

# 2008

## Solid-State Sensors, Actuators, and Microsystems Workshop

Greeting from the Chair

Committees

Acknowledgements

Table of Contents

Author Index

Keyword Index

Copyright

[www.hh2008.org](http://www.hh2008.org)



Sponsored by the  
Transducer Research Foundation, Inc.  
Additional support provided:  
Defense Advanced Research Projects Agency and the  
National Science Foundation

Hilton Head Workshop  
June 1 - 5, 2008 • Hilton Head, South Carolina  
Editors: Kimberly L. Turner and Leland "Chip" Spangler

TRF Catalog Number: 08TRF-0001  
Library of Congress Control Number: 2008924361  
ISBN Number: 0-9640024-7-7  
ISSN: 1539-2058 (Print) • ISSN: 1539-204X (Electronic)  
DOI: 10.31438/trf.hh2008.0

# Greetings from the General Chairman

Welcome to the 2008 Solid State Sensors, Actuators, and Microsystems Workshop; the fourteenth in the biannual series of regional meetings that alternate with the international Transducers Conference. This meeting will offer an open atmosphere of discussion, collaboration and interaction which has been its hallmark since the beginning in 1984. We'll see new ideas and new methods, hear about exciting applications and meet new colleagues. We'll also hear about progress on some older ideas and applications and renew relationships with old friends. The combination of ideas, opportunities and relationships has always been the objective of this meeting and we've worked to continue in this tradition.

The Workshop schedule remains organized around single session oral presentations with several poster presentations. Kimberly Turner has pulled together, and led a strong and opinionated program committee through a paper selection process resulting in the program published in this digest. Oral papers were selected on the basis of high quality content and likely broad interest to the meeting audience. Poster papers were selected on the basis of high quality as well, and for their probable high interest to a subset of the meeting attendees. The poster papers will be introduced by their authors using a "shotgun" session that has been popular for the last two years. We've also included late news oral and late news poster papers based on a selection process that occurred in mid-March. The program committee is to be congratulated for their efforts in reading, studying, ranking, debating, re-ranking, and selecting from the more than 250 submitted abstracts.

We also have significant unscheduled time for informal discussions among friends and colleagues. Technical brainstorming, collaborative ideas, job offers and business plans are usually topics for these breaks. We hope the relaxed environment here on the ocean helps to stimulate such interaction and creativity.

Several changes have been introduced this year in an attempt to keep the meeting fresh. Prior to this year, admission to the meeting was limited to those who were affiliated with an institution located in the Americas. For the first time this year, we have solicited abstract submissions and registrations from all previous alumni, regardless of the location of their current affiliation. This change recognizes that many of us have the opportunity to develop our careers in locations throughout the world and this experience can be an important factor in a meeting such as this.

We also streamlined the application process this year, allowing prior attendees to go directly to a web page which avoids the need to document qualifications. We also moved to an all electronic abstract submission process this year. This change has streamlined the collection, distribution and review of the abstracts and hopefully has simplified the abstract submission process. Along with these changes, we have updated the website to include "Frequently Asked Questions" providing supplemental information for new and prior attendees and their families. In addition, you will notice this digest is printed in color for the first time to allow for more vibrant figures and photographs to be published.

A tremendous "thank you" goes to Kimberly and the Technical Program Committee for their efforts in creating this program. Dave Monk is also to be acknowledged for taking on the new position of Development Chair. Dave has been responsible for establishing the benefactor and sponsorship programs as well as coordinating student travel support. Through Dave's efforts, we have been able for the first time, to offer a reduced registration fee for all student attendees.

Thanks also goes to the Transducer Research Foundation, DARPA, and the National Science Foundation for their continued support of travel for presenting student authors, thus enabling the meeting to continue the invigoration of our community with young talent, new ideas, and enthusiasm for the future of our community. Mark Allen has continued to provide excellent support of the local arrangements and thanks to Bob Sulouff for his oversight of our finances. Katharine Cline and her team at Preferred Meeting Management, Inc. are to be given special thanks for all of their hard work in pulling this meeting together and for making it run so smoothly. The work they do "behind the scenes" to make this meeting special is difficult to comprehend and our community and our meeting would suffer without them.

This meeting of course, belongs to all of you, thank you for your support. I would appreciate hearing your opinion regarding the changes that have been made this year as well as your suggestions for changes to future meetings so we can keep this meeting special. As well I sincerely hope you all have a great time.

Leland "Chip" Spangler  
General Chairman

# Organizing Committee

## General Chair

**Leland "Chip" Spangler**  
Aspen Technologies

## Technical Program Chair

**Kimberly L. Turner**  
University of California, Santa Barbara

## Promotions Chair

**David Monk**  
Freescale Semiconductor, Inc.

## Treasurer

**Bob Sulouff**  
Analog Devices

## Local Arrangements

**Mark G. Allen**  
Georgia Institute of Technology

## Technical Program Committee Members

Stephen Bart  
Analog Devices

Jack Judy  
University of California, Los Angeles

Sunil Bhave  
Cornell University

Aaron Knobloch  
General Electric Global Research Center

Victor M. Bright  
University of Colorado

Tina Lamers  
axept

Stephen Casalnuovo  
Sandia National Laboratory

Mehran Mehregany  
Case Western Reserve University

Abhi Chavan  
Guidant

Beth Pruitt  
Stanford University

Hemant Desai  
Freescale Semiconductor, Inc.

Michael Putty  
Delphi Research Labs

Reza Ghodssi  
University of Maryland

Andrei Shkel  
University of California, Irvine

Peter Hartwell  
Hewlett Packard

Leland "Chip" Spangler  
Aspen Technologies

Amy Herr  
University of California, Berkeley

Svetlana Tatic-Lucic  
Lehigh University

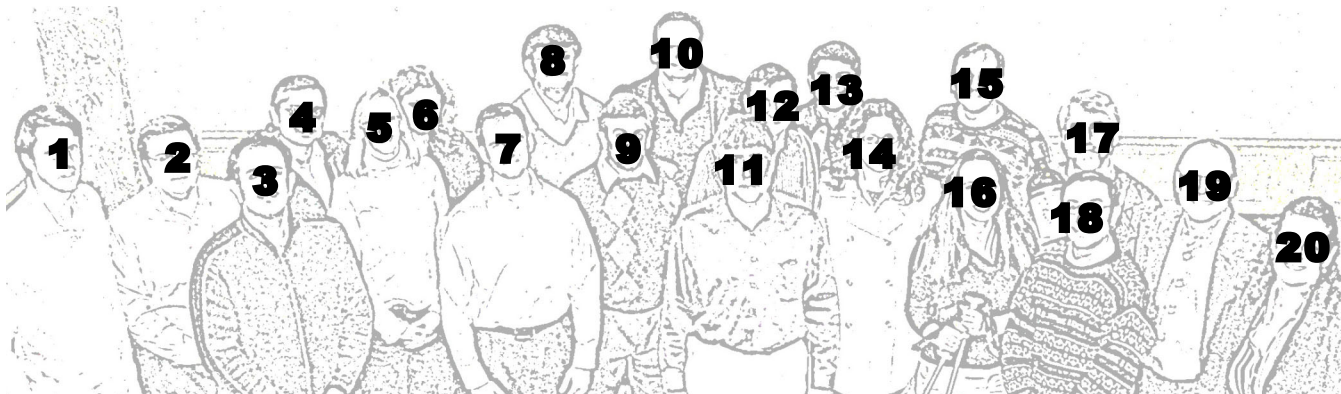
Michael A. Huff  
MEMS and Nanotechnology Exchange

William P. Taylor  
Allegro Microsystems, Inc.

Hal Jerman  
Coherent

Kimberly L. Turner  
University of California, Santa Barbara

# Technical Program Committee



- 1 – Jack Judy
- 2 – William P. Taylor
- 3 – Reza Ghodssi
- 4 – Abhi Chavan
- 5 – Tina Lamers
- 6 – Svetlana Tatic-Lucic
- 7 – Peter Hartwell
- 8 – Hemant Desai
- 9 – Michael Putty
- 10 – Victor M. Bright

- 11 – Stephen Casalnuovo
- 12 – Aaron Knobloch
- 13 – Sunil Bhave
- 14 – Kimberly L. Turner (Technical Program Chair)
- 15 – Andrei Shkel
- 16 – Amy Herr
- 17 – Hal Jerman
- 18 – Stephen Bart
- 19 – Leland "Chip" Spangler (General Chair)
- 20 – Beth Pruitt

not pictured: Mehran Mehregany and Michael A. Huff

# Acknowledgements

Special acknowledgement to the Transducer Research Foundation, Inc., Microsystems Technology Office (MTO) Program at the Defense Advanced Research Projects Agency (DARPA), and the National Science Foundation for their educational grant funding support of this Workshop.

## Exhibitors and Benefactors

We gratefully acknowledge the support of this Workshop from the following companies and institutions as of the printing of April 21, 2008:

**Aspen Technologies**

**Chipworks**

**Coventor, Inc.**

**Freescale Semiconductor**

**IEEE Sensors Council**

**MEMS and Nanotechnology Exchange**

**MEMS Investor Journal**

**MEMSCAP, Inc.**

**MEMSIC**

**OAI**

**Okmetic Silicon**

**Primaxx Inc.**

**Silex Microsystems Inc.**

**SoftMEMS LLC**

**Tousimis**

**Xactix, Inc.**

# Table of Contents

Scroll to the title and select a **Blue** link to open a paper. After viewing the paper, use the bookmark "Go to Previous Document" to return to the same page in the Table of Contents.

*Acrobat Reader 8 Users: Need to select View\Go To\Previous Document from the menu bar instead of using the bookmark.*

---

## Sunday, June 1, 2008

6:00 p.m. – **Registration and Welcome Reception**  
9:00 p.m.

## Monday, June 2, 2008

7:30 a.m. **Breakfast**

7:45 a.m. **Welcome and Introduction**  
Leland "Chip" Spangler, *Aspen Technologies, USA*  
Kimberly L. Turner, *University of California, Santa Barbara, USA*

### Session 1 - Packaging/Fabrication

Session Chairs:

Michael Putty, *Delphi Research Labs, USA*  
Kimberly L. Turner, *University of California, Santa Barbara, USA*

8:15 a.m. **Invited Speaker**  
**SILICON AS A BIOMEDICAL MATERIAL** ..... 1  
M.M.-C. Cheng<sup>1</sup>, E. Tasciotti<sup>1</sup>, and **Mauro Ferrari**<sup>1,2,3</sup>  
<sup>1</sup>*University of Texas Health Science Center, USA*, <sup>2</sup>*Rice University, USA* and  
<sup>3</sup>*The Alliance for Nanohealth, USA*

9:00 a.m. **AN ULTRA-THIN PACKAGED MEMS OSCILLATOR** ..... 6  
B.H. Stark, E. Radza, P. Gupta, J. Sharma, G. Peramaih, S. Deng, S. Suen,  
R. Sheridan, A. Partridge, and M. Lutz  
*SiTime Corporation, USA*

9:25 a.m. **FLIP-CHIP INTEGRATED SOI-CMOS-MEMS  
FABRICATION TECHNOLOGY** ..... 10  
P.J. Gilgunn and G.K. Fedder  
*Carnegie Mellon University, USA*

9:50 a.m. **NEW ARCHITECTURAL DESIGN OF A TEMPERATURE ROBUST MEMS GYROSCOPE WITH IMPROVED GAIN-BANDWIDTH CHARACTERISTICS** .....14  
A.A. Trusov, A.R. Schofield, and A.M. Shkel  
*University of California, Irvine, USA*

10:15 a.m. **Break**

### **Session 2 - Micro Switches**

Session Chairs:

Abhi Chavan, *Guidant, USA*

William P. Taylor, *Allegro Microsystems, Inc., USA*

10:40 a.m. **INTEGRATED MEMS SWITCH TECHNOLOGY ON SOI-CMOS** .....18  
J. Costa<sup>1</sup>, T. Ivanov<sup>1</sup>, J. Hammond<sup>1</sup>, J. Gering<sup>1</sup>, E. Glass<sup>1</sup>, J. Jorgenson<sup>1</sup>,  
D. Dening<sup>1</sup>, D. Kerr<sup>1</sup>, J. Reed<sup>1</sup>, S. Crist<sup>1</sup>, T. Mercier<sup>1</sup>, S. Kim<sup>1</sup>, and P. Gorisse<sup>2</sup>  
<sup>1</sup>RFMD, USA and <sup>2</sup>RFMD, FRANCE

11:05 a.m. **DUAL-BEAM ACTUATION OF PIEZOELECTRIC ALN RF MEMS SWITCHES MONOLITHICALLY INTEGRATED WITH ALN CONTOUR-MODE RESONATORS** .....22  
N. Sinha, R. Mahameed, C. Zuo, M.B. Pisani, C.R. Perez, and G. Piazza  
*University of Pennsylvania, USA*

11:30 a.m. **Poster/Oral Session Preview Presentations**  
Session Chairs:  
Victor Bright, *University of Colorado, USA*  
Stephen Casalnuovo, *Sandia National Laboratory, USA*

12:30 p.m. **Lunch**

2:00 p.m. – **Contributed Posters and Late News Posters**  
5:00 p.m.

## Tuesday, June 3, 2008

7:30 a.m. **Breakfast**

### Session 3 - Biomedical Applications

Session Chairs:

Peter Hartwell, *Hewlett-Packard Company, USA*

Reza Ghodssi, *University of Maryland, USA*

8:15 a.m. **Invited Speaker**

**BIO-INSPIRED ADHESION DEVICES** .....26

**Eduard Arzt** and A. del Campo

*INM - Leibniz Institute for New Materials, GERMANY*

9:00 a.m.

**CONCENTRATION OF CD8+ LYMPHOCYTES ON EWOD PLATFORM  
FOR MONITORING ORGAN TRANSPLANT REJECTION** .....28

G.J. Shah, J.L. Veale, Y. Korin, E.F. Reed, H.A. Gritsch, and C.-J. Kim

*University of California, Los Angeles, USA*

9:25 a.m.

**A WIRELESSLY-ACTIVATED PARYLENE ELECTROTHERMAL VALVE  
FOR MAPPING BRAIN FUNCTION IN FREELY MOVING SUBJECTS** .....32

P.-Y. Li, T.K. Givrad, D.P. Holschneider, J.-M.I. Maarek, and E. Meng

*University of Southern California, USA*

9:50 a.m.

**INTEGRATION OF A FILM BULK ACOUSTIC RESONATOR WITH  
MICROFLUIDIC CHANNELS FOR BIOMEDICAL SENSING IN LIQUID** .....36

W. Xu, X. Zhang, H. Yu, A. Abbaspour-Tamijani, and J. Chae

*Arizona State University, USA*

10:15 a.m. **Break**

## Session 4 - Resonant Devices

Session Chairs:

Sunil Bhawe, *Cornell University, USA*

Tina Lamers, *axept, USA*

10:40 a.m.	<b>THE MICROMECHANICAL RESONANT SWITCH ("RESOSWITCH")</b> .....	40
	Y. Lin, W.-C. Li, Z. Ren, and C.T.-C Nguyen <i>University of California, Berkeley, USA</i>	
11:05 a.m.	<b>PREAMPLIFYING CANTILEVERS FOR CONTACT RESONANCE MODE IMAGING</b> .....	44
	B. Zeyen <sup>1</sup> , B. Pittenger <sup>2</sup> , K. Virwani <sup>2</sup> , and K.L. Turner <sup>1</sup> <sup>1</sup> <i>University of California, Santa Barbara, USA</i> and <sup>2</sup> <i>Veeco Metrology Inc., USA</i>	
11:30 a.m.	<b>ELECTROSTATIC-TUNING OF HERMETICALLY ENCAPSULATED COMPOSITE RESONATOR</b> .....	48
	H.K. Lee, M.A. Hopcroft, R. Melamud, B. Kim, J. Salvia, S. Chandorkar, and T.W. Kenny <i>Stanford University, USA</i>	

## Late News Papers

11:55 a.m.	<b>A MEMS-RELAY FOR MAKE-BREAK POWER SWITCHING APPLICATIONS</b> .....	52
	A.C. Weber, J.H. Lang, and A.H. Slocum <i>Massachusetts Institute of Technology, USA</i>	
12:10 p.m.	<b>MEMS AND METAMATERIALS: A PERFECT MARRIAGE AT TERAHERTZ FREQUENCIES</b> .....	54
	H. Tao <sup>1</sup> , C. Bingham <sup>2</sup> , A. Strikwerda <sup>1</sup> , K. Fan <sup>1</sup> , W.J. Padilla <sup>2</sup> , R.D. Averitt <sup>1</sup> , and X. Zhang <sup>1</sup> <sup>1</sup> <i>Boston University, USA</i> and <sup>2</sup> <i>Boston College, USA</i>	
12:25 p.m. –	<b>Lunch</b>	
1:30 p.m.		
7:00 p.m. –	<b>Banquet</b>	
9:00 p.m.		

## Wednesday, June 4, 2008

7:30 a.m. **Breakfast**

### Session 5 - Micro Devices

Session Chairs:

Amy Herr, *University of California, Berkeley, USA*  
Jack Judy, *University of California, Los Angeles, USA*

8:15 a.m. **Invited Speaker**

**HUMAN IMPLANTABLE WIRELESS MICROSTIMULATORS  
AND MICROSENSORS** .....56

**Joseph H. Schulman**

*Alfred E. Mann Foundation for Biomedical Engineering, USA*

9:00 a.m. **DESIGN OF A SIX-AXIS MESO-SCALE NANOPositionER  
DRIVEN BY MOVING-COIL MICROACTUATORS** .....60

D.S. Golda and M.L. Culpepper

*Massachusetts Institute of Technology, USA*

9:25 a.m. **A SURFACE MICROMACHINED CAPACITIVE MICROPHONE  
FOR AEROACOUSTIC APPLICATIONS** .....64

D.T. Martin, K. Kadirvel, T. Nishida, and M. Sheplak

*University of Florida, USA*

9:50 a.m. **DEVELOPMENT OF A FULLY INTEGRATED MICRO-POWER  
SOURCE BASED ON A MICRO-SILICON FUEL CELL AND A  
MEMS HYDROGEN GENERATOR** .....68

L. Zhu<sup>1</sup>, K.Y. Lin<sup>1</sup>, R.D. Morgan<sup>1</sup>, H.S. Kim<sup>1</sup>, B. Gurau<sup>1</sup>, D. Kim<sup>2</sup>, B. Bae<sup>3</sup>,  
R.I. Masel<sup>1,3</sup>, and M.A. Shannon<sup>1,3</sup>

<sup>1</sup>*University of Illinois, Urbana-Champaign, USA,*

<sup>2</sup>*Sogang University, REPUBLIC OF KOREA, and* <sup>3</sup>*Cbana Labs, Inc., USA*

10:15 a.m. **Break**

## Session 6 - Optical Devices

Session Chairs:

Hal Jerman, *Coherent, USA*

Aaron Knobloch, *General Electric Global Research Center, USA*

- 10:40 a.m. **MEMS MICROSHUTTER ARRAY SYSTEM FOR JAMES WEBB SPACE TELESCOPE** .....72  
M.J. Li, T. Adachi, S.R. Babu, S. Bajikar, M.A. Beamesderfer, R. Bradley, K. Denis, N.P. Costen, A.J. Ewin, R. Fettig, D. Franz, L. Hess, R. Hu, K. Jackson, C.A. Jhabvala, M.D. Jhabvala, D. Kelly, T.T. King, G. Kletetschka, A.S. Kutyrev, B.A. Lynch, T. Miller, S.H. Moseley, V. Mikula, B. Mott, L. Oh, J. Pontius, D. Rapchun, C. Ray, K. Ray, E. Schulte, D.S. Schwinger, P.K. Shu, R.F. Silverberg, W.W. Smith, S. Snodgrass, D. Sohl, L.M. Sparr, R. Steptoe-Jackson, V. Veronica, L.L. Wang, Y. Zheng, and C. Zincke  
*NASA Goddard Space Flight Center, USA*
- 11:05 a.m. **TUNABLE-FOCUS MICROLENSES ACTUATED BY INFRARED-LIGHT-RESPONSIVE HYDROGELS WITH ENTRAPPED GOLD NANOPARTICLES FOR FIBER ENDOSCOPY** .....76  
X. Zeng and H. Jiang  
*University of Wisconsin, USA*
- 11:30 a.m. **RUGGED BOARD-TO-BOARD OPTICAL INTERCONNECT WITH CLOSED-LOOP MICROLENS SCANNER** .....80  
J.B. Chou<sup>1</sup>, K. Yu<sup>1</sup>, D.A. Horsley<sup>2</sup>, S. Mathai<sup>3</sup>, B. Yoxall<sup>2</sup>, M. Tan<sup>3</sup>, S.Y. Wang<sup>3</sup>, and M.C. Wu<sup>1</sup>  
<sup>1</sup>*University of California, Berkeley, USA*, <sup>2</sup>*University of California, Davis, USA*, and <sup>3</sup>*Hewlett-Packard Labs, USA*
- 11:55 a.m. **Lunch**

## Late News Papers

Session Chairs:

Mehran Mehregany, *Case Western Reserve University, USA*

Andrei Shkel, *University of California, Irvine, USA*

- 1:15 p.m. **A CMOS MONOLITHICALLY-INTEGRATED THREE-AXIS ACCELEROMETER BASED ON THERMAL CONVECTION**.....84  
Y. Cai<sup>1</sup>, M. Varghese<sup>1</sup>, A. Dribinsky<sup>1</sup>, Y. Hua<sup>1</sup>, F. Lu<sup>1</sup>, H. Gu<sup>1</sup>, M. Meng<sup>1</sup>,  
W. Zhang<sup>1</sup>, L. Jiang<sup>1</sup>, G. Pucci<sup>1</sup>, H. Liu<sup>1</sup>, A. Leung<sup>2</sup>, Y. Zhao<sup>1</sup>, and G. O'Brien<sup>1</sup>  
<sup>1</sup>*Memsic Inc., USA* and <sup>2</sup>*Simon Fraser University, CANADA*
- 1:30 p.m. **NOVEL ELECTRODE STRUCTURE OF A MICRO FUEL CELL INTEGRATING SERPENTINE FLOW FIELD CHANNEL**.....86  
D. Beloin St-Pierre, M. Paquin, and L.G. Fr chet  
*Universit  de Sherbrooke, CANADA*
- 1:45 p.m. **FEASIBILITY TEST OF A FAST MICRO GAS CHROMATOGRAPHY SYSTEM USING FIVE MICROVALVES AND A MICROCOLUMN** .....88  
B. Bae<sup>1,2</sup>, A.D. Radadia<sup>2</sup>, J. Han<sup>2</sup>, J. Yeom<sup>2</sup>, R.I. Masel<sup>1,2</sup>, and M.A. Shannon<sup>1,2</sup>  
<sup>1</sup>*Cbana Laboratories, Inc., USA* and <sup>2</sup>*University of Illinois, Urbana-Champaign, USA*
- 2:00 p.m. **FLIGHT CONTROL OF 10 GRAM INSECTS BY IMPLANTED NEURAL STIMULATORS**.....90  
H. Sato<sup>1</sup>, C.W. Berry<sup>2</sup>, and M.M. Maharbiz<sup>1,2</sup>  
<sup>1</sup>*University of California, Berkeley, USA* and <sup>2</sup>*University of Michigan, USA*
- 6:00 p.m. - **Open Posters**  
8:00 p.m. Session Chair:  
Michael A. Huff, *MEMS & Nanotechnology Exchange, USA*
- 8:00 p.m. - **Rump Session**  
10:00 p.m. Session Chair:  
Jack Judy, *University of California, Los Angeles, USA*

## Thursday, June 5, 2008

7:30 a.m. **Breakfast**

### Session 7 - Characterization

Session Chairs:

Stephen Bart, *Analog Devices, USA*

Hemant Desai, *Freescale Semiconductor, Inc., USA*

8:15 a.m. **Invited Speaker**

**THE APPLICATION OF INSTABILITIES IN MICROFLUIDIC JETS  
TO DIGITAL OFFSET-CLASS PRINTING**.....92

**Gilbert Hawkins**, J. Chwalek, C. Delametter, E. Furlani, D. Jeanmaire, J. Lebens,  
D. Trauernicht, and Q. Yang  
*Eastman Kodak Company, USA*

9:00 a.m. **ION IMPLANTED PIEZORESISTIVE CANTILEVER DESIGN AND  
PERFORMANCE**.....98

S.-J. Park, A.J. Rastegar, J.R. Mallon Jr., A.A. Barlian, T.H. Fung, and B.L. Pruitt  
*Stanford University, USA*

9:25 a.m. **OBSERVATIONS OF FIXED AND MOBILE CHARGE IN COMPOSITE  
MEMS RESONATORS**.....102

G. Bahl<sup>1</sup>, R. Melamud<sup>1</sup>, B. Kim<sup>1</sup>, S. Chandorkar<sup>1</sup>, J. Salvia<sup>1</sup>, M.A. Hopcroft<sup>1</sup>,  
R.G. Hennessy<sup>1</sup>, S. Yoneoka<sup>1</sup>, C.M. Jha<sup>1</sup>, G. Yama<sup>2</sup>, D. Elata<sup>1</sup>, R.N. Candler<sup>1,2</sup>,  
R.T. Howe<sup>1</sup>, and T.W. Kenny<sup>1</sup>  
<sup>1</sup>*Stanford University, USA* and <sup>2</sup>*Robert Bosch Corporation, USA*

9:50 a.m. **FRACTURE PREDICTION OF SINGLE CRYSTAL SILICON MEMS  
UNDER MULTI-AXIAL LOADING**.....106

A.M. Fitzgerald, D.M. Pierce, C.D. White, B.M. Huigens, and J.W. Eaton  
*A.M. Fitzgerald & Associates, LLC, USA*

10:15 a.m. **Break**

## Session 8 - Microfluidic Devices

Session Chairs:

Beth Pruitt, *Stanford University, USA*

Svetlana Tatic-Lucic, *Lehigh University, USA*

- 10:40 a.m. **INTERFACING MULTIPLEXED MICROFLUIDICS TO MALDI-MS BY HIGH-THROUGHPUT ROBOTIC SPOTTING** .....110  
C.W. Tsao<sup>1</sup>, T. Song<sup>2</sup>, C.F. Chen<sup>1,3</sup>, J. Liu<sup>1</sup>, C.C. Chang<sup>3</sup>, and D.L. DeVoe<sup>1</sup>  
*<sup>1</sup>Univeristy of Maryland, College Park, USA, <sup>2</sup>Calibrant Biosystems Inc., USA, and <sup>3</sup>Academia Sinica, TAIWAN*
- 11:05 a.m. **SMALL FOOTPRINT CONTINUOUS FLOW PCR DEVICES FOR A 96-WELL CFPCR MULTI-REACTOR PLATFORM** .....114  
D.S. Park<sup>1</sup>, P.-C. Chen<sup>1</sup>, B.H. You<sup>1</sup>, N. Kim<sup>1</sup>, T. Park<sup>1</sup>, T.Y. Lee<sup>1</sup>, P. Datta<sup>1</sup>, Y. Desta<sup>2</sup>, S.A. Soper<sup>1</sup>, D.E. Nikitopoulos<sup>1</sup>, and M.C. Murphy<sup>1</sup>  
*<sup>1</sup>Louisiana State University, USA and <sup>2</sup>BioFluidica Microtechnologies, USA*
- 11:30 a.m. **MULTI-INLET/OUTLET PRECONCENTRATOR WITH 3-D  $\mu$ -STRUCTURES COATED BY INKJET PRINTING OF TENAX TA** .....118  
B. Alfeeli<sup>1,2</sup>, M. Ashraf-Khorassani<sup>1</sup>, L.T. Taylor<sup>1</sup>, and M. Agah<sup>1</sup>  
*<sup>1</sup>Virginia Polytechnic Institute and State University, USA and <sup>2</sup>Kuwait Institute for Scientific Research, KUWAIT*
- 11:55 a.m. **ELECTROSTATICALLY-ACTUATED RECONFIGURABLE ELASTOMER MICROFLUIDICS** .....122  
M.-P. Chang<sup>1</sup> and M.M. Maharbiz<sup>1,2</sup>  
*<sup>1</sup>University of Michigan, USA and <sup>2</sup>University of California, Berkeley, USA*
- 12:20 p.m. **Closing Remarks**  
Leland “Chip” Spangler, Aspen Technologies, USA  
Kimberly L. Turner, University of California, Santa Barbara, USA
- 12:25 p.m. – **Lunch and Workshop Adjourns**  
2:00 p.m.

## Contributed Posters/Oral Papers

### Bio-Inspiration

- P1 **FLIGHT INITIATION AND DIRECTIONAL CONTROL OF BEETLES BY MICROTHERMAL STIMULATION** .....126  
K. Visvanathan<sup>1</sup>, N.K. Gupta<sup>1</sup>, M.M. Maharbiz<sup>2</sup>, and Y.B. Gianchandani<sup>1</sup>  
*<sup>1</sup>University of Michigan, USA and <sup>2</sup>University of California, Berkeley, USA*
- P2 **MICROFABRICATED DRY ADHESIVE DISPLAYING FRICTIONAL ADHESION** .....130  
D. Soto<sup>1</sup>, A. Parness<sup>1</sup>, N. Esparza<sup>1</sup>, T.W. Kenny<sup>1</sup>, K. Autumn<sup>2</sup>, and M. Cutkosky<sup>1</sup>  
*<sup>1</sup>Stanford University, USA and <sup>2</sup>Lewis and Clark College, USA*

### Biomedical Devices

- P3 **A NOVEL 3D MICRO MEMBRANE FILTRATION DEVICE FOR CAPTURE VIABLE RARE CIRCULATING TUMOR CELLS FROM WHOLE BLOOD** .....134  
S. Zheng<sup>1</sup>, H.K. Lin<sup>2</sup>, R.J. Cote<sup>2</sup>, and Y.-C. Tai<sup>2</sup>  
*<sup>1</sup>California Institute of Technology, USA and <sup>2</sup>University of Southern California, USA*
- P4 **A REAL-TIME PROTEIN DETECTOR UTILIZING THE VROMAN EFFECT ON SAM-FUNCTIONALIED SURFACES** .....138  
S. Choi, Y. Yang, and J. Chae  
*Arizona State University, USA*
- P5 **FLEXIBLE SHEAR STRESS SENSOR FOR IN VIVO CARDIOVASCULAR TESTING** .....142  
H. Yu<sup>1</sup>, L. Ai<sup>2</sup>, M. Rouhanizadeh<sup>2</sup>, R.A. Kloner<sup>2</sup>, E.S. Kim<sup>2</sup>, and T.K. Hsiai<sup>2</sup>  
*<sup>1</sup>Arizona State University, USA and <sup>2</sup>University of Southern California, USA*
- P6 **IMPLANTABLE MICROVALVE-PACKAGED GLAUCOMA DRAINAGE TUBE** .....146  
J.C.-H. Lin<sup>1</sup>, P.-J. Chen<sup>1</sup>, S. Saati<sup>2</sup>, R. Varma<sup>2,3</sup>, M. Humayun<sup>2,3</sup>, and Y.-C. Tai<sup>1</sup>  
*<sup>1</sup>California Institute of Technology, USA, <sup>2</sup>Doheny Eye Institute, USA, and <sup>3</sup>University of Southern California, USA*
- P7 **MICRO RF TAGS FOR MEDICAL IMAGING** .....150  
J.J. Bernstein<sup>1</sup>, M.G. Bancu<sup>1</sup>, R. Ciocan<sup>2</sup>, R.E. Lenkinski<sup>2</sup>, R. Marquis<sup>2</sup>, A. Ivanishev<sup>2</sup>, and J.V. Frangioni<sup>2</sup>  
*<sup>1</sup>The Charles Stark Draper Laboratory, USA and <sup>2</sup>Beth Israel Deaconess Medical Center, USA*
- P8 **RATIONALLY-DESIGNED SURFACE NANOPATTERNING: A POTENTIALLY NEW MEANS FOR ENHACING SAFETY & EFFICACY OF VASCULAR STENTS** .....154  
M.P. Rao<sup>1</sup>, J. Lu<sup>2</sup>, H.P. Aguilar<sup>1</sup>, D. Khang<sup>2</sup>, N.C. MacDonald<sup>3</sup>, and T.J. Webster<sup>2</sup>  
*<sup>1</sup>Purdue University, USA, <sup>2</sup>Brown University, USA, and <sup>3</sup>University of California, Santa Barbara, USA*

P9	<b>WIRELESS BILIARY STENT SYSTEM WITH WISHBONE-ARRAY RESONANT MAGNETOELASTIC (WARM) SENSOR AND CONFORMAL MAGNETIC LAYER</b> .....	158
	S.R. Green and Y.B. Gianchandani <i>University of Michigan, USA</i>	

## Characterization

P10	<b>CHARACTERIZATION OF MAGNETIC NANOPARTICLE-EMBEDDED SU8 FOR MICROACTUATION</b> .....	162
	K.L. Tsai, M. Ziaei-Moayyed, N. Klejwa, R.N. Candler, W. Hu, S.X. Wang, and R.T. Howe <i>Stanford University, USA</i>	
P11	<b>DESIGN OF ELECTROSTATICALLY ACTUATED MEMS UNDER UNCERTAINTIES</b> .....	166
	N. Agarwal and N.R. Aluru <i>University of Illinois, Urbana-Champaign, USA</i>	
P12	<b>DYNAMIC FRICTION AND MICROTURBINE PERFORMANCE USING A PLANAR-CONTACT ENCAPSULATED MICROBALL BEARING</b> .....	170
	M. McCarthy <sup>1</sup> , C.M. Waits <sup>1,2</sup> , and R. Ghodssi <sup>1</sup> <sup>1</sup> <i>University of Maryland, USA and</i> <sup>2</sup> <i>U.S. Army Research Laboratory, USA</i>	
P13	<b>INTEGRATED TESTING OF POLYMER MEMS MATERIAL PROPERTIES</b> .....	174
	D. Sameoto, C. Plesa, and M. Parameswaran <i>Simon Fraser University, CANADA</i>	
P14	<b>MEASURING CHARGE AND CHARGE DECAY IN FLOATING-ELECTRODE ELECTROSTATIC ACTUATORS</b> .....	178
	D. Elata <sup>1,2</sup> , R. Hennessy <sup>1</sup> , V. Leus <sup>2</sup> , N. Klejwa <sup>1</sup> , A. Hirshberg <sup>2</sup> , J. Provine <sup>1</sup> , and R.T. Howe <sup>1</sup> <sup>1</sup> <i>Stanford University, USA and</i> <sup>2</sup> <i>Technion - Israel Institute of Technology, ISRAEL</i>	
P15	<b>MICROSYSTEM FOR ELECTROMECHANICAL MEASUREMENTS OF CARBON NANOFIBER LOADING AND FAILURE</b> .....	182
	J.J. Brown <sup>1</sup> , J.W. Suk <sup>2</sup> , G. Singh <sup>1</sup> , D.A. Dikin <sup>3</sup> , R.S. Ruoff <sup>2</sup> , and V.M. Bright <sup>1</sup> <sup>1</sup> <i>University of Colorado, USA, </i> <sup>2</sup> <i>University of Texas, USA, and</i> <sup>3</sup> <i>Northwestern University, USA</i>	
P16	<b>RATE-DEPENDENT PULL-OFF FORCE - AN EXPERIMENTAL APPROACH TO IDENTIFY THE SEPARATION MODE IN MICROCONTACTS</b> .....	186
	L. Chen <sup>1</sup> , Y. Du <sup>2</sup> , N.E. McGruer <sup>3</sup> , and G.G. Adams <sup>3</sup> <sup>1</sup> <i>RF Micro Devices, Inc., USA, </i> <sup>2</sup> <i>Qualcomm, USA, and</i> <sup>3</sup> <i>Northeastern University, USA</i>	
P17	<b>TRACKING MICRORESONATOR Q-FACTOR IN CLOSED-LOOP OPERATION</b> .....	190
	J.H. Seo, K.S. Demirci, S. Truax, L.A. Beardslee, and O. Brand <i>Georgia Institute of Technology, USA</i>	

P18	<b>VISCOUS DAMPING OF LATERAL MEMS DEVICE WITHIN A FULLY-ENCLOSED CAVITY</b> .....	194
	W. Zhang, R. Walmsley, and P. Hartwell <i>Hewlett-Packard Laboratories, USA</i>	

## **Fabrication**

P19	<b>A NEW EXTRINSIC GETTERING TECHNIQUE IN THICK BONDED SILICON-ON-INSULATOR WAFERS ENABLING SENSOR-IC INTEGRATION</b> .....	198
	P. Sandow <sup>1</sup> , S. Whiston <sup>2</sup> , P. Daly <sup>2</sup> , J. Mäkinen <sup>3</sup> , J. Hintsala <sup>2</sup> , K. Nunan <sup>4</sup> , and W. Sawyer <sup>4</sup> <sup>1</sup> <i>Okmetic Inc., USA</i> , <sup>2</sup> <i>Analog Devices Inc., IRELAND</i> , <sup>3</sup> <i>Okmetic Oyj, FINLAND</i> , and <sup>4</sup> <i>Analog Devices, Inc., USA</i>	
P20	<b>ASSEMBLY OF PLANAR STRUCTURES BY PARALLEL ACTUATION OF MEMS MICROROBOTS</b> .....	202
	B.R. Donald <sup>1</sup> , C.G. Levey <sup>2</sup> , and I. Paprotny <sup>1,2</sup> <sup>1</sup> <i>Duke University, USA</i> and <sup>2</sup> <i>Dartmouth College, USA</i>	
P21	<b>CAPACITIVE TRANSDUCER STRENGTHENING VIA ALD-ENABLED PARTIAL-GAP FILLING</b> .....	208
	L.-W. Hung, Z.A. Jacobson, Z. Ren, A. Javey, and C.T.-C. Nguyen <i>University of California, Berkeley, USA</i>	
P22	<b>FABRICATION OF ATOM TRAPPING CHIPS WITH FEEDTHROUGH INTERCONNECTS FOR APPLICATIONS IN ATOM OPTICS</b> .....	212
	H.C. Chuang, D.Z. Anderson, and V.M. Bright <i>University of Colorado, USA</i>	
P23	<b>LOW-TEMPERATURE (&lt;300°C) LOW-STRESS SILICON CARBIDE SURFACE MICROMACHINING FABRICATION TECHNOLOGY</b> .....	216
	F. Nabki, T.A. Dusatko, S. Vengallatore, and M.N. El-Gamal <i>McGill University, CANADA</i>	
P24	<b>MICROFABRICATED HIGH DENSITY MULTIPLEXED ELECTROSPRAY</b> .....	220
	C.M. Waits <sup>1</sup> , B. Morgan <sup>1</sup> , W. Deng <sup>2</sup> , N.R. Jankowski <sup>1</sup> , A. Gomez <sup>2</sup> , and B. Geil <sup>1</sup> <sup>1</sup> <i>US Army Research Laboratory, USA</i> and <sup>2</sup> <i>Yale University, USA</i>	
P25	<b>OPTIMIZING DIRECT PRINTING OF PZT THIN FILMS</b> .....	224
	S. Bathurst <sup>1</sup> , J. Jeon <sup>1</sup> , P. Mardilovich <sup>2</sup> , H.W. Lee <sup>1</sup> , and S.G. Kim <sup>1</sup> <sup>1</sup> <i>Massachusetts Institute of Technology, USA</i> and <sup>2</sup> <i>Hewlett Packard, USA</i>	
P26	<b>PHOTOPATTERNABLE CONDUCTIVE PDMS AS A NEW MEMS MATERIAL</b> .....	228
	H. Cong and T. Pan <i>University of California, Davis, USA</i>	

P27	<b>IN-SITU TUNING OF MICRODEVICES FOR DIRECTIONAL MICROPHONE APPLICATIONS</b> .....	232
	S.-S. Je, J.C. Harrison, M.N. Kozicki, and J. Chae <i>Arizona State University, USA</i>	
P28	<b>PRINTING MEMS: FROM A SINGLE FLEXIBLE POLYIMIDE FILM TO THREE-DIMENSIONAL INTEGRATED MICROFLUIDICS</b> .....	236
	W. Wang, H. Cong, Z. Qiu, S. Zhao, H. Zhu, A. Revzin, and T. Pan <i>University of California, Davis, USA</i>	
P29	<b>SELF-ASSEMBLED 275NM-GAP ELECTRODES FOR CMOS-MEMS RESONATORS AND ITS PRECISION DC CHARGE-BASED CAPACITANCE MEASUREMENT</b> .....	240
	C.-C. Lo and G.K. Fedder <i>Carnegie Mellon University, USA</i>	
P30	<b>SYNTHESIS AND CHARACTERIZATION OF HYBRID ORGANIC-INORGANIC THIN FILMS VIA ATOMIC LAYER DEPOSITION FOR MEMS/NEMS</b> .....	244
	D. Seghete, Y.J. Chang, B. Davidson, V.M. Bright, and S.M. George <i>University of Colorado, USA</i>	

#### **Gas Sensors**

P31	<b>A MEMS PHOSPHONATE SENSOR</b> .....	248
	C.N. Monty, I. Oh, M.A. Shannon, and R.I. Masel <i>University of Illinois, Urbana-Champaign, USA</i>	
P32	<b>A MICRO-PRECONCENTRATOR/FOCUSER FOR A MICRO-GAS CHROMATOGRAPH: DEVICE AND MATERIALS CHARACTERIZATION</b> .....	252
	R.A. Veeneman and E.T. Zellers <i>University of Michigan, USA</i>	
P33	<b>DESIGN, MODELING AND FABRICATION OF MEMS-BASED MULTICAPILLARY GAS CHROMATOGRAPHY COLUMNS</b> .....	256
	M.A. Zareian-Jahromi, M. Ashraf-Khorassani, L.T. Taylor, and M. Agah <i>Virginia Polytechnic Institute and State University, USA</i>	
P34	<b>DRIE-SI GAS CHROMATOGRAPHY COLUMNS: EFFICIENCY AND THERMAL STABILITY OF STATIONARY PHASES FOR COMPREHENSIVE TWO-DIMENSIONAL (GCxGC) SEPARATIONS</b> .....	260
	G. Serrano, S.M. Reidy, K.D. Wise, and E.T. Zellers <i>University of Michigan, USA</i>	

## Microfluidics

- P35 **A THERMALLY IMPROVED QUANTITATIVE PCR CHIP**.....264  
Q.C. Quach and Y.C. Tai  
*California Institute of Technology, USA*
- P36 **CONTINUOUS FLOW SEPARATION OF SUSPENDED CELLS IN HUMAN WHOLE BLOOD USING DIELECTROPHORESIS**.....268  
Y. Jung<sup>1</sup>, K.-H. Han<sup>2</sup>, Y. Choi<sup>1</sup>, and A.B. Frazier<sup>1</sup>  
<sup>1</sup>*Georgia Institute of Technology, USA* and <sup>2</sup>*Inje University, SOUTH KOREA*
- P37 **CONTROLLED PICO-GRAM MATERIAL PLACEMENT ON SUSPENDED STRUCTURES USING SOLUTION WICKING**.....272  
S.S. Bedair and G.K. Fedder  
*Carnegie Mellon University, USA*
- P38 **OPTICAL IMAGE-BASED DYNAMIC MANIPULATION OF AQUEOUS DROPLETS IMMERSSED IN OIL MEDIUM**.....276  
S.-Y. Park, T.-H. Wu, K. Wei, S. Kalim, C. Callahan, M. Teitell, and E.P.Y Chiou  
*University of California, Los Angeles, USA*
- P39 **SMART MICROFABRICATED CHEMICAL PRECONCENTRATOR**.....280  
R.P. Manginell<sup>1</sup>, D.R. Adkins<sup>2</sup>, M.W. Moorman<sup>1</sup>, R. Hadizadeh<sup>3</sup>, D. Copic<sup>3</sup>,  
D. Porter<sup>3</sup>, J.M. Anderson<sup>1</sup>, D.R. Wheeler<sup>1</sup>, K.B. Pfeifer<sup>1</sup>, and A. Rumpf<sup>1</sup>  
<sup>1</sup>*Sandia National Laboratories, USA*, <sup>2</sup>*Defiant Technologies, Inc., USA*, and  
<sup>3</sup>*University of Louisville, USA*

## Optical Devices

- P40 **AN AGILE TIP-TILT-PISTON MICROMIRROR WITH LARGE APERTURE, LARGE SCANNING RANGE AND LOW DRIVING VOLTAGE** .....284  
K. Jia, S. Pal, and H. Xie  
*University of Florida, USA*
- P41 **MICROMACHINED "SIDE-VIEWING" OPTICAL SENSOR PROBE FOR NO-INVASIVE DETECTION OF ESOPHAGEAL CANCERS**.....288  
A. Garcia-Urbe<sup>1</sup>, K.C. Balareddy<sup>1</sup>, J. Zou<sup>1</sup>, A. Wojcik<sup>1</sup>, and L. Wang<sup>2</sup>  
<sup>1</sup>*Texas A&M University, USA* and <sup>2</sup>*Washington University, St. Louis, USA*
- P42 **MONOLITHIC INTEGRATION OF BINARY-PHASE FRESNEL ZONE PLATE OBJECTIVES ON 2-AXIS SCANNING MICROMIRRORS FOR COMPACT MICROENDOSCOPES** .....292  
K. Kumar, H. Cao, and X. Zhang  
*University of Texas, USA*

P43	<b>ROBUST OPTICAL DESIGN OF ANGLED MULTILAYER DIELECTRIC MIRRORS OPTIMIZED FOR RUBIDIUM VAPOR CELL RETURN REFLECTION</b> .....	296
	M.A. Perez <sup>1</sup> , J. Kitching <sup>2</sup> , and A.M. Shkel <sup>1</sup>	
	<sup>1</sup> University of California, Irvine, USA and	
	<sup>2</sup> National Institute of Standards and Technology, USA	

## Physical

P44	<b>A CAVITY-LESS MICROMACHINED CAPACITIVE PRESSURE SENSOR FOR WIRELESS OPERATION IN LIQUID AMBIENT</b> .....	300
	K. Takahata <sup>1</sup> and Y.B. Gianchandani <sup>2</sup>	
	<sup>1</sup> University of British Columbia, CANADA and <sup>2</sup> University of Michigan, USA	
P45	<b>A Laterally-Implanted Piezoresistive Skin-Friction Sensor</b> .....	304
	Y. Li, V. Chandrasekharan, B. Bertolucci, T. Nishida, L. Cattafesta, D.P. Arnold, and M. Sheplak	
	University of Florida, USA	
P46	<b>A MICROMACHINED WIRELESS GAMMA RADIATION DETECTOR USING BULK METAL CONVERSION LAYERS</b> .....	308
	C.K. Eun and Y.B. Gianchandani	
	University of Michigan, USA	
P47	<b>AN IMPLANTABLE CAPACITIVE MICROMACHINED ULTRASONIC IMAGER PROBE FOR PHOTOACOUSTIC IMAGING</b> .....	312
	X. Cheng <sup>1</sup> , J. Chen <sup>1</sup> , S.-W. Huang <sup>2</sup> , R.S. Witte <sup>3</sup> , and P. Lin <sup>4</sup>	
	<sup>1</sup> University of New Mexico, USA, <sup>2</sup> University of Michigan, USA,	
	<sup>3</sup> University of Arizona, USA, and <sup>4</sup> Infotonics Technology Center, USA	
P48	<b>FULLY BATCH-FABRICATED LINEAR QUADRUPOLE MASS FILTERS</b> .....	316
	K. Cheung, L.F. Velásquez-García, and A.I. Akinwande	
	Massachusetts Institute of Technology, USA,	
P49	<b>HOT SELF BOLOMETER PHOTONIC CRYSTAL BASED HYDROCARBON SENSOR</b> .....	320
	A.D. Oliver, M.U. Pralle, P. Loges, I. Puscasu, and E.A. Johnson	
	ICx Photonics, USA	
P50	<b>HYBRID ULTRA-COMPACT 4TH ORDER BAND-PASS FILTERS BASED ON PIEZOELECTRIC ALN CONTOUR-MODE MEM RESONATORS</b> .....	324
	C. Zuo, N. Sinha, C.R. Perez, R. Mahameed, M.B. Pisani, and G. Piazza	
	University of Pennsylvania, USA	
P51	<b>LOW VOLTAGE COMPLEMENTARY MEMS LOGIC USING PIEZOELECTRIC ACTUATORS</b> .....	328
	D.C. Judy, R.G. Polcawich, and J.S. Pulskamp	
	US Army Research Laboratory, USA	

P52	<b>MICRODISCHARGE-BASED PRESSURE SENSORS FOR OPERATION AT 1000°C</b> .....	332
	S.A. Wright and Y.B. Gianchandani <i>University of Michigan, USA</i>	
P53	<b>RADIOISOTOPE-POWERED IMPULSE RADIO FREQUENCY SENSOR NODE</b> .....	336
	S. Tin, R. Duggirala, A. Lal, and C. Pollock <i>Cornell University, USA</i>	
P54	<b>VERTICALLY ALIGNED SILICON NANOWIRE ACTUATORS AND SWITCHES</b> .....	340
	L. Tsakalakos, K. Subramanian, X. Wang, M.F. Aimi, C.F. Keimel, J.E. Balch, A.T. Byun, J.A. Fronheiser, J. Iannotti, L. Yan, T.P. Feist, and J.B. Fortin <i>General Electric – Global Research Center, USA</i>	

### Power Generation

P55	<b>A MEMS BASED MINIATURE HYDROGEN FUEL CELL FOR PORTABLE POWER GENERATION</b> .....	344
	K.Y. Lin, R.D. Morgan, H.S. Kim, L. Zhu, B. Gurau, M.A. Shannon, and R.I. Masel <i>University of Illinois, Urbana-Champaign, USA</i>	
P56	<b>A SELF-RESONANT, MEMS-FABRICATED, AIR-BREATHING ENGINE</b> .....	348
	F. Herrault <sup>1</sup> , T. Crittenden <sup>2</sup> , S. Yorish <sup>2</sup> , E. Birdsell <sup>1</sup> , A. Glezer <sup>1</sup> , and M.G. Allen <sup>1</sup> <sup>1</sup> Georgia Institute of Technology, USA and <sup>2</sup> Virtual AeroSurface Technologies, USA	

### Resonant Devices

P57	<b>AUTOMATIC MODE MATCHING FOR HIGH-Q VIBRATORY RATE GYROSCOPES</b> .....	352
	C.D. Ezekwe <sup>1,2</sup> and B.E. Boser <sup>1</sup> <sup>1</sup> University of California, Berkeley, USA and <sup>2</sup> Robert Bosch Research and Technology Center, USA	
P58	<b>FUNDAMENTAL AND OVERTONE ALUMINUM NITRIDE DUAL MODE RESONATOR FILTERS</b> .....	356
	R.H. Olsson III and M.R. Tuck <i>Sandia National Laboratories, USA</i>	
P59	<b>INFLUENCE OF SILICON ON QUALITY FACTOR, MOTIONAL IMPEDANCE AND TUNING RANGE OF PZT-TRANSDUCED RESONATORS</b> .....	360
	H. Chandrahalingam <sup>1</sup> , S.A. Bhavne <sup>1</sup> , R. Polcawich <sup>2</sup> , J. Pulskamp <sup>2</sup> , D. Judy <sup>2</sup> , R. Kaul <sup>2</sup> , and M. Dubey <sup>2</sup> <sup>1</sup> Cornell University, USA and <sup>2</sup> US Army Research Laboratory, USA	

P60	<b>NOISE ANALYSIS OF A TUNNELING ACCELEROMETER BASED ON STATE SPACE STOCHASTIC THEORY</b> .....	364
	L.A. Oropeza-Ramos, N. Kataria, C.B. Burgner, K.J. Åström, F. Brewer, and K.L. Turner <i>University of California, Santa Barbara, USA</i>	
P61	<b>PIEZORESISTIVE SENSING OF A DIELECTRICALLY ACTUATED SILICON BAR RESONATOR</b> .....	368
	D. Weinstein and S.A. Bhave <i>Cornell University, USA</i>	
P62	<b>POST-CMOS COMPATIBLE ALUMINUM NITRIDE RING WAVE GUIDE (RWG) RESONATORS</b> .....	372
	K.E. Wojciechowski, R.H. Olsson III, and M.R. Tuck <i>Sandia National Laboratories, USA</i>	

### Late News Posters

P63	<b>CARBON NANOTUBE MEMBRANE IN MICROCHANNEL FOR ELECTROPHORETIC SEPARATION OF PROTEINS</b> .....	376
	R. Dorairaj, T.J. Roussel, G. Sumanasekera, P. Sethu, C.M. Klinge, and R.S. Keynton <i>University of Louisville, USA</i>	
P64	<b>CHARACTERIZATION OF DUAL-AXIS PIEZORESISTIVE MEMS FORCE SENSORS</b> .....	378
	G.C. Hill, D.R. Soto, J.E. Oliver, and T.W. Kenny <i>Stanford University, USA</i>	
P65	<b>ENDOTOXIN REMOVAL USING MICROMACHINED SILICON NANOPOROUS MEMBRANES</b> .....	380
	R.A. Smith <sup>1,2</sup> , K. Goldman <sup>3</sup> , A.J. Fleischman <sup>1</sup> , W.H. Fissell <sup>1</sup> , C.A. Zorman <sup>2</sup> , and S. Roy <sup>1</sup> <i><sup>1</sup>Cleveland Clinic, USA, <sup>2</sup>Case Western Reserve University, USA, and <sup>3</sup>H-Cubed, Inc., USA</i>	
P66	<b>MECHANICAL ENERGY SCAVENGING FROM FLYING INSECTS</b> .....	382
	E.E. Aktakka <sup>1</sup> , H. Kim <sup>1</sup> , M. Atashbar <sup>1,2</sup> , and K. Najafi <sup>1</sup> <i><sup>1</sup>University of Michigan, USA and <sup>2</sup>Western Michigan University, USA</i>	
P67	<b>HIGH FREQUENCY ZNO-ON-DIAMOND MONOLITHIC FILTERS</b> .....	384
	R. Abdolvand <sup>1</sup> and F. Ayazi <sup>2</sup> <i><sup>1</sup>Oklahoma State University, USA and <sup>2</sup>Georgia Institute of Technology, USA</i>	
P68	<b>POLYMER-BASED MICROSYSTEM FOR MECHANICAL CHARACTERIZATION OF CELLS</b> .....	386
	M. Gnerlich <sup>1</sup> , W.-Y. Zhang <sup>1</sup> , H. Donahue <sup>2</sup> , A. Voloshin <sup>1</sup> , and S. Tatic-Lucic <sup>1</sup> <i><sup>1</sup>Lehigh University, USA and <sup>2</sup>Pennsylvania State University, USA</i>	

P69	<b>RAPID SACRIFICIAL GERMANIUM ETCHING USING XENON DIFLUORIDE</b> .....	388
	G.D. Cole and E. Behymer <i>Lawrence Livermore National Laboratory, USA</i>	
P70	<b>REAL-TIME SYNTHESIS AND MANIPULATION OF PHOTOPOLYMERIZED MICROSTRUCTURES USING OPTOFLUIDIC MASKLESS LITHOGRAPHY AND OPTICAL TWEEZERS</b> .....	390
	K. Yu <sup>1</sup> , H. Park <sup>2</sup> , N. Park <sup>2</sup> , and S. Kwon <sup>2</sup> <i><sup>1</sup>University of California, Berkeley, USA and <sup>2</sup>Seoul National University, KOREA</i>	

# SILICON AS A BIOMEDICAL MATERIAL

Mark Ming-Cheng Cheng<sup>1,2</sup>, Ennio Tasciotti<sup>1</sup>, and Mauro Ferrari<sup>1,2,3,4,5</sup>

<sup>1</sup>Center for Nanomedicine, Institute of Molecular Medicine, <sup>2</sup>Biomedical Engineering, The University of Texas Health Science Center at Houston, <sup>3</sup>Experimental Therapeutics, The University of Texas MD Anderson Cancer Center, <sup>4</sup>Bioengineering, Rice University, <sup>5</sup>The Alliance for Nanohealth, Houston, Texas, USA

## ABSTRACT

The cornerstone of microelectronics and MEMS, silicon-based manufacturing is taking over as a fundamental material in medicine. Research and laboratory diagnostic uses of biomolecular array technologies and microfluidics are well established. Novel sensor nanotechnologies are demonstrating features that make them an indispensable tool for the conquest of the post-genomic challenges, which present astronomical complexities in their requirement for multiplexed, real-time analyses. Controlled-release nanofluidic and microchip devices are under development as drug-delivery implants. Recently, nano-porous silicon has emerged as a material for medicine itself: it is biodegradable with tunable kinetics, eminently biocompatible, and provides suitable drug loading and release rates. Formed into micro- and nanoparticles of 'designer' size, shape and surface properties, nanoporous silicon is a particularly versatile material for the next generation of nanomedical therapeutic products.

## INTRODUCTION

With apologies to the purists of nomenclature and scientific taxonomy, in this article we employ the word 'silicon' not only to refer to the celebrated material itself, but also to refer to the top-down fabrication techniques employed in clean room to manufacture electronic and micro-electro-mechanical artifacts, the common denominator of which is the employ of photolithographic techniques. Begging further compositional license, we encompass under the rubric 'silicon' also those techniques that derived from the bubbling cauldron of clean room innovation, though they do not directly employ lithography proper – thus, soft lithographies also pertain within the scope of this article. With a final expansive thrust, we will encompass also a broad set of materials, but only within the context of their manufacture by means of the aforementioned set of techniques – thus, silicon oxides and nitride, several metals, biological and synthetic polymers... a large family indeed, the operational descendents of silicon proper and its processing protocols in semiconductor manufacturing techniques.

The connection between these materials and protocols will probably be obvious to the expert, and impenetrable to the occasional frequenter; the objective of this paper is to connect the dots and articulate the family tree, maintaining a focus on applications to biology and most notably in medicine. What will hopefully emerge is a portrait of 'silicon' as a key enabler of progress in medical diagnostics and therapeutics, and – surprise? – an enthusiastic endorsement of silicon itself as a great material for in-vivo use in the clinic.

## THE EMERGENCE OF SILICON-FAB AS AN ENABLING TECHNOLOGY IN BIOMEDICINE

The first thrust toward biomedical deployment of silicon fabrication technologies derived from microfluidics, which offered unprecedented performance in bioseparation and the controlled transport of reagents and analytes [1, 2]. Microfluidics has now become a household name in science worldwide, with academic journals, professional societies, and scientific congresses dedicated to the field. Many products have emerged for laboratory clinical and diagnostic uses, developed by companies ranging from the

start-up phase to publicly traded entities of the small- and mid-cap persuasion, to entire sector operations of large chip manufacturers. These products include separation technologies for blood into its components, the fractionation of complex biofluidic mixtures into, e.g., its protein and nucleic acid digest sub-populations, DNA amplification strategies via PCR-on-chip, precise fluidic dispensation technologies for automated high-throughput analyses, multiplexed analyte sensors for point-of-care diagnostics, and many more. A fundamental enabling breakthrough for the commercial and clinical transitions of microfluidics was the development of convenient methods of fabrication for polymers via soft-lithographic techniques, which do not require lithographic steps beyond the definition of an initial template or mold [3].

The transition from microfluidics to nanofluidics was enabled by the attainment of nanometer-scale resolution in UV photolithography, and the development of innovative, no-lithographic methods for nanometer-scale dimensional control. Our group has focused on nanofluidics for over a decade now, pioneering applications to cell transplantation [4], separation of biological molecules and nanoparticles [5], the encapsulation of implanted sensors to avoid biological fouling [6], and drug delivery from implants [7, 8]. The fundamental technique we have based our program on is the use of sacrificial oxide layers to define nanochannel dimensions [9, 10]. We have also explored the fundamental physical and chemical implications of nanochannel transport, developing and experimentally validating novel predictive laws for constrained non-Fickian diffusion [11, 12] and osmotic pressure [13].

Examples of microfluidic devices and approaches follow. The current standard for the separation of proteins or small nucleic acids (DNA, RNA, oligonucleotide), gel electrophoresis, suffers from labor-intensive processes as well as limited sensitivity and reproducibility. Microfluidics systems have been fabricated using photolithography and etching in glass to create microchannels with diameters between 10 -100 micrometers [14]. The devices utilize capillary electrophoresis and hydrodynamic pressure to implement the continuous-flow assays that automate and integrate sample injection, reaction, separation, staining and fluorescence detection steps. Different prototypes including binding assays, protein/enzyme assays, and cellular assays have been demonstrated [15]. Enzyme-linked Immunosorbent Assay (ELISA), commonly used in immunoassay to detect an antibody or an antigen in a sample involves a series of reaction/incubation and washing steps. It often takes many hours to two days because of the limited mass transport of antigen/antibody from the analytes to the surface. A polymer-based compact-disk (CD) like microfluidic platform has been developed to implement ELISA [16]. This device is fabricated using an UV-LIGA process. Different solutions involved in the ELISA process is stored in different reservoirs, followed by mixing and incubation that is controlled by centrifugal and capillary forces. Each step of the ELISA process is carried out by the rotation speed of the CD with no external power required. The advantages include reduction in reagent consumption and high-throughput; however, the non-specific adsorption on the polymer surface remains challenging.

The second avenue of import of UV- photolithography into medicine is in connection with microarrays for the sequencing of

nucleic acids, proteins, and an ever-growing taxonomy of biological molecules [17]. Photolithography was used to fabricate high density, spatially addressable DNA/RNA microarrays through and insight of Fodor, Stryer, and their coworkers [18, 19]. Contact lithography combined with the chemistry of light-sensitive removable protective groups allow for the synthesis of arbitrary polynucleotide bases at specified locations on the solid-state surface with a minimum of chemical steps. Current state-of-the-art microarrays have feature dimensions of 5 $\mu$ m and densities of about 4 $\times 10^6$ /cm<sup>2</sup>. It is expected the size will continue to scale down. While such high-density microarrays are suitable for gene expression analysis, it takes a very long time for passive hybridization. Using lithography-patterned planar microelectrode arrays, electronic microarrays have been developed for addressable, and fast DNA or RNA hybridization [20]. The application of a positive electric current to the individual electrodes enables rapid movement and concentration of negatively charged molecules. Porous hydrogel is coated on the electrode to serve as a soft support for attaching DNA probes and to reduce effects of electrolysis. Novel fabrication technologies for arrays of bioanalytes are explored by many groups worldwide [17].

## **SILICON NANOTECHNOLOGY FOR PROTEIN SENSORS AND PROTEOMICS**

An emerging application in biomedical research is the development of tools for reliable, rapid, quantitative, low-cost, and multiplexing identification of biomarkers using biological fluids (serum, urine, saliva) for screening, diagnostics, and staging of cancer and other pathologies. Early detection is particularly important in cancer, since the disease at its early stages, may be treated with the greatest probability of success.

However, the task is challenging because of the complexity and high dynamic range of protein and peptide biomarkers in the biofluids. It has been widely recognized that the number of different biomolecular species in the plasma proteome exceeds 300,000, and could be as high as 10<sup>6</sup>, with differences of as many as 12 orders of magnitude in relative abundances [21]. For quantitative detection of low-abundance biomarkers, new technologies are demanded including molecular recognition, bioconjugation protocols, and mechanisms for label-free, multiplexing detection. Three approaches are reviewed in what follows.

### **Cantilevers: Nanomechanical Detection of Biomolecules**

Detecting biomolecular interactions by measuring nanomechanical forces offers an exciting means to develop highly sensitive, miniature, and label-free biological sensors [22, 23]. When molecular adsorption/binding occurs on one-side of a cantilever, the silicon cantilever beam is subjected to surface stresses and a change of mass. The cantilever beam manifests the forces involved in the adsorption process by nanometer scale displacement as well as by changes in resonant frequency. Such a direct transduction eliminates the need for the analytes to be labeled. The displacement of the cantilever can be quantified simultaneously by using a number of techniques such as measuring variations in optical beam deflection, piezoresistivity, piezoelectric, and capacitance. These forces can also be measured as a resonance frequency although the sensitivity is usually low because of the low quality factor of the resonator and the viscosity of the liquid. To improve this, microchannels suspended in the cantilevers have also been developed in which the cantilever is placed in vacuum and the solution is allowed to flow inside a hollow resonator [24].

Silicon offers no intrinsic chemical selectivity so that the chemical recognition on cantilevers is achieved by affinity binding reactions. Self-assembled monolayers, DNA probes, antibodies, or peptides can be coated on the cantilever by mechanism such as adsorption, covalent binding, or affinity binding. DNA hybridization on cantilevers has been extensively investigated by a number of groups [22]. Detection of proteins by cantilever nanomechanics is challenging, mainly due to the lack of reproducible and robust immobilization techniques for antibodies. However, prostate specific antigen (PSA) has been successfully detected on cantilevers using immobilized antibodies [23]. It has been shown the amplitude of the bending is proportional to the concentration of the antigen adsorbed and to the time of exposure.

### **Silicon Nanotextured Surfaces for Proteomic Analysis**

It is hypothesized that the low molecular weight proteome (LMWP), comprising proteolytic fragments at extremely low concentration, contains a wealth of information of diagnostic and prognostic utility [25]. Because of the high range of variability of serum proteome, it is essential to develop fractionation technologies to deplete the most abundant interfering proteins. To overcome current limitations in sample processing and analysis, we developed nanoporous silicon chips (NSCs) to perform size exclusion, selective capture, and resultant enrichment of selected regions of the LMWP from body fluids and other biologic samples [26, 27].

NSCs incubated with human plasma mixtures spiked with peptide standards can be identified by Matrix Assisted Laser Desorption/Ionization Time-of-Flight (MALDI-TOF), one type of mass spectrometry analysis. The analytes can be detected with concentration as low as the ng/mL range, thus increasing the sensitivity of MS analysis by roughly 400-fold. In combination with the selective enrichment achieved by the use of NSCs, it represents a powerful tool to further improve the selectivity, sensitivity and reproducibility of peptide harvesting and identification in the search for disease-related biomarkers. They might provide clinical diagnostic tools for early detection of human diseases and for tracking individual patient's responses to treatment regimens.

### **Nanowires: Label-Free Electronic Biosensor**

Nanowire sensors operate on the basis that the change in chemical potential accompanying a target binding event, such as DNA hybridization, can act as a field-effect gate upon the nanowire, thereby changing its conductance [28, 29]. The high-density and high sensitivity of nanowires holds promise for monitoring local chemical, electrical or physical property changes in cells or tissues.

The ideal nanowire sensor is a lightly doped, high-aspect ratio, single-crystal nanowire with a diameter between 10 and 20 nm. If the nanowire is much smaller, it couples noises easily, whereas if it is too large, it is not as sensitive. Other design considerations include the length, sensor geometry of nanowires, fluidic conditions and ion concentrations in the aqueous solution.

One great advantage of nanowire sensor is that they can be integrated with the circuit. Large scale circuits can, in principle, be constructed within very small (microfluidic) environments, creating very dense sensor libraries, thus enabling measurement of many different genes and proteins from very small tissue samples, or even single cells. However, functionalization of the individual nanowires with multiple ssDNA molecules or protein capture agents does represent a serious challenge.

## SILICON-BASED THERAPEUTIC APPLICATIONS

Several implantable silicon-based microdevices have been explored in-vivo. For example, high-density silicon micromachined electrode arrays have been developed to interface with the central nervous system for the long-term monitoring of neural activity in vivo as well as the insertion of electronic signals into neural networks at the cellular level [30]. Another example is implantable silicon microchips for radio-frequency identification that have been approved by the FDA and commercialized.

Drug delivery is an extraordinarily exciting area of silicon-enabled nanomedicine [31]. For the chemotherapy of cancer, challenges remain to realize continuous local delivery of multiple drugs at a constant rate to the tumor microenvironment to overcome much of the systemic toxicity and to improve anti-tumour efficacy. The novel physical/chemical/biological properties of nanoscale materials offer new opportunities. For example, engineered particles for drug delivery can alter the pharmacokinetics and biodistribution of the drugs by immobilizing molecular recognition moieties (antibody, proteins, peptides, aptamers, etc) at the surface of particles. Another example is that we have shown when molecules transport through the nanochannels with a size approaching the hydrodynamic diameter of the molecules, the diffusion kinetics are linear, non-Fickian over a substantial period. This may be applied to drug delivery [32].

### Silicon Microchips for Controlled-Drug Delivery System

An array of miniature reservoirs have been fabricated using semiconductor processing for drug delivery applications [33, 34]. Each reservoir is loaded with drugs and sealed with a gold membrane. The membrane ruptures in the presence of chloride ions when anodic voltage is applied to the membrane of interest, allowing the drug within the reservoir to dissolve and diffuse into the surrounding tissue. This device allows for the release of multiple, active substances in a pulsatile manner. The reservoirs can also be made of time-dependent biodegradable polymer without the need for a stimulus to trigger drug release [34].

We discovered non-Fickian diffusion phenomena using nanochannels designed for the controlled release of molecules [11, 32]. The nanochannels were generated by removing a sacrificial silicon oxide layer, which is sandwiched between two structural layers. Nanochannels of width 7-50nm can now be routinely manufactured without E-beam lithography. By tailoring the channel size and chemistry according to the molecules of interest, it is possible to attain the desired constant release profiles of drugs for a period of several months. Furthermore, applying a very small electrical field across the channel gives the ability to actively control the release rates. This offers the opportunity to develop smart pre-programmed, remotely activated, and self-regulated delivery implants. Nanochannels can also be used for immunoisolation of cell transplantation to perform size-exclusion [6]. The physical geometry affords sufficient permeability to small molecules such as oxygen, glucose and insulin, while impeding the passage of immune molecules and graft-borne viruses. Encapsulated rat neonatal pancreatic islets have been demonstrated to significantly outlive and outperform controls in terms of insulin-secretion capability over periods of several weeks.

### Silicon Particles for Drug Delivery

Porous silicon particles can be formed using electrochemical etching in HF solution combined with lithography. These particles can carry drugs, proteins, peptides or small compounds. Large porous silicon particles of diameter 200 $\mu$ m have been investigated for oral delivery [35]. The particles carried FITC labeled insulin along with a permeation enhancer, sodium laurate. The release

profile was tested across differentiated human intestinal Caco-2 cell monolayers grown on Transwell® inserts. The flux of FITC-insulin from silicon particles across cell monolayers was nearly 10-fold higher as compared to liquid formulations.

Particles of diameter 30 $\mu$ m were used to carry radioisotope phosphorous 32 into close contact with the tumor [36]. The commercially available n-type silicon wafers contain dopant phosphorous 31 (0.001%), and it was irradiated to form 32P. These particles implanted intratumorally under local anesthesia directly into liver tumors under ultrasound or computed tomographic guidance showed a significant degree of antitumor efficiency at low doses.

### Multi-Stage Nanoporous Silicon Drug Delivery Systems

It is the consensus that only between 1 and 10 parts per 100,000 of intravenously administered drug molecules reach their tumor targets in vivo [31]. The human body's natural defenses or biobarriers act as obstacles to foreign objects injected in the blood stream. These barriers include enzymatic degradation, phagocytosis in peripheral blood and in the reticulo-endothelial system (RES), and the crossing of the vascular endothelium. Margination and adhesion onto vascular endothelia are governed by haemodynamic forces that are effective barriers for injected agents.

To overcome this challenge, we have developed a multifunctional multistage delivery system (MDS) that is able to navigate in the blood stream and to efficiently dock to the abnormal vasculature associated with diseased tissues [37, 38]. The MDS comprises stage 1 mesoporous silicon particles (S1MPs) that can be loaded with one or more types of stage 2 nanoparticles (S2NPs), which can in turn carry either active agents or higher-stage particles. By loading S2NPs inside the pores of the S1MPs, the enzymatic degradation and RES uptake of the S2NPs would be prevented. Vascular penetration enhancers and other molecules can also be simultaneously delivered by the MDS to increase the crossing of the endothelial barrier. Future embodiments of the MDS are envisioned to integrate biological recognition moieties to allow for their selective targeting. In addition, the treatment can be optimized for the specific pathology treated by loading the particles with drugs such as chemotherapeutic agents, humanized antibodies, small interfering RNAs, and other agents. This novel, multi-stage strategy may eventually lead to significant improvements in therapy efficacy, and reduced systemic toxicity as well reduction in the total amount of injected drugs.

## BIOCOMPATIBILITY AND BIODEGRADABILITY OF SILICON

Biocompatibility of medical device refers to its ability to perform its intended function, without eliciting any undesirable local or systemic effects in that host [39]. While silicon is a chemically-stable material, the oxidized silicon surface can show bioactivity, manifested in a layer of hydroxyapatite  $\text{Ca}_{10}(\text{PO}_4)_6(\text{OH})_2$ , which grows on the surface when exposed to a physiological solution. Recently, there have been reports on the testing of silicon and other MEMS materials as implantable candidates using ISO 10993 physicochemical and biocompatibility test [40, 41]. Silicon shows biocompatible but biofouling (the growth of adherent cells occurs)

Porous silicon has recently been discovered to have new biomedical properties [42, 43]. The bioactivity and biodegradation of porous silicon can be controlled by porosity and pore size. While high porosity silicon dissolves quickly in physiological buffers, biodegradation of medium porosity silicon is slower. Si dissolves mainly into monomeric silicic acid  $\text{Si}(\text{OH})_4$ , which is the

most natural form of Si in the environment and shows no toxicity. Silicon is an essential nutrient, and the average daily intake of silicon is about 20-50mg/day.

We showed in our pre-clinical studies that porous silicon is fully biodegradable and that the particles completely disappeared in 18-24 hours in physiologic solution, in 8-10 hours in serum and in less than 4 hours in whole blood. We cultured different cell types with porous silicon particles, and followed biocompatibility and cellular fate through proliferation assay, cytotoxicity assay, activation of the apoptotic program of the cells and cell cycle analysis. In all the experimental settings, the silicon particles proved to be completely harmless to cells.

## CONCLUSION

Photolithographic methods applied to silicon and an ever-expanding spectrum of organic and inorganic materials have beneficially impacted biology and medicine, in the context of research and diagnostic laboratories. Silicon and silicon-based materials and methods first demonstrated their biomedical applicability in microfluidic systems, biomolecular sensors and microarrays. Many novel technologies are emerging that will be instrumental for the post-genomic era, and the advent of personalized medicine. Therapeutic uses of silicon include the controlled-release delivery of drugs and radiation from implants. Biodegradable and biocompatible nanoporous silicon-based multistage particulates open a new frontier for the intravenous, biologically targeted delivery of therapy across biological barriers. With these, itself silicon graduates from the role of the fabrication support enabler and gains citizenship in the domain of the true biomedical materials.

## ACKNOWLEDGEMENT

These studies were supported by the following grants: DoDW81XWH-04-2-0035 Project 16, DoDW81XWH-07-2-0101, DoDW31P4Q-07-1-0008, NASA SA23-06-017, State of Texas, Emerging Technology Fund, NIH NCI 1R21CA1222864-01, 1R01CA128797-01, and NSF ECCS-0725886. The authors would like to recognize the support from the Alliance for NanoHealth (ANH) and Center of Nanomedicine, The University of Texas Health Science Center at Houston.

## REFERENCES

- [1] A. Manz, N. Graber, and H. M. Widmer, "Miniaturized Total Chemical Analysis System- A Novel Concept For Chemical Sensing," *Sensors and Actuators B-Chemical*, vol. 1, pp. 244-248, Jan 1990.
- [2] D. J. Beebe, G. A. Mensing, and G. M. Walker, "Physics and applications of microfluidics in biology," *Annual Review of Biomedical Engineering*, vol. 4, pp. 261-286, 2002.
- [3] Y. N. Xia and G. M. Whitesides, "Soft lithography," *Annual Review of Materials Science*, vol. 28, pp. 153-184, 1998.
- [4] T. A. Desai, W. H. Chu, J. K. Tu, G. M. Beattie, A. Hayek, and M. Ferrari, "Microfabricated immunoisolating biocapsules," *Biotechnology and Bioengineering*, vol. 57, pp. 118-120, Jan 1998.
- [5] J. K. Tu, T. Huen, R. Szema, and M. Ferrari, "Filtration of Sub-100nm Particles Using a Bulk-Micromachined, Direct-Bonded Silicon Filter," *Biomedical Microdevices*, vol. 1, p. 8, 1999.
- [6] T. A. Desai, D. J. Hansford, L. Leoni, M. Essenpreis, and M. Ferrari, "Nanoporous anti-fouling silicon membranes for biosensor applications," *Biosensors & Bioelectronics*, vol. 15, pp. 453-462, Nov 2000.
- [7] G. B. Lesinski, S. Sharma, K. A. Varker, P. Sinha, M. Ferrari, and W. E. Carson, "Release of biologically functional interferon-alpha from a nanochannel delivery system," *Biomedical Microdevices*, vol. 7, pp. 71-79, Mar 2005.
- [8] C. Cosentino, F. Amato, R. Walczak, A. Boiarski, and M. Ferrari, "Dynamic model of biomolecular diffusion through two-dimensional nanochannels," *Journal of Physical Chemistry B*, vol. 109, pp. 7358-7364, Apr 2005.
- [9] W. H. Chu and M. Ferrari, "Microfabricated Filter with Specially Constructed Channel Walls, and Containment Well and Capsule Constructed with Such Filters," *US Patent No. 5,798,042*, August 1998 1998.
- [10] T. A. Desai, D. J. Hansford, L. Kulinsky, A. H. Nashat, G. Rasi, J. Tu, Y. Wang, M. Zhang, and M. Ferrari, "Nanopore Technology for Biomedical Applications," *Biomedical Microdevices*, vol. 2, p. 20, August 1998 1999.
- [11] S. Pricl, M. Ferrone, M. Fermeglia, F. Amato, C. Cosentino, M. M. C. Cheng, R. Walczak, and M. Ferrari, "Multiscale modeling of protein transport in silicon membrane nanochannels. Part 1. Derivation of molecular parameters from computer simulations," *Biomedical Microdevices*, vol. 8, pp. 277-290, Dec 2006.
- [12] F. Amato, C. Cosentino, S. Pricl, M. Ferrone, M. Fermeglia, M. M. C. Cheng, R. Walczak, and M. Ferrari, "Multiscale modeling of protein transport in silicon membrane nanochannels. Part 2. From molecular parameters to a predictive continuum diffusion model," *Biomedical Microdevices*, vol. 8, pp. 291-298, Dec 2006.
- [13] A. Grattoni, M. Merlo, and M. Ferrari, "Osmotic pressure beyond concentration restrictions," *Journal of Physical Chemistry B*, vol. 111, pp. 11770-11775, Oct 2007.
- [14] L. Bousse, S. Mouradian, A. Minalla, H. Yee, K. Williams, and R. Dubrow, "Protein sizing on a microchip," *Analytical Chemistry*, vol. 73, pp. 1207-1212, Mar 2001.
- [15] S. A. Sundberg, "High-throughput and ultra-high-throughput screening: solution- and cell-based approaches," *Current Opinion in Biotechnology*, vol. 11, pp. 47-53, Feb 2000.
- [16] S. Lai, S. N. Wang, J. Luo, L. J. Lee, S. T. Yang, and M. J. Madou, "Design of a compact disk-like microfluidic platform for enzyme-linked immunosorbent assay," *Analytical Chemistry*, vol. 76, pp. 1832-1837, Apr 2004.
- [17] M. Ozkan, M. Heller, and M. Ferrari, *BioMEMS and Biomedical Nanotechnology, Vol. II: Micro/Nanotechnologies for Genomics and Proteomics*, 2006.
- [18] S. P. A. Fodor, J. L. Read, M. C. Pirrung, L. Stryer, A. T. Lu, and D. Solas, "LIGHT-DIRECTED, SPATIALLY ADDRESSABLE PARALLEL CHEMICAL SYNTHESIS," *Science*, vol. 251, pp. 767-773, Feb 1991.
- [19] R. J. Lipshutz, S. P. A. Fodor, T. R. Gingeras, and D. J. Lockhart, "High density synthetic oligonucleotide arrays," *Nature Genetics*, vol. 21, pp. 20-24, Jan 1999.
- [20] R. G. Sosnowski, E. Tu, W. F. Butler, J. P. Oconnell, and M. J. Heller, "Rapid determination of single base mismatch mutations in DNA hybrids by direct electric field control," *Proceedings of the National Academy of Sciences of the United States of America*, vol. 94, pp. 1119-1123, Feb 1997.
- [21] M. M. C. Cheng, G. Cuda, Y. L. Bunimovich, M. Gaspari, J. R. Heath, H. D. Hill, C. A. Mirkin, A. J. Nijdam, R. Terracciano, T. Thundat, and M. Ferrari, "Nanotechnologies for biomolecular detection and medical diagnostics,"

- Current Opinion in Chemical Biology*, vol. 10, pp. 11-19, Feb 2006.
- [22] J. Fritz, M. K. Baller, H. P. Lang, H. Rothuizen, P. Vettiger, E. Meyer, H. J. Guntherodt, C. Gerber, and J. K. Gimzewski, "Translating biomolecular recognition into nanomechanics," *Science*, vol. 288, pp. 316-318, Apr 2000.
- [23] G. H. Wu, R. H. Datar, K. M. Hansen, T. Thundat, R. J. Cote, and A. Majumdar, "Bioassay of prostate-specific antigen (PSA) using microcantilevers," *Nature Biotechnology*, vol. 19, pp. 856-860, Sep 2001.
- [24] T. P. Burg, M. Godin, S. M. Knudsen, W. Shen, G. Carlson, J. S. Foster, K. Babcock, and S. R. Manalis, "Weighing of biomolecules, single cells and single nanoparticles in fluid," *Nature*, vol. 446, pp. 1066-1069, Apr 2007.
- [25] L. A. Liotta, M. Ferrari, and E. Petricoin, "Clinical proteomics: Written in blood," *Nature*, vol. 425, p. 905, 2003.
- [26] D. Geho, M. M. C. Cheng, K. Killian, M. Lowenthal, S. Ross, K. Frogale, J. Nijdam, N. Lahar, D. Johann, P. Herrmann, G. Whiteley, M. Ferrari, E. Petricoin, and L. Liotta, "Fractionation of serum components using nanoporous substrates," *Bioconjugate Chemistry*, vol. 17, pp. 654-661, May 2006.
- [27] M. Gaspari, M. M. C. Cheng, R. Terracciano, X. W. Liu, A. J. Nijdam, L. Vaccari, E. di Fabrizio, E. F. Petricoin, L. A. Liotta, G. Cuda, S. Venuta, and M. Ferrari, "Nanoporous surfaces as harvesting agents for mass spectrometric analysis of peptides in human plasma," *Journal of Proteome Research*, vol. 5, pp. 1261-1266, May 2006.
- [28] G. F. Zheng, F. Patolsky, Y. Cui, W. U. Wang, and C. M. Lieber, "Multiplexed electrical detection of cancer markers with nanowire sensor arrays," *Nature Biotechnology*, vol. 23, pp. 1294-1301, Oct 2005.
- [29] Y. L. Bunimovich, G. L. Ge, K. C. Beverly, R. S. Ries, L. Hood, and J. R. Heath, "Electrochemically programmed, spatially selective biofunctionalization of silicon wires," *Langmuir*, vol. 20, pp. 10630-10638, Nov 2004.
- [30] K. D. Wise, D. J. Anderson, J. F. Hetke, D. R. Kipke, and K. Najafi, "Wireless implantable microsystems: High-density electronic interfaces to the nervous system," *Proceedings of the Ieee*, vol. 92, pp. 76-97, Jan 2004.
- [31] M. Ferrari, "Cancer nanotechnology: Opportunities and challenges," *Nature Reviews Cancer*, vol. 5, pp. 161-171, Mar 2005.
- [32] F. Martin, R. Walczak, A. Boiarski, M. Cohen, T. West, C. Cosentino, and M. Ferrari, "Tailoring width of microfabricated nanochannels to solute size can be used to control diffusion kinetics," *Journal of Controlled Release*, vol. 102, pp. 123-133, Jan 2005.
- [33] J. T. Santini, A. C. Richards, R. Scheidt, M. J. Cima, and R. Langer, "Microchips as controlled drug-delivery devices," *Angewandte Chemie-International Edition*, vol. 39, pp. 2397-2407, 2000.
- [34] A. C. R. Grayson, I. S. Choi, B. M. Tyler, P. P. Wang, H. Brem, M. J. Cima, and R. Langer, "Multi-pulse drug delivery from a resorbable polymeric microchip device," *Nature Materials*, vol. 2, pp. 767-772, Nov 2003.
- [35] A. B. Foraker, R. J. Walczak, M. H. Cohen, T. A. Boiarski, C. F. Grove, and P. W. Swaan, "Microfabricated porous silicon particles enhance paracellular delivery of insulin across intestinal Caco-2 cell monolayers," *Pharmaceutical Research*, vol. 20, pp. 110-116, Jan 2003.
- [36] A. S. W. Goh, A. Y. F. Chung, R. H. G. Lo, T. N. Lau, S. W. K. Yu, M. Chng, S. Satchithanatham, S. L. E. Loong, D. C. E. Ng, B. C. Lim, S. Connor, and P. K. H. Chow, "A novel approach to brachytherapy in hepatocellular carcinoma using a phosphorous(32) (P-32) brachytherapy delivery device - A first-in-man study," *International Journal of Radiation Oncology Biology Physics*, vol. 67, pp. 786-792, Mar 2007.
- [37] P. Decuzzi and M. Ferrari, "Design maps for nanoparticles targeting the diseased microvasculature," *Biomaterials*, vol. 29, pp. 377-384, Jan 2008.
- [38] E. Tasciotti, X. Liu, R. Bhavane, K. Plant, A. Leonard, B. Price, M. M. Cheng, P. Decuzzi, J. T. F. Robertson, and M. Ferrari, "Mesoporous silicon particles as a multistage delivery system for imaging and therapeutic applications " *Nature Nanotechnology*, March 2008.
- [39] A. Remes and D. F. Williams, "Immune Response in Biocompatibility," *Biomaterials*, vol. 13, pp. 731-743, 1992.
- [40] G. Kotzar, M. Freas, P. Abel, A. Fleischman, S. Roy, C. Zorman, J. M. Moran, and J. Melzak, "Evaluation of MEMS materials of construction for implantable medical devices," *Biomaterials*, vol. 23, pp. 2737-2750, Jul 2002.
- [41] G. Voskerician, M. S. Shive, R. S. Shawgo, H. von Recum, J. M. Anderson, M. J. Cima, and R. Langer, "Biocompatibility and biofouling of MEMS drug delivery devices," *Biomaterials*, vol. 24, pp. 1959-1967, May 2003.
- [42] L. T. Canham, "Bioactive silicon structure fabrication through nanoetching techniques," *Advanced Materials*, vol. 7, pp. 1033-&, Dec 1995.
- [43] L. T. Canham, C. L. Reeves, J. P. Newey, M. R. Houlton, T. I. Cox, J. M. Buriak, and M. P. Stewart, "Derivatized mesoporous silicon with dramatically improved stability in simulated human blood plasma," *Advanced Materials*, vol. 11, pp. 1505-+, Dec 1999.

# AN ULTRA-THIN PACKAGED MEMS OSCILLATOR

Brian H. Stark, Eric Radza, Pavan Gupta, Jason Sharma, Ganesh Peramaih, Sherwin Deng, Sunny Suen, Robbie Sheridan, Aaron Partridge, and Markus Lutz  
SiTime Corporation, Sunnyvale, California, USA

## ABSTRACT

This paper reports the world's thinnest packaged oscillator, the SiT8002UT (Figure 1). This device is a 370 $\mu\text{m}$  thick oscillator (3.0x3.5mm lateral dimensions) that can be programmed to a frequency between 1 and 125MHz with a 10ppm initial frequency resolution. The stability of the SiT8002UT over the industrial temperature range is evaluated to be +/-20ppm. The SiT8002UT is also, to our knowledge, the thinnest packaged MEMS product. In order to realize this device, functional 75 $\mu\text{m}$ -thick MEMS wafers are also demonstrated.

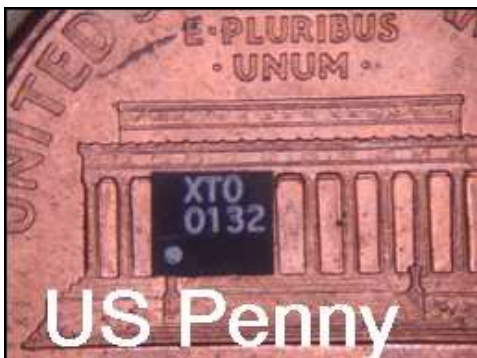
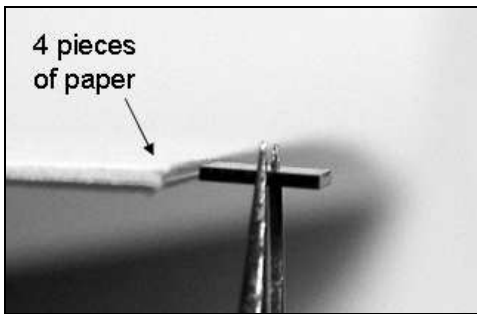


Figure 1: Images of the SiT8002UT. Nominal thickness is 370 $\mu\text{m}$  ( $\sigma=5\mu\text{m}$ ).

## INTRODUCTION

The quest for thinner oscillators is driven by the continuing decrease in the size of consumer electronics [1]. While many IC and passive components can be shrunk with relative ease, precision timing references heretofore have resisted the trend of extreme dimensional reduction [2]. In many portable applications, thickness is a more critical size metric than lateral dimensions. Comparative commercially viable oscillators (Figure 2) are at least 400 $\mu\text{m}$  thicker than the SiT8002UT. These oscillators are made from traditional quartz technology, which is limited in its ability to scale to thinner dimensions. As quartz must be vacuum encapsulated, the thickness of the package is fundamentally linked to the lateral dimensions of the part; to withstand the pressure of a vacuum cavity, the quartz package must have a relatively thick metal membrane around the package. As the membrane is thinned (to reduce package height), it must also be shrunk laterally to maintain stiffness. Shrinking lateral dimensions in quartz technology necessitates an increase in device cost, as solder seal rings are

reduced and process yields decrease dramatically. As a result, a further limitation of traditional quartz oscillators is that cost increases as device thickness shrinks. In comparison, semiconductor products evidence no fundamental linkage between device thickness and footprint. Furthermore in modern batch packaging technologies, price decreases with decreasing dimensions, as more units can be encapsulated in a single molding operation.

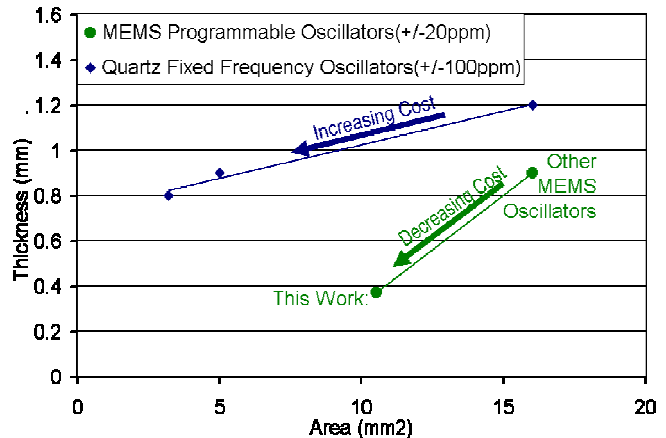


Figure 2: Size comparison of State-of-the-Art packaged oscillators. This work represents the thinnest device reported. Other oscillators are at least 400 $\mu\text{m}$  thicker than this work. Thickness is a critical metric for many space constrained consumer applications.

To reduce the height of a standard MEMS oscillator, two basic mechanisms are employed: 1) the stacked die configuration employed in current oscillators is replaced in favor of a side by side configuration and 2) the die are thinned as much as possible. At the onset of this project, it was unclear how much thinning could be reasonably achieved on a MEMS resonator without deleterious performance implications. Previously reported literature [3] has suggested that a thinned MEMS substrate results in an unacceptable deterioration of the Quality factor of the device. As a result (mitigating risk of thinned MEMS), two technologies to build a 370 $\mu\text{m}$  thick oscillator are explored (Fig. 3). One package is based upon a 240 $\mu\text{m}$  thick mold cavity (X2 mold thickness) on top of a 125 $\mu\text{m}$  thick Cu leadframe (X2QFN technology). The other utilizes a 370 $\mu\text{m}$  thick mold cavity (U mold thickness) on top of an 8 $\mu\text{m}$  thick Au/Ni/Au galvanically formed leadless land grid array pattern (ULLGA). The X2QFN requires thinner silicon die (reliability risk) and has worse stress behavior over temperature; the ULLGA allows for thicker silicon and exhibits less bimorph-induced stress, but can be more prone to delamination. In one variant of the X2QFN, to accommodate thicker MEMS die (again for risk mitigation if 75 $\mu\text{m}$  MEMS weren't practical – later shown unnecessary), a half-etched pocket was implemented in the leadframe. Both technologies were fabricated in high volume facilities that have installed manufacturing capacities exceeding one million units per day. Assembly yields are comparable to industry standards

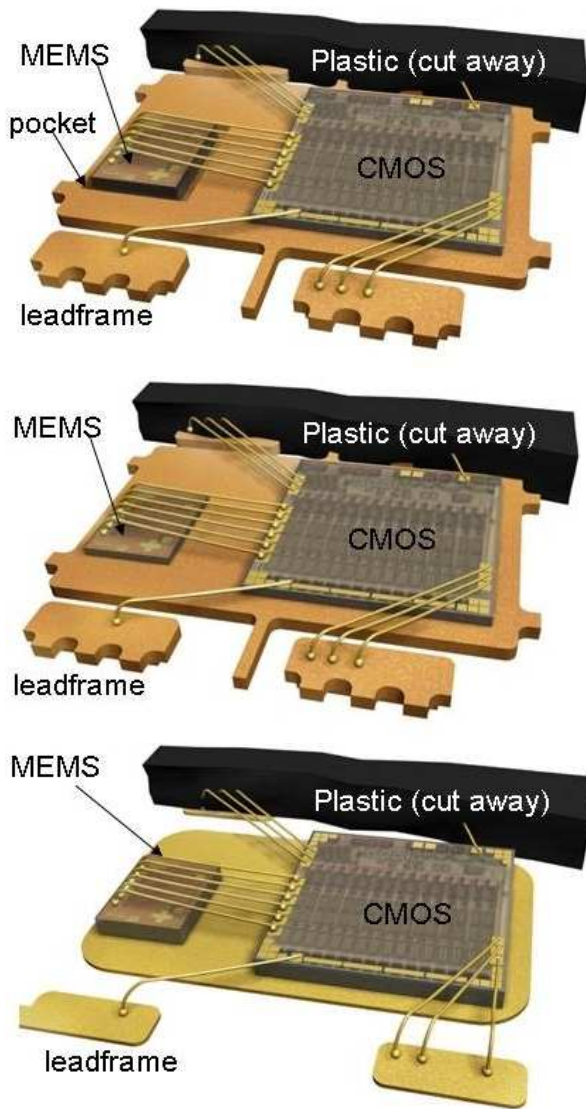


Figure 3: Diagram of the Ultra-Thin MEMS oscillator in different constructions. A X2QFN is made in two variants: 125 $\mu\text{m}$  thick MEMS with a half etched pocket (top) and 75 $\mu\text{m}$  MEMS in a standard leadframe (middle). The pocket was shown to be unnecessary as 75 $\mu\text{m}$  thick MEMS can be utilized without deleterious effects. The ULLGA is made with a center die paddle (bottom). The die in the ULLGA construction are 125 $\mu\text{m}$  thick.

### FABRICATION

In both package variants, construction begins with a leadframe (ULLGA process depicted in Figures 4a-d). MEMS and CMOS wafers (described in [4]) are ground and polished to either 75 $\mu\text{m}$  or 125 $\mu\text{m}$  and diced. This extreme height reduction (thinnest MEMS product reported) is possible due to the low-profile thin film encapsulation utilized in the MEMS process (Figure 5). Contrary to previously reported work [5], no decrease in Q is evidenced by thinning the substrate to these dimensions (Figure 6). After dicing, the chips are placed side by side on leadframe strips and wirebonded with 25 $\mu\text{m}$  gold wire. The populated leadframes are then transfer molded. Given the thin mold cap and the corresponding high mold pressures, extreme care has to be exercised in the molding process to prevent wire damage and latent

construction defects (Figure 7). The molded devices are then tested in strip and singulated.

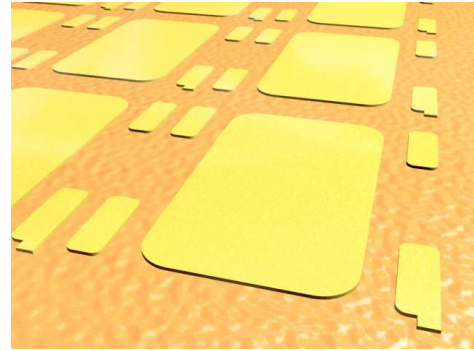


Figure 4a: ULLGA process. Fabrication begins with a galvanically formed lead pattern on a sacrificial copper substrate.

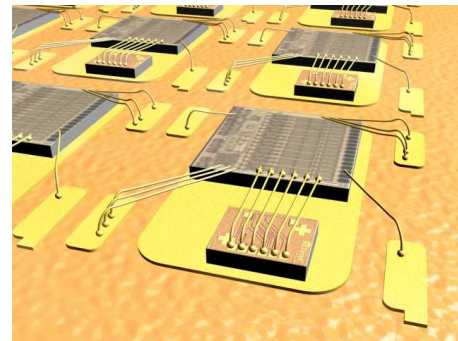


Figure 4b: ULLGA process. Thinned die are mounted and wirebonded.

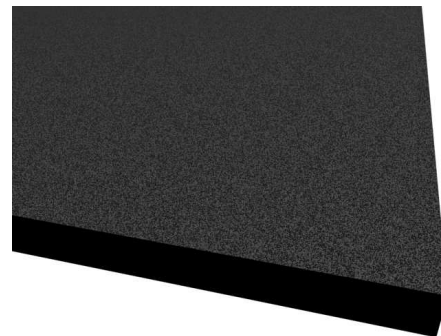


Figure 4c: ULLGA process. The part is molded. The copper substrate is removed after molding via a wet process.

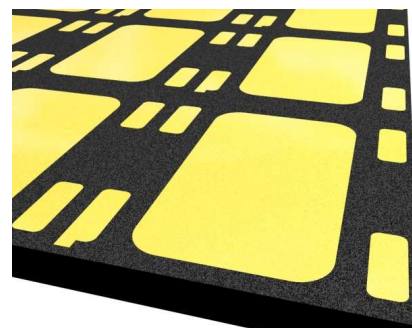


Figure 4d: ULLGA process. The parts are flipped upside down (dead bugged) and strip tested using a probe card.

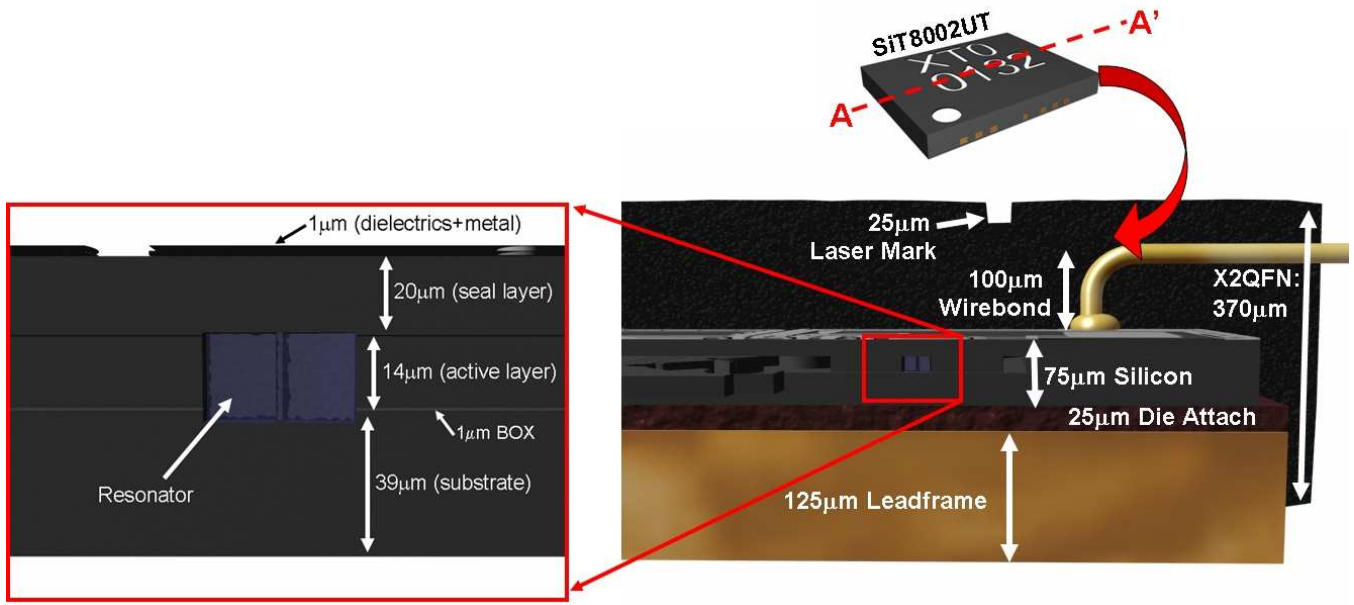


Figure 5: Cross section of the X2QFN showing manufacturing tolerances. In order to fit into the requirements of this package, 75µm-thick MEMS die are used. At this thickness, the substrate is thinned to ~39µm. As such, there is roughly an equal amount of silicon below the buried oxide as above it. This is the first MEMS resonator reported that achieves this thickness without deleterious performance implications. This extreme thinning is only possible with thin film encapsulation.

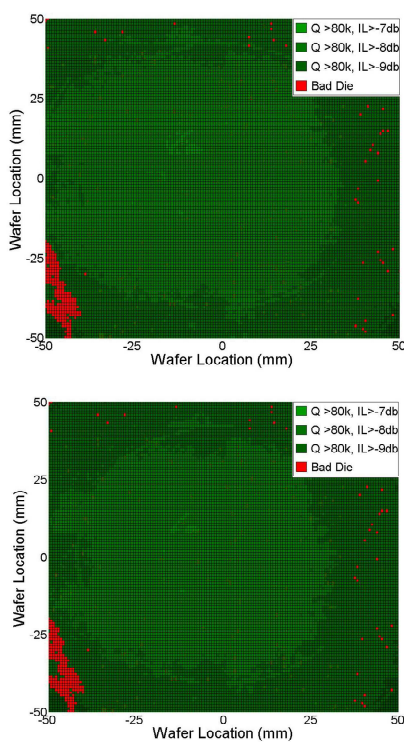


Figure 6: MEMS probe map of the center of the wafer showing resonator metrics at full thickness (top) and after thinning (bottom). Contrary to the results in [5], no significant decrease in  $Q$  (change from green at  $>80k$  to red at  $<80k$ ) is evident due to extreme thinning. Some change in insertion loss (change in shade of green) is observed; this is inaccuracy in the insertion loss measurement. This change does not materially impinge device performance.

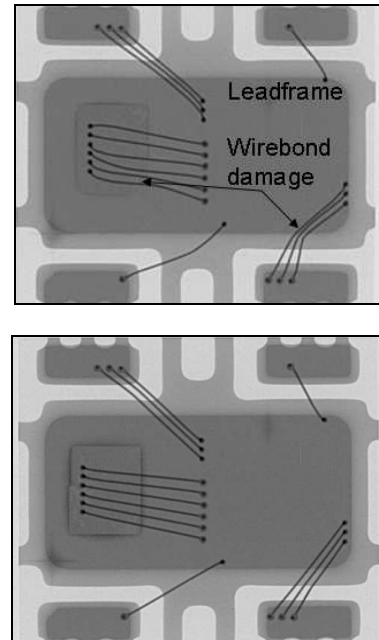


Figure 7: X-ray showing wirebond damage caused by poor molding conditions (top) and optimized construction (bottom).

## RESULTS

The packaged devices were measured to ensure compliance with thickness specifications. A Mitutoyo disk micrometer (accuracy 1µm) was used to measure the thickness of the entire package (including warpage) on 33 parts. The results are presented in Figure 8. As can be seen, the package is 370µm thick with a standard deviation of 5µm. This gives the package a 6σ confidence interval against a specification of 400µm thick.

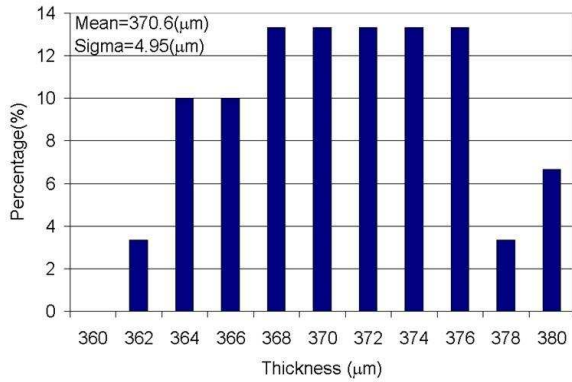


Figure 8: Histogram showing thickness measurements on the SiT8002UT.

The devices were extensively characterized. A key component of designing a thin oscillator is maintaining frequency stability of the part over temperature. Furthermore, the product must withstand the rigorous moisture requirements specified in JEDEC STD-020D. After assembly, 50 parts were randomly removed from carrier tape. The parts were placed into an oven and operated continuously from -40°C to 85°C (Industrial Temperature Range) for 5 cycles. Figure 9 shows the performance of these 50 SiT8002UT parts versus temperature (blue curve); these parts demonstrate +/-20ppm frequency stability. After the initial temperature screen, the parts were subjected to the JEDEC Moisture Sensitivity Level 1 (MSL 1) screen. The parts were then dried at 125°C for 24 hours, and then subjected to 168 hours at 85°C/85%RH and 3 260°C solder reflow cycles. As can be seen, performance is not noticeably impacted (red curve in Figure 9). The parts were also inspected with Scanning Acoustic Microscopy (C-SAM) to probe for delamination (Figure 10). As evidenced, there is no indication of delamination in these packages after MSL 1 exposure. These parts have been subsequently subjected to a full product qualification (HTOL, Biased Hast, Temp Shock, and Temp Cycle) and all units have passed the tests.

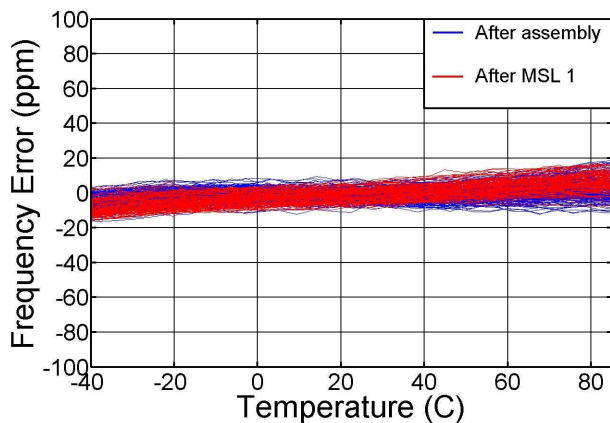


Figure 9: Frequency versus temperature (5 cycles) of the SiT8002UT (50 samples) after assembly (blue) and after MSL 1 exposure (168 hours at 85°C/85%RH, 3 cycles to 260°C). The frequency stability is +/-20ppm.

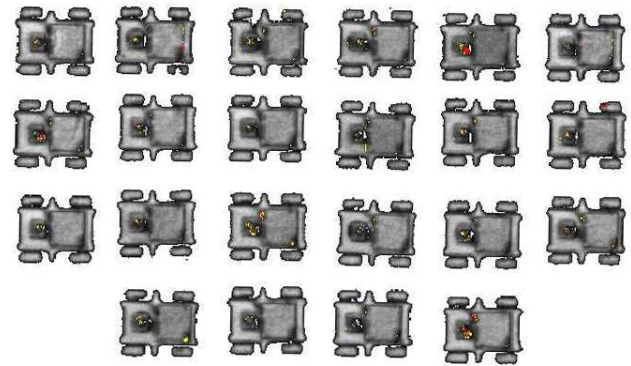


Figure 10: Scanning Acoustic Microscopy Photo of 22 SiT8002UT packages after MSL 1 exposure. No obvious package delamination can be observed. A delamination would evidence itself as a large red region within the package (this can be especially prevalent in the die attach epoxy)

## CONCLUSION

A 370μm thick, packaged MEMS oscillator has been demonstrated in multiple packaging technologies. In the course of developing this product, we have shown that it is possible to build 75μm thick MEMS resonators without noticeable deleterious performance implications. The parts were measured after fabrication and shown to have +/-20ppm frequency stability, which compares favorably with state of the art timing devices in this thickness range.

## REFERENCES

- [1] C. Beelen-Hendriks and M. Verguld, "Trends in electronic packaging and assembly for portable consumer products," *Proceedings of EPTC 2000*, pp. 24-32, 2000.
- [2] Y. Nagaura and S. Yokomizo, "The machining and characteristics of an ultra-thin, plano-convex-type quartz oscillator," *Proceedings of the 1998 IEEE Frequency Control Symposium*, pp. 844-7, 1998.
- [3] Y-H Park and K. C. Park, "High-Fidelity Modeling of MEMS Resonators – Part II: Coupled Beam-Substrate Dynamics and Validation," *IEEE Journal of Microelectromechanical Systems*, Vol. 13, No. 2, pp. 248-57, 2004.
- [4] M. Lutz, A. Partridge, P. Gupta, N. Buchan, E. Klaassen, J. McDonald, K. Petersen, "MEMS Oscillators For High Volume Commercial Applications," *Proceedings of Transducers '07*, Lyon, France, pp. 49-52, 2007.
- [5] A.-C. Wong, Y. Xie, and C. Nguyen, "A Bonded-Micro-Platform Technology for Modular Merging of RF MEMS and Transistor Circuits," *Proceedings of Transducers '01*, Munich, Germany, pp. 992-95, 2001.

# FLIP-CHIP INTEGRATED SOI-CMOS-MEMS FABRICATION TECHNOLOGY

P. J. Gilgunn<sup>1</sup>, G. K. Fedder<sup>1,2,3</sup>

<sup>1</sup>Electrical and Computer Engineering Dept., <sup>2</sup>The Institute for Complex Engineered Systems, and <sup>3</sup>The Robotics Institute, Carnegie Mellon University, Pittsburgh, Pennsylvania, USA

## ABSTRACT

A fully-dry, flip-chip fabrication technology was developed for the integration of high fill factor, silicon-on-insulator (SOI) structures and CMOS-MEMS actuators. An SOI mirror array with a fill factor of 95% and radius of curvature  $>1.3$  m was fabricated on CMOS-MEMS electrothermal actuators using this technology. The unloaded actuators achieved an optical scan range of  $>92^\circ$ . Following flip-chip bonding with high temperature epoxy, the structures were released using deep reactive ion etching (DRIE). Aspect ratio dependent etching (ARDE) modulated local structural silicon thickness on the CMOS-MEMS actuators and reduced notching and microtrenching on the posts of the SOI mirrors.

## INTRODUCTION

This paper describes a process flow in which high fill factor, silicon-on-insulator (SOI) structures were integrated with CMOS-MEMS [1] actuators using flip-chip bonding. The demonstration vehicle for this SOI-CMOS-MEMS fabrication technology was an array of 1-degree-of-freedom (1-DOF), Al-coated, single crystal silicon (SCS) mirrors, bonded with high temperature epoxy to pedestals formed in CMOS-MEMS (see Fig. 1) and anchored through electrothermal actuators. Aspect ratio dependent etch modulation (ARDEM) was a key technique in the process flow. Several artifacts, such as Al undercut on the mirror and non-planarity among array elements, can be observed in Fig. 1 and are yet to be resolved.

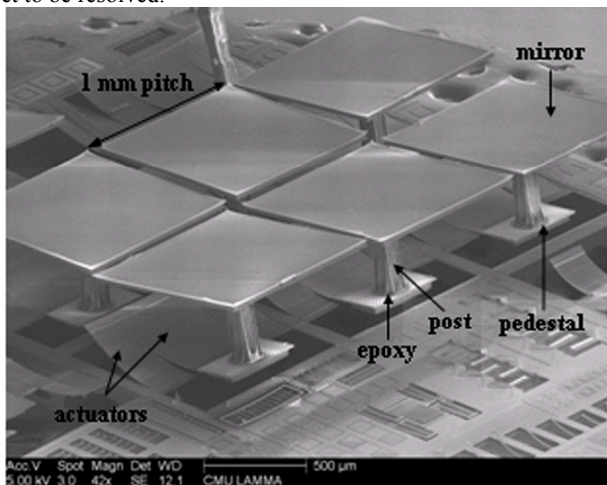


Figure 1. SEM image of a 3 x 2 array of 1-DOF, Al-coated, single crystal silicon (SCS) mirrors. The mirrors were  $25 \mu\text{m} \times 1 \text{mm} \times 1 \text{mm}$ . The SCS posts were  $500 \mu\text{m}$  tall and  $120 \mu\text{m}$  across at their widest point. The pedestals and electrothermal actuators were formed in CMOS-MEMS. SCS plates under the pedestals were bulk-Si micromachined from the backside of the CMOS substrate using aspect ratio dependent etch modulation (ARDEM). The posts were bonded to the pedestals with high temperature epoxy.

Dense packing and high fill factor in MEMS devices are desirable because they improve efficiency and resolution while reducing area consumption. Michalick [2] used flip-chip bonding to fabricate electrostatically actuated, piston-motion, MUMPS mirror arrays with a 98% fill factor. Tsai [3] demonstrated electrostatically actuated scanning mirrors for optical cross-

connects, with a fill factor of 96% in the SUMMiT-V technology. Packing densities of  $100$  cantilevers/ $\text{mm}^2$  for probe-based data storage devices were demonstrated by Despont [4] and Kim [5] using wafer-level transfer techniques and CMOS substrates.

Imaging applications benefit from large optical scanning angles and high fill factors which increase scan area, light coupling and spatial resolution. However, the goals of high fill factor and large actuator stroke have not been compatible up to now. Michalick's piston mirrors had a  $600 \text{nm}$  range of motion and Tsai's scanning mirrors had an optical scanning angle of  $17.6^\circ$ . In contrast, the electrothermally actuated CMOS-MEMS scanning mirror reported by Jain [6] had an optical scan angle of  $80^\circ$ , but a fill factor of only 60%.

We pioneered the SOI-CMOS-MEMS fabrication technology reported in this paper to simultaneously achieve high fill factor and large range of motion in arrayed MEMS devices. We decoupled mirror and actuator design so the properties and performance of each could be optimized independently. The material choices in this paper were made on the basis of the needs of the demonstration application and should not be considered as exclusive. Process scalability, manufacturability and robustness were concerns that we did not address experimentally, to date, and as such, no data on these subjects are presented.

## FABRICATION PROCESS FLOW

The fabrication technology consisted of three modules: 1. post-CMOS processing (Fig. 2), 2. SOI mirror-post processing (Fig. 3), and 3. Flip-chip bonding and release processing (Fig. 4). All processing was done at chip level.

Deep reactive ion etch (DRIE) processes were performed on a Surface Technology Systems (STS) Advanced Silicon Etch (ASE) inductively coupled plasma (ICP) etch tool [7]. Anisotropic silicon etching was done with a  $\text{SF}_6/\text{O}_2/\text{C}_4\text{F}_8$ , Bosch-type process [8]. A  $\text{SF}_6$  plasma was used for isotropic etching.

During plasma etch processes, CMOS-MEMS and SOI die were mounted on a resist-coated, silicon carrier wafer using  $150^\circ \text{C}$  Revalpha thermal release tape from Nitto Denko. This material proved resistant to 7+ hours of plasma etch processing, had very low residual adhesion following thermal release and left no observable defects on the die.

### Post-CMOS Process Module (Fig. 2)

CMOS-MEMS utilizes foundry CMOS die as a starting material (Fig. 2 (a)) [1]. The die used in this work was fabricated by Jazz Semiconductor, Newport Beach, CA in a four-metal,  $0.35 \mu\text{m}$ , SiGe BiCMOS process technology. The silicon substrate, as received from the foundry, was  $272 \pm 5 \mu\text{m}$ .

The group of steps from Fig. 2 (b) to (f) defined the final release etch mask and a SCS plate under the pedestal, which received the SOI post during flip-chip bonding. CMOS interconnect (a stack of Al and TiW, in this case) and ILD (various types of  $\text{SiO}_2$ ) hold residual stress that is relieved by bending after the CMOS substrate is removed. The effect of residual stress can be observed in the curling of the electrothermal actuators in Fig. 1, but the SCS plate prevented the pedestal from curling.

The backside of the die was DC sputtered with  $100 \text{nm}$  of Al at  $20^\circ \text{C}$  and patterned using backside-aligned, direct-write, chip-level, laser lithography on a Heidelberg Instruments DWL 66

(Fig. 2 (b)). The Al was wet etched to form a hardmask (Fig. 2 (c)) to protect the substrate during the CMOS-MEMS backside release etch process.

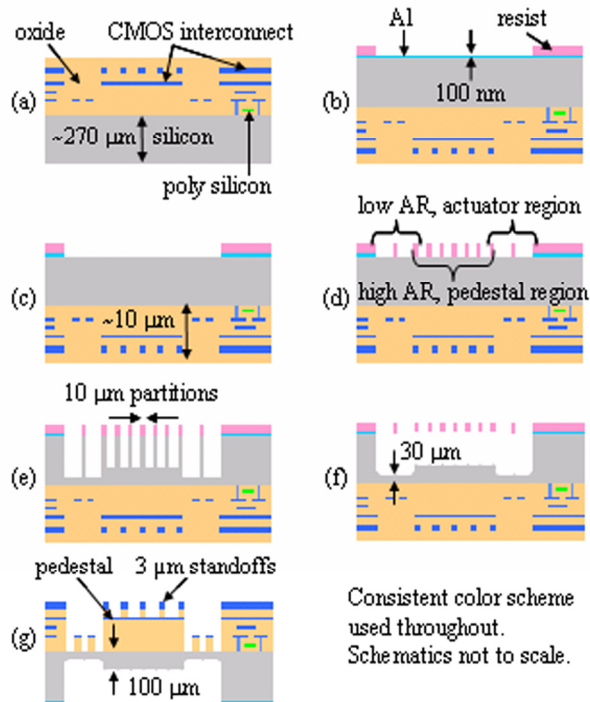


Figure 2. Post-CMOS process module schematic. Resist strip and clean steps not shown. (a) Foundry CMOS die. (b) CMOS backside Al hardmask DC sputter deposition. (c) Al hardmask patterning using backside-aligned, direct-write lithography and Al wet etch. (d) ARDEM patterning using backside-aligned, direct-write lithography. (e) Anisotropic, Bosch-type DRIE. (f) Isotropic  $SF_6$  plasma etch to remove ARDEM partitions. (g) Frontside sacrificial ILD etch using uppermost CMOS interconnect layer as etch mask.

Fig. 1 (d) and (e) show ARDEM applied during the anisotropic etch to create a backside mesa in the CMOS substrate that would eventually become the plate under the pedestal. ARDE is typically a reduction in etch rate with increasing aspect ratio (AR) of the feature being etched ( $AR = \text{feature depth}/\text{characteristic feature dimension}$ ) [9][10]. It is strongly coupled with the microloading and pattern shape effects [11]. We characterized ARDE using long, trench-like test structures ( $\text{length}/\text{width} \geq 4$ ). Our characterization was not sufficient to compensate for the microloading variation between the center and edge of the device array, so a consistent pattern was used. We believe our application is the first time ARDE has been used to fabricate structural silicon elements in a bulk-Si, backside, through-wafer etch process flow. An isotropic etch removed the ARDEM partitions (Fig. 2 (f)).

The post-CMOS process module ends with the removal of sacrificial ILD using a  $CF_4/CHF_3/O_2$  plasma etch process on a Plasmatherm 790 (Fig. 2 (g)). The uppermost CMOS interconnect layer in a stack acted as an etch mask and defined the final feature. The silicon substrate was exposed following this process step.

### SOI Mirror-Post Process Module (Fig. 3)

The mirror and post of the device was fabricated from a double-sided-polished SOI wafer to enable robust lithographic patterning of both sides of the wafer. The device layer was  $25 \mu\text{m}$  thick, the buried oxide was  $1 \mu\text{m}$  thick and the handle layer was

$500 \mu\text{m}$  thick. The thickness of the device layer was based on finite element simulations of the assembled device and the goal of placing the first plate mode of the mirror at least  $10\times$  the value of the highest bending mode of the actuator. The handle layer thickness was selected to enable a mechanical stroke of  $\pm 45^\circ$  for a  $1 \text{ mm} \times 1 \text{ mm}$  mirror. The buried oxide thickness was based on a measured Si:oxide selectivity of 150:1 for the anisotropic etch.

The mirror surface was formed in the first step (Fig. 3 (a)) by DC sputtering a  $100 \text{ nm}$  layer of Al at  $20^\circ \text{C}$ , patterning it using a Karl Suss MA56 contact aligner and wet etching it. The mirror surface also served as the hardmask for the final mirror release etch. A  $100 \text{ nm}$  layer of Al was DC sputtered on the handle layer to act as a secondary hardmask for the post etch. ARDEM patterning was done on a Karl Suss MA6 backside aligner (Fig. 3 (b)). The two mask layers were needed due to the process limitation of patterning a sufficiently thick layer of resist to withstand a 7 hour anisotropic post etch (Fig. 3 (c)). The Al was wet etched prior to post etch.

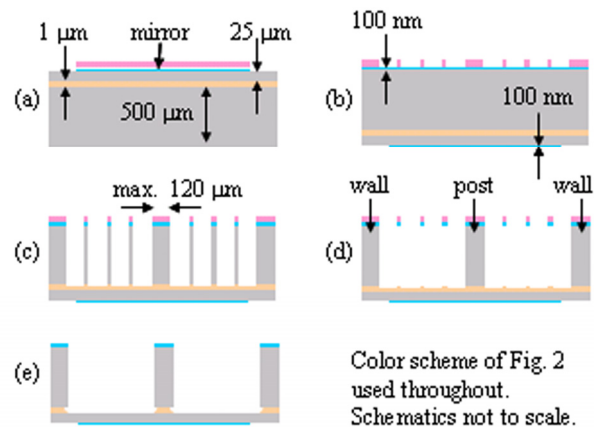


Figure 3. SOI mirror-post process module. Al wet etch, resist strip and clean steps not shown. (a) Al mirror sputter deposition and patterning using contact aligner. (b) Al hardmask sputter deposition and ARDEM patterning using backside-aligned contact aligner. (c) Anisotropic, Bosch-type DRIE. (d) Isotropic  $SF_6$  etch to remove ARDEM partitions. (e) Buried oxide layer removal in hydrofluoric acid.

ARDEM was applied in the post etch process to control the etch rate over the large exposed area ( $3 \text{ mm} \times 3 \text{ mm}$ ) in the manner of Kiihamaki [9] and to reduce microtrenching and notching after the buried oxide was exposed during the overetch, as demonstrated by Volland [12]. The etch/passivation ratio in the anisotropic etch step was varied from 11 s etch/9 s passivation in 45 minute steps up to 11.8 s etch/8.2 s passivation to further compensate for ion deflection and maintain ARDEM partition integrity throughout the post etch. Following anisotropic etch, a 30 s  $O_2$  polymer removal etch was performed, followed by a 2 min isotropic etch to remove the ARDEM partitions (Fig. 3 (d)).

In the final step, the buried oxide was removed in buffered hydrofluoric acid using the wall of the mirror chip as a container (Fig. 3 (e)). The wall provided structural integrity during handling and later as a mechanical buffer during flip-chip bonding.

### Flip-Chip Bonding and Release Process Module (Fig. 4)

Flip-chip bonding was performed on a Laurier M9-A device bonder. During bonding, the CMOS-MEMS die and the SOI die were held by vacuum. The device bonder was used for a dipping step and a bonding step. The SOI die was mounted on the bonder upper chuck for both flip-chip process steps.

A high-temperature, low viscosity, two-part epoxy (Epo-Tek 377) was applied to the mirror posts to a depth of 40  $\mu\text{m}$  using a dipping method (Fig. 4 (a) and (b)). The depth of epoxy coverage on the posts was fixed by the depth of the recess that accepted the wall. ARDEM was used to achieve a shallower depth for this recess than the epoxy well.

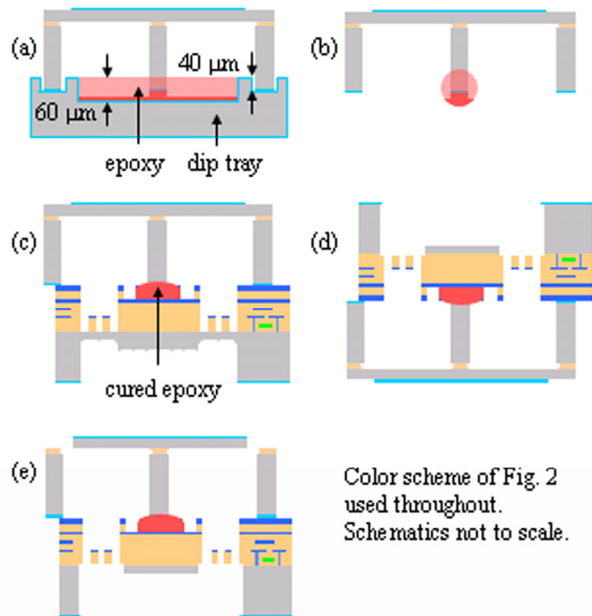


Figure 4. SOI-CMOS-MEMS flip-chip bonding and release etch process module. (a) SOI mirror die dipping in low viscosity, high temperature epoxy. (b) Conceptualization of epoxy ball on the end of the post. (c) Flip-chip bonded and cured SOI-CMOS-MEMS die. (d) Backside anisotropic release etch of CMOS-MEMS actuators. (e) Frontside anisotropic release etch of SOI mirrors.

The SOI and CMOS-MEMS die were bonded using an initial contact force of 2 N (770 kPa) (Fig. 4 (c)). The temperature was ramped up to 150° C and held for 30 mins to achieve a partial epoxy cure. During this time the applied force was allowed to float and reached a maximum of 10 N. The assembled die was cured for a further 12 hours in a 150° C oven.

The CMOS-MEMS actuators were released using an anisotropic etch with the Al from Fig. 2 (c) as hardmask (Fig. 4 (d)). The assembled die was flipped over to release the mirrors using an anisotropic etch (Fig. 4 (e)). The perimeter wall was removed manually to expose the assembled devices, however, the wall could be used as part of a chip level package to prevent fouling of the device.

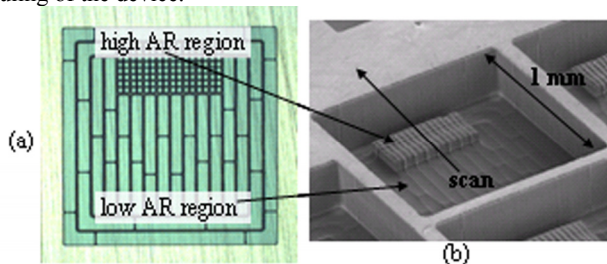


Figure 5. (a) Photo image of the CMOS backside resist pattern prior to DRIE. The high AR region is under the pedestal and the low AR region under the actuator. (b) SEM image of the backside etch pit following DRIE and ARDEM partition removal.

## PROCESS AND DEVICE CHARACTERIZATION

The mesa in the etch pit is shown in Fig. 5 (b). The difference in etch depth between the low AR actuator region and the high AR pedestal region (Fig. 5 (a)) was measured at 70  $\mu\text{m}$  using a profilometer.

Fig. 6 (a) shows the sacrificial ARDEM pattern on the device-side of the SOI wafer. The partitions were 10  $\mu\text{m}$  wide, and the space was 50  $\mu\text{m}$ , so the final AR was  $\sim 10:1$  when the buried oxide was exposed. A close-up of one of the posts is shown in Fig. 6 (c). Microtrenching can be observed approximately midway up the post and there was micron-scale notching at the base, but the post was structurally sound.

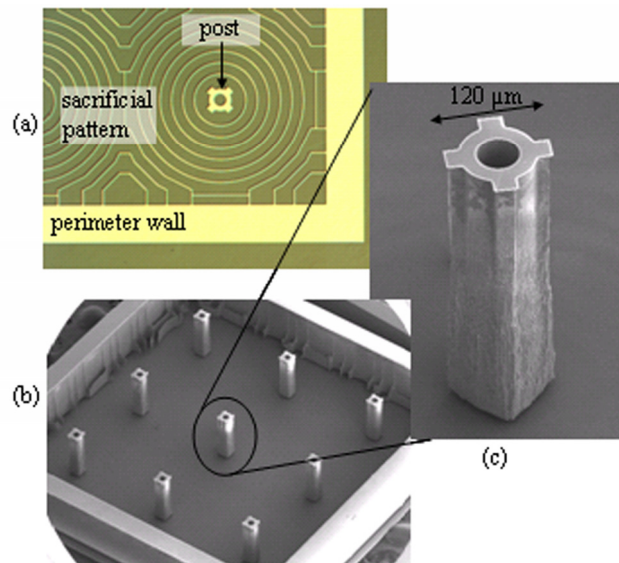


Figure 6. (a) Corner of post mask showing ARDEM pattern surrounding the post. (b) SEM image of the post side of the SOI mirror die following buried oxide removal. (c) SEM close-up of a post.

The assembled SOI-CMOS-MEMS die is shown in Fig. 7. The perimeter wall crushed some of the circuitry during flip-chip bonding, making the final device electrically inoperable. A mask revision was needed to resolve this issue, but a further integrated run has not been completed yet, so the electrical data shown in this section is for an unloaded actuator.

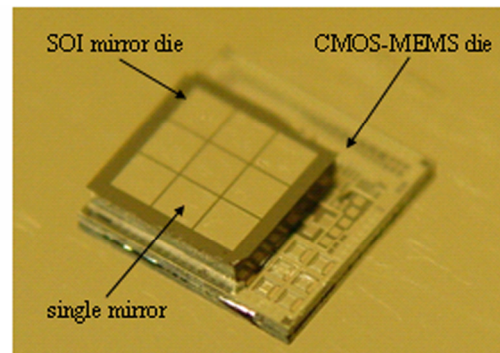


Figure 7. Flip-chip bonded SOI-CMOS-MEMS die before release.

The unloaded electrothermal actuators (Fig. 8) were tested by reflecting a laser off the pedestal and measuring the angular deflection of the beam on a curved screen of fixed radius. The positive sense actuator and negative sense actuator achieved an optical scan range of 59° and 33°, respectively, giving a total optical scan range of 92°. The actuator electrical resistance at

20°C was 220 Ω and the power consumption at maximum displacement was 13.7 mW and 21.1 mW for the positive and negative actuators, respectively.

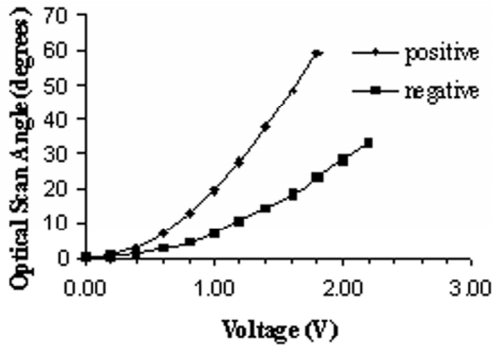


Figure 8. Optical scan range measurements of an unloaded electrothermal actuator.

The radius of curvature and the surface roughness of the released mirror was  $>1.3$  m and 8 nm, respectively, measured on a WYCO NT3300 using phase shifting interferometry. A mirror die was bonded directly to a silicon wafer to eliminate the Al undercut artifact from the characterization of mirror flatness (see Fig. 9) and released using the same anisotropic etch process.

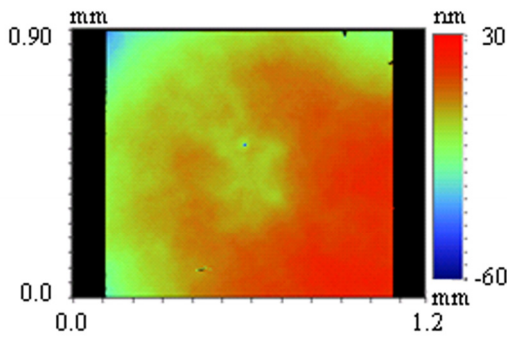


Figure 9. Phase shifting interferometric scan data for a mirror bonded directly to a silicon substrate and release etched.

The SCS plate under the pedestal is shown in Fig. 10. The final plate thickness was 50 μm and no stress relief curling was observed in the pedestal. 3 μm tall standoffs were designed on the pedestal to provide a constant thickness epoxy bond line and to increase the epoxy-device surface contact area.

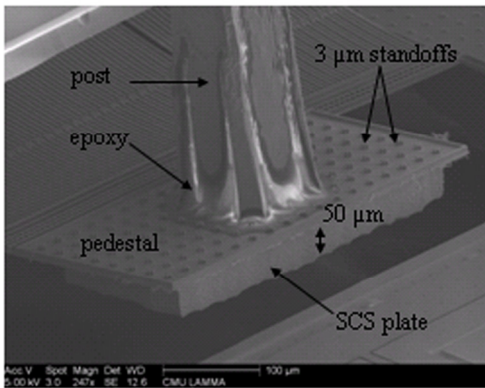


Figure 10. SEM image of a CMOS-MEMS pedestal and a SOI mirror, showing the SCS plate under the pedestal.

## IMPACT AND OUTLOOK

The design of large stroke CMOS-MEMS actuators was decoupled from the design of SCS mirrors formed in SOI to achieve 95% fill factor in a 3 x 2, 1-DOF mirror array, through the use of SOI-CMOS-MEMS flip-chip integration. A fully-dry release etch was performed separately on the CMOS-MEMS actuators and the SOI mirrors following flip-chip bonding.

ARDEM was used to achieve multi-thickness structures using a single photomask and to overcome notching and microtrenching in SOI etching. Additional characterization of pattern based etch rate variation would enable greater refinement in bulk-silicon structures using a single mask.

Future research and development will focus on the elimination of release etch artifacts, scaling the fabrication technology to smaller devices, demonstrating higher-DOF designs and quantifying the mechanical robustness and long-term operational reliability of the fabricated devices.

## ACKNOWLEDGMENTS

This work was sponsored by Boeing. The authors thank Chris Bowman and the CMU Nanofab staff for their equipment support.

## REFERENCES

- [1] G. Fedder, et al., "Laminated high-aspect-ratio microstructures in a conventional CMOS process," *Sens. Act. A Phys*, 57, 103 (1996).
- [2] M. A. Michalick, et al., "Flip-chip fabrication of advanced micromirror arrays," *Sens. Act. A*, 95, 152 (2002).
- [3] J. Tsai, M. C. Wu, "Gimbal-less MEMS two-axis optical scanner array with high fill factor," *J. MEMS*, 14, 1323 (2005).
- [4] M. Despont, et al., "Wafer-scale microdevice transfer/interconnect: Its application in an AFM-based data-storage system," *J. MEMS*, 13, 895 (2004).
- [5] Y. Kim, et al., "Thermo-piezoelectric Si<sub>3</sub>N<sub>4</sub> cantilever array on CMOS circuit for high density probe-based data storage," *Sens. Act. A*, 135, 67 (2007).
- [6] A. Jain, et al., "A two-axis electrothermal micromirror for endoscopic optical coherence tomography," *IEEE J. Sel. Top. Quantum Electronics*, 10, 636 (2004).
- [7] J. K. Bhardwaj, H. Ashraf, "Advanced silicon etching using high density plasmas," *Proc. SPIE 2639*, 224 (1995).
- [8] F. Laermer, A. Schilp, "Method of anisotropically etching silicon," U.S. Patent No. 5,501,893 (1996).
- [9] J. Kiihamäki, et al., "Depth and profile control in plasma etched MEMS structures," *Sens. Act. A*, 82, 234 (2000).
- [10] T. A. Chou, K. Najafi, "Fabrication of out-of-plane curved surfaces in Si by utilizing RIE lag," *Tech. Digest 15th IEEE Int. Conf. on Microelectromechanical Systems*, Las Vegas, NV, (2002), pp. 145 - 148.
- [11] T. F. Hill, et al., "Pattern density based prediction for deep reactive ion etch (DRIE)," *Tech. Dig. of the 2004 Solid-State Sensor, Actuator and Microsystems Workshop*, Hilton Head Isl., SC, 6/6-10/2004, Transducer Research Foundation, Cleveland (2004), pp. 320 - 323.
- [12] B. E. Volland, et al., "The application of secondary effects in high aspect ratio dry etching for the fabrication of MEMS," *Micro. Eng.*, 57 - 58, 641 (2001).

# NEW ARCHITECTURAL DESIGN OF A TEMPERATURE ROBUST MEMS GYROSCOPE WITH IMPROVED GAIN-BANDWIDTH CHARACTERISTICS

A.A. Trusov, A.R. Schofield, and A.M. Shkel

MicroSystems Laboratory, University of California, Irvine, CA, USA

## ABSTRACT

This paper reports a new MEMS vibratory rate gyroscope designed with increased robustness to fabrication imperfections and variations in environmental conditions. The distinct feature of the design is the increased response gain. The proposed architecture utilizes a single degree-of-freedom (DOF) drive-mode and a fully coupled 2-DOF sense-mode. The drive-mode operational frequency and the sense-mode bandwidth can be set independently, relaxing the tradeoff between the gain, die size, and detection capacitance, inherent to the previously reported robust gyroscopes with dynamic vibration absorber (DVA) architecture of the 2-DOF sense-mode. Prototypes with 2.5 kHz operational frequency were characterized in air and demonstrated sense-mode 3 dB bandwidth of 250 Hz. The uncompensated temperature coefficients of bias and scale factor were  $313\text{ }^{\circ}\text{h}/^{\circ}\text{C}$  and  $351\text{ ppm}/^{\circ}\text{C}$ , respectively. Using off-chip detection electronics, the rate sensitivity was  $56\text{ }\mu\text{V}/^{\circ}\text{s}$ ,  $\text{ARW} = 0.09\text{ }^{\circ}\text{s}/\sqrt{\text{Hz}}$ , bias instability  $= 0.08\text{ }^{\circ}\text{s}$ , and  $\text{ARRW} = 0.03\text{ }^{\circ}\text{s}/\sqrt{\text{Hz}}$ .

## INTRODUCTION

The operation of micromachined vibratory gyroscopes is based on a transfer of energy between two modes of vibration caused by the Coriolis effect [1]. Conventional implementations often utilize single degree of freedom (DOF) drive- and sense-modes [2, 3]. In mode-matched implementations, the mechanical gain is proportional to the sense-mode quality factor, which allows increasing the sensitivity, theoretically unlimitedly. However, the increase in quality factor of a mode-matched gyroscope is always at the cost of sensor robustness, temperature drift, bandwidth, and limited linear operational range. Also, precise matching of the operational modes over temperature ranges defined by application requirements is practically challenging. Alternatively, the modes of operation can be designed with a certain frequency mismatch [2, 3]. Even though this approach improves the robustness and the bandwidth characteristics, the limitations of the design space (1-DOF drive and 1-DOF sense) dictate a tradeoff between achieved robustness/bandwidth and gain.

For increasing robustness of vibratory gyroscopes, it is beneficial to design 1-DOF drive- and 2-DOF sense-modes so that the drive-mode resonant frequency is placed between the two resonant peaks of the sense-mode. A design of sense-mode with 2-DOF dynamic vibration absorber (VBA) architecture has been previously proposed and demonstrated to provide robust operation with a 200 Hz bandwidth using a micromachined prototype with a 750 Hz drive-mode operational frequency [4]. For this design concept, increasing the operational frequency would further increase the bandwidth, while also resulting in a decrease of the response gain. Adapting the DVA-based gyroscope design for operational frequencies above 1 kHz while maintaining the sense-mode peaks at a practical spacing is challenging due to the limitation of the design space and involves a stringent tradeoff between the die size and detection capacitance [5].

Most real-world applications, such as automotive, military, and consumer electronics, require robust yet sensitive gyroscopes with operational frequencies above several kHz in order to suppress the effect of environmental vibrational noise [6]. At the same time, the desired mechanical bandwidth of the sense-mode is

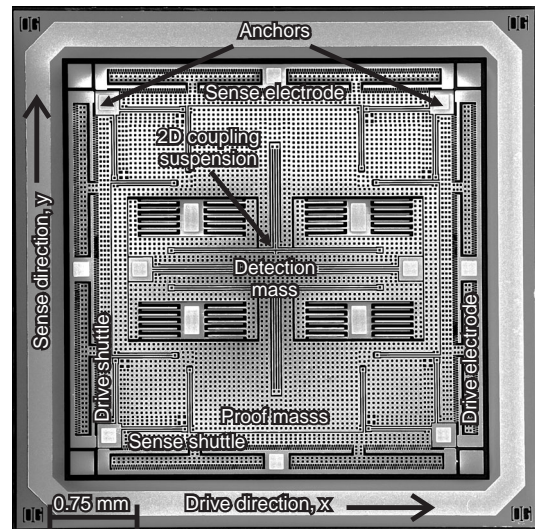


Figure 1: SEM image of a fabricated MEMS gyroscope with 1-DOF drive-mode and a fully coupled 2-DOF sense-mode providing wide, temperature-robust bandwidth while minimizing the sacrifice in gain.

typically above 100 Hz, but not more than 400 Hz [2, 3]. In this paper, we introduce an architecture, which extends the design space of the previously reported gyroscopes with 2-DOF sense-modes and overcomes the limitations imposed by the DVA dynamics. The device architecture is not just a minor optimization of previously reported designs, but rather a sharp conceptual deviation that introduces a new design architecture based on a different arrangement of structural components favorably shaping the response characteristics of robust gyroscopes.

## STRUCTURAL DESIGN AND DYNAMICS

### Structural Design

The structural implementation of the proposed gyroscope is shown in Fig. 1. It implements the novel fully coupled architecture shown in Fig. 2. The device consists of an anchored outer frame, two drive-mode and two sense-mode shuttles, a proof mass, a detection mass, and a central anchor. Each of the two drive-mode and two sense-mode shuttles is suspended relative to the fixed frame by two springs. These flexures restrict the motion of the shuttles to their respective axes. Similar suspension elements couple the four shuttles to the proof mass. The described configuration of 4 shuttles, 16 suspension elements, and a proof mass forms a symmetrically decoupled suspension. This suspension architecture was introduced in [7] and later adapted by several groups [8, 9] for conventional vibratory gyroscopes with 1-DOF drive- and 1-DOF sense-modes. In this work, the conceptual architecture of the suspension is utilized in a gyroscope with a 2-DOF sense-mode for the first time.

The proof mass  $m_p$  is suspended in  $x$ - $y$  plane with total drive and sense axes stiffnesses of  $k_1$ . Using the electrodes on the drive-mode shuttles, the mass is driven into a drive-mode oscillation to form a Coriolis element sensitive to rotation along the  $z$ -axis.

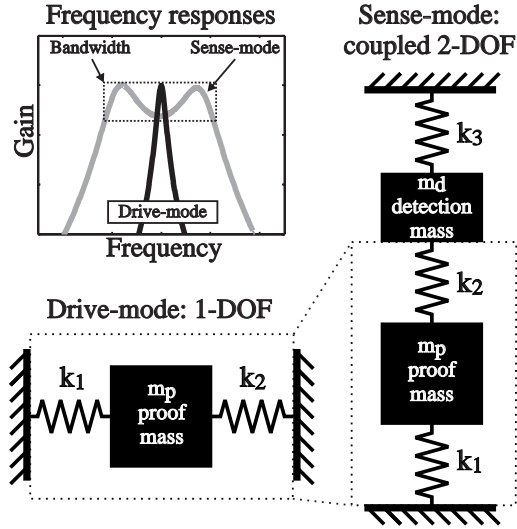


Figure 2: Drive- and sense-mode lumped models. The inset illustrates the response characteristics of the gyroscope.

Unlike the conventional case [8, 9], the Coriolis-induced motion is not directly picked-up from the proof mass,  $m_p$ , instead, the proof mass is coupled to a second, detection mass,  $m_d$ . The coupling flexure is bi-directional, with equal x and y stiffnesses  $k_2$ . The detection mass is also coupled to the substrate with an inner suspension,  $k_3$ . During rotation, the Coriolis acceleration of the proof mass is transferred to the detection mass, which responds in a wide frequency bandwidth due to the coupled dynamics of the proposed 2-DOF sense-mode.

Fig. 2 shows the lumped element drive and sense dynamic model of the proposed gyroscope. The drive-mode is a single-DOF system with mass  $m_p$  and stiffness  $k_1+k_2$ . The sense-mode is a complete 2-DOF system, with two masses,  $m_p$  and  $m_d$ , and three stiffnesses  $k_1$ ,  $k_2$ ,  $k_3$ . The damping terms  $c_1$ ,  $c_2$ , and  $c_3$  are located parallel to the respective spring elements.

### Dynamics and Selection of Parameters

The drive-mode of the gyroscope is a single-DOF resonator with undamped natural frequency  $\omega_n = \sqrt{(k_1+k_2)/m_p}$ . The sense-mode is a 2-DOF dynamic system with in-phase and anti-phase resonant modes. If the y-axis displacement of the proof mass is considered as an output of the system, the corresponding transfer function has a zero (“anti-resonance” condition) at the frequency  $\omega_0 = \sqrt{(k_2+k_3)/m_d}$ . The proof mass anti-resonance is always located between the two sense-mode resonances and provides a convenient design guideline for selecting parameters of the system.

The available structural design parameters for the proposed gyroscope are the two masses  $m_p$  and  $m_d$  and three stiffnesses  $k_1$ ,  $k_2$ , and  $k_3$ . These five parameters define the location of the drive-mode resonant frequency, i.e. the operational frequency of the gyroscope, and the locations of the two sense-mode resonant peaks, which define the bandwidth of the gyroscope. In practice, the operational frequency and bandwidth requirements are dictated by the specific application. We denote the desired operational frequency by  $\Phi$  and the sense-mode peak spacing by  $\Delta\Phi$ . To ensure the optimal positioning of the drive-mode resonance with respect to the 2-DOF sense-mode response, we require that the drive-mode resonance coincides with the proof mass anti-resonance in the sense-mode.

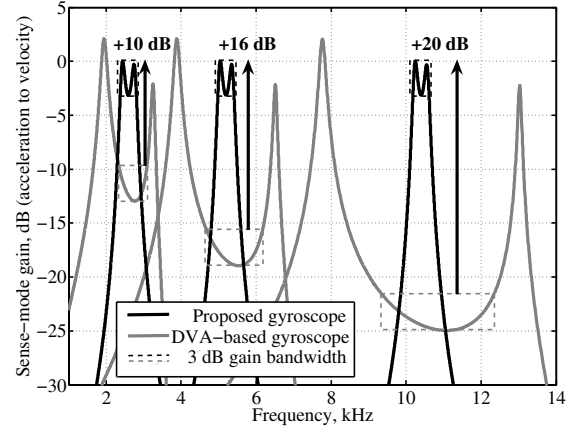


Figure 3: Frequency scaling of the sense-mode frequency response of the proposed and DVA-based gyroscopes.

We assume that the masses of the gyroscope together with the capacitive electrodes are implemented first. Then, the three stiffnesses  $k_1$ ,  $k_2$ , and  $k_3$  become functions of the two masses  $m_p$  and  $m_d$ , and selection of the desired operational frequency  $\Phi$  and the frequency spacing  $\Delta\Phi$ . By solving the algebraic eigenvalue equation, the stiffnesses of the 2-DOF sense-mode are obtained,

$$\begin{cases} k_1 = m_p \Phi^2 - k_2 \\ k_2 = \Delta\Phi \sqrt{m_p m_d} \sqrt{\Phi^2 - 0.25 \Delta\Phi^2} \\ k_3 = m_d \Phi^2 - k_2 \end{cases} \quad (1)$$

Unique solutions exist as long as  $\Phi \geq \Delta\Phi/2$ , which holds for any physically meaningful combination of the operational frequency and the frequency spacing.

For both the proposed gyroscope and the DVA-based design [4], the gain is inversely proportional to the sense-mode peak spacing. In the DVA-based design, the peak spacing cannot be adjusted freely without a sacrifice in detection capacitance and/or enlargement of the die due to the  $m_d/m_p$  mass ratio constraint [5]. This limitation is eliminated in the proposed device, where the peaks can be positioned arbitrary close to each other independent of the operational frequency and the mass ratio.

### Modeling of Gain and Bandwidth Scaling

Fig. 3 shows effects of the operational frequency scaling on the frequency response of the sense-mode for both the proposed and the DVA-based gyroscopes. Based on the parameters of the experimentally characterized devices, we set the values of the proof and detection masses to  $m_p = 4.72e-7$  kg and  $m_d = 1.35e-7$  kg. Assuming the device is operated in air, the damping coefficients are set to  $c_1 = 1e-4$  Ns/m,  $c_2 = 5e-6$  Ns/m, and  $c_3 = 2e-4$  Ns/m. The operational frequency is iterated through 2.6, 5.2, and 10.4 kHz, while the desired sense-mode frequency spacing is kept constant at 350 Hz. For the proposed gyroscope, the stiffnesses were obtained using (1).

The modeling confirms that the proposed design approach yields implementations with the prescribed operational frequency and the sense-mode frequency spacing is independent of the proof and detection mass values. Due to the flexibility of the extended design space of the proposed gyroscope, the two peaks can be placed close together. In this case, the sense-mode response of the detection mass has an increased bandwidth, composed of the two coupled resonant peaks and the region in between, while the gain is

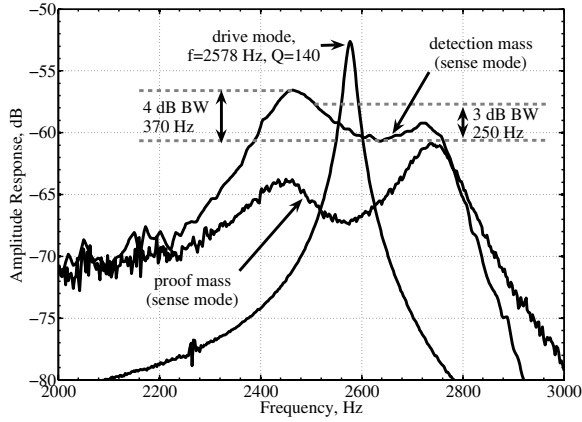


Figure 4: Experimental results demonstrate sense-mode bandwidth of several hundred Hz; the drive-mode resonance is located between the sense-mode peaks.

comparable to the mode-matched case. The described configuration is preferable for applications requiring operational frequencies in 2-20 kHz range and a bandwidth on the order of 100-350 Hz.

## EXPERIMENTAL RESULTS

### Fabrication

The fabrication of prototypes was done using an in-house, wafer-level, two-mask process using SOI wafers with 50  $\mu\text{m}$  thick device layer and 5  $\mu\text{m}$  buried oxide layer. The first mask was used to define metallization of bonding pads using a lift-off process, while the second mask defined the structural layout. After patterning photoresist with the second mask, the wafers were subjected to a Deep Reactive Ion Etching (DRIE) using a Surface Technology Systems (STS) tool. Individual dies were released in a HF acid bath. An SEM image of a fabricated device with lateral-comb drive electrodes is shown in Fig. 1.

### Structural Characterization

Experimental characterization of the lateral-comb device in atmospheric pressure is shown in Fig. 4. The measured drive-mode resonant frequency was 2.58 kHz which was located in-between the 2-DOF sense-mode resonances at 2.47 and 2.73 kHz, and the drive-mode quality factor was 140. A 250 Hz 3 dB bandwidth was formed in the sense-mode by the two resonant peaks and the flat region in-between.

### Thermal Characterization

Temperature robustness of the gyroscopes, characterized by sensitivity of the bias and scale factor to temperature variations, is a critical performance parameter of gyroscopes targeted for real-world, temperature varying environments. The prototypes were experimentally characterized in variable temperature environment using a custom made, package-level heater equipped with a feedback control. Fig. 5(a) shows characterization of the temperature drifts of the single-DOF drive-mode operated in air. Increase in system temperature from 25  $^{\circ}\text{C}$  to 125  $^{\circ}\text{C}$  resulted in a 2.25 dB drop in gain, yielding a temperature coefficient of 2404 ppm/ $^{\circ}\text{C}$ . Temperature coefficients of this order are typical in conventional gyroscopes with 1-DOF sense-modes.

Drive-mode temperature drifts are easily mitigated by closed loop operation. However, the drop of gain in the sense-mode can be detrimental to accuracy of conventional mode-matched gyroscopes. In the proposed gyroscope, the temperature drift of the

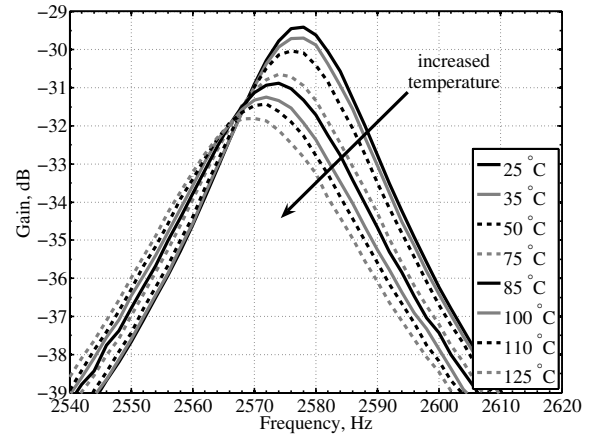


Figure 5(a): Effect of temperature variations on the drive-mode in air, showing a gain temperature sensitivity of 2404 ppm/ $^{\circ}\text{C}$ .

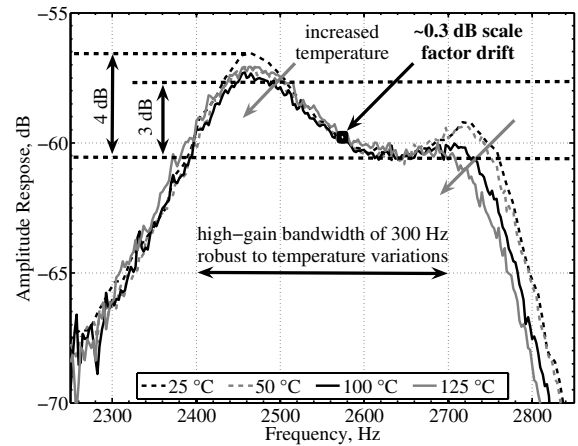


Figure 5(b): Effect of temperature variations on the sense-mode in air, revealing a robust bandwidth of 300 Hz. The uncompensated scale-factor temperature coefficient is approximately 351 ppm/ $^{\circ}\text{C}$ .

sense-mode is minimized by using the 2-DOF structure.

Sense-mode frequency-response of the detection mass was experimentally characterized at 4 different temperatures ranging from 25  $^{\circ}\text{C}$  to 125  $^{\circ}\text{C}$ , Fig. 5(b). Increase of temperature from 25  $^{\circ}\text{C}$  to 125  $^{\circ}\text{C}$  results in approximately 1 dB change of the gain in a 300 Hz bandwidth. The temperature change in the sense-mode gain evaluated at the corresponding drive-mode resonance frequency is approximately 0.3 dB over a 100  $^{\circ}\text{C}$  range. This yields the scale-factor temperature coefficient of 351 ppm/ $^{\circ}\text{C}$  – almost an 8 times improvement compared to the 1-DOF case of 2404 ppm/ $^{\circ}\text{C}$ , measured using the 1-DOF drive-mode. The temperature coefficient of the sense-mode phase was determined as 0.08  $^{\circ}/^{\circ}\text{C}$ .

### Angular Rate Characterization

The angular rate performance of the prototype was experimentally characterized in air using a computer controlled Ideal Aerosmith 1291BR rate table. The gyroscope was driven into 5  $\mu\text{m}$  peak-to-peak resonant motion using a combination of a 30 V DC bias and a 3.5 Vrms AC driving voltage applied to the anchored drive-mode lateral comb electrode. An electro-mechanical

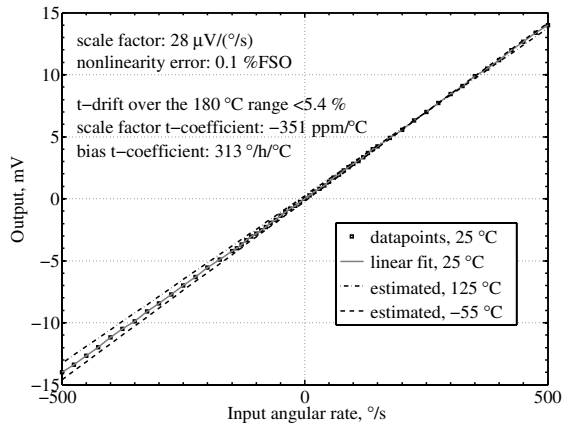


Figure 6: Experimental rate response at room temperature and estimated responses for -55 °C and 125 °C temperatures.

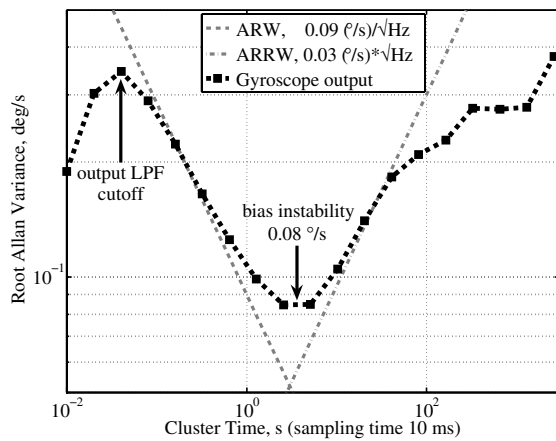


Figure 7: Allan Variance characterization of ARW, bias instability, and ARRW at zero rate, collected at 100 Hz for 4 hours.

amplitude modulation (EAM) technique was used to detect the Coriolis-induced motion in the sense-mode. The AC carrier voltage with 3.5 Vrms amplitude at 20.5 kHz frequency was applied to the mobile masses; the anchored sense-mode parallel-plate electrode was connected to the inverting input of an operational amplifier, configured as a transimpedance amplifier.

Fig. 6 shows the calibration curve obtained by programming the rate table to constant angular rate motion and observing the corresponding voltage output of the gyroscope. The collected datapoints were least squares fitted with a line to reveal the sensitivity of 28  $\mu\text{V}/\text{s}$ . As only a single sided capacitor was used, the total sensitivity of the device is 56  $\mu\text{V}/\text{s}$  for the same operational conditions. A 62.5  $^\circ/\text{s}$  rate equivalent quadrature was measured by observing the out-of-phase output of the gyroscope at zero rate.

From the structural characterization results above, the gyroscope's scale factor temperature sensitivity was estimated as 351 ppm/ $^\circ\text{C}$ . Based on the measured sense-mode phase temperature sensitivity and quadrature, the gyroscope's bias temperature sensitivity was estimated as 313  $^\circ/\text{h}/^\circ\text{C}$ . Fig. 6 shows the rate response curves for -55  $^\circ\text{C}$  and 125  $^\circ\text{C}$  temperatures calculated using the bias and scale factor temperature coefficients. The estimated maximum output drift over the 180  $^\circ\text{C}$  range is less than 5.4 %.

Fig. 7 shows experimental characterization of random noise modes using Allan Variance. The gyroscope's zero rate output

was collected for 4 hours at 100 Hz. With the off-chip detection electronics, the measured resolution (or angle random walk, ARW) at zero rate input was 0.09  $^\circ/\text{s}/\sqrt{\text{Hz}}$ , bias instability was 0.08  $^\circ/\text{s}$ , and angle rate random walk (ARRW) was 0.03  $^\circ/\text{s}/\sqrt{\text{Hz}}$ .

## CONCLUSIONS

We presented a novel gyroscope design which utilizes a 1-DOF drive-mode and a fully coupled 2-DOF sense-mode, comprising two masses with three suspension elements. To achieve optimal gain-bandwidth characteristics, the sense-mode bandwidth is defined by the two resonant peaks and the frequency region in-between. Due to the high symmetry of the structure, the operational frequency is guaranteed to be optimally placed between the sense-mode peaks even in presence of considerable fabrication imperfections. The rate sensitivity and quadrature of the gyroscope are comparable to the best reported performance numbers for MEMS gyroscopes operated in air [9]. At the same time, the gyroscope provides increased bandwidth as well as excellent robustness to fabrication imperfections and to in-operation temperature variations.

## ACKNOWLEDGEMENTS

This work was supported by the National Science Foundation grant CMS-0409923, BEI Technologies contract BEI-36974, and UC Discovery program ELE04-10202. The authors would like to acknowledge Lynn E. Costlow and Cenk Acar of Custom Sensors & Technologies Systron Donner Automotive for the useful discussions and UCI Integrated Nanosystems Research Facility (INRF) for help with the fabrication of prototypes.

## REFERENCES

- [1] A. M. Shkel, "Type I and Type II Micromachined Vibratory Gyroscopes," Proceedings of the 2006 IEEE/ION PLANS, San Diego, CA, 4/25-27/06, IEEE/ION, (2006), pp. 586-593.
- [2] M. Weinberg and A. Kourepenis, "Error Sources in In-Plane Silicon Tuning-Fork MEMS Gyroscopes," J Microelectromechanical Syst, 15, 3 (2006).
- [3] N. Yazdi, F. Ayazi, and K. Najafi, "Micromachined Inertial Sensors," Proceedings of the IEEE, 86, 8 (1998).
- [4] C. Acar and A. M. Shkel, "Inherently Robust Micromachined Gyroscopes with 2-DOF Sense-Mode Oscillator," J Microelectromechanical Syst, 15, 2 (2006).
- [5] A. R. Schofield, A. A. Trusov, and A. M. Shkel, "Structural Design Tradeoffs for MEMS Vibratory Rate Gyroscopes with 2-DOF Sense Modes," Proceedings of the ASME 2007 IDETC & CIE Conference, Las Vegas, NV, 9/4-7/07, ASME International, (2007).
- [6] A. Madni, L. Costlow, and S. Knowles, "Common Design Techniques for BEI Gyrochip Quartz Rate Sensors for Both Automotive and Aerospace/Defense Markets," IEEE Sensors Journal, 3, 5 (2003).
- [7] M. S. Kranz and G. K. Fedder, "Micromechanical Vibratory Rate Gyroscopes Fabricated in Conventional CMOS," Symposium Gyro Technology 1997, Stuttgart, Germany, 9/16-17/97, (1997), pp. 3.0-3.8.
- [8] W.-T. Sung, S. Sung, J. G. Lee, and T. Kang, "Design and Performance Test of a MEMS Vibratory Gyroscope with a Novel AGC Force Rebalance Control," J of Micromechanics and Microengineering, 17, 10 (2007).
- [9] S. E. Alper, K. Azgin, and T. Akin, "A High-Performance Silicon-on-Insulator MEMS Gyroscope Operating at Atmospheric Pressure," Sensors and Actuators, A: Physical, 135, 1 (2006).

# INTEGRATED MEMS SWITCH TECHNOLOGY ON SOI-CMOS

J. Costa<sup>1</sup>, T. Ivanov<sup>1</sup>, J. Hammond<sup>1</sup>, J. Gering<sup>1</sup>, E. Glass<sup>1</sup>, J. Jorgenson<sup>1</sup>, D. Dening<sup>1</sup>, D. Kerr<sup>1</sup>  
J. Reed<sup>2</sup>, S. Crist<sup>2</sup>, T. Mercier<sup>2</sup>, S. Kim<sup>2</sup>, P. Gorisse<sup>3</sup>

<sup>1</sup>RFMD, Greensboro, North Carolina, USA

<sup>2</sup>RFMD, Charlotte, North Carolina, USA

<sup>3</sup>RFMD, Toulouse, France

## ABSTRACT

We describe an RF MEMS contact switch technology that has been integrated above a 0.5um silicon RFCMOS-on-SOI process. This integration strategy combines a MEMS gold cantilever contact-switch with a custom silicon-on-insulator IC platform. This IC platform provides several power management functions critical for MEMS including high voltage generation, control and analog/digital/RF circuits... The technology also includes a wafer-level-package dielectric encapsulation process for the MEMS device which is hermetic and compatible with low cost packaging processes.

## INTRODUCTION

### MEMS switch requirements for wireless applications

Despite early demonstrations [1][2][3] of nearly ideal insertion loss, power handling, and linearity characteristics, RF MEMS switches, be it either contact- or capacitive-type, have failed to present day to penetrate any large or medium scale application in the RF market. Despite these obvious superior RF characteristics, four major factors have prevented RF MEMS switches from widespread use when compared to conventional solid-state FET switch solutions:

- 1) High actuation voltages (30-100V) which are typically required for reliable MEMS switch electrostatic actuation (versus 3-5V required for FET switches) require the user to provide external high voltage supplies;
- 2) MEMS switches require complex and expensive hermetic packaging solutions, whereas FET switches can be packaged using very low cost plastic overmold packaging technologies;
- 3) RF MEMS switches are typically slow (10us to 1ms typical) compared to sub-uS switching times for a solid-state FET. This is in part due to the mechanical nature of the switch which must move a conductor across a gap before final contact is established;
- 4) Long term reliability, RF power degradation and general lifetime requirements are not well understood for RF MEMS switches.

These factors, coupled with the relatively low cost and high process maturity of solid state FET switches, processed in either GaAs[4] or silicon-on-sapphire (SOS) [5] technology solutions, have essentially kept RF MEMS switches from having any significant participation in large-scale commercial applications. In particular, the cellular handset puts an even higher constraint on RF switching solutions utilizing MEMS due to high volume, large number of switching events, and typically low profit margin requirements of any of its RF chain components.

With the advent of 3G and 4G cellular communications platforms, the need for a high performance and highly integrated switch module as well as an adaptive power amplifier strategy capable of covering multiple bands and standards has become extremely desirable. These are complex applications that can greatly benefit from the higher performance of RF MEMS switches and can potentially tolerate the needed overhead (such as

charge pumps and voltage actuation circuitry) required.

In this paper we describe the development of RFMD's above-IC MEMS technology on SOI-CMOS. The MEMS switch is capable of meeting frequency and power (>2W) specifications needed for current cellular communication systems. This program is geared towards integrating a MEMS gold cantilever contact switch technology on a custom silicon-on-insulator IC platform to provide all of the necessary MEMS power management functions (high voltage charge pumps, control and timing signals), as well as an LDMOS silicon power amplifier and required digital and analog circuitry. This technology also includes a WLP (wafer level package) process which allows for a low cost hermetic packaging flow consistent with the industry's need to provide flip-chip solutions.

## FABRICATION

### SOI RFCMOS Technology

The above-IC MEMS process described in this work uses as a starting wafer a SOI (silicon-on-insulator) RFCMOS technology previously described in the literature [6]. This custom-developed technology is manufactured at JAZZ Semiconductor (Newport Beach, CA, USA). The SOI substrates used in this technology are fabricated by SOITEC (Bernin, France). The SOI silicon technology integrates on a single platform many of the necessary blocks needed for portable wireless applications, such as digital/analog mixed-mode components, solid-state power switches, as well as an RF power LDMOS transistor suitable for cellular PA operation (Figure 1).

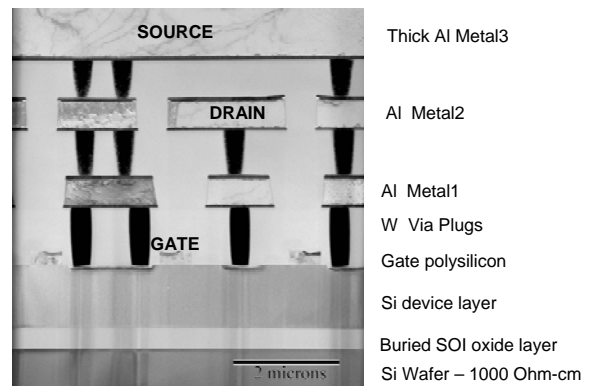


Figure 1. TEM cross-section of an LDMOS power FET built in the SOI silicon technology used as a starting wafer for our MEMS above-IC integration.

This 200mm SOI RFCMOS technology was selected for our MEMS process because of two distinct factors:

- 1) The handle wafer of SOI substrate utilized in this technology has a very high resistivity (1000 Ohm-cm typical), which is 2 to 3 orders of magnitude higher when compared with starting substrates used in conventional silicon CMOS technologies. The high

resistivity of the SOI silicon handle wafer yields superior RF characteristics compared with those measured on standard silicon substrates and also allows for the integration of higher Q matching components, such as inductors and Metal-Insulator-Metal capacitors.

- 2) The SOI technology allows for nearly ideal isolation of devices, since the different transistors and diodes do not share a common substrate terminal.

This latter feature of the SOI technology is particularly important for the development of the integrated MEMS technology, because the underlying PM (power management) block must be capable of internally boosting a 3V battery voltage to a MEMS actuation voltage  $> 50$  V. Without the isolation provided by the SOI substrate, one would be limited to much lower charge pump voltages, typically 20-35V for commonly available CMOS technologies. The SOI technology allows for the stacking of numerous NFET, PFET, diodes and bipolar transistors to create pseudo high voltage devices capable of meeting the high voltage requirements of our MEMS technology while consuming a minimum amount of DC current from the 3V battery. The SOI configuration also allows for the development and integration of devices not available in the bulk CMOS technology, such as very high breakdown FETs ( $BVDSS > 100V$ ) and SCR devices capable of triggering very high voltages with minimum amount of control charge. The suitability of SOI CMOS technology to deliver optimum power management capabilities for an integrated MEMS technology has also been identified by others in the literature [7].

### MEMS Switch Technology

The R&D development of our MEMS integrated process was done at RFMD's clean room fab in Charlotte (NC, USA). Since the CMOS process is complete at this point, it is obviously necessary to maintain all processing temperatures to less than 300 C. A picture of a finished MEMS switch inside a WLP on an SOI-CMOS wafer is shown in Figure 2.

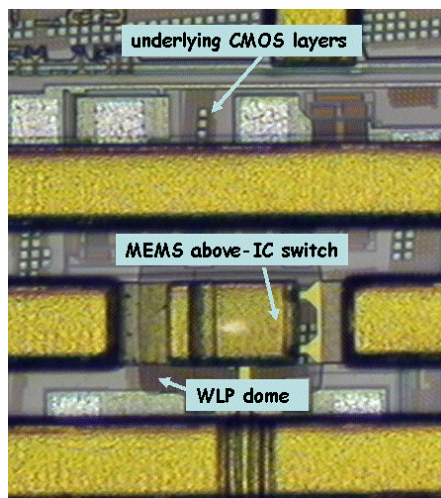


Figure 2. The above-IC MEMS contact switch technology, showing the underlying SOI CMOS layers, the Au cantilever beam and the WLP dielectric dome which encapsulates the structure.

As is typical of RFCMOS technologies manufactured in silicon foundries, the top metal layer consists of a thick final aluminum layer (3 $\mu$ m in our case), covered with a thin final dielectric passivation layer, which has been patterned to reveal the I/O pads. This starting configuration is highly non-planar. For optimum

performance and RF characteristics of the MEMS switch, it is also desirable to further isolate the MEMS structure from metallization layers utilized in the CMOS process.

The initial step in the MEMS flow therefore consists of multiple, thick PECVD oxide layer deposition and CMP (chemical-mechanical-polish) steps in order to yield a flat surface suitable for MEMS processing. Vias are then patterned and etched which will connect the CMOS aluminum layers with the top gold MEMS layers (see Figure 3).

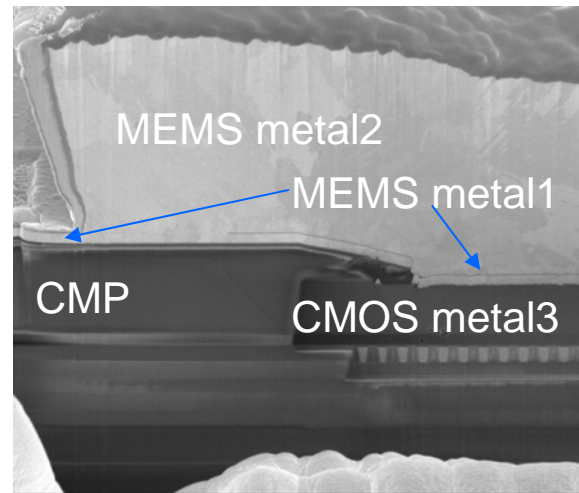


Figure 3. SEM cross-section of MEMS / CMOS vias. A thick PECVD oxide layer was deposited and planarized by CMP.

The first MEMS 0.5 $\mu$ m gold layer is then deposited and patterned (with the appropriate adhesion layer underneath). Our MEMS flow utilizes only Au-based metallization layers due to the superior electromigration and contact reliability characteristics of Au when compared with other metals typically available. The contact metal is then deposited and patterned to form the mechanical contact region of the MEMS switch. In our case, we utilize a gold alloy metal configuration engineered to give an optimal tradeoff between contact reliability and contact resistance.

The first sacrificial layer is deposited on the wafer. We utilize a polymer-based sacrificial material which can be reflowed to yield the necessary planarity for the top cantilever Au beam. Extreme care is necessary later on to ensure complete removal of this sacrificial polymer material over the entire MEMS region in order to yield the necessary reliability figures of merit needed for our MEMS application.

The second gold layer is electroplated to form the thick cantilever for the MEMS contact switch. We utilize a very thick Au layer in order to yield the necessary stiffness for the released MEMS cantilever beam and also to provide a high quality RF metal layer which is used for transmission lines and inductor designs. The MEMS cantilever structural design and process was engineered to meet the specific requirements for our MEMS switches (see Table 1). These include a relatively fast ON and OFF actuation cycle (5 $\mu$ s) and a high immunity to self-actuation from the large RF voltages present in a cellular PA. The stiffness of the thick gold beam also provides a much better immunity to stiction problems during the cantilever release step, which is necessary in a high yield, high volume applications.

Following the plating of the second MEMS metal, a second sacrificial layer is then deposited on the wafer which serves as the mold for the dielectric dome used in our WLP process. This

second sacrificial layer is thick enough to accommodate the height of the mechanical switch structure.

The WLP dome is formed using two low-stress PECVD depositions of silicon nitride. The combined thickness is optimized to provide a robust WLP dome as well as a short process time. The removal of all polymer sacrificial layers is done in between the first and the second dielectric depositions utilizing a proprietary patterning/cleaning process. The dielectric is then cleared over the I/O pad regions and the MEMS above-IC process is complete (see Figure 4).

Flip-chip processing is increasingly used in the wireless industry as the number of I/O's and RF intermodulation/isolation requirements increase[8]. This particular WLP process provides the low profile required..

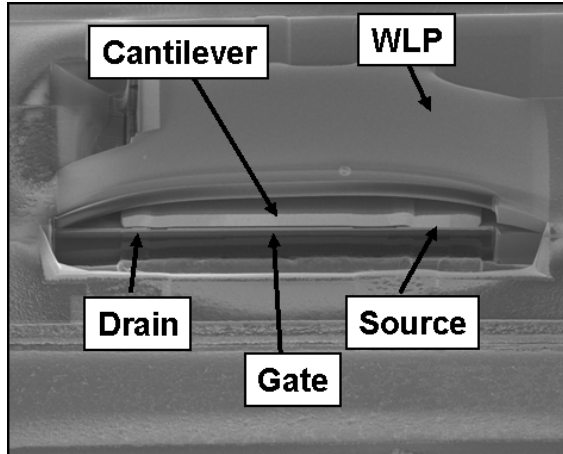


Figure 4. SEM cross-section (post FIB) of the completed MEMS contact switch, illustrating the different regions of the device. The drain corresponds to the metal contact region.

Note that in this particular WLP process, the cavity is sealed under a vacuum condition. This causes the mechanical quality factor of the switch to be very high since there is no air damping in the WLP enclosure, creating an unwanted large number of bounces for an ON transition. This effect is mitigated in our technology by a special Pulse Width Modulation (PWM) technique described in a later section.

## RESULTS

### MEMS Switch Requirements

In order to be used in a portable wireless application, MEMS switches have to demonstrate RF characteristics superior to solid-state FET devices, in addition to high yields and low cost. The MEMS switch must also withstand all of the required ruggedness tests associated with any RF part that is used in this application. Table 1 summarizes the measured characteristics of our MEMS contact switch.

### RF Characteristics

Extensive RF small and large signal characterization has been done on our WLP MEMS switches. Our switches demonstrate the desirable loss and isolation typical of a MEMS device (see Figures 5, 6).

Table 1: Measured RFMD MEMS Contact Switch Characteristics

Parameter		Unit
RF Power Handling (0.9/2GHz) 7:1 VSWR	36/33	dBm
Insertion Loss/ Isolation (2GHz)	0.1/30	dB
2 <sup>nd</sup> /3 <sup>rd</sup> Harmonic (Pin=35dBm@900MHz)	<-65	dBm
DC contact resistance	1	Ohms
Actuation Voltage	<100	V
Beam Collapse Voltage	150	V
ON / OFF time (with PWM pulse)	5	uS
Ruggedness (900 MHz, 15:1 VSWR)	36	dBm
Lifetime Cycles	100E6	cycles

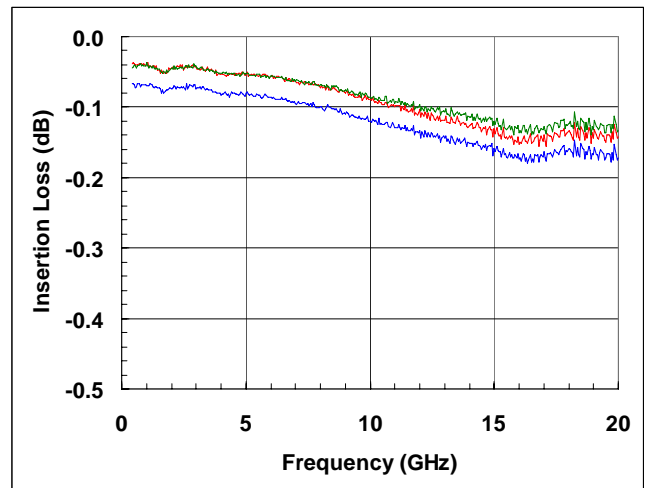


Figure 5. The insertion loss of our WLP MEMS switch is less than 0.1 dB up to 7 GHz.

As was mentioned earlier, our wafer level package is sealed under low pressure. This greatly reduces gas damping in the package and increases the Q of the MEMS switch. When the switch is actuated with a rectangular pulse the beam will bounce multiple times before settling in closed position. This behavior is illustrated in Figure 7. To mitigate this effect we employ a composite pulse actuation signal. The green trace is the high voltage signal seen by the gate and the blue trace is the switch response. The time needed for the transition from “open” to “closed” state can qualitatively be divided in three distinct segments. During the first one we apply a short pulse (“kick”) to initiate movement of the mechanical structure and to transfer enough energy in the system. During the second time segment (“coast”) the electrical stimulus is removed and the mechanical structure “coasts” through the remaining contact gap. Ideally, the movable structure should have zero kinetic energy when the contact is made. At this instant we apply a second actuation pulse (“hold”) to latch the switch closed and to apply the force needed for low contact resistance.

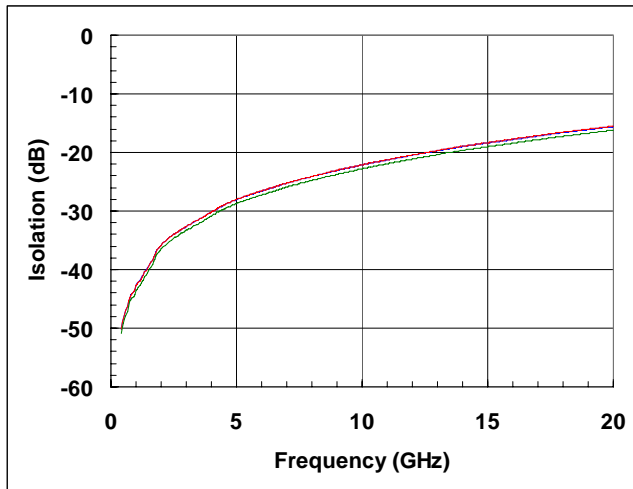


Figure 6. Isolation of our WLP MEMS switch on an SOI CMOS wafer is at least 30 dB up to 4 GHz.

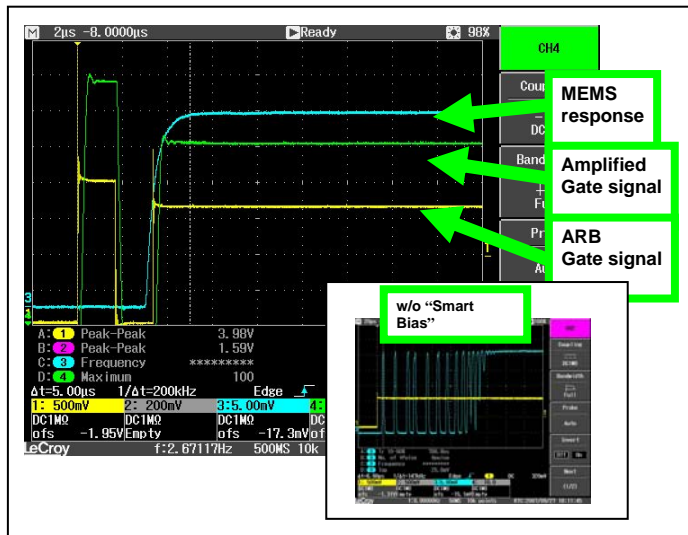


Figure 7. Pulse width modulation of switch actuation signal.

### Reliability

After plastic overmold packaging, the switches have been measured and verified to retain a hermetic seal within the dielectric membrane. Package level reliability testing is on-going.

These switches have been subjected to repeated cycle testing, under both DC and RF stress. Our most recent results are shown in Figure 8. Work is continuing in this area to meet the reliability requirements of a cellular Transmit/Receive switch, which depending on the modulation and architecture of the system, may exceed 100 billion cycles.

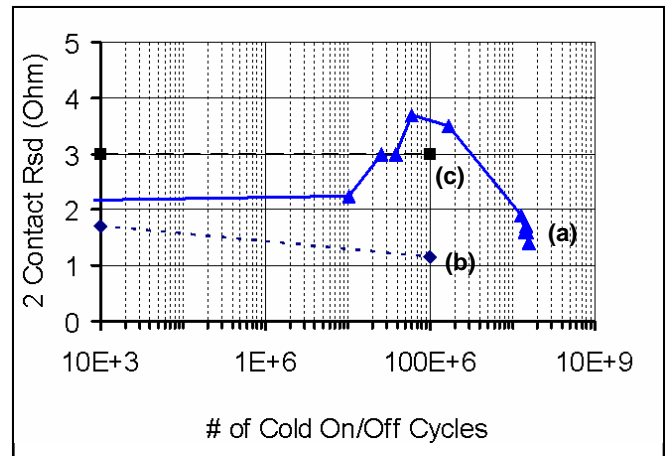


Figure 8. Cycle testing of RF MEMS switches at (a) 1 atm (without WLP), (b)  $1e-3$  atm (with WLP) without PWM actuation and (c)  $1e-3$  atm (with WLP) with PWM actuation.

### CONCLUSION

We have reported the development of an above-IC MEMS contact switch technology which meets many of the requirements for use in high volume RF front end applications including timing, ruggedness, insertion loss, and isolation. The metal cantilever contact switch is hermetically sealed inside a dielectric membrane strong enough to withstand plastic overmold packaging. They have been successfully fabricated and tested on top of 0.5  $\mu$ m SOI-RFCMOS wafers. Work is continuing on the reliability of the switches to meet a transmit/receive level switch specifications.

### REFERENCES

- [1] G. Rebeiz, "RF MEMS, Theory, Design and Technology", Chapter 1, John Wiley and Sons (2003).
- [2] H. de los Santos, "Micromechanical Microwave Systems", Chapter 3, Artech House (2004).
- [3] H. de los Santos, Y. Kao, A. Caigoy, E. Ditmars, "Microwave and mechanical considerations in the design of MEMS switches for aerospace applications", Proceedings of the 1997 IEEE Aerospace Conference, IEEE (1997), pp235-254.
- [4] W. Wolmouth, W. Liebl, V. Juneja, R. Hallgreen, W. Strubble, "E/D pHEMT technology for wireless components", proceedings of the 2004 IEEE Compound Semiconductor Integrated Circuits Symposium, (2004), pp 115-118.
- [5] D. Kelly, C. Brindle, C. Kemerling, M. Suber, "The state of the art of silicon-on-sapphire CMOS RF switches", proceedings of the IEEE Compound Semiconductor Symposium, (2005), pp 200-205.
- [6] J. Costa, M. Carroll, J. Jorgenson, T. McKay, T. Ivanov, T. Dinh, D. Kozuch, G. Remoundos, D. Kerr, A. Tombak, J. McMacken, M. Zybur, "A silicon RFCMOS SOI Technology for integrated cellular/WLAN RF TX applications", Proceedings of the IEEE MTS Microwave Symposium, (2007), pp(445-448).
- [7] L. Guan, J. Sin, H. Liu, Z. Xiong, "A Fully Integrated SOI RF MEMS technology for System-on-Chip applications", IEEE Trans. Elec. Devices, Vol. 53, No. 1, (2006), pp 167-172.
- [8] A. Morris, S. Cunningham, "Challenges and Solutions for cost-effective RF-MEMS packaging", Proceedings of the Electronic Manufacturing Technology Symposium, (2007) pp 278-285.

# DUAL-BEAM ACTUATION OF PIEZOELECTRIC ALN RF MEMS SWITCHES MONOLITHICALLY INTEGRATED WITH ALN CONTOUR-MODE RESONATORS

N. Sinha, R. Mahameed, C. Zuo, M. B. Pisani, C. R. Perez and G. Piazza

(The first two authors have contributed equally towards this work)

University of Pennsylvania, Philadelphia, Pennsylvania, USA

## ABSTRACT

This work reports on piezoelectric Aluminum Nitride (AlN) based dual-beam RF MEMS switches that have been monolithically integrated with AlN contour-mode resonators. The dual-beam switch design presented in this paper intrinsically compensates for the residual stress in the deposited films, requires low actuation voltage (5-20 V), facilitates active pull-off to open the switch and fast switching times (1 to 2  $\mu$ sec). This work also presents the combined response (cascaded S-parameters) of a resonator and a switch that were co-fabricated on the same substrate. The response shows that the resonator can be effectively turned on and off by the switch. A post-CMOS compatible process was used for fabrication of both the switches and the resonators. The single-chip RF solution presented herein constitutes an unprecedented step forward towards the realization of compact, low loss and integrated multi-frequency RF front-ends.

## INTRODUCTION

The last decade has seen an increase in the efforts for the development of RF MEMS switches that can be implemented in wireless communication systems. RF MEMS switches are known to have many advantages over FET and pin diode switches, such as lower power consumption, improved linearity, higher isolation, and lower insertion loss [1].

Various actuation methods have been employed in RF MEMS switches, such as electrostatic [2-4], piezoelectric [5-8], electromagnetic [9] and thermoelastic [10]. Electrostatic actuation is the most commonly used actuation method. However, this mechanism requires high voltages (>20V [1]) that necessitate the presence of a separate on-chip voltage source or charge pump to operate the switch. Reduction in the actuation voltage can be achieved by decreasing the switch stiffness; however, the restoring force that is usually employed for opening the switch and the switching time of the switch both lower with the associated decrease in stiffness. This also affects the ultimate reliability of the switch.

Piezoelectric technology has the ability to meet the requirements of high isolation, low insertion loss, low power consumption and at the same time has the potential to overcome

most of the drawbacks encountered in electrostatic switches. Lead Zirconate Titanate (PZT) is the most commonly used piezoelectric material for the development of RF MEMS switches. PZT has very high piezoelectric coefficient values, but the presence of lead makes its fabrication process CMOS incompatible. Few research groups [5-8] have already demonstrated PZT based switches that have the capability of low voltage actuation. AlN films have recently been introduced for RF applications and have demonstrated to be the preferred material for resonator applications [11-14]. AlN offers the ability of direct integration with CMOS over PZT. Furthermore, the monolithic integration of switches and contour-mode resonators [11-12] will tremendously impact the size and power efficiency of any RF front-end by drastically reducing parasitics and off-state leakage. In addition, such integration will enable new RF architectures based on massive arrays of multi-frequency AlN contour-mode resonators [14].

In this paper, we present the first AlN based piezoelectric switch that can be operated at low voltages and has been fabricated by building upon the well established process of fabrication of AlN based contour mode resonators and filters (as shown in Fig.1).

## DESIGN AND PRINCIPLE OF OPERATION

The schematic view of the dual-beam AlN piezoelectric switch is shown in Figure 2. The operating principle of each beam is based on the unimorph piezoelectric actuation design (Fig. 3) [15-16]. The routing of the bottom and middle metal layers (the layers that provide the actuation) is done in such a manner that two DC inputs can be used for actuating both beams simultaneously. The stack of layers that make up the unimorph are: one active and one passive layer of AlN, two layers of Platinum and a thick layer of Gold. The (bottom) active layer of AlN is sandwiched between two Platinum electrodes that are used for applying the actuation potential across the piezoelectric layer. The top AlN layer is used to isolate the RF signal from the actuation electrodes. A thick layer of electroplated gold was used on top of the aforementioned AlN stack. The gold layer serves two purposes: firstly as a low resistance carrier for the RF signal, and secondly as a structural layer used for offsetting the neutral axis of the beam needed to produce the bending moment for the switch actuation.

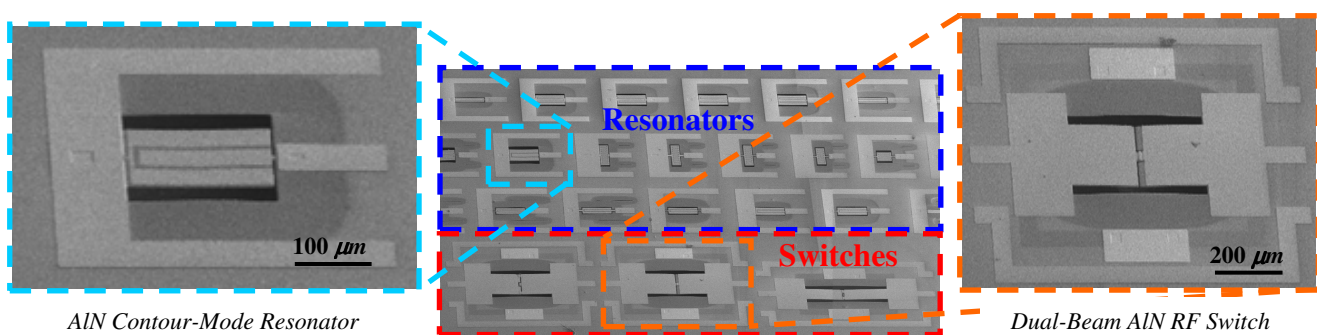


Figure 1: SEM showing dual-beam actuated AlN switches co-fabricated with AlN resonators on the same silicon substrate. The monolithic integration of AlN piezoelectric switches and resonators on a single chip gives us the advantage of achieving new levels of miniaturization for multi-band RF front-ends.

The switch has a gold-platinum contact and uses an amorphous silicon sacrificial layer for creating the nano (200-300 nm) air-gap (Fig. 5).

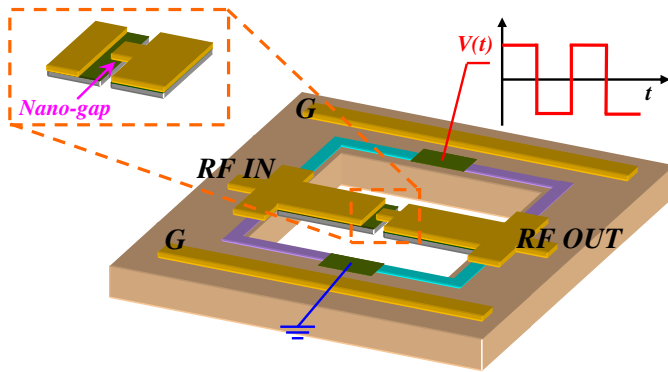


Figure 2: 3-D schematic view of the dual-beam AlN RF switch. This figure illustrates how both arms of the switch can be actuated at the same time. Both mating parts are released, therefore reducing the effect of any residual stress.

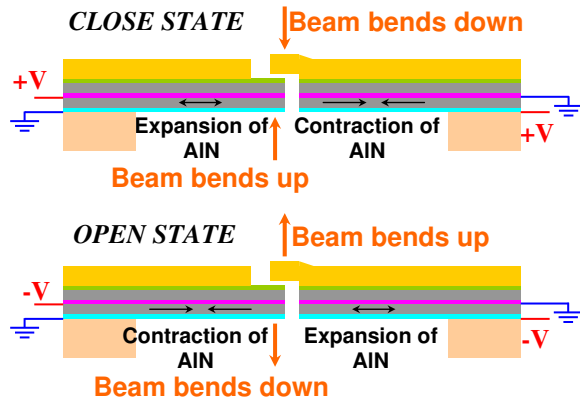


Figure 3: 2-D schematic view of the dual-beam switch showing the operating principle of the switch: The bottom layer of AlN is used for actuation; by reversing the polarity of the applied voltage (done by on-chip electrode routing) the switch can either be opened or closed.

The uniqueness of this work lies in the utilization of the dual-beam mechanism which uses two symmetric released beams for operating the switch. Both beams can be actuated simultaneously, thus giving: (i) low actuation voltage (halved), (ii) high contact forces (doubled for a given voltage), (iii) immunity to residual stress and process-induced variation in the initial nano-gap used to set the RF isolation level, (iv) active pull-off to open the switch and (v) faster switching times (halved).

## FABRICATION

A seven-mask post-CMOS compatible process is used for the co-fabrication of AlN based switches and contour-mode resonators (Fig. 4).

As shown in Figure 4:  $1\mu\text{m}$  of AlN is deposited on top of a 300 nm insulating layer of low stress nitride (LSN) and 200 nm of Pt patterned by lift-off. On this first layer of AlN, a second layer of AlN ( $1\mu\text{m}$ ) is deposited on top of a second layer of Pt (200 nm).

Opening to the bottom and middle electrodes are made by wet-etching of AlN using AZ400k<sup>®</sup> (a KOH based developer) at 70°C. This step shows an improvement in terms of sidewall angle control and reduced surface roughness over [10-11, 13] in defining the via opening. The AlN is patterned by a  $\text{Cl}_2$  based dry etch process using  $\text{SiO}_2$  as hard mask. The top Pt (200 nm) layer is deposited and patterned by lift-off to form part of the contact and provide access to the bottom and middle Pt layers. An amorphous silicon layer is evaporated and patterned by lift-off to form the sacrificial layer used to define the nano-gap. A gold seed layer is used for the electroplating of gold and a thick photoresist is employed as a mold for the electroplated layer. After wet etch of the seed layer, the sacrificial layer along with the structure are simultaneously dry-released using  $\text{XeF}_2$ . Dry release is used to eliminate stiction problems that would have otherwise been encountered with wet release techniques. Figure 5 shows a Scanning Electron Micrograph (SEM) of one of the microfabricated switches with a close up view of the nano gap.

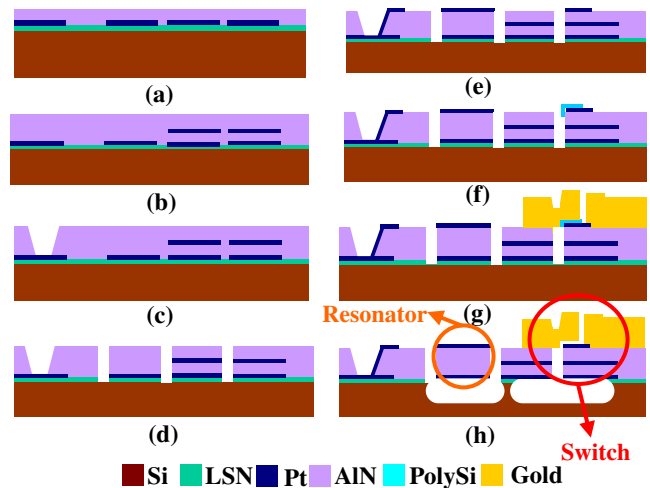


Figure 4: Process flow of the dual-beam switch fabricated with contour-mode resonators. (a) First AlN layer on top of Pt and LSN. (b) Second AlN layer on top of middle Pt. (c) Opening of via to bottom and middle Pt. (d) AlN Etch. (e) Top Pt deposition. (f) Si sacrificial layer. (g) Gold Electroplating. (h)  $\text{XeF}_2$  Release of structures.

## EXPERIMENTAL RESULTS

The experimental characterization of the switch focused on the measurement of the actuator displacement, the on resistance, the switching time and preliminary RF response.

Edge deflection measurements of the actuator were done using a Zygo optical profilometer. Figure 6 shows the edge deflection for a  $300 \times 100 \mu\text{m}$  unimorph actuator as function of applied voltage. These measurements (Fig. 6) exhibit very good agreement with FEM simulations (COMSOL<sup>®</sup>).

DC resistance measurements of the switches show that the contact resistance decreases with the applied voltage, proving that higher forces produce lower on-resistance ( $R_{\text{on}}$ ). Our dual-beam actuation scheme takes advantage of this concept and uses two actuators to double the force per unit voltage applied. To further validate this, we tested the change in on-resistance with the applied voltage when either one beam or both beams are actuated (Fig. 7).

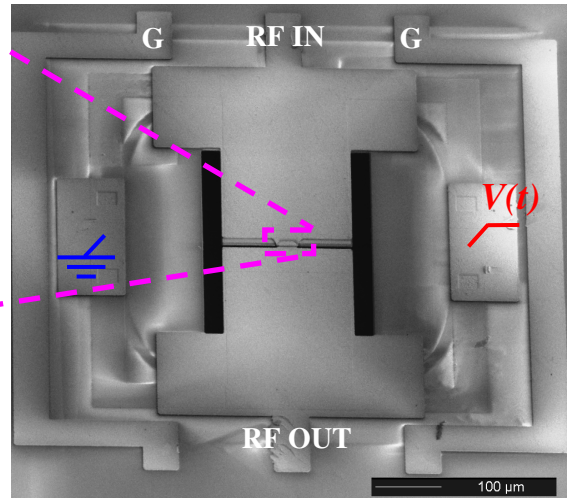
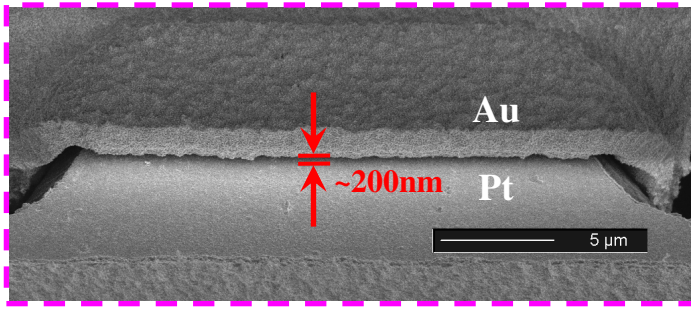


Figure 5: SEM of the fabricated AlN switch with a zoomed in view of the nano-gap and Au/Pt contact region. The nano-gap is realized by using evaporated amorphous silicon as sacrificial layer. The sacrificial layer is removed by using XeF<sub>2</sub> vapor phase release. The nano-gap definition is key in enabling switches with large forces and good RF isolation.

The plot in Figure 7 shows that 6.3 V are needed to establish contact (vs. 12 V for the single beam) when both beams are actuated and the on-resistance decreases to ~5.4 Ω at 40 V (vs. 8.4 Ω for a single beam at the same voltage). Some switches exhibited even lower on-resistance ( $R_{on}=3 \Omega$ ) for the same applied voltage.

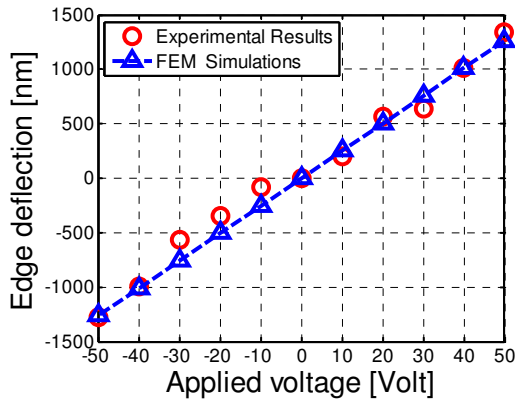


Figure 6: Edge deflection measured by optical profilometer (Zygo) for a 300x100 μm unimorph actuator. Experimental results show good agreement with COMSOL FEM simulations.

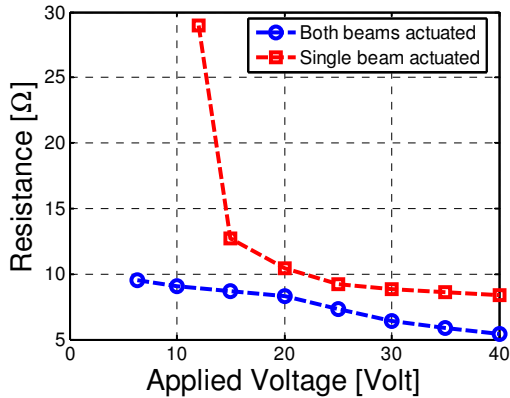


Figure 7: DC on resistance measurements of a switch (200x200 μm) for which single and both beams were actuated. The dual beam actuation shows lower resistance for a given voltage.

Preliminary RF measurements were performed in order to verify the RF response of this first AlN switch prototype. Figure 8 presents the isolation and the insertion loss of a 200x200 μm dual-beam AlN switch. In this switch, isolation > 26 dB and low Return Loss (RL) < 0.75 dB at 2 GHz were obtained. The current isolation response is limited by a combination of the switch contact and parasitics. Insertion Loss (IL) < 0.67 dB and RL > 34 dB were recorded at 2 GHz for this same switch. The higher than expected IL value is likely due to substrate parasitics, as shown in Figure 8 where the switch response is compared to a through-line on the same substrate. The additional losses are also likely to be due to an unwanted coupling between RF and DC signals and which can be avoided by improved care in the layout of the actuation signal.

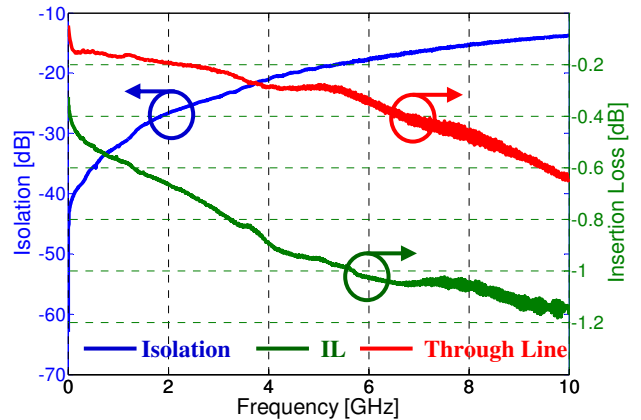


Figure 8: Measurement of isolation and insertion loss (IL) for a 200x200 μm dual-beam AlN switch from 100MHz to 10GHz. Switch IL is compared to the loss in a thru-line (of comparable length).

The same switch was fabricated in conjunction with several AlN contour-mode resonators on the same substrate. Figure 9 shows the combined response (cascaded S-parameters) of a 224 MHz resonator and the switch of Figure 8. The overlap between the resonator response with and without the switch shows that the introduction of the switch does not significantly alter the resonator performance. Furthermore, the switch effectively turns off the resonator by lowering the transmission response by at least ~39.5dB.

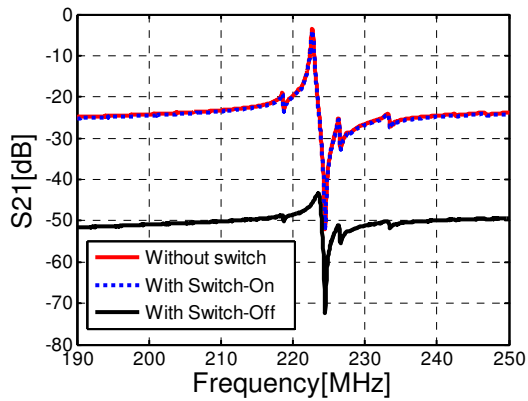


Figure 9:  $S_{21}$  plot (cascaded  $S$ -parameters) of a resonator monolithically integrated with the AlN switch presented in this work. The figure shows the response of a resonator with the switch in both on and off states.

In order to experimentally determine the switching time of the AlN switch, a square-wave at 40 Hz was used to turn the switch on and off, while the change in a DC signal applied across the RF line (i.e. across RF IN and RF OUT of Fig. 5) was monitored to measure the occurrence of contact. The switching time is defined as the time for the output DC signal (i.e. RF OUT, in Fig. 5) to rise from 10 to 90 % of the maximum output signal level in the on state. As shown in Figure 10, a switching time of  $\sim 1.6 \mu\text{sec}$  was recorded for the  $200 \times 200 \mu\text{m}$  switch. Repeated tests on other switches and at different actuation frequencies and voltages confirmed that the switching time lies between 1 and 2  $\mu\text{sec}$ .

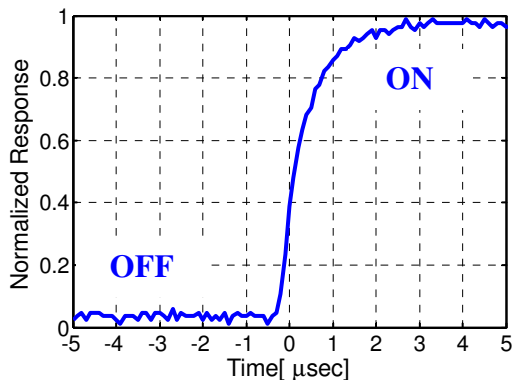


Figure 10: Response of the  $200 \times 200 \mu\text{m}$  switch to a square-wave form signal ( $\pm 44 \text{ V}$ ) at 40Hz.

## CONCLUSIONS

In this work the design, fabrication and experimental testing of the first piezoelectric AlN dual-beam switch monolithically integrated with AlN contour mode resonators has been demonstrated. The RF performance of the first prototype dual-beam switch has been evaluated and shows good isolation ( $>26 \text{ dB}$ ) and IL ( $< 0.67 \text{ dB}$ ) at 2 GHz. On-going research is focusing on long-term reliability testing and optimization of the switch in order to reduce IL and actuation voltage. Demonstration of integrated arrays of switches and AlN filters is also in progress.

## ACKNOWLEDGEMENTS

This work was supported by the DARPA ASP Project. The authors will like to acknowledge the help provided by Philip Stephanou and Justin Black at Harmonic Devices Inc. and the staff at the Penn Wolf Nanofabrication Facility.

## REFERENCES

- [1] G. M. Rebeiz, "RF MEMS Theory, Design and Technology", 1<sup>st</sup> Edition, John Wiley & Sons, Inc., 2003.
- [2] P. M. Zavracky, S. Majumder and N. E. McGruer, "Micromechanical switches fabricated using nickel surface micromachining," Journal of MicroElectroMechanical Systems, vol.6, no.1, pp.3-9, Mar 1997.
- [3] C. Bozler, R. Drangmeister, S. Duffy, M. Gouker, J. Knecht, L. Kushner, R. Parr, S. Rabe, and L. Travis, "MEMS microswitch arrays for reconfigurable distributed microwave components", IEEE MTT-S International Microwave Symposium Digest, Boston, MA (June 2000), pp. 153–156.
- [4] S. Duffy, C. Bozler, S. Rabe, J. Knecht, L. Travis, P. Wyatt, C. Keast, and M. Gouker, "MEMS microswitches for reconfigurable microwave circuitry", Microwave and Wireless Comp. Lett., 11/3/2001, pp. 106–108.
- [5] H. C. Lee, J. H. Park, J. Y. Park, H. J. Nam and J. U. Bu "Design, fabrication and RF performances of two different types of piezoelectrically actuated Ohmic MEMS switches", Journal of Micromechanics Microengineering, 15(2004), pp. 2098-2104.
- [6] J. H. Park, H. C. Lee, Y. H. Park, Y. D. Kim, C. H. Ji, J. Bu and H. J. Nam, "A fully wafer-level packaged RF MEMS switch with low actuation voltage using a piezoelectric actuator", Journal of Micromechanics Microengineering 16(2006), pp. 2281-2286.
- [7] S. J. Gross, S. Tadigadapa, and T. N. Jackson, S. Trolier-McKinstry, Q. Zhang "Lead-Zirconate-Titanate-Based Piezoelectric Micromachined Switch", Appl. Phys. Lett., 83/1/2003, pp. 174-176.
- [8] R. G. Polcawich, D. Judy, J. S. Pulskamp, S. Trolier-McKinstry and M. Dubey, "Advances in Piezoelectrically Actuated RF MEMS Switches and Phase Shifters", Microwave Symposium, (2007) IEEE/MTT-S International, pp.2083-2086.
- [9] M. Ruan, J. Shen, and C. B. Wheeler, "Latching Micromagnetic Relays", Journal of MicroElectroMechanical. Systems, 10/2001, pp. 511–517.
- [10] R. D. Streeter, C. A. Hall, R. Wood, and R. Madadevan, "VHF high-power tunable RF bandpass filter using microelectromechanical (MEM) microrelays", Int. J. RF Microwave CAE, 11/5/2001, pp. 261–275.
- [11] G. Piazza, P. J. Stephanou and A. P. Pisano, "Piezoelectric Aluminum Nitride Vibrating Contour-Mode MEMS Resonators", Journal of MicroElectroMechanical Systems, 15/6/2006, pp. 1406-1418.
- [12] G. Piazza, P. J. Stephanou and A. P. Pisano, "Single-Chip Multiple-Frequency AlN MEMS Filters Based on Contour-Mode Piezoelectric Resonators", Journal of MicroElectroMechanical Systems, 16/2/2007, pp. 319-328.
- [13] R. Ruby, P. Bradley, J. Larson III, Y. Oshmyansky and D. Figueredo, "Ultra-miniature high-Q filters and duplexers using FBAR technology", Solid-State Circuits Conference, 2001. Digest of Technical Papers. ISSCC. 2001 IEEE International, pp.120-121, 438.
- [14] G. Piazza, P. J. Stephanou and A. P. Pisano, "One and two port Piezoelectric Higher Order Contour-mode MEMS Resonators for Mechanical Signal Processing", Solid State Electronics, 51/ 11-12/2007, pp. 1596-1608.
- [15] J. G. Smits, S. Dalke and T. K. Cooney, "The Constituent Equations of Piezoelectric Bimorphs", Sensors and Actuators A, 28/1991, pp. 41-61.
- [16] D. L. DeVoe and A. P. Pisano, "Modeling and optimal design of piezoelectric cantilever microactuators", Journal of MicroElectroMechanical Systems, 6/3/1997, pp. 266-70.

# BIO-INSPIRED ADHESION DEVICES

E. Arzt and A. del Campo<sup>1</sup>

<sup>1</sup>INM – Leibniz Institute for New Materials, Saarbrücken, Germany

## ABSTRACT

Adhesive joining with molecular (van der Waals) interactions without chemical glue is presently receiving much attention because of many potential applications. Research on how insects, spiders and geckos stick to surfaces has inspired a new paradigm: fibrillar surfaces with appropriate design can show much higher adhesion performance than flat surfaces. The insight gained in studying biological systems can be transferred to the development of optimized artificial attachment devices. By systematic variations of fiber diameter, aspect ratio and contact shape, we have produced, on a laboratory scale, artificial structures with adhesion strengths similar to the gecko. Further advances with switchable adhesion (“smart adhesives”) have been demonstrated and may lead to interesting applications in medical products, sports good, construction materials and microfabrication.

## INTRODUCTION

A new paradigm has emerged over the last years in adhesion: enhanced sticking of patterned *versus* planar surfaces. This concept of “contact splitting” [1] arises from the observation of flies, spiders and geckos, which exhibit attachment organs with long micro to nano-sized hairs, e.g. [2, 3]. The complex design of these hairs seems to be the key to their smart adhesion behavior, which enables repeated attachment and easy release from almost any kind of surface.

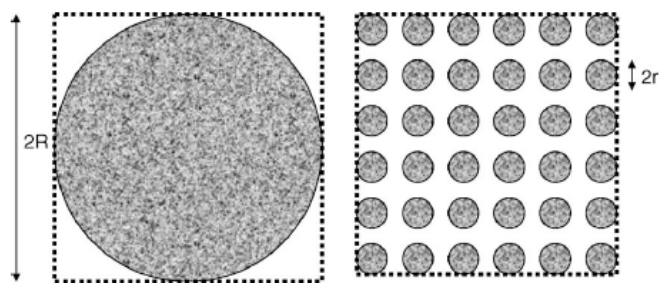


Figure 1: The principle of contact splitting: splitting of a reversible van der Waals contact (initially of radius  $R$ ) into many fine contacts (new radii  $r$ ) increases the adhesion force. This principle suggests the application of miniaturization technologies to achieve artificial adhesives.

Inspired by this principle, theory and experiment of reversible contact mechanics in small structures have made much progress in recent years, e.g. [4-16]. Yet attempts to produce such surfaces with significantly enhanced adhesion have so far met with mixed success. While individual fibers exhibited the expected attachment, larger surfaces often did not demonstrate superior adhesion performance. The reason for this failure very likely lies in the complexity of the problem: the design parameters and underlying adhesion mechanisms need to be understood and optimized on the nano, micro and macro scale. For this purpose, singular experiments, as are frequently published in the literature, fail to advance the subject; rather, systematic model studies backed by suitable modelling efforts are required. The present contribution describes some of our recent progress in this area.

## MICROPATTERNED MODEL SURFACES: EFFECTS OF FIBER SIZE AND SHAPE

We have fabricated model fibrillar structures by soft-molding elastomeric precursors on photolithographic molds [17]. Typical structures, with  $20\ \mu\text{m}$  diameter, are shown in Figure 2. Adhesion studies on regular arrays of Poly(dimethylsiloxane) (PDMS) micropillars (pillar radii were varied between  $2.5$  and  $25\ \mu\text{m}$  and aspect ratio between  $1$  and  $4$ ) have proved the enhanced adhesion of structured surfaces against flat controls. Systematic studies of the influence of the contact radius and aspect ratio of the pillars on the final adhesion performance have demonstrated that decreasing the contact radius and increasing the aspect ratio of the pillars enhances adhesion [18].

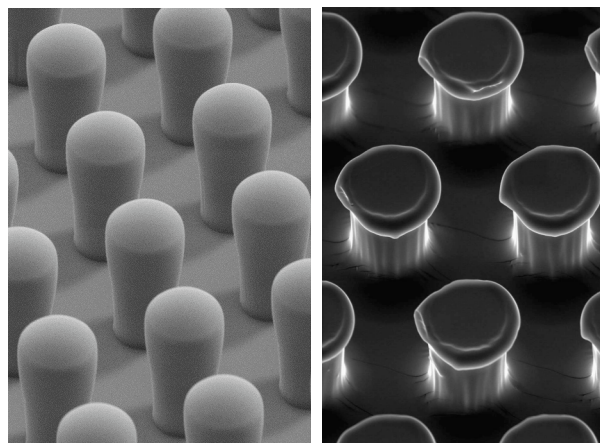


Figure 2: Micropatterned fibrillar PDMS surfaces: spherical tips (left) vs. mushroom-shaped tips (right). The diameter of both types of fibers is  $20\ \mu\text{m}$ . Adhesion is strongly enhanced by the presence of mushroom tips, which reach the adhesion strength of real gecko toes. (after del Campo et al. [21])

New methods for the fabrication of structured polymer surfaces possessing pillars with controlled 3D tip geometries were developed: spherical, spatula-like and suction cups [19, 20]. The fabrication strategies exploit the filling mechanism of lithographic templates by viscous polymers, combined with inking and printing steps using elastomeric precursors with various viscosities and crosslinking kinetics. Homogeneously structured areas were obtained which allow reproducible and reliable testing of adhesion behaviour and can be up scaled to prototypes. These fabrication routes do not require sophisticated 3D structuring equipment and can be extended to other materials, dimensions and geometries.

Our adhesion experiments show significant variation of the adhesion performance of the surfaces depending on the tip geometry and testing conditions [21]. The highest pull-off forces were found for mushroom-like pillars, which showed an increase of up to 30 times over the flat controls (see Fig. 2b and Fig. 3). This corresponds roughly to the adhesion strength of a gecko toe. Flat and spherical shapes showed lower adhesion, while concave shapes resulted in the poorest performance, coupled with an unusual preload dependence.

The fiber radius effect studied previously augments the shape effect, creating vastly different “splitting efficiencies” [5] for the

different shapes. Within the size range tested, mushroom and spatular shapes hold the greatest promise for further adhesion improvement through size reduction.

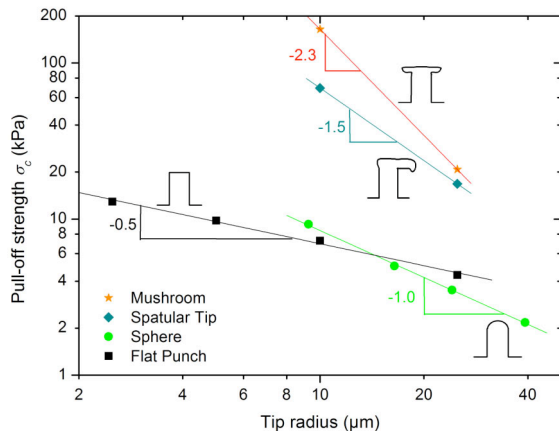


Figure 3: Adhesion strength (pull-off force divided by apparent contact area) of different contact shapes as a function of fiber radius. Mushroom and spatular tips scale most favorably to smaller dimensions. (after [21])

## TOWARDS SWITCHABLE ADHESION: “SMART” SURFACES

We have recently demonstrated that patterning technologies can be combined with responsive polymer materials to create microstructured surfaces with switchable adherence [22]. Application of an external field (e.g. temperature) causes changes in the topographical design and this influences the final adhesion performance. A shape memory polymer was selected for this purpose. Arrays of microfibers, with diameters between 0.5 and 50 μm and lengths between 10 and 100 μm, were patterned by soft molding. Mechanical deformation at the shape-memory transition temperature, followed by cooling to room temperature in the deformed position yielded a temporary non-adhesive surface consisting of pillars in a tilted position. By reheating above the transition temperature, the patterned surface switches from the temporary non-adhesive state to a permanent adhesive surface with at least a 200-fold increase in adherence. Such active structures may have interesting applications in responsive systems where adhesion or friction management is required.

## OUTLOOK

While some of the ingredients of biological attachment systems have been successfully emulated in artificial systems, several challenges still lie ahead. Obviously, biological devices are much more complex from a geometrical and materials point of view. These peculiarities still need to be analyzed theoretically; for example, the superiority of mushroom-type fibers has recently been explained by an improvement of the near-perimeter stress distribution by numerical methods [23]. The next challenge is to imitate the hierarchical structure of biological systems in order to achieve good adhesion to rough surfaces; a first attempt has been made [14], but the resulting adhesion strengths need to be improved to be of practical use. Biological fibers are most likely composed of gradient materials, e.g. to allow small fiber radii without the propensity to clumping [9]. Also asymmetric and anisotropic contact shapes, as they are present in flies and geckos, will need to be reproduced to combine reliable adhesion with easy detachment. Because of the large parameter space, experimental works needs to be accompanied by suitable modelling activities.

For example, the concept of “adhesion design maps” [9], which are useful graphical displays of the trade-offs in producing efficient attachment structures, need to be extended from simple spherical to more complex shapes [24]. Finally, of course, practical applicability will depend on cost-effective fabrication routes for large areas; such developments are currently underway [25].

## REFERENCES

- [1] E. Arzt, S. Gorb and R. Spolenak, “From micro to nano contacts in biological attachment devices”, *PNAS* 100 (19), 10603-10606 (2003)
- [2] S. Gorb, “Attachment Devices of Insect Cuticle”, Springer Netherland, 2001
- [3] K. Autumn et al., “Adhesive force of a single gecko foot-hair”, *Nature* 405, 681-685 (2000)
- [4] E. Arzt, “Biological and artificial attachment devices: lessons for materials scientists from flies and geckos”, *Mater. Sci. Eng. C* 26, 1245-1250 (2006)
- [5] R. Spolenak, S. Gorb, H. Gao and E. Arzt, “Effects of contact shape on the scaling of biological attachments”, *PRSL A* 461 (2054), 305-319 (2005)
- [6] B.N.J. Persson, “On the mechanism of adhesion in biological systems”, *J. Chem. Phys.* 118, 7614-7621 (2003)
- [7] C.Y. Hui et al., *J. Adhesion* 81 (7-8), 699-721 (2005)
- [8] L. Ma, R. McMeeking and E. Arzt, *Int. J. Mats. Res.* 98, 1156-1162 (2007)
- [9] R. Spolenak, S. Gorb and E. Arzt, “Adhesion design maps for bio-inspired attachment systems”, *Acta Biomater.* 1, 5-13 (2005)
- [10] H. Yao and H. Gao, *J. Mech. Phys. Solids* 54 (6), 1120-1146 (2006)
- [11] A.K. Geim et al., *Nature Mat.* 2 (7), 461-463 (2003)
- [12] A. Ghatak et al., *PRSL A* 460, 2725-2735 (2004)
- [13] J.Y. Chung and M.K. Chaudhury, *JRS Interface* 2 (2), 55-61 (2005)
- [14] M.T. Northen and K.L. Turner, *Nanotechnology* 16, 1159-1166 (2005)
- [15] M.Sitti and R.S. Fearing, *J. Adh. Sci. Tech.* 17 (8), 1055-1073 (2003)
- [16] A.J. Crosby et al., *Langmuir* 21 (25), 11738-11743 (2005)
- [17] A. del Campo and E. Arzt, “Design parameters and current fabrication approaches for developing bioinspired dry adhesives”, *Macromolecular Bioscience* 7, 118-127 (2007)
- [18] C. Greiner, A. del Campo and E. Arzt, “Adhesion of bioinspired micro-patterned surfaces: effects of pillar radius, aspect ratio and preload”, *Langmuir*, 23, 3495-3502 (2007)
- [19] A. del Campo, I. Alvarez, S. Filipe and M. Wilhelm, *Advanced Functional Materials* 17, 3590 (2007)
- [20] A. del Campo, C. Greiner, I. Alvarez and E. Arzt, “Patterning surfaces with pillars with controlled and 3D tip geometry mimicking bioattachment devices”, *Advanced Materials* 19, 1973 (2007)
- [21] A. del Campo, C. Greiner and E. Arzt, “Contact shape controls adhesion of bioinspired fibrillar surfaces”, *Langmuir* 23, 10235-10243 (2007)
- [22] S. Reddy, E. Arzt and A. del Campo, “Bioinspired surfaces with switchable adhesion made of shape memory polymers”, *Adv. Mats.* 19, 3833-3837 (2007)
- [23] A.V. Spuskanyuk, R.M. McMeeking, V.S. Deshpande and E. Arzt, “The effect of shape on the adhesion of fibrillar surfaces”, *Acta Biomaterialia*, in press
- [24] C. Greiner, R. Spolenak and E. Arzt, “Design Maps for Non-Spherical Contact Shapes”, in preparation
- [25] A. Altherr, P. Oliveira and E. Arzt, unpublished.

# CONCENTRATION OF CD8+ LYMPHOCYTES ON EWOD PLATFORM FOR MONITORING ORGAN TRANSPLANT REJECTION

Gaurav J. Shah<sup>1</sup>, Jeffrey L. Veale<sup>2</sup>, Yael Korin<sup>3</sup>, Elaine F. Reed<sup>3</sup>, H. Albin Gritsch<sup>2</sup>, and Chang-Jin “CJ” Kim<sup>1</sup>

<sup>1</sup>Mechanical and Aerospace Engineering Department, Henry Samueli School of Engineering and Applied Science

<sup>2</sup>Department of Urology, <sup>3</sup>Immunogenetics Center, David Geffen School of Medicine

University of California, Los Angeles (UCLA), Los Angeles, CA 90095

## ABSTRACT

As important developments in the effort to create a low-power portable lab-on-a-chip system, we demonstrate the concentration of human CD8+ T-lymphocytes on an electrowetting-on-dielectric (EWOD) platform using antibody-conjugated magnetic beads (MB-Ab). This is an important step of the protocol used to monitor the risk of rejection in organ transplant patients.

## INTRODUCTION

The ability to concentrate and separate specific cells is critical for cell-based biological assays and medical diagnostics. For instance, CD8+ cytotoxic T-lymphocytes play a critical role in transplant-rejection by infiltrating the transplanted organs and releasing proteins that attract additional lymphocytes to destroy the transplant cells. If CD8+ lymphocytes could be isolated from other peripheral blood components and then lysed, the concentration of these cells and their associated proteins could be measured to diagnose rejection non-invasively [1, 2]. While this protocol is well-established at the UCLA Immunogenetics Center, the transplanted patients have to visit the center for the tests. A portable device performing the lab test would not only obviate the post-transplantation visits but also facilitate early diagnosis and timely treatment. With its simplicity and low power-consumption, electrowetting-on-dielectric (EWOD)-based digital microfluidics is promising for such a point-of-care device.

In the quest to realize the entire lab protocol on a portable system, we report two main steps realized on the EWOD platform. First, we developed and quantitatively assessed binding of CD8+ cells to MB-Abs. Second, we developed the ability to separate CD8+ lymphocytes from a mixture of CD8+ and CD8- lymphocytes. While recent studies have shown concentration of MBs on EWOD platform is feasible in principle using simple water containing only the beads [3-5], this is the first report of success in advancing the concept to living cells.

## MATERIALS AND METHODS

### Cells Sample Preparation

Lymphocytes were isolated from whole blood using standard hematological procedures. Peripheral blood mononuclear cells were separated over a Ficoll-Hypaque gradient. Lymphocytes were obtained after macrophage depletion by adherence to a plastic flask. CD8+ and CD8- lymphocytes were separated using anti-CD8 MB-Ab (Dynabeads CD8 Positive Isolation Kit from Invitrogen, Inc., CA) before being detached from the MB's. Before EWOD experiments, the cells were spun down and resuspended in serum-free buffer. For visualization, the CD8+ cells were stained with fluorescent dye (CFSE).

### EWOD Device Fabrication

Typical UCLA EWOD fabrication processes [3] were used to prepare the device (Fig. 1). EWOD electrodes were defined on an Indium-Tin Oxide (ITO) (1400Å) layer over a 700 μm-thick glass (“EWOD”) substrate (TechGophers Inc.). Cr/Au (~100/1000 Å) was deposited and patterned to define the contact pads and electrode labels for easier visualization. Next, a Si<sub>3</sub>N<sub>4</sub> layer (~1

μm) was deposited using PECVD, and patterned to define the dielectric layer. A Cytop® (Asahi Inc.) layer (~1 μm) was spin-coated on top, and annealed at 200 °C to make the surface hydrophobic. 1.1 mm-thick glass substrates coated with ITO (1400 Å) (Delta Technologies Inc.) were used to fabricate the “Reference” substrate. A thinner PECVD Si<sub>3</sub>N<sub>4</sub> layer (~1000 Å) was deposited and patterned on it to expose the ITO for electrical ground connection, followed by Cytop® spin-coating and annealing (~1000 Å). A double-sided tape (~100 μm thick, 3M Inc.) was used as the spacer between the substrates.

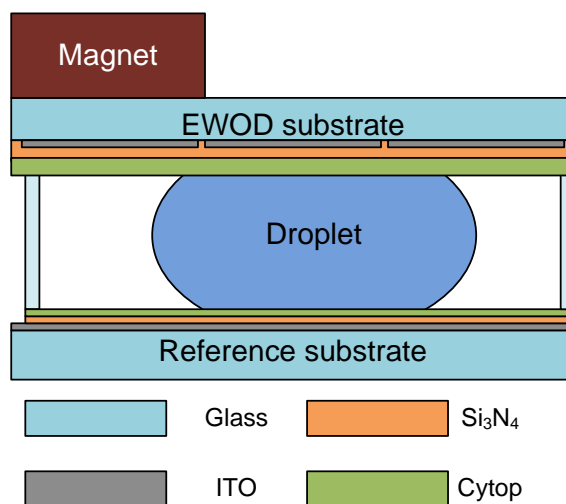


Figure 1: Cross section of the EWOD device (not precisely to scale). EWOD actuation electrodes were patterned on the ITO layer of the “EWOD” substrate. Contact pads were formed with Cr/Au (not shown). Electrodes were coated with silicon nitride as dielectric and cytop as hydrophobic coating. Thinner silicon nitride and cytop layers were deposited over the ITO-coated “Reference” substrate, connected to ground.

### Device Actuation and Image Capture

Droplet actuation was achieved by application of voltage (~70 Vac 1 kHz) to EWOD electrodes. Electronic control for the actuation sequence was controlled using LabVIEW (National Instruments Inc.) with the help of a digital I/O device (DAQPad 6507, National Instruments). Magnetic force was provided using a cylindrical permanent magnet (NdFeB, ½” dia. ½” thick) placed on top of the EWOD substrate (Fig. 1).

The device was mounted on an inverted fluorescence microscope (Nikon TE-2000U) for visualization. A video camera (Panasonic KR-222) was used to capture the droplet actuation movies, while still optical and fluorescence images were taken using a cooled CCD camera (Photometrics Coolsnap EZ).

## RESULTS AND DISCUSSION

### Flow cytometry Experiments

Before doing experiments on EWOD, the assay was verified using the conventional laboratory techniques.

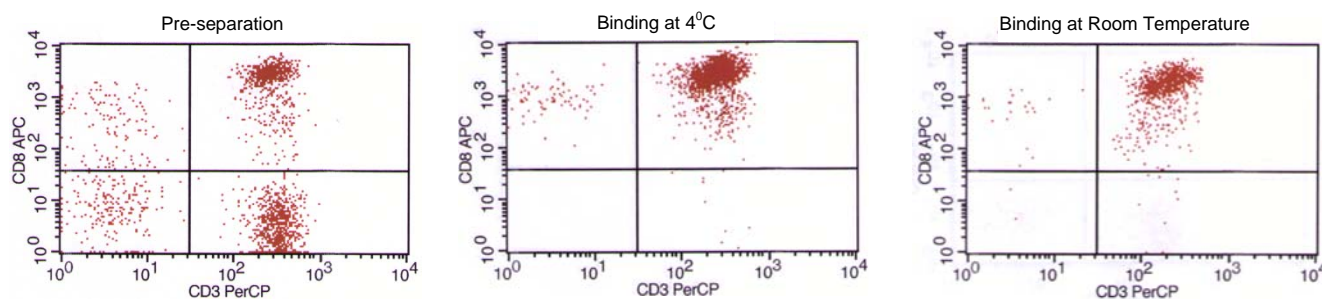


Figure 2: Test of the protocol to bind CD8+ cells to MBs under EWOD conditions. Flow cytometry data obtained for lymphocyte distribution before and after magnetic separation. Upper right corner indicates CD8+ T-lymphocytes. (Left) Before separation. (Middle) after magnetic separation for MB-cell binding done at 4°C as per protocol, (Right) after magnetic separation for MB-cell binding at RT in conditions similar to those during EWOD experiments. Collection efficiency is high (>95%) in both cases.

Flow-cytometry measurements were performed to determine the isolation efficiency for cell separation according to protocol. To ensure that MB-cell binding will also occur on an EWOD device, cell separation was also performed for binding conditions similar to EWOD (e.g. room temperature instead of the prescribed 2-8°C). Fig. 2 shows that CD8+ isolation efficiency was similarly high (>95%) under both conditions (Fig. 2 middle, right).

### Cell-MB Binding on EWOD

The steps to evaluate CD8+ cells binding with MBs on the EWOD device are schematically described in Fig. 3 and demonstrated in Fig. 4. A droplet containing MB-Ab (~10<sup>7</sup>/ml) and another containing fluorescently stained CD8+ cells (~10<sup>5</sup>/ml) were merged using EWOD (Figs. 3(a, b), 4(a, b)). The combined droplet was moved repeatedly over a circular path of electrodes to allow MB-cell mixing. After about 8-10 minutes (Fig. 3(c, d), 4(c, d)), an

NdFeB magnet was introduced (Fig. 3(e), 4(e)), attracting most MBs to the left-end of the droplet. (Earlier reports of MB separation on EWOD used meniscus-assistance [3], or performed separation immediately after sample introduction [4]. Although they are valid, a proprietary technique by Core Microolutions, Inc. (Los Angeles, CA) used here eliminates the need for either of these.) The droplet is subsequently cut to form the collected droplet (left) and the depleted droplet (right) (Fig. 5(a, b)).

By manually counting the fluorescent cells in these droplets, the cell-collection efficiency is conservatively estimated to be >92% (Fig. 5(c-f)). (Some cells in the collected droplet may be hidden behind MBs.) This high efficiency is attributed to the high interaction between MBs and cells confined inside a circulating droplet, as compared to a flow-through channel-microfluidics system.

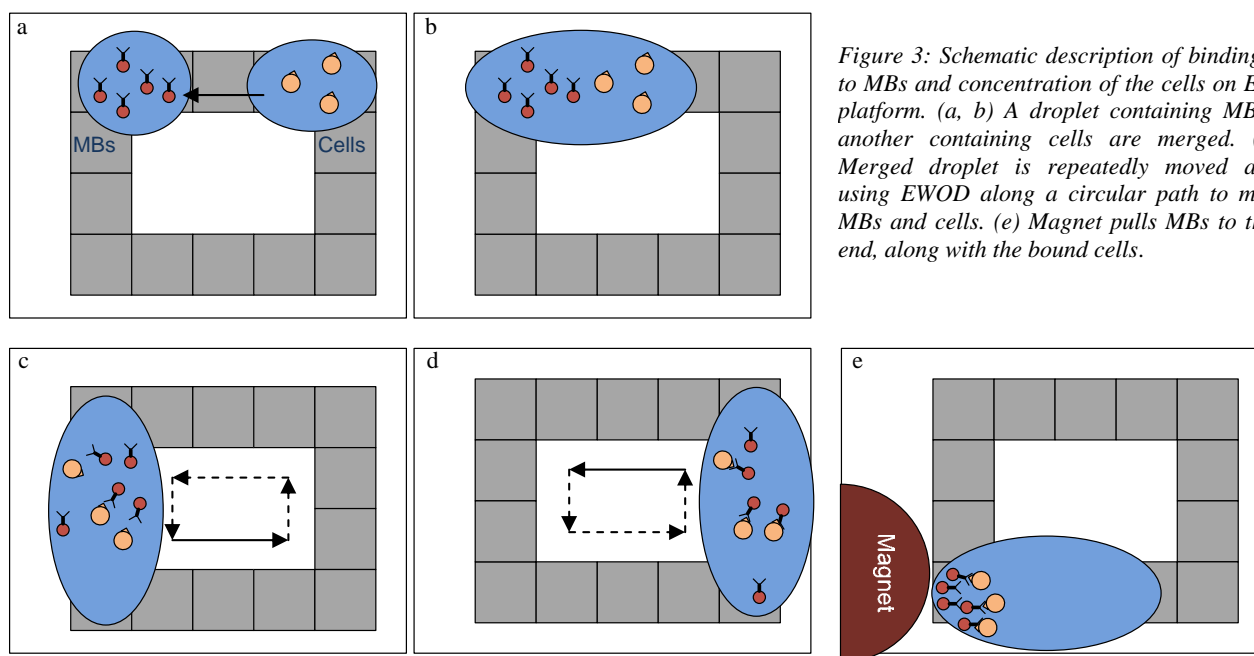


Figure 3: Schematic description of binding cells to MBs and concentration of the cells on EWOD platform. (a, b) A droplet containing MBs and another containing cells are merged. (c, d) Merged droplet is repeatedly moved around using EWOD along a circular path to mix the MBs and cells. (e) Magnet pulls MBs to the left end, along with the bound cells.

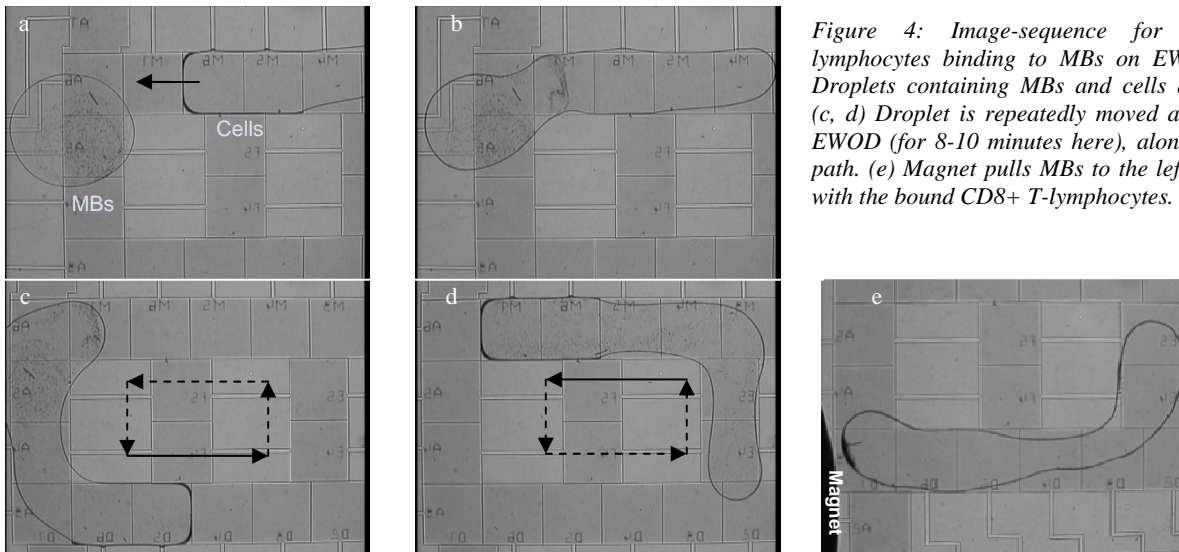


Figure 4: Image-sequence for CD8+ T-lymphocytes binding to MBs on EWOD. (a, b) Droplets containing MBs and cells are merged. (c, d) Droplet is repeatedly moved around using EWOD (for 8-10 minutes here), along a circular path. (e) Magnet pulls MBs to the left end, along with the bound CD8+ T-lymphocytes.

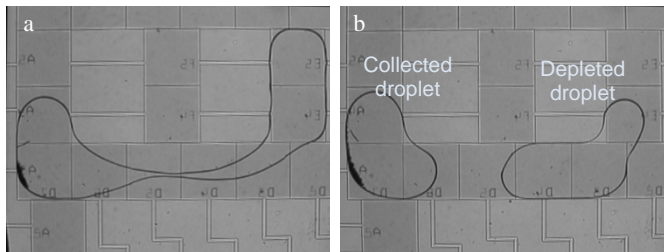
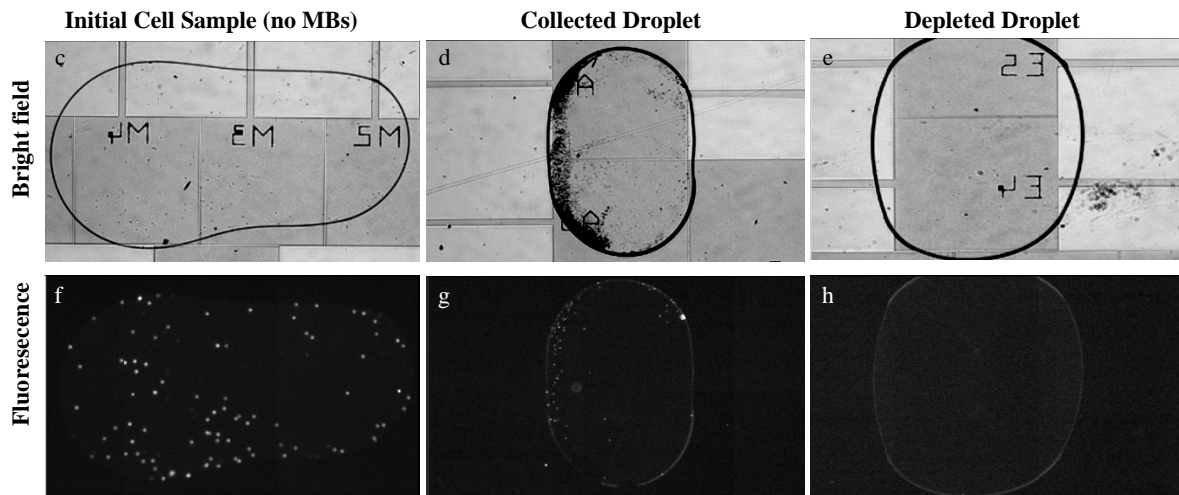


Figure 5: Assessment of binding efficiency. (a, b) Droplet is split after binding. Most CD8+ cells are bound to MBs and collected in the left droplet, as seen in the bright-field and fluorescence images. (c, f) Initial cell sample before merging with MB-containing droplet: ~88 stained cells counted. After binding, (d, g) Collected droplet: ~81 stained cells counted (Some may be hidden behind MBs.) (e, h) Depleted droplet: < 2 stained cells counted.



### Separation of CD8+ and CD8- lymphocytes

Fig. 5 shows the ability to separate CD8+ from CD8- cells. The initial sample contains fluorescently stained CD8+ cells pre-conjugated with MBs, mixed with unlabeled CD8- cells (~10<sup>5</sup>/ml total) (Fig. 6(a), 7(a,e)). On introduction of a magnet, the MB-CD8+ cells move to the left meniscus (Fig. 6(b), 7(b, f)). Fluorescence can be observed where MBs are. The droplet is then

cut using EWOD (Fig. 6(c, d), 7(c, d)), so that most MB-bound CD8+ cells are now collected in the left droplet.

Since they are not actively removed, some CD8- cells may also be collected. However, by adding wash buffer and repeating similar steps as above (Fig. 6(d,e)), CD8- cells can be eventually depleted, leaving mostly CD8+ cells in the final collected droplet (Fig. 6(f)).

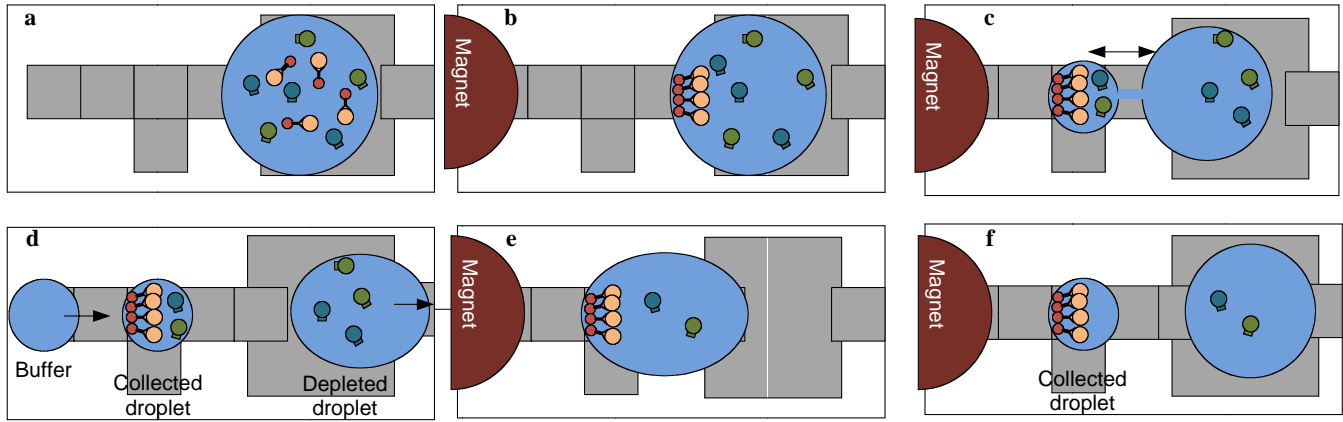


Figure 6: Schematic description of magnetic concentration of CD8+ cells. (a) Initial droplet containing fluorescently stained CD8+ cells (orange) pre-conjugated with MBs (red), and unlabeled CD8- cells (blue, green). (b) On introducing magnet, MB-bound CD8+ cells collected at left meniscus. (c, d) Droplet is cut into collected droplet, containing the MB-CD8+ cells, and depleted droplet with CD8- cells. (d-f) Remaining CD8- cells in the collected droplet can be removed by diluting it with a buffer droplet and repeating the process.

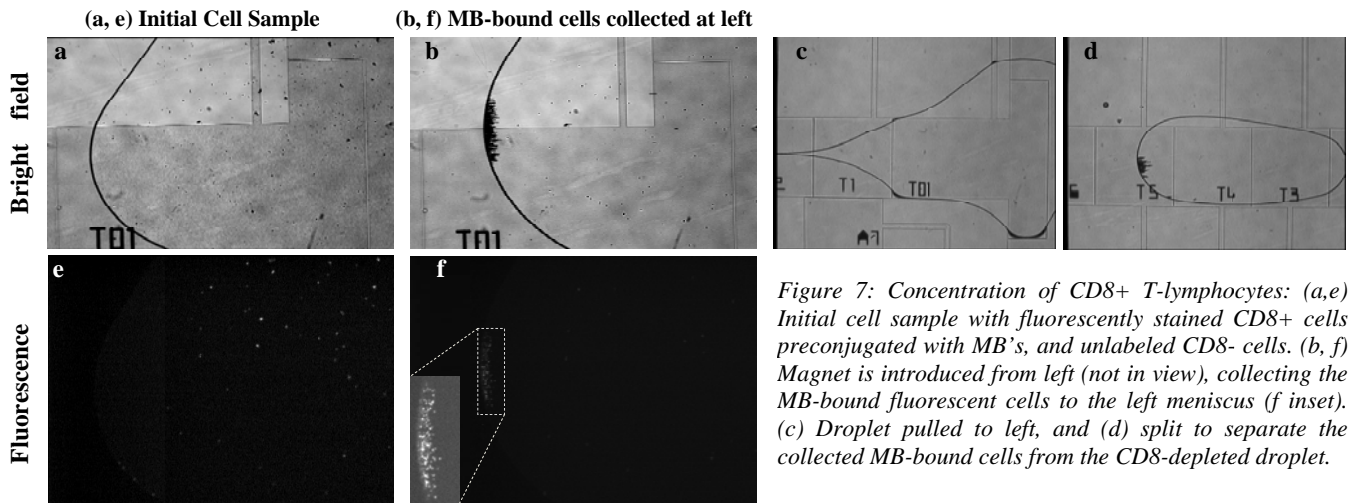


Figure 7: Concentration of CD8+ T-lymphocytes: (a,e) Initial cell sample with fluorescently stained CD8+ cells pre-conjugated with MB's, and unlabeled CD8- cells. (b, f) Magnet is introduced from left (not in view), collecting the MB-bound fluorescent cells to the left meniscus (f inset). (c) Droplet pulled to left, and (d) split to separate the collected MB-bound cells from the CD8-depleted droplet.

## CONCLUSION

We have demonstrated the binding of antibody-conjugated magnetic beads with CD8+ lymphocytes on an EWOD device. We also showed the separation of MB bound CD8+ lymphocytes from unbound CD8- lymphocytes, as a technique to concentrate the former. Improvement in concentration efficiency can be achieved through serial dilution, using EWOD microfluidic operations. The concentrated CD8+ cells can then be lysed, and the proteins from the lysate analyzed for monitoring of organ transplant patients, as per protocol.

Future work will be towards demonstrating the specificity of the MB-CD8+ cell binding on EWOD, and using less pre-processed blood derivatives as samples, so as to move closer to the laboratory protocol used to monitor organ transplant rejection. Cell-lysis and protein detection will also need to be integrated for the complete diagnostic device.

## ACKNOWLEDGEMENT

This work is supported by NASA through Institute for Cell Mimetic for Space Exploration (CMISE), NIH through Pacific Southwest RCE (grant AI065359), and Intramural Seed Grant of the UCLA Department of Urology.

## REFERENCES

- [1] A K Cashion, O M Sabek, C J Driscoll, L W Gaber, A O Gaber, "Serial Peripheral Blood Cytotoxic Lymphocyte Gene Expression Measurements for Prediction of Pancreas Transplant Rejection," *Transplantation Proceedings*, 2006, vol. 38, pp. 3676-3677.
- [2] J L Veale et al., "Noninvasive Diagnosis of Cellular and Antibody-Mediated Rejection by Perforin and Granzyme B in Renal Allografts," *Human Immunology*, 2006, vol. 67, pp. 777-786.
- [3] G J Shah, E Pierstorff, D Ho, C-J Kim, "Meniscus-Assisted Magnetic Bead Trapping on Ewod-Based Digital Microfluidics for Specific Protein Localization," *Proc. Transducers*, Lyon, France, June 2007, pp. 707-710.
- [4] Y Z Wang, Y Zhao, S K Cho, "In-Droplet Magnetic Beads Concentration and Separation for Digital Microfluidics," *Proc. Transducers*, Lyon, France, June 2007, pp. 711-714.
- [5] Y Z Wang, Y Zhao, S K Cho, "Efficient in-Droplet Separation of Magnetic Particles for Digital Microfluidics," *J. Micromechanics and Microengineering*, 2007, vol. 17, pp. 2148-2156.

# A WIRELESSLY-ACTIVATED PARYLENE ELECTROTHERMAL VALVE FOR MAPPING BRAIN FUNCTION IN FREELY MOVING SUBJECTS

Po-Ying Li<sup>1</sup>, Tina K. Givrad<sup>2</sup>, Daniel P. Holschneider<sup>2,3</sup>, Jean-Michel I. Maarek<sup>2</sup>, and Ellis Meng<sup>2</sup>

<sup>1</sup>Department of Electrical Engineering, University of Southern California, Los Angeles, California, USA

<sup>2</sup>Department of Biomedical Engineering, University of Southern California, Los Angeles, California, USA

<sup>3</sup>Department of Psychiatry, Neurology, Cell and Neurobiology, University of Southern California, Los Angeles, California, USA

## ABSTRACT

The first normally-closed Parylene valve operating on electrothermal principles for rapid and wireless drug delivery was designed, fabricated, modeled, and tested. This valve is a key component of an implantable microbolus infusion pump (MIP) for neuroimaging in freely-moving untethered animals. This low-power, lightweight MEMS valve enables an MIP suitable for studying functional brain activation in genetically engineered mice by replacing a large conventional solenoid valve used previously in larger animals.

## INTRODUCTION

In traditional neuroimaging, to avoid movement artifacts during data acquisition, subjects need to be immobilized or anesthetized. This is one of the major constraints on neuroimaging in animals which prevents study of fundamental behaviors linked to locomotor activities and introduces additional variables of stress or anesthetic agent that may confound meaningful interpretation. To acquire detailed understanding of the neural mechanisms underlying fundamental mammalian behaviors, such as aggression, mating, feeding, and fear, new techniques are required.

An implantable microbolus infusion pump (MIP) (Fig. 1) consisting of a drug reservoir, tuned inductive coil, catheter, and valve has been introduced for drug delivery in rats [1,2]. The MIP has allowed, for the first time, cerebral perfusion mapping in conscious freely-moving small animals. The remotely triggered valve initiates rapid release of a radioactive tracer from a pressurized reservoir directly into systemic circulation followed by rapid euthanasia. Regional cerebral blood flow is assessed using autoradiography. However, to apply the same drug delivery scheme to smaller animals, such as mice, a key requirement of the MIP system is the total weight and size of the implant which must be less than 3 grams and allow for subcutaneous implantation in a 40-gram mouse. In addition, the valve footprint should match the inner diameter of the catheter (330 or 500 $\mu$ m). Current technology in implantable drug delivery in small animals (constant rate infusion pump) is unable to achieve the rapid injection necessary to prevent nonspecific tracer distribution. A new valve is required that reduces the overall weight and size of the MIP (from 32 g to <3 g total

weight) for implantation in genetically engineered mice (~40 g) and maintains the ability to open quickly for on-demand release of a radiotracer.

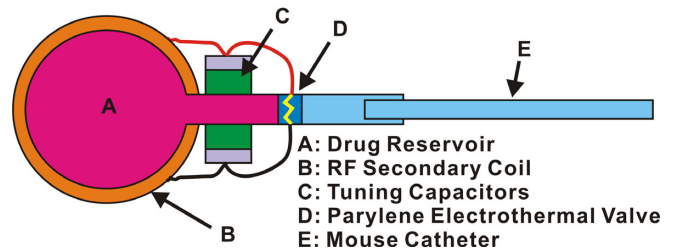
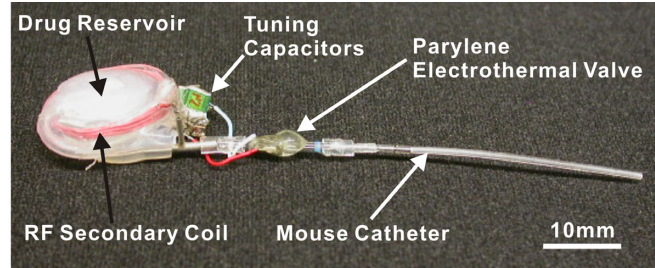


Figure 1: Miniature bolus infusion pump for neuroimaging in mice.

Normally-closed MEMS electrothermal valves capable of rapid opening provide a potential solution for the new MIP system. Previously, electrothermal valves have been developed but only one of these is suited for implantable drug delivery (Table 1) [3-8]. This valve consists of a resistive metallic membrane (Pt/Ti/Pt) suspended over a drug reservoir that opens when an applied current melts the membrane. However, melting the metallic membranes requires significant power to produce the necessary temperature. Here, we use a Parylene C/Pt composite membrane since Parylene C can be thermally degraded at much lower temperature (125-200 $^{\circ}$ C) [9] and can form large mechanically robust membranes for larger effective valve opening area (330-500  $\mu$ m in diameter).

Table 1: Comparison of the our valve with valves reported in research literature.

	Maloney [3]	Cardenas-Valencia [4]	Mueller [5]	Hong [6]	Guerin [7]	McDonald [8]	Our Device
Membrane Materials	Pt/Ti/Pt	SiN <sub>x</sub>	Doped Silicon	Un-crosslinked SU-8	PE/PET Film	PDMS	Parylene
Membrane Dimension L x W x T ( $\mu$ m)	50 x 50 x 0.01	3000 x 3000 x 3	N/A x N/A x 50	N/A x N/A x 50	N/A x N/A x 35	100 x 60 x 20	$\phi$ 500 x 10 (thick)
Thermal Element Materials	Pt/Ti/Pt	Pt/Ti	Doped Si	Ni	Cu	Pt	Pt
Thermal Element Thickness ( $\text{\AA}$ )	10/100/10	300/90	500000	50000	N/A	N/A	1000
Mass Transport Mechanism	Diffusion	Pressure Driven	Pressure Driven	Pressure Driven	Pressure Driven	Pressure Driven	Pressure Driven
Max. Pressure (kPa (psi))	N/A	500.0 (72.5)	20684.3 (3000)	96.5 (14)	200.0 (29)	N/A	689.4 (100)
Melting Temperature ( $^{\circ}$ C)	1770	700	1400	50	120	N/A	125
Opening Power (mW)	2250	16000	300	0.08	400	7.5	25.2
Applied Voltage (V)	N/A	70	N/A	0.7	1.5	420	3.6
Applied Current (mA)	1000	N/A	N/A	N/A	N/A	N/A	7
Opening Time (ms)	0.01	20	0.1	1000	1200	0.02	100
Energy (mJ)	0.025	320	30	0.08	400	150	2.52
Biocompatibility	Yes	No	No	No	No	No	Yes
Delivered Material (Solid/Liquid/Gas)	Solid/Liquid	Liquid	Gas	Gas	Liquid	Liquid	Liquid

Table 2: Valve design parameters.

Valve ID	33020	50020	50040
Layout			
Occupied Diameter (μm)	330	500	500
Element Line Width (μm)	20	20	40
Total Element Length(μm)	1780	3880	2380

## DESIGN

The electrothermal drug delivery valve consists of an electron-beam evaporated platinum thin film platinum resistive element embedded in a flexible Parylene C membrane (10 μm) (Fig. 2 and Table 2). Parylene further simplifies the valve design by obviating the etched silicon membrane support. The valve is situated in the lumen of a catheter and two contact pad flaps are wrapped along the catheter for connection to control circuitry (Fig. 2c). Current is applied to initiate Joule heating to thermally degrade or melt the Parylene membrane. When the electrical and mechanical connections are broken, the pressurized reservoir drives rapid release of fluids through the catheter and into the venous circulation. This convenient format can be implemented in many microfluidic applications where an inexpensive, disposable valve is required.

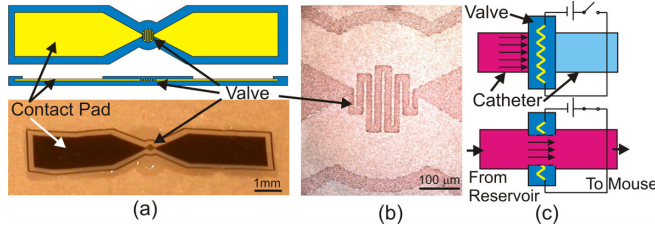


Figure 2: Parylene electrothermal drug delivery valve: (a) device layout, (b) close-up of valve element, and (c) illustration of operation principle of the valve.

## Modeling

To ensure that the Pt element can survive the instantaneous peak pressure from reservoir (1 atm), membrane mechanical performance was verified using both large deflection approximation (Parylene only) and nonlinear FEM models (Parylene/Pt/Parylene). First, in the large deflection theory [10], the nonlinear strain-displacement relations can be expressed as

$$\begin{aligned}\epsilon_x &= \frac{\partial u}{\partial x} + \frac{1}{2} \left( \frac{\partial w}{\partial x} \right)^2 \\ \epsilon_y &= \frac{\partial v}{\partial y} + \frac{1}{2} \left( \frac{\partial w}{\partial y} \right)^2 \\ \gamma_z &= \frac{\partial v}{\partial x} + \frac{\partial u}{\partial y} + \frac{\partial w}{\partial x} \frac{\partial w}{\partial y}\end{aligned}\quad (1)$$

where  $\epsilon_x$ ,  $\epsilon_y$ , and  $\epsilon_z$  and  $u$ ,  $v$ , and  $w$  are stresses and displacements in  $x$ ,  $y$  and  $z$  directions, respectively. The corresponding governing differential equations are

$$\begin{aligned}\frac{\partial^4 \phi}{\partial x^4} + 2 \frac{\partial^4 \phi}{\partial x^2 \partial y^2} + \frac{\partial^4 \phi}{\partial y^4} &= E \left[ \left( \frac{\partial^2 w}{\partial x \partial y} \right)^2 - \frac{\partial^2 w}{\partial x^2} \frac{\partial^2 w}{\partial y^2} \right] \text{ and} \\ \frac{\partial^4 w}{\partial x^4} + 2 \frac{\partial^4 w}{\partial x^2 \partial y^2} + \frac{\partial^4 w}{\partial y^4} &= \frac{t}{D} \left[ p + \frac{\partial^2 \phi}{\partial y^2} \frac{\partial^2 w}{\partial x^2} + \frac{\partial^2 \phi}{\partial x^2} \frac{\partial^2 w}{\partial y^2} - 2 \frac{\partial^2 \phi}{\partial x \partial y} \frac{\partial^2 w}{\partial x \partial y} \right]\end{aligned}\quad (2)$$

where  $\phi$  is the stress function,  $E$  is Young's modulus,  $t$  is the thickness of the plate,  $D$  is the flexural rigidity, and  $p$  is the applied pressure. By using the minimum strain energy method, the solution for a clamped thin circular plate subject to a uniform load  $p_0$  is

$$\frac{p_0 a^4}{64D} = 0.488 \left( \frac{w_{\max}}{t} \right)^3 \quad (3)$$

Nonlinear FEM analysis was also performed (Fig. 3). The results indicated that the maximum stress of the Pt element under 1 atm pressure (peak under normal operation) is 1.53GPa which is less than its tensile strength (1.83GPa). Thus, the electrical connections are expected to survive pressurized conditions during radiotracer loading. The nonlinear model results showed good agreement with load deflection experiments (composite membrane) obtained using a custom pressure testing setup (Fig. 4).

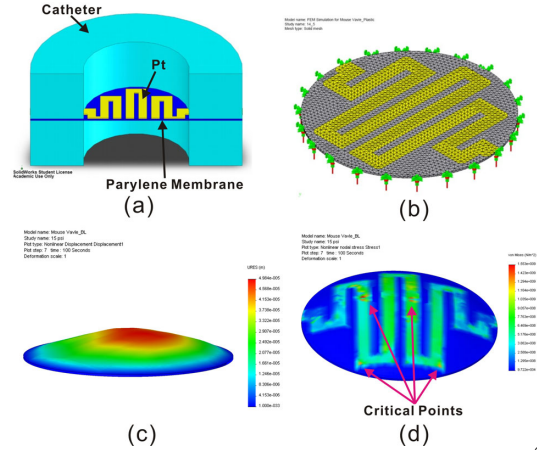


Figure 3: Finite element analysis using COSMOSWorks®: (a) nonlinear FEM model, (b) mesh, (c) vertical displacement (1 atm), and (d) stress distribution (1 atm).

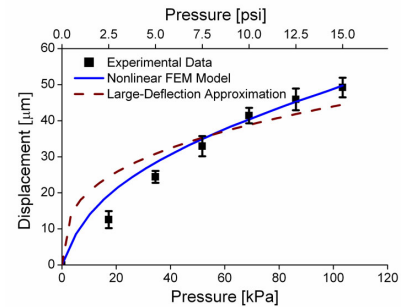


Figure 4: Comparison of experimental data with nonlinear FEM model and large-deflection approximation.

## FABRICATION

The valves were constructed using standard microfabrication techniques. The fabrication began with a 3 inch Si wafer with native oxide to facilitate Parylene C release. First, Parylene layer (5 μm thick) was deposited (Fig. 5A). This is the first layer of the Parylene/metal/Parylene sandwich. Two layers of photoresist (AZ1518 and AZ4400) were spun to create an undercut for Pt liftoff (Fig. 5B). Then liftoff lithography was performed and a 1000 Å Pt film was e-beam evaporated. Following liftoff, the resistive element and contact pad were defined (Fig. 5C). The top Parylene layer (5 μm thick) was then deposited (Fig. 5D). To reveal the contact pad openings, a thick photoresist layer (8 μm of AZ4400) was patterned as a mask for reactive ion etching (Fig. 5E). The Parylene over the contacts was removed by oxygen plasma. Then the photoresist was stripped and thermally annealed in vacuum with nitrogen backfill (200°C for 2 days) (Fig. 5F). The entire wafer was immersed into DI water to release the valves and the individual devices were manually cut from the wafer (Fig. 5G).

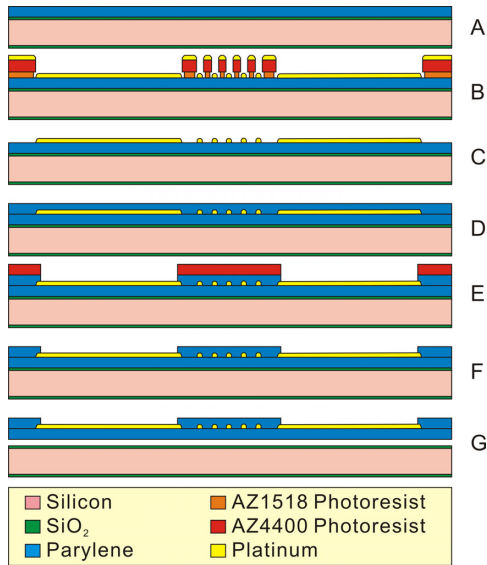


Figure 5: Fabrication process flow for the electrothermal valve.

### Valve Assembly

The valve is situated in the lumen of a catheter and two contact pad flaps are wrapped along the catheter for connection to control circuitry (Fig. 6). To package the valve, the device was first sandwiched between two catheter segments and two laser-cut double-sided adhesive rings (Fig. 6a). Then conductive epoxy was used to secure electrical wires to the contact pads (150°C for 15 hours) (Fig. 6b and d). Finally, the joined assembly was strengthened with a bead of epoxy (Fig. 6c and e). The assembly process was performed under a stereo microscope.

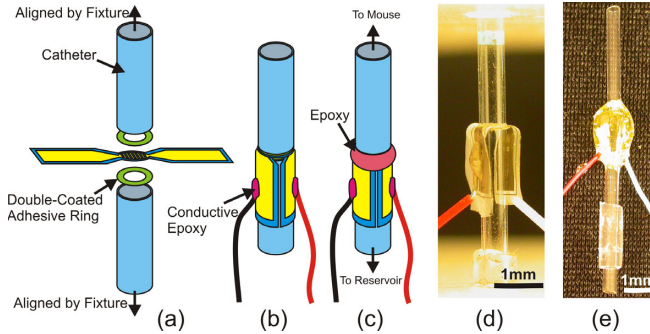


Figure 6: Assembly process for the electrothermal valve: (a) exploded view of components, (b) conductive epoxy for wire attachment, (c) epoxy bonding of the assembly, (d) wires attached to the contact pad by conductive epoxy, and (e) packaged device.

## EXPERIMENTAL METHOD

### Benchtop Testing

The temperature coefficient of resistivity (TCR), overheat temperature (OHT), and valve opening power of the Parylene C electrothermal valve were determined in benchtop experiments. TCR is an important parameter to predict Pt heater resistance at different temperatures. The temperature dependence of Pt is approximately linear over the range of interest and can be expressed as

$$R(T) = R(T_0)[1 + \alpha(T - T_0)] \quad (4)$$

where  $R(T)$  is the resistance at temperature  $T$ ,  $T_0$  is an appropriate reference temperature, and  $\alpha$  is the TCR. In addition, the OHT allows the temperature of the resistive element to be calculated from its resistance. Pt element resistances for different applied currents

were obtained. Then the valve element temperature can be estimated by using the following equation and the experimentally determined TCR:

$$T = T_0 + \frac{R(T) - R(T_0)}{\alpha R(T_0)} \quad (5)$$

The valve opening experiments were performed in both air and water. In air, the valve opening power and current were obtained by applying constant current starting from 1 mA and increasing in small increments; the current corresponding to valve opening was recorded. Corresponding opening power values were calculated. Current ramping was also examined for valve operation in water. Five ramping rates were tested to obtain reliable valve opening. The devices were evaluated by using a laser-machined test fixture to allow rapid electrical connections and facilitate visual observation of the valve. The entire process was monitored by a compound microscope connected to a computer-controlled CCD camera capable of recording time lapse images.

## RESULTS AND DISCUSSION

TCR calibration experiment results are presented in Fig. 7a. A typical TCR for our e-beam deposited thin film Pt heater was  $16.3 \times 10^{-4}/^\circ\text{K}$  which is lower than that expected for bulk Pt TCR ( $39.2 \times 10^{-4}/^\circ\text{K}$ ). This TCR value was applied to the OHT measurements to predict the Pt heater temperature at different applied currents (Fig. 4b). To prevent destructive thermal degradation of the device under test, the OHT experiments were performed at currents below opening values and the results were extrapolated to higher current ranges by using a 2nd-order polynomial curve fit. As depicted in Fig. 4b, a valve opening current between 10 to 15 mA was expected.

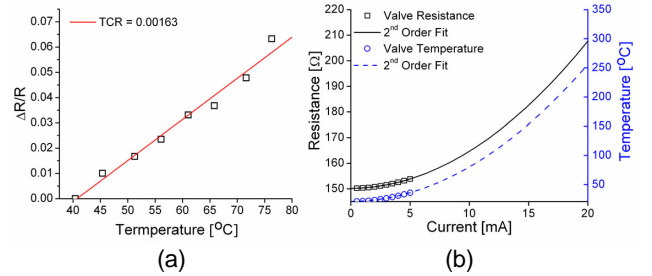


Figure 7: Representative valve electrothermal calibration curves (a) temperature dependence and (b) overheat temperature.

Valves were successfully opened in air (constant current) and water (current ramping) (Fig. 8-10). For constant current, opening current and power decreased with increasing resistance. The stages of valve opening (in water) were observed in real-time while simultaneously tracking the resistance by using current ramping. Five ramping rates (0.025 to 2 mA/sec) were tested to obtain the optimal opening rate (Table 3). Reliable valve opening was obtained for ramping rates less than 0.1 mA/sec.

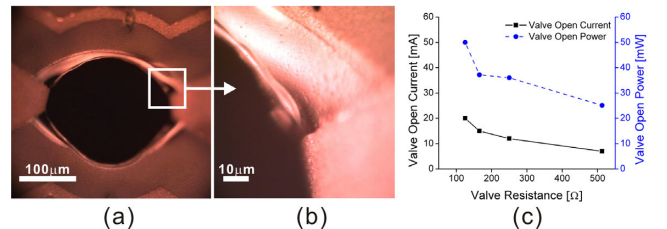


Figure 8: Valve opening (in air): (a) an open valve (15 mA), (b) magnified view of the edge of the valve orifice, and (c) valve opening current and power to resistance relationship.

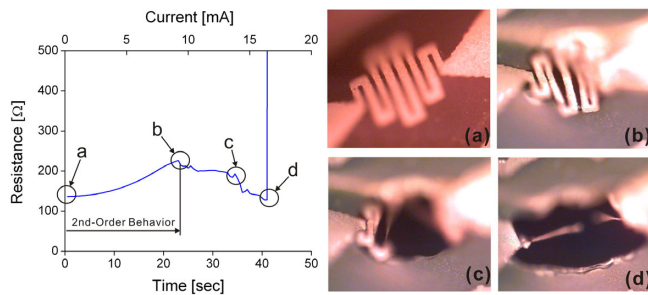


Figure 9: Valve opening (in water). Left: real-time response of the valve. Right: (a-d) time lapse images of valve opening corresponding to resistance measurement events in the left plot.

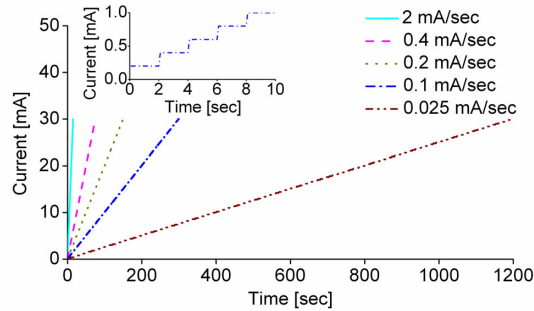


Figure 10: Current ramping rate. The inset shows a close up of the 0.1 mA/sec waveform.

Table 3: Optimization results for current ramping testing in water.

Ramping Rate (mA/sec)	Valve ID 33020		Valve ID 50020		Valve ID 50040	
	Open	Not Open	Open	Not Open	Open	Not Open
0.025	O		O		O	
0.1	O		O		O	
0.2		X		X	O	
0.4	O			X		X
2.0		X		X		X

## NEUROIMAGING

Valve integration into the new MIP design has commenced and wireless operation has already been demonstrated in the mouse emitter coil cage (Fig. 11a). Neuroimaging studies are planned and autoradiographic brain slices and optical density analysis will be obtained. Fig. 11b compares the dimensions of the MIP and a mouse.

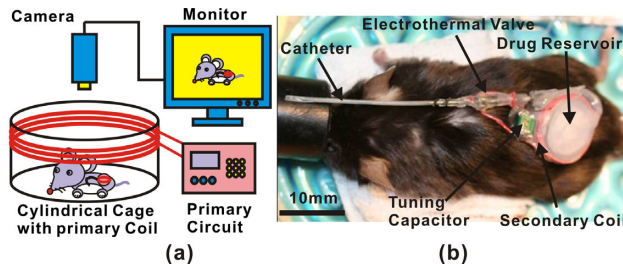


Figure 11: Neuroimaging: (a) in vivo testing setup in which the MIP is powered by inductive power transfer from a primary coil wrapped around the experimental cage, (b) relative size of the MIP and a mouse.

## CONCLUSION

We successfully developed a disposable, low-power Parylene C MEMS valve for neuroimaging applications. The design, modeling, fabrication, and benchtop characterization were performed and investigated. TCR and OHT experiments allowed prediction of the temperature of the heater and determination of the appropriate current to apply to open the valve. Opening powers of 25-50 mW were obtained in air and reliable valve opening in water using current ramping rate of 0.1 mA/sec was obtained. Further reduction in power consumption and optimization of valve performance is planned. Also, additional experiments will evaluate the performance of the valve in the presence of the radiotracer agent and in vivo.

## ACKNOWLEDGEMENTS

This work was funded in part by the NIBIB (1 R01 NS050171). The authors would like to thank Dr. Donghai Zhu, Dr. Tuan Hoang, Mr. Neil Sardesai, and members of the Biomedical Microsystems Lab at University of Southern California.

## REFERENCES

- [1] D. P. Holschneider, J.-M. I. Maarek, J. Harimoto, J. Yang, and O. U. Sremin, "An Implantable Bolus Infusion Pump for Use in Freely Moving, Nontethered Rats," *American Journal of Physiology*, 283, H1713 (2002).
- [2] D. P. Holschneider, J. Yang, Y. Guo, and J. M. I. Maarek, "Reorganization of functional brain maps after exercise training: Importance of cerebellar-thalamic-cortical pathway," *Brain Research*, 1184, 96-107 (2007).
- [3] J. M. Maloney, S. A. Uhland, B. F. Polito, J. N. F. Sheppard, C. M. Pelta, and J. J. T. Santini, "Electrothermally activated microchips for implantable drug delivery and biosensing," *Journal of Controlled Release*, 109, 244 (2005).
- [4] A. M. Cardenas-Valencia, J. Dlutowski, J. Bumgarner, C. Munoz, W. Wang, R. Popuri, and L. Langebrake, "Development of Various Designs of Low-Power MEMS Valves for Fluidic Applications," *Sensors and Actuators A*, 136, 374 (2007).
- [5] J. Mueller, E.-H. Yang, A. Green, V. White, I. Chakraborty, and r. reinicke, "Design and Fabrication of MEMS-Based Micropropulsion Devices at JPL," *Proceedings of SPIE*, San Francisco, CA, 10/22/01 (2001), pp. 57-71.
- [6] C.-C. Hong, J.-W. Choi, and C. H. Ahn, "Disposable Air-Bursting Detonators as an Alternative on-Chip Power Source," *The 15th IEEE International Conference on Micro Electro Mechanical Systems*, Las Vegas, NV, 1/20-24/02 (2002), pp. 240-243.
- [7] L. J. Guerin, L. J. Guerin, O. Dubochet, J. F. Zeberli, P. A. C. P. Clot, and P. A. R. P. Renaud, "Miniature One-Shot Valve," *The 11th IEEE International Conference on Micro Electro Mechanical Systems Heidelberg, Germany*, 01/17-21/98 (1998), pp. 425-428.
- [8] J. C. McDonald, S. J. Metallo, and G. M. Whitesides, "Fabrication of a Configurable, Single-Use Microfluidic Device," *Analytical Chemistry*, 73, 5645 (2001).
- [9] D. W. Grattan and M. Bilz, "The Thermal Aging of Parylene and the Effect of Antioxidant," *Studies in Conservation*, 36, 44 (1991).
- [10] T. von Karman, "Festigkeitsprobleme in Maschinenbau," *Encyklopadie der Mathematischen Wissenschaften*, 4, 348 (1910).

# INTEGRATION OF A FILM BULK ACOUSTIC RESONATOR WITH MICROFLUIDIC CHANNELS FOR BIOMEDICAL SENSING IN LIQUID

W. Xu, X. Zhang, H. Yu, A. Abbaspour-Tamijani and J. Chae

Department of Electrical Engineering, Arizona State University, Tempe, Arizona, USA

## ABSTRACT

This paper reports an integration of microfluidic channels with a film bulk acoustic resonator (FBAR) for in liquid biomedical sensing applications. The device consists of a zinc oxide (ZnO) film based longitudinal mode FBAR and parylene encapsulated microfluidic channels. By confining the liquid with the height comparable to the acoustic wavelength of the FBAR in the microfluidic channels, the quality factor ( $Q$ ) of the resonating system significantly increases, resulting in very high sensitivity FBAR sensor for liquid samples. We demonstrate a FBAR with  $Q$  up to 120, an improvement of more than 8 times over that of existing FBARs in liquid. A bio-molecular (streptavidine) sensing test presents a sensitivity of 638 Hz cm<sup>2</sup>/ng and an extremely fine resolution of 2.025 ng/cm<sup>2</sup> of the sensor.

## INTRODUCTION

Compared to fluorescent and radioactive labeling methods, label-free bimolecular sensors in liquid media are useful for various applications ranging from pharmaceutical research to medical diagnostics, partially due to the fact that label-free detection eliminates labeling process which may induce modification of chemical properties of target molecules [1]. However, widely used label-free protein detection techniques, such as surface plasmon resonance (SPR) [2, 3] and quartz crystal microbalances (QCM) [4, 5], are significantly less sensitive than labeling methods [1, 6]. In recent years, FBAR has shown great potentials of being high sensitivity biosensors. State-of-the-art ZnO-based FBAR biosensors reported in recent literature exhibit a mass sensitivity of up to 1000 Hz cm<sup>2</sup>/ng in air, over 1000 times higher than that of traditional QCMs [7-11]. Similar to QCMs, FBAR consists of a piezoelectric layer of 1-2 μm sandwiched between two metal electrodes, with an operating frequency above 1 GHz.  $Q$  of 500 at 1GHz can be easily achieved in the air or vacuum, which produces extremely high detecting resolutions. However, in the liquid environments  $Q$  significantly reduces due to the viscous damping of the contacting liquid. For instance in water  $Q$  usually drops by a factor of 10-100, which reduces the sensing ability of the sensor. As  $Q$  decreases the minimum detectable frequency shift increases, thus the sensible mass resolution reduces roughly by the same factor. Although shear mode vibration instead of longitudinal mode can reduce the  $Q$  degradation, it unavoidably lowers sensitivity [12, 13]. In shear mode,  $Q$  has been reported up to 100-150 in water; however the sensitivity drops approximately to 1/3 of the longitudinal mode resonators of similar dimensions. Clearly, a high  $Q$  resonator in liquid with uncompromised sensitivity is the key to achieve a high resolution, high sensitivity biosensor.

## APPROACH AND MODELING

A typical FBAR have a thickness of 1-2μm piezoelectric thin film such as ZnO or AlN mechanically supported by a dielectric layer, which has its fundamental resonance frequency above 1 GHz in longitudinal mode. FBARs usually have high  $Q$ s from several hundreds up to a couple of thousands in the air, because the acoustic energy is well entrapped in the resonator body due to very large impedance mismatch between solid materials and the air.

The  $Q$  drops significantly (12-25) in water since acoustic impedance mismatch between liquid and solid is much smaller than that between solid and air. Therefore the acoustic waves generated inside of the solid resonator partially transmit into the liquid and dissipate, consequently reduce  $Q$ .

The approach that we present is to form a very thin liquid layer on the solid resonator so that the acoustic wave length inside the liquid is comparable to the thickness of the thin liquid layer. This allows minimizing the energy dissipation inside the liquid. In order to form the thin liquid layer, we use microfluidic channels integrated with FBAR. Figure 1 illustrates the schematic design of the FBAR sensor integrated with microfluidic channels. A three-layer FBAR (Al/ZnO/Au) is fabricated on a suspended silicon nitride (SiN) membrane. A parylene enclosure built on top of the FBAR forms the microfluidic channels. The channel height is precisely defined by a sacrificial layer, and inlet / outlet ports are accessible from the backside of the device.

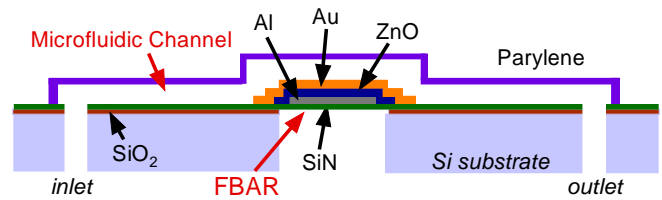


Figure 1: Schematic structure of an FBAR sensor integrated with the microfluidic channel.

We use a transmission-line model (Figure 2) for the multilayer composite resonator to estimate its  $Q$  behavior. The model consists of six physical layers of the device: SiN supporting membrane, Al electrode, piezoelectric ZnO layer, Au electrode, water layer confined in the microfluidic channel, and parylene microfluidic channel. Since the four solid layers have negligible loss compared to the liquid or polymer, we simplify the model that attenuation occurs only in liquid and polymer.

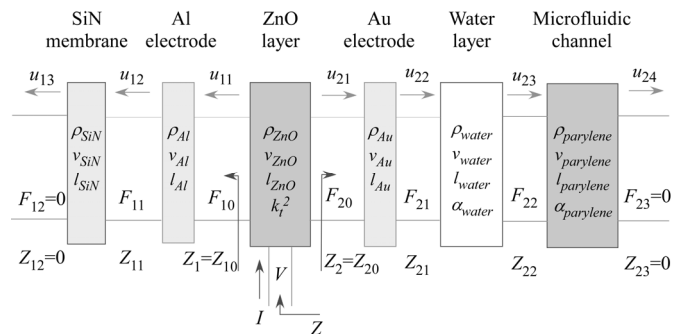


Figure 2: Equivalent transmission-line model of the FBAR with multilayer composites.

The piezoelectric ZnO layer is modeled as a three port component which has an electrical terminal pair (voltage  $V$  and

current  $I$ ), the back and front acoustic ports denoted as force  $F$  and displacement  $u$ . From the equivalent circuit model of Mason's in-line model of a piezoelectric film, the electric input impedance of the system can be written as [14]:

$$Z = \frac{1}{j\omega C_0} \left[ 1 - \frac{k_t^2}{\gamma} \cdot \frac{(z_1 + z_2) \cdot \sin \gamma + j \cdot 2(1 - \cos \gamma)}{(z_1 + z_2) \cdot \cos \gamma + j \cdot (1 + z_1 z_2) \cdot \sin \gamma} \right] \quad (1)$$

where  $C_0 = \epsilon_{33} \cdot S / l_{ZnO}$  is the static capacitance of the resonator,  $S$  is the effective area of the FBAR,  $\epsilon_{33}$  and  $l_{ZnO}$  are the permittivity and thickness of the ZnO layer,  $k_t^2$  is the electromechanical coupling coefficient of ZnO,  $\gamma = \omega l_{ZnO} / v_{ZnO}$  is the phase delay of the longitudinal acoustic wave with velocity  $v_{ZnO}$  in ZnO,  $\omega$  is the angular frequency,  $z_1 = Z_1 / Z_0$ ,  $z_2 = Z_2 / Z_0$  are the normalized acoustic loading impedance on both sides of the ZnO film,  $Z_0 = S \rho_{ZnO} v_{ZnO}$  is the acoustic impedance of the ZnO layer, and  $\rho_{ZnO}$  is the density, respectively.

$Z_1$  and  $Z_2$  are cascaded from the adjacent component and loading impedance by (Figure 2):

$$Z_{mn} = Z_{0mn} \frac{Z_{m,n+1} + Z_{0mn} \tanh \gamma_{0mn} l_{0mn}}{Z_{0mn} + Z_{m,n+1} \tanh \gamma_{0ij} l_{0mn}} \quad (2)$$

where  $m=1$  and  $2$ , indicating the impedance series on the left and right of ZnO,  $Z_{mn}$  is the loading impedance at the cross section after the  $n^{th}$  component either on the right or left of the ZnO,  $Z_{0mn}$ ,  $l_{0mn}$  are the acoustic impedance, thickness of the  $j^{th}$  component, respectively,  $\gamma_{0mn} = \alpha_{0mn} + j\beta_{0mn}$ ,  $\alpha_{0mn}$  is the attenuation coefficient and  $\beta_{0mn}$  is the angular wave number of the corresponding component. We define a boundary condition of  $Z_{12} = Z_{23} = 0$ , stating the mechanically free at the parylene/air or SiN/air interfaces. We use MATLAB to calculate  $Q$ :

$$Q = \frac{f}{2} \frac{\partial \varphi(Z)}{\partial f} \quad (3)$$

where  $\varphi(Z)$  is the phase of the impedance  $Z$  in eq. (1).

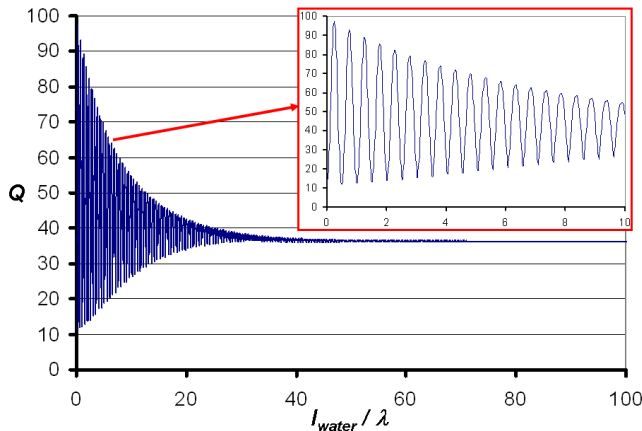


Figure 3: Theoretically predicted  $Q$  versus the ratio of fluidic channel height to the acoustic wavelength in water.

Figure 3 shows the MATLAB simulation of a  $0.5 \mu\text{m}$  thick ZnO FBAR. We plot  $Q$  in terms of the ratio of the thickness of water layer ( $l_{water}$ ) to acoustic wavelength in the water ( $\lambda$ ). The

FBAR has a resonance frequency of 2.0 GHz. As the ratio becomes large, above 30, the  $Q$  converges to low ( $< 40$ ). In other words, the large portion of the acoustic energy generated inside the FBAR dissipates in the water if the thickness of the water layer is more than 30 times of the acoustic wavelength in the water. This region is where typical FBAR operates at in liquid. However, when the ratio is less than 30,  $Q$  starts oscillating. This is because the acoustic waves reflected from ZnO/liquid and liquid/parylene boundaries alternatively interfere with each other constructively (in phase) or destructively (out of phase). If technologies allow implementing precisely ratioed structures of ZnO/liquid, it is possible to obtain high  $Q$  at contacting liquid.

## EXPERIMENTS AND EVALUATION METHODS

### Fabrication

Figure 4 illustrates the fabrication process flow. The FBAR sensor is fabricated using standard silicon micromachining technologies. Fabrication starts with a  $<100>$  silicon wafer;  $2000\text{\AA}$  thick oxide is first thermally grown on the wafer, followed by a  $6000\text{\AA}$  thick low-stress LPCVD SiN layer as a mechanical supporting membrane.  $1600\text{\AA}$  thick Al is evaporated and patterned on the SiN layer as the bottom electrode. The Al electrode determines the effective area of the FBAR. ZnO is then sputtered for  $0.55, 2.1, 4.2 \mu\text{m}$ .  $300\text{\AA}/1500\text{\AA}$  thick Cr/Au is sputtered and lift-off patterned on the ZnO layer as a top electrode. We use Au as the top electrode due to its excellent conductivity and good affinity to biomolecular binding [15].  $3\mu\text{m}$  thick photoresist is coated and patterned as a sacrificial layer on Au, followed by parylene C film coating to form the fluidic channel enclosures. The parylene C thin film is  $3 \mu\text{m}$  thick which provides enough mechanical strength.

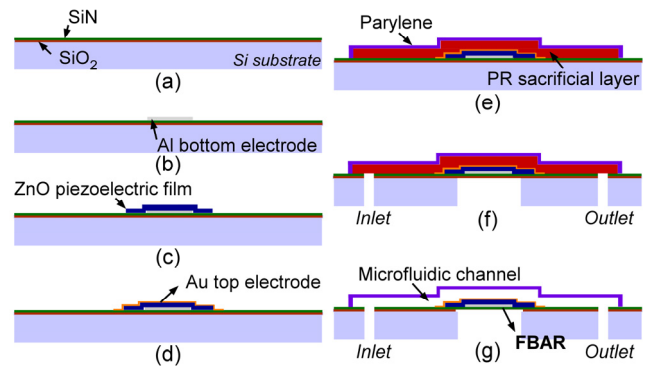


Figure 4: Fabrication process of a FBAR integrated with a microfluidic channel: a) thermally grown  $\text{SiO}_2$  and low stress SiN by LPCVD on Si substrate; b) Al deposition and patterning; c) ZnO deposition by sputtering and patterning; d) deposition of Cr/Au by patterning; e) photoresist patterns as sacrificial layer and coating of parylene C; f) Deep RIE to form inlet/outlet of channels and release the membrane; g) removing  $\text{SiO}_2$  beneath SiN and sacrificial PR; supercritical  $\text{CO}_2$  drying to release the microfluidic channel.

The wafer is etched through from the backside by Deep RIE (Reactive Ion Etch) to release the SiN membranes and to form the channel inlets/outlets. Finally, the sacrificial photoresist layer is removed by soaking devices in acetone for overnight and the microfluidic channels are dried by supercritical  $\text{CO}_2$  process. Additionally, the  $\text{SiO}_2$  layer underneath SiN which works as a stopping layer for Deep RIE is removed by buffered oxide etchant to achieve a smooth SiN supporting membrane. The  $\text{SiO}_2$  stopping

layer may not be very smooth due the physical bombardment during Deep RIE process. The fabricated FBAR integrated with the microfluidic channel is shown in Figure 5.

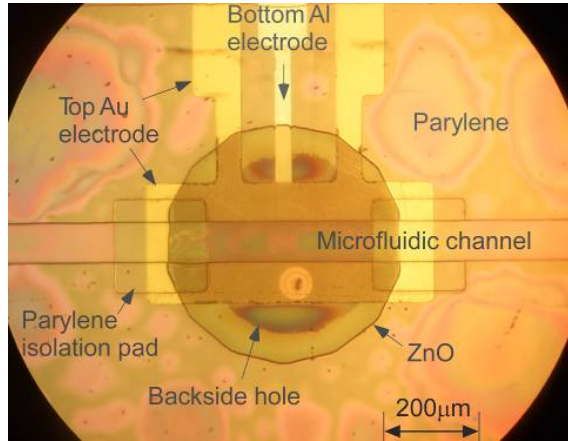


Figure 5: Top view of the fabricated FBAR integrated with the microfluidic channel.

### Q Measurements

$Q$  of the fabricated devices are measured for three different cases; in the air, drenched in the water and water in the microfluidic channel. These correspond to no damping, full damping and partial damping, respectively.

Chips are mounted on a probe station and characterized using HP 8510C network analyzer, 85105A millimeter-wave controller and 8517B S-Parameter test set. The test setup is shown in Figure 6. We record  $S_{11}$  and the impedance  $Z$  of the sensor is extracted from the  $S_{11}$  spectrum. Then, the  $Q$  of resonators is calculated by eq. (3).

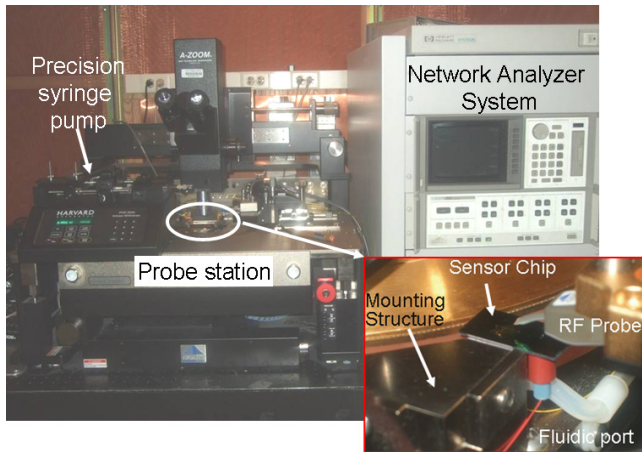


Figure 6: Test setups; testing device on a probe station, connected with a syringe pump and a network analyzer system.

2.1 $\mu$ m thick ZnO FBAR has a parallel resonant frequency of 1.05GHz. In the air,  $Q$  factor reaches  $\sim$ 250. We fill up the backside hole with water to measure the  $Q$  at full damping. The water is practically infinitely deep since the depth is more than 300  $\mu$ m, much larger than the acoustic wavelength in water ( $\sim$ 1.42  $\mu$ m).  $Q$  drops approximately to 7-15, which matches well with the previous reports [13, 16]. Now, we flow water through the

microfluidic channel to measure  $Q$  at partial damping. Water flows at a constant rate (25  $\mu$ L/hr) in the microfluidic channel driven by a precisely controlled infusion syringe pump. The  $Q$  drops from 250 to 120 when the water reaches the Au surface of the FBAR and remains nearly constant afterward. Compared to the reported longitudinal FBARs in water, our devices show 8 to 10 times higher  $Q$ , high enough to compete with the shear-mode FBARs.

Table 1 lists the measured  $Q$ , corresponding channel heights and the heights to wavelength ratios. Note that  $Q$  of partial damping varies widely. We believe this is due to the variation of water heights. As the water heights change  $Q$  changes significantly in the partial damping regime as shown in Figure 3. Figure 7 compares the measured impedance spectrum of no damping (in the air), full damping (drenched in water), and partial damping (water in microfluidic channels).

Table 1: Measured  $Q$  for different damping conditions.

ZnO thickness ( $\mu$ m)		0.55	2.1	4.1
Resonant freq. (GHz)		2.2	1.05	0.6
No damping	$l_{water}(\mu$ m)	--	--	--
	$l_{water}/\lambda$	--	--	--
	$Q$	<b>220</b>	<b>240</b>	<b>430</b>
Full damping	$l_{water}(\mu$ m)	500	500	500
	$l_{water}/\lambda$	--	--	--
	$Q$	<b>12</b>	<b>7</b>	<b>15</b>
Partial damping	$l_{water}(\mu$ m)	3.0	3.0	3.0
	$l_{water}/\lambda$	4.45	2.12	1.21
	$Q$	<b>35~40</b>	<b>65~120</b>	<b>85~110</b>

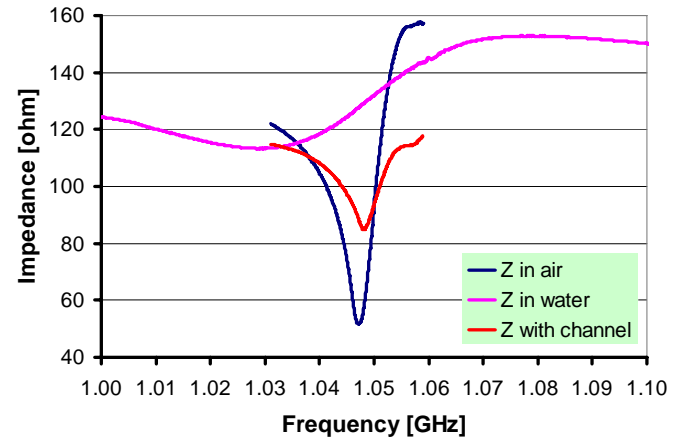


Figure 7: Impedance spectra of FBAR in the air (no damping), in water (full damping), and in the microfluidic channel (partial damping).

### Bio-sensing testing

Streptavidine is a protein which strongly binds to Au. As a proof-of-concept bio-sensing test, we use streptavidine molecules to characterize the fabricated FBAR sensor. The top electrode is made of Au, which forms a permanent bond with streptavidine flowing through the microfluidic channels.

Figure 8 shows the test sequence. Phosphate Buffer Solution (PBS) first flows through the microfluidic channel, at a constant

rate of 25 $\mu$ L/hr. After the flow stabilizes, the PBS is replaced by 0.1  $\mu$ M streptavidine solution. A frequency shift occurs immediately. This corresponds to the density and viscosity difference between these two solutions. After the streptavidine binding saturated the gold surface, we switch back to PBS. A permanent frequency shift of 90 kHz (86 ppm) is measured. The frequency shift indicates the mass loading by permanent streptavidine bound to the Au surface.

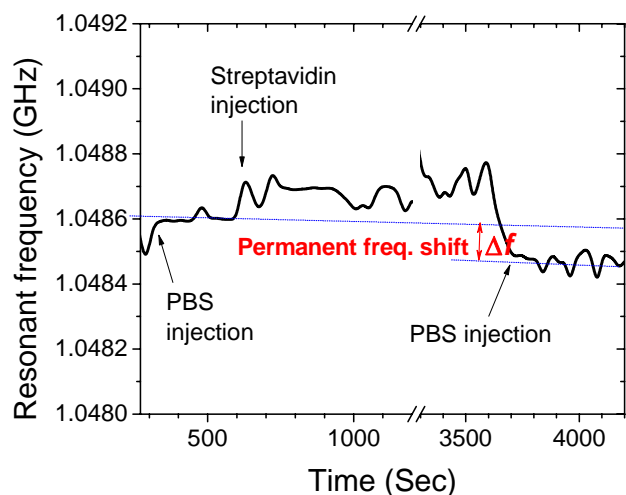


Figure 8: Measured parallel resonance frequency shift ( $\Delta f$ ) of the FBAR sensor over time ( $t$ ) due to the mass loading on gold electrodes resulted by streptavidine-gold bindings.

For the proof-of-concept test, the resonator has a  $Q$  of 80 in both PBS and streptavidine solutions. The sensitivity is calculated as 638 Hz  $\text{cm}^2/\text{ng}$ , which indicates a resolution of 2.025  $\text{ng}/\text{cm}^2$ , approximately 10 times better than reported resolution.

## CONCLUSION

We significantly improve  $Q$  of FBAR in liquid environments by confining the liquid in a micron range to minimize the acoustic energy dissipation. We demonstrate the  $Q$  of FBAR reaches 120, which is at least 8 times higher than reported  $Q$  in liquid environments. The  $Q$  improvement enhances the sensitivity of the FBAR sensor, thus increases the resolution of the sensor. Future efforts include optimizing the microfluidic channel to achieve higher  $Q$  and demonstrate high sensitivity biosensors for various biomolecules.

## REFERENCES

1. T. Burg, and S. Manalis, "Suspended microchannel resonators for biomolecular detection", *Appl. Phys. Lett.*, 83, 2698, (2003).
2. J. Homola, "Present and future of surface plasmon resonance biosensors", *Analytical and Bioanalytical Chemistry*, 377, 528 (2003).
3. J. Homola, S. Yee, and G. Gauglitz, "Surface plasmon resonance sensors: review", *Sensors and Actuators B, Chemical.*, 54, 3, (1999).
4. C. K. O'Sullivan, and G. Guilbault, "Commercial quartz crystal microbalances-theory and applications", *Biosensors and Bioelectronics.*, 14, 663, (1999).
5. M. Jonsson, et al., "Quartz crystal microbalance biosensor design", *Sensors and Actuators B (Chemical)*, 123, 21, (2007).
6. T. Burg, et al., "Vacuum-packaged suspended microchannel resonant mass sensor for biomolecular detection", *Journal of Microelectromechanical Systems*, 15, 1466, (2006).
7. J. Bender and J. Krim, "Applications of the Piezoelectric Quartz Crystal Microbalance for Microdevice Development", *Microscale Diagnostic Techniques*. 227, (2005).
8. R. Gabl, et al., "First results on label-free detection of DNA and protein molecules using a novel integrated sensor technology based on gravimetric detection principles", *Biosens. Bioelectron.*, 19, 615, (2004).
9. L. Yan, et al., "Piezoelectrically transduced low-impedance microelectromechanical resonators", *Appl. Phys. Lett.*, 87, 154103, (2005).
10. S. Lee, K.H. Yoon, and J. Lee, "Influence of electrode configurations on the quality factor and piezoelectric coupling constant of solidly mounted bulk acoustic wave resonators", *J. Appl. Phys.*, 92, 4062, (2002).
11. Z. Yan, et al., "ZnO-based film bulk acoustic resonator for high sensitivity biosensor applications", *Appl. Phys. Lett.*, 90, 143503, (2007).
12. G. Wingqvist, et al., "Shear mode AlN thin film electro-acoustic resonant sensor operation in viscous media", *Sens. Actuators B, Chem.*, 123, 466, (2007).
13. J. Weber, et al., "Shear mode FBARs as highly sensitive liquid biosensors". *Sens. Actuators A, Phys.*, 128, 84, (2006).
14. Y. Zhang, Z. Wang, and J. D. N. Cheeke, "Resonant spectrum method to characterize piezoelectric films in composite resonators", *IEEE Trans. Ultrason. Ferroelectr. Freq. Control*, 50, 321 (2003).
15. E. Ostuni, L. Yan, and G.M. Whitesides, "The interaction of proteins and cells with self-assembled monolayers of alkanethiolates on gold and silver", *Colloids and Surfaces B: Biointerfaces*, 15, 3, (1999).
16. H. Zhang, et al., "A film bulk acoustic resonator in liquid environments", *J. Micromech. Microeng.*, 15, 1911, (2005).

# THE MICROMECHANICAL RESONANT SWITCH (“RESOSWITCH”)

Yang Lin, Wei-Chang Li, Zeying Ren and Clark T.-C. Nguyen

Department of Electrical Engineering and Computer Sciences

University of California at Berkeley, Berkeley, California 94720, USA

## ABSTRACT

A micromechanical switch, dubbed the “resoswitch”, has been demonstrated that harnesses the resonance and nonlinear dynamical properties of its mechanical structure to greatly increase switching speed and cycle count (even under hot switching), and lower the needed actuation voltage, all by substantial factors over existing RF MEMS switches. The device comprises a wine-glass mode disk resonator driven hard via a 2.5V amplitude ac voltage at its 61-MHz resonance frequency so that it impacts electrodes along an orthogonal switch axis, thereby closing a switch connecting a 10V source to the switch electrode. The 61-MHz operating frequency corresponds to a switching period of 16ns with an effective rise time of <4ns, which is more than 200 times faster than the  $\mu$ s-range switching speeds of the fastest RF MEMS switches. Furthermore, since the voltage source is on during switching, the switch essentially *hot switches* with a demonstrated lifetime exceeding 16.5 trillion cycles without failure, but with some observed degradation.

## INTRODUCTION

RF MEMS switches operating at RF to millimeter-wave frequencies substantially outperform p-i-n diode and field-effect transistor (FET) counterparts in insertion loss, isolation, and switch figure of merit (*FOM*). Unfortunately, their much slower switching speeds (e.g., 1-15  $\mu$ s versus the 0.16-1ns [1] of FET’s) and cycle lifetimes on the order of 100 billion cycles (for the good ones) relegating them mainly to antenna switching, reconfigurable aperture, and instrumentation applications, and precludes them from much higher volume applications, such as switched-mode power amplifiers and power converters.

Indeed, the benefits afforded to switched-mode power applications that would ensue if the transistors they presently employ were replaced by switches with *FOM*’s on the order of those exhibited by RF MEMS switches would be enormous. For example, switched-mode power amplifiers that ideally should be able to achieve 100% drain efficiency presently cannot attain such values in practical implementations, in part because the transistors they use for switching exhibit large input capacitors (for small “on” resistances) and are often limited in the voltages they can support. MEMS switches, being made of metal, have very small “on” resistances and would be able to support higher voltages. However, if they are to be used in switched-mode power applications, their actuation voltages would need to be lowered substantially (from >50V down to the single-digit volt range), their speeds would need to be much higher (e.g., ns switching times), and their reliability enhanced substantially, since typical power amplifier and converter applications would require cycle counts in the 100’s of quadrillions.

Pursuant to achieving a switch suitable for power amplifier and converter applications, this work demonstrates a micromechanical switch, dubbed the “resoswitch”, that harnesses the resonance and nonlinear dynamical properties of its mechanical structure to greatly increase switching speed and cycle count (even under hot switching), and lower the needed actuation voltage, all by substantial factors over existing RF MEMS switches. The device comprises a wine-glass mode disk resonator driven hard via a 2.5V amplitude ac voltage at its 61-MHz resonance frequency so that it impacts electrodes along an orthogonal switch axis, thereby closing a

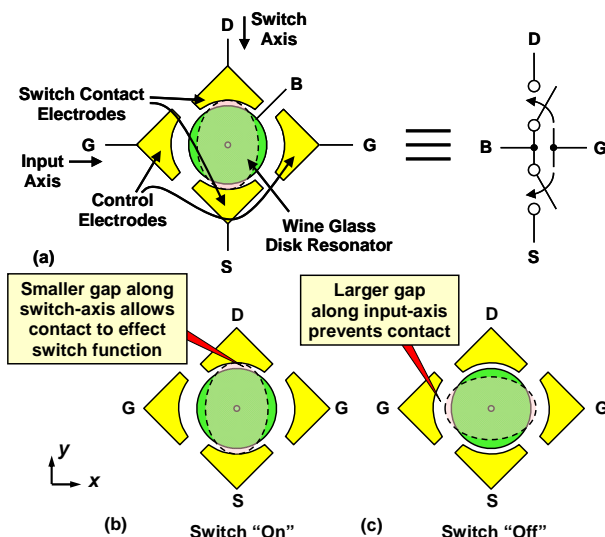


Fig. 1: Schematics showing (a) the physical structure of the micromechanical resoswitch, identifying its ports and equating it to a functional equivalent circuit; (b) its “on”; and (c) its “off” states.

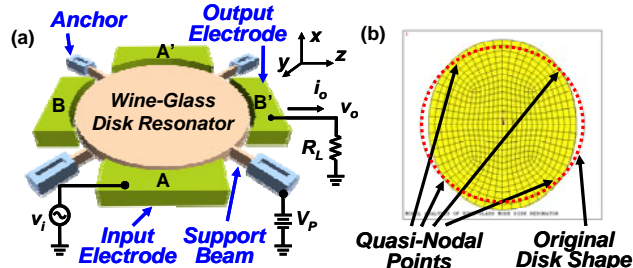


Fig. 2: (a) Perspective-view schematic of a micromechanical wine-glass-mode disk resonator in a typical two-port bias and excitation configuration (where A,A’ are electrically connected, as are B,B’); (b) ANSYS simulated wine-glass mode shape.

switch connecting a 10V source to the switch electrode. The 61-MHz operating frequency corresponds to a switching period of 16ns with an effective rise time of <4ns, which is more than 200 times faster than the  $\mu$ s-range switching speeds of the fastest RF MEMS switches. Furthermore, since the voltage source is on during switching, the switch essentially *hot switches* with a demonstrated lifetime exceeding 16.5 trillion cycles without failure, but with some observable degradation.

## RESOSWITCH STRUCTURE AND OPERATION

Fig. 1 presents schematics describing the structure and operation of one simple rendition of a resoswitch that comprises a capacitively-transduced wine-glass disk micromechanical resonator [2] (c.f., Fig. 2) made in a conductive material (preferably, a metal) and surrounded by four electrodes, two of which are situated along an indicated input axis having larger electrode-to-resonator gaps than their counterparts along an orthogonal switch axis. To operate the switch, an ac input voltage at the wine-glass mode disk resonance frequency is applied to the input electrodes (along the input

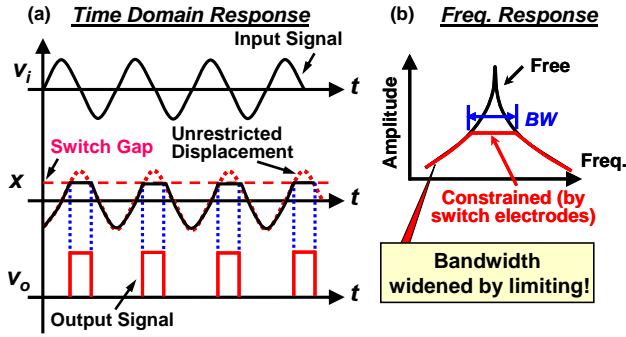


Fig. 3: (a) Time domain waveforms describing the relationships between the input signal, the ensuing displacement ( $90^\circ$  phase-shifted from the input), and the resulting output signal along the switch axis. In the displacement waveform, the red dotted curve indicates the displacement that would ensue if there were no limiting. (b) Expected frequency response illustrating bandwidth widening effect by impact limiting.

axis), electrically forcing the disk into the wine-glass mode shape delineated by the dotted curve in Fig. 1(a). As the resonance amplitude rises, the disk eventually impacts the (closer) electrodes along the switch axis, as shown in Fig. 1(b). This then ideally steals energy from the disk, effectively limiting its amplitude so that when the disk elongates along the input axis on the next cycle, it does not impact the (more distant) input electrodes, as shown in Fig. 1(c). Essentially, in this structure, control electrodes more distant from the disk are used to drive the disk into its resonance mode shape (indicated by the dotted curve), where at sufficient amplitude it impacts closer electrodes along the orthogonal axis, closing the switch at a frequency equal to the resonance frequency of the disk. Because the input is applied at the resonance frequency of the disk, the required input voltage amplitude that effects switching along the switch axis is quite small, on the order of 1-3V, which is much smaller than the >50V required by most RF MEMS switches.

The utility of a switch operating at resonance is immediately apparent upon recognition that some of the highest volume applications of switches, such as switched-mode power converters [3] and amplifiers [4], operate in a mode where their switches switch continuously with essentially constant period within specified bandwidths. The use of the present micromechanical resoswitch in place of the switching transistor in these applications (c.f., Fig. 4) stands to greatly enhance performance by allowing the use of much higher voltages (e.g., 10V vs. the 1V limit of conventional CMOS) [5], which raises the efficiency of switched-mode power amplifiers and raises the voltage levels achievable by power converters.

Of course, the cycle count of the resoswitch would need to be much larger than so far achieved by RF MEMS switches in order to be useful for such power applications. In this regard, the reliability of the present resoswitch benefits from two major advantages: 1) the stiffness of its actuating disk resonator is  $1.15 \times 10^6 \text{ N/m}$ , which is several orders larger than that of a conventional RF MEMS switch, so provides a substantially larger restoring force with which to overcome sticking forces; and 2) the energy stored via resonance vibration of the device provides a momentum that further increases the effective restoring force. The use of such a large spring restoring force is in turn made possible by resonance operation, under which the displacement of the actuator is  $Q$  times larger than off-resonance, allowing a mere 1-3V amplitude drive voltage to generate impacting switch axis amplitudes.

Fig. 3 presents the expected time domain waveforms generated by a direct contact version of the resoswitch under ideal operation. Here, the duty cycle of the output waveform is controlled

Table 1: On-Chip Switch Comparison

Parameter	FET	RF MEMS	Resoswitch
Actuation Voltage	1-3 V	20-80 V	2.5 V
Maximum Voltage	1-3 V	>100V	>100V
Switching Time	0.16-1 ns [1]	1-300 $\mu\text{s}$	$\sim 4$ ns
Life Time	Very Long	100 Billion [9]	> 16.5 Trillion
On Resistance	0.5 $\Omega$ [6]	0.1-1 $\Omega$ [9]	0.1-1 $\Omega^*$
Input Capacitance	20 pF [6]	1-10 fF [10]	20-30 fF
$FOM = 1/(2\pi R_{on} C_{off})$	590 GHz [7]	63 THz	>30 THz*

\* Potentially achievable by a metal version.

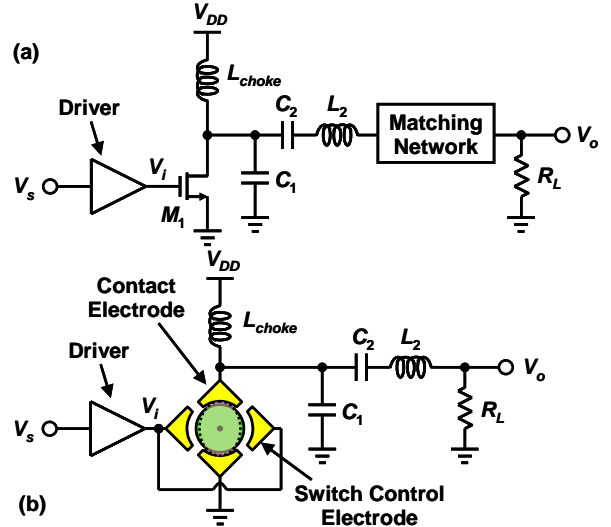


Fig. 4: Circuit topologies of (a) a conventional Class E amplifier using a transistor switch device; and (b) one simplified rendition of the proposed Class E amplifier utilizing the vibrating micromechanical resonator switch described herein. (The dashed line in (b) indicates how the resoswitch contorts to make contact.)

by how hard the resoswitch is driven. In particular, when the resoswitch is driven softly, so that it only barely touches the switch axis electrodes, the duty cycle is very small. When driven very hard, the duty cycle rises closer to its 50% maximum.

Not only is duty cycle adjustable, but so is the bandwidth of the resoswitch. In particular, as shown in Fig. 3(b), the bandwidth over which impacting occurs can also be controlled by the amplitude of the ac input voltage. In effect, the larger the input voltage amplitude, the lower is the frequency of first limiting on the frequency characteristic of the device, and the higher the frequency of last limiting. This bandwidth-widening is a nonlinear dynamical effect that simultaneously allows high  $Q$  along the input axis, which lowers the required input ac voltage; while also allowing a wide effective bandwidth along the switch (or output) axis. The availability of simultaneous high- $Q$  and wide bandwidth obviously benefits transmit power amplifier applications in communications, since it permits wide frequency modulations on the transmitted signal while simultaneously lowering the input capacitance for a given input signal amplitude needed to operate the device.

## RESOSWITCH ADVANTAGES

Table 1 compares the described micromechanical resoswitch with transistor FET and RF MEMS switch counterparts, showing clear advantages in maximum voltage and input capacitance over

transistor FET's, and in speed over RF MEMS switches. Although the device-to-device comparisons are already favorable for the resoswitch, the advantages provided by the described resoswitch are perhaps best elucidated in the context of an application. To this end, Fig. 4 shows the circuit topologies of (a) a conventional Class E power amplifier (PA) using a transistor switch device; and (b) one simplified rendition of the same amplifier utilizing the vibrating micromechanical resonant switch demonstrated in this work. The use of the present micromechanical resoswitch in place of the switching transistor in this application stands to greatly enhance performance in the following ways:

- 1) It allows the use of much higher voltages (e.g., 10V vs. the 1-3V limit of conventional CMOS) [5]. This then allows the resoswitch rendition to directly drive the 50Ω load, and thereby dispense with the lossy matching network needed by the transistor version. (Because of maximum voltage limitations, the voltage provided by the transistor FET is too small to deliver the required 1-2W of power into 50Ω. Thus, a matching network is required to lower the impedance driven by the transistor to ~2Ω.) Removal of the matching network and raising the driven impedance from 2Ω to 50Ω can raise the efficiency of a Class E power amplifier by as much as 23%.
- 2) The use of the resoswitch further allows the same or smaller "on" resistance than its FET counterpart, but with substantially smaller input capacitance, e.g., only 20fF for the resoswitch versus 20pF for a CMOS PA switch—a 1000× difference that removes much of the input power that would otherwise be needed to drive the PA. Again, better efficiency ensues.

## EXPERIMENTAL RESULTS

To demonstrate the resoswitch, doped polysilicon wine-glass mode disk resonators based on the design and fabrication process of [2] were employed. Fig. 5(a) presents the SEM of one of the 61-MHz wineglass disk resonators used in this work, with a zoom-in shot in (b) showing the tiny gap between the disk and its switch electrode. For most power amplifier and converter applications, the resoswitch should be constructed of metal, not polysilicon, to reduce its contact and series resistance. The use of doped polysilicon in this work does compromise resoswitch performance, especially with regards to the switch "on" resistance, which is dominated by the 1 kΩ parasitic resistance  $R_p$  of its polysilicon leads and interconnects. Nevertheless, it still allows demonstration of practically all other important resoswitch performance parameters. It should be noted that, despite its high series resistance, the polysilicon version of the resoswitch is actually still quite applicable for use in low current drain switch-mode on-chip dc-to-dc power converters (i.e., charge pumps), such as needed to supply the large dc-bias voltages often required by capacitively transduced vibrating RF MEMS devices [11].

For simplicity in this early demonstration, the strategy of using different electrode-to-disk spacings along the input and switch axes shown in Fig. 1 was not used in this implementation. Rather, the electrode-to-resonator gap spacings for both axes were 100 nm for direct contact switches, in which the conductive disk and electrode materials actually make electrical contact; and about 97 nm for capacitive switches, in which a thin layer of oxide exists over conductive surfaces that prevents electrical contact, but still allows switching through the large capacitance that results when the disk impacts its switch electrodes. For the direct contact version of the resoswitch, one obvious consequence of the use of identical input and switch axis electrode-to-resonator gaps is that the input gets shorted to the disk during operation, which then prevents deployment of the device in the fashion shown in Fig. 4, which would

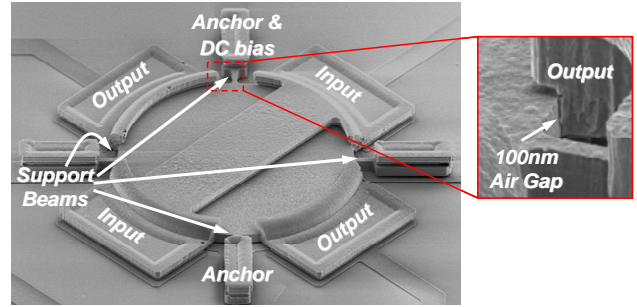


Fig. 5: (a) SEM of the polysilicon resoswitch demonstration vehicle used in this work, which essentially comprises a wine-glass disk resonator with properly spaced and positioned electrodes; and (b) zoom-in on the electrode-to-resonator gap of the device along the switch axis.

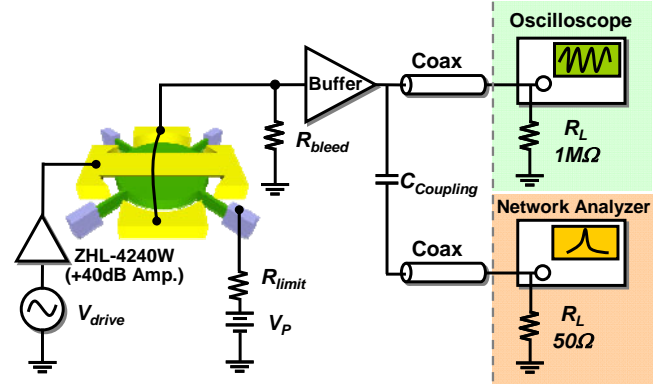


Fig. 6: Test set-up used to evaluate the micromechanical resoswitch.

otherwise be preferred.

To circumvent this problem, the test set-up used to measure resoswitch performance, depicted in Fig. 6, uses a less practical configuration, but one still very valid for evaluation of switch performance. Here, a dc-bias voltage  $V_p$  is applied to the disk structure that is effectively applied to the output node when the switch closes (i.e., comes "on") in the fashion shown in Fig. 1. As shown, this circuit allows both time domain (i.e., oscilloscope) and frequency domain (i.e., network analyzer) observation of the resoswitch output. The output buffer used in this circuit effectively removes the 80pF of coaxial capacitance that would otherwise load the output node of the resoswitch and greatly reduce the signal level due to 3dB bandwidth roll-off. The output buffer, however, is not perfect, as it still loads the output node of the resoswitch with about 4pF. This is large enough to round out the corners of the expected output square wave (c.f., Fig. 3) so that it looks more sinusoidal.

Fig. 7 and Fig. 8 present the oscilloscope waveform and swept frequency response spectrum, respectively, of the direct contact resoswitch, verifying switching operation, impact limiting, and also a bandwidth-widening effect that could be harnessed for wider-band power amplifier applications that should be accessible to future metal renditions of the resoswitch. Switching clearly occurs when the frequency response grows suddenly and limits with a "flat top", as shown on Fig. 8. This occurs when the voltage amplitude reaches 2.5V. The measured output signal on Fig. 7 has a peak-to-peak amplitude of about 1V, which is the value expected when considering attenuation via the finite 3dB bandwidth of the measurement circuit of Fig. 6, and when considering the voltage divider formed by the parasitic polysilicon interconnect resistance  $R_p$  and the bleed resistor  $R_{bleed}$ . The signal is not quite a square wave due to bandwidth limitations of the measurement circuit, but the amplitude is correct. To emphasize this point, Fig. 7 also includes a SPICE simulated waveform that includes the effects of 1.1 kΩ of parasitic

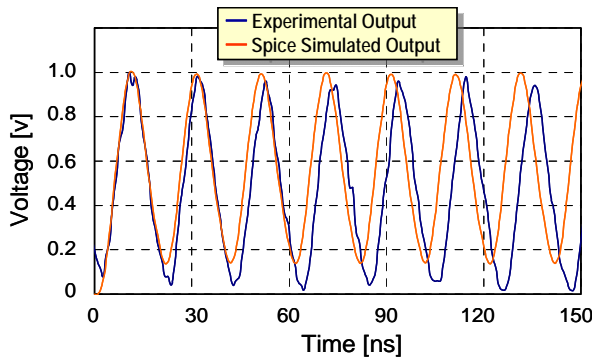


Fig. 7: Oscilloscope (i.e., time domain) waveform and SPICE simulated prediction seen at the resoswitch output node of Fig. 5 when driven by a resonance input signal with 2.5V amplitude.

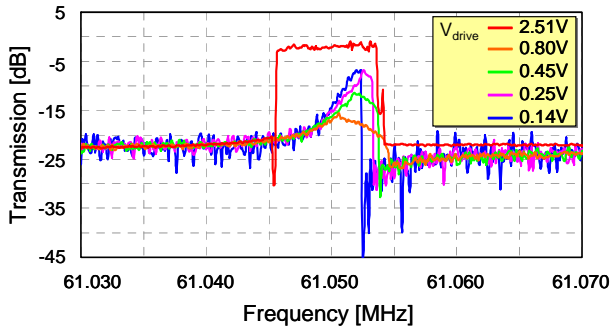


Fig. 8: Frequency response (in vacuum) as measured by a network analyzer of the direct contact version of the resoswitch for varying resonance input ac voltage amplitudes.

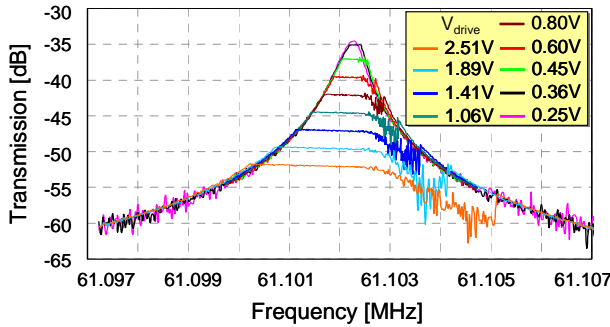


Fig. 9: Frequency response (in vacuum) as measured by a network analyzer of the capacitive version of the resoswitch for varying resonance input ac voltage amplitudes.

resistance  $R_p$  and 3.5 pF of capacitance, and that clearly matches the measured waveform.

Fig. 9 presents the swept frequency response for the capacitive resoswitch as measured via a network analyzer. Now, no dc electrical contact is made, so the transfer function flattens and reduces in gain value when switch impacting occurs, as expected. In addition, the bandwidth does indeed widen as the input voltage amplitude increases, clearly verifying nonlinear dynamical behavior.

To evaluate reliability, the resoswitch was operated continuously with  $V_p = 10V$  for 75 hours (~3 days or 16.5 trillion cycles) without failure at a frequency of 61 MHz, which is a frequency in the flat region of Fig. 8, and thus, a frequency where impacting occurs. Fig. 10 presents a plot of output amplitude versus time for the polysilicon version of the resoswitch. Although no failure is observed, degradation is seen, where after about 1.5 days, the output voltage begins to decrease significantly. Although 1.5 days corresponds to 7.7 trillion cycles at 61 MHz, which is more than

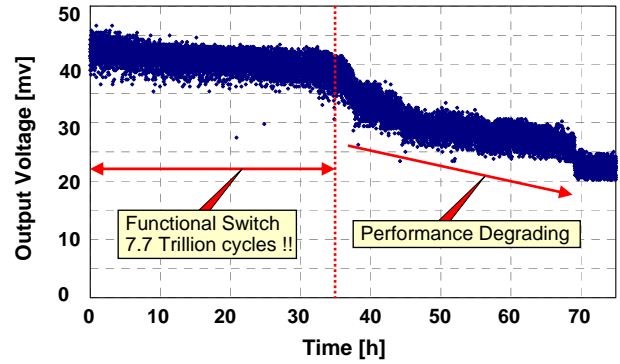


Fig. 10: Lifetime test of the polysilicon resoswitch

two orders of magnitude higher than the 100 billion cycles typically achieved by (good) RF MEMS switches, there is still cause for concern, here, since typical switched-mode power applications require much more than 3 days of operation. More study into the degradation mechanism is needed, but one possible reason for the observed degradation could be the growth of a thicker oxide or other dielectric on the switch contact interfaces. In the future, resoswitches constructed of metal with engineered contact surfaces will be investigated.

## CONCLUSIONS

In this work, the resonance and nonlinear dynamical properties of a micromechanical wine-glass disk have been harnessed to demonstrate an impacting micromechanical switch with substantially higher switching speed, better reliability (even under hot switching), and lower actuation voltage, all by substantial factors, over existing RF MEMS switches. Although next generation versions of this resoswitch constructed in metal material [12] should be more widely applicable, the present polysilicon version can still find application to low current drain applications, such as Dickson charge pumps [3], where replacement of diodes with resoswitches should allow a very high output voltage, suitable for dc-biasing of capacitively transduced micromechanical resonators.

**Acknowledgment:** This work was supported by DARPA.

## REFERENCES

- [1] H. Kamitsuna, et al., "A fast low-power 4x4 switch IC using InP HEMTs ...," *Proceeding, IEEE CSIC*, Jul. 2004, pp. 97-100.
- [2] Y.-W. Lin et al., "60-MHz wine glass micromechanical ... oscillator," *Tech. Dig.*, 2004 IEEE ISSCC, Feb. 15-19, 2004, pp. 322-323.
- [3] J. F. Dickson, "On-chip high-voltage generation in NMOS ...," *IEEE J. Solid-State Circuits*, vol. 11, no.3, pp.374-378, June 1976.
- [4] N.O. Sokal, et al., "Class E - A new class of high-efficiency tuned ...," *IEEE J. Solid-State Circuits*, vol. 10, no. 3, pp.168-176, June 1975.
- [5] S. Wolf, *Silicon processing for the VLSI era volume 3 - The submicron MOSFET*. Sunset Beach, CA: Lattice Press, 1995.
- [6] Agilent Technologies, "Agilent Solid State Switches-Selecting the right switch technology for your application," 2007.
- [7] D.A. Blackwell, et al., "X-band MMIC switch with ...," *IEEE Microwave and Millimeter-Wave Monolithic Circuits Symposium*, 1995.
- [8] J. B. Muldavin, et al., "High-isolation inductively-tuned X-band ...," *Tech. Dig.*, 2000 IEEE MTT-S, Boston, MA, pp. 169-172.
- [9] S.; Lampen, et al., "A packaged, high-lifetime ohmic MEMS ...," *Tech. Dig.*, 2003 IEEE MTT-S, pp. 1935-1938, vol.3, 8-13 June 2003
- [10] G. M. Rebeiz, et al., "RF MEMS Switches and switch circuits," *IEEE Microwave Magazine*, Dec. 2001, pp. 59-71.
- [11] J. Wang, et al., "1.51-GHz polydiamond ...," *Tech. Dig.*, 2004 IEEE MEMS Conf., Maastricht, The Netherlands, pp. 641-644.
- [12] W.-L. Huang, et al., "Fully monolithic CMOS nickel micromechanical ...," *Tech. Dig.*, 2008 IEEE MEMS Conf., pp. 10-13.

# PREAMPLIFYING CANTILEVERS FOR CONTACT RESONANCE MODE IMAGING

B. Zeyen<sup>1</sup>, B. Pittenger<sup>2</sup>, K. Virwani<sup>2</sup>, K.L. Turner<sup>1</sup>

<sup>1</sup>University of California, Santa Barbara, California, USA

<sup>2</sup>Veeco Metrology Inc., Santa Barbara, California, USA

## ABSTRACT

A novel preamplifying cantilever (PCL) design for scanning probe microscopes (SPM) that is capable of mechanically amplifying specimen movements is presented. The sample motions in both out-of-plane and in-plane directions are amplified by the PCL. The spatial resolution of the cantilever is in the nanometer scale and is comparable with existing SPM cantilevers. Some of the proposed applications are in the areas of ferroelectric domain imaging [1]-[5].

The amplification was demonstrated with measurements on ferroelectric materials- which included periodically poled lithium niobate (PPLN). Feasibility tests show that a 100x mechanical preamplification is possible with the current cantilever design, providing a much better signal to noise ratio on both amplitude and phase response measurements than the previous art (e.g. [8]).

## INTRODUCTION

Piezoresponse atomic force microscopy is used to study the inverse piezoelectric effect on thin films non-destructively with a very high lateral resolution.

For this purpose, an AC electric field is applied to the specimen through a conductive SPM tip. The specimen's vertical and lateral response is measured with the microscope's optical detector (see figure 1). The response is then analyzed for the amplitude and the phase shift using a lock-in amplifier. By operating the SPM in contact mode [6], a surface map of the piezoelectric response amplitudes and -phases is created.

When using a regular cantilever far below its contact resonance frequency, the measured amplitude of the cantilever corresponds directly to the amplitude of the specimen.

The response amplitudes of the specimen are often in the order of magnitude of  $10^{-12}$ m. In order to overcome the relatively low signal to noise ratios (about 3-5), either higher AC electric fields have to be applied or an actuation frequency close to the contact resonance frequency of the cantilever has to be used. At

contact resonance one benefits from the higher transfer function of the cantilever in bending. Both measures directly influence the output amplitude and the signal-to-noise ratio of the measurement [7]. However, number of times the required AC electric fields for a good signal-to-noise however are in the same order of magnitude to create polarization in the specimen, thereby affecting the measurement.

The signal levels can be highly improved by operating the cantilever close to its contact resonance frequency [8]. The interpretation of the results obtained with this method though is quite complex. Since in this mode in addition to the piezoelectric response, the mechanical response of the cantilever couples into the measured amplitude and phase signals.

## CANTILEVER DESIGN

One measure to enhance the signal-to-noise ratio is the use of a different cantilever architecture that optimizes the mechanical

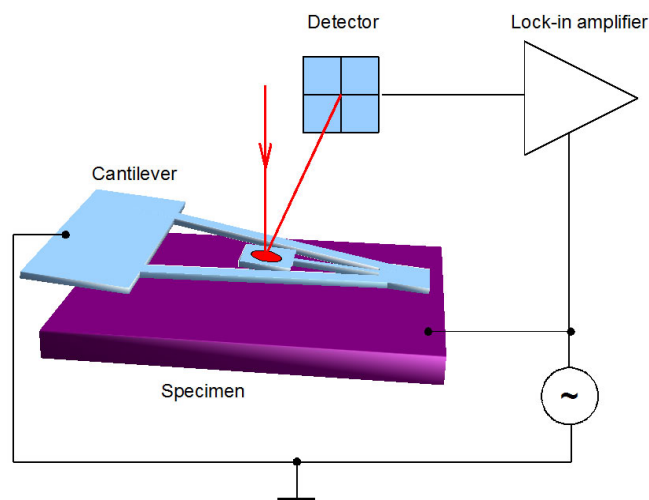


Figure 1: Piezo response imaging principle

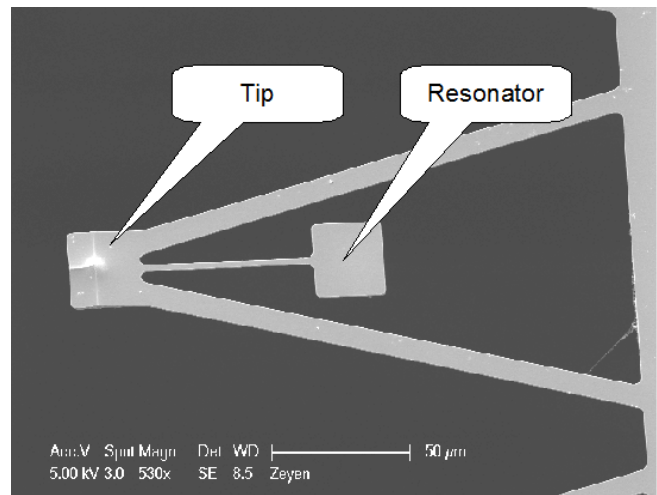


Figure 2. Preamplifying piezo response cantilever transfer function.

Figure 2 summarizes the basic design of the cantilever. It consists of a common triangular cantilever with its tip at the front end, and a resonator, attached via a coupling spring. This resonator, along with the coupling spring, serves as a tuning fork that reacts to (usually sample induced) movements in the tip in both vertical and lateral direction (compare [10]).

The laser of the atomic force microscope is focused onto the resonator during the measurements. Since the topographical features of the sample are scanned at a much lower rate than the resonator's frequency (in the order of 1kHz), the angular deflection changes of the tip due to the topography get directly transferred to the resonator and can be read out and used for the SPM's feedback control signal.

Since the frequency of the applied AC signal corresponds to the resonator's resonance frequency, the periodic mechanical response of the specimen gets maximally amplified by this

cantilever. It should be noted, that the measurements need a number of periods to settle as for any harmonic oscillator.

### FABRICATION

The cantilever was fabricated using standard processes using a Silicon on Insulator (SOI) wafer. The process is summarized in figure 3. In the first step, the tip geometry was transferred onto a hard mask of SiO<sub>2</sub>, then isotropically etched in a SF<sub>6</sub>- plasma and sharpened using low temperature thermal oxidation at 900°C. The resulting oxide was used as a hard mask for the overall cantilever contour shape, which was subsequently etched into the silicon with an anisotropic deep reactive ion etch step using CHF<sub>3</sub>. After patterning the backside consisting of SiO<sub>2</sub> and SiN<sub>x</sub> with CHF<sub>3</sub> and CF<sub>4</sub> and passivating the front-side with a rubber-based coating (Brewer Science Protek B3 [11]) the backside was anisotropically wet etched with KOH until the oxide etch stop layer was hit. In a final step the coating was solved with acetone. The etch stop layers as well as the hard masks were removed with buffered HF; the wafer cleaned with an oxide plasma and coated on the front- and back side with a thin layer of titanium and gold – the front side for electric conductivity and the backside for better optical properties.

These cantilevers can be operated in a regular SPM with the laser focused on the resonator.

### EXPERIMENTS ON PIEZOELECTRIC MATERIALS

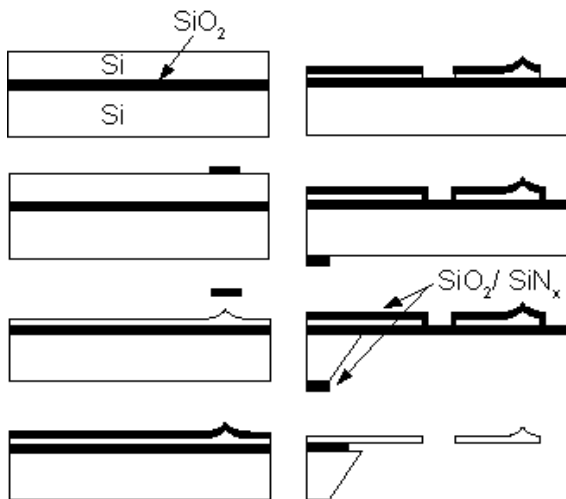


Figure 3. Fabrication process

The cantilever was tested with a Veeco Dimension V microscope using a Nanoscope 5 controller, sampling a periodically poled Lithium Niobate (PPLN) material. By applying an AC voltage between the tip and the sample, the mechanical reaction of the sample was characterized.

Figure 4 shows the vertical (ver.) and torsional (hor.) dynamic behavior of the cantilever while in contact with the specimen for the case where the laser was focused on the tip (tip) and then on the resonator (res.). The measurements indicate a total mechanical preamplification in the vertical direction of over 100. This was obtained by operating at the resonator's resonance.

The ratio of 100 was obtained by dividing vertical resonator deflection amplitude at resonance with the tip deflection amplitude out of resonance.

This curve was used to quantify the mechanical response: In the first step, the laser was focused onto the tip to statically measure the overall optical lever sensitivity (with a force-

deflection curve on a hard sample) and also its piezo response amplitude far below the cantilever's contact resonance frequency.

In the second step the laser was focused onto the resonator to measure the resonator optical lever sensitivity (again, with a force

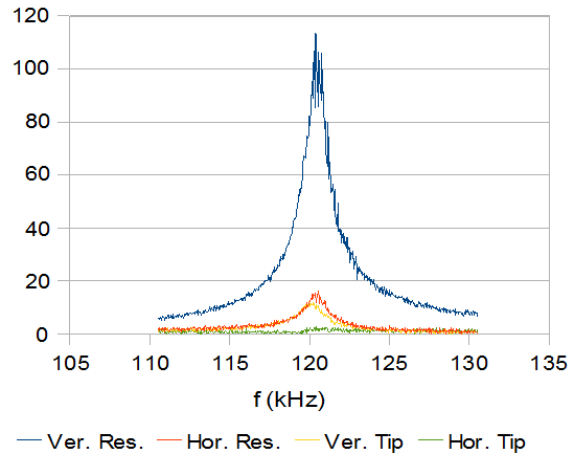


Figure 4. Dynamic behavior of the cantilever

curve on a hard sample) and the piezo response amplitude at the resonator's resonant frequency. Since the true piezo response amplitude is known from the first step of the calibration, the amplitude obtained with the laser on the resonator was used to determine the piezoresponse sensitivity.

Special caution had to be applied to the interpretation of the quantified signals however, as the response signal does not only contain the mechanical response of the piezoelectric material, but also an electrostatic contribution from the applied AC bias [8] and geometric effects of a locally induced piezoelectric strain [9]. The interpretation is still under investigation and will be a part of a future publication.

Figure 5 illustrates the vertical amplitude response of the cantilever close to (a) and far off resonance (b) using the same actuation amplitude to create the electric AC field in the sample. In (a), the domains and the domain changes between oppositely poled areas of the PPLN sample can be clearly seen as a small drop in the amplitude, whereas in (b) the overall amplitude ranges close to the noise level. The amplitude ranges used to create the images reflect the overall harmonic amplification of the cantilever.

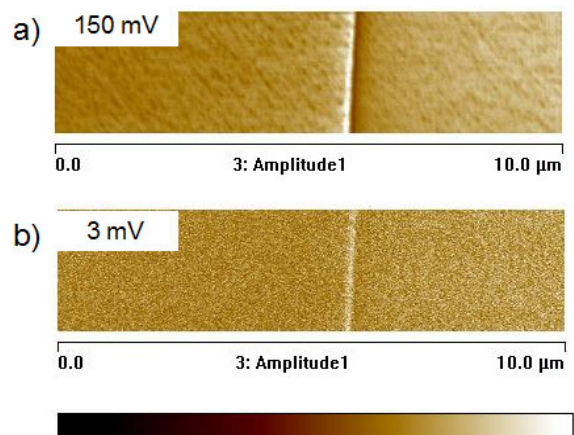


Figure 5. Amplitude response behavior for resonant and out-of-resonant actuation

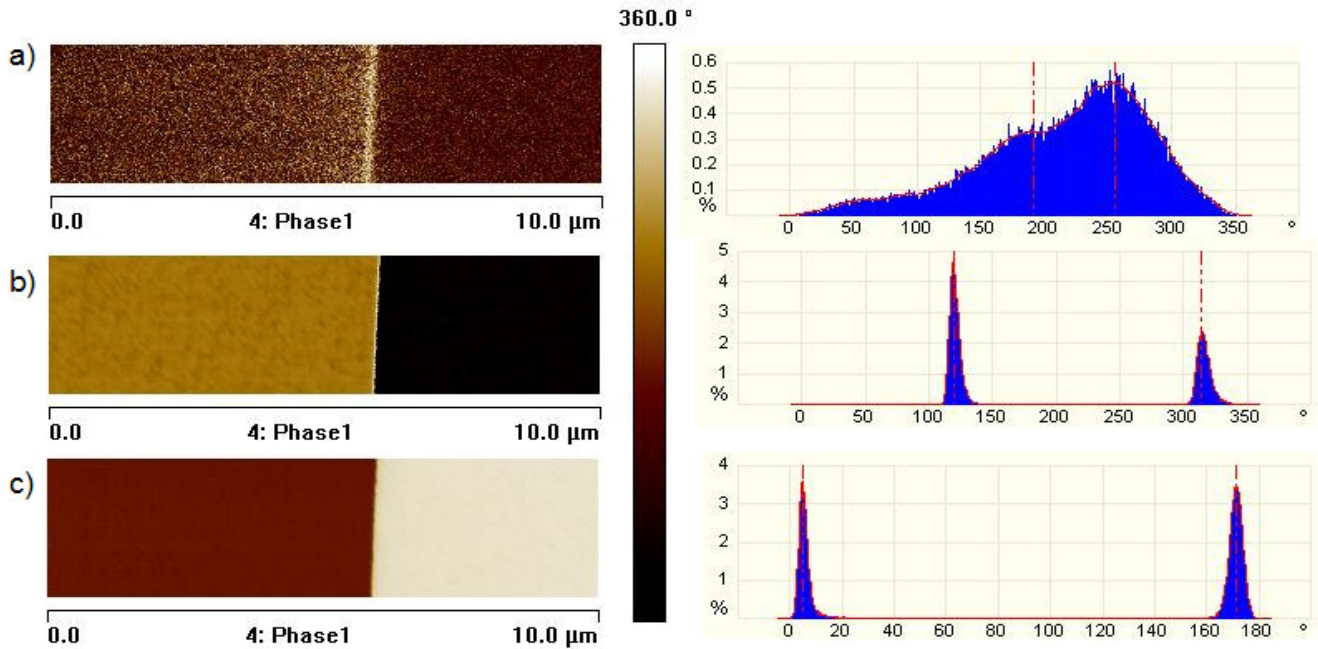


Figure 6. Phase response of the cantilever for a) out-of-resonance, b) subresonant and c) superresonant actuation

Figure 6 summarizes the phase images for an actuation of the sample out of resonance (a), slightly smaller than resonance (b) and slightly above resonance (c), using the same actuation voltage for all three experiments.

By comparing the phase contrast of the histograms close to resonance ( (b) and (c) ) to the histogram using an actuation out of resonance (a), the improvement of the signal-to-noise ratio can be demonstrated. For imaging phase maps of specimen close to the cantilever's contact resonance frequency it is important to take into consideration the phase shift in the response introduced by the cantilever. (b) and (c) show the phase shift when imaging the same part of the sample close below and above resonance. To obtain absolute quantitative results for phase image studies, the phase shift of the overall system, including the cantilever, has to be considered.

During our tests, the tip sample AC voltage at resonance could be reduced one order of magnitude (compared to previous cantilevers), overall to 200mV while still achieving a good signal-to-noise ratio. Figure 7 shows the resulting picture with a signal amplitude of 7.5mV. Applying the quantitative calibration scheme described above, we conclude that the specimen response amplitude in this figure was less than 5pm. For comparison – previously used commercial SCM-PIT cantilevers [12] exhibited a signal amplitude of 12mV for a 10V applied AC bias that corresponded to approximately 40pm sample response (the 5pm response amplitude is an upper bound). The discrepancies between the result and the comparison can originate from the elevated noise level when directly measuring response amplitudes far out of resonance as well as different conductivities, tip shapes of the cantilevers under study).

## SUMMARY

We have designed, fabricated and tested a new cantilever for piezo response imaging in contact mode by optimizing the cantilever geometry for a maximized transfer function. We have

characterized the cantilever using periodically poled Lithium Niobate thin films and demonstrated an one order of magnitude increase in sensitivity and signal-to-noise ratio that can be either used to achieve higher response- or lower excitation amplitudes.

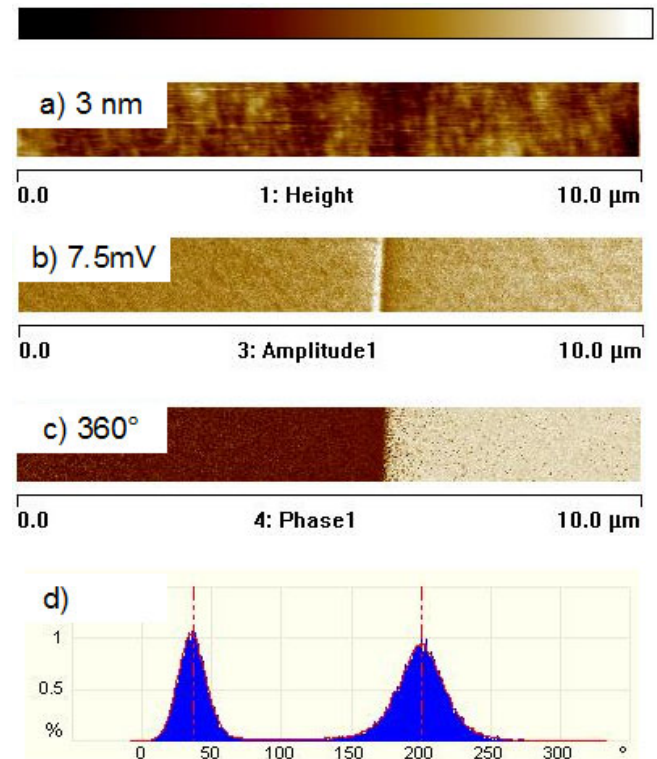


Figure 7. Results for specimen response amplitudes <5pm

## ACKNOWLEDGEMENTS

This research was partially supported by a grant from the Center for Nanoscale Mechatronics & Manufacturing, one of the 21st Century Frontier Research Programs, which are supported by Ministry of Science and Technology, KOREA

## REFERENCES

- [1] A. Gruverman, O. Auciello, H. Tokumoto: *Imaging and control of domain structures in ferroelectric thin films via scanning force microscopy*, Annu. Rev. Mater. Sci. No 28, 101-123 (1998)
- [2] T. Tybell, C.H. Ahn, J.-M. Triscone: *Control and Imaging of ferroelectric domains over large areas with nanometer resolution in atomically smooth epitaxial  $Pb(Zr_{0.2}Ti_{0.8})O_3$  thin films*, Appl. Phys. Lett., Vol 72, No. 12, 23 (1998)
- [3] C.S. Ganpule et al: *Imaging three-dimensional polarization in epitaxial polydomain ferroelectric thin films*, J. Appl. Phys., Vol 91, No. 3, 1 (2002)
- [4] E. Soergel: *Visualization of ferroelectric domains in bulk single crystals*, Appl. Phys. B 81,729-752
- [5] T. Jungk, A. Hoffmann, E. Soergel: *Quantitative analysis of ferroelectric domain imaging with piezoresponse force microscopy*, Appl. Phys. Lett. 89, 163507 (2006)
- [6] G. Binne, C.F. Quate: *Atomic Force Microscopy*, Phys. Rev. Lett. Vol. 56, No. 9 (1986)
- [7] K. Virwani, V. Kelley: *Piezoresponse Atomic Force Microscopy Using a NanoScope V Controller*, User Guide 013-444-000, Veeco Instruments
- [8] C. Harnagea, A. Pignolet, M. Alexe, D. Hesse: *Higher-Order Electromechanical Response of Thin Films by Contact Resonance Piezoresponse Force Microscopy*, IEEE Transactions on Ultrasonics, Ferroelectrics and Frequency Control, Vol. 53, No. 12, 2309-2322 (2006)
- [9] C. Harnagea, A. Pignolet, M. Alexe, D. Hesse: *Piezoresponse scanning force microscopy: What quantitative information can we really get out of piezoresponse measurement on ferroelectric thin films?* Integr. Ferroelectr. Vol 44, 113-124 (2002)
- [10] B. Zeyen, KL Turner: *Design and Test of a Novel Higher Harmonic Imaging AFM Probe With a Dedicated Second Cantilever for Harmonic Amplification*, Transducers& Eurosensors '07, 1545-1548 (2007)
- [11] <http://www.brewerscience.com/products/sm/product-information/temporary-etch-protective-coatings/>
- [12] [https://www.veecoprobes.com/probe\\_detail.asp?ClassID=103](https://www.veecoprobes.com/probe_detail.asp?ClassID=103)

# ELECTROSTATIC – TUNING OF HERMETICALLY ENCAPSULATED COMPOSITE RESONATOR

H.K. Lee<sup>1</sup>, M.A. Hopcroft<sup>1</sup>, R.Melamud<sup>1</sup>, B.Kim<sup>1</sup>, J.Salvia<sup>2</sup>, S.Chandorkar<sup>1</sup> and T.W. Kenny<sup>1</sup>

<sup>1</sup>Department of Mechanical Engineering, Stanford University, California, USA

<sup>2</sup>Department of Electrical Engineering, Stanford University, California, USA

## ABSTRACT

MEMS resonators have promising future as frequency references with high levels of stability. In this paper, we present electrostatic-tuning of frequency for temperature compensation in Si-SiO<sub>2</sub> composite resonators. This tuning technique uses the spring-softening effect for compensation. It is implemented by adjusting the DC bias voltage applied to the resonant structure. Electrostatic-tuning of silicon MEMS resonators has proven difficult because of the very large temperature induced frequency variation that must be overcome (2000 ppm). Si-SiO<sub>2</sub> composite resonators have at least 10x less frequency variation over temperature, and lend themselves to electrostatic-tuning for compensation. This paper presents our first results for a tuning-based compensation approach over a full (70°C-wide) commercial temperature range.

## INTRODUCTION

Silicon MEMS resonators have been considered as replacements for quartz crystal references in electronic products and systems [1]. Silicon resonators have many advantages over quartz references such as small size, low cost, less power consumption, and CMOS compatibility. Therefore, MEMS resonators are suitable for frequency references in miniaturized handheld electronic devices that have a large and growing market.

Although micro-machined silicon resonators have many promising attributes, commercial success depends on frequency stability comparable to quartz references; hence, research has been directed toward guaranteeing quartz-level frequency stability of MEMS resonators. The long-term stability of MEMS resonators was proven to be superior to that of quartz references [2]. This becomes possible due to recently developed ‘epi-seal’ encapsulation technology that provides a hermetic environment for resonator operation. Unfortunately, however, the resonant frequency of silicon resonators has a strong dependency on temperature since the Young’s modulus of silicon is a strong function of temperature. The temperature coefficient of frequency (TCf) of silicon resonators is about -30 ppm/°C. This results in ~2000 ppm frequency variation over 70°C-wide range while AT-cut quartz crystals have less than 30 ppm variation over the same temperature range. Therefore, compensating resonant frequency variation over ambient temperature change is a significant remaining problem to meet stability criteria.

Several methods have been proposed to overcome the effects of temperature. An encapsulated micro-oven inside the silicon die has achieved frequency stability better than ±0.1 ppm [3]. But, temperature control can require several mW of extra power consumption to maintain temperature of the resonant beams at the lowest ambient temperatures. Electrostatic-tuning of silicon resonators with sub-micron gaps (~100 nm) [4,5] has been demonstrated; however, bias-induced nonlinearities can be problematic, and the demonstrated frequency stability with this method is generally worse than 10 ppm. This is not enough to compete with widely used temperature compensated crystal oscillator (TCXO) which show ±0.5 ppm to ±5 ppm error. Material compensation using a Si-SiO<sub>2</sub> composite structure [6] and thermal expansion induced stress [7] has been demonstrated.

Although they are able to improve the inherent temperature stability, the frequency stability does not meet commercial product level requirements. Therefore, a new method that can achieve TCXO level stability with minimal additional power is imperative.

This work combines electrostatic-tuning and material Si-SiO<sub>2</sub> compensation to achieve TCXO level performance in a MEMS resonator with low power by taking advantages of both techniques. Electrostatic-tuning uses the spring-softening effect, and it only requires an adjustable bias voltage ( $V_{\text{bias}}$ ). Therefore, this method does not need significantly added power for compensation. However, electrostatic-tuning on our encapsulated silicon resonators is practically infeasible because of the relatively weak spring-softening effect that results from the micron-level electrostatic actuation gap. A sub-micron gap is needed to have strong spring-softening effect to overcome 2000 ppm frequency variation for tuning, but the ‘epi-seal’ process does not allow it. The recent development of Si-SiO<sub>2</sub> composite resonators [6] makes this method feasible since the composite resonators have inherently 10x smaller frequency variation than silicon resonators. In short, a weak spring-softening effect is good enough to apply electrostatic-tuning on composite resonators. In this paper, results from the combination of a composite resonator and electrostatic-tuning are presented that achieve commercial grade frequency stability.

## THEORY

### Si-SiO<sub>2</sub> composite resonators

Hermetically encapsulated flexural mode Si-SiO<sub>2</sub> composite resonators (Fig. 1) are fabricated using the ‘epi-seal’ technology introduced in [8]. The process results composite resonators that have thermal oxide coating on silicon resonant beams. For electrostatic actuation,  $V_{\text{bias}}$  is applied to the resonant structure through its anchor and an AC signal ( $V_{\text{AC}}$ ) is provided to two input electrodes. The output signal is detected by capacitive sensing. The resonator structure and electrodes for actuation and sensing are buried under epitaxial poly-silicon layer that provides hermetic encapsulation.

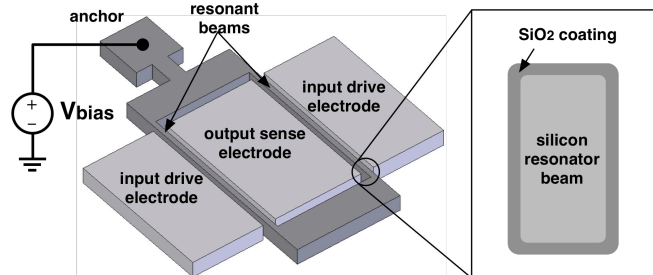


Figure 1: Left: Double-end tuning fork (DETF) type composite resonator for electrostatic-tuning. The beam length is 200 $\mu\text{m}$ , width is 6 $\mu\text{m}$ , and thickness is 20 $\mu\text{m}$ . Gap between resonant beam and electrode is 1.5 $\mu\text{m}$ . The resonant frequency is ~1.126MHz and  $Q \sim 12,000$ . Right: cross sectional view of the resonant beams of the Si-SiO<sub>2</sub> composite resonator.

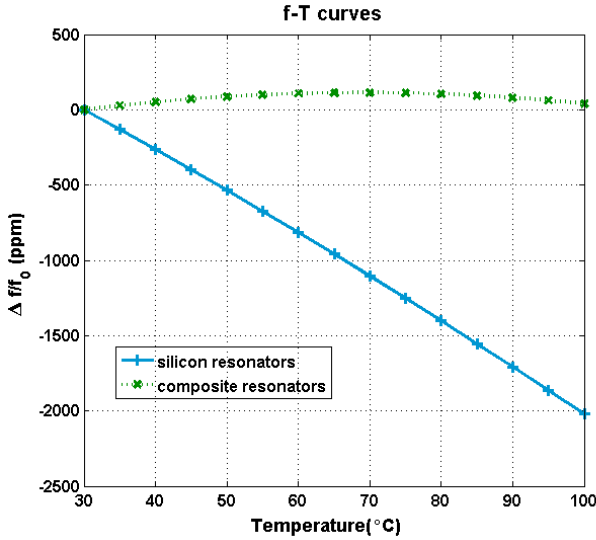


Figure 2: Frequency-Temperature curves of typical silicon and Si-SiO<sub>2</sub> composite resonators. For 30°C-100°C temperature range, the frequency variation of the composite resonator is ~200ppm while that of the silicon resonator is ~2000ppm.



Figure 3: Control loop for the electrostatic-tuning. Ambient temperature is measured, and this value is used to find the appropriate  $V_{bias}$  from the look-up table. The loop is designed to run once in every second.

The resonant frequency of a beam is given by:

$$f \propto \begin{cases} \sqrt{E_{Si} I_{Si}} & : \text{silicon resonator} \\ \sqrt{E_{Si} I_{Si} + E_{SiO_2} I_{SiO_2}} & : \text{Si-SiO}_2 \text{ resonator} \end{cases} \quad (1)$$

where  $f$  is the resonant frequency,  $E$  is a Young's modulus, and  $I$  is a second moment of inertial. The Young's modulus of silicon is a strong function of temperature; therefore, the bending stiffness of silicon beam varies a lot with change of temperature, and so does its resonant frequency. The Young's modulus of SiO<sub>2</sub> also has a strong dependency on temperature, but it has the opposite trend; Young's modulus of SiO<sub>2</sub> increases as temperature increases while that of silicon decreases. By growing an appropriate thickness of SiO<sub>2</sub> coating as shown in Figure 1, we can tune the overall bending stiffness of the Si-SiO<sub>2</sub> composite beams to be less sensitive to temperature variation. In this way, frequency variation can be reduced on the composite structure. Figure 2 shows typical frequency-temperature (f-T) characteristic of silicon resonators and Si-SiO<sub>2</sub> composite resonators. Over a wide temperature range, the frequency variation of the composite resonator is reduced by an order of magnitude.

### Electrostatic-tuning

Electrostatic-tuning uses the spring-softening effect in electrostatic actuation. By changing  $V_{bias}$  applied to resonant beams, the effective stiffness of the beams can be adjusted; therefore, this effect is called the spring-softening effect. Since we can modify the effective stiffness, the resonant frequency can be tuned by some amount. So, the spring-softening effect can be

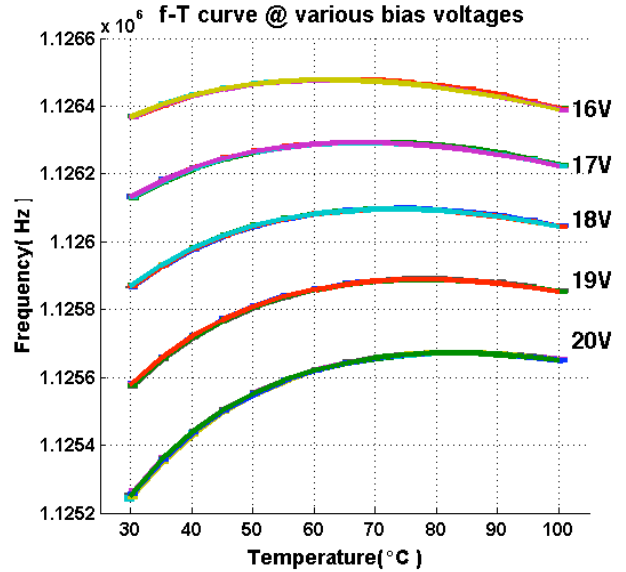


Figure 4: Multiple measurements of the resonant frequency at various temperature and bias voltage for characterization of device. 7 curves at each bias voltage look like one curve due to the consistent response of the resonator.

utilized for temperature compensation. The frequency sensitivity to  $V_{bias}$  of parallel plate resonators is given by:

$$\frac{df}{f_0 dV_{bias}} = \frac{-2\epsilon A_e V_{bias}}{k_m d^3} \quad (2)$$

where  $A_e$  is area of electrode,  $k_m$  is mechanical stiffness, and  $d$  is the size of the gap between the resonant beam and the electrode. As shown in equation 2, the sensitivity is a function of dimension and  $V_{bias}$ . The sensitivity of our device at usual operating condition ( $V_{bias} \sim 20$  V) is about 200 to 400 ppm/V, therefore; 1 V change of  $V_{bias}$  is necessary to compensate 200 ppm variation of composite resonators.

The most important thing in electrostatic-tuning is applying the proper  $V_{bias}$  at a given temperature that shifts the frequency to the target frequency. Therefore, a look-up table that has a list of temperature points and corresponding  $V_{bias}$  values to achieve constant target frequency is necessary. This look-up table can be built through device characterization. With a look-up table, electrostatic-tuning is implemented as an open loop control as shown in Figure 3.

## CHARACTERIZATION

### Repeatability check

Having a good look-up table is the most important requirement for open loop control. Therefore, the Si-SiO<sub>2</sub> composite resonator was characterized and analyzed to build a reliable look-up table from the relationships between ambient temperature,  $V_{bias}$  and frequency. The resonant frequency of the composite resonator is measured several times at various temperature and  $V_{bias}$  conditions (Fig. 4). As predicted in equation 2, the resonant frequency decreases as higher  $V_{bias}$  is applied. Frequency data is analyzed carefully to verify repeatability. Analysis is performed to check whether the measured frequency deviation comes from environmental changes or drifting device characteristics. Since temperature deviation and noise in  $V_{bias}$  are the two most dominating environmental factors that cause frequency variation, analysis is based on those two variables.

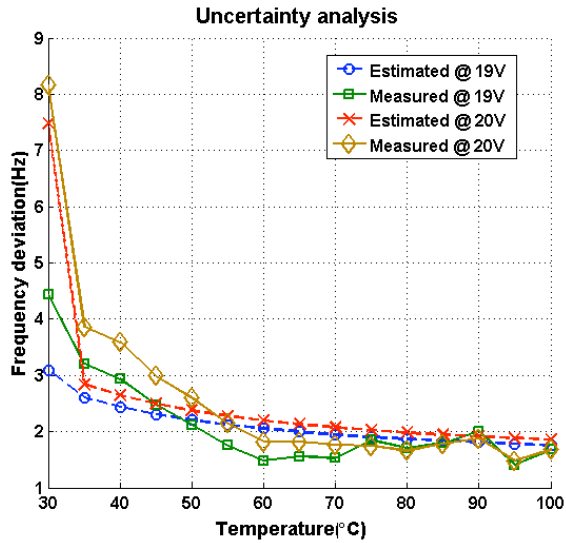


Figure 5: Measured and estimated deviation of frequency at 19V and 20V. Uncertainty analysis is done with those two voltages since they have comparably large frequency deviation.

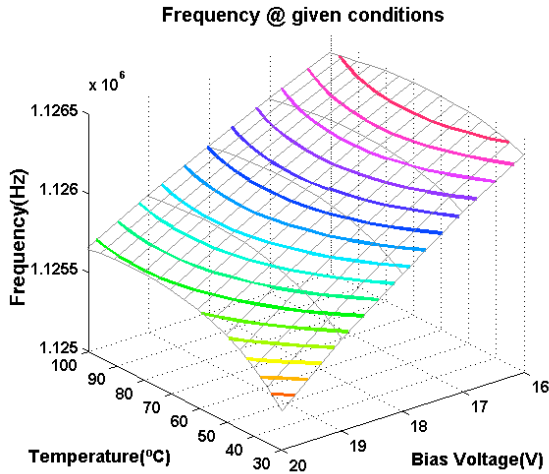


Figure 6: Surface plot of the empirical equation that describes the resonant frequency as a function of bias voltage and ambient temperature.

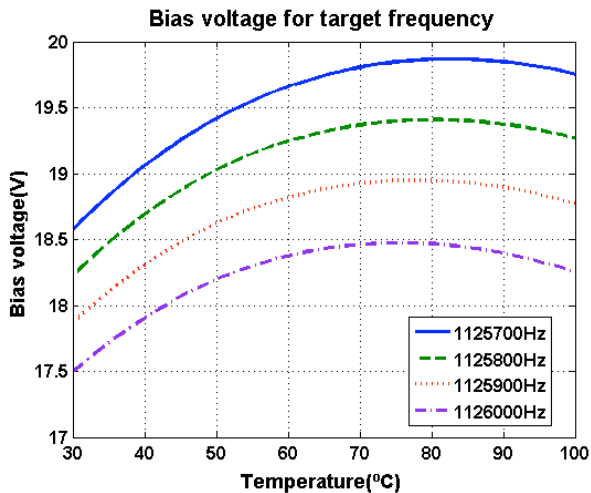


Figure 7: Look-up table for several target frequencies.

First, standard deviation of the measured frequencies at each temperature and  $V_{bias}$  condition are plotted. Afterwards, it is compared with estimated standard deviation of frequency (Fig. 5). The estimation is based on the uncertainty analysis given by:

$$\sigma_f = \sqrt{\left(\frac{\partial f}{\partial T} \sigma_T\right)^2 + \left(\frac{\partial f}{\partial V_{bias}} \sigma_{V_{bias}}\right)^2} \quad (3)$$

where  $f$  is the resonant frequency,  $T$  is temperature, and  $\sigma$  is standard deviation. It is true that there are some other minor factors that affect the resonant frequency, but they are neglected since their effects are negligible and it is difficult to identify them. As shown in Figure 5, the measured standard deviation of frequency and estimated standard deviation of frequency do not match perfectly; however, we can see that they show the same trend of deviations with values in a similar range. Considering other minor factors that are neglected in the estimation, we can conclude that frequency-temperature-bias voltage relationship is repeatable.

### Look-up table

The look-up table is built after the repeatability of characterization is guaranteed. First, the frequency is plotted as a function of bias voltage and temperature. Next, two variable polynomial fitting is performed to obtain an empirical equation. The empirical equation is plotted on Figure 6. The empirical equation is obtained because it helps to get intermediate values that are not measured in characterization run. The two variable polynomial fitting is based on equation given by:

$$f = \sum_{j=0}^5 \sum_{i=0}^5 a_i b_j T^i V_{bias}^j \quad (4)$$

where  $a_i, b_j$  is fitting coefficient.

The order of the polynomial equation is decided after error analysis. The maximum error between measured data and fitted data is targeted to be sub-ppm to achieve TCXO level stability. A 5<sup>th</sup> order polynomial is chosen according to the criteria. From the polynomial equation, a look-up table that has a list of temperatures and bias voltages for several target frequencies (Fig. 7) is built by finding the iso-frequency lines.

### Experimental setup

A resonator chip and a Platinum RTD are mounted on a PCB and placed in a temperature-controlled chamber. An oscillator circuit is connected to the resonator to sustain oscillation. An Agilent 34420A nano volt/micro ohm meter is connected to the

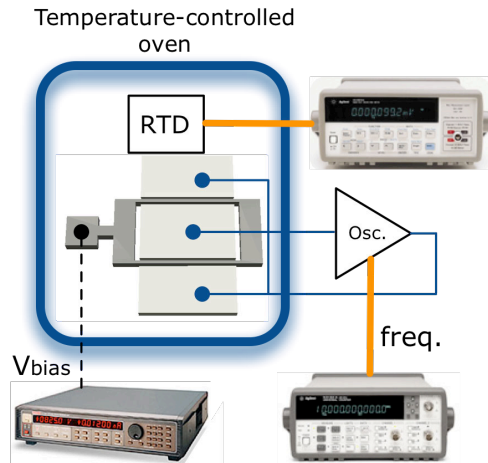


Figure 8: Experimental setup for electrostatic-tuning.

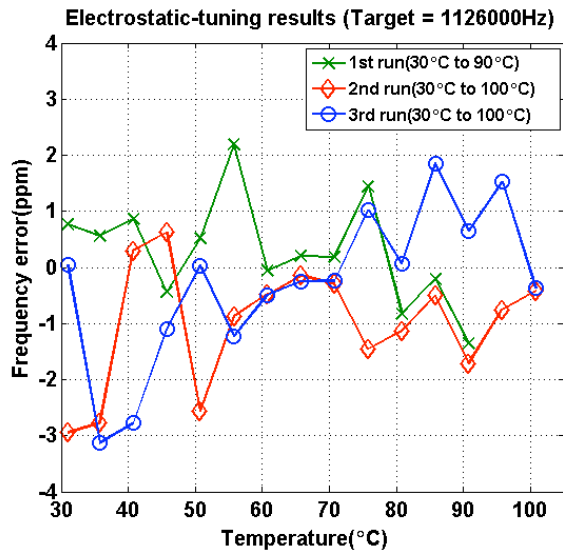


Figure 9: Results from electrostatic-tuning on the composite resonator.

RTD to read the temperature of the resonator and an Agilent 53132A universal counter is connected to the oscillator circuit to get the resonant frequency. A Keithley 236 current/voltage source is wired to the resonant beam to supply stable voltage. Resolution of the Keithley 236 is 10 mV in the voltage range of interest. Considering the frequency sensitivity to resonator  $V_{bias}$ , the tuning resolution is given as 2 to 4 ppm. The  $\pm 5$  V power supply for the oscillator circuit and the computer that runs control code are omitted in Figure 8.

## RESULTS

The full experiment was performed 3 times and frequency was maintained within  $\pm 3.2$  ppm from the target frequency over a wide temperature range (Fig. 9). The demonstrated result is in the level of stability of commercial TCXO [9], and it is a 6x improvement over the previous electrostatic-tuning result [5]. If we consider that the tuning resolution is 2 to 4 ppm,  $\pm 3.2$  ppm is within the expected resolution. Also, it implies that there is a room for further improvement of temperature stability with a more precise voltage source for  $V_{bias}$ .

Unlike the combination of micro-oven and Si-SiO<sub>2</sub> composite resonator [3], the reported method doesn't require additional power consumption but can still achieve commercial level frequency stability. In addition, temperature gradients are not generated on resonator chip since heat source such as micro-oven does not exist inside the chip; therefore, a relatively simple temperature sensor, unlike complicated ones [10,11] for ovenized devices, is good for temperature sensing. Relatively easy temperature sensing can be another benefit of electrostatic-tuning. Furthermore, this method has an advantage of programmable output frequency; a single device can generate various frequency outputs if a look-up table that has several target frequencies (Fig.7) is used.

## CONCLUSIONS

We have first demonstrated electrostatic-tuning on Si-SiO<sub>2</sub> composite resonator to achieve TCXO level temperature stability. With other advantages such as less power consumption, simple temperature sensing, and programmable output frequency, electrostatic-tuning of composite resonators becomes a promising technology for commercialization of MEMS resonators.

## ACKNOWLEDGMENTS

This work was supported by DARPA HERMIT (ONR N66001-03-1-8942), the Bosch Palo Alto Research and Technology Center, and the National Users Network facilities funded by the National Science Foundation under award ECS-9731294. The authors would especially like to thank Clark Nguyen and Amit Lal for their DARPA HERMIT program management.

## REFERENCES

- [1] C. T. C. Nguyen, "MEMS technology for timing and frequency control," IEEE transactions on ultrasonics, ferroelectrics, and frequency control, vol. 54, pp. 251-70 (2007).
- [2] B. Kim, R. N. Candler, M. Hopcroft, M. Agarwal, W.-T Park, and T. W. Kenny, "Frequency Stability of Encapsulated MEMS Resonator," Sensors and Actuators, A: Physical, vol. 136, pp. 125-131 (2007).
- [3] M.A. Hopcroft, H.K. Lee, B. Kim, R. Melamud, S. Chandorkar, M. Agarwal, C.M. Jha, J. Salvia, G. Bahl, H. Mehta, and T.W. Kenny, "A High-Stability MEMS Frequency Reference," in 14th International Conference on Solid-State Sensors, Actuators and Microsystems, Lyon, France (2007), pp. 1307-1309.
- [4] W.-T. Hsu and C. T. C. Nguyen, "Stiffness-compensated temperature-insensitive micromechanical resonators," in IEEE International Workshop on Micro Electro Mechanical Systems (MEMS'02), Las Vegas, Nevada, USA (2002), pp. 731-734.
- [5] G. K. Ho, K. Sundaresan, S. Pourkamali, and F. Ayazi, "Temperature compensated IBAR reference oscillators," in 19th IEEE International Conference on Micro Electro Mechanical Systems (MEMS'06), Istanbul, Turkey (2006), pp. 910-913.
- [6] R. Melamud, B. Kim, S. Chandorkar, M. A. Hopcroft, M. Agarwal, C. M. Jha, and T. W. Kenny, "Temperature-compensated high-stability silicon resonators," Applied physics letters, vol. 90, 244107 (2007).
- [7] W. T. Hsu, J. R. Clark, and C. T. C. Nguyen, "Mechanically temperature-compensated flexural-mode micromechanical resonators," in IEEE International Electron Devices Meeting (IEDM), San Francisco, California, USA (2000), pp. 399-402.
- [8] B. Kim, R. Melamud, M. A. Hopcroft, S. A. Chandorkar, M. Agarwal, G. Bahl, M. Messana, R. N. Candler, G. Yama, and T. W. Kenny, "Si-SiO<sub>2</sub> Composite MEMS Resonators in CMOS Compatible Wafer-scale Thin-film Encapsulation," in IEEE Frequency Control Symposium, Geneva, Switzerland (2007), pp. 1213-1218.
- [9] [http://www.vectron.com/products/tcxo/tcxo\\_index.htm](http://www.vectron.com/products/tcxo/tcxo_index.htm)
- [10] M.A. Hopcroft, M. Agarwal, K. K. Park, B. Kim, C. M. Jha, R. N. Candler, G. Yama, B. Murmann, and T. W. Kenny, "Temperature Compensation of a MEMS Resonator Using Quality Factor as a Thermometer," in IEEE International Workshop on Micro Electro Mechanical Systems (MEMS'06), Istanbul, Turkey (2006), pp. 222-225.
- [11] C. M. Jha, G. Bahl, R. Melamud, S. A. Chandorkar, M. A. Hopcroft, B. Kim, M. Agarwal, J. salvia, H. Mehta, and T. W. Kenny, "High Resolution Microresonator-based digital temperature sensor," Applied physics letters, vol. 91, 074101 (2007).

# A MEMS-RELAY FOR MAKE-BREAK POWER SWITCHING APPLICATIONS

A.C. Weber<sup>1</sup>, J.H. Lang<sup>2</sup>, and A.H. Slocum<sup>1</sup>

<sup>1</sup>Mechanical Engineering, Massachusetts Institute of Technology, Cambridge, MA, USA

<sup>2</sup>Electrical Engineering and Computer Science, Massachusetts Institute of Technology, Cambridge, MA, USA

## ABSTRACT

This paper presents the design, modeling, fabrication and testing of a horizontal-displacement, electrostatically-actuated, MEMS relay for make-break power switching applications. The relay features {111}-plane silicon-etched electrical contacts. It is etched in (100) Si through a combination of KOH etching and DRIE, bonded to a glass substrate, and plated with a 10  $\mu\text{m}$  thick copper, and a 2  $\mu\text{m}$  thick palladium-cobalt film. Experimental relays exhibit a minimum total on-state contact resistance of 130 m $\Omega$ , a response time of 750  $\mu\text{s}$ , a theoretical electrical isolation in excess of 1 kV (tested to 450 V with available equipment), and a current carrying capacity of 800 mA. They have been hot-switched in excess of  $10^5$  cycles without signs of performance degradation.

## INTRODUCTION

MEMS relays and switches are of interest in applications such as test equipment, radars, communications and power systems, amongst others [1, 2]. Unlike solid state devices, mechanical relays provide galvanic isolation between the control and power ports. Heat dissipation and tribology impose significant constraints on MEMS relays which typically operate at contact forces on the order of  $\mu\text{N}$  to mN [1, 2]. Telecom relays, for example, may be subject to surges of up to 2.5 kV and several Amperes [3]. The purpose of this research is to develop a MEMS-relay capable of reliably hot-switching currents on the order of 1 A, and providing galvanic isolation in excess of 1 kV.

## DESIGN AND MODELING

In order to achieve reliable operation, high on-state current carrying capacity, high off-state breakdown voltage, and the capability of reliably hot-switching resistive and inductive loads, the following functional requirements must be met.

- Contact travel must exceed 10  $\mu\text{m}$  to prevent arcing while operating in air at atmospheric pressures, as expressed by Paschen's law [4, 5]. Contact travel over 30  $\mu\text{m}$  is preferred for hot-switching, as contact erosion may lead to bridging [6].
- A minimum closing force of 0.1-0.6 mN is required to achieve stable contact performance, and 5-10 mN is required to achieve low contact resistance with hard metals such as Ru [7].
- A minimum opening force of 0.1-2.7 mN is required to overcome contact adhesion [7].
- Contact wipe is desired to increase the reliability of the contacts by removing oxide and organic films.
- Adequate contact materials and metallization processes are desired, to provide stable and low contact-resistance, prevent material transfer, and achieve high arc voltages and currents. Materials with high melting and boiling temperatures are preferred [3].

## Device Architecture

Based on the functional requirements, we designed a single pole, single-throw, serial metal-contact MEMS relay. This relay, shown in Figure 1, is comprised of four double-parallelgram flexures (1) which serve as bearings, eight pairs of engaging and disengaging electrostatic "zipper" actuators (2), one moving {111} contact (3), and a pair of static {111} contacts (4a, 4b).

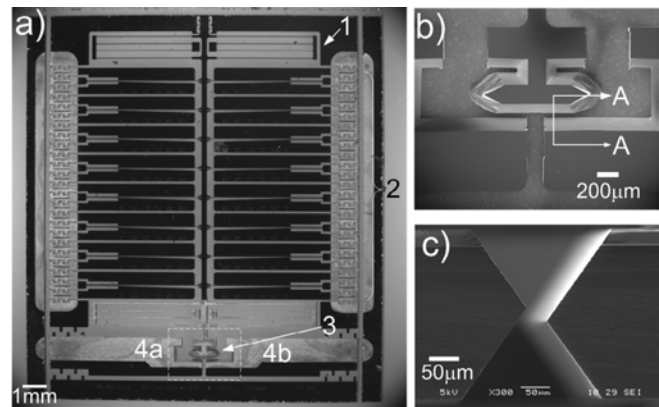


Figure 1: Fabricated relay. Die top view (a); contact detail, prior to metal deposition (b); contact cross section A-A, as shown in Figure 1b, without the metal film (c).

## {111} Silicon Etched Contacts

The {111}-plane contacts offer several advantages over traditional MEMS-relay metal contacts such as vertical displacement contacts (VDC) and horizontal displacement contacts (HDC). VDC, shown in Figures 2a and 2b, have a contact travel on the order of 1-5  $\mu\text{m}$  [1, 2], which is less than the 30  $\mu\text{m}$  required to withstand contact erosion [6] and the 10  $\mu\text{m}$  required to prevent arcing [4, 5]. Traditional HDC, shown schematically in Figures 2c and 2d, have resistances on the order of 1-10 Ohms [8, 9], which leads to excessive Joule heating while handling the currents in our application; further it is difficult to deposit metal onto these contacts, making continuity challenging. The {111} contacts [10], shown schematically in Figures 2e and 2f, provide large travel, on the order of 70  $\mu\text{m}$ , which prevents arcing, and introduces contact wipe which is known to enhance the contact reliability. Further, the oblique geometry allows for an enhanced metallization process which provides low on-state contact resistance values.

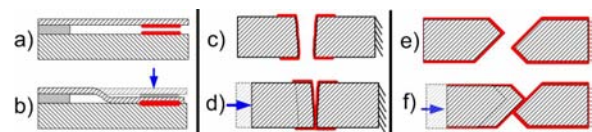


Figure 2: Contact architecture. Vertical displacement contacts (VDC) in open (a) and closed (b) states; horizontal displacement contacts (HDC) in open (c) and closed (d) states; {111} Si etched contacts in open (e) and closed (f) states.

## Actuation

Eight pairs of compliant-starting-zone zipper (CSZZ) actuators [11] provide a theoretical force of 40 mN during the closing and opening events, a pull-in voltage of 65 V and a 70  $\mu\text{m}$  travel. Electrostatic actuation was chosen due to its low, virtually negligible, power consumption and heat generation; CSZZ actuators were selected to reduce the pull-in voltage, while providing the required displacement and force.

## Contact Material

The {111}-plane contacts were electroplated with 10  $\mu\text{m}$  of copper (Cu) and 2 $\mu\text{m}$  of palladium-cobalt (Pd-Co) over an evaporated gold (Au) seed layer. Pd was selected for its low and stable contact resistance, robustness to material transfer, high minimum arc voltages and arc currents, high melting and boiling temperatures; the alloying material Co was selected to increase the hardness of the Pd alloy. However, it was found during testing that the Co readily oxidized in the presence of an arc, thus pure Pd could yield better results than those presented here.

## FABRICATION

The MEMS relay fabrication process, shown in Figure 3, proceeds as follows: the device layer is etched in (100) Si through a combination of deep-reactive-ion-etching (DRIE) and crystalline-orientation-dependant etching with KOH using nested silicon-dioxide and silicon-nitride masks (a-k); a Au seed layer is evaporated through a shadow wafer onto both sides of the device wafer (l); the device layer is bonded to a glass substrate (m); the conductive metal films are electroplated over the seed-layer onto the contacts; the device is released by dicing through the device layer; finally, the device is wire-bonded to a pin grid array IC package for testing.

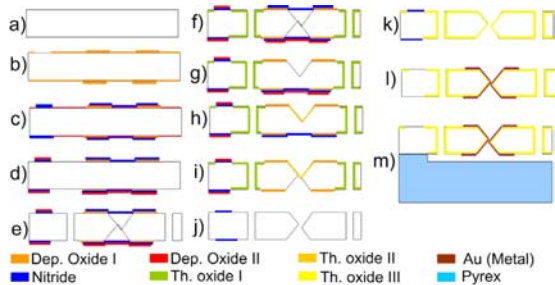


Figure 3: Fabrication process.

## EXPERIMENTAL RESULTS

During testing, voltages and currents are continuously monitored as the relay cycles, and the instantaneous total contact resistance is computed, as shown in Figures 4 and 5.

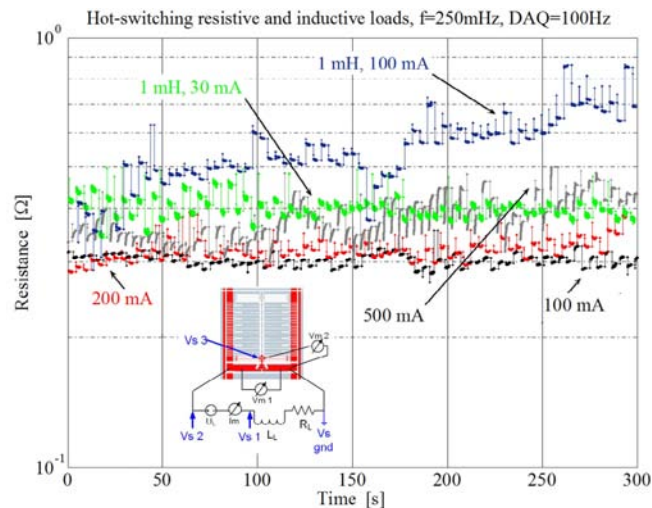


Figure 4: Continuous sampling of total contact resistance during hot-switching. Inset: Experimental setup.

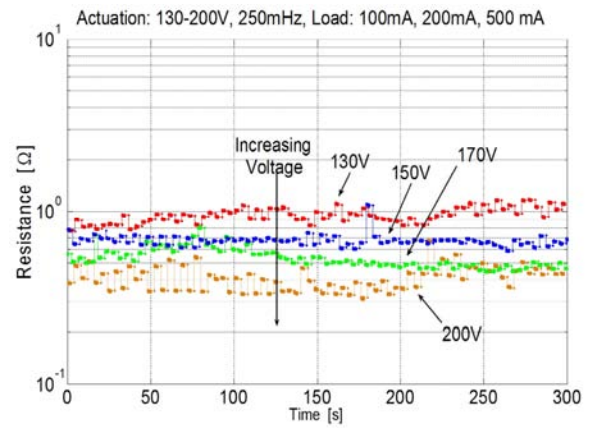


Figure 5: Total contact resistance at various actuation voltages.

The test setup is shown in the inset of Figure 4. Voltage and current are sampled continuously and synchronously via multimeters ( $I_m$ ,  $V_{m1}$ ,  $V_{m2}$ ), while an oscilloscope is used for the transient response ( $V_{s1}$ ,  $V_{s2}$ ,  $V_{s3}$ ).

The load current and voltage were increased until the relay showed any signs of temporary contact-sticking during any actuation cycle. The sticking was found to be reversible, the contacts recovered after cycling without the load connected. Thus no permanent damage was caused to the contact surfaces. The maximum hot-switched current achieved without any signs of contact sticking was 800 mA with a resistive load and 350 mA with a 1 mH inductive load. The integrity of the contact surfaces was attested with a scanning electron microscope before and after hot-switching.

## CONCLUSIONS

The MEMS relay exhibits theoretical isolation in excess of 1 kV (tested to 450 V with available equipment), repeatable and reliable hot-switching characteristics with load currents up to 800 mA and 350 mA with resistive and inductive loads respectively. The relay was tested over  $10^5$  cycles. The Pd-Co film was found to readily oxidize in the presence of an arc and during hot temperature processing in an oxidizing environment. In order to improve device performance, the Pd-Co film should be replaced by pure Pd or by a refractory metal.

## ACKNOWLEDGMENT

Microfabrication was performed at the Microsystems Technology Laboratories at MIT. The electroplating was performed at FormFactor Inc., 7005 South Front Rd., Livermore, CA 94551. The authors thank Dr. Mike Armstrong and Dr. Rod Martens for their assistance and the insightful discussions.

## REFERENCES

- [1] G.M. Rebeiz, RF MEMS theory design and tech., JW&S '03.
- [2] J.J. Yao, J. Micromech. Microeng., Vol. 10, '00, pp. R9-R38.
- [3] W. Jöhler, IEEE TCPT, 27(1), March '04, pp. 19-29.
- [4] J.-E. Wong, et. al. MEMS 2000, Japan, '00, pp. 633-638.
- [5] H. Hosaka, et. al., Sens. and Act. A., (40-1), Jan '94, pp. 41-47.
- [6] S.T. Patton, et. al., Tribology Lett., 18-2, Feb '05, pp. 215-230.
- [7] J. Schimkat, Sensors and Actuators, 73(1999), pp. 138-143
- [8] J. Qiu, et. al., JMEMS, Vol. 14(5), Oct. 2005, pp. 1099-1109
- [9] W.P. Taylor, et. al., JMEMS, Vol. 7(2), 1998, pp. 181-191.
- [10] A.C. Weber, et. al., 53<sup>rd</sup> Holm Conf., Sept. '07, pp. 156-159.
- [11] J. Li, et. al., JMEMS, Vol. 14(6), 2005, pp. 1283-1297.

# MEMS AND METAMATERIALS: A PERFECT MARRIAGE AT TERAHERTZ FREQUENCIES

H. Tao<sup>1</sup>, C. Bingham<sup>2</sup>, A. Strikwerda<sup>1</sup>, K. Fan<sup>1</sup>, W.J. Padilla<sup>2</sup>, R.D. Averitt<sup>1</sup> and X. Zhang<sup>1</sup>  
<sup>1</sup>Boston University, USA and <sup>2</sup>Boston College, USA

## ABSTRACT

This paper reports our recent progress on creating active structures and devices to enhance the ability to manipulate and detect far-infrared, or terahertz (THz), radiation by combining electromagnetic metamaterials with MEMS technologies. We have designed, simulated, and fabricated state-of-the-art THz components which include a THz resonance switch, flexible THz metamaterials, and 3D THz metamaterials. Preliminary results demonstrate the potential of MEMS-enhanced metamaterials for THz applications.

## INTRODUCTION

The terahertz region of the electromagnetic spectrum extends from 100 GHz to 10 THz (1 THz corresponds to a wavelength of 300 microns). This region, alternatively called the far-infrared, lies below visible and infrared wavelengths and above microwave wavelengths. This narrow portion of the electromagnetic spectrum is the least developed and therefore the least understood.

Motivating our effort to advance THz science and technology is the unique characteristics of THz radiation which includes transparency to materials such as cardboard, plastic, and styrofoam which are opaque at other wavelengths, and sensitivity to molecular signatures of gas phase and solid phase materials including biological agents and chemical explosives. While there have been laboratory-based demonstrations, further improvements in THz sources, components, and detectors are required for systems which are sufficiently compact and robust for real-world operation.

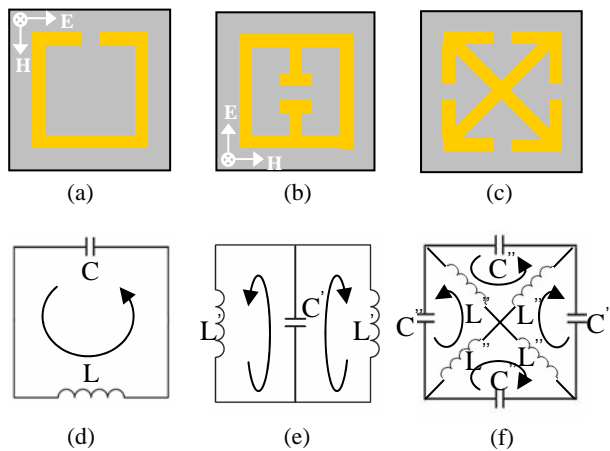


Figure 1: Some THz metamaterial split-ring resonators (SRRs) and equivalent circuits: a) & d) Single-SRR, which shows bianisotropic responses, coupling to both electric and magnetic fields. b) & e) Double-SRR, which couples strongly to a uniform electric field, and negligibly to a uniform magnetic field. c) & f) Quad-SRR, which couples only to electric field, and is polarization non-sensitive due to high structure symmetry.

Recently, artificially structured electromagnetic materials have become an extremely active research area because of the possibility of creating materials which exhibit novel electromagnetic responses not available in natural materials, such as negative

refractive index. Such electromagnetic composites, often called metamaterials, are sub-wavelength composites where the electromagnetic response originates from oscillating electrons in highly conducting metals such as gold or copper allowing for a design specific resonant response of the electrical permittivity or magnetic permeability, which are especially important for the technologically relevant THz frequency regime, as shown in Fig. 1.

## EXPERIMENTS

In this paper, three different but correlated THz structures and components are developed through the intelligent design of metamaterial/MEMS composites, which show extreme power at microscale for sensing/imaging applications:

### Cantilever-based THz resonance switch

An individual THz metamaterial resonance switch element consists of a split ring resonator (SRR) with a cantilever sitting above the gap, as shown in Fig. 2. Our device exhibits tunable electrically resonant response amplitude of nearly 50% at 0.75 THz and operates by shorting the SRR gap with the bimaterial cantilevers. The modulation can be further improved by choosing high-Q SRRs and by optimizing the geometry of cantilevers.

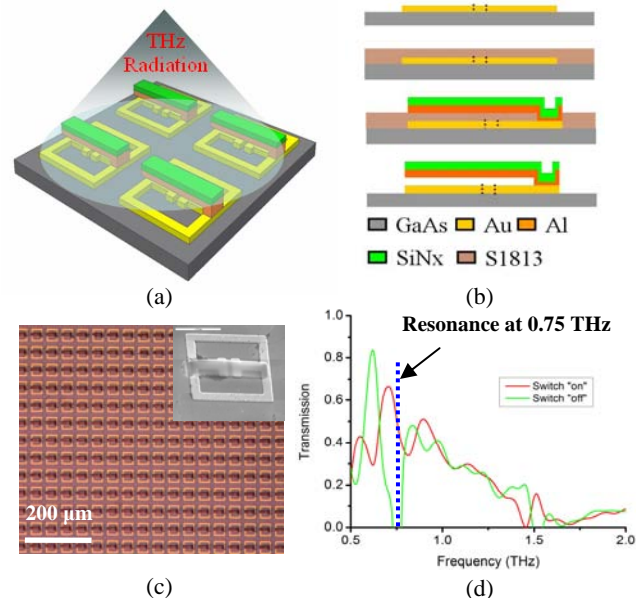


Figure 2: Cantilever-based THz resonance response switch: a) Planar periodic array exposed to normal incident radiation; b) Fabrication process flow; c) Photographs of the fabricated samples; d) Preliminary testing results showing a modulated resonance response of ~50%.

The switch was fabricated by using surface microfabrication process. A semi-insulating GaAs wafer was chosen because it is highly transmitting at THz frequencies; AZ5214e image reversal photoresist was patterned using direct laser writing with a Heidelberg™ DWL 66 laser writer; 200 nm-thick Au/Ti was

E-beam evaporated followed by lift-off with rinsing in Acetone for several minutes; 1.3  $\mu\text{m}$ -thick photoresist of Shipley S1813 was spin-coated as the sacrificial layer; anchors were patterned by standard photolithography; a 200 nm-thick Al layer was E-beam evaporated, followed by sputtering of a 200 nm-thick  $\text{SiN}_x$  layer; cantilevers were patterned by standard photolithography, and etched by reactive ion etch of  $\text{SF}_6/\text{He}$  and Al etchant respectively; isotropic release etching of photoresist was conducted by high density oxygen plasma asher.

Active controls of narrow band resonance response have been demonstrated before by optical pumping [1] and electric modulation [2]. This paper reports the first demonstration of the tunable metamaterial resonance response using the thermal-driven bimaterial cantilever switch realized by MEMS technologies.

### Flexible THz metamaterials

A main charming of metamaterial is the potential of realization of “invisible cloak”. The very first cloak device fabricated on PCB substrate was demonstrated at microwave frequency ( $\sim 8.5$  GHz), and named one of Science’s top ten “Breakthroughs” of 2006 [3]. In this paper, we further pushed it into THz range by using MEMS technologies. Polyimide is chosen as the substrate material for THz “cloaking” because of: 1) its high transmission at THz frequencies; 2) its good mechanical flexibility – this is extremely important in the design of THz cloak, which composes multi-curved layers to provide gradually varying dielectric constants. In this paper, we demonstrate, for the first time, the advances for creating flexible metamaterials operating at the THz frequency range, as shown in Fig. 3.

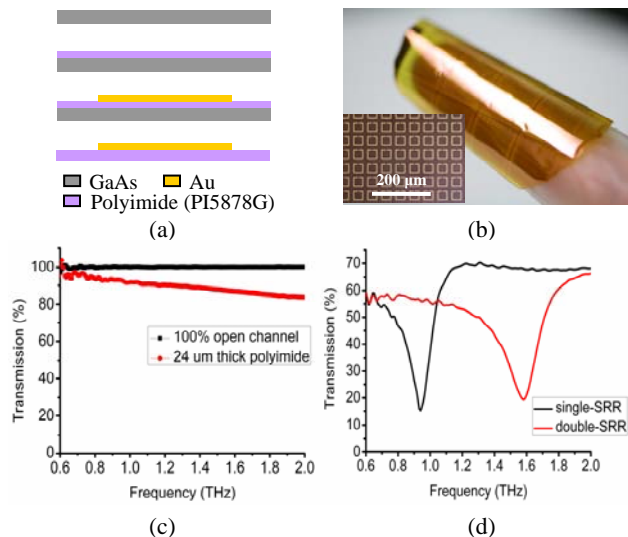


Figure 3: Flexible THz metamaterials: a) Fabrication process flow. (A 24  $\mu\text{m}$ -thick polyimide was spin-coated and cured on a silicon wafer; the SRR structures were patterned by using standard lift-off process, and then peeled off from the substrate.) b) A flexible “skin” applied to a finger. c) Transmission spectrum of the as-fabricated polyimide film. d) Measured resonance responses of single-SRR and double-SRR structures fabricated on flexible polyimide substrates.

### 3D THz metamaterials

Most THz metamaterials are made in single planar layer and/or stack of multi planar layers. Although 3D structures were fabricated on silicon by using self-assembling techniques [4], the out-of-plane angle was relatively small and the silicon substrate was not transparent to THz radiation. In this paper, we demonstrate the first

3D THz metamaterials with large/controllable bending angles and high-filling factor using periodic pop-up structures suspended on low-stress  $\text{SiN}_x$  films. The out-of-plane angle of  $\sim 45^\circ$  was realized by bimaterial legs and further modified by rapid thermal annealing (RTA), as shown in Fig. 4.

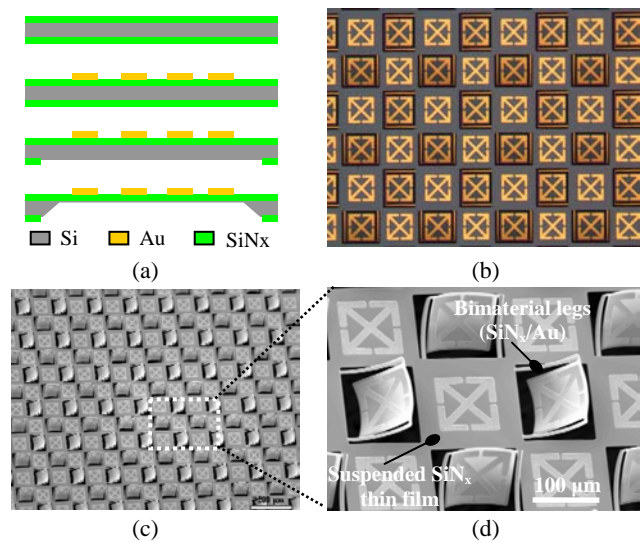


Figure 4: 3D THz metamaterials: a) Fabrication process flow: The SRR structures were patterned by using standard lift-off process on a silicon wafer with 400 nm-thick  $\text{SiN}_x$  thin films deposited on both sides; the bimaterial legs were patterned by using lithography and RIE; open windows were patterned on the backside and then etched through in KOH solution to release the structure. b) Released structures before RTA. c) & d) SEM photographs showing pop-up structures after 10 min RTA at 500°C.

### CONCLUSION

This paper introduces a compelling new research frontier in which functional THz metamaterial components were developed using MEMS technologies. It is believed that the results could set the stage for the marriage of metamaterials with MEMS, enabling technological advances that would otherwise be difficult to achieve.

### ACKNOWLEDGEMENTS

This work is supported by DOD/Army Research Laboratory under grant W911NF-06-2-0040.

### REFERENCES

- [1] W.J. Padilla, A.J. Taylor, C. Highstrete, M. Lee, and R.D. Averitt, “Dynamical electric and magnetic metamaterial response at terahertz frequencies”, *Physical Review Letters*, 96, 107401 (2006).
- [2] H.T. Chen, W.J. Padilla, J.M.O. Zide, A.C. Gossard, A.J. Taylor, and R.D. Averitt, “Active terahertz metamaterial devices”, *Nature*, 444, 597 (2006).
- [3] D. Schurig, J.J. Mock, B.J. Justice, S.A. Cummer, J.B. Pendry, A.F. Starr, and D.R. Smith, “Metamaterial electromagnetic cloak at microwave frequencies”, *Science*, 314, 977 (2006).
- [4] M.S. Islam and L. VJ, “Microfabrication of self-assembling elements for 3D negative-index materials”, *SPIE News room*, DOI:10.117/2.1200612.0515, (2006).

# HUMAN IMPLANTABLE WIRELESS MICROSTIMULATORS AND MICROSENSORS

J.H. Schulman, Ph.D.\*

Alfred E. Mann Foundation for Biomedical Engineering, Valencia, California, USA

## ABSTRACT

Stroke, spinal cord injury, and other injuries have today left over 5 million patients with partial or complete paralysis in one or more limbs. These patients often have viable skeletal muscles with attached viable motor neurons, but no way to activate their neural-muscular system to contract their paralyzed muscles. In 1989 the National Institute of Health (NIH) requested the development of magnetically powered injectable stimulators to restore function to these patients. This request has led to the development of a system of wirelessly coordinated battery powered rechargeable implantable microdevices specifically designed to restore function to these patients with a minimum of surgery, and external equipment.

## INTRODUCTION

There have been many attempts to provide function to paralyzed or partially paralyzed limbs using implantable multi-lead stimulators during the last 40 years. Two of these attempts which are no longer on the market are shown in Figure 1 and Figure 1A.

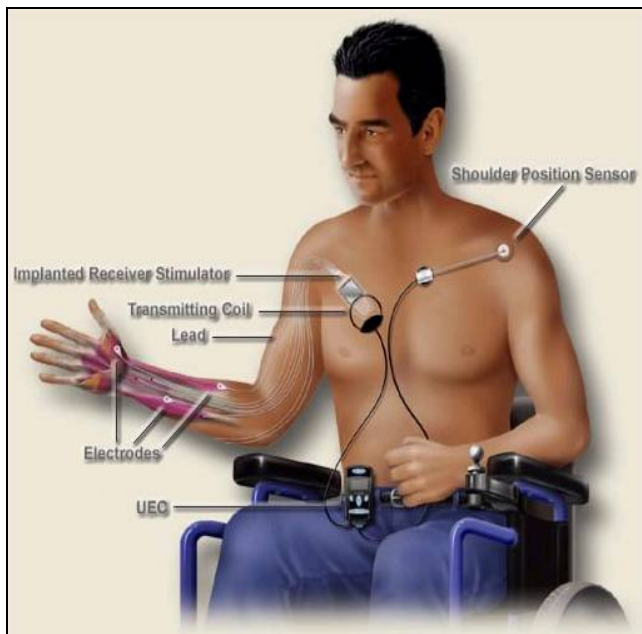


Figure 1: *The Free Hand System by NeuroControl Corp.* has 8 or more stimulating leads to restore function to the hand. It is triggered by a shoulder movement.

\*Chief Scientist at the Alfred E. Mann Foundation for Biomedical Engineering

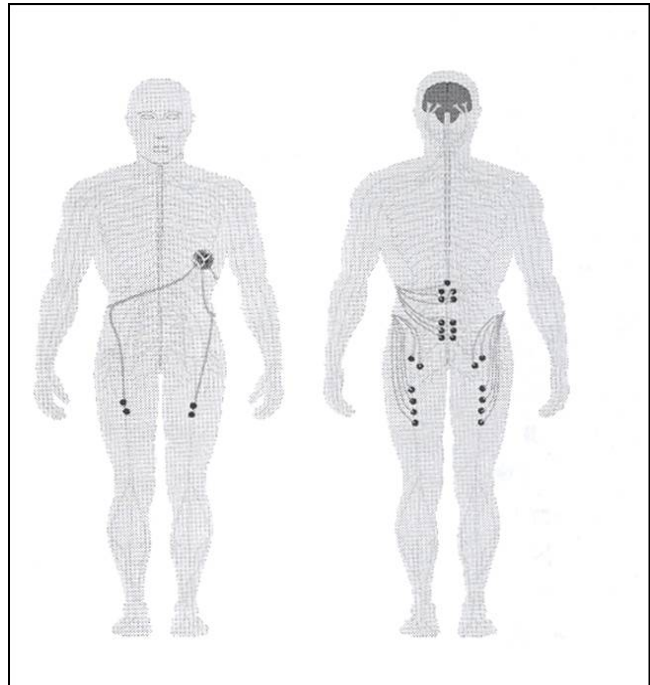


Figure 1A: *The Nucleous FES 22 by Neopraxis Pty Ltd* has 22 stimulating leads. It was designed to restore partial function to the legs and provide some urinary control.

The problems associated with these and other multi-leaded Functional Electrical Stimulation (FES) systems are:

1. Extensive surgery requiring on the order of 4 or more hours, and in some cases several days of surgery to tunnel long wires thru the body, attach the different electrode terminations onto the correct anatomical locations of the targeted nerves and muscles, and make the pocket for the implantable device.
2. Threat of infection: The surfaces of the wires, electrodes and devices seem to protect infectious microorganisms from the body's immune system. By the time a bacterial infection is detected, it is always assumed that the entire interconnected system has become contaminated. This requires that the entire implant system be surgically removed. In some cases the explant procedure is more difficult than the implant surgery and can take longer. There is also always the danger for serious damage to the patient from the explant procedure.
3. External coil orientation and position: External magnetic powering requires a coil to be worn by the patient in close proximity to the implanted device, and to be oriented correctly. If the coil is displaced by a relatively small distance the entire system becomes intermittent or shuts down.
4. Significant advanced planning and inflexibility: The precise number and type of sensors, stimulators, lead lengths and device locations specific to each patient and

his/her condition must be planned for in advance. Adding extra channels that were not planned for can become a major engineering project.

5. Coordination of sensors and stimulators and external wires: Many systems had implantable stimulator channels and external sensing channels. The external sensors required wires outside the body running between the sensor and the external powering/control unit, in addition to the wires from the coil.

As a result of these problems, multi-leaded multichannel implantable stimulator-sensing systems to provide daily functional support for paralyzed limbs have not been successfully commercialized. Only multichannel stimulators with all the electrodes on one or two cables such as spinal cord stimulators and cochlear implants that operate at a specific anatomical location have been successfully commercialized.

### A PRACTICAL MULTI-CHANNEL FUNCTIONAL ELECTRICAL STIMULATION SYSTEM

A practical FES system needs to be wireless to prevent the entire system from getting infected. The body's immune system is quite effective. Foreign objects provide a partial shield over which the infection can migrate. If different components of an implantable system were not connected, the probability that an infection of one of the components could migrate to another would be significantly reduced. In 1989 NIH funded the development of a magnetically powered wireless injectable stimulator. Three glass encased microstimulators were demonstrated to the NIH in 1982 and shown to be independently programmable. (See Fig. 2A). The stimulation energy and timing of up to 255 of these microstimulators could be independently controlled and powered thru a single magnetic field. Thus the infection problem was dealt with. If one microstimulator got infected, there was a high probability that the infected device could be removed without infecting the others.. This design was later improved with a more efficient assembly (Fig. 2B) and a strong ceramic case with eyelet (Fig. 2C). Figures 3 and 4 show x-rays with five devices which were injected to stimulate certain nerves. When stimulated, these nerves could move the arm, thumb, fingers, and wrist of a stroke patient. The photo on the right is a demonstration of the control unit and the coils mounted on an arm to power and control the five injected micro-stimulators.

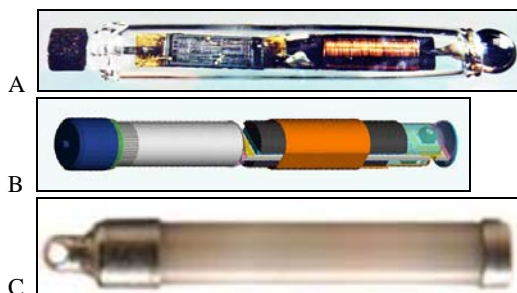


Fig 2: A) Glass microstimulator 1992, left to right: Tantalum oxide anodic-electrode-capacitor, integrated circuit (IC), and ferrite wound coil. B) Internal components, electrode, capacitor, and coil wound on ferrite sandwiched IC. C) Advanced design in a hermetic ceramic case.



Figure 3: Left: X-ray of three microstimulators between the wrist and elbow positioned to stimulate the nerves that cause the fingers to open, the thumb to rise, and the wrist to move upward. Right x-ray of the two microstimulators positioned between elbow and shoulder to stimulate the nerves to cause the arm to straighten out.

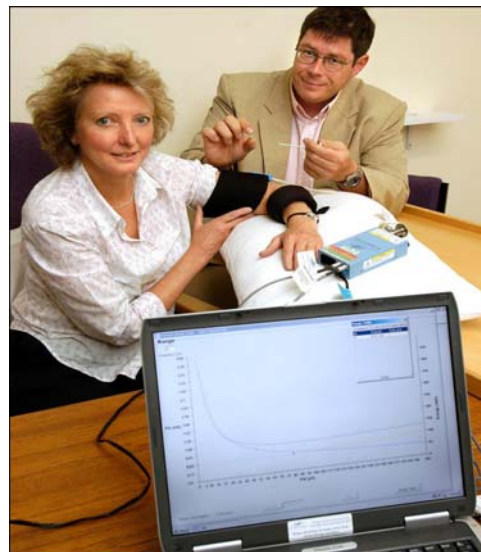


Figure 4: Demonstration of the coils (black) mounted on the arm to power and control the five microstimulators, and the blue control unit on the table next to the hand. The demonstrators are Dr. Jane Burridge of South Hampton England (the principal clinical investigator) and Dr. Gregoire Cosendai (The AMF Field Bioengineer).

These magnetically powered microstimulators satisfy problems 1 and 2 mentioned in the introduction above, i.e. the wireless requirement and the minimization of surgery. In clinical studies on six patients it was determined that with training, a surgeon can learn to inject these devices in the correct location at a rate of about 15 minutes per microdevice. However, we need microsensors, and have to get rid of the external coils and wires that power and control the microstimulators. This requires new technologies inside each of the micro devices, a battery, a propagated electromagnetic wave radio transceiver, and the addition of sensing technology. This also requires a small external

computerized controller (master control unit or MCU) with a matching transceiver, initially outside the body since its program will have to be modified as we add microdevices, and later inside the body if a totally implanted system was desired.

### POWER SOURCE FOR EACH MICRODEVICE

In about 1995 it was decided that the battery should be a hermetic 10 mWhr Lithium Ion (LI) cylindrical cell. The LI cell has about five times the energy density of nickel cadmium batteries, and has excellent charge retention properties. In about 1998, a hermetic LI cell meeting our requirements was developed by Quallion Corp. [1] See Figure 5. This cell was about 2.5mm in diameter and 12 mm long. It had a capacity of about 10 mWhrs (3 mAHrs at about 3.6 volts).



Figure 5. 10 mWhrs Lithium Ion rechargeable battery that is about 2.7 mm in diameter and about 12mm long.

### BATTERY CHARGING SYSTEM

The wireless powering system to recharge the battery was similar to that used to power the glass microstimulator, (i.e. transformer coupling). The constraints however were less demanding. A small amount of intermittency and coils could be allowed as long as the battery was charged in a reasonably short time. The goal is one hour per week or five minutes per day. A ferrite tube was used for the core of the coil. Most of the electronics is located inside the ferrite tube. See Fig. 6. The coil is about 2.5 cc in diameter, and about 8 mm long. The charging coil is very large, (about two or more inches in diameter and several inches long), and thus there is negligible loading of the large coil's field by the microdevice's coil. By designing the large coil with a high "Q" and not having any modulation on the magnetic field, it is possible to efficiently generate a very large magnetic field with a small amount of power, and permit recharging microdevices deep inside the body (e.g. more than four inches inside the body). 125Mhz is used for the charging field.

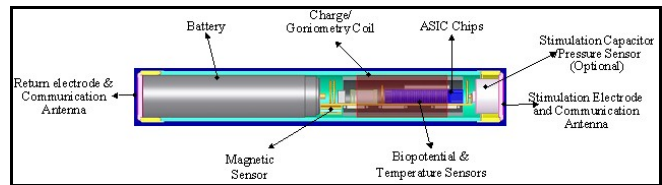


Figure 6: Left to right: battery, two vertical inductors, capacitor half in ferrite tube. The blue represents several integrated circuit chips, with a crystal on top inside the ferrite tube, and the output capacitor on the right.

### BIDIRECTIONAL TELEMETRY SYSTEM

The requirement is a low power telemetry system, capable of communicating from any part of the human body to the MCU which could be 4 meters away on a nightstand.. The lowest power wireless scheme is to use propagated electromagnetic waves, i.e. radio signals. It has been estimated that if certain muscles in a persons leg were more than 50 mSec late in responding while running, that person could fall down.[2] Also electrical noise could introduce an error in the message. Thus we need error detection codes, and need to be able to resend the message. Based on these situations, we decided to perform all communications within a 10 mSec time frame. This time frame would allow us to repeat the same message five times before we were physiologically late. The data to each device requires the selection of one out of about a hundred parameters plus about 8 bits to implement a new value. The response would usually be an eight bit value for a preprogrammed parameter, plus two special bits. One special bit indicates the error check status of the previously received transmission, and the other special bit indicates whether or not an alerting condition was detected. The alerting condition could be low battery capacity, unsafe overcharging, an undesired temperature rise, etc. Thus in every frame 15 and 10 data bits plus an equal number of forward error detecting bits are transmitted to and from each micro device respectively.

### TRANSCIEVER COMMUNICATION POWER CONSIDERATIONS

The first amplifier component (field effect transistor or current transistor) in a receiver front end for the band 400 to 460MHz needs a powering current of about one milliamp to be able to lower the noise floor to detect microvolt signals. A transmitter located 4 inches inside the body needs an equivalent radiated power (ERP) of about 1 mW (if it were in air) to get a radio signal out of the body that is reliably detectable 4 meters away by a sensitive receiver. The power to the transmitter output stage needs to be about three times the ERP. This means that about 1 mA at 3.5 volts is needed for the transmitter.

Continuous reception is out of the question since the 3mAHr battery would be drained in 3 hours with a continuous 1mA drain.. Besides the transceiver power requirement, we also need the battery power to do jobs like stimulating nerves and sensing various parameters. The solution we came up with is to have a very short transmit and receive duty cycle (about 0.1%) that is accurately synchronized. For each 10 mSec frame the implant would receive for 5 μSec, and then at a later time in the frame transmit for 5 μSec. With a 0.1% duty cycle one mA of power drain becomes an average of one μA. of power drain. This scheme requires a clock accurate to a fraction of a microsecond every ten mSec. The receiver also has to be designed to start up quickly.

If the total transmit and receive time is only ten microseconds, this also means that the transmitter and receiver is off for 9,990 μS. Thus another device can transmit and receive during the off time.

In fact if the timing were very exact, 999 other devices can communicate during the off time. In reality we were restricted to about 850 devices during the off time.

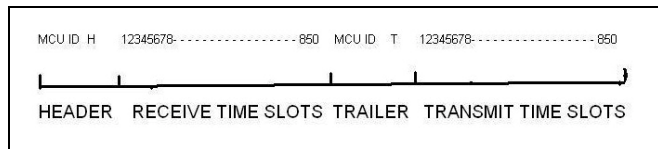


Figure 7: Upload and download timing diagram: The header, trailer, and time slots are shown for a single frame.

### SYNCHRONIZING TO TIME SLOTS

The MCU contains a microprocessor, an accurate clock, and a transceiver designed to communicate with each of the microdevices used in the system. At time of implant, each micro device will be assigned a time slot, and the ID of its MCU. Time slots will be assigned in numerical sequence. The MCU has a program that determines the coordination of all of its microdevices. At the beginning of each frame the MCU broadcasts a header with 11 time slots, and half way into the frame it also transmits a trailer involving 11 time slots. The header contains the MCU ID and other information. When the microdevice initially turns on it starts looking for the header or trailer. After it locates the start of the header, it synchronizes its clock to that of the MCU, and then locates its own time slot. From that point onward, it only listens to its own time slot, and continues to synchronize its own clock using the time slot information. Fig. 7 is a diagram showing the header, time slots, and trailer.

### SENSORS

In the initial versions, we intend to have two programmable sensor features, voltage, and distance measurement for joint angles.

### VOLTAGE AMPLIFIER

A programmable voltage amplifier capable of detecting muscle or neural potentials. Signals between 3  $\mu$ V and 0.1 V with 30,000 sample/second resolution. The voltage signal is analyzed during each frame, and either the number of nerve spikes or muscle potentials are transmitted back for each frame, or a rectify and integrate circuit indicates the average amplitude of all the signals in a single frame. During fitting, the clinician can have an oscilloscopic view of the signal at 30,000 samples/second, and decides which analysis parameters he wishes to set up.

### GONIOMETRY

The pickup coil for charging the battery is used as a 125 kHz magnetic field transmitter in one microdevice, and as a magnetic field strength detector in another microdevice. The distance between a transmitting and receiving device can be determined within a few percent accuracy between one and twenty centimeters by the strength of the received signal. A reading is sent every frame. This is useful in monitoring and controlling the opening and closing of a limb joint.

### TEMPERATURE

Temperature is also monitored for engineering purposes. This is obtained by amplifying the thermal coefficient of a transistor base-emitter junction. It is accurate to about 0.2 degrees centigrade. A block diagram of the circuit is shown in Fig. 8 and the system diagram is shown in Fig. 9.

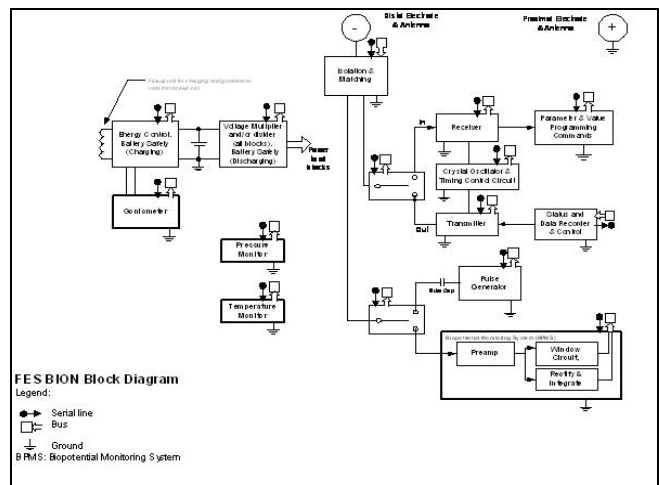


Figure 8: Block diagram of implantable microdevice.

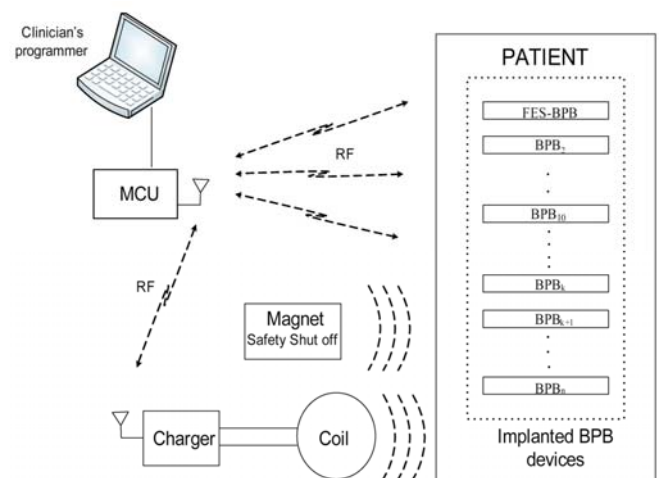


Figure 9: SYSTEM DIAGRAM: The magnet safety shut off is an optional feature in case the microdevices are used in a stand alone mode. In that situation, the only safe stimulation shut off is to bring a permanent magnet near the implant. If the MCU is used, the implants can be programmed to stop stimulating if radio signals stop being received for a predetermined time

At the present time the project is close to releasing the final integrated circuits for the first version.

### ACKNOWLEDGEMENTS

I wish to thank Phil Troyk and Jerry Loeb for bringing me into this project. I also wish to thank Al Mann and the staff at the Alfred Mann Foundation for the great work in bringing these devices to fruition. Partial funding for this project came from the U.S. National Institute of Health under contact No. 1-NS-2-2322.

### REFERENCES

- [1] About 1995 the AMF made a major effort to obtain such a battery from each of the three best quality major international battery manufacturers. The small size of the medical market compared to the large cell phone and computer markets prevented these companies from having an economically feasible relationship with us. In the end Alfred Mann personally founded a company, "Quallion" specifically to make these high reliable Li-I batteries.
- [2] Private communication from Dr. Don McNeal when he was at Rancho Los Amigos Hospital

# DESIGN OF A SIX-AXIS MESO-SCALE NANOPositionER DRIVEN BY MOVING-COIL MICROACTUATORS

*Dariusz S. Golda and Martin L. Culpepper*

Massachusetts Institute of Technology, Cambridge, Massachusetts, USA

## ABSTRACT

This paper presents the design, fabrication, and characterization of a high-speed, six-axis, meso-scale nanopositioner with applications in nanomanufacturing, probe-based microscopy, and data storage. The nanopositioner consists of a silicon flexure bearing, sample stage, and magnetic moving-coil microactuators. A new fabrication process was generated to integrate a silicon flexure and planar copper coils. The nanopositioner was measured to have a range of 10 micrometers and 1 micrometer in the lateral and out-of-plane directions, respectively, an angular range of 0.5 degrees, and a first mode resonant frequency at 900 Hz. Open-loop calibration has been shown to minimize parasitic in-plane motion to less than 100 nm.

## INTRODUCTION

Nanopositioners enable the motion control of large or small parts with nanometer-level or better precision in multiple axes. They therefore set limits on the ability to measure and manipulate physical systems. Macro-scale nanopositioners are designed to position payloads such as wafers and optical elements. The large size (tens of centimeters) and mass (kilograms) of macro-scale nanopositioners limits their bandwidth to a few hundred Hertz. They are inherently sensitive to thermal drift in position and orientation because of their large size. Meso- or millimeter-scale nanopositioners enable a combination of larger bandwidth, improved thermal stability, portability, and the potential for parallel operation in a small package. Meso-scale nanopositioners are suited to position modest payloads such as probe tips, millimeter-sized data storage media, and cell samples. Meso-scale nanopositioners are envisioned to impact applications in data storage [1], nanomanufacturing [2], and probe-based metrology. These applications may benefit from low-cost, portable, multi-axis nanopositioners that position samples with (i) nanometer-level precision, (ii) at bandwidths of 100s Hz and (iii) over a working envelope that is larger than  $10 \times 10 \times 10 \mu\text{m}^3$ . Previously reported meso-scale nanopositioners were limited to five axes of motion or less, and maximum force density has limited the range or natural frequency when using flexure bearings [3-5]. An electrothermal six-axis meso-scale system has been demonstrated [6]; however its range was limited to a few micrometers.

The paper presents the design, fabrication, and experimental characterization of a meso-scale, six-axis nanopositioner wherein silicon flexure bearings and moving-coil microactuators have been combined to yield improved performance over previous designs.

## NANOPositionER DESIGN

### System Concept

The six-axis nanopositioner is designed to (1) operate in open-loop with a range-of-motion that is larger than 10 micrometers in the X-, Y- and Z- directions; and 0.5 degrees in the  $\theta_x$ ,  $\theta_y$ , and  $\theta_z$  directions, (2) possess a natural frequency of several 100 Hz, (3) exhibit better than 10 nm resolution and 50 nm repeatability in open-loop, and (4) possess a footprint of less than 20 mm on a side. The nanopositioning system that was constructed in this work is shown in Figure 1. The system is comprised of three sets of magnet-coil microactuators, a silicon flexure mechanism, sample stage, alignment features, and magnet

fixture package. The microfabricated silicon chip was aligned to the permanent magnets with DRIE alignment features that mate to pins in a precision-machined magnet alignment fixture.

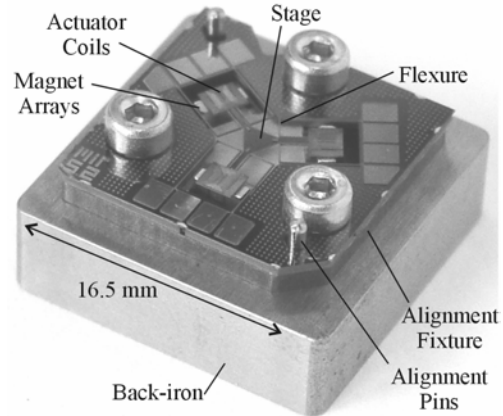


Figure 1: Six-axis nanopositioner with magnet fixture.

The six-axis actuation concept is based upon the HexFlex flexure system that is shown in Figure 2 [7]. Two orthogonal forces were applied to the planar flexure bearing at each of the three actuator paddles in the lateral and out-of-plane directions. Six independent actuator forces were combined through linear bending and torsion of the flexure bearings to yield six-axis motion of the stage in the X-, Y-, Z-,  $\theta_x$ -,  $\theta_y$ - and  $\theta_z$ - directions.

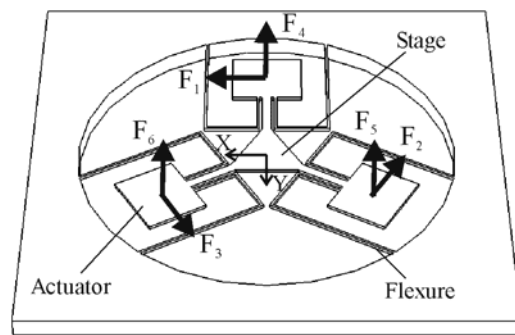


Figure 2: Meso-scale HexFlex six-axis actuation concept.

The actuator inputs,  $\mathbf{i}$ , that are required to generate a commanded stage displacement,  $\mathbf{x}$ , is given by:

$$\mathbf{i} = (\mathbf{TK}_a)^{-1} \mathbf{Kx} \quad (1)$$

where  $T$  is the force transformation matrix,  $K_a$  is the actuation matrix, and  $K$  is the stiffness matrix of the flexure bearing. The actuation matrix relates the input currents to the actuator forces. The force transformation matrix transforms the forces applied at the paddles to a set of forces applied to the stage. The nanopositioner requires three actuators that are capable of generating orthogonal and independent linear forces in two axes in order to achieve six-axis motion in the system.

### Actuator Concept

A new two-axis, magnetic moving-coil actuator was created to drive the nanopositioner [8]. Each actuator consists of stacked micro-coils that are suspended above an alternating array of  $1 \text{ mm}^3$  permanent magnets via a silicon flexure system as shown in Figure 3. The silicon flexure beams support copper traces that provide electrical current to each of the actuator coils.

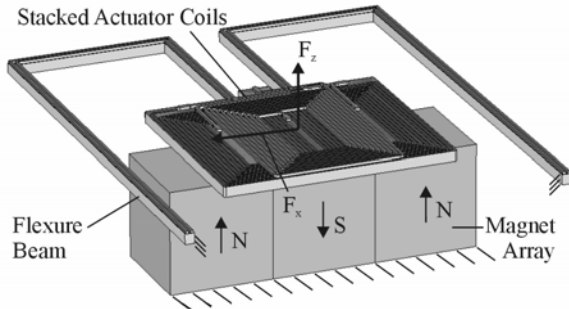


Figure 3: Rendering of two-axis moving-coil actuator concept.

The actuator consists of two independent coils that are stacked upon each other and that apply in-plane and out-of-plane forces to the flexure as shown in Figure 4.

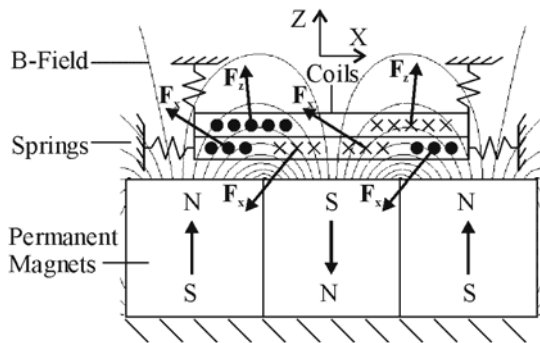


Figure 4: Cross-section of the actuator concept that illustrates the directions of Lorentz forces that act on the y-directed coil segments

The working coil segments that are directed in the Y-direction interact with the permanent magnet field to generate Lorentz forces in the X- and Z-directions. An upper “racetrack” coil generates a net Z-directed force, while a lower “figure-eight” coil generates a net X-directed force. The force properties of the actuator were optimized by adjusting the lateral dimensions of the coils [8]. The actuator inputs are combined to control the stage position in six axes. This actuator outperforms previous designs as it exerts orthogonal, linear forces while minimizing parasitic forces.

### FABRICATION

A new microfabrication process was created to integrate multi-layer, copper actuator coils, silicon flexure bearings, and alignment features. Figure 5 shows the process flow diagram. The process was developed at the MIT Microsystems Technology Lab (MTL). The process used SOI wafers with a  $100 \mu\text{m}$  device layer and  $1 \mu\text{m}$  buried oxide. Trenches for the copper coil mold with cross-sections of  $30 \mu\text{m} \times 30 \mu\text{m}$  were created via DRIE in step (2) and then thermally oxidized in step (3). A Ti/Cu seed layer was sputtered in step (4). The trenches were electroplated into a silicon mold using a deep-filling chemistry at Nexx Systems (BillERICA, MA) in step (5). The overflow copper was polished in step (6) by

chemical-mechanical planarization (CMP). In step (7) a PECVD silicon dioxide interlayer dielectric was deposited and patterned by wet etch to electrically isolate the copper coils. The oxide pattern was also used as the etch mask for the flexure beams in step (12). A second Ti/Cu seed layer was evaporated in step (8). The second copper coil layer was then electroplated into a photoresist mold in step (9). The resist-molded coils had a cross-section width and height of  $25 \mu\text{m} \times 28 \mu\text{m}$ . The resist was removed with acetone after plating and the Ti/Cu seed layer was wet-etched. The backside of the wafer was etched with DRIE to the buried oxide in step (10) in order to define the thickness of the device. Photoresist was used as the etch mask. The buried oxide was then etched with vapor HF in step (11). The front of the wafer was protected with photoresist in order to prevent the HF vapors from attacking the PECVD oxide and the Ti adhesion layer beneath the exposed coils. The upper copper coil layer and silicon dioxide were then used as a mask to etch the silicon flexure mechanism and alignment features with DRIE in step (12). The wafers were mounted on a bare silicon wafer in this step in order to enable the through-etch. The exposed copper structures were not observed to be damaged by the DRIE etch gases. The mean width of the silicon flexure beams after etching was less than  $80 \mu\text{m}$ . The wafer was dismounted in acetone and cleaned in low-power oxygen plasma after etching of the flexures and alignment features. The dies were then separated by laser ablation in step (13). Fabrication process details are available in Ref. [9].

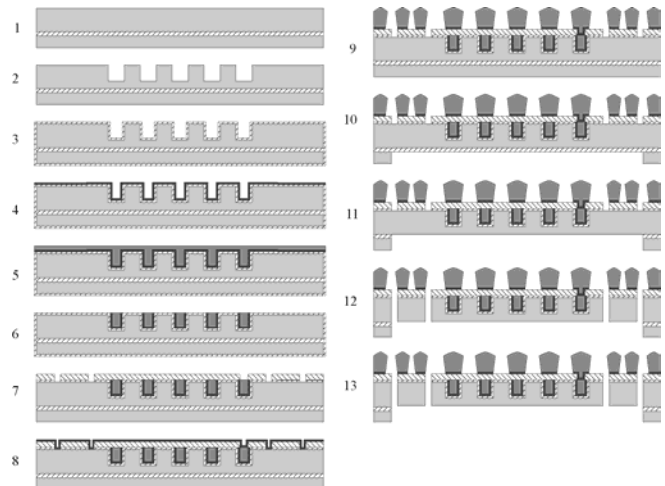


Figure 5: Microfabrication process for meso-scale nanopositioner

Figure 6 shows an optical image of the completed chip. The chip contains copper actuator coils and leads, silicon flexures, alignment features, fastener holes, and bond pads.

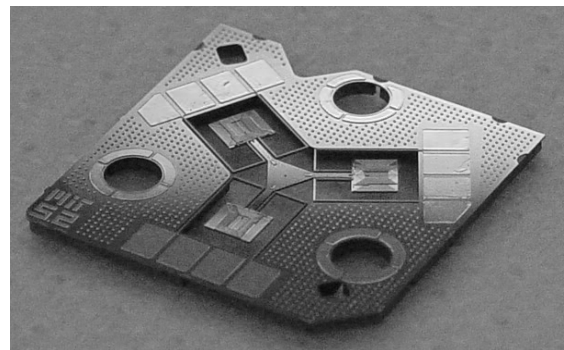


Figure 6: Optical images of the completed nanopositioner die.

The chip was then aligned and fastened to a fixture that contained permanent magnet arrays, alignment features, and a permeable back-iron as shown in Figure 1.

Figure 7 shows the released actuator paddle after assembly to the permanent magnet fixture. The coils, jumpers, and via plugs are visible on the paddle. Permanent magnets are visible beneath the actuator paddle. The air gap between the paddle and magnets was set by the thickness of the alignment fixture and adjusted with polyester shims. Debris that accumulated below the magnets, and assembly errors, resulted in variations in the position of magnets with respect to the coils. The mean, minimum, and maximum air gaps were measured to be 80, 20, and 120  $\mu\text{m}$ , respectively.

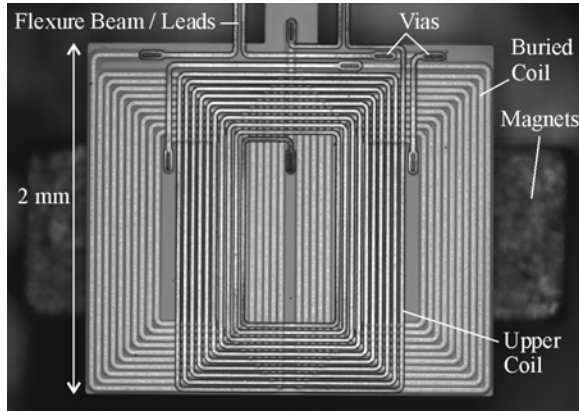


Figure 7: Optical image of a released actuator paddle that is suspended above a magnet array.

## EXPERIMENTAL RESULTS

In-plane frequency response and static range-of-motion were measured at the stage center with a uMech MEMS Motion Analyzer. The out-of-plane frequency response and step response were measured at the stage center with a Polytec MSA-400 laser vibrometer. The device was driven with a 6 channel current controller that possessed an electrical bandwidth of over 3 MHz.

### Frequency Response

Figure 8 shows the measured in-plane frequency response of the nanopositioner. In this experiment, the system was driven by three in-plane actuators. The first mode frequency was observed to be an underdamped rotational mode about the Z-axis at 900 Hz. The peak at 1780 Hz represents the X- and Y- translation modes.

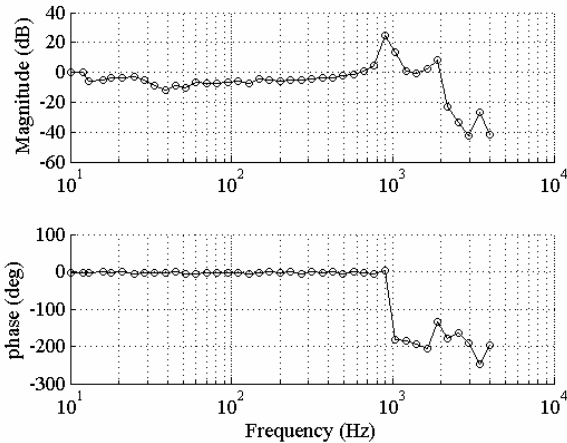


Figure 8: Measured frequency response for pre-calibrated actuation in the  $\theta_z$ -direction.

Figure 9 shows the measured out-of-plane frequency response due to one out-of-plane actuator input. The underdamped peak near 1 kHz is composed of two closely spaced resonances. The lowest resonant frequency was measured at 1040 Hz and observed to be a tilting mode about the X-axis. The translational mode in the Z-direction was measured at 1060 Hz. The higher order modes at 4.5 kHz and 10 kHz are structural deformation modes of the stage.

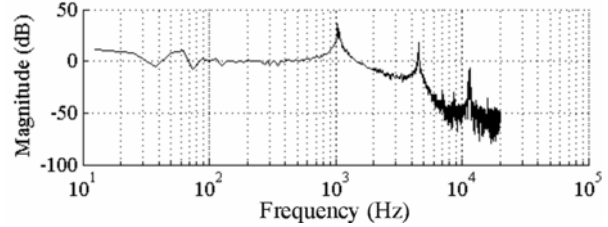


Figure 9: Measured frequency response for pre-calibrated actuation in the Z-direction.

### In-Plane Static Response

The nanopositioner was calibrated for open loop operation in the plane by constructing a 3 x 3 calibration matrix from experimental data. The resultant X-, Y-, and  $\theta_z$  stage motions were measured for each of three combinations of actuator inputs. The calibration matrix was measured to be

$$\begin{bmatrix} \Delta x \\ \Delta y \\ \Delta \theta_z \end{bmatrix} = \begin{bmatrix} 9.8005 & -4.2330 & -6.5472 \\ 0.3061 & -6.8919 & 8.5796 \\ 0.0075 & 0.0053 & 0.0076 \end{bmatrix} \begin{bmatrix} i_1 \\ i_2 \\ i_3 \end{bmatrix}. \quad (2)$$

The input current has units of Amps, displacement has units of  $\mu\text{m}$ , and rotation has units of radians. Figure 10 shows the measured quasistatic response of the nanopositioner in the X- and Y-directions to calibrated commands in the X-direction.

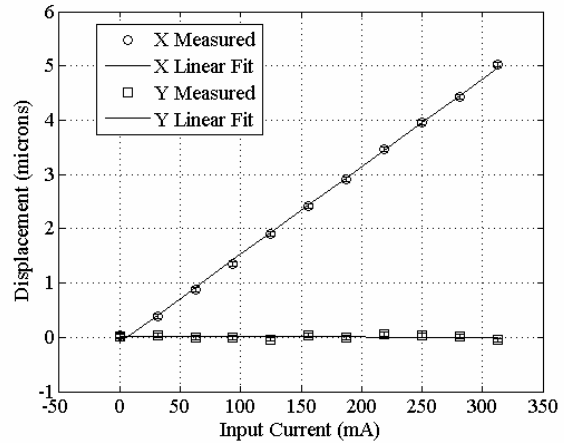


Figure 10: Measured in-plane quasistatic response to calibrated commands in the X-direction.

The measurement error bars of  $\pm 40$  nm are plotted in the figure. The input current plotted in the figure represents the maximum current applied to any of the three actuators. The data indicates that the nanopositioner has a unidirectional range-of-motion that is larger than 5  $\mu\text{m}$  and therefore has a bidirectional range greater than 10  $\mu\text{m}$ . The input current was limited to less than 350 mA in these experiments, while the temperature-limited

maximum current is larger than 450 mA. The nanopositioner may therefore have a useful range that is greater than 14  $\mu\text{m}$ , but this has yet to be measured. Less than 100 nm of parasitic translation was recorded during the commanded translations.

The data in this section demonstrates that the parasitic motions that are due to parasitic moments and forces may be minimized during open-loop operation by linear calibration. In addition to the translational motion, the system was measured to have a calibrated angular range of more than 0.5 degrees in the  $\theta_z$  direction.

### Out-of-Plane Step Response

Out-of-plane motion in the Z-direction was measured prior to calibration with a laser vibrometer. Square wave inputs were commanded to one Z-actuator. The input square wave oscillated between 0 and 50 mA, which is well below the actuator coil current limit of 450 mA. Figure 11 shows the pre-calibrated, out-of-plane step response.

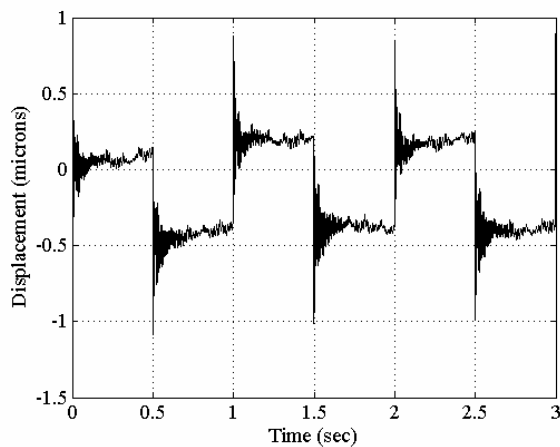


Figure 11: Measured out-of-plane response to pre-calibrated step commands in the out-of-plane Z-direction.

The data indicates that the nanopositioner has a unidirectional range of 0.5  $\mu\text{m}$  in the Z-direction with a calibration constant of 10  $\mu\text{m}/\text{A}$ . The bidirectional range is therefore at least 1  $\mu\text{m}$ . An input of  $\pm 100$  mA would result in  $\pm 1$   $\mu\text{m}$  of motion in the Z-direction.

The data in Figure 11 also indicates that system settling time is less than 250 ms. The excessive settling time and greater than 200 nm drift may be due to thermally-induced error motions from power dissipated in the actuator coils. The power dissipation induces thermal bimorph bending of the flexure beams which may cause the observed drift. Experiments are in progress to investigate the effects of thermally-induced error motions that are caused by power dissipation within the microcoils.

### CONCLUSIONS

This paper presented the design, microfabrication, and initial experimental characterization of a six-axis, meso-scale nanopositioner. The nanopositioner uses a silicon flexure bearing and a set of two-axis linear moving-coil actuators to enable in-plane and out-of-plane motion in open-loop. The system was measured to have a range of motion of 10  $\mu\text{m}$  in the lateral directions, a range of 1  $\mu\text{m}$  in the out-of-plane direction, an angular range of 0.5 degrees, and a first mode resonant frequency at 900 Hz. Experiments are in progress to calibrate the system in six-axis and investigate the thermally-induced error motions. The system

is envisioned to provide a platform for future low-cost, high-performance instruments and equipment that are used in nano-scale research and nano-manufacturing.

### ACKNOWLEDGEMENTS

This material is based upon work supported by the National Science Foundation under Grant 0348242 – PECASE: Research and Education Plans for Modeling and Design of Fixtures and Six-Axis Manipulators for Nanomanufacturing. The authors would like to thank the staff of the MIT MTL for their guidance and use of microfabrication facilities, Nexx Systems for the use of their electroplating services, Professors Jeff Lang and Dennis Freeman for use of experimental equipment, and Polytec for the use of the laser vibrometer.

### REFERENCES

- [1] E. Eleftheriou, T. Antonakopoulos, G. K. Binnig, G. Cherubini, M. Despont, A. Dholakia, U. Durig, M. A. Lantz, H. Pozidis, H. E. Rothuizen, and P. Vettiger, "Millipede - a MEMS-based scanning-probe data-storage system," *IEEE Transactions on Magnetics*, 39, 2 (2003).
- [2] A.P. Malshe, K. Virwani, K. P. Rajurkar, and D. Deshpande, "Investigation of nanoscale electro machining (nano-EM) in dielectric oil," presented at 55th CIRP General Assembly, Antalya, Turkey, 8/21-27/05.
- [3] J.J. Choi, H. Park, K. Y. Kim, and J. U. Jeon, "Electromagnetic micro x-y stage for probe-based data storage," *Journal of Semiconductor Technology and Science*, 1, 1 (2001).
- [4] H. Rothuizen, U. Drechsler, G. Genolet, W. Haberle, M. Lutwyche, R. Stutz, R. Widmer, and P. Vettiger, "Fabrication of a micromachined magnetic X/Y/Z scanner for parallel scanning probe applications," *Microelectronic Engineering*, 53, 1 (2000).
- [5] H. Rothuizen, M. Despont, U. Drechsler, G. Genolet, W. Haberle, M. Lutwyche, R. Stutz, and P. Vettiger, "Compact copper/epoxy-based electromagnetic scanner for scanning probe applications," *Proceeding of the 2002 IEEE International Conference on MEMS*, Las Vegas, NV, 1/20-24/2002, IEEE 2002, pp. 582-585.
- [6] M. L. Culpepper and S. Chen, "Design of a Compliant, Micro-scale, Six-axis Nanopositioner-The Micro-HexFlex," *Precision Engineering*, 30 (3) 314-24, 2006.
- [7] M. L. Culpepper and G. Anderson, "Design of a Low-cost Nano-manipulator Which Utilizes a Monolithic, Spatial Compliant Mechanism," *Precision Engineering*, 28 (4), 469-82, 2004.
- [8] D. Golda and M. L. Culpepper, "Two-axis electromagnetic moving-coil micro-actuator," *Proceedings of the 2006 ASME International Mechanical Engineering Conference and Exposition*, Chicago, IL, 11/5-10/2006, ASME 2006.
- [9] D. S. Golda "Design of High-speed Meso-scale Nanopositioners Driven by Electromagnetic Actuators," Ph.D. Thesis, Massachusetts Institute of Technology, February 2008.

# A SURFACE MICROMACHINED CAPACITIVE MICROPHONE FOR AEROACOUSTIC APPLICATIONS

D. T. Martin<sup>1</sup>, K. Kadirvel<sup>1</sup>, T. Nishida<sup>1</sup>, and M. Sheplak<sup>2</sup>

<sup>1</sup>Department of Electrical and Computer Engineering

<sup>2</sup>Department of Mechanical and Aerospace Engineering

Interdisciplinary Microsystems Group, University of Florida, Gainesville, FL

## ABSTRACT

This paper presents improved results for a micromachined dual-backplate condenser microphone designed for aeroacoustic applications. Previous microphone characterization yielded an unacceptably high noise floor. This paper presents improvements to the noise floor through the use of a low-noise voltage amplifier and improved packaging. With bias voltages of  $\pm 9.3$  V, an average sensitivity of  $166 \mu\text{V}/\text{Pa}$  and a noise floor of  $22.7 \text{ dB}/\sqrt{\text{Hz}}$  for a 1 Hz bin centered at 1 kHz are obtained. The noise floor is reduced to a level below that of other MEMS-based aeroacoustic microphones while maintaining sufficient bandwidth and maximum pressure.

## INTRODUCTION

The goal of this research is to develop a microphone for aeroacoustic testing that equals the performance of conventional commercial measurement microphones. The applications for such a microphone include wind-tunnel testing using arrays consisting of a large number of microphones [1]. To be suitable for aeroacoustic measurements, a microphone must operate linearly up to a sound pressure level of 160 dB and have a bandwidth extending to 100 kHz. Furthermore, the noise floor should be as low as possible. The Brüel and Kjær 4138 1/8<sup>th</sup> inch condenser microphone meets these requirements with a noise floor of 18 dB/ $\sqrt{\text{Hz}}$  for a 1 Hz bin at 1 kHz [2]. However, due to the high cost of these microphones, a low-cost MEMS microphone of adequate performance would enhance these measurements by allowing a greater number of microphones to be used.

There have been many MEMS microphones developed in the past; however, most of these have focused on audio applications [3]. While there has been limited development in the area of aeroacoustic microphones, their overall performance is far from that of the B&K 4138 condenser microphone [4-7]. Several previous MEMS microphones have sufficient bandwidth and maximum pressure [4-6]; however, the noise floor of these devices is too high.

A dual-backplate capacitive microphone has been designed to meet the specifications for aeroacoustic measurements. Previously reported results for this microphone yielded an unacceptably high 41 dB/ $\sqrt{\text{Hz}}$  noise floor [8]. This was obtained using a charge amplifier located far from the microphone, resulting in high parasitic capacitance. This paper presents results obtained with a low-noise voltage amplifier with packaging designed to reduce the parasitic capacitance.

## MICROPHONE STRUCTURE

The dual-backplate capacitive microphone consists of three circular conducting plates. These plates are separated by two air gaps. Each layer is comprised of conductive doped-polysilicon, thus forming two capacitors. The outer plates are perforated with holes to allow the incident pressure to deflect the diaphragm. A photograph of the microphone is shown in Figure 1 and a schematic cross-section is shown in Figure 2.

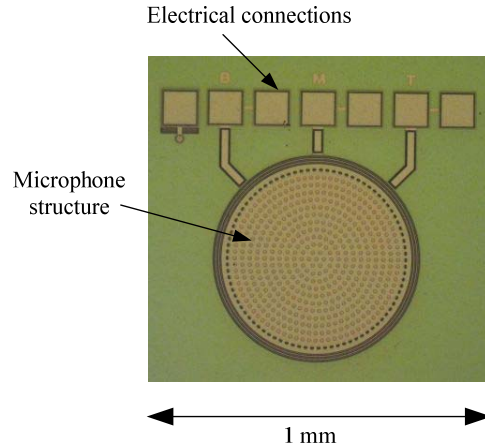


Figure 1: Photograph of the dual-backplate capacitive microphone.

The operation of this type of device is similar to that of the common single-backplate microphone. As the incident pressure impinges on the microphone, it deflects the diaphragm. This changes the values of the two capacitors causing one to increase while the other decreases. Bias voltages are applied to the two backplates, and the output is the voltage on the diaphragm.

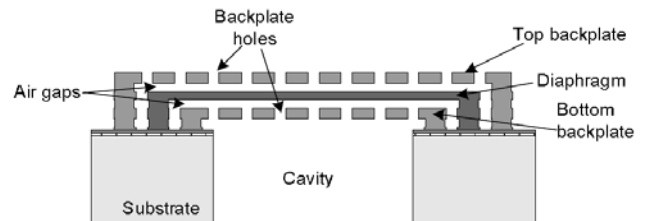


Figure 2: Cross-section of the dual-backplate capacitive microphone showing the key elements.

The microphone is fabricated using the SUMMiT V process at Sandia National Laboratories [9]. The 5-layer, planarized polysilicon process is well suited for this microphone. The conductive polysilicon is used to realize the three electrodes, and the use of chemical mechanical polishing (CMP) in the process results in uniform air gap spacing. This feature is also a major drawback of the process; the use of CMP results in high variability in the air gap thicknesses, which is manifested as a variability in device sensitivity [8]. A summary of the microphone physical specifications is given in Table 1.

## PACKAGING AND CIRCUITRY

A schematic of the microphone and interface circuit is shown in Figure 3. The microphone, represented by  $C_1$  and  $C_2$ , is biased with symmetric voltages  $\pm V_B$ , and the diaphragm electrode is connected to the voltage amplifier. Due to the small capacitance of this microphone, it is essential to minimize the capacitance load

presented by the parasitic capacitance,  $C_p$ , and the amplifier input capacitance,  $C_i$ . As these capacitances increase, the sensitivity of the microphone is reduced [3].

Table 1: Microphone physical specifications.

Property	Nominal value
Diaphragm diameter	460 $\mu\text{m}$
Diaphragm thickness	2.25 $\mu\text{m}$
Air gap spacing	2.0 $\mu\text{m}$
Top capacitance	867 fF
Bottom capacitance	632 fF

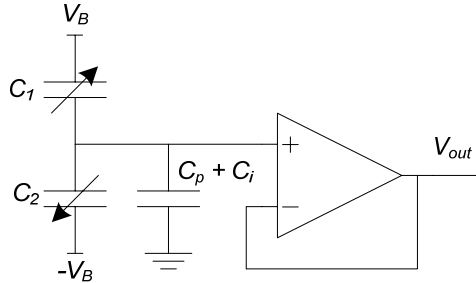


Figure 3: Circuit schematic showing the microphone and buffer amplifier.

To achieve minimal attenuation due to these capacitances, an amplifier with a very low input capacitance is used. The SiSonic Microphone Amplifier, courtesy of Knowles Electronics, is used for the interface circuitry. This amplifier has an input capacitance of approximately 0.3 pF [10].

The microphone package was designed to contain the amplifier and the MEMS die in close proximity to minimize parasitic capacitance introduced by cabling and electrical interconnect. This hybrid package was also designed to minimize interference with the acoustic field by mounting the microphone flush with the front surface of the package. A photograph of the assembled microphone package is shown in Figure 4. In sequence, the microphone is first mounted in a printed circuit board (PCB). The amplifiers are mounted on the reverse side of the circuit board. This preserves the flush surface, while minimizing the parasitic capacitance. This PCB is then secured in a Lucite block designed to be compatible with the acoustic test setup. Photographs of the front- and rear-views of the microphone package are shown in Figure 5. This shows the flush-mounted microphone die, which contains four microphones as well as several test structures. Gold wirebonds connect the MEMS die to the circuit board. These bond wires are covered in a protective epoxy.

The final package has a frontal surface area of 0.75 in. x 0.75 in. This is considerably larger than an individual microphone. However, each die contains four microphones, thus the package contains four amplifiers. A smaller package footprint is possible for a re-designed die containing only one amplifier.

## EXPERIMENTAL RESULTS

Previous results reported for the microphone employed a charge amplifier located off-package [8]. In this configuration, a sensitivity of 390  $\mu\text{V}/\text{Pa}$  was achieved with a noise floor of 41  $\text{dB}/\sqrt{\text{Hz}}$  at 1  $\text{kHz}$ . The resonant frequency of the microphone was determined to be 178  $\text{kHz}$ . The dominant source of noise for this initial characterization was due to the charge amplifier interface circuit. The results presented in this section show a significantly improved noise floor with a modest reduction in sensitivity.

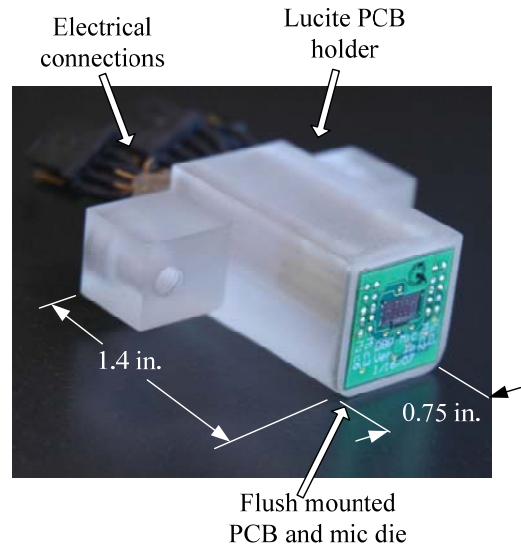


Figure 4: Photograph of the packaged microphone.

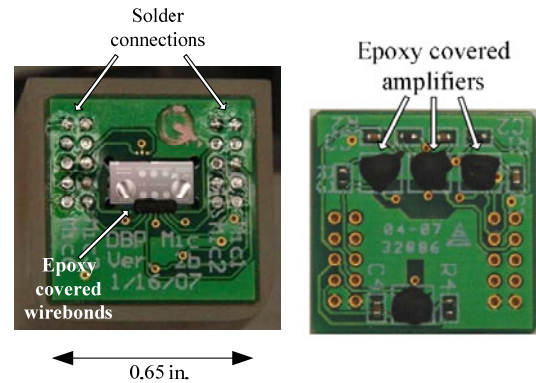


Figure 5: (Left) Front view of the microphone package showing the flush mounted MEMS die. (Right) Back view of the PCB showing four covered, mounted amplifier die.

A total of seven microphones are characterized with the improved circuitry. Experimentation is performed to determine the microphone linearity and frequency response. These acoustic tests are performed using a plane wave tube [11] with a maximum frequency of 20  $\text{kHz}$ , as shown in Figure 6. The noise floor of the microphone is estimated by measuring the output of the microphone/amplifier system without an acoustic input. Bias voltages of  $\pm 2\text{ V}$  are used unless otherwise specified. The experimental setups are described in detail by Martin et al. [8].

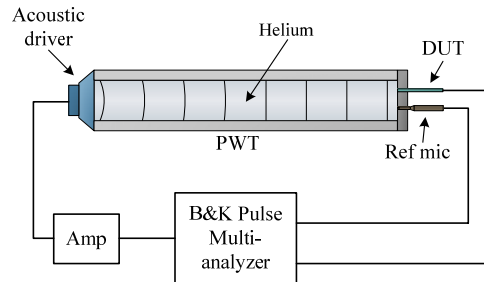


Figure 6: Experimental setup for acoustic experiments.

Figure 7 shows the output of the microphones for varying incident pressure. The amplitude of a 1  $\text{kHz}$  tone is varied from

approximately 40 dB to 160 dB re. 20  $\mu\text{Pa}$ . The output voltage of each microphone is plotted vs. the incident pressure. The dashed lines indicate the predicted output voltage. The average sensitivity is 166  $\mu\text{V}/\text{Pa}$  with a variation of  $\pm 20 \mu\text{V}/\text{Pa}$  between the seven microphones.

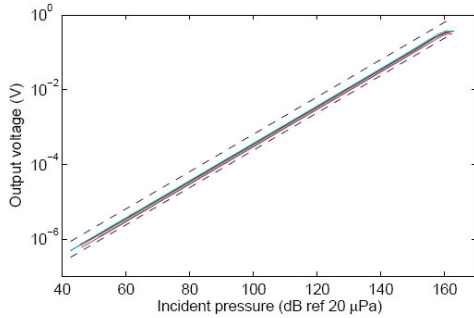


Figure 7: The output voltage of seven microphones vs. incident pressure at 1 kHz.

The microphone output saturates near 160 dB; at this pressure, the microphone output voltage exceeds the input voltage of the amplifier. To quantify the distortion generated by the microphone, the bias voltage is reduced to 2 V to lower the sensitivity. This eliminates any distortion generated by the amplifier for the range of sound pressure levels tested. The total harmonic distortion of the seven microphones is given in Figure 8. The microphones show an average distortion of 4% at 164 dB.

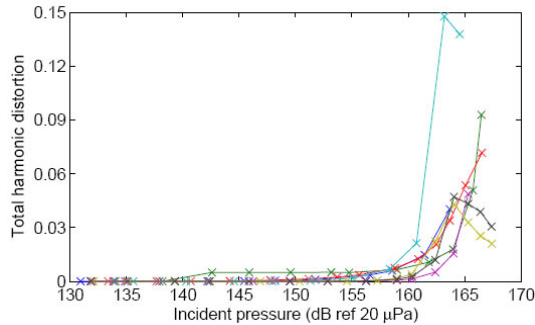


Figure 8: Total harmonic distortion of the seven microphones versus incident pressure at 1 kHz.

The frequency response of the seven microphones is measured from 300 Hz to 25 kHz. The magnitude response is plotted in Figure 9 and the phase response is plotted in Figure 10. The upper frequency for plane-waves in the acoustic waveguide is 20 kHz. Below this frequency, the device under test and a reference microphone are exposed to the same incident pressure. However, above this frequency, the two microphones are sensing a different pressure. Therefore, the magnitude response above 20 kHz is a qualitative measurement demonstrating microphone sensitivity up to this frequency. This measurement confirms the close sensitivity matching of the seven microphones.

The phase response shown in Figure 10 is plotted from 300 Hz to 20 kHz. For the majority of the frequency range, the phase is matched to within  $\pm 1^\circ$ . The dip near 10 kHz corresponds to a reduced output of the acoustic driver. The cut-on of higher modes in the plane wave tube near 20 kHz is evident in the phase response.

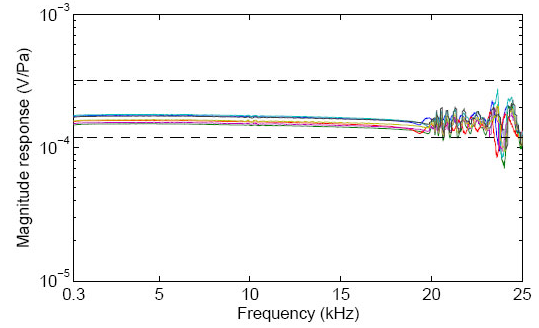


Figure 9: Magnitude response plotted over the range of 300 Hz to 25 kHz.

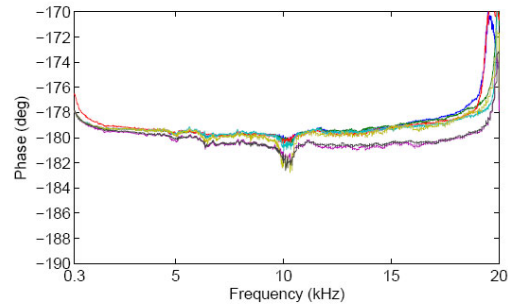


Figure 10: Phase response of the seven microphones plotted over the range of 300 Hz to 20 kHz.

The final measurements performed on the microphones with the improved circuitry determined the noise. The packaged microphones were placed in a Faraday cage to reduce the effects of electromagnetic interference [12]. With no acoustic input to the microphone, the output noise voltage power spectral density (PSD) of the amplifier was measured with a spectrum analyzer over the range of 10 Hz to 100 kHz. Dividing the square root of the PSD by the microphone sensitivity yields the input referred noise, plotted in Figure 11. For a 1 Hz bin centered at 1 kHz, the average noise level of the seven microphones is 22.7 dB/ $\sqrt{\text{Hz}}$ . The input referred noise for the seven microphones falls within  $\pm 1 \text{ dB}$ . Table 2 shows the average noise floor in several equivalent units including a minimum detectable force and capacitance change. The average A-weighted noise figure for the seven microphones is 60.4 dBA.

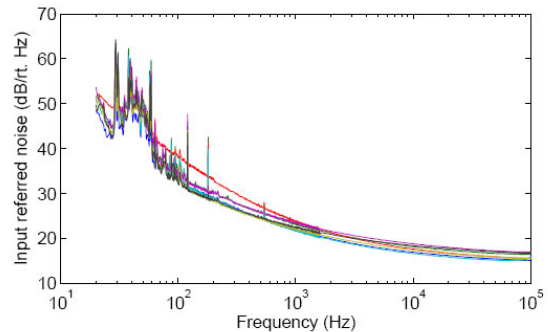


Figure 11: Input referred noise spectrum of the seven microphones.

These results demonstrate the importance of the interface circuitry on the performance of the capacitive MEMS microphone. The lower noise voltage amplifier and hybrid package reduced the noise floor by 18 dB. This improvement was due to a large

reduction in the amplifier noise. The acoustic noise generated by the microphone structure was less significant than the electronic noise [8].

Table 2: The average minimum detectable signal of the seven microphones expressed in several equivalent units at 1 kHz in a 1 Hz bin.

Average Minimum detectable Signal	Value
Pressure	22.7 dB
Pressure	273 $\mu$ Pa
Force	15.1 pN
Displacement	75.4 fm
Capacitance	17.9 zF

The performance of the dual-backplate capacitive microphone is compared to other MEMS microphones, as well as the Brüel and Kjør 4138 condenser microphone in Table 3. The other microphones are sufficient in two specifications listed; however, all fall short of the B&K 4138 in at least one. The present work exceeds the performance of the other MEMS microphones and compares most favorably to the commercial microphone. It is within 4 dB of the 4138's maximum pressure and 3 dB of the noise floor. However, the diameter of the dual-backplate microphone is significantly smaller. With the appropriate packaging, this device has the potential to enable microphone placement in locations prohibited by the size of the B&K 4138 microphone.

Table 3: Comparison of the present work to other aeroacoustic microphones.

Microphone	Diameter	Max Pressure	$f_{max}$	Noise Floor
Present Work	460 $\mu$ m	164 dB	178 kHz	22.7 dB <sup>1</sup>
B&K 4138. [2]	3.2 mm	168 dB	140 kHz	18 dB <sup>1</sup>
Arnold <i>et al.</i> [4]	1.0 mm	160 dB	100 kHz	52 dB <sup>1</sup>
Scheeper <i>et al.</i> [5]	3.9 mm	141 dB	20 kHz	23 dBA
Horowitz <i>et al.</i> [6]	1.8 mm	169 dB	59 kHz	35.7 dB <sup>1</sup>
Pedersen [7]	360 $\mu$ m	140 dB	75 kHz	22 dB <sup>1</sup>

<sup>1</sup>Noise figure at 1 kHz in a 1 Hz bin

## CONCLUSIONS

An instrumentation-grade dual-backplate capacitive microphone has been designed for aeroacoustic measurements. Improvements in the packaging and the use of a low-noise voltage amplifier significantly improved the device performance over the initial characterization results. The noise floor has been reduced while maintaining adequate bandwidth and maximum pressure. The device characterization demonstrates performance that exceeds that of existing MEMS aeroacoustic microphones. In addition, the dual-backplate capacitive microphone compares favorably to the Brüel and Kjør 4138 condenser. For applications not requiring measurements at the extreme ends of the 4138's dynamic range, the designed MEMS microphone is suitable.

## ACKNOWLEDGMENTS

Financial support for this project was provided by the National Science Foundation grant #ECS-0097636 and Sandia National Laboratories. The authors gratefully acknowledge Dr. Pete Loeppert, from Knowles Electronics, for providing the SiSonic microphone amplifier used as part of this work.

## REFERENCES

- [1] T. J. Mueller, *Aeroacoustic Measurements*. Berlin, Germany: Springer-Verlag, 2002, pp. 158–179.
- [2] Brüel and Kjør, Product Data, Condenser Microphone Cartridges—Types 4133 to 4181, p. 6. [Online]. Available: <http://www.bksv.com/pdf/Bp0100.pdf>
- [3] P. R. Scheeper, A. G. H. van der Donk, W. Olthuis, and P. Bergveld, "A review of silicon microphones," *Sens. Actuators A, Phys.*, vol. 44, no. 1, pp. 1–11, Jul. 1994.
- [4] D. P. Arnold, S. Gururaj, S. Bhardwaj, T. Nishida, and M. Sheplak, "A piezoresistive microphone for aeroacoustic measurements," in *Proc. ASME IMECE*, 2001, pp. 281–288.
- [5] P. R. Scheeper, B. Nordstrand, B. L. J. O. Gullov, T. Clausen, L. Midjord, and T. Storgaard-Larsen, "A new measurement microphone based on MEMS technology," *J. Microelectromech. Syst.*, vol. 12, no. 6, pp. 880–891, Dec. 2003.
- [6] S. Horowitz, T. Nishida, L. Cattafesta, and M. Sheplak, "Development of a micromachined piezoelectric microphone for aeroacoustic applications," *J. Acoust. Soc. Amer.*, vol. 122, No. 6, 2007, pp. 3428–3436.
- [7] M. Pedersen, "Development of microelectromechanical systems capacitive microphone for high-frequency applications," in *Proc. of 151st Meeting of the Acoust. Soc. Amer.* Providence, RI, 2006.
- [8] D. T. Martin, J. Liu, K. Kadirvel, R. M. Fox, M. Sheplak, and T. Nishida, "A Micromachined Dual-Backplate Capacitive Microphone for Aeroacoustic Measurements," *Journal of Microelectromechanical Systems*, Vol. 16, No. 6, 2007, pp. 1289–1302
- [9] J. J. Sniegowski and M. S. Rodgers, "Multi-layer enhancement to polysilicon surface-micromachining technology," in *Proc. IEDM Tech. Dig.*, 1997, pp. 903–906.
- [10] P. V. Loeppert and S. B. Lee, "SiSonic—The first commercialized MEMS microphone," in *Proc. Solid-State Sensor Actuator Workshop*, Hilton Head Island, SC, 2006, pp. 7–30.
- [11] T. Schultz, L. Cattafesta, and M. Sheplak, "Modal decomposition method for acoustic impedance testing square ducts," *J. Acoust. Soc. Amer.*, vol. 120, no. 6, pp. 3750–3758, Dec. 2006.
- [12] R. Dieme, G. Bosman, M. Sheplak, and T. Nishida, "Source of excess noise in silicon piezoresistive microphones," *J. Acoust. Soc. Amer.*, vol. 119, no. 5, pp. 2710–2720, 2006.

# DEVELOPMENT OF A FULLY INTEGRATED MICRO-POWER SOURCE BASED ON A MICRO-SILICON FUEL CELL AND A MEMS HYDROGEN GENERATOR

L. Zhu<sup>1</sup>, K. Y. Lin<sup>2</sup>, R. D. Morgan<sup>2</sup>, H. S. Kim<sup>2</sup>, B. Gurau<sup>2</sup>, D. Kim<sup>3</sup>, B. Bae<sup>4</sup>, R. I. Masel<sup>2,4</sup>, M. A. Shannon<sup>1,4</sup>

<sup>1</sup>Department of Mechanical Science and Engineering, University of Illinois, Urbana, IL USA

<sup>2</sup>Department of Chemical and Biomolecular Engineering, University of Illinois, Urbana, IL USA

<sup>3</sup>Department of Mechanical Engineering, Sogang University, Seoul, Republic of Korea

<sup>4</sup>Cbana Labs, Inc. Champaign, IL USA

## ABSTRACT

This paper introduces a fully integrated millimeter scale power source based on a micro-silicon fuel cell and a MEMS hydrogen generator. The integrated devices are fabricated from silicon wafers using conventional MEMS fabrication processes. In this design, hydrolysis reaction of calcium hydride and water is used to generate hydrogen and the hydrogen generation rate is controlled by a microfluidic self-regulating mechanism, which can control the hydrolysis reaction based on the load. Design, fabrication, and testing results of a prototype system are described. One of the devices can produce 90  $\mu\text{W}$  for 6 hrs with a maximum power of 0.17 mW, and another one can produce 30  $\mu\text{W}$  for 26 hours with a total energy density of 100 Whr/L.

## INTRODUCTION

Sub-millimeter power sources are needed for micro-sensors, cognitive arthropods, subdermal drug delivery systems, and other applications. Generally, the devices need microwatts of continuous standby power with peak power levels above one milliwatt, and have mission durations of an hour to a few months. At present, sub-millimeter power sources with such power and energy densities have not yet been demonstrated due to constraints on packaging, fuel storage, fuel delivery, and power generation.

To this end, both micro-batteries and micro-fuel cells have been explored to build millimeter scale power sources and some effort have been done to miniaturize the power sources to sub-millimeter scale. For example, the all solid state thin film lithium battery is the highly promising and mature system already under development by a number of entities with ties to the original work at Oakridge National Laboratory [1, 2]. Although planar thin film micro-battery has relatively high power per unit volume, the current density per unit area is low (1-10 mA/cm<sup>2</sup>) due to its cm-scale surface area. If the area of the thin film battery is decreased to mm-scale, the maximum power would be in micro-watt range. Therefore, the multiple thin film cells have to be stacked in z direction to meet the peak power requirement. This process could increase difficulties in fabrication and packaging. A 3-D integrated all-solid-state rechargeable micro-battery has been proposed [3], but it is still at the early stage of development. Recently, micro-fuel cells have attracted lot of attention to make millimeter scale power sources due to their inherently higher energy and power densities. Most of the current research work is focused on the development of portable PEM fuel cells that meet the demand of portable electronic devices with 1 to 10 W electric power [4-6]. Several groups have worked on micro-silicon fuel cells [7, 8], but none of them included an integrated micro-fuel storage system to complete an integrated micro-power source.

In this paper, we present for the first time the design, fabrication, and initial testing results of a fully integrated micro-power source based on a micro-silicon fuel cell and a MEMS hydrogen generator. The device schematic is shown in Figure 1 and the volume of the whole device is 10.9 mm<sup>3</sup>. Both of the micro-silicon fuel cell and the MEMS hydrogen generator are

fabricated from silicon wafers using standard MEMS fabrication processes, which would enable us to miniaturize the micro system even further to make a sub-millimeter power source. In this work, calcium hydride (CaH<sub>2</sub>) is used as fuel storage due to its high energy density, fast and complete reaction, and low volume expansion [9]. CaH<sub>2</sub> is not typically used for large scale mobile hydrogen generators due to its higher weight per hydrogen stored, but here small volumes are more important than low weight. As shown in Figure 1, a microfluidic self-regulating mechanism is integrated into the MEMS hydrogen generator to control the hydrogen generation based on the load. The self-regulating mechanism is fully passive and it does not cause any parasitic power loss. This design provided a feasible approach to build the sub-millimeter power source in the future.

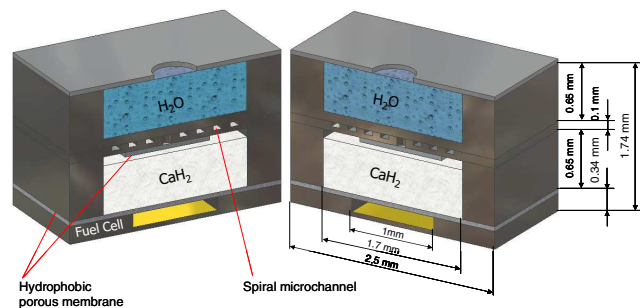


Figure 1: Schematic of the all silicon integrated micro-power source based on self-regulating MEMS hydrogen generator and micro-silicon fuel cell.

## FABRICATION

The micro-silicon fuel cell depicted in Figure 2 is fabricated from a 100 mm P type boron-doped double sided polished prime <1-0-0> SOI wafer (Ultrasil Corp., Hayward, CA) with 300  $\mu\text{m}$  thick handle wafer (0.1-1.0 ohm-cm resistivity), 40  $\mu\text{m}$  thick device layer (1-10 ohm-cm resistivity), and 0.5  $\mu\text{m}$  thick buried oxide using conventional MEMS fabrication processes. Square windows of 2.4 mm x 2.4 mm were patterned on the handle wafer (anode side) while a 6 x 6 array of circular windows of 100  $\mu\text{m}$  diameter and 100  $\mu\text{m}$  apart were patterned on the device layer (cathode side). Figure 3 shows the microfabrication processes for making of the Si dies: (A) The native oxide layer was removed by immersion in the buffered oxide etch (BOE) solution and the wafer was cleaned using piranha etch (3:1 sulfuric acid and 30 wt% hydrogen peroxide); (B) roughly 100 nm thick silicon nitride layer was grown on both sides of the wafer by low pressure chemical vapor deposition (LPCVD); (C) Photolithography using AZ 4620 photoresist (Clariant Co.) was applied to pattern on the silicon nitride of the handle wafer (anode side) to make the square windows (2.4 mm sides); (D) Dry etching using ICP-DRIE was done to create square windows in the nitride layer on the anode side; (E) Photoresist was removed by photoresist stripper AZ-400T

(Clariant Co.), then the exposed silicon substrate was wet etched down to the oxide layer using a 35% potassium hydroxide (KOH) solution at 85°C with silicon nitride as the mask; (F) Again, using standard photolithography, a 6 x 6 array of circular windows (100 μm diameter) was patterned on the silicon nitride of the device layer (cathode side); (G) Dry etching using ICP-DRIE was done to create the circular windows in the silicon nitride on the cathode side; (H) Dry etching using the BOSCH process was done to etch 40 μm of the exposed silicon substrate down to the oxide layer; (I) Dry etching using a Freon reactive ion etcher system (Freon RIE, PlasmaLab) was done to etch through the oxide layer; (J) Using a DC-Magnetron sputtering system, roughly 150 nm of gold (50 nm of chrome as an adhesion layer) was sputtered (everywhere on both sides of the wafer except the openings on both sides) to serve as the current collector.

The membrane electrode assembly (MEA) was directly applied on the fabricated silicon structure as shown in Figure 2. To prepare the MEA, ~28 μL of 5 wt% Nafion® ionomer 1100 EW (Solution Technology Inc.) was applied to the membrane area to fill the channels for proton conduction as well as to serve as an adhesion layer for the anode and cathode catalyst layers. The Nafion® layer was then allowed to dry. Catalyst inks were prepared by dispersing platinum black (HiSPEC 1000, Alfa Aesar) with Nafion® solution, Millipore water, and iso-propanol via sonication. Using the direct paint method, the catalyst inks were painted onto the Nafion® layer of the anode and cathode to form the membrane electrode assembly. The resulting catalyst loading was approximately 20 mg/cm<sup>2</sup>. In addition to the membrane area, a small amount of catalyst ink was painted onto the gold current collectors to provide electrical connection.

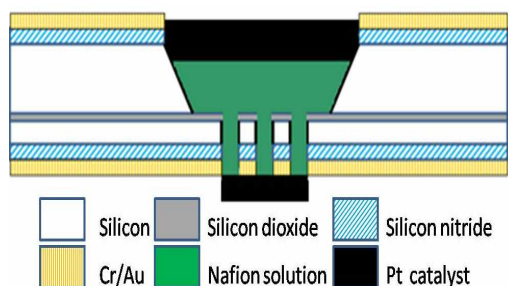


Figure 2: Schematic of Si based hybrid membrane hydrogen fuel cell.

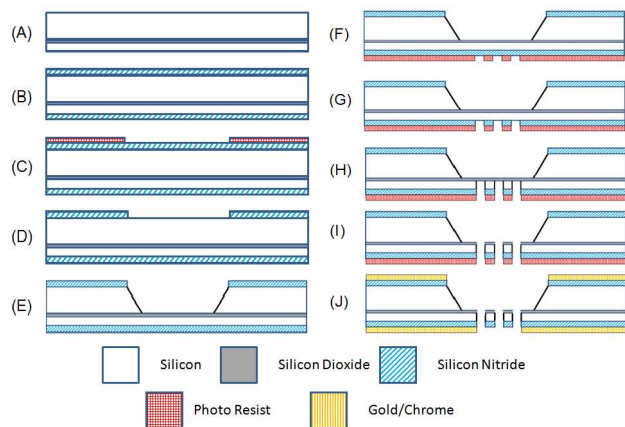


Figure 3: Microfabrication processes for silicon fuel cell dies.

As shown in Figure 1, the MEMS hydrogen generator was fabricated from three silicon wafers. The water reservoir and hydride reservoir were fabricated from 650 μm thick, double side polished prime wafers using ICP-DRIE. The hydride reservoir is 1.7 mm × 1.7 mm × 0.65 mm and the water reservoir is 1.7 mm × 1.7 mm × 0.55 mm with a 200 μm through hole at the corner. The microfluidic self-regulating mechanism was fabricated from a 100 μm thick, double side polished prime wafer. A 100 μm wide, 30 μm deep, and 11.9 mm long spiral microchannel and a 200 μm diameter hole at center end of the spiral microchannel were fabricated on this wafer using ICP-DRIE. To make the surface of water reservoir and microchannel hydrophilic, 0.5 μm of silicon dioxide was grown on the surface in an 1100°C oxidation tube furnace for 12 hr. The water reservoir was aligned and bonded to the microfluidic control layer by adhesive bonding [10] to seal the microchannel and make fluidic connection. A 50 μm thick porous hydrophobic PTFE membrane (GE Osmonics Labstore, Minnetonka, MN) was bonded to the control layer to prevent liquid water flowing into the hydride reservoir through the microchannel. Then the hydride reservoir was bonded to the stack (water reservoir and control layer) to complete the fabrication of MEMS hydrogen generator. Finally, CaH<sub>2</sub> powder (Aldrich chemical company, St. Louis, MO) was loaded into the hydride reservoir in a nitrogen glove box, then the MEMS hydrogen generator was bonded to the micro-fuel cell separated by a porous PTFE membrane. A photograph of a fabricated device using this approach is shown in Figure 4.

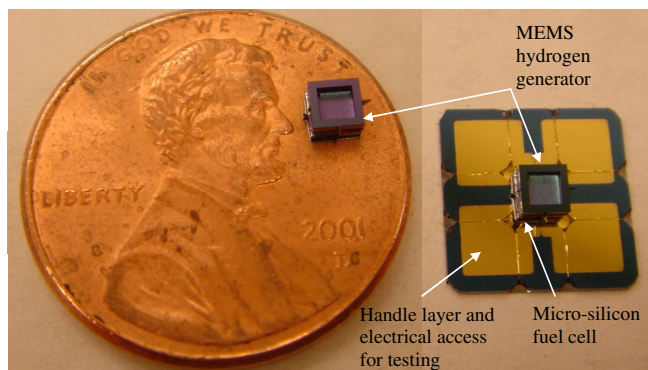


Figure 4: Pictures of the MEMS hydrogen generator and integrated micro power source with micro silicon fuel cell.

## RESULTS AND DISCUSSION

In order to compare the fuel cell performance before and after integration, the micro-silicon fuel cell was tested using a potentiostat (Solartron SI 1287, Solartron Analytical, Hampshire, UK) before integration. Dry hydrogen from hydrogen tank was passed over to the anode, and oxygen was allowed to diffuse to the cathode from ambient air. As shown in Figure 5, the fuel cell has an open cell potential of 0.98 V and a peak power density of 237 mW/cm<sup>2</sup>.

Two prototype devices were fabricated to evaluate the performance of the integrated micro-power source. A hydrogen purging system was built and the device was purged with hydrogen for three cycles to replace trapped nitrogen with hydrogen. The water reservoir was filled with Millipore water and sealed by Parafilm. The device was operated by vapor diffusion. Water flows from the water reservoir into the hydrophilic micro-channel where it contacts the porous hydrophobic membrane. Water vapor diffuses through the membrane and spontaneously reacts with

CaH<sub>2</sub> to release hydrogen ( $\text{CaH}_2 + 2\text{H}_2\text{O} \rightarrow \text{Ca(OH)}_2 + 2\text{H}_2$ ). The hydrogen then flows to the anode of the fuel cell. The cathode of the fuel cell is exposed to ambient air to breathe oxygen. The polarization curve and power density plot of one of the integrated micro-power sources are shown in Figure 6. The device has an open cell potential of 0.95 V and a peak power density of 16.8 mW/cm<sup>2</sup>. The mass transport limit was reached at 0.3 V with current density of 48 mA/cm<sup>2</sup>. Compared with the fuel cell performance before integration shown in Figure 5, the performance of the integrated device is about one order of magnitude lower. This reduction in power is because the Nafion® membrane was dehydrated by the strongly hygroscopic calcium hydride powder that is located on top of Nafion® membrane. Most of the water in Nafion® membrane from ambient air or from the cathode reaction can permeate through the membrane and react with the calcium hydride to release hydrogen. However, the proton conductivity of Nafion® is related to the water content within it [11]. Low water concentration in Nafion® can result in low fuel cell performance.

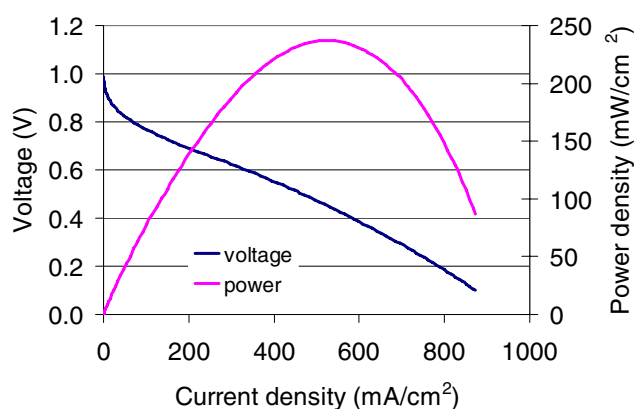


Figure 5: Polarization curve and power density plot of the micro-silicon fuel cell before integration. Hydrogen was supplied from a hydrogen tank.

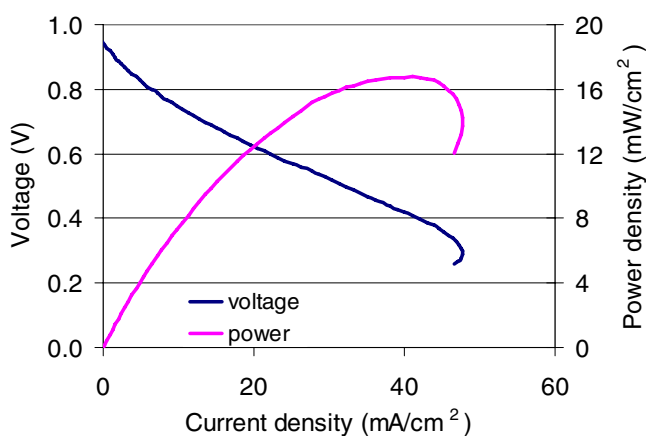


Figure 6: Polarization curve and power density plot of the integrated device. Mass transfer limit was reached at 0.3 V.

Chemical hydrides have been used to generate hydrogen for fuel cell applications for decades [12-14]. In this design, hydrogen production from CaH<sub>2</sub> is controlled by a microfluidic self-

regulating mechanism. As shown in Figure 7, water flows from water reservoir into the hydrophilic microchannel and a hydrophobic porous membrane can prevent liquid water flowing into the hydride reservoir. Instead, the water vapor diffuses into hydride reservoir through the hydrophobic porous membrane and reacts with the hydride to generate hydrogen. When hydrogen is being consumed at a low rate at the anode under a low load, the water/gas interface is forced to move back to the water reservoir. Therefore, the hydrogen generation rate decreases due to the longer water vapor diffusion length. As hydrogen is consumed by the fuel cell during periods of load, the water-gas interface self-regulates to generate only the required amount of hydrogen. However, this self-regulating mechanism has both minimum and maximum hydrogen generation rate, when the water/gas interface is at the two ends of the microchannel, respectively. The integrated device was operated at 0.8, 0.6, and 0.4 V alternatively to test the self-regulating mechanism. Figure 8 shows current density plot of the integrated device at each voltage. Although the current density can quickly change when the voltage was changed, it stabilizes in about 30 min. This data indicates that the self-regulating mechanism can regulate the hydrogen generation with the load.

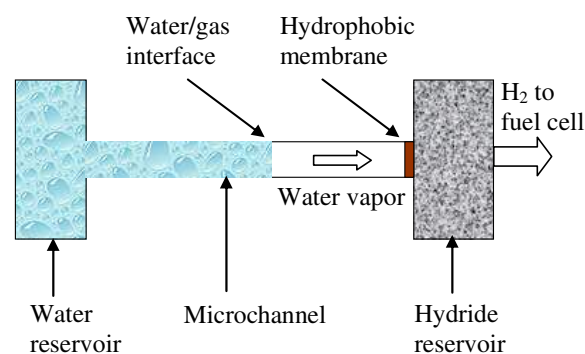


Figure 7: Schematic of the microfluidic self-regulating mechanism for controlling hydrogen generation.

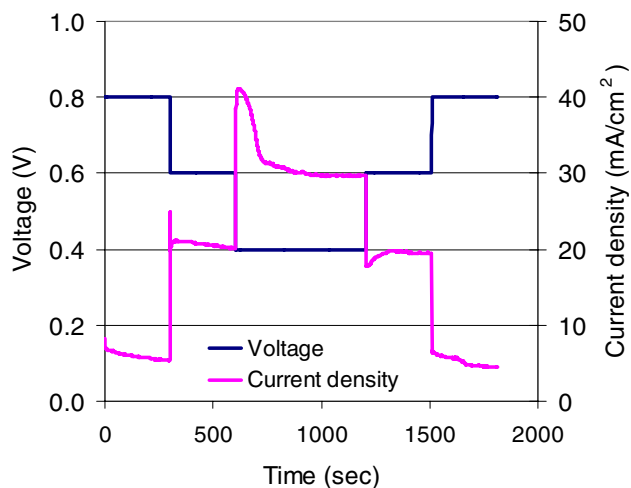


Figure 8: Current density curve of the integrated device at 0.8, 0.6, and 0.4 V alternatively. The device was operated at each voltage for 30 min.

Table 1: Summary of the testing results for two fabricated devices based on micro-silicon fuel cell and MEMS hydrogen generator.

	Device volume (mm <sup>3</sup> )	Open cell potential (V)	Energy density (Whr/L)	Maximum power density (W/L)
Device 1	10.9	0.99	61.3	15.6
Device 2	10.9	1.01	99.9	5.1

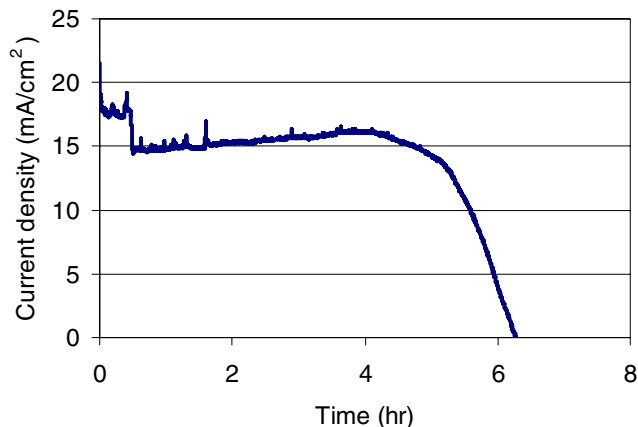


Figure 9: Life time test for the integrated micro power source. The micro fuel cell was running at constant voltage 0.6 V for more than 6 hours, and the total energy density (based on the volume of the whole device) is 61.3 Whr/L.

Life time tests were also performed at constant voltage (0.6 V) with the two fabricated devices. As shown in Figure 9, one of the devices ran at 0.6 V for more than 6 hours until the reaction was complete. Another device ran at 0.6 V with lower current density for more than 26 hours. A summary of the testing results for two devices is provided in Table 1. Device 2 showed an energy density of 100 Whr/L, which is close to the energy density of current microbatteries [1]. The energy density can be improved if the fuel volume to device volume ratio (32% for current device) and fuel utilization rate (about 35% for current device) can be increased. Device 1 has power density of 15.6 W/L, which is equal to an average power of 0.17 mW. As described previously, the micro-silicon fuel cell can provide maximum power density of 237 mW/cm<sup>2</sup> and the lower power density of the integrated device is due to the drying of the Nafion® membrane. If this problem can be solved in the future design, the integrated device has the ability to provide peak power above 1 milliwatt.

## CONCLUSIONS

A fully integrated micro-power source based on a micro-silicon fuel cell and a MEMS hydrogen generator has been demonstrated in this paper. Two integrated devices were fabricated using MEMS fabrication processes. A microfluidic self-regulating mechanism has been successfully integrated into the micro-system, and it can control the hydrogen generation with changes in the applied electrical load. The performance of the integrated device is one order of magnitude lower than the micro-silicon fuel cell before integration due to the drying out of the Nafion® membrane by the hygroscopic calcium hydride in contact with it. But one device still has energy density of 100 Whr/L, which is close to the energy density of current microbatteries. The performance is expected to be improved in future designs that mitigate the dryout of the Nafion®.

## ACKNOWLEDGEMENTS

This research is funded by the Defense Advanced Research Projects Agency (DARPA) under grant 2007-0299513-000. Any opinions, findings, and conclusions or recommendations expressed in this manuscript are those of the authors and do not necessarily reflect the views of the US Government. Micro-Nano-Mechanical Systems Cleanroom along with Micro and Nanotechnology Laboratory in University of Illinois at Urbana-Champaign provided the microfabrication facilities.

## REFERENCES

- [1] N.J. Dudney, Materials Science and Engineering B-Solid State Materials for Advanced Technology, 116 (2005), pp. 245-249.
- [2] J.B. Bates, N.J. Dudney, B. Neudecker, A. Ueda, and C.D. Evans, Solid State Ionics, 135 (2000), pp. 33-45.
- [3] P.H.L. Notten, F. Roozeboom, R.A.H. Niessen, and L. Baggetto, Advanced Materials, 19 (2007), pp. 4564-4567.
- [4] J.D. Morse, International Journal of Energy Research, 31 (2007), pp. 576-602.
- [5] K. Cowey, K.J. Green, G.O. Mepsted, and R. Reeve, Current Opinion in Solid State & Materials Science, 8 (2004), pp. 367-371.
- [6] O.J. Adlhart, P. Rohonyi, D. Modroukas, and J. Driller, Asaia J., 43 (1997), pp. 214-219.
- [7] T. Pichonat and B. Gauthier-Manuel, Fuel Cells, 6 (2006), pp. 323-325.
- [8] K.L. Chu, M.A. Shannon, and R.I. Masel, Journal of the Electrochemical Society, 153 (2006), pp. A1562-A1567.
- [9] L. Zhu, D. Kim, M.A. Shannon, and R.I. Masel, in American Chemical Society 234th National Meeting & Exposition. 2007. Boston, MA.
- [10] B.R. Flachsbarth, K. Wong, J.M. Iannacone, E.N. Abante, R.L. Vlach, P.A. Rauchfuss, P.W. Bohn, J.V. Sweedler, and M.A. Shannon, Lab on a Chip, 6 (2006), pp. 667-674.
- [11] R. O'Hayre, S.W. Cha, W. Colella, and F.B. Prinz, Fuel cell fundamentals 2006, Hoboken, NJ John Wiley & Sons.
- [12] Z.T. Xia and S.H. Chan, Journal of Power Sources, 152 (2005), pp. 46-49.
- [13] D. Linden, Handbook of Batteries and Fuel Cells. 1984, New York: McGraw-Hill Inc.
- [14] P.P. Prosini and P. Gislou, Journal of Power Sources, 161 (2006), pp. 290-293.

# MEMS MICROSHUTTER ARRAY SYSTEM FOR JAMES WEBB SPACE TELESCOPE

M.J. Li, T. Adachi, S.R. Babu, S. Bajikar, M.A. Beamesderfer, R. Bradley, N.P. Costen, K. Denis, A.J. Ewin, R. Fettig, D. Franz, L. Hess, R. Hu, K. Jackson, C.A. Jhabvala, M.D. Jhabvala, D. Kelly, T.T. King, G. Kletetschka, A.S. Kutryev, B.A. Lynch, T. Miller, S.H. Moseley, V. Mikula, B. Mott, L. Oh, J. Pontius, D. Rapchun, C. Ray, K. Ray, E. Schulte, D.S. Schwinger, P.K. Shu, R.F. Silverberg, W.W. Smith, S. Snodgrass, D. Sohl, L.M. Sparr, R. Steptoe-Jackson, V. Veronica, L.L. Wang, Y. Zheng, C. Zincke  
NASA Goddard Space Flight Center, Greenbelt MD 20771 USA

## ABSTRACT

A complex MEMS microshutter array system has been developed at NASA Goddard Space Flight Center (GSFC) for use as a multi-object aperture array for a Near-Infrared Spectrometer (NIRSpec), one of the four major instruments carried by the James Webb Space Telescope (JWST). The microshutter arrays (MSAs) are designed for the selective transmission of light (0.6 to 5  $\mu\text{m}$ ) with high efficiency (100 times over current technology) and high contrast ( $>2000$ ). The MSAs are close-packed shutters (100x200 $\mu\text{m}$  pixel size), hybridized with ASIC584 driving components, and packaged using a novel single-side indium bump bonding technology. The MSA system, a mosaic of 2x2 MSA quadrants, is operated with magnetic actuation and electrostatic latching and addressing. Complete MSA quadrant assemblies have been successfully manufactured and fully functionally tested.

## INTRODUCTION

A complex MEMS microshutter array system has been developed at NASA GSFC for use as a multi-object aperture array for a NIRSpec. The NIRSpec is one of the four major instruments carried by JWST, the next generation of space telescope after the Hubble Space Telescope retires. The MSAs are designed for the selective transmission of light with high efficiency and high contrast. It is demonstrated in Figure 1 how a MSA is used as a

multiple object selector in deep space. The MSAs empower the NIRSpec instrument simultaneously collect spectra from more than 100 targets therefore increases the instrument efficiency 100 times or more. The MSA technology is one of three major innovations on JWST and the first major MEMS devices serving observation missions in space. The NIRSpec instrument is being built-up by a collaborative effort among NASA, the European Space Agency (ESA), and the Canadian Space Agency (CSA). The JWST launching is scheduled for 2013.

## MICROSHUTTER ARRAY DESIGN

Major scientific requirements<sup>1</sup> for the MSA system include: random access addressing, -- must allow the opening of any shutter distribution and equal to or more than 100 objects simultaneously targeted; field of view, -- must cover the field of view of NIRSpec (3.4' x 3.4'); contrast, -- must have an open to closed transmission ratio of  $>2000$ ; life time, -- must operate for  $9.4 \times 10^4$  cycles with minimal failures; and operating environment, -- must operate in the JWST test and operation environments, including the entire 300K to 35K temperature range, the power dissipation of 40 mW average (at 35K), a volume fitting the envelope in NIRSpec instrument, a mass of 10 kg, and the radiation within a life dose of 48 kRad. To meet the requirements, the MSA flight concept consists of a MEMS mosaic of 2 x 2 format of four fully addressable 365 x 171 arrays fitting in the JWST optical path at the focal plane. The MSA system has

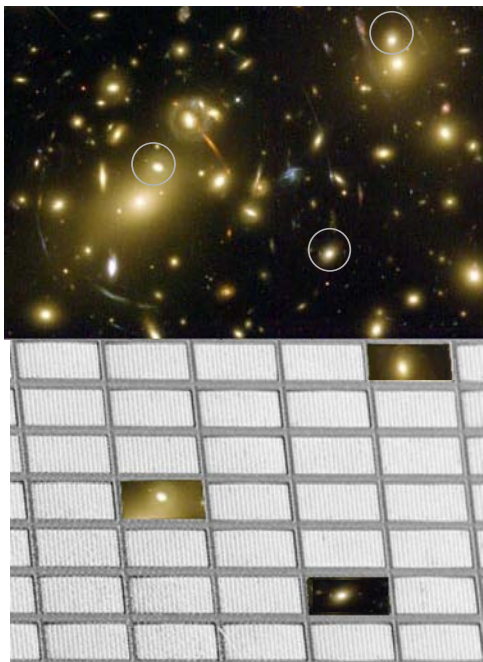


Figure 1. Demonstration of a microshutter array used as an aperture (bottom) to select multiple objects from sky (top)

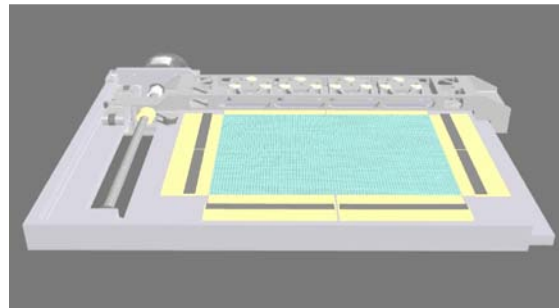


Figure 2. Schematic of an early model for demonstration of the MSA actuation mechanism. A linear magnet sweeps in y direction across the array

a mechanism of magnetic actuation and electrostatic latching and addressing<sup>1,2</sup>. Conductive thin films are tailored on the top of shutters as column electrodes and on the sidewalls in shutter frame windows as row electrodes, respectively. A linear permanent magnet aligned with the shutter rows is positioned on the top of a flipped up-side-down array, as demonstrated in Figure 2, and sweeps across the array in a direction parallel to shutter rows (moving towards readers). As the magnet sweeps across the

array, sequential rows of shutters are rotated from their natural horizontal orientation to a vertical open position, where they can be latched to the row electrodes on the sidewalls by a DC bias, typically 40 V. As the bias is removed or insufficient, shutters return to their horizontal closed position upon an elastic restoring force from a torsion flexure on the shutters (see next section).

**MICROSHUTTER ARRAY FABRICATION**

As shown in Figure 3, each MSA is fabricated out of a 4” silicon-on-insulator (SOI) wafer using MEMS bulk-micromachining technology. Individual shutters are close-packed

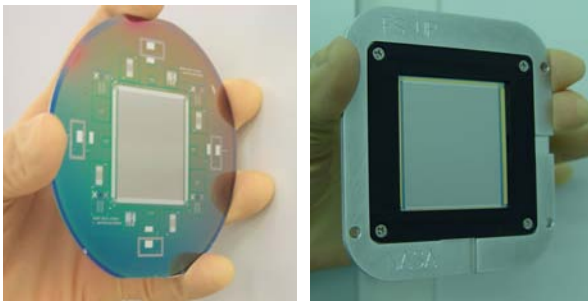


Figure 3. A flight-format 365x171 microshutter array (right) is fabricated out of a 4” SOI wafer (left)

silicon nitride membranes with a pixel size close to 100x200 μm (Figure 4). Shutters are patterned with a fine torsion flexure that connects to the frame permitting shutters to open 90 degrees with a minimized mechanical stress concentration. Silicon nitride is utilized as the shutter blades based on its excellent mechanical

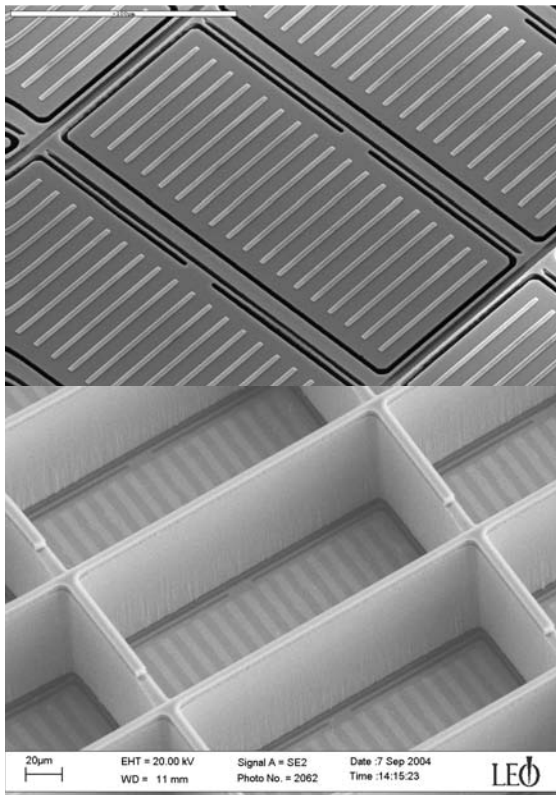


Figure 4: SEM images of the front side (top) and backside (bottom) of a 64x128 microshutter array with zoom-in images of shutter cells.

and thermal mechanical performances<sup>2</sup>. A cobalt-iron thin film processed on shutter blades functions as the magnetic element that responds to the external magnetic field for actuating shutters. The thin film is patterned into stripes so to make the magnetic domains in the film parallel to the external magnetic field as much as possible. The design helps to minimize uneven motion of shutters during actuations. In order to prevent light leak, light shields are fabricated on to the surrounding frame of each shutter to cover the gaps between the shutters and the frame, as shown in Figure 5(a). Sub-micron bumps and micro-ribs are tailored on light shields and back walls, respectively, to prevent sticktion, as shown in Figures 5(a) and (b).

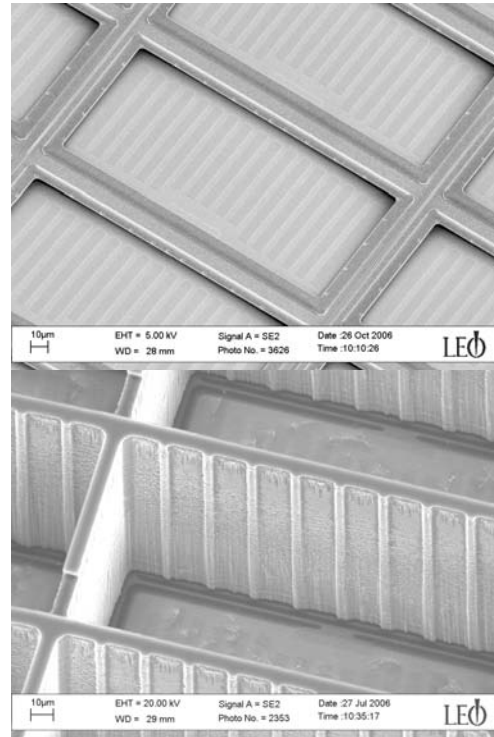


Figure 5. Light shields are patterned to cover the gaps between shutters and frame (top); sub-micron-bumps are made on light shields (top), and micron-ribs on back walls to prevent sticktion (bottom).

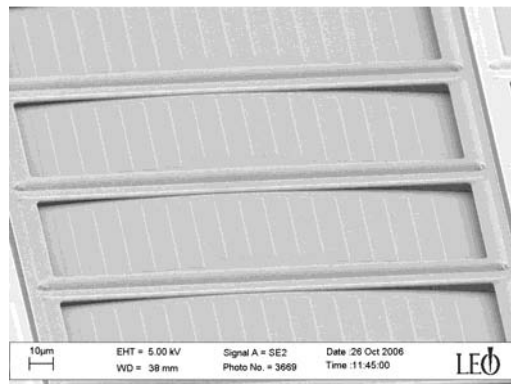


Figure 6. Shutters are slightly bowing down at room temperature and will become flat when the temperature reaches 35K

JWST instruments are required to operate at cryogenic temperatures as low as 35K, though they are to be subjected to

various levels of ground tests at room temperature. The shutters should therefore maintain nearly flat in the entire temperature range between 35K and 300K. An optically opaque and electrically conductive metal-nitride thin film is utilized as a coating material deposited on the shutters with the best thermal-expansion matching to silicon nitride -- the shutter blades themselves. A shutter image shown in Figure 6 was taken at room temperature, presenting shutters slightly bowing down as expected. Shutters become flat when the temperature decreases to 35K.

## PACKAGING

MSA substrates are made of single crystal silicon, in the thickness of 2 mm, for the best thermal match to the shutter arrays. The bonding between a MSA and a substrate is conducted using a novel single-sided indium flip-chip bonding technology<sup>3</sup>. The indium pumps function as mechanical support as well as electrical paths that connect the column electrodes on a MSA to its substrate. Indium bumps, as shown in Figure 6, are patterned on a substrate through a lift-off patterning process. There are 180,000 indium bumps for attaching a flight-format MSA array to its substrate. Single-side indium bump patterning on the substrate eliminates the risk of damaging MSAs in the lift-off process. Further advantages are no heating or under-fill required in the bonding process that minimize the thermal stress and simplify the packaging process. This bonding technology permits the flatness over the entire MSA within 1  $\mu\text{m}$ .

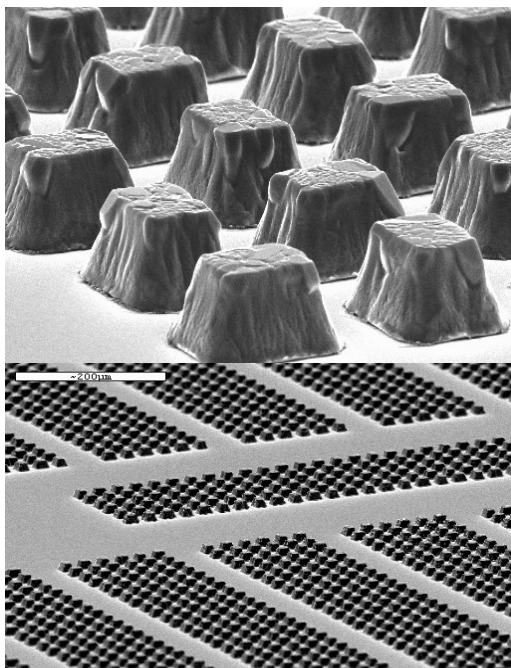


Figure 6. Indium bumps (top) are patterned on a MSA substrate (bottom) for flip-chip bonding between MSAs and their substrates

One of the four quadrants in a 2x2 mosaic MSA system is shown in Figure 7. The substrate is fully populated with 2-dimensional addressing components. Besides a MSA, each substrate houses five customer-designed ASIC (Application Specific Integrated Circuit) multiplexer/address chips, twenty capacitors, two temperature sensors, numbers of resistors and all necessary inter-

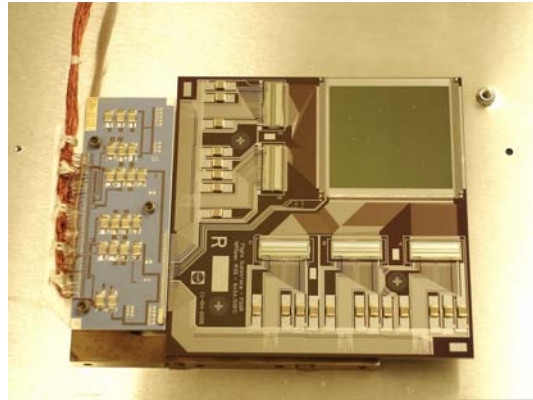


Figure 7. A MSA quadrant assembly consists of a MSA array (top right), a silicon substrate populated with ASIC 2-D addressing components, a daughter board (left), and a flexure (underneath the substrate)

connects. The substrate is electronically connected to a daughter board. Both the substrate and the daughter board are mounted on a flexure that can be seen underneath the substrate. Flexures are designed with the consideration of protecting the silicon substrates from thermal stresses introduced by CTE mismatch between the substrates and a large metal plate. The metal plate is the foundation of the MSA system, housing all four quadrants. A permanent praseodymium quadrupole magnet is designed for the actuation of all four 171x365 MSA arrays.

## QUALIFICATION TESTING

A series of qualification inspection and testing are conducted at the MSA level and the quadrant level, respectively. The qualification inspection includes the prescreening, open/close test, electrical test, and bowing test, while the qualification testing covers the 2-D addressing, life cycling, optical test, and environmental tests.

In the MSA open/close testing, two failure modes are characterized: the failed open and the failed close. The former is defined as the light leak through a supposedly closed shutter, while the latter as the light blocked by a supposedly open shutter.

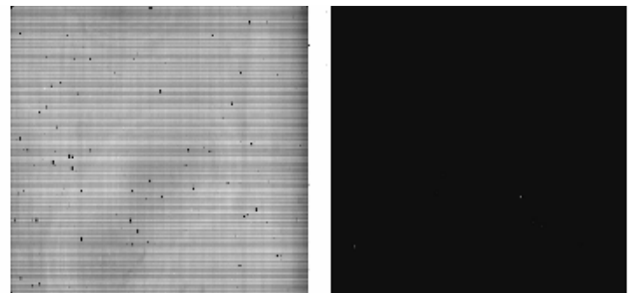


Figure 8. Images of a MSA in an open/close test. A homogenous magnetic force is applied keeping shutters open (left), and withdrawn so to release shutters to their close position (right). Shutters in failed-open/failed-close are enumerated.

In the NIRSpec instrument is required typically the failed-closed shutters < 5% and the rows with failed-open shutters < 3 % at the beginning of the life (BOL), and the failed-closed shutters < 20% and rows with failed-open shutters < 6% at the end of the life (EOL). Before a life cycling test, MSAs are exposed to a

homogenous magnetic field. Failed-closed and failed-open shutters are counted and recorded automatically. Over thousands of photos are taken from each MSA with details of individual shutters for the records at BOL that will be compared with those taken at EOL. Two images, as shown in Figure 8, present the failed-closed and failed-open shutters in a flight-format MSA (171x365 pixels) with 150 failed-closed shutters (0.2%) and 3 failed-open shutters (1.8%). Shutter bowing tests are conducted using a confocal imaging system. Shutter bowing is monitored over a temperature span typically from 300K to 35K with a resolution of 0.1um. Bowings along the short and long dimensions of shutters, as well as shutter tilting are evaluated.

The series of qualification testing are conducted at the MSA quadrant level. During the 2-D addressing test, the permanent magnet positioned on the backside of the shutter array (on the grid side) scans across the array. The scan opens shutters into the grid, column by column, to the position against back walls. The magnetic force can be adjusted by a programmed control of the distance between the shutter array and the magnet. Shutters are latched by applying voltages typically around 40V. A 2-D addressing is done by typically keeping 20 V at the selected shutters to hold them open, and turning off the bias to the rest of shutters to release them back to their closed position. The release process is synchronized with a sweep of the magnet so to gently send shutters back without impact to the light shields. Various 2-D addressing patterns are programmed into the MSAs to test functional responses of shutters. A 2-D addressing pattern with programmed “ESA” letters in a MSA is shown in Figure 9. Shutters with transmitted light (bright) were latched open, while the rest (dark) were released and kept closed.



Figure 9. A 2-D addressing pattern from a flight-format 365x171 microshutter array showing “ESA” letters

Life cycling testing is conducted in a cryogenic chamber. MSAs tested at a cycling rate of 4Hz passed 1 million cycles with minimal increase of failed open and failed closed shutters. Optical tests are performed to evaluate optical performance of MSAs, mainly the contrast. Shutter arrays fabricated with light shields are able to achieve a contrast of > 10,000 that well exceeds the NIRSpec instrument requirement of 2000. Environmental tests consist of the radiation, acoustic and vibration tests. Radiation tests are conducted to simulate effects of ionizing particle radiation in space, while the acoustic and vibration tests are to simulate the environments at the JWST launching. MSAs we fabricated passed all the qualification tests.

## CURRENT STATUS AND FUTURE WORK

Complete MSA quadrant assemblies have been successfully manufactured and fully functionally tested<sup>4</sup>. The assemblies have passed a series of critical reviews required by JWST project in satisfying all the design specifications.

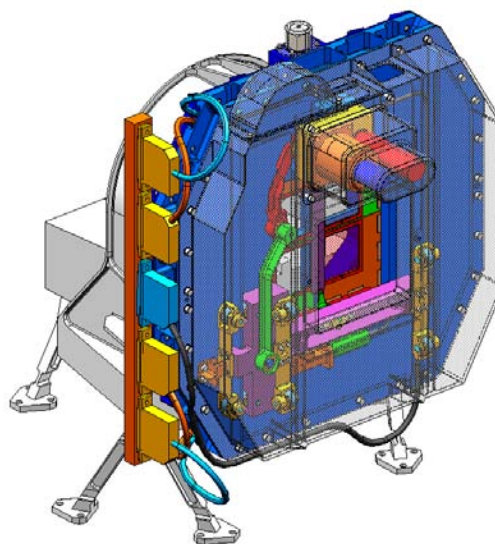


Figure 10. Final design of a microshutter array assembly with four MSA quadrants located in the center, a permanent magnet (pink) in up-down motion programmed to synchronize shutter open and close, step motors, and harnesses connected to the NIRSpec instrument

MSA teams are now making progress in final fabrication and testing the MSA system assembly (Figure 10). The delivery of flight-format MSA system is scheduled at the end of 2008 to be integrated to the focal plane of the NIRSpec detectors at ESA.

## ACKNOWLEDGEMENTS

We express our appreciation to Drs. Reza Ghodssi, Wen-Hsien Chuang and Mr. John Barry at UMPC, Dr. Shu-Fan Cheng at NRL, Mr. John Lehtonen and Ms. Katherine Mach at JHU/APL for their tremendous technical supports.

## REFERENCES

- <sup>1</sup> S. H. Moseley, et al, “Microshutter Arrays for the JWST Near-infrared Spectrometer”, Proc. SPIE Vol. 5487, pp. 645-652, Optical, Infrared, and Millimeter Space Telescopes; John C. Mather; Ed., SPIE conference “Astronomical Telescopes and Instrumentation 2004: Space Telescopes and Astronomy”, Glasgow, Scotland 2004.
- <sup>2</sup> M. Li, et al., invited paper “Microshutter Array Development for the James Webb Space Telescope”, Smart Structures, Devices, and Systems II, Proc. SPIE, **5650**, pp. 9-16, 2005.
- <sup>3</sup> Christine A. Allen, et al, “Flip Chip Integration of a Large Format Array of MOEMS Devices for Space Infrared Astronomy”, Proc. of the SMTA International Conference, Emerging Technologies Summit, 2006
- <sup>4</sup> M. Li, et al, invited paper “Complex MEMS Device: Microshutter Array System for Space Applications”, Micro (MEMS) and Nanotechnologies for Defense and Security, Proc. SPIE, **6556**, 2007.

# TUNABLE-FOCUS MICROLENSSES ACTUATED BY INFRARED-LIGHT-RESPONSIVE HYDROGELS WITH ENTRAPPED GOLD NANOPARTICLES FOR FIBER ENDOSCOPY

X. Zeng and H. Jiang

Department of Electrical & Computer Engineering, University of Wisconsin – Madison, Madison, WI, USA

## ABSTRACT

We report on liquid microlenses with tunable focal length actuated by infrared- (IR-) light-responsive hydrogel with entrapped gold nanoparticles. A curved water-oil interface forms the liquid microlens; this water-oil meniscus is pinned at a hydrophobic-hydrophilic boundary at the top edge of an aperture. IR-light responsive hydrogel microstructures are photopatterned under ultraviolet light. The volumetric change in the hydrogel, when controlled by IR-light, regulates the pressure difference across the water-oil interface, varying its curvature and the resulting focal length of the microlens. The focal length of the microlens varies from  $-17.4$  mm (slightly *divergent*) to  $-\infty$  (*flat*) and from  $+\infty$  to  $8.8$  mm (*convergent*) in 4 seconds under IR-light irradiation. The spherical aberration of the microlens is  $-0.245$   $\mu\text{m}$ .

## INTRODUCTION

Fiber endoscopes [1] are important diagnostic and surgical

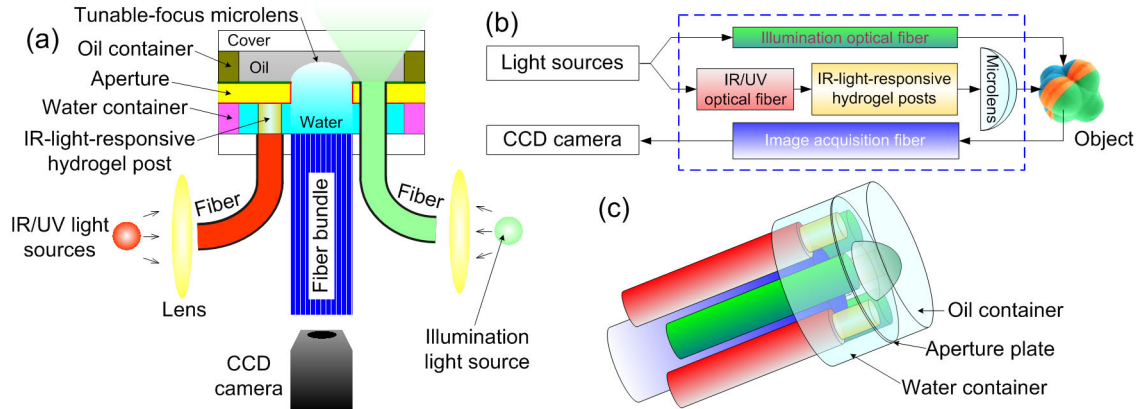


Figure 1: Schematics of potential application of IR-light-responsive tunable liquid microlenses in fiber endoscopes: (a) cross-section, (b) mechanism and (c) 3-D schematic of the distal end. The hydrogel actuators controlled by IR light tune the focal length of the liquid microlens formed by a water-oil meniscus. The hydrogel is first patterned under ultraviolet (UV) exposure, and is later controlled by IR-light, all from the same set of fibers. Another set of fibers illuminates the area of interest. Central fiber bundle guides the acquired image to image acquisition devices such as a CCD camera.

## PRINCIPLE AND STRUCTURES

Fig. 2 describes the structure and mechanism of a tunable-focus microlens. An aperture plate and water container is fabricated through liquid phase photopolymerization ( $LP^3$ ). A microlens is formed through a curved interface between water and oil. The sidewalls and bottom surfaces of the aperture are chemically treated hydrophilic, as shown in the red lines in Fig. 1(a), 2(c) and 2(d), while the top surfaces are naturally hydrophobic. Thus a water-oil meniscus is pinned at this hydrophobic-hydrophilic (H-H) boundary at the top edge of the aperture. Oil prevents the evaporation of water and serves as lens material along with water since the refractive index of oil (1.48) is larger than that of water (1.33).

Multiple IR-light-responsive hydrogel micro posts are formed in the water container to actuate the microlens under IR-light irradiation. IR-light-responsive hydrogel consists of a thermo-responsive reversible *N*-isopropylacrylamide (NIPAAm) hydrogel [3, 4] and water-soluble gold nanoparticles with distinct

tools. Current fiber endoscopes use non-tunable lenses at the distal tip for imaging; hence their operation requires constant skillful manual maneuver. Tunable-focus microlenses integrated at the end of endoscopes to scan the areas of interest with minimum movements of the scopes themselves would therefore greatly advance endoscopy.

However, current tunable microlens technologies [2] are not best suited for this purpose due to their relative large size, complicated fabrication and demanding actuation. Here, we demonstrate a relatively simple procedure to fabricate tunable microlenses. The microlenses are actuated by compact infrared- (IR-) light-responsive hydrogel microstructures with entrapped gold nanoparticles. Patterning and actuation of the hydrogel actuators (thus focal length tuning) are both realized with light, as shown in Fig. 1; hence the microlenses are intrinsically integratable with fibers optics for fiber endoscopy.

and strong optical absorption of IR-light, which has high heat efficiency [5]. With the IR-light turned on, the gold nanoparticles absorb the IR-light, generating heat to cause the hydrogel to contract. With the IR-light turned off, the heat dissipates and the hydrogel expands back to the original volume. The resultant net change between the hydrogel and water regulates the pressure difference across the water-oil interface. The curvature of the interface varies from *divergent* to *convergent* and the focal length of the microlens changes from negative to positive, as shown in Fig 2(c) and 2(d).

## FABRICATION METHODS

### Synthesis of Gold Nanoparticles

The water-soluble gold nanoparticles with thiolated ligands are synthesized using Brust method [6, 7], as shown in Fig. 3(a). First, 2.19 g of tetraoctylammonium bromide ( $[\text{CH}_3(\text{CH}_2)_7]_4\text{NBr}$ ) is dissolved in 80 mL of toluene, and 30 mL of a 30 mM aqueous hydrogen tetrachloroaurate ( $\text{HAuCl}_4$ ) solution is added. Under stirring, 100 mg of hexanethiol is added, followed by slowly adding

25 mL of 0.4 M aqueous sodium borohydride ( $\text{NaBH}_4$ ) solution. After the mixture is stirred for 1 hour, the solvent is evaporated and the organic layer is isolated. The particles are washed three times with ethanol. The gold particles are then collected and dispersed in 10 mL of dichloromethane (DCM). Next, 10 mL of 1.82-mM aqueous polyethylene glycol (PEG) solution is added for the exchange reaction. After 24 hours, DCM is removed under reduced pressure with mild heat and the particles with excessive PEG are redispersed in DCM and stirred for another 48 hours. The particles are again evaporated to dry, redispersed in deionized (DI) water, and centrifuged to remove insoluble particles. The concentration of gold nanoparticles in the solution is around 4.7 mg/mL.

Fig. 3(b) shows the scanning electron microscope (SEM) image of the synthesized gold nanoparticles coated with PEG-thiol polymer. The diameter of the gold nanoparticles is between 10 nm to 20 nm.

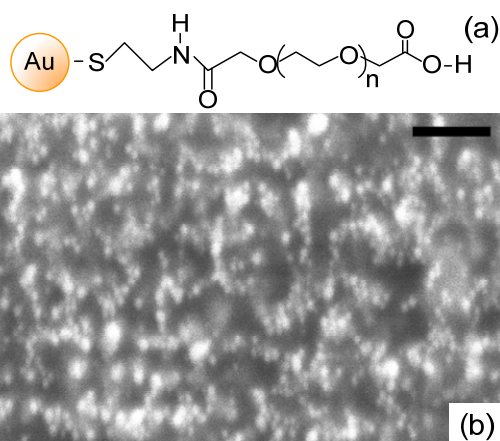


Figure 3: (a) Chemical structure of the water-soluble gold nanoparticles. (b) SEM image of the gold nanoparticles coated with PEG-thiol polymer. The scale bar represents 100 nm.

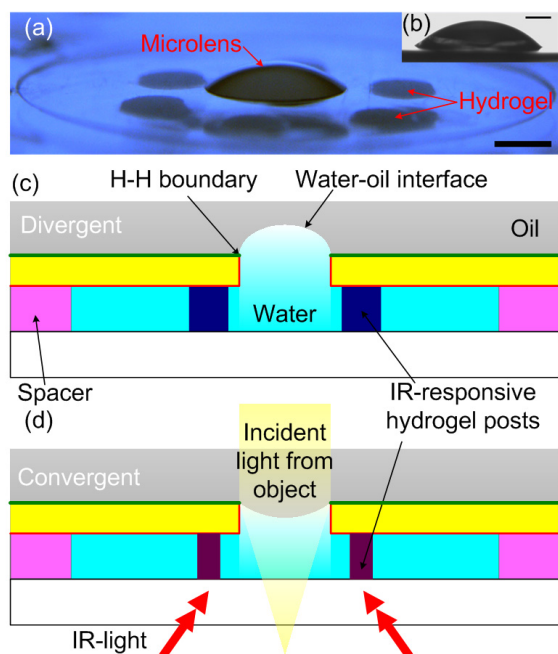


Figure 2: Structure and mechanism of an IR-light actuated tunable-focus microlens. (a) Picture of the microlens taken with a stereoscope from an oblique angle. The scale bar is 1 mm. (b) Side profile of the water meniscus of the microlens at the starting point taken with a goniometer. The scale bar is 0.5 mm. Oil is not yet added for a clearer image. (c) Divergent microlens with expanded hydrogel posts and (d) convergent microlens with contracted hydrogel posts under IR-light irradiation.

### Polymer Precursors

Two pre-polymer solutions are used in the fabrication process: isobornyl acrylate (IBA) and IR-light-responsive hydrogel [8]. IBA pre-polymer solution is used for the structural polymers, such as aperture plate and water container. Under UV radiance, IBA pre-polymer solution is polymerized, called poly-IBA.

IR-light-responsive hydrogel pre-polymer solution consists of five components: NIPAAm 0.545 g as the monomer, 0.0385 g 2,2-dimethoxy-2-phenylacetophenone (DMPA) as the co-monomer, 0.031 g  $N,N'$ -methylenebisacrylamide (NMBA) as the cross-linker, 0.75 mL dimethyl sulfoxide (DMSO) and 0.25 mL gold nanoparticles solution as the solvents. Exposure to a UV-light source causes the pre-polymer solution to harden because of the photopolymerization.

### Fabrication

Fig. 4 shows the whole process based on LP<sup>3</sup> to fabricate the microlens [8, 9]. First, a polycarbonate cartridge cavity is filled with IBA pre-polymer solution. The cartridge cavity consists of top cartridge plates and bottom liner plates. The thickness of the cavity is defined by the spacer and is 250  $\mu\text{m}$ , as shown in Fig. 4(a). The film photomask (Photomask I) is aligned on top of the cartridge to pattern the poly-IBA aperture in the cavity using LP<sup>3</sup> under UV radiance (intensity,  $I_{UV} = 8.2 \text{ mW/cm}^2$ ; time,  $t = 23 \text{ s}$ ), as shown in Fig. 4(b). The bottom liner plate is peeled off and the cartridge plate is flipped over. Next, another film mask (Photomask II) is used as the top plate and a cavity around 800  $\mu\text{m}$  thick is formed. A microchannel is formed on top of the aperture plate using the similar LP<sup>3</sup> procedure ( $I_{UV} = 8.2 \text{ mW/cm}^2$ ;  $t = 35 \text{ s}$ ), as shown in Fig. 4(c). Side walls and top surfaces of the poly-IBA plate are rendered with oxygen plasma (power supply 50 W; oxygen flow rate 20.0 sccm; gas pressure 20 mtorr; treatment time 30 s) from hydrophobic to hydrophilic, shown as red lines in Fig. 4(d), to form the H-H pinning boundaries. Then, the mask plate is peeled off and the poly-IBA plate is flipped over and bonded onto a glass slide, forming the water container, as shown in Fig. 4(e). Multiple IR-light-responsive hydrogel posts are fabricated in the water container with a photomask (intensity,  $I_{UV} = 12.5 \text{ mW/cm}^2$ ; time,  $t = 19 \text{ s}$ ), as shown in Fig. 4(f). To achieve better hydrophobicity on the top surface of the aperture plate, an octadecyltrichlorosilane (OTS) solution diluted by hexadecane (0.2% v/v) is brushed onto it, as shown in Fig. 4(g). Finally, a polydimethylsiloxane (PDMS) ring, whose surface is treated under high frequency electric field to improve adhesion, is bonded on top of the aperture plate and covered by a glass slide to form an oil container, as shown in Fig. 4(h).

## EXPERIMENTS AND RESULTS

### Spectra of Gold Nanoparticles Solution

The absorption spectrum is measured by Edmund Industrial Optics CCD Spectrometer. The scanning wavelength range is from 400 to 1100 nm. All liquid samples are measured in cuvetts with 1 mm long light-path. The hydrogel with entrapped gold nanoparticles is polymerized in a cuvet under UV radiance for 10 minutes. Fig. 5 shows the absorption spectra of the gold nanoparticle solution, the polymerized IR-light-responsive hydrogel with entrapped gold nanoparticles, DI water and the IR-light source. Gold nanoparticles in the solution and entrapped in the hydrogel have high absorption of light in the IR range.

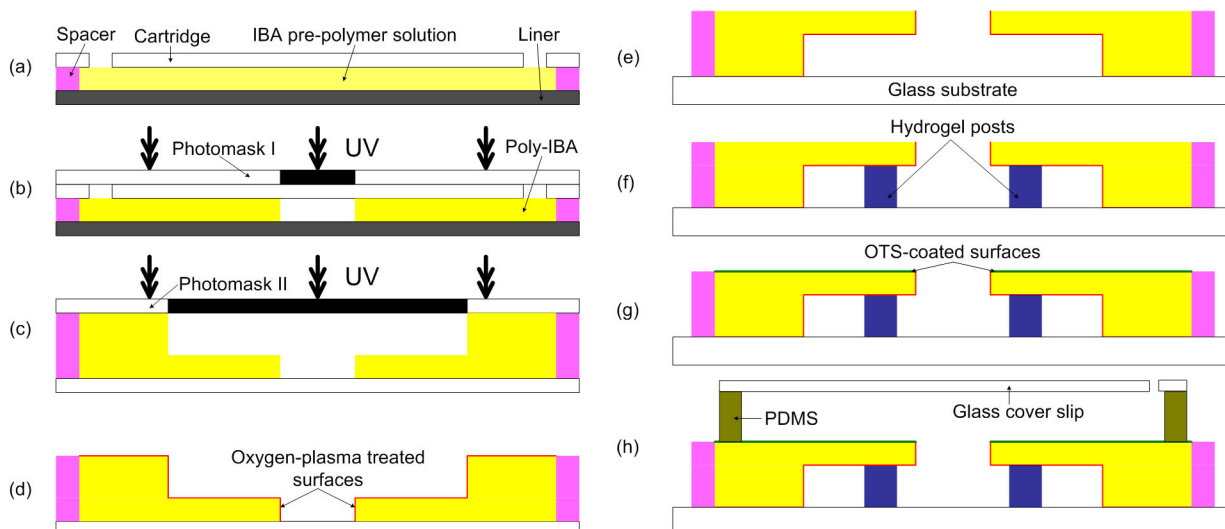


Figure 4: Fabrication process flow of an IR-light actuated tunable-focus microlens.

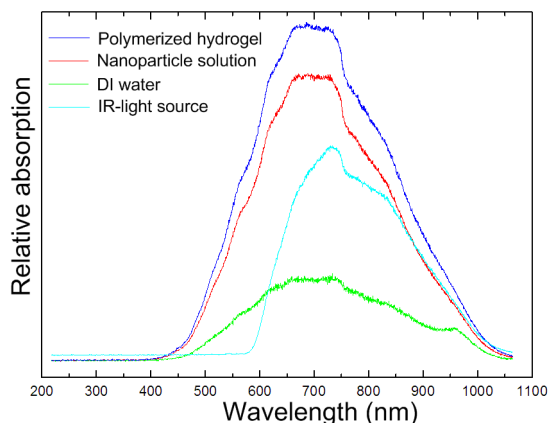


Figure 5: Absorption spectra of the gold nanoparticle solution, the polymerized IR-light-responsive hydrogel with entrapped gold nanoparticles, DI water and the IR-light source.

### Contact Angles of Surfaces

Surfaces of poly-IBA are treated by oxygen plasma and OTS. The contact angles of DI water on the surfaces of natural, oxygen-plasma treated and OTS-coated poly-IBA are measured by a goniometer and are  $105^\circ$ ,  $47^\circ$  and  $116^\circ$ , respectively. With

oxygen-plasma treatment, the surface is rendered hydrophilic; with OTS coating, the surface is more hydrophobic than untreated.

### Response Times of Hydrogel

IR-light-responsive hydrogel begins to contract when the temperature increases from lower than to above the lower critical solution temperature (LCST) of hydrogel [10]. A small amount of an ionizable monomer, 3-(methacryloylamino) propyl trimethylammonium chloride (MAPTAC) is added into IR-light-responsive hydrogel pre-polymer solution to increase the LCST of hydrogel. Two concentrations of MAPTAC are mixed into the hydrogel pre-polymer solution and the LCST shifts from  $32^\circ\text{C}$  to  $42^\circ\text{C}$  (0.15% v/v) and  $48^\circ\text{C}$  (0.30% v/v), respectively.

Fig. 6 shows the contraction and expansion time of a hydrogel posts with different concentration of MAPTAC under IR-light irradiation. The IR-light-responsive hydrogel post is polymerized in a  $250\text{-}\mu\text{m}$  thick cavity under UV radiance (intensity,  $I_{UV} = 12.5 \text{ mW/cm}^2$ ; time,  $t = 11 \text{ s}$ ). The power intensity of the IR-light source at the surface of hydrogel posts is measured by an IR sensor and to be  $1.42 \text{ W/cm}^2$ . The full contraction of IR-light-responsive hydrogel post takes about ten seconds [Fig. 6 (b)], while the full expansion takes longer time due to the reliance on heat dissipation to cool down the hydrogel [Fig. 6 (c)].

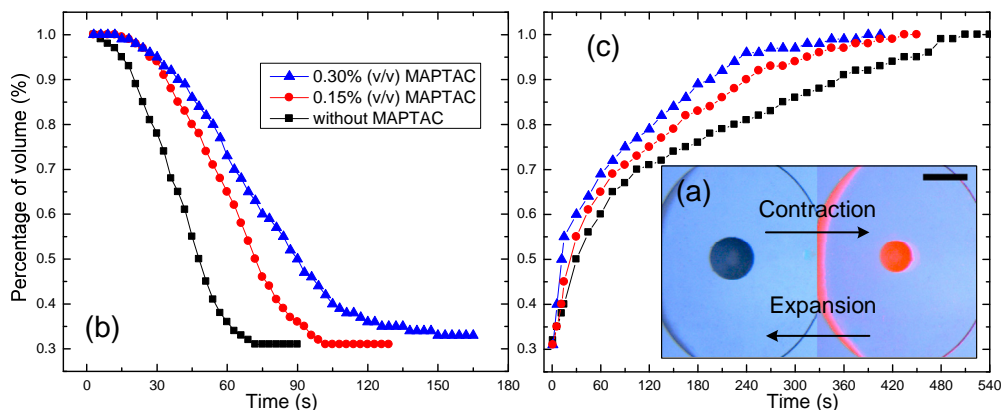


Figure 6: (a) IR-light-responsive hydrogel changes from the expanded state (left) to the contracted state (right) under IR-light irradiation. (b) Contraction and (c) expansion time of IR-light-responsive hydrogel with three different concentrations of MAPTAC.



Figure 7: Sequence of frames taken from a video demonstrates the dynamic magnification using a tunable-focus microlens. The scale bar represents 1 mm.

### Optical Properties of Tunable-Focus Microlenses

To reduce the response time of the microlens, multiple hydrogel posts are used and the volume change in each post adds up. Here, the focal length of the microlens changes from *divergent* to *convergent* in 4 seconds under IR-light irradiation.

Fig. 7 shows the image magnification using a microlens with six hydrogel posts by tuning its focal length. The observed image plate with *MNSA* logo, printed on a transparency film, is located 1.0 mm under the back side of the device substrate. A CCD-coupled stereoscope is placed above the microlens to record the video. The IR-light lamp is irradiated from an oblique angle and the power intensity at the plate of IR-responsive hydrogel posts is measured to be  $1.42 \text{ W/cm}^2$ .

Initially, the microlens is slightly *divergent* and the image is slightly reduced. At the time instant of 1.0 s, the water-oil interface becomes *flat* and the image is the same size as the object. From 1.0 s on, the microlens becomes *convergent*; thus its focal length decreases and the resultant image is gradually magnified. For the *convergent* microlens, the focal length is measured by determining optically the minimum focused point of a collimated input light beam along the optical axis. At 4.0 s, the microlens reaches its minimum focal length ( $f = 8.8 \text{ mm}$ , limited by the height of the current water container). A close-to-flat starting profile of the microlens [Fig. 1(b)] can further decrease the tuning time needed from *divergent* to *convergent*.

The spherical aberration of the microlens calculated from the profile shown in Fig. 2(b) using an optical simulation tool (Zemax) is  $-0.245 \mu\text{m}$ .

### CONCLUSION

A tunable-focus microlens driven by IR-light in seconds for fiber endoscopy is presented. A liquid microlens is formed through the water-oil interface and pinned at the H-H boundary at the top edge of the aperture. Under IR-light irradiation, the total water volume in the water container is changed by IR-light-responsive hydrogel, varying the focal length of the microlens from  $-17.4 \text{ mm}$  to  $8.8 \text{ mm}$  in 4 seconds.

In future studies, the hydrogel posts can be directly patterned and actuated by, thus self-aligned to, optical fibers; hence the demonstrated microlenses can be intrinsically integrated with fiber endoscopes. To reduce the response time of the microlens to sub-seconds, more hydrogel posts can be fabricated and different hydrogels can be used [11]. To enhance the mechanical robustness of the microlenses, more robust H-H boundaries will be investigated. The microlenses can be extended to tunable microlens arrays for larger field of view. These microlenses may also be used in other optical imaging applications.

### ACKNOWLEDGEMENTS

This work was supported by NSF (ECCS 0702095) and Wisconsin Institutes for Discovery. The authors thank Richard K. Noll for assistance in taking SEM images, Professor David Beebe for access to his facilities, Professor Franco Cerrina for access to Zemax, and Professor Leon McCaughan, Chad Staus, Chi-Wei Lo and Professor Liang Dong for their insightful discussions.

### REFERENCE

1. B. I. Hirschowitz, L. E. Curtiss, C. W. Peters, and H. M. Pollard, "Demonstration of a new gastroscope, the fiberscope", *Gastroenterology*, 35, 50, (1958).
2. H. Jiang and L. Dong, "Smart lenses", *Phys. World*, 19, 29, (2006).
3. D. J. Beebe, J. S. Moore, J. M. Bauer, Q. Yu, R. H. Liu, C. Devadoss, and B. H. Jo, "Functional hydrogel structures for autonomous flow control inside microfluidic channels", *Nature*, 404, 588, (2000).
4. L. Dong, A. K. Agarwal, D. J. Beebe, and H. Jiang, "Adaptive liquid microlenses activated by stimuli-responsive hydrogels", *Nature*, 442, 551, (2006).
5. S. R. Sershen, G. A. Mensing, M. Ng, N. J. Halas, D. J. Beebe, and J. L. West, "Independent optical control of microfluidic valves formed from optomechanically responsive nanocomposite hydrogels", *Adv. Mater.*, 17, 1366, (2005).
6. M. Brust, M. Walker, D. Bethell, D. J. Schiffrin, and R. Whyman, "Synthesis of Thiol-Derivatized Gold Nanoparticles in a 2-Phase Liquid-Liquid System", *J. Chem. Soc., Chem. Commun.*, 801, (1994).
7. A. H. Latham and M. E. Williams, "Versatile routes toward functional, water-soluble nanoparticles via trifluoroethylster-PEG-thiol ligands", *Langmuir*, 22, 4319, (2006).
8. A. K. Agarwal, S. S. Sridharamurthy, D. J. Beebe, and H. R. Jiang, "Programmable autonomous micromixers and micropumps", *J. Microelectromech. Syst.*, 14, 1409, (2005).
9. D. J. Beebe, J. S. Moore, Q. Yu, R. H. Liu, M. L. Kraft, B. H. Jo, and C. Devadoss, "Microfluidic tectonics: A comprehensive construction platform for microfluidic systems", *Proc. Nat. Acad. Sci. U.S.A.*, 97, 13488, (2000).
10. J. Wang, Z. Y. Chen, M. Mauk, K. S. Hong, M. Y. Li, S. Yang, and H. H. Bau, "Self-actuated, thermo-responsive hydrogel valves for lab on a chip", *Biomed Microdevices*, 7, 313, (2005).
11. A. Richter, D. Kuckling, S. Howitz, T. Gehring, and K. F. Arndt, "Electronically controllable microvalves based on smart hydrogels: Magnitudes and potential applications", *J. Microelectromech. Syst.*, 12, 748, (2003).

# RUGGED BOARD-TO-BOARD OPTICAL INTERCONNECT WITH CLOSED-LOOP MICROLENS SCANNER

J.B. Chou<sup>1</sup>, K. Yu<sup>1</sup>, D.A. Horsley<sup>2</sup>, S. Mathai<sup>3</sup>, B. Yoxall<sup>2</sup>, M. Tan<sup>3</sup>, S.Y. Wang<sup>3</sup>, and M.C. Wu<sup>1</sup>

<sup>1</sup>University of California, Berkeley, CA, USA

<sup>2</sup>University of California, Davis, CA, USA

<sup>3</sup>Hewlett-Packard Labs, Palo Alto, CA, USA

## ABSTRACT

This paper discusses a free-space optical interconnect system capable of dynamic closed-loop optical alignment using a microlens scanner and a proportional integral and derivative (PID) controller. Electrostatic microlens scanners based on combdrive actuators are designed, fabricated, and characterized with vertical cavity surface emitting lasers (VCSELs) for adaptive optical beam tracking in the midst of mechanical vibration noises. We demonstrate optical beam positioning noise reduction of approximately 20 dB with a 400 Hz bandwidth in the presence of up to a 3g ( $g = 9.8m/s^2$ ) vibration.

## INTRODUCTION

Optical interconnect technologies can significantly increase the chip-to-chip and board-to-board communication bandwidth, relieving the bottleneck of traditional backplane-based computer systems [1]. Especially, free-space optical interconnects using arrays of VCSELs and photo-receivers allow for cheaper, lower power, higher bandwidth, and more compact alternatives to traditional copper-based interconnects [1-4]. However, alignment between the optical source and detector is critical for optical interconnect applications, and mechanical noises due to vibration and temperature variation inside the computer systems have prevented the wide deployment of such technology.

We present an adaptive free-space optical interconnect using electrostatic microelectromechanical systems (MEMS) lens scanners with closed-loop control to circumvent such difficulties. Although various strategies to adaptively compensate for the misalignment using MEMS devices [3, 4] with feed-forward [5] and feedback control [6] have been attempted, a vibration-resistant free-space optical interconnect system with an intensity-modulated optical beam has never been fully demonstrated. Figure 1 shows the schematic view of our device correcting a misalignment  $\Delta x$  by steering the optical beam across the board-to-board gap.

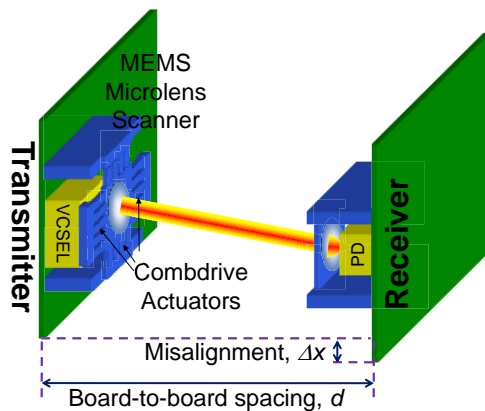


Figure 1: Schematic diagram of MEMS based free-space board-to-board optical interconnect. Although the optical transmitter and receiver are laterally misaligned by  $\Delta x$ , the MEMS microlens scanner steers the optical beam to the correct position.

## DEVICE DESIGN AND FABRICATION

The light source (VCSEL) is located near the back focal plane of the polymer microlens (focal length:  $f$ ), and the beam deflection angle due to the MEMS lens scanner is approximately given by  $(\theta_x, \theta_y) = (d_x/f, d_y/f)$ , when the microlens lateral displacement on the  $X$  and  $Y$  direction are  $d_x$  and  $d_y$ , respectively ( $f \gg d_x, d_y$ ) [3, 7]. For example, to compensate for the misalignment of  $\Delta x$  at the board-to-board spacing of  $d$ , as schematically depicted in Fig. 1, the microlens should be laterally translated by  $\Delta x f/d$  toward the photodetector (PD). Design parameters for the microlens size, displacement requirement, and footprint are summarized in Table 1.

Table 1: Design parameters for MEMS lens scanner devices.

Parameter	Value
Board-to-board spacing, $d$	2 cm
Maximum misalignment, $\Delta x_{max}$	500 $\mu m$ (one direction)
Mechanical noise bandwidth	400 Hz
Microlens scanner footprint	1.8 mm $\times$ 1.8 mm
Microlens diameter	300 $\mu m$
Combdrive gap width	3 $\mu m$
Combdrive finger length	40 $\mu m$

To compensate for the misalignment in both  $X$  and  $Y$  direction, the MEMS lens scanner should be able to steer the optical beam in two orthogonal directions. We use electrostatic combdrive actuators to laterally scan the lens [4, 7, 8], and the four operating modes (left, right, up, and down) are schematically described in Fig. 2. For this paper, however, only one-dimensional actuation (right direction in  $X$ -axis with outer combdrives as shown in Fig. 2a) is used to demonstrate vibration-resistant optical interconnect.

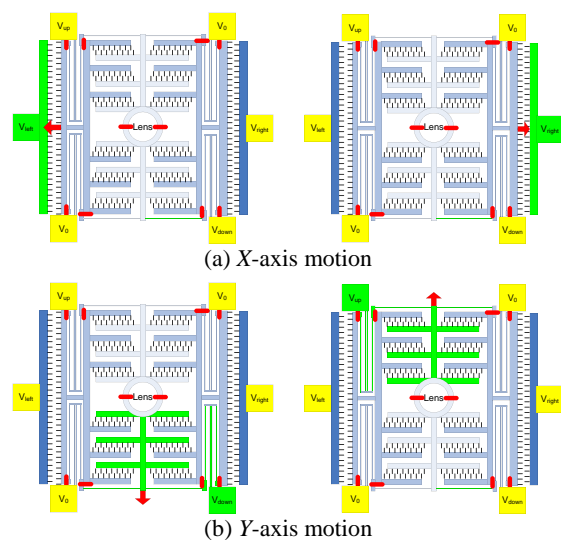


Figure 2: Scanning modes of operation for two orthogonal axes. Electrical isolation trenches are indicated by red lines.

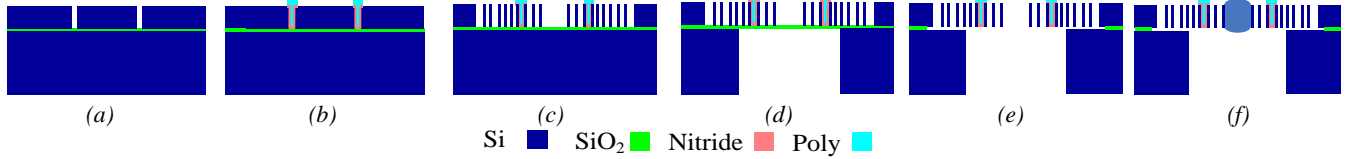


Figure 3: Fabrication process flow of two-dimensional MEMS lens scanner. (a) DRIE front side isolation trenches on 20  $\mu\text{m}$  device layer. (b) Deposit and pattern low-stress nitride and polysilicon for electrical isolation. (c) DRIE for MEMS structures, such as combdrives and springs. (d) DRIE backside through-wafer etching on 500  $\mu\text{m}$ -thick silicon substrate. (e) HF vapor for release etch on 1  $\mu\text{m}$ -thick buried oxide layer. (f) Directly apply ultraviolet-curable polymer on the lens frame, and cure for 5 minutes.

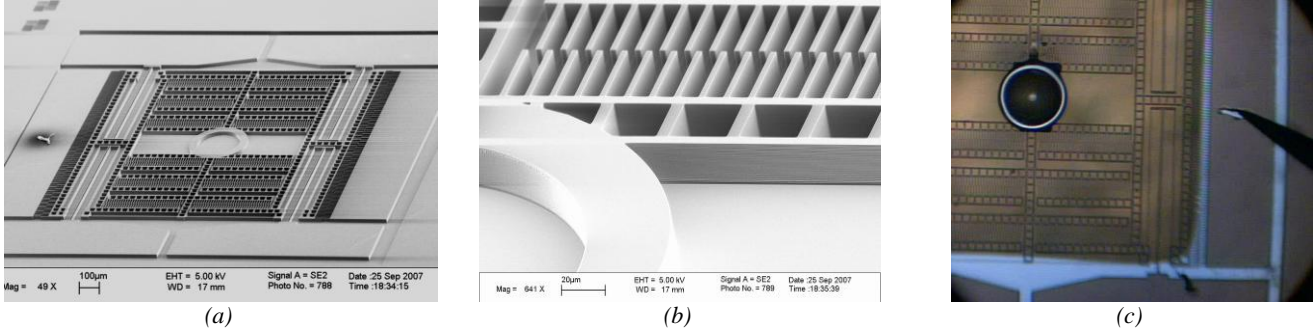


Figure 4: Scanning electron micrograph (SEM) and microscope images of the fabricated MEMS devices. (a) SEM of the entire device after front side etching (Fig. 3c). (b) Zoom in on comb structures and lens frame. The outer diameter of the lens frame is 300  $\mu\text{m}$ . (c) An optical microscope image of complete MEMS structure with polymer microlens. (The electrical isolation steps (Fig. 3a and 3b) are skipped.)

Our MEMS lens scanner is fabricated by bulk-micromachining of 6-inch silicon-on-insulator (SOI) wafer with a 20  $\mu\text{m}$  device layer. The details of our process flow and the pictures of the fabricated devices are shown in Fig. 3 and 4, respectively. A deep reactive ion etching (DRIE) process is used to define front and backside features with high aspect ratios. A backside through-wafer etch (Fig. 3d) was performed for two reasons, to create an optical path for the laser output and to eliminate undesired out-of-plane electrostatic actuation.

An ultraviolet-curable polymer lens, with a refractive index of 1.55, was used to collimate and deflect the optical beam from a directly-modulated VCSEL with the center wavelength of  $\lambda=850$  nm (Fig. 3f and 4c) [4, 8]. Assuming the beam profile evolution according to Gaussian beam theory, the beam diameter at the scanning lens is approximately given by  $2\sqrt{d\lambda/\pi}$ , if the board-to-board spacing,  $d$ , is twice the Rayleigh length of the collimated beam. The clear aperture size of the steering lens is designed to be larger than the optical beam diameter to reduce any clipping loss.

For two-dimensional actuation of the polymer lens, low stress nitride and polysilicon can be used to create plugs to electrically isolate yet mechanically couple segments of the device (Fig. 2, 3a, and 3b). The electrical isolation plug locations are indicated by short red lines in Fig. 2. Because of these electrical isolation trenches, only one device layer is required for two-dimensional lateral motion. Previous works using electrostatic actuators, such as [7], use two device layers for mechanical/electrical isolation.

## EXPERIMENTS AND RESULTS

We first measure the static and dynamic characteristics of the MEMS lens scanner device. Figure 5a shows the quadratic relationship between the laser beam deflection angle ( $\theta_x$ ) and the input voltage ( $V_x$ ). The focal length of the lens is estimated to be  $f\sim 1.3$  mm, and the optical beam position ( $d_x$ ) is measured by the PSD as shown in Fig. 6 ( $\theta_x=d_x/f$ ). The lateral microlens displacement is very small compared to the microlens diameter of

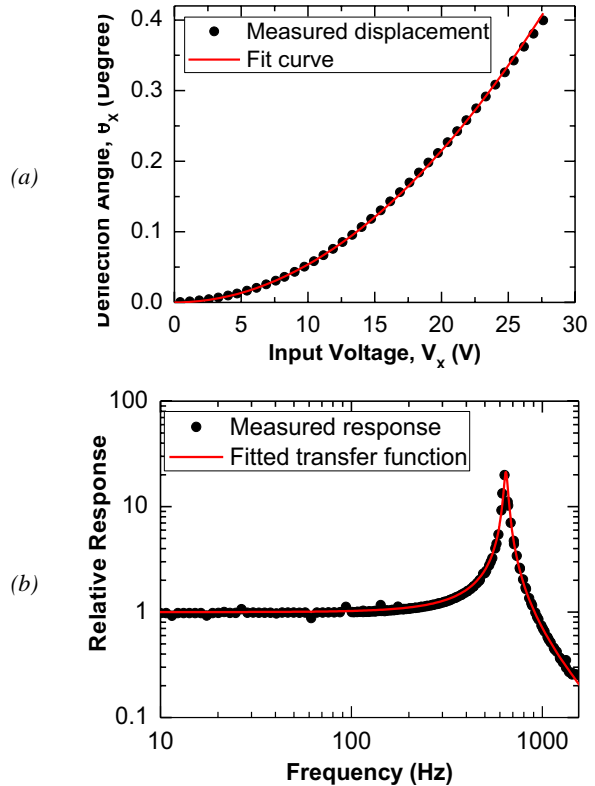


Figure 5: Static and dynamic characteristics of the MEMS lens scanner for its X-axis motion (Fig. 2a). (a) Measured and fitted optical beam deflection angle ( $\theta_x$ ) as a function of input voltage ( $V_x$ ). (b) Measured and fitted transfer functions when the input bias voltage is 22V. The output signal amplitude is normalized to the DC level.

300  $\mu\text{m}$  ( $d_x < 10 \mu\text{m}$  at  $V_x = 25 \text{ V}$ ), and, therefore, the steering angle dependant clipping loss is negligible. The maximum input voltage before the combdrive pull in effect is observed is approximately 47 V, which corresponds to a single sided maximum beam deflection of about  $1^\circ$ . The lens focal length is currently not optimized for the board-to-board spacing of 2 cm as described in Table 1, but adjusted for the distance between the transmitter and receiver in our system-level experimental setup shown in Fig. 6 (~130 mm).

The transfer function of the device at the input bias voltage of 22 V is shown in Fig. 5b, which indicates that the resonant frequency of the lowest mode (translational motion along the X-axis) is around 640 Hz. To obtain transfer function measurements, the small signal amplitude is kept small (~1 V) to prevent nonlinear effects. Under this regime, the MEMS scanner can be modeled as an underdamped second-order linear system with the natural frequency of  $f_0$ . Under this model, the fitted transfer function of the MEMS structure in Fig. 5b is given by  $F(s) = \omega_0^2 / (s^2 + 2\zeta\omega_0 s + \omega_0^2)$  where the angular natural frequency and the damping ratio are  $\omega_0 = 2\pi f_0 = 2\pi \times 644.5 \text{ Hz}$  and  $\zeta = 0.0234$ , respectively. Our computer simulations based on finite element methods confirm our measurements, and the estimated resonant frequencies of the two lowest order modes along the X and Y direction are 0.64 and 1.6 kHz, respectively, when the polymer lens mass is taken into consideration. According to the simulation results, the resonant frequencies for other higher order modes are much greater than our target mechanical bandwidth of 400 Hz as well as the resonant frequencies for the two lowest order modes. For example, the third mode is the in-plane torsional motion, and its eigen frequency is 2.6 kHz.

As described in Fig. 1 and 6, our system-level experimental setup is designed to simulate one-dimensional mechanical vibration between two computer boards and to use the MEMS lens scanner to eliminate the mechanical noise of free-space optical interconnect. Instead of vibrating the whole transmitter or receiver, we used a  $45^\circ$  turning mirror and a voice coil shaker to introduce time-varying translational offset  $\Delta x(t)$  to the optical beam position on the PSD and a high-speed photodetector. The VCSEL with the center wavelength of  $\lambda = 850 \text{ nm}$  is directly modulated at 100 Mbits/s with  $2^{23}-1$  pseudo random bit sequence using a pulse pattern generator, and the MEMS lens scanner collimates and steers the optical beam toward the PD in the receiver side. The data rate of the optical communication system is currently limited by the bandwidth of the PD and VCSEL modulation, which can be significantly improved. The bandwidth of the PSD is approximately 10 kHz, and, therefore, its output signal is almost insensitive to the high-speed intensity

modulation, and proportional to the optical beam position.

A data acquisition system obtains the optical beam position information by sampling the PSD signals at a rate of 20 kHz, and a software-based real-time PID controller calculates and generates the closed-loop feedback voltage signal to the MEMS lens scanner within a 50  $\mu\text{s}$  period. The PID controller has a transfer function of  $H(s) = sK_D + K_P + s^{-1}K_I$ , and, therefore, the cascaded transfer function of the MEMS device and the PID controller becomes

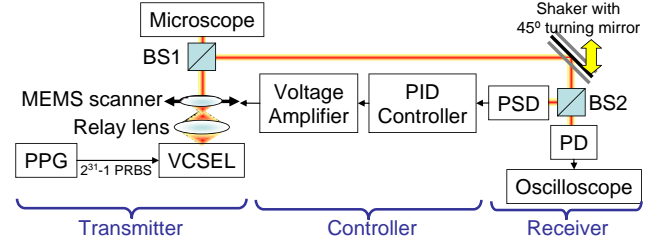


Figure 6: Schematic diagram of our experiment setup.

BS: Beam splitter. PPG: Pulse pattern generator at 100 Mbits/s. PD: high-speed photodetector with 100 MHz 3-dB bandwidth.

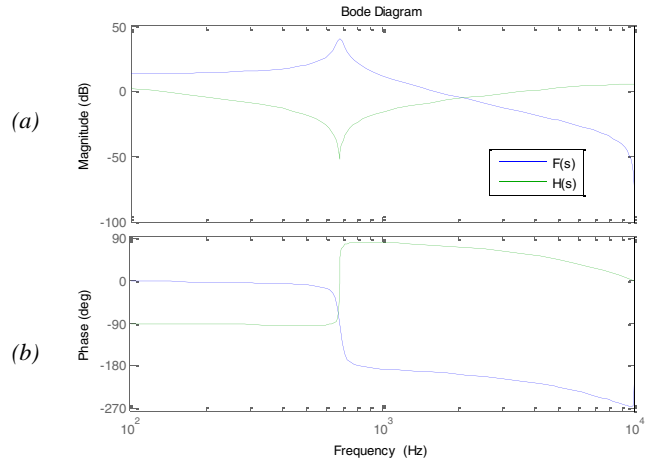


Figure 7: Simulated response curves of the PID ( $H(s)$ ) controller and MEMS device ( $F(s)$ ). (a) The magnitude of the transfer function shows the tuned PID controller zero cancels out the resonant frequency of the MEMS device. (b) The phase plot of the PID and MEMS transfer function.

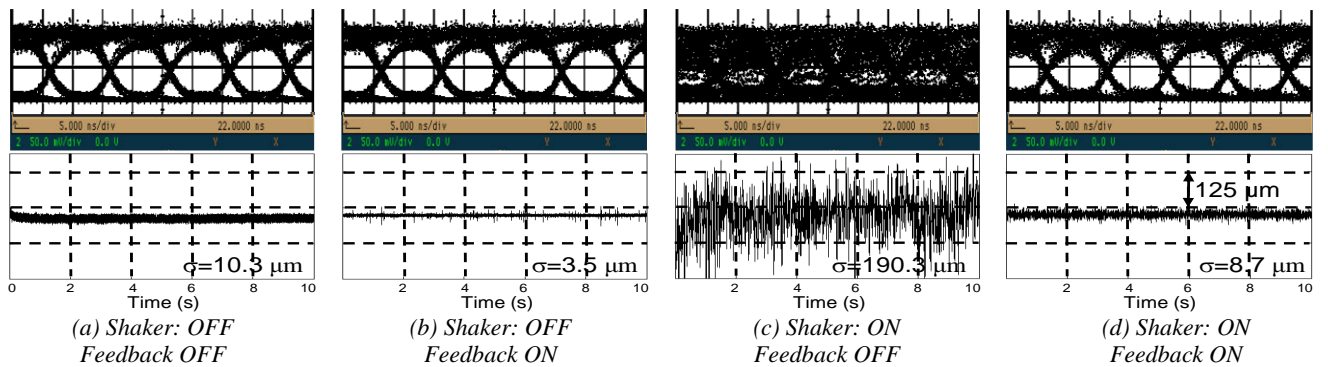


Figure 8: Measured eye diagrams (upper row) and optical beam positions (lower row) in the four different operating regimes. The optical beam position signals are measured when the VCSEL is not modulated. When the shaker is turned on and the feedback control mechanism is not used, the signal quality is severely degraded and the eye is almost closed as shown in Fig. 8c. However, the active optical tracking, with the MEMS lens scanner, can compensate for the mechanical vibration, and restores signal quality as shown in Fig. 8d.

$F(s)H(s)$ . By tuning the coefficients  $K_D$ ,  $K_P$ , and  $K_I$ , we are able to change the zeros of the PID controller in the numerator, and compensate for the underdamped response of the MEMS lens scanner [9]. In our experiment, the PID zero effectively cancels out the MEMS pole at 644 Hz as shown in Fig. 7. The coefficients used are  $K_P = 2.58 \times 10^{-3}$ ,  $K_I = 871$ , and  $K_D = 4.84 \times 10^{-5}$ , which are sensitive to VCSEL position, ambient light, and sampling frequency. Our device is demonstrated under room temperature with ambient room light fully exposing the system.

The eye diagrams and beam position signals in Fig. 8 demonstrate the improved optical communication link with the closed-loop feedback microlens scanner. With Gaussian white noise vibration with a standard deviation of  $190.3 \mu\text{m}$ , the eye diagram is severely degraded as shown in Fig. 8c. However, when the feedback controller is turned on, the standard deviation of the noise attenuates by a factor of over 20, which results in an even cleaner signal than the static case in Fig. 8a.

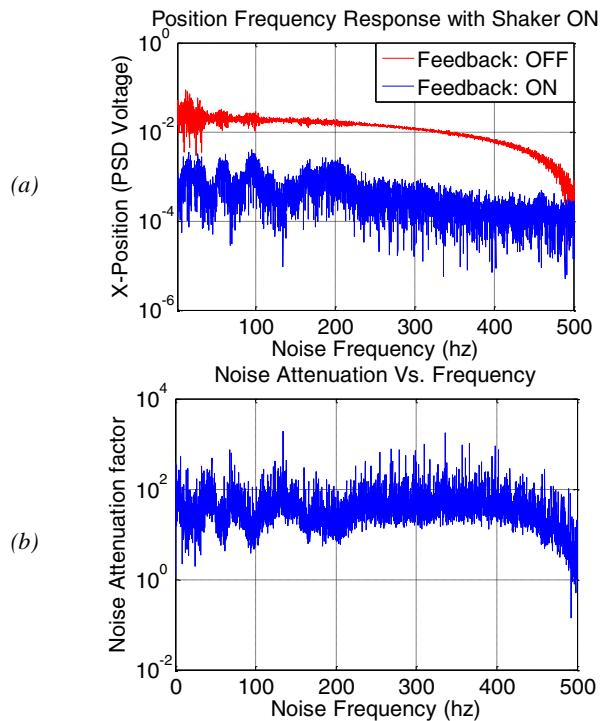


Figure 9: (a) Power spectral density of beam positioning noise when the closed-loop feedback controller is turned on and off. (b) Noise attenuation factor obtained by dividing the signal without feedback over with feedback. Noise attenuation cutoff near 400 Hz is due to the mechanical vibration bandwidth of the voice coil shaker itself.

Finally, Fig. 9 shows that the demonstrated system is capable of a noise attenuation factor of about 100 with a bandwidth of 400 Hz. We measured the optical beam position as a function of time using the PSD while the driving signal to the voice coil shaker is white Gaussian. By taking the Fourier transform of the measured PSD output, we can estimate the power spectral density of the beam positioning noise. The cutoff frequency of the noise power spectral density at  $\sim 400$  Hz when the feedback control is off is due to the maximum driving frequency of the mechanical shaker. Because of force constraints, the shaker cannot be driven much faster than the cutoff frequency, and this fact limits our ability to measure the noise power spectral density beyond the cutoff frequency. The voice coil shaker also has several resonant modes at low frequencies ( $<100$

Hz), which distorts the power spectral density curve. By comparing the noise power spectral density curves before and after the feedback controller is turned on, we can conclude that the MEMS lens scanner can suppress the beam positioning error significantly at least up to 400 Hz.

## CONCLUSION

We successfully demonstrate a one-dimensional robust optical interconnect with a closed-loop microlens scanner capable of correcting mechanical misalignment up to 100 times with a bandwidth of 400 Hz. We present eye diagrams to show the dramatic improvement of the free-space optical link quality in the midst of vibration noise with and without the feedback control activated. The MEMS scanner was designed, fabricated, and characterized with an intensity-modulated VCSEL, and has a maximum beam deflection of  $\sim 1^\circ$  with a resonant frequency of 644 Hz in the  $X$  direction. A PID controller was tuned to provide a stable feedback control for reliable optical beam tracking. Aside from optical interconnects, these types of devices can be applied to an array of optical systems, such as digital imaging, photo-lithography, and optical monitoring/tracking, that require fine position control and real-time adaptability. We believe our device can provide a compact, low cost, and low power solution to adaptive optical steering systems.

## REFERENCES

- [1] N. Savage, "Linking with Light - Having proven their worth in long-distance communications, photons will soon take over inside the computer," *IEEE Spectrum*, vol. 39, pp. 32-36, 2002.
- [2] E.M. Strzelecka, D.A. Louderback, B.J. Thibeault, G. B. Thompson, K. Bertilsson, and L. A. Coldren, "Parallel free-space optical interconnect based on arrays of vertical-cavity lasers and detectors with monolithic microlenses," *Appl. Optics*, vol. 37, pp. 2811-2821, 1998.
- [3] A. Tuantranont, V. M. Bright, J. Zhang, W. Zhang, J. A. Neff, and Y. C. Lee, "Optical beam steering using MEMS-controllable microlens array," *Sens. Actuators A: Phys.*, vol. 91, pp. 363-372, 2001.
- [4] K. Hedsten, J. Melin, J. Bengtsson, P. Modh, D. Karlen, B. Lofving, R. Nilsson, H. Rodjegard, K. Persson, P. Enoksson, F. Nikolajeff, and G. Andersson, "MEMS-based VCSEL beam steering using replicated polymer diffractive lens," *Sens. Actuators A: Phys.*, vol. 142, pp. 336-345, 2008.
- [5] V. Milanovic and K. Castelino, "Sub-100  $\mu\text{s}$  settling time and low voltage operation for gimbal-less two-axis scanner," in *Proc. the 2004 IEEE/LEOS International Conference on Optical MEMS, Takamatsu, Japan, 2004*.
- [6] J. H. Park, T. Chung, I. H. Park, J. A. Jeon, B. W. Yoo, M. Kim, and Y. K. Kim, "Fast tracking of light source with micromirror and associated feedback circuit," in *IEEE/LEOS International Conference on Optical MEMS and Nanophotonics, Taiwan, 2007*, pp. 59-60.
- [7] K. Takahashi, H. N. Kwon, M. Mita, K. Saruta, J. H. Lee, H. Fujita, and H. Toshiyoshi, "A silicon micromachined f- $\theta$  microlens scanner array by double-deck device design technique," *IEEE J. Select. Topics Quantum Electron.*, vol. 13, pp. 277-282, 2007.
- [8] S. Kwon and L. P. Lee, "Micromachined transmissive scanning confocal microscope," *Opt. Lett.*, vol. 29, pp. 706-708, 2004.
- [9] B. Borovic, A. Q. Liu, D. Popa, H. Cai, and F. L. Lewis, "Open-loop versus closed-loop control of MEMS devices: choices and issues," *J. Micromech. Microeng.*, vol. 15, pp. 1917-24, 2005.

# A CMOS MONOLITHICALLY-INTEGRATED THREE-AXIS ACCELEROMETER BASED ON THERMAL CONVECTION

Y. Cai<sup>1</sup>, M. Varghese<sup>1</sup>, A. Dribinsky<sup>1</sup>, Y. Hua<sup>1</sup>, F. Lu<sup>1</sup>, H. Gu<sup>1</sup>, M. Meng<sup>1</sup>,  
W. Zhang<sup>1</sup>, L. Jiang<sup>1</sup>, G. Pucci<sup>1</sup>, H. Liu<sup>1</sup>, A. Leung<sup>2</sup>, Y. Zhao<sup>1</sup>, G. O'Brien<sup>1</sup>

<sup>1</sup>Memsic Inc., Andover, MA, USA

<sup>2</sup>Simon Fraser University, Burnaby, BC, Canada

## ABSTRACT

We report on the design, fabrication and testing of the first low-cost CMOS monolithically-integrated three-axis accelerometer based on thermal convection. A novel single sensor element measures accelerations in all three axes. Differential temperature readout is used in the X-Y axis and pseudo-differential mode readout is used for the Z-axis. On-chip, low-noise, analog electronics are used to pre-amplify and condition sensor signals prior to on-chip digital calibration and compensation. This device has a bandwidth of 10 Hz in all three axes, noise floor of  $0.1\text{mg}/\sqrt{\text{Hz}}$  in the X-Y axis and  $1.5\text{mg}/\sqrt{\text{Hz}}$  in the Z-axis. Non-linearity in the X, Y, and Z axes is less than 5% of full scale. The 3-axis die is 30% smaller in area than our current 2-axis production die and device power remains unchanged at 6mW.

## INTRODUCTION

MEMSIC has been building two axis thermal convection based accelerometers for over ten years ([1], [2], [3]). These sensors have been demonstrated to have high reliability and ultra-low manufacturing cost. Since no proof mass is required for this sensor, the thermal bridge may be designed to have very low mass and high resonant frequency (above 50 kHz), and as a result can survive in-use shock loads above 50,000g. A die image of our two-axis sensor is shown in Figure 1.

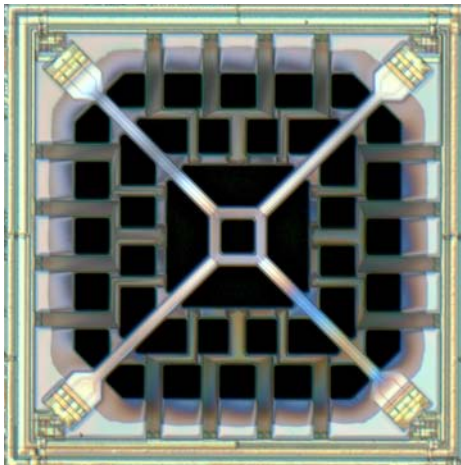


Figure 1: Photograph of a MEMSIC 2-axis sensor element. CMOS circuitry surrounds the sensor on all four sides. The sensor element is approximately 1mm by 1mm in size.

A heater in the center of the structure sets up a symmetric temperature field (Figure 2) as a result of thermal conduction, which in turn creates a gas density gradient around the structure. Any acceleration in the X-Y directions (due to gravity or otherwise) modifies convection currents around the heater that transfer thermal power in the direction of the acceleration and perturb the temperature field asymmetrically. Although these temperature changes are small at the size scales of interest they

may be measured differentially using thermopiles on either side of the heater. The convection currents are set up almost instantly with step changes in accelerations, however, the bandwidth of the sensor is limited by the time constant associated with heating or cooling the thermopile elements.

## THREE-AXIS ACCELEROMETER

Ideally, a three dimensional sensing element with thermopiles distributed above and below the heater plane could be fabricated to measure Z-axis accelerations. However, this type of structure is difficult to implement in our standard CMOS-MEMS process. An alternative implementation utilizes the asymmetry of the temperature field in the Z-direction (Figure 2) caused by the cavity below the sensor element. Any Z-axis acceleration would move the isothermal surfaces up or down and modify the common mode temperature of the X and Y thermopiles (a symmetric temperature field would produce no common mode signal). The signal must be differentiated from that due to ambient temperature changes. This is achieved using the pseudo-differential readout where a signal proportional to the ambient temperature is subtracted from the sensor common mode signal. It should be pointed out that this technique is inherently less sensitive than a true differential readout and can be more susceptible to drift errors.

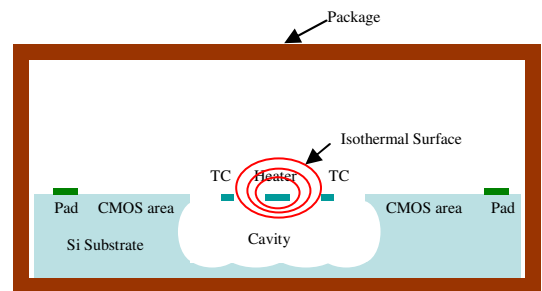


Figure 2: Cross-section view of a thermal accelerometer showing z-axis asymmetric temperature field. A cavity under the suspended heater and thermopile is formed by a combination of DRIE and isotropic etches. The cavity depth is approximately 300um. The overall power of the 3-axis device is equal to that of our 2-axis device (approximately 6mW).

The design has been implemented in a 0.25um CMOS process (Figure 3) that enables implementation of trimming and sophisticated signal processing functions to be moved to the digital domain. Examples include temperature compensation, free fall detection, I<sup>2</sup>C and SPI interfaces. Calibration data is also stored on chip using a one time programming memory (OTP).



Figure 3: Photograph of a MEMSIC 3-axis sensor element. CMOS circuitry surrounds the sensor on all four sides. The sensor element is identical in size to our 2-axis design, approximately 1mm by 1mm in size.

### EXPERIMENTAL RESULTS

The Z-axis noise spectral density in the sensor’s analog output is shown in Figure 4. X-axis and Y-axis noise is over fifteen times smaller than noise in the z-axis due to higher sensitivity in these directions and approximately equal to that in our existing 2-axis devices. Measurements were taken with an HP 3582A spectrum analyzer.

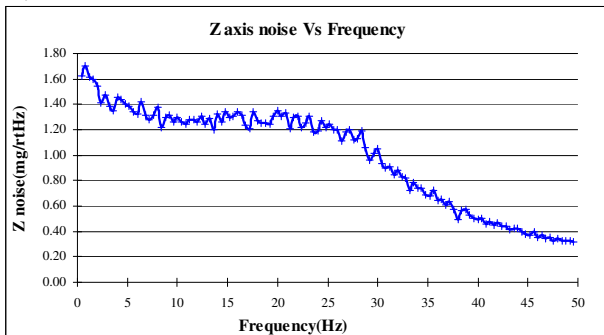


Figure 4: Noise spectral density of the Z-axis signal.

Figure 5 shows the Z-axis output measured through the digitized I<sup>2</sup>C interface. The sensor was rotated by 360 degrees around the X-axis in 6 degree increments. Linearity error was defined as the difference between the measured Z-axis signal (square dots) and a perfect sinusoid (solid line) normalized to 1g amplitude. Linearity error was less than 5% (dashed line with diamonds) after on-chip compensation.

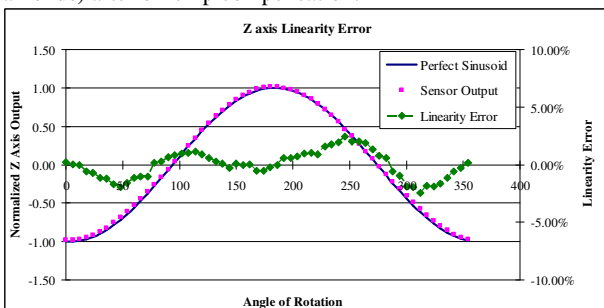


Figure 5: Z-axis linearity measurement.

Figure 6 shows data from a free fall detector that may be used in applications such as hard disk protection. The device is released at 650ms from a height of 25cm and takes approximately 230ms before hitting a table surface. Large accelerations in all three axes are observed upon impact. Free fall is detected within 40ms of release, and more than 190ms before impact for a 25cm drop. When free-fall is detected, a high interrupt signal is generated on an output pin (blue line). A second interrupt signal is observed when the device bounces and begins a second free-fall.

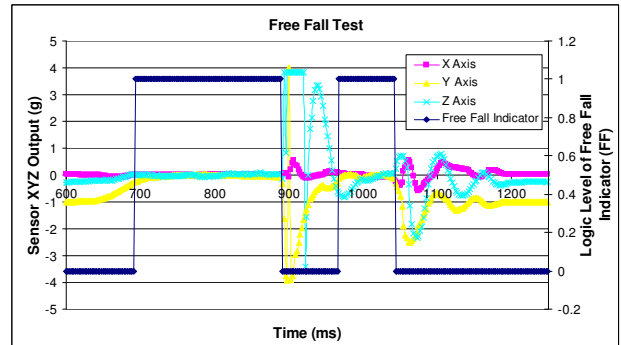


Figure 6: Free fall detection measurement.

### CONCLUSION

We have reported on the first CMOS monolithically-integrated three-axis accelerometer based on thermal convection. A novel single sensor element is used to detect accelerations in all three axes. Differential mode sensing is used for X and Y axes and a pseudo-differential mode is used for the Z-axis. The device is fabricated in a 0.25um CMOS process with on-chip amplification, digital signal processing and calibration. Total die area is reduced by 30% from our 2-axis designs while keeping overall power unchanged.

### REFERENCES

- [1] A. M. Leung, J. Jones, E. Czyzewska, J. Chen, B. Woods 1998 Micromachined accelerometer based on convection heat transfer. Proc. 11th IEEE Int. Workshop Micro Electro Mechanical Systems (MEMS '98), Heidelberg, Germany, pp. 627–630
- [2] Y. Zhao, P. Brokaw, M. E. Rebeschini, A. M. Leung, G. P. Pucci, A. Dribinsky “Thermal convection accelerometer with closed-loop heater control”, U.S. Patent 6795752, issued 2004
- [3] Y. Zhao, Y. Hua, “Method of etching a deep trench in a substrate and method of fabricating”, U.S. Patent 6712983, issued 2004

# NOVEL ELECTRODE STRUCTURE OF A MICRO FUEL CELL INTEGRATING A SERPENTINE FLOW FIELD CHANNEL

Didier Beloin St-Pierre, Mathieu Paquin, and Luc G. Fréchette

Université de Sherbrooke, Dept of Mechanical Engineering, Sherbrooke, Québec, Canada

## ABSTRACT

We demonstrated a fully-micromachined polymer electrolyte membrane fuel cell ( $\mu$ PEMFC) configuration that integrates the flow field with novel electrode structures done within a simple two-mask process. The silicon-based electrodes are designed to maximize platinum utilisation and are located within a serpentine flow channel for stable operation. This complements other work on  $\mu$ PEMFC that has focused mostly on microfabricated flow fields and membranes, but less on novel electrode structures and their integration.

## INTRODUCTION

Most of the conventional PEMFC electrodes are composed of Nafion® as the proton conductor, platinum as the catalyst, and carbon particles as the electric conductor. Mixed together, they create porous electrodes with ad-hoc tri-contacts sites in which the hydrogen and oxygen gas will diffuse. A tri-contact is a catalytic site where ions, molecules, and electrons are joined through respective conducting paths for the chemical reaction. The small scale of these reaction sites represents a good opportunity for microfabrication to optimise performances and ensure access to all tri-contacts sites. Microfabrication of the electrode structure has been studied by others [1, 2], although with less consideration of the ionic transport within the electrodes. MEMS research has also shown to be beneficial for the implementation of flow channels, gas diffusion layers (GDL) and the electrolyte membrane of micro-PEMFC [3, 4].

In this work, we replace the ill-defined tri-contacts found in porous media with well defined catalytic sites and conduction paths implemented using microfabrication techniques. In our previous work, we designed a microfabricated electrode structure to optimize the use of expensive platinum catalyst [5]. Here, we integrated the electrodes structure within a microchannel flow field (Fig. 1), microfabricated the devices and successfully demonstrated their operation and the high usage of platinum area.

## DESIGN AND FABRICATION

Two main aspects are novel in the micro-PEMFC presented here: the approach to integrate the electrodes within the flow channels and the electrode microstructure formed by DRIE and capillary wicking of a liquid polymer electrolyte. The process is shown in Fig. 2.

In opposition to conventional PEMFC for which flow field channels are placed on the surface of a gas diffusion layer over the electrodes, here the electrodes are integrated within the serpentine flow channel. This configuration, shown in Fig. 1, leads to a simple two-mask process where column-shaped electrodes are formed simultaneously with the flow channel, using DRIE (Fig. 3).

The electrodes themselves are formed of highly doped silicon columns coated sequentially with a sputtered Pt layer and a film of polymer electrolyte (Nafion®). The electrolyte on the columns serves as the ionic conductor and is expected to be a major resistance for this configuration [5]. To alleviate this limitation, we gather columns into packs of four such that small gaps between them will increase capillary pressure and tend to improve wicking of a solution of Nafion® into the electrode structure (Fig. 3). This aims to allow better ionic conduction channels by having more Nafion® between the columns without blocking the gas flow. The process consists of soaking a Nafion® membrane into a solution of Nafion® at 5% (Liquion®), then pressing it between two microfabricated electrodes to allow capillary forces to draw the solution into the column matrix. The device was then hot-pressed to bond and

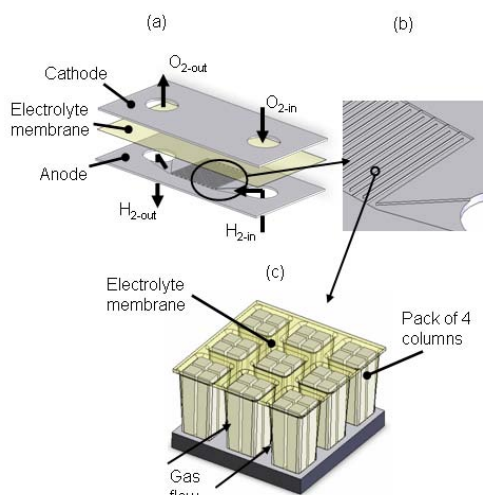


Figure 1: Configuration of the column matrix electrode structure with serpentine flow field. (a) Exploded view of the fuel cell showing the gas holes and gas flow path for  $O_2$  and  $H_2$  through the anode and the cathode. (b) Zoom on the serpentine flow field. Dimensions of the channel are  $60 \mu\text{m}$  deep by  $400 \mu\text{m}$  wide with  $20 \mu\text{m}$  thick walls. (c) Zoom on the columnar electrode structure in the serpentine channel. Columns are gathered in packs of four to ease wicking of Nafion® through capillary forces. Dimensions of the columns are  $6 \mu\text{m} \times 6 \mu\text{m} \times 60 \mu\text{m}$ . Separation between packs of 4 columns is  $6 \mu\text{m}$  and separation between adjacent columns is  $2 \mu\text{m}$ .

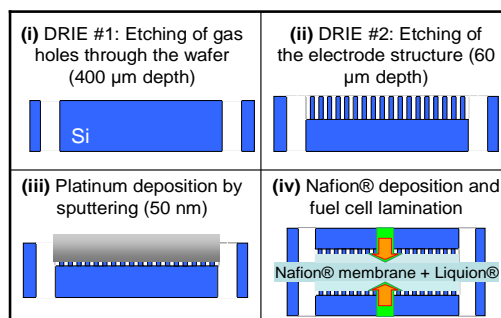


Figure 2: Cross-section view of the device showing the main steps involved in the fabrication. (i) Large gas holes are etched through the wafer by deep reactive ion etching (DRIE). (ii) A second DRIE step generates the column matrix and the serpentine flow field channel simultaneously. (iii) Platinum is sputtered over the column matrix structure. (iv) Solution of Nafion® (Liquion®) is deposited by capillary force on the column matrix and a membrane is hot pressed between two microfabricated electrodes.

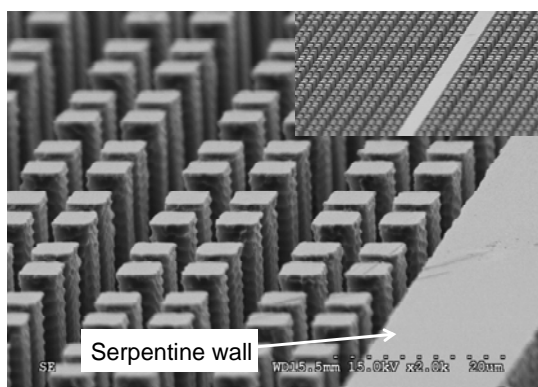


Figure 3: SEM image of the columns matrix electrode and the serpentine flow field formed by DRIE. Each electrode of 1 cm<sup>2</sup> has a serpentine channel of 240 mm length and approximately 960,000 columns.

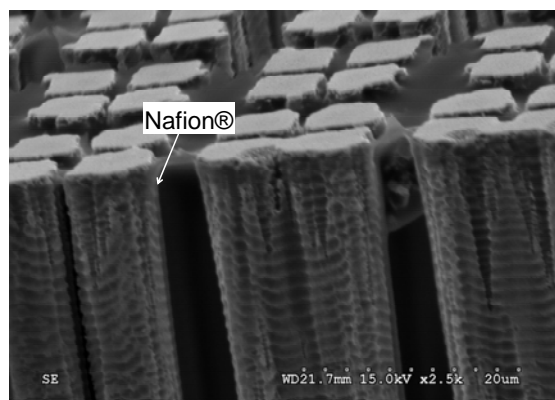


Figure 4: SEM image of the Liquion® deposition by capillary force on the column matrix structure after peeling off the Nafion® membrane for imaging. Nafion® appears to fill the smallest gaps between columns, but also some of the largest gaps, so further process improvement is required and higher levels of performance should be achievable.

seal the parts together at 6 psi and 100°C for 15 minutes and at 50°C for 30 minutes. Figure 4 shows the Nafion® coating on the columns.

## EXPERIMENTAL RESULTS

A first configuration, consisting of a simple matrix of equally spaced columns, showed unstable performance, probably due to water management problems that also brought bad ionic conduction. Transient performance up to 37.4 mW/cm<sup>2</sup> and 123 mA/cm<sup>2</sup> was however achieved. The second configuration, with the serpentine channel and improved capillary wicking discussed above, showed stable and repeatable operation (Fig. 5), achieving a maximum power density of 13.5 mW/cm<sup>2</sup>. The serpentine configuration was found to greatly improve the stability in operation, probably due to better gas flow control compared to a simple matrix of columns without the serpentine channel. When considering the power per unit area of platinum, we achieved up to 3.4 mW/cm<sup>2</sup> of Pt for the first device, which is slightly greater than conventional porous electrodes with 3.2 mW/cm<sup>2</sup> of Pt [6]. It should be noted that power per unit mass of Pt is however less interesting since a relatively thick layer of catalyst was applied; alternate nanocoatings of Pt should be considered instead of sputtering.

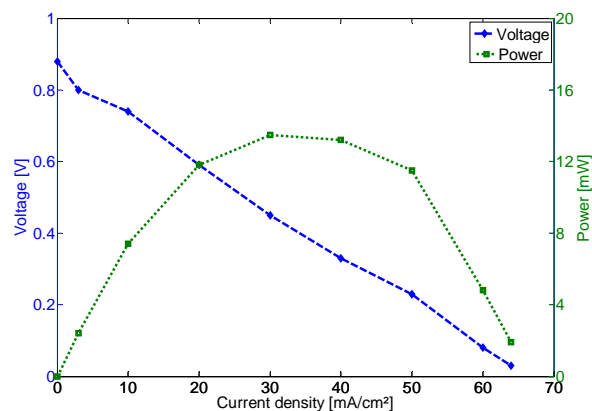


Figure 5: Experimental results showing polarisation and power curves for a device. Operating conditions: anode: 15 sccm of humidify hydrogen at 55°C with a back pressure of 9 psi, cathode: 20 sccm of humidify oxygen at 55°C with a back pressure of 8 psi, cell temperature of 30°C. Linear polarisation curve suggests that mass transport problems are not the limiting problem and that electric or ionic resistance is the limiting parameter.

## CONCLUSION

The simple fabrication process, the ability to tailor the electrode microstructures, the high Pt utilisation, and the interesting power levels achieved make this design promising and interesting for future research and applications in portable power generation. Future work should be done on Nafion® deposition to improve ionic conduction and minimise water management problems. This should reduce voltage loss in the fuel cell which is the biggest problem for the device at this point. Alternate deposition methods of the catalyst layers should also be considered.

## REFERENCES

- [1] W.Y. Sim, G.Y. Kim, S.S. Yang, "Fabrication of micro power source (MPS) using a micro direct methanol fuel cell ( $\mu$ DMFC) for the medical application", Technical Digest of the 14th IEEE International Conference on MEMS, Interlaken, Switzerland, pp.341-344 (2001)
- [2] J. Yeom, G.Z. Mozsgai, B.R. Flachsbar, et al., "Microfabrication and characterization of a silicon-based millimeter scale, PEM fuel cell operating with hydrogen, methanol, or formic acid", Sensors and Actuators B, 107, pp. 882–891 (2005)
- [3] T. Pichonat, B. Gauthier-Manuel, "Recent developments in MEMS-based miniature fuel cells", Microsyst Technol, 13, pp.1671-1678 (2007)
- [4] G.J. La O, H. Jin In, E. Crumlin et al., "Recent advances in microdevices for electrochemical energy conversion and storage", International Journal of energy Research, 31, pp. 548-575 (2007)
- [5] D.B. St-Pierre, M. Paquin, L.G. Fréchette, "Design and Microfabrication of a PEM Fuel Cell with Silicon-Supported Electrodes in a Column Matrix Configuration", Technical Digest of the 2006 International Workshop on Micro and Nanotechnology for Power Generation and Energy Conversion Applications, Berkeley, U.S.A., pp. 93-96 (2006)
- [6] H.A. Gasteiger, S.S. Kocha, B. Sompalli, et al., "Activity benchmarks and requirements for Pt, Pt-alloy, and non-Pt oxygen reduction catalysts for PEMFCs", Applied Catalysis B: Environmental, 56, pp.9-35 (2004)

# FEASIBILITY TEST OF A FAST MICRO GAS CHROMATOGRAPHY SYSTEM USING FIVE MICROVALVES AND A MICROCOLUMN

Byunghoon Bae<sup>1,2</sup>, Adarsh D. Radadia<sup>2</sup>, Jaehyeong Han<sup>3</sup>, Junghoon Yeom<sup>3</sup>, Richard I. Masel<sup>1,2</sup>, and Mark A. Shannon<sup>1,3</sup>

<sup>1</sup>Cbana Laboratories, Inc., Champaign, IL 61820

<sup>2</sup>Department of Chemical and Biomolecular Engineering, University of Illinois, Urbana, IL 61801

<sup>3</sup>Department of Mechanical Science and Engineering, University of Illinois, Urbana, IL, 61801

## ABSTRACT

We present a new type of a fast MEMS Gas Chromatography (GC) system that integrates five microvalves and microcolumn for rapid detection of species for a flame ionization detector (FID). The integrated GC samples mixed-gas species, preconcentrates them, and injects a sharp band into the microcolumn with 50  $\mu$ s pulse width. The microcolumn can then separate and detect 8 components in the species within 10 seconds with 25 psi of the carrier gas. The fast speed of this GC is enabled by microsecond switching microvalve, low dispersion design, and a new coating technique on the microcolumn.

## INTRODUCTION

Many efforts have been made to build fast and portable micro-GC systems for various applications. Homeland security and many on-site industrial applications need fully integrated micro-GC systems with injector microvalves, preconcentrator (PC), microcolumn, detector, and a micropump for sampling. However, no fully integrated system has been developed yet. MEMS PCs including [1] have been published but without integration of other components. A micropump-driven GC system was developed by Kim *et al.* [2], but their system still employs a separate injection system, lowering GC speed and resolution. Microvalves integrated with a PC was reported by Bae *et al.* [3].

In this paper, we present a new type of a fast MEMS GC system that integrates five microvalves and microcolumn for rapid detection of species for an FID.

## SYSTEM CONFIGURATION

Figure 1 shows a schematic diagram and device pictures of five microvalves and a microcolumn. Figure 2 shows photographs of all

the layers of the microvalves and how they are stacked. To achieve fast operation, the five microvalves employs electrostatic actuation, and each valve can switch states in 50 microseconds [4]. The five integrated microvalves consist of two microvalves to load the sample gas, and three microvalves to route and inject the sweep gas through a one- $\mu$ L chamber to the microcolumn that is designed for low dispersion and has a new deactivation method applied. The microcolumn has 34 cm-long serpentine channels whose cross-section is 100 x 100  $\mu$ m<sup>2</sup> with a design generates the lower dispersion than spiral [5]. The integrated GC samples mixed-gas species, preconcentrates them, and injects a sharp band into the microcolumn with 50  $\mu$ s pulse width. The microcolumn can then separate and detect 8 components in the species within 10 seconds with 25 psi of the carrier gas. The fast speed of this GC is enabled by MEMS sizing and fabrication, microsecond switching microvalve, low dispersion design, and a new coating technique on the microcolumn, which enables the detection of poisonous gases, toxic industrial compounds, and other volatile compounds to be separated in seconds, rather than tens of minutes with conventional GC systems.

## RESULTS

Figure 3 shows a separation of 8 chemical components using a standalone microcolumn with 25 psi H<sub>2</sub> carrier gas and temperature setting of 90~98°C. As an injected plug moves down the column, the plug experiences broadening due to diffusion, velocity-induced shearing, and smearing at bends. Figure 4 shows toluene peaks through the same microcolumn as the one used in the previous experiment. Toluene vapor is sampled at ambient temperature and injected every 10 seconds by the microvalves following the sequence in Fig. 1a to the microcolumn. The H<sub>2</sub> sweep gas is 3 psi,

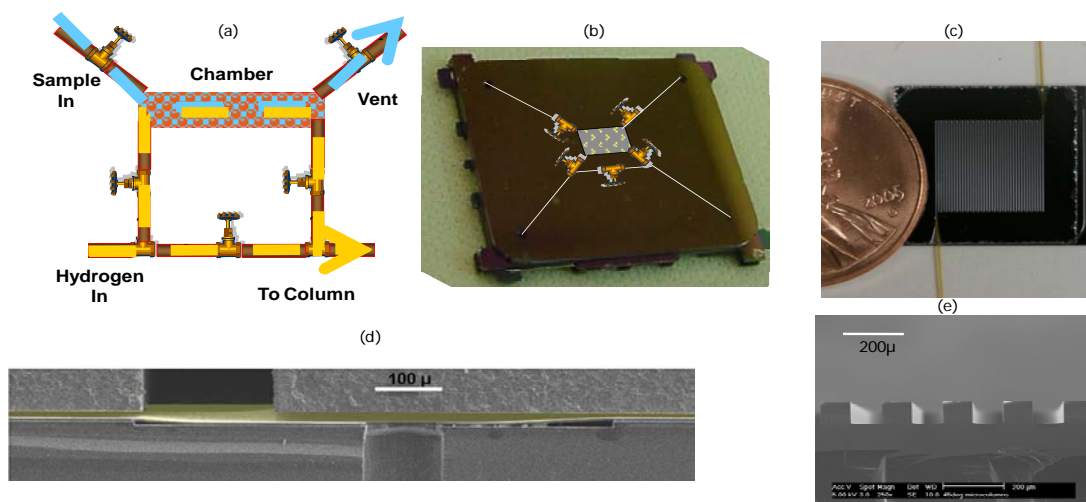


Figure 1: (a) A schematic diagram shows how all the five valves are used for sampling gas (blue line) and for sweeping the sample through to the column with H<sub>2</sub> (yellow line); device pictures of (b) five microvalves and (c) microcolumn; and SEM images of the cross-sections of (d) a microvalve and (e) the microcolumns.

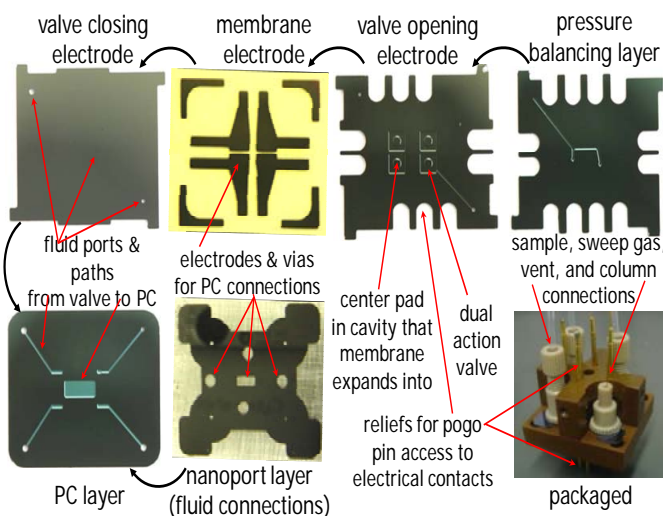


Figure 2: Photos of all the layers of the microvalves and how they are stacked.

which is more than 8 times less than the pressure used for the standalone column in Fig. 3. Figure 4 (b) shows that the 100 ms width peaks are as sharp as and slightly faster than the peak from the standalone microcolumn. This result is attributed to the microsecond switching performance of the microvalves in addition to the design of the low dispersion microcolumn. To integrate the five microvalves and microcolumn, a connecting layer was fabricated that not only connects the five microvalves to the microcolumn, but also has inlet and outlet fluidic ports where Nanoports<sup>®</sup> are used as shown in Fig. 5.

## CONCLUSIONS

The feasibility of a micro-GC system that uses five fast-acting microvalves and a microcolumn has been shown through

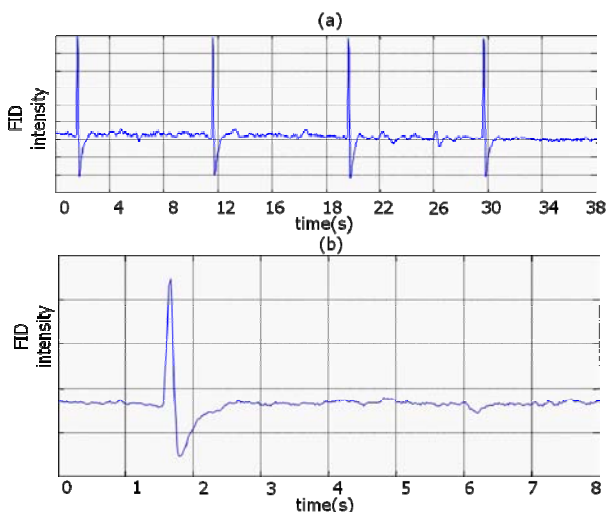


Figure 4: Toluene peaks through the same microcolumn as the one used in the previous experiment. (a) Toluene vapor at ambient temperature being sampled and injected every 10 second by five microvalves to the microcolumn via a capillary, with  $H_2$  carrier gas at 3 psi, which is more than 8 times less than the pressure used for the standalone column. (b) The 100 ms width peaks are as sharp as and slightly faster than the peak from the standalone microcolumn. This result is attributed to microsecond switching performance of the microvalves in addition to the design of the low dispersion microcolumn.

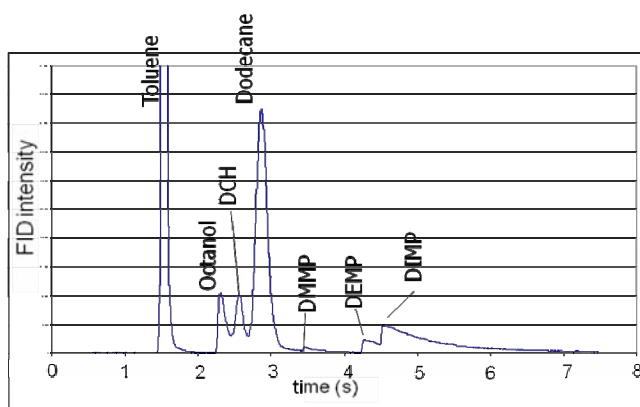


Figure 3: A separation of 8 chemical components using a standalone microcolumn with 25 psi  $H_2$  carrier gas at a temperature between 90–98°C. As an injected plug moves down the column, the plug experiences broadening due to diffusion, velocity-induced shearing, and smearing at bends.

simple testing. The peak width will be even sharper by removing a dead volume between components that increases band broadening, allowing higher pressures to be used, and thereby reducing analysis time further.

## ACKNOWLEDGEMENTS

We gratefully acknowledge financial support from the Defense Advanced Research Projects Agency (DARPA) under U.S. Air Force grant FA8650-04-1-7121. Any opinions, findings, and conclusions or recommendations expressed in this manuscript are those of the authors and do not necessarily reflect the views of the Defense Advanced Projects Research Agency or the U.S. Air Force.

## REFERENCES

- [1] W.C. Tian, H.K.L. Chan, C.J. Lu, S.W. Pang and E.T. Zellers, "Multiple-Stage Microfabricated Preconcentrator-Focuser for Micro Gas Chromatography System," *Journal of Microelectromechanical Systems*, Vol. 14, No. 3, pp 498-507, 2005.
- [2] H. Kim, W. H. Steinecker, S. H. Reidy, G. R. Lambertus, A. A. Astle, K. Najafi, E. T. Zellers, L. P. Bernal, P. D. Washabaugh, K. D. Wise, "A Micropump-Driven High-Speed MEMS Gas Chromatography System," *Transducers 07'*, pp. 1505-1508, 2007.
- [3] B. Bae, J. Yeom, R. I. Masel, M. A. Shannon, "A Five-Microvalve Fully Integrated Preconcentrator," *IEEE Sensors conference*, pp. 1353-1356, 2007.
- [4] B. Bae, J. Han, R. I. Masel, M. A. Shannon, "A Bidirectional Electrostatic Microvalve With Microsecond Switching Performance," *Journal of Microelectromechanical Systems*, Vol. 16, No. 6, pp.1461-1471, 2007.
- [5] A. D. Radadia, R. I. Masel, and M. A. Shannon, "New Columns Design for MicroGC," *Transducers 07'*, pp. 2011-2014, 2007.

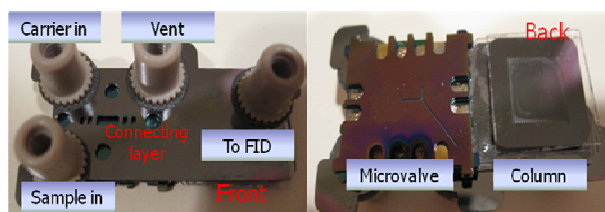


Figure 5: A photo of the five microvalves integrated with the microcolumn.

# FLIGHT CONTROL OF 10 GRAM INSECTS BY IMPLANTED NEURAL STIMULATORS

*Hirota Sato*<sup>1</sup>, *Chris W. Berry*<sup>2</sup> and *Michel M. Maharbiz*<sup>1,2</sup>

<sup>1</sup>Electrical Engineering and Computer Science, University of California, Berkeley, CA, USA

<sup>2</sup>Electrical Engineering and Computer Science, University of Michigan, Ann Arbor, MI, USA

## ABSTRACT

We present several important advances on the flight-control microsystem for a cyborg beetle presented recently [1]. Giant beetles (*Mecynorhina torquata*) were employed to achieve larger payloads than the previously used *Cotinis texana* beetles. A new turning control method based on direct neural stimulation of the optic lobes (compound eyes) was achieved as well as initiation, cessation and elevation controls. A new variant of the initiation/cessation stimuli is also presented. Additionally, we report that operational neural stimulators and an entire working microcontroller were successfully implanted into *Japanese rhinoceros* beetles at the pupal stage; these beetles subsequently emerged into adults.

## INTRODUCTION

Micro air vehicles (MAV's) have been the subject of intense research and development. Despite major advances, MAV's are still limited in size, payload, flight range and performance [2]. Various species of insects, among flies (Diptera), moths (Lepidoptera), dragonflies (Odonata) and beetles (Coleoptera) have unparalleled flight performance and increasingly understood muscular and nervous systems [3]. Additionally, insects undergoing complete metamorphosis (*i.e.* forming pupae) are very amenable to implantation and internal manipulation during pupation [1,4,5]. In this study, we extend our previous work to the *Mecynorhina torquata*, which has 7 – 10 g body weight and 1.4 – 2.0 g payload capacity.

## EXPERIMENTAL

The complete microsystem is shown in Fig. 1. The neural stimulation system consisted of three neural wire electrodes: one dorsally implanted at the pupal stage between compound eyes into the insect brain and the other two were implanted either a) into the optic lobes or b) under the basalar flight muscles. A fourth wire inserted into dorsal metathorax was used as a counter electrode. As with our previous study, the neural stimulators were driven by a TI MSP430 microcontroller (some characterization used a function generator); flight command sequences were stored in the 2 KB memory (~1000 flight commands with current program). The microcontroller was powered by a microbattery which was dorsally mounted on the beetle platform. Beetles were attached on custom gimbals to measure flight responses; the torsional stiffness constant of the gimbal was  $3.32 \times 10^{-5}$  Nm/rad.

Prior to pupation, *Mecynorhina* makes and encases itself inside a pupal chamber. For the implantation of the neural wire electrode, first the pupal chamber was split and the electrode was inserted into the brain (Fig. 2(a)). The split pupal chambers were then glued together with a starch paste (Fig. 2(b)). For the implantation of the entire flight control system, the neural wire electrodes were soldered directly onto the microcontroller pins and all surfaces were coated with a clear nail polish. The dorsal thorax of a *Japanese rhinoceros* beetle was slit, and the assembly was inserted 2 weeks into the 3 week pupation period.

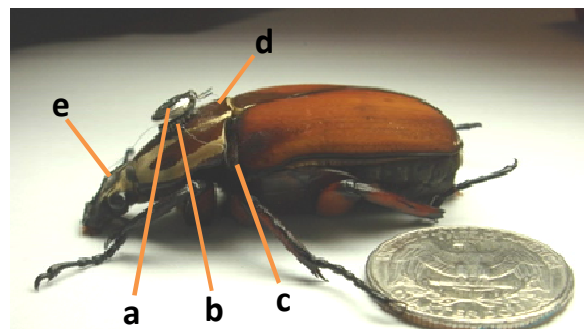


Figure 1: Cyborg beetle microsystem consisted of microbattery (a, rechargeable lithium ion coin battery, Panasonic, ML614, 3 V, 160 mg,  $\varnothing 6.8$  mm  $\times$  1.4 mm, 3.4 mAh), microcontroller (b, Texas Instruments, MSP430F2012IPWR, 63 mg, 5.0 mm  $\times$  4.5 mm  $\times$  1.0 mm), stimulating electrodes implanted into basalar flight muscle (c), metathorax (d), brain (e), and beetle platform of *Mecynorhina torquata* (7 - 10 g, 6 - 8 cm).

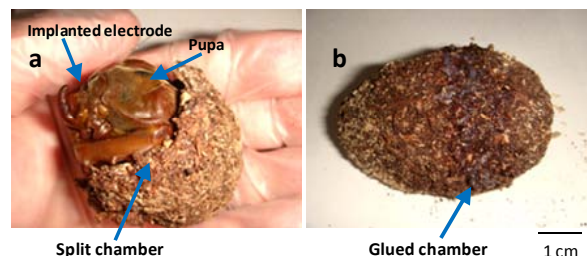


Figure 2: implantation of the neural wire electrode into a pupa of *Mecynorhina torquata*. (a) the electrode was inserted into the brain after splitting the pupal chamber. (b) the split chambers were glued together with a starch paste.

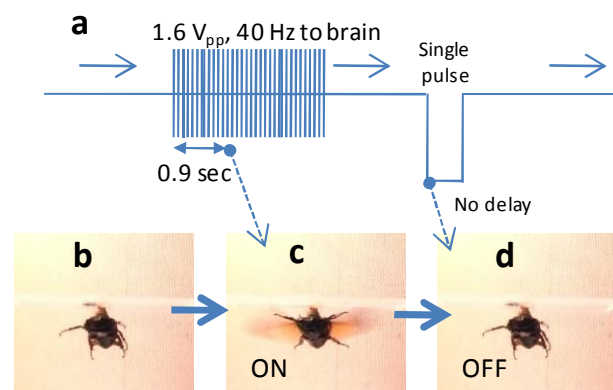


Figure 3: Initiation and cessation control of beetle flight (front views). (a) indicates typical sequential flow of pulse trains. Neural stimulation pulse trains of  $1.6 V_{pp}$  and 40 Hz to the beetle brain started wingbeat following a 0.9 sec induction time (b-c) and 2 V single pulse stopped the flight without delay of response (c-d).

## RESULTS AND DISCUSSION

The same on/off, throttling and turning behavior presented in [1] can be extended to other beetle systems with much larger payloads (payloads: *Cotinis texana* 0.2 - 0.4 g, *Mecynorhina torquata* 1.4 - 2.0 g, *Japanese rhinoceros* 1.4 - 1.8 g). Figure 3 shows the initiation and cessation controls. When appropriate voltage (1.6 V<sub>p-p</sub> on average) pulse trains at 40 - 110 Hz were applied between the right and left optic lobes, the beetle began beating wings following a short period (0.9 sec on average). A single pulse of higher magnitude voltage (> |2| V) stopped the flight without a delay of response. When initiation pulse trains were applied during flight, they lowered flight power without stopping the flight (Fig. 4). We do not yet know if both these developments (flight initiation with pulse trains and the modified throttle response) apply also to *Cotinis texana*. We additionally identified a new turning stimulus. Stimulation of the optic lobes with 0.8 V and 100 Hz pulse trains elicited turns towards the lobe stimulated (Fig. 5). Importantly, these results indicate that all flight controls including flight initiation, cessation, throttling and turning can be performed by using only brain-implanted neural stimulators.

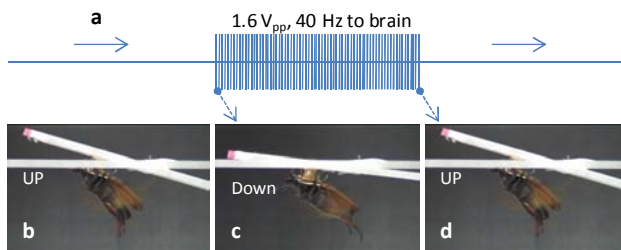


Figure 4: Elevation control of beetle flight (side views). (a) indicates typical sequential flow of pulse trains. Neural stimulation pulse trains of 1.6 V<sub>pp</sub> and 100 Hz to beetle brain altered pitch of flying beetle. The beetle was mounted on a custom pitching gimbal (Fig. 2). The red marker on the gimbal follows as the beetle climbed up (b, d) or down (c). The beetle decreased climbing rate whenever the stimulation pulse trains were applied to the brain. No response delay in 30 fps video was detected.

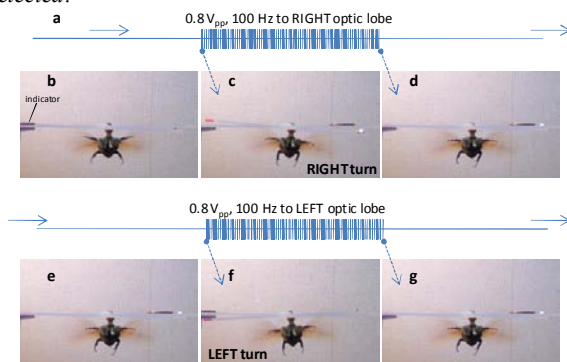


Figure 5: Tracking of optic lobe (compound eye) stimulation by pulse trains of ~0.8 V<sub>pp</sub> and 100 Hz (back views). The beetle was mounted on a custom rolling gimbal. (a) indicates typical sequential flow of pulse trains. The red marker on the left side of the gimbal is an indicator to signify left and right turns. The stimulation to right optic lobe elicited right turn (b-c-d), and vice versa (e-f-g). No response delay in 30 fps video was detected.

To test the plasticity of pupal implantation, the entire system except for the microbattery was fully implanted into the dorsal metathorax of *Japanese rhinoceros* beetles at the pupal stage. Figure 6 shows white light and X-ray images of representative

implants at both the pupal and emerged adult stages; success rate for these implants was 50% (N = 12). These implanted controllers were functional in flight-ready emerged adults.

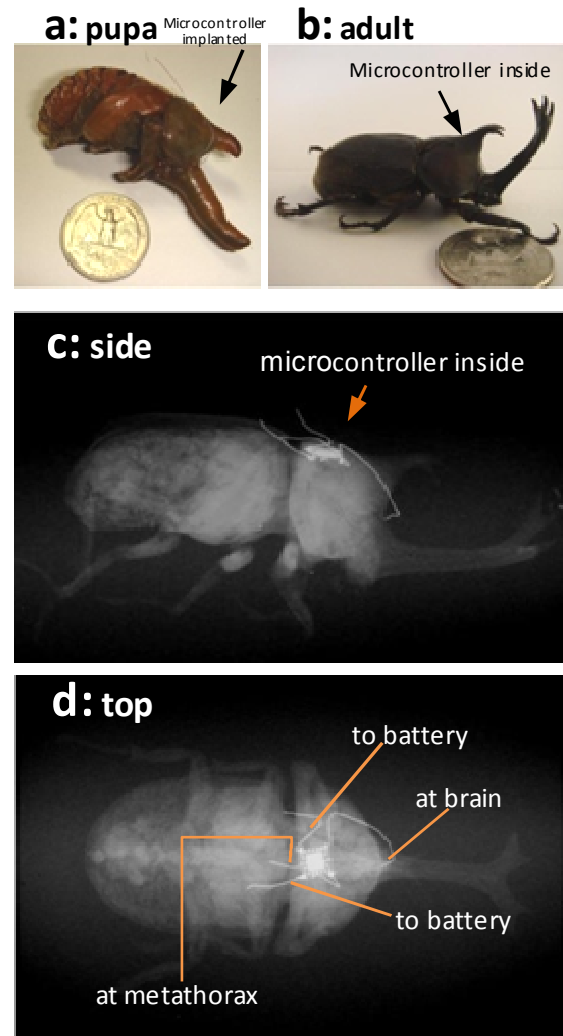


Figure 6: White light (a, b) and X-ray (c, d) images of entire stimulator implant; pupa (a), emerged adult (b), side and (c) top (d) views of the emerged adult. This implant was done on a *Japanese rhinoceros* beetle.

## ACKNOWLEDGEMENT

This work was financially supported by Defense Advanced Research Projects Agency (DARPA) and Marubun Research Promotion Foundation.

## REFERENCES

- [1] H. Sato, C. W. Berry, B. E. Casey, G. Lavella, Y. Yao, J. M. VandenBrooks and M. M. Maharbiz, *Proc. MEMS 2008*, pp. 164-167.
- [2] D. J. Pines and F. Bohorquez, *J. Aircraft*, 43 (2006), 290-305.
- [3] M. Dickinson, G. Farman, M. Frye, T. Bekyarova, D. Gore, D. Maughan and T. Irving, *Nature*, 433 (2005), pp. 330-333.
- [4] A. Bozkurt, A. Paul, S. Pulla, A. Ramkumar, B. Blosssey, J. Ewer, R. Gilmour and A. Lal, *Proc. MEMS 2007*, pp. 405-408.
- [5] A. Bozkurt, R. Gilmour, D. Stern and A. Lal, *Proc. MEMS 2008*, pp. 160-163.

# THE APPLICATION OF INSTABILITIES IN MICROFLUIDIC JETS TO DIGITAL OFFSET-CLASS PRINTING

Gilbert Hawkins, James Chwalek, Christopher Delametter, Edward Furlani, David Jeanmaire,  
John Lebens, David Trauernicht, and Qing Yang  
Eastman Kodak Company, Rochester, New York, USA

## ABSTRACT

The tendency of fluid jets to break up into droplets of multiple sizes has been well known since the times of Lord Rayleigh.<sup>1</sup> However the ability to make and control individual droplets from arrays of such jets has come only recently, due in part to the availability of microstructure manufacturing technologies and to the recognition of the potential importance of such arrays to variable data printing. We describe a new inkjet printing technology based on thermally stimulated drop breakup of jets of complex fluids that allows variable data printing to move into "high-speed," "offset class" markets, which include publication and short-run commercial printing markets, often served today by offset lithography, and transactional printing markets, often served by lithography print technologies. The physics of microjet instabilities and the ability to make low-cost microfluidic devices enable such high-speed digital applications.

## INTRODUCTION

Inkjet printing for consumer applications has revolutionized desktop printing of documents, including high-quality color images. The two currently commercialized printhead technologies, thermal and piezo drop-on-demand (DOD) technologies, contribute substantially to the revenues attributed to MEMS devices. These technologies have been slow to penetrate commercial applications because the printing speed of consumer devices is far less than that typically associated with technologies such as offset lithography. Of course, the speed of offset printing derives from the fact that identical images are produced without variable data content. The desirability to print variable data at the speed and cost of offset printing has long been recognized but not yet achieved. We believe that the continuous inkjet (CIJ) technology described here offers a practical path for such offset class digital printing, due to the convergence of new principles of device operation, the availability of integrated electronic/fluidic device manufacturing, as well as new developments in ink and media formulations.

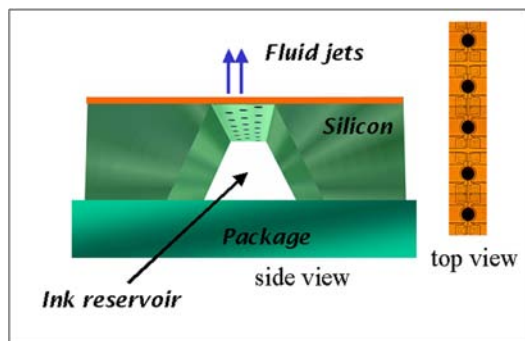


Figure 1a: A new principle of inkjet printing, based on thermal pinch-off of continuously jetted fluid streams.

Figure 1a illustrates schematically a new type of silicon-based CIJ printhead based on thermally stimulated drop formation. Ink in

the reservoir is pressurized and jets through the nozzles in the form of fluid columns that propagate (vertically in Fig. 1a) and eventually break up into drops. Figure 1b shows a cross-section of a CIJ device of the thermal stimulation type, which is made by integrated CMOS-MEMS processing using deep reactive ion etching to form the ink reservoirs as channels through the silicon wafer. The nozzle bores are etched through all of the various dielectric layers of the CMOS process and are typically 10  $\mu\text{m}$  in diameter and located on 20–40  $\mu\text{m}$  centers. The choice of silicon as a material technology is an important one, both because silicon-based materials have historical precedence for their compatibility with liquid inks, and because the ability to integrate electronic logic for nozzle addressing greatly simplifies the already complex fluidic packaging of devices with thousands of nozzles.

As opposed to the case of DOD printheads, the energy supplied to eject fluids in CIJ technology is not local to the nozzles. For example, the reservoir in Fig. 1a contains fluid pressurized by a pump external to the printhead. Due to the strength of the silicon materials and to the fact that the energy does not have to be supplied by micro devices located at each nozzle, it is possible to eject a very wide variety of fluids by continuously maintaining many atmospheres of pressure in the reservoir. Because the pressure is constant in CIJ technology, rather than being pulsed as in DOD technology, the duty cycle for fluid ejection is 100% and the velocity of the jets can be varied over a wide range, for example 10–40 m/s.

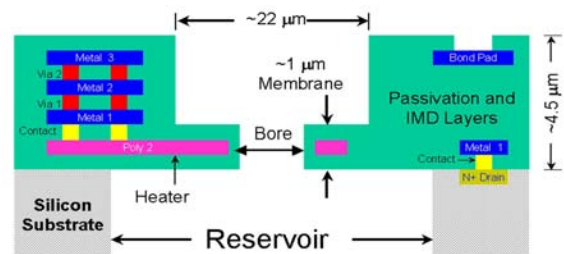


Figure 1b: Cross-section of CMOS-MEMS integrated printhead.

## PHYSICS OF DROP FORMATION

The ability to rapidly eject fluids from closely spaced arrays of nozzles allows CIJ devices to print at very high speeds. In general, a fixed amount of colorant (dye or pigment) is required per unit area of printed media to achieve the required maximum optical density, and thus ink flux scales with speed. Also, because of the ability of CIJ devices to jet very viscous fluids, the concentration of colorants in the ink can be quite high, further enabling high print speeds; CIJ print speeds can exceed a thousand feet per minute. With such potential come problems to be solved, the first of which is the need to form drops of known and controlled volumes and the second of which is to select the drops to be printed. The solution to these two problems forms the basis of the technology discussions below.

A "chaotic" sequence of drop formation is shown in Fig. 2. This formation was generated from a linear array of 70 jets of fluid

that are propagating vertically downward; each jet flows from a separate nozzle bore opening. Pressurized jets emerge from the nozzle bores as fluid columns each about the diameter of the bore and travel rapidly, typically 20 m/s, for a distance of a few mm before breaking up “randomly” to form discrete drops moving along the same vertical paths. Figure 2 shows only the discrete drops; the printhead and the fluid columns are about 1 mm above the image. Although the fluid flux from each jet is constant, the volumes of the drops vary widely, and the largest drops may even touch drops from neighboring jets.

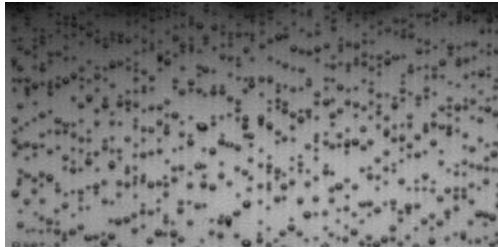


Figure 2: Chaotic breakup of jetted fluid streams.

Chaotic drop formation is not of use for image printing, which requires control over drop volumes, velocities, and trajectories, preferably using very low energies for reasons of thermal management. We achieve drop control at very low energies by introducing small thermal perturbations using heaters surrounding the nozzle bores.<sup>2</sup> The perturbations are spaced along the jet in the form of heat “bands,” each a fraction of the jet radius in length along the jet, and having a surface temperature rise of a few degrees C. These perturbations locally reduce the surface tension around the jet and initiate a hydrodynamic process of collapse or pinch-off of the jet at the point of the heat band. The energy required for pinch-off is low because surface tension perturbations capitalize on the natural propensity of the jet to break up into drops in order to minimize the surface free energy. This technique is applicable to a wide variety of fluids because most free fluid surfaces exhibit reduced surface tension upon heating. The surface tension gradients, and hence surface forces, associated with thermal stimulation are the underlying perturbations responsible for initiating pinch-off of the column; a drop is formed between adjacent pinch-off points. As is well known,<sup>1</sup> drops spaced at about nine times the radius of the jet are formed most rapidly, and a very low energy stimulation at this spatial frequency is sufficient to lock droplet formation into a repetitive pattern of nearly equal drop volumes, as shown in Fig. 3, in which the jets are shown propagating left to right. In past CIJ inkjet devices, such stimulation has been achieved by acoustic resonance of the printhead, at frequencies as high as 1 MHz. However, acoustic stimulation cannot be applied to a single jet independent of other jets in an array, due to acoustic cross talk; and uniform acoustic stimulation in an array of jets is difficult to achieve.

The jets in Fig. 3 were thermally modulated to form drops of regular volumes at frequencies near 1 MHz using independent heaters at each nozzle. At the left of Fig. 3, the fluid columns shown are just starting to pinch off at the locations where heat was originally applied. The heat pulses, typically of 1  $\mu$ s duration, need produce a rise of only about 2 °C at the surface of the jet to cause the column to pinch off or “collapse” after a delay time of typically 20  $\mu$ s. Each heat pulse, by reducing the surface tension in a “band” around its associated fluid column, sets in place a time-delayed collapse of the jet at the location of the centroid of temperature gradient. Satellite drops in Fig. 3 that form during jet collapse

rapidly recombine with the main drops due to the pull of surface tension during their separation.

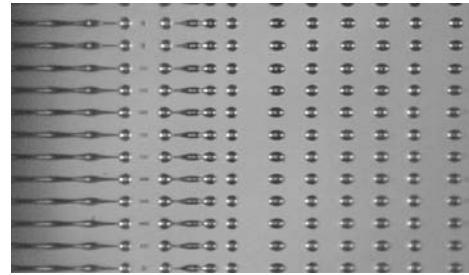


Figure 3: Thermally stimulated formation of drops.

Figures 4a and 4b are SEM micrographs of a nozzle bore formed in a CMOS interlayer dielectric stack and of the associated embedded heater formed in first gate polysilicon in accordance with the schematic illustration of Fig. 1b. The heater ring closely surrounding the bore in Fig. 4a cannot be seen on the surface of the membrane through which the bore is formed due to the planarity of the fabrication process. The rectangular structures in Fig. 4a are metal traces connecting the CMOS driver to the heater. The use of VLSI processing results in very precise geometries for the jet exit orifice and for the heater. This precision is important to ensure accurate jet directionality. The membrane surrounding the 10  $\mu$ m diameter nozzle bore is less than 2  $\mu$ m in thickness.

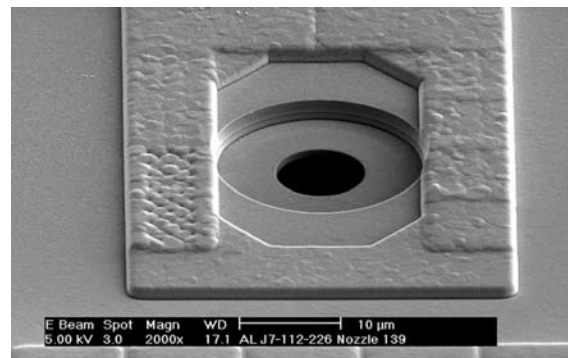


Figure 4a: Silicon nozzle; the bore diameter is about 8  $\mu$ m. The 1  $\mu$ m width thin-film heater is buried in the adjacent dielectric.

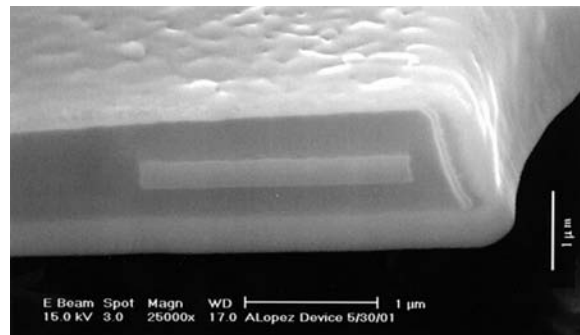


Figure 4b: Imbedded heater, first gate polysilicon, provides thermal stimulation.

The rather small aspect ratio of the bore membrane thickness to the bore diameter is not found to limit directional accuracy of the

jet, which is instead governed by the membrane flatness and the flow pattern of fluid in the underlying channel in the silicon substrate. In fact, such a small aspect ratio is a requirement for thermal steering of the jets, as will be discussed, and is a requirement that would be difficult to achieve without MEMS processing technology.

Figure 5 illustrates the geometrical model input used for 3D computational simulation of jet breakup. The model applies voltage pulses of about 1  $\mu$ s duration to a heater ring surrounding the nozzle and solves for both the thermal and hydrodynamic system responses using known silicon materials parameters.

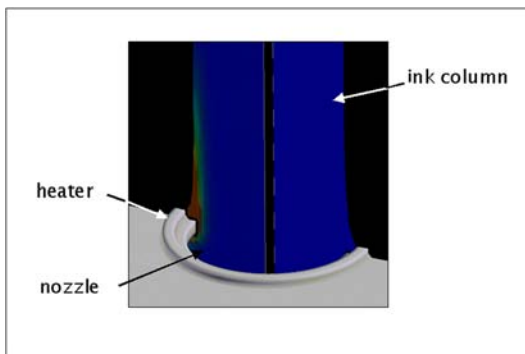


Figure 5: Device geometry for coupled thermal and hydrodynamic modeling. Material covering the heater and planarizing the top surface is not shown. The axisymmetric distribution of heat is shown only on one side of the fluid column to illustrate the radial temperature distribution.

Computational modeling results are shown in Fig. 6, left side, for the temperature profile at pinch-off of the jet in Fig. 5 subjected to a single 1- $\mu$ s heat pulse having amplitude sufficient to increase the surface temperature of the jet by about 2  $^{\circ}$ C. The model heat pulse was applied at the exit orifice, shown at the bottom of Fig. 6, about 20  $\mu$ s before the Fig. 6 snapshot. The delay time between application of the heat pulse and pinch-off depends strongly on the radius and surface tension of the jet and weakly on pulse amplitude.<sup>2</sup> The band of heat applied to the jet has lengthened more than twofold along the jet during this time, principally due to convection induced by the surface tension gradient; the pinch-off point nearly coincides with the temperature centroid in the case of a spatially symmetrical heat pulse.

Just as a single heat pulse later creates a pinch-off point on the jet, two temperature pulses, spaced apart in time (and hence spaced apart in space on the moving fluid jet), will create two pinch-off points along the jet and thereby form a drop, whose volume scales with the time delay between the pulses and the velocity of the jet. By applying heat pulses at various positions along the fluid column, as illustrated by the arrows on the right side of Fig. 6, drops of arbitrary volume can be formed. It should be understood that although these concepts are useful guides, the actual experimental situation can be complicated by the fact that each pinch-off point can trigger the formation of secondary pinch-off points spaced about the primary by multiples of the Rayleigh length (about 9 times the jet radius). These secondary drops usually coalesce with the primary drops or are swept into fluid catchers. Pulses spaced closer than about 7 radii interfere with one another and may not produce a simple drop; pulses spaced more than about 40 radii may result in multiple drops that do not coalesce.

Figure 7 illustrates drops formed by the device of Fig. 3 using

heat pulses applied at various positions along the fluid column. The larger drops shown in Fig. 7 are not constrained to volumes that are integer multiples of the smallest drop volume, a property that can be used advantageously in contone printing applications.

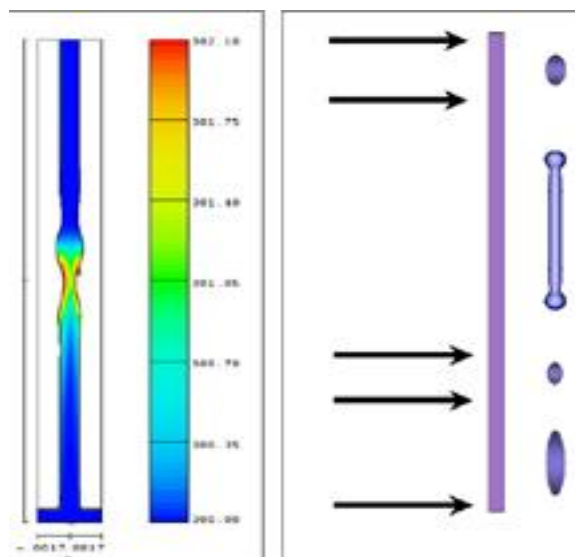


Figure 6: Model of thermal stimulation and pinch-off of a fluid jet. Left: pinch-off due to a single heat pulse (orange). Right: multiple heat pulses (arrows) spaced variably in time form multiple drop volumes.

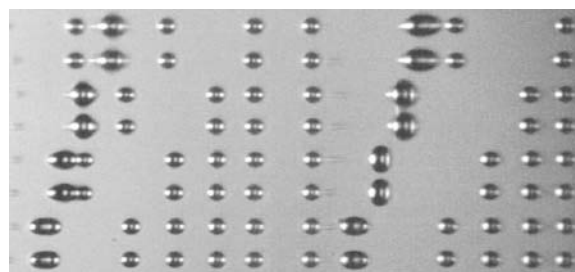


Figure 7: Variable sized drops, not constrained to integer volume ratios.

The experimental results of Figs. 3 and 7 correspond to simple, low-viscosity fluids such as dye-based inks. However, most practical inks are complex fluids containing polymers and pigments and/or exhibiting non-Newtonian behavior such as shear thinning. Such fluids behave qualitatively similarly to the case of simple fluids, because their instabilities are also driven by surface tension, but they yield more complex modes of breakup, as shown in the comparison of model and experiments in Fig. 8 for a practical ink with substantial polymer content. Under the assumption that shear-induced changes in rheology relax slowly on the time scale of drop formation, model predictions are seen to reproduce the experiments surprisingly well. The breakup modes depend sensitively on the spacing of the heat pulses compared to the jet radius, consistent with the models.

## DROP SELECTION

The ability to form drops of various sizes at very high frequencies, using low excitation energies for a wide variety of fluids, is not sufficient to print images. As opposed to DOD inkjet

technology, the CIJ drop ejectors are always “on” and the printed page would be saturated with ink unless a subset of drops is selected for printing. (Those drops not printed are typically gathered in a catcher and reused, similar to the working principle of a CRT display.) A large variety of methods have been proposed to select printing drops; some are simpler to implement than others. To capitalize on the very high frequencies of operation of CIJ technology, the means of selecting drops must be equally fast, i.e., it must be responsive in about 1  $\mu$ s. One method, electrostatic deflection of charged drops, is in commercial use today. However, the images produced are limited in resolution for many reasons, including restrictions on inks and repulsion of like-charged drops. Also, the electric fields required to deflect drops are quite high. Another method of drop selection, mechanical steering by MEMS devices in contact with the jets or drops, has been proposed, but the technical hurdles are formidable. Dense arrays of mechanisms would be required, each capable of a large range of motion (>100  $\mu$ m) on a microsecond time scale. Also, problematic for a mechanical technology is the fact that liquids generally adhere to and build up on solid surfaces, even initially hydrophobic surfaces.

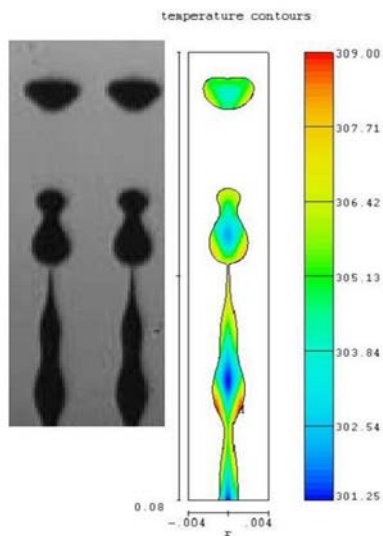


Figure 8: Experimental and CFD model results for drop break-off of a complex fluid.

Two other methods of drop selection, which suffer fewer practical limitations, have been developed at Kodak for thermally stimulated CIJ. The first is asymmetric heating of jets as they exit the nozzles, and the second relies on airflow to separate large from small drops. These methods are illustrated schematically in Figs. 9 and 10, respectively. Steering by asymmetric heating relies on the fact that the formation of drops requires only a perturbation of the fluid jet, not a symmetrical perturbation. By splitting the heating ring into two or more segments, drop formation may be accomplished in a manner virtually identical to that described above by applying heat pulses to one or more segments. However, when heat is asymmetrically applied, in addition to drop formation, the drop trajectories are steered, typically in a direction away from the side of the nozzle heated. Steering is a complex phenomenon<sup>3</sup> based on temperature-induced changes in viscosity, density, and surface tension. Understanding the effects of surface tension requires 3D modeling, since the forces on the jet viewed from above the nozzle derive from surface tension gradients that torque the fluid stream. For many practical types of ink, the dominant steering mechanism is modulation of the velocity of horizontal

flow of fluid under the activated heater due to a reduced fluid viscosity near the heated surface. Horizontal momentum flow is transmitted through the nozzle bore, provided the membrane surrounding the bore is very thin, so that the velocity profile in the bore cannot equilibrate to a parabolic distribution. Such a case is modeled on the left of Fig. 9, which shows the fluid column deviating from the vertical axis by a few degrees. Because this angle is principally determined by momentum conservation, fluid flowing vertically up through the bore represents a disadvantageous weight component that reduces steering of the jet. Hence, the patented structure shown on the right of Fig. 9, with a mechanical membrane blocking the path of fluid flow vertically from the reservoir to the bore, exhibits several-fold greater steering, as is confirmed experimentally. In the model in Fig. 9, an additional heater has been included in the blocking membrane, as that inclusion is without cost in the fabrication process steering and can be reversed.

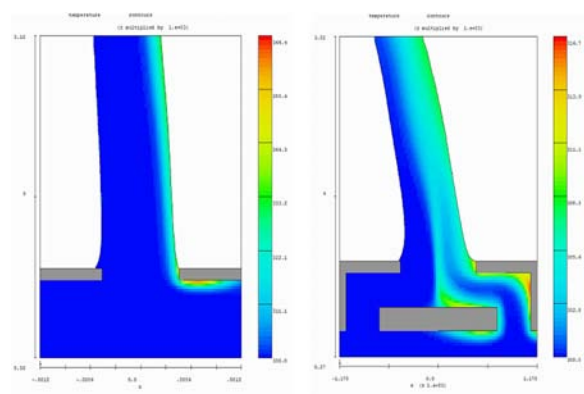


Figure 9: Thermal steering by asymmetric heating of fluid jets. Left: Open chamber geometry. Right: Central flow blocked.

The mechanism of drop selection by airflow makes use of the ability of thermal stimulation to control drop size on a drop-by-drop basis, as illustrated in Fig. 10. A force that depends on drop size is applied perpendicular to the drop trajectories. One such mechanism is laminar gas flow, simply depicted in Fig. 10 as applied by a vacuum channel adjacent the streams of drops. Small drops in this case are pulled into the tube while larger drops (typically 2x–4x larger) travel onto the media and are printed. The difference in trajectory deflection is due to the scaling of inertia vs. drag, the deflection margin scaling approximately as the inverse drop radius. This drop selection technique favors small drops, which is advantageously an industry trend for reasons of image quality. Alternatively, the large drops may be intercepted by a fluidic catcher and the small drops printed. Other methods of drop selection capitalizing on the attributes of thermal stimulation as well as combinations of methods have also been proposed and deserve further study.

## A NEW LOOK AT AN OLD THEORY

In the linear theory of slender jets,<sup>1</sup> the time required for the collapse of a fluid column into a series of drops subject to a sinusoidal perturbation of the column depends on the wavelength of the perturbation approximately in accordance with Fig. 11, the classic “growth rate” of the perturbation vs. the perturbation wave vector  $k$ , defined as twice  $\pi$  divided by the spatial wavelength. The perturbation can be one in radial profile, temperature profile, velocity profile, pressure profile, or some combination thereof;

there are generally three independent boundary conditions. The column collapses at an extremum of the perturbation, and while the solutions differ slightly depending on what is perturbed, the wavelength dependence is always similar to that shown in Fig. 11, because collapse is driven by geometrical reduction of the surface free energy, which is a maximum at a spatial wavelength of about 9 times the column radius.

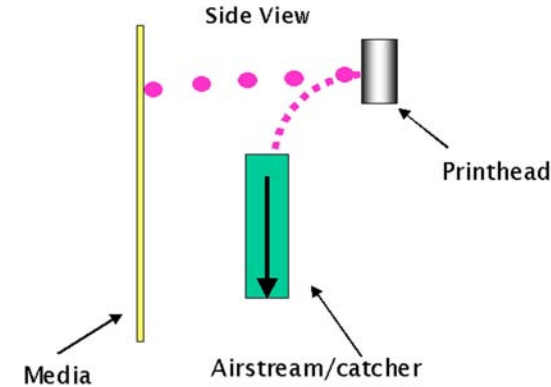


Figure 10: Separation of drops by air deflection.

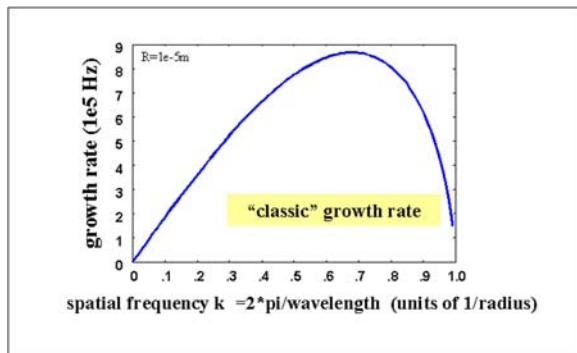


Figure 11: Classic growth rate of sinusoidal perturbations on a fluid jet.

In Fig. 11, at spatial frequencies higher than those on the extreme right of the graph,  $k = 1/\text{radius}$ , the jet fails to collapse, limiting the size of droplets that can be produced for a given jet radius. For this case, the time dependence of the radius is shown in Fig. 12; the jet radius oscillates in time, behaving as a viscously damped simple harmonic oscillator (SHO). In fact, it can be shown that the equations governing the evolution of thin jets are isomorphic to those of a SHO with effective mass, spring constant, and damping parameters shown in Table 1. The terms in Table 1 are the conventional SHO mass  $m$ , spring constant  $K$ , resonant frequency  $\omega$ , damping coefficient  $\alpha$ , damping time  $\tau$ , and resonant Q-factor  $Q$  for a column of fluid of density  $\rho$ , surface tension  $\sigma$ , and viscosity  $\mu$ , perturbed at reciprocal wavelength  $k$ . These terms have straightforward physical interpretations: the effective oscillating mass  $m$  scales as the moving mass of a capillary wave, the effective spring constant is related to the surface tension and the geometrical distortion of the surface, and the damping is governed by viscosity. Note that the spring constant is negative for wavelengths associated with jet collapse, which for all of the wavelengths is shown in Fig. 11. For these wavelengths, just as for a mass-and-spring harmonic oscillator with a negative spring

constant, the position of the mass or, analogously, the radius of the jet, diverges, so that the system is releasing, not storing, potential energy. In this regime,  $Q$  could be said to be formally negative. For shorter wavelengths for which the jet radius oscillates rather than collapses,  $Q$  is only on the order of unity for an aqueous jet, as shown in Table 2. Note that it is important to distinguish between periodicity in time for a given spatial wavelength along a fluid column vs. the time response of a spatial periodic perturbation along the jet. These very different concepts become entangled because the spatial perturbation along a jet is frequently the result of a temporal perturbation applied at the nozzle on a moving jet, a very natural concept experimentally.

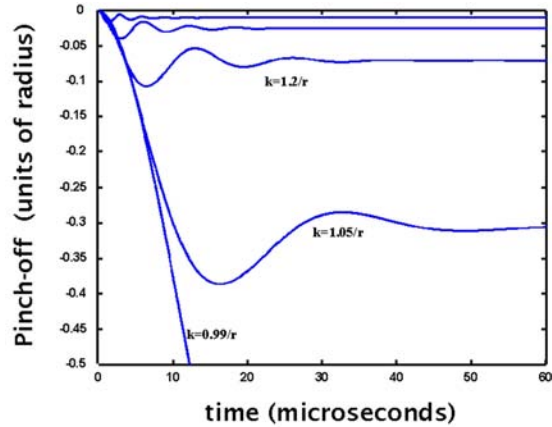


Figure 12: Time dependence of jet radius for stimulation at various spatial wavelengths of an imposed perturbation in surface tension. The perturbation is imposed at time equal zero and thereafter remains constant.

Table 1: Effective harmonic oscillator parameters for a fluid jet excited at wave vector  $k$ .

Parameter	SHO	JET
mass	$m$	$\frac{\rho r_0 \lambda^2}{2\pi^2}$ cap. depth $\sim \lambda$
spring const.	$K$	$\sigma_0 [r_0^2 k^2 - 1]$
res. freq.	$\omega_0^2 = K / m$	$\omega_0^2 = \frac{\sigma_0 k^2}{2\rho r_0} [r_0^2 k^2 - 1] \Theta_{\pm}$
coef. friction	$\alpha$	$6r_0\mu$
damping	$\tau^{-1} = \alpha / m$	$\frac{3\mu}{\rho} k^2$
Q	$Q = \frac{\omega_0 \tau}{2\pi}$	$Q = \frac{\omega_0 \tau}{2\pi}$

The analogy of a jet to a harmonic oscillator is useful in understanding drop formation in printing. This analogy is illustrated by the potential energy surface of Fig. 13, in which the z-axis represents a generalized potential energy, the x-axis a spatial variable (position of a mass on a spring, a puck sliding in a bowl, or the radius of a fluid jet), and the y-axis an effective restoring constant (spring constant). The straight white line on the surface corresponds to a change in sign of the spring constant. Toward the back of the surface, the spring constant is positive and the spatial coordinate oscillates, for example, following the white trajectory of positive curvature, the usual behavior of a SHO. Toward the front

of the surface, the spring constant is negative; the trajectory generally diverges, following, for example, the white trajectory with negative curvature. This is the behavior expected of a SHO having a negative spring constant as well as that of a collapsing jet. Mathematically, the solution sets are related by transforming the frequency-dependent solutions of an oscillator to the time domain by integration in the complex plane.

Table 2: Numerical values for the effective oscillator parameters of an aqueous jet perturbed at a spatial wavelength of about 4 times the radius.

Parameter	Numerical values for perturbations half the Rayleigh wavelength	Jet parameters
mass	$e^{-13}$ kg (0.1 pL)	$\frac{\rho r_0 \lambda^2}{2\pi^2}$ cap. depth $\sim \lambda$
spring const.	0.1 N/m	$\sigma_0 [r_0^2 k^2 - 1]$
res. freq.	800,000 Hz	$\omega_0^2 = \frac{\sigma_0 k^2}{2\rho r_0} [r_0^2 k^2 - 1] \Theta_H$
coef. friction	$3e^{-8}$ kg/s	$6r_0 \mu$
damping	Inverse $3.5e^6$ s	$\frac{3\mu}{\rho} k^2$
Q	$\sim 1$	$Q = \frac{\omega_0 \tau}{2\pi}$

The energy required for jet pinch-off is understandably small, since the system itself is providing the energy and the applied perturbation serves to synchronize pinch-off events. On the other hand, in the region of Fig. 13 for short wavelength perturbations, the radius of the fluid column exhibits damped oscillation, not pinch-off. Of course, it is possible to perturb the system so strongly in the short wavelength regime that very small droplets of some type are produced. The very large energies required would characterize a DOD ejector, in which the system-free energy is overwhelmed by the applied perturbation.

The graph of Fig. 11 suggests that the ability to rapidly change drop size would energetically be costly, as it is tempting to view the system as a resonant oscillator preferring a periodic perturbation of wavelength about 9 times the jet radius. Fortunately for applications in printing, where variable drop size is generally advantageous, this conclusion is incorrect. As shown in Fig. 14, a “delta-function” train of heat pulses, arbitrarily spaced, is more effective in forming drops than are sinusoidal perturbations of equal heat content. A single “delta-function” heat pulse collapses a jet nearly as effectively as a sinusoidal perturbation at the peak of the growth rate curve in Fig. 11. This frequently overlooked fact stems from the role of the surface tension gradient as the driving force for drop breakup. It is consistent with the oscillator analogy of a system of low Q and is essential to enable the applications to printing described here.

In conclusion, although continuous inkjet was an historically early printing technology, its use has not become widespread due to perceived limits in resolution and image quality. Now, changes in the physical principles of CIJ operation that allow control over drop breakup independently at each nozzle and changes in the ability to fabricate arrays of devices have given new life to a growing segment of variable data printing that allow it to compete in offset class image quality, cost, speed, and substrate flexibility (ink latitude). Our learnings along the way include appreciation for simplicity of device fabrication, avoidance of “creeping elegance of design,” a need to capture at least one aspect of device

performance that on fundamental grounds appears superior to any competition, the ability to scale devices physically to cover multiple applications, a technical vision of extensible functionality, and the ability to enable at least one very large market in which one can afford the luxury, often a necessity, of realistic development times.

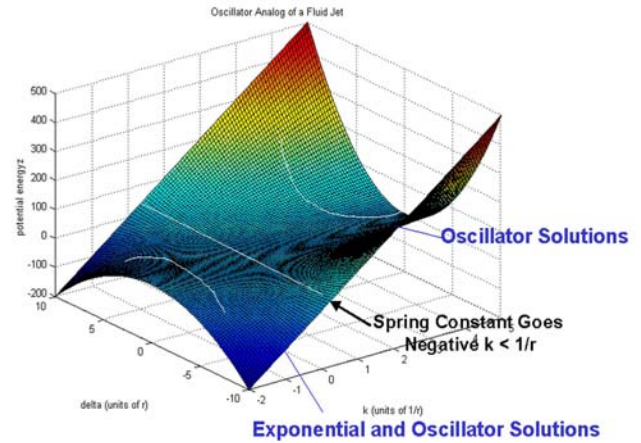


Figure 13: Solution plane for trajectories of a linear fluid jet: Potential energy (vertical axis) vs. jet radius and wave vector k of an applied surface tension perturbation.

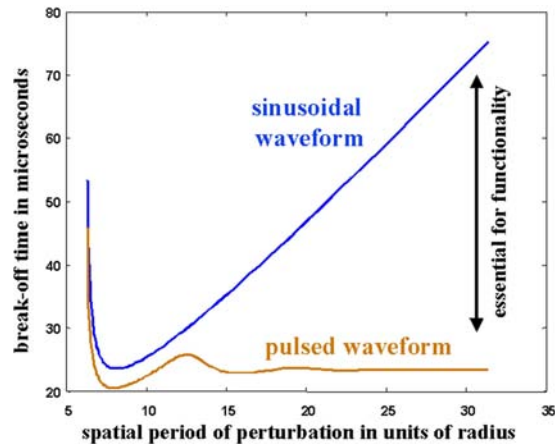


Figure 14: The delay time between application of a periodic temperature perturbation and jet collapse as a function of the wavelength of the perturbation for sinusoids and for pulses of equal average heat.

## REFERENCES

- [1] Lord Rayleigh, “On the instability of jets,” Proc. Lond. Math. Soc. 10, 4-13 (1878).
- [2] E. P. Furlani, “Temporal instability of viscous liquid microjets with spatially varying surface tension,” J. Phys. A: Math. and Gen. 38, 263-276 (2005); E. P. Furlani, B. G. Price, G. Hawkins, and A. G. Lopez, “Thermally Induced Marangoni Instability of Liquid Microjets with Application to Continuous Inkjet Printing”, Proc. NSTI Nanotechnology Conference (2006).
- [3] Unpublished results.

# ION IMPLANTED PIEZORESISTIVE CANTILEVER DESIGN AND PERFORMANCE

S.-J. Park<sup>1</sup>, A.J. Rastegar<sup>1</sup>, J.R. Mallon Jr.<sup>2</sup>, A.A. Barlian<sup>1</sup>, T.H. Fung<sup>2</sup> and B.L. Pruitt<sup>1</sup>

<sup>1</sup>Department of Mechanical Engineering, Stanford University, Stanford, California, USA

<sup>2</sup>Department of Electrical Engineering, Stanford University, Stanford, California, USA

## ABSTRACT

We present design guidelines for ion implanted piezoresistive cantilevers. Most analytical models assume cantilevers have uniform doping profiles, whereas ion implanted piezoresistors with graded doping profiles are commonly fabricated in commercial force and pressure sensors. To address this issue, we modified existing models to predict the performance of ion implanted piezoresistors. Experiment, simulation, and our analytical model of force sensitivity and force resolution agree with less than 20% error. Using the analytical model, we also demonstrate a method to choose design and operating parameters to optimize performance.

## INTRODUCTION

MEMS piezoresistive microcantilevers have become increasingly popular as force and displacement sensors since the first piezoresistive AFM cantilevers by Tortonese [1]. Piezoresistors have advantages such as large dynamic range, large deflection, relatively small size, simple fabrication, and straightforward signal-conditioning circuitry. Piezoresistive cantilevers are used where other transduction methods are impractical [2] and Harley and Kenny's [3] analyses of noise and sensitivity are widely used in maximizing sensitivity for limited power. However, piezoresistor design remains challenging due to the many coupled parameters such as cantilever dimensions (width, length, and thickness), piezoresistor dimensions, fabrication process parameters (doping concentration, annealing time and temperature), and bias voltage which must be chosen carefully to optimize performance (bandwidth, stiffness, resolution, power dissipation and nonlinearity). For example, increasing sensitivity by reducing piezoresistor doping and increasing bias voltage increases power dissipation and noise. Harley [3] first showed a method to design piezoresistive cantilevers, but only for epitaxial piezoresistors with uniform doping profiles [4]. However, ion-implanted piezoresistive sensors with non-uniform doping profiles are commonly specified for their low cost and simple fabrication. Here, we extend analytical model to predict sensitivity and resolution of piezoresistive cantilevers with arbitrary doping profiles. We validate the model with simulation and experimental measurements. We also show how to choose optimal design parameters that satisfy the complex parameter interaction of piezoresistive cantilevers.

## ANALYICAL MODEL

To calculate sensitivity and resolution of piezoresistive cantilevers with an arbitrary dopant profile, we should consider two profiles: stress distribution and doping concentration profile. Stress is distributed across the length and thickness of a cantilever as per Euler's beam equation; and doping concentration varies in the thickness of cantilever for common doping techniques such as epitaxial growth and ion-implantation. Therefore, we model the piezoresistor in depth as a composite of many thin slices of piezoresistors connected in parallel, with the change in resistance in each slice depending on the stress and piezoresistive coefficient for that slice. By integrating the change in resistance in thin slices of a piezoresistor, we can compute force sensitivity in terms of resistance change ( $\Delta R/R$ ), cantilever dimension (length,  $l$ , width,  $w$ , thickness,  $t$ ), piezoresistor length ( $l_p$ ), maximum longitudinal

piezoresistivity as a function of direction at 300° K ( $\pi_{l_{max}}$ ), electronic charge ( $q$ ), mobility ( $\mu$ ), doping concentration ( $p$ ), piezoresistance factor ( $P$ ), distance from neutral axis ( $z$ ):

$$S_{F\Omega} = \frac{\Delta R}{R} = \frac{12(l - \frac{1}{2}l_p)\pi_{l_{max}}}{wt^3} \frac{\int_{-t/2}^{t/2} q\mu p P z dz}{\int_{-t/2}^{t/2} q\mu p dz} [\Omega], \quad [1]$$

We define an efficiency factor,  $\beta^*$ , by dividing force sensitivity by the theoretical maximum force sensitivity which can be achieved if the dopant atoms exist only at the surface ( $z = t/2$ , Fig. 1) and the doping concentration is small enough to maintain the maximum piezoresistance factor ( $P=1$ ):

$$\beta^* = \frac{2}{t} \frac{\int_{-t/2}^{t/2} q\mu p P z dz}{\int_{-t/2}^{t/2} q\mu p dz}. \quad [2]$$

$\beta^*$  is function only of cantilever thickness and process parameters, so the  $\beta^*$  of cantilevers from the same wafer is constant and independent of cantilever length and width.  $\beta^*$  differs from the efficiency factor ( $\beta$ ) defined by Tortonese and Harley [3].  $\beta^*$  includes the piezoresistance factor ( $P$ ) inside the integral of the numerator only. While  $\beta$  represents the conductivity and piezoresistivity weighted average of stress,  $\beta^*$  is the conductivity weighted average of the product of piezoresistivity and stress.  $\beta$  neglects the depth-weighted, piezoresistivity effect on force sensitivity because the piezoresistance factors in the numerator and denominator cancel, as in the case of epitaxy. Because  $\beta^*$  is a ratio of the depth-weighted and maximum force sensitivities, we can now calculate sensitivity by multiplying  $\beta^*$  and maximum force sensitivity. This extended model predicts the sensitivity of ion-implanted cantilevers, where the piezoresistance factor rapidly varies with depth.

Using  $\beta^*$  and considering a 1/4-active Wheatstone bridge

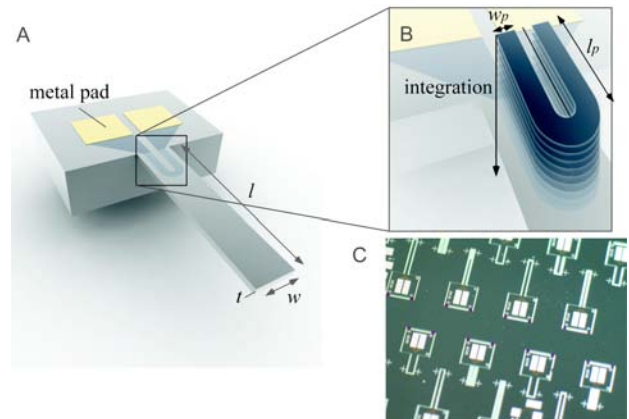


Figure 1: Piezoresistive microcantilever: (A) geometry of cantilever, (B) geometry of piezoresistor. We can compute force sensitivity by integrating the change in resistance in thin slices of a piezoresistor. (C) custom made piezoresistive cantilevers.

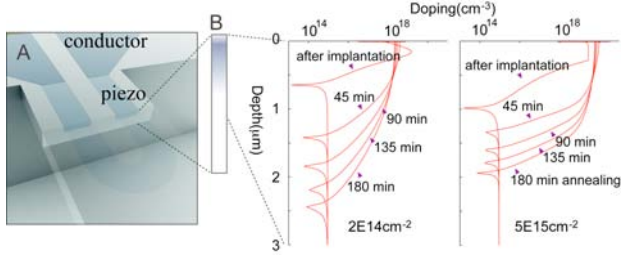


Figure 2: TSUPREM4 simulation of doping concentration profile of cantilever every 45 min annealing. Inert  $N_2$  anneal at  $1100^\circ\text{C}$  for low dose ( $2E14\text{ cm}^{-2}$ , left), and at  $1000^\circ\text{C}$  for high dose ( $5E15\text{ cm}^{-2}$ , right).

configuration (voltage output,  $V_{out} \approx V_{bias}/4 \cdot \Delta R/R$ ), force sensitivity may be expressed in terms of voltage as,

$$S_{FV} = \frac{3(l - \frac{1}{2}l_p)\pi\epsilon_{l\_max}}{2wt^2} \beta^* \gamma V_{bias}, \quad [3]$$

where  $V_{bias}$  is bias voltage and  $\gamma$  is a geometric factor defined as the ratio of the resistance of the strained region in the piezoresistor and total resistance including unstrained regions, interconnects, and contact pads (Fig. 1). Because these regions do not change resistance with applied force, force and displacement sensitivity are decreased.

Noise and force sensitivity determine force resolution:

$$F_{min} = \frac{\sqrt{\frac{\alpha V_{bias}^2}{2l_p w_p N_z} \ln\left(\frac{f_{max}}{f_{min}}\right) + 8k_B T R_s \frac{l_p}{w_p} (f_{max} - f_{min})}}{\frac{3(l - \frac{1}{2}l_p)\pi\epsilon_{l\_max}}{2wt^2} \beta^* \gamma V_{bias}}, \quad [4]$$

where  $\alpha$  is the Hooge noise parameter [5],  $w_p$  is piezoresistor width,  $N_z$  is the integration of doping concentration across thickness,  $k_B$  is Boltzmann's constant,  $T$  is operating temperature,  $R_s$  is sheet resistance,  $f_{max}$  and  $f_{min}$  are respectively the maximum and minimum frequency. The first term in the numerator is  $1/f$  noise and the second term is Johnson noise of the U-shaped piezoresistor.

To predict force resolution of a cantilever with an arbitrary doping profile, we first calculate  $\beta^*$  (Eq. 2) using the doping profile simulated by TSUPREM4 (Fig. 2). We then compute the predicted sensitivity by multiplying  $\beta^*$  and the maximum sensitivity (Eq. 3).

Force resolution is calculated by dividing noise by the sensitivity (Eq. 4).

## VALIDATION

We validated the analytical model by comparing it with numerical simulation and experimental measurements of custom fabricated, ion-implanted cantilevers. We designed and fabricated ion-implanted piezoresistive cantilevers with varied dimensions ( $l$ : 1.7 to 6 mm;  $w$ : 30 to 400  $\mu\text{m}$ ;  $t$ : 7 to 50  $\mu\text{m}$ ,  $l_p$ : 200 to 350  $\mu\text{m}$ ,  $w_p$ : 10 to 20  $\mu\text{m}$ ) and varied fabrication process conditions (implantation energy: 50 keV, dose:  $5E15$  to  $5E16\text{ cm}^{-2}$ , annealing temperature: 1000 to  $1150^\circ\text{C}$ , oxidation time: 15 to 45 min,  $N_2$  annealing time: 5 to 35 min) as described previously [2, 6]. We measured the effective spring constants, force sensitivities, and first-mode resonant frequencies of cantilevers experimentally using a Laser Doppler Vibrometer (Polytec OFV3001) and resonance techniques [6, 7]. In addition, we computed resistance change by integrating the stress and stress-induced resistivity change of each piezoresistor element for a force applied at the tip of cantilever using a commercial finite element method code, COMSOL. We calculated  $\beta^*$ , force sensitivity and force resolution using our analytical model (Eq. 2, 3, and 4) based on two different piezoresistance factors: Harley's empirical model [3] and Kanda's theoretical values [8] (Fig. 3A).

The analytical model agrees with experimental data ( $< 20\%$  error, Fig. 3) and the numerical solution ( $< 5\%$  error). Fig. 3A shows the changes in resistance based on the analytical model and experimental results when a point force is applied at the tip. Our experimental data are closer to the analytical prediction using Harley's piezoresistance factor rather than Kanda's (Fig. 3A). Fig. 3B and Fig. 3C show  $\beta^*$  and force sensitivity, respectively, as a function of diffusion length for a 15  $\mu\text{m}$  thick piezoresistive cantilever. The predicted  $\beta^*$  and force sensitivity of cantilevers with various dimension and process conditions are in good agreement with experimental results. As expected,  $\beta^*$  of high dose cantilevers with long diffusion lengths significantly decreases with increasing diffusion length, because diffusion causes the dopant atoms to move away from the top surface (highest stress region) resulting in decreased  $\beta^*$  and force sensitivity. In addition,  $\beta^*$  and force sensitivity of high dose, short diffusion length cantilevers are independent of dose because of the solid solubility limit. We also found that  $\beta^*$  and force sensitivity of low dose cantilevers increase with annealing because the piezoresistance factor effect more than

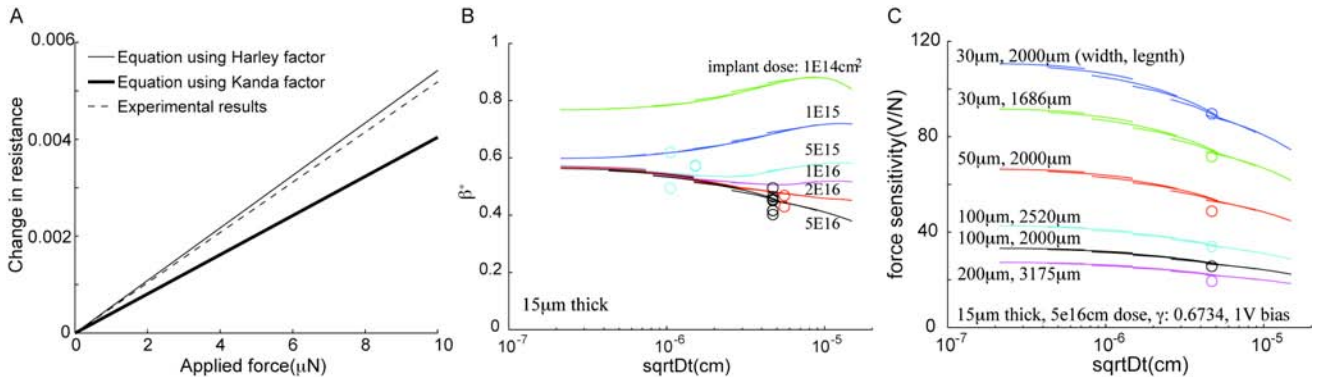


Figure 3: Validation of the analytical model: (A) Comparison of analytical model and experimental results of changes in resistance of a typical piezoresistive cantilever (2000  $\mu\text{m}$  long, 30  $\mu\text{m}$  wide, 15  $\mu\text{m}$  thick cantilever with 350  $\mu\text{m}$  long by 10  $\mu\text{m}$  wide U-shaped piezoresistor) based on piezoresistance factors of Harley's empirical model [3] and Kanda's theoretical values, (B)  $\beta^*$  of 15  $\mu\text{m}$  thick piezoresistive cantilever, and (C) force sensitivity of piezoresistive cantilevers with various cantilever dimensions. The analytical model (solid lines) is in good agreement with experimental results (circles).

compensates for depth effects (lower doping concentrations have higher piezoresistance factors, while bending stress decreases linearly with depth).

## OPTIMIZATION

We present four parameter categories for optimizing piezoresistive cantilever performance: 1) cantilever dimension (width, length, and thickness), 2) piezoresistor dimension, 3) bias voltage, and 4) fabrication process parameters (doping concentration, annealing time and temperature).

### Cantilever Dimensions

Measurement bandwidth, desired stiffness of cantilever and desired cantilever thickness determine cantilever length and width. The maximum bandwidth is usually limited by the resonant frequency ( $f_n$ ) of the cantilever. The stiffness ( $k_c$ ) of cantilever is set by the sample stiffness: a soft cantilever is good for a soft sample because stiff cantilevers can damage soft samples. The minimum useful cantilever thickness is limited by selected process parameters, such as ion implant energy, dose, anneal temperature and time.

The desired bandwidth, stiffness and cantilever thickness determine the optimal cantilever length and width:

$$l = \left(\frac{E}{\rho_s}\right)^{1/4} \left(\frac{t}{2\pi f_n}\right)^{1/2} \quad [5]$$

$$w = \frac{4k}{E} \left(\frac{l}{t}\right)^3 \quad [6]$$

where  $E$  is Young's modulus and  $\rho_s$  is density of the beam. Fig. 4 suggests lengths of silicon cantilevers over a range of resonant frequency and thickness.

### Piezoresistor Dimensions

We choose piezoresistor length and width to minimize force resolution. Force resolution is inversely proportional to the piezoresistor width (Eq. 4). Therefore, we select a piezoresistor width as large as possible ( $w_p = w/2$ ). However, the choice of piezoresistor length is not simple: while a longer piezoresistor is better for  $1/f$  noise, a shorter piezoresistor is better for Johnson noise and force sensitivity (Eq. 4). We find the optimal ratio of cantilever and piezoresistor length ( $a = l_p/l$ ) by differentiating the force resolution with respect to  $a$ . The optimal  $a$  is function of the ratio of  $1/f$  noise and Johnson noise, integrated over the bandwidth, when piezoresistor length extends the full cantilever length (Fig. 5):

$$\sqrt{\frac{a^3 + 2a^2}{2 - 3a}} = \left(\frac{1/f \text{ noise (V)}}{\text{Johnson noise (V)}}\right)_{l_p=l} \quad [7]$$

The optimal  $a$  is  $2/3$  for  $1/f$  noise dominant cantilevers and  $0$  for Johnson noise dominant cantilevers. Thus, the optimal piezoresistor length can be between  $0$  and  $2/3$  of cantilever length depending on the ratio of  $1/f$  noise and Johnson noise. Piezoresistor thickness is subsequently determined once we select the fabrication process.

### Bias Voltage

Once the cantilever and piezoresistor dimensions are determined from Eq. 5, 6 and 7, we choose a bias voltage by considering power dissipation of the piezoresistor. Although higher bias voltage has little effect on the force resolution of a  $1/f$  noise dominant cantilever, it significantly improves force resolution of Johnson noise dominant cantilevers (Eq. 4). However, high bias voltage will increase power dissipation and operating temperature,

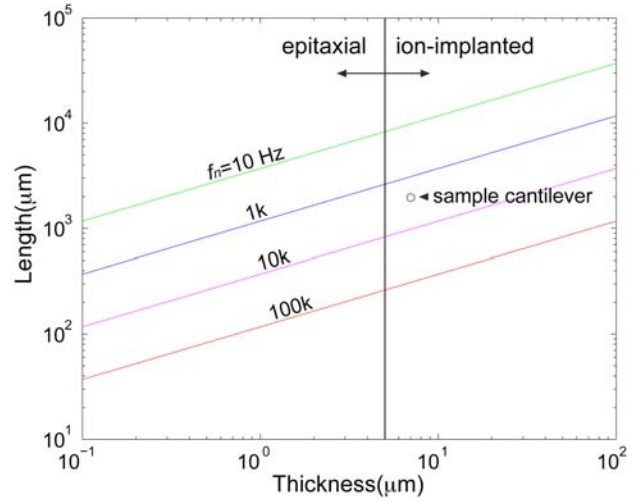


Figure 4: Relation of piezoresistive cantilever dimensions. Target resonant frequency (bandwidth) determines cantilever dimensions. The circle (2000  $\mu\text{m}$  long and 7  $\mu\text{m}$  thick, and 2.5kHz resonant frequency) is one of our sample cantilevers.

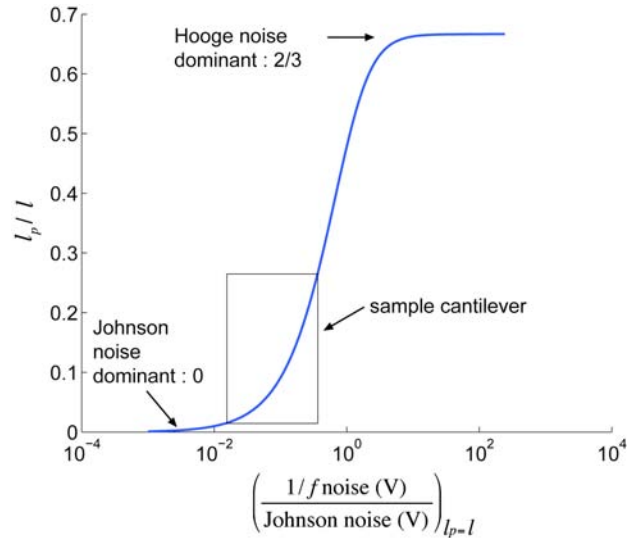


Figure 5: Optimization of piezoresistor length. The optimal piezoresistor length can be determined by the ratio of  $1/f$  noise and Johnson noise when piezoresistor extends the full cantilever. We found that the optimal length ratio of  $1/f$  noise dominants and Johnson noise dominant cantilever is  $2/3$  and  $0$  respectively. The box indicates optimal piezoresistor length range of a typical cantilever.

and could lead to mechanical destruction or piezoresistance reduction (piezoresistivity is inversely proportional to temperature). Therefore, we should choose as high a bias voltage as power dissipation will allow.

### Fabrication Process Parameters

Once cantilever and piezoresistor dimensions and bias voltage are set, then we can calculate force resolution for a variety of process conditions using Eq. 2, 3, and 4. Fig. 6 shows force resolution performance of a sample cantilever over a range of process conditions (dose and diffusion length). We can choose desired fabrication process parameters such as doping concentration, annealing time and temperature from Fig. 6.

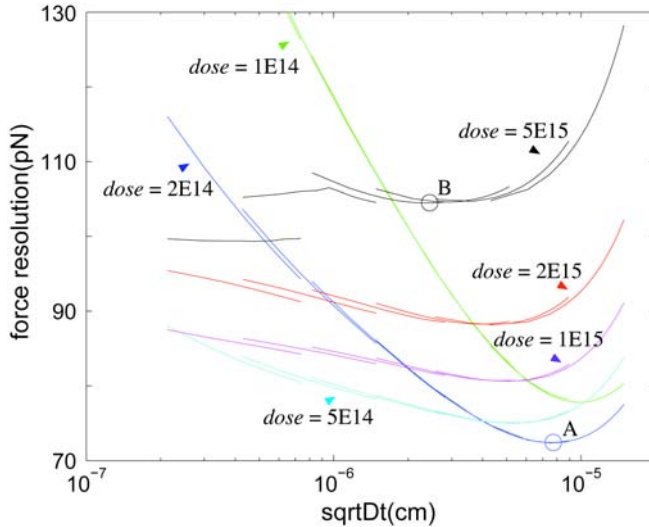


Figure 6: Optimization of typical piezoresistive cantilevers. Target design conditions are 2.5 kHz bandwidth, 0.05 N/m stiffness, <10 mW power, < 5V bias voltage, and 700  $\Omega$  resistance. Circle A and B indicates the lowest force resolution of cantilevers with low dose and high dose respectively. The design parameters and specification of these cantilevers are summarized in Table 1.

### Sample Piezoresistive Cantilever Optimization

We chose design and operating parameters to optimize a sample piezoresistive cantilever for use with an INA 103, Texas Instruments, USA, a low Johnson noise commercial instrumentation amplifier. The desired design conditions included 1 to 2500 Hz bandwidth, 0.05 N/m stiffness, <10 mW power dissipation, <5 V bias voltage, >700  $\Omega$  resistance, and a 7  $\mu\text{m}$  thick silicon on insulator (SOI) wafer. From Eq. 5 and 6, the cantilever should be 2000  $\mu\text{m}$  long and 30  $\mu\text{m}$  wide (circle in Fig.4). Based on TSUPREM4 simulation data for a variety of ion implantation and annealing conditions (1E14 to 5E16  $\text{cm}^{-2}$  dose, 900 to 1150  $^{\circ}\text{C}$  and 0 to 180 minutes anneals), we calculated  $a$ , bias voltage,  $\beta^*$ , force sensitivity, noise and force resolution from Eq. 2, 3, 4, 7 (Fig. 5 box and Fig. 6 circles). The parameters are summarized in Table 1 for low vs. high dose cases.

### CONCLUSION

We have presented an analytical model to predict force sensitivity and resolution of ion implanted piezoresistive microcantilevers. We characterized several piezoresistive cantilevers over a range of process conditions and verified that the model agrees with simulation and experiment with less than 20% error. We have also shown this model can be used for optimization of cantilever performance for a given process. This optimization technique is useful in the design of piezoresistive sensors for a variety of applications with complex design conditions, e.g. broad bandwidth (>100kHz), small force resolution (~pN), large dynamic range (nN~mN), or CMOS compatible sensors.

### ACKNOWLEDGEMENTS

This work was performed in part at the Stanford Nanofabrication Facility (a member of the National Nanotechnology Infrastructure Network) which is supported by the National Science Foundation under Grant 9731293, its lab members, and the industrial members of the Stanford Center for Integrated Systems. Funding was also provided under NSF ECCS-0449400,

Table 1: Design and operating conditions and specification of piezoresistive cantilevers with low dose (circle A in Fig. 6) and high dose (circle B in Fig. 6).

Parameters	Low Dose (2E14 $\text{cm}^{-2}$ )	High Dose (5E15 $\text{cm}^{-2}$ )
$lwt$ ( $\mu\text{m}$ )	2000 $\times$ 30 $\times$ 7	2000 $\times$ 30 $\times$ 7
$l_p w_p t_p$ ( $\mu\text{m}$ )	80 $\times$ 15 $\times$ 2.18	220 $\times$ 15 $\times$ 1.79
anneal temperature ( $^{\circ}\text{C}$ )	1100	1000
anneal time (min)	135	135
bias voltage (V)	5	2.6
<b>Specification</b>		
resistance ( $\Omega$ )	2500	700
resonant frequency (kHz)	2.5	2.5
stiffness (N/m)	0.05	0.05
power dissipation (mW)	10	10
$\beta^*$	0.68	0.44
force sensitivity (V/N)	4910	1630
noise (nV)	356	170
force resolution (pN)	72	104

ECCS-0425914, and NIH 1 R01 EB006745-01A1. S-JP was supported by a Samsung fellowship.

### REFERENCES

- [1] M. Tortonese, R. C. Barrett, and C. F. Quate, "Atomic Resolution with an Atomic Force Microscope using Piezoresistive Detection," Appl. Phys. Lett., 62, 834 (1993).
- [2] S.-J. Park, M. B. Goodman, and B. L. Pruitt, "Analysis of Nematode Mechanics by Piezoresistive Displacement Clamp," Proc. Natl. Acad. Sci. USA, 104, 17376 (2007).
- [3] J. A. Harley and T. W. Kenny, "1/f Noise Considerations for the Design and Process Optimization of Piezoresistive Cantilevers," J. Microelectromech. Sys, 9, 226 (2000).
- [4] J. A. Harley and T. W. Kenny, "High-sensitivity Piezoresistive Cantilevers under 1000A thick," Appl. Phys. Lett., 75, 289 (1999).
- [5] F.N. Hooge, "1/f Noise Sources," IEEE Trans. Electron Devices, 41, 1926 (1994).
- [6] B. L. Pruitt and T. W. Kenny, "Piezoresistive Cantilevers and Measurement System for Characterizing Low Force Electrical Contacts," Sens. Actuators A, 104, 68 (2003).
- [7] B. L. Pruitt, W. T. Park, and T. W. Kenny, "Measurement System for Low Force and Small Displacement Contacts," J. Microelectromech. Sys, 13, 220 (2004).
- [8] Y. Kanda, "Piezoresistance Effect of Silicon," Sens. Actuators A, 28, 83 (1991).

# OBSERVATIONS OF FIXED AND MOBILE CHARGE IN COMPOSITE MEMS RESONATORS

G. Bahl<sup>1</sup>, R. Melamud<sup>1</sup>, B. Kim<sup>1,3</sup>, S. Chandorkar<sup>1</sup>, J. Salvia<sup>1</sup>, M.A. Hopcroft<sup>1,3</sup>, R.G. Hennessy<sup>1</sup>, S. Yoneoka<sup>1</sup>, C.M. Jha<sup>1</sup>, G. Yama<sup>2</sup>, D. Elata<sup>1</sup>, R.N. Candler<sup>2</sup>, R.T. Howe<sup>1</sup>, and T.W. Kenny<sup>1</sup>

<sup>1</sup>Stanford University, Stanford, CA, USA

<sup>2</sup>Robert Bosch Corporation, USA

<sup>3</sup>currently at University of California Berkeley, CA, USA

## ABSTRACT

This paper investigates dielectric charge in oxide-coated composite-beam silicon electrostatic resonators. The effects of charge in the oxide layers on resonant frequency are theoretically modeled. Evidence for the presence of both fixed and mobile charge is presented through experimental studies. It is shown that the motion of charge is controllable through the bias voltage applied to the resonator. These studies are relevant for improving the reliability of non-contacting MEMS where dielectrics may be present such as timing references, inertial sensors, and optical actuators.

## INTRODUCTION

Dielectric charging in contacting structures such as RF capacitive switches has been studied extensively. In these structures capacitance measurements are used to infer charge through partial deflection or complete pull-in measurements [1, 2]. In stiff non-contacting structures such as resonators, accelerometers and gyroscopes, charge build-up can also affect the stability and reliability of the transducer. Pull-in measurements are often impractical for such structures and do not emulate standard operating conditions. Here, the use of resonant frequency measurements can complement pull-in measurements as a non-contact method to study the evolution of charge in dielectrics under low-field conditions.

We utilize oxide-coated composite-beam silicon resonators designed for passive temperature compensation as test structures [3]. This paper presents evidence for trapped charge in the resonator oxides by two methods: observing frequency dependence on bias voltage to show the existence of built-in electric fields within the resonating device, and examination of transient behavior of frequency under controlled bias and temperature conditions.

## DEVICE DESCRIPTION

### Resonator fabrication

Single-anchor double-ended tuning fork resonators are fabricated on 20  $\mu\text{m}$  device layer SOI wafers using the “epi-seal” single-wafer encapsulation process (Fig.1) [4]. Each resonator beam is 200  $\mu\text{m}$  in length and the width  $W$  is the design variable.

The devices fabricated in this technology are vacuum encapsulated with pristine silicon surfaces and are protected from environmental agents. Native oxide on silicon surfaces is destroyed during the high temperature sealing step performed during the final steps of the encapsulation process. No additional oxide is expected to grow within the encapsulation since nitrogen and hydrogen are flooded in during the sealing step and are later annealed out. Long-term frequency stability within the encapsulation has previously been shown for silicon-only devices [5].

### Dielectric Coating

An oxidation step can be performed prior to sealing the devices with the silicon cap layer. The oxide is thermally grown at 1100°C in a wet ambient. The process duration varies with the oxide thickness desired. Since this oxide is significantly thicker (compared to a native oxide layer) it can survive the high temperature sealing step.

The SOI wafers used in fabrication have a (100) crystal

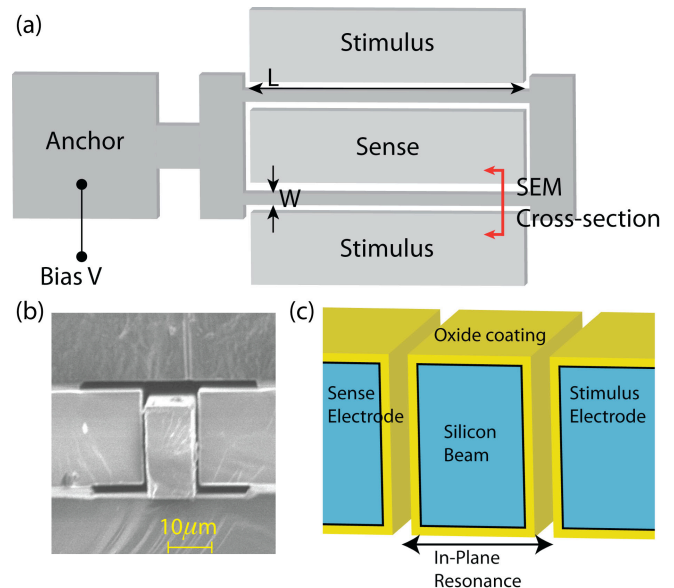


Figure 1: (a) Top view schematic of resonator with electrical setup of the device. (b) SEM of cross-section shown. (c) Schematic of SEM cross-section.

orientation at the surface. The devices are oriented such that the etched device layer side-walls primarily expose the (110) plane. The oxide thickness on the wafer surface is measured and the corresponding sidewall oxide thickness can then be estimated using the Deal-Grove oxidation model [6]. The devices presented in this paper have an estimated 0.45  $\mu\text{m}$  oxide coating on (110) surfaces.

### Electrical setup

In all experiments the resonator is connected to a source of fixed bias voltage  $V$  (Fig.1). The stimulus and sense electrodes are nominally held at ground, though they do also support a small amplitude AC resonance signal. All AC signals are assumed to be negligible in the theoretical analysis, though higher order effects are expected for large signal amplitudes [7].

## MODELING CHARGE EFFECTS

Each resonator beam forms two capacitors with the stimulus and sense electrodes adjoining it. The resonator beam height defined by the device layer ( $\sim 20 \mu\text{m}$ ) and length ( $L \sim 200 \mu\text{m}$ ) are significantly greater than the gap width ( $\sim 1.5 \mu\text{m}$ ) so it is reasonable to model these capacitors with the parallel plate approximation. The stimulus and sense electrodes are nominally held at DC ground potential. Thus, the four individual capacitors for both tuning fork beams are structurally and electrically (DC) identical and can thus be treated as a single capacitor with the same bias voltage across it but with four times the area (Fig.2). The spatial distribution of charge within the dielectrics is unknown but can be modeled as an equivalent uniform surface charge at the vacuum-dielectric interface.

Electrostatic spring softening explains how the resonance frequency of a parallel-plate resonator depends on the applied bias

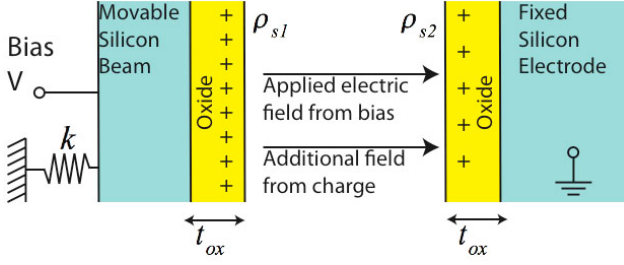


Figure 2: Single-capacitor equivalent model of the resonator system.

voltage [8]. In the absence of additional electric fields, the polarity of the bias voltage does not affect the spring softening since the voltage term is squared. However, when charge is present in the dielectrics additional field may arise within the actuation gap. This additional field can be modeled as a built-in voltage  $\Delta V$ , additive or subtractive to the applied bias depending on bias polarity. This changes the effective bias voltage and modifies the frequency.

Under electrical spring softening with small resonance amplitude the resonant frequency is calculated as

$$f \approx f_o \left( 1 - \frac{\Delta k_e}{2k} \right) \quad (1)$$

where  $k$  is the mechanical spring constant. The electrical spring softening  $\Delta k_e$  due to both charge and applied bias voltage can be analytically calculated. Specifically, the dependence on voltage can be calculated to be

$$\Delta k_e \propto (V + \Delta V)^2 \quad (2)$$

The built-in voltage can be expressed as a function of the uniform vacuum-oxide surface charge densities as follows

$$\Delta V = \frac{t_{ox}}{\epsilon_{ox}} (\rho_{s1} - \rho_{s2}) \quad (3)$$

If the amount of surface charge on the two dielectrics is identical i.e.  $\rho_{s1} = \rho_{s2}$ , the built-in electric field will be canceled out and there is no effect on frequency.

Using equations 1-3, when frequency is plotted as a function of bias voltage  $\Delta V$  appears as a translation along the voltage axis. As a consequence when frequency is plotted against magnitude of bias, the frequency appears to shift in opposite directions depending on bias polarity (see Fig.3). Although the zero charge state ( $\Delta V = 0$ ) cannot be observed in a given resonator that has charge built-in, the polarity dependent splitting of the frequency-

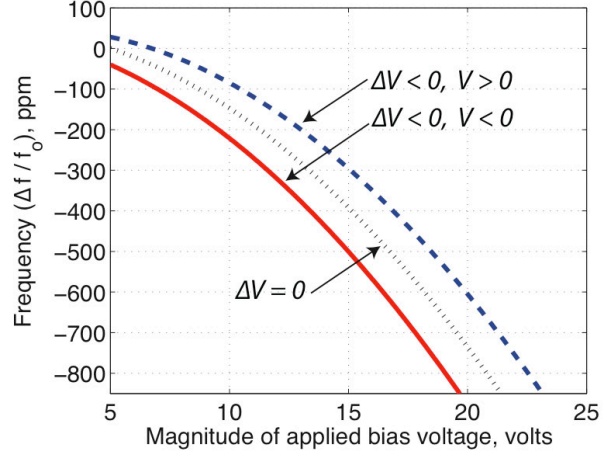


Figure 3: Simulation result for a 1MHz resonator based on the charge model with the  $\Delta V = 0$  and  $\Delta V < 0$  cases plotted. Resonance frequency depends on bias polarity when charge is present in the oxide coating, i.e. when  $\Delta V \neq 0$ .

bias curve should still be seen. In recently published work the use of frequency-bias curves to extract the uncharged mechanical resonance frequency has been discussed [9].

## RESULTS

Environmental factors (such as humidity) known to affect charge states on dielectrics cannot act on the sealed devices. The primary control variables on the system are temperature and bias voltage. The possibility of unintentional electrostatic discharge occurring within the encapsulation and having affected the behavior of these devices is unlikely, though it cannot be entirely ruled out.

### Fixed oxide charge

The frequency of the resonant peak is monitored for various bias voltages and is plotted against the magnitude of bias. All measurements were made in a temperature-stabilized oven using a HP 4395A Network Analyzer with an amplifier at the resonator output to boost the signal. By fitting this data to the theoretical model  $\Delta V$  can be extracted. Some representative data sets are shown in Fig.4.

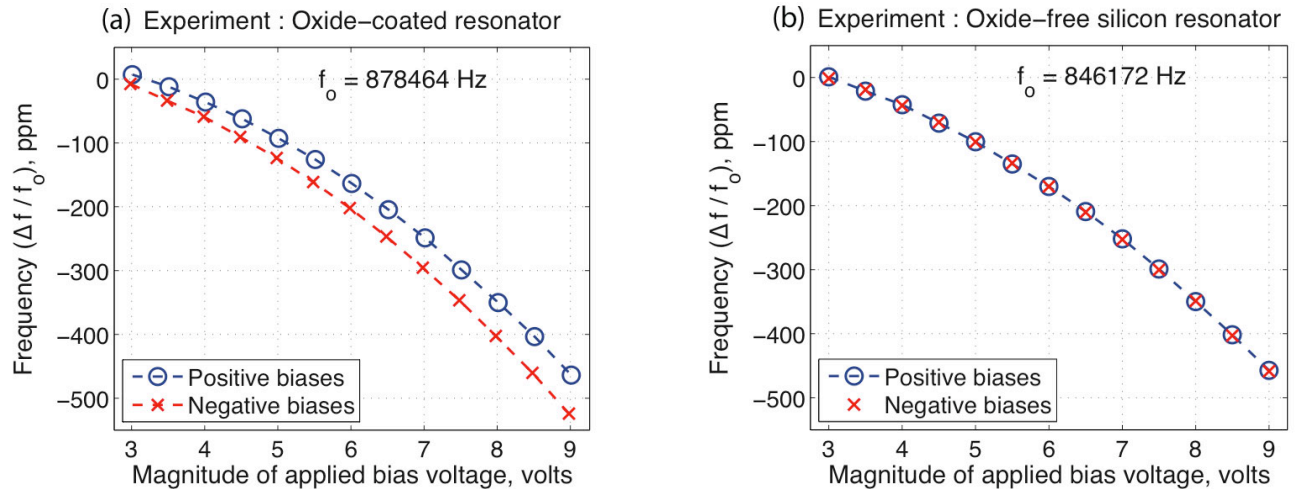


Figure 4: Bias polarity dependence in oxide-coated resonators. (a) Oxide-coated resonators show both positive and negative  $\Delta V$  indicating the presence of fixed charge in the dielectric. The frequency-bias curve of a resonator with  $\Delta V < 0$  is shown here. (b) Oxide-free silicon devices show no measurable bias polarity dependence.

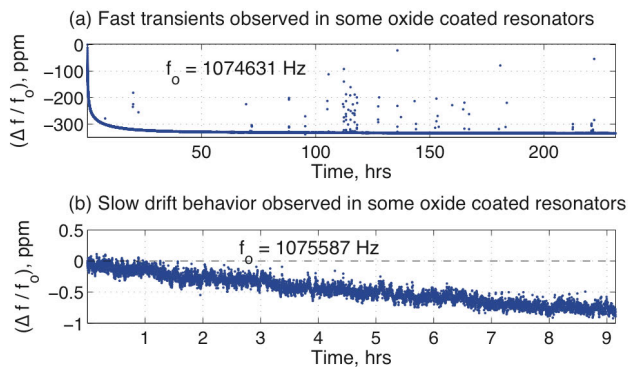


Figure 5: Frequency drift behavior seen in some oxide-coated resonators.

Of the 21 oxide-coated resonators that were tested all exhibit non-zero  $\Delta V$  values in the range of -250 mV to +340 mV. Notably, most oxide-coated resonators from this wafer exhibit negative values of  $\Delta V$ . In these resonators we note that an observed voltage shift of 100 mV corresponds to an equivalent surface charge imbalance ( $\rho_{s1} - \rho_{s2}$ ) of approximately  $7.67 \times 10^{-10} \text{ C/cm}^2$  as calculated from equation 3. The reasons for this variation in oxide charge imbalance over the wafer and predominance of negative values of  $\Delta V$  are being investigated. Silicon-only resonators of identical design were also tested (9 devices) and showed no measurable frequency asymmetry (fitted  $\Delta V = -1 \pm 4 \text{ mV}$ ).

#### Mobile oxide charge

Mobile charge observations are made with the oxide-coated resonators constantly actuated at their resonant frequency when connected in a closed-loop oscillator circuit. Frequency readings are taken using an Agilent 53132A Universal Frequency Counter.

Some devices exhibit large decaying transients over short durations immediately after the bias voltage is changed. These transients are the focus of this study (Fig.5a). Additionally, some devices show very little drift over long durations of time, and no transients (Fig.5b). Finally, many devices appear to show no drift or transient behavior over currently tested observation intervals and are usable for frequency stability experiments. The reason why certain oxide-coated resonators exhibit frequency transients while others do not is presently under investigation. This behavior is absent in silicon-only resonators made with the same “epi-seal”

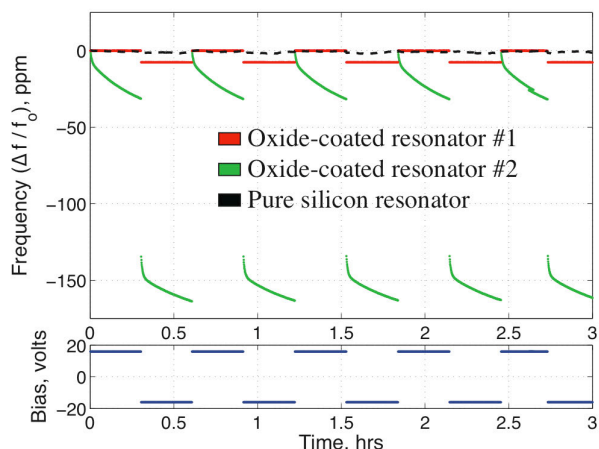


Figure 6: Frequency trends of three lithographically identical devices ( $W = 5.75 \mu\text{m}$ ) showing transients and bias polarity dependence.

technology [5].

The bias-frequency sensitivity of these resonators can be extracted from the frequency-bias curves shown previously and is around 60–100 ppm/Volt depending on beam width  $W$ . Bias voltage is controlled using a Valhalla 2701C voltage calibrator to a stability better than 1 mV. As a result the bias voltage cannot account for the observed transients in frequency. Although temperature is kept constant in a stabilized oven environment there are still some random fluctuations that affect the frequency. Since the resonators are passively temperature-compensated with the oxide [3], temperature fluctuations can only account for frequency variations on the order of 3 ppm or less at the operating temperature of 40°C. The oscillator circuit boards are reusable and are often exchanged between devices to ensure that any drifts are not oscillator artifacts.

Fig.6 shows the frequency trends of three lithographically identical devices ( $W = 5.75 \mu\text{m}$ ) as the bias is alternated between +18 V and -18 V. Bias polarity dependence of frequency is visible in the oxide-coated resonators. In addition, oxide-coated resonator #2 shows transient behavior in time. Both effects are absent in silicon resonators and the data from one silicon device is shown. Reproducibility of the short duration transients in oxide-coated resonators strongly indicates that shape change, fatigue, and other burn-in processes or material issues can be ruled out.

The transient behavior of frequency can be controlled using various bias alternation schemes. In the experiment shown in Fig.7, a negative bias  $V_2$  is applied momentarily to partially reverse the effect of charge movement due to positive bias  $V_1$ . Frequency readings are not taken at bias  $V_2$  since the oscillator does not operate at low bias magnitudes ( $V_2 = 0 \text{ V}, -5 \text{ V}$  in this experiment). A comparison of four experiments plotted against a common reference frequency  $f_0$  reveals a level of control over the net frequency drift.

Since the frequency is seen to be a function of the biasing history, to replicate an experiment the initial conditions and stimuli must be restored exactly. The dielectrics have an unknown volume charge distribution, however, and the only observable quantities from the system are the frequency and amplitude of resonance. It is thus unlikely that the actual charge distribution at the beginning of any experiment can be determined or restored using this measurement method.

Transients in frequency at a fixed bias voltage seem to

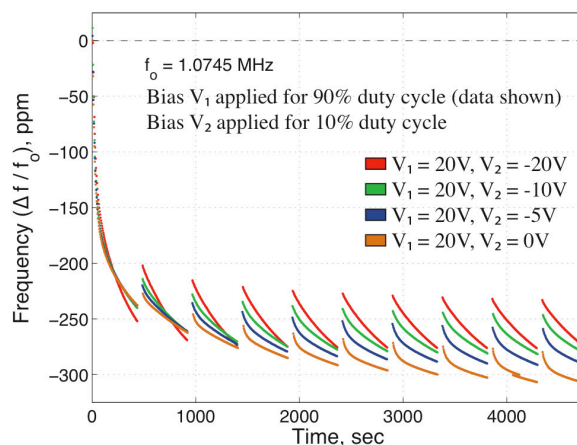


Figure 7: Bias control of frequency transients in an oxide-coated resonator. Multiple experiments are superimposed to show frequency dependence on biasing scheme.

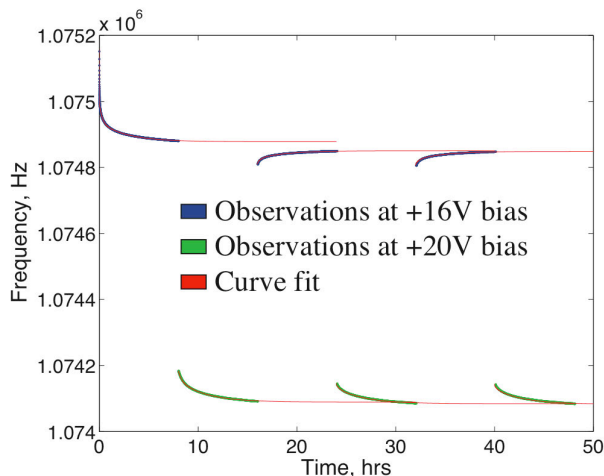


Figure 8: Demonstration of bias-dependent steady states.

approach a steady state when given enough time to stabilize. As is seen in Fig.7, however, the transients reappear at the same voltage  $V_i$  after the devices are rested for some time with zero applied voltage. This suggests that there may be a restoring effect acting on the charge that does not require an externally applied electric field.

This effect can be further studied with the experiment shown in Fig.8. Here, the bias voltage polarity is maintained constant at all times while its magnitude is varied. The device is initially primed by bringing the frequency close to its steady state at  $V = 16$  V bias. This transient can be interpreted as an *increase* of  $\Delta V$  with time under the influence of the applied electric field (charge redistribution) to reach an equilibrium state. The bias voltage  $V$  is then increased to 20 V to increase the electric field across the gap. The frequency is allowed to drift to its new steady state. This second downward transient indicates a further movement of charge and a further *increase* in  $\Delta V$ . Then when the field is reduced by reducing applied bias to 16 V, the frequency is observed moving in the opposite direction back towards the 16 V state. This indicates that  $\Delta V$  is *decreasing* over time although the applied electric field is still in the same direction (since bias polarity is maintained). It must be concluded then that the applied electric field is no longer the dominant driving force on the charge. It is seen that this back and forth movement between two steady states happens consistently as bias is alternated in this manner.

It should also be noted that frequency transients appear to accelerate with increasing temperature, though the specific time constants and temperature-dependence is a direction for future study. It is yet to be determined whether the long-duration drifts are also caused by mobile charge.

## CONCLUSIONS

The devices that show frequency transients offer an excellent opportunity to study the behavior, mechanisms and mitigation of mobile charge. It must be noted that there are also oxide-coated resonators fabricated in this same process and on the same wafers that exhibited much smaller bias splits and much smaller transients and smaller long-term drifts. The presence of a significant fraction of oxide-coated resonators that do not exhibit the effects described in this paper is an important indication that the elimination of these effects may be possible.

Currently we are investigating process non-uniformities, plasma charging, and other possible sources of the trapped charge, and the negative predominance of the built-in potential  $\Delta V$  in non-transient devices. Hermeticity of the resonator environment and the ability to control the amount of oxide in identical resonators provides a well-controlled and highly sensitive scientific tool to non-destructively study the effects and time-evolution of charge on dielectrics in MEMS under low-field conditions.

## REFERENCES

- [1] C. Goldsmith, J. Ehmke, A. Malczewski, B. Pillans, S. Eshelman, Z. Yao, J. Brank, and M. Eberly, "Lifetime Characterization of Capacitive RF MEMS Switches," IEEE International Microwave Symposium, 1, (2001)
- [2] R.W. Herfst, H.G.A. Huizing, P.G. Steeneken, and J. Schmitz, "Characterization of Dielectric Charging in RF MEMS Capacitive Switches," IEEE International Conference on Microelectronic Test Structures, (2006), pp.133-136
- [3] R. Melamud, B. Kim, S.A. Chandorkar, M.A. Hopcroft, M. Agarwal, C.M. Jha, and T.W. Kenny, "Temperature-Compensated High-Stability Silicon Resonators," Applied Physics Letters, 90, 244107
- [4] R.N. Candler, M.A. Hopcroft, B. Kim, W.-T. Park, R. Melamud, M. Agarwal, G. Yama, A. Partridge, M. Lutz, and T.W. Kenny, "Long-Term and Accelerated Life Testing of a Novel Single-Wafer Vacuum Encapsulation for MEMS Resonators," Journal of Microelectromechanical Systems, 15, (2006), pp.1446-1456
- [5] B. Kim, R.N. Candler, M.A. Hopcroft, M. Agarwal, W.-T. Park, and T.W. Kenny, "Frequency Stability of Wafer-Scale Film Encapsulated Silicon Based MEMS Resonators," Sensors and Actuators, A: Physical, 136, pp.125-131, (2007)
- [6] J.D. Plummer, M.D. Deal, and P.B. Griffin, *Silicon VLSI Technology*. New Jersey: Prentice Hall, 2000
- [7] M. Agarwal, S.A. Chandorkar, R.N. Candler, B. Kim, M.A. Hopcroft, R. Melamud, C.M. Jha, T.W. Kenny, and B. Murmann, "Optimal Drive Condition for Nonlinearity Reduction in Electrostatic Microresonators," Applied Physics Letters, 89, 214105, (2006)
- [8] S.G. Adams, F.M. Bertsch, K.A. Shaw, P.G. Hartwell, F.C. Moon, and N.C. MacDonald, "Capacitance Based Tunable Resonators," J. Micromech. MicroEng., 8, (1998), pp.15-23
- [9] S. Kalicinski, H.A.C. Tilmans, M. Wevers, and I. De Wolf, "A New Method to Determine the Mechanical Resonance Frequency, Quality Factor and Charging in Electrostatically Actuated MEMS," IEEE MEMS 2008, Tuscon, Arizona, USA, Jan 13-17, (2008)

## ACKNOWLEDGEMENTS

This work was supported by DARPA CIEMS, Bosch, Epson, HP, Agilent, Boeing, Qualcomm, DARPA HERMIT (ONR N66001-03-1-8942), and the National Nanofabrication Users Network facilities funded by the National Science Foundation under award ECS-9731294, and the National Science Foundation Instrumentation for Materials Research Program (DMR 9504099), and the Stanford Graduate Fellowship support for R. Melamud. We thank Andrew Graham, Wes Smith and Scott Lord for their support.

# FRACTURE PREDICTION OF SINGLE CRYSTAL SILICON MEMS UNDER MULTI-AXIAL LOADING

A.M. Fitzgerald, D.M. Pierce, C.D. White, B.M. Huigens, and J.W. Eaton  
A.M. Fitzgerald & Associates, LLC, San Carlos, California, USA

## ABSTRACT

We describe and validate a new failure prediction methodology specifically designed for single-crystal MEMS devices under general service loadings. The methodology uses experimental data efficiently generated from fracture testing of simple test specimens to calculate a series of Weibull parameters descriptive of specific surface conditions. These data, combined with finite element modeling, are used to predict the fracture load distribution for any MEMS device fabricated by the same process, under any type of loading. We demonstrate the accuracy of our method by comparing predicted fracture probabilities against actual fracture test results for a micro-mirror in two distinct multi-axial loading configurations.

## INTRODUCTION

The reliability of a MEMS design, even with state-of-the-art simulation tools, can only be determined through destructive tests on finished devices. Determination of reliability therefore occurs very late in the development cycle, after significant time and funds have already been expended. This predicament occurs because traditional finite element (FE) simulations are incapable of calculating failure predictions for MEMS devices, due to the nature of the brittle materials from which they are made.

Brittle materials fail when the applied stress at a critically-sized flaw exceeds the fracture toughness of the material. If every flaw in and on a MEMS device could be measured and mapped, the principles of fracture mechanics would allow for a deterministic calculation of the fracture strength. However, while such a metrology-oriented approach is theoretically possible using tools such as Scanning Electron Microscopy (SEM) or Atomic Force Microscopy (AFM), from a practical standpoint it would be prohibitively time-consuming and expensive.

Statistical characterization of flaw populations provides a practical solution for brittle structure analysis. The material volume in a single-crystal silicon MEMS structure is, conveniently, essentially flaw-free due to the high purity and crystallinity of the silicon wafer. The etch processing used to machine silicon, by its nature, creates significant surface flaws, and the remaining flaw shapes and sizes are sensitive to process recipe [1,2]. Test-driven, statistical characterization of the process-specific surface flaw distributions is therefore a cornerstone of this prediction method.

Our methodology employs FE simulation, calibrated by experimental data, to predict fracture in MEMS devices under service conditions. First, simple four-point bend test specimens are used to generate fracture stress distribution data descriptive of the specific etch processes used to manufacture the MEMS device under study [3]. Next, a computational model of the MEMS device is created using commercial FE software. Our algorithm then merges the experimental data and the FE model results to calculate the fracture probability of the device under a range of given applied loads.

Although other researchers have explored similar methods, all previous studies are limited to fracture prediction of beams in uniaxial stress [4-6]. We believe this is the first demonstration of accurate fracture prediction for a MEMS device with realistically complex geometries, loadings, and stress fields. As an additional

benefit, our approach does not require time-consuming fractographic inspection or modeling of individual test specimens to generate accurate results.

## METHODOLOGY

Our method assumes that fracture initiation in single-crystal MEMS devices depends only on the following: (i) the condition of the device surface areas, and (ii) the stress distributions on those areas. These assumptions are well supported in the literature [1,7]. While applied stresses can be calculated in a straightforward manner using FE, a quantitative description of the surface conditions is more challenging.

### Weibull Statistics

The only practical approach to characterizing the surface conditions is to use a statistical description. We use the Weibull probability function to describe the fracture stress distribution of a population of test specimens fabricated by a specific process, which in turn provides a relevant, quantitative description of the surface characteristics of that process [2,8].

The Weibull probability density function is commonly employed to characterize failure in brittle materials at the macro- and micro-scales, for both single-crystal and polycrystalline materials [4,9]. A two-parameter Weibull fit to a sample population of fracture stresses provides a characteristic strength,  $\sigma_0$ , defined as the stress at which 63.2% of the specimens fail, and the Weibull modulus,  $m$ , which describes the scatter in the distribution (lower values of  $m$  correspond to greater scatter.) Independent Weibull parameters are required to describe each different type of surface condition present in a MEMS device to be analyzed, including the polished surface of the wafer.

### Four-Point Bend Beam

Test specimens are required to determine the Weibull parameters that characterize the various surface conditions. Although any type of test specimen geometry may be used, the four-point bend beam has a simple geometry and loading which is particularly advantageous. In this type of test specimen, the maximum stress develops uniformly on the surface of the beam within a well-defined area [3]. As a result, the fracture stress,  $\sigma_f$ , is calculated analytically according to Eqn. (1).

$$\sigma_f = 3PL/4bd^2 \quad (1)$$

Where  $P$  is the applied load at fracture,  $L$  is the support span,  $b$  is the width of the beam, and  $d$  is the beam depth.

In order to generalize the Weibull parameters to multi-axial loading conditions, a reference area from the test specimen,  $A_0$ , is required. The reference area is defined as the entire area upon which the maximum stress (and therefore the fracture stress) develops and by definition includes the region in which the fracture initiates. The reference area is used to area-normalize the test specimen results and allow their application to MEMS devices with more complex geometries.

In the four-point bend beam, the parameter  $A_0$  is simply the product of the distance between the inner two load points and the

width of the beam,  $b$ .

The use of a four-point bend beam eliminates the need for FE analysis to calculate maximum stresses and reference areas, which complicated previous analyses of cantilever specimens [10], and for detailed inspection of every sample to determine the location of fracture initiation [11]. The elegance of the four-point bend beam simplifies gathering experimental data and enables cost-effective surface characterization.

### Probability Calculation

Once the surfaces of the test specimens have been characterized, a FE model of the MEMS device to be analyzed is constructed. To capture the mechanical response of the device, orthotropic material properties are defined for the silicon volume. In cases where solution speed is critical, such as parametric design optimization, isotropic material properties for silicon may be substituted. This assumption leads to an error in the stress distribution of approximately 3% or less [1].

Standard FE modeling practice is used to calculate the stress distribution in the entire MEMS device under service loading. After solution, the first, second and third principal stresses ( $S_1$ ,  $S_2$ ,  $S_3$ ) are readily available at each surface node of the entire device. The tensile principal stresses ( $\hat{S}_1$ ,  $\hat{S}_2$ ,  $\hat{S}_3$ ) at each node of interest are then calculated according to Eqn. (2). As is common in the reliability analysis of brittle materials, compressive stresses are ignored [12,13].

$$\hat{S}_i = \begin{cases} S_i & \text{if } S_i \geq 0, \text{ for } i = 1,2,3 \\ 0 & \text{otherwise} \end{cases} \quad (2)$$

To facilitate further discussion, it is necessary to define some terms. First, let  $n_{type}$  be the total number of surface types associated with a particular MEMS device to be analyzed, where  $k = 1$  to  $n_{type}$ . Hence, the analysis requires  $n_{type}$  sets of Weibull parameters ( $\sigma_{0k}$ ,  $m_k$ ,  $A_{0k}$ ). Next, let  $n_{area}$  be the total number of areas associated with a particular surface type (specific etch), where  $j = 1$  to  $n_{area}$ . Finally, let  $n_{node}$  be the total number of nodes associated with a single surface area, where  $i = 1$  to  $n_{node}$ . The value of  $n_{node}$  will vary from area to area, according to the size of the area and the density of the FE mesh.

To continue, the scalar failure probability per unit area,  $\psi_i$ , at each surface node, is calculated from the tensile principal stresses using an isotropic failure probability function as shown in Eqn. (3) [1,12,13]. Although the fracture toughness,  $K_{IC}$ , varies with crystal axis orientation, the difference is small, and thus the use of an isotropic failure probability function is justified for single-crystal silicon [1].

$$\psi_i = \frac{1}{A_{0k}} \left[ \left( \frac{\hat{S}_1}{\sigma_{0k}} \right)^{m_k} + \left( \frac{\hat{S}_2}{\sigma_{0k}} \right)^{m_k} + \left( \frac{\hat{S}_3}{\sigma_{0k}} \right)^{m_k} \right] \quad (3)$$

Once the nodal values of the failure probabilities are determined per unit area, these values are multiplied by the total area contribution per node,  $\Delta A$ , the area increment. This yields the scalar failure probability,  $f_i$ , at each surface node, as shown in Eqn. (4).

$$f_i = \psi_i \Delta A_i \quad (4)$$

Next, the total probability of failure for the device under

service conditions,  $P_s$ , is estimated as shown in Eqn. (5).

$$P_s(A) = \exp \left[ - \int_A \psi dA \right] \approx \exp \left[ - \sum_{k=1}^{n_{type}} \sum_{j=1}^{n_{area}} \sum_{i=1}^{n_{node}} \psi_i \Delta A_i \right] \Bigg|_j \Bigg|_k \quad (5)$$

Finally, the total device survivability, or reliability,  $R$ , is related to the total failure probability as shown in Eqn. (6).

$$R = 1 - P_s \quad (6)$$

### VERIFICATION EXPERIMENT

We demonstrate our methodology and its accuracy by predicting the reliability of a representative MEMS device. A doubly-suspended MEMS micro-mirror was chosen because it can be loaded in two distinct states, tension and torsion, that produce different complex stress fields in the device.

Following the outlined methodology, four-point bend beam specimens were fabricated and fractured to gather data for both the polished and etched surfaces of the beam, thereby capturing the specific surface conditions that would be present on the micro-mirror. The data were used to make a prediction of the fracture load distributions for the micro-mirror in both load states. Finally, we fractured actual micro-mirror samples in both tension and torsion in order to verify the accuracy of our predictions.

### Specimen Fabrication

Test specimen four-point bend beams and micro-mirrors were fabricated using oxidized, double-polished (100)-orientation silicon wafers (310  $\mu\text{m}$  thickness) as a starting material. The specimen patterns were defined in a single contact lithography step, followed by a plasma etch to remove oxide in the areas to be etched (the remaining field oxide served as a hard mask during the long silicon etch). Next, a Surface Technology Systems (STS) Multiplex ICP etcher was used to deep reactive ion etch entirely through the silicon wafer to define the specimens. The oxide was stripped in buffered oxide etch, and the wafer was sawed to separate the individual specimens. Special precautions were taken during sawing to protect the etched sidewalls from damage.

The four-point bend beams used to calibrate the micro-mirror analysis were designed to fracture in a load range that was easily measured using a macro-scale apparatus. Handling lugs at each end of the beam prevent accidental contact with the etched surface areas (and hence possible damage) during specimen handling, and also facilitate alignment in the test fixture (Fig. 1).

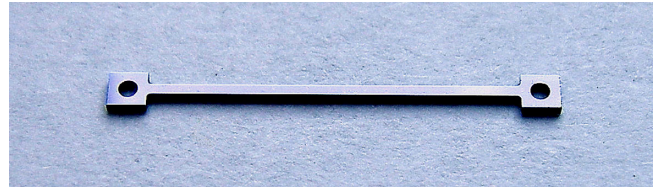


Figure 1: The silicon four-point bend test specimen used for calibration (length = 11.7 mm, width = 300  $\mu\text{m}$ , height = 310  $\mu\text{m}$ , gage length = 8 mm).

The silicon micro-mirrors used to verify the prediction methodology were designed with a support frame which facilitated handling and clamping in the test fixture (Fig. 2). Two alignment holes in the frame allow the sample to be accurately positioned via locating pins in the test fixture.

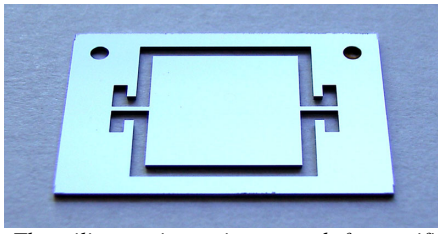


Figure 2: The silicon micro-mirror used for verification (the mirror: 8 x 8 mm, and the flexures: length = 2 mm, width = 300  $\mu\text{m}$ , height = 310  $\mu\text{m}$ ).

### Test Apparatus

A specially designed load fixture was installed on an Instron<sup>®</sup> 5542 mechanical tester. The fixture was designed specifically to accurately locate the samples, to allow easy placement and removal of the samples, and to remove any mechanical play in the tester and load cell (Fig. 3). Careful design of the test fixture allowed for repeatable and efficient collection of the necessary fracture data. All loads were measured using a Transducer Techniques GS0-1K (10N) piezoresistive load cell. The Instron<sup>®</sup> was operated under load control and all specimens were loaded at a rate of 300  $\mu\text{m}/\text{min}$  until fracture.

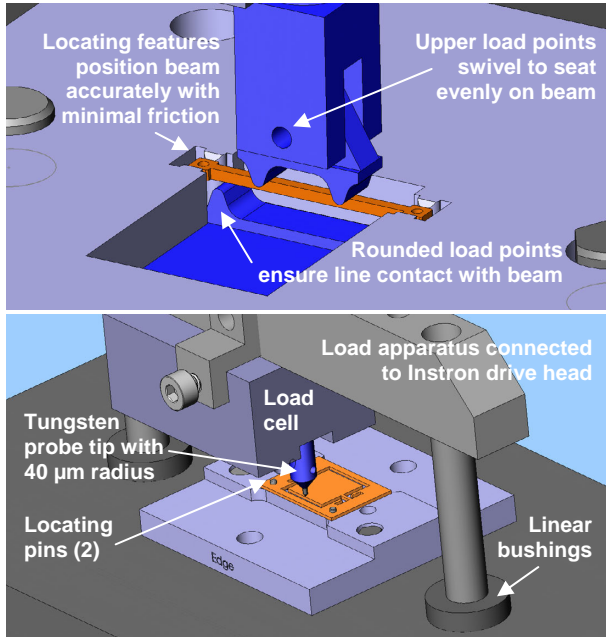


Figure 3: Schematic of loading apparatus and specimen fixtures. Top: Four-point bend fixture. The four-point support design was based on ASTM D-6272-02. Bottom: Fixture plate for edge-loading of micro-mirror. The silicon specimens are in orange.

### Four-Point Bend Beam Calibration Data

Two groups of test specimen beams ( $N = 50$  for each group) were created by randomly sampling twenty-five beams from each of two wafers. One group of beams was loaded in four-point bend to fracture with the polished surface in tension, while the second group was loaded with the etched surface in tension. The fracture stress of each beam was calculated from the fracture load, according to Eqn. (1). A two-parameter Weibull fit was used to characterize the fracture stress distribution of each set of beams, and hence  $n_{type} = 2$ , due to the two types of surfaces (Fig. 4).

As shown in Fig. 4, the polished surface of the beam has a characteristic strength of 636 MPa, which is 15% greater than the

etched surface characteristic strength of 555 MPa. These data provide an illustration of the sensitivity of fracture strength to surface condition.

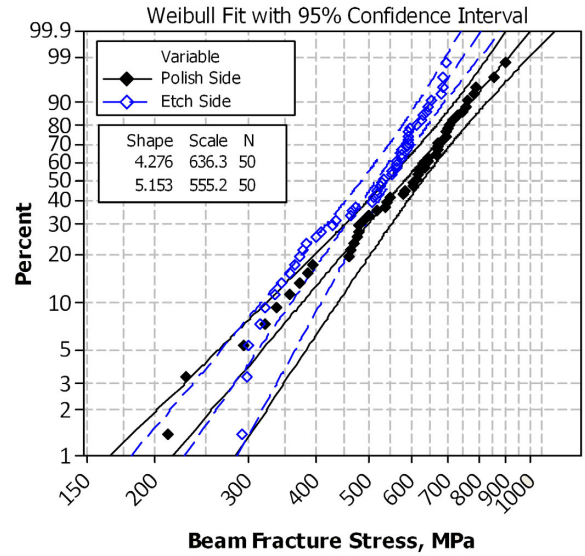


Figure 4: Probability plot of fracture stress data from test specimens ( $Shape = m$ ,  $Scale = \sigma_0$ ).

### Reliability Prediction

Following the outlined methodology, a FE model of the MEMS micro-mirror was created in ANSYS<sup>®</sup> Multiphysics v. 11.0 (Fig. 5). The model employs half-symmetry and a varying mesh density (highest in anticipated high stress-gradient areas) to reduce computational cost. Displacement boundary conditions are applied to the model such that the range of reaction forces in the loading direction spanned the experimentally-measured applied load.

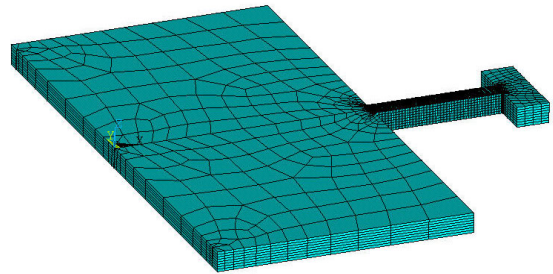


Figure 5: Finite element half-symmetry model of the MEMS micro-mirror constructed in ANSYS<sup>®</sup>.

Equations (2)-(6) were implemented in a numerical algorithm scripted in APDL, the ANSYS<sup>®</sup> scripting language. The experimentally-determined Weibull parameters from the two groups of test beams (polish and etch surfaces) were used to predict the micro-mirror failure probabilities under a range of loads in both center (tension) and edge (torsion) loading configurations.

### MEMS Micro-Mirror Verification Data

Two groups of micro-mirrors were created by random sampling from two wafers. Employing the same test apparatus, one group of mirrors was loaded in the center, to create a tension load/stress distribution in the flexure ( $N = 20$ ). The second test group was loaded at the edge of the mirror, thus generating a torsion load/stress distribution in the flexure ( $N = 18$ ). The micro-mirrors were loaded to failure under load control. The reliability

data from this testing were compared to the results of the reliability prediction.

## RESULTS AND DISCUSSION

The predicted and experimental failure probabilities (versus applied load) matched with reasonable accuracy (Figs. 6 and 7). The difference in characteristic load (defined at 63.2% probability of failure) between the actual data and the prediction is -12% for tension and 6.9% for torsion.

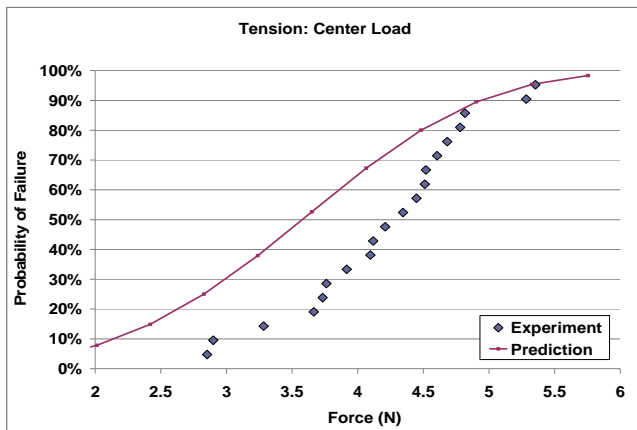


Figure 6: Predicted failure probability for mirrors loaded in tension compared with actual data ( $N=20$ ).

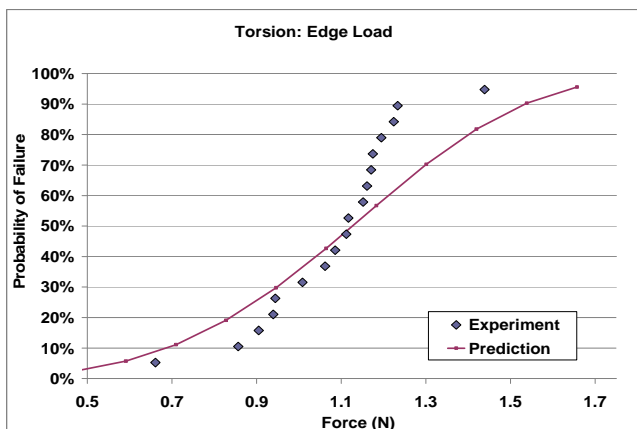


Figure 7: Predicted failure probability for mirrors loaded in torsion compared with actual data ( $N=18$ ).

The method appears to be quite robust. Despite variations in the four-point bend beam dimensions due to manufacturing variability, and the analytical determination of both the fracture stress,  $\sigma_f$ , and of the area-normalization parameter,  $A_0$ , the method predicted the true device reliability with acceptable accuracy.

Furthermore, despite the relatively large device size, we contend that the method is valid at any length scale provided that: (i) the single-crystal material acts as a continuum, and (ii) the etching processes used to build the four-point beam specimens (and hence generate the surface-specific data) is representative of the etching processes used to manufacture the devices to be analyzed.

## CONCLUSION

We have demonstrated accurate fracture prediction in single-crystal silicon MEMS subjected to realistically complex, multi-

axial loadings. Importantly, the experimental methods are efficient, cost effective, and repeatable. Once a particular set of manufacturing processes is characterized using simple beam specimens, accurate reliability estimates can be made for future devices of any complexity to be fabricated using the same processes. Failure probability estimates for any subset of specific device features or types of surfaces (and hence their impact on overall device reliability), as well as parametric design optimization, are also possibilities. Our method and algorithm stand to improve predictive design of brittle microstructures, enabling reduction of development time, and of the cost, size, and complexity of the resulting MEMS devices.

## ACKNOWLEDGEMENTS

The authors would like to thank Kathy Jackson for her assistance with fabrication of the silicon specimens and Karl Malchar of Instron Corporation. All silicon specimens were fabricated at the Stanford Nanofabrication Facility. This research was funded entirely by A.M. Fitzgerald & Associates, LLC.

## REFERENCES

- [1] K.-S. Chen, A. Ayon, and S. M. Spearing, "Controlling and Testing Fracture Strength of Silicon on the Mesoscale", *J. Amer. Cer. Soc.*, 83 (2000)
- [2] A. M. Fitzgerald, "Crack Growth Phenomena in Micro-Machined Single Crystal Silicon and Design Implications for Micro Electro Mechanical Systems (MEMS)", Stanford University Ph.D. Thesis (2000)
- [3] ASTM Standard D-6272-02 (2002)
- [4] J. Bagdahn, W. N. Sharpe Jr., and O. Jadaan, "Statistical Characterization of Fracture of Brittle MEMS Materials", *J. MEMS*, 12, 3 (2003)
- [5] N. N. Nemeth, L. J. Evans, O. M. Jadaan, W. Sharpe, G. Beheim, and M. Trapp, "Fabrication and Probabilistic Fracture Strength Prediction of High-Aspect-Ratio Single Crystal Silicon Carbide Microspecimens with Stress Concentration", *Thin Solid Films*, 515 (2007)
- [6] R. Boroch, J. Wiaranowski, R. Mueller-Fiedler, M. Ebert and J. Bagdahn, "Characterization of strength properties of thin polycrystalline silicon films for MEMS applications", *Fatig. Fract. Eng. Mat. Struct.*, 30 (2007)
- [7] W. R. Rice, J. J. Mecholsky, and P. F. Becher, "The effect of Grinding Direction on Flaw Character and Strength of Single Crystal and Polycrystalline Ceramics", *J. Mat. Sci.*, 16 (1981)
- [8] O. M. Jadaan, N. N. Nemeth, J. Bagdahn, and W. N. Sharpe Jr., "Probabilistic Weibull Behavior and Mechanical Properties of MEMS Brittle Materials", *J. Mat. Sci.*, 38, 20 (2003)
- [9] B. L. Boyce, J. M. Grazier, T. E. Buchheit, and M. J. Shaw, "Strength Distributions in Polycrystalline Silicon MEMS", *J. MEMS*, 16, 2 (2007)
- [10] C. J. Wilson, A. Ormeggi, and M. Narbutovskih, "Fracture Testing of Silicon Microcantilever Beams", *J. Appl. Phys.*, 75, 5 (1996)
- [11] W. N. Sharpe Jr., O. Jadaan, G. M. Beheim, G. D. Quinn and N. N. Nemeth, "Fracture Strength of Silicon Carbide Microspecimens", *J. MEMS*, 14, 5 (2005)
- [12] S. F. Duffy and J. M. Manderscheid, "Noninteractive Macroscopic Reliability Model for Ceramic Matrix Composites with Orthotropic Material Symmetry", *J. Eng. Gas Turb. Pow.*, 112 (1990)
- [13] CARES Theory Guide 8.1, Connecticut Reserve Technologies, Inc. (2006)

# INTERFACING MULTIPLEXED MICROFLUIDICS TO MALDI-MS BY HIGH-THROUGHPUT ROBOTIC SPOTTING

C.W. Tsao<sup>1</sup>, T. Song<sup>2</sup>, C.F. Chen<sup>1,3</sup>, J. Liu<sup>1</sup>, C.C. Chang<sup>3</sup> and D.L. DeVoe<sup>1</sup>

<sup>1</sup>Department of Mechanical Engineering, University of Maryland, College Park, MD, USA

<sup>2</sup>Calibrant Biosystems Inc., Gaithersburg, MD, USA

<sup>3</sup>Division of Mechanics, Research Center for Applied Science, Academia Sinica, Taipei, Taiwan

## ABSTRACT

Direct and automated spotting of analyte from multichannel microfluidic chips is demonstrated as a simple, robust, and high-throughput method for interfacing arrays of parallel microchannels with matrix-assisted laser desorption/ionization mass spectrometry (MALDI-MS). Using cyclic olefin copolymer (COC) chips containing 8 parallel 100  $\mu\text{m}$  x 46  $\mu\text{m}$  channels connected to a single input port, excellent spotting volume repeatability and MALDI-MS signal uniformity are achieved for a panel of sample peptides. Using the robotic spotting approach, chip-based reversed-phase liquid chromatography (RPLC) separations are interfaced with nanofilament silicon LDI-MS, demonstrating the potential for this approach towards high-throughput on-chip bioanalysis coupled seamlessly with back-end mass spectrometry.

## INTRODUCTION

The ability to perform high-throughput bioanalysis in a multiplexed platform is a substantial benefit promised by microfluidics technology. For applications which require analyte detection with high mass accuracy, interfacing microfluidics with mass spectrometry is a necessity. There are several examples of microfluidic systems containing multiplexed microchannels interfaced to electrospray ionization (ESI) tip arrays for ESI-MS analysis.[1-3] In practice, such systems are not well suited to parallel analysis since ESI-MS is an on-line method, with data acquisition performed in real-time. Coupling multiple electrospray tips with parallel MS analysis would thus require multiple MS tools, substantially limiting the practicality of this approach. A more compatible solution is to couple on-chip analyses with laser desorption/ionization methods such as MALDI-MS. In contrast to ESI-MS, MALDI-MS is an off-line soft ionization method in which sample is deposited onto a target plate and co-crystallized with a UV-absorbing organic matrix which aids in the ionization process during UV laser irradiation.[4] The off-line nature of MALDI-MS allows parallel deposition of analyte from multiplexed microchannels onto the MALDI target plate, followed by serial analysis of the deposited analyte spots. Because the laser spot size is typically on the order of 200  $\mu\text{m}$ , closely spaced sample spots may be analyzed without concern for crosstalk, allowing dense microchannel arrays to be effectively interfaced to off-line MS.

A variety of approaches for interfacing microfluidic systems to MALDI-MS have been demonstrated.[5, 6] In a particular approach explored by Knapp et al., a multichannel cyclic olefin copolymer (COC) chip developed for parallel RPLC[7] was interfaced with a MALDI target through an electrically-mediated deposition technique[8] which was shown to be robust for the case of a 2-channel chromatography chip. Here we describe a simpler approach based on direct hydrodynamic contact spotting from multichannel microfluidic chips. Contact spotting provides a generic approach to LDI-MS interfacing which is straightforward to implement and integrate, robust even for large numbers of multiplexed microchannels, and compatible with a wide range of

flow rates.

## HYDRODYNAMIC CONTACT DEPOSITION

The 8-channel chip design used in this work, shown in Figure 1(a), consisted of a symmetric 3-stage splitter connecting a single input port to an array of 8 parallel microchannels with 2 mm spacing. Each channel was nominally 100  $\mu\text{m}$  wide and 46  $\mu\text{m}$  deep, with geometric variances of less than 1.5% measured across all channels prior to chip bonding. The overall microchannel network was 50 mm long from input port to spotting tips.

Chip fabrication employed thermal embossing from a silicon master template and solvent bonding. After solvent bonding, the chip was shaped using a high precision CNC milling machine to produce regions with cross-sections 1 mm wide and 500  $\mu\text{m}$  thick surrounding each of the spotting tips, followed by a final cut to expose the fluid exit points using a semiconductor wafer dicing saw. Finally, a film of Teflon AF was deposited on the tip exit, thereby forming a hydrophobic surface to prevent fluid from wicking along the chip edge.

Two versions of the chip design were fabricated, one containing a methacrylate monolith within each spotting channel, and one without the monolith. Monoliths are highly porous inorganic or organic materials originally developed for conventional capillary HPLC separations. In comparison to packed columns, monoliths can offer fast and efficient separations using relatively low pressures, and by tuning the prepolymer composition and fabrication process, monoliths can be readily adapted for different separation mechanisms without further treatments. One of the most attractive characteristics of monolithic materials, especially the polymethacrylate/acrylate types, is that their photopolymerization-based synthesis enables the preparation of well-defined monoliths within specific regions of microchannel networks. The monolith was fabricated by first modifying the COC microchannel surface using a photografting method to enhance monolith/wall adhesion. The reversed-phase monolith was then fabricated *in situ* using a UV photolithography process first described by Frechet et al [9], resulting in a monolith with a morphology well suited for application to liquid chromatography applications.

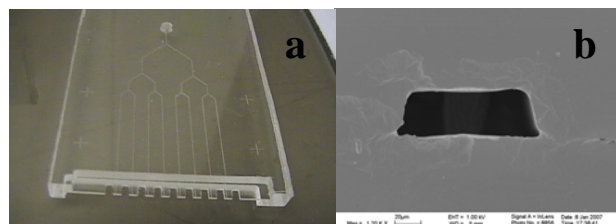


Figure 1: (a) An 8 channel COC chip with on-chip spotting tips connected to a single flow source, and (b) electron micrograph showing a typical spotting tip exit surface following chip dicing.

Custom microstructured MALDI target plates were fabricated by first spin-coating a thin Teflon AF layer onto an optically-

smooth stainless steel plate. The Teflon AF film, approximately 1  $\mu\text{m}$  thick, was baked at 250  $^{\circ}\text{C}$  for 2 hr to produce a dense hydrophobic layer over the entire stainless steel surface. A 300 nm thick gold film was then deposited by e-beam evaporation using a shadow mask to pattern four 8 x 8 arrays of 250  $\mu\text{m}$  diameter gold pads on top of the Teflon AF film.

The experimental system used for spotting tests is shown in Figure 2. The chip inlet was interfaced to a syringe pump through a 100  $\mu\text{m}$  i.d. capillary using an Upchurch Nanoport connector. The chip was mounted to a single-axis positioning stage to control the displacement of the chip relative to the target plate, which was mounted to a separate two-axis stage. The on-chip deposition tips were aligned to a first row of gold anchor pads and positioned 2 mm from the target surface. Following initial positioning, all control over the deposition process was automated using custom LabView software which controlled positioning of the stages through micro-stepper motors with a resolution of 5  $\mu\text{m}$ .

Automatic spotting was performed by moving the chip 200  $\mu\text{m}$  from the target surface to transfer droplets to the gold pads, then returning to the initial 2 mm gap and indexing the stage for the next row. Sequential images of the robotic spotting process are shown in Figure 3. Each of the 8 channels deposited droplets in parallel onto the MALDI target plate, with a total of 8 spotting events to fill the array. For each experiment, peptide sample premix with matrix solution was deposited onto 64 target spots in an 8 x 8 array.

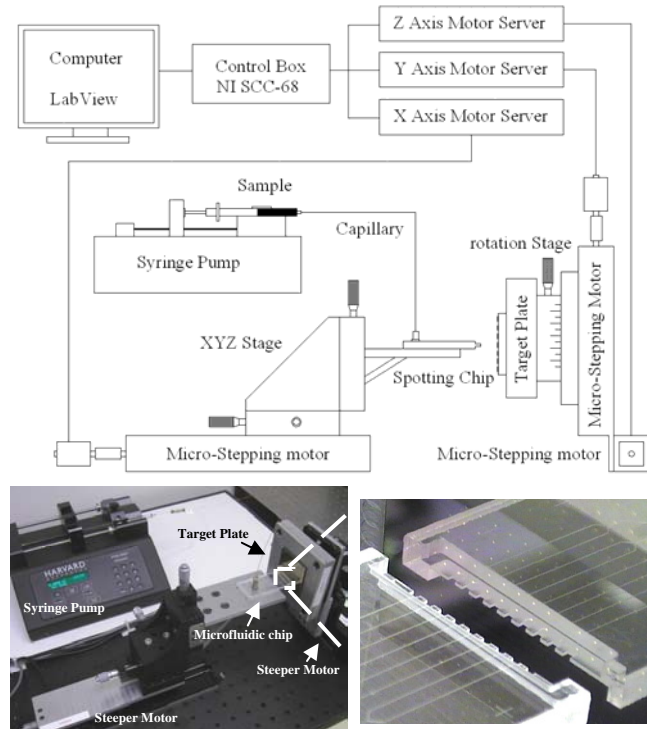


Figure 2: Experiment set of the robotic spotting system, with the multiplexed microfluidic chip and MALDI target fixed and aligned on their respective robotic stages.

The average droplet volume and coefficient of variation (CV) transferred from the COC chip to the MALDI target substrate is shown in Figure 4. The chip containing monoliths for liquid chromatography applications showed a CV of 12.9% for multiple droplets from a single channel, and up to 7.0% for single spotting events across all 8 channels. This compares favorably with values

of 34.7% and 25.2% from a single channel and across all channels, respectively, without monolith inside the multiplexed channel array. [10]

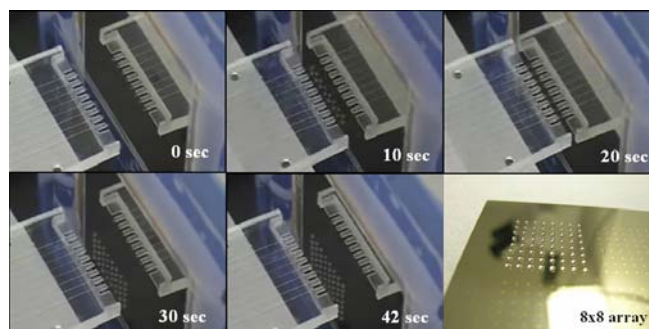


Figure 3: Consecutive images of the automated contact spotting process using a 12  $\mu\text{L}/\text{min}$  total flow rate and 6 sec interval between spotting events, resulting in an 8x8 array of 150 nL droplets deposited on the microstructured MALDI target surface.

Following spotting, the array of droplets was air dried, leaving co-crystallized sample and matrix on the gold anchors. The hydrophilic anchor pads were found to be effective in encouraging the efficient transfer of droplets from the hydrophobic chip spotting tips. The anchor pads also served to maintain the positions of the deposited droplets once transferred to the MALDI target. Figure 5 shows sequential images of the solvent evaporation and sample/matrix co-crystallization process on a single gold anchor pad.

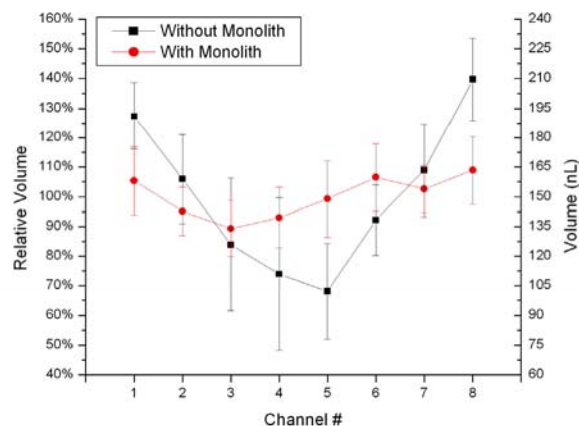


Figure 4: Average droplet volume transfer based on 8 consecutive spot runs comparing channels with and without monoliths.

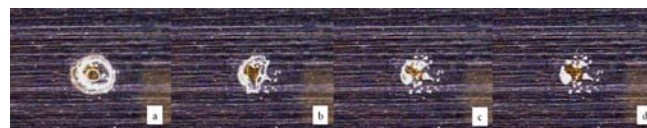


Figure 5: Sequential images showing the process of solvent evaporation and sample/matrix co-crystallization on a gold target anchor.

## MULTIPLEXED MALDI-MS MEASUREMENTS

Uniformity of MALDI-MS measurements using the spotting system was characterized with a panel of model peptides consisting of RASG-1 (MW 1000.5), angiotensin fragment 1 (MW 898.7), angiotensin II (MW 1045.5), bradykinin (MW 1059.6),

angiotensin I (MW 1295.7), renin substrate (MW 1758.0), enolase T35 (MW 1872.0), enolase T37 (MW 2827.3), and melittin (MW 2845.7). Sample was mixed with a MALDI matrix solution consisting of 10  $\mu\text{g}/\mu\text{L}$   $\alpha$ -cyano-4-hydroxycinnamic acid (CHCA) mixed into acetonitrile, DI water, and acetic acid 5:4:1 v/v/v. The matrix solution was mixed with the peptide sample 1:1 v/v, for final peptide concentrations of 0.5 pmol/ $\mu\text{L}$ .

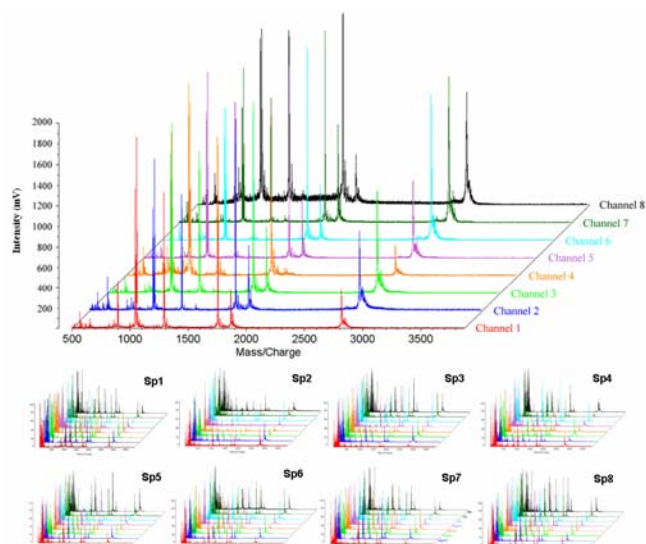


Figure 6: MALDI-MS spectra for sample deposited from all 8 channels during a single spotting event, revealing excellent repeatability

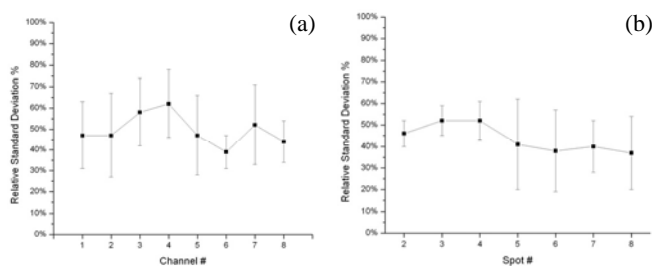


Figure 7: Uniformity of MALDI-MS signal (a) between different spotting events averaged over all channels, and (b) between different channels averaged over all spotting events.

Except for the m/z value at 1000.5 corresponding to RASG-1, which presents a relatively low signal intensity with a signal-to-noise ratio (S/N) less than 3, MALDI-MS spectra acquired from the 64 sample spots provided repeatable identification for 8 of the 9 model peptides for all spotting events. Figure 6 shows the mass spectra from all 8 channels during a single spotting event. The MALDI-MS measurements were performed on a Kratos Amixa time-of-flight (TOF) mass spectrometer. All LDI-MS spectra were acquired in linear, positive ion mode using between 25 and 50 laser pulses from a 337 nm nitrogen laser with a 3 ns pulse width. Laser energy was optimized based on signal-to-noise ratio using a test sample spot, and held constant during all experiments. The resulting uniformity of MALDI-MS signal intensities is displayed in Figure 7. Figure 7(a) shows the deviation of intensity values between different spotting events averaged over all channels, while Figure 7(b) reveals deviations between each channel averaged over

all spotting events. Compared with traditional spotting methods, which can often result in > 100% variations in signal intensity, the measured RSD values are encouraging.

## INTERFACING CHIP-RPLC WITH LDI-MS

The key to achieving highly repeatable droplet generation from the 8-channel spotting chip was to integrate monoliths into the spotting channels, thereby reducing the effects of capillary forces on the relative flow rates among the channels within the array. This fact makes the spotting approach attractive for multiplexed RPLC separations, since monoliths can provide excellent stationary phases for a range of chromatographic separations, including RPLC.

The RPLC chip design used here is shown in Figure 8. The chip consists of a sample injection channel, an LC pump connection, and a single serpentine RPLC separation channel containing a 15 cm long monolith. Each channel is nominally 100  $\mu\text{m}$  wide and 46  $\mu\text{m}$  deep, with geometric variances of less than 1.5% measured across all channels prior to chip bonding. Chip fabrication employed thermal embossing from a silicon master template and solvent bonding using procedures identical to previously-reported process. After solvent bonding, the chip was cut to expose the fluid exit points using a semiconductor wafer dicing saw. Because high pressures are used during RPLC separation, surgical stainless steel needles were used as high pressure and low dead-volume interconnections between off-chip components and the on-chip sample injector and separation channels.

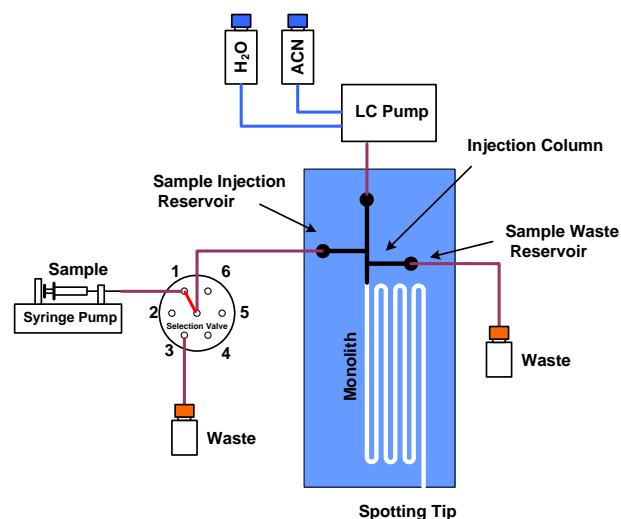


Figure 8: LC/MS chip design and experiment setup

Unlike the previous MALDI-MS characterization results (Figs. 6-7), which were generated using a traditional stainless steel MALDI target during deposition and analysis (Figs. 6-7), the RPLC separations were interfaced with a nanofilament silicon (nSi) target which eliminates the need for organic matrix to be added to the sample [11]. The nSi substrates were fabricated by a metal-assisted oxidative silicon etching process.[12] A 3 nm thick gold layer was deposited onto silicon wafer by e-beam evaporation followed by immersion into a solution of HF, H<sub>2</sub>O<sub>2</sub>, and EtOH (1:1:1 v/v/v) in a teflon beaker for 32 s. The etched wafer was oxidized by a 30 min UV/ozone treatment (PSD-UV, Novascan Technologies, Ames, IA) and the oxidized surface was then fluorinated by (pentafluorophenyl)propyldimethylchlorosilane.

To evaluate the system, model peptides consisting of [leu5]-enkephalin (MW 555.62), angiotensin II (MW 1046.18), bradykinin (MW 1060.61) and neurotensin (MW 1672.92) were first dissolved in 10 mM sodium carbonate/bicarbonate buffer (pH 9.0) to a concentration of 2 mM. Equal volumes of each peptide solution were mixed and then diluted 5-fold with HPLC grade water before being injected into the microfluidic chip. Separation of peptides on the 15 cm long monolith was achieved using a piecewise linear acetonitrile (ACN) solvent gradient, with an initial gradient of 5% to 20% ACN during the first 15 min, followed by 20% to 50% ACN over the next 5 min, and a constant 50% ACN concentration for the remainder of the separation. The total flow rate was set at 1.5 mL/min using the LC pump, with the on-chip splitter delivering a flow rate of 0.2~0.5  $\mu$ L/min through the monolith-filled separation channel.

Throughout the separation, automatic spotting was performed by moving the chip 200  $\mu$ m from the target surface to transfer droplets to the nanofilament substrate, then returning to the initial 2 mm gap and indexing the stage for the next spot. A total of 20 droplets were eluted onto the nSi substrate, with 2 min between each spotting event over the full 40 min separation time. The resulting mass spectra measured from each of the 20 deposited spots is shown Figure 9. Each of the sample peptides was observed in specific fractions deposited on the nSi surface, with [leu5]-enkephalin identified from spots #2 and #3, angiotensin II from spot #5 and bradykinin and neurotensin together from spot #10. The co-elution of [leu5]-enkephalin across two adjacent fractions indicates a relatively large bandwidth for this peptide, while the simultaneous elution of bradykinin and neurotensin within a single fraction suggests that more fractions should be sampled to fully resolve these components with similar hydrophobicity.

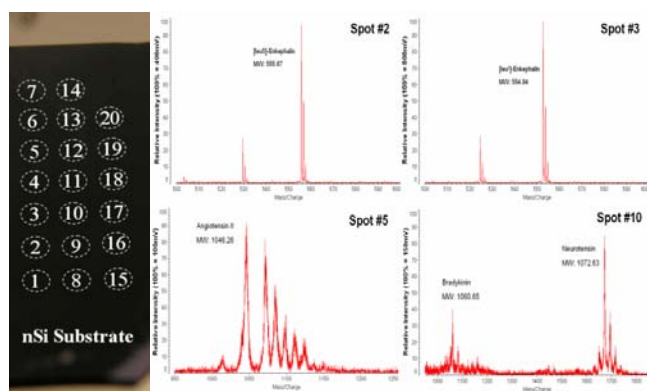


Figure 9: Nanofilament LDI-MS spectra from four nSi target spots containing peptides separated by the microfluidic chip-RPLC system.

## CONCLUSION

Automated contact spotting is an exceptionally simple and robust approach for coupling microfluidic separations to off-line LDI-MS mass spectrometry. Spotting from multiplexed arrays of parallel microchannels revealed good uniformity in both droplet volume and MALDI-MS signal intensity across all channels and multiple spotting events, while spotting from a single separation channel onto an nSi LDI-MS target demonstrated that hydrodynamic contact spotting may be effectively coupled with microfluidic RPLC separations. Further work to demonstrate parallel RPLC interfaced to nSi LDI-MS as an approach to high-throughput bioanalysis leveraging the unique benefits of microfluidic technology is ongoing.

## REFERENCES

- [1] Q. F. Xue, F. Foret, Y. M. Dunayevskiy, P. M. Zavracky, N. E. McGruer, and B. L. Karger, "Multichannel microchip electrospray mass spectrometry," *Analytical Chemistry*, vol. 69, pp. 426-430, 1997.
- [2] K. Q. Tang, Y. H. Lin, D. W. Matson, T. Kim, and R. D. Smith, "Generation of multiple electrosprays using microfabricated emitter arrays for improved mass spectrometric sensitivity," *Analytical Chemistry*, vol. 73, pp. 1658-1663, 2001.
- [3] S. Le Gac, S. Arscott, C. Cren-Olive, and C. Rolando, "Two-dimensional microfabricated sources for nanoelectrospray," *Journal of Mass Spectrometry*, vol. 38, pp. 1259-1264, 2003.
- [4] M. Karas and F. Hillenkamp, "Laser Desorption Ionization of Proteins with Molecular Masses Exceeding 10000 Daltons," *Analytical Chemistry*, vol. 60, pp. 2299-2301, 1988.
- [5] F. Foret and J. Preisler, "Liquid phase interfacing and miniaturization in matrix-assisted laser desorption/ionization mass spectrometry," *Proteomics*, vol. 2, pp. 360-372, 2002.
- [6] D. L. DeVoe and C. S. Lee, "Microfluidic technologies for MALDI-MS in proteomics," *Electrophoresis*, vol. 27, pp. 3559-3568, 2006.
- [7] K. W. Ro, J. Liu, and D. R. Knapp, "Plastic microchip liquid chromatography-matrix-assisted laser desorption/ionization mass spectrometry using monolithic columns," *J. Chromatography A*, vol. 1111, pp. 40-47, 2006.
- [8] C. Ericson, Q. T. Phung, D. M. Horn, E. C. Peters, J. R. Fitchett, S. B. Ficarro, A. R. Salomon, L. M. Brill, and A. Brock, "An automated noncontact deposition interface for liquid chromatography matrix-assisted laser desorption/ionization mass spectrometry," *Analytical Chemistry*, vol. 75, pp. 2309-2315, 2003.
- [9] T. B. Stachowiak, T. Rohr, E. F. Hilder, D. S. Peterson, M. Q. Yi, F. Svec, and J. M. J. Frechet, "Fabrication of porous polymer monoliths covalently attached to the walls of channels in plastic microdevices," *Electrophoresis*, vol. 24, pp. 3689-3693, 2003.
- [10] C. W. Tsao, J. Liu, and D. L. DeVoe, "Droplet formation from hydrodynamically coupled capillaries for parallel microfluidic contact spotting," *Journal of Micromechanics and Microengineering*, vol. 18, pp. 025013, 2008.
- [11] C. W. Tsao, P. Kumar, J. Liu, and D. L. DeVoe, "Dynamic electrowetting on nanofilament silicon for matrix-free laser desorption/ionization mass spectrometry," *Analytical Chemistry*, 2008, In press.
- [12] X. Li and P. W. Bohn, "Metal-assisted chemical etching in HF/H<sub>2</sub>O<sub>2</sub> produces porous silicon," *Applied Physics Letters*, vol. 77, pp. 2572-2574, 2000.

# SMALL FOOTPRINT CONTINUOUS FLOW PCR DEVICES FOR A 96-WELL CFPCR MULTI-REACTOR PLATFORM

D. S. Park<sup>1</sup>, P.-C. Chen<sup>1,2</sup>, B. H. You<sup>1,2</sup>, N. Kim<sup>1,2</sup>, T. Park<sup>1,2</sup>, T. Y. Lee<sup>1,2</sup>, P. Datta<sup>4</sup>, Y. Desta<sup>5</sup>, S. A. Soper<sup>1,3</sup>,  
D. E. Nikitopoulos<sup>1,2</sup>, and M. C. Murphy<sup>1,2</sup>

<sup>1</sup>Center for Bio-Modular Multi-Scale Systems, <sup>2</sup>Department of Mechanical Engineering

<sup>3</sup>Department of Chemistry, <sup>4</sup>Center for Advanced Microstructures and Devices

Louisiana State University, Baton Rouge, LA, USA

<sup>5</sup>BioFluidica Microtechnologies, Baton Rouge, LA, USA

## ABSTRACT

Incorporation of spiral continuous flow (CF) polymerase chain reaction (PCR) devices into a 96-well titer plate format will enable highly parallel analyses of many nucleic acids under steady-state temperature control for the realization of a high throughput CFPCR multi-reactor platform. Prior to realization of the full platform, verifying the feasibility of small footprint CFPCR devices, each device confined to a footprint of 8x8 mm<sup>2</sup>, throughout the manufacturing and amplification processes was essential. Small footprint, CFPCR devices in a CFPCR multi-reactor module were designed and double-side hot embossed on one side of a substrate and structures for thermal isolation on the other to improve thermal management. Successful amplification of 99 bp target DNA fragments from  $\lambda$ -DNA template was demonstrated in the small footprint, 20- and 25-turn CFPCR devices.

## INTRODUCTION

The polymerase chain reaction (PCR) is a powerful technique for DNA amplification. It has been widely used in nucleic acid analysis for diverse fields such as molecular diagnosis, treatment monitoring, food technology, forensics, agriculture, and environmental sciences [1, 2]. Target DNA can be exponentially amplified through multiple, multi-step temperature cycles: 90-95°C for denaturation of double-stranded target DNA molecules, 50-70°C for annealing of primers to single-stranded DNA target sites, and 70-77°C for primer extension with a thermostable DNA polymerase. Most commercial PCR instruments are bulky and have high thermal capacitance and slow heat transfer. These lead to high power requirements and limited reaction speeds due to the constrained heating and cooling rates.

Many efforts have been made to miniaturize PCR in Si, glass, and polymers using microelectromechanical systems (MEMS) technologies for the faster reaction speeds and reduced reagent consumption over commercial PCR instruments [3]. Micro chamber-type stationary PCR devices demonstrated faster amplification due to lower thermal capacitance and faster heat transfer [4-5]. In contrast, microfabricated continuous flow PCR (CFPCR) devices can provide the advantages of steady-state temperature control and much shorter times required to heat and cool only the fluidic PCR mixtures in microchannels compared to micro chamber-type PCRs [2, 6-7].

For parallel analysis of many nucleic acids in high throughput applications such as exploitation of the accumulated genetic information from the Human Genome Project, several micro chamber-type PCR multi-reactors have been reported. Liu et al. developed an integrated PCR-CE array, glass-PDMS microdevice with resistance temperature detectors and heaters for genetic analysis [8]. A miniaturized PCR multi-chamber array for high throughput PCR was fabricated using several Si micro chambers with microfabricated heaters and sensors, and integrated onto a printed circuit board substrate using flip-chip bonding [9].

In order to overcome the slow, transient temperature control in

the micro chamber-type PCR multi-reactors, microfabricated CFPCR devices can be incorporated into a polymer 96-well titer plate format [10] for the realization of a high throughput CFPCR multi-reactor platform at significantly lower cost. Figure 1 shows a schematic representation of a CFPCR multi-reactor platform, consisting of three key modules including a fluidic control module, a CFPCR multi-reactor module, and a heater module. PCR samples are introduced into common inlet ports and distributed to the inlet vias in the fluidic control network, amplified in the CFPCR multi-reactor platform, and collected from individual outlet ports using standard multi-pipettes and/or robotic equipment for PCR analysis. A heater array with precise temperature controllers can be realized using metal blocks for uniform temperature distribution with commercial strip heaters and thermocouples.

Prior to realization of the full platform, verifying the feasibility of small footprint CFPCR devices, with each device confined to a footprint of 8x8 mm<sup>2</sup>, in a 1<sup>st</sup> generation CFPCR multi-reactor module was essential throughout the manufacturing and amplification processes. Small footprint, double-sided CFPCR devices were designed, double-side hot embossed, and used to amplify DNA fragments as part of a 96-well CFPCR multi-reactor platform.

## DESIGN OF A CFPCR MULTI-REACTOR MODULE

A single, spiral-type CFPCR device in a hot embossed polycarbonate (PC) chip was demonstrated to investigate its performance as a function of reaction speed and identify the

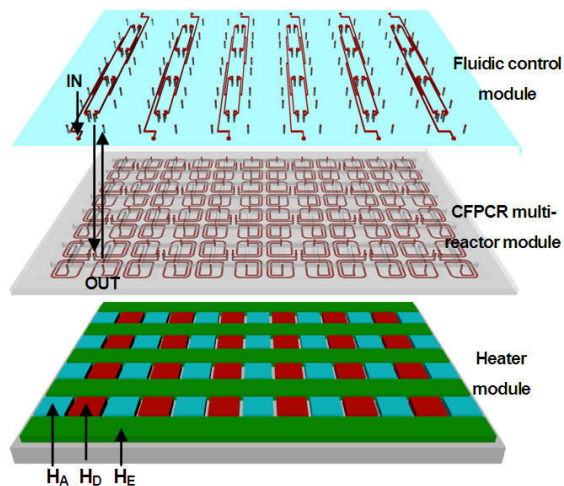


Figure 1: Schematic representation of a CFPCR multi-reactor platform with three key modules: a fluidic control module, a CFPCR multi-reactor module, and a heater module.  $H_D$  denotes for denaturation heaters (90-95°C),  $H_A$  for annealing heaters (50-70°C), and  $H_E$  for extension heaters (70-77°C).

residence time limits for DNA amplification [7]. The spiral-type CFPCR device concept was implemented in the design of a single-sided 1<sup>st</sup> generation CFPCR multi-reactor module and manufacturing of a single-sided 96-well CFPCR module was successfully demonstrated [11]. In order to utilize double-sided hot embossing of a 96-well CFPCR multi-reactor chip, two 6-inch large area mold inserts were designed: a nickel mold insert with the microfluidic channels for the CFPCR devices on one side, and a brass mold insert for the grooves and fins for thermal isolation on the other side with alignment marks (Fig. 2).

For the design of a nickel mold insert, each CFPCR device was confined in the effective area of 8x8 mm<sup>2</sup> because of the standardized format of the 96-well titer plate used [10]. A set of twelve CFPCR devices (channel widths: 10–40 μm, depth: 40 μm, channel wall width: 10–55 μm) with 20- and 25-turns was designed and extended to a 96-well format (Fig. 2(a)). The channel widths and lengths in the extension zone of each device were doubled compared to those in the denaturation and extension zones for keeping the residence time ratio of 1 : 1 : 4 (denaturation : annealing : extension) [7]. Sharing of temperature zones for four adjacent PCR devices was used for efficient thermal control and use of fewer heaters and thermocouples (Fig. 3) and extended to all 96 CFPCR devices.

Grooves (width: 1 mm, depth: 1.2 mm) were used between different temperature zones in the design of a brass mold insert for thermal isolation to improve thermal management [12]. Additional fins (width: 0.4 mm, height: 1.2 mm) were used inside the grooves for the transition from the denaturation to the annealing zones (Figs. 4(a) and (b)). The temperature distribution of four adjacent CFPCR devices on one side with grooves and fins on the other side were estimated via finite element simulations with ANSYS (v11.0,

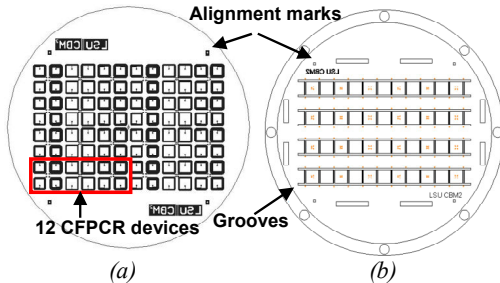


Figure 2: Layouts of (a) a nickel mold insert with a set of twelve CFPCR devices and (b) a corresponding brass mold insert with grooves and alignment marks.

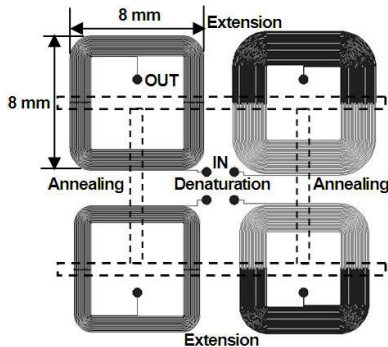


Figure 3: A layout of four CFPCR devices (each device in 8x8 mm<sup>2</sup>) sharing temperature zones for more efficient thermal control (dotted lines show grooves on the backside).

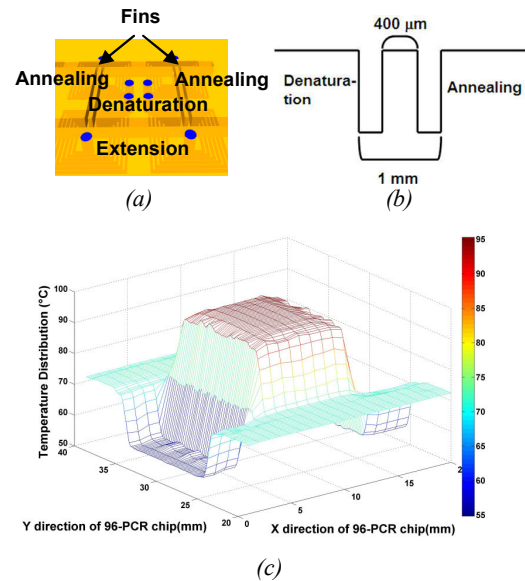


Figure 4: (a) 3-D view of CFPCR devices with grooves and fins, (b) a cross-section view of grooves and fins, and (c) temperature distribution of four adjacent CFPCR devices obtained via FE simulations with ANSYS (v11.0, Canonsburg, PA).

Canonsburg, PA) and the desired distinct temperature transitions between the different temperature zones were observed (Fig. 4(c)).

## FABRICATION OF A CFPCR MULTI-REACTOR MODULE

A CFPCR multi-reactor module with small footprint CFPCR devices was fabricated and manufacturing feasibility was carefully investigated throughout the fabrication of two nickel and brass mold inserts, double-sided micro molding, sealing by thermal fusion bonding, and leakage testing.

Fabrication of a nickel mold insert was reported elsewhere [11, 13]. In brief, electroplating templates were prepared by SU-8 based optical lithography on Si substrates with an electron beam evaporated seed layer of Cr/Au (20 nm/50 nm). Nickel overplating was carried out to fabricate metallic mold inserts in a custom-designed electroplating setup using a nickel sulfamate solution. Post-plating processes were carried out to produce a nickel mold insert mounted in a stainless steel (SS) hot embossing fixture, including: planarization of the overplated nickel mold insert surface, water jet cutting to a circular shape, removal of the Si substrate and SU-8, and mounting of the planarized nickel mold insert onto the SS fixture using laser-welding. A brass mold insert was precisely machined using a micro-milling machine (KERN MMP2522, KERN Micro- und Feinwerktechnik GmbH & Co. KG, Germany). Fig. 5(a) shows an image of the high precision and high quality nickel and brass mold inserts.

Double-sided micro molding was done in polycarbonate (PC, 2.3 mm thick, Lexan 9034 sheet, GE Structured Products, Pittsfield, MA) using hot embossing with two metallic mold inserts. A molding pressure of about 160 psi was used for one minute at a mold temperature of 187°C and the demolding temperature was 140°C. Acceptable replication fidelity over the entire surface area was obtained, but some CFPCR devices with 10 μm wide microchannel walls (height: 40 μm) showed incomplete filling and deformation. Alignment accuracy between the top and bottom reservoirs was within 100 μm (Fig. 5(b)), which can be improved by further alignment process optimization. Figure 5(c) shows fluidic paths

between the top and bottom reservoirs machined into the hot embossed CFPCR multi-reactor PC chips using laser ablation (Resonetics Rapid X<sup>®</sup> 1000 Series laser system, Nashua, NH).

Sealing of the molded PC chips with PC covers (250  $\mu\text{m}$  thick) was done in a custom-designed thermal bonding apparatus (Fig. 5(d)). The apparatus was composed of two stainless steel plates with 35 evenly spaced spring plungers [11]. Wing-nuts were used to compress the spring plungers, applying evenly distributed, multiple point loads on the glass plates, resulting in a more uniform load applied to the polymer chips. The gap between the two steel plates was used to determine the total load applied based on a calibration curve for compressed displacement of the spring plunger tips as a function of the applied load from a load cell. The bonding temperature and bonding pressure were varied parametrically for a fixed bonding time to determine the best conditions for acceptable sealing over the large surface area. A typical sealed PC chip, thermally bonded at a bonding temperature of 154°C and bonding pressure of 110 lb-force for a fixed bonding time of 2 hours, can be seen in Figure 5(e). A close-up of the sealed microchannels confirmed good sealing without deformation, even in the areas where grooves and fins were present underneath (Fig. 5(f)).

The sealed PC chips were cut into 10-well or 12-well sets for easier leakage and amplification testing (Fig. 6(a)). Two poly ether ether ketone (PEEK) capillaries (1543, Upchurch, Oak Harbor, WA) were inserted into inlet and outlet of CFPCR devices and fixed by epoxy. Flow of a fluorescent dye through the system confirmed

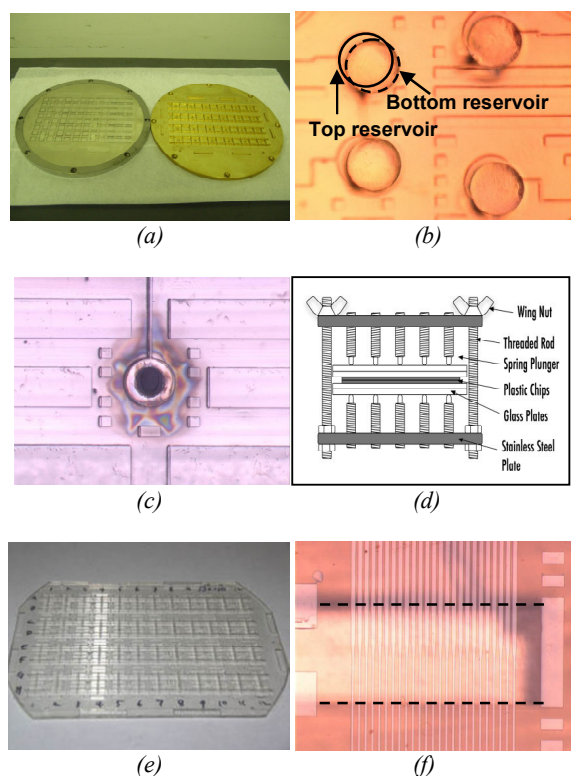


Figure 5: Images of (a) a nickel (left) and a brass (right) mold inserts, (b) four pairs of top and bottom reservoirs in a double-side molded chip, (c) a fluidic path between top and bottom reservoirs made by laser ablation, (d) a schematic view of the custom-designed thermal bonding apparatus, (e) a sealed, 1<sup>st</sup> generation 96-well CFPCR multi-reactor module in PC, and (f) a close-up view of sealed microchannels (dotted lines show grooves on the backside).

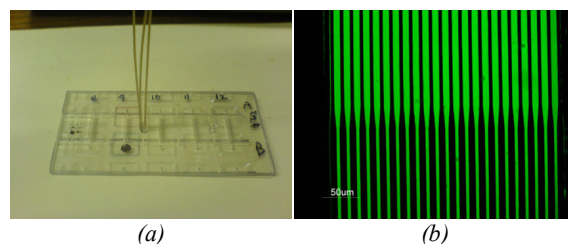


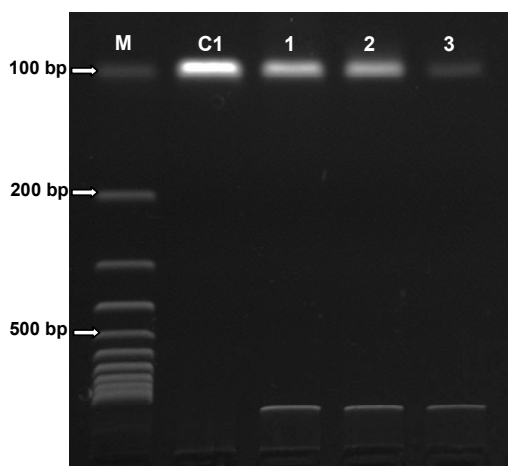
Figure 6: Images of (a) leakage testing setup using fluorescent dye with a sealed chip, cut into a 10-well (or 12-well) format; and (b) 40  $\mu\text{m}$  wide microchannels in the extension zone and 20  $\mu\text{m}$  wide microchannels in the denaturation (or annealing) zone filled with fluorescent dye showing no leakage between microchannels.

no leakage between the microchannels (Fig. 6(b)) and showed smooth flow of the dye for CFPCR devices with microchannel widths of 20  $\mu\text{m}$  or larger.

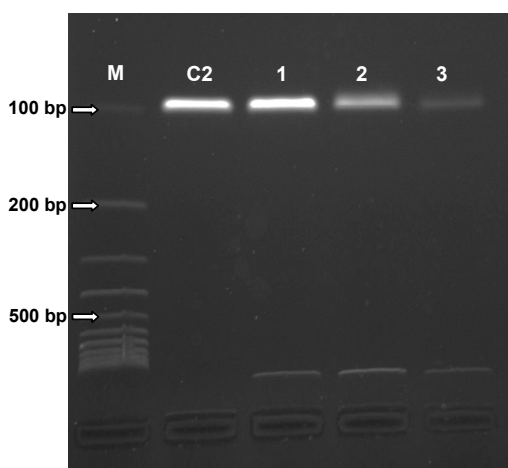
## DNA AMPLIFICATION

Small footprint, 20- and 25-turn CFPCR devices with microchannel widths of 20  $\mu\text{m}$  or larger were used for verifying the DNA amplification capability. The overall dimensions and volumes of the devices were: the width of the microchannels in the extension zone was 40  $\mu\text{m}$  (channel wall width: 20  $\mu\text{m}$ ); the widths of the microchannels in the denaturation and annealing zones was 20  $\mu\text{m}$  (channel wall width: 40  $\mu\text{m}$ ); the depth of the microchannels for all temperature zones was 40  $\mu\text{m}$ ; and the enclosed volumes were 739 nL for a 20-turn CFPCR device and 990 nL for a 25-turn CFPCR device, respectively. The DNA template was a 48 kbp  $\lambda$ -DNA c1857Sam7. Primers were designed to generate 99 bp DNA amplicons. The forward primer was 25 bp and its sequence was 5'-GATGAGTTCGTGTCCTACAACCTGG-3'. The reverse primer was 24 bp and its sequence was 5'-GACGGGCAATCA GTTCATCTTTCG-3'. The PCR cocktail contained 10 mM Tris-HCl (PH 8.3), 1.5 mM MgCl<sub>2</sub>, and 50 mM KCl. The concentrations of the nucleotides were 200  $\mu\text{M}$ , the template was 5 ng/ $\mu\text{L}$ , each forward and reverse primer was 0.2  $\mu\text{M}$ , bovine serum albumin (BSA) was 0.5  $\mu\text{g}/\mu\text{L}$ , and the *Taq* DNA polymerase was 0.1 units/ $\mu\text{L}$ . This DNA cocktail was amplified in a bench-top thermal cycler to validate the composition and as a reference to the CFPCR results. The cycling conditions were 2 min at 94°C for preheating, 7 min at 72°C for a final extension, and 20 cycles consisting of denaturation for 1 minute at 94°C, annealing for 1 minute at 63°C, and extension for 1 minute at 72°C.

The single CFPCR device was placed on three separate copper plates [12] to maintain the three distinct temperature zones of 94°C (denaturation), 63°C (annealing), and 72°C (extension). Thermal double-sided tape was used to assure the good contact between the copper plates and the device. The DNA cocktail for amplifying 99 bp target DNA fragments from  $\lambda$ -DNA template was pumped into the microchannels from a 50  $\mu\text{L}$  syringe by a syringe pump and collected from the outlet port into a 0.2 ml tube. The amplicons were mixed with 1X Blue/Orange Dye and injected into an agarose gel for electrophoresis. The product was imaged using a Gel Logic 200 Imaging System (Kodak, New Haven, CT) with UV light. There was neither preheating of the DNA cocktail nor BSA coating for the microchannels. Flow velocities of 1 mm/s, 2 mm/s, and 3 mm/s, corresponding to 0.048  $\mu\text{L}/\text{min}$ , 0.096  $\mu\text{L}/\text{min}$ , and 0.144  $\mu\text{L}/\text{min}$ , were used. Figure 7 shows the successful amplification results from the small footprint 20- and 25-turn CFPCR devices at different flow velocities. Total reaction times as fast as 5.1 min (15.3 s cycle<sup>-1</sup>) were achieved for the 20-turn CFPCR device at a



(a)



(b)

Figure 7: Gel electrophoresis images of the 99 bp DNA fragments generated from (a) 20-turn and (b) 25-turn small footprint CFPCR devices. Lane m represents DNA sizing markers (from 100 to 1000 bp); C1: 20-turn control from a commercial PCR cycler; C2: 25-turn control from a commercial PCR cycler; 1: flow velocity of 1 mm/s, 2: flow velocity of 2 mm/s, 3: flow velocity of 3 mm/s.

flow velocity of 3 mm/s.

## CONCLUSIONS

Small footprint CFPCR devices, each device confined to a footprint of  $8 \times 8 \text{ mm}^2$ , were designed and double-side hot embossed as part of a high throughput 96-well CFPCR multi-reactor platform. Acceptable replication fidelity over the entire surface area was obtained from double-sided micro molding of CFPCR PC chips. A custom-designed thermal bonding apparatus yielded proper sealing of double-side molded PC chips without leakage between the microchannels. Such small footprint, 20- and 25-turn CFPCR devices showed successful DNA amplification of 99-bp target DNA fragments from a 48 kbp  $\lambda$ -DNA template at different flow velocities.

Small footprint CFPCR devices demonstrated in this work will enable processing of multiple PCR samples in parallel with the development of a heater module and a fluidic control module in a titer plate-based CFPCR multi-reactor platform for fast PCR process optimization and high throughput PCR applications, and

will also offer the capability of integration with other microfluidic analytical devices.

## ACKNOWLEDGEMENTS

This work was supported by the National Science Foundation and the State of Louisiana Board of Regents Support Fund under grant number EPS-0346411, and the State of Louisiana Board of Regents Support Fund, Industrial Ties Program through grant number LEQSF(2005-08)-RD-B-04. The authors thank the Center for Advanced Microstructures and Devices (CAMD) at Louisiana State University for the microfabrication support.

## REFERENCES

- [1] T. K. Christopoulos, 1999, "Nucleic Acid Analysis", *Anal. Chem.*, 71, pp. 425R-438R (1999).
- [2] P. J. Obeid, T. K. Christopoulos, H. J. Crabtree, and C. J. Backhouse, "Microfabricated Device for DNA and RNA Amplification by Continuous-Flow Polymerase Chain Reaction and Reverse Transcription-Polymerase Chain Reaction with Cycle Number Selection", *Anal. Chem.*, 75, pp. 288-295 (2003).
- [3] C. Zang and D. Xing, "Miniaturized PCR Chips for Nucleic Acid Amplification and Analysis: Latest Advances and Future Trends", *Nucleic Acids Research*, 35(13), pp. 4223-4237 (2007).
- [4] M. A. Northrup, M. T. Chang, R. M. White, and R. T. Watson, "DNA Amplification in a Microfabricated Reaction Chamber", *Proceedings of the 7th International Conference on Solid-State Sensors and Actuators (Transducers '93)*, Yokohama, Japan, 6/07-10/93, pp. 924-926.
- [5] C. J. Easley, J. M. Karlinsey, and J. P. Landers, "On-Chip Pressure Injection for Integration of Infrared-Mediated DNA Amplification with Electrophoretic Separation", *Lab Chip*, 6, pp. 601-610 (2006).
- [6] M. U. Kopp, A. J. deMello, and A. Manz, "Chemical Amplification: Continuous-Flow PCR on a Chip", *Science*, 280, pp. 1046-1048 (1998).
- [7] M. Hashimoto, P.-C. Chen, M. W. Mitchell, D. E. Nikitopoulos, S. A. Soper, and M. C., Murphy, "Rapid PCR in a Continuous Flow Device", *Lab Chip*, 4, pp. 638-645 (2004).
- [8] C. N. Liu, N. M. Toriello, and R. A. Mathies, "Multichannel PCR-CE Microdevice for Genetic Analysis", *Anal. Chem.*, 78, pp. 5474-5479 (2006).
- [9] Z.-Q. Zou, X. Chen, Q.-H. Jin, M.-S. Yang, and J.-L. Zhao, "A Novel Miniaturized PCR Multi-Reactor Array Fabricated Using Flip-Chip Bonding Techniques", *J. Micromech. Microeng.*, 15, pp.1476-1481 (2005).
- [10] Microplate Standards Development Committee (2004) For Microplates – Footprint Dimensions – ANSI/SBS 1-2004, eds. Secretariat Society for Biomolecular Screening. Danbury, CT.
- [11] D. S. Park, P.-C. Chen, B. H. You, N. Kim, T. Park, P. Datta, Y. Desta, S. A. Soper, D. E. Nikitopoulos, and M. C. Murphy, "Optimization of Geometry for Continuous Flow PCR Devices in a Titer Plate-Based PCR Multi-Reactor Platform", *Proc. ASME IMECE 2007*, IMECE2007-42135.
- [12] P.-C. Chen, D. E. Nikitopoulos, S. A. Soper, and M. C. Murphy, "Temperature Distribution Effects on Micro-CFPCR Performance", *Biomedical Microdevices*, 10(2), pp. 141-152 (2008).
- [13] D. S.-W. Park, M. L. Hupert, M. A. Witek, B. H. You, P. Datta, J. Guy, J.-B. Lee, S. A. Soper, D. E. Nikitopoulos, and M. C. Murphy, "A Titer Plate-Based Polymer Microfluidic Platform for High Throughput Nucleic Acid Purification", *Biomedical Microdevices*, 10(1), pp. 21-33 (2008).

# MULTI-INLET/OUTLET PRECONCENTRATOR WITH 3-D $\mu$ -STRUCTURES COATED BY INKJET PRINTING OF TENAX TA

B. Alfeeli<sup>1,2</sup>, M. Ashraf-Khorassani<sup>1</sup>, L. T. Taylor<sup>1</sup>, and M. Agah<sup>1</sup>

<sup>1</sup>Virginia Polytechnic Institute and State University, Blacksburg, Virginia, USA

<sup>2</sup>Kuwait Institute for Scientific Research, Kuwait City, Kuwait

## ABSTRACT

The design, simulation, fabrication and testing of a thermally desorbed micro preconcentrator ( $\mu$ -TPC) is presented. The device consists of multiple inlets/outlets with novel high-aspect-ratio (240 $\mu$ m) crisscross  $\mu$ -pillar structures and on-chip thermal desorption capability. The  $\mu$ -TPC has a total inner surface area of 200 mm<sup>2</sup> and a total inner volume of 6.5  $\mu$ L resulting in a surface to volume ratio of 31 mm<sup>-1</sup>. The 3-D structures were coated with Tenax TA based on polymer inkjet printing methods. The 7 mm  $\times$  7 mm  $\mu$ -TPC was capable of collecting volatile organic compounds (VOCs) with a preconcentration factor > 1000.

## INTRODUCTION

Sample pre-treatment methods, such as preconcentration, are used to increase the detection sensitivity and selectivity of many analytical instruments such as gas chromatography, mass spectrometry, and ion mobility spectrometry. Preconcentration is very useful as it aids in the detection of trace compounds such as pollutants, explosives, and drugs. The key feature of a preconcentrator is to collect an analyte or a group of analytes by adsorption over a period of time and to release them on command by thermal desorption. Conventional thermally desorbed preconcentrators (TPCs) consist of a short-length microbore tubing packed with an adsorbent material and a heating element coiled around the tube for thermal desorption. However, they are troubled by large pressure drops, dead volumes, and high power consumptions. Different configurations for MEMS-based TPCs have been reported to overcome these issues [1-4]. The development of  $\mu$ -TCPs enables small, sensitive, and portable analytical instruments for field measurements.

This paper reports, for the first time, a  $\mu$ -TCP consisting of multiple inlets/outlets with novel crisscross  $\mu$ -pillar structures and on-chip heaters and temperature sensors. An Optical image of the fabricated device and scanning electron microscopy (SEM) monographs of the inner structure are shown in Fig. 1. The device was placed in front of a U.S. penny to give a size prospective. The

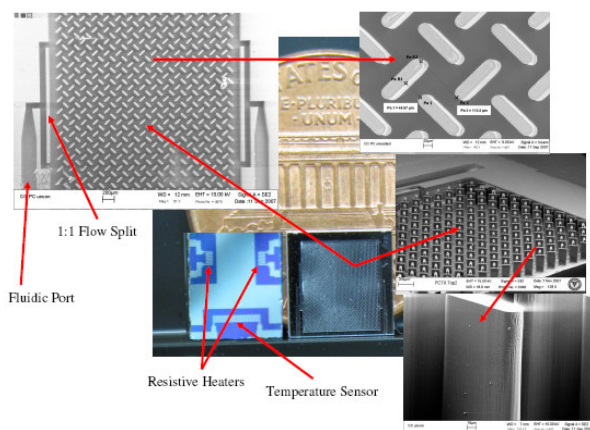


Fig. 1 Optical image of the  $\mu$ -TPC showing the front and back sides of the device, insets are SEM monographs of the etched 3-D structures and the fluidic ports

heaters and temperature sensors are evident on the backside of the chip. The metal layer covering the rest of the surface enhances heat distribution over the entire device. The SEM monographs show the shape and arrangement of the micropillars. The fluidic ports act as an adapter to connect the capillary tubing to the device for sample delivery and transfer. The multiple inlets/outlets were achieved by splitting the flow into a 1:1 ratio as shown in Fig 1. Since conventional particulate adsorbents are not suitable for this structure, a new method based on polymer inkjet printing principle [5] has been also developed to deposit Tenax TA (2,6-diphenylene oxide) on the micropillars.

## DESIGN AND FABRICATION

The most important figure of merit for TPCs is the preconcentration factor (PF). It is the ratio of an analyte's concentration delivered to the detector after preconcentration to the concentration originally present in the sample. Since preconcentration relies on adsorption/desorption processes, PF is mainly dependent on the adsorption surface area. Conventional TPCs are packed with granular adsorbents. However, one effective method to enhance PF without significant pressure drops is to utilize embedded pillars and realize a hybrid configuration combining packed (large surface area) and wall-coated (small flow restrictions) structures [4].

Using computational fluid dynamics, the effectiveness of different micropillar structures was simulated in terms of flow uniformity by defining a two dimensional geometry of the device. The steady state flow through the crisscross and square pillars (for comparison) are shown in Fig 2(a-b). In the square design, the flow in the perpendicular direction cannot pass to the other side due to the relatively fast flow in the parallel direction. This forces

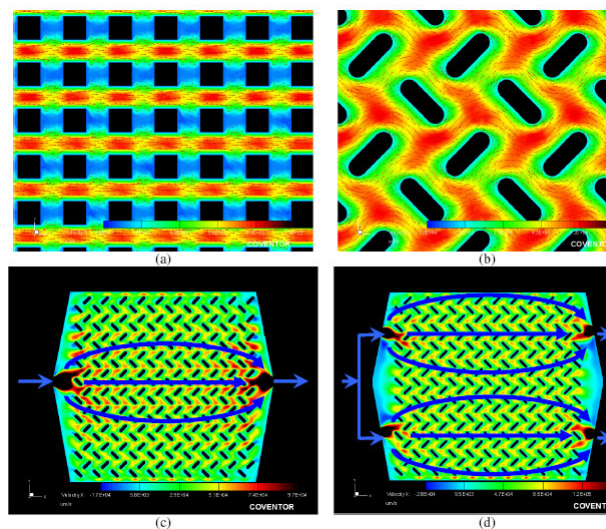


Fig. 2 CFD simulation of the flow in (a) ordered square pillars, (b) crisscross pillars, (c) crisscross pillars with single inlet/outlet showing the flow path, (d) crisscross pillars with multiple inlet/outlet showing the flow path

the fluid to come to rest at that region creating a stagnation point as depicted by the blue region in Fig. 2(a). The sharp corners of the square pillars also contribute to stagnation. This flow pattern indicated that the sample molecules do not effectively collide with half of the pillar surfaces, thus decreasing the adsorption surface. In the crisscross design, the sharp corners were eliminated and the flow was directed in a zigzag pattern to ensure non-zero velocity in all direction. The simulation analysis also showed that the multiple inlet/outlet design spreads the flow more evenly among the pillars (Fig. 2c-d). In the single inlet/outlet design, the flow velocity was highest in the middle giving rise to an undesired flow concentration. The use of a double inlet/outlet lessened this effect allowing more interaction between the pillars and the gaseous sample.

Fig. 3 shows the fabrication process. Using the standard photolithographic technique, the micropillars and the fluidic ports were patterned on a 4" silicon wafer. Deep reactive ion etching (DRIE) was utilized to form the 240 $\mu\text{m}$ -deep pillars and fluidic

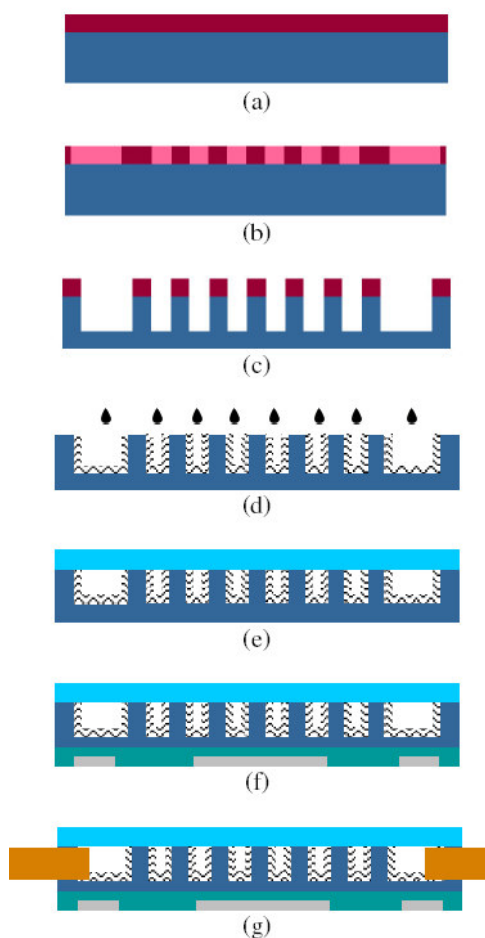


Fig. 3 (a) Spinning of high-resolution, superior aspect ratio thick film photoresist (PR9260), (b) Photolithography of  $\mu$ -pillars and the fluidic ports, (c) The pattern was etched using deep reactive-ion etching (DRIE) to form 240  $\mu\text{m}$ -deep 3D structures, (d) Dispensing of one-by-one droplets of adsorbent polymer solution on the microstructures, (e) Anodic bonding with Pyrex glass wafer to seal the structures, (f) PECVD oxidation followed by the deposition of thin-film resistive heaters and temperature sensors, (g) Attaching deactivated fused silica tubing to the fluidic ports by high temperature silica based bonding agent.

ports. Tenax TA particles were dissolved in dichloromethane at 2 mg/mL concentration to create a solution for inkjet printing. Before bonding,  $\mu$ -droplets were dispensed one-by-one on the 3-D microstructures. The volatility of the solvent and the large surface to volume ratio of the  $\mu$ -droplets caused instant evaporation which left behind a film of Tenax TA on the surface. This method resulted in a uniform and high-coverage coating as demonstrated in Fig. 4. The  $\mu$ -TPC was then sealed by anodic bonding the silicon substrate to a Pyrex wafer at 1250 V and 250 $^{\circ}\text{C}$  instead of conventional 350-400 $^{\circ}\text{C}$  bonding temperature to avoid damaging the polymer. After depositing a 3000 $\text{\AA}$  PECVD oxide layer on the backside, Ti/Pt was evaporated and patterned to form resistive heaters and temperature sensors.

## EXPERIMENT SETUP

To maintain isothermal temperature condition, the testing was carried out inside a commercial GC oven. The built-in auxiliary systems such as gas flow controller and flame ionization detector (FID) were also utilized to ensure consistent testing parameters. Helium carrier gas was supplied via the GC inlet and controlled by the flow controller. The sample adsorption/desorption was measured by the FID. The on-board resistive heaters and temperature sensor were not used in this experiment. Instead, an off-board high-performance ceramic heater (ultra-fast ramp rate) was used for thermal desorption along with K-type thermocouple for manual temperature monitoring and control. In future work, the on-chip thermal desorption capability will be used.

The experimental testing was performed by loading the chip with pure n-nonane ( $\text{C}_9$ ) and then thermally desorbing it at 100 $^{\circ}\text{C}/\text{sec}$  up to 250 $^{\circ}\text{C}$ . This was done for uncoated devices with

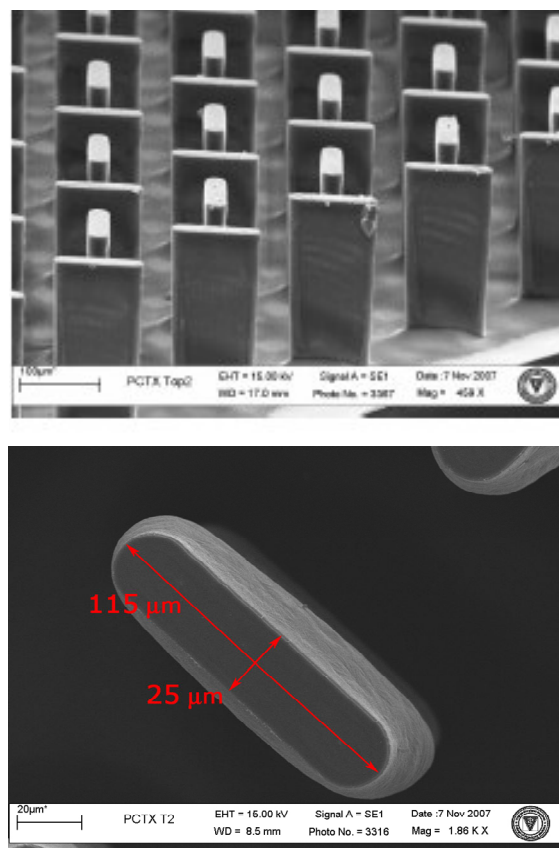


Fig. 4 SEM monographs of Tenax TA coated pillars.

the following configurations: without pillars, with square pillars, and crisscross pillars. This initial test was carried out to confirm the simulation results. All subsequent tests were performed on the crisscross design coated with Tenax TA since it was the focus of this work.

To examine the use of the  $\mu$ -TPC as an injector, the device was put on-line with a 2 m-long, 100  $\mu$ m-ID fused silica capillary column coated in-house with a methyl polysiloxane stationary phase. The  $\mu$ -TPC was then loaded with a diluted mixture of n-octane ( $C_8$ ), n-nonane ( $C_9$ ), n-decane ( $C_{10}$ ), n-dodecane ( $C_{12}$ ), and n-tetradecane ( $C_{14}$ ). The injection of the mixture into the GC column was initiated by the fast thermal desorption. The column ramp was 10°C/min from 35°C to 150°C.

## RESULTS AND DISCUSSION

Using the aforementioned fabrication process,  $\mu$ -TPC devices with high-aspect-ratio structures (240 $\mu$ m) were developed on a 7 mm square die. The  $\mu$ -TPC with crisscross pillars has a total inner surface area of about 200 mm<sup>2</sup> and a total inner volume of about 6.5  $\mu$ L resulting in  $\sim$ 31 mm<sup>-1</sup> surface area to volume ratio (S/V). For comparison, a 25 cm-long, 250  $\mu$ m-ID capillary tube yields the same surface area but has an inner volume of 12.5  $\mu$ L, and S/V of 16 mm<sup>-1</sup>.

The effect of the pillar design and configuration as well as the number of inlet/outlet on the  $\mu$ -TPC performance was studied by testing the performance of the uncoated and coated devices. Testing uncoated devices enabled performance characterization without interference effects from the adsorbent material. Table 1 lists the preconcentration factor for no-pillars, square and crisscross pillars along with single and multiple inlet/outlet crisscross devices. As predicted by the simulation analysis, the double inlet/outlet crisscross device produced the highest concentration factor among the other designs. The elimination of

Table 1: Preconcentration factor for different designs

Design	inlet/outlet	Spacing between posts ( $\mu$ m)	PF factor
No posts	1	-	4
 Ordered	1	50	7
 Crisscross	1	80	22
 Crisscross	2	80	32
 Crisscross	1	80 + Tenax TA	700
 Crisscross	2	80 + Tenax TA	1000

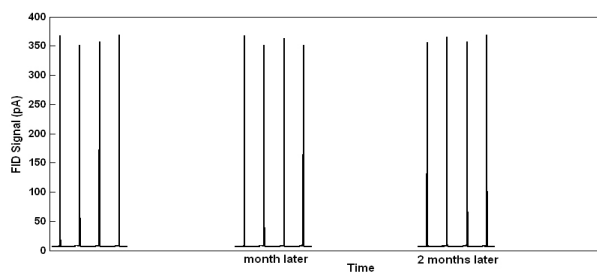


Fig. 5 Series of  $\mu$ -TPC generated desorption pulses over a three-month period.

stagnation and the effective dispersing of the sample among pillars produced more vapor/surface interaction. Moreover, the double inlet/outlet splits the flow into two flows with half the magnitude of the incoming flow (See Fig. 2 (d)). This led to a slower flow within the device compared to the flow in the single inlet/outlet configuration making the adsorption process more effective.

Fig. 5 demonstrates a series of desorption pulses generated over three months by a coated  $\mu$ -TPC consisting crisscross pillars with double inlet/outlet configuration. Reproducibility in terms of peak height and width was excellent (relative standard deviation 3% and 6% respectively).

Fig. 6a and 6b represent the chromatogram obtained by injecting the sample through the GC conventional injector and the  $\mu$ -TPC, respectively. The fast thermal desorption enabled sharp peak injection comparable to what could be produced by the GC injection port. The solvent peak was significantly smaller in the  $\mu$ -TPC injection pulse indicating that the device did not concentrate most of the solvent (dichloromethane). Yet, most of the separated compounds show a higher peak when injected through the  $\mu$ -TPC as clearly demonstrated in the zoomed-in chromatograms. Comparing the peak magnitudes of the solvent shows that the  $\mu$ -TPC has the advantage of discriminating between VOCs and the solvent. Therefore, the device can be used as a split injector to reduce the amount of solvent entering the GC column. The slight shift in the elution time of compounds is attributed to the change in the flow due to the placement of the  $\mu$ -TPC.

## CONCLUSIONS

The sensitivity and selectivity of an analytical instrument could be improved with preconcentration as a sample pretreatment. This report has demonstrated the possibility of developing MEMS-based  $\mu$ -TPCs that have smaller sizes, lower pressure drops, lower power consumptions, and higher efficiencies compared to conventional counterparts. By utilizing novel crisscross pillars with zigzag configuration and multiple inlet/outlet design, we have demonstrated a hybrid configuration combining packed (large surface area) and wall-coated (small flow restrictions) structures.

The simulation analyses verified by experimental results have shown the effect of the distributed inlet/outlet as well as the pillar geometry and configuration on the  $\mu$ -TPC performance. Future work will aim to better understand and model the behavior of the  $\mu$ -TPC under different conditions

The Sharp reproducible desorption peaks needed for fast on-field analytical analysis has been demonstrated by the  $\mu$ -TPC. The presented device was successful in concentrating a diluted multi-compound hydrocarbon mixture.

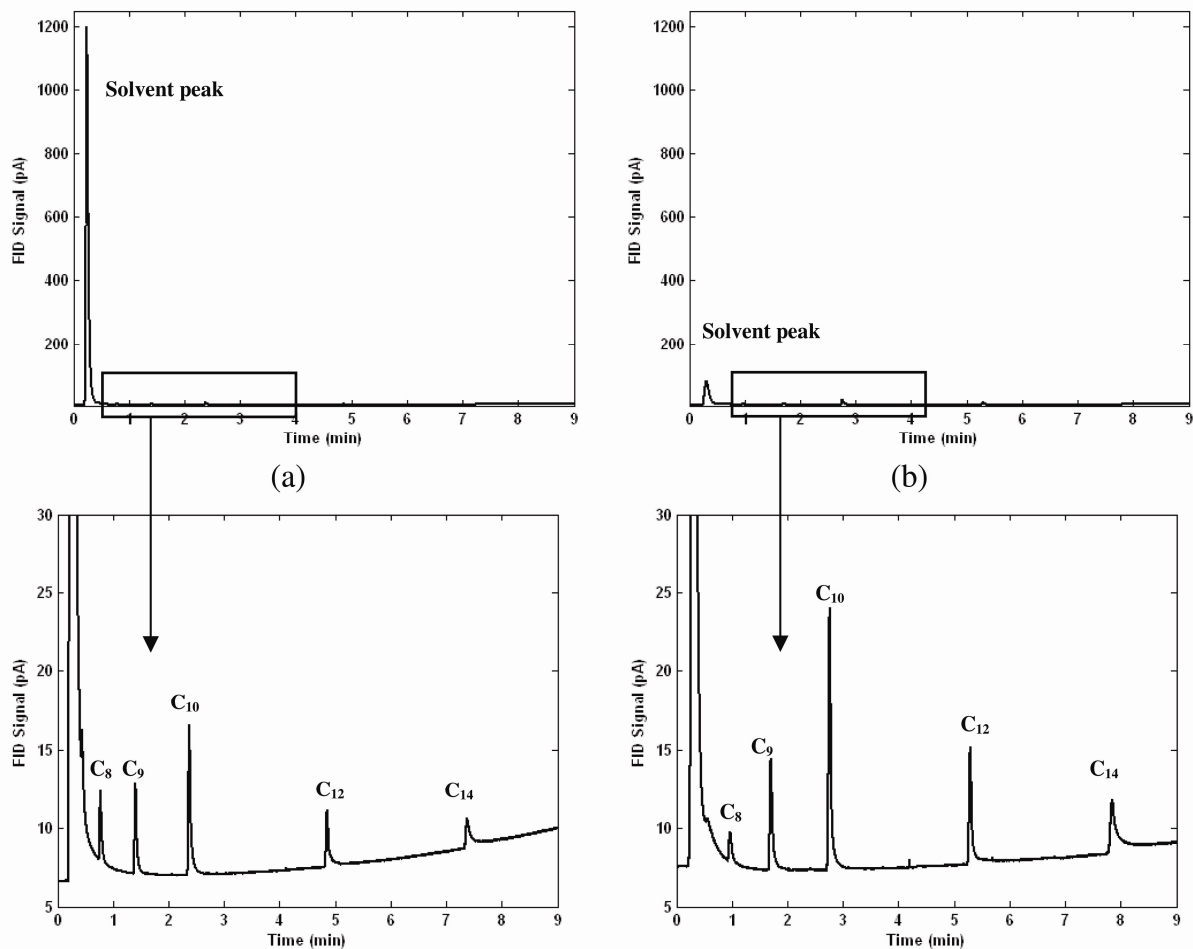


Fig. 6 Sample injection chromatograms, (a) represents the sample injected through the GC conventional injection port with a zoomed-in version below it, and (b) represents the sample injected by the  $\mu$ -TPC fast thermal desorption ability with a zoomed-in version below it

## REFERENCES

- [1] P. R. Lewis, P. Manginell, D. R. Adkins, R. J. Kottenstette, D. R. Wheeler, S. S. Sokolowski, D. E. Trudell, J. E. Byrnes, M. Okandan, J. M. Bauer, R. G. Manley and C. Frye-Mason, "Recent advancements in the gas-phase MicroChemLab," *IEEE Sens. J.* 6, 3, (2006)
- [2] W.-C. Tian, H. K. L. Chan, L. Chia-Jung, S. W. Pang and E. T. Zellers, "Multiple-stage microfabricated preconcentrator-focuser for micro gas chromatography system," *J. Microelectromech. Syst.* 14, 3, (2005)
- [3] M. Kim and S. Mitra, "A microfabricated microconcentrator for sensors and gas chromatography," *J. Chromatogr. A* 996, 1-2, (2003)
- [4] Y. Tang, J. Yeom, J. Han, B. Bae, R. I. Masel and M. A. Shannon, "A Micro-post preconcentrator for a microscale gas chromatography system", 9th International Conference on Miniaturized Systems for Chemistry and Life Sciences, Boston, MA, (2005), 660-662
- [5] P. Calvert, "Inkjet Printing for Materials and Devices," *Chem. Mater.* 13, 10, (2001)

# ELECTROSTATICALLY-ACTUATED RECONFIGURABLE ELASTOMER MICROFLUIDICS

Meng-Ping Chang<sup>1</sup>, and Michel M. Maharbiz<sup>2,3</sup>

<sup>1</sup>Department of Mechanical Engineering, University of Michigan, Ann Arbor, USA

<sup>2</sup>Department of Electrical Engineering and Computer Science, University of California, Berkeley, USA

<sup>3</sup>Department of Electrical Engineering and Computer Science, University of Michigan, Ann Arbor, USA

## ABSTRACT

We present a user-programmable reconfigurable elastomer microfluidic system which employs electrostatic actuation of water-filled elastomer microfluidic channels. Device actuation was achieved by applying 5 MHz, 15-20 V voltages to induce “wet” electrostatic gap-closing of nano-liter PDMS microfluidic chambers embedded with metal flexure electrodes. The primary contributions of this technology are: a) elastomer microfluidics that do not require external pneumatics to actuate when filled with air, oil, or water, b) a fabrication process compatible with standard PDMS microfluidics, and c) actuation voltages low enough to be driven by off-the-shelf RF IC’s.

## INTRODUCTION

For the past fifteen years, microfluidics has been a research field of intense scientific and engineering interest [1]. Technologies based on elastomers such as polydimethylsiloxane (PDMS) and parylene have become very popular due to ease of fabrication and use [2, 3, 4]. Most these technologies require external pneumatic connections for liquid control, but this manipulation becomes problematic as the system advances toward high-density large-scale integration. The lack of local low power actuation also prevents *in vivo* applications of these devices [5].

In this paper, we present a completely reconfigurable distributed elastomer microfluidic network system, as shown in Fig. 1. The operation of the device and two designs of the fabricated chips are shown in Fig. 2. The device consists of 7 (hexagon) or 9 (square) micro chambers which can be actuated independently by electrostatic pull-in of a PDMS-metal membrane [6]. The embedded metal flexure forms the top capacitor plate and the ITO electrode forms the bottom plate. When a voltage above the pull-in voltage is applied, the PDMS-metal “roof” collapses onto the “floor” (Fig. 2 a) and liquid within this actuated chamber is expelled into adjacent open micro chambers. This applied signal had a 5 MHz frequency to prevent electrical double layer screening of the electrostatic forces [7]. This makes possible the design of VLSI fluidic systems with many actuated components each driven by digitally synthesized signals. The device can actuate in air, water, and oil without external fluidic connections. These micro devices are also scalable to nanofluidic regimes and are compatible with general PDMS microfluidics.

## THEORY AND DEVICE DESIGN

A key issue of designing this micro device is the pull-in voltage which is affected by the device geometry, mechanical properties and dielectric constants of the membranes and working liquids. A closed form of the pull-in voltage can be expressed as [7, 8]:

$$V_{PI} = \sqrt{\frac{8k(g + t_{ox}\epsilon_L/\epsilon_{ox})}{27\epsilon_0\epsilon_L A} \cdot \left(1 + \frac{2(1-\nu^2)\sigma_R A}{9Et^2}\right)} \quad (1)$$

where  $k$  = spring constant;  $t_{ox}$  = oxide thickness;  $g$  = channel height;  $\epsilon_{ox}$  = oxide permittivity;  $\sigma_R$  = membrane residual

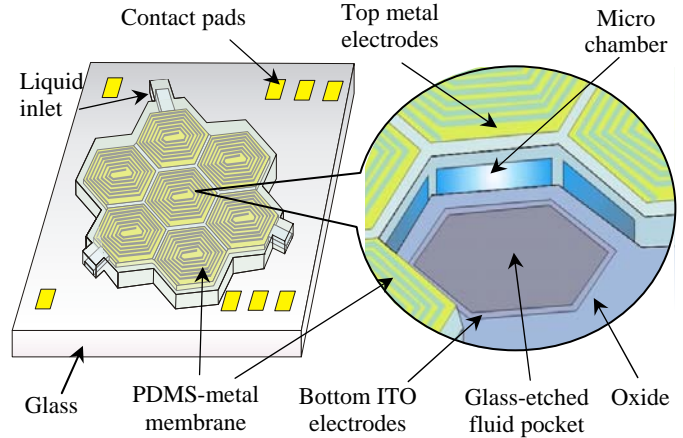


Figure 1: Conceptual view of a reconfigurable microfluidic device built on a glass substrate. The top PDMS-metal membrane and the bottom ITO form the capacitor plates. Each valve chamber is connected to adjacent chambers and can be electrostatically actuated independently. A valve seat is made by glass wet etching. An insulating oxide layer is deposited on the ITO electrode.

stress,  $A$  = capacitor area;  $\epsilon_L$  = liquid dielectric permittivity;  $\nu$  = Poisson’s ratio;  $E$  = Young’s modulus, and  $t$  = membrane thickness.

Devices with square elements measured  $300 \mu\text{m} \times 300 \mu\text{m}$  and hexagonal elements had  $200 \mu\text{m}$  edges, as shown in Fig. 2b. Hexagonal chambers were found preferable due to 1) compact footprint 2) shorter liquid transport path and 3) more uniform membrane deflection. The patterned spiral metal line was only for electric conduction of the PDMS, and its stiffness could be neglected when compared to that of PDMS membrane. The spring constant [9] of the devices and the pull-in voltage were calculated to be 20-30 N/m and 15-20 V. We previously characterized the pull-in behavior of this type of device [6]. The inlets connecting to each micro chamber were  $50 \mu\text{m}$  in width and 5 mm in length.

Table 1: Parameter values used in equation (1).

Square area	$9 \times 10^4 \mu\text{m}^2$
Hexagon area	$1 \times 10^4 \mu\text{m}^2$
Channel height gap	2.5 – 5.0 $\mu\text{m}$
Oxide permittivity	3.9
Oxide thickness	0.4 $\mu\text{m}$
Liquid permittivity	78.0
Membrane Young’s modulus	370.0 MPa [12]
Membrane residual stress	6.4 MPa [12]
Membrane Poisson’s ratio	4.8 [12]
Membrane thickness	7.2 $\mu\text{m}$

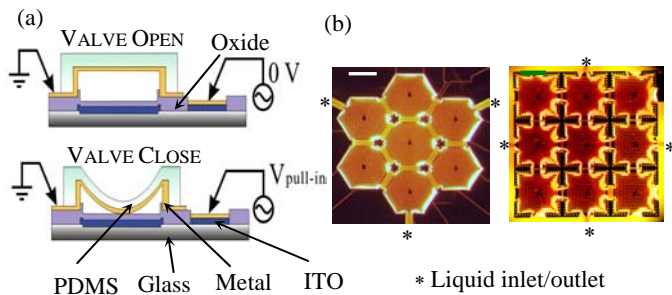


Figure 2: (a) The valve is closed when applying a 5 MHz signal at the pull-in amplitude (15-20 volt). By varying the sequence of actuation signal the chambers can function as independent micro channels, valves, and pumps. (b) White-light micrograph of fabricated devices. Scale bar, 200  $\mu\text{m}$ .

## FABRICATION

Figure 3 shows the fabrication flow of a basic single valve. The glass substrate was first wet etched in diluted buffered HF to form a 1  $\mu\text{m}$  recess. Indium tin oxide (ITO, 1000  $\text{\AA}$  thickness) was patterned, annealed at 700 $^\circ\text{C}$ , and covered with a layer of 4000  $\text{\AA}$  plasma-enhanced chemical vapor deposition (PECVD) oxide. This oxide layer was annealed at 550 $^\circ\text{C}$  for better dielectric insulation. Photoresist (AZ-9260, 10  $\mu\text{m}$ ) was then spun, baked and patterned into a micro channel mold. A thin film of Cr/Au (150/5000  $\text{\AA}$ ) was then sputtered and patterned using wet-etching to form the top capacitor plate. A stiff PDMS (Dow Corning WL-5351) was then spun and cured to form the micro chambers and channels. After releasing in acetone and methanol, the final channel height and the thickness of PDMS-metal membrane were 2.5 - 4  $\mu\text{m}$  and 7.2  $\mu\text{m}$ , respectively. The device was mount and wire bonded onto a PCB board.

## EXPERIMENTAL

### Microscopy and Fluidic Characterization

Figure 4 (a) shows the experiment apparatus of flow measurement by fluorescent or white-light microscopy on a Nikon TE-2000 inverted microscope. Food color and fluorescent dyes (fluorescein and ruthenium tris(bipyridine) chloride) were used as

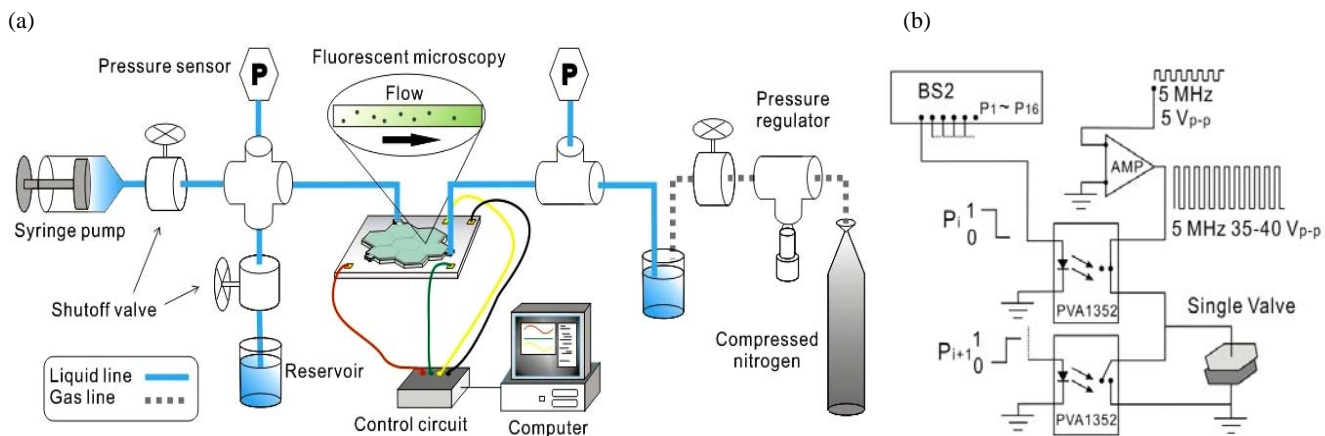


Figure 4: Experiment apparatus. (a) A syringe pump is connected at the upstream to flush/fill the system prior to any test. Two pressure transducers are installed to measure the pressure difference across the chip. A nitrogen bottle is used as pressure source to generate backpressure for pressure characterization. The flow velocity is measured by detecting the displacement of 0.5  $\mu\text{m}$  microspheres. (b) Control circuitry. Photovoltaic relay is controlled by a signal from the BS2 microcontroller. Signals from two adjacent ports  $P_i$  and  $P_{i+1}$  in BS2 are always out of phase, so the 5 MHz signal can be periodically switched between 15-20 V and ground.

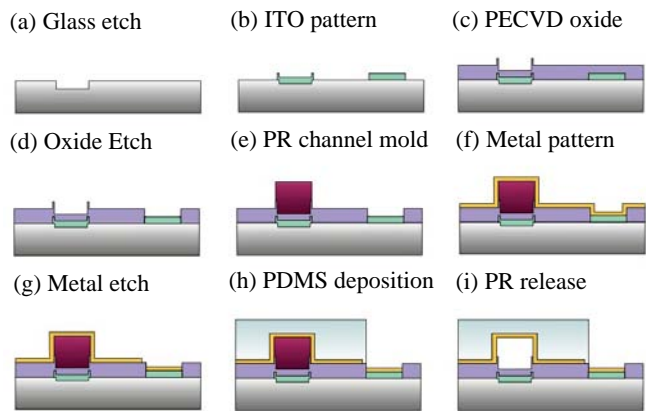


Figure 3: Fabrication flow.

visual indicators of valving actuation, flow movement and liquids mixing. Surfactant (Triton X-100) was mixed with water into 1% w/w and filled the device by capillary force. Polystyrene microspheres (PolySciences, 0.5  $\mu\text{m}$  diameter) were mixed in the solution for flow rate measurement. A syringe pump (KD Scientific) was used to flush and fill the fluidic network. The counter pressure could be generated by a nitrogen bottle or hydrostatic pressure for pressure and flow rate characterization. Two pressure transducers (Honeywell 40PC-150) were installed on both stream sides of the device to measure pressure drop across the device.

### Control Circuitry

The control circuitry is shown in Fig. 4 (b). A single valve device was actuated by a 5 MHz signal, switched between 15-20 V amplitude and ground. An initial 5 MHz, 5 V<sub>p-p</sub> signal was generated by a function/arbitrary waveform generator (Agilent 33250A, 80MHz), and amplified to 35-40 V<sub>p-p</sub> by either high speed IC amplifiers (Analog Devices AD815) or commercial RF amplifiers (Amplifier Research). The drive signal was applied via a pair of photovoltaic relay IC's (International Rectifier PVA13N) each of which was controlled by two digital signals ( $P_i = \bar{P}_{i+1}$ ) from the micro controller (Parallax BS2). The micro controller was programmed to provide the various actuation sequences used.

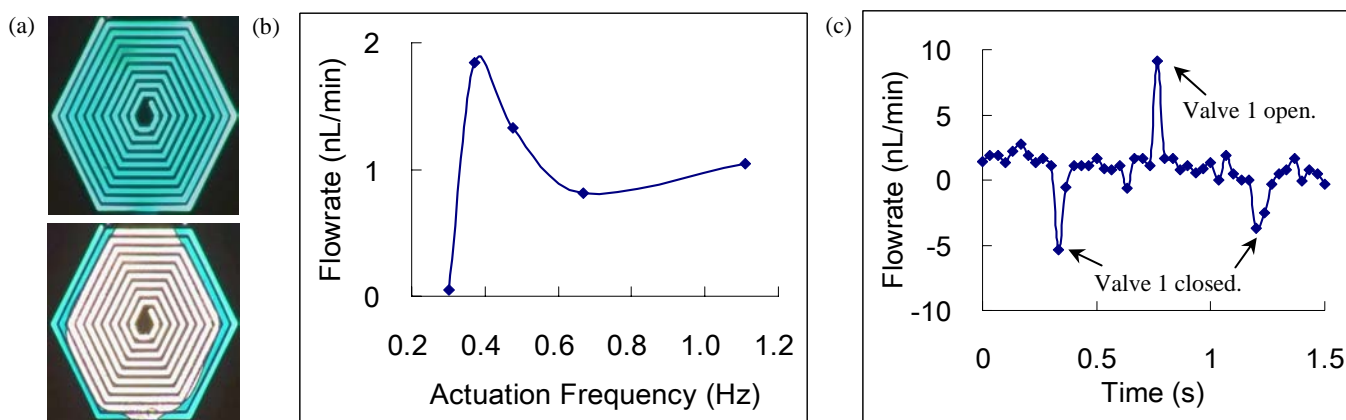


Figure 5: Valving and peristaltic pumping. (a) Top: an open valve filled with blue liquid. Bottom: as the valve closed, the liquid was expelled. (b) Average flow rate versus pumping frequency. The maximum average flow rate was found at 0.4 Hz actuation. After this frequency the flow rate decreased as actuation frequency increased. The measured flow rate was on the order of nL/min. (c) Flow rate versus time with 1.11 Hz actuation frequency. Peristaltic pumping generated pulsating flow, as indicated by the positive and negative spikes in the plot. The span between the two negative spikes has the same time span as the actuation period (0.9 second).

## RESULTS AND DISCUSSION

### Single Valve

Figure 5 (a) shows the basic valve operation. An earlier design of square units was reported to hold a 6 psi pressure [10]. The peak current was less than 1  $\mu$ A.

### Peristaltic Pump

Figure 5 (b) shows the average flow rate versus actuation frequency of a three-valve peristaltic pump. The maximum flow rate is 4.45 valve volume/min (1.85 nL/min) at 0.37 Hz. After this frequency the flow rate decreased as frequency increased. Figure 5 (c) presents the time response of the pump flow rate at 1.1 Hz actuation frequency. The liquid movement was a pulsating flow, with a nominal flow rate about 2 nL/min. As expected, positive and negative velocity peaks were observed at the same frequency as the pump actuation frequency.

### Reconfigurable Distributed Microfluidics

Table 2 shows the different actuation patterns used for valving, pumping and mixing. Figure 6 shows single-valve circulation actuation using a ruthenium tris(bipyridine) chloride dye as a fluorescent indicator. The actuation time of a single element was approximately 150 ms. We also achieved bi-valve circulation, full vertical, full horizontal, “Y” pumping and mixing; all these videos

are available online [11].

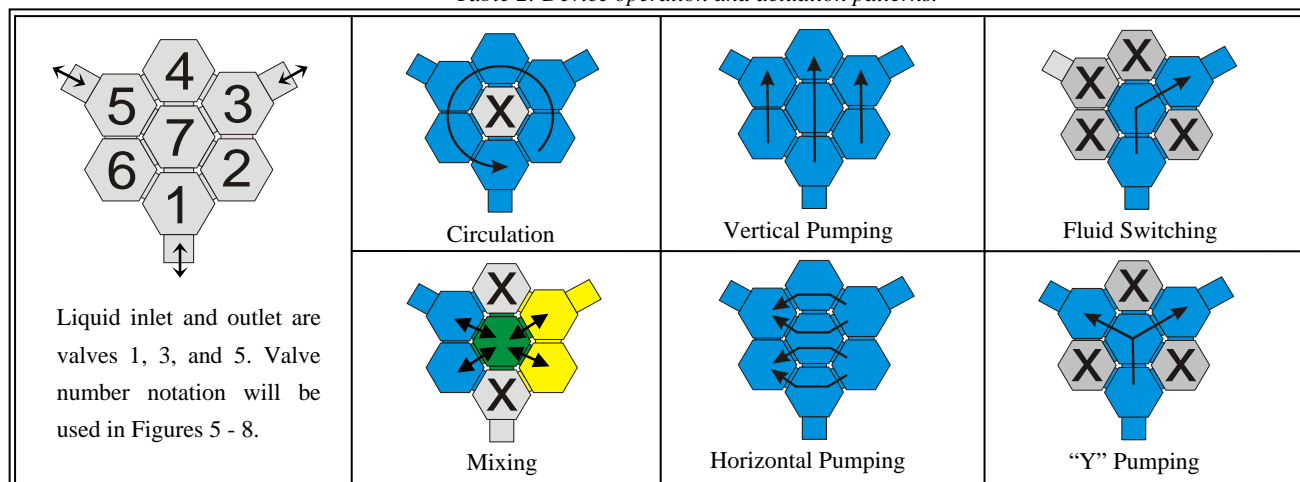
Fluid switching, as shown in Fig. 7, was realized by peristaltically actuating any three adjacent valves and closing all other undesignated valves. Blue food color was used to indicate flow direction.

Figure 8 shows mixing of two liquids. Two liquids, yellow and blue, were induced into the device from two separate liquid inlets. By actuating two pairs of diagonal valves sequentially, the liquids were actively mixed into green liquid. The whole mixing process was accomplished within 1 second.

## CONCLUSIONS

We have designed, fabricated, and tested an electrostatic reconfigurable distributed microfluidic device. This technology is compatible with modern PDMS microfluidics and CMOS drive voltages. The device requires no external pneumatic connections, operates at low voltage and is conceptually scalable to nanofluidic regime. We have demonstrated the device is capable of single valving, peristaltic pumping, and multi-position serial valving, “Y” pumping, fluid switching, and mixing, all of which are essential liquid movement manipulations for large-scale parallel biological or biochemical analysis. Current work focuses on eliminating leakage by etching valve seats similar to those used in pneumatically-actuated valves [13].

Table 2: Device operation and actuation patterns.



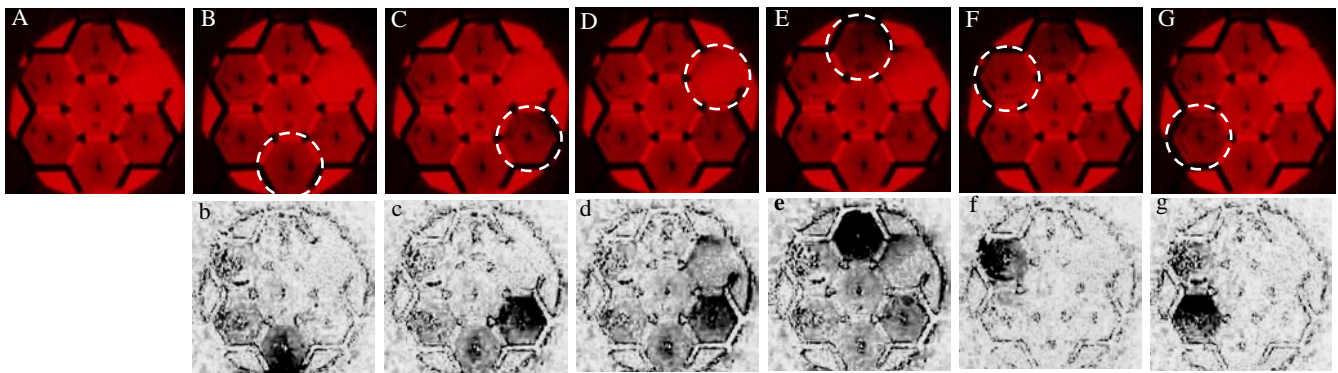


Figure 6: Single valve circulation actuation. Fluorescent microscopy images: image (A) is an unactuated device, and images B-G show independent actuation of each valve. White dashed circles indicate the actuated valve. Actuation voltage was 40 Vp-p, and each individual actuation was 150 ms. The motion of fluorophore is more apparent when images are subtracted from the background (A).

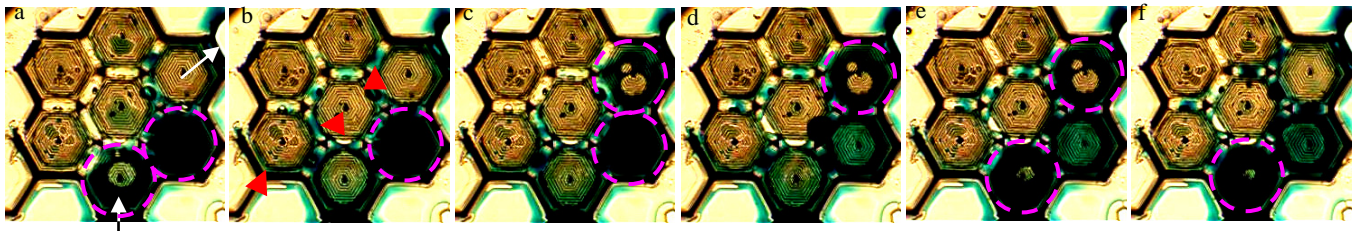


Figure 7: Fluid switching to the right. Liquid was pumped from valve 1 to valve 3, as indicated by the arrows in a). Valves 4, 5, 6, 7 were permanently closed, and valves 1, 2, 3 were actuated in sequence: 1+2  $\rightarrow$  2  $\rightarrow$  2+3  $\rightarrow$  3  $\rightarrow$  1+3  $\rightarrow$  1. Dashed circles show the actuated valve for that phase of the peristaltic pumping. Each actuation period was 150 ms, pumping frequency was 1.1 Hz. Slight leakage (red arrowhead in b) occurred between the actuated chambers.

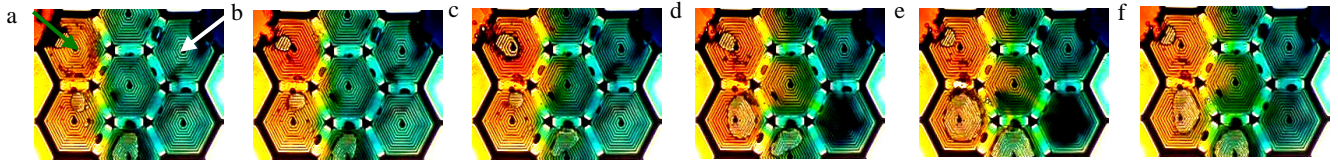


Figure 8: Mixing of two liquids in central chamber (valve 5). Time interval between each frame is 200 ms. When  $t = 0$  (a), the chip was pre-filled with blue liquid (valve 3, white arrow) and yellow liquid (valve 5, green arrow). At  $t = 200$  ms, valve 5 actuated and yellow liquid in valve 5 was expelled and started to mix with blue liquid in the central valve. This semi-mixed liquid was pushed into the lower-right valve (valve 2, d). As valve 2 actuated ( $t = 800$  ms, fig. e) liquid was pushed back into valve 7, and completed one mixing cycle.

## ACKNOWLEDGEMENT

The authors thank the Michigan Nanofabrication Facility, Neural Engineering Laboratory, Wise/Najafi Laboratory for experiment setup, Dr. Hiroataka Sato and Ruba Borno for discussion, and the funding support from the Engineering Research Centers Program of the National Science Foundation (EEC-9986866).

## REFERENCES

- [1] A. Manz, S. J. Harrison, E. M. J. Verpoorte, J. C. Fettinger, A. Paulua, H. Ludi, and H. M. Widmer, "Planar Chips Technology for Miniaturization and Integration of Separation Techniques into Monitoring Systems : Capillary Electrophoresis on a Chip", *J. Chromatogr., A*, 593 (1992).
- [2] M. A. Unger, H. P. Chou, T. Thorsen, A. Scherer, and S. R. Quake, "Monolithic Microfabricated Valves and Pumps by Multilayer Soft Lithography", *Science*, 288 (2000).
- [3] W. H. Grover, A. M. Skelley, C. N. Liu, E. T. Lagally, and R. A. Mathies, "Monolithic membrane valves and diaphragm pumps for practical large-scale integration into glass microfluidic devices", *Sens. Actuators, B*, 89, 3 (2003).
- [4] J. Xie, J. Shih, Q. Lin, B. Yang, and Y.-C. Tai, "Surface Micromachined Electrostatically Actuated Micro Peristaltic Pump", *Lab Chip*, 4 (2004).
- [5] N. A. Cellar, R. T. Kennedy, "A Capillary-PDMS Hybrid Chip for Separations-Based Sensing of Neurotransmitters in vivo", *Lab Chip*, 6 (2006).
- [6] T. Bansal, M.-P. Chang, and M. M. Maharbiz, "A Class of Low Voltage, Elastomer-Metal "Wet" Actuators for Use in High-Density microfluidics", *Lab Chip*, 7 (2007).
- [7] B. Legrand, A. S. Rollier, D. Collard, L. Buchailot, "Suppression of the Pull-in Instability for Parallel-Plate Electrostatic Actuators Operated in Dielectric Liquids", *Appl. Phys. Lett.*, 88 (2006).
- [8] P.-C. Hsu, C. H. Mastrangelo, K. D. Wise, "A High Sensitivity Polysilicon Diaphragm Condenser Microphone", *Proceedings of 1998 MEMS*, 01//1998, Heidelberg, Germany (1998), pp. 580 - 585.
- [9] W. C. Young, "Roark's Formulas for Stress and Strain", McGraw-Hill International Edition, (1989).
- [10] M.-P. Chang, T. Bansal, and M. M. Maharbiz, "Electrically Actuated PDMS Microvalves and Pumps for VLSI Microfluidics" *The 11th  $\mu$ TAS*, 10//2007, Paris, France (2007).
- [11] <http://www-personal.umich.edu/~mpchang/HH2008/>
- [12] Dow Corning WL-5351 product information.
- [13] W. H. Grover, R. H. C. Ivester, E. C. Jensen, and R. A. Mathies, "Development and multiplexed control of latching pneumatic valves using microfluidic logical structures", *Lab Chip*, 6 (2006).

# FLIGHT INITIATION AND DIRECTIONAL CONTROL OF BEETLES BY MICROTHERMAL STIMULATION

Karthik Visvanathan<sup>1</sup>, Naveen K. Gupta<sup>1</sup>, Michel M. Maharbiz<sup>2</sup> and Yogesh B. Gianchandani<sup>1</sup>

<sup>1</sup>Department of Mechanical Engineering, University of Michigan, Ann Arbor, USA.

<sup>2</sup>Department of Electrical Engineering and Computer Science, University of California at Berkeley, USA.

## ABSTRACT

This paper presents the efforts at micro thermal stimulation to initiate the flight and control the direction of beetles. Experiments were carried out by mounting micro thermal stimulators at the base of the antenna of the Green June beetle (*Cotinis nitida*). Preliminary *in vivo* experiments with resistive micro-heaters demonstrate that the beetle generates a torque of 18mN-mm at an estimated temperature of 43°C at the beetle-heater interface. These experiments utilized a micromachined resistive heater fabricated from bulk Ni foil. Additional experiments with a beetle carcass indicate that ultrasonic heating could be more effective, providing an estimated interface temperature of 43°C with 160 mW power. A circular PZT-5H disk of 3.2 mm diameter was used in the experiments.

## INTRODUCTION

The design and development of a reliable autonomous micro air vehicle (MAV) for environment monitoring and military applications has been an important challenge for researchers over the past decade. Apart from the efforts of creating a mechanical MAV, research is underway to explore the control of insect flight, motivated by flying agility and maneuverability of insects over a significant range of mass and size.

There has been a long standing interest among the researchers to understand the factors controlling the locomotion of various species of insects. For example, the role of the motion sensitive horizontal cells in the lobula plate of the fly in controlling the yaw torque generated was discussed in [1-2]. The dependence of the flight stability during maneuvers of the hawk moth on the mechanosensory input from the antenna was demonstrated by Sane *et al.* [3]. The removal of the antennal flagellum of these moths was found to severely disrupt the flight stability, thereby indicating the crucial role played by the antenna in their flight. In the past there have been preliminary efforts utilizing neural stimulation to initiate and control the direction of flight in beetles [4]. An implantable flight control microsystem consisting of multiple inserted neural and muscular stimulators, a visual stimulator and a microcontroller was developed. Electroneural sensing techniques were developed to observe the neural activities and control the locomotion of freely moving cockroach in [5-6]. However,

developing a reliable method for initiating the flight and control the direction of flight of insects have remained a major limitation in the development of insect based MAV.

Recent advances in micro fabrication have made it possible for the researchers to make sensors weighing less than a gram that can be attached as a “backpack”. Further, surgical implantation of microsystems in hawk moth was demonstrated by Paul *et al.* [9-10]. A permanently anchored base was created in an adult moth by inserting a biocompatible balsa titanium anchor in the late pupal stage of the moth.

This paper presents an effort at microthermal stimulation, which exploits the natural propensity of insects to escape fire, to initiate the flight and control the direction of beetles. The Green June beetle (GJB) of the genus ‘Cotinis’ and species ‘Nitida’ has active flight behavior and appreciable load capacity, which favors it as a biological carrier for multiple sensing applications (Fig. 1) [11]. It has been observed that the head of the beetle is most sensitive to thermal stimulation, particularly in the vicinity of the antennae [12]. This work explores the feasibility of both resistive and piezothermal stimulators and analyzes their relative performance. The present technique, while being less intrusive, is potentially widely applicable due to its independence from any specific neurological or physiological structures of the concerned insect. The following sections present the analytical model for thermal stimulation followed by device structure, fabrication technique, experimental results and finally the relevant discussion and conclusion.

## ANALYTICAL MODEL

In the present analysis microthermal stimulators are mounted near the base of the antennae and are operated in appropriate sequence to stimulate the desired flight response. The beetle and the non-conductive epoxy (used to bond the thermal stimulator to the beetle surface) are assumed to be two semi-infinite bodies in thermal equilibrium with each other. The equilibrium temperature,  $T_0$  at the interface of these two semi-infinite bodies is given by [13]:

$$T_0 = \frac{T_1 \sqrt{\rho_1 c_1 k_1} + T_2 \sqrt{\rho_2 c_2 k_2}}{\sqrt{\rho_1 c_1 k_1} + \sqrt{\rho_2 c_2 k_2}} \quad (1)$$

where,  $T_1, T_2$  are the temperatures of the first and the second semi-infinite bodies;

$\rho_1, \rho_2$  are the densities of the two bodies;

$c_1, c_2$  are the specific heat capacities of the two bodies, and

$k_1, k_2$  are the thermal conductivities of the two bodies.

Table 1: Properties of beetle shell and epoxy used in the analytical model.

Beetle shell properties	Epoxy Properties
Initial Temp., $T_1=300\text{K}$	Initial Temp., $T_2=393\text{K}$
Density, $\rho_1=1496 \text{ kg/m}^3$	Density, $\rho_2=870 \text{ kg/m}^3$
Heat Capacity, $c_1=3700\text{J/kgK}$	Heat Capacity, $c_2=1100\text{J/kgK}$
Thermal Conductivity, $k_1=1\text{W/m/K}$	Thermal Conductivity, $k_2=0.25 \text{ W/m/K}$

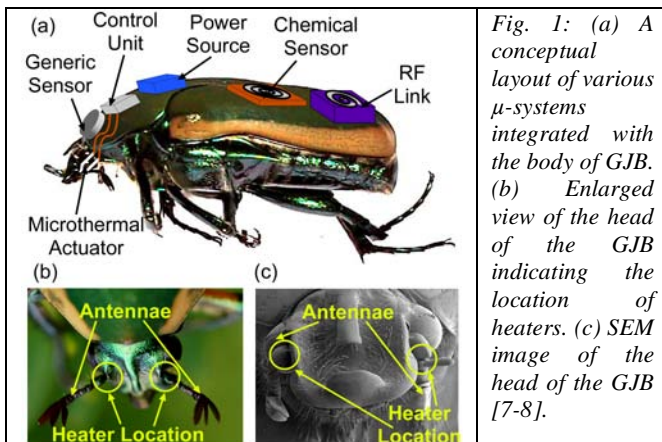


Fig. 1: (a) A conceptual layout of various  $\mu$ -systems integrated with the body of GJB. (b) Enlarged view of the head of the GJB indicating the location of heaters. (c) SEM image of the head of the GJB [7-8].

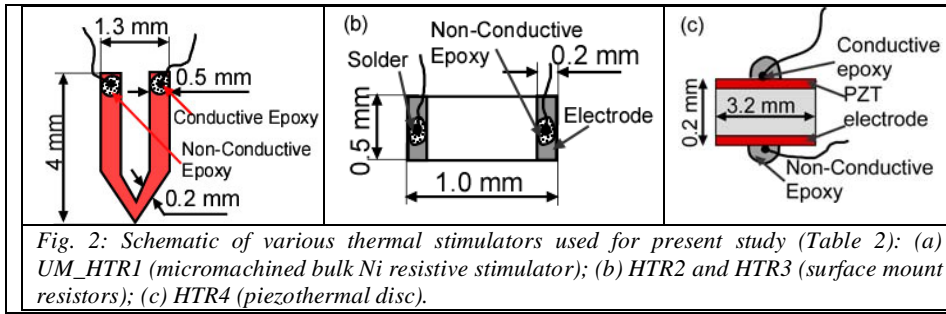


Fig. 2: Schematic of various thermal stimulators used for present study (Table 2): (a) UM\_HTR1 (micromachined bulk Ni resistive stimulator); (b) HTR2 and HTR3 (surface mount resistors); (c) HTR4 (piezothermal disc).

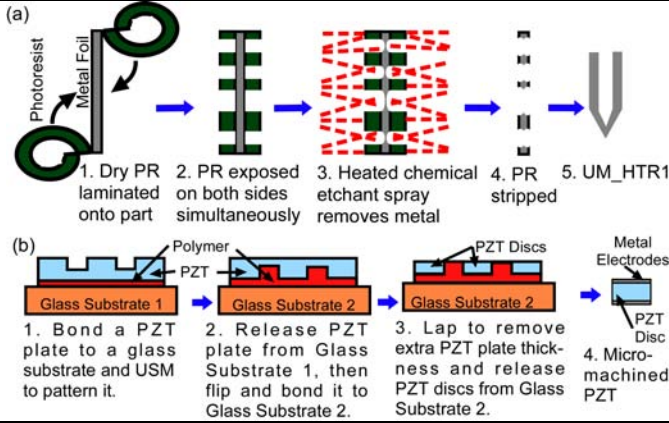


Fig. 3: (a) Fabrication of bulk Ni heater (UM\_HTR1) – metal foil is covered with dry PR, which is used to mask spray etch (b) Piezothermal stimulator can be ultrasonically machined (USM) – PZT plate is ultrasonically patterned, which is subsequently lapped from back to get the piezo discs [14].

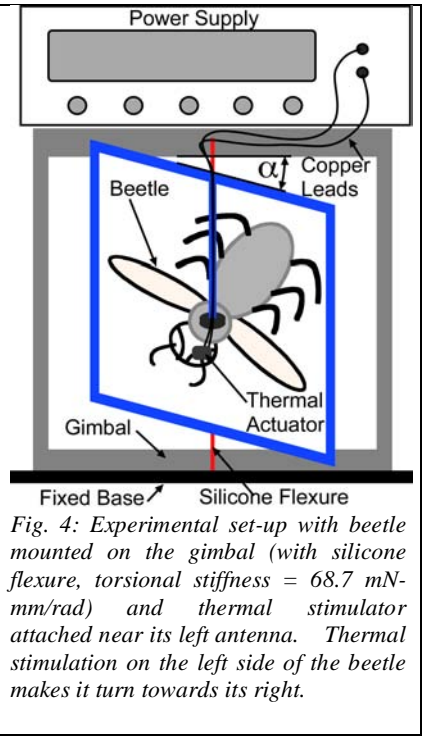


Fig. 4: Experimental set-up with beetle mounted on the gimbal (with silicone flexure, torsional stiffness = 68.7 mN-mm/rad) and thermal stimulator attached near its left antenna. Thermal stimulation on the left side of the beetle makes it turn towards its right.

Table 2: Comparison chart for different types of thermal stimulators used in flight response characterization of green june beetle (GJB).

	UM_HTR1	HTR2	HTR3	HTR4
Description	Micromachined bulk Ni stimulator	Surface mount resistors	Surface mount resistors	Piezothermal stimulator
Suffixes	'a' – in air 'b' – bonded to beetle	'a' – in air 'b' – bonded to beetle	'a' – in air 'b' – bonded to beetle	'g' – bonded to glass 'b' – bonded to beetle
Dimensions	4x1.3x0.05 mm <sup>3</sup>	1x0.5x0.35 mm <sup>3</sup>	1x0.5x0.35 mm <sup>3</sup>	Φ = 3.2 mm & thk. = 0.2 mm
Electrical Prop.	Resistance = 2 Ω	Resistance = 2.7 Ω	Resistance = 24 Ω	Capacitance = 0.65 nF
Mechanism	Resistive	Resistive	Resistive	Piezoelectric

The subscripts '1' and '2' refer to beetle shell and epoxy, respectively. The properties of these materials assumed for the analysis are given in Table 1. The beetle-epoxy interface temperature generated by the stimulator was estimated to be 43°C.

### DEVICE DESIGN AND FABRICATION

Four different kinds of externally mounted microthermal stimulators were investigated: custom micro-machined bulk nickel resistive heaters (UM\_HTR1), surface mount resistors (HTR2/3), and piezothermal PZT disks (HTR4) (Fig. 2, Table 2). Each of them was connected to the power supply through thin copper wire (gauge ≈ 38, length ≈ 40 cm, resistance ≈ 0.2 Ω).

UM\_HTR1, the 'V' shaped bulk Ni heaters (4x1.3x0.05 mm<sup>3</sup>) were fabricated by laminating dry resist on both sides of a Ni sheet, patterning and spray etching it, followed by electrochemical polishing (Fig. 3a). In order to concentrate the thermal energy at the tip of the stimulator, an additional time etch step was performed to yield a thinned tip of the stimulator. (Some of these fabrication steps were outsourced.) Electrode wires were connected using conductive epoxy followed by an insulating layer of non-conductive epoxy. A fabricated device is shown in Fig. 5.

The rectangular surface mount resistors (Fig. 3c, Table 2), while being commercially available and compact in size (1x0.5x0.35 mm<sup>3</sup>), have limited options on resistance and dimensions. Electrode wires were soldered in place with Indalloy #42 solder with an insulating layer of non-conductive epoxy.

Circular PZT devices (Φ = 3.2 mm & thickness = 0.2 mm) were fabricated by ultrasonic machining from a PZT plate, followed by metallization (Fig. 3b). The fabrication of piezothermal stimulators was a two step process. The first step involved micromachining of steel tool using serial micro electro discharge machining [14]. In the next step, the pattern formed on this tool was transferred to the PZT-5H plate using ultrasonic machining with the help of tungsten carbide abrasive powder. The plate was then finally flipped over and lapped from behind to release the pattern imprinted by the steel tool. Electrode wires were connected to the PZT discs by using conductive epoxy followed by an insulating layer of non-conductive epoxy.

### EXPERIMENTAL RESULTS

The response of the beetles was quantified by attaching them to a custom fabricated gimbal with an acrylic frame and silicone flexures (Fig. 4). The gimbal was designed such that it offers least resistance for rotation about its axis, while constraining the spatial movement. The torsional stiffness of the silicone flexures was experimentally measured to be 68.7 mN-mm/rad. The microthermal stimulators were mounted in close vicinity of the two antennae (Fig. 5). The stimulators were bonded using epoxy in order to prevent it from being dislodged by the beetle. A DC power supply (HP E3630A) and an AC function generator (HP 33520A) was used to actuate the resistive stimulators and piezothermal stimulators respectively.

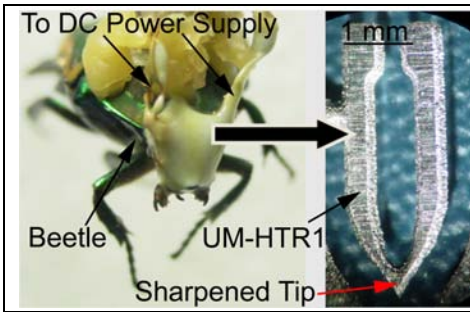


Fig. 5: Photograph of beetle with Ni resistive stimulators (UM\_HTR1, Table 2) bonded near its antennae. The sharpened heater tip localizes stimulation.



Fig. 6: Photograph of beetle turning towards its left due to thermal stimulation near its right antenna.

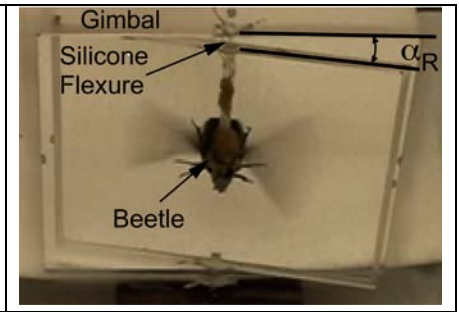


Fig. 7: Photograph of beetle turning towards its right due to thermal stimulation near its left antenna.

Preliminary results confirmed an aversion of beetle to the thermal stimulation. The microthermal stimulator UM\_HTR1 repeatedly demonstrated flight initiation and directional control of the GJB when a voltage of 1.75 V was applied, resulting in an estimated temperature of 43°C at the beetle-heater interface (Fig. 6-7) [11]. The beetle turned away from the side being heated by approximately 15° (0.26 rad), which resulted in a torque of 18 mN-mm.

The maximum temperature attained and specific time constant (*i.e.*, STC, the time constant per unit mass) were measured for various resistive and piezothermal stimulators (UM\_HTR1 and HTR2/3/4), for different thermal boundary conditions: in air, on beetle and on glass substrate. Figure 8 shows the experimental setup used for characterizing various thermal stimulators. For the resistive stimulators, both the voltage and the current through the stimulator was measured using HP E3630A DC power supply. The power consumed was given by the product of voltage across the stimulator and the current flowing through it. Similarly, the voltage and current across the PZT was measured using an Agilent DSO6014A oscilloscope and Tektronix CT1 (1 GHz) current probe respectively. The power dissipated by the PZT is given by:

$$P_c = V_{\text{rms}} I_{\text{rms}} \cos(\varphi) \quad (2)$$

where  $\varphi$  is the phase difference between the current and the voltage obtained by measuring the difference in time axis between the maxima of voltage and the current signals. The temperatures in both experiments were measured using a K-type thermocouple read using HH506A multilogger thermometer.

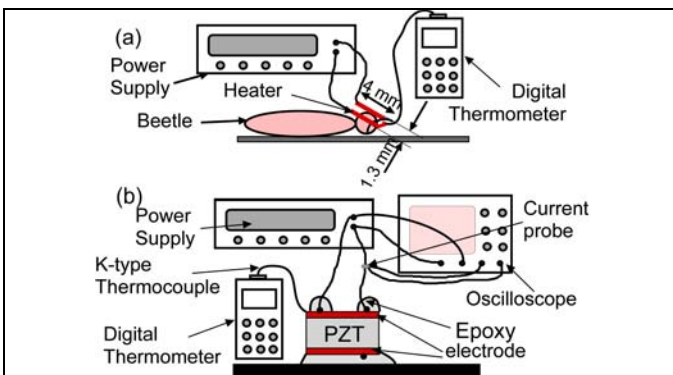


Fig. 8: Schematic layout of the test set-up to characterize heater performance. (a) UM\_HTR1B – Custom micromachined nickel heater (UM\_HTR1) mounted on the beetle and related electrical connections, (b) HTR4G – Piezothermal actuator bonded to the glass slide and related electrical connections.

Figure 9 suggests that the thermal efficiency (temperature rise/power) for resistive stimulators improves with decrease in size and with increase in resistance of the stimulator. This is mainly due to the decrease in the power loss due to convection and the resistance of the connecting leads. The plot indicates that HTR3 is about 1.25 times as efficient as HTR2, considering the thermal performance of heaters in air.

Further, a similar analysis of the piezothermal stimulator, HTR4, suggests that it offers about three times greater efficiency than resistive micro stimulators. HTR4 is further investigated for optimal operating frequency to generate desired stimulation temperature. Figure 10 shows the steady state temperature attained by the bulk PZT assembly bonded to the exoskeleton of the beetle, as a function of the frequency of the sinusoidal voltage input. The frequency corresponding to the maximum temperature attained is then further used to generate a steady state response of the piezothermal stimulator for varying input power (Fig. 10). The existence of an optimal operating frequency of the piezothermal actuator is shown by the resonance peak observed in Fig. 10. This frequency (650 kHz) corresponds to one of the resonance frequencies of the PZT structure measured using the impedance analyzer (Agilent 4395A). As expected, the system attains a maximum temperature at resonance frequency. Finally, the piezothermal stimulator is characterized for steady state thermal efficiency (temperature rise per milliwatt) attained at different frequencies (Fig. 11). Moreover, HTR4 achieves a maximum thermal efficiency of 0.93°C/mW at 600 kHz, slightly below its resonance frequency (650 kHz).

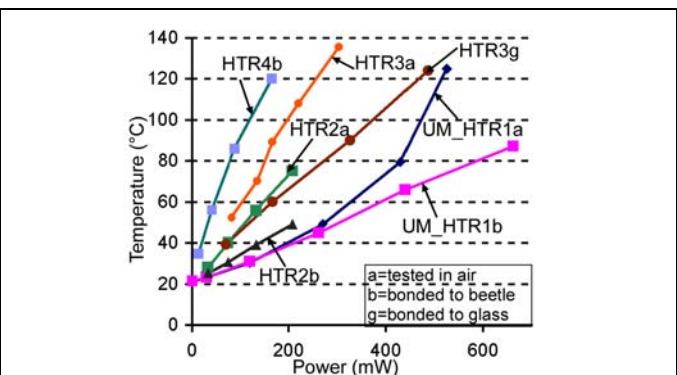


Fig. 9: Maximum temperatures attained by various stimulators for specified power inputs, with different thermal boundary conditions. Suffixes a, b and g denote air, beetle and glass slide substrate respectively. The voltage and current across the PZT was measured using an oscilloscope and current probe respectively.

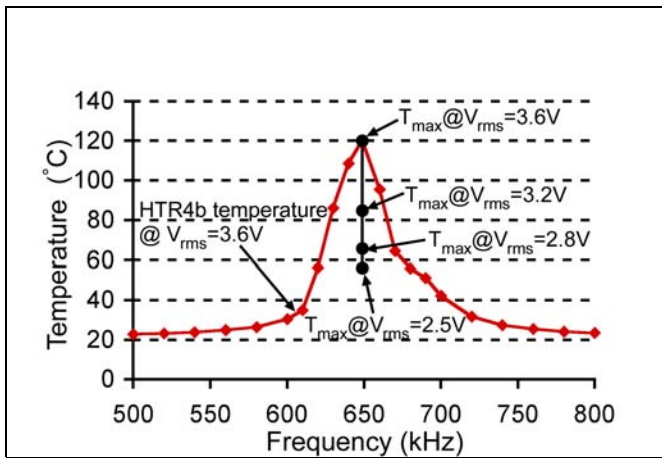


Fig. 10: Temperature generated by the piezothermal stimulator for different actuation frequencies. The piezothermal stimulator (HTR4b) shows a resonance at about 650 kHz and achieves a maximum temperature of 120 °C at resonance. The maximum temperature attained at resonance frequency for various input voltages is also plotted.

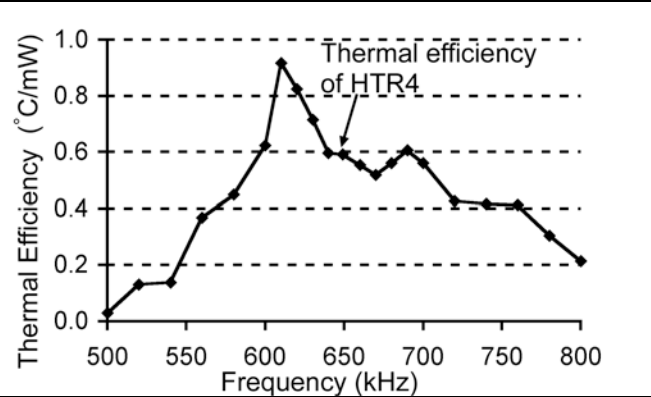


Fig. 11: The thermal efficiency (temperature rise/unit power) of HTR4b as a function of frequency of the sinusoidal input voltage. The thermal efficiency of the PZT stimulator was found to attain its maximum around 600 kHz.

Table 3: Specific time constant for various heating elements.

Heating element	Specific time constant (sec/mg)
UM_HTR1b (on beetle)	0.18
HTR2b (on beetle)	0.22
HTR4b (on beetle)	0.11
HTR3g (on glass)	0.22
HTR4g (on glass)	0.09

The fundamental theoretical STC limits of various stimulators are also calculated. This determines the latency time for the beetle to respond to thermal stimulation. The STC of HTR4 is 90 msec/mg as compared to 180 msec/mg for UM\_HTR1 and 220 msec/mg for HTR2/3 (Table 3). Apart from having a comparatively low STC, UM\_HTR1 also provides more thermal localization than the surface mount stimulators. Further, its 'V'-shape is also easier to mount around the antenna making it most ideal for the experiment.

## CONCLUSION

The study suggests that microthermal stimulation can be used as a reliable technique to initiate and control the flight of GJB. Both resistive and piezothermal stimulation appear to be feasible.

Piezothermal stimulation has lower specific time constant and proved to be more power efficient particularly around resonance, as compared to the resistive stimulators. Since the PZT has a Curie temperature of 350°C, which is far in excess of the stimulation requirements, resonant piezothermal stimulation is very attractive for continuing efforts.

## ACKNOWLEDGEMENTS

The authors would like to thank Tao Li for his invaluable suggestions and Hirotaka Sato for his help in rearing the beetles. This study is supported in part by Defense Advanced Research Projects Agency Microsystems Technology office (DARPA-MTO). YG acknowledges support through the IR/D program while working at the National Science Foundation. The findings do not necessarily reflect the views of the NSF. KV acknowledges partial support by a fellowship from the Mechanical engineering department.

## REFERENCES

- [1] K. Hausen, C. Wehrhahn, "Neural Circuits Mediating Visual Flight Control in Flies. I. Quantitative Comparison of Neural and Behavioural Response Characteristics," *Journal of Neuroscience*, 9 (11), 1989.
- [2] K. Hausen, C. Wehrhahn, "Neural Circuits Mediating Visual Flight Control in Flies. II. Separation of Two Control Systems by Microsurgical Brain Lesions," *Journal of Neuroscience*, 10 (1), 1990.
- [3] S.P. Sane, A. Dieudonne, M.A. Willis, T.L. Daniel, "Antennal Mechanosensors Mediate Flight Control in Moths," *Science*, 315, 2007.
- [4] H. Sato, C.W. Berry, B.E. Casey, G. Lavella, Y. Yao, J.M. VandenBrooks, M.M. Maharbiz, "A Cyborg Beetle: Insect Flight Control Through an Implantable Tetherless Microsystem," *IEEE MEMS*, Tucson, USA, Jan. 2008, pp. 164-167
- [5] S. B. Crary, T. E. Moore, T. A. Conklin, F. Sukardi, and D. E. Koditschek, "Insect biobotics: Electro-neural control of cockroach walking," *IEEE Robotics and Automation workshop WT3, Bio-Mechatronics*, 1996, pp. 42-54.
- [6] S. Takeuchi, I. Shimoyama, "An RF- Telemetry System with Shape Memory Alloy Microelectrodes for Neural recording of Freely Moving Insects," *IEEE Special Topic Conf. on Microtech. in Medicine & Biology*, 2000, pp. 491-96,
- [7] <http://www.uglybug.org/images02/bug69.jpg>, accessed on 3<sup>rd</sup> March 2008
- [8] [http://redwhisk.com/pictures/longwoodgardens/july2006/dsc\\_0082a\\_greenjunebeetle.jpg](http://redwhisk.com/pictures/longwoodgardens/july2006/dsc_0082a_greenjunebeetle.jpg), accessed on 3<sup>rd</sup> March 2008
- [9] A. Paul, A. Bozkurt, J. Ewer, B. Blosssey, A. Lal, "Surgically Implanted Micro-platforms in Manduca Sextamoth," *2006 Solid-State Sensor & Actuator Workshop*, Hilton Head, SC, pp. 209- 211
- [10] A. Lal, Hybrid Insect MEMS, <http://www.darpa.mil/MTO/Programs/himems/index.html>
- [11] J. M. Domek, D. T. Johnson, "Demonstration of Semiochemically Induced Aggregation in Green June Beetle, *Cotinis Nitida*," *Environmental Entomology*, 17 (2), 1988
- [12] P. J. Gullan, P. Cranston, "The Insects: An Outline of Entomology," *Blackwell Publishing*, 2004, pp. 85-111.
- [13] Y. A. Cengel, "Heat Transfer – A Practical Approach," *McGraw Hill*, 1997, pp. 244-271.
- [14] T. Li, Y. B. Gianchandani, "A Micromachining Process for Die- scale Pattern Transfer in Ceramics and its Application to Bulk Piezoelectric Actuators," *JMEMS*, 15 (3), 2006.

# MICROFABRICATED DRY ADHESIVE DISPLAYING FRICTIONAL ADHESION

D. Soto<sup>1</sup>, A. Parness<sup>1</sup>, N. Esparza<sup>1</sup>, T. Kenny<sup>1</sup>, K. Autumn<sup>2</sup>, M. Cutkosky<sup>1</sup>

<sup>1</sup>Stanford University, Stanford, California, USA

<sup>2</sup>Lewis and Clark College, Portland, Oregon, USA

## ABSTRACT

Gecko adhesion has inspired many engineered adhesives. Many of these gecko-like synthetic adhesives (GSAs) only replicate the fibrillar aspect of gecko adhesion. We present here a new GSA, MicroWedges, which demonstrates the gecko properties of dynamic adhesion, frictional adhesion, and massive reusability. MicroWedge fibers individually attach and detach during shear sliding, maintaining shear and normal adhesion. MicroWedges also exhibit the gecko-like property of frictional adhesion. Increasing the shear load on a patch of MicroWedges increases the normal adhesion. MicroWedges also demonstrate the gecko-like properties of anisotropy and high  $\mu'$ . MicroWedges are fabricated in PDMS from a reusable mold formed from SU-8. The SU-8 is exposed in a dual-side, dual-angle lithography process on transparent wafers.

## INTRODUCTION

Biomimetic adhesives inspired by the gecko adhesive system have emerged as a major research field. The gecko adhesive garners this attention since its adhesive system is unlike conventional pressure sensitive adhesives. Conventional adhesive materials are soft, with bulk moduli below 100 kPa.[1] The gecko uses micron and nanometer scale hairs of  $\beta$ -keratin, which has a bulk modulus of 1.6 GPa,[2] to form its adhesive. We have taken inspiration from the architectural principles of the gecko's adhesive and previous work with SU-8[3] to create this adhesive. There have been many demonstrations of fibrillar adhesives made from materials that do not have bulk adhesive properties.[4, 5, 6, 7, 8] This work builds on previous work by introducing a geometry that allows for frictional adhesion,[9] dynamic adhesion, and excellent longevity. This asymmetrical structure has a sharp angled tip that allows the adhesive to present a variable surface area based on the amount of loading. This allows for adhesive anisotropy, building on the theme of switchability in previous work.[10] The MicroWedges' anisotropic adhesion is described by the frictional adhesion model, which is unlike the familiar embedded friction cone model exhibited by pressure sensitive adhesives such as those on tape or Post-it<sup>®</sup> Notes (Figure 2).

## FABRICATION

This adhesive is created using a molding process depicted in Figure 3. The reusable mold is created using SU-8 on a quartz wafer with a unique lithography process. We then vacuum cast and cure polydimethylsilox-

ane rubber (PDMS) in the mold and peel out to release. To create the mold, we deposit and pattern a thin layer of aluminum on a double polished quartz wafer to create a hardmask. We then spin coat and bake a 200  $\mu\text{m}$  layer of SU-8 on top of the aluminum surface. We process the SU-8 according to recommended practice[11]. After SU-8 application, the wafer is placed on a tilted exposure stage. We adjust the stage, correcting for the index of refraction of the SU-8, to achieve the desired angle for the slanted surfaces of the mold. In this work we chose the MicroWedge angle to be  $14.8^\circ$  giving the wedges a 4:1 aspect ratio. We then expose the wafer to ultraviolet light from the underside. We perform a planar exposure with the second mask in an aligner so that the vertical surfaces are aligned with respect to the slanted surfaces. The SU-8 was then baked and developed using standard processes. With the mold complete, we use it to vacuum cast PDMS. The PDMS was prepared and placed in a vacuum chamber with the mold. The chamber is evacuated and air trapped in the PDMS is liberated. Still under vacuum, the PDMS is poured on the wafer. Air trapped in the mold bubbles through the PDMS and is removed. We then remove the mold from vacuum and spin it to planarize the PDMS backing to the desired thickness. Our backings are in the range of

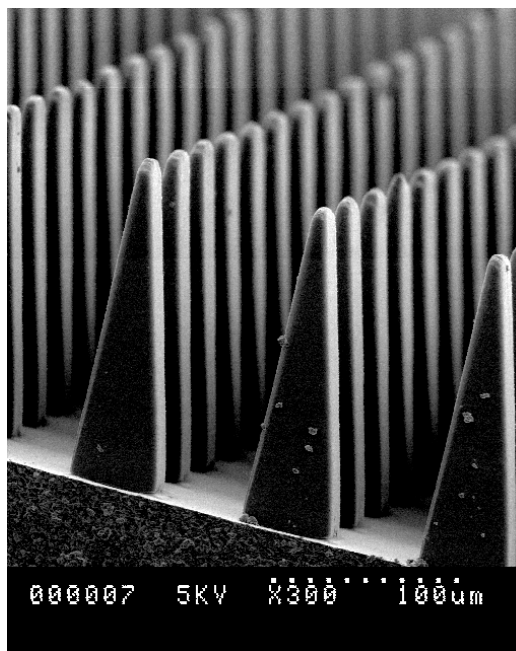


Figure 1: SEM Image of MicroWedges. Structures are 50  $\mu\text{m}$  square at the base and are 200  $\mu\text{m}$  tall.

300  $\mu\text{m}$  to 1200  $\mu\text{m}$ . The PDMS is allowed to cure. The MicroWedges are released by gently peeling the backing layer from the mold.

## TESTING

We test the MicroWedge adhesive on a custom built force testing apparatus with a three-axis motor stage[12] to control friction and loading at arbitrary angles (Figure 4). A MicroWedge patch of  $\sim 1\text{cm}^2$  is affixed by a conventional tape adhesive to a fixture on a load cell. The fixture sits atop a two-axis tilt stage that provides for the sample to be coplanar with the glass test surface. The glass stage is lowered and brought into contact with the adhesive. After initial contact, the glass is lowered further, compressing the sample. This compression phase is referred to as the preload. At this point, the stage is moved at an angle to the sample. If the sample is moved at an angle normal to the sample, it is called a load-pull (LP) test. In the case of the stage moving parallel and shearing the adhesive, the test is called a load-drag-pull (LDP) test. Intermediate angles are also tested. We collect data for both shear force and normal force adhesion during the period of contact. We also record the forces at the moment that the adhesive breaks contact by either detachment or slipping.

## RESULTS

### Dynamic Adhesion

The force trace plot (Figure 5) allows us to see the forces exerted by the adhesive as a function of time. The plot shows that dynamic sliding adhesion is obtained where despite slipping, both shear and normal adhesion forces are exerted. The adhesive is able to simultaneously maintain 4 kPa of adhesion and 20 kPa of shear. This implies that individual hairs that have detached are able to reattach and exert adhesive force. This property

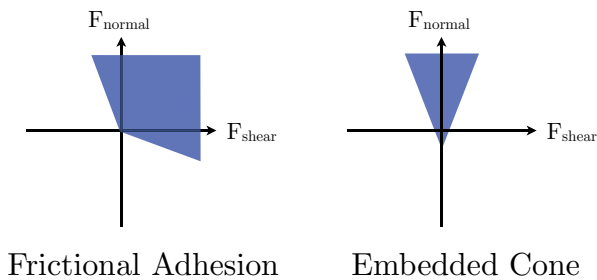


Figure 2: Comparison of Frictional Adhesion and Embedded Cone models. The shaded areas represent regions of stability. The unshaded areas represent areas where the adhesive will pull away or slip relative to the substrate. The frictional adhesion model is unique as increasing the shear on the adhesive generates more adhesion. Another unique feature is that the adhesion vanishes when the shear is removed.

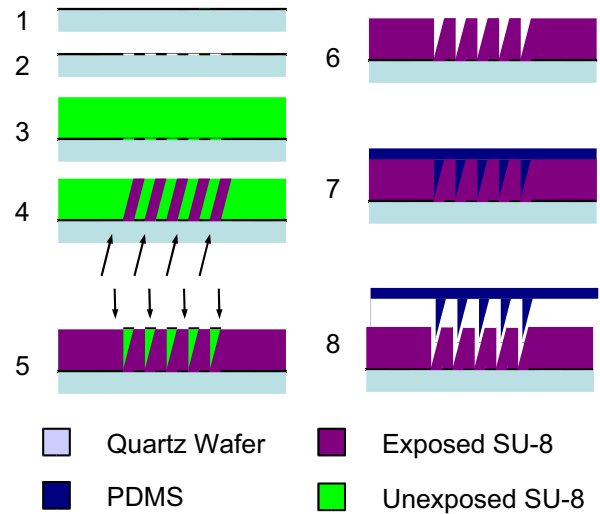


Figure 3: Fabrication Sequence 1) Deposit aluminum on quartz wafer 2) Pattern aluminum to create self-aligned mask 3) Deposit SU-8 on top of aluminum 4) Angled self-aligned UV exposure from backside 5) Align mask to topside and UV expose 6) Develop 7) Cast and spin PDMS 8) Peel out cast MicroWedges and backing layer

allows the MicroWedge adhesive a graceful failure mode desirable for robotics or locomotion applications. Other GSAs have demonstrated similar results using a spherical surface with a radius of  $\sim 5\text{mm}$ . [8] These tests don't necessarily demonstrate the reattachment of fibrils since only a portion of the sample's fibers are in contact.

### Frictional Adhesion

The limit surface in Figure 6, obtained through many trials over a range of preload angles, preload depths, and exit angles, is a map of the release points for different

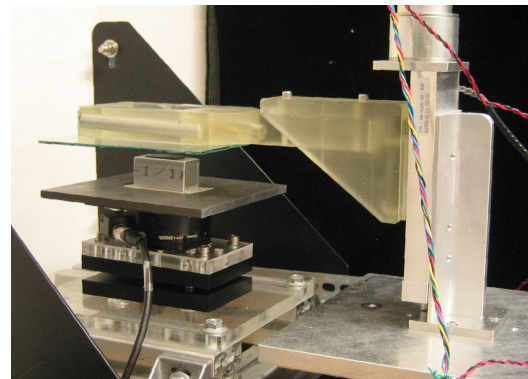


Figure 4: Force measurement apparatus. Photo shows MicroWedge adhesive samples on mounting plate affixed to load cell. Load cell is above two-axis tilt plate for plane-plane alignment. The glass plate (not in contact) is above the sample. The motorized stages are seen on the right side of the photo.

shear to adhesion ratios. The curve creates a limit surface of conditions where the adhesive contact will fail, either by shear or normal movement. The limit surface shows that as greater shear is exerted, the adhesion increases. The limit surface of the flat control in Figure 7, shows behavior similar to the embedded cone model where increasing shear decreases the available normal force. Also, the limit surface of the flat control does not pass through the origin. This implies that there must be a normal force exerted at detachment when there is no shear.

### Longevity

We have performed testing of the adhesive over thousands of LDP cycles. When loaded to a constant displacement depth, the MicroWedges retain 50% of their adhesion and 86% of their shear over the 30,000 trials. This is in contrast to conventional pressure sensitive adhesives as well as other synthetic fibrillar adhesives which degrade more quickly with repeated use. Each of these trials was a 10mm drag resulting in a total dragged distance of 300m.

### DISCUSSION

We believe that this adhesive is an important advancement in applications where shear force, anisotropy, and reusability are key properties. These properties are especially important for climbing applications. Traditional pressure sensitive adhesives are not suitable for climbing since they require large forces of detachment. This adhesive exhibits frictional adhesion and as can be seen in Figures 2 and 6, when the shear force is removed, the normal adhesion vanishes, allowing effortless detachment. This ease of detachment enables climbing stability. Another key property for climbing applications is the dynamic adhesion. The MicroWedge adhesive is able to maintain adhesion while sliding. This prevents

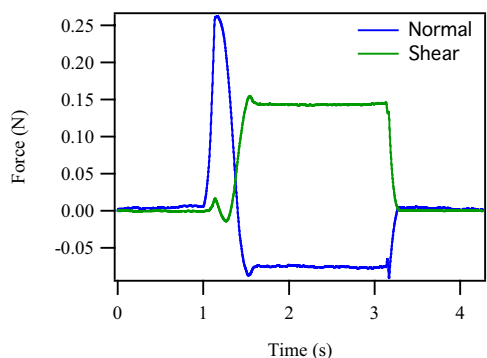


Figure 5: MicroWedge Force Trace. The normal trace shows the initial compression phase followed by a region of adhesion during the parallel drag. In the shear trace, we see that there is a shear force created by the adhesive at the same time as the normal adhesion force.

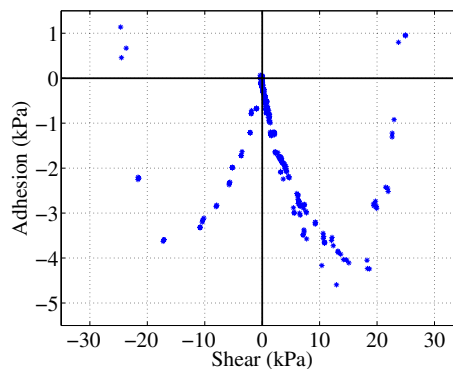


Figure 6: Frictional Adhesion Plot for 50  $\mu\text{m}$  Diameter MicroWedges. We see that the adhesion is increased as the shear increases. Also, if the shear is decreased to zero, the adhesion vanishes and the adhesive can be removed with no force.

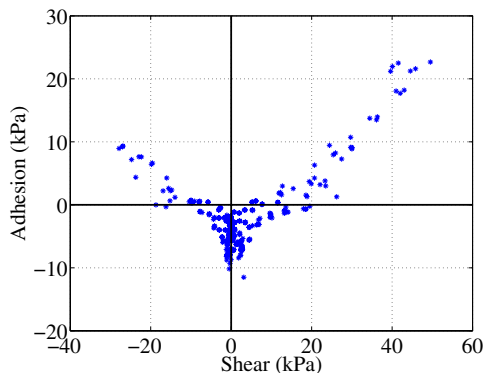


Figure 7: Frictional Adhesion Plot for PDMS Flat Control Sample. The limit surface does not intersect the origin and increasing shear leads to diminished adhesive capability.

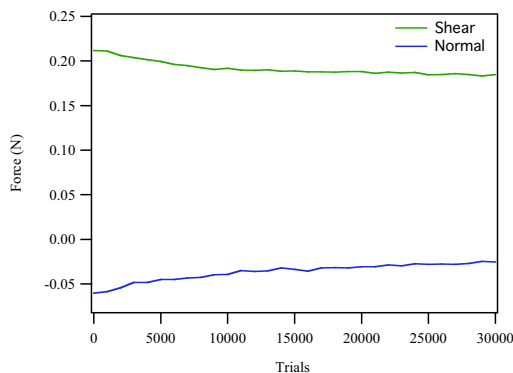


Figure 8: Lifetime Test of MicroWedge Adhesive. 30,000 trials performed of 10mm drag. Adhesion fell to 50% of initial and shear fell to 86% of initial during test. This longevity is superior to other pressure sensitive adhesives.

catastrophic failures of adhesion. For a climbing robot, graceful failures in adhesion leading to sliding are preferable to complete detachment.

## CONCLUSION

A novel geometry for a GSA has been fabricated and tested. The MicroWedge adhesive displays increasing adhesion with increasing shear, the ability to maintain adhesion while sliding, and maintains 56% of its initial adhesion after 30,000 cycles. Future work will investigate the effect of material properties and device geometry on performance.

## ACKNOWLEDGEMENTS

Work was performed in part at the Stanford Nanofabrication Facility (a member of the National Nanotechnology Infrastructure Network) which is supported by the National Science Foundation under Grant ECS-9731293, its lab members, and the industrial members of the Stanford Center for Integrated Systems. This work was supported by the CIS New User Grant Program at the Stanford Nanofabrication Facility.

## REFERENCES

- [1] C. Gay and L. Leibler, "Theory of Tackiness", *Physical Review Letters*, (1999).
- [2] A. Peattie, C. Majidi, A. Corder, and R.J. Full, "Ancestrally high elastic modulus of gecko setal  $\beta$ -keratin", *The Journal of the Royal Society Interface*, 4, (2007).
- [3] H. Sato, Y. Houshi, and S. Shoji, "Three-dimensional micro-structures consisting of high aspect ratio inclined micro-pillars fabricated by simple photolithography", *Microsystem Technologies*, 10, (2004).
- [4] A. Geim, S. Dubonos, I. Grigorieva, K. Novoselov, A.A. Zhukov, and S.Y. Shapoval, "Microfabricated adhesive mimicking gecko foot-hair", *Nature Materials*, 2, (2003).
- [5] S. Gorb, M. Varenberg, A. Peressadko, and J. Tuma, "Biomimetic mushroom-shaped fibrillar adhesive microstructure", *Journal of The Royal Society Interface*, 4, (2007).
- [6] L. Ge, S. Sethi, L. Ci, P. Ajayan, and A. Dhinjwala, "Carbon nanotube-based synthetic gecko tapes", *Proceedings of the National Academy of Sciences*, 104, 26, (2007)
- [7] B. Schubert, J. Lee, C. Majidi, and R.S. Fearing, "Sliding-induced adhesion of stiff polymer microfibre arrays. II. Microscale behaviour" *Journal of The Royal Society Interface* (2008)
- [8] M.P. Murphy, B. Aksak, M. Sitti "Adhesion and anisotropic friction enhancements of angled heterogeneous micro-fiber arrays with spherical and spatula tips", *Journal of Adhesion Science and Technology*, 21, (2007)
- [9] K. Autumn, A. Dittmore, D. Santos, M. Spenko, and M. Cutkosky, "Frictional adhesion: a new angle on gecko attachment", *The Journal of Experimental Biology*, 209, (2006).
- [10] M. T. Northen, K.L. Turner, C. Greiner, and E. Arzt, "A hierarchical gecko-inspired switchable adhesive", *Technical Digest of the 2006 Solid-State Sensor and Actuator Workshop*, Hilton Head Isl., SC, 2006, Transducer Research Foundation, Cleveland (2006), pp. 43-46.
- [11] <http://www.microchem.com>
- [12] D. Santos, M. Spenko, A. Parness, S. Kim, and M. Cutkosky, "Directional adhesion for climbing: theoretical and practical considerations", *Journal of Adhesion Science and Technology*, 21, (2007)

# A NOVEL 3D MICRO MEMBRANE FILTRATION DEVICE FOR CAPTURE VIABLE RARE CIRCULATING TUMOR CELLS FROM WHOLE BLOOD

Siyang Zheng<sup>1</sup>, Henry K. Lin<sup>2</sup>, Richard J. Cote<sup>2</sup>, and Yu-Chong Tai<sup>1</sup>

<sup>1</sup>Department of Electrical Engineering, California Institute of Technology, Pasadena, California, USA

<sup>2</sup>Department of Pathology, University of Southern California, Los Angeles, California, USA

## ABSTRACT

Cancer is one of the most serious diseases facing human being. Improvement on cancer diagnostics has proved to be important for the outcome of cancer patients. We report here a novel micro membrane filtration device that captures rare circulating tumor cells from whole blood for early cancer diagnostics and treatment monitoring. The device is fabricated with multi layers of polymer material parylene-C. Tested with the model system, the device can capture tumor cells from whole blood with 86.5% capture efficiency. Different from previous membrane filtration devices, the cells are alive up to at least two weeks after isolation.

## INTRODUCTION

Cancer has become the leading cause of death for persons younger than eighty-five years old in US since 1999 [1]. Over 90% of the solid tumor patients are killed by secondary metastatic tumors. Unfortunately, the metastasis process remains a major challenge for basic cancer research [2]. Imaging has been the primary tool for tumor diagnostics, but it requires the tumor to reach certain size to be detectable. During the metastasis process, tumor cells from the primary tumor travels to distant sites through circulation system (bloodstream or lymphatic circulation). Circulating tumor cells (CTC) are tumor cells shed into bloodstream during metastasis. If these CTCs can be detected, it can provide an invaluable tool for cancer early diagnostics and patient treatment monitoring. Technical difficulties for CTC detection include extremely low concentration (e.g.,  $\sim 1/\text{mL}$  or  $1/10^{10}$  blood cells), and thus large sample volume for micro devices ( $\sim 7.5\text{mL}$  whole blood). Therefore, a sensitive, efficient, and fast method for the separation and detection of CTCs at low cost is highly desirable and such a method may revolutionize the cancer diagnostics and prognostics [3-5].

Current clinical practice of CTC detection is primary based on gradient centrifugation [6]. A centrifugation reagent Ficoll-paque, which has specific gravity matched to mononuclear cells, is mixed with whole blood and centrifuged. The cell fraction including most of the lymphocytes and CTCs is extracted and immunohistochemically stained before laid on tens of glass slides. It can take a pathologist hours to read the slides. The only FDA approved automated system for CTC detection is based on immunomagnetic separation [7, 8]. Antibody conjugated magnetic beads capture CTCs while other blood cells are flushed away. The assay and the instrument are very expensive and the fundamental problem of variable antigen expression on CTC surface limits the capture efficiency. Recently an immunoaffinity based "CTC chip" [4], where CTCs are captured with antibodies conjugated to device surface, has successfully demonstrated high enrichment CTC detection with patient samples from multiple metastatic cancers. While viable CTCs with high purity can be obtained, the capture efficiency and throughput need to be improved.

Previously, we reported a single-layered parylene membrane filter device that can capture CTCs from 7.5mL of whole blood with  $\sim 90\%$  efficiency and  $10^7$  enrichment [9]. Our filter utilizes size-based filtration because CTCs (15-30 $\mu\text{m}$  in diameter) are significantly larger than erythrocytes (6-9 $\mu\text{m}$ ) and leukocytes (5-16 $\mu\text{m}$ ). However, the blood samples needs to be fixed (i.e.,

hardened) before filtration. Without fixation, cell membrane of CTC is ruptured during the filtration process. Fixation not only lengthens the sample preparation procedure and increases the back pressure, but, more importantly, kills the tumor cells, which limits further study of these rare cells. In this paper, we present a new 3D filter device that eliminates the need of blood fixation and reduces the shear stress exerted on the tumor cells during the filtration process. Experimentally, CTCs captured by the new device can stay alive for at least two weeks.

## DESIGN AND FABRICATION

Parylene-C (poly-para-xylylene) is an ideal building material for this filtration device because of its unique properties. It is a mechanically strong (Young's modulus 4GPa and tensile strength: 70MPa) while malleable (elongation to break 200%) polymer. It is optically transparent in visible range, which facilitates direct pathological observation of stained cells under microscope. Chemically, it is inert to most of the chemicals and solvents used in standard chemical and biological laboratories, so all the post-processing (e.g. cell fixation, cell lysing, cell staining) can be performed after cell capture on devices. Parylene is a highly biocompatible polymer and can meet the highest standard for long-term implantation. Parylene membrane filtration devices will experience less clogging and membrane fouling due to reduced protein absorption and cell adhesion. Finally, high quality pin-hole free parylene thin film can be obtained with room-temperature chemical vapor deposition (CVD), and further patterned with standard lithography and oxygen plasma in a reactive ion etcher (RIE).

The fabrication started with 1 $\mu\text{m}$  thermal oxidation of prime Si wafer (Fig.1). The backside oxide was patterned and the front-side was stripped. A 5 $\mu\text{m}$  parylene-C thin film was deposited on front-side, and then melted at 350°C. TMAH etching from backside made nine through-wafer cavities on each of the 1x1cm<sup>2</sup> die, with silicon dioxide as etching mask and molten parylene as front-side protection layer. A 2.5 $\mu\text{m}$  second parylene layer was deposited from both sides and patterned with oxygen plasma. On the cavity regions, this second parylene layer sandwiched with the molten parylene layer and formed the bottom filter layer of the membrane filtration device. Then 6.5 $\mu\text{m}$ -thick sacrificial photoresist was spin-coated and patterned, followed by 10 $\mu\text{m}$  parylene deposition and patterning from front-side. This is the top filter layer of the membrane filtration device. Finally sacrificial photoresist was dissolved in acetone and all the parylene layers were annealed at 190°C for forty-eight hours to strengthen the overall structure. The pore size, shape and density are defined by the photolithography process. The gap between the top and bottom membranes is defined by the thickness of the sacrificial photoresist. All these parameters can be controlled by design.

To keep device integrity during filtration, within each cavity there are 99 hexagonal patches (Fig.2). The top and bottom parylene membrane layers are in contact and annealed at the regions between the patches. Each patch has thirty-six 9 $\mu\text{m}$  diameter pores on the top parylene membrane and thirty-seven 8 $\mu\text{m}$  diameter pores on the bottom parylene membrane (Fig.3). The pore positions on the top and bottom membranes are shifted so that a

flow-through particle has to traverse the gap in between, which effectively acts as a third dimension during filtration.

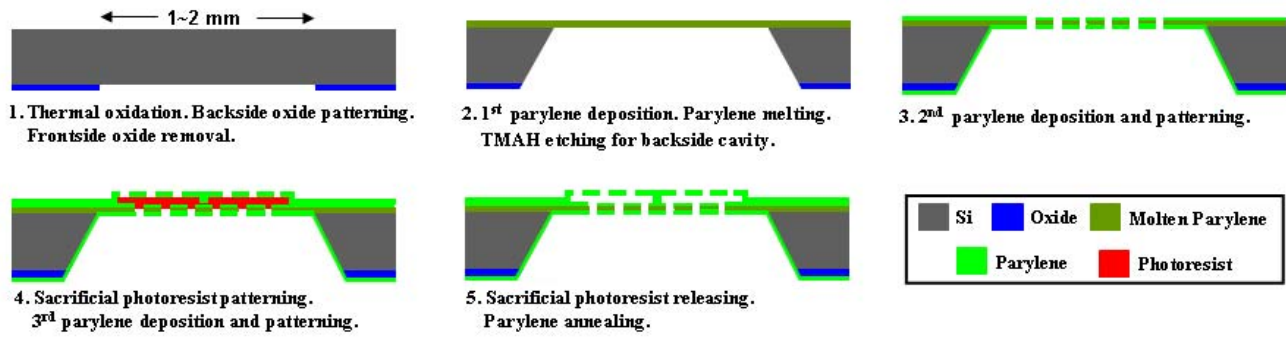


Figure 1: Process flow.

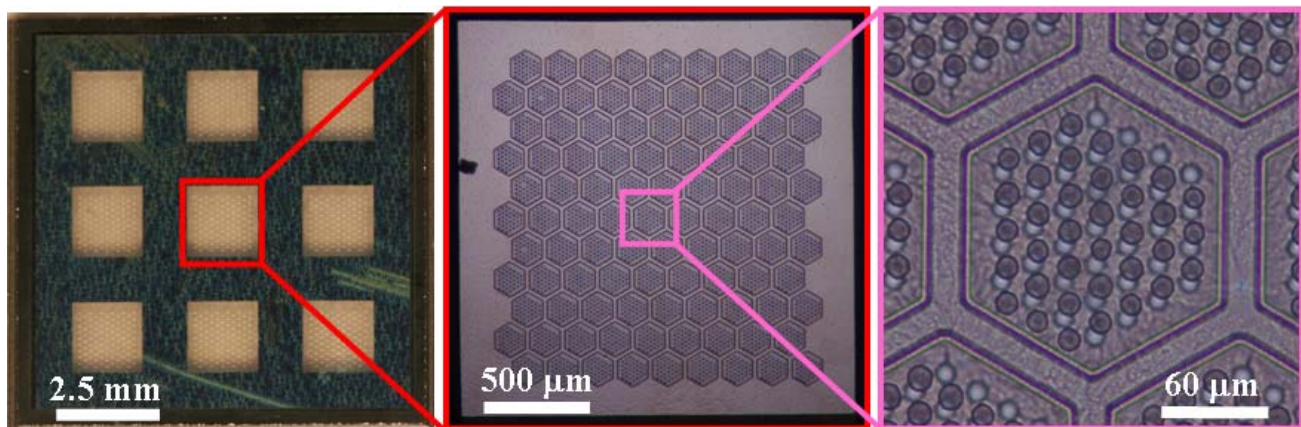


Figure 2: Fabricated device pictures. Left: each device has a 3x3 array of Si cavities. Middle: each cavity has 99 hexagonal patches. Right: each patch contains two layers of parylene filters with shifted pore positions. The gap between the two layers is 6.5 μm and acts as the 3rd filtration dimension.

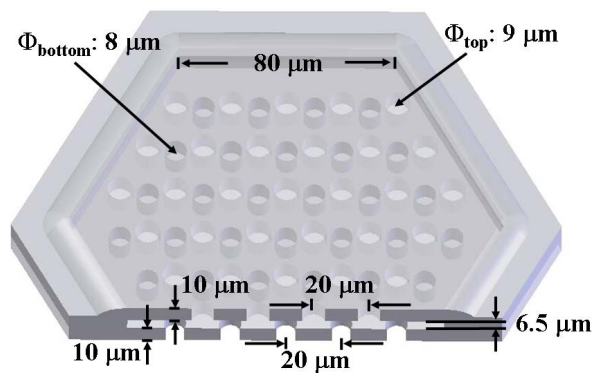


Figure 3: Device design showing the geometry of a single patch.

## EXPERIMENTAL

Human breast adenocarcinoma cancer cell line MCF-7 is treated with green fluorescent stain carboxyfluorescein diacetate succinimidyl ester (CFSE), centrifuged and then resuspended in phosphate buffered saline (PBS) before testing. Live cells with intact cell membrane can keep CFSE inside and thus fluoresce, while CFSE leaks out in dead cells. CFSE stained MCF-7 cells in

the stock solution are counted manually with a hemacytometer under an epi fluorescent microscope with a blue excitation green emission filter block (Nikon B-2E/C). The cells are diluted with PBS to the desired concentration before use. Cells are cultured in standard cell culture facility at 37°C and 5% CO<sub>2</sub>. Dulbecco's modified eagle's medium (DMEM) with 10% fetal calf serum (FCS) is used as cell culture media.

For testing, a jig was made by two acrylic pieces with central holes (Fig.4). Four pieces of PDMS were used to sandwich the chip to form a top and a bottom chamber and as the sealing material to prevent leakage. The acrylic pieces and the PDMS pieces are clamped together. Sample is loaded into a syringe and the tip is inserted into a matching hole on the top PDMS piece. The sample is hand-pushed through the device. The back pressure experienced during filtration is normally very low.

## RESULTS AND DISCUSSION

For the previous one layer parylene membrane filter, the cells have to be fixed before applying to the devices. Fixation hardens the cells by chemically crosslink cellular proteins. Without fixation, the cells are disintegrated during the filtration process due to the mechanical shear stress acting on the cell membrane during the filtration process (Fig.5A and Fig.5B). The 3D micro filtration devices have two layers of membrane filters and the pore positions on the bottom membrane are shifted from those on the top membrane. The cells are trapped in the pores of the top membrane

and the bottom membrane provides mechanical support to the trapped cells. In this way, the shear stress exerted on cell membrane during the filtration process is minimized. As a result, in contrast to the faint green “ghost rings” on previous single-layered filter, the CFSE labeled MCF-7 cells show bright green fluorescence on the 3D microdevices after filtration, meaning the cell membrane is well preserved (Fig.5C).

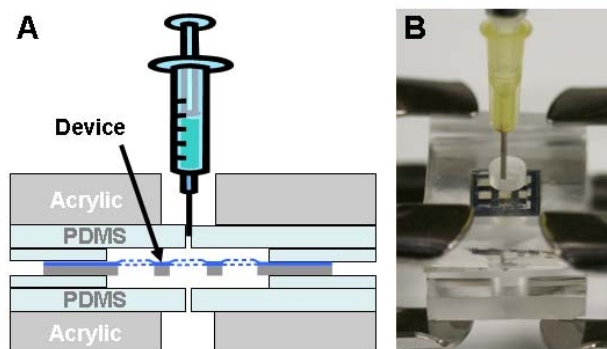


Figure 4: Device assembled for testing.

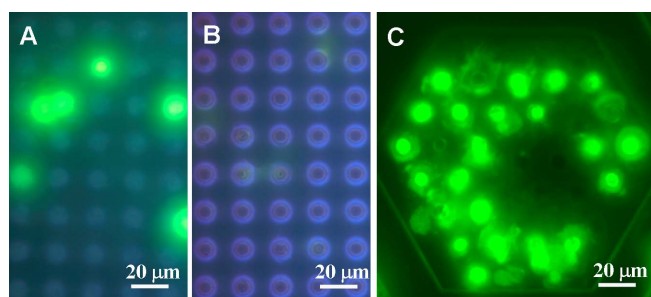


Figure 5: Experiments with MCF-7 tumor cells. A: positive control, CFSE labeled MCF-7 cells loaded on top a single layered parylene filter without filtering through. B: CFSE labeled MCF-7 cells filtered through a single layered parylene filter. The image is over exposed to show the faint green color around the pore edge. C: CFSE labeled MCF-7 cells filtered through a 3D filtration device.

Capture efficiency is an important parameter for CTC isolation and we characterized it with a model system. The model system is constructed by spiking a known number of CFSE labeled human breast cancer cell line MCF-7 cells into dilute whole blood. In the results shown in Table 1, MCF-7 cells were counted manually under hemacytometer for five times.  $342 \pm 58$  MCF-7 cells were then spiked in 1 mL ten times diluted whole blood, and passed through the devices. Cells are counted under fluorescent microscope right after filtration. The MCF-7 cells are green fluorescent because of CFSE labeling while blood cells do not fluoresce. Capture efficiency is measured to be  $86.5 \pm 16.5\%$  with the model system, which is comparable to that of the previous single layer membrane filter ( $\sim 90\%$ ).

To study the viability of the captured tumor cells, the devices were taken out from the jig assembly and put immediately into a petri dish filled with cell culture media and kept in cell culture incubator for further observation. After seven days in cell culture media, over 80% of the tumor cells still fluoresce brightly (Fig.6). In spite of the overwhelming number of blood cells around, the cellular membrane of these tumor cells is intact. It's interesting to note some of bright spots, which presumably are viable cells right after filtration, are missing after seven days. In three of these cases in

Fig.6, the cells are actually on the surface of the top filter, instead of being trapped in pores. So it is likely that these three cells detached from the device surface and moved into cell culture media during cell culture or device manipulation after filtration. For the rest nine cases where the cells seem to be trapped in pores of the top membrane on the first day but missing after seven days, there might be two possibilities. These cells might die during the seven day period and thus the CFSE dye leaks out, making them not fluoresce. Or these cells might migrate out of the pores. In fact tumor cells are famous for their ability to migrate during the metastasis process and this ability is an important characteristic of a metastatic tumor cell.

Table 1: Capture efficiency measurement.

Experiment Number	Tumor Cell Count
1	288
2	317
3	281
4	299
Average	$296 \pm 16$

To further confirm the viability of the captured tumor cells, red fluorescent stain  $C_{12}$ -resazurin (dodecyl-resazurin) purchased from Invitrogen, CA, USA is used to measure the metabolic level inside cells.  $C_{12}$ -resazurin is readily diffused into cell through cellular membrane. In metabolically active cells, non-fluorescent  $C_{12}$ -resazurin is reduced to red-fluorescent  $C_{12}$ -resorufin by some cellular enzymes. To use  $C_{12}$ -resazurin for cell viability test, green fluorescent dye CFSE labeled MCF-7 cells were spiked into ten times dilute whole blood, and then filtered through a 3D filtration device. After checking the captured cells under epi fluorescent microscope with green emission filter, the device was kept in cell culture media for fourteen days. On the fifteenth day,  $C_{12}$ -resazurin with a final concentration of  $5\mu\text{M}$  was introduced to the device and the system was incubated in cell culture incubator for fifteen minutes. Then the device was taken out and observed under epi fluorescent microscope with green excitation red emission filter block (Nikon G-2E/C). Only metabolically active cells fluoresce red due to the reduction of  $C_{12}$ -resazurin to red fluorescent  $C_{12}$ -resorufin. As shown in Fig.7, all metabolically active cells including blood cells fluoresce red. Compared with the green fluorescent image which indicates positions of the CFSE labeled MCF-7 tumor cells only, almost all the tumor cells with complete cell membrane (green fluorescent) also show strong red fluorescent signals. Compared with green fluorescent image taken right after filtration, more than 70% of the CFSE labeled tumor cells are metabolically active after 14 days.

## CONCLUSION

A novel 3D membrane filtration device was designed and fabricated with integrated parylene technology. The pore positions on the bottom membrane are shifted from the positions on the top membrane. The mechanical support provided by the bottom membrane to cells trapped in the pores of the top membrane effectively reduces the shear stress exerted on cell membrane. As a result, the tumor cells can be captured alive without any sample preparation other than dilution with PBS. The viability of the captured tumor cells are validated with two approaches. Green fluorescent dye CFSE assays for the integrity of the cell membrane, while red fluorescent labeling reagent  $C_{12}$ -resazurin tests the cellular metabolic activity. In both cases, the results show at least 70% of the tumor cells isolated from the tumor cell spiked model

system are alive for at least two weeks after filtration. The capture efficiency measured from the model system is 86.5%, which is comparable to previous single layer parylene filter and higher than

most of the other approaches for CTC isolation. The 3D micro filtration devices can be a valuable tool for metastasis research and clinical diagnostics of metastatic cancer.

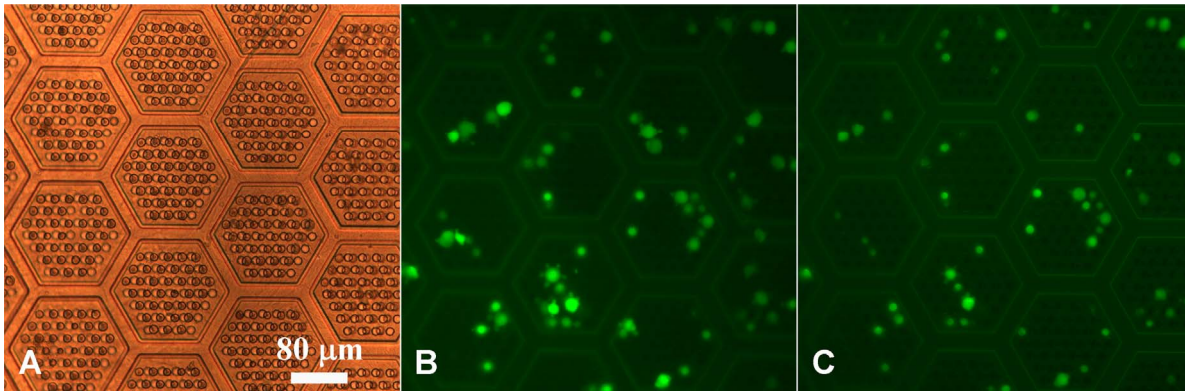


Figure 6: Experiments with the model system. CFSE labeled MCF-7 cells are mixed with ten times diluted whole blood and then passes through the 3D filtration devices. A: Microscope image of the device after filtration under bright field illumination. B: Epi fluorescent image of the device right after the filtration. C: Epi fluorescent image of the device 7 days after the filtration.

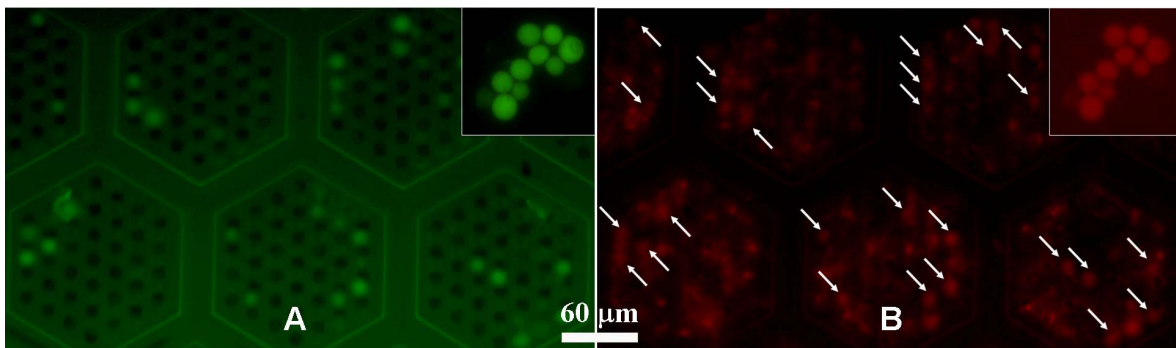


Figure 7: Cell viability tests. A: Epi fluorescent image (green channel) of a device 14 days after filtered with the model system mixture. B: Epi fluorescent image (red channel) of same device stained with C12-resazurin at the 14th day. Arrows points to the positions of MCF-7 cells as indicated by figure 7A. Note metabolic active blood cells are also stained red. Insets are a positive control of MCF-7 cells 14 days after loaded onto a device without filtration.

#### ACKNOWLEDGE

The funding of the project is provided by NIH 1R21 CA123027-01. The authors would like to thank members of the Caltech Micromachining Laboratory for their valuable assistance.

#### REFERENCES

- [1] A. Jemal, T. Murray, E. Ward, A. Samuels, R. C. Tiwari, A. Ghafoor, E. J. Feuer, and M. J. Thun, "Cancer Statistics, 2005," *CA Cancer J Clin*, vol. 55, pp. 10-30, January 1, 2005 2005.
- [2] R. A. Weinberg, *The biology of cancer*. New York: Garland Science, Taylor & Francis Group, LLC, 2007.
- [3] G. P. Gupta and J. Massague, "Cancer metastasis: Building a framework," *Cell*, vol. 127, pp. 679-695, Nov 17 2006.
- [4] S. Nagrath, L. V. Sequist, S. Maheswaran, D. W. Bell, D. Irimia, L. Ulkus, M. R. Smith, E. L. Kwak, S. Digumarthy, A. Muzikansky, P. Ryan, U. J. Balis, R. G. Tompkins, D. A. Haber, and M. Toner, "Isolation of rare circulating tumour cells in cancer patients by microchip technology," *Nature*, vol. 450, pp. 1235-U10, Dec 2007.
- [5] K. Pantel and R. H. Brakenhoff, "Dissecting the metastatic cascade," *Nature Reviews Cancer*, vol. 4, pp. 448-456, Jun 2004.
- [6] O. Lara, X. D. Tong, M. Zborowski, and J. J. Chalmers, "Enrichment of rare cancer cells through depletion of normal cells using density and flow-through, immunomagnetic cell separation," *Experimental Hematology*, vol. 32, pp. 891-904, Oct 2004.
- [7] U. Bilkenroth, H. Taubert, D. Riemann, U. Rebmann, H. Heynemann, and A. Meye, "Detection and enrichment of disseminated renal carcinoma cells from peripheral blood by immunomagnetic cell separation," *International Journal Of Cancer*, vol. 92, pp. 577-582, May 15 2001.
- [8] E. Racila, D. Euhus, A. J. Weiss, C. Rao, J. McConnell, L. Terstappen, and J. W. Uhr, "Detection and characterization of carcinoma cells in the blood," *Proceedings Of The National Academy Of Sciences Of The United States Of America*, vol. 95, pp. 4589-4594, Apr 14 1998.
- [9] S. Zheng, H. Lin, J.-Q. Liu, M. Balic, R. Datar, R. J. Cote, and Y.-C. Tai, "Membrane microfilter device for selective capture, electrolysis and genomic analysis of human circulating tumor cells," *Journal of Chromatography A*, vol. 1162, pp. 154-161, 2007.

# A REAL-TIME PROTEIN DETECTOR UTILIZING THE VROMAN EFFECT ON SAM-FUNCTIONALIZED SURFACES

Seokheun Choi, Yongmo Yang, and Junseok Chae

Electrical Engineering, Arizona State University, Tempe, AZ, USA

## ABSTRACT

We report a new SPR (surface plasmon resonance) protein sensor using the Vroman effect for real-time, sensitive and selective detection of protein. The sensor relies on the competitive nature of protein adsorption to the surface, directly depending upon protein's molecular weight. We, for the first time, utilize the Vroman effect for real-time protein microsensors using three different proteins including annexin (36 kDa), streptavidine (53 kDa), and isolectin (114 kDa) on three different surfaces which are a bare-gold surface and two others modified by OH- and COOH-terminated SAM (Self Assembly Monolayer). The real-time adsorption and displacement of the proteins are monitored by SPR demonstrating very high sensitivity and selectivity label-free protein sensor. The biosensor can distinguish at least 17 kDa in molecular weight with 100 % selectivity. The protein detector can be integrated with microfluidic systems to provide extremely sensitive and selective analytical capability.

## 1. INTRODUCTION

Biosensors comprise a specific bio-receptor and a sensitive transducer. The bio-receptor requires high selectivity and affinity whereas the transducer demands high sensitivity and large dynamic range. Depending upon detection mechanisms, biosensors can largely be categorized as either labeled or label-free system. Labeling techniques have been broadly employed to allow automation of detection process. However, the chemical labeling may modify the target proteins characteristics so that their natural activity is impaired [1]. Moreover, the labeling is time-consuming and labor-intensive and often it is difficult to achieve accurate quantification due to different labeling efficiency for different proteins. Label-free system, on the other hand, does not require labeling process and has started to be attractive for biological analysis [2]. Among various label-free mechanisms, SPR has been one of the leading techniques due to its extremely high sensitivity (The detection limit of the SPR is up to a few ppt ( $\text{pg mL}^{-1}$ )) [3]. For selectivity, researchers use antibodies, protein lysates, lectins, peptides, and aptamers, which are single stranded DNAs or RNAs synthesized in a combinatorial fashion, as bio-receptors [4]. However, weak binding affinity with analytes, non-specific adsorption, and low reproducibility still remains critical limitations.

In this paper, we present a new proof-of-concept high sensitivity and selectivity SPR protein sensor operating without using a bio-receptor. The selectivity, typically offered by bio-receptors, is provided by a competitive nature of protein adsorption to the surface, directly depending upon protein's molecular weight, namely Vroman effect [5]. Leo Vroman first observed that fibrinogen adsorbed from plasma disappeared within minutes of surface contact. The loss was the first described example of the fibrinogen displacement phenomenon by other high molecular weight plasma proteins. Fig. 1 describes the Vroman effect; a low-molecular-weight (LMW) protein, initially covers the surface, is displaced by a high-molecular-weight (HMW) protein. It is more energetically stable when HMW proteins replace LMW ones in nature. However, when HMW proteins cover the surface first, LMW ones arriving later do not displace the former. We utilize the molecular weight differences as selectivity of our biosensor.

In section 2, surface preparation and device fabrication are

discussed. Experimental and evaluation methods are presented in section 3. In section 4, we demonstrate SPR measurements results using three different proteins. Finally, concluding remarks follow in section 5.

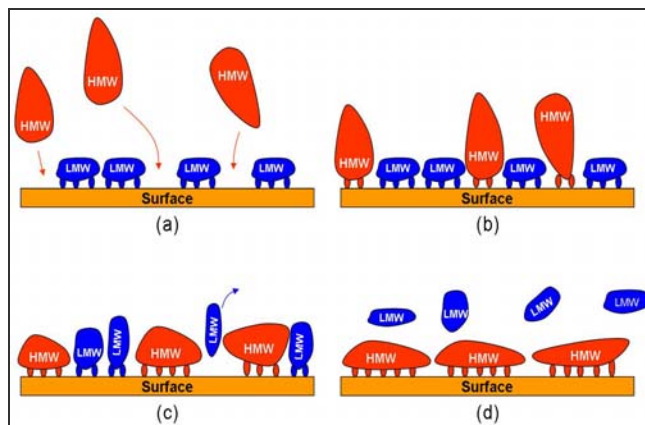


Figure 1. Schematic of the Vroman effect

## 2. SURFACE PREPARATION AND MICROFLUIDIC DEVICE FABRICATION

We use three different proteins; annexin (36 kDa), streptavidine (53 kDa), and isolectin (114 kDa). All proteins are commercially available from Sigma Aldrich and Invitrogen. The proteins are diluted using Phosphate Buffered Saline (PBS) 1X (Mediatech Inc.).

We prepare three different surfaces; bare-gold, OH-terminated SAM, and COOH-terminated SAM. This is to observe Vroman effect on three different hydrophobicity surfaces. Bare-gold is the most hydrophobic and OH-SAM provides the most hydrophilic surfaces. Vroman effect occurs based upon energy preference of hydrophobicity / hydrophilicity surfaces; thus the surface modification greatly affects biosensor performance. Details are presented in section 4. Glass substrates (BK7,  $n=1.517$ ) are first cleaned in piranha solution (a 3:1 ratio of  $\text{H}_2\text{SO}_4$  and  $\text{H}_2\text{O}_2$ ) for 10 min. The cleaned glass is coated with Cr/Au (3nm/48nm) by thermal evaporation. Then the substrates are cleaned by oxygen plasma (Harrick Plasma Inc.) and immersed in an ethanol solution of different alkane-thiols at 1mM for 24h at room temperature to form SAMs. COOH- and OH- terminated SAMs are formed on the substrate with 11-mercaptoundecanoic acid and 11-mercapto-1-undecanol. Finally the substrates are rinsed with ethanol and water, and thoroughly dried using nitrogen.

### 2.1 Surface Characterization

The three different surfaces are characterized by contact angle measurement and FTIR (Fourier Transform Infrared Spectroscopy). A droplet (2ul) of water is dispensed on the surfaces and the contact angle is measured (Easy Drop FM 40, Krüss GmbH Inc.). The contact angles for bare-gold, COOH-, and OH-terminated SAM are  $82.6 \pm 0.77^\circ$ ,  $41.4 \pm 0.63^\circ$ , and  $38.2 \pm 0.32^\circ$ , respectively. As expected, the bare-gold surface is very hydrophobic and OH- and COOH-SAM surfaces are hydrophilic. The contact angle difference

between OH- and COOH- SAM surfaces is not large; yet this small difference makes significant impact on the protein adsorption / desorption.

The compositions of the SAM surfaces are determined by FTIR (Nicolet Continuum, Thermo Electron Corp.). Figure 2 shows that the methylene stretching of the alkyl chains for both COOH- and OH- terminal SAMs are clearly visible with two absorption bands at 2917 and 2846  $\text{cm}^{-1}$ . The spectrum of the COOH-SAM shows the C=O stretching band at 1706  $\text{cm}^{-1}$  in the mid-IR spectrum, which suggest most terminal acid groups participate in intermolecular hydrogen bonding process. The OH-SAM spectrum shows the C-O stretch absorption at 1040  $\text{cm}^{-1}$ , thus validating the formation of SAMs on gold substrate.

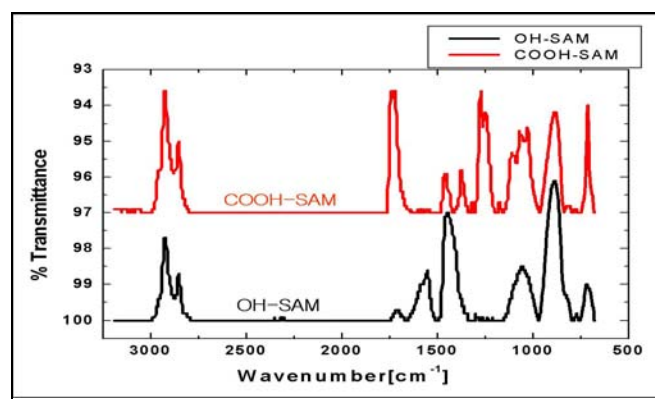


Figure 2. FTIR spectra of OH- and COOH-SAMs

## 2.2. Microfluidic Device

In order to facilitate potential integration with microfluidic systems, the sensor is enclosed by microfluidic channels/chambers (Figure. 3). On a Pyrex glass substrate (500 $\mu\text{m}$ ), Cr/Au are deposited (3nm/48nm). A cover glass is patterned and etched to have 1mm wide and 50 $\mu\text{m}$  deep fluidic channels. Ports for inlets and outlets are 9.7mm tall and 6.4mm in diameter. The Pyrex substrate and cover glass are bonded by epoxy thin films (Upchurch Scientific) and cured at 120  $^{\circ}\text{C}$  for 20 min.

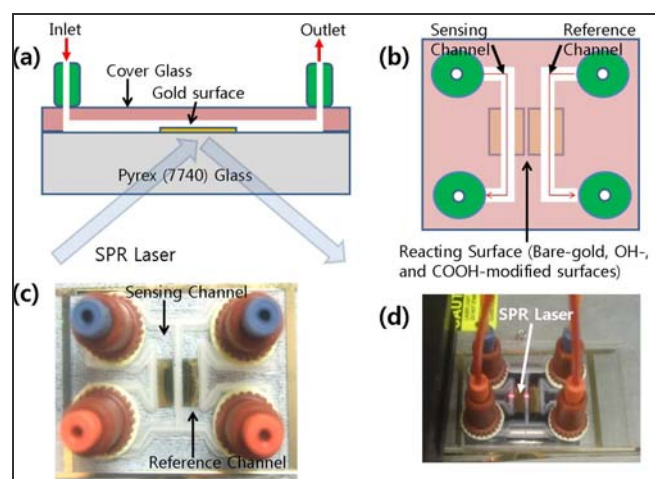


Figure 3. Schematics of (a) the cross sectional view, (b) the top view, (c) microfluidic enclosure, and (d) the bio-sensor chip on a SPR

## 3. EXPERIMENTAL AND EVALUATION METHODS

The fabricated device is mounted on SPR analytical system (Biosensing Instrument Inc.). We monitor the angle shift in real time as protein solution flows through the channels driven by an external syringe pump. First, PBS is circulated for 20 min until the SPR output stabilizes. The protein solution (1 $\mu\text{M}$ ) flows through the channels at 20 ml/min, which generates the angle shift proportional to molecular interactions on the surface. When protein absorption completes, we let PBS wash the surface to remove excess weakly bound proteins. As shown in figure 4, in order to observe Vroman effect, we first flow LMW proteins such as annexin (36kDa) or streptavidine (53kDa) to cover the surface. The bond strength depends upon the hydrophobicity of the surface; the more hydrophobic the surface is, the stronger the bond is [6]. Then, HMW proteins such as streptavidine (53kDa) or isolectin (114kDa) flow through the channels and replace existing bonds formed by the LMW proteins. We also perform the reverse configuration, HMW to LMW proteins, to confirm Vroman effect (figure 4 (3)).

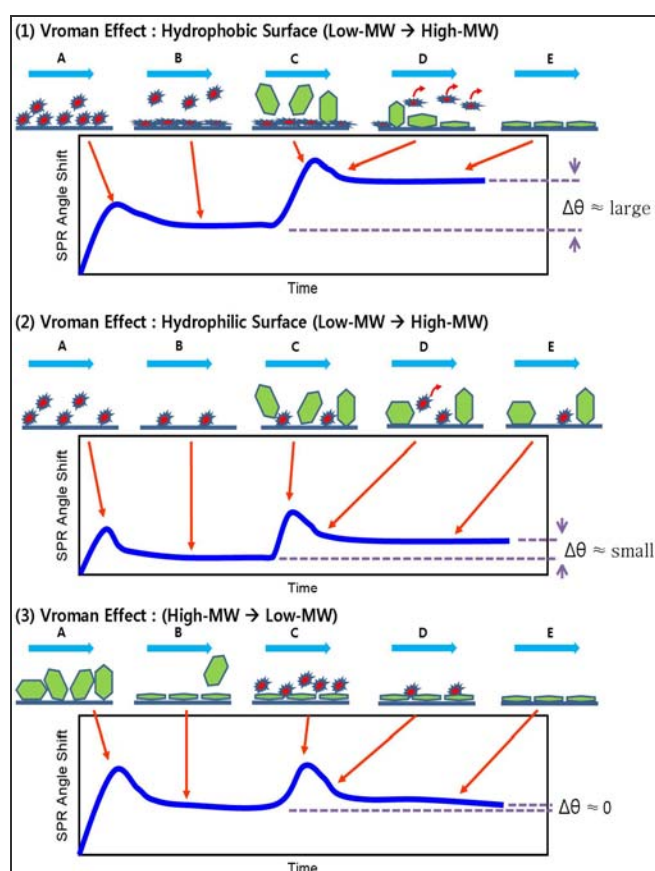


Figure 4. A schematic of SPR profiles & illustration of the Vroman effect (1) on the hydrophobic and (2) the hydrophilic surfaces when the LMW protein adsorbs first and then the HMW protein arrives later to the surface. If the HMW protein adsorbs first and the LMW protein comes later, (3) no angle change occurs.

## 4. RESULTS AND DISCUSSION

The SPR angle shifts of each protein on three different surfaces (bare-gold, COOH- and OH-terminated SAM) are listed in Table 1. The SPR angle shifts are proportional to the size of the proteins. HMW proteins generate larger angle shifts than LMW ones.

Obviously, the larger proteins have stronger molecular interactions on the surfaces. Proteins that we use tend to adsorb more on the hydrophobic than hydrophilic surfaces. This phenomenon is due to the nature of proteins. Generally, proteins have hydrophobic residues buried within the core and their hydrophilic residues facing outside [7]. For any protein structure, when the protein adsorbs to a solid surface, the adsorption behavior is highly related to hydrophobic attraction [8]. Hydrophilic residues influence the orientation of the adsorbed protein, not absorption process. Therefore, the protein rapidly adsorbs to a hydrophobic surface, unfolds and spreads its hydrophobic residues over the surface. On the other hand, hydrophilic surfaces have weaker protein adsorption; thus, the adsorbed proteins are easily detached by subsequent PBS solution.

Table 1. The SPR angle shifts of proteins adsorption

	SPR Angle Shift [mDeg]		
	Bare-gold	COOH-SAM	OH-SAM
Annexin (36 kDa)	195 mDeg	22 mDeg	8 mDeg
Streptavidine (53 kDa)	380 mDeg	35 mDeg	11 mDeg
Isolectin (114 kDa)	550 mDeg	72 mDeg	18 mDeg

In order to monitor Vroman effect, it is important to saturate the surfaces. This is because HMW proteins adsorb the space between LMW proteins if the LMW proteins do not form a fully packed protein monolayer. We saturate the surfaces using 1 $\mu$ M proteins, more than enough to form a full packed monolayer. Figure 5 shows the SPR adsorption / displacement profiles of sequentially injected two proteins with different molecular weights on bare-gold, COOH- and OH-SAM, respectively. The angle shift increases at each protein adsorption and the peak decreases to stabilized angle after washing any weakly bound proteins from the surface. The final SPR angle shift represents fully adsorbed monolayer on the surfaces, the equilibrium state.

The monolayer of LMW proteins is displaced by subsequent HMW proteins, which produce the SPR angle shift. The angle shift demonstrates Vroman effect, indicating how many LMW proteins are replaced by HMW ones. Figure 6 presents the angle shifts of the three different proteins on the three different surfaces. Table 2 summarizes all experiments matrix. The larger the difference of molecular weight between LMW and HMW proteins is, the larger the angle shift is. Regardless of surface properties, we get the largest the angle shift from the smallest, annexin, to the largest protein, isolectin.

The angle shift also depends upon the surfaces; the hydrophilic surfaces have higher replacement percentage than the hydrophobic surface. On the bare-gold surface, LMW proteins strongly bind to the surface and be induced to conformational spreading. Subsequent HMW proteins do not replace all the adsorbed proteins from the surface. However, hydrophilic surfaces show much higher displacement ratio because weak bonds between the hydrophilic residues of the proteins and the surface do not induce the conformational spreading. The weak bond allows the high percentage displacement.

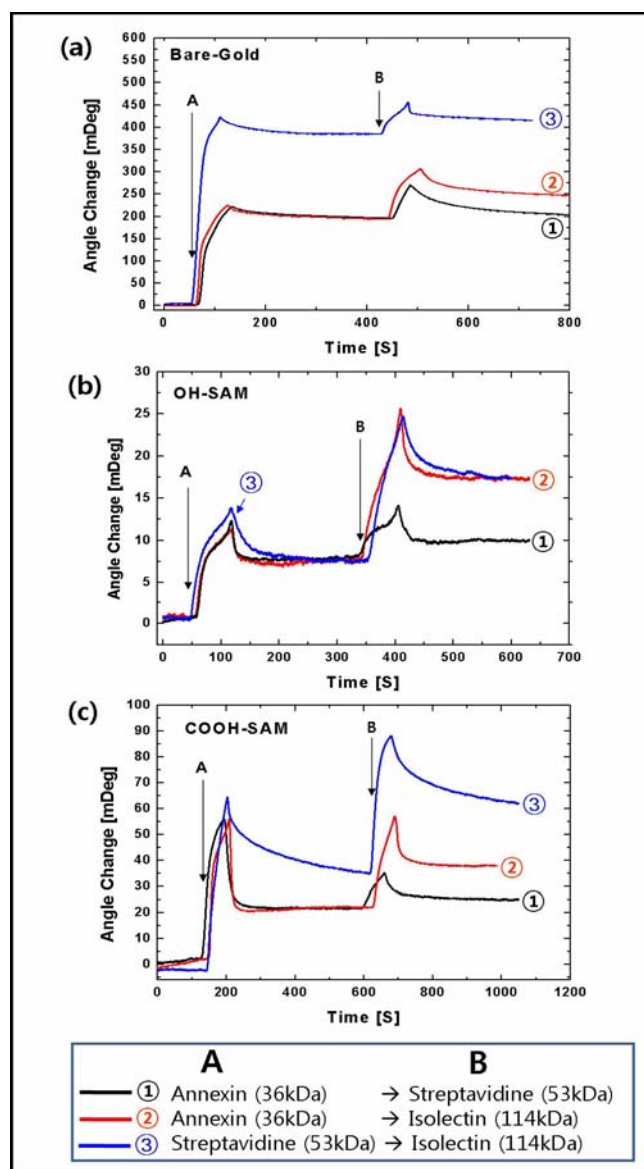


Figure 5. Real-time SPR adsorption profiles of proteins on the bare-gold, OH- and COOH-SAM surfaces, respectively.

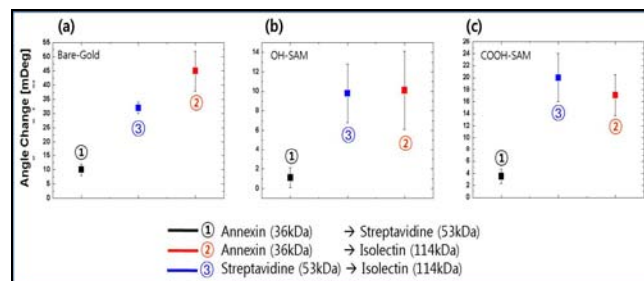


Figure 6. The SPR angle shifts on the bare-gold, OH- and COOH-SAM surfaces, respectively.

Table 2. Summary of the SPR angle shifts on the bare-gold, OH-, and COOH-SAM surfaces. Angle shifts represent sensitivity and the sequential angle shifts indicates selectivity. Bare-gold shows the highest sensitivity yet limited selectivity. On the other hand OH-SAM offers the best selectivity yet low sensitivity.

		Annexin → Isolectin		Streptavidine → Isolectin		Annexin → Streptavidine	
		Annexin (36kDa)	Isolectin (114kDa)	Streptavidine (53kDa)	Isolectin (114kDa)	Annexin (36kDa)	Streptavidine (53kDa)
Angle change [mDeg] & Rate of protein displacement	Bare-Gold Substrate	++++ (~195 mDeg)	++ (~50 mDeg) ~44% displacement	++++ (380 mDeg)	++ (~33 mDeg) ~75% displacement	++++ (~195 mDeg)	+ (~10 mDeg) ~54% displacement
	OH-SAM Substrate	+ (~8 mDeg)	+ (~9mDeg) ~94% displacement	+ (~8mDeg)	+ (~9mDeg) ~94% displacement	+ (~8mDeg)	+ (~2mDeg) ~91% displacement
	COOH-SAM Substrate	++ (~22mDeg)	++ (~16mDeg) ~53% displacement	++ (~35mDeg)	++ (~27mDeg) ~86% displacement	++ (~22mDeg)	+ (~3mDeg) ~71% displacement

Angle change [mDeg] : + (0~10), ++(11~50), +++(51~100),  
++++(101~200), +++++(>201)

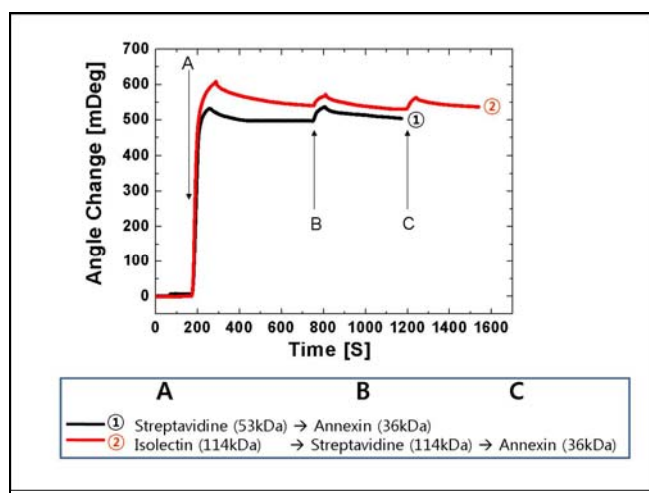


Figure 7. The SPR profiles of the opposite sequence injection (HMW proteins → LMW proteins)

In order to evaluate the selectivity of the protein sensor, we now reverse the proteins injection sequence; HMW proteins are injected first and then LMW ones arrive later. On all surfaces, the angle shifts are almost negligible, less than 0.3 mDeg, representing Vroman effect has nearly 100% selectivity as protein sensors. This data also support the SPR angle changes in figure 5 are not due to multilayer protein-protein interaction but solely due to Vroman effect.

#### 4. CONCLUSION

Conventional protein sensors are limited to satisfy both high selectivity and sensitivity requirements at very low concentration because of complex structure and multiple forms of proteins. Existing protein sensors utilize a bio-receptor to capture target molecules; yet many challenges exist on integrating bio-receptors into the transducer. In this paper, we present a biosensor using Vroman effect. The biosensor utilizes a competitive nature of proteins adsorptions on the surfaces and read real-time molecular interactions using SPR. LMW proteins are displaced by HMW

proteins, but the reverse sequence does not occur. Vroman effect and SPR offer extremely high selectivity and sensitivity. We use three different proteins, annexin, streptavidine, and isolectin, to demonstrate high selectivity and high sensitivity biosensor. The biosensor can distinguish at least 17kDa in molecular weight with 100 % selectivity.

We also examined the effects of surface properties on protein adsorption / displacement using well-defined SAMs of alkane-thiols. Strong interaction of protein with hydrophobic surface induces conformational spreading and transitions to an irreversibly adsorbed state. The strong binding causes the protein displacement very difficult. On the other hand, COOH- and OH-SAM modified hydrophilic surfaces allow very weak binding with proteins, resulting high chance of displacement, thus high selectivity.

#### 5. REFERENCES

- [1] B.B. Haab, "Antibody Arrays in Cancer Research", Molecular & Cellular Proteomics, 4, 4 (2003), pp.377-383
- [2] X. Yu, D. Xu, and Q. Cheng, "Label-free detection methods for protein microarrays", Proteomics, 6 (2006), pp.5494-5503
- [3] K.V. Gobi, K. Matsumoto, K.Toko, H.Ikezaki, and N.Miura "Enhanced sensitivity of SAM-based SPR immunosensor for detection of benzaldehyde using a single-step multi-sandwich immunoassay", Anal. Bioanal. Chem., 387 (2007), pp.2727-2735
- [4] R. Chaerkady and A. Pandey "Applications of Proteomics to Lab Diagnosis", Annu. Rev. Pathol. Mech. Dis.,3 (2008), pp.485-489
- [5] T.A. Horbett and J.L.Brash "Proteins at Interfaces II: Fundamentals and Applications", American Chemical Society, Washington, DC 1995. pp.112-128
- [6] C.F.Wertz et al. "Effect of surface hydrophobicity on adsorption and relaxation kinetics of albumin and fibrinogen: single-species and competitive behavior", Langmuir, 17 (2001), pp.3006-3016
- [7] R. A. Latour, Jr. "Biomaterials : Protein-Surface Interactions" Encyclopedia of Biomaterials and Biomedical Engineering (2005), pp.1-15
- [8] J.J. Gray, "The interaction of proteins with solid surfaces", Current Opinion in Structural Biology, 14 (2004), pp.110-115

# FLEXIBLE SHEAR STRESS SENSOR FOR IN VIVO CARDIOVASCULAR TESTING

H. Yu<sup>1</sup>, L. Ai<sup>2</sup>, M. Rouhanizadeh<sup>2</sup>, R. A. Kloner<sup>2</sup>, E. S. Kim<sup>2</sup> and T. K. Hsiai<sup>2</sup>

<sup>1</sup>Arizona State University, Tempe, Arizona, USA

<sup>2</sup>University of Southern California, Los Angeles, California, USA

## ABSTRACT

A catheter-based intravascular micro sensor was deployed into the aorta of New Zealand White (NZW) rabbits for real-time shear stress measurement. The sensor body was built on a biocompatible polymer Parylene C, and packaged with a flexible coaxial wire while the sensing element was composed of Titanium (Ti) and Platinum (Pt). With the newly developed sensor, we translated the MEMS sensors for real-time focal measurements in the arterial system of NZW rabbits for the first time. In the abdominal aorta, shear stress was measured to vary from 0 to 43 dynes/cm<sup>2</sup> in response to the heart beats at ~180 beats/min and the respiratory variations at ~30 breaths/min.

## INTRODUCTION

Acute coronary syndromes remain the leading cause of death in the industrialized nations [1]. Hemodynamic forces, specifically, fluid shear stress, play an important role in the development of coronary artery disease [2]. The development of Micro Electro Mechanical Systems (MEMS) sensors provides an entry point to assess small-scaled hemodynamics with high spatial and temporal variations [3] that is difficult with Computed Tomography (CT), Magnetic Resonance Imaging (MRI), ultrasound, and laser Doppler velocimetry.

MEMS shear stress sensors have been developed for aerodynamics and fluid mechanics [4, 5]. A flexible shear-stress sensor skin containing a 1-D array of 36 shear-stress sensors has been designed to acquire shear stress measurement on the non-planar surfaces [6]. We have previously fabricated MEMS shear stress sensors with backside wire bonding to address micro-scale hemodynamics with high temporal and spatial resolution [3]. However, to assess shear stress in the complicated arterial geometry in the presence of time-varying component of blood flow, we hereby developed a new generation of polymer-based sensors that are flexible, biocompatible, and deployable into the arterial system.

Our sensor design addressed hemocompatibility of the sensor function in the rabbit blood, and integration of sensors with the catheter to transmit voltage signals to the external electronics. We demonstrated that the flexible and biocompatible polymer-based sensor allowed for direct real-time shear stress analysis in the abdominal aorta of NZW rabbits. The direct shear stress measurement agreed with that of the computational hemodynamics (CFD) code within an acceptable range of experimental differences. Thus, the polymer-based sensors provide a basis to investigate the interplay between hemodynamics and arterial plaque formation with a potential for clinical diagnostics.

## THEORY

Fluid shear stress ( $\tau$ ) is a frictional force per unit area that is tangential to the surface of vascular endothelial cells (EC). For a Newtonian fluid at steady state, shear stress is defined as:

$$\tau = \mu \frac{du}{dy} \quad (1)$$

where  $\mu$  and  $du/dy$  are viscosity and vertical velocity gradient along the y-axis perpendicular to the wall surface, respectively [7]. Our

device works as a thermal anemometer to measure the shear stress. The operation principle is based on convective cooling of a heated sensing element as fluid flows over its surface (Fig. 1). The heat transfer from the heated surface to the fluid depends on the flow characteristics in the viscous region of the boundary layer [5]. We measure the resistance change of the sensing element due to temperature perturbation, and convert it to the shear stress.

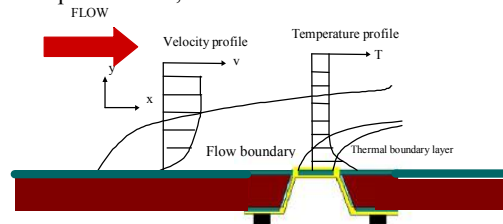


Fig. 1. Bulk micromachined Si-based hot anemometer for shear stress sensing.

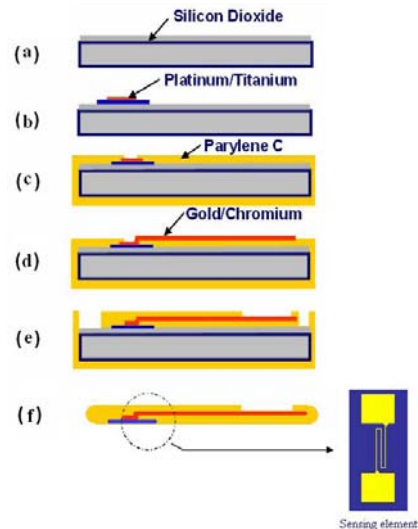


Fig. 2. The fabrication process of intravascular shear stress sensor.

## FABRICATION

The sensor was fabricated using surface micromachining with biocompatible materials including parylene C, Ti and Pt. To dovetail to the arterial circulation, we have fabricated the sensors with the steps illustrated in Fig. 2 that are consisted of (1) dry thermal growth of 0.3 $\mu$ m thick SiO<sub>2</sub> and deposition of a 1  $\mu$ m thick sacrificial amorphous silicon layer using E-beam evaporator, (2) deposition (and patterning) of Ti/Pt layers with thicknesses of 0.06 $\mu$ m/0.015 $\mu$ m for the sensing element with E-beam evaporator, (3) deposition of 9 $\mu$ m thick Parylene C with Parylene vacuum coating system (PDS2010, Specialty Coating System, Inc., IN), (4) deposition (and patterning) of a metal layer of Cr/Au (Au being 2 $\mu$ m thick) for electrode leads with E-beam evaporator, (5) deposition and patterning of another 12  $\mu$ m thick layer of Parylene C to form device structure, (6) etching the underneath silicon sacrificial layer with XeF<sub>2</sub> etching system to release the device.

The resulting sensor bodies were 4 cm in length, 320  $\mu$ m in

width and 21  $\mu\text{m}$  in thickness (Fig. 3). The fabrication process illustrates the application of Ti and Pt as the heating and sensing element (Fig. 2f). The Ti/Pt sensing elements (Strip of 280  $\mu\text{m}$  in length by 2  $\mu\text{m}$  in width) were encapsulated with parylene which was in direct contact with the blood flow. The Ti/Pt sensing element offers low resistance drift, large range of thermal stability, low 1/f noise with absence of piezoresistive effect, and resistance to corrosion/oxidation.

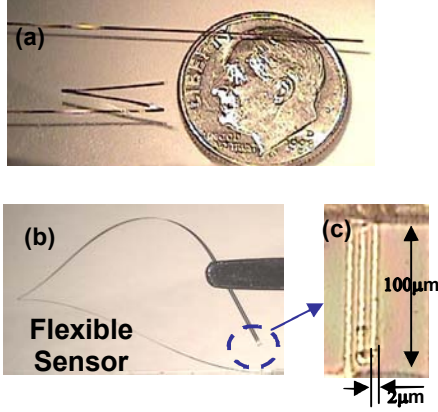


Fig. 3. Flexible intravascular sensors. (a) The sensor was bended or folded in a zigzag fashion without structural or functional damage. (b) The sensor was measured at 4 cm in length, 320  $\mu\text{m}$  in width and 21  $\mu\text{m}$  in thickness; (c) The sensing element was positioned at the tip of the sensor, and the sensing element resistor was made of 2  $\mu\text{m}$  wide Ti/Pt strip with a dimension of 280  $\mu\text{m}$ .

The sensors then were integrated to an electrical coaxial wire as catheter's guide wire application for intravascular shear stress analysis (Fig. 4). The Cr/Au electrode leads were connected to an electrical coaxial wire (Precision Interconnect Portland, OR) using the biocompatible conductive epoxy (H20E, www.epotek.com) that was cured at 90°C over 3 hours. The electrical coaxial wire allowed for transmitting the electrical signals from the arterial circulation to the external circuitry. The sensor was mounted to the coaxial wire at 4 cm from the tip analogous to the entrance length required to deliver well-defined laminar flow field. This distance avoided flow disturbance at the tip of the coaxial wire. The biocompatible epoxy anchored the sensing elements on the coaxial wire surface. The coaxial wire was 0.4 mm in diameter, and the sensing element pad was 80  $\mu\text{m}$  in width and 240  $\mu\text{m}$  in length.

Using the fluoroscope in the animal angiographic lab, the operator was able to visualize and steer the sensor wire in the aorta of the New Zealand White rabbits to the anatomic regions of interest; namely, aortic arch and abdominal aorta (Fig. 5a). Contrast dye was injected to delineate the position of the wire in relation to the inner diameter of the aorta (Fig 5b).

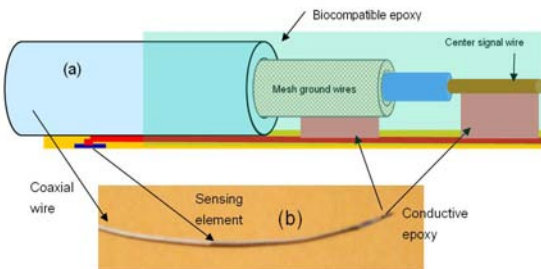


Fig. 4. Packaging of the polymer shear stress sensor.

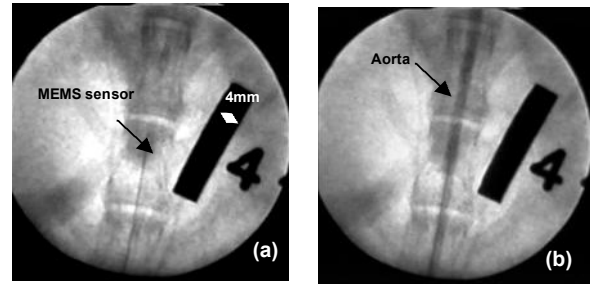


Fig. 5. Fluoroscope images of In vivo testing of the MEMS sensor.

## CALIBRATION AND MEASUREMENT

Based on the heat transfer principle, the output voltage of the MEMS sensors under the constant current detection circuits was sensitive to the fluctuation in ambient temperature. The temperature overhear ratio ( $\alpha_T$ ) is defined as temperature variations of the sensor over the ambient temperature ( $T_0$ ) [4]:

$$\alpha_T = \frac{(T - T_0)}{T_0} \quad (2)$$

where T denotes the temperature of the sensor. The relation between resistance and temperature overhear ratios is expressed as:

$$\alpha_R = \frac{(R - R_0)}{R} = \alpha(T - T_0) \quad (3)$$

where  $\alpha$  is temperature coefficient of resistance (TCR). For shear stress measurement, we applied a high overhear ratio (~3%) by passing higher current and by generating a "hot" sensing element to stabilize the sensor. Calibration was performed in a 2-D flow channel for individual sensors to establish a relationship between heat exchange (from the heated sensing element to the flow field) and shear stress over a range of steady flow rates ( $Q_n$ ) in the presence of rabbit blood flow at 37.8°C (Fig. 6).

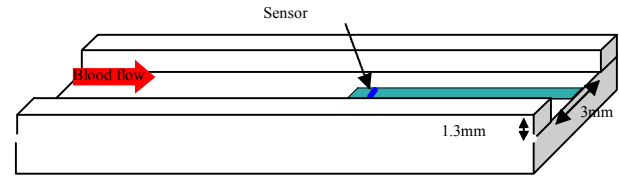


Fig. 6. The schematic diagram of 2-D micro PDMS channel for sensor calibration in the rabbit blood.

For a Newtonian fluid at steady state, the theoretical shear stress value in relation to the flow rate in the 2-D flow channel was established using the following formula based on the analysis of Truskey, et al. [26]:

$$\tau_w \Big|_{y=\frac{H}{2}, x=0} = \mu Q \cdot \frac{6 - \sum_{n=0}^{\infty} \frac{48}{(2n+1)^2 \pi^2 \cosh\left(\frac{(2n+1)\pi W}{2H}\right)}}{WH^2 - \sum_{n=0}^{\infty} \frac{96H^3}{(2n+1)^5 \pi^5 \cosh\left(\frac{(2n+1)\pi W}{2H}\right)} \cdot \exp\left(-\frac{(2n+1)\pi W}{2H}\right)} \quad (4)$$

$$y \in \left(-\frac{H}{2}, \frac{H}{2}\right), \quad x \in \left(-\frac{W}{2}, \frac{W}{2}\right)$$

where  $\tau_w$  is the wall shear stress;  $\mu$  is the blood viscosity; Q is ; and H and W are the height and width of the flow channel, respectively ( $H/W = 0.433$ ). The viscosity used in the above equation was obtained from the published data for rabbit blood [7]. The individually calibrated sensors were then deployed to the NZW rabbit's aorta for real-time shear stress assessment.

### In Vivo Assessment of Intravascular Shear Stress

Under the fluoroscopic guidance, the catheter integrated with the micro vascular device was deployed into the abdominal aorta above the renal arteries of the rabbit for shear stress measurements under fluoroscopy guidance (Fig. 5). Periodic blood pressure measurement was obtained with an automated tail cuff. The shear stress recordings were synchronized with the rabbit's cardiac cycle via ECG. After measurement, the catheter was removed and the femoral artery was tied off.

The position of the catheter in relation to the arterial wall was visualized via the contrast dye under fluoroscope. The output voltage of the sensor was high when the sensor was facing the blood whereas the signal was attenuated as we steered the sensor toward the arterial wall. Unlike our previously published wall shear stress measurement for an *in vitro* bifurcating model [8], the unique feature of our catheter-based approach allowed for intravascular shear stress analysis in response to pulsatile blood flow in the abdominal aorta of NZW rabbit.

### Data Acquisition

The constant current circuit was used to measure the shear stress in Aorta. Electrical current of 0.9833mA was input from a Multimeter (HP34401A, Santa Clara, CA, USA), which was working at resistance measurement mode. When the current passed through the sensor, sensing element was heated up at an overhear ratio of ~3%. The voltage across the sensing element was monitored by LabView data acquisition board (NI USB-6251, Austin, TX, USA) and BNC adaptor board (BNC-2110, Austin, TX, USA) which was connected to a laptop computer (Thinkpad T61, Lenovo, China). The main source of noise source was electrical magnetic interference from the environment at 60Hz. We analyzed the data to filter out 60Hz noise and improved the noise floor from 1.2mV to 0.5mV. The sampling rate for data acquisition was at 800 points/sec.

### Development of Computational Fluid Dynamic Stimulation

Computational fluid dynamic (CFD) code was developed for non-Newtonian fluid to simulate real-time shear stress in the abdominal aorta and to compare with the experimental measurements. The luminal geometrical model of the rabbit abdominal aorta was constructed and meshed using a specialized pre-processing program GAMBIT (Fluent Inc., Gambit 2.3.16, Lebanon, NH, USA). The local effects of branching arteries were assumed to be negligible. The meshed models were then imported into the main CFD solver FLUENT (Fluent Inc., Fluent 6.2.16, Lebanon, NH, USA) for pulsatile flow simulation. The grid was generated by meshing the inlet surface using Pave scheme type to create unstructured mesh, followed by generating a volume mesh using Cooper scheme type to sweep the mesh node patterns that specified the inlet surface as the "source" faces. The model was composed of 174,510 cells which were primarily the wedge elements. For simulation of wall shear stress, boundary layers immediately adjacent to the wall were constructed to generate sufficient information for characterization of the large fluid velocity gradients near the wall. The diameter of the rabbit abdominal aorta,  $D$ , which was measured from angiography during sensor deployment, was set at 2.4 mm. The total length was set at 8.27 times of the diameter to provide sufficient entrance length for the flow to develop [9].

The pulsatile centerline flow velocity information was applied to compute a complex Fourier series approximation for the inlet flow rate pulse using Womersley solution [10]. The blood flow was simulated by applying the 3-D Navier-Stokes equations. The governing equations, including mass and momentum equations, were solved by the FLUENT software for laminar, incompressible,

and non-Newtonian flow. The arterial wall of rabbit abdominal aorta was assumed to be rigid and impermeable.

At the inlet of the abdominal aorta, a physiological flow waveform was introduced. The transient flow rate information was used to compute a complex Fourier series approximation for the pressure gradient pulse using Womersley solution. This profile was implemented by the user defined C++ code. The flow outlet was far downstream where traction-free condition was prescribed. This approach allowed the velocity profile to become a solution to the 3-D Navier-Stokes equations, and the velocity profile was propagated downstream along the aorta. No-slip boundary condition was implemented along the inner walls.

The flow field was initialized by propagating the constant time-averaged inlet velocity profile downstream into the computational domain. The initial pressure was set to zero in the entire domain as were the two cross-stream velocity components. An iterative scheme that marched toward a converged solution was employed by FLUENT. The second order implicit formulation of the solver was applied for the unsteady simulations. Second order-upwind discretization was applied for the governing equations. The pressure-velocity coupling was based on the SIMPLEC technique.

### RESULTS

The resistance of the sensing element was ~1.0 kOhm, and the temperature coefficient of resistance was measured to be approximately 0.16%/°C (Fig. 7). These properties were compatible for *in vivo* analysis. The relation between the resistance and temperature was linear, suggesting that the thermal coefficient of resistance (TCR) over this temperature range remained constant.

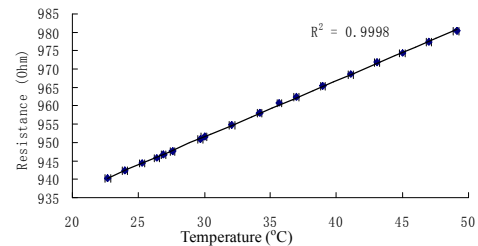


Fig. 7. Measured data of the sensing element (Ti/Pt) resistance versus temperature.

To account for the non-Newtonian properties of the blood flow, we collected 10ml blood from the NZW rabbits and calibrated the sensor at 37.8 °C in a 2-D flow channel (Fig. 6). The sensing element (240 x 80x 0.1  $\mu\text{m}^3$ ) was positioned in a PDMS flow channel (1.32mm high and 3.0mm wide) for sensor calibration in the presence of rabbit blood flow at 37.8 °C. We obtained a non-linear relation between changes in the sensor output voltage (due to heat dissipation from the sensing element) and the blood flow (converted to the shear stress) (Fig. 8).

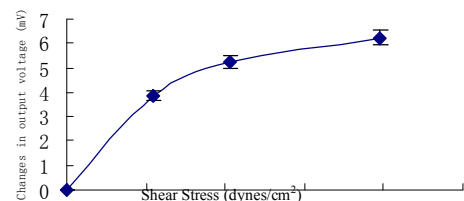


Fig. 8. Calibration curve for changes in the sensor output voltage and shear stress in response to the rabbit blood flow.

Using the calibration curve, we obtained the intravascular

shear stress in the abdominal aorta from the real-time voltage measurement (Fig. 9a), and show it in Fig. 9b. The real-time voltage output was recorded in response to pulsatile flow at a heart rate of approximately 180 beats/min. The noise floor was 0.5 mV, giving signal-to-noise ratio of at least 4.8. Shown in Fig. 9a is a representative output voltage tracing over six cardiac cycles with an interval of 0.33 seconds per heart beat in the abdominal aorta, which is shown in the dashed line enveloping the signal. Fig. 9b is the corresponding intravascular shear stress profile.

The experimental shear stress value (green) is compared with the CFD solution (red) in Fig. 10. The measured shear stress peaked at 44 dynes/cm<sup>2</sup> during systole and bottomed at 5 dynes/cm<sup>2</sup> during diastole. The noise floor was approximately 1 dynes/cm<sup>2</sup>. The CFD solution revealed a peak wall shear stress value at 48 dynes/cm<sup>2</sup>. Despite the distinct waveforms between the intravascular shear stress (experimental) and the wall shear stress (CFD simulation), the two peak values vary by 9%, and the waveform profiles overlap within the range of acceptable experimental errors for wall shear stress measurement.

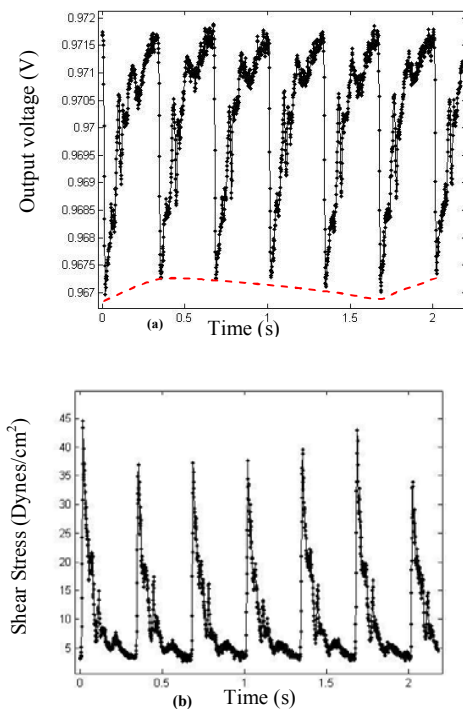


Fig. 9. (a) Measured real-time voltage signals that were obtained from the abdominal aorta of NZW rabbits. (b) Shear stress obtained from the measured voltage signals and the calibration curve.

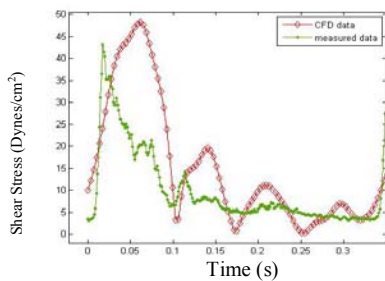


Fig. 10. Shear stress tracing (in green) in one cardiac cycle was compared with CFD simulation.

## CONCLUSIONS

In this paper, we describe the first flexible polymer sensors to acquire real-time shear stress measurement *in vivo* with a potential for clinical applications. The feasibility to translate a micro-device to *in vivo* real-time analysis represents an advance in the field of MEMS technology, and the *in vivo* measurements contribute to the understanding of hemodynamics and vascular disease. Our sensor design successfully addressed hemocompatibility of the sensor function in the rabbit blood and challenging fabrication issues of integrating a sensor with a catheter to transmit voltage signal to external electronics.

## ACKNOWLEDGEMENTS

This work was supported by American Heart Association GIA 0655051Y (TKH), NIH HL 83015 (TKH), NIH HL068689 (TKH), American Heart Association Post-Doctoral Fellowship 0725016Y (HY), and AHA Pre-Doctoral Fellowship 0615063Y (MR). The authors would like to thank Prof. Ellis Meng and Po-Ying Li for helps on the construction of the 2D flow channel and Jie Zhu for the manuscript preparation.

## REFERENCES

- [1] R. Ross, "Atherosclerosis is an inflammatory disease," *American Heart Journal*, vol. 138, no.5 part 2, pp: S419-420, 1999.
- [2] R. M. Nerem, R. W. Alexander, D. C. Chappell, R. M. Medford, S. E. Varner, and W. R. Taylor, "The study of the influence of flow on vascular endothelial biology," *The American journal of the medical sciences*, vol. 316, no. 3, pp:169-175, 1998.
- [3] M. Rouhanizadeh, G. Soundararajan, R. Lo, D. Arcas, F. Browand and T. Hsiai, "MEMS sensors to resolve spatial variations in shear stress in a 3-D blood vessel bifurcation model," *IEEE Sensors*, vol. 6, no. 1, pp: 78-88, 2006.
- [4] Q. Lin, F. K. Jiang, X. Q. Wang, Y. Xu, Z. G. Han, Y. C. Tai, J. Lew and C. M. Ho, "Experiments and simulations of MEMS thermal sensors for wall shear-stress measurements in aerodynamic control applications," *Journal of Micromechanics and Microengineering*, vol. 14, no.12, pp:1640-1649, 2004.
- [5] C. Liu, Y. C. Tai, J.B. Huang and C.M. Ho, "Surface Micromachined Thermal Shear Stress Sensor," *The First ASME Symposium on Application of Micro-Fabrication to Fluid Mechanics*, Chicago, IL, pp. 9-15, November 1994.
- [6] Y. Xu, Y.-C. Tai, A. Huang, and C.-M. Ho, "IC-Integrated Flexible Shear-Stress Sensor Skin," *Journal of Microelectromechanical Systems*, vol. 12, pp. 740-747, 2003.
- [7] P. W. Longest, C. Kleinstreuer, G. A. Truskey and J. R. Buchanan, "Relation Between Near-Wall Residence Times of Monocytes and Early Lesion Growth in the Rabbit Aorto-Celiac Junction," *Ann. of Biomed. Eng.*, vol. 31, no. 1, pp: 53-64, 2003.
- [8] M. Rouhanizadeh, L. Lin, D. Ascara and T. Hsiai, "Spatial variations in Shear stress at low Reynolds number flow," *Annals of Biomedical Engineering*, vol. 33, no. 10, pp: 1425-1440, 2005.
- [9] T. Kim, T. Seo and A. I. Barakat, "Numerical simulations of fluid mechanical interactions between two abdominal aortic branches," *Korea-Australia Rheology Journal*, vol. 16, pp: 75-83, 2004.
- [10] J. R. Womersley, "Method for the calculation of velocity, rate of flow and viscous drag in arteries when the pressure gradient is known," *J. Physiol.* Vol. 127, pp: 553-563, 1955.

# IMPLANTABLE MICROVALVE-PACKAGED GLAUCOMA DRAINAGE TUBE

Jeffrey Chun-Hui Lin<sup>1</sup>, Po-Jui Chen<sup>1</sup>, Saloomeh Saati<sup>2</sup>, Rohit Varma<sup>2,3</sup>, Mark Humayun<sup>2,3</sup>, Yu-Chong Tai<sup>1</sup>

<sup>1</sup>California Institute of Technology, Pasadena, California, USA

<sup>2</sup>Doheny Eye Institute, Los Angeles, California, USA

<sup>3</sup>University of Southern California, Los Angeles, California, USA

## ABSTRACT

This paper presents the first tube-type microvalved glaucoma drainage device (GDD) incorporating two parylene-based micro check valves in a needle-implantable form factor for minimally invasive implantation. Dual micro check valves are exploited in back-to-back configuration to realize a specified pressure-bandpass flow regulation profile for effective intraocular pressure regulation. Post-fabrication packaging of the microvalves in a glass capillary tube carrier facilitates hypodermic needle implantation of the device to the anterior chamber of the eye. This capillary tube then effectively provides a regulatory eye fluid drainage control with minimal surgical complications. Bench top flow tests successfully characterize the pressure/flow rate behavior of the tube device consistent with our design in the 0-200 mmHg and 0-80  $\mu$ L/min regulation ranges. In addition, preliminary *ex vivo* implantation test of tapered hollow tube mockup verifies the concept of subconjunctival tube placement with proposed device dimensions, which is promising for future study of tube implantation.

## INTRODUCTION

Glaucoma is associated with abnormally high intraocular pressure (IOP) due to a patient's inability to drain excessive eye fluid from the anterior chamber of the eye through trabecular meshwork [1]. If not reduced with adequate treatment, the high IOP would continuously suppress and damage a patient's optical nerves as the disease progresses, leading to loss of vision or even total blindness in the end. Current clinical treatment involves medication typically in the form of eye drops with dosages depending on the severeness of the disease. However, it accompanies with certain concerns such as difficulty of continuous treatment, inefficient dosage style, and potential side effects or patient refractoriness to the drug composition. In order to have an alternative addressing those issues, glaucoma drainage device (GDD) has been a desirable with the concept of physically draining the excessive intraocular fluid through the artificial drainage path so as to reduce the associated IOP. Such a device should be capable of regulating the IOP to be below 20 mmHg while not causing hypotony (i.e., IOP < 5 mmHg) with time. It is further necessary to have the valve closed if high IOP (e.g., >50 mmHg) happens due to normal external interferences like eye rubbing or bumping. Therefore, it is ideal to have dual back-to-back valves consisting of an opened normally-closed (NC) valve above 20 mmHg and a closed normally-open (NO) valve above 50 mmHg in order to realize the desirable pressure-bandpass flow regulation.

Micromachined valves have long been widely made and used in microfluidic devices for flow controls in micro-total-analysis systems ( $\mu$ TAS) [2][3]. In 2007, Chen et al. reported on-chip surface-micromachined parylene-based dual check valves with a potential application of using them as a passive IOP regulator [4]. To accomplish a stand-alone implantable device, however, the microvalves must be extensively released and packaged into a capillary tube to become a real valve-in-tube system for real device implantation. As a result, a novel post-microfabrication tube packaging technology using an auxiliary glass capillary tube as a coupler in this work is developed to help us assemble the valve

system. These valves have smaller planar size than the inner diameter (I.D.) of the coupling tube so that the valve surface would not be contaminated during packaging and such makes it easier to load the valves into appropriate capillary tubes. A subconjunctival needle implantation would be executed to mimic the normal aqueous humor drainage pathway (Figure 1). As such, the shape and length of the capillary tubes are also carefully designed so that the implantation can be performed using a specific needle-in-needle introducer setup. The front end of the tube is tapered for convenient device placement after injected from the needle with not penetrating the conjunctiva. The length is chosen based on that the back end of the tube can still be observed through cornea during surgery.

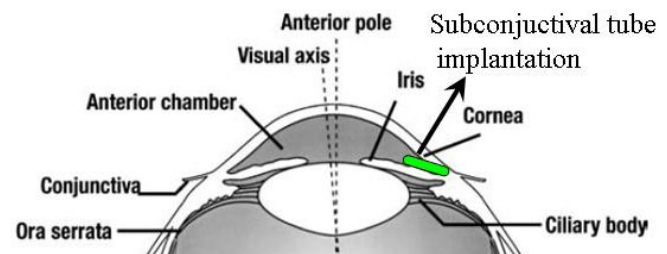


Figure 1: Subconjunctival implantation idea of the GDD implanted through the anterior chamber of the eye.

## DESIGN

In microflow control component design of the glaucoma drainage tube, one NC valve is chosen to achieve the necessary low-pressure-off response and one NO valve is chosen to behave as a high-pressure stopper (Figure 2). Dual NC and NO parylene micro check valves artificially regulate the intraocular fluid drainage without any external power consumption, further control the IOP drainage profile of glaucoma patients. The back-to-back configuration prevents the GDD from water leakage if the fluid flows in the opposite direction. In NO valve design, the twisted-arm tether length is carefully designed considering the stiction effect to guarantee free-standing valve membrane after release [5]. On the contrary, the NC valve utilizes a stiction process that normally happens during drying process [6]. This self-stiction effect facilitates spontaneous anchoring of the NC valve with predetermined cracking pressure by pre-stressing the center sealing part of the valve through straight tethers connecting to the anchoring part (Figure 3). It greatly simplifies the multi-layer parylene micromachining process into single-layer parylene deposition. Both NC and NO valves are made separately by surface micromachining parylene C, which is biocompatible (USP Class VI grade) and compatible with CMOS/MEMS processes. The mechanical properties of the microvalves were simulated using COMSOL Multiphysics™ to design their pressure/flow rate characteristics. The cracking pressure and the fluidic conductance of the device can be controlled by the geometry and numbers of the tethers, the thickness of parylene, and the height difference between stiction anchoring part and the center sealing part.

In order to fulfill a real implantable GDD, valves are designed with circular releasing trenches on the back side of the wafer (Figure 3) to be introduced in an extra coupling capillary during packaging. All valves are encircled by 65  $\mu\text{m}$  wide, 150  $\mu\text{m}$  deep grooves defined by DRIE on the top side for convenient assembly afterwards. The I.D. of the coupling tubes is 320  $\mu\text{m}$ , which is slightly larger than the 300  $\mu\text{m}$  valve diameter. The outer diameter (O.D.) of the coupling tube is 400  $\mu\text{m}$ , smaller than the I.D. of the outside protecting tube. The protecting tube can perfectly accommodate the valves given its 530  $\mu\text{m}$  I.D., and it fits into 19-gauge needle given its 670  $\mu\text{m}$  O.D. so that hyperdermic needle implantation is feasible. The front tip of the protecting tube is tapered to be 30° for convenient device placement at subconjunctiva site. The length of the protecting tubes could be trimmed to 2-10 mm depending on the size of individual eye for good observation during surgery.

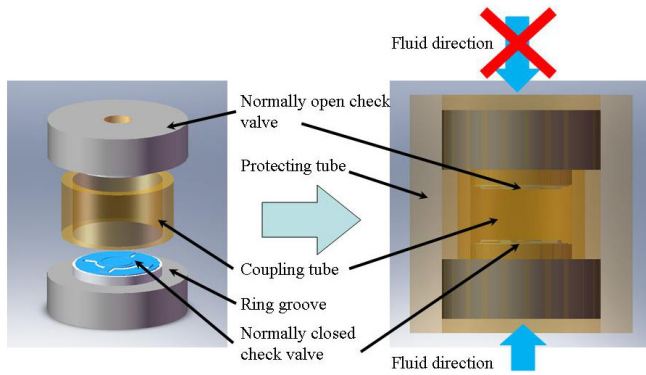


Figure 2: Schematics of valve-in-tube system: (left) Combination of one NC valve and one NO valve with a coupling tube; (right) Final finished valve-in-tube system.

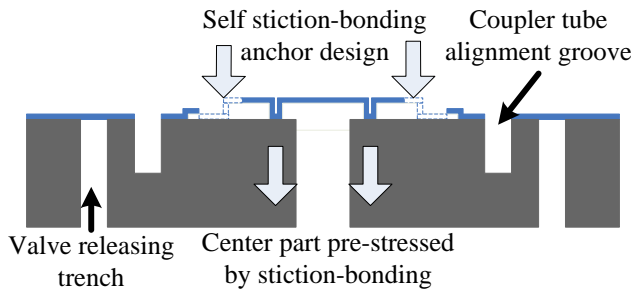


Figure 3: Cross-section of NC valve design.

### FABRICATION AND PACKAGING

The fabrication process started from growing thermal oxide on silicon wafer surface (Figure 4). Through-wafer holes and releasing trenches of the valves were etched using backside DRIE until 50  $\mu\text{m}$  silicon membranes were left. A three-step lithography was performed to create three different heights of sacrificial photoresist for the NC valve. A 150  $\mu\text{m}$  deep groove was created surrounding the valves using additional DRIE after parylene C coating and patterning for convenient coupling tube packaging alignment afterwards. Through holes were then opened by completely etching away the silicon membrane so as to strip the sacrificial photoresist with acetone. After photoresist stripping and air drying of the devices, stiction happened on NC valves and the anchoring parts bonded onto wafer surfaces, providing the necessary pre-stressed force. Figure 6 shows the completed devices after air drying.

The microfabricated valves were packaged into a glass

capillary tube to fulfill the valve-in-tube system. The coupling tube was attached to the valve with a tiny epoxy drop gently applied onto the alignment groove (Figure 5). The valve-with-coupler package was then inserted into the protecting tube and the entire tube-in-tube system was further secured by epoxy sealing (Figure 7). The finished valved tube could be trimmed to 2-10 mm long, suitable for 19-gauge needle implantation (Figure 8).

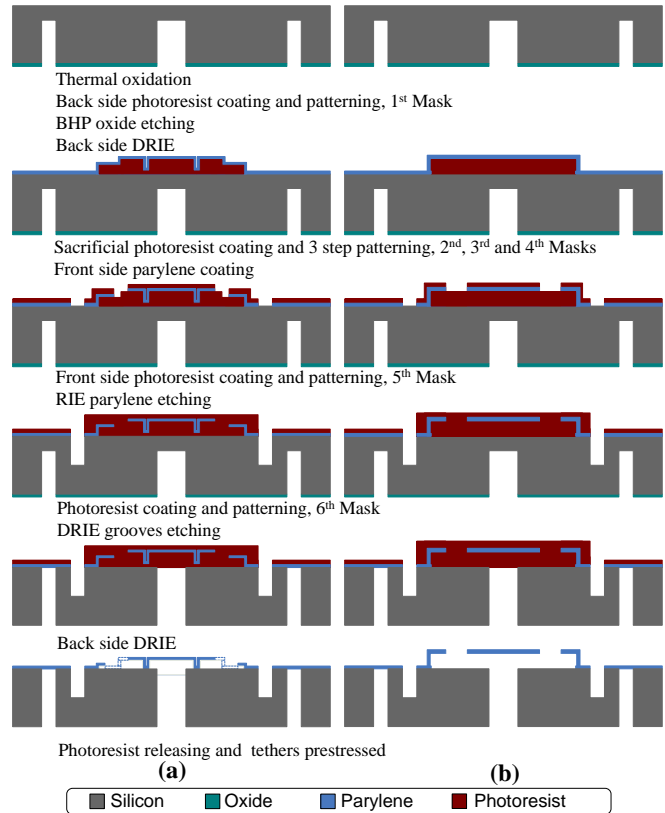


Figure 4: Fabrication process flow: (a) NC valve; (b) NO valve.

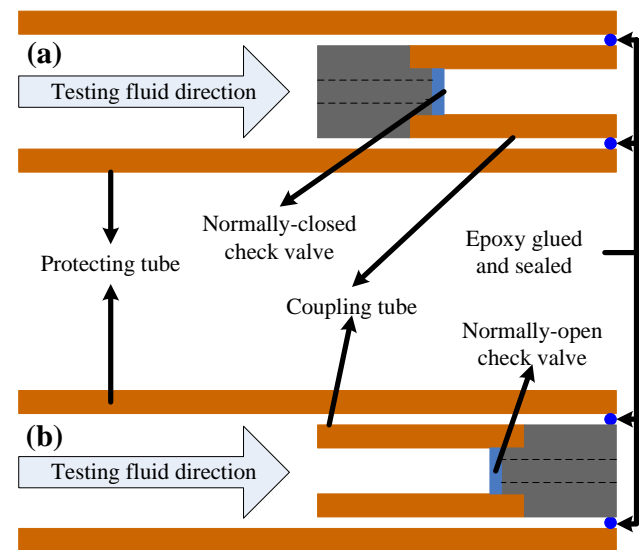


Figure 5: Valve-in-tube system packaging procedure: (a) NC valve; (b) NO valve. Two valves share opposite packaging direction.

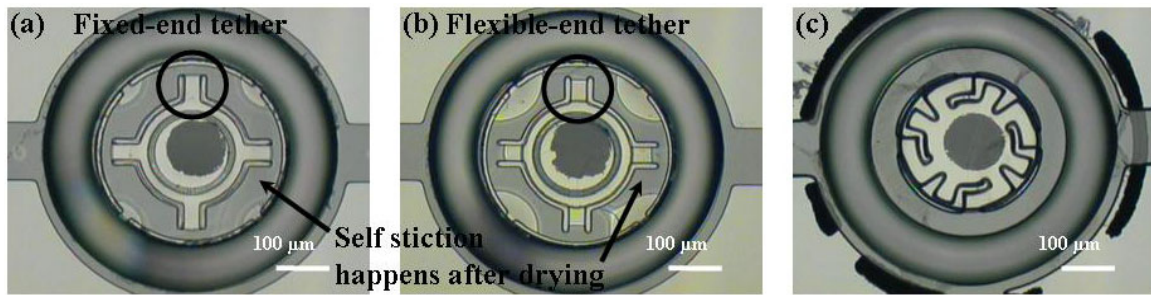


Figure 6: Micrographs of fabrication results: (a) NC valve with fixed-end tether boundary; (b) NC valve with flexible-end tether boundary; (c) NO valve with free-standing twisted-arms.

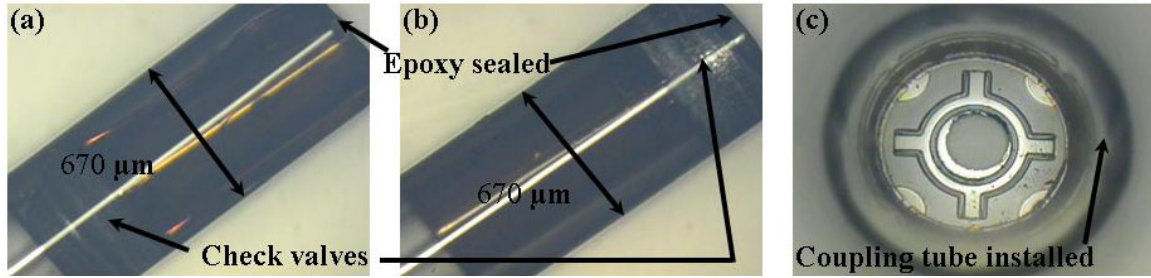


Figure 7: Valve packaging results: (a) NC valve and (b) NO valve in the tube; (c) Top view of NC valve inside a coupling tube.

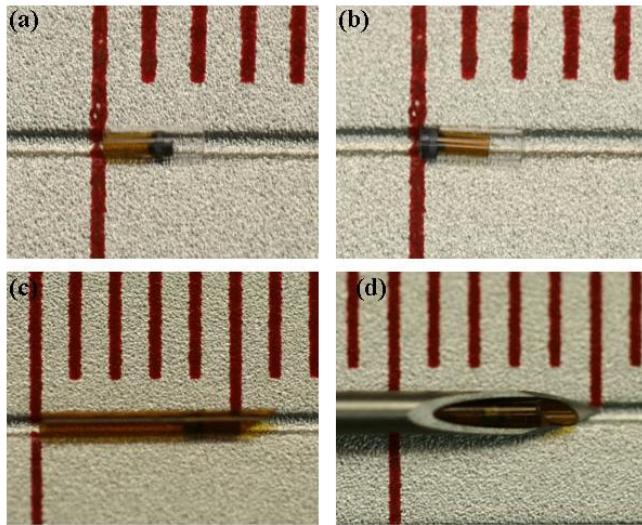


Figure 8: Final valved tube results: (a) 2 mm long NC valved tube; (b) 2 mm long NO valved tube; (c) 6 mm long valved tube with 30 degree tapered tip; (d) Tapered valved tube in 19-gauge needle. 1 div. in pictures = 1 mm.

## TEST AND DISCUSSION

### Bench top test

Two different testing setups were built up for valve-on-chip and valve-in-tube test (Figure 9), respectively. Water was chosen as the working fluid to simulate the intraocular environment. Controlled pressure-driven water flow was injected and monitored by pressure gauge with tuning resolution up to 0.01 psi (~0.5 mmHg). For on-chip valve test, working fluid flowed into a customized jig with specially designed channels conducting water to fluidic ports of the tested valves. For valved tubes, an adapter was introduced to connect from columns of the testing setup to

valved tubes with different diameter. A protective tubing sleeve was also used to protect the valved tubes and provided tightly mounting. The flow rate was calculated from measuring the flowing speed of water front in the columns of the testing setup.

Pressure/flow testing results are shown in Figure 10. For NC valves, it could be shown that there is a good agreement with data from valves on chips and valves in tubes. The characterization results of NC valve show that cracking pressure was measured approximately 0.2 psi (~10 mmHg), which is consistent with our valve simulation results. No water flow was observed under pressure loading below cracking pressure point, giving the support that the sealing part was well pressed by the four straight tether arms with the predetermined snapping force. This result also indicates that the epoxy well secured the valved tube opening with no water leakage. NO valves were characterized directly in valved tubes. No significant cracking pressure was obtained during tests. The high-off behavior with greatly decreased flow rate from approximately 1.0-1.5 psi (~50-75 mmHg) was demonstrated. A small amount of water leakage was observed because of the misalignment of fluidic ports of the valves occurred from the nature of double-sided pattern alignment on the wafer throughout the fabrication processes.

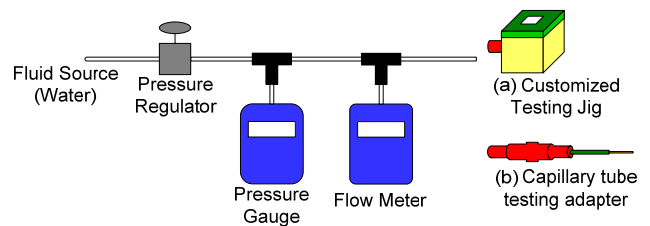


Figure 9: Schematic of testing setup: (a) Customized testing jig was used to test valve on chip; (b) An adapter was used to test valve-in-tube system.

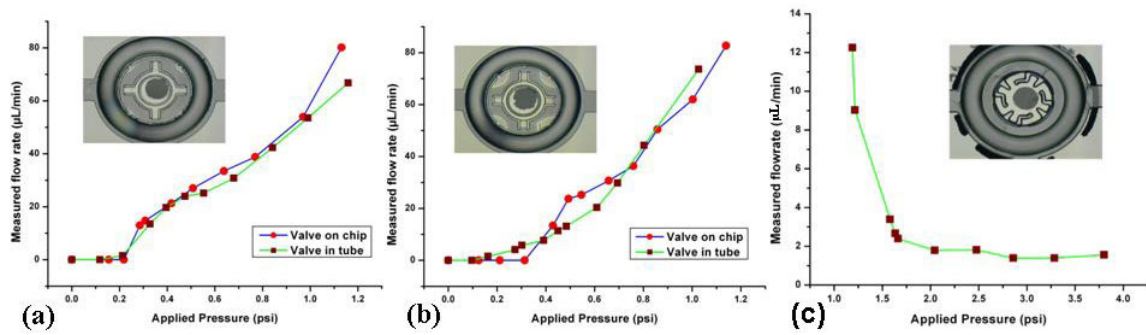


Figure 10: Testing results: (a) NC valve with fixed-end boundary; (b) NC valve with flexible-end boundary; (c) NO valve tested in tube.

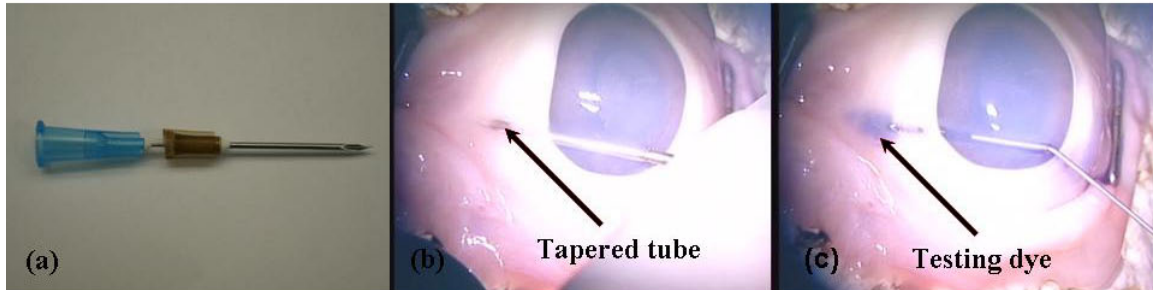


Figure 11: (a) Needle in needle introducer setup; (b) A hollow tube subconjunctivally implanted into an enucleated porcine eye; (c) Testing dye shunted into the hollow tube.

#### Ex vivo implantation test

An implantation test using an enucleated porcine eye model and a tapered hollow tube mockup was performed to verify the implantation concept. A customized needle-in-needle introducer using 19-gauge and 25-gauge needles was developed to facilitate the minimally invasive needle incision and device injection (Figure 11) that the tube device would not dislodge during introducer retraction. Testing dye was injected into the hollow tube and it drained out to the diffusive subconjunctival location as expected. Dual-valve tube packaging is currently underway for further study and analysis.

#### CONCLUSION

A new post-microfabrication tube packaging technology has been developed to facilitate a valve-in-tube device for intraocular pressure regulation. Testing results have verified that valved tubes can be secured with epoxy with no observable water leakage. The finished tubes are designed with a form factor for needle-based minimally invasive implantation. Both normally-close and normally-open valves have been characterized respectively with experimental verification that their pressure/flow rate behaviors meet the IOP regulation requirements. *Ex vivo* implantation using tapered hollow tube prototype was performed with successful testing dye drainage demonstration. Optimized tube lengths can be determined from preliminary surgery results and incorporated in future GDD design. The coupling tube can serve as an adaptor to realize a back-to-back dual valve system as a practical pressure-bandpass IOP regulator (Figure 12).

#### ACKNOWLEDGEMENTS

This work was supported in part by the Engineering Research Centers Program of the National Science Foundation under NSF Award Number EEC-0310723 and by Bausch and Lomb. The authors would also like to thank Mr. Trevor Roper for his valuable

fabrication assistance.

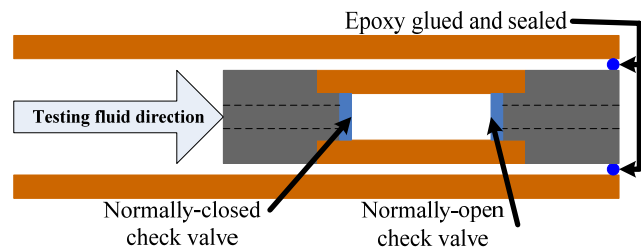


Figure 12: Schematic of a back-to-back dual-valved IOP regulator.

#### REFERENCES

- [1] M. Yanoff and J.S. Duker (Eds.), *Ophthalmology*, Second Edition, Mosby, St. Louis, 2003.
- [2] A. van den Berg and T. S. J. Lammerink, "Micro Total Analysis Systems: Microfluidic Aspects, Integration Concept and Applications," *Topics in Current Chemistry*, vol. 194, pp. 21-50, 1997.
- [3] S. Shoji, "Fluids for Sensor Systems," *Topics in Current Chemistry*, vol. 194, pp. 163-188, 1998.
- [4] P.-J. Chen, D. C. Rodger, E. M. Meng, M. S. Humayun, and Y.-C. Tai, "Surface-Micromachined Parylene Dual Valves for On-Chip Unpowered Microflow Regulation," *J. Microelectromech. Syst.*, vol. 16, pp. 223-231, 2007.
- [5] N. Tas, T. Sonnenberg, H. Jansen, R. Legtenberg, and M. Elwenspoek, "Stiction in Surface Micromachining," *J. Micromech. Microeng.*, vol. 6, pp. 385-397, 1996.
- [6] H. Zhang, S. Wang, and Y. Xu, "Study and Applications of A Parylene Self-Sealing Structure," *Technical Digest, The 19th IEEE International Conference on MicroElectroMechanical Systems (MEMS 2006)*, Istanbul, Turkey, Jan. 22-26, pp. 282-285.

# MICRO RF TAGS FOR MEDICAL IMAGING

J.J. Bernstein<sup>1</sup>, M.G. Bancu<sup>1</sup>, R. Ciocan<sup>2</sup>, R.E. Lenkinski<sup>2</sup>, R. Marquis<sup>2</sup>, A. Ivanishev<sup>2</sup>, and J.V. Frangioni<sup>2</sup>

<sup>1</sup>The Charles Stark Draper Laboratory, Cambridge, Massachusetts, USA

<sup>2</sup>Beth Israel Deaconess Medical Center, Boston, Massachusetts, USA

## ABSTRACT

This paper presents Micro Resonant Devices (MRD's) which are visible in MRI scans. These LC resonators are fabricated using electroplated spiral inductors combined with thin-film Ta<sub>2</sub>O<sub>5</sub> capacitors, formed by a novel oxy-nitride plasma oxidation process. Arrays of resonators were fabricated with diameters of 0.3, 0.5 and 1 mm. To compensate for process variations, resonators were fabricated with parametrically varying capacitor areas. In this study, we characterize the first such devices for their detectability as a function of size, in salt-containing aqueous media and in vivo, using a clinical MRI scanner and a scanning UHF microscope.

## INTRODUCTION

### Magnetic Resonant Imaging

Magnetic Resonant Imaging (MRI) works by imaging the density of hydrogen nuclei, as well as variations in the spin relaxation times in the presence of a strong magnetic field [1]. The spin energy states of a hydrogen nucleus are split in a magnetic field, creating a small net magnetic moment. Transitions between the two states occur at the Larmor frequency which is proportional to the magnetic field. The classical interpretation of nuclear spin in a magnetic field gives a precession frequency equal to the Larmor frequency, which is a useful way of visualizing the magnetic moments in an MRI sample. In a 3T field, the Larmor frequency is 127.7 MHz.

Most MRI contrast agents perturb the RF B1 field or the spin relaxation times T1 and T2 [1], using elements with unpaired spins which can exchange energy with the proton magnetic spins. Examples are transition metal ions Fe<sup>3+</sup>, Mn<sup>2+</sup>, and Gd<sup>3+</sup>. Other contrast agents consist of non-stoichiometric iron oxide nano-particles called MIONS [2].

The long term goal of this research is to detect a single device, in a single cell, anywhere in a living subject. This will require tags on the order of 10 μm in size, capable of being endocytosed by cells. The devices presented here are a first step towards the tiny tags which can be inserted in single cells.

In this work, we present a novel RF MEMS tag which is visible in an MRI because it is resonant at the Larmor frequency. It can therefore exchange energy with the hydrogen nuclei and perturb the RF (B1) field and the spin relaxation times. The device consists of a spiral inductor and a thin film capacitor. The inductor also serves as an antenna, coupling to the external RF pulses and the nearby protons.

## DESIGN OF MICRO RESONANT DEVICES

The goal was to fabricate Micro-Resonant Devices (MRD's) with a resonant frequency of 127.7 MHz. The process to make the capacitor dielectrics was developed simultaneously with the spiral inductors, and the process variability was unknown. Hence, the mask set was created with an array of parametrically varied resonators to cover the frequency range from 0.6 to 1.5X the Larmor frequency (77 MHz to 190 MHz) at 3% frequency intervals. Inductors were constrained to 3 sizes: 0.3 mm, 0.5 mm and 1.0 mm. For each inductance size, the capacitor areas were varied to achieve the desired resonant frequency range. While this technique yields only a few devices resonant near the

desired frequency, it was designed to yield some good resonators in the presence of unknown process variations in capacitance or inductance.

## Spiral Inductors and Capacitors

Calculations of lumped spiral inductance were made using the modified Wheeler formula and checked with the current sheet formula [3]. These formulas agreed within a few %. The skin depth  $\delta$  for Cu is 5.8 microns at 127.7 MHz. The inductor trace width was kept  $< 2 \delta$  to efficiently use the Cu in the traces.

The capacitors were placed either at the inner or outer diameter of the spiral inductor, leaving an opening free of metal at the inductor center to allow free passage of magnetic flux. A simple lumped capacitor element was assumed.

## FABRICATION

### Capacitors

To achieve the smallest possible LC resonator with the correct resonant frequency, capacitors with a high capacitance/area are required. Currently such dielectric films are being used as gate dielectrics in advanced MOSFETs. Atomic Layer Deposition (ALD) is used to deposit discrete monolayers of oxide films such as HfO<sub>2</sub> and Ta<sub>2</sub>O<sub>5</sub>. A metal-dielectric-metal capacitor (not MOS) is required for our tags, hence we chose a plasma oxidation process on a thin film of Ta, rather than ALD. A literature search showed that tantalum oxy-nitrides have superior dielectric properties compared to pure oxides [4], so experiments were performed with both pure O<sub>2</sub> and O<sub>2</sub>/N<sub>2</sub> mixtures. An Oxford Plasma Technologies RIE was used to oxidize the Ta surface. Temperature and gas composition were varied to yield a high value of capacitance and reasonable uniformity across the wafer. A mixture of 50% O<sub>2</sub> / 50% N<sub>2</sub> and substrate temperature of 250 °C was found to give a repeatable value of 0.028 F/m<sup>2</sup>.

### Inductors

To achieve a large inductance and low resistance in a small area, thick Cu coils were electroplated on a temporary seed layer. Two photoresists were used: KMPR [5], a high aspect ratio negative resist, and AZ 4620, a conventional positive thick resist. Although the KMPR yielded superior high aspect ratio plated structures (Fig. 1), difficulty removing the cross-linked KMPR caused us to ultimately revert to AZ 4620 which is easily removed in standard solvents and resist strippers.

### Fabrication Process Sequence

The process is shown in cross-sections in Fig. 2. 100 mm glass wafers were used as substrates. A tri-layer stack of Cr/Au/Ta was sputtered and patterned using a liftoff technique (2a). This layer serves as the bottom conductor for the capacitors, and also to cross-under the inductor. The top Ta layer is plasma oxidized to form the capacitor dielectric (2 b). A contact mask is applied and the resultant Ta<sub>2</sub>O<sub>5</sub> and Ta layers are plasma etched in the contact areas. A 2 μm thick layer of positive photoresist is patterned and hard baked to form a sacrificial layer for creating an air-gap between the inductor and the cross-under layer (2c). A seed layer of Ti/Cu is then

sputtered everywhere as a plating base (2d). The plating resist mask is applied and patterned to define the spiral inductor and the top capacitor metal (2e). A commercial Cu bath is used to plate up 15 microns of Cu, after which the resist plating mask, seed layer, and sacrificial photoresist layer are removed (2f). Finally the wafer is coated with photoresist and diced to the desired size. A completed resonator is shown in Fig. 3. A unit cell containing an array of resonators and test structures, coated in Agar gel is shown in Fig. 4. These arrays were further diced to provide individual resonators when required for in-vivo testing.

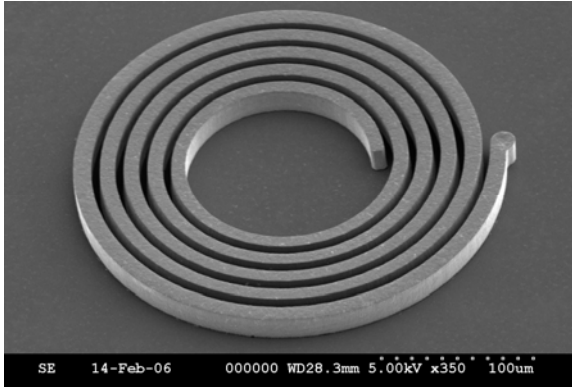


Figure 1. Electroplated Cu coil 15  $\mu\text{m}$  thick, plated through high aspect ratio KMPR negative resist. Coils are 10  $\mu\text{m}$  wide with a 5  $\mu\text{m}$  gap.

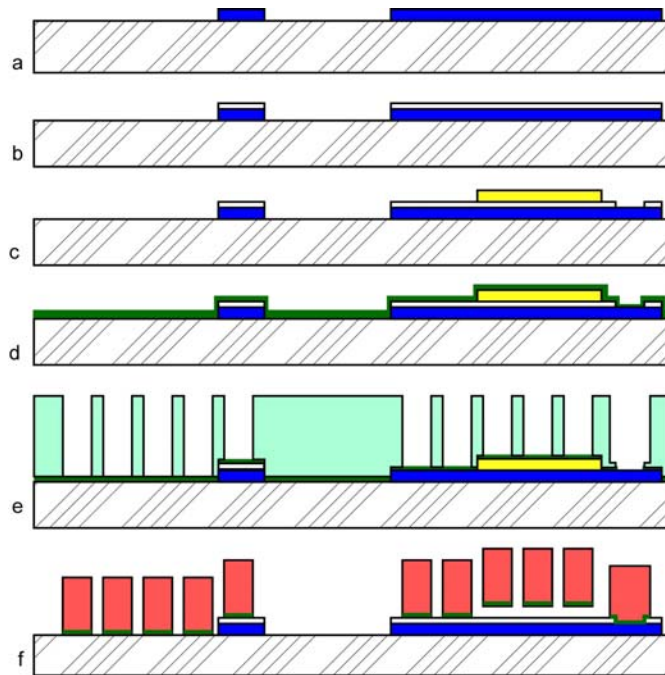


Figure 2. Fabrication sequence for the resonant micro-tags.

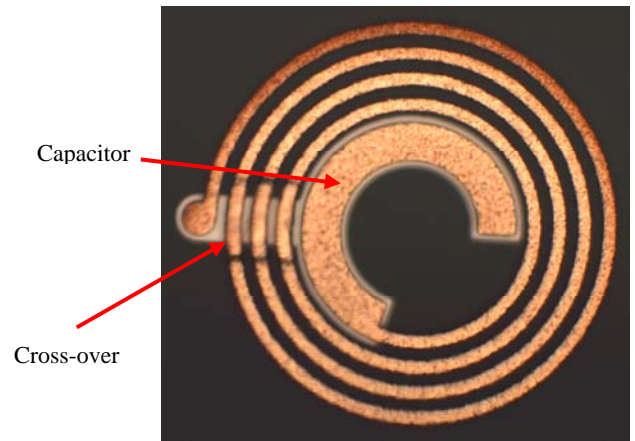


Figure 3. LC resonator with spiral inductor, air-bridge and capacitor. Device diameter is 370 microns.

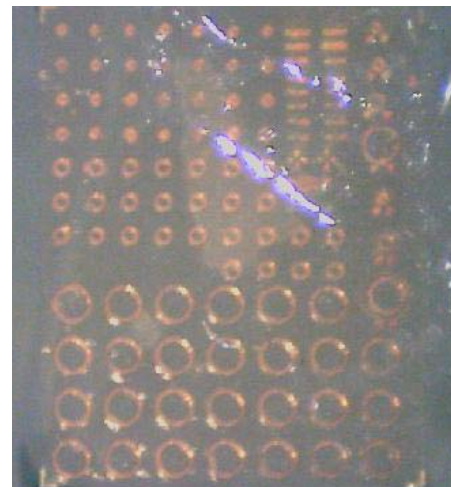


Figure 4. Array of resonators with 0.3, 0.5, and 1 mm diameters encapsulated in Agar gel.

## RESULTS

### Spiral Inductors

Test inductors included on the mask set were measured using an HP LCR meter. Measured vs. calculated values of inductance are shown in Fig. 5. The measured values are about 70-80% of the calculated values, perhaps due to stray capacitance and inductance of the test leads.

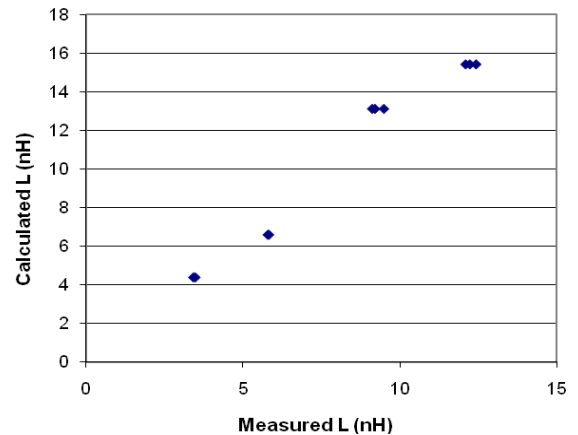


Figure 5. Measured vs. calculated inductances.

## SCANNING RF MICROSCOPE AND MRI IMAGES

A technique similar to that used in scanning near field microwave microscopy [6] was used in order to characterize the MRDs. We call this technique ultra high frequency scanning microscopy (UHF microscopy) because the frequency range of interest is typically 87- 207 MHz. This technique involves scanning a coil with a diameter of 1.5 mm (detection coil) that couples inductively to the MRDs without contacting them. The linear magnitude and phase of the reflection coefficient ( $S_{11}$ ) measured by a network analyzer (HP 8751A) is stored along with the spatial coordinates using custom software. By plotting the  $S_{11}$  coefficient as a function of position an RF image of the MRDs can be obtained for a specific frequency (Fig. 6). A good correlation was obtained between the location of MRDs in MRI spin echo image (Fig 8a) and the UHF microscopy image (Fig 8b). A good concordance between MRI and UHF microscopy can be seen for 300 and 500 microns resonators.

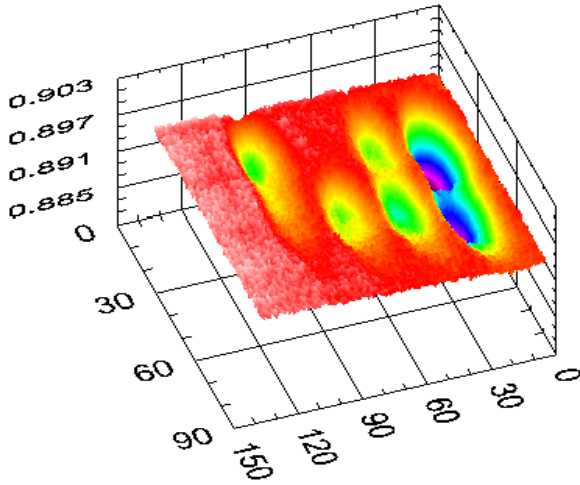


Figure 6. Scanning UHF image ( $S_{11}$ ) of array of MRD's.

The variation of  $S_{11}$  recorded during UHF microscopy experiment is analyzed as a function of frequency for a given  $x$ ,  $y$  position and, as a result, the frequency response of MRD is obtained. To understand these variations and to predict which MRDs can be visualized in MRI experiments we developed an analytical model. This model is based on the analogy between UHF microscopy and Radio Frequency Identification (RFID) systems. The detection coil and MRDs are similar to the transmitter coil and the transponder in an RFID system. In an RFID system, mutual inductance between the readout coil and the LC circuit of the tag allows readout. Based on this analogy, we can use the relationship derived by Finkenzeller [7] for the complex transformed impedance  $Z'_T$  of MRDs "seen" in detection circuit:

$$Z'_T = \frac{\omega^2 k^2 L_1 L_2}{R_2 + j\omega L_2 + Z_2} \quad (1)$$

where  $L_1$  and  $L_2$  are inductances of detection and MRDs coils, respectively;  $\omega$  is angular frequency;  $R_2$  is the MRD coil resistance,  $Z_2$  is the MRD non-inductive impedance (given by Equation 3) ;  $k$  coupling coefficient [7] was computed as:

$$k(x) = \frac{r_{MRD}^2 r_{reader}^2}{\sqrt{r_{MRD} r_{det}} \left( \sqrt{x^2 + r_{det}^2} \right)^3} \quad (2)$$

where  $r_{MRD}$  and  $r_{det}$  are the average radius of MRD and detection coils, respectively placed at distance  $x$ .  $Z_2$  impedance from Equation 1 is associated with the capacitor  $C_2$  made up of a parallel tuning capacitor ( $C_T$ ) and a parasitic capacitance ( $C_p$ ) from the real circuit. A load resistor ( $R_L$ ) that describes the current consumption in the RFID circuit was also considered, which could represent leakage current (if any) through the dielectric. In these conditions, the MRD non-inductive impedance becomes:

$$Z_2 = \frac{R_L}{1 + j\omega R_L C_2} \quad (3)$$

MEMS chips were attached on a microscope slide, immersed in a Phosphate-Buffer Saline (aqueous media supplemented with 150mM NaCl) and imaged in a 3T MRI scanner (GE) using an 8 - leg birdcage coil (110 mm in length and 60 mm in diameter). Fig. 7 is a spin-echo image with the following experimental MRI parameters: repeat time - TR=300 ms; echo time -TE = 10 ms; the field of view (FOV) was 80 mm  $\times$  80 mm with a 256 by 128 data matrix.

Relatively B1 sensitive spin-echo sequences showed good MRD contrast, whereas relatively B1 insensitive gradient echo-sequences showed none, demonstrating that the MRD contrast mechanism is due to perturbation of the B1 field.

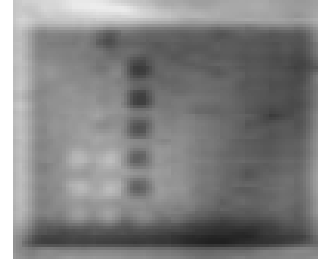


Figure 7. MRI image of MRD array.

Computed and experimentally determined frequency responses for an MRD in are shown in Figure 8c. The analytical model and experimental data show that a quality factor of 7.2 was measured for this device. The frequency analysis of MRDs based on UHF microscopy allowed us to select the devices that will be visualized in MRI experiments. MRD active devices contain the Larmor frequency 127.7 MHz (green line in Figure 8c) within their 3dB region.

Two active and two non-active MRDs were subcutaneously implanted in a mouse flank (Fig. 9). The MicroCT image (InVeon, Siemens Medical Solutions) shows that at least 3 MRDs are placed in the same plan (Fig. 9C). These devices have been imaged using MRI in a clinical 3T scanner (Fig. 9b). The magnetic field generated by the MRDs was mapped (Figure 9a) using an algorithm [8] that considers two gradient - echo scans at flip angles of 30 degrees and 60 degrees. These pictures show that only the active devices have been located due to their self generated magnetic field. The maximum B1 value determined from MRD (labeled 1 in Figure 8) was  $8.6 \cdot 10^{-7}$  Tesla.

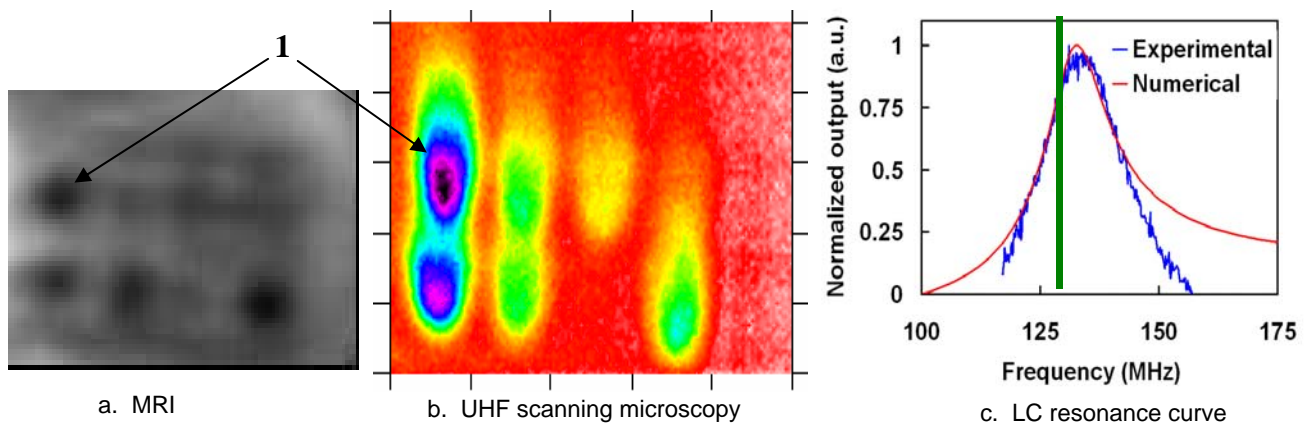


Figure 8. Comparison of MRI image (a) and UHF scanning image (b). Measured LC resonance with peak near 127.7 MHz (green line).



Fig. 9. Comparison of MRI B1 magnetic field map (a), MRI image (b) and micro-CT image (c). Devices are implanted in a mouse flank.

## CONCLUSIONS

We have demonstrated that micro-solid-state resonant devices are capable of being imaged *in vivo* and *in vitro* using a clinical 3T MRI, and that they can serve as B1 contrast agents. A novel plasma oxidation process was utilized to fabricate high value capacitance in a small area. A novel UHF microscope was built to image the devices. All types of MRDs (300, 500 and 1000 microns) designed and manufactured were detected in clinical 3T MRI. The scanning time was less than 10 minutes for each scan.

Future studies will focus on miniaturizing these devices to the cellular scale, on generating contrast at radiofrequencies not present in the human body, and on probing the limits of MRI sensitivity.

## ACKNOWLEDGEMENTS

Supported by an Application Development award from the Center for the Integration of Medicine and Innovative Technology (CIMIT), US Army DAMD17-02-2-0006.

## REFERENCES

- [1] M. H. Levitt, "Spin Dynamics", pp. 315-335, (Wiley and Sons, 2001).
- [2] Feridex and Combidex are products of Advanced Magnetics: <http://www.amagpharma.com/>.
- [3] S.S. Mohan et. al., "Simple Accurate Expressions for Planar Spiral Inductances", IEEE Journal of Solid-State Circuits, Vol. 34, No. 10, October 1999, pp. 1419-1424.
- [4] H. Jung, K. Im, D. Yang, and H. Hwang "Electrical and Reliability Characteristics of an Ultrathin TaOxNy Gate Dielectric Prepared by ND<sub>3</sub> Annealing of Ta<sub>2</sub>O<sub>5</sub>" IEEE ELECTRON DEVICE LETTERS, VOL. 21, NO. 12, DECEMBER 2000, pp. 563-565.
- [5] KMPR photoresist, MicroChem Inc.: <http://www.microchem.com/products/kmpr.htm>
- [6] R. Ciocan and N. Ida, IEEE Transactions on Magnetics, **40**, 651 (2004).
- [7] K. Finkenzerler "RFID Handbook Fundamentals and Applications in Contactless SmartCards and Identification", (John Wiley & Sons Inc New York, 2003), pp 88-91.
- [8] E.K. Insko and L. Bolinger, Journal of magnetic resonance, series A, **103**, 82(1993).

# RATIONALLY-DESIGNED SURFACE NANOPATTERNING: A POTENTIALLY NEW MEANS FOR ENHANCING SAFETY & EFFICACY OF VASCULAR STENTS

M.P. Rao<sup>1,2,3,4</sup>, J. Lu<sup>5,6</sup>, H.P. Aguilar<sup>1,3</sup>, D. Khang<sup>5,6</sup>, N.C. MacDonald<sup>7</sup>, and T.J. Webster<sup>5,6</sup>

<sup>1</sup>School of Mechanical Engineering, Purdue University, West Lafayette, IN, USA

<sup>2</sup>School of Materials Engineering, Purdue University, West Lafayette, IN, USA

<sup>3</sup>Birk Nanotechnology Center, Purdue University, West Lafayette, IN, USA

<sup>4</sup>Center for Advanced Manufacturing, Purdue University, West Lafayette, IN, USA

<sup>5</sup>Division of Engineering Brown University, Providence, RI, USA

<sup>6</sup>Department of Orthopaedic Surgery, Brown University, Providence, RI, USA

<sup>7</sup>Department of Mechanical Engineering, University of California, Santa Barbara, CA, USA

## ABSTRACT

This paper presents preliminary data supporting the feasibility of an innovative new therapeutic strategy that seeks to address the limitations of current drug-eluting stents via rational design of stent surface topography at the nanoscale. Using recently-developed anisotropic metal micromachining techniques, we have created bulk metal substrate surfaces patterned with arrays of micrometer to sub-micrometer scale parallel grooves. The rationale for this pattern geometry is based upon the presumption that such features will facilitate healing by accelerating reestablishment of the endothelium, the native lining of the vessel wall. Results from our preliminary *in vitro* studies show that these surfaces accelerate endothelialization, promote more native cellular morphology, and significantly enhance competitive adhesion of endothelial cells over vascular smooth muscle cells. As such, these data suggest that rationally-designed nanopatterned surfaces may provide a robust new means for enhancing efficacy and safety of vascular stents, possibly without the need for drug-elution.

## INTRODUCTION

Coronary heart disease (CHD) currently represents one of the most pressing health concerns of our time. Worldwide, CHD kills over 7 million people per year and is the cause of one in seven deaths [1]. In the United States, over 16 million are affected by the disease and it is the leading cause of death, killing well over 500,000 yearly [2]. Furthermore, nearly 50% of men and 30% of women over the age of 40 are at risk of developing the disease [2]. The economic burden of the disease in the United States is staggering, with estimated costs of nearly \$150 billion in 2006 [2]. As such, the need for efficacious and economical treatment methods for CHD is clearly evident.

CHD is characterized by arterial narrowing (stenosis) due to the accumulation of plaque beneath the endothelium, the layer of cells that make up the innermost lining of the blood vessel. This accumulation, known as atherosclerosis, can cause restriction of blood flow, thus depriving the heart muscle of oxygen. In severe cases, stent implantation has become the preferred method for restoring normal blood flow. Stents are metallic, lattice-like scaffolds that are implanted into stenosed arteries to maintain vascular patency. In their first embodiment, bare metal stents (BMS) simply served as mechanical supports to prevent vascular recoil after balloon angioplasty. However, they have since evolved to incorporate biological functionality as well, in order to mitigate neointimal hyperplasia, the vascular response to implantation-induced injury. This response is characterized by excessive tissue proliferation within the lumen, which can cause re-narrowing over time (restenosis).

Of the numerous solutions developed to address restenosis, the most successful to date has been the drug-eluting stent (DES), which suppresses hyperplastic response via slow release of

antiproliferative or immunosuppressive drugs from a polymer coating applied to the stent. There is growing evidence, however, that potential for thrombogenic stimulus (clotting) is higher in DES than BMS, particularly after drug-elution has ceased. While incidence of this so-called late stage thrombosis in DES is generally low (< 5%), there is cause for concern nonetheless because fatality in such cases can be as high as 45% [3]. Although the mechanism has yet to be fully understood, the cause is likely multifactorial, with delayed intimal healing caused by inhibition of endothelialization potentially playing a significant role [4]. This therefore provides the impetus to develop new therapeutic strategies that facilitate rather than delay healing.

A number of studies have begun to show the promise of pro-healing strategies. All presume that rapid restoration of the endothelium over the stent will enable its isolation from circulating blood, and therefore reduce potential for thrombosis. To date, most have focused on use of bioactive agents, such as growth factors, peptides, and antibodies, which are delivered locally via coating-based elution, surface-immobilization, or porous balloon catheter. However, the efficacy of such approaches is often critically dependent upon spatial and/or temporal control of delivery. Moreover, consideration must also be given to the potentially detrimental consequences of unintended systemic exposure [5]. Thus, there is still distinct need for development of more robust and reliable solutions. In this paper we demonstrate preliminary evidence supporting the feasibility of a new therapeutic strategy that seeks to promote healing via rational design of the surface topography at the nanoscale.

## INFLUENCE OF NANOSCALE TOPOGRAPHY IN CELL-SUBSTRATE INTERACTIONS

Numerous studies have demonstrated the often beneficial effects of nanoscale topography on cellular function in a variety of implant applications. With regard to cardiovascular applications and endothelial cells in particular, studies have shown distinct improvements in cellular behavior on nanostructured surfaces, including enhanced adhesion, spreading, and migration [6-12]. It has also been demonstrated clinically that, contrary to prevailing belief, nanoscale surface roughness may actually decrease hyperplastic response slightly [13].

In each of the above mentioned studies, surface topography was essentially random in nature, with only limited control over the distribution of feature sizes, their spatial arrangement, or their morphology (i.e. shape). However, cellular response is known to be strongly affected by small variations in each of these parameters, thus suggesting the need for greater control to elicit more uniform and reproducible response. It has also been shown that specifically-shaped surface features may elicit desirable cellular responses. For example, arrays of sub-micrometer scale linear grooves have been shown to enhance endothelial alignment

and elongation significantly compared to micropatterned surfaces [14], thus providing the potential for improved mimicry of the native endothelium. Moreover, micrometer scale linear groove arrays have been shown to produce significant acceleration of endothelialization, due to alignment-induced reduction of contact inhibition between cells [15]. Since many of these responses are observed to scale favorably with decreasing feature size, this suggests that precisely-controlled and rationally-designed topographical variation of the stent surface at the nanoscale may provide considerable promise for enhancing healing and endothelial function in vascular stenting.

## EXPERIMENTAL METHODS

### Patterned substrate fabrication

Polished titanium wafer substrates (99.6% Ti, 100 mm diameter, 500  $\mu\text{m}$  thickness,  $R_a \sim 10$  nm RMS), were cleaned in ultrasonic baths of acetone and isopropanol, followed by deionized (DI) water rinsing. The wafers were then dried with  $\text{N}_2$  and dehydration baked. The wafers were primed with hexamethyldisilazane, coated with photoresist, and pre-exposure baked. The coated wafers were then lithographically exposed using a wafer stepper. After exposure, the wafers were post-baked, developed, rinsed in DI, and dried with  $\text{N}_2$ .

Each die pattern was composed of an assemblage of 5 x 5 mm sub-patterns, each made up of a periodic array of parallel lines and space of equal width. The sub-patterns were arranged such that they were orthogonally aligned to their nearest neighbors. A different line width was used for each sub-pattern (ranging from 0.75  $\mu\text{m}$  to 100  $\mu\text{m}$ ), thus providing the opportunity for simultaneous evaluation of a broad pattern parameter space within the same sample and, therefore, within the same cell culture conditions. The range of chosen feature sizes was bounded at the lower end by the resolution limit of the wafer stepper, and at the upper end by the recognition that the widths of stent struts are typically on the order of 100-150  $\mu\text{m}$ .

The photoresist patterns were transferred into the underlying titanium substrates using inductively coupled plasma reactive ion etching (conditions: 100 sccm  $\text{Cl}_2$ , 5 sccm Ar, 400 W source power, 100 W substrate power, 2 Pa chamber pressure) [16]. Afterwards, the residual photoresist was removed in ultrasonic solvent baths, followed by DI rinsing and  $\text{N}_2$  drying. Resulting groove depths of  $\sim 2$   $\mu\text{m}$  were achieved with etch times of 2 – 3 min. Due to the limited scope of this preliminary study, groove depth was not varied. However, it is anticipated that groove depth may strongly influence cellular response.

### Substrate characterization

Scanning electron microscopy was used to characterize the patterned Ti substrates. Prior to imaging, the substrates were sputter-coated with a thin layer of gold-palladium (these samples were not used for subsequent cell culture experiments). Surface topography was further characterized by atomic force microscopy. Commercially available AFM tips (radius of tip curvature less than 10 nm) were used in tapping mode. Tips with full tip cone angle less than  $10^\circ$  in the last 200nm of the tip apex were used (25  $\mu\text{m}$  full tip height,  $30^\circ$  full cone angle after initial 200 nm, 40 N/m force constant). Scan rate was fixed at 0.5Hz.

### Cell culture

Before cell culture experiments, all substrates were rinsed in acetone for 5 min, ethanol for 5 min, and finally in DI water for another 5 min. They were then sterilized by autoclaving (115-120  $^\circ\text{C}$ ) for 30 min. Competitive endothelial and vascular smooth muscle cell proliferation on patterned titanium substrates was

evaluated in the following manner: endothelial and vascular smooth muscle cells previously incubated with fluorescent stains were suspended in cell culture media (DMEM containing 10% FBS), seeded randomly (2,500 cells/ $\text{cm}^2$  surface area) onto the substrate surface, and cultured under standard static cell culture conditions for periods ranging from 4 hours to 5 days. At the conclusion of the experiments, non-adherent cells were removed by rinsing with phosphate-buffered saline. In all experiments conventional wrought Ti surfaces ( $R_a=4.1$  nm) served as controls representative of conventional stent surfaces. Endothelial monoculture assays (i.e. endothelial cells alone) were also performed using the above-listed procedures.

### Cellular adhesion and proliferation characterization

Adherent cells were fixed and counted using fluorescent microscopy. Cell preparations were examined using a fluorescence microscope with cell density (cells per unit surface area) determined by averaging the number of cells in five random fields. Proliferating cells were also visualized using computer-based image analysis. Special attention was given to analysis of cell morphology on the patterned substrates. All cell experiments were run in triplicate and repeated a minimum of three times per substrate type. Numerical data was analyzed using Analysis of Variance (ANOVA) with proliferation as the observed response; values of  $p < 0.05$  were considered significant difference between substrate types.

Endothelial cell morphology after culture was also quantified using SEM. Endothelial cells were fixed with formalin for 5 min, then dehydrated by soaking serially in 10%, 30%, 50%, 70%, and 90% ethanol for 30 min, followed by soaking in 100% ethanol for 15 min three times. The substrates were then critical point dried before visualization.

## RESULTS

Figures 1 & 2 illustrate the highly precise and anisotropic nature of the grooved surface topography of the patterned titanium substrates. The results of 3 day competitive endothelial and vascular smooth muscle cell proliferation assays on the patterned titanium substrates are shown in Figure 3. The data clearly show that decreasing feature sizes promote strong enhancement of endothelial proliferation and concurrent inhibition of smooth muscle cells; both of which are critical to improving vascular stent efficacy and safety. This stands in stark contrast to the behavior observed on representative conventional stent surfaces (i.e. wrought Ti control samples), where endothelial proliferation is strongly inhibited relative to smooth muscle cells.

Endothelial monoculture assays produced similar trends of enhanced response with decreasing size scales. Endothelial spreading behavior under 3 day monoculture conditions is shown in Figure 4. Increasing cell density, better spreading, and greater alignment was observed with decreasing feature size. Figure 4(d) provides further evidence of strong contact guidance, as indicated by the sharp transition of cellular alignment from one orthogonally aligned sub-pattern to the next. A scanning electron micrograph of endothelial spreading after 3 day monoculture on a 0.75  $\mu\text{m}$  patterned substrate is shown in Figure 5 and further demonstrates the strong alignment induced by the sub-micrometer patterned surfaces. Additional monoculture experiments (data not shown) also demonstrated that time to endothelial confluence decreased with decreasing feature size. Specifically, confluence was achieved within 3 days on 0.75  $\mu\text{m}$  features, whereas confluence was not achieved even after 5 days on wrought Ti control surfaces. Collectively, these data suggest potential for strong affect of nanopatterning on endothelialization *in vivo*.

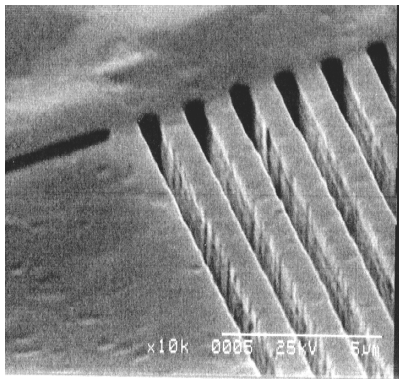


Figure 1: Scanning electron micrograph (inclined view) of patterned titanium substrate with 0.75 μm wide grooves and space. Scale bar = 5 μm.

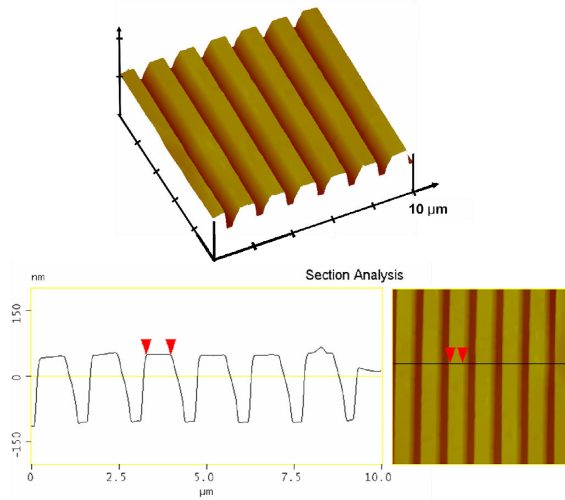


Figure 2: Atomic force micrographs of patterned titanium substrate with 0.75 μm wide grooves and space.

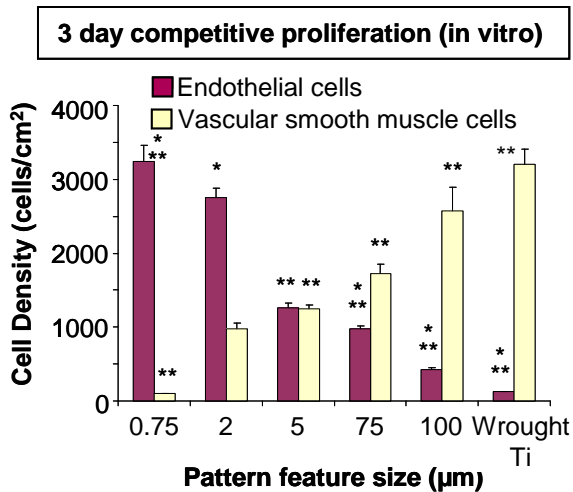


Figure 3: 3 day competitive cell proliferation on patterned titanium substrates as a function of feature size. Feature sizes correspond to groove width and spacing. Data = mean +/- SEM; N = 3; \* p < 0.01 (compared to vascular smooth muscle cells on same feature dimension); \*\* p < 0.01 (compared to 2 μm features).

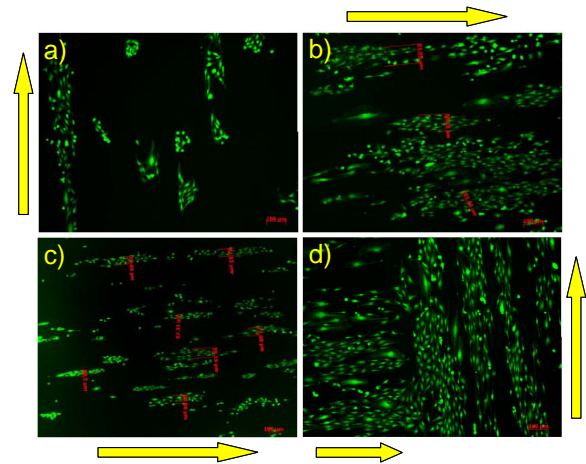


Figure 4: Endothelial spreading (live, stained) for 3 day monocultures on patterned titanium substrates with: a) 100 μm; b) 25 μm; c) 2 μm; and d) 0.75 μm grooves & space. Arrows indicate approximate direction of pattern alignment. Scale bar at bottom right of each image = 100 μm.

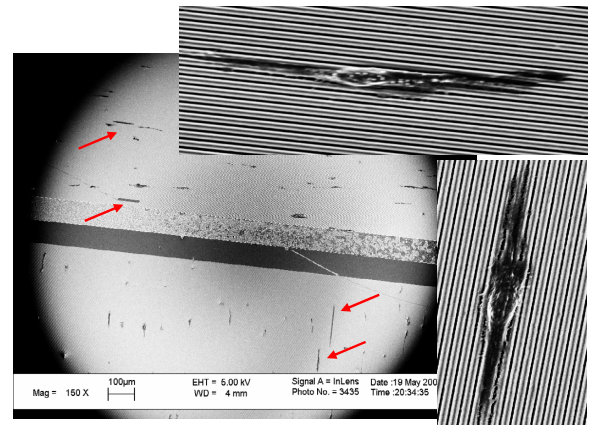


Figure 5: Scanning electron micrographs of 3 day monocultured endothelial cells adhered to patterned titanium substrate with 0.75 μm grooves and space. Background: Low magnification view of two adjacent patterned regions; the upper is horizontally aligned, while the lower is vertically aligned. Arrows mark examples of highly aligned cells. Foreground: High magnification views demonstrating strong endothelial alignment along ridge tops of two patterns.

## DISCUSSION

This preliminary study represents the first demonstration of enhanced competitive endothelial cell response relative to vascular smooth muscle cells on patterned titanium substrates. Clear evidence is presented of improved endothelial proliferation, higher cell density, and greater alignment with decreasing pattern feature size, particularly as feature sizes are pushed into the sub-micrometer realm. This suggests that subsequent cellular function may be improved with decreasing feature size. Perhaps more importantly, however, it also provides compelling first evidence of the potential for mitigation of restenosis and thrombosis solely through rational design of the surface topography of the stent material itself. As such, the inherent simplicity, robustness, and reliability of this approach is immediately apparent, as is its potential for improving the efficacy and safety of vascular stents.

The exact mechanisms by which such surface features affect cellular response are still unknown, however prevailing theories suggest that they may either: a) modulate the interfacial forces that guide cellular structure and intracellular signaling [17]; or b) influence the nature of protein adsorption on the surface, thus affecting the expression of integrin receptors that regulate subsequent cellular adhesion and function [18]. With regard to vascular cells in particular, recent evidence has been reported supporting the latter hypothesis. It was noted that adsorption and unfolding of fibronectin, a key protein involved in endothelial cell adhesion, were both enhanced on randomly nanostructured surfaces of biodegradable polymers [6,19]. The same results have since been observed for vitronectin. It would therefore be presumed that endothelial response would be enhanced by not only the increased number of binding sites produced by higher concentrations of adsorbed protein, but also by their more favorable conformation, since unfolding may promote expression of key cell-adhesive integrin receptors, such as RGD. However, vascular smooth muscle cells also adhere to RGD contained in fibronectin and vitronectin, yet their competitive adhesion is observed to decrease with decreasing feature size. This suggests that competitive pressure from endothelial cells may play a strong role in inhibiting smooth muscle cell proliferation on patterned titanium surfaces.

Although enhanced competitive endothelial response was observed with decreasing feature size in the preliminary study, the smallest features probed were still only within the sub-micrometer range, i.e. 0.75  $\mu\text{m}$  and above. It is well known, however, that many important cellular and extracellular matrix components are of far smaller dimensions, with most within the range of tens to a few hundreds of nanometers [20]. Filopodia, are one particularly important example within the context of cell-substrate interactions. These tendril-like cellular projections are used probe the substrate in advance of establishment of focal adhesions. They have been shown to preferentially attach to nanoscale surface features [9] and it has been suggested they may be responsible for cellular alignment along patterned features (i.e. contact guidance) [14]. They have also been shown to increase in number in response to nanoscale surface features [21]. Consequently, this suggests that further reduction of feature sizes in the patterned titanium substrates may increase filopodia-based interactions which may then yield even greater endothelial response. As such, the implications for vascular stents are enormous. Improved competitive endothelial proliferation, higher cell density, and improved alignment might enable rapid and robust endothelialization of the stent, thus reducing potential for thrombosis and restenosis.

## CONCLUSION

The current study represents the first demonstration of nanopatterning-enhanced endothelialization in materials of immediate relevance to vascular stents. Furthermore, the current study presents the first demonstration of strongly enhanced competitive endothelial proliferation over vascular smooth muscle cells on nanopatterned surfaces. Finally, the current study represents the first demonstration of such behavior in patterned metallic surfaces created using fabrication techniques that are intrinsically scalable to low-cost/high-volume manufacturing of vascular stents. This is a particularly key distinction, since it demonstrates a clear path towards clinical translation. Consequently, this study provides compelling evidence of a potentially robust and reliable new means of improving the safety and efficacy of vascular stents.

## REFERENCES

- [1] The atlas of heart disease and stroke. Ed. J. Mackay and G. Mensah, World Health Organization, Geneva, Switzerland, 2004.
- [2] W Rosamond *et al.* Heart disease and stroke statistics – 2007 update: A report from the American Heart Association Statistics Committee and Stroke Statistics subcommittee. *Circulation*, 115:E69-E171, 2007.
- [3] I Iakovou *et al.* Incidence, predictors, and outcome of thrombosis after successful implantation of drug-eluting stents. *JAMA*, 293(17):2126-2130, 2005.
- [4] M Joner *et al.* Pathology of drug-eluting stents in humans. *J Am Coll Cardiol*, 48(1):193-202, 2006.
- [5] KL March, *et al.* Cardiovascular gene therapy using adenoviral vectors: Distant transduction following local delivery using a porous balloon catheter. *J Am Coll Cardiol*, 23(1):177A, 1994.
- [6] DC Miller, A Thapa, KM Haberstroh, and TJ Webster. Endothelial and vascular smooth muscle cell function on poly(lactic-co-glycolic acid) with nano-structured surface features. *Biomaterials*, 25(1):53-61, 2004.
- [7] S Choudhary, M Berhe, KM Haberstroh, and TJ Webster. Increased endothelial and vascular smooth muscle cell adhesion on nanostructured titanium and CoCrMo. *Int J Nanomedicine*, 1(1):41-49, 2006.
- [9] MJ Dalby *et al.* In vitro reaction of endothelial cells to polymer demixed nanotopography. *Biomaterials*, 23(14):2945-2954, 2002.
- [11] S Buttiglieri *et al.* Endothelialization and adherence of leucocytes to nanostructured surfaces. *Biomaterials*, 24(16):2731-2738, 2003.
- [12] TW Chung, DZ Liu, SY Wang, and SS Wang. Enhancement of the growth of human endothelial cells by surface roughness at nanometer scale. *Biomaterials*, 24(25):4655-4661, 2003.
- [13] A Dibra *et al.* Influence of stent surface topography on the outcomes of patients undergoing coronary stenting: A randomized double-blind controlled trial. *Catheter Cardio Inte*, 65(3):374-380, 2005.
- [14] CJ Bettinger *et al.* Micro fabrication of poly (glycerol-sebacate) for contact guidance applications. *Biomaterials*, 27(12):2558-2565, 2006.
- [15] C Fuss *et al.* Surface micro grooves (MG) improve endothelialization rate in vitro and in vivo. *J Am Coll Cardiol*, 37(2):70A-70A Suppl. A, 2001.
- [16] ER Parker *et al.* Inductively coupled plasma etching of bulk titanium for MEMS applications. *J Electrochem Soc*, 152(10):C675-C683, 2005.
- [17] ASG Curtis *et al.* Cells react to nanoscale order and symmetry in their surrounding. *IEEE Trans Nanobioscience*, 3(1):61-65, 2004.
- [18] TJ Webster, LS Sadler, RW Siegel, and R Bizios. Mechanisms of enhanced osteoblast adhesion on nanophas alumina involve vitronectin. *Tissue Eng*, 7(3):291-301, 2001.
- [19] DC Miller, KM Haberstroh, and TJ Webster. Mechanism(s) of increased vascular cell adhesion on nanostructured poly(lactic-co-glycolic acid) films. *J Biomed Mater Res*, 73A(4):476-484, 2005.
- [20] RG Flemming *et al.* Effects of synthetic micro- and nanostructured surfaces on cell behavior. *Biomaterials*, 20(6):573-588, 2000.
- [21] MJ Dalby *et al.* Polymer-demixed nano-topography: Control of fibroblast spreading and proliferation. *Tissue Eng*, 8(6):1099-1108, 2002.

# WIRELESS BILIARY STENT SYSTEM WITH WISHBONE-ARRAY RESONANT MAGNETOELASTIC (WARM) SENSOR AND CONFORMAL MAGNETIC LAYER

Scott R. Green<sup>1</sup> and Yogesh B. Gianchandani<sup>1,2</sup>

<sup>1</sup>Department of Mechanical Engineering, University of Michigan, Ann Arbor, Michigan, USA

<sup>2</sup>Department of Electrical Engineering, University of Michigan, Ann Arbor, Michigan, USA

## ABSTRACT

Stents are used to maintain bile duct patency after duct narrowing occurs due to various pathologies. Unfortunately, stent placement results in sludge accumulation within a variable timeframe, leading to complications such as jaundice or liver damage. This paper presents a system for wirelessly monitoring the accumulation of sludge, comprising an integrated magnetoelastic system with a sensor and biasing permanent magnet layer that conform to the meshed topology and tubular curvature of a biliary stent. The sensors have an active area of 7.5 mm x 29 mm and a mass of 9.1 mg. A 38% decrease in the resonant frequency – from 61.6 kHz to 38.2 kHz – after application of a sludge simulant totaling 20.9 mg - 2.3X the mass of the sensor – was measured with the integrated system.

## INTRODUCTION

Stents are mesh tubular structures used to impart and maintain patency in a variety of vessels and ducts that have become constricted as a result of stenotic pathology. Though the act of implanting a stent relieves symptoms caused by the constriction, in-stent restenosis – a reappearance of the narrowing, typically due to the reaction of the body to the presence of the stent – is a risk associated with all stenting procedures.

An example of a stent application area – and the focus of this work – is the bile duct, which transports bile between the liver, gall bladder, pancreas, and small intestine. The constriction relieved by stent implantation is often due to pancreatitis, cholangitis, tumors, or gallstones. Restenosis can occur in an average of 4-5 months via formation of a bacterial matrix known as biliary “sludge” [1].

The timeframe for clinically significant restenosis to occur is highly variable from case to case. Current techniques for diagnosing a blockage are indirect and rely on detecting enzyme levels that may not increase until after the blockage is significant. The combined effect of the unknown pathogenesis time course and the indirect testing methods can result in either unnecessary, pre-scheduled interventions or in untimely interventions after patients exhibit outward symptoms of the blockage (and liver damage has already occurred). As such, a direct method of diagnosis – such as that shown in Fig. 1 – would enable timely intervention and eliminate unnecessary procedures.

We have previously reported on magnetoelastic wireless sensing of sludge accumulation utilizing externally applied AC interrogative and stent-integrated DC biasing magnetic fields [2]. The magnetic fields cause a magnetoelastic sensor integrated with the stent to resonate at a frequency that changes as local viscosity increases and as sludge accumulates. The mechanical resonance generates an oscillating magnetic field that can be measured with an external pick-up coil. Our previous work utilized discrete neodymium magnets to optimally bias the anisotropy of a ribbon sensor – i.e. a rectangular strip of magnetoelastic material – that was similar in design to sensors used in industrial/environmental applications [3-5]. Although this combination was shown to be effective in benchtop testing, the discrete nature of the magnet and sensor components leaves room for improvement – especially with regards to maintaining important distributed flexibility of the biliary stent. Components that conform to or mimic the open, flexible structure of the stent would lead to a system that is better

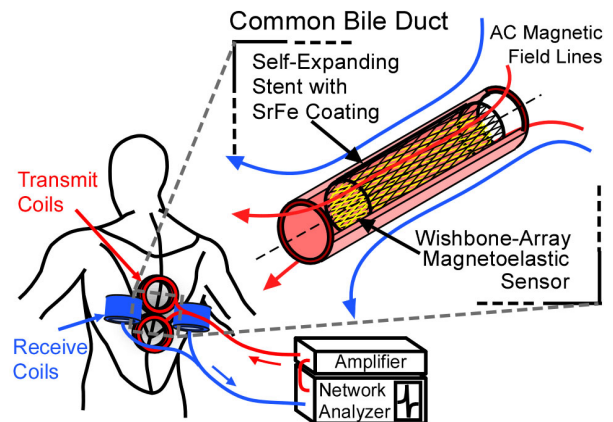


Figure 1: Conceptual diagram of *in vivo* magnetoelastic sensing of sludge accumulation for biliary stents.

able to withstand and accommodate the deformations required during catheter-based delivery, as well as lead to a system that preserves the structural functionality of the stent. With this viewpoint, this work focuses on an integrated magnetoelastic system with a sensor and biasing permanent magnet layer that conform to the meshed topology and tubular curvature of a biliary stent. Further, we investigate the impact of structural patterning, sensor shaping, and sensor material optimization.

## DESIGN AND MODELING

### Wishbone-Array Sensor

Biliary stents generally reach their final *in situ* diameter via an elastic self-expansion. This is in opposition to the plastic expansion of typical balloon-assisted cardiac stents. The need for large elastic diameter recovery in biliary stents leads to not only the utilization of materials with superior elastic properties (e.g. chrome-nickel Elgiloy or nickel-titanium Nitinol) but also to the use of open diamond-shaped patterns. Often these patterns are formed by braiding filaments into a tubular shape.

In keeping with the philosophy of mimicking the design of the stent with the design of the magnetoelastic sensor, we would like to use a material with superior elastic properties and to shape the material in diamond-shaped patterns. Fortunately, Metglas<sup>TM</sup> alloys are materials with excellent magnetostrictive properties as well as excellent elastic properties. For instance, the 2826MB alloy as used in this work is reported to have a yield strain of 1.6% [6], which is even higher than most cold-reduced Elgiloy yield strains of ~1% [7]. Metglas<sup>TM</sup> is not, however, readily available in filament form. It is also likely that a resonant sensor fashioned from braided filaments would have low structural coupling and high damping at braid cross-over points, limiting efficiency as a resonator. For these reasons, both the stent and sensor in this work are batch-fabricated from foils of different base materials utilizing a photochemical machining (PCM) process [2]. As shown in Figure 2, an elongated wishbone-array pattern is used; this pattern allows good mechanical flexibility for both the stent and sensor while maintaining mechanical coupling and minimizing joint damping for efficient resonant operation of the sensor. To ensure that plastic strain in the sensor was avoided during deformation that is required during catheter-based delivery, an FEA model was

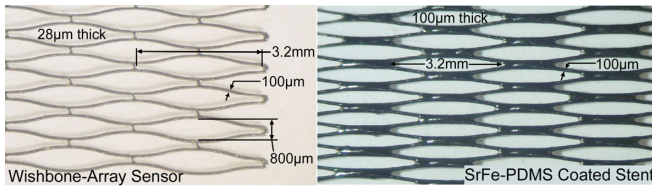


Figure 2: LEFT: A portion of a wishbone-array sensor, along with important dimensions. RIGHT: Stent with SrFe-PDMS coating.

utilized (Fig. 3). With the fabricated dimensions, FEA suggests that the wishbone-array sensor can undergo a 50% reduction in circumference without plastic strain that may result in degradation of sensor performance.

Because the wishbone-array pattern represents a significant departure from typical ribbon sensors – which are analyzed for this application in detail in [2,8] – we developed an FEA tool that is appropriate for estimating mode shapes and expected signal amplitudes from sensors with complicated structures. The crux of this tool is in its use of linearized constitutive equations describing the coupling between flux, field strength, stress, and strain in a magnetostrictive material:

$$\vec{\sigma} = [C]\vec{\epsilon} - \frac{[d][d]^T}{\mu_0\mu_r}\vec{B} \quad (1)$$

$$\vec{H} = -\frac{[d][C]}{\mu_0\mu_r}\vec{\epsilon} + \frac{1}{\mu_0\mu_r}\vec{B} \quad (2)$$

Equations (1) and (2) are versions of the so-called “piezomagnetic” equations – a name that highlights their similarity to piezoelectric equations – where  $\sigma$  is the stress vector,  $C$  is the stiffness matrix,  $\epsilon$  is the strain,  $d$  is the magnetostrictivity matrix,  $B$  is the magnetic flux density vector,  $H$  is the field strength vector,  $\mu_0$  is the permeability of free space, and  $\mu_r$  is the relative permeability. Magnetostrictive materials are nonlinear, but linearization about an operating point in a resonant magnetoelastic analysis is prudent, with a rationale analogous to that used in small-signal models of transistor-based circuits. Equations (1) and (2) are implemented in this work utilizing COMSOL Multiphysics and coupled time-harmonic (frequency response) induction current and stress-strain modes. A detailed look at an FEA implementation for magnetostrictive materials is in [9]; the approach used in this work is modified for application to resonant sensors. In Figure 4, calculated mode shapes for planar wishbone-array sensors are shown. The mode shapes displayed are at frequencies corresponding to significant peaks in the measured frequency response for the planar sensors, with the mode shape at 61.6 kHz resulting in the largest response amplitude. Note that the mode shapes combine significant longitudinal and transverse motion, whereas mode shapes of traditional ribbon sensors are

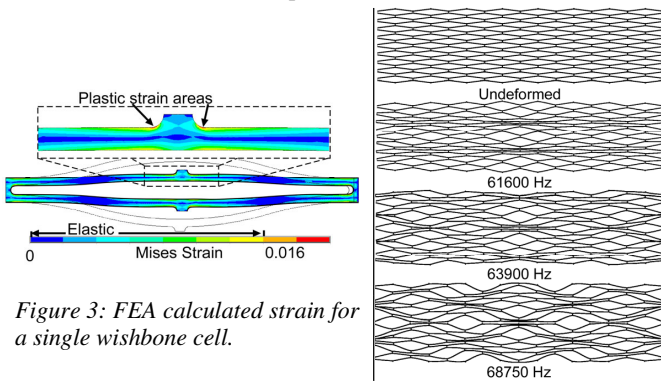


Figure 3: FEA calculated strain for a single wishbone cell.

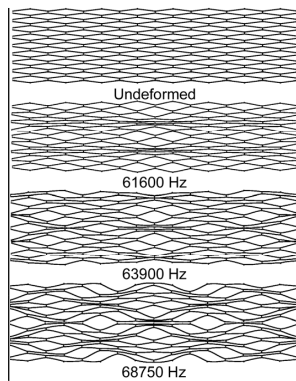


Figure 4: FEA calculated mode shape and frequency predictions.

limited to longitudinal motion. The model also predicts signal amplitude trends for various sensor geometries.

### Conformal Magnetic Layer

To achieve optimal magnetomechanical coupling, the magnetoelastic material must be biased with a DC magnetic field. This field offsets the as-fabricated anisotropy of the magnetic domains in the material, and the optimal field is dependent not only on the material of the sensor, but also on the feature sizes or aspect ratio of the final sensor. The process of selecting a bias field magnitude can be considered analogous to selecting an operating point for a transistor in an electrical circuit.

Our past work with integrated discrete magnets showed that sensor performance is improved when the bias field is as uniform as possible. This uniformity is difficult to achieve with integrated discrete magnets, because the field strength will necessarily decay as the distance from the magnets increases. However, if the magnetized portion of the system were to be continuously distributed, the field strength could be maintained more uniformly. This improves the sensor performance and eradicates high magnetic field gradients that lead to undesirable magnetic forces.

The distributed magnet is chosen in this work to be a layer of strontium ferrite (SrFe) particles (~1 µm average diameter, Hoosier Magnetics) suspended in polydimethylsiloxane (PDMS, Sylgard 184, Dow Corning). This choice is made again in keeping with minimally altering the functionality and structure of the biliary stent with the additional components. In this case, the polymer-suspended particles can be applied in a thin, flexible layer conforming exactly to the stent structure (Fig. 2).

Other polymers have been used as a base for SrFe particles in microfabricated magnets described elsewhere [10]. SrFe particles have the advantages of being chemically inert (owing to their ceramic nature), and of being widely and inexpensively available in very small particle sizes. The chemical inertness is especially valuable in our implantable application. PDMS is chosen in this work due to its generally accepted biocompatibility and due to processing ease. In fact, the entire polymer-suspended magnet fabrication process (as described later) is preferable in terms of ease compared with alternative options such as sputtering or electrodeposition of a thin-film magnetic layer.

### FABRICATION

#### Wishbone-Array Sensor

The wishbone-array sensors for this work are batch fabricated from a 28 µm thick foil of 2826MB Metglas™ utilizing the PCM process. Feature sizes of the individual struts are 100 µm, which is near the feature size limit for the technology. The overall size of the active portion of the sensor (not including the anchor areas discussed later) is 7.5 mm x 29 mm, with a mass of 9.1 mg.

PCM is a planar process, so the as-fabricated sensors are also planar. Because the stent application calls for a tubular shape, and the lateral dimension of the sensor is larger than the diameter of the stent, the sensor must be curved into a tubular or semi-tubular shape to best match the stent geometry. Initial attempts to add curvature to the sensor via mechanical stress proved catastrophic for the sensor signal. Instead, the tubular shape is achieved in this work by placing the sensor against the inner wall of a fixture tube and annealing for 30 minutes. Various final radii can be achieved by either changing the fixture tube radius or by changing the anneal temperature. For instance, a 4.6 mm radius results from annealing at 375 °C for 30 minutes inside a 3.6 mm radius tube, while a 1.6 mm radius results from annealing inside a 1.25 mm radius tube. Lower temperatures lead to lesser final curvature.

### Conformal Magnetic Layer

To form the conformal magnetic layer, the PDMS is first mixed in a 10:1 base-to-curing-agent ratio. Subsequently, the SrFe particles are introduced in 1:1, 3:1, or 1:3 SrFe-to-PDMS by weight ratios and mixed in by hand until the mixture is consistent (usually about 1 minute of mixing time). The mixture is then poured or spread into a mold containing the stent. The stent is then peeled out of the mold, with a conformal layer of the magnetic suspension adhered due to surface tension. The layer is then cured for 30 minutes at 60 °C. Thicker layers can be built up by repeating the process. Finally, the layer is magnetized uniformly along the long axis of the stent using a benchtop pulse magnetizer. In general, the 1:1 SrFe:PDMS ratio offered the best combination of workability and remnant strength of the ratios tested.

### Stent

The stent is also batch fabricated using the PCM process, in this case from a 100 µm thick foil of Elgiloy. As intended, the feature sizes and patterns are identical to those of the sensor (Fig. 2). The overall stent size is 5 mm (dia.) x 40 mm.

### System Assembly

Lateral portions of the wishbone-array sensor are connected to the active area with single struts. These areas act as anchors, and the single struts isolate the vibrating active area from the anchors. The anchors are bonded to the stent with a thin layer of PDMS.

Subsequently, the stent is rolled into a tubular shape and the resulting seam where the edges of the stent adjoin is also bonded with a thin layer of PDMS. The process is shown in Figure 5, and assemblies are shown in Figures 6 and 7.

## EXPERIMENTAL METHODS AND RESULTS

### Isolated Sensors

Prior to integration, as-cast planar sensors were evaluated using a uniform but variable bias field applied by Helmholtz coils located coaxially with the long axis of the sensor. For all tests, a swept-frequency network analyzer signal was amplified and sent through a transmit coil, while the same analyzer measured the EMF generated on a receive coil. The sensors were located concentrically with these coils. Results from the initial evaluation for the largest modal response of four sensors are shown in Figure 8. The optimal bias field – where the amplitude of the response is largest (10 mV) – is around 5 Oe. A clear dependence of resonant frequency on bias field can be seen – a manifestation of the  $\Delta E$  effect. The frequency and amplitude show repeatable performance across the tested sensors, as do frequencies and amplitudes from other modes, indicating a repeatable PCM fabrication process.

The sensors were then thermally treated either above (375 °C) or below (325 °C) the material Curie temperature (353 °C) and either remained planar or were given curvature. The resulting frequency characteristics are shown in Fig. 9. Post-treatment evaluation showed lower optimal biasing field (~1.5 Oe) and

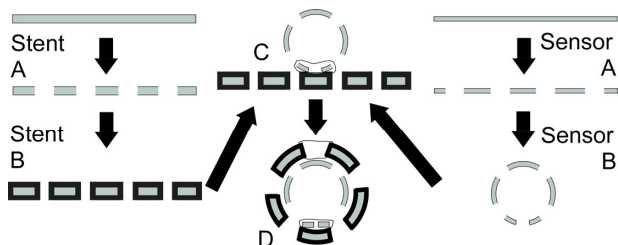


Fig. 5: Fabrication process. A) PCM patterning of Elgiloy (stent) and Metglas™ (sensor). B) Stent coated in SrFe-PDMS layer and magnetized. Sensor annealed in a tube. C) Sensor anchors bonded to stent with PDMS. D) Stent seam bonded with PDMS.

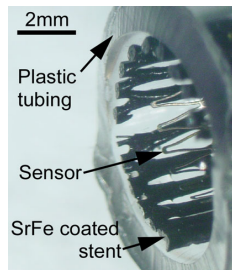


Figure 6: Assembled sensor, stent, and magnet layer.

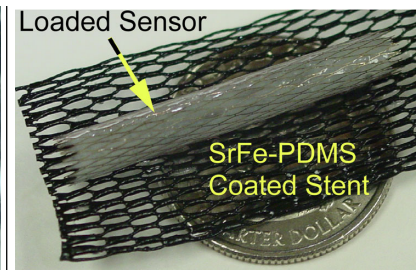


Figure 7: Assembled sensor, stent, and magnet layer. The stent seam is not bonded here for clarity.

improved signal level (up to 13.5 mV p-p). This important result shows that thermal treatment facilitates thinner SrFe-PDMS layers, which simplifies fabrication and minimizes concerns about large chronically implanted magnetic fields.

As-cast and thermally treated sensors were compressed through 1.5 mm diameter tubes – a circumferential deformation of at least 37% – without signal degradation. The repeatable performance of this test across both as-cast and thermally treated sensors implies that the thermal treatment process does not lead to impaired mechanical properties. The slight discrepancy with the FEA model predictions may be due to an imperfect correlation between the onset of plastic strain and the onset of strains that change the magnetomechanical properties of the material.

Bile viscosity changes are precursors to sludge accumulation, so sensor response to viscosity was evaluated (Fig. 10). The tested viscosity range is much greater than the physiological range of bile (1-12 cP), but the results show that sensitivity and signal amplitude is maintained over a very large range that might be suitable for other applications. Note that a 2.5 mm x 37.5 mm ribbon sensor resonant frequency will drop by only 6% over this viscosity range.

Accumulation of sludge results in a mass-loading effect on the sensor. This process was simulated by the application of two different materials – paraffin and a spray-on acrylate terpolymer – to as-cast and thermally treated wishbone-array sensors, as well as to 2.5 mm x 37.5 mm ribbon sensors. As shown in Figure 11, each of the sensor types reacts similarly in terms of resonant frequency to both sludge simulants. Further, the full scale range of each sensor type extends into the “critical zone”, where accumulation begins to significantly narrow the cross-sectional flow area.

### Integrated System

The integrated system, which consists of a curved wishbone-array sensor and a SrFe-PDMS coated stent, was evaluated in a manner similar to the isolated sensors but without the bias field supplied by the Helmholtz coils. In this way, all biasing of the sensor was provided by the conformal SrFe-PDMS magnetic layer. For the integrated system, sensitivity to viscosity over a physiologically appropriate range was measured even as mass was added. This experimental process showed that the normalized frequency response of the sensor to viscosity changes was not significantly affected by mass buildup (Fig. 12). Application of the acrylate terpolymer sludge simulant as a mass load showed that the frequency and signal amplitude of the integrated sensor reacted to mass loads similarly to those of the isolated sensors (Fig. 13).

## DISCUSSION

Three important advantages of the wishbone-array sensor over typical ribbon sensors in this application are made clear by this work. First, the fine features sizes and large open area of the pattern present little obstruction to bile flow, which is the primary objective of a biliary stent. Second, the sensors are much more accommodating of the large deformations required for catheter-

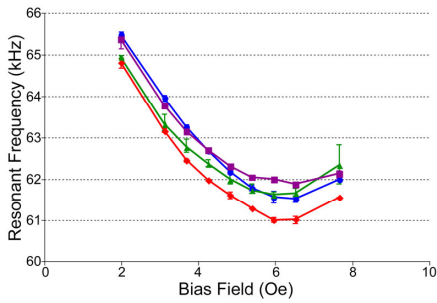


Figure 8: Evaluation of four as-cast planar wishbone-array sensors. The points in these figures represent the mean of three trials, and the error bars represent the minimum and maximum recorded values.

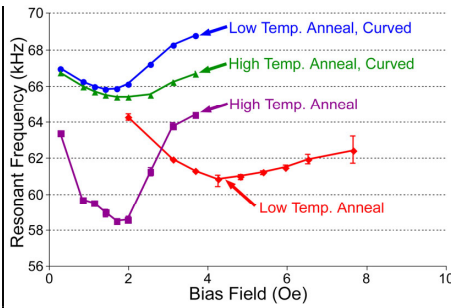


Figure 9: Characterization of wishbone-array sensors after thermal treatment.

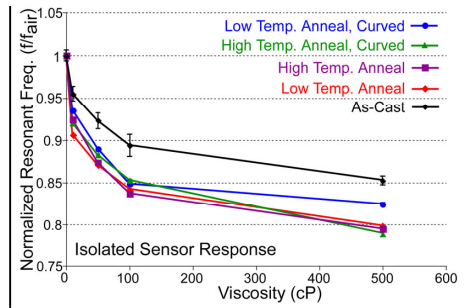


Figure 10: Isolated sensor response to changes in viscosity.

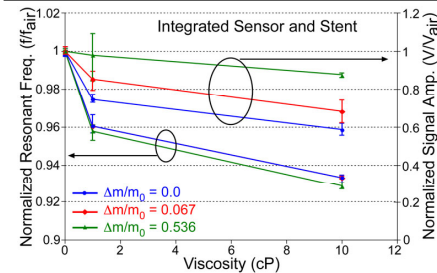


Figure 12: Response of the system to viscosity changes as mass accumulates.

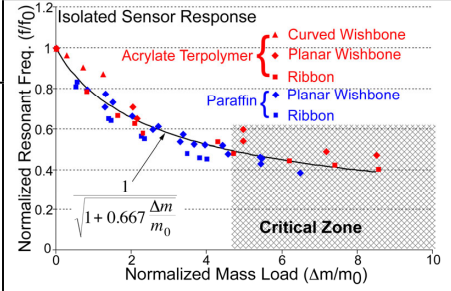


Fig. 11: Isolated wishbone and ribbon sensor response to mass loading from different sludge simulants. The curve is determined with a least-squares regression using the points and an equation of the form shown.

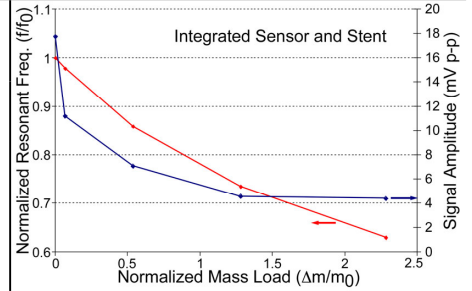


Figure 13: Response of the system to mass buildup. Mass added to the sensor was difficult to separate from mass added to the stent, so the equation for the curve in Fig. 11 was used to back-calculate the mass load.

based delivery. Third, the sensors have a higher sensitivity to viscosity changes, which is a clinically relevant parameter in many pathological conditions [11]. The principal disadvantage of the wishbone-array sensor, at least with the present design, is the smaller signal amplitude. However, preliminary results show that the signal amplitude scales with the overall sensor length, so this disadvantage may be mitigated with a longer sensor design.

Prior to *in vivo* testing of the system, further evaluation of the mechanical properties of the stent must be done. Analytical models imply that the sludge simulants used in this work represent a worst-case scenario, as biofilms like sludge are likely to be less stiff than the test materials [12].

## CONCLUSION

This work integrates a flexible wishbone-array magnetoelastic sensor and conformal magnetic layer with a biliary stent as a wireless system that monitors the stent environment. The system is sensitive to physiologically appropriate viscosity changes, showing a 7% decrease in resonant frequency in 10 cP fluid. The system also is capable of measuring mass buildup that is associated with sludge accumulation, showing a 38% decrease in the resonant frequency after an applied mass load of 20.9 mg, or 2.3X the mass of the sensor. The integrated system is robust to deformations required for delivery and provides a uniform biasing layer that minimally affects stent mechanics. With appropriate scaling, the sensing methodology may be applicable in any stent, including cardiovascular and esophageal stents. Additionally, the improved viscosity sensitivity of the wishbone-array sensor may find use in industrial applications like monitoring oil refinement.

## ACKNOWLEDGEMENTS

The authors acknowledge Dr. Grace Elta and Dr. Richard Kwon for discussions regarding stent usage. Mark Richardson assisted with test setup design and implementation. Metglas Inc., Hoosier Magnetics, and Dow Corning provided samples for this project. This work was supported in part by a NSF Graduate

Research Fellowship, the NSF ERC for Wireless Integrated Microsystems (WIMS), and the University of Michigan. Y. Gianchandani acknowledges support through the IR/D program while working at the National Science Foundation. The findings do not necessarily reflect the views of the NSF.

## REFERENCES

- [1] G. Donnelly, et al., "Plastic Biliary Stent Occlusion: Factors Involved and Possible Preventive Approaches," *Clinical Medicine & Research*, Vol. 5, No. 1, 2007, pp. 53-60.
- [2] S. R. Green, et al., "Photochemically Patterned Biliary Stents with Integrated Permanent Magnets and Deformable Assembly Features for Wireless Magnetoelastic Tissue Growth Sensing," *Transducers 2007*, June 2007, pp. 213-217.
- [3] C. Grimes, et al., "Magnetoelastic Microsensors for Environmental Monitoring," *IEEE Transducers 2001*, pp. 278-281.
- [4] M. Jain, et al., "A Wireless Micro-sensor for Simultaneous Measurement of pH, Temperature, and Pressure," *Smart Mat. and Struc.*, Vol. 10, 2001, pp. 347-353.
- [5] C. Grimes, et al., "Simultaneous measurement of liquid density and viscosity using remote query magnetoelastic sensors", *Rev. Sci. Inst.*, Vol. 7, Issue 10, 2000, pp. 3822-3824.
- [6] J.-J. Lin, et al., "Embrittlement of Amorphous Fe<sub>40</sub>Ni<sub>38</sub>Mo<sub>4</sub>B<sub>18</sub> Alloy by Electrolytic Hydrogen," *Met. and Mat. Trans. A*, Vol. 26, No. 1, 1995, pp. 197-201.
- [7] www.matweb.com
- [8] M.T. Richardson, et al., "Magnetoelastic Wireless Sensing of Tissue Growth for Self-Expanding Biliary Stents," *IEEE MEMS 2007*, pp. 469-472.
- [9] J. Benatar, "FEM Implementations of Magnetostrictive-Based Applications", MS thesis, University of Maryland, 2005.
- [10] L. Lagorce, et al., "Magnetic and Mechanical Properties of Micromachined Strontium Ferrite/Polyimide Composites," *JMEMS*, Vol. 6, No. 4, 1997, pp. 307-312.
- [11] H. Zhang et al., "Role of Bile Mucin in Bacterial Adherence to Biliary Stents," *J. Lab Clin Med*, 139(1), pp. 28-34, Jan 2002.
- [12] A.W. Cense, et al., "Mechanical Properties and Failure of *Streptococcus mutans* Biofilms, Studied Using a Microindentation Device," *J. Microbiological Methods*, Vol. 67, 2006, pp. 463-472.

# CHARACTERIZATION OF MAGNETIC NANOPARTICLE-EMBEDDED SU8 FOR MICROACTUATION

K.L. Tsai, M. Ziaei-Moayyed, N. Klejwa, R.N. Candler, W. Hu, S.X. Wang, and R.T. Howe  
Stanford University, USA

## ABSTRACT

SU8 polymer with embedded magnetic nickel nanoparticles (SU8-Ni) can be used as a structural material for microsystems and has the potential to be used for biomedical applications where remote actuation is needed. A composition of SU8-Ni (12.5% Ni nanoparticles and 87.5% SU8-2010 by weight) is investigated in this paper. Polysilicon torsional actuators were fabricated to measure the saturation magnetic moment of the material, and measurements were validated with alternating gradient magnetometry (AGM). Optical transmittance of the magnetic polymer was measured with a spectrophotometer and compared to standard SU8-2010.

## INTRODUCTION

SU8 is an epoxy based negative photoresist that has several advantages as a micromechanical system material, including biocompatibility [1], chemical resistance, thermal stability, low cost, and mechanical compliance for large deflections [2]. Using primarily SU8, Hill et al. [3] created a Fabry-Perot pressure sensor for blood pressure measurements. Chen et al. [4] used SU8 on silicon cantilevers to create underwater shear sensors. Magnetized SU8 could combine the advantages of SU8 for biomedical applications (specifically biocompatibility and chemical resistance) with the possibility of long-distance non-invasive magnetic actuation. Previous work [5] demonstrated the feasibility of magnetically deflecting cantilevers made from SU8-Ni but did not fully characterize the magnetic properties of the material. A full understanding of the material properties of nanoparticle embedded polymers is necessary if they are to be successfully used *in vivo*. In this work, the magnetic and optical properties (e.g., saturation magnetic moment and transmittance) for one nickel concentration of this material are measured, which is a critical starting point for understanding its capabilities for use in microsystems.

## MAGNETIC CHARACTERIZATION

A magnetic MEMS actuator previously developed for micromirror applications consisted of electroplated nickel on a polysilicon plate supported by a pair of torsional beams [6, 7]. Its torsional design allowed for large angular displacement under moderate magnetic forces.

A similar device design is used here as a platform for magnetic characterization of the SU8-Ni material (Figure 1). The large deflections give a large sensitivity to force, which enables finer resolution measurements of magnetic properties of the material on the device.

## Fabrication Process

The SU8-Ni was prepared by mixing SU8-2010 photoresist (MicroChem, MA, USA), 87.5% by weight, and nickel powder (100 nm diameter, Argonide, FL, USA), 12.5% by weight, with a rotisserie device for at least 12 hours to achieve a uniform suspension. Figure 2 shows the fabrication process for the torsional actuator used to characterize the magnetic properties of the SU8-Ni material.

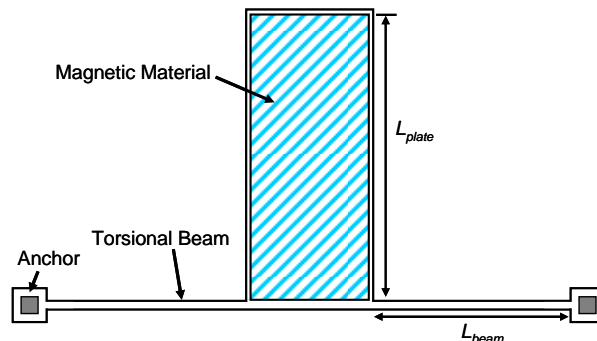


Figure 1. Top view of the torsional magnetic actuator used to characterize the SU8-Ni.  $L_{plate} = 430 \mu\text{m}$  and  $L_{beam} = 400 \mu\text{m}$  (figure not to scale).

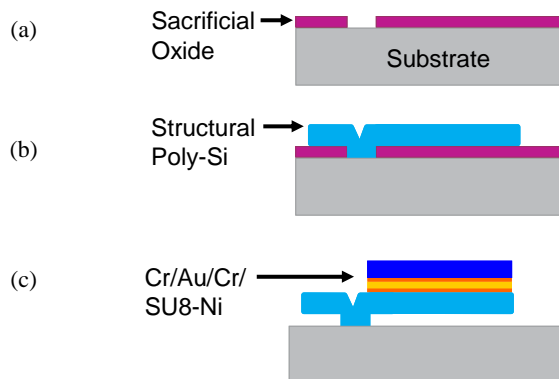


Figure 2. Fabrication process. (a) Deposit and pattern sacrificial oxide. (b) Deposit and pattern polysilicon structure layer. (c) Deposit and pattern Cr/Au/Cr/SU8-Ni. Release device with HF oxide etch and CPD.

A  $1 \mu\text{m}$  thick sacrificial oxide layer was first deposited on a  $\langle 100 \rangle$  silicon substrate at  $400^\circ\text{C}$  by low pressure chemical vapor deposition (LPCVD) and patterned via plasma etching. A  $1.4 \mu\text{m}$  thick structural polysilicon layer was then deposited by LPCVD and patterned via plasma etching. Next, a  $10 \text{ nm Cr}/100 \text{ nm Au}/10 \text{ nm Cr}$  metal stack was deposited via sputtering. This metal stack was necessary for proper adhesion of the SU8-Ni during device release. A  $15 \mu\text{m}$  thick layer of the SU8-Ni was then spin-coated and patterned according to standard processing procedures for SU8-2010. The spin speed used for the SU8-Ni was the same as that for standard SU8-2010 (e.g., 1625 rpm for  $15 \mu\text{m}$  thickness). Scanning electron micrograph (SEM) images were taken to measure the thickness of the SU8-Ni and confirmed that the SU8 viscosity was not affected by the addition of the nanoparticles. To prevent the SU8-Ni layer from cracking, extra care was taken to avoid sudden temperature changes during the baking steps. Finally, devices were released in 6:1 buffered HF and dried using critical point drying to prevent stiction (Figure 3).

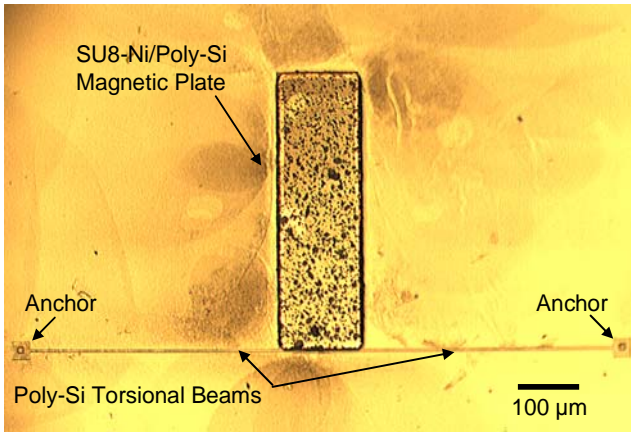


Figure 3. Optical micrograph of magnetic actuator composed of a SU8-Ni/Poly-Si plate (SU8-Ni:  $430\ \mu\text{m}$  (l)  $\times$   $130\ \mu\text{m}$  (w)  $\times$   $15\ \mu\text{m}$  (t)) suspended by a pair of poly-Si torsional beams ( $400\ \mu\text{m}$  (l)  $\times$   $3.2\ \mu\text{m}$  (w)  $\times$   $1.4\ \mu\text{m}$  (t)).

### Experimental Results

Devices were tested using a permanent magnet mounted onto a micropositioner for precision position control and a probe station for rough position control (Figure 4). The actuator chip was mounted vertically under the microscope for optical measurement of deflection. The magnet position was controlled by the micropositioner.

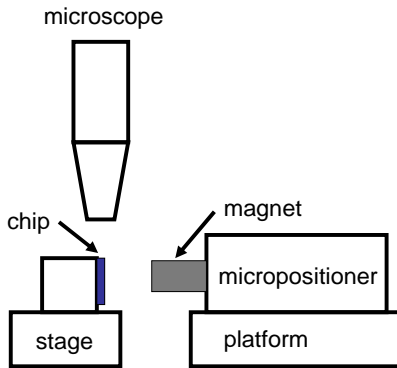


Figure 4. Schematic of probe station test setup for measuring actuator deflection vs. magnet distance (not to scale). The chip holder is non-magnetic.

A Hall probe was used to measure the magnetic field strength as a function of distance from the magnet surface (Figure 5).

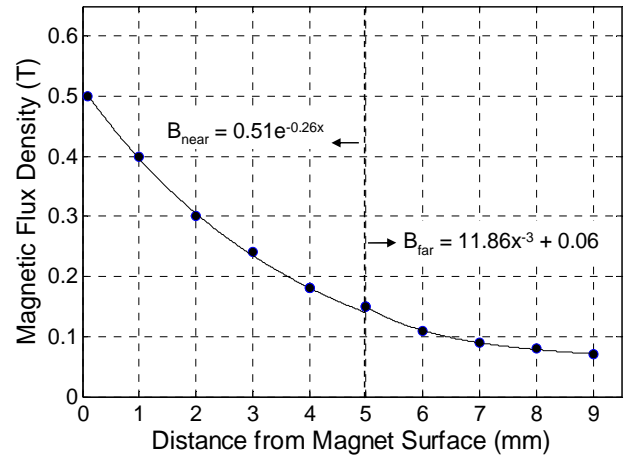


Figure 5. Calibration experiment results showing magnetic flux density ( $B$ ) as a function of distance from magnet surface ( $x$ ). Near field approximation (i.e.,  $x < 5\ \text{mm}$ ) shows exponential relationship between  $B$  and  $x$ , while far-field approximation (i.e.,  $x > 5\ \text{mm}$ ) shows  $1/x^3$  relationship between  $B$  and  $x$ .

A magnetic actuator composed of 12.5% Ni nanoparticles (100 nm diameter) and 87.5% SU8-2010 by weight was tested. Deflection of the actuator was observed when the magnet was brought into close proximity to the actuator (Figure 6).

Figure 7a shows the bending angle and vertical displacement as a function of magnet distance. The data obtained from the calibration experiment (Figure 5) was used to convert magnet distance to magnetic field strength (Figure 7b), assuming the magnetic actuator has a negligible effect on the magnetic field.

Quantitative measurements of the bending angle ( $\theta$ ) were used to determine the vertical displacement ( $d$ ) at the free end of the magnetic plate using the relation:

$$d = \sin(\theta)L_{plate} \quad (1)$$

where  $L_{plate}$  is the length of the magnetic plate ( $430\ \mu\text{m}$ ).

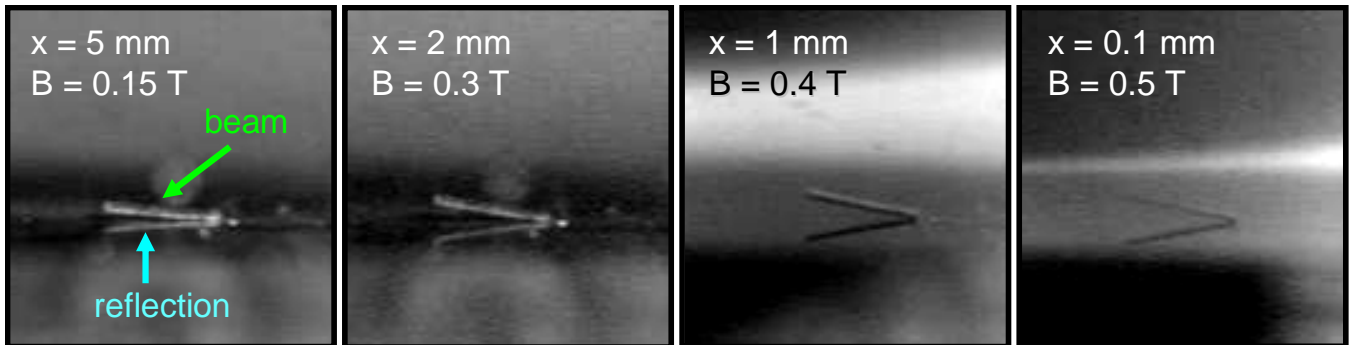


Figure 6. (Side view) Deflection of the magnetic actuator with decreasing magnet distance ( $x$ ) and increasing magnetic flux density ( $B$ ).

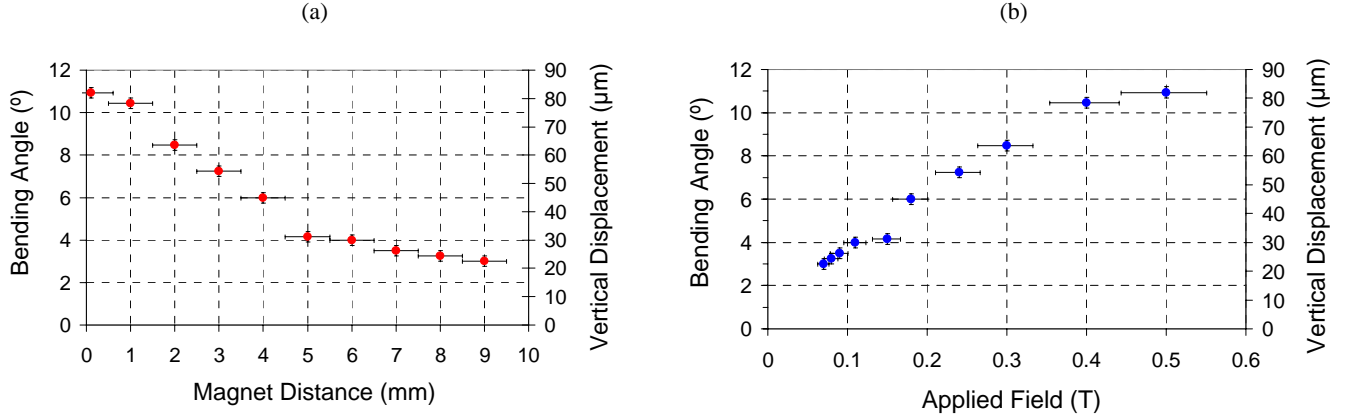


Figure 7. Bending angle and vertical deflection of magnetic actuator (a) as a function of magnet distance and (b) as a function of applied magnetic field.

The bending angle was also used to calculate the torque ( $T$ ) exerted on the magnetic plate using the general expression for torsional deformation of a rectangular beam (Figure 8):

$$T = \frac{2KG}{L_{beam}} \theta \quad (2)$$

where  $L_{beam}$  is the length of a single torsional beam (Figure 1) and  $G = E/[2(1+\nu)]$  is the shear modulus of elasticity. For polysilicon,  $E = 169$  GPa [8] and  $\nu = 0.22$ , and the shear modulus was found to be 69.3 GPa.  $K$  is the polar moment of inertia for a torsional bar with rectangular cross section [9, 10]. For a torsional bar with width and thickness of  $2a$  and  $2b$ , respectively, it is given by the equation:

$$K = ab^3 \left[ \frac{16}{3} - 3.36 \frac{b}{a} \left( 1 - \frac{b^4}{12a^4} \right) \right] \quad \text{for } a \geq b \quad (3)$$

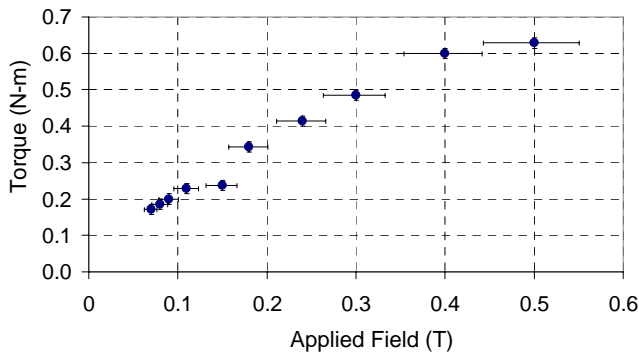


Figure 8. Torque vs. applied magnetic field.

A basic model was developed to calculate the magnetic moment of the SU8-Ni from the experimentally-derived torque on the magnetic plate. Because the magnetic nanoparticles are suspended uniformly throughout the plate, the torque can be approximated as a function of the average magnetic moment ( $m_{avg}$ ), assumed to be at the center of the plate, and the field gradient at the center of the plate:

$$T = F_{mag} \frac{L_{plate}}{2} = \nabla(m_{avg} \cdot B) \frac{L_{plate}}{2} \quad (4)$$

where  $m$  = magnetic moment and  $B$  = magnetic flux density.

In saturation, the magnetization is constant, so  $\nabla m_{avg} = 0$ . Therefore, (4) can be simplified as:

$$T = (m_{s,avg} \cdot \nabla B) \frac{L_{plate}}{2} \quad (5)$$

and

$$m_{s,avg} = \frac{2T}{(\nabla B)L_{plate}} \quad (6)$$

where  $m_{s,avg}$  is the average magnetic moment in saturation and  $\nabla B$  is the field gradient at the center of the plate. Alternating gradient magnetometry (AGM) measurements (Figure 9) suggest the SU8-Ni is in saturation for  $B > 0.2$  T, so this was the range of data used to calculate  $m_{s,avg}$ . Substituting  $\nabla B$  from the calibration experiment (Figure 5) and  $T$  from the deflection experiment (Equation 2) into (6), the average saturation magnetic moment, of the SU8-Ni was found to be 6.4 nA-m<sup>2</sup>.

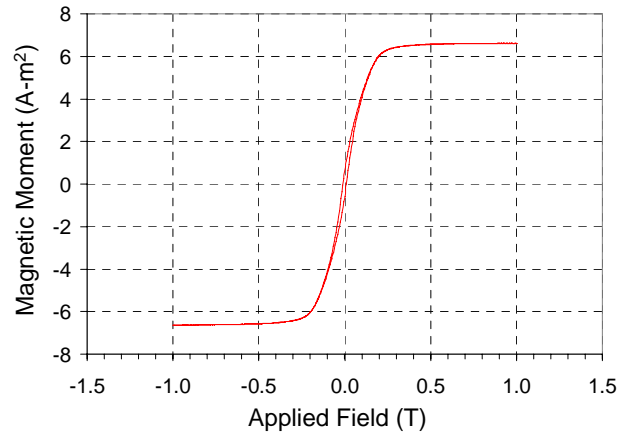


Figure 9. Alternating gradient magnetometry (AGM) results showing magnetic moment vs. applied magnetic field. Measurement shows narrow hysteresis and small coercivity.

The AGM measurements confirmed the validity of the experimentally-derived value for  $m_{s,avg}$  and provided further insight into the magnetic properties of SU8-Ni (Figure 9). Specifically, its small coercivity and narrow hysteresis verified that the ferromagnetic property of the Ni nanoparticles was not affected by the SU8. The measurements and their interpretation using the first-order analytical model were consistent with the saturation magnetic moments expected from this class of nanoparticles combined with their density in SU8 (Table 1).

Table 1. Comparison of expected and measured  $m_s$  values.

Saturation Magnetic Moment ( $m_s$ )	Value
Expected (based on 12.5% wt Ni concentration)	6.8 nA-m <sup>2</sup> (SI) μemu (CGS)
Measured (based on AGM results (Fig 9))	6.6 nA-m <sup>2</sup> (SI) μemu (CGS)
Measured (based on deflection experiment (Eq 6))	6.4 nA-m <sup>2</sup> (SI) μemu (CGS)

## OPTICAL CHARACTERIZATION

A 4" quartz substrate was spin-coated with a 15 μm thick layer of SU8-Ni (87.5% SU8-2010 and 12.5% Ni by weight) for characterizing the optical properties of the magnetic polymer. The SU8-Ni film was imaged and cured following standard processing guidelines for SU8-2010 (e.g. pre-baking, exposing, post-exposure baking, developing, and hard-baking). The transmittance spectrum of the SU8-Ni film was then measured using a spectrophotometer (Figure 10).

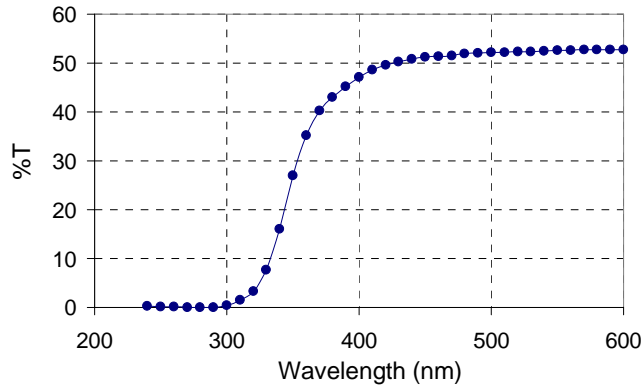


Figure 10. Transmittance of SU8-Ni (12.5% Ni by weight).

Compared to standard SU8-2010, the SU8-Ni composite showed lower transmittance in the 350-600 nm range (53% vs. 91%), but the transition between absorption and transmission (i.e. at 350 nm) was almost unaffected. This was to be expected since the diameter of the nanoparticles (100 nm) is well below the wavelength of the transmitted light. Assuming the SU8-Ni behaves as a dispersive medium, the transmittance can be formulated according to the Beer-Lambert law:

$$T = e^{-(\alpha_{SU8} + \alpha_{Ni})x} \quad (7)$$

where  $\alpha_{SU8}$  is the attenuation coefficient of the SU8,  $\alpha_{Ni}$  is the attenuation coefficient of the Ni particles, and  $x$  = path length (i.e., film thickness). Using the transmittance data at a particular wavelength, the attenuation coefficients for pure SU8-2010 and the SU8-Ni (12.5% Ni by weight) were determined. For  $\lambda = 500$  nm,

$T_{SU8} = 0.91$  and  $T_{SU8-Ni} = 0.53$ . Therefore,  $\alpha_{SU8} = 62.87 \text{ cm}^{-1}$  and  $\alpha_{SU8-Ni} = 423.25 \text{ cm}^{-1}$ . This measurement is important for determining the maximum concentration of Ni allowable in a sample with a minimum required transmittance.

## CONCLUSION

Magnetic SU8 holds promise as an enabling material for novel sensors and actuators. The saturation magnetic moment of a SU8-Ni composite was measured with a torsional actuator platform and was within 6% of the expected value. The optical transmittance of the material was also measured. Future work includes analyzing different concentrations of Ni nanoparticles as well as investigating other magnetic and polymer materials, which will allow the engineering of novel composite or polymer-only microactuators with optimized magnetic and optical properties.

## ACKNOWLEDGEMENTS

Fabrication work was performed at the Stanford Nanofabrication Facility (a member of the National Nanotechnology Infrastructure Network) supported by the NSF under Grant ECS-9731293, its lab members, and the industrial members of the Stanford Center for Integrated Systems. This work was supported by an NSF Graduate Research Fellowship. The authors would like to thank J Provine for helpful discussions.

## REFERENCES

- [1] N. Chronis and L. P. Lee, "Electrothermally Activated SU-8 Microgripper for Single Cell Manipulation in Solution", *Journal of Microelectromechanical Systems*, 14, 4 (2005).
- [2] H. Lorenz, M. Despont, N. Fahmi, N. LaBianca, P. Renaud, and P. Vettiger, "SU-8: A Low-cost Negative Resist for MEMS", *Journal of Micromechanics and Microengineering*, 7 (1997).
- [3] G.C. Hill, R. Melamud, F.E. Declercq, A.A. Davenport, I.H. Chan, P.G. Hartwell, and B.L. Pruitt, "SU-8 MEMS Fabry-Perot Pressure Sensor", *Sensors and Actuators A: Physical*, 138, 1 (2007).
- [4] N. Chen, J. Chen, J. Engel, S. Pandya, C. Tucker and C. Liu, "Development and Characterization of High Sensitivity Bioinspired Artificial Haircell Sensor", *The 12<sup>th</sup> Solid State Sensors, Actuator, and Microsystems Workshop (Hilton Head 2006)*, Hilton Head Island, SC, 6/4-8/06.
- [5] N. Damean, B. A. Parviz, J. N. Lee, T. Odom, and G. M. Whitesides, "Composite Ferromagnetic Photoresist for the Fabrication of Microelectromechanical Systems", *Journal of Micromechanics and Microengineering*, 15 (2005).
- [6] J. W. Judy and R. S. Muller, "Magnetic Microactuation of Torsional Polysilicon Structures", *8<sup>th</sup> International Conference on Solid-State Sensors and Actuators Digest of Technical Papers (Transducers 1995)*, Stockholm, Sweden, 6/25-29/95, vol. 1, pp. 332-335.
- [7] J. W. Judy and R. S. Muller, "Magnetically Actuated, Addressable Microstructures", *Journal of Microelectromechanical Systems*, 6, 3 (1997).
- [8] W. C. Young and R. G. Budynas, *Roark's Formulas for Stress and Strain, 7<sup>th</sup> Edition*, McGraw-Hill (2002).
- [9] C. Liu, *Foundations of MEMS*, Upper Saddle River, NJ, Pearson/Prentice Hall (2006).
- [10] W. N. Sharpe, Jr., B. Yuan, R. Vaidyanathan, and R. L. Edwards, "Measurements of Young's Modulus, Poisson's Ratio, and Tensile Strength of Polysilicon", *10<sup>th</sup> Annual International Workshop on Micro Electro Mechanical Systems*, Nagoya, Japan, 1/26-30/97, pp. 424-429.

# DESIGN OF ELECTROSTATICALLY ACTUATED MEMS UNDER UNCERTAINTIES

Nitin Agarwal and N. R. Aluru

University of Illinois at Urbana-Champaign, Urbana, Illinois, USA

## ABSTRACT

This work presents a stochastic framework based on stochastic collocation approach to quantify the effect of uncertain parameters on the performance of electrostatic MEMS devices. We consider an example of a MEMS switch to demonstrate that the proposed methodology can be used to design effective and reliable MEMS devices. The approach is straightforward to implement and can be orders of magnitude faster than the Monte Carlo method.

## INTRODUCTION

State-of-the-art design methodologies for MEMS are based on deterministic approaches [1-2] where the geometrical and physical properties of the device are assumed to be known precisely. However, low cost manufacturing processes often result in significant uncertainties in MEMS. For example, in the case of the transverse comb drive shown in Figure 1, depending on the manufacturing process used, there is always some uncertainty associated with the geometrical features such as the thickness of the movable fingers or fixed teeth, overlap length between the two set of teeth or material properties such as the Young's modulus etc. The inability to account for these uncertainties during computational design can significantly affect the reliability of MEMS. To this end, we seek to develop a stochastic framework with a twofold objective -- firstly, to quantify the effect of variation in various input parameters on the output parameters such as deflection, pull-in behavior etc., relevant to the design of electrostatic MEMS devices. Secondly, to employ this uncertainty quantification data to identify the parameters which are critical to the device performance.

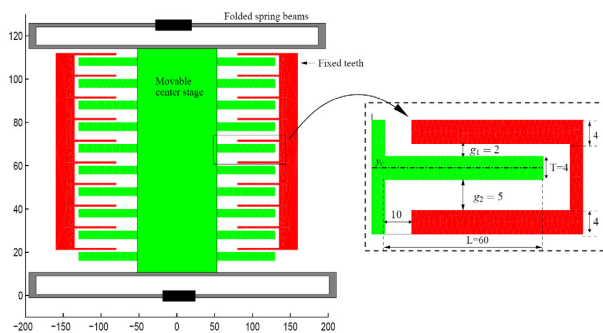


Figure 1: Transverse comb drive.

Typically in MEMS, uncertainties are taken into account through safety factors, which may lead to over conservative designs. Uncertain parameters can also be handled by using sampling based methods such as Monte Carlo (MC) method. For example, the effect of uncertainty in various geometrical parameters on the design of a comb drive has been considered in [3]. The variability in the performance of a ceramic actuator resulting from the variation in the shape of the actuator and the air gap in the condenser has been studied in [4]. Although MC based methods are straightforward to apply and generate the required statistics easily, they can be prohibitively expensive, as their accuracy depends on the sample size. In [5] we presented a framework for stochastic modeling of MEMS based on a spectral discretization technique – *generalized polynomial chaos (GPC)*,

which provides fast convergence. However, the GPC based approach leads to a set of coupled deterministic equations that need to be solved, and hence the implementation may be non-trivial (see [5] for details).

In this work, we propose an efficient framework based on the stochastic collocation approach [6-8] to handle uncertain parameters during the design of electrostatic MEMS. The novel features of this approach are – firstly, since it involves sampling at a pre-determined set of points, it is straightforward to implement. Secondly, for the number of uncertain parameters one usually needs to consider for the analysis of MEMS devices, this approach is orders of magnitude faster than the Monte Carlo method to obtain the same level of accuracy. The proposed methodology has been applied to design a MEMS switch under uncertainties.

The paper is organized as follows: first, we present the deterministic formulation for the coupled electromechanical problem. The stochastic formulation and the solution methodology are detailed in next section. In following section we then present a numerical example, and finally conclude the discussion.

## DETERMINISTIC FORMULATION

Figure 2 shows a typical MEM device – a deformable cantilever beam over a fixed ground plane. When a potential difference is applied between the beam and the ground plane, it induces electrostatic pressure acting normal to the surface of the beam, which causes it to deflect.

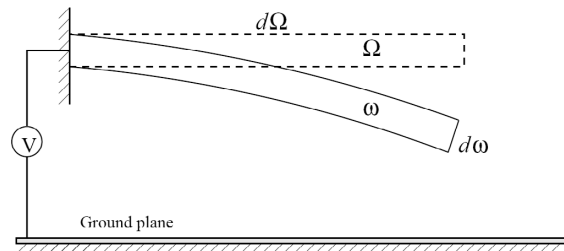


Figure 2: MEM beam under deformation.

Physical level analysis of such a device requires a self-consistent solution of the coupled mechanical and electrostatic equations. A framework for the deterministic analysis is presented in [1]. In the absence of any free charges, the electrostatic potential can be obtained by solving the Laplace equation, given as,

$$\nabla^2 \phi = 0 \text{ in } \varpi, \quad (1)$$

where  $\phi$  is the potential field in the dielectric medium  $\varpi$ , surrounding the conductors. A boundary integral formulation (see [1] for details) of Eq. (1) is used to compute the surface charge density  $\sigma$  on the conductors. The electrostatic pressure  $P_e$  acting on the microstructures can be computed from  $\sigma$  as  $P_e = \sigma^2 / 2\epsilon$ , where  $\epsilon$  is the dielectric constant of the medium.

The mechanical deformation of the microstructure due to the electrostatic pressure is obtained by performing 2-D large deformation elastic analysis. The governing equation for the deformation  $\mathbf{u}$ , in the absence of any body force, is given as,

$$\nabla \cdot (\mathbf{FS}) = 0 \text{ in } \Omega, \quad (2)$$

where  $\Omega$  represents the undeformed configuration of the microstructure,  $\mathbf{F} = \mathbf{I} + \nabla \mathbf{u}$  is the deformation gradient and  $\mathbf{S}$  is the second Piola-Kirchhoff stress tensor. Appropriate displacement and surface traction boundary conditions (from electrostatic analysis) are applied. Eqs. (1) and (2) are solved in a self-consistent manner using relaxation or Newton scheme, as described in [1]. We can represent the coupled electromechanical system as,

$$L(\mathbf{u}, \sigma; \mathbf{x}) = 0 \quad \mathbf{x} \in \Omega. \quad (3)$$

Such a system can be solved easily using Finite Element method (FEM) and Boundary Element method (BEM). In the next Section, we present the stochastic formulation which employs repetitive usage of such a deterministic solver, in order to generate the desired statistics of various output parameters, relevant to the design of electrostatic MEMS.

### STOCHASTIC FORMULATION

The stochastic formulation employs stochastic quantities to model uncertainties – uncertain random parameters are modeled as random variables and uncertain spatial functions are represented as random fields. The basic idea is to treat uncertainty as a separate dimension in addition to space and time (for dynamical problems). The random probability space is characterized using  $n$  independent random variables  $\xi = [\xi_i]_{i=1}^n$ , using which all uncertain parameters are represented as  $(n+d)$ -dimensional functions, where  $d$  refers to the dimension of the physical space. The stochastic formulation for the coupled electromechanical system can be written as: we seek uncertain displacement  $\mathbf{u}(\mathbf{x}, \xi)$  and surface charge density  $\sigma(\mathbf{x}, \xi)$ , such that

$$L(\mathbf{u}, \sigma; \mathbf{x}, \xi) = 0 \quad (\mathbf{x}, \xi) \in \Omega \times \Gamma, \quad (4)$$

where  $\Gamma$  represents the random domain.

### Monte Carlo method

Monte Carlo simulation has been traditionally used for systems with random input parameters. It involves generating various realizations of the input parameters according to the underlying probability distribution, and repeatedly employing the deterministic solver for each realization. Eq. (4) can be easily solved using MC method as follows:

1. For the given number of samples  $K$ , generate independent and identically distributed (iid) random variables  $\{\xi^j\} = [\xi_i^j]_{i=1}^n, j = 1, \dots, K$ , according to the underlying distribution.
2. For each of the realizations, solve the deterministic problem  $L(\mathbf{u}^j, \sigma^j; \mathbf{x}, \xi^j) = 0$ , and obtain the solution  $(\mathbf{u}^j, \sigma^j)$ , for  $j = 1, \dots, K$ .
3. Compute the required statistics such as mean  $\mu$  and variance  $\nu$ , for e.g.,

$$\mu(\mathbf{u}) = \frac{1}{K} \sum_{j=1}^K \mathbf{u}^j, \quad \nu(\mathbf{u}) = \frac{1}{K} \sum_{j=1}^K (\mathbf{u}^j - \mu(\mathbf{u}))^2. \quad (5)$$

The amount of work required for a MC simulation to converge to

achieve the required accuracy  $\tau$  is given as  $\tau(K) = O(1/\sqrt{K})$ , which represents very slow convergence.

### Stochastic collocation method

The basic idea of the stochastic collocation approach is to approximate the stochastic dependent variables by a polynomial interpolation function in the multi-dimensional random space. The interpolation is constructed by sampling the dependent variables at a pre-determined set of points  $\Theta_K = \{\xi^j\}_{j=1}^K$ . The set of points  $\Theta_K$  are chosen as the sparse grid points generated using the Smolyak algorithm (see [6] for details), unlike the MC approach where the sampling points are chosen in a statistical manner.

Using the polynomial approximation, the interpolated displacement and surface charge density can be written as:

$$\hat{\mathbf{u}} = \sum_{j=1}^K \mathbf{u}(\mathbf{x}, \xi^j) \psi_j(\xi), \quad \hat{\sigma} = \sum_{j=1}^K \sigma(\mathbf{x}, \xi^j) \psi_j(\xi), \quad (6)$$

where  $\{\psi_j\}$  are the Lagrange interpolation functions such that  $\psi_j(\xi^i) = \delta_{ij}$ . Using the interpolated form in the stochastic system given by Eq. (4), we obtain  $K$  decoupled deterministic systems (see [7-8] for details),

$$L(\mathbf{u}(\mathbf{x}, \xi^j), \sigma(\mathbf{x}, \xi^j); \mathbf{x}, \xi) = 0, \quad j = 1, \dots, K. \quad (7)$$

The statistics of the random solution, such as mean, can be computed as:

$$\mu(\mathbf{u}) = \sum_{j=1}^K \mathbf{u}(\mathbf{x}, \xi^j) w_j, \quad w_j = \int_{\Gamma} \psi_j(\xi) \rho(\xi) d\xi, \quad (8)$$

where  $\rho(\xi)$  represents the joint probability density function of the random variables  $\xi$ , and  $\{w_j\}$  are the weights that can be pre-computed and stored. The complexity of the sparse grid collocation approach is given as,

$$\tau(K) = O(K^{-r} (\log K)^{(r+1)(d-1)}), \quad (9)$$

for solutions with bounded mixed derivatives up to order  $r$ . Thus, for sufficiently smooth functions, this approach would be orders of magnitude faster than the MC method. In addition to the faster convergence rate, the fact that the procedure only requires solving the deterministic problem at a set of sample points makes the implementation straightforward. The solution methodology has been detailed in Figure 3.

### NUMERICAL EXAMPLE

We consider a MEMS switch, modeled by a silicon cantilever beam, which is  $80 \mu\text{m}$  long,  $1 \mu\text{m}$  thick and  $10 \mu\text{m}$  wide, located over a ground plane. As the applied potential difference  $V$  between the beam and the ground plane is increased, the beam increasingly deflects towards the ground plane. At a voltage  $V_p$  (known as the pull-in voltage), when the electrostatic force can no longer be balanced by the restoring elastic force, the beam finally collapses onto the ground plane, which signifies the *ON* state of the switch. In order to design reliable switches, it is required that we consider the variations in material properties and geometrical parameters, and quantify their effect on device performance parameters such as deflection and pull-in voltage etc.

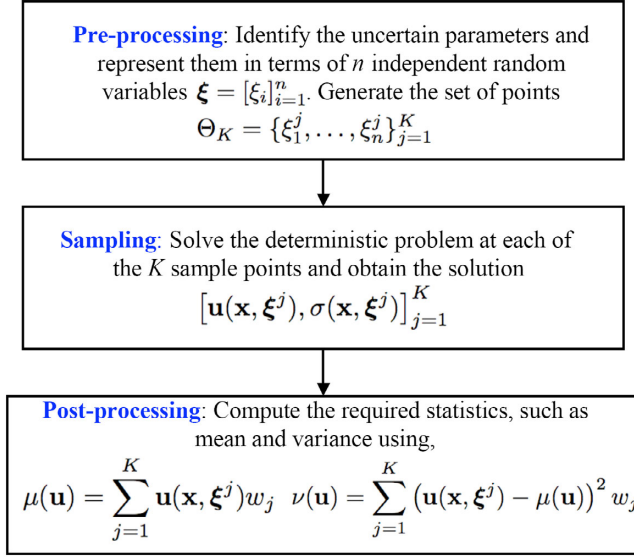


Figure 3: Solution methodology for stochastic collocation method.

Specifically, we consider the effect of uncertain Young's modulus  $E$  and the initial gap  $g$  between the beam and the ground plane, which are given as:

$$E = E_0(1 + \nu_E \xi_1); \quad g = g_0(1 + \nu_g \xi_2), \quad (10)$$

where  $E_0 = 169$  GPa and  $g_0 = 1 \mu\text{m}$  are the mean values,  $\nu_E = \nu_g = 0.1$ , which represents a 10% variation in both parameters, and  $\xi_{1,2}$  are independent uniformly distributed random variables on  $[-1, 1]$ .

#### Pull-in behavior

The pull-in voltage  $V_p$  and the vertical tip deflection at  $V = V_p^-$  (deflection just before pull-in), computed by solving the deterministic coupled problem, for various values of  $E$  and  $g$  are tabulated in Table 1. As can be seen, for the given variation in the parameters, the pull-in voltage varies between 7.3 V and 11.4 V.

Table 1: Pull-in voltage and tip deflection for the cantilever beam.

Sample	$E / E_0$	$g / g_0$	$V_p$ (V)	Vertical tip displacement ( $\mu\text{m}$ )
S0	1.0	1.0	9.2	-0.3431
S1	0.9	0.9	7.3	-0.3007
S2	1.1	1.1	11.4	-0.4217

In Figure 4 we plot the mean vertical tip displacement with various applied potential difference, as obtained from the stochastic collocation approach. We also plot the pull-in curves obtained by solving the deterministic problem for two samples given by S1 and S2. We note that for the applied potential difference higher than the pull-in voltage, the tip displacement is equal to initial gap  $g$ . Clearly, the realizations S1 and S2 mark the two boundaries for the pull-in curve and are indicative of the worst case behavior of the switch. Thus for all possible values ( $E, g$ ), the vertical tip deflection of the beam would be between the values indicated by these two curves. In Figure 5 we plot the mean and

the error bars, based on standard deviation, for the vertical tip displacement. One could use the information regarding the worst-case behavior to design reliable switches, but such designs may be over conservative. However, the information obtained in terms of the error bars quantifies the variability of the performance of the switch, and may be used to design reliable and efficient switches.

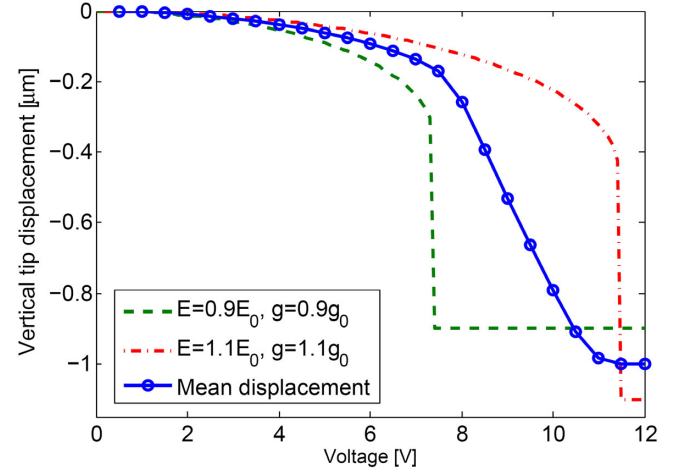


Figure 4: Worst case and mean pull-in behavior for the MEMS switch.

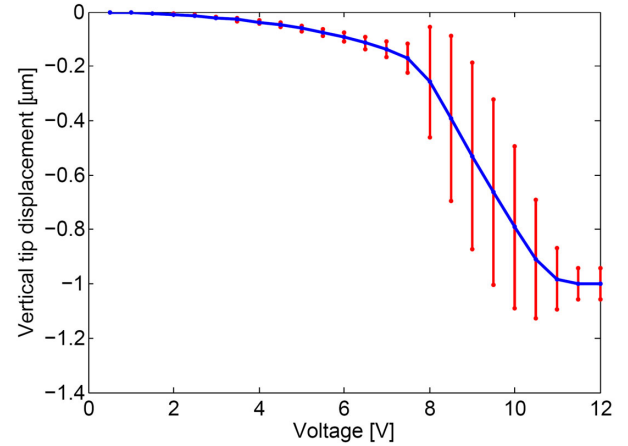


Figure 5: Mean vertical tip displacement with error bars (based on standard deviation).

#### Design under uncertainties

In addition to quantifying the effect of uncertain parameters on the device performance, the methodology based on GPC (described in [5]) and the stochastic collocation approach can also be used to identify critical design parameters, which one may need to control carefully, in order to improve reliability. In Figure 6 we plot the mean sensitivity of the tip deflection to the variations in

Young's modulus  $s_E = \frac{1}{\nu_E} \frac{\partial v_{tip}}{\partial \xi_1}$  and gap  $s_g = \frac{1}{\nu_g} \frac{\partial v_{tip}}{\partial \xi_2}$  obtained

using GPC approach, and conclude that the variations in gap are more critical to the performance of the switch as compared to the Young's modulus.

In Figure 7 we plot the probability of pull-in with various applied voltages obtained using the stochastic collocation approach. As the applied voltage increases from 7.3 V to 11.4 V,

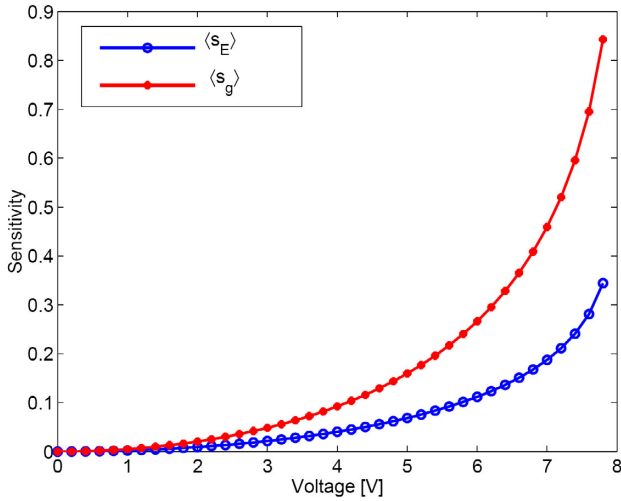


Figure 6: Sensitivity of tip deflection to the variations in Young's modulus and gap (using GPC based approach [5]).

the probability increases from 0 to 1. From a design viewpoint, we observe that the probability of pull-in for  $V = 9.2$  V is 0.47. Using this, one can argue that if the switch was designed for the mean values of the parameters (given by the realization  $S_0$ ), the probability that the switch may fail to operate is 53%. It can also be said that if the operating voltage of the switch is specified as  $V = 10.5$  V, the probability that the switch will operate successfully is 88%, which may be acceptable. In the absence of such information, one may have no choice but to operate the switch at  $V = 11.4$  V, which will lead to higher power consumption. Such observations can be effectively used to design reliable and efficient MEMS devices, which would give desired performance and improve reliability.

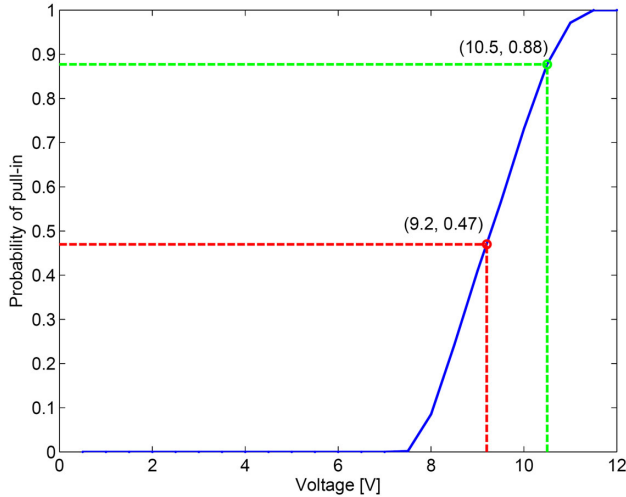


Figure 7: Probability of pull-in with various applied voltage.

In Figure 8 we plot the probability density functions (PDF) of the vertical tip displacement for various applied voltages. As expected, for voltages between 7.3 V and 11.4 V, we observe two peaks in the PDF, which indicates a non-zero probability of pull-in.

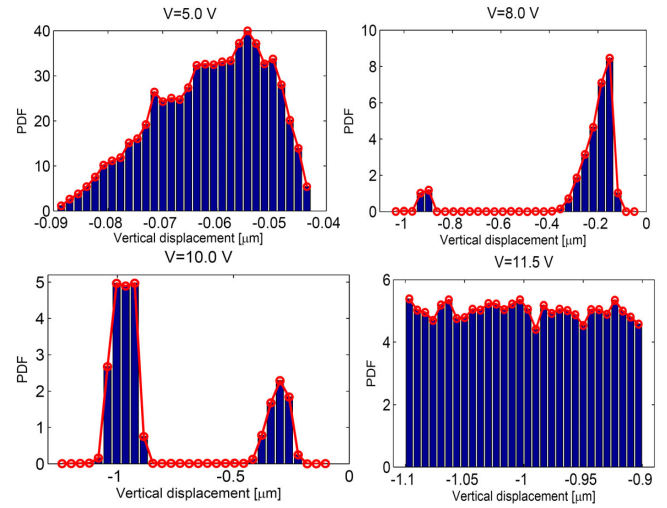


Figure 8: Probability density function (PDF) of vertical tip displacement for various applied voltage.

## CONCLUSION

We presented a stochastic framework to quantify the effect of uncertain parameters on the performance of MEMS devices. The approach can also be used to identify those design parameters which are critical to the performance of the device. We demonstrated by considering the example of a MEMS switch that this framework can be used to design effective and reliable devices, which would give desired performance and improve reliability.

## REFERENCES

- [1] S. K. De and N. R. Aluru, "Full-Lagrangian schemes for dynamic analysis of electrostatic MEMS", *Journal of Microelectromechanical Systems*, 13(5), 737 (2004).
- [2] S. K. De and N. R. Aluru, "Coupling of hierarchical fluid models with electrostatic and mechanical models for the dynamic analysis of MEMS", *Journal of Micromechanics and Microengineering*, 16(8), 1705 (2006).
- [3] S. Reh, P. Lethbridge, and D. F. Ostergaard, "Quality based design and design for reliability of Micro Electro Mechanical Systems (MEMS) using probabilistic methods", *International Conference on Modeling and Simulation of Microsystems*, San Diego, CA (2000).
- [4] M. Allen, M. Rauli, K. Maute, and D. Frangopol, "Reliability based analysis and design optimization of electrostatically actuated MEMS", *Computers & Structures*, 82, 1007 (2004).
- [5] N. Agarwal and N. R. Aluru, "Stochastic modeling of coupled electromechanical interaction for uncertainty in electrostatically actuated MEMS", *Comput. Methods Appl. Mech. Engrg.*, doi:10.1016/j.cma.2008.01.005 (2008).
- [6] A. Klimke and B. Wohlmuth, "Algorithm 847: *spinterp*: piecewise multi-linear hierarchical sparse grid interpolation in MATLAB", *ACM Trans. Math. Software*, 31, 561 (2005).
- [7] D. Xiu and J. S. Hesthaven, "High-order collocation methods for differential equations with random inputs", *SIAM Journal of Scientific Computing*, 27(3), 1118 (2005).
- [8] B. Ganapathysubramanian and N. Zabaras, "Sparse grid collocation schemes for stochastic natural convection problems", *J. Comput. Phys.* 225, 652 (2007).

# DYNAMIC FRICTION AND MICROTURBINE PERFORMANCE USING A PLANAR-CONTACT ENCAPSULATED MICROBALL BEARING

M. McCarthy<sup>1</sup>, C. M. Waits<sup>2,1</sup>, and R. Ghodssi<sup>1</sup>

<sup>1</sup>University of Maryland, College Park, Maryland, USA

<sup>2</sup>U.S. Army Research Laboratory, Adelphi, Maryland, USA

## ABSTRACT

Successful demonstration and characterization of a radial inflow microturbine supported on a planar-contact encapsulated microball bearing is presented. Reliable operation of the air-driven silicon microturbine is shown for nearly 1,000,000 revolutions at speeds, pressure drops, and flow rates of up to 10,000rpm, 0.45psi, and 3.5slm, respectively. Incorporation of a gas thrust plenum enables comprehensive spin-down friction characterization of the encapsulated microball bearing. An empirical power-law model for dynamic friction has been developed for speeds and loads of 250-5,000rpm and 10-50mN, respectively, corresponding to torques of 0.0625-2.5 $\mu$ Nm and friction coefficients of 0.0005-0.025.

## INTRODUCTION

Microball bearings provide a simple, stable, and robust support mechanism for PowerMEMS devices. With inherent tribological and systems-level benefits, microball bearings represent a compromise between the more extensively studied gas-lubricated and contact bearings. While gas-lubricated systems have superior speed and friction characteristics [1-2], microball bearing support mechanisms are notably simpler to fabricate and operate. Similarly, microball bearings provide increased tribological performance over sliding contact bearings, where friction and wear substantially impact the operation and life of such devices [3]. Accordingly, our group has demonstrated several microball bearing supported devices exploiting these benefits [4-9]. While microball bearings have been shown to be a reliable and robust support mechanism, the modeling and reduction of friction and wear is necessary for high performance applications.

In our linear and rotary ball bearing-supported variable-capacitance micromotors [4-5], a silicon slider (or rotor) sits on top of steel microballs ( $\text{\O} = 285\mu\text{m}$ ) housed in rectangular trenches and is actuated via in-plane electrostatic forces. These electric motors are synchronous machines where the maximum operating speed and force/torque is directly dictated by the bearing friction. Friction increases with speed until the motors cannot generate enough force/torque to maintain synchronization with the moving element, corresponding to maximum linear and rotary speeds of 7mm/s and 500rpm, respectively. Similarly, high-speed microturbines supported on encapsulated microball bearing structures have been demonstrated for speeds up to 37,000rpm [7-9]. These devices, however, suffer from excessive wear, leading to particle contamination and geometric deviations. Accordingly, the reduction of friction and wear is critical to the realization of high-speed micromachines like MEMS turbogenerators and electric pumps. The devices and apparatus in this work provide a platform to investigate and mitigate friction and wear in microball bearings.

Characterizing friction in our previous devices was significantly limited by the coupled nature of actuation and normal forces. In the previously published micro-motors and turbines [4-7], the normal forces were solely dependent on the actuation forces. Using a thrust plenum, these forces have been decoupled in this work allowing for comprehensive spin-down friction testing under a variety of operating conditions relevant to next-generation microball bearing supported PowerMEMS devices.

## DEVICE

To investigate the dependence of speed and normal load on dynamic friction in a MEMS encapsulated ball bearing, microturbines packaged together with a bottom-side thrust plenum have been developed. Figure 1 shows the geometries of the various microturbine components. To minimize friction and wear, the encapsulated microball bearing fabrication process developed by Waits *et al.* [7-8] was modified to provide planar (Fig. 1a), rather than point, contact between the silicon race and steel microballs. Figure 1b & 1c show the radial-inflow microturbine geometry, designed using an incompressible laminar flow velocity triangle method, and a cross-section of the fabricated device. The topside of the device consists of a radial array of inlet orifices and a central outlet where the rotor speed bump structures can be seen (Fig. 1d). Figure 1e shows the underside of the encased rotor which acts as a thrust surface. By pressurizing the backside of the device the rotor is lifted into proper contact with the microballs and spun using pressurized nitrogen passing through the radial-inflow microturbine, as seen in Fig. 2.

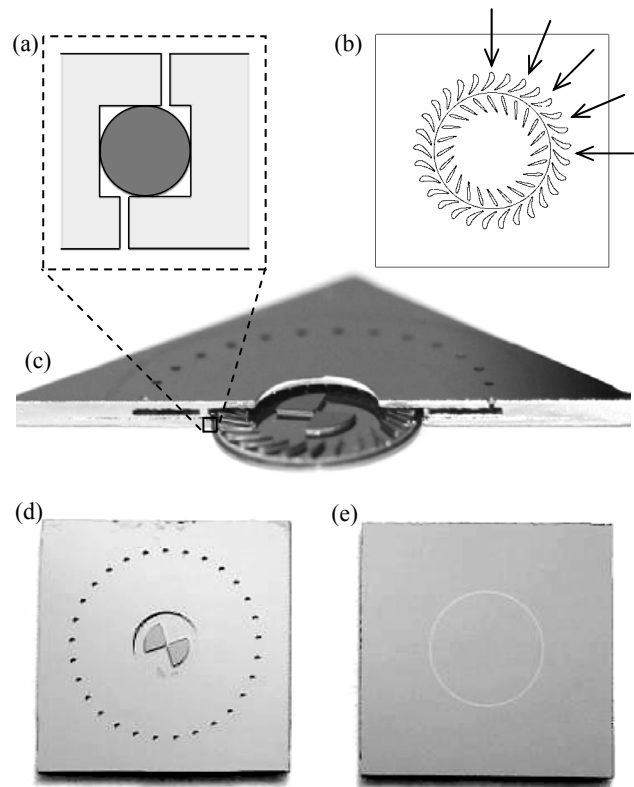


Figure 1: Microturbine device showing (a) the microball bearing geometry ( $\text{\O} = 285\mu\text{m}$ ), (b) the blade design and flow direction, and optical photos of (c) the device cross-section with 10mm rotor, (d) top side with ports and speed bumps, and (e) the bottom side thrust surface. The total device dimensions are 23mm x 23mm x 1.5mm.

## FABRICATION AND TESTING

The microturbine fabrication process consists of wafer-level construction of encapsulated rotors followed by die-level temporary bonding of a capping layer to create internal flow paths. The microball housing is defined with a nested deep reactive ion etch (DRIE) in a pair of silicon wafers and approximately ninety stainless steel microballs are encased between the wafers using a gold/tin eutectic bond. The wafer stack is diced and individual die are deep-etched using patterned SiO<sub>2</sub> masks to define turbine structures and release the rotors, this is followed by photoresist bonding of a capping layer containing fluid inlet and outlet ports.

Complete characterization of dynamic friction in the planar-contact encapsulated microball bearing requires independent control of rotor speed and normal load. These parameters are decoupled through the use of a hydrostatic thrust plenum defined by a novel packaging assembly. Figure 2 shows schematics of the device cross-section and operation while Figure 3 is an optical photo of a packaged device being tested. Complete details of the device fabrication and testing apparatus have been reported previously at *PowerMEMS '07* [9].

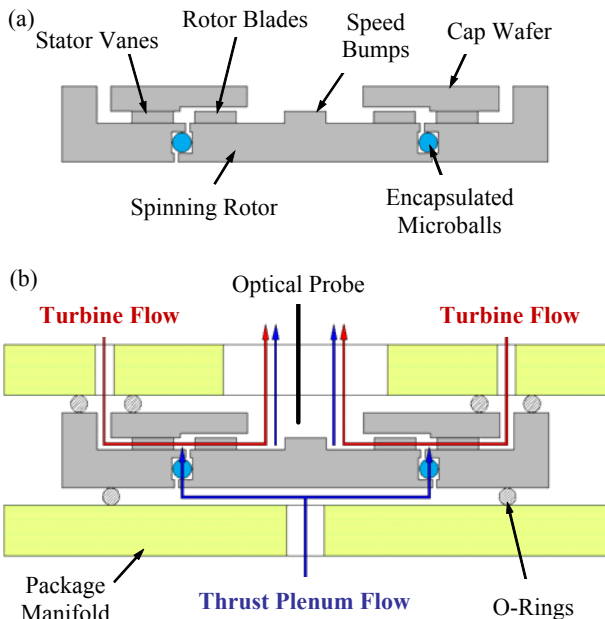


Figure 2: Schematic showing (a) the microturbine cross-section and (b) the experimental operation of the device indicating flow paths for the turbine and thrust plenum.

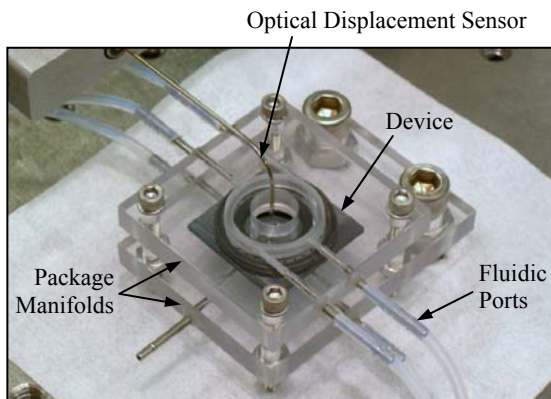


Figure 3: Photo of a packaged microturbine being tested.

## RESULTS AND DISCUSSION

### Microturbine Characterization

Using the packaging scheme shown in Figs. 2-3, the microturbine has been characterized up to 10,000rpm. As turbine flow passes over the rotor periphery (Fig. 2b), the underside is pressurized resulting in a net upward normal force without the addition of thrust plenum flow. While this novel packaging approach decouples normal and rotational forces during spin-down testing, the two are very much coupled during turbine actuation. Rotational speed, normal force, and flow rate are plotted in Figure 4 as a function of turbine inlet pressure, in the absence of thrust plenum flow. Figure 4a shows alternate paths for increasing and decreasing actuation at low speeds; this can be attributed to a variety of factors. First and foremost, this is a likely product of higher static friction than dynamic. Other possible contributors are net radial forces and a varying slide-to-roll ratio of the microballs during start-up. Figure 4b shows a linear relationship between inlet pressure and rotor normal force, demonstrating the coupled nature of normal and rotational forces during actuation.

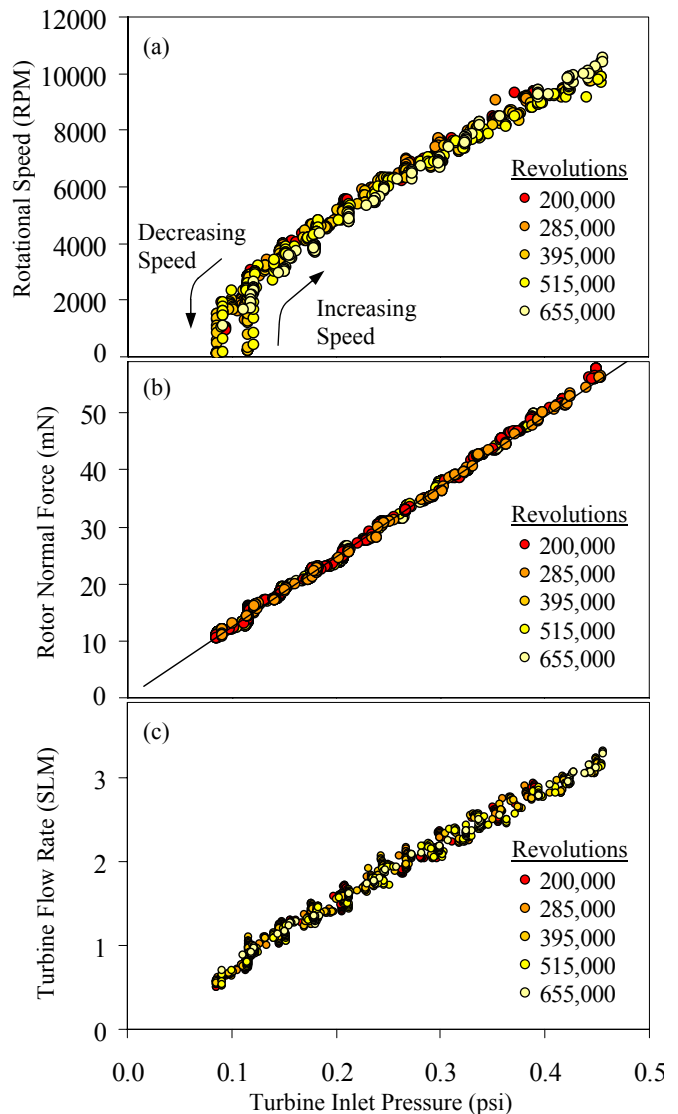


Figure 4: Turbine operating curves for (a) rotational speed, (b) rotor normal force, and (c) turbine flow rate as a function of turbine inlet pressure, with no thrust plenum flow.

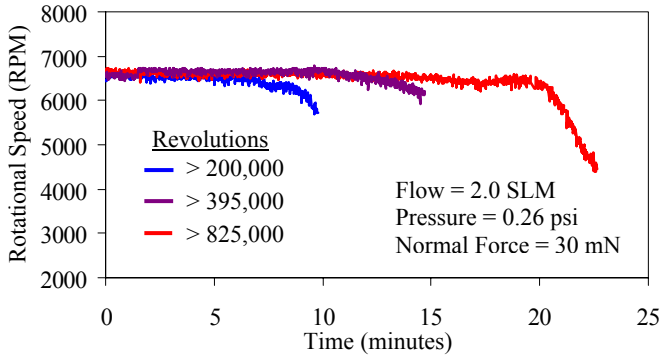


Figure 5: The effect of wear debris on turbine performance after prolonged operation. After each data set the device is cleaned and returns to the expected behavior.

### Effect of Wear Debris

After continuous operation, wear debris builds up slowing the turbine due to increased friction. Accordingly, the device is cleaned periodically in an ultrasonic bath to remove wear particles. After cleaning, the turbine performance returns to the expected behavior, showing longer operation with increased revolutions, as seen in Fig. 5. Each data set of the characterization curves (Fig. 4a-c) was collected after ultrasonic cleaning. This shows that while wear debris limits the duration of the device, wear itself (geometric deviation from the as-fabricated state) has virtually no effect on performance, for the loading conditions considered.

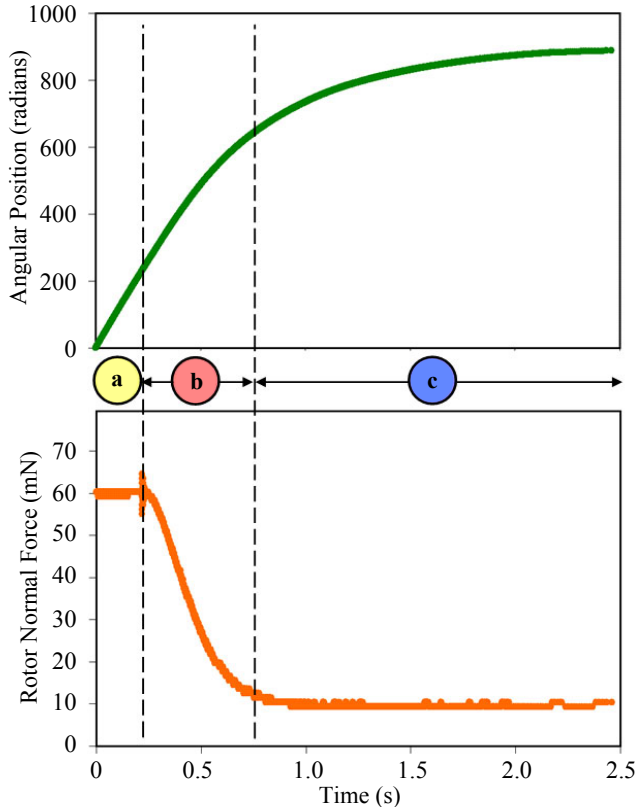


Figure 6: Spin-down data acquisition procedure. (a) The turbine is spun at a constant speed of 10,000rpm. (b) The turbine flow is shut off and the speed and normal force decrease. (c) The normal force equilibrates to the pre-set value (10mN). Spin-down data is acquired during this stage as the rotor decelerates under a specified constant normal force.

### Spin-Down Friction Testing

Comprehensive characterization of dynamic bearing friction is achieved through spin-down testing using the backside thrust plenum (Fig. 2b) to achieve a desired normal rotor force. The spin-down response of the microturbine (Fig. 6) can be separated into three distinct stages. Initially, the turbine is spinning at a constant speed ( $\sim 10,000$ rpm) corresponding to a linear increase in angular position and an elevated constant thrust force (**stage a**). The turbine flow is shut off and the thrust force decreases dramatically as the rotor begins to slow down (**stage b**). Finally, **stage c** corresponds to the period after the thrust load equilibrates to within 10% of the pre-set desired value (10mN in this case). Spin-down data is acquired during **stage c**. An optical probe measures angular position,  $\theta$ , as the rotor decelerates under a prescribed constant normal force provided by the thrust plenum.

To characterize the effects of speed and load on dynamic bearing friction, this testing procedure is repeated for several normal loads. Figure 7 shows spin-down data acquired at several thrust forces, showing faster spin-down at higher loads, as would be expected. These position versus time data sets fit well to an exponential function of the form

$$\theta = A(1 - e^{-Bt}) \quad (1)$$

(with coefficients A & B). The result is a linear relationship between angular acceleration ( $\ddot{\theta}$ ) and angular velocity ( $\dot{\theta}$ ),

$$\ddot{\theta} = -B\dot{\theta}, \quad (2)$$

and therefore a linear relationship between friction torque, calculated as the product of the angular acceleration and rotor mass moment of inertia ( $\tau_F = I\ddot{\theta}$ ), and bearing speed ( $\omega = \dot{\theta}$ ). Accordingly, each spin-down at a constant normal force ( $F_N$ ) corresponds to a single ratio of friction torque to bearing speed

$$\frac{\tau_F}{\omega} = |I \cdot B| = f(F_N) \quad (3)$$

where  $I$  is the rotor mass moment of inertia and  $B$  is the coefficient determined from numerical fitting.

This testing and data reduction scheme is repeated sequentially at various intervals up to 825,000 revolutions for normal loads from 10-50mN. These loads correspond to the range of expected values in next-generation electrostatic and magnetic micromotors and microgenerators being developed by our group.

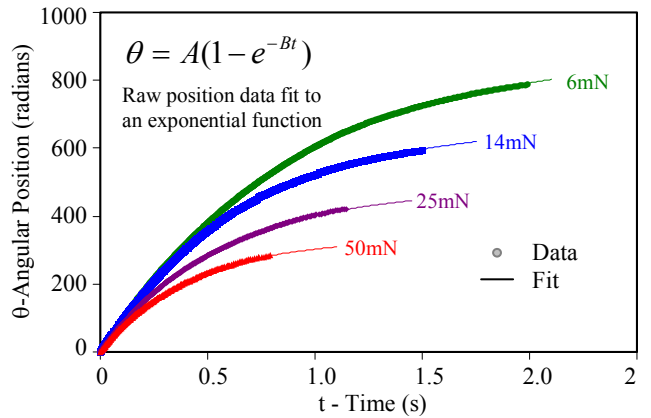


Figure 7: Spin-down trajectory data for several normal loadings fit to an exponential function with constants A&B, resulting in a linear relationship between deceleration and speed.

The dependence of the ratio of friction torque to bearing speed ( $\tau_F/\omega$ ) on the normal load ( $F_N$ ) is plotted in Figure 8 for intervals up to 825,000 revolutions. Accordingly, an empirical power-law model for friction torque of the form  $\tau_F = C F_N^D \omega$  has been developed for speeds and loads of 250-5,000rpm and 10-50mN, respectively, corresponding to 0.0625-2.5 $\mu$ Nm of friction torque. This results in coefficients of dynamic rolling friction varying from 0.0005 (at 250rpm and 50mN) to 0.025 (at 5,000rpm and 10mN). Figure 9 shows the evolution of the modeling constants (C&D) at every interval. After an initial period of 'run-in', repeatable results from 100,000 to 825,000 revolutions are observed corresponding to the developed model shown in Fig 8.

The test device and experimental apparatus presented in this work provide a platform to characterize and optimize friction and wear in encapsulated microball bearing support mechanisms. This is the first demonstration of such a system, independently investigating the effects of speed and load. Using this platform complete characterization of bearing friction over a range of relevant operating conditions has been achieved. Additionally, the onset and effects of wear have been identified. Continued work will focus on the incorporation of thin-film hard-coatings into the bearing housings to mitigate the effects of friction and wear.

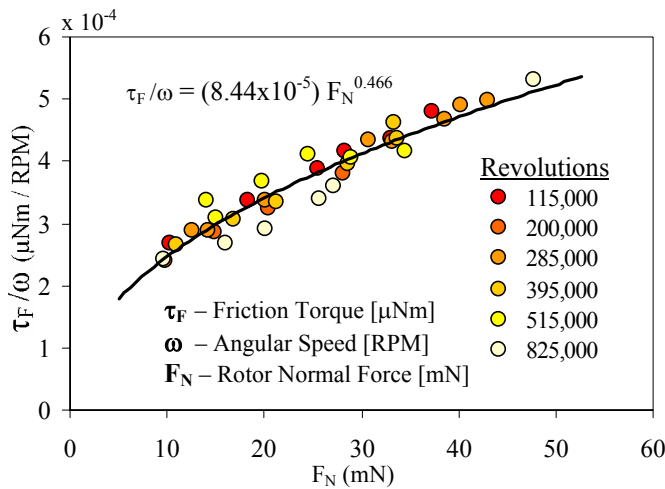


Figure 8: Linear proportionality between friction torque and speed as a function of rotor normal force at various intervals, showing good agreement with a power-law relation up to 825,000 revolutions.

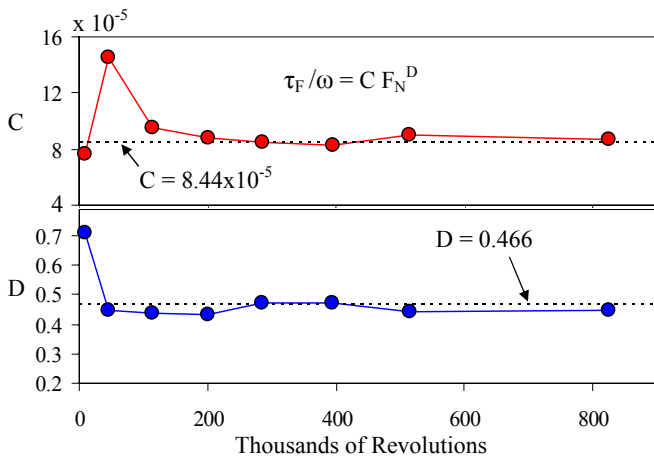


Figure 9: Empirical modeling constants from spin-down friction tests, equilibrating after an initial period of wear.

## CONCLUSIONS

Reliable and stable operation of a silicon microturbine supported on a planar-contact encapsulated microball bearing has been demonstrated. A novel testing apparatus has enabled the first characterization and empirical modeling of dynamic friction in microball bearings over operating conditions relevant to the development of a wide range of rotary micromachines. This apparatus has provided quantitative and qualitative information on the nature and prominence of friction and wear in such bearing systems. Additionally, this platform will allow the investigation and optimization of these critical bearing parameters through the use of hard-film coatings. The technologies presented here will act as robust drive and support mechanisms for the high-speed rotary micro-generators, motors, electric-pumps and turbopumps currently in development by our group.

## ACKNOWLEDGMENTS

This work was supported by the U.S. Army Research Laboratory under Grant No. CA#W911NF-05-2-0026.

## REFERENCES

- [1] L. Fr chet, S. Jacobson, K. Breuer, F. Ehrlich, R. Ghodssi, R. Khanna, C. Wong, X. Zhang, M. Schmidt, and A. Epstein, "High-Speed Microfabricated Silicon Turbomachinery and Fluid Film Bearings", *Journal of Microelectromechanical Systems*, 14, 1, pp.141-152 (2005).
- [2] C. Livermore, A. Forte, T. Lyszcza, S. Umans, A. Ayon, and J. Lang, "A high-power MEMS electric induction motor," *Journal of Microelectromechanical Systems*, 13, pp.465-471 (2004).
- [3] M. Mehregany, S. D. Senturia, and J. H. Lang, "Measurement of wear in polysilicon micromotors," *IEEE Transactions on Electron Devices*, 39, pp.1136 (1992).
- [4] N. Ghalichechian, A. Modafe, J. H. Lang, and R. Ghodssi, "Dynamic Characterization of a Linear Electrostatic Micromotor Supported on Microball Bearings," *Sensors and Actuators: A. Physical*, 136, 2, pp.416-503, (2007).
- [5] N. Ghalichechian, A. Modafe, M. Beyaz, and R. Ghodssi, "Design, Fabrication, and Characterization of a Rotary Micromotor Supported on Microball Bearings," *Journal of Microelectromechanical Systems*, In Press, December 2007.
- [6] N. Ghalichechian, M. McCarthy, M. Beyaz, and R. Ghodssi, "Measurement and Modeling of Friction in Linear and Rotary Micromotors Supported on Microball Bearings," *Technical Digest of the IEEE International Conference on Microelectromechanical Systems (MEMS)*, Tucson, AZ, USA, January 13-17, 2008.
- [7] C. M. Waits, N. Jankowski, B. Geil, and R. Ghodssi, "MEMS Rotary Actuator using an Integrated Ball Bearing and Air Turbine", *Technical Digest of the International Conference on Solid-State Sensors and Microsystems (Transducers)*, Lyon, France, June 10-14, 2007.
- [8] C. M. Waits, B. Geil, and R. Ghodssi, "Encapsulated Ball Bearings for Rotary Micromachines," *Journal of Micromechanics and Microengineering*, 17, pp. S224-S229 (2007).
- [9] M. McCarthy, C. M. Waits, and R. Ghodssi, "Development of a Hybrid Gas/Ball Bearing Support Mechanism for Microturbomachinery," *International Workshop on Micro and Nanotechnology for Power Generation and Energy Conversion Applications (PowerMEMS)*, Freiburg, Germany, Nov. 28-29, 2007.

# INTEGRATED TESTING OF POLYMER MEMS MATERIAL PROPERTIES

D. Sameoto<sup>1</sup>, C. Plesa<sup>1</sup>, and M. Parameswaran<sup>1</sup>

<sup>1</sup>Institute of Micromachine and Microfabrication Research, Simon Fraser University, Burnaby, BC, Canada

## ABSTRACT

We present a novel method for rapidly testing the material properties and fabrication qualities of polymer MEMS structures that uses an external vibration source and an all optical measurement system. A combination of static and dynamic test structures are designed and fabricated in SU-8 to test the basic performance of the system, and automatic measurements of device dimensions are used to correct for non-ideal fabrication effects. A piezoelectric actuator directly connected to the substrate excites all compliant structures in-plane simultaneously, and the resonance response is measured optically. The Young's modulus of SU-8 is found to be  $3.88 \pm 0.20$  GPa using this system.

## INTRODUCTION

Polymers are becoming increasingly popular for MEMS applications due to their wide range of material properties, low temperature processing and generally low costs. Polymers have been used for rapid MEMS prototyping [1], fabrication of micro-fluidics [2], and for thermal isolation of sensors [3]. More recently, novel composite structures have been developed that add electrical functionality to polymer MEMS devices [4] for sensing or actuation purposes. In order to achieve good yields and determine material properties for new composites or processing parameters, an integrated system for rapidly testing polymer MEMS properties is required.

The evaluation of material properties in MEMS is extremely important for determining performance of fabricated devices, expected failure modes, and long term reliability. Non-integrated testing may be performed by removing components and performing macroscale type tests for stress-strain relations, fracture strength etc., but they are not practical for rapid material property extraction. Previous publications have identified three major types of integrated test structures: M-test, strain gauge and resonance [5]. Of these three, only strain gauges and resonance structures are appropriate for the thin and thick structures that can be fabricated with polymer MEMS [5]. A standard test die was designed for this work that includes many of these test structures (Figure 1).

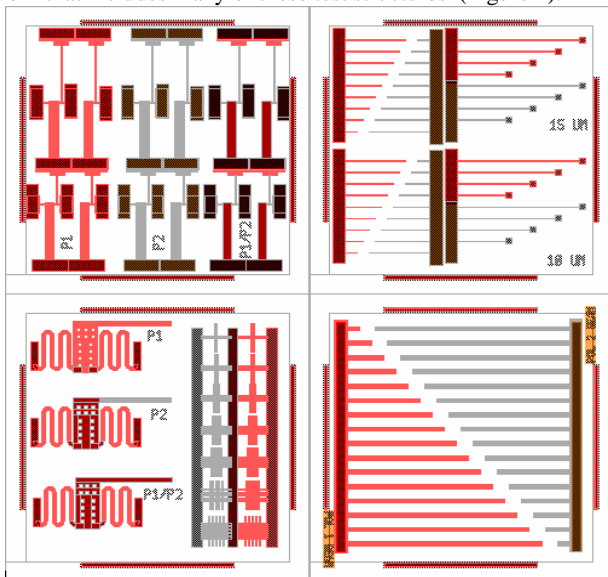


Figure 1: L-Edit layout of a 1x1 cm polymer MEMS test die.

The resonance of MEMS structures has often been used to determine Young's modulus [6], but electrostatic actuation for high frequency excitation is not possible with electrically insulating polymers. To overcome this problem, an external excitation source is used on the whole die or wafer at a single time, while in-plane dynamic response is measured optically. In-plane resonance is easily observed with a standard microscope, and is theoretically independent of device thickness. Fixed-free cantilevers can provide values for Young's modulus, while fixed-fixed beams can be used to evaluate residual stress. Other static structures like strain gauges [7], or cantilevers attached to out-of-plane pop-up structures [8] may be used to directly observe residual strain or curvature, but cannot be used directly to find stress or stress gradients unless the Young's modulus is known. When combined with data from the resonance structures, these structures can be used to extract other material properties. However, the focus of this work is how to best measure polymer material properties through frequency response.

## FABRICATION

Fabrication of the polymer MEMS test die follows a very similar method to that described in [1]. Rather than a polystyrene sacrificial layer used in previous work [1], a polyimide based sacrificial layer (Prolift [9]), is used. Prolift dissolves rapidly in TMAH-based developers, can be processed above 200 °C while remaining soluble, and is unaffected by most organic solvents. Therefore, it is an excellent sacrificial layer for many spin-coated polymers. A thick layer of Shipley 1827 photoresist is spun-coat on the Prolift and patterned with an underexposure, so as not to remove Prolift during the development step. A second, blanket underexposure can also be used through a bare Mylar sheet to roughen the remaining photoresist surface significantly (Figure 2).

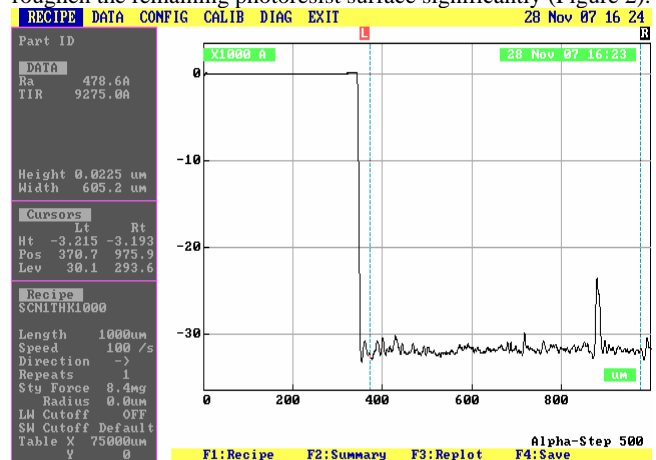


Figure 2: Profilometer data of an underexposed anchor in photoresist defined using a Mylar mask. Optical imperfections in the Mylar produce a very rough photoresist surface.

An O<sub>2</sub> RIE step transfers the photoresist topology to the Prolift and results in a very rough sacrificial layer that minimizes stiction after a wet release while also significantly increases the visibility of transparent polymers. With thicker polymer MEMS structures, fabricated dimensions must be experimentally measured to ensure accurate measurements of material properties from strain

gauges and resonant structures. SU-8 is used as a structural layer in this work because it is a common polymer used in MEMS and material properties can be compared with previously published results. Two different structural thicknesses are defined on each test die, either 18 or 38  $\mu\text{m}$  thick in this work, to determine the effects of the resonating test structures with different aspect ratios. The basic process steps are shown in Figure 3.

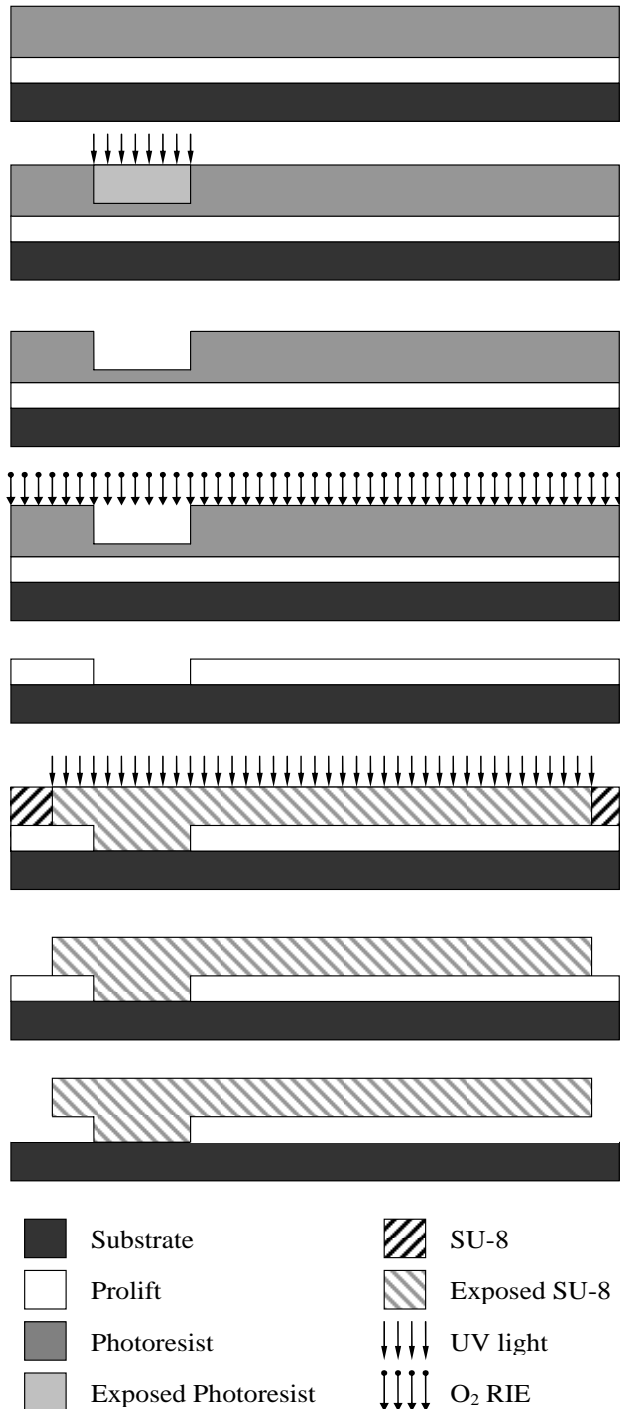


Figure 3: Generalized process steps for the creation of SU-8 MEMS cantilevers for dynamic testing.

### TEST SETUP

Individual test die, or wafer sections are placed under a

microscope after release and examined using either a Moticom 1300 (resolution 1024x768), or a BigCatch EM-500M eyepiece camera (resolution 2592x1944). The higher resolution of the BigCatch camera is offset by a much lower refresh rate, making it better suited for static images or slower frequency sweeps. A National Instruments PCI-5401 function generator card is used to step a sinusoidal signal through a frequency range. This signal is input to a Trek model PZD-700 high voltage amplifier capable of outputting  $\pm 700\text{V}$  to a piezoelectric actuator. This piezoelectric actuator excites the substrate in-plane for dynamic characterization of polymers with the same microscope setup used for static measurements (Figure 4). Images are captured corresponding to each input frequency, with each step taking approximately 4 seconds.

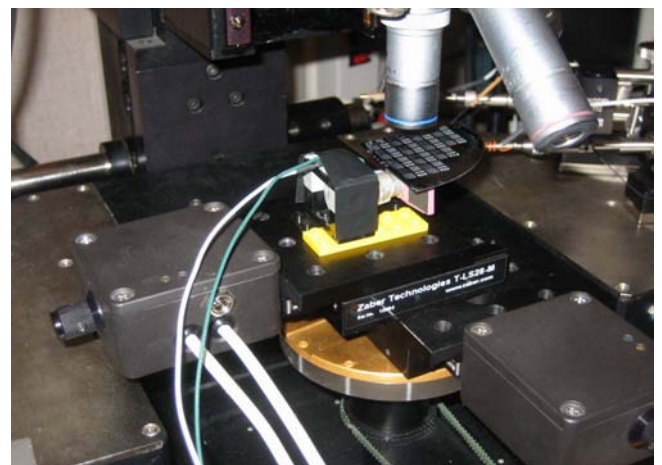
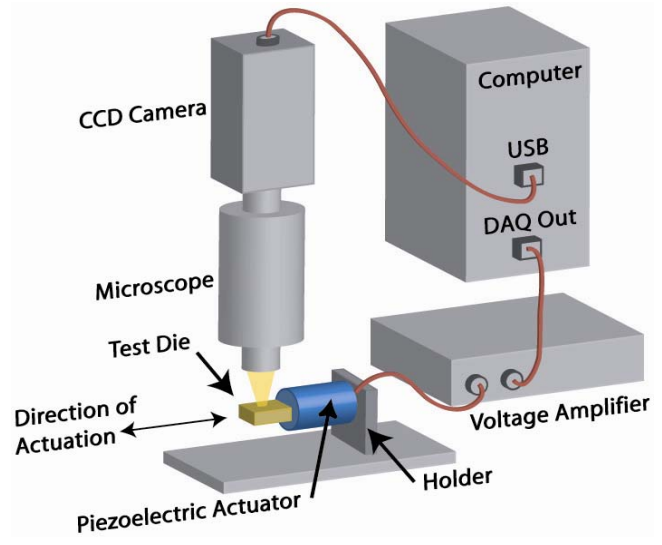


Figure 4: Schematic of test setup and image of a quarter wafer in position for testing. The existing test system can work on a few die at once, but should be able to eventually measure whole wafers automatically.

The substrate motion is lower than the optical threshold of the system and can be ignored while taking measurements. Polymer structures typically have low values for Young's modulus ( $<10\text{ GPa}$ ), and can resonate at frequencies below the resonance of the piezoelectric crystal (Figure 5). After all the images are captured during the frequency sweep, National Instruments Vision Builder for Automated Inspection is used to determine device dimensions and resonance points. Edge detection in regions of interest allows

the response of multiple structures within the field of view to be measured and evaluated. Matlab® is then used to calculate material properties from the dimensions and resonance frequencies of multiple structures, and average values and standard deviation for Young's modulus are found.

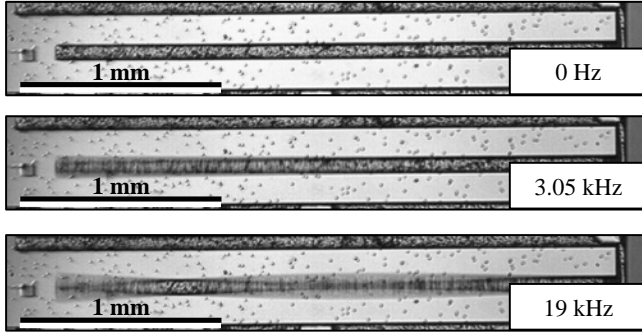


Figure 5: Dynamic response of a long, low aspect ratio (~1:2) SU-8 cantilever at different input frequencies. Two resonance modes are observed below the resonance frequency of the piezoelectric crystal (25 kHz).

## THEORY

Basic beam theory allows Young's modulus to be found from the undamped resonance frequency of a cantilever beam by the following relationship assuming a rectangular cross section:

$$f_n = \frac{C_n}{2\pi} \sqrt{\frac{Ew^2}{12\rho L^4}} \quad (1)$$

Where  $\rho$  is the density of the material,  $L$  is length,  $E$  is Young's modulus and  $w$  is beam width. In this case,  $C_n$  is the coefficient corresponding to the resonant mode of the beam (3.52 for the first mode of a cantilever). Matlab® is used to determine mechanical properties based on the measured device geometries and resonant frequencies. The density of SU-8 is assumed to be 1200 kg/m<sup>3</sup> for these calculations. For new polymers or composites tested in the future, data may be calibrated based on measured densities. The out-of-plane structures used for curvature measurement can also be used to directly observe the sidewall angle to provide correction factors for the equations used for resonance based on trapezoidal cross-sections (Figure 6). The average sidewall angle was measured to be approximately 85°.

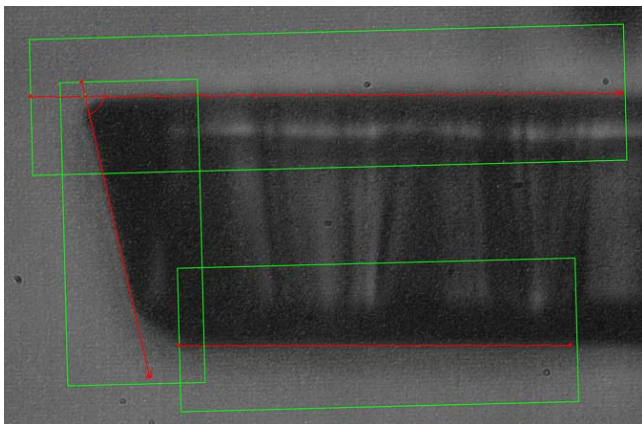


Figure 6: Negative sidewalls in SU-8 structures due to exposure through a Mylar emulsion mask.

The corrected natural frequency for a trapezoidal beam

resonating in-plane is found by the following equation, where  $w_b$  is the bottom width, and  $w_t$  is the top width.

$$f_n = \frac{C_n}{2\pi} \sqrt{\frac{E(w_b^3 + w_b^2 w_t + w_b w_t^2 + w_t^3)}{12\rho L^4(3w_b + w_t)}} \quad (2)$$

## RESULTS

Measurements were made on over 90 different SU-8 resonant structures across the test wafer. The majority of narrow compliant SU-8 structures fabricated in early experiments (upper right quadrant of the test die), had feature swelling due to contact problems with the flexible Mylar masks. This swelling increased the natural frequency of all structures. In addition, many of the smaller structures with swollen features demonstrated negative curvature, due to lower exposure dose per area [10], and could not vibrate freely. The swelling of fixed-fixed beams meant that nearly all of the structures had resonance frequencies above that of the piezoelectric actuator, making measurements of these structures unreliable. Wider and thinner structures demonstrated the best fabrication yields and were also the least sensitive to errors in measurements of sidewall angle (Figure 7) and beam width.

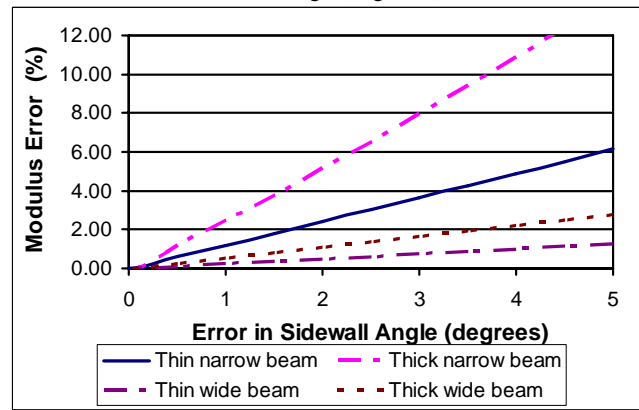


Figure 7: Theoretical error introduced into measurements of Young's modulus from sidewall angle for different beam geometries as fabricated on the test die.

The measured quality factor of tested cantilevers was greater than 30 in air, indicating that the damping introduces less than 1% error. Multiple tests on resonating structures also indicate that the material properties of SU-8 remain stable and the optical measurements are repeatable (Figure 8).

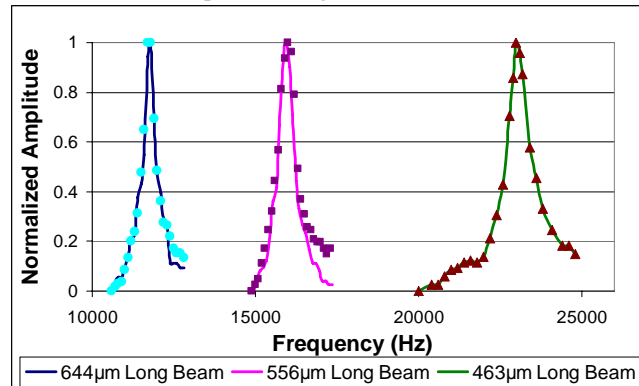


Figure 8: Resonance peaks of three narrow beams, 38 µm thick on a single die measured 1 week (solid line), and 60 days (dots), after fabrication. Little change in  $Q$  factor or resonance frequency of SU-8 cantilevers is observed.

The full analysis of all beams results in a range of measured Young's modulus between 3.5 and 4.3 GPa. The majority of structures however, clustered around an average Young's modulus of  $3.88 \pm 0.20$  GPa which agrees well with previously published values [11]. The average Young's modulus and standard deviation of differently designed cantilever geometries is shown below in Figure 9. Thinner, wider cantilevers demonstrate the lowest range of measured Young's modulus.

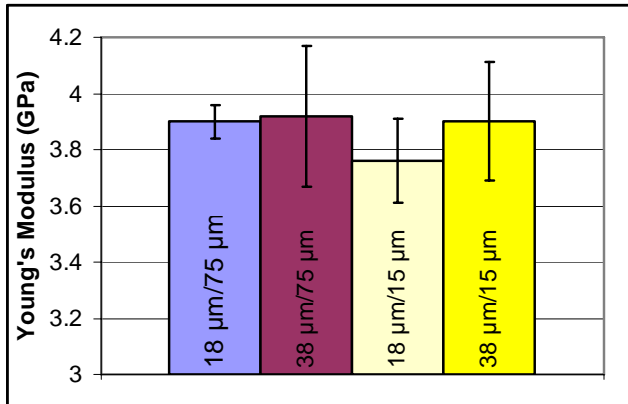


Figure 9: Measured Young's modulus for SU-8 from resonance of different thicknesses and designed widths of SU-8 cantilevers post exposure baked at 120 °C for 30 minutes.

Given that the thinnest, longest structures showed greatest reliability, different analysis techniques were tested to determine a minimum number of tests to provide accurate results. A series of curve fits were completed on the 18 μm thick, 75 μm nominal width cantilevers with non-linear least squares fit from the Matlab® curve fitting toolbox (Figure 10). On average, the results agreed with the full analysis to within 0.06 GPa, indicating that acceptable extraction of Young's modulus may be achieved with as little as five different resonance measurements on the low aspect ratio beams.

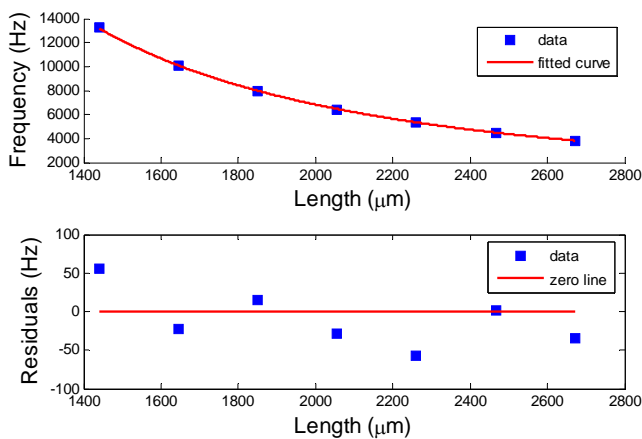


Figure 10: Least squares fit of resonance data from a set of low aspect ratio SU-8 cantilevers on a single die.

## CONCLUSIONS

A novel test system for integrated testing of polymer MEMS has been developed that overcomes challenges with respect to actuating insulating structures and observing transparent polymers without the addition of extra materials. It is to the authors' knowledge, the first test mechanism to actuate MEMS on multiple die simultaneously and to use resonance of low aspect ratio

structures in-plane to extract material properties. This system is designed to account for fabrication problems which may arise during the creation of polymer structures through lithography, direct molding or dry etching. The in-plane actuation of full die or quarter wafers using a piezoelectric actuator allows multiple structures to be tested within an optical field of view which reduces analysis times. Analysis of failure modes and data obtained from different structures indicates that low aspect ratio structures are more likely to provide acceptable data from in-plane excitation due to the more accurate measurements of structure width and smaller effect of non-vertical sidewalls. Future improvements to this system will include the introduction of piezoelectric actuators with higher resonant frequencies and lower operating voltage, so that excitation of cantilevers and fixed-fixed bars over a larger frequency range and at different frequency modes may be completed.

## ACKNOWLEDGEMENTS

We would like to thank the Natural Sciences and Engineering Research Council of Canada for financial support of this work.

## REFERENCES

- [1] D. Sameoto, S. H. Tsang, and M. Parameswaran, "Polymer MEMS processing for multi-user applications," *Sensors and Actuators A*, vol. 134, pp. 457-464, 2007.
- [2] S. Metz, S. Jiguet, A. Bertsch, and P. Renaud, "Polyimide and SU-8 microfluidic devices manufactured by heat-depolymerizable sacrificial material technique," *Lab on a Chip*, vol. 4, pp. 114-120, 2004.
- [3] S. H. Tsang, A. H. Ma, K. S. Karim, M. Parameswaran, and A. M. Leung, "Monolithically fabricated polymer MEMS 3-axis thermal accelerometers designed for automated wirebonder assembly," presented at IEEE MEMS 2008, Tucson, AZ, pp. 880-883.
- [4] J. M. Engel, N. Chen, K. Ryu, S. Pandya, C. Tucker, Y. Yang, and C. Lie, "Multi-level embedment of conductive and non-conductive PDMS for all-elastomer MEMS," *Solid State Sensors, Actuators and Microsystems Workshop (Hilton Head, SC, June 2006)*, pp. 316-319.
- [5] V. T. Srikanth and S. M. Spearing, "A critical review of microscale mechanical testing methods used in the design of microelectromechanical systems," *Experimental Mechanics*, vol. 43, pp. 238-247, 2003.
- [6] K. E. Petersen and C. R. Guarnieri, "Young's modulus measurements of thin films using micromechanics," *Journal of Applied Physics*, vol. 50, pp. 6761-6766, 1979.
- [7] L. Lin, A. P. Pisano, and R. T. Howe, "A micro strain gauge with mechanical amplifier," *Journal of Microelectromechanical Systems*, vol. 6, pp. 313-321, 1997.
- [8] S.-H. Tsang, D. Sameoto, I. G. Foulds, R. W. Johnstone, and M. Parameswaran, "Automated assembly of hingeless 90° out-of-plane microstructures," *J. Micromech. Microeng.*, vol. 17, pp. 1314-1325, 2007.
- [9] <http://www.brewerscience.com/?id=134#27>, "Prolift Data Sheet," Brewer Science, 2008.
- [10] D. Sameoto, S. H. Tsang, I. G. Foulds, S.-W. Lee, and M. Parameswaran, "Control of the out-of-plane curvature in SU-8 compliant microstructures by exposure dose and baking times," *Journal of Micromechanics and Microengineering*, vol. 17, pp. 1093-1098, 2007.
- [11] H. Lorenz, M. Despont, N. Fahrni, N. LaBianca, and P. Renaud, "SU-8: a low-cost negative resist for MEMS," *J. Micromech. Microeng.*, vol. 7, pp. 121-124, 1997.

# MEASURING CHARGE AND CHARGE DECAY IN FLOATING-ELECTRODE ELECTROSTATIC ACTUATORS

D. Elata<sup>1,2</sup>, R. Hennessy<sup>1</sup>, V. Leus<sup>2</sup>, N. Klejwa<sup>1</sup>, A. Hirshberg<sup>2</sup>, J. Provine<sup>1</sup> and R.T. Howe<sup>1</sup>

<sup>1</sup>Stanford University, Stanford, California, USA

<sup>2</sup>Technion - Israel Institute of Technology, Haifa, Israel

## ABSTRACT

We consider electrostatic actuators that are pre-energized with charge, which amplifies their response to input voltages. Floating-electrode actuators were designed, fabricated, and characterized. A non-disruptive measurement of charge is proposed and demonstrated. When the floating electrode is charged, the system has two distinct pull-in voltages. It is shown that the amplitude of charge is proportional to the average of the two pull-in voltages. In this work, we present the correct way of using energy methods to analyze systems that are loaded by both charge and voltage.

## INTRODUCTION

In recent years, much attention is given to the effect of dielectric charging in microelectromechanical actuators [1-6]. Proper operation of RF-MEMS capacitive switches requires a predictable and stable pull-in voltage (e.g. [7]), but this voltage is strongly affected by dielectric charging [6]. An even worse effect is a total lock-down of capacitive switches caused by spatial distribution of injected charges [6]. Dielectric charging has adverse effects in other microsystems as, for example, inducing drift in resonators [8, 9].

A rigorous analysis of the effect of injected charge on the electromechanical response of electrostatic actuators was presented by Rottenberg et al. [6, 10]. In these investigations, electrostatic forces due to applied voltage and injected charge were derived, and used to solve the equilibrium equation of the system. An alternative approach is using energy methods to derive the system response. The advantage of energy methods is that they can be used to directly compute critical parameters of the *dynamic* response, without having to integrate the momentum equations in time [11]. However, with reference to dielectric charging, energy methods must be used with care to avoid physically inconsistent results, as explained in this work.

This manuscript has two purposes. The first is to demonstrate the correct way of using energy methods to analyze electrostatic actuators that are subjected to both voltage and charge. The second purpose is to analyze a simple electrostatic actuator that is loaded by voltage and charge, and to show theoretically and experimentally how the charge can be deduced from measured parameters of the electromechanical response.

## ANALYSIS

As a simple model of an electrostatic actuator that is loaded by charge and driven by voltage, we consider the floating-electrode actuator schematically described in Fig. 1. The floating electrode of mass  $m$  has a single degree-of-freedom  $x$ , and is suspended on a linear spring with stiffness  $k$ . The floating electrode is electrically isolated and may carry a total charge  $Q$ , and the driving electrode is subjected to a voltage  $V$ . A fixed parasitic capacitance  $C_p$  is also considered. Throughout this work, damping is neglected.

The capacitance of the variable driving capacitor is given by

$$C_d = \varepsilon_0 A / (g - x) \quad (1)$$

where  $\varepsilon_0$  is the permittivity of free-space,  $A$  is the area of the driving electrode, and  $g$  is the gap at the unloaded state (i.e.  $V = 0$ ,  $Q = 0$ ). For brevity, fringing fields are neglected in the analysis.

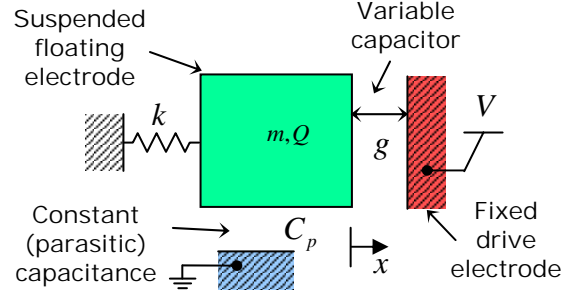


Figure 1: Schematic view of a floating-electrode actuator. The floating electrode with charge  $Q$  is suspended on a linear spring and is driven by voltage  $V$  on the driving electrode.

When the floating electrode is charged, the driving and parasitic capacitors are effectively connected in parallel. The charge on the driving electrode  $q_{dQ}$  and the charge on the ground-side of the parasitic capacitance,  $q_{pQ}$ , are given by

$$q_{dQ} = -\frac{C_d Q}{C_p + C_d}, \quad q_{pQ} = -\frac{C_p Q}{C_p + C_d} \quad (2)$$

such that  $Q + q_{pQ} + q_{dQ} = 0$ .

In this actuator, both charge  $Q$  and voltage  $V$  are the driving parameters of the system. In practice, charge does not change as fast as voltage and accordingly, we assume that the system is first loaded quasi-statically by charge  $Q$  while  $V = 0$ , and only then the voltage is applied. This charging may be achieved by connecting the floating electrode to a source with the appropriate voltage. During charging, the suspended floating electrode moves due to the developing electrostatic forces, and reaches an equilibrium state  $x = x_0$  as derived later on. At this equilibrium state, the charge on the driving electrode reaches the value  $q_{d0}$ , which is a function of the charge  $Q$

$$q_{d0} = -Q \frac{\varepsilon_0 A}{C_p} \left( g + \frac{\varepsilon_0 A}{C_p} - x_0 \right)^{-1} \quad (3)$$

Once the floating electrode is charged, the system may be subjected to a voltage  $V$ . This voltage may be applied gradually so that the loading is quasi-static, or may be applied in a step-function such that a dynamic response is induced. In either case, when a voltage  $V$  is applied to the system that was pre-loaded with a charge  $Q$ , the charge on the driving electrode  $q_d$  and the charge on the ground-side of the parasitic capacitance  $q_p$ , are given by

$$q_d = \frac{C_d (VC_p - Q)}{C_p + C_d}, \quad q_p = -\frac{C_p (VC_d + Q)}{C_p + C_d} \quad (4)$$

When the system is loaded by voltage, the driving and parasitic capacitances are effectively connected in series. At this state, the electrostatic potential energy  $U_E$  of the two capacitors is given by

$$U_E = \frac{1}{2} \frac{q_p^2}{C_p} + \frac{1}{2} \frac{q_d^2}{C_d} = \frac{1}{2} \frac{Q^2}{C_p + C_d} + \frac{1}{2} \frac{V^2}{\frac{1}{C_p} + \frac{1}{C_d}} \quad (5)$$

The mechanical potential  $U_M$  of the suspension is given by

$$U_M = \frac{1}{2}kx^2 \quad (6)$$

To consider the energy of the entire system, we include the potential energy of the voltage source (e.g. battery) [12]. The potential energy of an ideal voltage source is  $U_B = -q_B V$  where  $q_B$  is the charge that flows from the source to the driving electrode. Accordingly, the potential energy of the voltage source is given by

$$U_B = -(q_d - q_{d0})V = \frac{VQ/C_p - V^2}{\frac{1}{C_p} + \frac{1}{C_d}} + q_{d0}V \quad (7)$$

The total potential of the system is the sum of the mechanical potential, the electrostatic potential, and the potential energy of the voltage source [12]

$$\begin{aligned} \psi(V, Q, x) &= U_M + U_E + U_B \\ &= \frac{1}{2}kx^2 + \frac{1}{2} \frac{Q^2}{C_p + C_d} - \frac{1}{2} \frac{V^2}{\frac{1}{C_p} + \frac{1}{C_d}} + \frac{VQ/C_p}{\frac{1}{C_p} + \frac{1}{C_d}} + q_{d0}V \end{aligned} \quad (8)$$

The careful accounting for the potential energy terms in Eq. (8), especially that of the voltage source in Eq. (7), is essential to correctly account for the electromechanical response of the floating electrode actuator.

### Static Response

Following the methodology in [12], for any given loading  $Q$  and  $V$ , the system may be held at an arbitrary location  $x$  by application of a reactive mechanical force. This reactive force is given by the partial derivative of the total potential with respect to the displacement

$$f = \frac{\partial \psi}{\partial x} = kx - \frac{1}{2} \varepsilon_0 A \left( V - \frac{Q}{C_p} \right)^2 \left( g + \frac{\varepsilon_0 A}{C_p} - x \right)^{-2} \quad (9)$$

Equilibrium is a state in which the reactive force vanishes

$$2kx = \varepsilon_0 A \left( V - \frac{Q}{C_p} \right)^2 \left( g + \frac{\varepsilon_0 A}{C_p} - x \right)^{-2} \quad (10)$$

The stiffness of the system is the partial derivative of the reactive force with respect to the degree of freedom

$$K(V, Q, x) = \frac{\partial f}{\partial x} = k - \varepsilon_0 A \left( V - \frac{Q}{C_p} \right)^2 \left( g + \frac{\varepsilon_0 A}{C_p} - x \right)^{-3} \quad (11)$$

The stability of the system can now be determined by the sign of the stiffness. The system is stable for  $K > 0$ , is unstable for  $K < 0$  and is critically stable at  $x_c$  if  $K(V, Q, x_c) = 0$  and  $K(V, Q, x_c + \delta) < 0$  where  $\delta$  is a small perturbation from  $x_c$ . Stability of an equilibrium state may be determined by substituting (10) into (11) which yields

$$K_{Eq} = k - 2kx \left( g + \frac{\varepsilon_0 A}{C_p} - x \right)^{-1} \quad (12)$$

Stability of equilibrium is lost (i.e.  $K_{Eq} = 0$ ) at the pull-in state of the system. It follows that the pull-in displacement is always

$$x = \frac{1}{3} \left( g + \frac{\varepsilon_0 A}{C_p} \right) \quad (13)$$

which is compatible with analysis of related systems [12].

The term  $V - Q/C_p$  in Eqs. (9)-(11) is the effective electrostatic load applied to the suspended electrode, henceforth written as

$$V^* = V - \frac{Q}{C_p} \quad (14)$$

Substituting the displacement (13) back into the equilibrium equation (10), it follows that there are *two static* pull-in voltages given by

$$\begin{aligned} V_{SPI(I)} &= \frac{Q}{C_p} + V^*_{SPI} \\ V_{SPI(II)} &= \frac{Q}{C_p} - V^*_{SPI} \end{aligned} \quad (15)$$

where

$$V^*_{SPI} = \sqrt{\frac{8}{27} \frac{k}{\varepsilon_0 A} \left( g + \frac{\varepsilon_0 A}{C_p} \right)^{3/2}} \quad (16)$$

It is deduced that in the initial loading (i.e.  $V = 0$ ), static equilibrium is only possible if the charge is within the range

$$-V^*_{SPI} < \frac{Q}{C_p} < V^*_{SPI} \quad (17)$$

Furthermore, from (15) it follows that the normalized charge is equal to the average of the two pull-in voltages

$$\frac{Q}{C_p} = \frac{1}{2} (V_{SPI(I)} + V_{SPI(II)}) \quad (18)$$

and that the critical effective electrostatic load is given by

$$V^*_{SPI} = \frac{1}{2} (V_{SPI(I)} - V_{SPI(II)}) \quad (19)$$

Therefore, by measuring the positive and negative pull-in voltages (without discharging the floating electrode) we can deduce the amount of charge on the floating electrode. We emphasize that this measurement is insensitive to the mechanical parameters of the system (i.e. mass and stiffness). At the same time, since the system constant  $V^*_{SPI}$  is independent of charge, we can use property (19) to monitor the quality of measurement.

We may now extract the initial equilibrium displacement resulting from the charge alone (i.e.  $V = 0$ ), and extract the charge  $q_{d0}$  on the driving electrode in that equilibrium state from (3). Actually, it is simpler to compute  $Q$  and  $q_{d0}$  in terms of the equilibrium displacement  $x_0$  within its stable range  $0 \leq x_0 < \frac{1}{3} (g + \varepsilon_0 A / C_p)$ . Setting  $V = 0$  in the equilibrium equation (10) and solving for  $Q$  yields

$$\frac{Q}{C_p} = \pm \sqrt{2 \frac{kx_0}{\varepsilon_0 A} \left( g + \frac{\varepsilon_0 A}{C_p} - x_0 \right)} \quad (20)$$

A typical equilibrium curve of a floating-electrode actuator is schematically illustrated in Fig. 2. This specific equilibrium curve relates to a positive charge  $Q > 0$ . Loading the actuator with charge  $Q$  results in the initial displacement  $x_0$ . From this initial state, the system can be subjected to a gradually increasing, positive or negative voltage, until a pull-in instability occurs. In the charged actuator, there are two distinctly different pull-in voltages. For  $Q > 0$  one pull-in voltage is negative with small amplitude, and the other is positive with large amplitude. In the case  $Q = 0$ , the curve is symmetric in  $V$ , both positive and negative pull-in voltages have the same amplitude, and in that case we commonly consider only the upper half of the equilibrium curve.

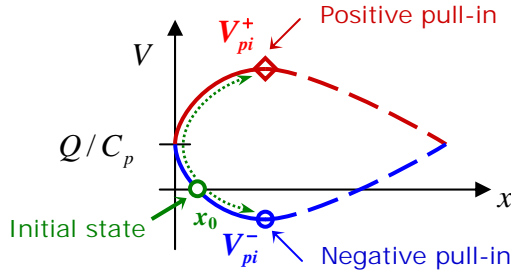


Figure 2: Equilibrium curve of the floating-electrode actuator for a given charge. The charge works like a bias, shifting the curves by  $Q/C_p$ , such that the two pull-in voltages have different amplitudes.

### A Modeling Error to be Avoided

For electrostatic actuators that are driven by voltage only, it turns out that  $U_B = -2U_E$  (e.g. set  $Q = 0$  in (5), (7) and (3)). However, it is incorrect to identify the total potential as  $\psi^v = U_M - U_E$ . In electrostatic actuators that are driven only by voltage this error has no consequence. However, in cases such as the floating-electrode actuator with  $Q \neq 0$ , the equilibrium equation that is derived using the wrong total potential is given by

$$2kx = \varepsilon_0 A \left( V^2 - \cancel{Q^2/C_p^2} \right) \left( g + \frac{\varepsilon_0 A}{C_p} - x \right)^{-2} \quad (21)$$

This incorrect result predicts that the equilibrium displacement depends on only the magnitudes of the voltage and charge and not on their polarities [13, 14], in contrast to Eq. (10) which is verified by experimental results on our actuator.

### Dynamic Response

The location of the suspended floating electrode as function of time can be computed by integrating the momentum equation in time. When the charged actuator is at rest and is subjected to a low step-function voltage, the dynamic response is a periodic vibration, with stagnation states  $\dot{x} = 0$  at  $x > 0$ . If the step-function voltage is sufficiently high, a non-periodic switching response occurs. The step-function voltage, which is in between the periodic and switching responses, is the dynamic pull-in voltage. By running many such time-integration simulations, we can try to extract the dynamic pull-in voltage, but this is obviously very time-consuming.

An alternative approach is to use energy methods to extract the dynamic pull-in voltage *without any time integration* [11, 12].

To this end, we consider the Hamiltonian of the system

$$H = \frac{1}{2} m \dot{x}^2 + \psi(V, Q, x) \quad (22)$$

Immediately after application of the step-function voltage, and before the floating electrode begins to move, the Hamiltonian is equal to the total potential  $\psi(V, Q, x_0)$ , and assuming there is no damping in the system, from this moment ( $t = 0$ ) the Hamiltonian is constant

$$H = \frac{1}{2} m \dot{x}^2 + \psi(V, Q, x) = \psi(V, Q, x_0) \quad (23)$$

We can now define the dynamic response function which relates the displacement  $x$ , velocity  $\dot{x}$ , and applied voltage  $V$ , at any time  $t > 0$

$$D = \frac{1}{2} m \dot{x}^2 + \psi(V, Q, x) - \psi(V, Q, x_0) \quad (24)$$

The stagnation states of the system are those states in which velocity vanishes, and are described by the stagnation function

$$S = \psi(V, Q, x) - \psi(V, Q, x_0) \quad (25)$$

For any given charge  $Q$  and initial displacement  $x_0$ , the stagnation function relates the displacement at stagnation points to the applied step-function voltage. One trivial solution of (25) is  $x = x_0$  which results from the fact that the initial state is static equilibrium (i.e.  $\dot{x} = 0$ ) regardless of the step-function voltage  $V$  which is about to be applied. By simultaneously solving the equilibrium equation (10) and the stagnation function (25), we may extract the other non-trivial dynamic pull-in displacement and the associated dynamic pull-in voltage

$$x_{DPI} = \frac{1}{2} \left( g + \frac{\varepsilon_0 A}{C_p} - x_0 \right) \quad (26)$$

$$V_{DPI} = \frac{Q}{C_p} \pm \frac{1}{2} \sqrt{\frac{k}{\varepsilon_0 A} \left( g + \frac{\varepsilon_0 A}{C_p} + x_0 \right) \left( g + \frac{\varepsilon_0 A}{C_p} - x_0 \right)} \quad (27)$$

where  $Q$  is given by (20).

As in the case of static measurements, the average of the dynamic pull-in is proportional to the charge

$$\frac{Q}{C_p} = \frac{1}{2} (V_{DPI(I)} + V_{DPI(II)}) \quad (28)$$

### EXPERIMENT

Actuators were fabricated using SOI technology (Fig. 3), with a large mass and soft suspension to slow the dynamic response (natural frequency of  $f_n = 268\text{Hz}$ ) and thus increase the measurement accuracy.

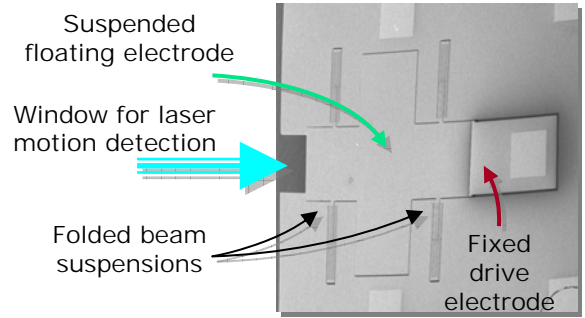


Figure 3: SEM image of floating-electrode actuator. The large rotor plate is suspended on four folded-beam springs. Stoppers that are electrically connected to the floating electrode, prevent contact between the rotor and the fixed driving electrode.

An opening was etched in the device layer to allow accurate measurement of in-plane motion using a Polytec laser vibrometer. The actuator includes stoppers that prevent contact and shorting of the rotor and drive electrode.

The floating electrode is charged by application of voltage through a probe-tip, which is then lifted leaving the charged electrode electrostatically floating. In order to prevent charging of the floating electrode where it faces the driving electrode, the latter is subjected to the same voltage during charging. The parasitic capacitance of the tested actuator is 48.2pF so when it is charged by a 6Volt source, the total charge is  $Q = 2.89 \cdot 10^{-10} \text{C} = 1.8 \cdot 10^9 e$ .

Figure 4 presents the measured positive and negative pull-in voltages for various levels of charge. As predicted by the theory, the average of the two pull-in voltages is proportional to the charge. The pull-in voltages were measured a short time after the floating electrode was charged.

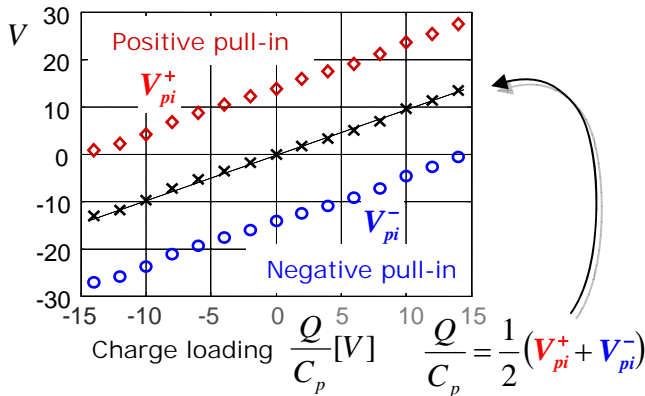


Figure 4: Measured pull-in voltages for different values of charge on the floating electrode. The average of the two pull-in voltages (dashed line) is equal to the charge loading  $Q/C_p$ .

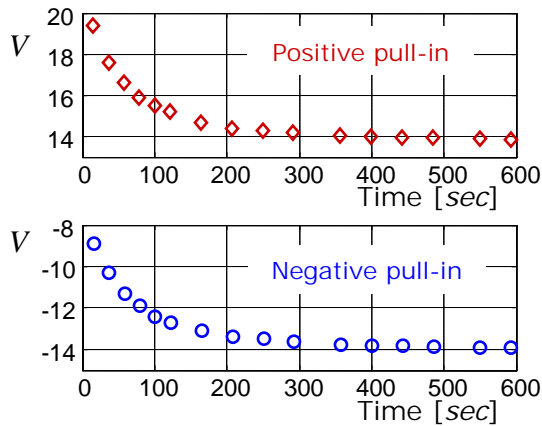


Figure 5: Time decay of positive and negative pull-in voltages. Measurement was performed in ambient conditions of 22°C and 50% relative humidity.

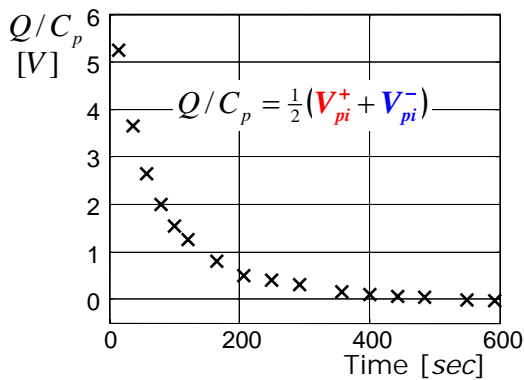


Figure 6: Charge decay as a function of time in the unpackaged actuator. Initial charge was  $Q/C_p=6$  Volts. The rapid leakage is attributed to high relative humidity.

To measure charge decay, the two pull-in voltages are sequentially and repeatedly measured at fixed time intervals. Figure 5 presents the change in the two pull-in voltages after the floating electrode was charged with a source of 6 Volts. The average of the two, presented in Fig. 6, shows the decay of charge from its initial value. This experiment was performed with an unpackaged device with an ambient relative humidity of 50%. We plan to use our methodology to measure charge and its decay in encapsulated devices, in which pull-in will be identified by the change in capacitance of the driving electrode. It is expected that charge retention will be excellent in a hermetically sealed microshell encapsulation.

#### ACKNOWLEDGEMENT

This work was supported by DARPA grant HR0011-06-1-0049 through the Center on Interfacial Engineering in Microelectromechanical Systems (CIEMS), at Stanford University.

#### REFERENCES

- [1] E.K. Chan, K. Garikipati, and R.W. Dutton, "Characterization of contact electromechanics through capacitance-voltage measurements and simulations," *JMEMS*, **8**, 208-217, 1999.
- [2] C. Goldsmith, et al., "Lifetime characterization of capacitive RF MEMS switches," presented at International Microwave Symposium, *IEEE MTT-S*, 2001.
- [3] J.R. Reid, "Simulation and measurement of dielectric charging in electrostatically actuated capacitive microwave switches," *MSM 2002*, San Juan, Puerto Rico, 2002.
- [4] W. M. van Spengen, R. Puers, R. Mertens, and I. De Wolf, "A comprehensive model to predict the charging and reliability of capacitive RF MEMS switches," *JMM*, **14**, 514-521, 2004.
- [5] R.W. Herfst, H.G.A. Huizing, P.G. Steeneken, and J. Schmitz, "Characterization of dielectric charging in RF MEMS capacitive switches," *IEEE Microelect. Test Structures*, 2006.
- [6] X. Rottenberg et al. "Analytical model of the DC actuation of electrostatic MEMS devices with distributed dielectric charging and nonplanar electrodes," *JMEMS*, **16**, 1243-1253, 2007.
- [7] P. Farinelli et al., "MEMS Switches with Stepped Pull-Down Voltage for Tunable Phase Shifters," *MEMSWAVE 2007*, Barcelona, 2007.
- [8] R. Melamud et al. "Temperature-compensated high-stability silicon resonators," *App. Phys. Letters*, **90**, 244107, 2007.
- [9] G. Bahl et al., "Observations of fixed and mobile charge in composite MEMS resonators," *Hiton Head workshop*, 2008.
- [10] X. Rottenberg, B. Nauwelaers, W. De Raedt, and H. A. C. Tilmans, "Distributed dielectric charging and its impact on RF MEMS devices," *34th European Microwave Conf.*, 2004.
- [11] D. Elata and H. Bamberger, "On the dynamic pull-in of electrostatic actuators with multiple degrees of freedom and multiple voltage sources," *JMEMS*, **15**, 131-140, 2006.
- [12] D. Elata, "On the static and dynamic response of electrostatic actuators," *Bulletin Polish Acad. Sciences*, **53**, 373-384, 2005.
- [13] Y. Nemirovsky et al. "A methodology and model for the pull-in parameters of electrostatic actuators," *JMEMS*, **10**, 601-615, 2001.
- [14] O. Bochobza-Degani et al. "On the effect of residual charges on the pull-in parameters of electrostatic actuators," *Sens. & Act. A*, **97**(8), 563-568, 2002.

# MICROSYSTEM FOR ELECTROMECHANICAL MEASUREMENTS OF CARBON NANOFIBER LOADING AND FAILURE

J.J. Brown<sup>1</sup>, J.W. Suk<sup>2</sup>, G. Singh<sup>1</sup>, D.A. Dikin<sup>3</sup>, R.S. Ruoff<sup>2</sup>, and V.M. Bright<sup>1</sup>

<sup>1</sup>Department of Mechanical Engineering, University of Colorado, Boulder, CO, USA.

<sup>2</sup>Department of Mechanical Engineering, University of Texas, Austin, TX, USA.

<sup>3</sup>Department of Mechanical Engineering, Northwestern University, Evanston, IL, USA.

## ABSTRACT

A thermally actuated uniaxial testing stage for nanofiber materials has been designed and fabricated. Electrical separation of portions of the stage allows two-point electrical measurements simultaneously with mechanical testing. Using this stage, a carbon nanofiber was subjected to mechanical loading and simultaneous electrical impedance characterization, which provides a means to derive fiber resistance measurements when a fiber is mechanically coupled using highly resistive contacts.

## INTRODUCTION

Electromechanical measurements on nanoscale fibers are of interest to enable integration of these materials into sensors and other microdevices. [1,2] Uniaxial testing is desirable in mechanical testing to ensure uniform loading throughout a fiber specimen [3,4], and to this end several devices have been developed to perform uniaxial mechanical testing on a nanofiber. [5-8] Furthermore, electrical coupling to a fiber specimen can allow thermomechanical characterization. The novelty of the device presented here lies in the ability to perform electrical measurement of a fiber specimen under mechanical loading, and mechanical loading of an electrically heated specimen.

## DESIGN

### Actuation

Stage actuation is realized by thermal expansion through Joule heating of a set of angled beams. Beams symmetrically connected to the stage ensure uniaxial motion and also serve as heat sinks. Using the actuator geometry and a plane strain condition, it was estimated through solid mechanics mathematical analysis that the thermal actuator would be capable of providing up to 400  $\mu$ N force. In order to avoid the specimen temperature changes caused by the actuator in [5,6], the moving specimen stage was separated from the thermal actuator and mechanically anchored.

### Mechanical Measurements

Tensile measurement is enabled by fixing a material specimen across a gap between the moving and fixed portions of the stage. The experiment reported here uses SEM observation as a direct means of measuring the carbon nanofiber strain. Microscopy

requires the interpretation of micrographs in order to derive strain data, which can be a slow process. Sensors could provide a faster approach to acquisition of strain data, and to that end, several indirect strain measurement mechanisms were built into the reported device. These alternative devices can be seen at left in Figure 2, and as built in the center of Figure 1. These measurement approaches include a diffraction grating, piezoresistive beam bending, and electron emission or gas ionization. All these approaches require further characterization. The diffraction grating is designed to measure submicron stage displacement by examination of a reflected laser beam. The electron or ion sensor works by comparing an electron or ion current arriving at a fixed and a moving electrode.

For the piezoresistive beam measurements, electrical current is carried in two of the polysilicon anchoring beams. As the stage moves, the beams bend, modifying the electrical resistance of each beam. This concept has been explored in [9], but experimental results thus far have been inconclusive.

The successful implementation of one of the displacement sensors above can be used in combination with bending of a beam to derive a measured force as applied to the fiber, as in the approach taken in [8]. Direct force measurement has not yet been implemented in this design. An alternative approach to force measurement can be developed from measurements of the actuator input power and the stage displacement. The simulation shown in Figure 4 indicates that at any given applied voltage, there is a linear relation between force and displacement. This suggests that it may be possible to develop a map that translates electrical and stage displacement data into force measurements.

### Electrical Characterization

Although two gold connections have been provided on the moving stage, they are electrically linked by the underlying polysilicon layer. Two separate electrical contacts were defined on the fixed side of the stage, effectively enabling a 3 point conductivity measurement. In practice, the difficulty of carbon nanofiber placement limited actual connections to only two: one on the moving stage, and one on the closest portion of the fixed stage. The fiber was mechanically clamped to the stage with amorphous carbon deposits created in an SEM, and these

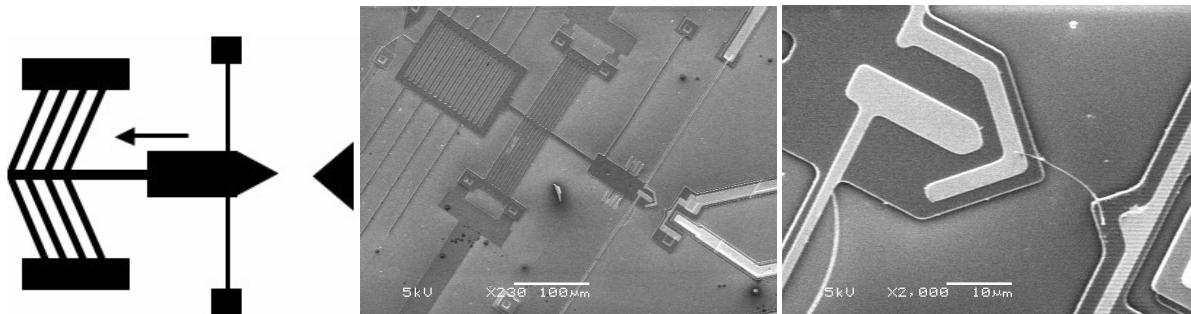


Figure 1. Left: Diagram of actuator and stage system. The moving stage at left is linked by bending beams to rectangular anchor points. A thermal actuator pulls the moving stage away from the fixed stage, at right. Center: SEM image of overall system. Right: Close-up of stage showing mounted carbon nanofiber, 120 nm diameter, before loading.

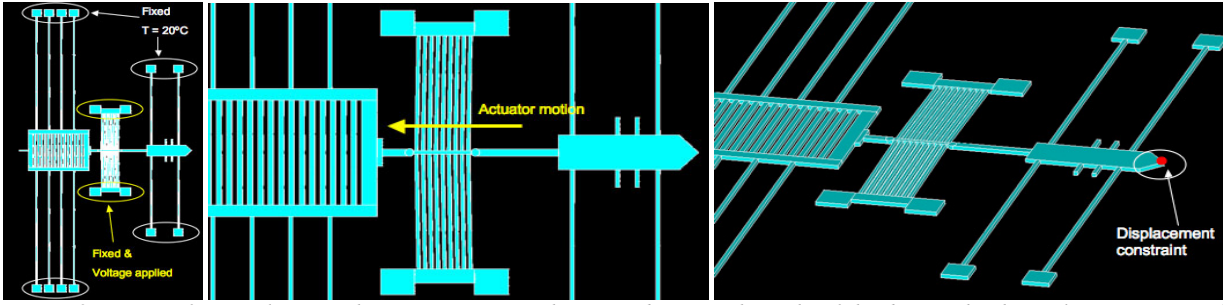


Figure 2: Layout for simulation. The moving stage is the pointed part at the right of the device, the thermal actuator is at the center, and the springs and large grating at the left were added to test several indirect means of displacement measurement.

amorphous carbon “welds” also served as the electrical connections. These amorphous carbon contacts present a high electrical resistivity, similar to the behavior of diamond-like carbon. Typically, only a very small amount of direct current can pass through these contacts. The structure of the contacts is one of a highly resistive material in a thin layer between two more conductive materials. In essence, these contacts are capacitors with lossy dielectrics. These capacitors lie in series with the fiber specimen, whose resistance is of interest in relation to strain behavior. Capacitors in a series circuit create a high-pass filter. At low frequencies and for DC currents, current must flow directly through the contacts and is therefore limited by the high resistance of the amorphous carbon contacts. As the frequency of an alternating current increases, the capacitors at the fiber contact points will begin to behave as if the contacts were shorted. Current at higher frequencies will capacitively couple across the contact points and the contact resistance will become irrelevant. A measurement of the AC circuit impedance will therefore be dominated by the resistance of the fiber and a reactance due to the contact capacitances.

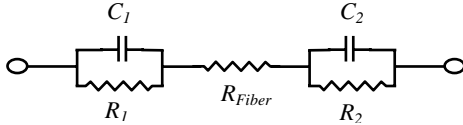


Figure 3. Circuit diagram for a fiber specimen with amorphous carbon contacts. Each contact has contact resistance  $R_1$  and  $R_2$ , and contact capacitance  $C_1$  and  $C_2$ . For fiber piezoresistive measurements, the resistance of the fiber  $R_{Fiber}$  must be resolved.

Although the electrical connection to the moving stage is made on a bending beam, the piezoresistive change experienced by this beam is not significant for measurement of the fiber specimen. This is possible because a gold layer patterned on top of the connecting beam provides much greater conductivity, and the carbon specimen is connected only to this gold layer. Consequentially, current will be conducted primarily in the gold layer and only to a small extent in the polysilicon layer. The circuit probing the nanofiber resistance has some inherent resistance, and there may be some temperature-induced variation of the mounting stage resistance as the stage is warmed by the actuator. However, the small cross-section of the nanofiber implies that the nanofiber itself should have a large resistance that dominates other circuit resistances except for contact resistances.

The circuit from the LCR meter to the fiber specimen and back will have some inductance  $L$  which may reduce the magnitude of the reactance observed. Inductive reactance  $X_L$  is proportional to angular frequency  $\omega$  and inductance, and capacitive reactance  $X_C$  is inversely proportional to angular frequency and capacitance  $C$ .

$$X_L = \omega L \quad X_C = -1/\omega C$$

When both inductance and capacitance are small, and the AC frequency is kept relatively low (below the MHz range), the capacitive reactance will have a much larger value than the inductive reactance, and will therefore dominate.

### Electrical Connections

Three electrical circuits are tied together by the moving stage. These are the thermal actuator circuit, the nanotube resistance measurement circuit, and, if desired, a displacement measurement circuit. If these circuits are not tied together at any other point, for instance if no more than one of the circuits is grounded, then the three circuits can operate independently.

Table 1. Polysilicon material properties used as simulation inputs. Data derived from references [10-12].

Material Properties of Polysilicon	
Thickness	3.5 $\mu\text{m}$
Electrical Resistivity	$4.0 \times 10^{-4} \Omega\text{-m}$
Thermal Conductivity	150 W/m-K
Poisson Ratio	0.29
Modulus of Elasticity	165 GPa
Coefficient of Thermal Expansion	$3 \times 10^{-6} /\text{K}$
Yield Strength	1.2 GPa
Density	$2.33 \times 10^3 \text{ kg/m}^3$

### SIMULATIONS

A simulation was performed to define the thermomechanical behavior of the system across a range of applied input voltages. The simulation used the values in Table 1, the structure in Figure 2, and a tetrahedral coupled-field element, SOLID98, in ANSYS 10.0 software. The simulation did not include the temperature dependence of polysilicon electrical resistivity. In order to estimate the force applied from the stage to a mounted nanofiber, a displacement boundary condition was assigned to the moving stage. When no displacement constraint is assigned, corresponding to the absence of a test specimen, the simulation provides a parabolic curve of displacement versus voltage, similar in shape to the measured behavior, Figure 4. The discrepancy between the two curves can be explained in that the voltage was measured some distance away from the actuator.

At fixed voltages, with varying displacement constraints, the moving stage exhibits a linear reaction force versus displacement. The actuator effectively serves as a variably stiffened spring. Force simulation as shown in Figure 4 indicates the analytical estimate of 400  $\mu\text{N}$  to be a reasonable order of magnitude for a zero micron displacement constraint. The actuator experimentally demonstrated  $>1.60 \mu\text{m}$  displacement, also in good agreement with the values estimated in Figure 4. At 15V, the simulation predicts a stage temperature of 229°C, significantly lower than the actuator temperature of 437°C.

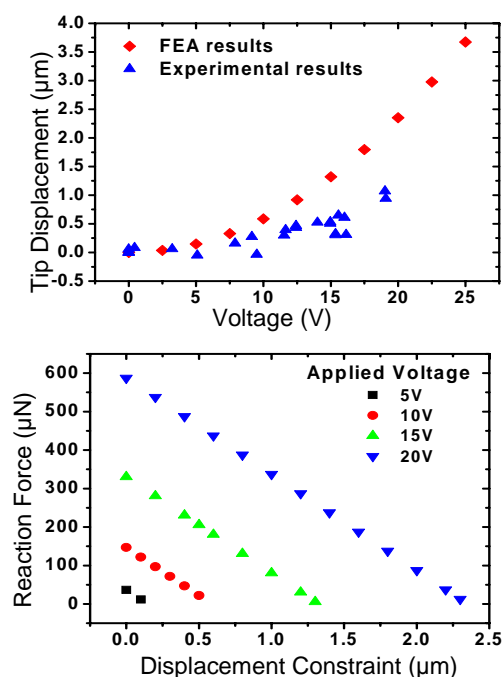


Figure 4. Simulation results. Top: Tip displacement versus voltage across the actuator for the freely moving stage. Bottom: Simulation output of the reaction force at the tip of the stage for different values of actuator voltage and constraints on the tip displacement.

## EXPERIMENTAL

The device was fabricated from polysilicon with Au contacts using the PolyMUMPs service from MEMSCAP, Inc. The polysilicon layers were released using a 3 minute etch in 48% HF<sub>(aq)</sub> followed by drying in a CO<sub>2</sub> supercritical dryer.

Nanotube-core carbon nanofibers were synthesized using Fe thin film catalyst in a thermal chemical vapor deposition (CVD) reactor at 725°C; they were subsequently ultrasonicated for 3 hours in a toluene solution and dried into the form of a mat. A 3-axis piezoelectric micro-manipulator (Kleindiek™) with a tungsten microscopy probe was used for separating an individual nanofiber from the mat using the procedures described in [13]. It was then transferred and glued on to the MEMS tensile stage by performing electron beam induced deposition (EBID) for 10 minutes with the JEOL JSM-6480LV scanning electron microscope in spot mode with 30 kV accelerating voltage. Subsequently, the device substrate was bonded to a chip carrier, with wire-bonding for electrical connections, and this system was mounted in an SEM.

A DC power supply provided electrical current to the thermal actuator, and voltage on the power supply was varied to control the amount of power delivered to the thermal actuator. Voltage and current supplied to the actuators were measured using a Hewlett Packard 34401A multimeter. Using an Agilent 4263B LCR meter, the fiber resistance and reactance were observed as strain was varied. For these measurements, coaxial connectors were used to tie together the voltage and current lines on each side of the measured specimen. The stage displacement and nanofiber length were extracted from SEM images using ImageJ software.

## RESULTS AND DISCUSSION

Before loading, DC resistance across the nanofiber was >10 MΩ. However, measurement at 100 kHz found 5.0 kΩ resistance and -55.5 kΩ reactance, indicating that contact resistance may dominate the DC measurement. The negative reactance indicates

that the reactance is dominated by the capacitance. If the capacitance is inferred from the total reactance, an inline capacitance of 28.7 pF is indicated by the measured reactance. This corresponds to a capacitance of 57.4 pF at each contact if both contacts are assumed to have equal dimensions and permittivities. Measurement at 10 kHz gave a value of 44 pF for inline capacitance.

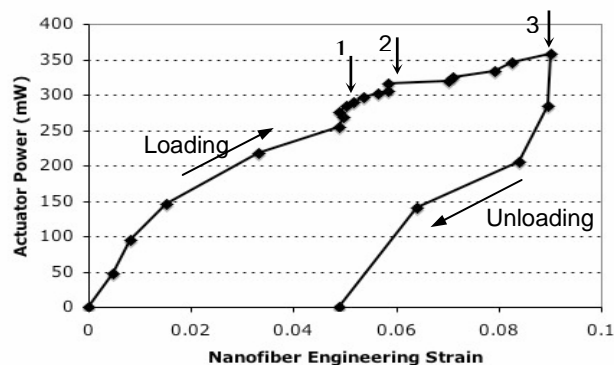


Figure 5. Strain determined from extension of the nanofiber from its length when completely unloaded. Following from the origin, the three marked inflection points indicate (1) where the fiber had straightened, (2) a point where the specimen resistance changed spontaneously under a constant strain, and (3) the point just after failure, seen at right in Fig. 7, where the fiber began to be unloaded.

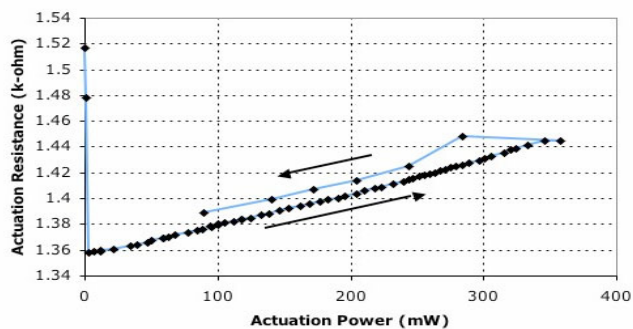


Figure 6. The polysilicon actuator shows a linear increase in electrical resistance with increasing input power, with a small hysteresis in resistivity upon reduction of the input power, possibly due to reduced loading from the nanofiber as the actuator power was reduced after the yielding of the fiber.

As the nanofiber was loaded, first it straightened and simultaneously elongated, until direct tensile load was applied to the length of the fiber. Failure eventually occurred in an outer layer of the fiber as seen in Figure 7. As the moving stage was allowed to return to its original position, the nanofiber buckled upon itself as seen in Figure 8, indicating that the failure seen in Figure 7 was not a complete fracture. In Figure 5 it can be seen that some strain was recovered as the fiber was unloaded, indicating that the observed nanofiber failure was a plastic deformation. Another interpretation of this data could be that the fiber moved out of the plane of observation as the stage was allowed to retract.

In Figure 6, it can be seen that the actuator resistance increases with the input power and therefore with the temperature of the actuator. This indicates that the thermomechanical simulation of the actuator could be more accurate if it were to include temperature-dependent electrical resistivity. However, the actuator

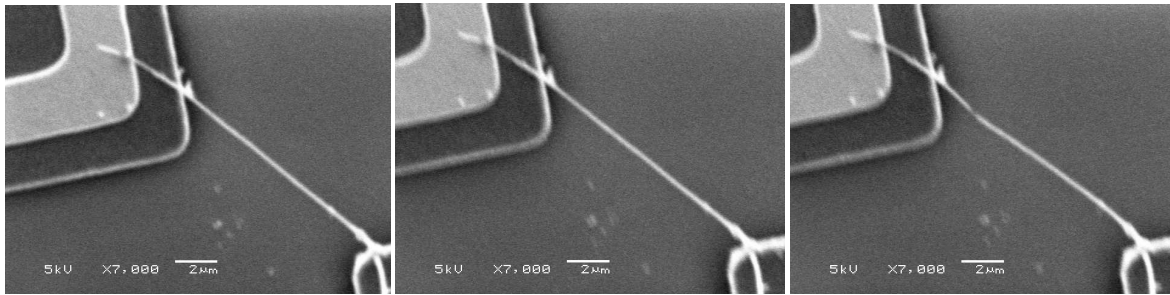


Figure 7: Tensile observation. Left: Slack removed from nanofiber before significant loading,  $R=5.01\text{ k}\Omega$  (measured at 100 kHz). Center: Nanofiber just before failure,  $\epsilon=5.3\%$ .  $R=4.98\text{ k}\Omega$ . Right: Failure of an outer layer.  $R=4.98\text{ k}\Omega$ . Reactances ranged from  $X=-54.7\text{ k}\Omega$  to  $-57.0\text{ k}\Omega$ . No significant trends in resistance or reactance were observed for this sample during the tensile test.

exhibits a hysteresis in resistance as the actuator is unloaded. A typical temperature-dependent resistance simulation would not account for this behavior. Some possible explanations of this hysteresis include a piezoresistive effect on the loaded actuators, or microstructural changes due to the elevated temperatures.

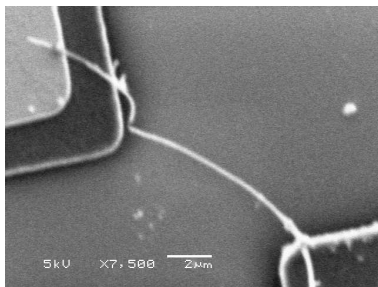


Figure 8. Image of the nanofiber after the moving stage has been allowed to return to its original position.

## CONCLUSIONS

A novel stage for electromechanical testing of micro and nanoscale fibers has been designed, simulated, and fabricated. Further thermal design is required to minimize fiber resistance measurement error due to stage temperature deviations caused by the thermal actuators.

For carbon nanofiber testing, specimens were placed using a micromanipulator and bonded using amorphous carbon deposited in an SEM. Specimen manipulation and placement, and derivation of strain data from micrographs are key limiting steps to data collection. The development of faster approaches to displacement measurement and to nanofiber placement is needed to improve the quality of mechanical characterization data of nanoscale fibers.

The use of AC two-point impedance measurements has been demonstrated as an approach to bypassing the high contact resistance from mechanical welds to tensile specimens. Impedance measurements may additionally provide an estimation of the capacitance of these welds.

## ACKNOWLEDGEMENTS

This research was supported by DARPA Award # HR0011-06-1-0048 and the DARPA Focus Center for Integrated Micro/NanoMechanical Transducers (iMINT Center) at the University of Colorado, Boulder. This material is based upon work supported under a National Science Foundation Graduate Research Fellowship, which supports J.J. Brown. The authors wish to thank NIST-Boulder and Paul Rice at the University of Colorado for help with the nanotubes and the micromanipulator.

## REFERENCES

- [1] A. Jungen, C. Stampfer, J. Hoetzel, V.M. Bright, C. Hierold, "Process integration of carbon nanotubes into microelectromechanical systems", *Sensors & Actuators A*, 130, 588 (2006).
- [2] C. Stampfer, A. Jungen, and C. Hierold, "Fabrication of discrete nanoscaled force sensors based on single-walled carbon nanotubes", *IEEE Sensors Journal*, 6, 613 (2006).
- [3] M.F. Yu, O. Lourie, M.J. Dyer, K. Moloni, T.F. Kelly, and R.S. Ruoff, "Strength and Breaking Mechanism of Multiwalled Carbon Nanotubes Under Tensile Load", *Science*, 287, 637 (2000).
- [4] M.-F. Yu, B.S. Files, S. Arepalli, and R.S. Ruoff, "Tensile Loading of Ropes of Single Wall Carbon Nanotubes and their Mechanical Properties", *Phys. Rev. Letters*, 84, 5552 (2000).
- [5] S. Lu, D.A. Dikin, S. Zhang, F.T. Fisher, J. Lee, and R.S. Ruoff, "Realization of nanoscale resolution with a micromachined thermally actuated testing stage", *Rev. Sci. Instr.*, 75, 2154 (2004).
- [6] S. Lu, Z. Guo, W. Ding, and R.S. Ruoff, "Analysis of a microelectromechanical system testing stage for tensile loading of nanostructures", *Rev. Sci. Instr.*, 77, 056103 (2006).
- [7] M. Kiuchi, S. Matsui, and Y. Isono, "Mechanical Characteristics of FIB Deposited Carbon Nanowires Using an Electrostatic Actuated Nano Tensile Testing Device", *Journal of Microelectromechanical Systems*, 16, 191 (2007).
- [8] Y. Zhu, A. Corigliano, and H.D. Espinosa, "A thermal actuator for nanoscale in situ microscopy testing: design and characterization", *Journal of Micromechanics and Microengineering*, 16, 242 (2006).
- [9] T.L. Waterfall, G.K. Johns, R.K. Messenger, B.D. Jensen, T.W. McLain, and L.L. Howell, "Observations of piezoresistivity for polysilicon in bending that are unexplained by linear models", *Sensors & Actuators A*, 141, 610 (2008).
- [10] T. Moulton and G.K. Ananthasuresh, "Micromechanical devices with embedded electro-thermal-compliant actuation", *Sensors and Actuators, A*, 90, 38 (2001).
- [11] C.-S. Oh and W.N. Sharpe, Jr., "Techniques for measuring thermal expansion and creep of polysilicon", *Sensors & Actuators, A: Physical*, 112, 66 (2004).
- [12] W.N. Sharpe, Jr., B. Yuan, R. Vaidyanathan, and R.L. Edwards, "Measurements of Young's modulus, Poisson's ratio, and tensile strength of polysilicon", *Proceedings of IEEE MEMS '97*, (1997), pp. 424-429.
- [13] G. Singh, P. Rice, K.E. Hurst, J.H. Lehman, and R.L. Mahajan, "Laser-induced exfoliation of amorphous carbon layer on an individual multiwall carbon nanotube", *Applied Physics Letters*, 91, 033101 (2007).

# RATE-DEPENDENT PULL-OFF FORCE – AN EXPERIMENTAL APPROACH TO IDENTIFY THE SEPARATION MODE IN MICROCONTACTS

L. Chen<sup>1</sup>, Y. Du<sup>2</sup>, N.E.McGruer<sup>3</sup>, and G.G.Adams<sup>3</sup>

<sup>1</sup>RF Micro Devices, Inc., Charlotte, North Carolina, USA

<sup>2</sup>Qualcomm, San Jose, California, USA

<sup>3</sup>Northeastern University, Boston, Massachusetts, USA

## ABSTRACT

In this paper, we report our observation of rate-dependence of the pull-off force in microcontacts. Two rate-dependent features have been observed during contact cycling tests. One is a larger pull-off force at a low rate (LFLR), and the other is a larger pull-off force at a high rate (LFHR). Further investigation using SEM demonstrates that these two rate-dependent features can be related to two distinct separation modes, i.e. brittle and ductile modes. LFLR behavior may be due to surface effects in brittle separation, whereas LFHR behavior could be due to viscous effects in ductile separation. By monitoring the rate-dependency of the pull-off force, the separation mode could be identified.

## INTRODUCTION

Applications of MEMS switches generally require reliable closing and opening of microcontacts over many billions of contact cycles [1]. During operation, topographical and/or material changes can alter the contact resistance and contact adhesion, leading to fail-to-close or fail-to-open switch failures. In order to study microcontact evolution, a scanning probe microscope (SPM) based contact tester was built [2]. Contact tests were performed between hemispherical contact bumps and planar substrates. The contact bumps were microfabricated on silicon test cantilevers. Both the bumps and substrates were coated with the contact test material. Using this contact tester, we have studied different contact materials [3], contact adhesion [4], and separation modes [5]. However in the previous studies, we were unable to identify the separation mode during the cycling test.

In general, there are two separation modes in microcontacts. One is the brittle mode in which rupture occurs abruptly with little or no plastic deformation. The other is the ductile mode in which rupture occurs more gradually with significant plastic deformation. Figure 1 shows typical differences in the force displacement curves for the two separation modes.

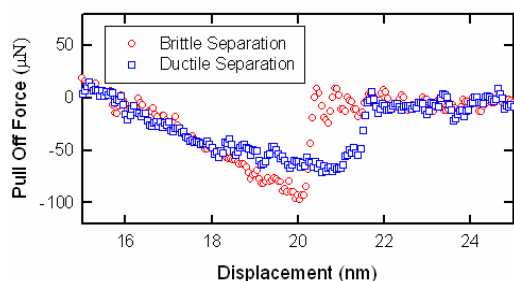
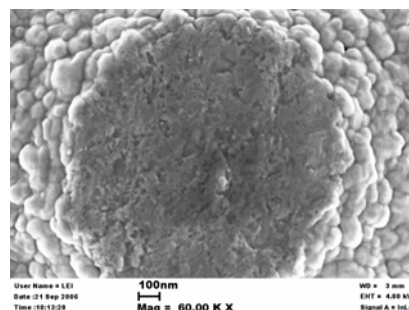


Figure 1: Force displacement curves for the two separation modes. Ductile separation shows a change in slope of the force vs. displacement characteristic due to plastic deformation and a gradual separation. Brittle separation shows a constant slope followed by a sudden separation with ringing of the cantilever. Both force-displacement curves were measured at an unloading rate of  $35\mu\text{m/s}$ .

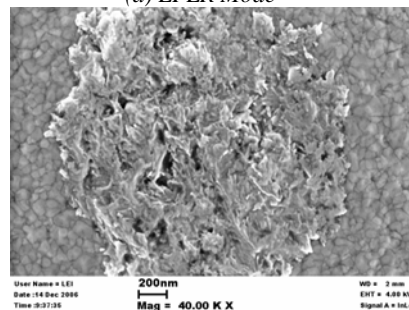
Depending on the separation mode, the surface morphology of the microcontacts can change, leading eventually to large changes in the pull-off force (the force needed to separate the contacts) [4, 5]. In this paper we report our observations of the *rate-dependence* of the pull-off force. In particular we find that the magnitude of the pull-off force depends on the cycling and separation rates, and this rate-dependence is related to the separation mode. This behavior allows the separation mode to be identified during testing without SEM observation.

## EXPERIMENT

To study the rate-dependent pull-off force, a 250 nm gold thin film was sputtered on the stiff test cantilever and also on the mating planar substrate. The tests were performed in laboratory air with a relative humidity of 30% to 40%. The cycling test uses an additional piezo-actuator to achieve a high cycling rate. The pull-off force is measured using the SPM. The rate-dependent pull-off force is studied by: (i) comparing the pull-off force at two cycling rates (0.5Hz and 300Hz); (ii) comparing rate-dependence at different loading; (iii) comparing the pull-off force by sweeping the cycling rate between 0.5Hz and 1000Hz; and, (iv) comparing pull-off force at different unloading rates.



(a) LFLR Mode



(b) LFHR Mode

Figure 2: SEM micrograph of gold contact bumps with a maximum loading force of  $200\mu\text{N}$ . (a) For the bump with a radius of curvature of  $4\mu\text{m}$ , the pull-off force at 0.5Hz is  $172\pm 11\mu\text{N}$  and the pull-off force at 300Hz is  $94\pm 9.5\mu\text{N}$ ; (b) For the bump with a radius of curvature of  $50\mu\text{m}$ , the pull-off force at 0.5Hz is  $130\pm 9.7\mu\text{N}$ , and the pull-off force at 300Hz is  $165\pm 7.2\mu\text{N}$ .

### Rate Switching Test

We first compared the pull-off force at two cycling rates (0.5Hz and 300Hz), by suddenly switching from one frequency to the other. The maximum contact force was controlled at 200 $\mu$ N during the cycling. After the test, the samples were inspected in the SEM. For gold contacts, we observed two distinctive rate-dependent features in the pull-off force. One feature shows a larger pull-off force at low cycling rates (LFLR). The other feature shows a larger pull-off force at high cycling rates (LFHR). SEM observation shows plastically flattened features (Figure 2a), at the surface of the contact in the LFLR mode. However, in the LFHR mode, ductile necks and/or signs of material transfer are always seen (Figure 2b).

### Force Sweeping Test

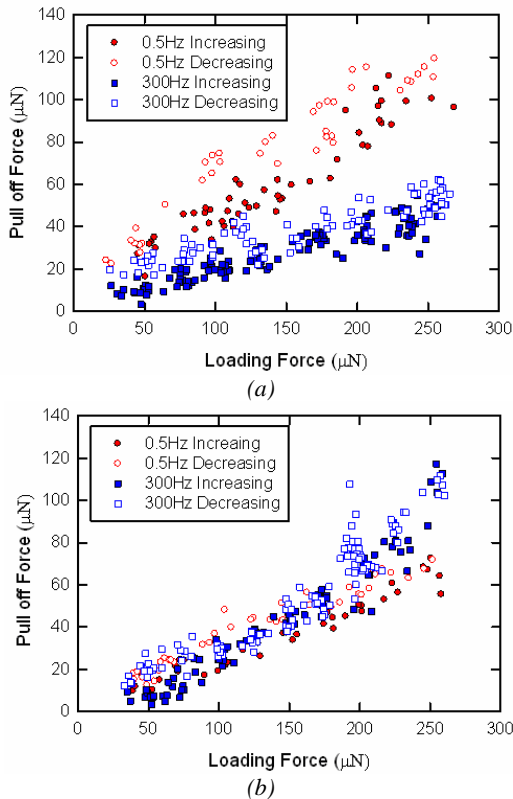


Figure 3: Rate-dependent pull-off force for separation with (a) larger force at low rate (LFLR), and (b) larger force at high rate (LFHR).

We then investigated the loading effects on the rate related pull-off force. The loading force was manually changed while cycling the contact. For one load sweep, the loading was increased from 0 to 250  $\mu$ N, and then decreased back to zero. Each sweeping process took about 120~180 seconds (without strict control). Two cycling rates were used, 0.5Hz and 300Hz. The load sweep was first performed at 0.5Hz, and then followed by the 300Hz test. The samples are gold bumps with radius of curvature of 15 $\mu$ m. The pull-off force was recorded during the cycling. The test results are shown in Figure 3. In both LFLR mode and LFHR mode, the pull-off force increases with an increase in the loading force. However, the response of the pull-off force is different in each mode according to the change in the loading.

In LFLR mode, as shown in Figure 3 (a), a larger pull-off force is measured at 0.5Hz than at 300Hz. The difference between the

two rates increases from 20 $\mu$ N at a loading of 150 $\mu$ N to 40  $\mu$ N at a loading of 250 $\mu$ N. It is also noted that the pull-off force, as the loading is decreased, is slightly higher than the force as the loading is increased. This is probably due to the wear of the surface film during the test.

On the other hand, in LFHR mode, as shown in Figure 3 (b), the pull-off force measured at the two rates (0.5Hz and 300Hz) are almost the same for a loading force less than 200 $\mu$ N. However, at loading forces greater than 200 $\mu$ N, the pull-off force measured at 300Hz becomes larger than the force measured at 0.5Hz. For a loading force of 250 $\mu$ N, there is a 40 $\mu$ N difference in the pull-off force between the two cycling rates. It is also noted that the increase of the pull-off force is more random in the LFHR mode than in the LFLR mode.

### Rate Sweeping Test

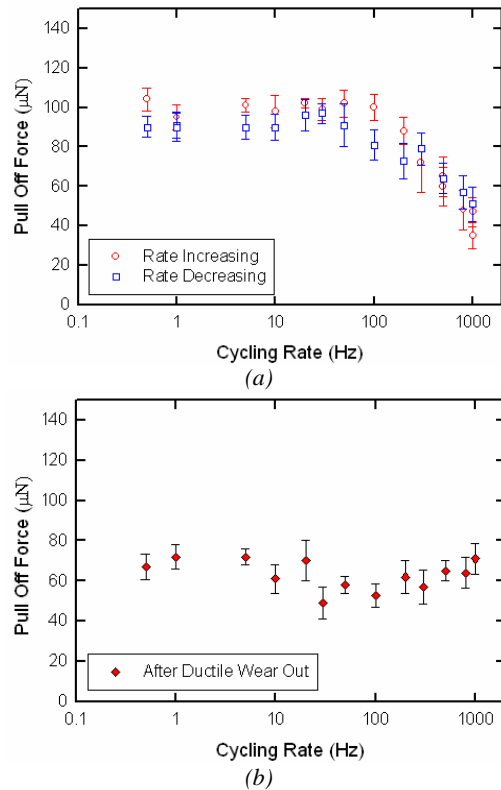


Figure 4: The rate-dependent response of the pull-off force by sweeping the cycling rate. The maximum loading force is maintained at 200 $\mu$ N. (a) is the pull-off force response for less than 10<sup>5</sup> cycles (LFLR); (b) is the response after 10<sup>6</sup> cycles of testing.

We also studied the rate-dependent pull-off force properties by sweeping the cycling rate from 0.5Hz to 1000Hz. The sample used for test was a gold bump with a radius of curvature of 15 $\mu$ m. During the test, the maximum loading force was controlled at 200 $\mu$ N. The cycling rate was increased from 0.5Hz to 1000Hz, and then decreased back to 0.5Hz. During the rate sweep, 13 different cycling rates were tested. At each cycling rate, the sample was cycled for 30 seconds for pull-off force measurement. The sampling rate for data acquisition was 500k/s for cycling rates of 100Hz~1000Hz 50k/s for the rates of 10~100Hz, and 2k/s for the rates of 0.5Hz~10Hz respectively.

One such result is shown in Figure 4. A LFLR mode is clearly

demonstrated in Figure 4 (a). It is shown that the pull-off force is constant at a low cycling rate, and starts to decrease for cycling rates larger than 100Hz. The pull-off force changed from 100 $\mu$ N measured at 0.5Hz to 40  $\mu$ N measured at 1000Hz. A rate of 100Hz appears to be a transition point during the rate sweeping test. It is also noted that such a transition feature can disappear after a certain number of cycles. Figure 4(b) shows the same rate sweeping test result from the same contact after being cycled for 10<sup>6</sup> times. There is no clear rate-dependent feature, and the pull-off forces measured at different rates were similar. After this test, the contact surface was inspected in the SEM. The SEM images show damage or material transfer on the contact surface. Surface wear could be the reason for the disappearance of the LFLR features.

We found that it was not easy to observe the LFHR mode during the rate sweeping test. However, we were able to characterize the LFHR mode by using the unloading rate test.

### Unloading Rate Test

The unloading rate test is performed by using a series of pulse signals. Each signal has the same rise time (10ms), the same resting time (10ms), but different unloading times. The unloading rate is related to the unloading time. A longer unloading time provides a lower unloading rate. By varying unloading time, eight unloading rates, from 0.05 $\mu$ m/s to 50 $\mu$ m/s, have been tested. At each unloading rate, the pull-off force is measured with two different maximum loading forces (100 $\mu$ N and 200 $\mu$ N). Some results are shown in Figure 5. It is clear that a LFHR feature was recorded. At a maximum loading of 200 $\mu$ N, the pull-off force increased with an increase of the unloading rate. However, such a trend is not clear at a lower loading (100 $\mu$ N).

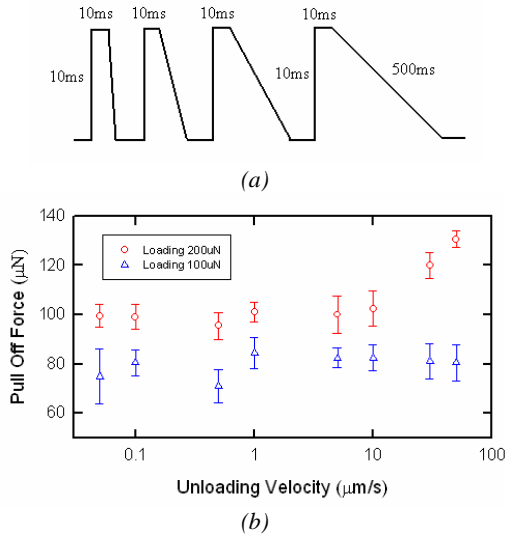


Figure 5: Pull-off force test with different unloading velocity. (a) The driving waveform for the test. Each pulse with the same loading time and the same time in contact, but with different unloading time; (b) measured unloading rate-dependent pull-off force in the LFHR mode.

## DISCUSSION

According to our rate-dependent pull-off force contact tests, there are two different rate-dependent features that have been identified. One feature shows a larger pull-off force at low cycling rates (LFLR). The other feature shows a larger pull-off force at high cycling rates (LFHR). Based upon our SEM inspection, the

contacts with LFLR features usually have plastically flattened surfaces. However, for the samples found with LFHR features, surface damage has always been observed. These observations suggest that the LFLR mode is associated with brittle separation, and the LFHR mode is associated with ductile separation.

For a brittle separation, the magnitude of the pull-off force depends on the bonding strength at the interfaces. The longer time in contact, the stronger bonding could develop, which in turn leads to a larger pull-off force to separate the contacts. Observed LFLR features could be due to the contact time and load effects on the interfacial bonding strength.

A simple calculation shows a possible surface film effect in the LFLR mode. Assuming elastic separation in LFLR mode, the pull-off force  $F_{pulloff}$  can be estimated by using the JKR contact adhesion model:

$$F_{pulloff} = 1.5\pi wR \quad (1)$$

where  $R$  is the radius of curvature of the contact bump, and  $w$  is the work of the adhesion. In our contact test, we observed a plastic deformation region on top of the contact bump. Due to plastic deformation, the effective asperity radius of curvature  $R_{eff}$  after elasto-plastic or fully plastic deformation is different than its initial value  $R$ . Correspondingly, the pull-off force can be expressed in term of  $R_{eff}$ ,

$$F_{pulloff} = 1.5\pi wR_{eff} \quad (2)$$

Further assuming that all the plastic deformation occurs during the first cycle of loading, the unloading and the next cycle of loading are elastic. To estimate the effective radius of curvature after a single loading event, we use the Kogut-Etsion (KE) curve-fit solutions from finite element analysis [6]. Based upon the KE model, the bump with original radius of curvature  $R=15\mu$ m, hardness  $H=500$ MPa, and loading force 200 $\mu$ N, the effective radius of curvature  $R_{eff}$  can be calculated as 45 $\mu$ m. Using Equation (2), we calculated that the work of adhesion is 0.37J/m<sup>2</sup> for 80  $\mu$ N pull-off force; the work of adhesion is 0.18J/m<sup>2</sup> for 40 $\mu$ N pull-off force. These works of adhesion are much smaller than the work of adhesion between clean metal contacts (1~3J/m<sup>2</sup>). This calculation indicates that there are surface films between the gold contacts. These interposed films usually lower the surface energy and can keep the separation in the brittle mode.

The kinetics of forming or destroying the interposing surface film could contribute to the observed LFLR rate-dependent features. Since gold is a hydrophilic surface and the tests were all done in room air, such surface film effects could be due to the meniscus force effect.

For a meniscus effect, there is a time constant for forming meniscus bridges. The experiments by Szoszkiewicz [7] have shown that at 37% relative humidity, the mean meniscus nucleation time is around 0.7~4.2ms at room temperature. For contact times less than the mean nucleation time, the number of menisci formed will be reduced. The longer the time in contact, the more menisci can be developed, hence the larger meniscus force. Our rate sweeping experiment shows that the pull-off force drops when the cycling rate is larger than 100Hz. This may indicate the equilibrium time for meniscus condensation is about 5ms, which is in the range of the meniscus nucleation time scales observed by Szoszkiewicz. Further increasing the cycling rate could cause some meniscus bridges to fail to nucleate.

Furthermore, we can verify that, in LFLR mode, the measured difference in pull-off force at two rates is of the same magnitude as the meniscus force effect. It was shown that the force difference

between the high cycling rate and low cycling rate is in the range of 20~60 $\mu$ N. For a water thin film between a hemispherical bump and a flat surface, the meniscus force can be estimated by:

$$F_m = 4\pi R \gamma_{lv} \cos\theta \quad (3)$$

where  $\gamma_{lv}$  is surface tension of water film, equal to 72.7dyn/cm. Since there is an intrinsic layer of water thin film on a gold surface, the contact angle is chosen as zero. Using an effective radius of 45 $\mu$ m, the meniscus force can be calculated as 40 $\mu$ N, which is the force difference between 0.5Hz and 300Hz. Both the transition time and the magnitude of the force suggest that the LFLR effect could be due to the meniscus force effect in brittle separation. The LFLR feature could be used to identify a brittle separation.

On the other hand, ductile separation is usually associated with bulk material stretching and nanostructure separation. Such nanostructure separation could activate viscous effects in the gold. Usually, for inelastic deformation in a metal, time-independent yield flow is the dominant deformation mechanism. The yield flow is activated by nucleation of dislocations, which defines the perfectly plastic behavior observed in macroscopic crystalline metal. However, when the structure scale reduces to the nanoscale, the dislocation sources are largely reduced. Under this situation, a time-dependent "creep" flow becomes dominant. In "creep" flow, diffusion is a dominant mass transport mechanism. The low barrier height for atom diffusion around the nanostructure allows atoms to move fast on the surface. Surface tension driven diffusion has been observed in the separation of Au/Au [8] and Pb/Au [9] nano junctions. Even though it is unrealistic to assume the nano junction is a liquid, it is believed that at the last stage of the separation, (when the neck is narrowing down to several nanometer), the junction behaves like a "liquid" [10].

Due to the "creep" flow in nanojunctions, we would expect a viscous effect in ductile separation. Such viscous effects could be the reason for observed LFHR features, which gives a larger pull-off force at a high cycling rate. In particular, we found that, by increasing the unloading rate, independent of the cycling rate, the pull-off force increased in the LFHR mode.

In ductile separation, the magnitude of the pull-off force is then related to the volume of the ductile area. The increase in the pull-off force in the LFHR mode may indicate an increase of the ductile area.

Two features in LFHR mode have been observed: (1) the force increase in LFHR mode is random. This could be due to a random distribution of the ductile area. (2) In the LFHR mode, a larger pull-off force is observed at large loading and a high unloading rate. This could be because larger loading can activate more ductile region and lead to larger viscous effects.

## CONCLUSION

Two rate-dependent pull-off force features have been observed in gold micro contacts. One is a larger pull-off force at low rate (LFLR), and the other is larger pull-off force at high rate (LFHR). We found that the rate-dependent features could be related to two separation modes: brittle and ductile.

For LFLR features, the rate dependences may be due to surface effects during brittle separation. Longer contact times at lower rate can help to develop a larger surface force between contacts. Since all these tests were performed in room air with 30%~40% humidity, such surface effects could be due to menisci between contacts. We found that the measured force and rate features are consistent with the characteristics of meniscus condensation. SEM inspections show that the contact surfaces in LFLR usually are plastically flattened.

For LFHR features, the rate effects could be due to the viscous effects in ductile separation. During the ductile separation, there are nano tips drawn out of the surfaces. Surface tension driven diffusion in these nanostructures causes viscous effects during separation. The viscous effects can lead to a larger pull-off force at a higher unloading rate. We observed that the increase of pull-off force in the LFHR mode has considerable scatter. This could be due to the random nature of ductile separation. In general, once the ductile separation has been identified during the cycling test, the surface is found to be damaged. SEM inspection shows that the contact surfaces in LFHR mode are rough, with significant wear and sharp peaks characteristic of ductile separation.

The significance of this work is the identification of the rate-dependence of the pull-off forces in metal contacts and its relation to the separation modes. By monitoring rate-dependent features during cycling tests, the separation mode can be identified in situ. This method can be a useful technique for metal contact microswitch reliability studies.

## REFERENCES

- [1] M. Rebeiz, J.B. Muldavin, "RF MEMS Switches and Switch Circuits", *IEEE Microwave Magazine*, 12, 59 (2001).
- [2] L. Chen, N.E. McGruer, and G.G. Adams, "AFM-Based Testing and Measurements of Contact and Stiction in a Micromechanical Switch" in *Proc., ASME/STLE Inter. Joint. Tribol. Conf., Long Beach, California USA, TRIB 2004-64347* (2004).
- [3] L. Chen, H. Lee, Z.J. Guo, N.E. McGruer, K.W. Gilbert, S.Mall, K.D. Leedy, and G.G.Adams, "Contact Resistance Study of Noble Metals and Alloy Films Using a Scanning Probe Microscope Test Station", *Journal of Applied Physics*, 102, 074910 (2007).
- [4] N.E. McGruer., G.G. Adams, L. Chen, Z. Guo, and Y. Du, "Mechanical, Thermal, and Material Influence on Ohmic-Contact-Type MEMS Switch Operation", in *Proc. IEEE Microelectromech. Syst., Turkey, 1* (2006), pp. 230-233.
- [5] Y. Du, L. Chen, N.E. McGruer, G.G. Adams, I. Etsion, "A Finite Element Model of Loading and Unloading of an Asperity Contact with Adhesion and Plasticity", *Journal of Colloid and Interface Science*, 312, 522 (2007).
- [6] L. Kogut and I. Etsion, "Adhesion in Elastic-Plastic Spherical Microcontact", *Journal of Colloid and Interface Science*, 261, 372 (2003).
- [7] R. Szoszkiewicz and E. Riedo, "Nucleation Time of Nanoscale Water Bridges", *Physical Review Letter*, 95, 135502 (2005).
- [8] T. Kizuka, "Atomic Process of Point Contact in Gold Studied by Time-Resolved High-Resolution Transmission Electron Microscopy", *Physical Review Letters*, 81, 4448 (1998).
- [9] L. Kuipers and J.W.M. Frenken, "Jump to Contact, Neck Formation, and Surface Melting in Scanning Tunneling Microscope", *Physics Review Letters*, 70, 3907 (1993).
- [10] N. Agrait, A.L. Yeyati, and J.M. van Ruitenbeek, "Quantum Properties of Atomic-Sizes Conductors" *Physics Reports*, 377, 81 (2003).

# TRACKING MICRORESONATOR Q-FACTOR IN CLOSED-LOOP OPERATION

*J.H. Seo, K.S. Demirci, S. Truax, L.A. Beardslee and O. Brand*

School of Electrical and Computer Engineering, Georgia Institute of Technology, Atlanta, Georgia, USA

## ABSTRACT

A method to extract and track the quality factor (Q-factor) of microresonators in closed-loop operation is presented. The proposed Q-factor tracking approach relies on a controlled stiffness modulation of the resonator introduced by a second feedback loop and, thus, solely requires frequency measurements. Furthermore, the proposed concept is applicable to all resonant microstructures featuring excitation and detection elements. The feasibility of the proposed method is verified experimentally by tracking the Q-factor variations of a micromachined resonator caused by ambient temperature changes.

## INTRODUCTION

In resonant sensors utilizing a frequency output, the Q-factor is one of the key parameters, which affects the (short-term) frequency stability and, thus, the sensor resolution. The Q-factor is related to the mechanical properties of the resonator, namely its stiffness, mass, and damping. Any property variation of the microresonator in response to a measurand results in a quality factor change. Therefore, the Q-factor can be used to investigate the response of a resonant sensor to environmental changes. This fact has been exploited by using the Q-factor to sense e.g. temperature [1, 2], fluidic properties such as viscosity and density [1, 3, 4], and pressure [5]. By measuring both resonance frequency and quality factor changes, simultaneous sensing of multiple measurands becomes possible.

The Q-factor change of a resonator is generally detected either by measuring its oscillation amplitude [2] or its open-loop transfer characteristic [4]. Approaches based on an amplitude measurement require precise A/D conversion, in which case the advantages of a resonant sensor are not fully utilized. Methods based on the open-loop transfer characteristic of the resonator typically require expensive equipment, such as a network analyzer, and continuous in-situ monitoring of Q during normal sensor operation is not feasible.

In this work, we propose a new Q-factor extraction and tracking method in closed-loop operation based on a controlled stiffness change of the resonator, relying solely on frequency data. Thereby, the Q-factor is measured along with the measurand-induced frequency shift during normal sensor operation. This simultaneous operation allows realization of multi-functional resonant sensing systems, in which environmental (e.g. temperature) changes as well as the main measurand of a resonant sensor are detected at the same time without need for additional sensing devices.

## PRINCIPLE OF Q-FACTOR TRACKING

In a sensing application, the microresonator is generally incorporated in an amplifying feedback loop as the frequency-determining element, and the measurand can simply be detected by measuring the resonance frequency change using a frequency counter. To sustain the harmonic oscillation of a microresonator at a specific resonance mode, the excitation force generated by the feedback loop is phase matched with the vibration velocity of the resonator to compensate for the damping force (see main loop in Fig. 1). This way, the effective damping coefficient of the overall

closed loop system becomes zero and a self-sustaining oscillation can be initiated and maintained.

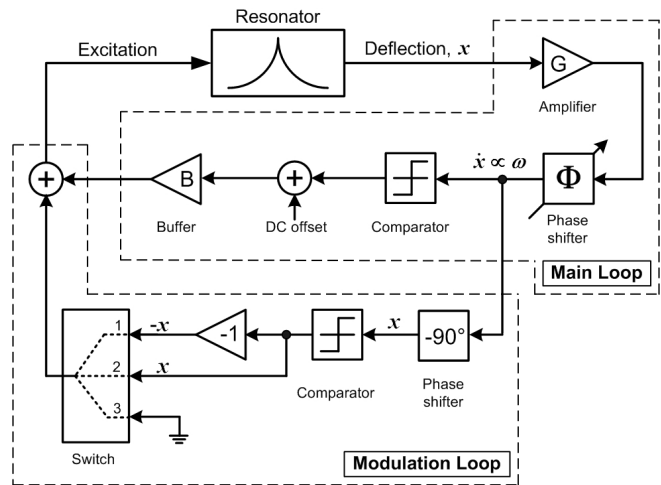


Figure 1: Schematic diagram of feedback circuitry with main loop and modulation loop for the proposed Q-factor tracking.

If an excitation force having the same phase as the resonator deflection signal is generated by a secondary electronic feedback loop (see modulation loop in Fig. 1) and applied to the resonator in addition to the force generated by the main loop, the effective stiffness of the resonator can be modulated by the additional feedback loop [6]. Depending on the direction of the applied force with respect to the resonator deflection, the effective stiffness of the resonator can be either reduced or increased. As a result, the resonance frequency of the harmonic oscillator is changed in response to the modulated effective stiffness.

This effective stiffness modulation method has been applied to extract relative stiffness changes of a microresonator for temperature compensation [7]. To extract the relative stiffness change, the additional feedback loop was composed of a phase shifter and a linear amplifier. A more detailed description of the above mentioned method can be found in [8].

If the linear amplifier of the modulation loop is replaced by a comparator, relative Q-factor changes  $\Delta Q/Q$  can be extracted by analyzing the frequency changes caused by the additional feedback loop. Using the describing function of a comparator, defined as the complex ratio of the fundamental harmonic component of the comparator output signal to its input sinusoidal signal [9], the motion of a resonator with enabled modulation loop can be described by Eq. (1). Thereby, the microresonator is approximated by a simple second-order system consisting of mass  $m$ , damper  $b$  and spring  $k$ .

$$m\ddot{x} + b\dot{x} + kx = \psi_{main} \frac{\dot{x}}{|\dot{x}|} + \psi_{mod} \frac{x}{|x|} \quad (1)$$

The force amplitudes  $\psi_{main}$  and  $\psi_{mod}$  in Eq. (1) are defined as:

$$\psi_{main} = \chi\gamma \frac{4M_{main}}{\pi}, \quad \psi_{mod} = \chi\gamma \frac{4M_{mod}}{\pi} \quad (2)$$

Here,  $\chi$  is the transfer function of the generated mechanical force to an applied electrical excitation signal,  $\gamma$  is the transfer function of the electrical read-out signal to the resonator deflection, and  $M_{main}$  and  $M_{mod}$  are the amplitudes of the square wave signals generated by the main loop and modulation loop, respectively. By combining Eqs. (1) and (2), the system equation for the resonator shown in Fig. 1 is expressed by:

$$m\ddot{x} + \left[ b - \frac{\psi_{main}}{|\dot{x}|} \right] \dot{x} + \left[ k - \frac{\psi_{mod}}{|x|} \right] x = 0 \quad (3)$$

Considering that the force generated by the main feedback loop is the same as the damping force to sustain a harmonic oscillation at the mechanical resonance frequency, the magnitude of the steady-state vibration velocity  $\dot{x}$  and the vibration amplitude  $x$  of the resonator embedded in the feedback circuit are obtained from Eq. (3) by forcing the effective damping force (second term in Eq. (3)) to zero, i.e.  $|\dot{x}| = \psi_{main} b^{-1}$  and  $|x| = \psi_{main} b^{-1} \omega^{-1}$  (with  $|\dot{x}| = \omega |x|$ ). Thus, the equation of motion becomes:

$$m\ddot{x} + \left[ k - \frac{\psi_{mod}}{\psi_{main}} b \omega \right] x = 0 \quad (4)$$

Using the relation  $Q = k b^{-1} \omega^{-1}$ , Eq. (4) can be expressed by:

$$m\ddot{x} + \left[ k \left( 1 - \frac{\psi_{mod}}{\psi_{main}} \frac{1}{Q} \right) \right] x = 0 \quad (5)$$

If the amplitudes of the excitation signals generated by the main and modulation loops are equal, i.e.  $\psi_{main} = \psi_{mod}$ , Eq. (5) is simplified to:

$$m\ddot{x} + \left[ k \left( 1 - \frac{1}{Q} \right) \right] x = 0 \quad (6)$$

Eq. (6) shows that the relative stiffness change induced by the modulation loop is related to the Q-factor of the resonator. In fact, the stiffness is modified by a factor of  $(1 - Q^{-1})$  by the modulation loop in Fig. 1.

Depending on the polarity of the signal in the modulation loop, either positive or negative effective stiffness changes can be produced resulting in an increase or decrease of the resonance frequency. Assuming that the additional spring force caused by the modulation loop has a spring constant of  $C$ , the resonance frequencies with positive and negative stiffness modulation, respectively, become:

$$\omega_{pos} = \sqrt{\frac{k+C}{m}}, \quad \omega_{neg} = \sqrt{\frac{k-C}{m}} \quad (7)$$

From the ratio of the frequencies  $\omega_{pos}/\omega_{neg}$ , the Q-factor of the resonator can be calculated:

$$Q = \frac{\alpha+1}{\alpha-1}, \quad \alpha = \left( \frac{\omega_{pos}}{\omega_{neg}} \right)^2 \quad (8)$$

Therefore, the Q-factor (or the relative Q-factor change) of a microresonator can be extracted and tracked by measuring the resonance frequency changes caused by the periodically enabled modulation loop of Fig. 1.

It should be noted that Eqs. (1)-(9) only hold when the excitation signals generated by main and modulation loop are exactly phase matched with the vibration velocity  $\dot{x}$  and the deflection of the resonator  $x$ , respectively. In a real system, the phase-tuning is done by an electronic circuit, such as an all-pass filter, and there is a possibility of a tuning error, which will introduce an error in the estimated Q-factor. However, the error caused by the phase tuning can be minimized if both the positive and the negative frequency changes induced by the modulation loop are used in extracting the relative Q-factor change of the resonator.

## EXPERIMENTAL SETUP

To verify the feasibility of the proposed Q-factor tracking method, the experimental setup shown in Fig. 2 has been implemented.

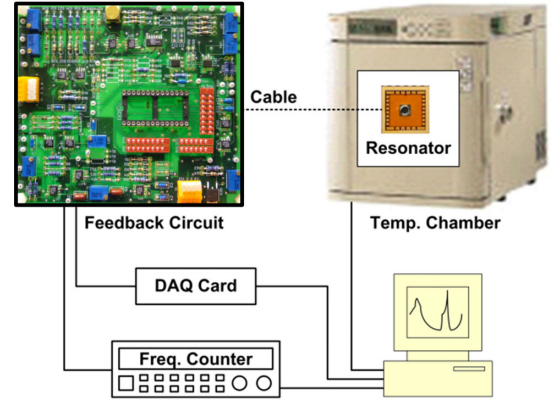


Figure 2: Schematic diagram of the experimental setup.

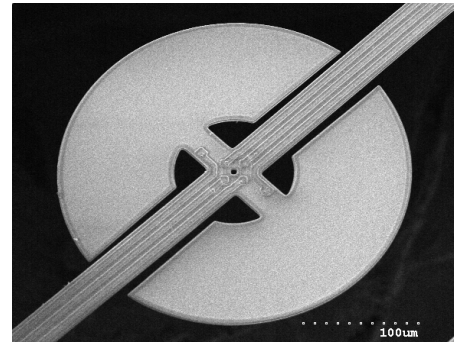


Figure 3: SEM photograph of silicon-based disk-type resonator with electrothermal excitation and piezoresistive detection elements.

In the experiment, the temperature of the microresonator is varied to introduce a Q-factor change. A custom-made printed circuit board includes the feedback circuitry shown in Fig. 1. A disk-type resonator [10] with on-chip electrothermal excitation and piezoresistive detection elements (see Fig. 3) is placed inside an ESPEC SH-241 environmental test chamber. A LabView program controls the switch position shown in Fig. 1 via a National Instruments DAQ card and reads the chamber temperature and resonance frequency of the resonator.

## RESULTS

During the measurements, the negative and positive stiffness modulation loops (switch position 1 and 2 in Fig. 1) are enabled for 2 seconds each, every 54 seconds (see Fig. 4). To prevent variations in resonance frequency by different static power dissipations with enabled and disabled modulation loop, the static power dissipation produced by the electrothermal excitation elements is kept constant during the experiment.

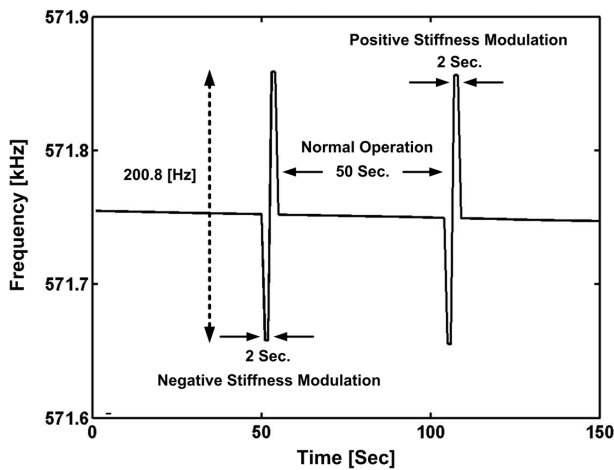


Figure 4: Resonance frequency of disk-type resonator with periodically enabled positive/negative stiffness modulation at a temperature of  $\approx 10^\circ\text{C}$ .

The disk-type resonator with a 571.8 kHz resonance frequency showed a frequency change ( $f_{\text{pos}} - f_{\text{neg}}$ ) of approximately 200.8 Hz at  $10^\circ\text{C}$  by the enabled modulation loop (see Fig. 4). As the ambient temperature increases, the frequency difference  $f_{\text{pos}} - f_{\text{neg}}$  also increases (see Fig. 5), indicating that the Q-factor of the resonator is inversely proportional to the temperature. The extracted Q-factor from Eq. (8) is plotted in Fig. 6 as solid lines when the disk resonator is subjected to temperature variations between  $-20^\circ\text{C}$  and  $40^\circ\text{C}$ . The Q-factors extracted from open-loop transfer characteristics of the disk resonator are plotted in Fig. 6 (symbols) for comparison.

A slight discrepancy between closed-loop and open-loop Q-factor values is observed in Fig. 6. This difference is believed to be caused by experimental errors in extracting the Q-factor of the disk resonator from open-loop measurements. The open-loop Q-factors of the disk resonator were measured only twice at the same temperature and show considerable variations (see Fig. 6). On the contrary, Q-factors estimated using the proposed stiffness modulation showed quite good repeatability and small variations over the temperature range from  $-20$  to  $40^\circ\text{C}$ . Furthermore, a slight slope change in the temperature dependence of the Q-factors is noticeable around  $12^\circ\text{C}$ ; the origin of this effect is not fully

understood yet and requires further investigation.

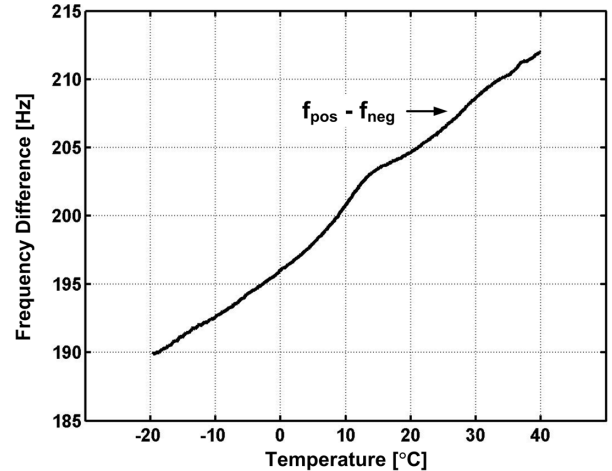


Figure 5: Frequency difference  $f_{\text{pos}} - f_{\text{neg}}$  between resonator with positive and negative stiffness modulation as a function of temperature.

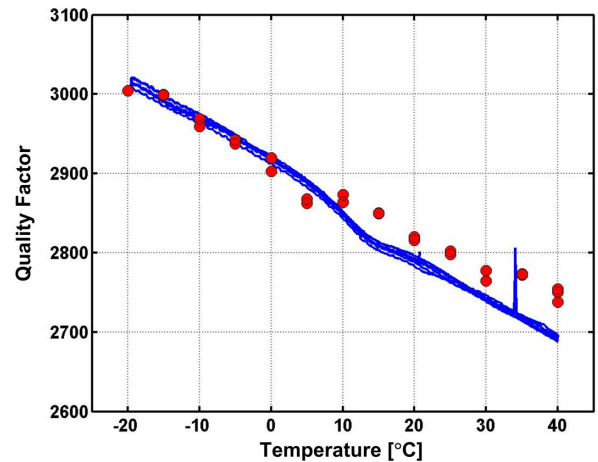


Figure 6: Comparison of quality factor extracted from Eq. (8) (solid lines) and from 3-dB bandwidth of the open-loop amplitude transfer characteristic (symbols) as a function of ambient temperature.

As a possible application of the proposed Q-factor extraction method, the extracted Q-factor change is used for temperature compensation of the microresonator using the almost linear relationship between Q-factor and temperature (see Fig. 6). The relation between temperature and Q-factor is first determined during an initial calibration step and then used to extract the temperature-induced frequency drift of the disk-type resonator. Fig. 7 shows the resonance frequency of the disk-type resonator as a function of temperature before and after temperature compensation. In this experiment, the resonator temperature is varied from  $30^\circ\text{C}$  to  $60^\circ\text{C}$ . The disk-type resonator showed relative frequency changes around 1000 ppm over the  $30^\circ\text{C}$  temperature range, while the temperature compensated frequency change was less than 50 ppm. In other words, the temperature coefficient of the resonance frequency is reduced from 33 to less than  $2 \text{ ppm}/^\circ\text{C}$ .

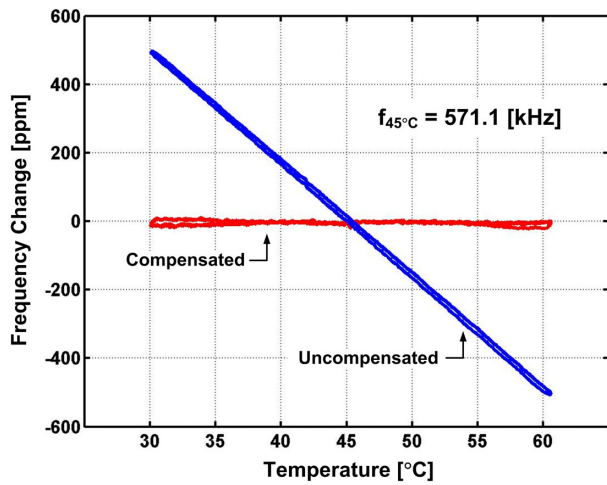


Figure 7: Relative resonance frequency change of disk-type microresonator as a function of temperature without temperature compensation (blue line) and with temperature compensation based on the Q-factor (red line); the reference frequency is 571.1 kHz at 45°C.

## DISCUSSION

As mentioned earlier, a similar controlled-stiffness-modulation method has been used to extract the relative stiffness change of a resonator [7]. By combining the method presented in [7] and the Q-factor estimation method described in this paper, the relative stiffness change and the relative Q-factor change of a resonator can be estimated at the same time without disturbing the oscillation of a resonator at its mechanical resonance frequency. Once the relative stiffness, Q-factor and frequency changes are extracted, the changes of the remaining mechanical properties ( $m$ ,  $b$ ) of the resonator can be estimated using:

$$\frac{\Delta m}{m} = \frac{\Delta k}{k} - 2 \frac{\Delta \omega}{\omega} \quad (9)$$

$$\frac{\Delta b}{b} = \frac{\Delta k}{k} - \frac{\Delta Q}{Q} - \frac{\Delta \omega}{\omega} \quad (10)$$

Thus, potentially all system constants of a resonator can be monitored using the proposed Q-factor tracking method in combination with the approach to extract stiffness changes [7].

## SUMMARY

A method for extracting and tracking the Q-factor of a resonator during closed-loop operation at its mechanical resonance frequency is proposed and verified experimentally. The proposed method solely requires frequency measurements and can be

implemented easily and cost effectively using a simple electronic feedback loop, thus avoiding expensive equipment for Q-factor measurement. By combining the Q-factor tracking method with a method for extracting relative stiffness changes, all system parameters of a resonator can potentially be monitored.

## ACKNOWLEDGEMENTS

The authors would like to thank the staff of the Georgia Tech Microelectronics Research Center for their help. This work has been funded in part by the National Science Foundation under award 0601467.

## REFERENCES

- [1] M. K. Jain, S. Schmidt, and C. A. Grimes, "Magneto-Acoustic Sensors for Measurement of Liquid Temperature, Viscosity and Density," *Applied Acoustics*, vol. 62, pp. 1001-1011, 2001.
- [2] M. A. Hopcroft, M. Agarwal, K. K. Park, B. Kim, C. M. Jha, R. N. Candler, G. Yama, B. Murmann, and T. W. Kenny, "Temperature Compensation of a MEMS Resonator Using Quality Factor as a Thermometer," *Proc. IEEE Conf. Micro Electro Mechanical Systems (MEMS 2006)*, pp. 222-225, 2006.
- [3] S. J. Martin, R. W. Cernosek, and J. J. Spates, "Sensing Liquid Properties with Shear-Mode Resonator Sensors," *Proc. Transducers '95*, vol. 2, pp. 712-715, 1995.
- [4] R. Thalhammer, S. Braun, B. Devic-Kuhar, M. Groschl, F. Trampler, E. Benes, H. Nowotny, and P. Kostal, "Viscosity Sensor Utilizing a Piezoelectric Thickness Shear Sandwich Resonator," *IEEE Trans. Ultrasonics, Ferroelectrics and Frequency Control*, vol. 45, pp. 1331-40, 1998.
- [5] S. Bianco, M. Cocuzza, S. Ferrero, E. Giuri, G. Piacenza, C. F. Pirri, A. Ricci, L. Scaltrito, D. Bich, A. Merialdo, P. Schina, and R. Correale, "Silicon Resonant Microcantilevers for Absolute Pressure Measurement," *J. Vacuum Science Technology B*, vol. 24, pp. 1803-9, 2006.
- [6] R. Sunier, T. Vancura, Y. Li, K.-U. Kirstein, H. Baltes, O. Brand, "Resonant Magnetic Field Sensor with Frequency Output," *J. Microelectromechanical Systems*, vol. 15, pp. 1098-1107, 2006.
- [7] J.H. Seo, K.S. Demirci, A. Byun, S. Truax, O. Brand, "Novel Temperature Compensation Scheme for Microresonators Based on Controlled Stiffness Modulation," *Proc. Transducers '07*, pp. 2457-2460, 2007.
- [8] J. H. Seo, "Silicon-Based Resonant Microsensor Platform for Chemical and Biological Applications," Ph.D. Thesis, Georgia Institute of Technology, 2007.
- [9] K. Ogata, *Modern Control Engineering*, 4th ed., Prentice Hall, 2002.
- [10] J.H. Seo, O. Brand, "High-Q Factor Resonant Sensor Platform for Chemical and Biological Applications," *Proc. Transducers '05*, pp. 593-596, 2005.

# VISCOUS DAMPING OF LATERAL MEMS DEVICE WITHIN A FULLY-ENCLOSED CAVITY

Wenhua Zhang, Robert Walmsley, and Peter Hartwell

Hewlett-Packard Laboratories, 1501 Page Mill Rd., Palo Alto, CA 94304

## ABSTRACT

A new viscous damping model has been proposed for analyzing damping performance of a laterally moving MEMS device inside a fully-enclosed cavity. Trench Pressure Damping, identified as a new damping term and not included in previous models, becomes dominant in the total viscous damping in a MEMS device. The cavity height inside the enclosed package is a critical dimension in determining the damping performance. The analytical results from the new model agree well with the measured results.

## INTRODUCTION

Fully enclosing MEMS devices has been common practice in many applications, including accelerometers, gyroscopes, and resonators, where Couette flow (Stokes) and squeeze-film damping models have been used extensively to estimate air damping. Several analytical models have been suggested applicable for MEMS devices with uncapped packages, where air is assumed free to move in and out to the outside environment as the device moves. Previous work by Yasumura et. al. [1] has shown that viscous damping in an enclosed MEMS device can be significantly altered from that observed in an open environment. Damping is enhanced inside the chamber by a pressure gradient formed during device movement that changes the dominant dissipative mechanism from the Stokes or Couette flow of slide-film damping [2, 3] to Poiseuille flow damping. Evidence in our study shows that the pressure difference between two sides of the device resulting from forced air movement inside the cavity adds another damping term not included by Yasumura. A new analytical damping model has been proposed for analyzing viscous damping performance of a laterally moving MEMS device inside a fully-enclosed cavity. The analytical results agree well with the measured results. This new term plays a significant role in the damping of a MEMS device under test and is the dominant term compared to either Stokes flow damping or pressure driven damping enhancement.

## DEVICE

Figure 1a shows a schematic section view of the device in this study. The moving component of the device (*TRANSLATOR*) is sandwiched between a *CAP WAFER* and *STATOR WAFER* which form a fully enclosing cavity. The dimensions of the *TRANSLATOR* and enclosing cavity are shown in Figure 1b. The *TRANSLATOR* has a height (*h*) ~100µm, width (*W*) and length (*L*) ~1800µm. Typical gap dimensions were ~2 µm for the bottom cavity gap, *g*<sub>2</sub>, and ~30 µm for the upper cavity gap, *g*<sub>1</sub>. The width of side trenches, *W*<sub>t</sub>, was about 20 µm. The pressure inside the device cavity could be adjusted and monitored using the variable pressure system shown in Figure 2. A venting hole was introduced that connected the internal device cavity to the external volume of the 68-pin CLCC package whose pressure could be controlled between 10<sup>-4</sup> Torr and 1 atm (760 Torr).

## THEORY

### Classic Damping Theory

According to traditional damping theory, without an enclosing top cover, sliding film damping between the *TRANSLATOR* bottom surface and the fixed cavity floor should be a dominant

damping source, since the device cavity has a small bottom gap, *g*<sub>2</sub>, in microns, while other cavity dimensions were in 10's of microns. Considering damping from the upper gap, *g*<sub>1</sub>, the total sliding film shear force is:

$$\tau_{s, g_1, g_2} = \frac{\mu u_0}{g_1} + \frac{\mu u_0}{g_2} = \frac{\mu u_0 (g_1 + g_2)}{g_1 g_2} \quad (1)$$

where  $\mu$  is air viscosity and  $u_0$  is the velocity of the *TRANSLATOR* when moving.

Squeeze-film damping losses in the side trenches due to vertical flow out of the trenches may be included using a model from Veijola et. al., which includes border flow effects [4]. Since the length and width of the proof mass are much larger than its height, a one-dimensional model may be employed. The total squeeze length, will include the twice the proof mass Length, *L*. The squeeze-film damping coefficient is given by:

$$b_{sq} = \frac{\mu_{eff, trench} L (2h + 1.3W_t)^3}{W_t^3} \quad (2)$$

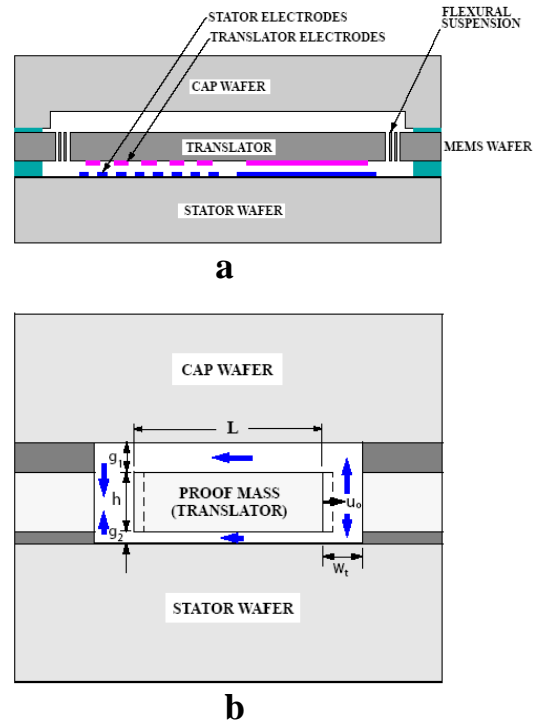


Figure 1 Schematics of the device package and damping physical model, (a) Device model, (b) Damping model. The moving structure has a height of *h*, width and length of *L*. The bottom gap is *g*<sub>2</sub> and the upper gap is *g*<sub>1</sub>. The side trenches between the device sidewall and the package have width of *W*<sub>t</sub>. Lateral resonant frequency, *f*<sub>r</sub>, of the device was ~1100 Hz.

### Yasumura's Correction

Yasumura's work reported that the damping inside an enclosed volume was enhanced due to the forced air movement inside the cavity [1]. The air flow physics in the bottom and top

gaps is changed from Couette flow to Poiseuille flow and an extra damping term (Shear Pressure) must be added in this case. Yasumura et. al. assumed incompressible flow such that the full displaced volume resulting from lateral motion was assumed to flow through the upper and lower gaps from one side of the rotor to the other [1]. The  $-1/\rho(dp/dx)$  term can no longer be neglected and the pressure driven velocity is then given by [1]:

$$u(y, g)_p = -\frac{1}{2\mu} \frac{dP}{dx} (gy - y^2) \quad (3)$$

where  $g$  is the gap ( $g_1$  or  $g_2$ ) through which air flows and  $dP/dx$  is the induced gradient. Pressure driven shear force is then:

$$\tau(y, t)_p = -\mu \frac{\partial}{\partial x} u(y, t) \Big|_{y=0} = -\frac{1}{2} \frac{dP}{dx} (g - 2y) \Big|_{y=0} \quad (4)$$

By equating mass flows as:

$$\rho h w u_0 = \int_0^w \int_0^{g_1} \rho u(y, g_1) dy dw + \int_0^w \int_0^{g_2} \rho u(y, g_2) dy dw \quad (5)$$

And combining Equations 3 and 5, one can solve for  $dP/dx$  in terms of  $h$ ,  $g_1$ ,  $g_2$  and  $u_0$ .

### Rarefaction effect correction

In order to investigate pressure dependent damping, correction for rarefaction effects must be included. A typical method, in this case for lateral motion, assumes an effective viscosity that depends on the Knudson number,  $K_n$ , for each gap:

$$\mu_{eff,1} = \frac{\mu}{(1 + 2K_{n,1} + 0.2K_{n,1}^{0.788} \exp(-\frac{K_{n,1}}{10}))} \quad (6)$$

where  $K_{n,1}$  is the Knudson number for gap 1,  $K_{n,1} = \lambda/g_1$ , and  $\lambda$  is the gas mean-free-path [2]. An alternative effective viscosity that was formulated for ‘‘squeeze’’ gaps subject to Poiseuille flow is given by (for gap 1) [5]:

$$\mu_{eff,1} = \frac{\mu}{(1 + 9.638K_{n,1}^{1.159})} \quad (7)$$

Since pressure-induced flow in upper and lower gaps is expected to be Poiseuille-like, Equation 7 is considered more applicable.

Combining Equations 3 and 5 and solving for  $dP/dx$ , we have:

$$\frac{dP}{dx} = \frac{12hu_0}{\left(\frac{g_1^3}{\mu_{eff,1}} + \frac{g_2^3}{\mu_{eff,2}}\right)} \quad (8)$$

The total pressure-driven shear force is:

$$\tau_{p,g_1,g_2,V} = \frac{6hu_0(g_1 + g_2)}{\left(\frac{g_1^3}{\mu_{eff,1}} + \frac{g_2^3}{\mu_{eff,2}}\right)} \quad (9)$$

Correction to the Stokes shear force would take the form:

$$\tau_{s,g_1,g_2,V} = \frac{\mu_{eff,1}u_0}{g_1} + \frac{\mu_{eff,2}u_0}{g_2} \quad (10)$$

Using the Veijola rarefaction correction, the total shear force is assumed to be the sum of Stokes and Pressure terms as:

$$\tau_{total,V} = \tau_{p,g_1,g_2,V} + \tau_{s,g_1,g_2,V} = \frac{6hu_0(g_1 + g_2)}{\left(\frac{g_1^3}{\mu_{eff,1}} + \frac{g_2^3}{\mu_{eff,2}}\right)} + \frac{\mu_{eff,1}u_0}{g_1} + \frac{\mu_{eff,2}u_0}{g_2} \quad (11)$$

### Trench Pressure Damping

In addition to the shear forces in top and bottom gaps, an additional pressure term resulting from a pressure difference between trenches must be included. This term was not included in Yasumura’s formulation, but its necessity was made clear by FEA results. The resulting trench pressure term is:

$$F_T = (P_{T1} - P_{T2})A_T = \frac{dP}{dx} L(Lh) = \frac{12L^2h^2u_0}{\frac{g_1^3}{\mu_{eff,1}} + \frac{g_2^3}{\mu_{eff,2}}} \quad (12)$$

where  $F_T$  is the net force acting between trenches,  $P_{T1}$  and  $P_{T2}$  are trench pressures,  $A_T$  is the area of the Translator ends, and  $dP/dx$  is from Equation 8. The damping coefficient term is given by:

$$b_{trench,V} = \frac{12L^2h^2}{\frac{g_1^3}{\mu_{eff,1}} + \frac{g_2^3}{\mu_{eff,2}}} \quad (13)$$

Using Veijola rarefaction corrections (Equations 6 and 7), the corresponding damping coefficient are then:

$$b_{T,V} = \frac{6Ah(g_1 + g_2) + 12L^2h^2}{\left(\frac{g_1^3}{\mu_{eff,1}} + \frac{g_2^3}{\mu_{eff,2}}\right)} + \frac{\mu_{eff,1}A}{g_1} + \frac{\mu_{eff,2}A}{g_2} \quad (14)$$

Note:

$$b = \frac{\tau A}{u_0} \quad (15)$$

where  $A$  is the area of the translator bottom surface in contact with the air gap.

### Device Damping and Quality Factor

Using the Veijola rarefaction corrections, the total damping coefficient combines Equations 2 and 14 as:

$$b = \frac{6Ah(g_1 + g_2) + 12L^2h^2}{\left(\frac{g_1^3}{\mu_{eff,1}} + \frac{g_2^3}{\mu_{eff,2}}\right)} + \frac{\mu_{eff,1}A}{g_1} + \frac{\mu_{eff,2}A}{g_2} + \frac{\mu_{eff,trench}L(2h + 1.3W_t)^3}{W_t^3} \quad (16)$$

For the micro-mover with a square geometry, the total damping coefficient can also be written as:

$$b = \frac{6Ah(g_1 + g_2 + 2h)}{\left(\frac{g_1^3}{\mu_{eff,1}} + \frac{g_2^3}{\mu_{eff,2}}\right)} + \frac{\mu_{eff,1}A}{g_1} + \frac{\mu_{eff,2}A}{g_2} + \frac{\mu_{eff,trench}L(2h + 1.3W_t)^3}{W_t^3} \quad (17)$$

The quality factor,  $Q$ , is then given by:

$$Q = \frac{m\omega}{b} \quad (18)$$

where  $b$  is the total damping coefficient,  $\omega$  is the resonant angular frequency (radians/sec), and  $m$  is the moving mass.

## TESTING SETUP AND RESULTS

A vacuum test system has been built and constructed to test the packaged device that has been vented by laser drilling into the device cavity over a pressure range from  $\sim 0.1$  mTorr to 760 Torr. The schematics of the vacuum test setup are shown in Figure 2. The device under test (DUT) is mounted and wire bonded into a Kyocera ceramic open-top 68 pin CLCC package. The DUT is inserted into a CLCC socket on a special test board so that a vacuum housing can be clamped over the top making an O-ring seal to the face of the CLCC package, hence, forming a vacuum cavity with the package. Two ports allow this volume to be evacuated and the pressure sensed. Because the pressure gauges are upstream from the test volume, measured pressures should set an upper bound on the actual device pressure. The system has been designed to minimize pressure differences between gauge and device. Pressure control above base vacuum is accomplished using a combination of a pump throttling valve and a leak valve, both downstream from the test volume. By this means, we hope to insure minimal flow in the gauging arm of the test chamber and therefore minimal pressure difference between gauge and device.

In Figure 3, a typical measurement at a pressure of 1 mTorr is shown by physically tapping the package. The measurement shows that it takes more than 60 s for the proof mass to ring down (dissipate the energy). The quality factor,  $Q$ , is about 135,000. This is significant for a device with a resonance frequency of  $\sim 1$  kHz.

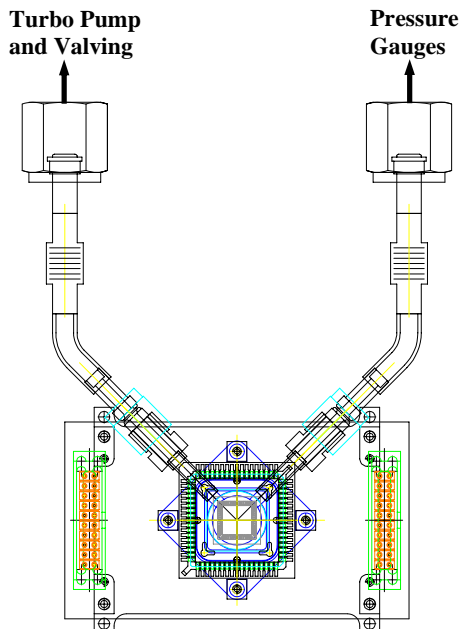


Figure 2 Schematic of the vacuum test setup. A vacuum cavity is formed between a vacuum housing on top of a Kyocera ceramic open-top 68 pin CLCC package with an O-ring to seal the vacuum. The pressure can be adjusted from  $10^{-4}$  Torr to 1 atm.

A square voltage signal is input into the electrodes to move the proof mass laterally, so that the translator oscillates eventually decaying to a new equilibrium position. As the trailing edge of the pulse arrives, the electrostatic force is removed. Therefore the translator moves back to its original position by the restoring force of the spring, decaying exponentially as well. The decay rate of the resulting oscillations provides a measure of the quality factor,  $Q$ , and through  $Q$ , the damping coefficient of resistance can be found. Figure 4 shows a  $Q$  versus pressure measurement of a device packaged as described above.

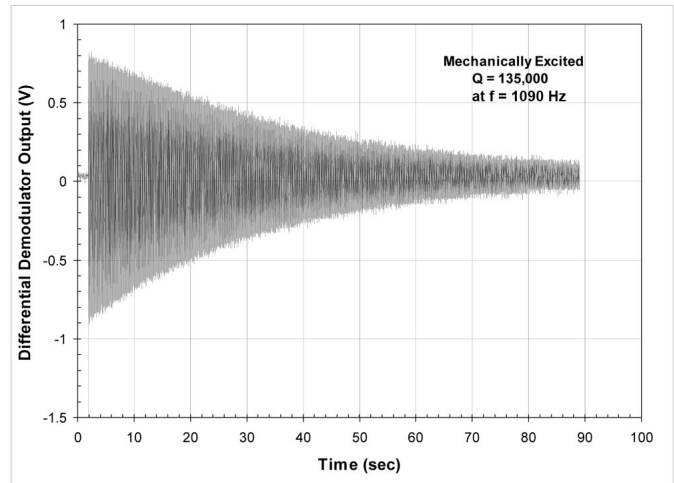


Figure 3 X-axis ringdown curve for the Translator at 1 mTorr. The observed  $Q$  is 135,000.

Analytical results from several models are shown in Figure 4 as well. Both the results from the traditional Couette flow damping and pressure-enhanced-damping from Yasumura's work underestimated the damping. The dash-dot curve in Figure 4 shows the analytical result after adding the new damping term, Trench Pressure Damping, which agrees well with measured results. The deviation from theory at low pressure (i.e.,  $< 10$  mTorr) indicates that other damping phenomena, likely thermo-elastic damping [6, 7], would need to be included in this pressure regime.

## ANALYSIS AND DISCUSSION

The encapsulation of the device in a sealed chamber has changed the damping physics from seemingly Couette flow dominant damping to pressure driven dominant damping. At 1 atm, the Quality factor of the device is about 166 from Couette flow damping theory and 70 from Yasumura's pressure-enhanced-damping theory, compared to 14 in actual device. The encapsulation package dramatically enhanced air damping in the device. As the device moves, a pressure difference is formed between trenches from both sides of the device in the moving axis. This pressure difference not only increases damping due to the pressure driven flow in the upper and lower gap, but the existence of the pressure differential in the trenches is also an obvious damping source for the device.

According to the Equation 17, air damping coefficient is a function of the depth of the cavity in the cap wafer. Therefore by varying the depth, air damping of the device can be tuned. Increasing the cavity depth causes the corresponding pressure drop to decrease. Figure 5 shows the calculated damping coefficient and quality factor dependence on the cavity depth from Equation 17 at 1 atm (760 Torr). Figure 5 also shows three testing results of damping coefficient at cavity gap of 33, 41, and 99  $\mu\text{m}$ , which agree with the analytical results.

In an enclosed volume, the total height of the device cavity becomes a critical dimension controlling viscous damping. Utilizing this design parameter would allow individual damping adjustment of multiple devices which share the same cavity volume (and hence, cavity pressure). Quality factor ( $Q$ ) can be improved by increasing the cavity, until it "saturates" at certain depth, where further increase has little effect on damping. In this case, the damping of the device is governed by traditional damping theory.

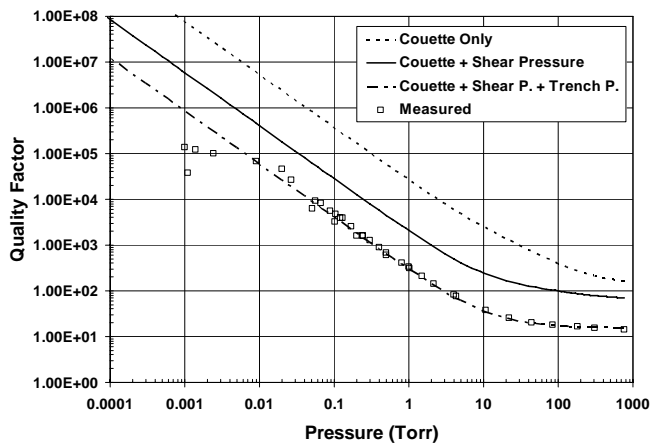
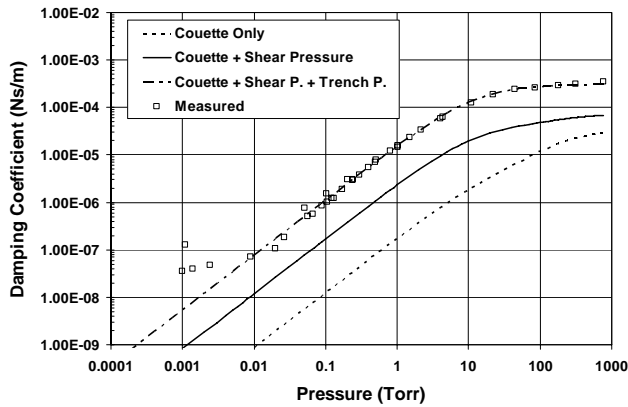


Figure 4 Damping Coefficient ( $b$ ) and Quality Factor ( $Q$ ) versus pressure of a MEMS device including Trench Pressure Damping. Also shown are Damping Models based on Couette Flow damping (top, dash curve) and on Couette+Shear Pressure (solid curve). Device Parameters: Resonant Frequency ( $f_r$ )  $\sim$  1100 Hz, Translator Mass ( $m$ ) = 780  $\mu$ g, Length ( $L$ ) = 1800  $\mu$ m, Width ( $W$ ) = 1800  $\mu$ m, Height ( $h$ ) = 100  $\mu$ m.

## CONCLUSION

Air damping of a MEMS sensor or actuator inside an encapsulated chamber can be quite different from uncapped package. Traditional Couette flow and squeeze film damping theories are no longer enough to accurately characterize the damping. Yasumura improves the theory by including a pressure enhanced damping term, but still overestimates the Quality factor of the device under test. In this work, pressure buildup in the side trenches of the translator as it moves was observed and proved to form an extra drag to the movement of the proof mass. Trench Pressure Damping has been identified as a new and dominant damping term, with analytical results that agree well with the experimental results in the devices in this work. The device damping in an encapsulated package has a strong dependence on the cavity depth in the cap-wafer and can therefore be tuned. An accurate analytical damping model has great utility in the design and optimization of lateral resonator-based MEMS sensors allowing for improved performance of accelerometers [8], gyroscopes, and mass sensors.

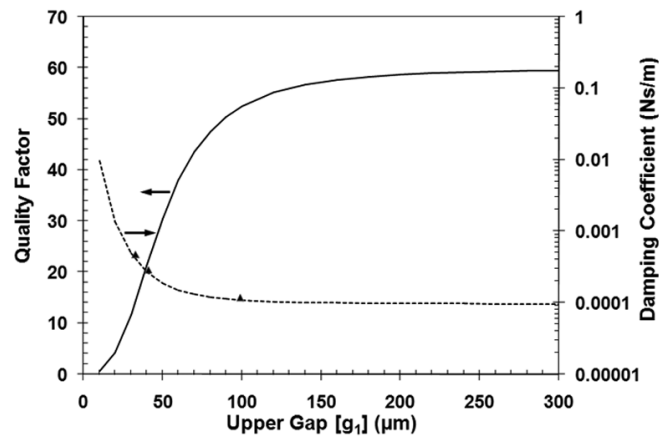


Figure 5 Damping Coefficient ( $b$ ) and Quality Factor ( $Q$ ) versus Upper Cavity Gap,  $g_1$ , for the MEMS device in this study at one atmosphere. All damping terms in Equation 17 are included. Solid triangles show the testing results of damping coefficient at cavity gap of 33, 41, and 99  $\mu$ m respectively.

## REFERENCES

- [1] K. Yasumura and H. Jerman, "Pressure-Enhanced Air-Damping in Enclosed Laterally Oscillating Microstructures", Technical Digest of the 2006 Solid-State Sensor and Actuator Workshop, Hilton Head Isl., SC, 6/04-08/06, Transducer Research Foundation, Cleveland (2006), pp. 320-323.
- [2] T. Veijola and M. Turowski, "Compact Damping Models for Laterally Moving Microstructures with Gas-Rarefaction Effects", Journal of Microelectromechanical Systems, 10, 263 (2001).
- [3] Y.-H. Cho, A. P. Pisano, and R. T. Howe, "Viscous Damping Model for Laterally Oscillating Microstructures", Journal of Microelectromechanical Systems, 3, 81 (1994).
- [4] T. Veijola, A. Pursula, and P. Raback, "Extending the validity of squeezed-film damper models with elongations of surface dimensions", Journal of Micromechanics and Microengineering, 15, 1624 (2005).
- [5] T. Veijola, H. Kuisma, and J. Lahdenpera, "Model for gas film damping in a silicon accelerometer", Digest of Technical Papers of 1997 International Conference on Solid State Sensors and Actuators (TRANSDUCERS '97), Chicago. (1997), pp. 1097-1100.
- [6] R.N. Candler, H. Li, M. Lutz, W.T. Park, A. Partridge, G. Yama, and T.W. Kenny, "Investigation of Energy Loss Mechanisms in Micromechanical Resonators", Digest of Technical Papers of Transducers '03, Boston, (2003), pp. 332-335.
- [7] W. Zhang and K. L. Turner, "Pressure-Dependent Damping Characteristics of Micro Silicon Beam Resonator for Different Resonant Modes", 2005 IEEE Sensors, Irvine, CA, (2005), pp. 357-360.
- [8] T. B. Gabrielson, "Mechanical-Thermal Noise in Micromachined Acoustic and Vibration Sensors", IEEE Transactions on Electron Devices 40, 903 (1993).

# A NEW EXTRINSIC GETTERING TECHNIQUE IN THICK BONDED SILICON-ON-INSULATOR WAFERS ENABLING SENSOR – IC INTEGRATION

*P. Sandow<sup>1</sup>, S. Whiston<sup>2</sup>, P. Daly<sup>2</sup>, J. Mäkinen<sup>3</sup>, J. Hintsala<sup>3</sup>, K. Nunan<sup>4</sup>, W. Sawyer<sup>4</sup>*

<sup>1</sup>Okmetic Inc., 301 Ridgmont Drive, Allen, TX 75002, USA

<sup>2</sup>Analog Devices Inc., Raheen Business Park, Raheen, Limerick, Ireland

<sup>3</sup>Okmetic Oyj, Piitie 2, 01510 Vantaa, Finland

<sup>4</sup>Analog Devices, Inc., 21 Osborn St., Cambridge, MA 02139, USA

## ABSTRACT

A new technique for gettering of transition-metal impurities in thick bonded SOI (BSOI) wafers is demonstrated. A thin poly-Si interlayer was placed between the active silicon layer and the buried oxide by direct wafer bonding. Testing of wafers in CMOS processes showed a clear improvement of the gate oxide integrity, even approaching that of conventional bulk silicon wafers. Poly-Si interlayer layer showed no measurable effects on BSOI characteristics such as bond strength, interfacial voids, or sacrificial oxide etching, and the residual stress was very low. The results suggest that a thin poly-Si layer has minimal effect on fabrication of the MEMS elements.

## INTRODUCTION

Integration of MEMS with integrated circuits is one of the major attractions of silicon micromachining. From the technical solution viewpoint, integrating MEMS and signal processing circuitry on a single chip has some distinct advantages. Significantly smaller signals can be processed on-chip as compared to the MEMS element and the electronics on separate chips, allowing smaller silicon sensor size and low power consumption. Also, package size constraints or high interconnection densities can justify integration. However, due to incompatibilities of MEMS and IC processes the development cycles have been long and complex device and process integration has made it less common in MEMS.

Processing options that combine thick BSOI wafers and deep reactive ion etching can considerably simplify process integration. In particular, it is possible to design the process to include the MEMS process steps in the beginning and in the end, not interrupting the CMOS processing at all. The buried oxide of the SOI wafer makes it possible to release the MEMS devices by deep reactive ion etching after the IC processing is completed, and standard IC foundry processes can be used. In CMOS integrated systems – or equally in power or mixed signal devices made on thick SOI wafers – the techniques for gettering fabrication-induced metal impurities need to be addressed.

Poor gettering of metal impurities is a fundamental problem on thick BSOI wafers. Transition metal contaminants in CMOS devices is known to lead to oxide breakdown device failures and decrease in gate oxide integrity [1]. The methods that are in widespread use for gettering transition-metal contaminants include e.g. SiO<sub>2</sub> precipitates in the bulk of Czochralski (CZ) silicon wafers, mechanical damage, deposited polycrystalline silicon film on the backside of the wafer, or substrates with high boron concentration [2, 3, 4]. In SOI wafers the buried oxide forms a diffusion barrier for most transition metals. It prevents the use of any of the standard gettering methods in which the sinks for diffusing impurities are located in the back surface of the wafer or in the bulk of the handle Si wafer. Oxygen precipitation within the active device layer would lead to SiO<sub>2</sub> precipitates and associated defects also on the surface of the device layer. Heavy boron implantation at the start of the CMOS process at defined areas has been used for gettering with BSOI wafers [5, 6]. Lateral gettering

techniques have several drawbacks as the implanted areas must be designed as part of the circuit layout, and the gettering efficiency depends on the distance to the active device area.

In this paper, use of polycrystalline silicon interlayer for effective gettering of metal impurities in thick BSOI wafers is demonstrated and discussed. In the BSOI structure, a thin LPCVD polycrystalline silicon (poly-Si) film is placed as a gettering layer between the active silicon layer and the buried oxide by direct bonding. The distance between the active device area and the gettering layer is short and constant, yet the poly-Si layer is in the noncritical region for CMOS processing.

## EXPERIMENTAL

BSOI structures with and without a poly-Si interlayer were fabricated by direct bonding, mechanical grinding and polishing. The device wafers were p-type, <100> -oriented 150 mm Czochralski silicon wafers with resistivity of 1 – 15 Ω cm. Undoped poly-Si film was formed on the device wafer by LPCVD, and the poly-Si surface was polished by CMP. The thickness of the poly-Si film varied from 0.2 to 1.0 μm. The device wafer was then bonded to the handle wafer with a thermally grown oxide (oxide thickness 0.2-2 μm), and the bonded wafer pairs were annealed for 2 h at 1100°C. The bonded wafer was thinned down by grinding and polishing. The final thickness of the BSOI layer was from 2 μm to 20 μm, with thickness uniformity better than ± 0.5 μm. Some of the wafers were run through a high temperature process cycle (total time at ≥ 1000°C 24 h, with maximum temperature of 1150°C for 4 h) to simulate wafer processing.

Two methods were applied to measure the efficiency of metal impurity gettering. Some wafers were intentionally contaminated with Fe by dipping in SC-1 solution and subsequent heat treatment was used to drive contaminants into the bulk. Fe concentration in the active region of the SOI wafer was analyzed with DLTS measurements based on surface contact method. The detection limit of DLTS depends on the active layer thickness and resistivity, and it was approximately 1·10<sup>11</sup> at/cm<sup>3</sup> in the studied wafers.

SOI wafers with a poly-Si interfacial layer and a final active layer thickness of 10 μm were processed through a 0.6 μm CMOS flow. To ensure the effect on gate oxide quality, if any, of the buried poly-Si layer could be quantified, bulk Si wafers with intrinsic gettering and SOI wafers without an intrinsic gettering mechanism were processed at the same time in the same lots. Extensive wafer level testing was carried out to quantify relative gate oxide quality on the experimental splits by measuring gate oxide capacitor dielectric breakdown. To determine capacitor breakdown the voltage across the dielectric was ramped into accumulation until catastrophic breakdown was triggered.

The fabricated thick BSOI structures were examined with several techniques. Cross sectional analysis was done with Scanning Electron Microscopy (SEM) and defect etching. Wafers were analyzed for interfacial voids using Scanning Acoustical Microscope (SAM). The smallest detectable defect size in a bonded interface was from 25 to 30 μm in diameter. Bond strength was examined with crack opening method [7] and with HF etching

test [8]. In the former technique, the bond strength is calculated from observed crack length by a blade inserted between bonded wafers. The latter technique is based on the measurement of the lateral buried oxide etch rate in hydrofluoric acid (HF) solution. In these tests 50% HF at room temperature and with 10 minute etching time was used. The surface roughness of poly-Si interlayer after removing the handle silicon wafer and the buried oxide was measured with Atomic Force Microscopy (AFM).

Stress in the poly-Si layer was measured with FSM-128 film stress measuring tool (laser scanner) and also by optically measuring the curvature of HF released beams. Samples for the latter method were prepared by dicing SOI wafers to get several pieces which were etched in 49% HF solution in order to release the beams from the handle wafer. Stress was calculated from the curvature results using Stoney's equation after Klein [9].

## RESULTS AND DISCUSSION

### Cross-sectional poly structure

Cross-sectional SEM image of the SOI structure with interfacial poly-Si layer is presented in Fig. 1. The poly-Si layer is just beneath the active device layer, and the bonded interface is between the poly-Si layer and the buried oxide layer (oxide thickness 1.0  $\mu\text{m}$ ). The polycrystalline region consists of randomly oriented grains with diameters varying from few tens of nanometers to few hundreds of nanometers. In the active silicon region there are no dislocations originating from the poly-Si layer.

The effect of high temperature heat treatment (> 1000°C for 24 h, maximum temperature of 1150°C for 4 h) on the polycrystalline structure can be seen in Fig. 2 where cross sectional SEM image of BSOI structure with 0.6  $\mu\text{m}$  thick poly-Si interlayer is presented. Defect etching was made for enhancing the visibility of grain boundaries. The number of individual poly grains has decreased and their respective size has increased. As grain boundaries act as gettering centers for impurities, gettering efficiency will decrease as grains grow during heat treatment. However, the poly structure has remained relatively unaffected by the heat treatment when compared to literature results [10]. It is proposed that the presence of both single-crystal silicon and buried oxide next to the poly layer is responsible for this enhanced stability.

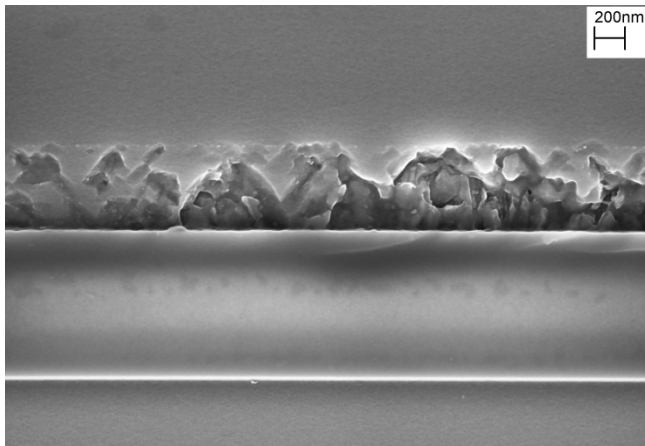


Figure 1: Cross sectional SEM image of bond interface in BSOI wafer structure with buried 0.6  $\mu\text{m}$  poly-Si interlayer between the active silicon layer and the buried oxide.

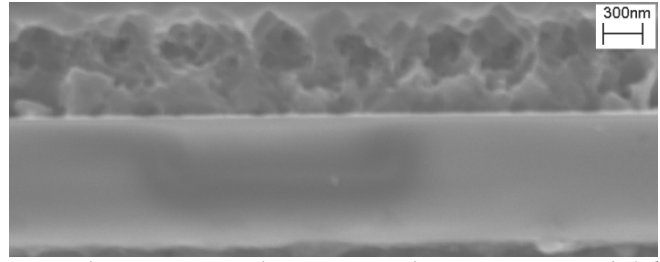


Figure 2: Cross sectional SEM image of BSOI structure with 0.6  $\mu\text{m}$  thick poly-Si interlayer after high temperature heat treatment (> 1000°C for 24 h, maximum temperature of 1150°C for 4 h) and defect etching for enhancing the visibility of grain boundaries.

### Gettering efficiency

Active layer iron concentrations of different SOI samples measured with DLTS and calculated gettering efficiencies are presented in Table 1. Intentional contamination of BSOI wafers with no poly-Si interlayer induces Fe concentration in the bulk of the active layer from  $2 \cdot 10^{13}$  to  $4 \cdot 10^{13}$   $\text{at}/\text{cm}^3$ . With poly-Si interlayer (layer thickness 0.6  $\mu\text{m}$ ) the Fe bulk concentration was below the detection limit of the DLTS measurement ( $1 \cdot 10^{11}$   $\text{at}/\text{cm}^3$ ). Compared to reference BSOI wafers, the Fe concentration decreases by at least two orders of magnitude. It is attributed to the polycrystalline Si interlayer forming a sink to diffusing Fe atoms. Gettering efficiency was calculated to be over 99%, and the exact value was limited by the DLTS detection limit.

Part of the wafers went through a high temperature heat treatment before intentional contamination and in these wafers the Fe concentration in the active device layer was  $1.2 \cdot 10^{12}$   $\text{at}/\text{cm}^3$  with poly-Si interlayer. As indicated above, recrystallization at high temperatures increases the polycrystalline grain size reducing the area of grain boundaries resulting in fewer gettering sites. However, even after high temperature annealing cycle the gettering efficiency was as high as 96.5%.

Table 1: Fe concentrations in intentionally contaminated BSOI wafers with and without 0.6  $\mu\text{m}$  poly-Si interlayer as measured with DLTS. Part of the wafers went through a high temperature heat treatment cycle before the intentional Fe contamination (> 1000°C for 24 h, maximum temperature of 1150°C for 4 h).

Wafer type	Heat treatment	Fe ( $\text{at}/\text{cm}^3$ )	Gettering efficiency (%)
SOI with poly	NO	< DL	> 99.4
SOI w/o poly	NO	$1.9 \cdot 10^{13}$	NA
SOI with poly	YES	$1.2 \cdot 10^{12}$	96.5
SOI w/o poly	YES	$3.4 \cdot 10^{13}$	NA

### CMOS processing

The gettering effectiveness of the buried polysilicon layer was determined by comparing the spread of catastrophic gate oxide breakdown on the wafers with the poly-Si interlayer with that of traditional SOI wafers with no additional gettering and normal bulk wafers, after processing through a 0.6  $\mu\text{m}$  CMOS flow. The CMOS flow is a well established, long running bulk wafer process which employs oxygen precipitate induced stacking faults in the bulk of the wafer to getter low levels of background metallics present in a typical state of the art processing environment. On traditional SOI wafers with no additional gettering gate oxide quality is degraded compared to bulk wafers. A midfield distribution in the breakdown is observed, indicative of reduced gettering of background metallics [Fig. 3]. When wafers with the

buried polysilicon layer are processed, this midfield distribution is substantially reduced leading to gate oxide quality approaching that of the bulk CMOS process [Fig. 4]. Additionally SEM images of cross sectioned wafers post processing show the continued presence of grain boundaries. This indicates that even after a thermal budget including cycles up to 1100°C the polysilicon retains some grain structure and so the gettering mechanism will remain active even through a significant thermal budget.

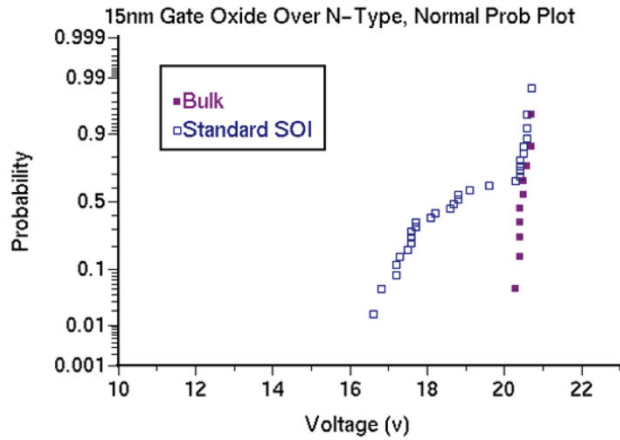


Figure 3: Cumulative probability plot of  $V_{bd}$  comparing standard BSOI to conventional bulk wafers.

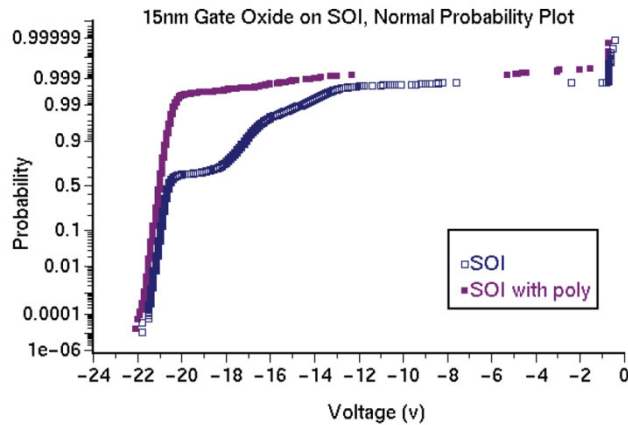


Figure 4: Cumulative probability plot of  $V_{bd}$  comparing BSOI with buried polysilicon to standard BSOI.

### Stress in the poly-Si interlayer

The stress in the as-grown LPCVD polysilicon film and in the poly-Si interlayer was measured using FSM-128 film stress measuring tool. The polycrystalline film is initially in high compression, and the film stress was in the range 280-350 MPa independent of the poly thickness (0.2-1.0  $\mu\text{m}$ ). Film stress in the poly-Si interlayer after SOI wafer processing was measured by removing the handle silicon wafer and the buried oxide. Small compressive stress of 1.5 MPa was found in a 0.6  $\mu\text{m}$  poly-Si layer.

The film stress was also calculated from the radius of curvature induced by the poly-Si layer on release etched 20  $\mu\text{m}$  thick beams. Film stress was 1.4 MPa with 0.6  $\mu\text{m}$  poly and 1.1 MPa with 1.0  $\mu\text{m}$  poly. The stress was tensile in both cases.

In conclusion it can be stated that the residual stress in poly-Si interlayer is relatively low ( $\leq 10$  MPa) as bond annealing relaxes the initial high stress.

### Bond interface characterization

Bond strengths measured with crack opening method were in the range of 2.1-2.5  $\text{J/m}^2$  for BSOI wafers with and without poly-Si interlayer. The values are in good agreement with typical surface energy of hydrophilic silicon/oxide bonds annealed at  $\geq 1100^\circ\text{C}$ .

Etching of the buried oxide can be used to characterize the bonded interface. Also, sacrificial oxide etching is a standard step in MEMS processing to release mechanical structures, and it is critical to have a well-defined oxide etching rate. Both the etching rate and the profile of the etched oxide are characteristic of the bond quality. For full strength of the bond the etched oxide edge is nearly straight. If HF etching proceeds faster along the bonded interface, a notch is formed and the oxide starts to etch also in vertical direction resulting in high effective etching rate. For hydrophilic silicon/oxide bonds the recorded values of the etching rate in 50% HF for 10 min at room temperature for a large number of different types of SOI products range from 1.4 to 1.6  $\mu\text{m}/\text{min}$ .

In these tests the etching rate of buried oxide was measured with cross-sectional SEM. One cross-sectional image is shown in Fig. 5. The etched oxide profile is almost vertical indicating that the etch rate along the polySi-SiO<sub>2</sub> bond interface is very close to the etch rate along the thermal oxide interface. HF etch rate results of different SOI samples can be found in Table 2. These are calculated as average values from three points in each sample wafer. The poly-Si interlayer or polySi-SiO<sub>2</sub> bond interface have no influence on etching of the buried oxide.

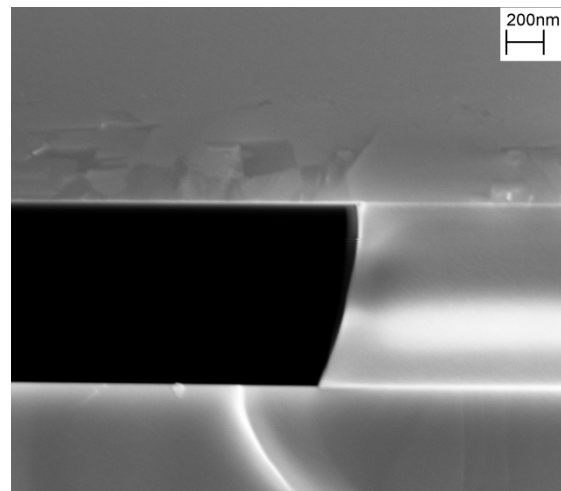


Figure 5: Cross-sectional SEM image for measuring the HF etching rate of buried oxide. BSOI wafer with 10  $\mu\text{m}$  active layer, 1.0  $\mu\text{m}$  buried oxide, and 0.6  $\mu\text{m}$  poly-Si interlayer.

Table 2: Etching rate of the buried oxide (50% HF for 10 min) in different BSOI samples. Poly-Si interlayer thickness 0.6  $\mu\text{m}$ .

Wafer type	Heat treatment	Etch rate ( $\mu\text{m}/\text{min}$ )
SOI with poly	NO	1.45
SOI with poly	YES	1.47
SOI w/o poly	NO	1.46

Bond interface quality was inspected with SAM using measurement mode detecting voids larger than or equal to 20 - 30  $\mu\text{m}$  in diameter. Image of a high-resolution SAM measurement of BSOI wafer with 0.6  $\mu\text{m}$  poly-Si interlayer is presented in Fig. 6 showing defect-free interface down to 30  $\mu\text{m}$  void diameter.

The number of voids was also evaluated by fabricating 100

BSOI wafers with a poly-Si interlayer, and scanning the whole wafer area with SAM. The smallest detectable defect size in a bonded interface was approximately 70  $\mu\text{m}$  due to the scan resolution. The wafers had on average less than one void per wafer, and no voids larger than 1.0 mm. High temperature heat treatment had no effect on the void distribution. The results indicate good quality of the bonding between polycrystalline silicon and thermal oxide.

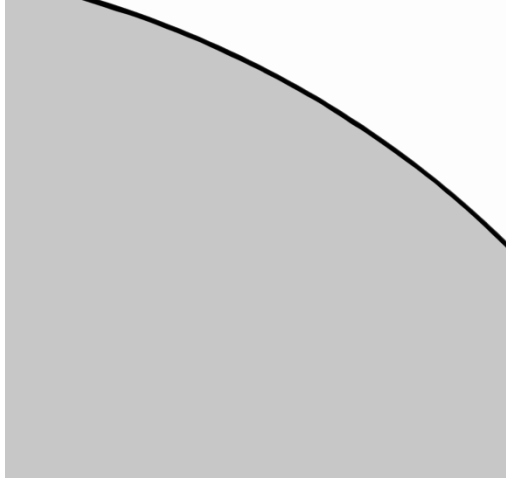


Figure 6: Bond interface quality of 200 mm BSOI wafer with 0.6  $\mu\text{m}$  poly-Si interlayer measured with SAM (50 mm  $\times$  50 mm area).

The micro-roughness of the polySi-SiO<sub>2</sub> bond interface in BSOI wafer with 0.6  $\mu\text{m}$  poly as measured with AFM was  $R_q = 0.296 \text{ nm}$  (AFM with 5  $\mu\text{m} \times 5 \mu\text{m}$  scan area) [Fig. 7]. This is higher than in standard SOI wafers in which the Si-SiO<sub>2</sub> bond interface roughness was around 0.1 nm. Thermal wet oxidation (0.2  $\mu\text{m}$ ) of the poly-Si interlayer surface and oxide removal increased the surface roughness to  $R_q = 5.0 \text{ nm}$ . With short oxidation and oxide removal after sacrificial oxide etching to release of the mechanical structures the polysilicon surface roughness might be high enough to reduce sticking of released active layer structures.

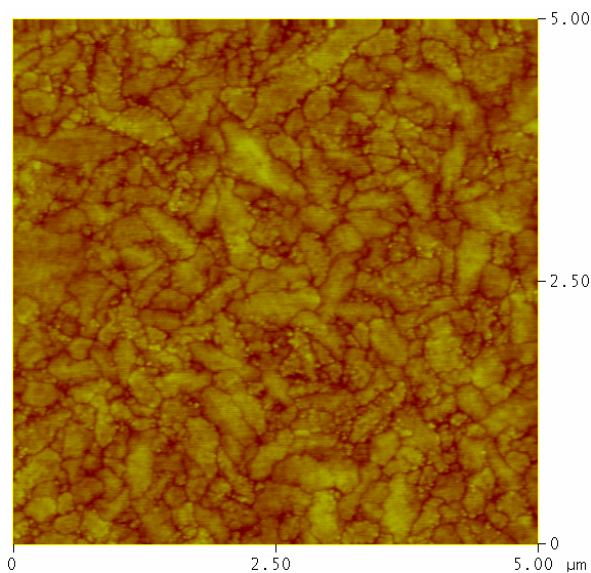


Figure 7: AFM image of active layer bond interface in gettered SOI wafer with 0.6  $\mu\text{m}$  poly-Si interlayer ( $R_q$  0.296 nm).

## CONCLUSIONS

Thick BSOI wafers with and without a thin polycrystalline silicon film between the active device layer and the buried oxide were fabricated, and their properties were evaluated. With a poly-Si interlayer, the quality of the gate oxide after a full CMOS process flow was approaching that in standard silicon wafers. The significant improvement in the gate oxide integrity as compared with standard SOI structure is associated with effective gettering of fabrication-induced metal impurities by the poly-Si layer. One obvious application is for IC-integrated MEMS processing options that build on thick BSOI wafers. Implementation of gettering by a poly-Si interlayer provides effective gettering sinks that are built in the BSOI substrate. Evaluation of the wafer properties suggests that the thin poly-Si layer has minimal effect on fabrication of the MEMS elements. The quality of the bonded interface is similar to that in standard bonded wafers, there is no influence to the sacrificial etching of the buried oxide, and the residual stress in the poly-Si film is very low.

## ACKNOWLEDGEMENTS

The authors wish to thank Mrs. Anna Chekurova, Okmetic Oyj, for SEM measurements, Mr. Pasi Kostamo, Helsinki University of Technology, for stress measurements and Dr. Marko Yli-Koski, Helsinki University of Technology, for DLTS measurements.

## REFERENCES

- [1] W. A. Nevin and A. Hoelke, "Effect of Intrinsic Gettering on Semiconductor Device Performance in SOI Substrates", ECS Transactions, 3, 469 (2006).
- [2] S. M. Myers, M. Seibt and W. Schröter, "Mechanisms of Transition-metal Gettering in Silicon", Journal of Applied Physics, 88, 3795 (2000).
- [3] T. Y. Tan, "Recent Progresses in Understanding Gettering in Silicon", Materials Research Society Symposium Proceedings 719 (2002), pp. F4.1.1-F4.1.12.
- [4] A. A. Istratov, H. Hieslmair and E. R. Weber, "Advanced Gettering Techniques in ULSI Technology", MRS Bulletin, 25, 33 (2000).
- [5] K. L. Beaman, O. Kononchuk, S. Koveshnikov, C. M. Osburn and G. A. Rozgonyi, "Lateral Gettering of Fe on Bulk and Silicon-on-Insulator Wafers", Journal of The Electrochemical Society, 146, 1925 (1999).
- [6] S. Q. Hong, T. Wetteroth, H. Shin, S. R. Wilson, D. Werho, T.-C. Lee and D. K. Schroder, "Improvement in Gate Oxide Integrity on Thin-film Silicon-on-Insulator Substrates by Lateral Gettering", Applied Physics Letters, 71, 3397 (1997).
- [7] Q. Y. Tong and U. Gösele, Semiconductor Wafer Bonding: Science and Technology, John Wiley & Sons, pp. 25-28, New York (1999).
- [8] T. Suni, J. Kiihamäki, K. Henttinen, I. Suni and J. Mäkinen, "Characterization of Bonded Interface by HF Etching Method", in Semiconductor Wafer Bonding: Science, Technology and Applications VII, C. Hunt, H. Baumgart, S. Bengtsson and T. Abe, Editors, PV 2003-19, The Electrochemical Society Proceedings Series, Pennington, NJ (2003), pp. 70-75.
- [9] C. A. Klein, "How Accurate are Stoney's Equation and Recent Modifications", Journal of Applied Physics 88, 5487 (2000).
- [10] B. Y. Tsauro and L. S. Hung, "Epitaxial Alignment of Polycrystalline Si Films on (100) Si", Applied Physics Letters 37, 648 (1980).

# ASSEMBLY OF PLANAR STRUCTURES BY PARALLEL ACTUATION OF MEMS MICROROBOTS

B.R. Donald<sup>1,2,\*</sup>, C.G. Levey<sup>3</sup>, and I. Paprotny<sup>4,1</sup>

<sup>1</sup>Department of Computer Science, Duke University, Durham, North Carolina, USA

<sup>2</sup>Department of Biochemistry, Duke University Medical Center, Durham, North Carolina, USA

<sup>3</sup>Thayer School of Engineering, Dartmouth College, Hanover, New Hampshire, USA

<sup>4</sup>Department of Computer Science Dartmouth College, Hanover, New Hampshire, USA

## ABSTRACT

Parallel motion and cooperation of multiple microrobots has many potential applications, including microassembly. In this paper, we present designs, theory and the results of fabrication and testing for an untethered multi-microrobotic system of stress-engineered MEMS microrobots that implements a novel microassembly scheme. Our work constitutes the first implementation of an untethered, mobile multi-microrobotic system. The robots are designed such that multiple devices can be independently maneuvered using a single, global control signal. We used a novel stress-engineering fabrication process to build 15 microrobots and used these to demonstrate microassembly of five types of planar structures from two classes of initial conditions. The final assemblies matched their target shapes by 96% (average), measured as the percentage of the area of the target shape covered by the assembled structure.

## INTRODUCTION

Mobile microrobotic devices have many potential applications, including medicine, surveillance, and assembly [1]. This paper presents designs, theory and experimental results for a novel microassembly scheme, which aggregates planar structures from a group of parallel-actuated MEMS microrobots. In this work, parallel-actuated (as opposed to serial) refers to the robots moving simultaneously under the application of a single, global control and power-delivery signal. The robots are 240-280  $\mu\text{m} \times 60 \mu\text{m} \times 7\text{-}20 \mu\text{m}$  in size, and consist of untethered scratch-drive actuators [2] that provide forward motion, and steering-arm actuators that control whether the robots move forward or turn [3]. We present fabrication methods, designs, control algorithms, and experimental results demonstrating the first simultaneous control of multiple untethered microrobots, and report the application of such multi microrobotic systems to the assembly of planar micro-structures. The aggregation and assembly of these structures is controlled and programmed by docking the individual robots, while defect formation is avoided by using non-colliding paths, enabling virtually defect-free assembly.

A system of  $n$  of our microrobots operating within the same operating environment is both non-holonomic (robots can only move in the direction they are facing) and highly underactuated, because all the robots receive a single, common control signal. Since all  $n$  robots are electrically coupled (and via compliance, intermittently mechanically coupled), the generalization of our earlier work [3] from one to  $n$  robots required advances in design, fabrication, control and programming to defeat the coupling and the potentially exponential explosion in complexity due to added degrees of freedom of the configuration space (C-space). In this paper, we present microrobot designs that efficiently demultiplex the common control signal for a group of  $n$  microrobots, and a control strategy that implements microassembly, transforming the problem of parallel control of  $n$  devices to parallel control of two robots, followed by sequential control of single robots. We used this control strategy to assemble several planar micro-structures. Innovations in designs and fabrication include designs of independently controllable microrobot species, an improved stress engineering process, single-device trimming to further reduce process variability, and a batch transfer mechanism for parallel transfer of robots from the die to their operating environment.

Fig. 1 shows scanning-electron micrographs of five *microrobot species* that we used to implement microassembly. Four of these species are *independent*, i.e. can be maneuvered as independent non-holonomic systems during microassembly. The micrographs of five types of planar structures assembled by these microrobots are shown in Fig. 2. The final assemblies matched their target shapes (portion of the area of the target shape covered by the assembling structure) by 96%, on average. All assembly experiments were conducted within a small (1.5 mm<sup>2</sup>) area.

While previous MEMS-robotic systems are assembled from microfabricated components, the dimension of these robots are on the order of millimeters or centimeters [4]. Scaling laws cause power delivery to be challenging as the dimensions of the robots are reduced to the micro-scale. The ability of our microrobot [3] to receive power from its environment [2] allows us to reduce its size by almost two orders of magnitude from other MEMS robotic

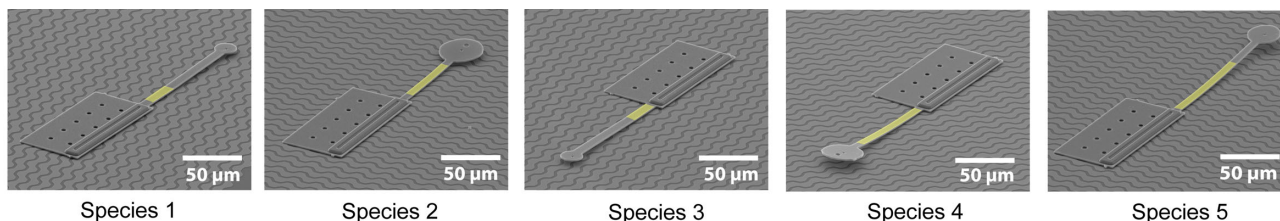


Figure 1: Scanning electron micrographs of the five microrobot species used to implement microassembly. Sets of independent microrobot species are: 1,3,4,5 or 2,3,4,5. The snap-down and release voltages of species 1 and 2 are similar, despite different steering-arm designs. Yellow color is used to highlight the areas of the steering-arms covered by the stress layer.

\* Corresponding author: D101 Levine Science Research Center, Duke University, Durham, NC.

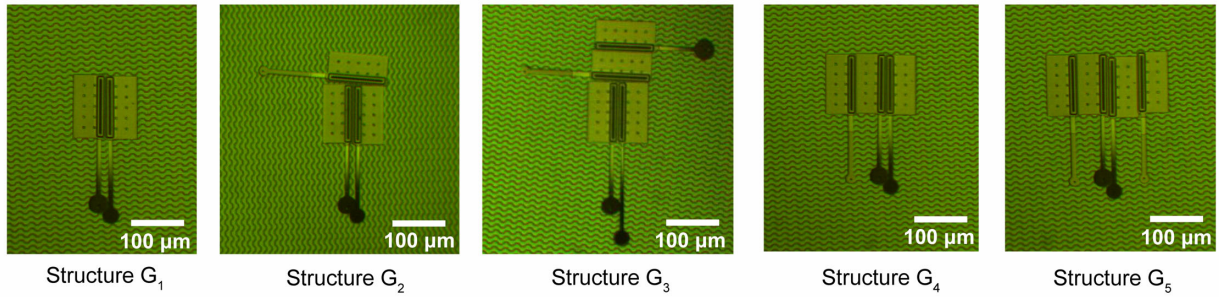


Figure 2: Optical micrograph of planar structures assembled using microrobot species shown in Fig. 1. The image of structure  $G_3$  was taken using an earlier version of species 5 (lower-right device), with a slightly longer steering-arm actuator than what was used in the assembly experiments reported in Table 1.

devices. Recently, a  $950\ \mu\text{m}$  MEMS micro-needle powered by external magnetic fields has also been demonstrated [5].

Most proposed microrobotic applications envision simultaneous operation of many microrobots. Micro-scale multi-robotic cooperation has not been previously attempted; however there are many examples of macroscopic multi-robotic systems that aggregate form or functionality through cooperation or mutual interaction. Coordination of macroscale multirobotic systems is achieved by message passing, implicit communication, or local rules. However, most of these approaches assume the robots have sufficient onboard hardware resources to receive and process sensory inputs and/or communicate with other devices. In contrast, our robots are much simpler and can only partially decode the broadcasted control signal. While the control of such systems have not been previously studied, the concept of selective response to a global control signal (Global Control, Selective Response (GCSR) [6]) is common in micro- or nano-scale biological systems. Our work demonstrates theoretically and experimentally that by designing microrobots so that each responds differently to a global control signal, we can control a group of robots to achieve useful tasks, such as microassembly.

Microassembly is generally performed in one of two ways: robotic manipulation through the use of macro-scale robotic manipulators with micro-scaled end-effectors [7], or self-assembly, where structures are aggregated through stochastic motion and interactions of components [8]. Robotic manipulation is in general inefficient, while defect formation is a common problem in self-assembly. Furthermore, in self-assembly the geometry of the assembly is programmed upon fabrication of the individual components (one set of parts can only assemble one type of structure). Our assembly scheme controls structure aggregation through intersecting trajectories, virtually eliminating defect formation, and allowing us to generate a large variety of structures from the same set of components. This assembly scheme does not require external actuators to maneuver the individual parts, resulting in an efficient, controllable assembly with a yield comparable to assembly using robotic manipulation.

### STRESS-ENGINEERED MEMS MICROROBOT

Fig. 3 presents a schematic design of a stress-engineered MEMS microrobot (a detailed description of the robot can be found in [3]). It consists of an untethered scratch-drive actuator (USDA) [2] that provides forward motion, and a out-of-plane curved steering-arm actuator that determines whether the robot moves straight or turns. The robot moves in straight line when the arm is elevated, and turns when the arm is down. A lithographically-patterned stress layer defines the out-of-plane

curvature of the steering arm. The robot operates on a grid of zirconia-insulated interdigitated electrodes. When a voltage is applied between sets of electrodes, the electrodes and the conductive chassis of the microrobot form a capacitive circuit, and an electrical potential is induced on the microrobot. Varying this potential (in the form of a waveform) allows us to control the state of the steering-arm actuator as well as to provide the power to the USDA.

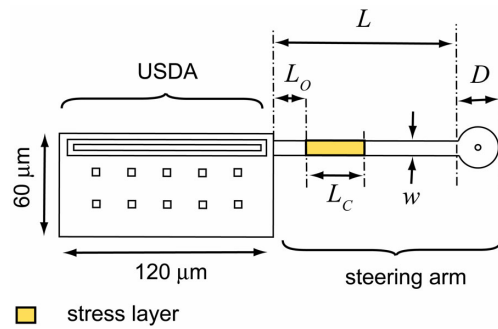


Figure 3: A schematic design of a stress-engineered MEMS microrobot.

The steering-arm actuator consists of an  $80\text{--}130\ \mu\text{m}$  long cantilever beam ( $L$ ) attached to a circular pad of  $20\text{--}40\ \mu\text{m}$  in diameter ( $D$ ) with a  $0.75\text{--}1.2\ \mu\text{m}$  deep dimple at the center of the pad to prevent irreversible stiction. Similar to an electrostatic cantilever beam, each steering-arm has two distinct transition voltages at which the arm abruptly changes states. These are the *snap-down* voltage ( $V_{\text{down}}$ ) at which the arm is pulled in contact with the substrate as the robot is commanded to turn, and the *release* voltage ( $V_{\text{up}}$ ) at which the arm is released when the robot is commanded to move straight. These transition voltages are determined by the steering-arm designs. Microrobots with the same steering-arm design are classified as the same microrobot species.

### FABRICATION

The fabrication of the microrobot chassis is performed through the surface micromachining MEMSCAP PolyMUMP's foundry process. The chassis is formed from the top layer of polysilicon, referred to as the Poly2-layer, while the bushing is formed from both the Poly1 and Poly2 layers. After the PolyMUMP's process is complete, a portion of each arm is coated with a stress layer of evaporated chromium (stress-engineering). The tensile residual

stress of the chrome-layer curves the steering-arms upward and is one of the factors determining their transition voltages. However, stress-engineered MEMS microrobots are highly susceptible to galvanic attack (GA) because the under-etch bath exposes polysilicon structures to Buffered Hydrofluoric Acid (BHF) prior to chrome deposition, and the release-etch exposes the polysilicon structures to Hydrofluoric Acid (HF) in the presence of metal from the stress layer. Both the BHF-exposure and HF-exposure in presence of metal have been shown to promote GA and corresponding polysilicon degradation. The effects of GA are often localized, and can result in scorching, *viz.* dark and granular silicon surfaces, as well as variations in the thickness of the polysilicon structures. We found that poor chrome adhesion during the release-etch is correlated with such polysilicon scorching. We have also measured significant thinning of the polysilicon layer on die with visible GA-scorching. In some cases, the structure thickness was degraded by up to 100 nm. To reduce the effects of GA, the stress-engineering process from [3] was modified to incorporate two consecutive baths during the BHF undercut stage, as well as the HF release stage. We have found this double bath system greatly reduced the GA-attributed structural thinning.

The microrobots are fabricated attached to larger structures, called *transfer frames*, which are used to move multiple devices from the die to the operating environment. The relative position of the robots is set in design, and the attached transfer frame allows us to move this entire configuration to the operating environment. Fig. 4 shows an optical micrograph of a transfer frame. Microrobots are fabricated attached to the frame through notched sacrificial beams (i). The frame is anchored to the substrate through another set of sacrificial beams (ii). These beams are broken, and the frame is lifted of the substrate, and subsequently transferred to the operating environment, using micro-probes inserted into hinged ears at the perimeter of the frame (iii), or using a vacuum microprobe. Once on the operating environment, the notched beams (i) are broken, and the robots are released while maintaining their designed configuration.

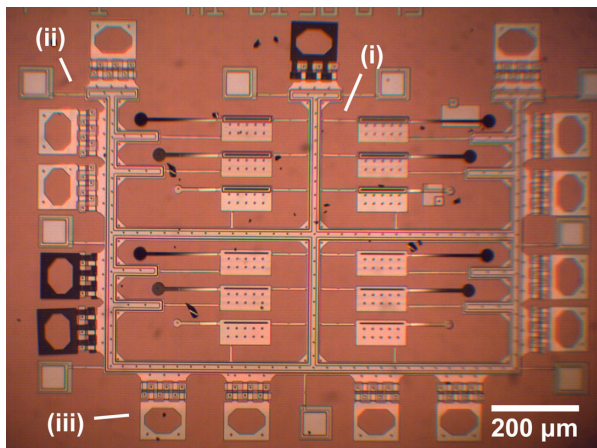


Figure 4: Optical micrograph of a batch transfer structure called a Transfer Frame.

In the infrequent cases when compounding process variability due to GA or other factors causes the transition voltage of the steering-arms to deviate significantly from their design, a novel post-release trimming method can be used to further increase or decrease the curvature of the individual steering-arms. Fig. 5 shows a schematic illustration of the post-release trimming concept (left) and optical micrographs showing device from species 5

before and after the trimming operation (right). A prefabricated fixture (i) is used to immobilize a released microrobot, such that additional chrome can be deposited on its steering-arm. Chrome is deposited on the top surface of the arm to increase the curvature, or on the bottom surface of the arm to decrease it. The fixture is anchored to a handle substrate through a linear spring that provides a normal force immobilizing the microrobot. The handle substrate is subsequently placed in a thermal evaporator for additional chrome deposition. The fixture also functions as a shadow-mask, limiting the chrome deposition to the surface of the steering-arm actuator (ii).

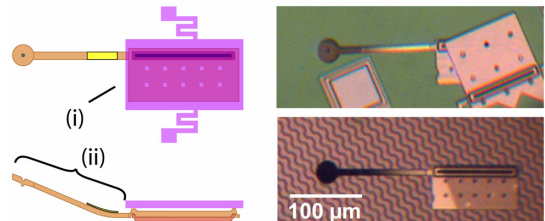


Figure 5: The post-release trimming method used to adjust the deflection of the steering-arm actuators.

The operating environment for our microrobots consists of zirconia-insulated wavy interdigitated electrodes. The electrodes are composed of a 500 Å gold layer, patterned through a liftoff process. They reside on a silicon substrate, covered with a 3 µm - thick layer of thermal silicon oxide. The electrodes are coated with 0.5 µm of reactive-evaporated zirconium dioxide, followed by a 300 Å passivation layer of evaporated silica. A more detailed description of the fabrication process for the operating environments is given in [3].

## INDEPENDENT MICROROBOT SPECIES

We designed and fabricated five microrobot species using three separate stress-engineering runs, resulting in 15 fabricated microrobots. Species 1, 3, 4, and 5 are independent and 2, 3, 4, and 5 are independent, *i.e.* can be controlled as independent non-holonomic systems. Our control algorithms ensure species independence if the snap-down and release voltage pairs for all robots are *unique*, *i.e.* either  $V_{down}$  or  $V_{up}$  is unique.

The design parameters for each of the five species are summarized in Table 1. Species 2 used a 1.2 µm tall dimple, while all other species used a 0.75 µm dimple. Single-device trimming was used to adjust the steering-arm transition voltages of one device from species 2 and one device from species 5. However, damage to the device from species 2 (caused by arcing due to dielectric breakdown) prevented us from fully completing the adjustment, reducing the number of operational devices to 14.

Table 1: Design parameters for the steering-arms of microrobot species 1-5. All dimensions are in µm.

Species	$D$	$w$	$L$	$L_C$	$L_O$
1	20	10	120	33.5	9.5
2	40	8	80	59.5	9.5
3	20	10	120	33.5	1.5
4	36	8	107	94.5	1.5
5	30	8	130	91.5	1.5

Fig. 6 illustrates the five control and power-delivery waveforms, called *control primitives*, that are used to control the microrobots. Experimentally-measured trajectories of the microrobots during the

application of each control primitive are presented in Fig. 7. For each control primitive, two trajectories are shown for each stress-engineering run of each microrobot species. A total of 140 such trajectories are shown; 28 for each of the five control primitives. Note that the control primitives are labeled (A-E) and ordered left-to-right such that independent microrobot species progressively switch from turning to straight-line motion. This order is exploited in our strategy for controlling the microrobots during microassembly.

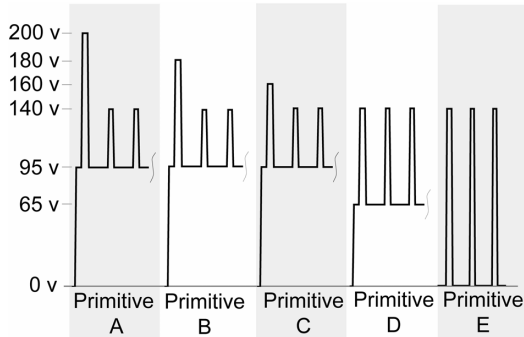


Figure 6: The waveform sequences (first three pulses only) of the five control primitives (A-E) used to control the five microrobot species (1-5 in Figure 1). Voltages may deviate up to  $\pm 10$  V from the actual voltages used.

### CONTROL STRATEGY FOR MICROASSEMBLY

We implemented microassembly by exploiting the ordering described above. The corresponding progressive change in the behavior of our microrobots allows us to transform the problem of parallel control of  $n$  microrobots to a simpler problem of simultaneously controlling two devices, followed by sequential control of single robots. The integrity of the intermediate assemblies is maintained through mutual compliance, and we restrict the structures that can be assembled to those that can be reached via the progressive assembly of *compliant-stable* structures. Compliant-stable structures do not change their configuration while the devices are powered; the sum of forces (including friction) and moments, generated by all the robots and transmitted through compliant interaction, equals to zero.

Consider a system of  $n$  microrobots, devices  $D_i$ ,  $i \in \{1 \dots n\}$  belonging to independent microrobot species, and labeled according to increasing transition voltages of their steering arms, and  $n+1$  control primitives,  $P_j$ ,  $j \in \{1 \dots n\}$  labeled according to

decreasing number of turning devices. The assembly of  $n$  robots takes place in  $n-1$  steps:

#### Step 1: Assembly of the Initial Stable Shape

In step 1, we assemble the initial stable shape, ( $G_1$  from Fig. 2) by simultaneously controlling microrobots  $D_{n-1}$  and  $D_n$  to dock together using primitives  $P_1$ ,  $P_2$ , and  $P_3$ . These primitives invoke both turning and straight-line motion in robots  $D_{n-1}$  and  $D_n$ , but *only* invoke turning behavior in the remaining devices. Thus, regardless of the trajectory of  $D_{n-1}$  and  $D_n$ , the remaining  $n-2$  robots “idle” by orbiting in circular trajectories. We use simple geometric trajectory planning to simultaneously control  $D_{n-1}$  and  $D_n$  to dock at an intersecting point of their trajectories. Fig. 9b shows the implementation of this first step of the control strategy on the system of four microrobots.

#### Steps 2, ..., $n-1$ : Subsequent Addition of Single Robots

In subsequent steps, the goal shape is progressively assembled through sequential addition of single robots while maintaining the stability of the accumulating structure. The robots are added in the order  $D_{n-2}$ ,  $D_{n-3}$ , ...,  $D_1$  using the pairs of control primitives ( $P_3, P_4$ ), ( $P_4, P_5$ ) ... ( $P_n, P_{n+1}$ ). For example, primitive pair ( $P_3, P_4$ ) provides turning and straight-line motion to robot  $D_{n-2}$ , while  $D_{n-3}$ , ...,  $D_1$  orbit, and  $D_{n-1}$ ,  $D_n$  are immobilized in the assembling structure (see Fig. 9c and d).

#### Self-Aligning Compliance

Microrobots that dock to form the initial stable shape self-align, reducing any remaining alignment error. The straight front edge of the scratch-drive actuator causes two opposing microrobots to slide relative to one another until both robots reach a stable configuration. Self-alignment is a form of local, pairwise self-assembly. Fig. 8 shows an example of self-aligning compliance between two docking robots. Configurations of the two devices measured four times during a self-aligning experiment are shown, illustrating the reduction in relative misalignment.

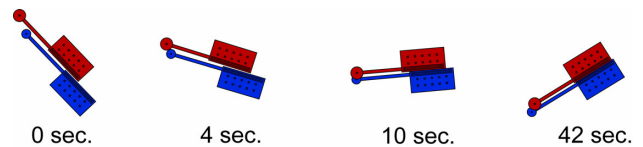


Figure 8: An example of self-aligning compliance. Outlines of devices from species 4 (red) and 5 (blue) recorded four times during a self-aligning experiment. The structure rotates by  $79^\circ$  overall.

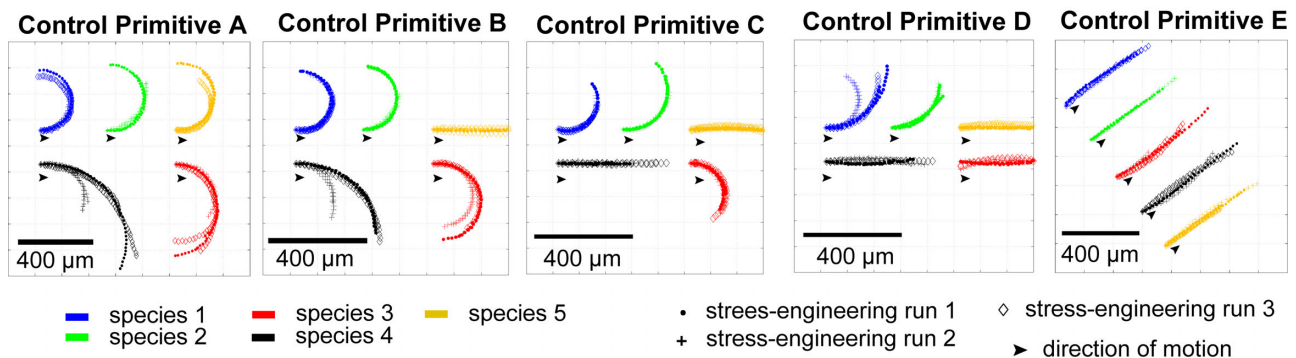


Figure 7: Experimentally-measured trajectories showing the reproducibility of motion for the five microrobot species (1-5 in Fig. 1) during the application of each control primitive (A-E) in Fig. 6.

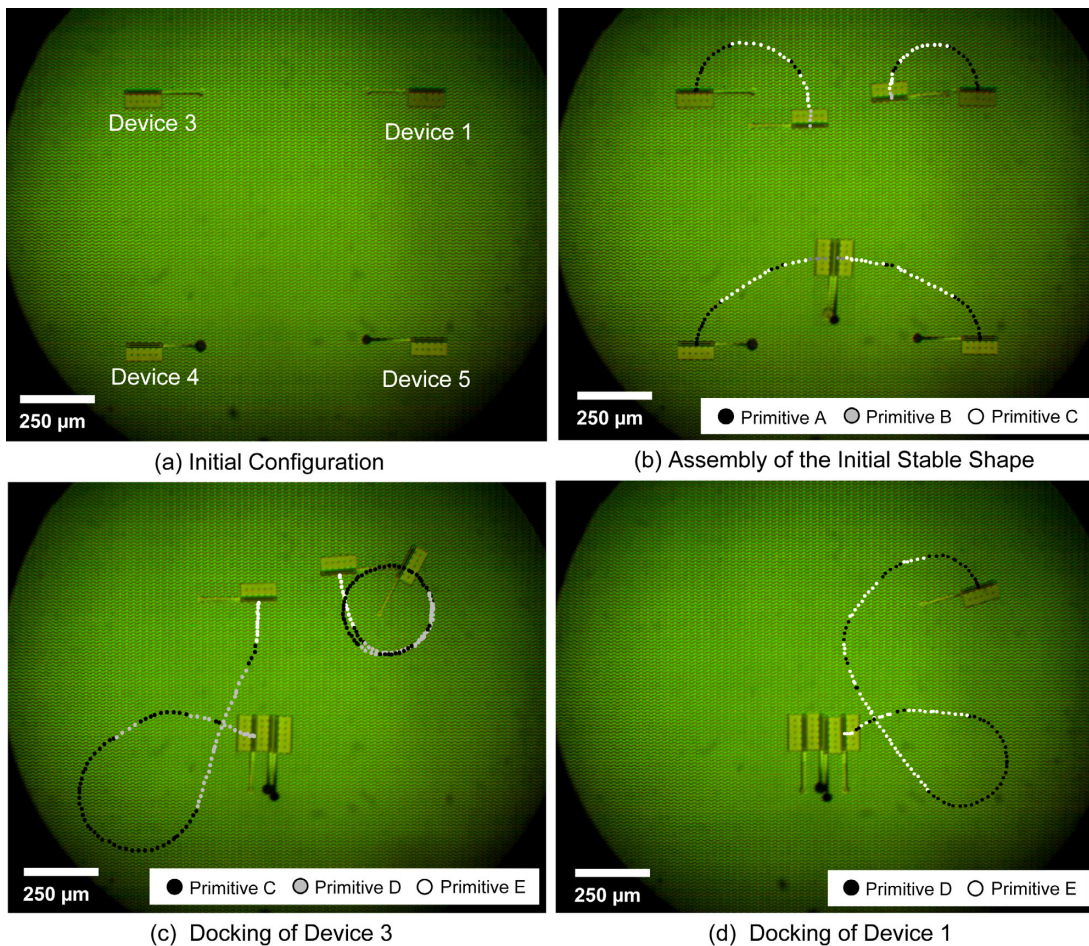


Figure 9: Composite optical micrograph of experimental assembly data using devices from species 1,3,4 and 5. The devices are labeled according to the number of their respective species. **a:** Initial configuration. **b:** Docking of device 4 and 5 to form the initial stable shape, while device 1 orbits. **c:** Docking of device 3 with the initial stable shape, while device 1 orbits. **d:** Docking of device 1 to complete the assembly. Black denotes trajectory segments where both robots that are being maneuvered towards the goal turn, gray denotes segments where one robot moves straight while the other robot turns, white denotes segments where both robots move straight. A movie of this assembly sequence is available online at: <http://www.cs.duke.edu/donaldlab/Supplementary/HH08/>.

## MICROASSEMBLY IMPLEMENTATION

We implemented microassembly using groups of four independent microrobots during five independent assembly experiments generating a total of 14 structures. Fig. 9 illustrates data from one of the assembly experiments. The robots were operated on a  $1.5 \text{ mm}^2$  environment, and their position was observed using a digital video-camera attached to an optical microscope with a  $6.7\times$  objective lens. The position of the devices was extracted with a precision of  $\pm 2.1 \mu\text{m}$ . During the operation of the microrobots, the humidity was controlled below 4% RH using a continuous stream of dry nitrogen. The waveforms defining the control primitives were produced using an Agilent 33120A arbitrary waveform generator, and amplified with a Trek PZD700-1 high-voltage power amplifier with a gain of 200.

The table in Fig. 10 indicates the average match (portion of the target structure covered by the assembled shape) for each type of generated shapes. The experiments were conducted starting from two different classes of initial configurations:  $R_1$  - robots are arranged along the corners of a rectangle with sides 1 by 0.9 mm, all devices oriented along the y-axis, and  $R_2$  - robots are arranged in a line with average separation of  $360 \mu\text{m}$ , and variable orientation. The initial position of the microrobots was set using

microprobes. We used common geometric shapes (a line and a rectangle) to demonstrate the ability to achieve successful assembly from arbitrary different initial configurations. Five types of planar structures were assembled, denoted as  $G_1$ - $G_5$  (see Fig. 2). Due to the absence of external fixtures that would constrain the position of the assembled structure, we consider the assembly a success regardless of the pose of the assembled structure, as long as the structure is entirely contained within the operating environment.

The average match across all assembled structures was 96%,  $\pm 3\%$  (st. dev.). This average does not include completely failed assemblies. We recorded an 11% failure rate during consecutive assembly of nine structures over the course of three assembly experiments: the single failure was due to the loss of stability of an intermediate structure.

The average docking misalignment across all experiments was  $5 \mu\text{m} \pm 5 \mu\text{m}$  (st. dev.). In all experiments, compliance was used to self-align the initial stable structures. Two of the five experiments were conducted with the initial shape purposefully misaligned by at least  $50 \mu\text{m}$  to test self-alignment. In these experiments, the average misalignment after completed self-alignment was  $9 \mu\text{m} \pm 8 \mu\text{m}$ . In the remaining three initial

		Target Structure G					
							Average $G_1 - G_5$
		$G_1$	$G_2$	$G_3$	$G_4$	$G_5$	
Initial Configuration	 $R_1$	96 % (4) 3 runs	98 % (3) 2 runs	96 % (2) 2 runs	96 % (na) 1 run	93 % (na) 1 run	96 % (3) 3 runs
	 $R_2$	99 % (2) 2 runs	98 % (na) 1 run	93 % (na) 1 run	89 % (na) 1 run	na	95 % (4) 2 runs
Average $R_1$ and $R_2$		97 % (3) 5 runs	98 % (2) 3 runs	95 % (2) 3 runs	93 % (5) 2 runs	93 % (na) 1 run	96 % (3) 5 runs

Figure 10: Summary of the assembly experiments, showing the average match (portion of the area of the target shape covered by the assembled structure) for each of the generated shapes. A total of five assembly experiments were conducted starting from two classes of initial configurations  $R_1$  and  $R_2$ . The standard deviation (in parenthesis) and the number of experimental runs from each class of initial configurations are also shown.

shape docking experiments, precise control was applied to minimize the initial misalignment. In these experiments, the average docking misalignment was  $6 \mu\text{m} \pm 7 \mu\text{m}$  before the self-alignment, and  $2 \mu\text{m} \pm 3 \mu\text{m}$  after the self-alignment was complete.

When docking a single robot with a stable structure, the average docking misalignment was  $3 \mu\text{m} \pm 3 \mu\text{m}$ , which is on the order of the minimum feature-size of the fabrication process.

## CONCLUSION

In this work we demonstrated the first example of parallel operation of multiple untethered MEMS microrobots. We presented designs and fabrication of independent stress-engineered microrobot species, as well as control algorithms that implement a new microassembly scheme, generating planar structures with a high level of accuracy. The average match between the generated structures and the desired target configurations was 96%, with an average misalignment of  $5 \mu\text{m}$  across all experiments, and  $3 \mu\text{m}$  in experiments where error correction and self-aligning compliance were fully implemented.

In the presence of a global, broadcast-type control signal, a multi microrobotic system composed of many individual devices will naturally be highly-underactuated, necessitating the type of control algorithms presented in this work. Successful control of highly underactuated systems is likely to be important as the size of the assembling components is reduced even further, since parallel operation, broadcast communication, and selective response are ubiquitous in the architecture of micro- and nano-scale biological systems.

## ACKNOWLEDGEMENTS

This work was supported by grant number GM-65982 to B.R.D. from NIH, and 2000-DT-CX-K001 to B.R.D., from the Office for Domestic Preparedness, Department of Homeland Security, USA. The electron micrographs were taken at the Dartmouth Ripple Electron Microscopy Laboratory, with the help of C. P. Daghljan. We would like to extend our thanks to D. Rus for her advice and collaboration. We thank C. McGray for the initial work on the stress-engineered MEMS microrobot. We

thank J. Gibson for the use of equipment in her lab. We further thank D. Balkcom, C. Bailey-Kellogg, A. Lebeck, K. Böhringer, and J. Reif for their advice and suggestions.

## REFERENCES

- [1] D. Popa, and H. E. Stephanou, "Micro and meso scale robotic assembly", SME Journal of Manufacturing Processes, 6, 1 (2004).
- [2] B. R. Donald, C. G. Levey, C. McGray, D. Rus, and M. Sinclair, "Power delivery and locomotion of untethered micro-actuators," Journal of Microelectromechanical Systems, 10, 6 (2003).
- [3] B. R. Donald, C. G. Levey, C. McGray, I. Paprotny and D. Rus, "An untethered, electrostatic, globally-controllable MEMS micro-robot", Journal of Microelectromechanical Systems, 15, 1 (2005).
- [4] S. Bagilo, S. Castorina, L. Fortuna, and N. Savalli, "Technologies and architectures for autonomous MEMS microrobot," in the proceedings of the IEEE International Symposium on Circuits and Systems (ISCAS 2002), 2, (2002), pp. II-584 – II-587.
- [5] K. B. Yesin, K. Vollmers, and B. J. Nelson, "Modeling and control of untethered boimicrorobots in fluid environment using electromagnetic fields," International Journal of Robotics Research, 25, 5-6 (2006).
- [6] B. R. Donald, "Building very small mobile micro robots," Inaugural Lecture, Nanotechnology Public Lecture Series, MIT (Research Laboratory for Electronics, EECS, and Microsystems Technology, Laboratories). Cambridge, MA., April 2007, available online at: <http://mitworld.mit.edu/video/463/>.
- [7] G. Skidmore, M. Ellis, A. Geisberger, K. Tsui, K. Tuck, R. Saini, T. Udeshi, M. Nolan, R. Stallcup, and J. V. E. the 2nd, "Assembly technology across multiple length scales from the micro-scale to the nano-scale", the Proceedings of the 17th IEEE International Conference on MEMS, (2004), pp. 588 – 592
- [8] G. M. Whitesides and B. Grzybowski, "Self-assembly at all scales," Science, 295, (2002).

# CAPACITIVE TRANSDUCER STRENGTHENING VIA ALD-ENABLED PARTIAL-GAP FILLING

Li-Wen Hung, Zachery A. Jacobson, Zeying Ren, Ali Javey, and Clark T.-C. Nguyen  
Department of Electrical Engineering and Computer Sciences  
University of California, at Berkeley, CA 94720, U.S.A

## ABSTRACT

The electromechanical coupling factors ( $\eta_e$ 's) of capacitively-transduced micromechanical resonators have been increased by a factor of  $8.1\times$  via a process technology that utilizes atomic layer deposition (ALD) to partially fill the electrode-to-resonator gaps of released resonators with high- $k$  dielectric material and thereby achieve effective electrode-to-resonator gap spacings as small as 32 nm. The electromechanical coupling increase afforded by gaps this small not only lowers termination impedances for capacitively-transduced micromechanical filters from the  $k\Omega$  range to the sub- $100\Omega$  range, thereby making them compatible with board-level RF circuits; but does so in a way that reduces micromechanical filter termination resistance  $R_Q$  much faster than the electrode-to-resonator overlap capacitance  $C_o$ , thereby also substantially increasing the  $1/(R_Q C_o)$  figure of merit (FOM).

## INTRODUCTION

To date, capacitively transduced micromechanical resonators have posted the highest  $Q$ 's of room temperature on-chip resonator technologies, with  $Q$  values exceeding 200,000 in the VHF range and exceeding 14,600 in the GHz range [1]. This makes them strong candidates for use as RF channel-selectors in next generation software-defined cognitive radios [2], or as ultra-low noise oscillators in high performance radar applications.

Unfortunately, the exceptional  $Q$ 's of these resonators are not easy to access, because the impedances they present are often much larger than that of the system that uses them. For example, many of today's board-level systems are designed around  $50\Omega$  impedance, which is much smaller than the 2.8 k $\Omega$  termination resistors required by the 163-MHz differential disk array filter of [3]. Thus, even though the filter of [3] attains an impressively low insertion loss of 2.43 dB for a 0.06% bandwidth, it requires an  $L$ -network to match to  $50\Omega$ . While it is true that as micromechanical filters are integrated together with transistors on single silicon-chips impedance requirements will grow to the  $k\Omega$  range for best performance [4], off-chip board-level applications will still need lower impedances.

Pursuant to attaining lower capacitive micromechanical resonator impedances, this work employs atomic layer deposition (ALD) [5] to partially fill the electrode-to-resonator gaps of released disk resonators with high- $k$  dielectric material and thereby achieve substantially smaller gap spacing, as small as 32 nm. This reduction in gap spacing increases the electromechanical coupling factors ( $\eta_e$ 's) of capacitively-transducers by a factor of  $8.1\times$ , which not only lowers termination impedances for *capacitively transduced* micromechanical filters from the  $k\Omega$  range to the sub- $100\Omega$ -range, thereby making them compatible with board-level RF circuits; but does so in a way that reduces micromechanical filter termination resistance  $R_Q$  much faster than the electrode-to-resonator overlap capacitance  $C_o$ , thereby also substantially increasing the  $1/(R_Q C_o)$  figure of merit (FOM). The increase in the FOM is also  $n^2\times$  faster (hence, better) than that of fully-filled solid-dielectric gap methods for  $R_x$  reduction [6]. This partial dielectric-filling based approach further prevents shorting of the resonator to its electrode, hence, greatly improves the resilience of micromechanical resonators against ESD or other

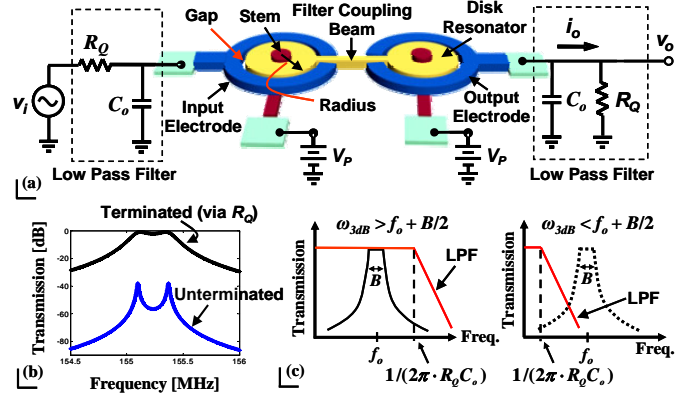


Fig. 1. (a) Perspective-view schematic of a two-resonator micromechanical filter with termination resistors  $R_Q$ 's and the low-pass filters they form with the  $C_o$ 's enclosed by dashed lines. (b) Frequency characteristics of an unterminated and a terminated filter with smooth passband. (c) Impact of the low-pass filters in (a) on filter response.

events that might pull a resonator into its electrode.

## APPROACHES TO IMPROVING FOM

The utility of a  $1/(R_Q C_o)$  figure of merit is perhaps best conveyed by considering a typical micromechanical filter [3][8], such as shown in Fig. 1, and examining how its termination resistance  $R_Q$  and its input capacitance  $C_o$  affect its performance. As shown in Fig. 1, the  $R_Q$  and  $C_o$  essentially combine to generate a pole at  $\omega_b = 1/(R_Q C_o)$  that sets the 3dB bandwidth of a low-pass filter. If  $\omega_b$  is lower than the center frequency  $\omega_o$  of the filter, then it will add undesired passband loss. This problem is actually fixable by using an (on-chip) inductor to resonate out the  $C_o$ , but it would be preferable if an inductor were not needed.

The needed value for termination resistance  $R_Q$  is given by

$$R_Q = \left( \frac{Q}{qQ_{fltr}} - 1 \right) \cdot R_x \approx \frac{Q}{qQ_{fltr}} \cdot \frac{m_r \omega_o}{Q\eta_e^2} \approx \frac{m_r B}{q\eta_e^2} \quad (1)$$

where  $R_x$  is the motional resistance of a constituent end resonator, such as shown in Fig. 1;  $Q$  is the unloaded quality factor of the resonator;  $Q_{fltr} = f_o/B$ ,  $B$  being the filter passband width;  $q$  is a normalized parameter obtained from a filter cookbook [7];  $m_r$  is the dynamic mass of the resonator at its point of maximum displacement; and  $\eta_e$  is the electromechanical coupling factor, given by

$$\eta_e = V_p \frac{\partial C}{\partial x} \approx V_p \cdot \frac{A \epsilon_r \epsilon_o}{d^2} \quad (2)$$

where  $V_p$  is a dc-bias applied to the conductive resonator structure;  $\partial C/\partial x$  is the change in electrode-to-resonator overlap capacitance per displacement;  $A$  is the electrode-to-resonator overlap area;  $\epsilon_r$  is the relative permittivity of the electrode-to-resonator gap material ( $=1$ , if not present);  $\epsilon_o$  is the permittivity in vacuum; and  $d$  is the electrode-to-resonator gap spacing.

Using (1)-(2), the expression for figure of merit becomes

Table 1: Comparison of Approaches for  $R_Q$  Reduction

Approach	$\eta_e$	$R_Q$	$C_o$	$FOM$
Arraying with $n$ resonators	$n \times$	$(1/n) \times$	$n \times$	$1 \times$
Solid-gap filling with $\epsilon_r = n$	$n \times$	$(1/n^2) \times$	$n \times$	$n \times$
Air gap reduction from $d_o$ to $d = d_o/n$	$n^2 \times$	$(1/n^4) \times$	$n \times$	$n^3 \times$

$$FOM = \frac{1}{R_Q C_o} \approx \frac{q}{B} \frac{\phi}{\pi} \frac{\epsilon_o}{\kappa \rho R} \frac{\epsilon_r}{d^3} \quad (3)$$

where  $\phi$  is the angle over which the input electrode subsides;  $\kappa$  is a modifier that accounts for the integration needed to obtain dynamic stiffness [8];  $\rho$  is the density of the disk structural material;  $R$  is the radius of the disk (as indicated in Fig. 1); and (3) was reduced to its final form by recognizing that the dynamic mass of the disk at a maximum velocity point on the disk is  $m_r = \kappa \pi R^2 t$ , where  $t$  is thickness.

Of the variables in (3), only  $\epsilon_r$  and  $d$  are truly adjustable, although  $R$  can often be minimized by operating at a fundamental mode, rather than higher modes. This implies that arraying approaches to lowering  $R_Q$  [9] that essentially increase the electrode-to-resonator overlap area do not in fact raise the  $FOM$ . On the other hand, solid-gap filling methods, such as in [6][10], that raise  $\epsilon_r$ , do improve the  $FOM$ , although the improvement ends up being much less than the factor by which  $\epsilon_r$  increases, since the need to compress the gap material often greatly reduces the benefits. Thus, it seems to still be gap spacing reduction that provides the largest gain in  $FOM$ , with very strong third power dependence. In particular, a reduction in gap spacing by  $5 \times$  yields a  $125 \times$  increase in  $FOM$ . Of course, linearity issues will need to be curtailed, as the  $IIP3$  of the disk will reduce as the gaps shrink [11], but the effects are less consequential as frequencies rise (e.g., at GHz) and can be alleviated in certain mechanical circuit networks.

Table 1 summarizes the efficacy of different approaches to reducing  $R_Q$  and increasing  $FOM$ .

### GAP REDUCTION VIA PARTIAL GAP FILLING

Evidently, from an  $FOM$  perspective, reducing the electrode-to-resonator gap spacing is perhaps the best way to reduce  $R_Q$ . Achieving smaller gaps, however, might not be so straightforward. In particular, the process of [3] achieves its sub-100nm lateral gaps using a sacrificial oxide sidewall film that is sandwiched between the resonator and electrode during intermediate process steps, but then removed via a liquid hydrofluoric acid release etchant at the end of the process to achieve the tiny gap. Fig. 2 shows the last step of the fabrication process. Here, sacrificial layers, including sidewall layers, are removed via wet etching to release structures that will eventually move. This approach to achieving lateral gaps, while effective for gap spacings above 50 nm, proves difficult for smaller gap spacings. In particular, smaller gap spacings make it more difficult for etchants to diffuse into the gap and get to the etch front; and for etch by-products to diffuse away from the etch front. While there is some evidence that a gaseous etchant capable of more easily accessing and escaping the gap, such as vapor phase HF, might prove effective for releasing structures with 50nm gaps [12], gaps so small (once released) might be overly susceptible to inadvertent shorting, due to ESD or other catastrophic events.

Rather than removing material by etching, one alternative approach to attaining both sub-50nm high-aspect-ratio gaps and protection against ESD events is to partially fill an already released gap

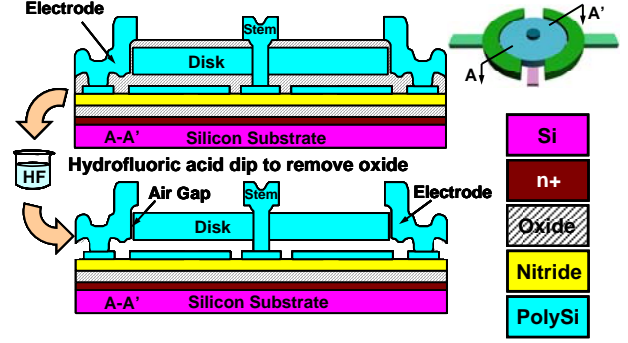


Fig. 2: Cross-sections depicting the final release step in the fabrication sequence for a laterally driven wine-glass disk resonator.

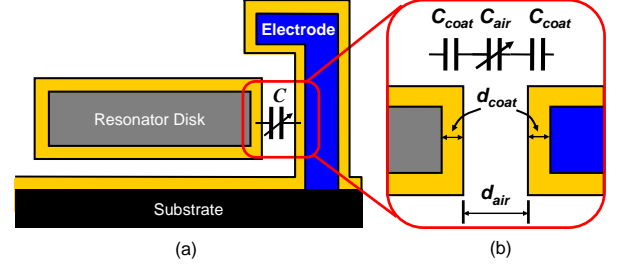


Fig. 3: (a) Schematic of a partial-ALD-filled gap. (b) Enlarged view of the gap and its equivalent series capacitances.

with a non-conductive dielectric material, as shown in Fig. 3(a). Here, filling via a dielectric is just as effective as if filling were done with a metal if the permittivity of the dielectric is high enough to allow the air (or vacuum) gap of Fig. 3(b) to set the overall capacitance value. Specifically, the capacitance between the electrode and resonator of Fig. 3(a) can be modeled by the series connection shown in Fig. 3(b). Here, the total electrode-to-resonator capacitance is given by

$$C(x) = C_{coat} \parallel C_{air}(x) \parallel C_{coat} = \frac{C_{coat}}{2} \parallel C_{air}(x) \quad (4)$$

from which  $(\partial C / \partial x)$  can be written (for small  $x$ ) as

$$\frac{\partial C}{\partial x} = \frac{1}{\epsilon_o A_o} \left[ \frac{C_{coat}}{2} \parallel C_{air} \right]^2 = \frac{1}{d_{air} C_{air}} \left[ \frac{C_{coat}}{2} \parallel C_{air} \right]^2 \quad (5)$$

where  $C_{air}$  is the capacitance across the air gap for  $x = 0$  (i.e. no displacement);  $C_{air}(x)$  is this capacitance as a function of displacement  $x$ ;  $C_{coat}$  is the capacitance across each dielectric-coated region; and any dimensions used are defined in Fig. 3. Obviously, if  $C_{coat} \gg C_{air}$ , then the capacitance and  $(\partial C / \partial x)$  reduce to

$$C(x) = C_{air}(x) \rightarrow \frac{\partial C}{\partial x} = \frac{C_{air}}{d_{air}} \quad (6)$$

which are the values that would ensue if there were no dielectric and if the electrode-to-resonator gap were equal to  $d_{air}$ . In practice,  $C_{coat}/2$  should be at least 10 times larger than  $C_{air}$  in order for (7) to hold, which means that the dielectric constant of the filling material should be at least

$$\epsilon_{coat} \geq 20 \epsilon_o \frac{d_{coat}}{d_{air}} \rightarrow C(x) \cong C_{air}(x) \quad (7)$$

where the gap dimensions  $d_{coat}$  and  $d_{air}$  are indicated in Fig. 3. For the case where the gap spacing of a disk resonator is reduced from 94 nm to 32 nm using ALD, achieving a  $(d_{coat}/d_{air})$  ratio of (31/32) and providing a 74 times decrease in  $R_Q$ , (7) suggests that the relative permittivity of the dielectric filling material should be  $>19.4$  to allow the use of (7) to determine  $(\partial C / \partial x)$ ; otherwise (6) should be

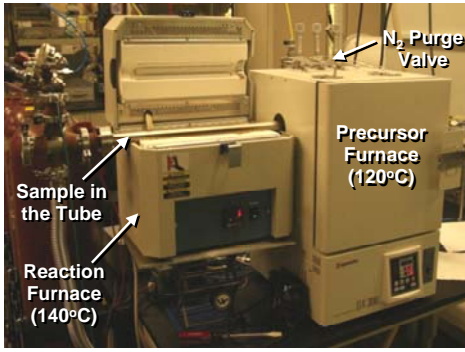


Fig. 4: Photo of the custom-built ALD tool used in this work.

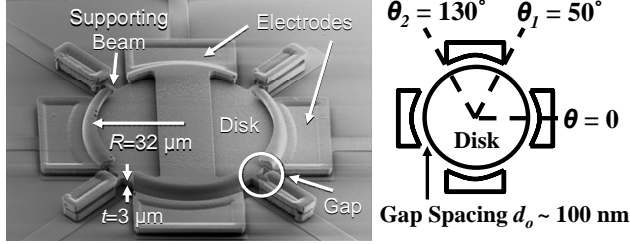


Fig. 5: SEM of a 61-MHz wine-glass disk and some key design parameters.

used. Hafnium oxide ( $\text{HfO}_2$ ) comes close, so is a reasonable choice of dielectric.

## EXPERIMENTAL RESULTS

To attain high-aspect-ratio sub-50nm gaps, the starting gap should already be very small, e.g., on the order of 100 nm, so the method used to fill gaps should be very conformal. Recognizing this, atomic layer deposition (ALD) is uniquely adept for this gap-coating process, since its two-step precursor, monolayer-by-monolayer deposition methodology effects very precise film thicknesses with conformality sufficient to uniformly cover the surfaces of the 30:1 aspect ratio 100nm (initial) gaps of the resonators. The post-release process used to reduce gap spacings in this work then consisted merely of an ALD step using a custom-built system (c.f., Fig. 4) to deposit  $\text{HfO}_2$  into the gaps of already released disk resonator devices, such as shown in Fig. 5; then a simple lithography and HF dip step to remove  $\text{HfO}_2$  over bond pads. The ALD of  $\text{HfO}_2$  was done at  $140^\circ\text{C}$  using tetrakis (ethylmethylamido) hafnium and water vapor prepared at  $120^\circ\text{C}$ .

Fig. 6 presents the measured frequency response characteristics for a 94 nm-gap wine-glass mode disk resonator, with design summarized in Fig. 5, and one coated with 30.7 nm of ALD'ed  $\text{HfO}_2$  using the process described above, then sintered in forming gas at  $400^\circ\text{C}$  for 3 minutes (for reasons to be described later). Here, the measured  $Q$  of the coated resonator is considerably lower than that of the uncoated one—an observation to be discussed in more detail later. For now, though, accounting for the reduced  $Q$ , the extracted  $\eta_e$ 's are  $19.84 \mu\text{C}/\text{m}$  and  $2.44 \mu\text{C}/\text{m}$  at  $V_p = 16\text{V}$  for the coated and uncoated devices, respectively, yielding an  $\eta_e$  improvement of  $8.1\times$ , which is very close to the expected  $8.6\times$  difference from (3). The motional resistance  $R_x$  at this point is  $966 \Omega$ . After another 3 minutes of sintering at  $400^\circ\text{C}$ , the same device achieves  $R_x=685 \Omega$  and  $Q = 7,368$  at  $V_p = 19\text{V}$ .

Perhaps the most accurate way to determine the electrode-to-resonator gap spacing for any capacitively transduced resonator is to utilize the dependence of resonance frequency on gap spacing, seen in the expression for resonance frequency

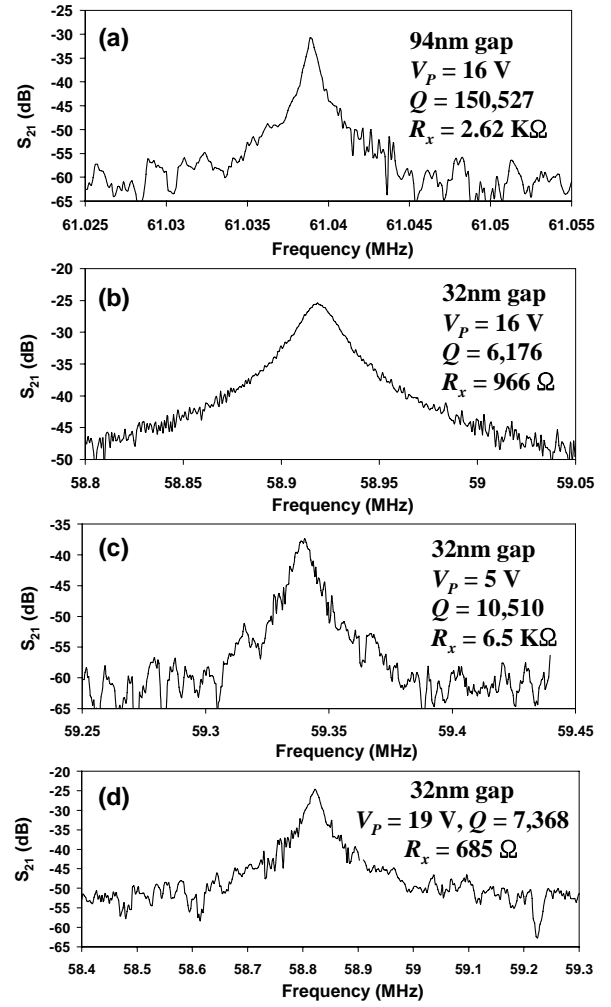


Fig. 6: Frequency characteristics of an initially 94nm-gap resonator before and after ALD coating. From top to bottom: (a) right after HF release; (b) after partially filling the gap with 30.7 nm  $\text{HfO}_2$  and sintering at  $400^\circ\text{C}$  for 3 minutes, showing  $R_x < 1 \text{ k}\Omega$ ; (c) after the same conditions as (b) but with lower  $V_p$ , showing  $Q > 10,000$ ; and (d) after sintering at  $400^\circ\text{C}$  for another 3 minutes, showing even lower  $R_x$  at  $V_p=19\text{V}$ .

$$f_o = \frac{1}{2\pi} \sqrt{\frac{k_m - k_e}{m_r}} = \frac{1}{2\pi} \sqrt{\frac{k_m}{m_r} \left( 1 - \left\langle \frac{k_e}{k_m} \right\rangle \right)} \quad (8)$$

where  $k_m$  is the mechanical stiffness,  $k_e$  the electrical stiffness, and

$$\left\langle \frac{k_e}{k_m} \right\rangle = \int_{\theta_1}^{\theta_2} \frac{1}{k_m(\theta)} \cdot \left( V_p^2 \frac{\epsilon_o R t d \theta}{d^2} \right) \quad (9)$$

where  $\theta_1$  and  $\theta_2$  are given in Fig. 5. From (9), the dependence of  $f_o$  on  $V_p$  is strongly influenced by the gap spacing  $d_o$ , suggesting that plots of  $f_o$  versus  $V_p$  can be used to very accurately extract  $d_o$ .

Fig. 7(a) plots frequency versus dc-bias  $V_p$  for two devices before and after  $\text{HfO}_2$  coating. The data in (a) is for a device different from that of Fig. 6, for which curve-fitting with the theoretical prediction of (8) yields gaps of 97nm for the uncoated disk; and 37 nm for the  $\text{HfO}_2$ -coated one—both very close to expectations given that  $\sim 30 \text{ nm}$  of  $\text{HfO}_2$  was deposited, all attesting to the precision by which ALD can achieve a specific film thickness. Fig. 7 (b) plots similar measured and theoretical curves for the device in Fig. 6 after  $\text{HfO}_2$  ALD, but this time also plotting the theoretical prediction for a

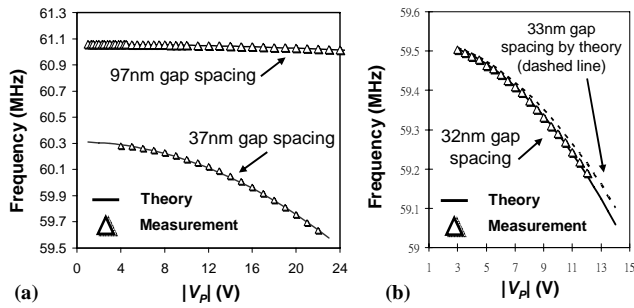


Fig. 7: Resonance frequency  $f_o$  vs. dc-bias  $V_P$  plots of measurement data and theory (a) a 97nm-gap resonator before and after 30nm  $\text{HfO}_2$  coating; and (b) a 32nm-gap partial-filled  $\text{HfO}_2$  device.

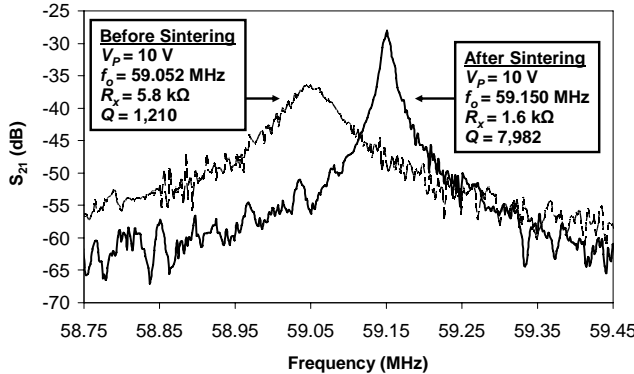


Fig. 8: Frequency characteristic of a 37nm-gap resonator before and after sintering, showing marked improvement in  $Q$ .

33nm gap (dashed line). The offset in the curves shows just how sensitive the  $f_o$  versus  $V_P$  can be in determining  $d$ .

Part of the reason for the reduction in  $Q$  seen in Fig. 6 derives from the fact that the  $Q$  of a resonator with a smaller  $R_x$  is loaded more heavily by parasitic interconnect resistance than one with a large  $R_x$ . But comparisons of  $Q$  versus dc-bias  $V_P$  plots suggest that more of the  $Q$  reduction seems to derive from surface losses introduced by the  $\text{HfO}_2$  film. In this respect, the quality of the  $\text{HfO}_2$  deposited film very likely governs the final  $Q$  of an ALD-filled device. To gauge to degree to which  $Q$  depends upon film quality, ALD-filled devices were sintered at  $400^\circ\text{C}$  in forming gas for varying time periods in order to improve  $\text{HfO}_2$  film quality, as done for VLSI transistors [13]. Fig. 8 presents measured frequency characteristics for a 61-MHz wine-glass disk resonator with ALD-coated gaps, showing a marked improvement in  $Q$  after 6 minutes of sintering at  $350^\circ\text{C}$ . More work is needed to find the best recipe, but it appears that a method to restore  $Q$  is at least feasible. It should also be noted that the thicker the ALD coating, the lower the  $Q$  of a  $\text{HfO}_2$  ALD-coated disk. Thus, another approach to retaining  $Q$ 's  $>100,000$  for disk resonators is to merely start with a smaller initial gap and deposit a much thinner ALD coating. For example, if the initial gaps were 50 nm, then only 9 nm of ALD would be needed to match the 32 nm gaps of this work, and the  $Q$  should be higher.

In addition to  $Q$ -reduction, another concern regarding oxide-partial-filled devices is charging. In particular, any charge in the ALD'ed oxide, or at the oxide-silicon interface, will impose a change in electrical stiffness that will pull the frequency of the resonator up or down, according to the sign of the net charge. The existence of such charge is easily discernable by again comparing plots of  $f_o$  versus  $V_P$ , one with positive  $V_P$ , another with the polarity of the  $V_P$  reversed (i.e., with  $V_P = -V_P$ ). Here, a shift in the curve identifies the presence of charge.

Fig. 9 presents plots of  $f_o$  versus  $V_P$  and reverse polarity  $V_P$  for a

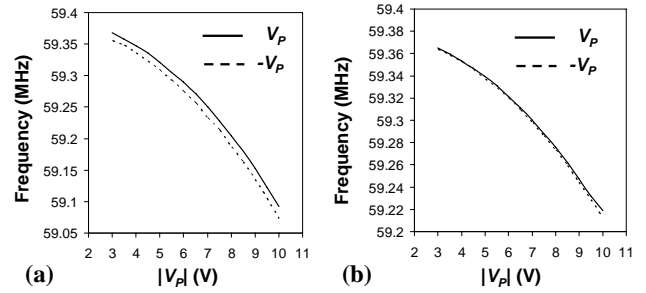


Fig. 9: Resonance frequency  $f_o$  vs. dc-bias  $V_P$  plots of a 32nm-gap resonator (a) before sintering; and (b) after sintering.

partial-ALD-filled gap device before and after sintering at  $400^\circ\text{C}$  in forming gas for 3 minutes. Before sintering, the curve of positive  $V_P$  is horizontally right-shifted from that of negative  $V_P$ , while no difference is seen after sintering. It seems that sintering is a very effective means by which to virtually eliminate the oxide charging issue, at least for  $\text{HfO}_2$  ALD gap coatings.

## CONCLUSIONS

Even with  $Q$  reductions caused by partial-ALD-gap filling that in turn result in  $R_x$ 's only 2.7X better than those of larger air gap devices, the impact of this work is still enormous. This impact is perhaps best gauged by considering the effect of partial-ALD-gap filling on the demonstrated differential disk array filter of [3]. Here, a reduction in gap spacing from 80nm to 32nm of the resonators used in this micromechanical circuit would reduce the needed filter termination resistors  $R_D$  from 2.8k $\Omega$  to only 72 $\Omega$ , which is now compatible with present-day board-level impedances. Since the  $Q$ 's of the radial-mode disk resonators used in the work of [3] were only 10,500, the  $Q$  of 10,510 of this work can maintain the same low insertion loss of 2.43dB for 0.06% bandwidth performance of that filter, but with much smaller matching impedances. Work to actually demonstrate such a filter using partial-ALD-filled gaps is in progress.

**Acknowledgment:** This work was supported by DARPA.

## REFERENCE

- [1] S.-S. Li, *et al.*, "Micromechanical "hollow-disk" ring resonators," *Proceedings, MEMS'04*, pp. 821-824.
- [2] C. T.-C. Nguyen, "Integrated ...," *Proceedings, Int. Symp. on VLSI Tech., Systems, and Apps.*, 2008, to be published.
- [3] S.-S. Li, *et al.*, "MSI micromechanical differential ...," *Tech. Dig., Transducers'05*, pp. 307-311.
- [4] Y. Xie, *et al.*, "1.52-GHz micromechanical ...," *IEEE Trans. Ultrason., Ferroelect., Freq. Contr.*, to be published.
- [5] D. M. Hausmann, *et al.*, "Atomic layer deposition of hafnium and zirconium oxide ...," *Chem. Mater.*, 2002, pp. 4350-4358.
- [6] Y.-W. Lin, *et al.*, "Vibrating ...," *Proceedings, IEEE Int. Frequency Control Symposium*, 2005, pp. 128-134.
- [7] A. I. Zverev, *Handbook of Filter Synthesis*. NY: Wiley, 1967.
- [8] F. D. Bannon III, *et al.*, "High-Q HF microelectromechanical filters," *IEEE J. Solid-State Circuits*, vol. 35, no. 4, pp. 512-526, April 2000.
- [9] M. Demirci *et al.*, "Mechanically corner-coupled square microresonator array for reduced ...," *IEEE/ASME J. Microelectromech. Syst.*, vol. 15, no. 6, pp. 1419-1436, Dec. 2006.
- [10] H. Chandralalim, *et al.*, "Channel-select micromechanical filters using high-k ...," *Proceedings, MEMS'06*, pp. 894-897.
- [11] R. Navid, *et al.*, "Third-order intermodulation distortion ...," *Tech. Dig., MEMS'01, Interlaken, Switzerland*, Jan. 21-25, 2001, pp. 228-231.
- [12] K. Hamaguchi, *et al.*, "3-nm gap fabrication using gas phase sacrificial etching for quantum ...," *Tech. Dig., IEEE MEMS'04*, pp. 418-421.
- [13] S. Jeong, *et al.*, "HfO<sub>2</sub> gate insulator formed ...," *Thin Solid Films*, vol. 515, pp. 5109-5112, April 2007.

# FABRICATION OF ATOM TRAPPING CHIPS WITH FEEDTHROUGH INTERCONNECTS FOR APPLICATIONS IN ATOM OPTICS

*H.C.(Rick) Chuang<sup>1</sup>, D.Z. Anderson<sup>2</sup>, and V.M. Bright<sup>1</sup>*

<sup>1</sup>Department of Mechanical Engineering, University of Colorado, Boulder, Colorado, USA

<sup>2</sup>Department of Physics, University of Colorado, Boulder, Colorado, USA

## ABSTRACT

This paper presents a new method to fabricate the feedthrough vias in atom trapping chips used in ultra-high-vacuum (UHV) atom-optics cells for Bose-Einstein Condensation (BEC) experiments. A process was developed which uses silicon nitride thin film and copper electroplating to seal the vias. The atom trapping chips offer simple microfabrication and reduced volume of the atom trapping cell. The results demonstrate that 8 Amps current can be conducted through the vias while the vacuum can be held under  $4 \times 10^{-11}$  Torr at room temperature. The via fabrication yield after anodic bonding (425 °C) is 97%, a considerable change over our prior results of 30% using a different process [1].

## INTRODUCTION

BECs have been realizable for several years now and some of the advantages of microscopic magnetic traps for cold atoms on a chip have been described [2, 3]. W. Hansel [2] demonstrated that the formation of BEC can be simplified using a magnetic atom trap on a chip in a glass cell under UHV. The electrical connections to the chip were made by wires soldered on the connector inside the cell. The wires and solder areas were found to be vulnerable, resulting in an unreliable vacuum seal. Previously our group [4] proposed a different portable atom trapping chip system in which the chip itself forms one wall of the vacuum cell by attaching a mirrored silicon plate (50  $\mu\text{m}$  thick) anodically bonded to the cell (Figure 1). However, the electrical connection is realized by pin connectors along the chip edges which again require much soldering in a small area.

In the last decade, a large number of sensors and actuators have been developed using MEMS processes. Each application puts specific requirements on the package dimensions, materials, cost and reliability. Through-wafer electrical connections are now becoming increasingly important for three-dimensional integrated circuits, microelectromechanical systems packaging and radio-frequency components. Therefore, wafer through-hole interconnect technology has been studied extensively [5,6]. Most research teams report their results on the formation of through-wafer metal plugs using copper electroplating techniques. However, all of the previous works reviewed simply require electrical conduction from one side of substrate to the other side; none of them require an ultra-high vacuum (UHV) seal (below  $10^{-9}$  Torr) on the feedthrough vias. Here, we propose the new fabrication of feedthrough atom trapping chips based on a simple microfabrication process.

In this paper, we present our feedthrough atom trapping chip fabrication process by copper electroplating inside through-wafer vias. With the new feedthrough atom chips, the atom chips can be anodically bonded to the glass cell instead of using the epoxy. Therefore, the glass cell baking temperature can be raised up to 400°C without any leaking problems, giving a much better vacuum quality for BEC experiments. After the glass cell baking process, a custom connector can be directly clipped on the back side of the atom chip for electrical connections, thus eliminating any soldering.

## FABRICATION PROCESS

The atom chip, Figure 2, is made from a double side polished, 3

inch diameter silicon wafer (100 cut, 380  $\mu\text{m}$  thick). A 1  $\mu\text{m}$  thick low stress silicon nitride layer (LPCVD) was grown on both sides of the wafer as an insulating layer. Etch windows on the silicon nitride layer are patterned by RIE and the electrical feedthrough vias (120  $\mu\text{m} \times 120 \mu\text{m}$  square) are then etched through the wafer by KOH (30% in DI water, 80 °C). After KOH etching, the 1  $\mu\text{m}$  thick silicon nitride thin film was left on the other side of the substrate. An adhesion layer, chromium (15 nm), and a gold layer (400 nm) were evaporated on both sides of the substrate and inside the vias as a mask layer for HF etching. The front side anodic bonding areas were patterned and the silicon nitride layer is etched away by HF (48%) in these locations. The rest of silicon nitride layer was protected by the gold mask. After HF etching, the gold layer and chromium layer were stripped by aqua regia solution and CR-7. A 100 nm oxide layer was thermally grown on both sides of the substrate and inside the vias as an insulating layer between vias. An adhesion layer, titanium (30 nm), and a copper seed layer (250 nm) were evaporated on both sides of the substrate and inside the vias. A photoresist (AZ 4620) was spin coated on both sides of the substrate. The backside pads and via openings were patterned. A 15  $\mu\text{m}$  thick copper layer was then plated by electroplating. The copper electroplating current density was set to 40 mA/cm<sup>2</sup> and the deposition rate was around 0.5  $\mu\text{m}/\text{min}$ . The total plating time was 30 mins. After backside pad plating, the front side via openings were patterned and then the copper seed layer and titanium adhesion layer were etched away using copper and titanium etchants. The copper etchant consisted of 500 ml DI water, 5 ml Sulfuric acid and 60 g Microetch 85 powder from Technic, Inc. The etching rate was approximately 0.25  $\mu\text{m}/\text{min}$  at room temperature. The titanium etchant consisted of 40 parts DI water, 1 part Nitric acid and 1 part Hydrofluoric acid. The silicon nitride layer (1 $\mu\text{m}$ ) and oxide layer (100 nm) inside the front side via opening were removed by RIE. The atom chip wires (100  $\mu\text{m}$  wide) were patterned on the front side and 15  $\mu\text{m}$  thick copper was deposited by copper electroplating with the same plating parameters setup mentioned previously. After the vias were sealed by copper electroplating, the adhesion layer, titanium and copper seed layers were stripped off the chip. The final step was to pattern and etch away the oxide layer for anodic bonding of the chip to the glass cell of the portable vacuum system. The main steps of the fabrication process are described in Figure 2 and the microscopic cross-sectional images (optical microscope) of the diced fabricated vias are shown in Figure 3. Microscope images of the front sides of fabricated vias are shown in Figure 4 and photographs of atom trapping chip anodically bonded to a glass cell are shown in Figure 5.

## VACUUM GLASS CELL CONSTRUCTION

After anodic bonding, a miniature BEC glass system assembled with atom trapping chip was attached to the pumping station as shown in Figure 6. The glass cell is assembled without epoxy being used in the vacuum. The anodic bonding process makes this possible, and allows the vacuum cells to be processed at much higher temperatures than was possible with earlier cell fabrication techniques [4]. The atom trapping chip with electrical feedthrough vias simplifies electrical connections to the vacuum regions of the system.

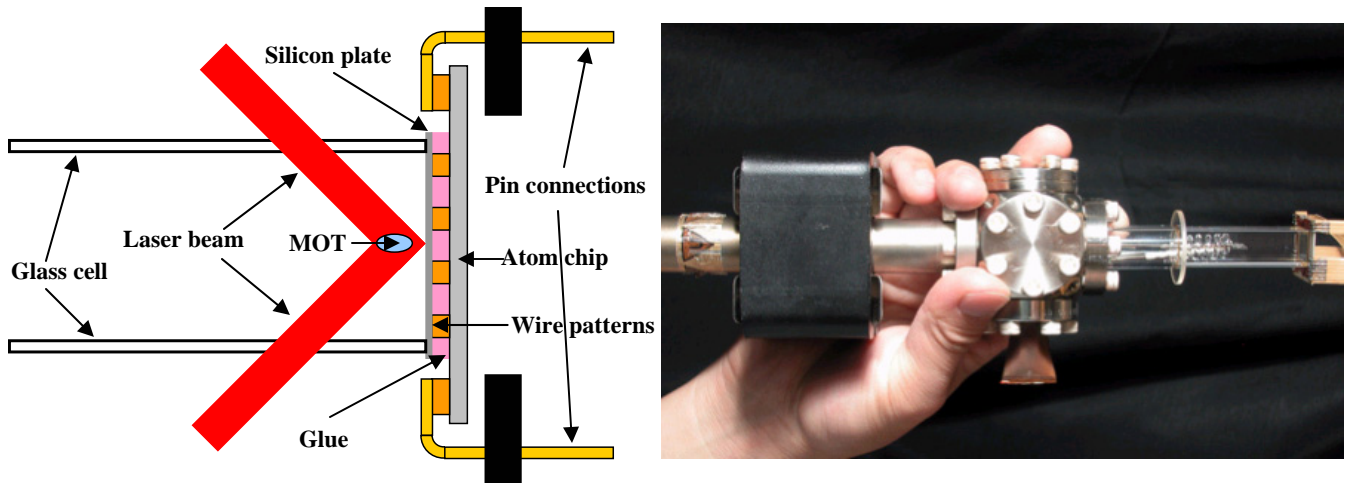


Figure 1: Schematic drawing and photograph of the portable BEC vacuum system in which MOT is created (Magneto-Optical Trap).

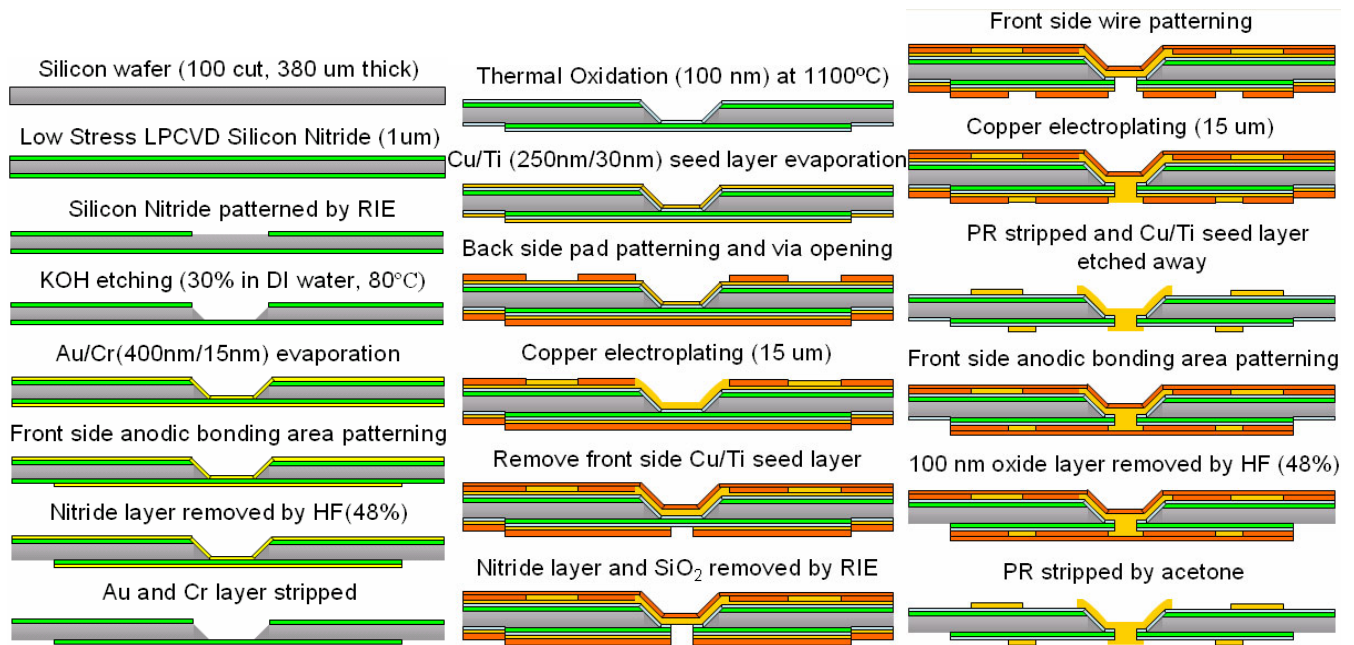


Figure 2: Fabrication process for creating feedthrough atom trapping chips.

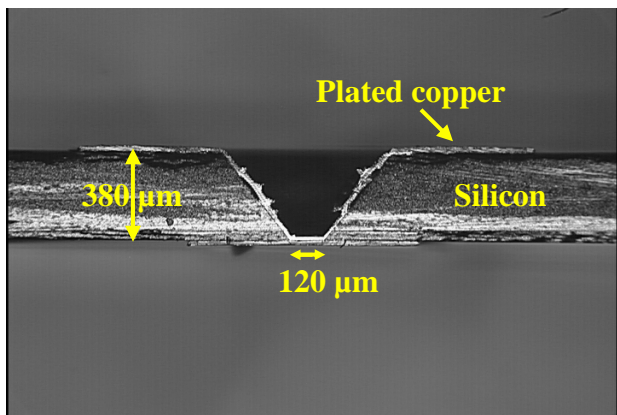


Figure 3: Cross-sectional view of the diced vias.

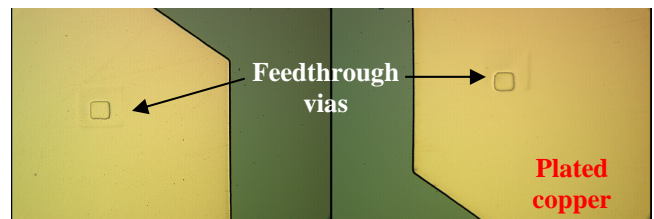


Figure 4: Microscope images of the fabricated vias on the front side of the atom chip.

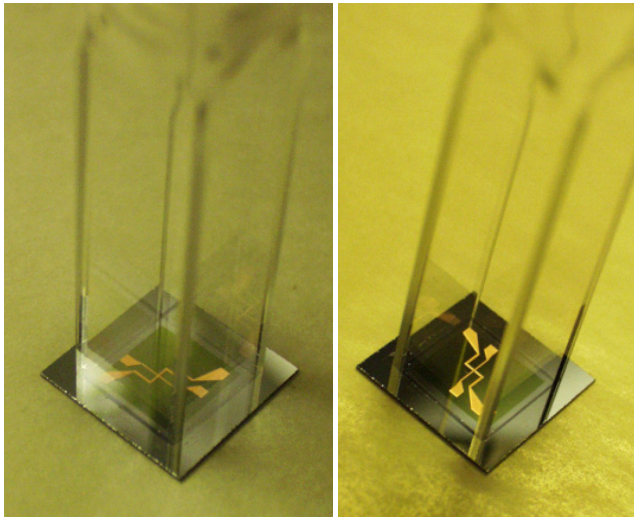


Figure 5: Photographs of atom trapping chip anodically bonded to a glass cell.

As show in Figure 6 the vacuum chamber has 4 general parts: the atom chip, the BEC cell, the center six way flange, and the 2D MOT cell. The 2D MOT cell is made from a 1cm Pyrex flourimeter cell (Starna Cells 3-Px-10). The cell is lapped and polished on the open end, and a rubidium source tube is glass blown to one of the side walls of the cell. The source tube is a 12mm Pyrex tube that is closed by a Pyrex disk with four pin press electrical feedthroughs. Attached to the pin presses are a non-evaporable getter (SAES getters HI/7-6) and a SAES rubidium dispenser. The getter is used to pump the hydrogen released by the Rb dispenser and to help maintain the vacuum in the 2D MOT cell. The 2D MOT cell is joined to the BEC cell and vacuum pumps by the center vacuum flange. The flange itself is a 6 way mini-conflat cube (Kimball Physics MCF133-SC6). A 2l/s ion pump mounted perpendicular to the MOT cells maintains the pressure in the BEC cell. Additionally a second non-evaporable getter (SAES getters HI 7/6) is connected to a conflat mounted power feedthrough and is used in lieu of a titanium sublimation pump. A copper pinch off tube is brazed to a third conflat flange. The pinch off tube is attached to a vacuum pumping station for the initial pump down and bakeout. After bakeout the copper tube is pinched off so the vacuum cell can be separated from the pumping station. The BEC cell is made by glass blowing a custom made (New Era Enterprises) square 1cm ID Pyrex cell to a Pyrex glass to metal mini-conflat adaptor. The other end of the cell is lapped and polished for anodic bonding. A fabricated silicon atom chip with UHV electrical vias is anodically bonded to this polished surface.

## ELECTRICAL AND VACUUM TEST RESULTS

After the feedthrough atom trapping chips were made, a quick vacuum test was performed by a helium vacuum detector in order to check if there were any immediate leaks on the feedthrough vias. The atom chip was placed on a chuck with an O-ring and the leak detector is pumped to high vacuum. Once the vacuum reaches a reasonable value ( $1 \times 10^{-6}$  ~  $1 \times 10^{-7}$  Torr), the helium gas probe is placed close to the vias in order to check for leaking. If the vias leak, the helium detector detects helium that comes through the feedthrough vias and the vacuum pressure readout of the helium detector will increase immediately. No leaking of the feedthrough vias was detected.

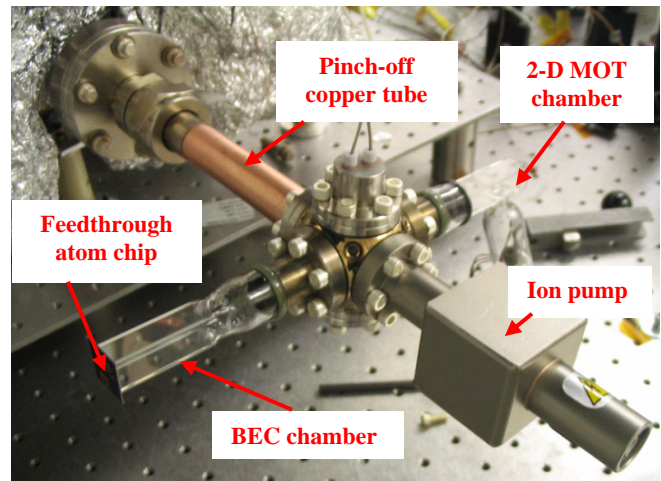


Figure 6: A miniature BEC system attached to the pumping station.

## Resistance measurement

The BEC experiments require high current (5 Amps) to run through the feedthrough vias. Therefore, resistance measurements become important to examine the ability of fabricated feedthrough vias to handle such high currents. In order to deal with the problem of contact resistance when measuring the resistance from the vias, a four point resistance measurement method was performed. The resistances across the feedthrough vias were measured by a Multimeter (Keithley, 2002 Multimeter). The measurement results are shown in Figure 7. All of the measured resistances from randomly selected 20 vias are all below 0.1 ohms, which is low enough to allow sufficient current for the BEC experiments.

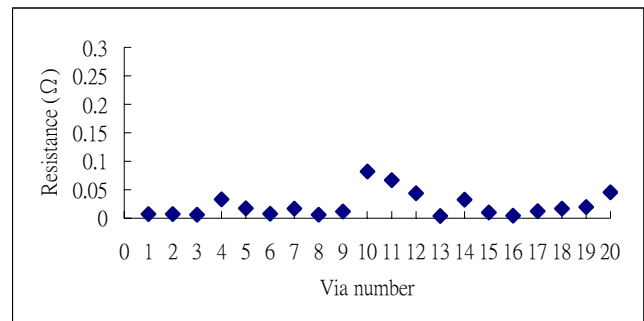


Figure 7: Resistances measurement from 20 vias (The measured resistances of the 20 vias are all below 0.1 Ω).

## Current measurement

In order to create adequate magnetic fields to trap atoms in BEC experiments, no more than 5 Amps current running through the copper wires is required, and thus through the feedthrough vias as well. Five randomly selected vias on the atom chip were soldered to wires on the bonding pads of the atom chip. Current, ranging from zero to 8.7 Amps, was applied through soldered wires by a high current power supply (Sorensen, DCS8-125E) for 1 minute. The test results show that all of the five feedthrough vias survived during the high current test. From this current test results, 8 Amps of current can be successfully run through the feedthrough vias for 1 minute without burning them out. Therefore, all of the tested vias were suitable for BEC experiments, which run typically under 1 minute. The measured voltage as a function of applied current is shown in Figure 8.

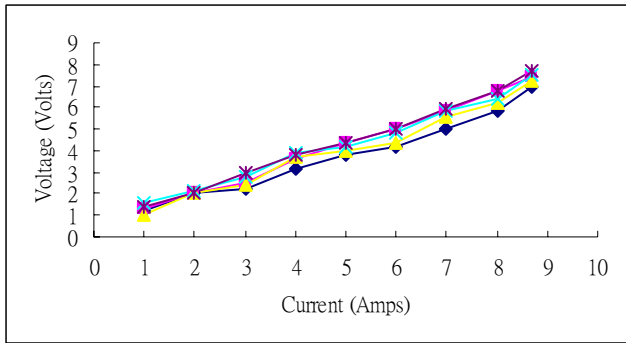


Figure 8: The measured voltage as a function of applied current for 5 feedthrough vias.

In addition to current tests, the measurement of the vias life time with different currents applied was also performed. A current range from 10 to 13 Amps was applied to four randomly selected feedthrough vias until they burned out. The measurement results are shown in Figure 9. In Figure 9, vias with 10 and 11 Amps of current applied lasted longer than 1 minute which satisfies the requirement of BEC experiments, 1 minute. However, running such high current for BEC experiments is risky since the life time is very close to 1 minute. The other vias with 12 and 13 Amps of current applied burned out after few seconds of testing.

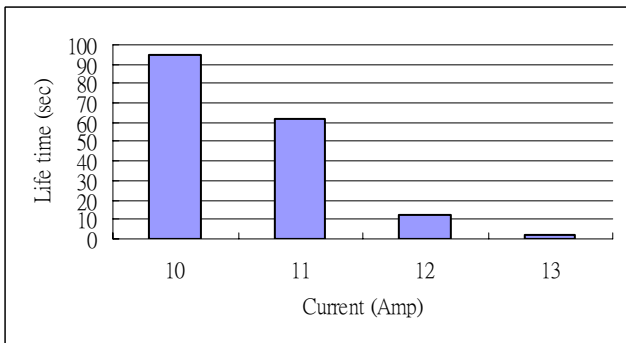


Figure 9: Feedthrough vias life time measurement with different applied current.

### Pressure Measurement

After the miniature BEC system was assembled with all the components, including the atom chip, it was attached to the vacuum pumping station for initial pump down and bakeout. The whole BEC system was baked out at 350 °C for 80 hours in order to remove contamination inside the glass cell. The overall pumping time was around 3 days to reach cell pressure of  $4 \times 10^{-11}$  Torr, which is low enough to pinch off for BEC experiments. No leak was found from the feedthrough vias and anodic bonding areas during the pump down and bakeout process. Next, the miniature BEC system was pinched off after the cell pressure reached  $4 \times 10^{-11}$  Torr. The measured pressure curve as a function of time is shown in Figure 10. In Figure 10, there were sharp pressure peaks every 4 hours. This is because of the action of a titanium sublimation pump, which was triggered every 4 hours. When the pump was triggered, titanium was released into the cell to absorb hydrogen and then was pumped away by a turbo pump (Varian, Turbo-V70LP). After pumping for 76 hours, the bakeout process was complete and the BEC cell began to cool down, thus the cell pressure dropped substantially as shown in Figure 10. Meanwhile, the ion pump on the BEC system was activated to maintain the pressure inside the

cell. At 60 hours, the BEC system was switched from the turbo pump to an Ion pump so that the system can be separated from the pumping station after pinch off. At switchover, a jump can be seen in the pressure curve. After couple hours, however, the ion pump was able to return the cell pressure to  $4 \times 10^{-11}$  Torr at room temperature and it is low enough to pinch off for BEC experiments. The atom chip vias were able to hold the pressure during the entire pump and bake out process.

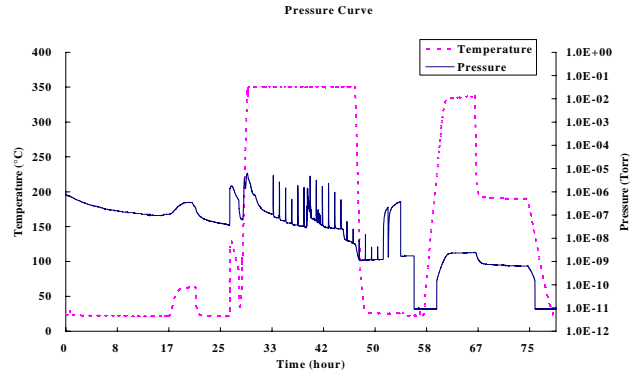


Figure 10: Pressure curve as a function of BEC cell baking time.

### CONCLUSIONS

A fabrication process for the purpose of creating feedthrough atom trapping chips for BEC experiments has been developed. The fabricated feedthrough vias and anodically bonded areas were successfully tested by a helium vacuum detector. A feedthrough via fabrication yield rate of 97% was achieved after anodic bonding (required heating to 425 °C). The resistances of 20 random feedthrough vias were measured by a four point resistance measurement method and were all below 0.1 ohms. Electrical current measurement showed that at least 8 Amps can be conducted through the vias with no leaking under vacuum. After baking out the cell (350 °C) on the vacuum pumping station, the final cell pressure of  $4 \times 10^{-11}$  Torr at room temperature was achieved. The cell was then pinched off to maintain the vacuum for BEC experiments.

### REFERENCES

- [1] H.C. Chuang, T.K. Hakala, D.Z. Anderson, and V.M. Bright, "Fabrication of feedthrough atom trapping chips", Technical Digest of the 14<sup>th</sup> International Conference on Solid-State Sensors, Actuators and Microsystems (TRANSDUCERS 2007) Lyon, France, June 10-14, Vol. 2, pp. 2059-2062.
- [2] W. Hansel, P. Hommelhoff, T.W. Hansch, and J. Reichel, "Bose-Einstein condensation on a microelectronic chip", Nature, vol. 413, pp. 498-501 (2001).
- [3] D. Muller, D.Z. Anderson, R.J. Grow, P.D.D. Schwindt, and E.A. Cornell, "Guiding neutral atoms around curves with lithographically patterned current-carrying wires", Phys. Rev. Lett., vol. 83, pp. 5194 (1999).
- [4] S.W. Du, M.B. Squires, V.M. Bright, K. Reichel, T.W. Hansch, and D.Z. Anderson, "Atom-chip Bose-Einstein condensation in a portable vacuum cell", Phys. Rev. A, vol. 70, 053606 (2004).
- [5] N.T. Nguyen, E. Boellaard, N.P. Pham, V.G. Kutchoukov, G. Craciun and P.M. Sarro, "Through-wafer copper electroplating for three-dimensional interconnects", J. Micromech. Microeng., vol. 12, pp.395-399 (2002).
- [6] V.G. Kutchoukov, M. Shikida, J.R. Mollinger and A. Bossche, "Through-wafer interconnect technology for silicon", J. Micromech. Microeng., vol. 14, pp.1029-1036 (2004).

# LOW-TEMPERATURE (<300°C) LOW-STRESS SILICON CARBIDE SURFACE MICROMACHINING FABRICATION TECHNOLOGY

Frederic Nabki<sup>1</sup>, Tomas A. Dusatko<sup>1</sup>, Srikar Vengallatore<sup>2</sup>, and Mourad N. El-Gamal<sup>1</sup>

<sup>1</sup>Department of Electrical and Computer Engineering, <sup>2</sup>Department of Mechanical Engineering  
McGill University, Montreal, CANADA

## ABSTRACT

A low temperature (<300°C), low-stress micro electromechanical systems fabrication process based on a silicon carbide structural layer is presented. A Hexoloy-SG target enables low-temperature DC sputtering of amorphous silicon carbide. The process is designed for low-cost implementation and CMOS post-integration stemming from chemical and thermal compatibility. Process flow, deposition, etching, and stress control are discussed, and the electrical transfer characteristic of a fabricated resonator device is reported to demonstrate a process application.

## INTRODUCTION

Historically, silicon has been the structural layer of choice for microelectromechanical systems (MEMS) fabrication as it is commonly used by the semiconductor industry. However, the mechanical properties of silicon are not optimal for many applications, and other materials such as silicon carbide (SiC) are being developed to improve performance, enhance reliability, and enable new functionalities in MEMS. In contrast with silicon, SiC exhibits higher acoustic velocity, higher fracture strength, hardness, and desirable tribological properties [1]. In addition, SiC can operate at higher temperature, and withstand corrosive and erosive environments, which makes this material suitable for use in harsh [2] and biological [3] environments. These factors, along with the maturation of deposition and patterning techniques, make SiC a natural choice for next generation MEMS processing.

Adding MEMS capabilities to integrated circuits processes (such as CMOS) is very desirable in many sensing and control applications. However, low-temperature processing of SiC is non-trivial, and most SiC MEMS processes do not intrinsically lend themselves to CMOS integration (<400°C). This work demonstrates for the first time a metallized, low-temperature, low-stress amorphous silicon carbide (*a*-SiC) surface micromachining process for the fabrication of micro electromechanical systems. It is designed to be CMOS-compatible, both chemically and thermally [4].

This paper outlines the process flow, and discusses the deposition and etching of SiC. Several devices are shown, and the measured characteristics of a microelectromechanical (MEM) resonator are reported to demonstrate the capabilities of this CMOS-compatible fabrication process.

## DEPOSITION TECHNOLOGY

The technology is based on the use of Hexoloy-SG, which is an electrically conductive sintered SiC alloyed with 6 wt% carbon. This material permits DC sputtering of thin films at relatively high rates and low temperatures, with simple implementation and low cost. Residual stresses of the films can be tuned by changing the argon pressure during deposition.

SiC deposition has generally not lent itself to be CMOS compatible, because of the high temperatures involved (>800°C) in traditional polycrystalline SiC (poly-SiC) chemical vapor deposition (CVD) [5-7]. Plasma enhanced CVD (PECVD) has been used to deposit *a*-SiC at reduced temperatures [8], but annealing at around 600°C was required to reduce film stress [9]. Amorphous SiC has similar properties to poly-SiC, with variations in properties

such as the Young's modulus [10]. Low-temperature PECVD of *a*-SiC tends to form hydrogenated films (*a*-SiC:H) with lower Young's modulus than sputtered *a*-SiC [10]. Table 1 compares different SiC types, with poly-silicon as a reference. In accordance with the Hexoloy-SG properties [11], nanoindentation analysis of the DC sputtered SiC thin films yielded a higher Young's modulus than that of poly-silicon and other *a*-SiC films [12].

Table 1: Properties of different materials.

Material	Dep. type	Temp. (°C)	Young's mod. (GPa)	Acoustic Velocity (km/s)
poly-Si	LPCVD	1050	169 [13]	8.52
3C-SiC	LPCVD	900	401 [14]	11.18
<i>a</i> -SiC	RF Sput.	-	231 [10]	8.48
<i>a</i> -SiC:H	PECVD	600 (anneal)	153 [10]	6.90
This work ( <i>a</i> -SiC)	DC Sput.	<170	258 [12]	9.50

## THE PROCESS FLOW

The process provides a total of three metallic layers for routing signals and electrostatic actuation. Polyimide is used as the sacrificial layer in this surface-micromachining process. A layer of chromium is used as an etch stop for the SiC plasma etch, and also protects the underlying polyimide from fluorination [15]. Finally, a thick aluminum layer is available to lower the resistivity of interconnects, and to create bonding pads.

Figure 1 illustrates the process flow to create clamped-clamped beam resonators. A DC sputtered 60 nm aluminum layer is wet etched to pattern the bottom electrode (Fig. 1a). Subsequently, a variable thickness (>200 nm) polyimide sacrificial layer is spun-on, cured, and patterned to form the anchors (Fig. 1b). Another 60 nm aluminum layer renders the bottom surface of the SiC conductive (Fig. 1c).

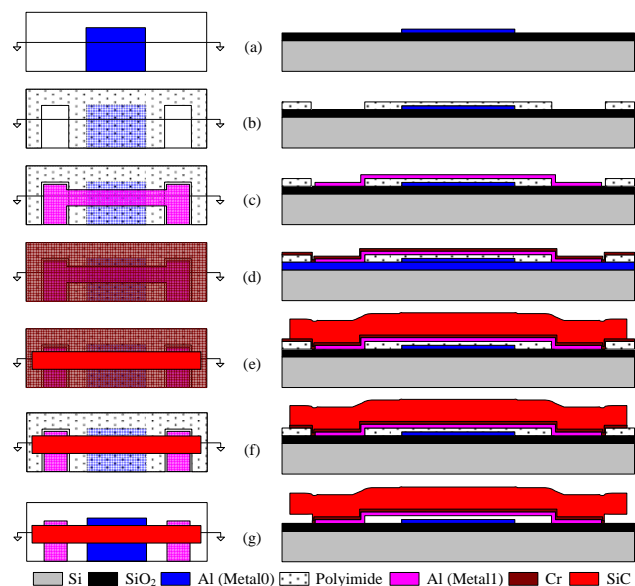


Fig. 1: Process flow for a clamped-clamped beam resonator.

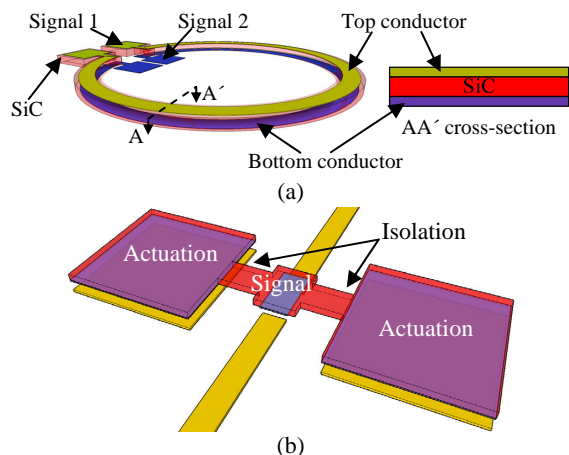


Fig. 2: (a) A released MEM inductor with two isolated conductive layers, and (b) a MEM switch with signal/actuation isolation.

An 80 nm chromium etch-stop layer is then DC sputtered (Fig. 1d) followed by the 2  $\mu\text{m}$  SiC structural layer. The etch-stop protects the underlying polyimide from fluorination for subsequent release [15]. The SiC is then patterned through  $\text{NF}_3$  reactive ion etching (RIE) (Fig. 1e). Finally, a wet etch removes the etch-stop (Fig. 1f), then oxygen plasma releases the structures (Fig. 1g). Not shown in Fig. 1 is an aluminum layer that can be added to the process flow on top of the structural layer. This interconnect layer can be patterned after the SiC etch, or be self-aligned to the SiC layer, by patterning it after the chromium mask.

The low-temperature SiC process allows for the deposition of a metal underneath the SiC, and hence provides the ability to route signals both on top and bottom of the structural layer. This yields interesting design advantages. For example, electrical isolation of signals across the structural layer is possible, such as in the released inductor shown in Fig. 2a, or as depicted in Fig. 2b, where this is exploited in a MEM switch to isolate the actuation and signal voltages.

## DETAILS OF DEPOSITION AND ETCHING

### Characterization of SiC thin films

Thin films deposited by physical or chemical vapor deposition are invariably subjected to intrinsic residual stresses. The choice of DC magnetron sputtering to deposit *a*-SiC permits good control of film stress. Figure 3a shows the effect of the argon pressure during deposition on the biaxial residual stress in the film. The stresses reported on this graph were measured using the wafer-curvature technique. The measured stress of the deposited film goes from compressive to tensile at a working pressure of approximately 6 mTorr. This is consistent with previously reported studies of DC sputtered Hexoloy-SG thin films [16]. Repeated depositions of films at this condition confirmed stress values of  $\pm 50$  MPa. Fracture due to tensile stresses of these magnitudes is not a concern for SiC; however, compressive stresses of tens of megapascals can lead to buckling in slender microfabricated beams. Therefore, the deposition pressure is selected to ensure a low level of tensile stress in the film. Figure 3b shows a scanning electron micrograph of doubly-clamped SiC structures confirming the absence of stress-induced buckling or fracture.

Although the deposition was performed at room temperature with no external heating, the substrate experienced an increase in temperature due to ion bombardment during film growth.

By using adhesive temperature labels on the wafer, the maximum temperature of the substrate was monitored continuously during the deposition of a 2  $\mu\text{m}$  thick SiC. The maximum temperature experienced by the substrate was below 170°C, which is significantly lower than in chemical vapor deposition processes. Furthermore, the film can be grown in stages without vacuum break to lower substrate heating. A growth rate of 75 nm/minute was achieved at a deposition power of 2 kW. This is significantly higher than the 18-30 nm/min reported for *a*-SiC RF sputtering [17, 18].

Energy-dispersive X-ray (EDX) spectroscopy was used to obtain an approximate value for the SiC films' atomic composition. The incident electron beam had an effective volume of interaction which is typically on the order of the thickness of the films used in this work. Therefore, the SiC films were deposited on aluminum substrates to prevent any convolution of silicon signals from the films and substrates. Calibrated measurements yielded an average atomic composition of 47.7% silicon, 51.6% carbon, and 0.7% oxygen. The carbon to silicon ratio of 1.08 is consistent with expectations based on deposition from a Hexoloy-SG target.

The resistivity of the SiC was investigated by probing isolated micro-striplines using DC needles. A lower bound of 40 M $\Omega$  was established for the electrical resistance using a multimeter. The corresponding bound on the bulk resistivity of the film is  $\sim 550$   $\Omega\text{-cm}$ . For comparison, the value reported in [16] for the electrical resistivity of deposited Hexoloy thin films was  $\sim 2000$   $\Omega\text{-cm}$ .

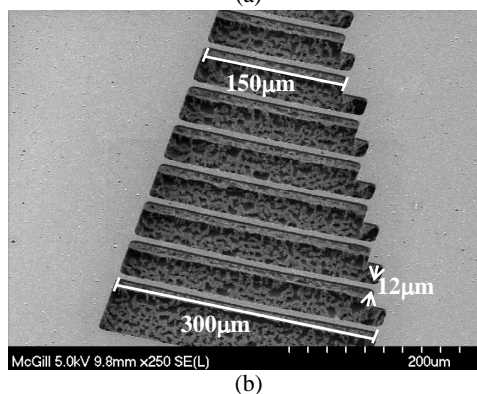
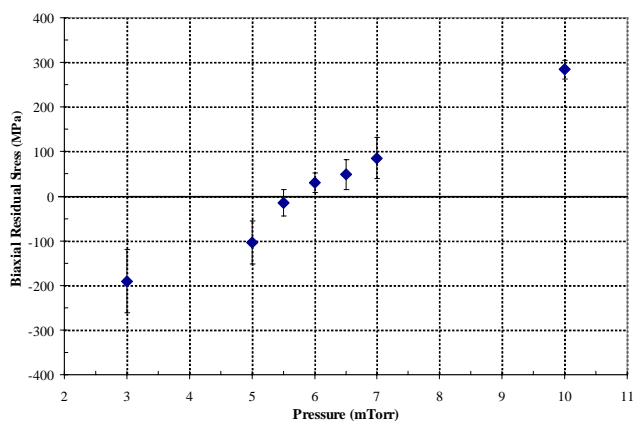


Fig. 3 (a) Biaxial residual stress of an SiC film versus working pressure at 2 kW of power (error bars indicate standard deviation). (b) Scanning electron micrograph of released stress-free clamped-clamped SiC beams.

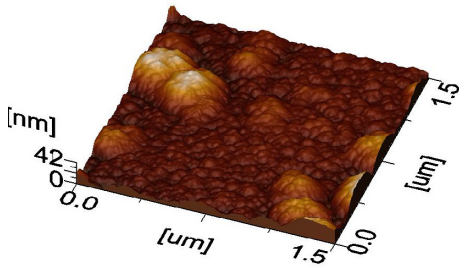


Fig. 4 Atomic force microscopy of the SiC film surface indicating an RMS roughness of  $\sim 20$  nm.

X-ray diffraction (XRD) analysis ascertained the amorphous nature of the film. The surface morphology of the SiC films was examined using electron microscopy and atomic-force microscopy (AFM). The image from an AFM scan of a  $1.5 \mu\text{m} \times 1.5 \mu\text{m}$  area is shown in Fig. 4. The measured RMS roughness ranges from 10 to 30 nm from a series of AFM scans. A remarkable feature of the surface is the presence of irregular mounds, which has also been previously reported for Hexoloy thin films [16].

### Reactive-Ion Etching of SiC

SiC patterning is more difficult than other commonly used materials because of the strong inter-atomic bond of the silicon and carbon atoms. Therefore, etching using aqueous solutions must be performed at temperatures greater than  $600^\circ\text{C}$  [19], which is not compatible with low-temperature processes. As a result, dry techniques such as RIE and lift-off are better suited. Lift-off of SiC can yield good results [20], but entails multiple steps, requires sacrificial materials, and can be difficult to optimize for the desired resolutions. RIE is a more commonly used technique, and can yield better etch profiles and resolution.

A magnetically enhanced (ME) RIE with  $\text{NF}_3$  was used in this work.  $\text{NF}_3$  yields fluorine ions efficiently and, as a consequence, has one of the highest etch rates of all fluorinated gases. SiC RIE can lead to excessive etch residue formation from mechanisms such as micro-masking [21]. Fig. 5 shows an un-optimized etch recipe that yields a grassy etch field. The long columnar structures are attributed to re-deposited non-volatile material landing in the etch field, creating localized masks. This residue can significantly reduce the contact quality of the underlying metal layers. Optimizations in masking material and etch parameters were necessary to mitigate these effects. An etched SiC sample masked with chromium is shown in Fig. 6. The etch rate obtained was  $2079 \text{ \AA}/\text{min}$ , and no residue is present in either the etch field or on the sidewalls.

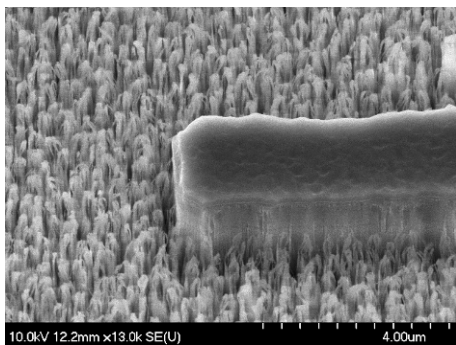


Fig. 5: SiC test structure etched using non-optimal process parameters, yielding etch field residue.

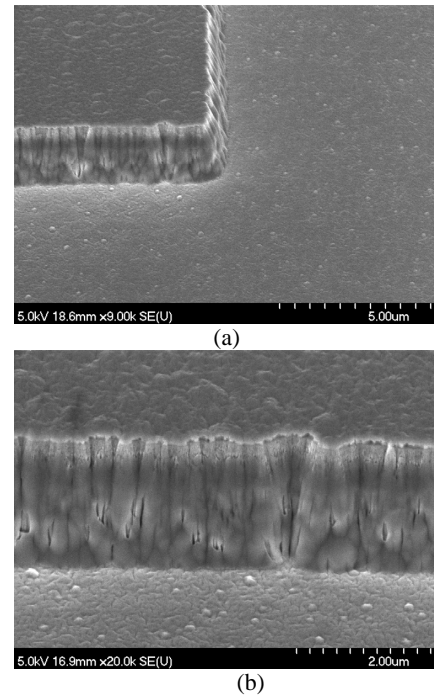


Fig. 6: Scanning electron micrographs of (a) an SiC corner, and of (b) a sidewall, both etched with optimal process parameters.

### FABRICATION RESULTS

Several test devices were fabricated (Fig. 7) using the process flow outlined in Fig. 1. These include beam resonators, inductors, and variable capacitors. All devices clearly exhibited low stresses and low stress gradients in the structural layers. Fig. 7a and 7b show electron micrographs of a clamped-clamped beam resonator and its transducer gap, respectively. The gap is clear of residue, and confirms successful release of the devices. Fig. 7c and 7d show a released variable capacitor with release holes, and a released inductor. Stress control is apparent in the capacitor which shows no signs of plate deformation due to intrinsic stress.

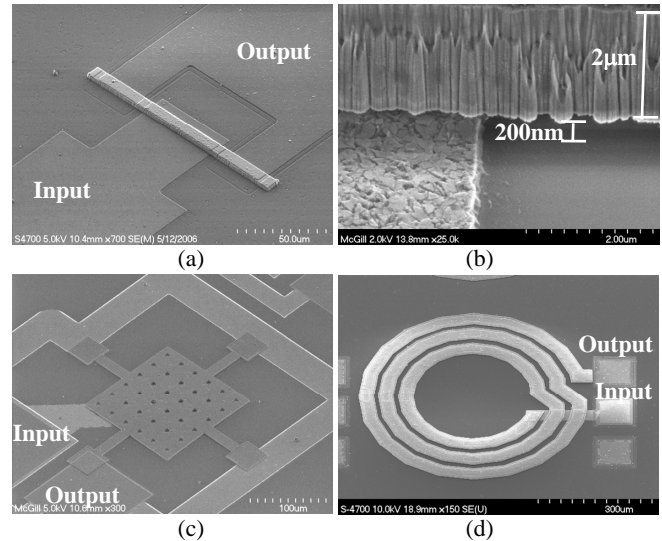


Fig. 7: Scanning electron micrographs of (a) a released clamped-clamped beam MEM resonator, (b) its transducer gap, (c) a variable capacitor, and (d) a released inductor.

Similarly, the released inductor exhibits low stress gradients. This is important, as warping of large structural membranes, such as the parallel plates in a variable capacitor, can result in a significant loss in tuning performance or even device malfunction due to interlayer stray contacts.

The measured transfer function of a clamped-clamped beam resonator device with a natural frequency of 8.3 MHz is shown in Fig. 8. The mechanical quality factor (Q) measured in vacuum is 815, which compares favorably with values reported for similar SiC beam-type resonators (e.g. Q=490 in [20]).

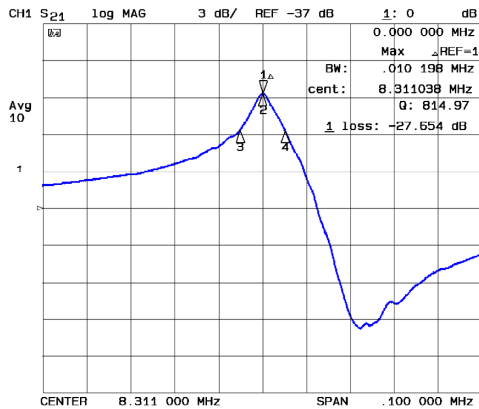


Fig. 8: Transfer function of an 8.3 MHz clamped-clamped beam resonator.

## CONCLUSIONS

This work presented a low-temperature and low-stress process for *a*-SiC that was demonstrated with functional fabricated MEM resonators. This process features double-sided metallization that allows for high quality conduction of two separate signal paths. The SiC structural layer allows for higher acoustic velocity, operation in harsh environment, and increased reliability. DC sputtering is used for metals and SiC, making the process low-cost and easy to integrate with standard integrated circuits processes. Additionally, the sacrificial spun-on polyimide allows for low-cost creation of the small gaps required for devices such as MEM resonators. This process enables processing of SiC through innovative masking techniques that reduce aluminum micro-masking issues. These results establish a strong foundation for the integration of high-performance MEMS with CMOS devices.

## ACKNOWLEDGMENT

The structures reported in this paper were fabricated in the NanoTools Microfabrication Facility (funded by CFI, MDEIE and McGill University). The staff of this Facility provided invaluable assistance during process development. The financial support of McGill University, ReSMiQ, and FQRNT are highly appreciated.

## REFERENCES

- [1] G. L. Harris, "Properties of Silicon Carbide", London, Inspec/IEE (1995).
- [2] R. Cheung, "Silicon Carbide Microelectromechanical Systems for Harsh Environments", London, Imperial College Press (2006).
- [3] S.Santavirta et al., "Biocompatibility of silicon carbide in colony formation test in vitro", Archives of Orthopaedic and Trauma Surgery, 118, 1-2 (1998), pp. 89-91.
- [4] F. Nabki, T. Dusatko, M. N. El-Gamal, and S. Vengallatore, "Low temperature ceramic microelectromechanical structures," US Patent Application, December 2007.

- [5] C. R. Stoldt et al., "A low-temperature CVD process for silicon carbide MEMS", Sensors and Actuators A, 97-98, (2002), pp. 410-415.
- [6] R. F. Wiser, J. Chung, M. Mehregany, and C. A. Zorman, "Polycrystalline silicon-carbide surface-micromachined vertical resonators-part I: growth study and device fabrication", Journal of Microelectromechanical Systems, 14, 3 (2005), pp. 567-578.
- [7] D. Gao et al., "High modulus polycrystalline 3C-SiC technology for RF MEMS", International Conference on Solid State Sensors, Actuators and Microsystems, 2, (2003), pp. 1160-1163.
- [8] L. S. Pakula, H. Yang, and P. J. French, "A CMOS compatible SiC accelerometer", Proceedings of the IEEE Sensors Conference, 2, (2003), pp. 761-764.
- [9] D. S. Kim and Y. H. Lee, "Annealing effects on a-SiC:H and a-SiC:H(F) thin films deposited by PECVD at room temperature", Thin Solid Films, 261, 1-2 (1994), pp. 192-201.
- [10] M. A. E. Khakani et al., "Hardness and Young's modulus of amorphous a-SiC thin films determined by nanoindentation and bulge tests", Journal of Materials Research, 9, 1 (1994), pp. 93-103.
- [11] A. Wolfenden, A. C. Anthony, and M. Singh, "Measurement of Young's modulus and damping for Hexoloy SG silicon carbide", Scripta Materialia, 41, 6 (1999), pp. 611-615.
- [12] J. Crocker, G. Sosale, and S. Vengallatore, "Nanomechanical characterization of Hexoloy-SG silicon carbide thin films", Proceedings of the 21st Canadian Congress of Applied Mechanics, (2007), pp. 678-679.
- [13] W. N. Sharpe, B. Yuan, and R. Vaidyanathan, "Measurements of Young's modulus, Poisson's ratio, and tensile strength of polysilicon", IEEE International Workshop on Micro Electro Mechanical Systems, (1997), pp. 424-429.
- [14] J. S. Mitchell et al., "Examination of bulge test for determining residual stress, Young's modulus, and Poisson's ratio of 3C-SiC thin films", Journal of Aerospace Engineering, 16, 2 (2003), pp. 46-54.
- [15] L. J. Matienzo et al., "Surface composition and distribution of fluorine in plasma-fluorinated polyimide", Journal of Vacuum Science & Technology A, 6, 3 (1988), pp. 950-953.
- [16] M. Tenhover and I. B. Ruppel, "DC-magnetron sputtered silicon carbide", Proceedings of the Thin Films Symposium, (1995), pp. 227-232.
- [17] N. Ledermann et al., "Sputtered silicon carbide thin films as protective coating for MEMS applications", Journal of Surface and Coating Technology, 125, 1-3 (2000), pp. 246-250.
- [18] A. K. Costa and S. S. Camargo, "Properties of amorphous SiC coatings deposited on WC-Co substrates", Journal of Materials Research, 6, 1 (2003), pp. 39-42.
- [19] P. H. Yih, V. Saxena, and A. J. Steckl, "A Review of SiC Reactive Ion Etching in Fluorinated Plasmas", Physica Status Solidi B, 202, 1 (1997), pp. 605-642.
- [20] R. F. Wiser, M. Tabib-Azar, M. Mehregany, and C. A. Zorman, "Polycrystalline silicon-carbide surface-micromachined vertical resonators - part II: electrical testing and material property extraction", Journal of Microelectromechanical Systems, 14, 3 (2005), pp. 579-589.
- [21] P. H. Yih and A. J. Steckl, "Effects of hydrogen additive on obtaining residue-free reactive ion etching of  $\beta$ -SiC in fluorinated plasmas", Journal of the Electrochemical Society, 140, 6 (1993), pp. 1813-1824.

# MICROFABRICATED HIGH DENSITY MULTIPLEXED ELECTROSPRAY

C. M. Waits<sup>1</sup>, B. Morgan<sup>1</sup>, W. Deng<sup>2</sup>, N. R. Jankowski<sup>1</sup>, A. Gomez<sup>2</sup>, and B. Geil<sup>1</sup>

<sup>1</sup>US Army Research Laboratory, Adelphi, Maryland, USA

<sup>2</sup>Yale University, New Haven, Connecticut, USA

## ABSTRACT

We present the fabrication, assembly, and testing of novel compact fuel atomization devices for portable power systems. Silicon multiplexed electro spray devices with nozzle densities  $>11,500$  nozzles/cm<sup>2</sup> are demonstrated for the first time exhibiting liquid fluxes  $>400$  mL/hour/cm<sup>2</sup> with droplet diameters  $<5$   $\mu$ m. Compared to prior electro spray devices, these results represent a 40x increase in nozzle density and a 50% reduction in driving voltage and droplet diameter enabling more efficient small-scale combustion.

## INTRODUCTION

Small-scale portable power systems based on the combustion of liquid hydrocarbons have had increasing interest since the mid-1990's [1-3]. These combustion-based devices take advantage of the significantly higher energy density available in liquid hydrocarbons when compared to conventional batteries (at only 10% efficiency, diesel fuel can yield 4.2 MJ/kg, 10 times more than the 0.36 MJ/kg for primary batteries). When scaling down the size of the combustor volume to the cm<sup>3</sup> range and below, catalytic conversion and diffusion-controlled combustion will likely be used and require the fuel to be delivered as small and rapidly evaporating droplets [4]. Using liquid hydrocarbons such as JP-8, the logistical fuel of choice for the Army, a compact and reliable method to atomize the fuel has yet to be developed for portable power systems.

Multiplexed electro spray systems were previously demonstrated to be effective in atomizing liquid fuel into fine droplets enabling meso-scale combustion [4]. However, minimizing combustor volume requires smaller droplet diameters to reduce evaporation time and promote better mixing with the oxidizer. Smaller droplets can be obtained only at the cost of decreasing the flow rate per nozzle because of the monotonic dependence of droplet size on flow rate in typical electro spray operation. Therefore, maintaining or even increasing liquid flux levels requires increasing the level of multiplexing to counteract the smaller per nozzle flow rates.

Previous fabrication and assembly methods produced up to 250 nozzles/cm<sup>2</sup>, but could not accommodate further scaling up of multiplexed electro spray devices for the small droplet diameters ( $<10$   $\mu$ m) and higher flow rates ( $>100$  mL/hour) required in small-scale combustion applications [5-7]. Therefore, a new microfabrication and assembly technique was developed in this work to obtain a high density of electro spray sources that enables the smaller droplet diameters and larger flow rates. The operation of a 19-nozzle array is reported, demonstrating the capability of the high density multiplexed electro spray developed.

## MULTIPLEXED ELECTROSPRAY

The design and configuration of a multiplexed electro spray was previously reported in [7]. The microfabricated multiplexed electro spray is composed of three layers: (1) a nozzle array, (2) an extractor electrode and (3) an electrically insulating spacer (Fig. 1). The device is operated with a potential drop between the conductive fluid within the nozzles and the extractor electrode (HV1-HV2). The fluid forms a cone at the nozzle tip through the balance of surface tension and the electrohydrodynamic force induced by the applied electric field. Above a critical field, a liquid ligament issues

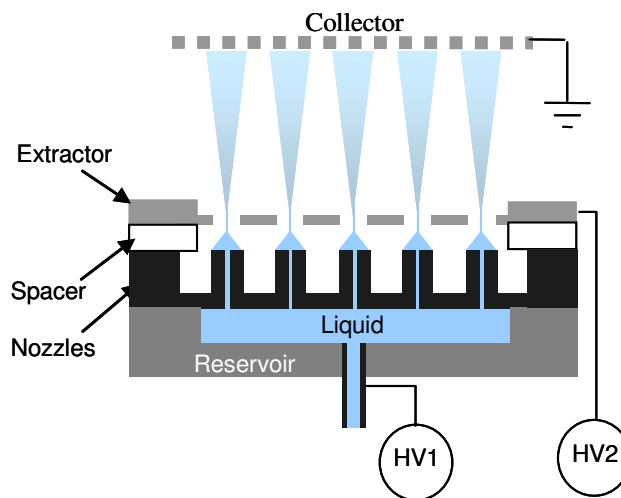


Figure 1: Schematic drawing of a multiplexed electro spray device and setup for testing. The grounded screen acts to draw the fuel droplets away from the device in place of a combustor or air flow.

from the cone tip and breaks up into monodispersed droplets. The Coulomb repulsion of the charged fluid causes the fluid droplets to disperse into a fine mist. A driving field was established between the extractor and grounded collector downstream (HV2-Gnd) to provide a removal force large enough to counteract the space charge effect that may cause satellite droplets to fly back and flood the electrode [8].

The critical geometric features of the multiplexed electro spray are shown in Table 1 for a nozzle array density greater than 11,500 nozzles/cm<sup>2</sup>. Arrays of nozzles ranging from 1 to 91 nozzles were designed onto individual 1.6 cm<sup>2</sup> die. The nozzle outer diameter, height, and pitch, combined with the spacer distance dictate the electric field at the tip of the liquid cone that enables the electro spray operation. Meanwhile, the nozzle inner diameter and length determine the fluidic characteristics of the device.

Table 1. High density multiplexed electro spray design quantities.

Nozzle Parameters	Quantity	Units
Outer diameter	30	$\mu$ m
Inner diameter	15	$\mu$ m
Height	80	$\mu$ m
Pitch	100	$\mu$ m
<b>Extractor Parameters</b>		
Hole diameter	60	$\mu$ m
Membrane thickness	40	$\mu$ m
Layer thickness	200	$\mu$ m
<b>Spacer Parameters</b>		
Spacer Distance	60	$\mu$ m
Anticipated electric field	0.8-1.7	$\times 10^5$ V/cm

The spacer must provide electrical insulation with high electrical breakdown strength to support the electric field required to sustain the electrospray. Additionally, the spacer must provide mechanical stability between the extractor and nozzle layers and maintain micron-level alignment accuracy. Slight misalignment between the 30  $\mu\text{m}$  nozzles and the 60  $\mu\text{m}$  extractor holes may cause the dispersed sprays to impinge on the extractor and cause flooding. Quartz optical fibers were chosen as the spacing element with the dual purpose of providing good insulation as well as precise alignment capability when combined with alignment trenches.

### HIGH DENSITY ELECTROSPRAY FABRICATION

The nozzle and extractor layers were fabricated on separate wafers and then bonded together at the die level using a novel optical fiber alignment technique and room temperature cured epoxy. Figure 2 illustrates the optimized fabrication process flow for the silicon nozzle and extractor layers.

The nozzle layer was fabricated using a 4-inch, 425  $\mu\text{m}$   $\pm 25 \mu\text{m}$ , double sided polished silicon wafer with a 1.1  $\mu\text{m}$  thermally grown silicon dioxide layer. The first step in the nozzle fabrication defines the nozzle rings and alignment trenches into the silicon dioxide using photolithography and subsequent reactive ion etching (RIE). Then, a second photolithography step patterns only the inner hole of the nozzle into a thick photoresist masking layer. The inner holes were then etched using deep reactive ion etching (DRIE) to a depth greater of 100  $\mu\text{m}$ . After this step, the backside silicon dioxide layer on the nozzle wafer was patterned with 60  $\mu\text{m}$  diameter holes. The larger diameter hole enables a higher etch rate, lower aspect ratio, and larger alignment tolerance than if a 15  $\mu\text{m}$  hole were used to match the inner diameter of the nozzle. The larger hole on the backside was etched to approximately 295  $\mu\text{m}$ . The depths chosen for the nozzle inner diameter and backside hole create a 50  $\mu\text{m}$  thickness at the base of the nozzles after the 80  $\mu\text{m}$  nozzle etch. If the base becomes thinner than 50  $\mu\text{m}$  it may be too fragile for arrays having a large nozzle count.

The final fabrication step before dicing of the wafer was to etch the nozzles to the desired depth of 80  $\mu\text{m}$ . Given the thin nozzle wall (7.5 $\mu\text{m}$ ), and photolithography alignment tolerance (1  $\mu\text{m}$ ), even a small negative taper creates a very thin sidewall at the bottom of the silicon nozzle. This can lead to punch through for sidewall angles as small as  $\sim 86^\circ$  (Fig. 3a) or the nozzle breaking off during dicing and bonding. Tuning the deposition cycle time and the etch cycle time in the DRIE multiplexing process resulted in a nearly vertical sidewall profile, as shown in Fig. 3b. The DRIE process must be tuned for different pitches and nozzle outer/inner diameter combinations due to changing silicon loading conditions.

The extractor layer fabrication, shown in Fig. 2 was performed using a 4-inch, 200  $\mu\text{m}$ , double sided polished silicon wafer with a 1.1  $\mu\text{m}$  silicon dioxide. The silicon dioxide layers were patterned using photolithography and RIE, while the silicon was etched using conventional DRIE. The extractor hole above the nozzle layer and the alignment trenches were etched together to a depth of 50  $\mu\text{m}$  to ensure the optical fiber does not touch the bottom of the trench during assembly, as well as ensure the topside etch breaks through. The topside was etched 155  $\mu\text{m}$ , leaving a 45  $\mu\text{m}$  thick extractor membrane. The diameter of the extractor hole and the thickness of the membrane were designed leave excess space for the dispersed spray to pass through without impinging onto the sidewalls. The use of a 200  $\mu\text{m}$  wafer thickness allowed a smaller surface area on the sidewalls of the extractor, thereby minimizing possible space charge effects at the edge of the spray region.

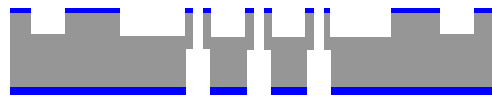
#### Nozzle Fabrication



1. Pattern silicon dioxide for nozzles and alignment trenches



2. Pre-etch nozzle inner diameter using a patterned photoresist masking layer and DRIE.



3. Nozzle formation using silicon dioxide masking layer and DRIE on both top and bottom. Alignment trench depths are defined at the same time.

#### Extractor Fabrication



1. Pattern silicon dioxide on top to define cavity, and bottom to define extractor holes and alignment trenches.



2. Etch extractor holes and alignment trenches using silicon dioxide masking layer and DRIE.

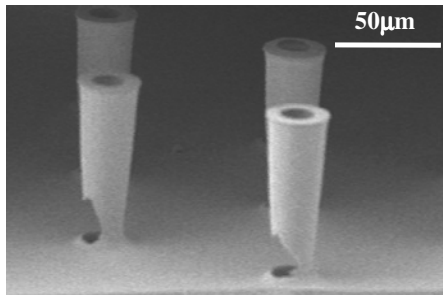


3. Define extractor membrane by etching cavity from the top using the silicon dioxide masking layer and DRIE.

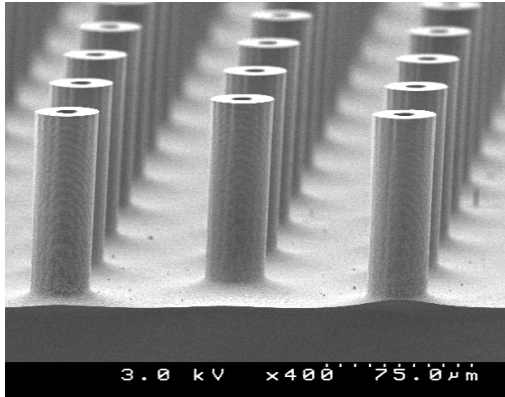


Figure 2. Fabrication flow for the nozzle and the extractor layers.

Conventional bond alignment techniques are limited to wafer level alignment and, furthermore, state-of-the-art machines can only achieve a 1  $\mu\text{m}$  alignment tolerance. In testing of the electrospray devices, it is convenient to employ an impermanent bond, which then requires bond alignment to be performed at the die level. A novel alignment and bonding technique was developed to assemble the nozzle array and extractor electrode layers with high alignment and gap precision. Our technique used 125  $\mu\text{m}$  diameter with  $\pm 1 \mu\text{m}$  diameter tolerance bare optical fibers resting in opposing



(a)



(b)

Figure 3. SEM images of fabricated 30 μm O.D., 100 μm pitch nozzle arrays for nozzles with (a) initial poor sidewall verticality and alignment and (b) good sidewall verticality.

trenches, eliminating the need for specialized alignment equipment. The tight diameter tolerance of the optical fiber enables both alignment and gap control by lithographically tailoring the width of the alignment trenches, as shown in Fig. 4. The nozzle and extractor layers are then assembled using epoxy to secure the optical fibers in 108 μm wide alignment trenches and achieve a gap of 60 μm (Fig. 5).

### FABRICATION RESULTS AND TESTING

Hexagonal arrays of 1, 7, 19, and 91 nozzles and matching extractors were fabricated having a pitch of 100 μm. Varying pitches can be accomplished using the same tuned DRIE etch recipe by including inactive nozzles to maintain silicon loading and aspect ratio. A cross-sectioned device having 91 nozzles is shown in Fig. 6a with close-ups showing the optical fiber alignment and the nozzles in Fig. 6 b and c respectively.

The alignment accuracy and gap precision using the alignment trenches and the optical fiber were measured using an optical profilometer. The alignment accuracy was evaluated by how centered the nozzle was to the extractor opening when looking from the top of the extractor. The measurements showed in-plane alignment to be consistently below 1 μm due to the self-centering nature of a cylindrical fiber within rectangular trenches. Gap uniformity across a 3.5mm wide test membrane was measured to be  $\Delta_{\text{gap}} \leq 1.5 \mu\text{m}$ . Potential errors in this alignment technique include the  $\pm 1 \mu\text{m}$  optical fiber tolerance, fabrication accuracy of alignment trenches, and inconsistent contact between fiber and trench corners. Nonetheless, this new technique has proven quite simple and accurate as an insulating spacer and chip-level alignment/assembly technique.

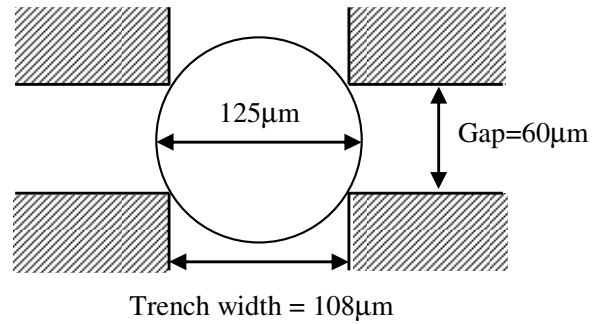


Figure 4. Illustration of alignment and gap control using an optical fiber and tailored alignment trenches.

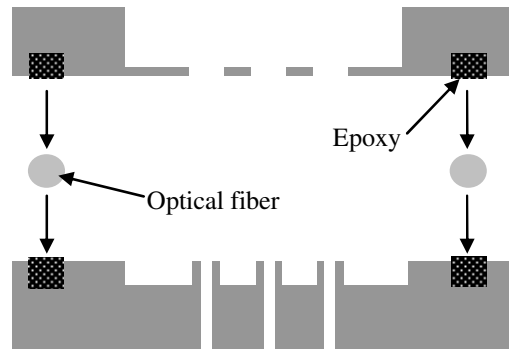


Figure 5. Illustration showing the assembly technique using an optical fiber to align and maintain a prescribed gap between nozzle and extractor layers.

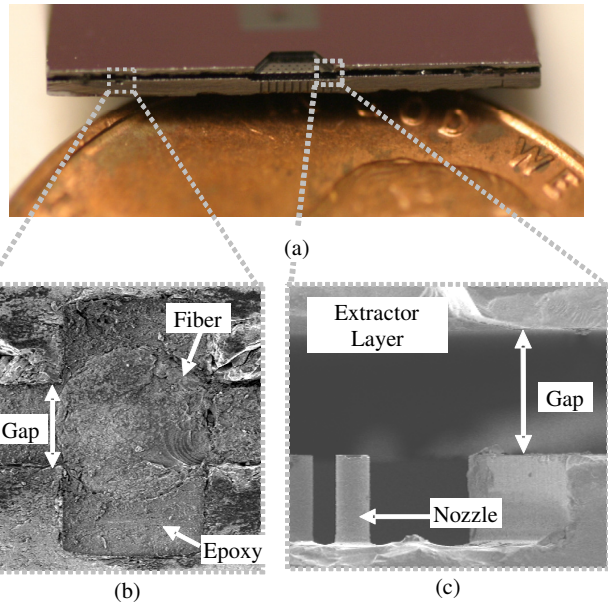


Figure 6. (a) Optical picture showing the cross-section of an assembled electro spray device and SEM images of (b) the optical fiber alignment using the silicon trench and epoxy (see Figure 5) and (c) gap between the nozzle and extractor layers.

Successful electro spray operation with pure ethanol and flow rates on the order of 0.04 mL/hour per nozzle for a 19-nozzle, 100  $\mu\text{m}$  pitch array were achieved using a potential difference of 880 V between the nozzle layer and the extractor layer (HV1-HV2). The bias voltage between the grounded collector, shown in Fig. 1, and the nozzle layer was set to 5kV with the collector 5.5 mm away from the extractor layer, establishing a driving field of 9.1 kV/cm. Figure 7 shows an optical image of the 19-nozzle device operating in electro spray mode.

An average droplet diameter of 4.5  $\mu\text{m}$  was measured using a TSI Phase Doppler Particle Analyzer (PDPA) downstream of the electro spray close to the collector using an equal-distance scan with a step of 100  $\mu\text{m}$ . Figure 8 shows the average droplet diameter as the scan is stepped across the spray from A to A' in Fig. 7. The overall relative standard derivation of the diameter was 13%, which is comparable to that of the uncertainty of the PDPA at 0.5  $\mu\text{m}$ , or 11%. Furthermore, the spatial resolution of the optical technique may be inadequate to sort out primary droplets from satellites in each electro spray. As a result, the recorded spread in droplet size may be artificial and, in part, consequent to averaging both primary and satellite droplets in unequal proportion from point to point.

## CONCLUSION

A new microfabrication process was developed for a high density of nozzles to be fabricated and assembled with an extractor electrode forming the multiplexed electro spray device. A novel alignment technique utilizing bare optical fibers was presented, with die level alignment accuracy below 1  $\mu\text{m}$  demonstrated. The new microfabrication process and assembly techniques presented enabled the first demonstration of a multiplexed electro spray having a source density greater than 11,500 nozzles/cm<sup>2</sup>. Results of a 19-nozzle array showed a liquid flux greater than 400 mL/hour/cm<sup>2</sup> with an average droplet diameter of 4.5  $\mu\text{m}$ , which is sufficient for envisioned compact combustor volumes. Future work will focus on the integration of these electro spray fuel atomizers into Army portable power generator systems operating on JP-8.

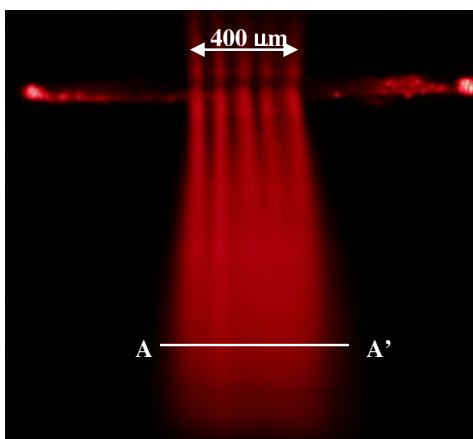


Figure 7. Optical photograph demonstrating electro spray action using pure ethanol and a 19-nozzle array at >11,500 nozzles/cm<sup>2</sup>.

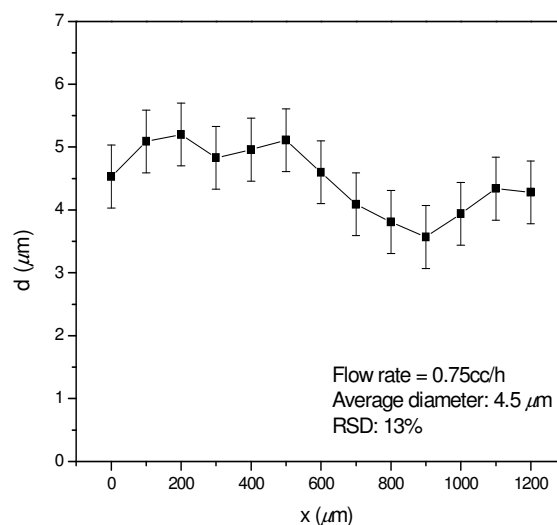


Figure 8. Scan from A-A' in Figure 7 showing the average droplet diameter is 4.5  $\mu\text{m}$  for a 19-nozzle, 100  $\mu\text{m}$  pitch nozzle array at 0.75cc/h.

## REFERENCES

- [1] A.H. Epstein, "Millimeter-scale, MEMS Gas Turbine Engines," Proceedings of ASME Turbo Expo 2003, Power for Land, Sea, and Air, June 16-19, Atlanta (2003), pp. 1-28.
- [2] N. Müller and L.G. Fréchet, "Performance Analysis of Brayton and Rankine Cycle Microsystems for Portable Power Generation," Proceedings of IMECE2002, November 17-22, New Orleans (2002), pp. 1-10.
- [3] Y. Suzuki, Y. Okada, J. Ogawa, S. Sugiyama, and T. Toriyama, "Experimental study on mechanical power generation from MEMS internal combustion engine," Sensors & Actuators: A. Physical, 141, 2, pp. 654-661 (2008).
- [4] W. Deng, J.F. Klemic, X. Li, M. Reed, and A. Gomez, "Liquid Fuel Combustor Miniaturization via Microfabrication," Proceedings of the Combustion Institute, 31, pp. 2239-2246 (2007).
- [5] Tang, K., Lin, T., Matson, D.W., Kim, T., and Smith, R.D., "Generation of multiple electro sprays using microfabricated emitter arrays for improved mass spectrometric sensitivity, Analytical Chemistry", Analytical Chemistry 73, pp. 1658-1663 (2001).
- [6] R. Bocanegra, D. Galán, M. Márquez, I.G. Loscertales, and A. Barrero, "Multiple electro sprays emitted from an array of holes," Journal of Aerosol Science, 36, pp. 1387-1399 (2005).
- [7] W. Deng, J.F. Klemic, X. Li, M.A. Reed, and A. Gomez, "Increase of electro spray throughput using multiplexed microfabricated sources for the scalable generation of monodisperse droplets," Journal of Aerosol Science, 37, pp. 696-714 (2006).
- [8] W. Deng and A. Gomez, "Influence of space charge on the scale-up of multiplexed electro sprays," Journal of Aerosol Science, 38, pp. 1062-1078 (2007).

# OPTIMIZING DIRECT PRINTING OF PZT THIN FILMS

S. Bathurst<sup>1</sup>, J. Jeon<sup>1</sup>, P. Mardilovich<sup>2</sup>, H.W. Lee<sup>1</sup>, and S.G. Kim<sup>1</sup>

<sup>1</sup>Massachusetts Institute of Technology, Cambridge, Massachusetts, USA

<sup>2</sup>Hewlett Packard, Corvallis, Oregon, USA

## ABSTRACT

We recently reported a new method for depositing lead zirconate titanate (PZT) thin films via thermal ink jet (TIJ) printing of a modified sol-gel [1]. The use of PZT in MEMS has been limited due to the lack of process compatibility with existing MEMS manufacturing processes. Direct printing of PZT thin films eliminates the need for photolithographic patterning and etching, allows for controlled deposition over non-planar topographies, and enables the fabrication of devices with varying thickness which cannot be accomplished with conventional spin coating processes. This paper reports conditions of deposition and crystallization for PZT thin films via thermal ink jet printing. Included are details of the solution chemistry developed, printing conditions required for MEMS quality films, and thermal processing parameters that enable a strong piezoelectric response.

## INTRODUCTION

The high degree of piezoelectric and ferroelectric coupling in perovskite phase lead zirconate titanate (PZT) makes it an attractive material for use in MEMS. Due to the strong piezoelectric response and low operating voltage, many groups have worked to integrate thin film PZT into a wide range MEMS devices including: actuators, energy harvesters, resonators, pressure sensors, pumps, nano-positioning stages, and MEMS switches [2]-[4]. However, processing of thin film PZT is not readily compatible with existing MEMS fabrication processes and significant design constraints exist when integrating thin film PZT.

While some recent work has demonstrated novel ways of forming sol-gel based films, spin coating remains the dominant method of forming thin film PZT for MEMS. Not only is spin coating inherently wasteful of the expensive and difficult to manufacture sol, but it prevents the deposition of PZT films on or around out of plane features. Spin coating is not the best fabrication method for PZT based MEMS, but it is the most compatible at the present time. Figure 1 shows the cracking and thinning that occurs when PZT is spin coated over a step about 2 $\mu$ m in height. The sol is also very sensitive to other deposition parameters, including humidity, particle contamination, and substrate condition and as a result device yields are often low. Reliable deposition requires great care and often a good deal of experience processing PZT thin films. Consequently a flexible new approach is needed to easily and effectively deposit high quality PZT thin films in MEMS applications.

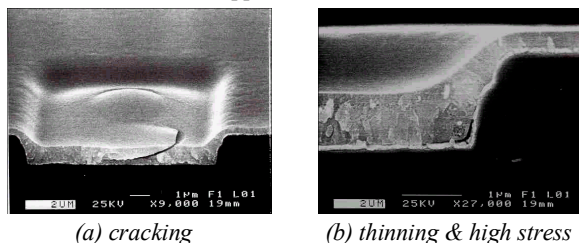


Figure 1: SEM images of poor step coverage of spin coated sol-gel PZT films [5].

In recent years dot-on-demand (DOD) printing has been studied as a robust, flexible, and inexpensive method of material

deposition for MEMS [6]. Some of the benefits of DOD printing for MEMS can be summarized as follows. First, no mask or patterning is required. Direct printing enables the designer to deposit a film based on a digital pattern file only. This file can be generated in many ways, including from computer aided design (CAD) software, manually, or based on images. Digital deposition in this way eliminates the need for photolithography and subsequent etching steps in the manufacturing process flow. Furthermore the short cycle time required for pattern generation makes rapid prototyping possible and allows multiple design iterations that were previously not possible in MEMS product development. A further advantage of direct printing is the cost savings due to a reduction in the material consumption during manufacturing and in chemical waste produced. The result is a manufacturing process that is both cleaner and cheaper than other common deposition techniques.

Perhaps the most compelling benefit of direct printing of PZT is that it provides a freedom of geometry that eliminates many of the design constraints currently associated with PZT MEMS. Since high quality thin films can be achieved with deposition control that is not possible with spin coating, novel functionalities can be incorporated into PZT MEMS. Specifically, PZT printing is able to deposit material over and around large out-of-plane features. In addition, the thickness of thin film PZT can vary deterministically across a device or across a wafer. Thickness can be controlled from tens of nanometers for sol-gel based inks, all the way to very high aspect ratio features 100 $\mu$ m tall or thicker with particle based inks [7]. Together, these improvements enable a new geometry of device designs that were previously not possible with simple manufacturing processes. While it is unclear yet what novel devices this new manufacturing method will yield, it is possible that the precise deposition control achieved with PZT printing could have a significant impact on the way MEMS structures are designed in the future.

In order to achieve the potential benefit of direct printing of PZT, three process requirements must be addressed. First, the ink must print reliably, forming discrete drops without clogging. Second, the geometry of the printed film must be highly uniform and controllable. Finally the properties of the printed PZT film, both mechanical and electrical, must be comparable to those of the spin coated PZT film.

## SOLUTION CHEMISTRY

The sol-gel used in this work was Mitsubshi A6 50/49 PZT. As purchased, this sol is 85%(wt) 2-methoxyethanol and 15%(wt) a mixture of lead, zirconium, and titanium oxides. Dilution is required to control the evaporation rate of the ink and prevent decomposition of the metal-organic molecules on the ink jet heater. Combinations of 2-methoxyethanol, isopropanol, and 2-ethylhexanoic acid were added to the sol to create the diluted PZT inks. 2-methoxyethanol is the same solvent used in the manufacture of the PZT sol and helps to control hydrolysis. 2-propanol is a common mild solvent with a low boiling point that is known to be reliable in thermal inkjet printing. Finally 2-ethylhexanoic acid was used to control overall ink volatility as it has a high boiling point and is also known to be compatible with thermal ink jet head.

To prevent clogging of the printer nozzle and defects in the

film, three sources of particle contamination were addressed and controlled. First, to eliminate external particle contamination each ink was filtered with a  $0.45\mu\text{m}$  PTFE syringe filter and deposition was carried out in a hermetically sealed glove box filtered with 99.99% efficient removal of 0.2 micron and larger airborne particles. Particle formation during the printing process was also a concern due to the decomposition of the metal-organic molecules during the thermal event. Throughout this work, over thirty ink chemistries, with dilution levels ranging from the as purchased 15%wt of metal oxides down to 2%wt, were tried and empirically the appropriate levels of dilution were observed. Table 1 shows observations of the concentration required for reliable printing for different nozzle sizes. Finally, preventing clogging also requires controlling the evaporation rate of the ink such that a stable meniscus is formed at the nozzle. If the solvent evaporates too quickly, metal oxide particles are built up inside the nozzle and firing chamber and concentrations that exceed stable printing requirements result. This was prevented by maintaining a low rate ink flow through the nozzle at all times.

Table 1: Maximum allowable metal oxide concentrations for reliable printing with different droplet sizes.

Nozzle size, droplet volume (pl)	Maximum Acceptable Concentration (%wt)
180	15
80	4.7
35	2.3

To ensure predictable substrate wetting and stable droplet formation, certain dimensionless numbers known to govern drop on demand printing dynamics were calculated and observations were made to ensure the accuracy of the predicted results. The forming of a film on a substrate is characterized by the Bond number, which for these droplet sizes will be no larger than approximately  $4 \cdot 10^{-3}$ . As for most ink jet printing, the Bond number for this work is sufficiently low to ensure the film shape on the surface will be dominated by surface tension, forming spherical caps for single drops and cylindrical slices for a printed line. Figure 2 shows an image of a spherical cap of 2-methoxyethanol forming on a platinum substrate during contact angle measurements. The contact angle was measured between  $10^\circ$ - $12^\circ$ , although accuracy can not be guaranteed for measurements at such low angles. Previous work has shown that the ratio of the Reynolds number to the square root of the Weber number dictates the dynamics associated with droplet formation [8]. Most dot-on-demand inks have  $1 < Z < 10$ . Viscous dissipation can prevent droplet ejection for  $Z < 1$  and for  $Z > 10$  multiple drops, or even a constant stream, can result.  $Z$  is estimated to be 1-3 for the smaller nozzle sizes used in this work.

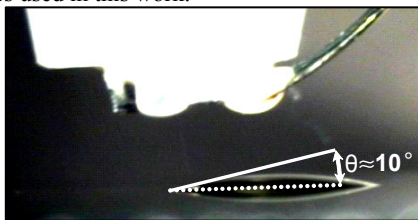


Figure 2. Advancing contact angle measurement of 2-methoxyethanol on platinum.

## CONTROLLING FILM GEOMETRY

This work characterized the resolution limits of two methods of printed PZT patterning. The first involved printing into a predefined mold and the second, free printing method, was based

only on droplet size and wetting angle with the substrate. Printing into a mold to pattern the PZT removes the coupling between pattern resolution and film uniformity that occurs due to the dependence both parameters have on film evaporation rate. When using a mold, droplet spreading and solute diffusion can be independently controlled. Therefore the evaporation rate can be very low, allowing for highly uniform films without a loss of resolution. Figure 3 demonstrates the resolution achieved for cast PZT films. In general, the in plane geometry PZT films printed into lithographically pattern molds was controlled to the accuracy of the mold itself. Thickness uniformity was also good: for printed films with a bulk mean thickness of 147 nm, the RMS roughness was 9 nm.

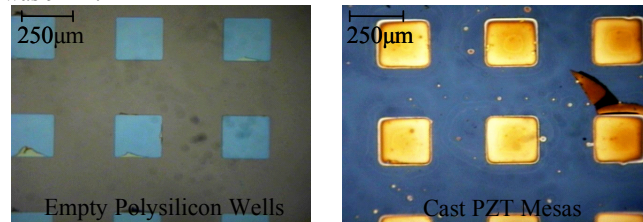


Figure 3. Results of thermal ink jet printing of PZT into preformed polysilicon molds.

Mold-free printing for MEMS is attractive because the mold removal step after printing adds complexity to the process. However, printing without a mold makes it more difficult to achieve the geometric control required. The diffusion of solutes towards the film edges during solvent evaporation known as the coffee stain effect can lead to significant non-uniformity []. Figure 4 shows how early printed PZT films exhibited this effect. In order to overcome this non-uniformity a study was conducted to determine the ink volatility and substrate temperature required to achieve the optimum level of spreading and diffusion.

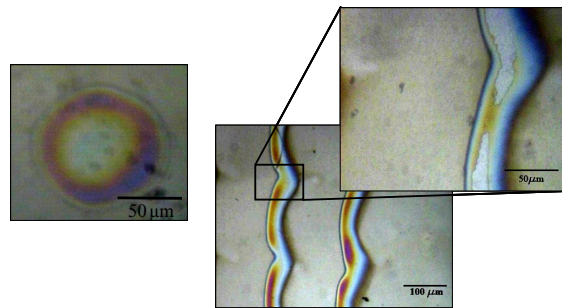


Figure 4. The influence of the coffee stain effect on dot on demand printing of PZT

Controlling the thickness uniformity of free printed PZT films requires controlling the amount of diffusion of the metal oxides towards the film edges that can occur as the volatile solvents evaporate. It was observed that ink chemistries with an excess of 2-methoxyethanol always exhibited significant metal oxide diffusion flow, and therefore substantial non-uniformity. Given the relatively high levels of dilution required, isopropanol was selected to make up the bulk of the ink given that it had a lower boiling point and would evaporate more quickly controlling diffusion of the oxides. It was found that inks that were made up of 50% isopropanol and 15% PZT sol would both print reliably as required by the clogging constraints, and evaporate quickly enough to prevent significant solute diffusion.

To achieve highly uniform films, precise control over evaporation rate is required. This was accomplished by adjusting

the substrate temperature. However, the range of substrate temperatures available is limited to approximately 70°C to prevent clogging as a result evaporation of ink from the printer nozzle. Due to this limit, the volatility of the ink was controlled to bring the substrate temperature into the specified range. This was accomplished using the remaining 35 % of the ink which was comprised of a mixture 2-methoxyethanol and 2-ethylhexanoic acid. The boiling point of ethylhexanoic acid is significantly higher than the other solvents (228°C), and therefore the concentration of ethylhexanoic acid was used to control the overall ink volatility, with anhydrous 2-methoxyethanol making up the remainder of the ink. Figure 5 demonstrates the control over mold free film geometry that can be achieved by adjusting the substrate temperature when the ink volatility is set at an acceptable level.

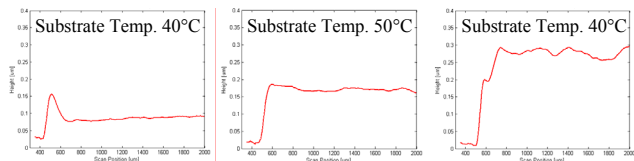


Figure 5. Profilometry of thermal ink jetted PZT, deposited at different substrate temperatures. Ink composition: 6% EHA, 15%PZT sol-gel, 50%IPA, 29%ME.

In order to determine the optimal substrate temperature for this ink (6% EHA, 15%PZT, 50%IPA, 29%ME), 15 samples were prepared at different temperatures. The results of the study clearly showed an optimum deposition temperature at 60°C. However, to ensure that clogging of the nozzle due to excessive solvent evaporation would not be a problem, it is desirable to reduce the substrate temperature during deposition. A new ink was prepared made up of 5% EHA, 15%PZT, 50%IPA, 30%ME, and the study was conducted again. The results of the second uniformity vs. substrate temperature study show a reduction in optimum deposition temperature from 60°C to 50°C (Figure 6). These two studies demonstrate the effectiveness of using substrate temperature to control deposition uniformity, and using ink volatility to ensure that the substrate temperature doesn't cause clogging.

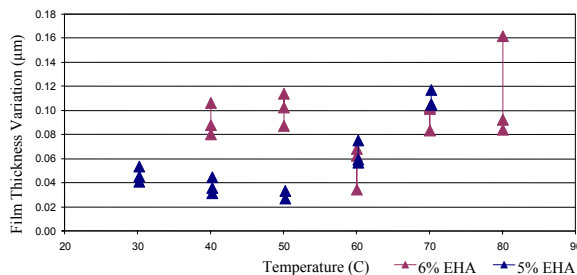


Figure 6: Study of thickness variation vs. substrate temperature for thermal ink jetted PZT on Pt.

After optimization of solution chemistry and substrate temperature, PZT films of between 100 - 500 nm thickness with less than 40nm variation could be printed with a droplet size of 80pl. Spot sizes as small as 43µm were achieved with a 10pl droplet of PZT ink deposited on Pt substrate. The edge variation of printed lines was controlled within +/- 10µm.

### THERMAL PROCESSING OF PRINTED PZT FILMS

There are three steps to properly crystallize a sol gel based PZT thin film into a piezoelectric, perovskite phase. The first is the

drying of the solvent in which the metal organics are dispersed. The second is the decomposition of the metal organics into an amorphous film. Finally the film must be annealed into a perovskite structure. The thermal processing of the early printed PZT films was determined based on manufacturer's recommendation and authors' experience in processing spin coated films of the Mitsubishi A-6 50/49 PZT sol gel (Table 2). With the same thermal treatment, the printed PZT showed very poor piezoelectric performance and low film resistivity. At 5V the film resistivity measured was  $4.5 \cdot 10^{10} \Omega \cdot \text{cm}$ , however at 15V the resistivity dropped to  $8.3 \cdot 10^2 \Omega \cdot \text{cm}$ .

Table 2: Thermal processing conditions for spin coated PZT films.

Processing Step	Temp. [°C]	Time [min]
Dry	260	3
Pyrolysis	360	8
Anneal	650	20

In order to improve piezoelectric performance, the drying and pyrolysis steps were lengthened to ensure complete evaporation of the solvent and removal of added organics prior to annealing. FTIR analysis after 2 hours of pyrolysis showed the removal of a significant fraction of the organic material (Figure 7).

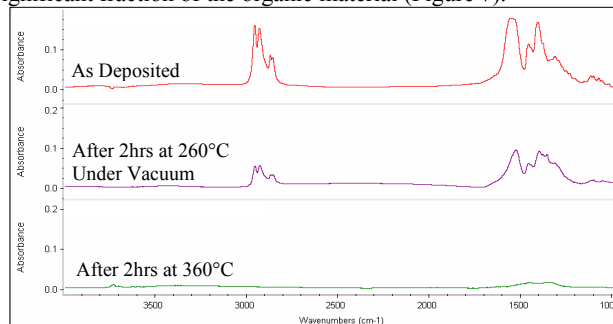


Figure 7: FTIR of a printed PZT thin film during heat treatment.

Under this new thermal treatment the dielectric properties of printed films were significantly increased. At 5V the film resistivity measured was  $6.4 \cdot 10^{10} \Omega \cdot \text{cm}$ , and at 15V the resistivity was still  $6.2 \cdot 10^{10} \Omega \cdot \text{cm}$ .

X-ray diffraction was performed after annealing to investigate the influence of pyrolysis time on crystallization. All films had a pure perovskite, pyroclor free, crystal phase. The study further showed that the amount of crystalline PZT increase significantly with pyrolysis time.

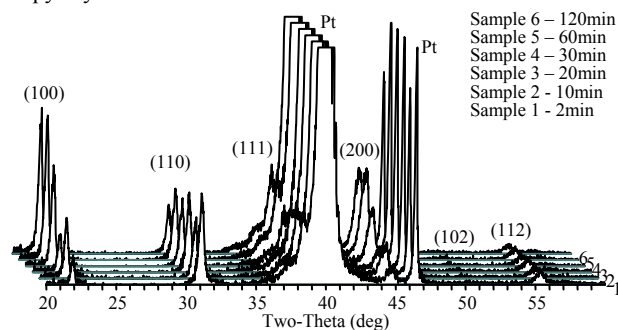


Figure 8: X ray diffraction of printed PZT films pyrolysed for different times.

The substantial improvement of the polarization-voltage curve of the extended pyrolysis is shown in Figure 9. When compared to

a spin coated film, the remnant polarization of the extended pyrolysis film (approx.  $\pm 5 \mu\text{C}/\text{cm}^2$ ) is still lower than desired, but shows much improved dielectric performance and a piezoelectric performance that is still greater other piezoelectric materials. The test device fabricated was a simple capacitor structure with approximately 400nm thick printed PZT between two platinum electrodes. The bottom electrode on which the PZT was printed was platinum (200nm Pt / 20nm Ti / 200nm SiO<sub>2</sub> / Si). The capacitor area was  $6.25 \cdot 10^{-4} \text{ cm}^2$ .

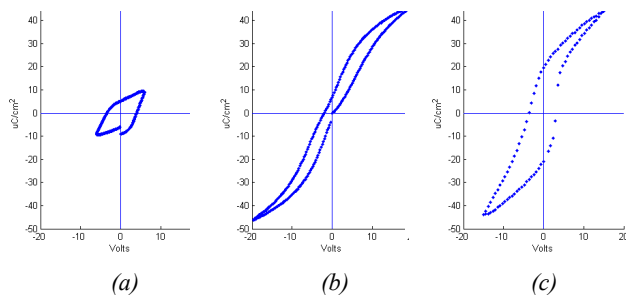


Figure 9: Polarization vs. voltage hysteresis curve for a thermal ink jetted PZT thin film a) after standard pyrolysis and b) after extended pyrolysis as well as c) for a spin coated film after standard pyrolysis.

It is believed that the relatively low remnant polarization is due to defects/voids forming at the grain boundaries (Figure 10). These defects are likely due to incomplete removal of organics before annealing, which were added when the sol was dilute to become ink jettable. This theory is supported by the FTIR spectrum in figure 7 showing some organics remaining after pyrolysis, as well as the increase in crystallinity with increased pyrolysis indicated by the x-ray diffraction in figure 8. Furthermore, thermal gravimetric analysis, not shown, indicates that increasing the ramp rate of the pyrolysis leads to a greater organic removal. Work to optimize pyrolysis conditions to eliminate these defects is underway.

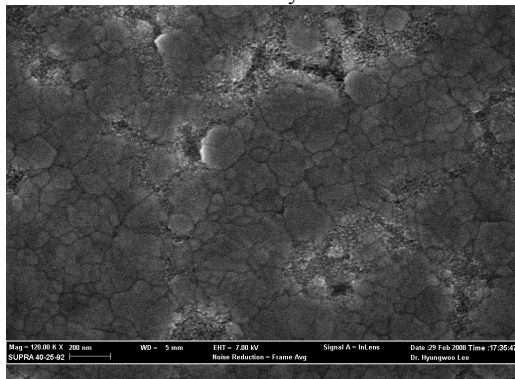


Figure 10: SEM image of printed PZT film showing intergranular defects.

## CONCLUSION

A new solution based, dot-on-demand (DOD) PZT deposition method has been developed that provides increased flexibility and lower manufacturing costs over standard deposition methods. Ink chemistry that can be reliably ink jetted has been developed and optimized; printing conditions are optimally determined; the appropriate thermal processing parameters are identified and characterized to ensure a high resistivity and good perovskite phase of crystallized PZT films after annealing. This required

implementing particle control measures, determining the right amount of dilution required to control droplet formation, and ensuring minimal evaporation at the printer nozzle.

Analysis was performed on droplet formation dynamics and on substrate wetting conditions. A method for determining the optimum deposition temperature for dot on demand printing of highly uniform thin films on a nonporous surface was presented. Furthermore, a method for creating and using cast features as mold for thin film deposition was developed. Printing of cast films was demonstrated to have significantly improved resolution and uniformity over standard drop on demand deposited films.

Finally the thermal processing conditions were determined for the annealing of printed PZT films into pure perovskite phase polycrystalline films. Pyrolysis time was investigated as a means for controlling film crystallization. Fourier transform infrared spectroscopy was used to confirm sufficient removal of the organic material in our highly diluted PZT ink and X-ray diffraction test was used to confirm the final crystalline phase.

The results from this study will provide a robust and efficient method of depositing PZT thin films for MEMS applications. This will also enable many novel MEMS device designs that were not previously possible.

## ACKNOWLEDGEMENTS

This study was supported by the DARPA Grant HR0011-06-1-0045 and Hewlett Packard. The authors would like to thank Paul Benning and Murali Chaparala of HP for their contributions and help.

## REFERENCES

- [1] S. Bathurst, H.W. Lee and S.G. Kim, "Direct Printing of Lead Zirconate Titanate Thin Films," IEEE MEMS 2008, Tucson, AZ, 2008
- [2] P. Muralt, "PZT Thin Films for Microsensors and Actuators: Where Do We Stand?" Ultrasonics, IEEE Transactions on Ferroelectrics and Frequency Control, vol. 47, pp. 903-915, July 2000.
- [3] Z. Traina and S.G. Kim, "A Large Strain Piezoelectric Microactuator by Folding Assembly," M.S. thesis, Massachusetts Institute of Technology, Cambridge, MA, 2005.
- [4] R. Sood and S.G. Kim, "Piezoelectric Micro Power Generator (PMPG): A MEMS-Based Energy Scavenger," M. Eng. thesis, Massachusetts Institute of Technology, Cambridge, MA, 2003.
- [5] S.G. Kim, M.K. Koo, "Design of a microactuator array against the coupled nature of microelectromechanical systems (MEMS) processes", in Annals of the CIRP, vol. 49, no. 1, 2000
- [6] S. B. Fuller, E. J. Wilhelm, and J. M. Jacobson, "Ink-Jet Printed Nanoparticle Microelectromechanical Systems," Journal of Microelectromechanical Systems, vol. 11, no. 1, February 2002
- [7] R. Noguera, C. Dossou-Yovo, M. Jejeune, and T. Chartier, "Fabrication of 3D fine scale PZT components by ink-jet prototyping process," Journal de Physique IV, vol. 128, pp. 87-93, 2005
- [8] J.E. Fromm, IBM J. Res. Dev. 28 (1984) p. 322.
- [9] R.D. Deegan, O. Bakajin, T.F. Dupont, G. Huber, S. R. Nagel, T.A. Witten, "Capillary flow as the cause of ring stains from dried liquid drops", Letters to Nature, vol 389, no. 6653, pp 827-829, 1997

# PHOTOPATTERNABLE CONDUCTIVE PDMS AS A NEW MEMS MATERIAL

H. Cong<sup>1</sup> and T. Pan<sup>1</sup>

<sup>1</sup>Department of Biomedical Engineering, University of California, Davis, USA

## ABSTRACT

Polydimethylsiloxane (PDMS) elastomer has been widely used in various biological and medical applications. However, high electrical impedance and poor adhesion to metal limit its further applications in the area of electrical sensing and flexible circuits. In this paper, we first developed conductive photodefineable PDMS composites addressing both electrical conductivity and photopatternability. The photosensitive composite, consisting of a photosensitive reagent, a conductive filler and PDMS pre-polymer, can be used as a regular photoresist. A standard photolithographic approach has been used to fabricate the conductive elastomer microstructures. Highest conductivity of 0.01  $\Omega$ -cm and minimal resolution of 10  $\mu$ m have been achieved using the conductive PDMS composite.

## INTRODUCTION

Polydimethylsiloxane (PDMS) elastomer has been widely used in a variety of academic and industrial applications, due to its unique physical and chemical properties. With recent advances in soft lithography and polymer microelectromechanical systems (MEMS), PDMS has been constructed into a large array of micro and nano-scale devices for biological and medical applications [1-3]. However, PDMS has high electrical impedance and poor adhesion to metal, which prevent its further applications in the area of electrical sensing and flexible circuits [4]. Moreover, molding method, commonly used to construct PDMS microstructures, creates fabrication compatibility and integration issues [3].

An alternative approach to PDMS processing is to make the PDMS pre-polymer sensitive to ultraviolet wavelengths by adding photoinitiators into it, and then, it can be directly photopatternable [5-7]. The photodefinable mixture of PDMS and a photoinitiator, which eliminates the need of a master mold and the issues related to molding, provides a more efficient way to rapid prototyping of polymer MEMS devices.

To overcome the low electrical conductivity of PDMS, highly conductive fillers are usually introduced into the polymer matrix and provide continuous conductive pathways for electron migration, which greatly expands its usage to the field of electrical sensing and flexible circuits [8-13]. However, to our knowledge, the fabrication of those PDMS composite-based devices has only been achieved by using the traditional molding methods [3].

In this paper, we first developed conductive photodefineable PDMS composites addressing both electrical conductivity and photopatternability at the same time. Highest conductivity of 0.01  $\Omega$ -cm and minimal resolution of 10  $\mu$ m have been achieved using the conductive PDMS composite.

## EXPERIMENTAL

The photosensitive composite, consisting of a photosensitive reagent, a conductive filler and PDMS pre-polymer, can be used as a regular photoresist. To prepare the composite, the PDMS base and curing agent (Sylgard® 184) were mixed at 10:1 (w/w) ratio. Benzophenone (3 wt%) and silver powder (17–22 vol%, 2  $\mu$ m) were added to the PDMS mixture and degassed for 15 minutes. The prepared PDMS-Ag photoresist mixture was then spin-coated

onto a flat substrate (e.g., glass, silicon, polyester or silicone) for 30 seconds. The spin-coated wafer was loaded towards photomask in an approximate mode with 50  $\mu$ m spacing. Ten-minute UV exposure at 12 mW/cm<sup>2</sup> was followed by a post-exposure bake for 50 seconds at 120 °C. Heavy UV exposure dosage (7200 mJ/cm<sup>2</sup>) was necessary to induce complete photochemical reactions under significant decay of light transmission by silver particles. During the post-exposure bake, the unexposed region got fully crosslinked while the exposed region remains uncured. The uncured PDMS was then removed in toluene for 5 seconds during the development. Finally, the wafer was rinsed in 2-propanol and blow-dried in nitrogen flow.

## RESULTS AND DISCUSSION

### Spin Curve

Figure 1 shows spin curves of different film thicknesses achieved at various spin rates and silver composition ratios. The thickness of the composite films can be controlled by variation of the spin coating speeds. Adding silver powders into the PDMS matrix increases the thickness of the composite film as a result of viscosity change. At 22 vol% or above of silver powder, the composite becomes highly viscous and is not able to achieve uniform coating.

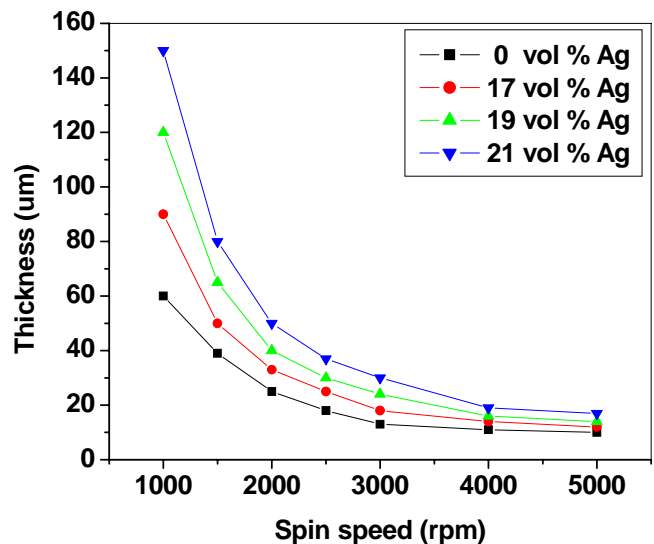


Figure 1: Spin curves of the PDMS-Ag conductive photoresist at various spin rates and silver composition ratios.

### Resolution

Minimal feature size of 10  $\mu$ m was successfully demonstrated using the photolithographic method in Figure 2. The further miniaturization is limited by strong scattering of UV light from silver particles.

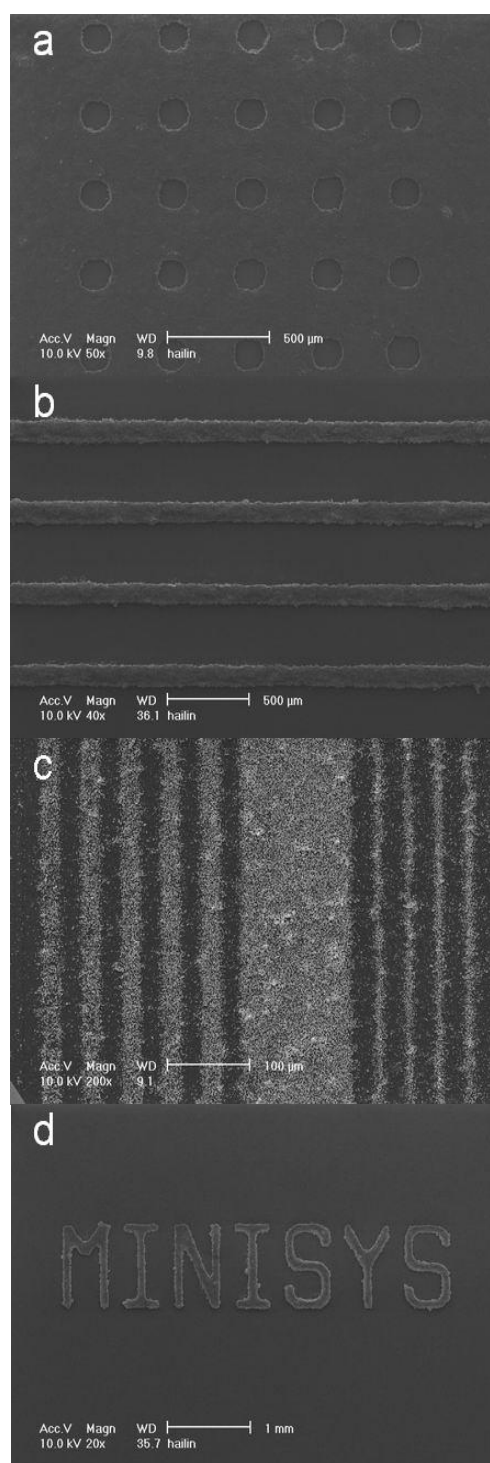


Figure 2: SEM photographs of the lithographic patterns of the conductive PDMS with various dimensions: (a) 150µm-wide holes, (b) 150µm-wide and 30µm-thick lines, (c) 10µm-wide line, and (d) MINISYS lab logo.

### Electrical Conductivity

Electrical conduction mechanism is based on establishing electronic paths through the percolation and contacts between filler particles in the insulating matrix [14-17]. Increasing content of the

conductive filler reduces the electrical resistivity of the PDMS composite matrix by adding more interconnected clusters of silver particles into conducting paths. Figure 3 shows a sudden decrease of electrical resistivity at the percolation threshold around 18 vol%, compared with theoretic prediction of 16 vol% as a simple binary composites (assuming a simple binary composite with spherical particles distributed statistically) [18-20].

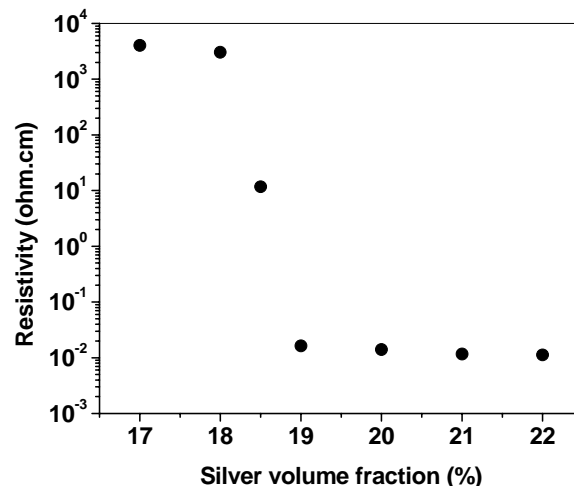


Figure 3: Electrical resistivity of the PDMS-Ag conductive photoresist versus silver volume fraction.

### Mechanical and Thermal Properties

As a conductive filler, silver powders significantly improve electrical conductivity of the PDMS polymer, but also present enhanced mechanical and thermal properties as well as interesting surface properties. Table 1 summarizes the mechanical and thermal properties of the PDMS-Ag conductive photoresist. The silver particles in the PDMS matrix participate in physical crosslinking, and thus, greatly improve the mechanical strength of PDMS composites. Significantly enhanced thermal conductivity of the composites is attributed to excellent thermal conductivity of the silver filler in the percolation path.

Mechanical bending and stretching tests have been performed to evaluate the stability of the conductive property. The excellent elastomeric nature of PDMS allows extensive bendability and stretchability of the conductive polymeric film. No apparent change in the electrical conductivity of the conductive film has been observed for both 100-cycle tests of 150° bending and 50 % stretching. The result implies that well-established network of conductive paths through the percolation and contacts between filler particles in the PDMS matrix can be recovered after bending and stretching. Further studies on the transient electrical properties under various mechanical loads are currently under investigation.

Table 1: Properties of the PDMS-Ag conductive photoresist.

Sample PDMS-Ag (vol % of Ag)	0	17	19	21
Hardness (Shore A)	49	63	67	72
Tensile modulus (MPa)	1.3	2.7	3.0	3.2
Elongation at Break (%)	58	59	58	57
Thermal conductivity (W/m K)	0.2	71	76	81

## Surface Properties

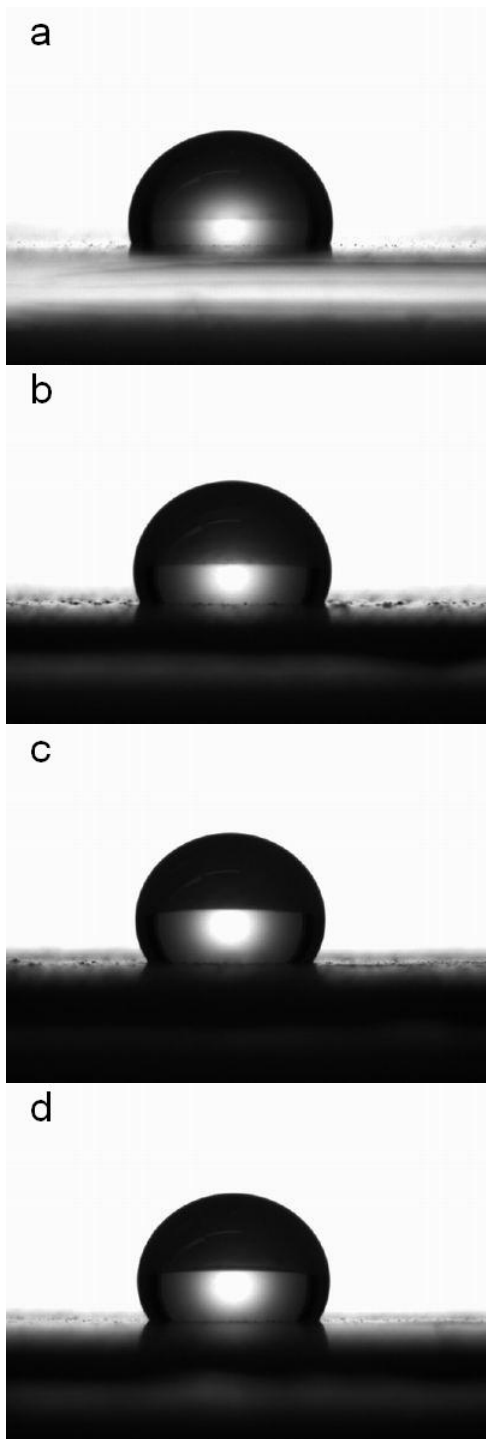


Figure 4: Contact angle of water on cured PDMS-Ag photoresist surface with (a) 0 vol %, (b) 17 vol %, (c) 19 vol %, (d) 21 vol % silver powders.

Figure 4 shows water contact angles of the composite surfaces. The measured contact angles of the PDMS surfaces containing 0, 17, 19 and 21 vol % silver powder are  $109^\circ$ ,  $119^\circ$ ,  $127^\circ$  and  $131^\circ$ , respectively. Thus, adding silver powder

substantially changes the contact angle of the PDMS surfaces, which become more hydrophobic than that of the pure PDMS. The increased surface hydrophobicity results from the high surface roughness of the formed PDMS-Ag composites, as shown in Figure 5.

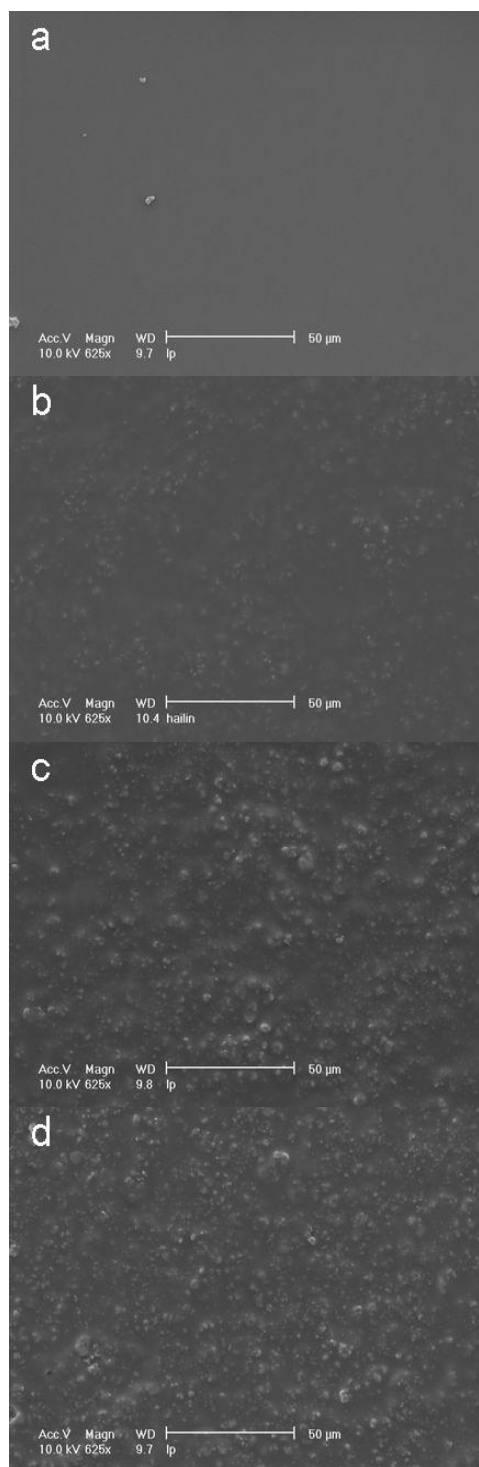


Figure 5: SEM morphology of the cured PDMS-Ag photoresist surface with (a) 0 vol %, (b) 17 vol %, (c) 19 vol %, (d) 21 vol % silver powders.

## MEMS Application

Figure 6 demonstrates a prototype of a micro sensing array fabricated from the PDMS-Ag conductive photoresist. It is first patterned as both sensing components and connecting circuitry onto a pure PDMS flexible substrate (Fig 6-a). And then, two sides of the sensing circuits are folded over, aligned with the aid of surrounding alignment marks, and covalently bonded through free radical reactions generated in oxygen plasma (for 30 sec at 30 W) (Fig 6-b).

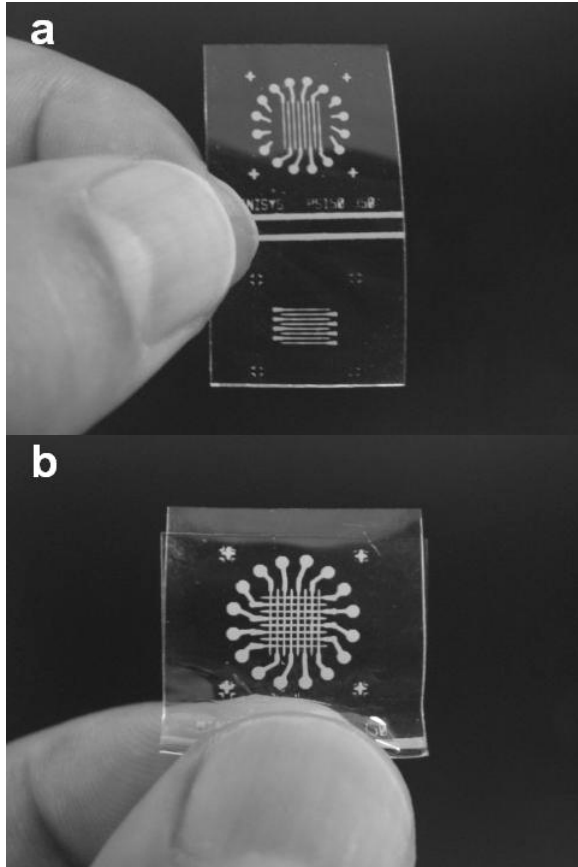


Figure 6: Prototype of a micro pressure sensing array using PDMS-Ag conductive photoresist. (a) single-layer process of PDMS-Ag on PDMS layer, (b) the folding-bonded micro-sensing chip.

## CONCLUSIONS

In this paper, the first conductive photodefineable PDMS composites is developed addressing both electrical conductivity and photopatternability at the same time. A standard photolithographic approach has been used to fabricate the conductive elastomer microstructures. Highest conductivity of 0.01  $\Omega$ -cm and minimal resolution of 10  $\mu$ m have been achieved using the conductive PDMS composite. As a conductive filler, silver powders significantly improve electrical conductivity of the PDMS polymer, but also present enhanced mechanical and thermal properties. The combined electrical, mechanical, and thermal properties along with photopatternability make the photopatternable conductive PDMS an excellent processing and structural material for various MEMS applications.

## REFERENCES

- [1] S. K. Sia, and G. M. Whitesides, "Microfluidic Devices Fabricated in Poly(dimethyl siloxane) for Biological Studies", *Electrophoresis*, 24, 3563 (2003).
- [2] B. H. Jo, L. M. V. Lerberghe, K. M. Motsegood, and D. J. Beebe, "Three-dimensional Micro-channel Fabrication in Polydimethylsiloxane (PDMS) Elastomer", *JMEMS*, 9, 76 (2000).
- [3] C. Liu, "Recent Developments in Polymer MEMS", *Adv. Mater.*, 19, 3783 (2007).
- [4] X. Niu, S. Peng, L. Liu, W. Wen, and P. Sheng, "Characterizing and Patterning of PDMS-Based Conducting Composites", *Adv. Mater.*, 19, 2682 (2007).
- [5] A. A. S. Bhagat, P. Jothimuthu, and I. Papautsky, "Photodefinable Polydimethylsiloxane (PDMS) for Rapid Lab-on-a-chip Prototyping", *Lab on a Chip*, 7, 1192 (2007)
- [6] K. Tsougeni, A. Tserepi, and E. Gogolides, "Photosensitive Poly(dimethylsiloxane) Material for Microfluidic Applications", *Microelectronic Engineering*, 84, 1104 (2007).
- [7] "Patternable Silicones for Electronics", *Product Data Sheet*, Dow Corning (2005).
- [8] C. Liu, "Nanocomposite Conductive Elastomer: Microfabrication Processes and Applications in Soft-Matter MEMS Sensors", *Mater. Res. Soc. Symp. Proc.*, 0947-A07-01 (2007).
- [9] J. Engel, J. Chen, N. Chen, S. Pandya, and C. Liu, "Multi-walled Carbon Nanotube Filled Conductive Elastomers: Materials and Application to Micro Transducers", *IEEE MEMS*, 246 (2006).
- [10] M. A. Unger, H. P. Chou, T. Thorsen, A. Scherer, and S. R. Quake, "Monolithic Microfabricated Valves and Pumps by Multilayer Soft Lithography", *Science*, 288, 113 (2000).
- [11] V. T. S. Wong, A. Huang, and C. M. Ho, "SU-8 Lift-off Patterned Silicone Chemical Vapor Sensor Arrays", *IEEE MEMS*, 754 (2005).
- [12] A. J. Gawron, R. S. Martin, and S. M. Lunte, "Fabrication and Evaluation of Carbon-based Dual-electrode Detector for Poly(dimethylsiloxane) Electrophoresis Chips", *Electrophoresis*, 22, 242 (2001).
- [13] S. P. Rwei, F. H. Ku, and K. C. Cheng, "Dispersion of Carbon Black in a Continuous Phase: Electrical, Rheological, and Morphological Studies", *Colloid Polym. Sci.*, 280, 1110 (2002).
- [14] S. Jiguel, A. Bertsch, H. Hofmann, and P. Renaud, "Conductive SU8 Photoresist for Microfabrication", *Adv. Funct. Mater.*, 15, 1511 (2005).
- [15] R. Biller, "AC Conductivity for the Two-dimensional Bond-percolation Problem", *J. Phys.*, 18, 989 (1985).
- [16] A. Y. Dovzhenko, and P. V. Zhirkov, "The Effect of Particle Size Distribution on the Formation of Percolation Clusters", *Phys. Lett. A*, 204, 247 (1995).
- [17] R. Zallen, "The Physics of Amorphous Solids", Wiley, New York (1983).
- [18] S. Kirkpatrick, "Percolation and Conduction", *Rev. Mod. Phys.*, 45, 574 (1973).
- [19] F. Carmona, P. Prudhon, and F. Barreau, "Percolation in Short Fibres Epoxy Resin Composites: Conductivity Behavior and Finite Size Effects near Threshold", *Solid State Commun.*, 51, 255 (1984).
- [20] S. Jiguel, A. Bertsch, H. Hofmann, and P. Renaud, "SU8-Silver Photosensitive Nanocomposite", *Adv. Eng. Mater.*, 6, 719 (2004).

# IN-SITU TUNING OF MICRODEVICES FOR DIRECTIONAL MICROPHONE APPLICATIONS

Sang-Soo Je, Jere C. Harrison, Michael N. Kozicki, and Junseok Chae  
Department of Electrical Engineering, Arizona State University, Tempe, AZ

## ABSTRACT

This paper presents a new method to manipulate microdevices' membranes using nano-electrodeposits for directional microphones in hearing aid applications. The key to achieving high directionality is to minimize the mismatch of the omni-directional microphones using *in-situ* tuning by the integrated electrodeposition of metallic nanostructures. The nanostructures can be grown/retracted upon external bias at room temperature. The growth/retraction changes mass/stress distribution on the diaphragm of microdevices to precisely manipulate sensitivities to incoming acoustic waves. The omni-directional microphones are capacitive and have a parylene membrane integrated with the nanostructures. The microphone capacitance can be tuned up to 0.7 dB and acoustic mismatch reduces by 1.2 dB. This represents directivity index (DI) increase of 1.2 dB, which is crucial to achieve high directionality in composite microphones. The technology has many applications, including post-packaging trimming and calibration of micro-devices.

## INTRODUCTION

Directionality is one of the most demanded features in modern hearing aids [1-3]. It is essential if directional microphones are to pick up sounds efficiently in the presence of ambient noise. To achieve a high directionality, each omni-directional microphone should pick up sound from all directions almost equally to the other. Technically, multiple omni-directional microphones must be matched precisely, within 0.25 dB [4], otherwise directionality is lost. Figure 1 shows directionality over two omni-directional microphones' gain mismatch in hearing aids. As indicated, a DI greater than 4.5 is required for excellent directionality in directional hearing aid applications, which corresponds to less than 0.25 dB gain mismatch between two omni-directional microphones at audio frequencies.

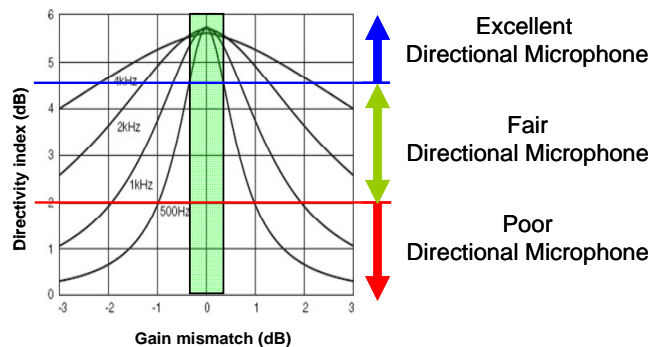


Figure 1: DI vs. gain mismatch between two omni-directional microphones for hearing aid applications. Less gain mismatch indicates better directionality.

Many techniques exist to allow to improve the directionality of microphones, including electronic calibration and compensation [5]. The electronic methods are complex, have large system size, high cost, and large power consumption. Few techniques that tune mechanical elements have been demonstrated [6], partially because it is hard to manipulate micro-size mechanical components *in-situ* with extremely low power and high precision at room temperature.

We have demonstrated precise manipulation of micro-size

membranes using electrodeposited nanostructures. The operating principle is similar to electrodeposition in liquid electrolyte, except this technique uses solid-state electrolyte. AgGeSe solid electrolyte allows  $Ag^+$  ions to transfer from an anode toward a cathode upon the application of voltage.  $Ag^+$  ions reaching the cathode are reduced to form electrodeposits which grow toward the anode. The nano-electrodeposit causes the surface to become rough and heterogeneous, and consequently, changes the mass and stress distribution [7]. The proposed MEMS capacitive microphone associated with a thin GeSe film on a parylene membrane is illustrated in Figure 2. There are 3 major parts; top/bottom electrodes, a multiple layered membrane including Ag-rich GeSe and parylene layer, and cathode/anode electrodes. The suspended membrane is made of parylene. On the parylene membrane a solid-electrolyte Ag-doped GeSe film and two electrodes to grow and retract Ag nano-electrodeposits. The GeSe film is saturated with Ag ions by UV (Ultra Violet) photo-dissolution to be a conductive film. The Ag nano-electrodeposits start to grow from the Ni tip (cathode electrode) toward to the Ag tip (anode). The air gap between top and bottom electrode is defined as small as 1  $\mu m$ .

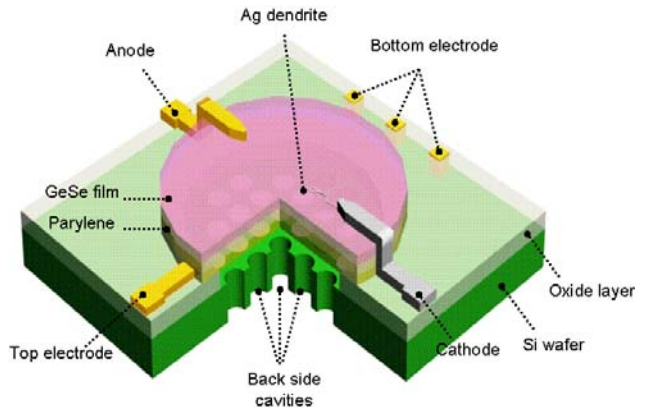


Figure 2: The proposed 3D view of the capacitive microphone integrated with nano-electrodeposits.

## FABRICATION AND MEASUREMENT SETUP

### Fabrication

The fabrication process of the capacitive microphone integrated with the nano-electrodeposit mechanism is illustrated in Figure 3. It is a seven-mask process including evaporated AgGeSe solid-state electrolyte on a parylene membrane suspended on a silicon substrate. The back side of the substrate is etched by Deep Reactive Ion Etch (DRIE) and  $SiO_2$  is used as a sacrificial layer to release the parylene membrane. (a) 3000Å thick parylene is coated on top of a 3000Å thick top electrode (Cr/Au) on a 1 $\mu m$  thick sacrificial oxide layer. (b) 2400Å thick GeSe solid-state electrolyte and 800Å thick Ag layer are deposited on the membrane. (c) Photo-dissolution is performed for 15 min under the UV exposure to dissolve the Ag into the GeSe layer. (d) The anode (Ag) and cathode (Ni) are evaporated and patterned to form electrodes to grow and retract the electro-deposits from the end of cathode tip. (e) To contact the silicon substrate the bottom electrode (Cr/Au) is evaporated and patterned. (f) Finally, the membrane is defined by

etching the back side of the silicon wafer using DRIE at an etch rate of  $3 \mu\text{m}/\text{min}$ . The membrane is released by removing the sacrificial oxide layer at the end of the process using HF for 15 min.

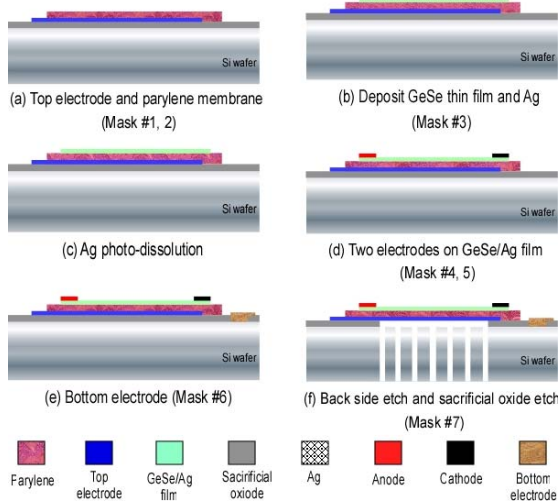


Figure 3: Fabrication process flow.

The fabricated single microphone covered by AgGeSe solid electrolyte is shown in Figure 4 (a). Ag is electrochemically deposited from the Ni cathode tip toward the Ag anode tip by applying an external bias from 3 to 5 V (Figure 4 (b)). The dual microphones for the directionality test are shown in Figure 4 (d). Figure 5 (a) shows the fully grown silver electrodeposits at the cathode (Ni) tip on the membrane. Figure 5 (b) shows that the height of the grown silver nano-electrodeposits is up to 90 nm while the film roughness is less than 10 nm. The growth is dendritic but generally moves toward the anode. Due to the grown and retracted silver nano-electrodeposits on the suspended parylene membrane, the membrane deflects and consequently changes the spring constant. However, after full retraction, traces and residues of silver electrodeposits remain on the membrane and prevent it from returning to its original state [8].

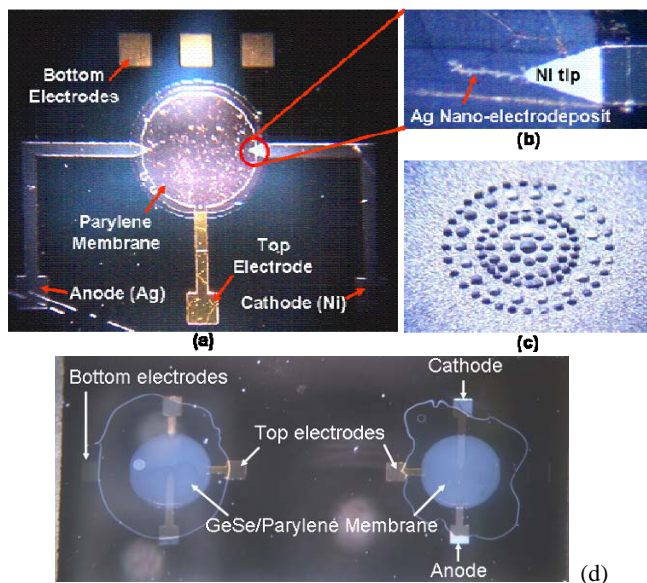


Figure 4: The fabricated single microphone integrated with nano-electrodeposits (a) Top view, (b) Grown Ag nano-electrodeposits, (c) backside view, and (d) the fabricated dual microphone integrated with nano-electrodeposits.

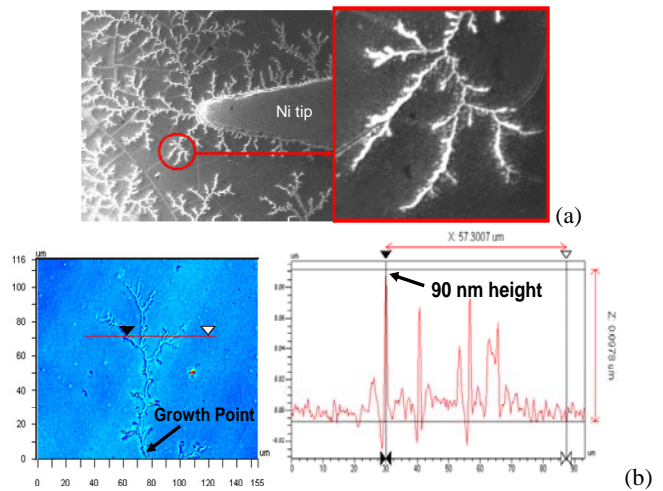


Figure 5: SEM photographs of grown silver dendrite from a Ni tip on parylene membrane (top) and an optical profilometer (Veeco NT9800) photograph of the height of the silver dendrite and film roughness (bottom).

### Electrical/Acoustic Measurement Setup

The microphone is glued on a PCB where the capacitance to voltage converter for readout is implemented (Figure 6). The fabricated dual microphone and electrical/acoustic test setup (top) and a manipulator with  $1 \mu\text{m}$  resolution in the Faraday cage (bottom) are shown in Figure 7. The readout circuits and microphone are placed inside of the Faraday cage to avoid electromagnetic noise. An additional shield for the readout circuit is provided to protect from electrical coupling. Operation of the circuit is described below.

With no acoustic excitation, electric current through a  $10 \text{ M}\Omega$  resistor balances ohmic leakage through the microphone to bias the top microphone electrode with a constant charge at 135 mV. When the microphone is excited acoustically, a change in capacitance causes a voltage change in the charge fixed to the microphone membrane. The induced voltage change on the microphone passes through an isolation capacitor as displacement current, and is amplified by an AD8607 amplifier with 37x closed circuit gain. The circuit output is analyzed using an Agilent 35670a Dynamic Signal Analyzer. The microphone is excited acoustically by a Knowles FK-6260 micro-speaker, which is aligned precisely  $5 \text{ mm}$  above the microphone using  $1 \mu\text{m}$  resolution translation stages.

The acoustic readout circuit response shows a passband starting at 2 kHz and ending at 58 kHz, with a peak capacitance to voltage conversion of  $250 \text{ mV}/\text{pF}$  for a microphone with a steady state capacitance of  $20 \text{ pF}$ . The response shows both high and low frequency loss, including loss in the audible frequencies we intend to measure. Circuit response at low frequencies is reduced due to charge retaining limitations of the bias resistor. When the RC time constant is the same order of magnitude as the signal period, voltage discharge across the bias resistor dominates the circuit loss. Assuming the microphone capacitance is  $20 \text{ pF}$  (the theoretically expected value), the RC time constant is 200 ms. As a result, signals below 5 kHz see significant attenuation. The low frequency cutoff can be improved with a larger resistor; however, doing so reduces the overall amplification of the circuit. The bias resistance of  $10 \text{ M}\Omega$  is chosen to balance the circuit bandwidth and peak output. Circuit response at high frequencies is reduced due to bandwidth limitations in the amplifier, and at sufficiently high frequencies, signal leakage as displacement current through the microphone.

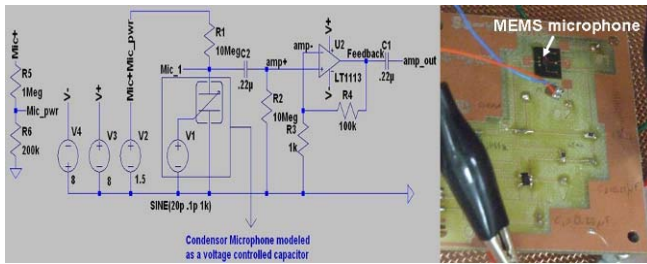


Figure 6: The schematic of the capacitive readout circuits (left) and PCB implementation with the fabricated single microphone (right)

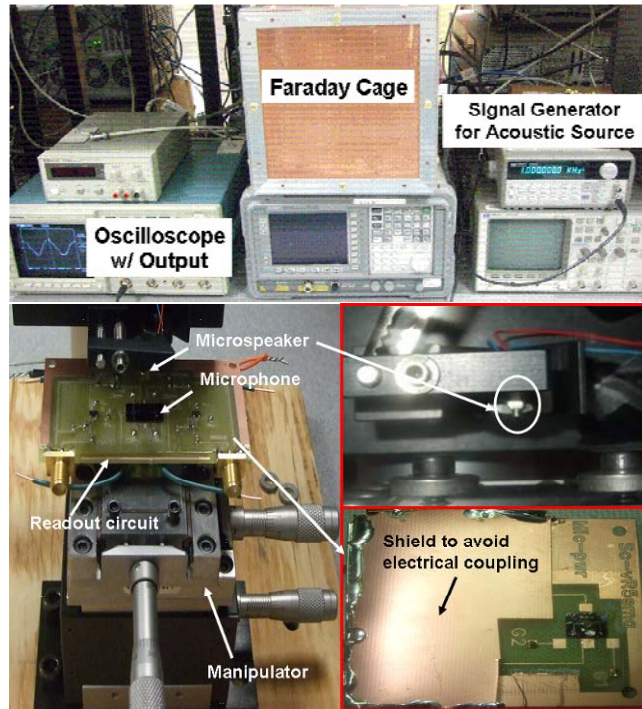


Figure 7: Electrical and acoustical test setup (top) and a Knowles microspeaker and the fabricated dual microphone on a manipulator with 1  $\mu\text{m}$  resolution in the Faraday cage. The implemented PCB is shield to protect undesired electrical coupling (bottom).

## DEVICE CHARACTERIZATION AND RESULTS

We first characterize the microphone using the readout circuits. The microspeaker (FK-6260 from Knowles electronics) generates acoustic input and the output of the readout circuits is measured (Figure 8). The fabricated microphone was vertically separated 5 mm away from the microspeaker using the 1  $\mu\text{m}$  resolution XYZ linear translation stages. The customized readout circuits show from -38 dB (given 75 dB SPL input, which corresponds to 0.1 V microspeaker input) to -25 dB (given 88 dB SPL input, which corresponds to 0.4 V microspeaker input).

The dual microphone mismatch is characterized electrically by an LCR meter, Agilent 4284A (Figure 9). The gain mismatch of the microphone is monitored *in-situ* while the nano-electrodeposits are grown. Initial gain mismatch of the dual microphone at 0.2 V DC bias is the blue line. Now we grow the nano-electrodeposits on the selected microphone. The mismatch between microphones decreases by more than 7.3% when the electrodeposits are grown for 20 sec and at 3 V DC external bias. Upon the growth of nano-electrodeposits the microphone mismatch is improved by at least 0.7 dB at all over the audible frequency ranges (the red line).

Finally, we measure *in-situ* tuned microphone acoustic readout circuit response over audible frequencies between 1 kHz to 10 kHz and monitor the mismatch reduction upon the growth of the nano-electrodeposits. Figure 10 (a) shows that the tuned microphone produces smaller capacitance changes due to reduced membrane displacement. It is believed that the modification of membrane stiffness is changed by grown and retracted nanostructures. The microphone mismatch shown in Figure 10 (b) is improved from 0.6 dB to 0.16 dB after the tuning, which corresponds to fair directionality improving to excellent directionality at 3 kHz.

Figure 11 shows acoustic responses over electrodeposit growth time. The mismatch after *in-situ* tuning reduces from 2.76 dB to 1.56 dB, which represents DI increases from 3.5 dB (fair directionality) to 4.7 dB (excellent directionality). The gain mismatch of microphones is precisely controlled by *in-situ* silver nano-electrodeposits growth/retraction under a normal operating environment such as room temperature and no specific setup. Specifically, if the initial mismatch of non-tuned microphones is small, then it can be manipulated to reduce the mismatch to within 0.25 dB.

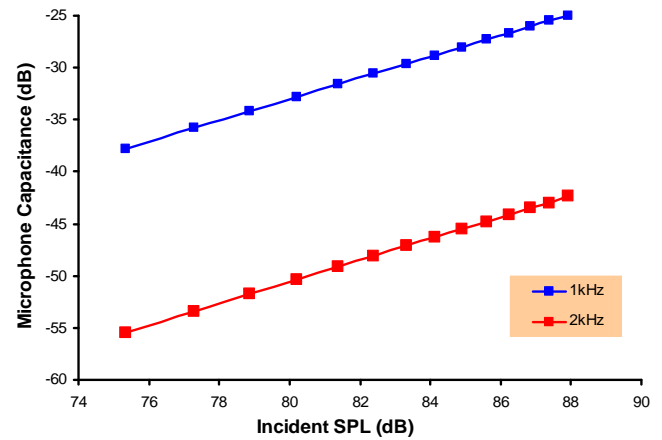


Figure 8: Capacitance output of a microphone from readout circuits over input sound pressure from the Knowles microspeaker (dB SPL).

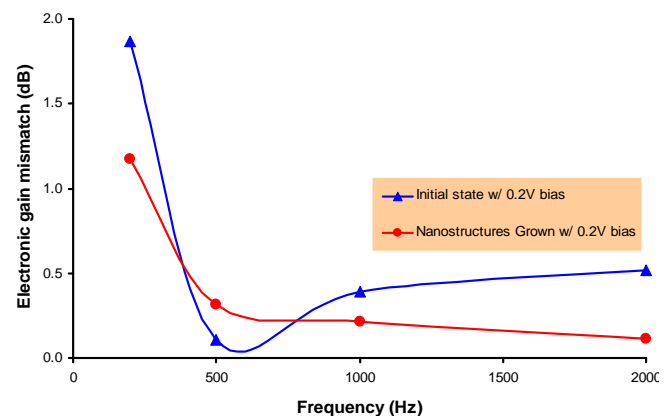
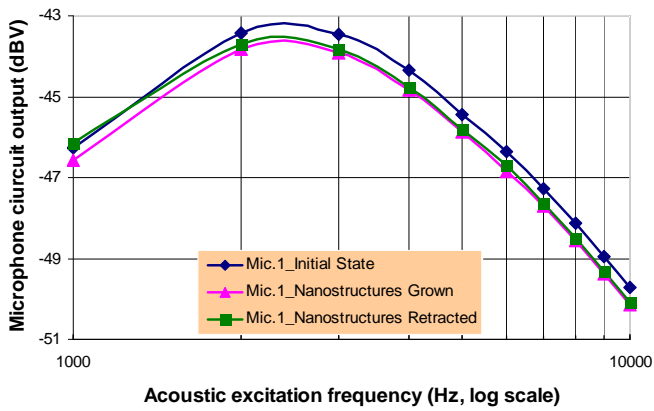
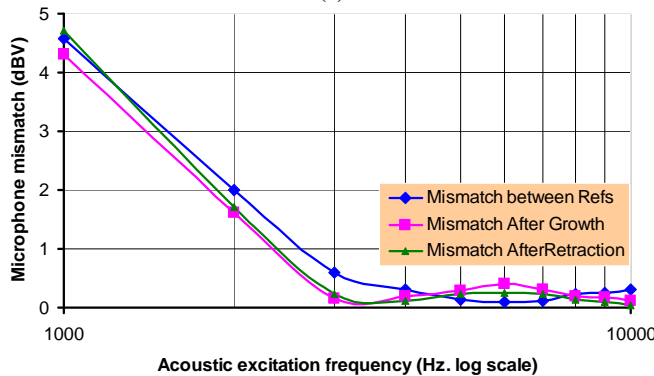


Figure 9: Mismatch reduction upon the growth of the nano-electrodeposits in electrical *in-situ* measurement using the LCR meter.



(a)



(b)

Figure 10: (a) Nanostructures tuned microphone acoustic readout circuit response over an audio frequency range and (b) reduced mismatch using nanostructures tuned microphone acoustic response over a selected frequency range.

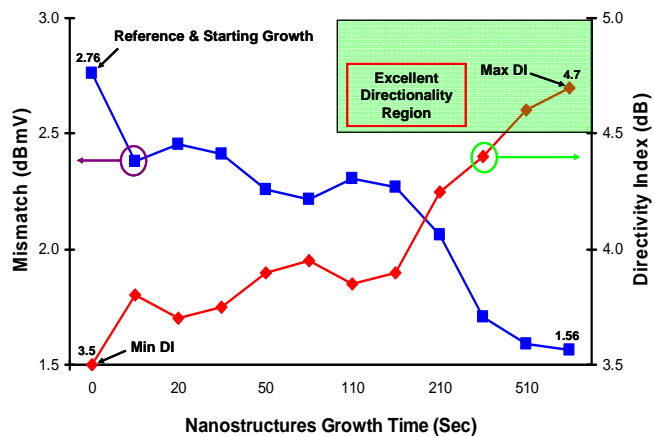


Figure 11: Acoustic responses upon nano-electrodeposits growth; showing the improvements of gain mismatch and DI.

## CONCLUSION

We demonstrate a directional microphone using multiple *matched* omni-directional microphones. It is performed by an *in-situ* tuning technique using integrated nanostructures on the membrane of a microphone. The tuning is to minimize the mismatch of multiple microphones to achieve better directionality. The omni-directional microphones are capacitive and have a parylene membrane integrated with the nanostructures. The silver nanostructures with approximately 100 nm heights are controlled by

external bias at room temperature. The nanostructures can be grown and retracted to precisely manipulate the sensitivity to incoming acoustic waves by the change of mass/stress distribution on the parylene diaphragm of the microphone. The readout circuits to interface MEMS microphones have bandwidth of 56 kHz and SNR of approximately 40 dB at 1 kHz. To reduce noise sources, such as 60 Hz coupling from the power grid we place the acoustic measurement setup in a custom built Faraday cage. The microphone capacitance is tuned up to 0.7 dB at all over the frequency ranges and acoustic mismatch reduces by 1.2 dB. This represents DI increase of 1.2 dB, which is crucial to achieve a highly directional microphone. The presented technique has many potential applications, including post-packaging trimming and calibration of micro-devices.

## ACKNOWLEDGMENT

The authors would like to acknowledge Mr. Yongmo Yang, the staff of the Center for Solid State Electronics Research (CSSER) at Arizona State University, Prof. Tom Milster's group at the University of Arizona, and Knowles electronics for their continuing support. We also appreciate the US National Science Foundation (US NSF) supporting this work under Grant #0627777 and #0652136.

## REFERENCES

1. M. C. Killion, R.S., L. Christensen, D. Fabry, L. Revit, P. Niquette, and K. Chung, "Real world performance of an ITE directional microphone," *Hear. J.* vol. 51, No. 4, pp. 24–38 (1998).
2. D. B. Hawkins and W. S. Yacullo, "Signal-to-noise ratio advantage of binaural hearing aids and directional microphones under different levels of reverberation," *J. Speech Hear Disord.*, vol. 49, pp. 278–286 (1984).
3. S. Kochkin, Customer satisfaction with single and multiple microphone digital hearing aids, Better hearing ([www.betterhearing.org](http://www.betterhearing.org)).
4. J. Tchorz, Effects of microphone mismatch in directional hearing instruments, *Hearing review* (2001).
5. J. J. Yao and N. C. MacDonald, "A micromachined, single-crystal silicon tunable resonator," *J. Microelectromech. Syst.*, vol. 6, pp. 257-264 (1996).
6. W. Zhang, R. Baskaran, and K. L. Tumer, "Changing the behavior of parametric resonance in MEMS Oscillators by tuning the effective cubic stiffness," *MEMS 2003 conference*, pp. 173-176 (2003).
7. M. N. Kozicki and M. Mitkova, "Mass transport in chalcogenide electrolyte films - materials and applications," *Journal of Non-Crystalline Solids*, vol. 352, pp. 567-577 (2006).
8. S. Je and J. Chae, "Precise manipulation of micro-device membranes using electrodeposited nano-structures," *NEMS 2008* (2008).

# PRINTING MEMS: FROM A SINGLE FLEXIBLE POLYIMIDE FILM TO THREE-DIMENSIONAL INTEGRATED MICROFLUIDICS

W. Wang, H. Cong, Z. Qiu, S. Zhao, H. Zhu, A. Revzin, and T. Pan

Department of Biomedical Engineering, University of California, Davis, USA

## ABSTRACT

With the major advances in soft lithography and polymeric materials, use of microfluidic lab-on-a-chip device has attracted tremendous attention recently. A simple and fast micromachining process is highly in demand to prototype such a device. In this paper, we first reported an out-of-cleanroom printing-based integrated microfabrication process, referred to as printing microelectromechanical system (*Printing MEMS*). Using the *Printing MEMS* process, we demonstrated the potential to accomplish an entire design-to-fabrication cycle within an hour, including 50  $\mu\text{m}$ -resolution non-lithographic patterning, well-controlled polyimide etching, three-dimensional pattern alignment and multilayer wax fusion bonding. A microfluidic mixer was prepared by this method and tested for the process validation.

## INTRODUCTION

Over the last two decades, design and fabrication of integrated microfluidic devices and systems for biological and medical applications have experienced extensive growth [1-3]. Lab-on-a-chip system, an emerging technique of precisely handling extremely tiny volume of fluid, plays a key role in the modern analytical chemistry and biomedical studies [1-3]. Although various lab-on-a-chip devices have been demonstrated by conventional microfabrication techniques with high reliability and ultra fine resolution, expensive equipment, extensive usage of cleanroom as well as lengthy processing cycle present a major obstacle in the research-oriented prototype development. Therefore, rapid prototyping approaches are highly demanded to manufacture microfluidic chips with feature sizes ranging from tens microns to several millimeters.

With recent advances in the soft lithography and polymeric microelectromechanical systems, a large number of rapid prototyping techniques for microfluidic devices have been demonstrated [4-6]. However, the PDMS-based soft lithography technique still heavily relied on the master mold created by conventional micromachining within a clean-room environment [2-4]. More recently, a progress on "printing and peeling" technique, using a commercial laser printer to create master mold for PDMS features, showed the potential of a cleanroom-independent soft lithography process [5,6]. However, geometrical dimensions of the molded micropatterns were highly limited by the printer performance and the interactions between the toner and printed surface. Only low aspect ratio microchannels of less than 15  $\mu\text{m}$  in height were achieved by this process [5,6]. Considering the defects and irregularities on the printed surface, the fluidic performance within the molded PDMS microchannels might not be optimized. Moreover, none of the current approaches demonstrates fully integrated fabrication capability, for instance, customized alignment and packaging techniques are typically involved.

In this paper, we present the first out-of-cleanroom integrated printing microelectromechanical systems, *Printing MEMS*, including non-lithographic patterning, etching process, alignment and packaging. In this process, a special solid wax ink was printed onto a commercial available flexible polyimide film using a solid-ink laser printer. Using the wax patterns as wet etching barrier, the polymeric substrate was able to be selectively removed in a base

solvent to form embedded micro structures. Finally, three-dimensional structures were aligned by special folding structures created in the etching process and packaged using thermal fusion bonding through the wax layers. Figure 1 shows a microfluidic mixer fabricated onto the polyimide film only using a solid-ink laser printer and wet etching.

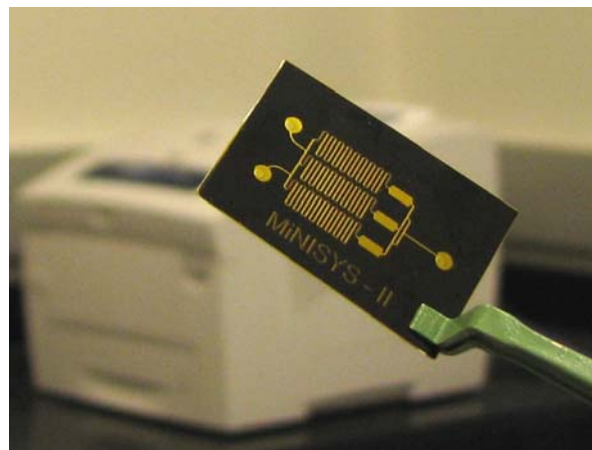


Figure 1: Photograph of a microfluidic mixer fabricated by *Printing MEMS* process with a solid-ink laser printer setting as the background. (the polyimide substrate shows its intrinsic yellow color while having black wax prints as an adhesive layer)

## MICROFABRICATION

Solid-ink printing utilizes molten wax to produce images on the print instead of fluid inks and toner cartridges. The solid ink stick is melted and produces images on the substrate in offset-printing manner. The solid-ink printing technique is usually used for vibrant-color patterning and can print on a wide range of media, including flexible polymeric substrate as we used in this work [7].

In our *Printing MEMS* fabrication process, the patterned solid wax serves several important functions as: 1) a non-lithographic patterning layer, 2) a chemical etching barrier, and 3) a self adhesive layer for packaging. A polyimide film (Kapton™, DuPont) was chosen as the substrate for its excellent chemical and physical properties as well as the flexibility [8], which is widely used in flexible circuits and biological MEMS devices.

Figure 2 illustrates the fabrication scheme of the *Printing MEMS*. All the microscale patterns were first created in a graphic design software (CorelDraw™, Corel) and then directly printed onto the film using transparency settings in a solid-ink printer (Phaser™ 8560DN, Xerox). To implement three-dimensional structures in a single film print, all the layers were printed and processed at once but separated by folding marks. In addition, double-sided printing technique was used to pattern both sides of the film simultaneously (Fig 2-a). A subsequent annealing at 65 °C improves adhesion between the wax layer and underlying film. Then a KOH-based etchant (KOH: H<sub>2</sub>O: Ethanolamine=1: 2: 2 wt)

was used to perform an isotropic etching into the polyimide substrate (Fig 2-b). Finally, the film was folded over along the etched folding grooves and thermal fusion bonded through the wax layer at 65 °C (Fig 2-c, 2-d).

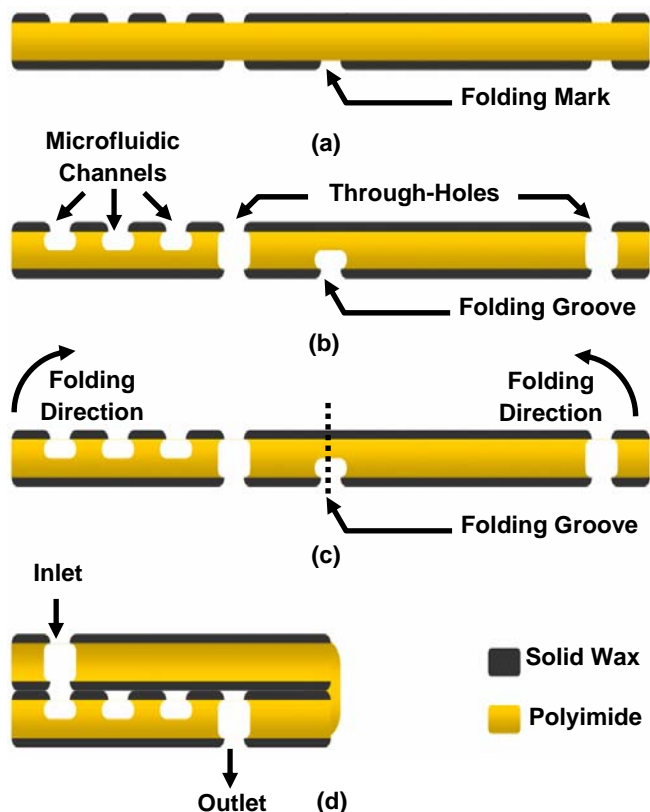


Figure 2: Schematic illustration of the Printing MEMS process: (a) Solid wax was double-sided printed onto a polymeric film using the solid-ink laser printer, (b) the polymeric film was selectively etched with the printed solid wax as the mask, where microfluidic channels and through-holes were fabricated simultaneously, (c) the etched film was folded over along the folding groove which provides a good alignment for the multilayer structures, and (d) wax fusion bonding was used to seal the microchannel and realize a 3D microfluidic chip.

## RESULTS AND DISCUSSION

### Printing Performance

As a non-lithographic patterning layer, the resolution of solid wax print is largely set by the printer performance and the interfacial energy between the wax and printed surface. Although Xerox claims Phaser 8560 laser printer resolution is up to 2,400 dpi, equivalent to 10.6  $\mu\text{m}$ , we could not verify this result experimentally. Figure 3 compares the printed line/gap widths with their original computer designs. The design and printing results follow a linear relationship as expected. However, the printed features appear to be enlarged from the design by a systemic offset, which may result from pattern transfer from the offset print drum to the film, and limits the minimal printable feature size. As shown in Figure 3, the narrowest line can be printed reliably is 170  $\mu\text{m}$  wide with a minimum gap width of 50  $\mu\text{m}$ . Figure 4 shows a scanning electron microscopic (SEM) photo of typical printing results.

Compared with regular toner-based laser printing techniques, solid ink printing provides better adhesion between wax layer to a non-textured smooth surface due to melting and re-solidifying of wax, which is critical to form miniaturized features onto the smooth surface of the polyimide substrate. Furthermore, thermal annealing of the wax layer at an elevated temperature serves as an important step to eliminate printing defects and irregularities, and therefore, significantly improve the chemical resistivity in the following chemical etching step. Under the KOH-based etchant, the annealed wax layer shows excellent selectivity to the underneath polyimide substrate.

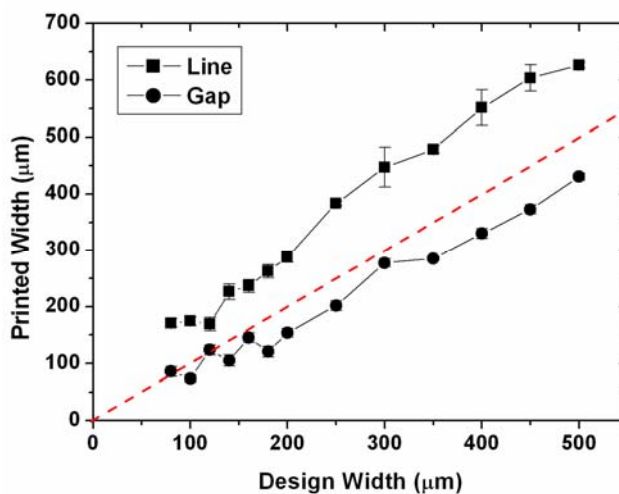


Figure 3: Calibration of the printed lines and gaps with their original designs in the computer.

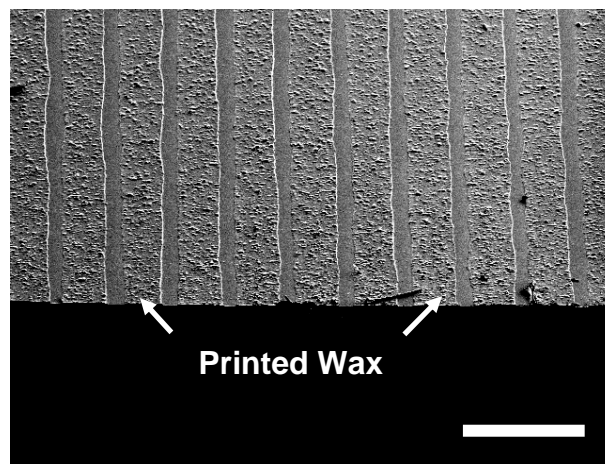


Figure 4: Printed wax lines and gaps on a polyimide film. (the scale bar is 500  $\mu\text{m}$ , the printed line is 170  $\mu\text{m}$  wide with a minimum gap width of 50  $\mu\text{m}$ )

### Etching Performance

We have characterized polyimide wet etching in a KOH-based etchant. The ethanolamine in the KOH etchant acts as an organic solvent to speed the residue removing in the wet etching process.

As exhibited in Figure 5, etching rate of polyimide increases with elevated temperature, and achieves  $\sim 15 \mu\text{m}/\text{min}$  at  $70^\circ\text{C}$ , beyond which the wax melts and peels off rapidly in the etching bath. Although higher etching temperature leads to fast processing, the surface roughness increases while uniformity decreases over the substrate at high etching rate. In addition, the etchant may leak through the wax layer and severely undercut the substrate at higher temperature. Therefore, compromising etching rate and etching profile, a processing temperature between  $30$  and  $50^\circ\text{C}$  has been used, leading to a highly controllable etching rate within the range from  $1$  to  $4 \mu\text{m}/\text{min}$ . Figure 6 shows a SEM photo of wet etched polyimide substrate, on which the microchannels are  $45 \mu\text{m}$  deep with noticeable undercut underneath the wax layer through the isotropic etching process.

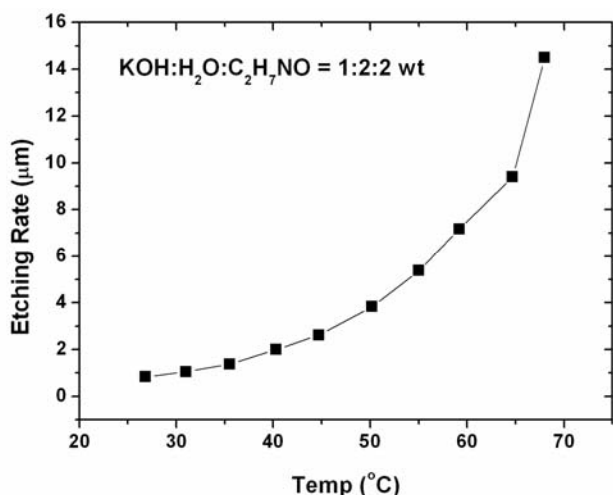


Figure 5: Various etching rates of polyimide substrate at different processing temperatures.

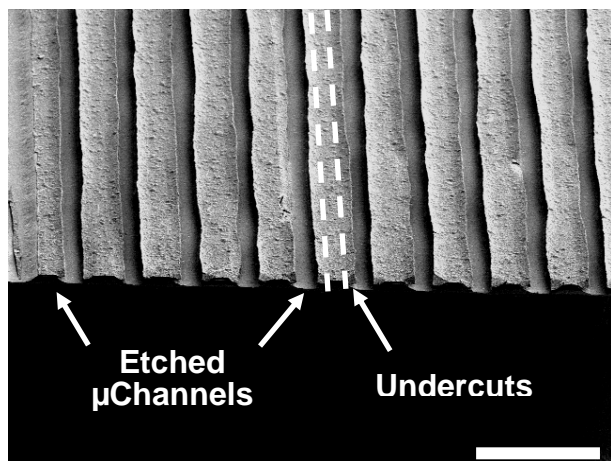


Figure 6: Wet etched microchannels of  $45 \mu\text{m}$  in depth. (the scale bar is  $500 \mu\text{m}$ )

In the *Printing MEMS*, the double-side printing can be used to construct three-dimensional multilayer structures from a single

processed film. Patterning solid wax on the both sides of a polyimide film and annealing the wax in an oven ( $\sim 65^\circ\text{C}$ ), lateral and transverse microfluidic channels were etched out on both sides of the polyimide surfaces simultaneously as shown in Figure 7. Through holes were also created at the crossovers where the overetched microchannels on each side are connected.

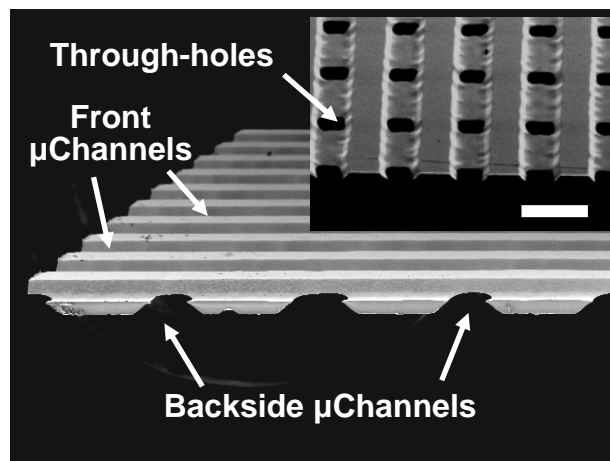


Figure 7: Double side printing and etching for a 3D microfluidic channel network with through holes at the crossovers. (inset is the top view of the crossover, the scale bar is  $500 \mu\text{m}$ )

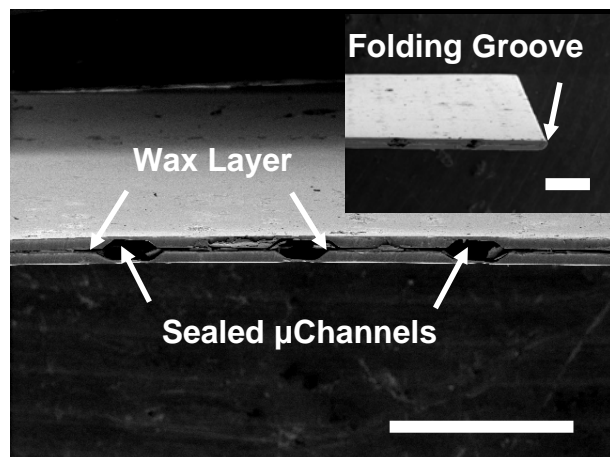


Figure 8: Sealed microchannel with fusion bonding of the wax. (inset is the folding groove, all the scale bars are  $500 \mu\text{m}$ )

#### Folding Alignment and Wax Fusion Bonding

Pre-defined folding grooves between each patterned area play an important role in our alignment design. Folding along the etched grooves, misalignment less than  $10 \mu\text{m}$  can be achieved manually. The printed wax layer is used as a reusable adhesive layer in the following fusion bonding step, which allows possible adjustment on the alignment even after initial bonding. Figure 8 reveals a cross-section view of enclosed microfluidic channels using the wax thermal fusion bond. A folding groove structure in the inset provides alignment capacity. Compared with the alignment of multi-layer printing technique, the alignment with the folding

groove achieves higher precision.

The fusion bonding of the wax layer was processed at 65 °C with a slight physical pressure (<1 kPa) applied to make conformal contact of the bonding surfaces. Current fusion bonding technique achieves a bonding strength of ~10 kPa, primarily contributed from van der Waals interaction between wax and polyimide molecules. This may not be sufficient for high-pressure large-flow operation. Therefore, a surface chemical modification of polyimide is currently under investigation. Our preliminary results indicate more than 0.5 MPa bonding strength between two polyimide substrates can be repetitively achieved using a two-step surface treatment of diluted KOH and HCl solutions. In that case, microfluidic device also benefit from keeping the optical transparency.

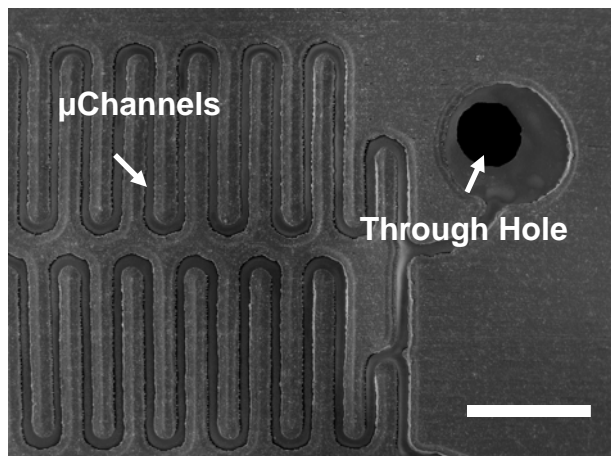


Figure 9: Microchannel and the through hole for inlet. (the scale bar is 2mm)

### Gradient Mixing Test

To verify the *Printing MEMS* process, a microfluidic mixer was prepared to create chemical gradient. Multiple printing and etching processes were demonstrated in the fabrication. First, through-holes of fluidic inlets and outlet were defined on the polyimide substrate by the first wax printing. Followed by a 3-minute etching at 50°C, the wax layer on the film was removed in Hexane as aforementioned. This results in a 10 μm etching step into the polyimide film. The second printing was used to pattern microfluidic channels and folding alignment grooves simultaneously. Alignment between two sequential prints may lead to a systemic offset more than 50 μm, basically caused by mechanical feeding. The same KOH-based wet etching was conducted consequently till the inlet and outlet holes were completely etched through. Then, the micromachined film was rinsed in DI water and blow-dried in nitrogen flow. Figure 9 illustrates the SEM photo of the micromixing channels and a through-hole inlet. Finally, the patterned polyimide film was folded over along the etched folding groove and thermal fusion bonded through the wax layer at 65 °C.

Red color dye and DI water separately loaded to the two inlets were used to generate a mixing gradient. The outlet was connected to a vacuum line (at ~0.2 atm), which provided the pressure gradient across the microfluidic device and pulled the dye and DI water through mixing channels. Figure 10 shows mixing results achieved at the downstream reaction chambers.

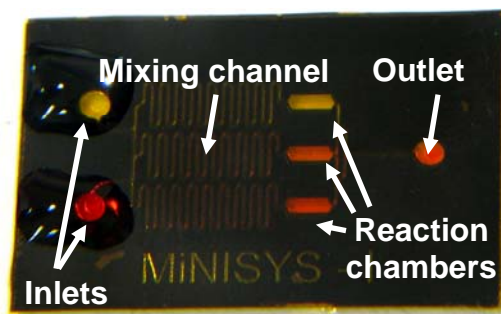


Figure 10: Gradient mixing result of a red dye buffer with DI water.

### CONCLUSIONS

In this paper, a novel out-of-cleanroom rapid-prototyping technique, *Printing MEMS*, was first reported only using a solid-ink laser printer and wet etching. Using this process, we demonstrated the potential to accomplish an entire design-to-fabrication cycle, including 50 μm resolution non-lithographic patterning, well-controlled polyimide etching, three-dimensional pattern alignment and multilayer wax fusion bonding. Moreover, the patterned solid wax served several important functions as a non-lithographic patterning layer, a chemical etching barrier, as well as a self adhesive layer for packaging. In addition, a special folding alignment technique was shown to create three-dimensional structures from a single processed polyimide film. Overall, from the original layout design to the final functional device, the *Printing MEMS* technique only takes less than an hour to process, which offers an inexpensive rapid-prototyping solution for lab-on-a-chip applications.

### ACKNOWLEDGEMENT

This research is partially supported by California Healthcare Foundation and the University of California, Davis. The authors would like to thank Dupont Corporation for the kindly supply of polyimide films.

### REFERENCES

- [1] P. S. Dittrich, K. T. Tachikawa, and A. Manz, "Micro Total Analysis Systems. Latest Advancements and Trends", *Analytical Chemistry*, 78, 3887 (2006).
- [2] A. Grimes, D. N. Breslauer, M. Long, J. Pegan, L. P. Lee, and M. Khine, "Shrinky-Dink Microfluidics: Rapid Generation of Deep and Rounded Patterns", *Lab on a Chip*, 8, 170 (2008).
- [3] C. Khoury, G. A. Mensing, and D. J. Beebe, "Ultra rapid prototyping of microfluidic systems using liquid phase photopolymerization", *Lab on a Chip*, 2, 50 (2002).
- [4] D. C. Duffy, J. C. McDonald, O. J. A. Schueller, and G. M. Whitesides, "Rapid Prototyping of Microfluidic Systems in Poly(dimethylsiloxane)", *Analytical Chemistry*, 70, 4974 (1998).
- [5] V. I. Vullev, J. Wan, V. Heinrich, P. Landsman, P. E. Bower, B. Xia, B. Millare, and G. Jones, "Nonlithographic Fabrication of Microfluidic Devices", *Journal of the American Chemical Society*, 128, 16062 (2006).
- [6] G. V. Kaigala, S. Ho, R. Penterman, and C. J. Backhouse, "Rapid Prototyping of Microfluidic Devices with a Wax Printer", *Lab on a Chip*, 7, 384 (2007).
- [7] [http://en.wikipedia.org/wiki/Solid\\_ink](http://en.wikipedia.org/wiki/Solid_ink).
- [8] S. Metz, R. Holzer, and P. Renaud, "Polyimide-based Microfluidic Devices", *Lab on a Chip*, 1, 29 (2001).

# SELF-ASSEMBLED 275NM-GAP ELECTRODES FOR CMOS-MEMS RESONATORS AND ITS PRECISION DC CHARGE-BASED CAPACITANCE MEASUREMENT

Chiung-C. Lo<sup>1</sup> and Gary K. Fedder<sup>1,2</sup>

<sup>1</sup>Department of Electrical and Computer Engineering  
and <sup>2</sup>The Robotics Institute of Carnegie Mellon University, USA

## ABSTRACT

A self-assembled electrode (SAE) technique and a precise DC charge-based capacitance measurement (CBCM) method are introduced for integrated on-chip characterization of lateral gap MEMS capacitance. A SAE with a 275 nm gap is applied in CMOS-MEMS free-free flexural mode resonators (FMRs) to enlarge input and output capacitive coupling. A 23 dB gain enhancement illustrates the importance of the method. The CBCM method can measure MEMS electrode capacitances down to a few femto-Farads with the existence of large parasitic capacitance to ground. A modified finite-element model verifies the relation between the measured capacitance to the electrode geometry. A temperature stability test demonstrates the SAE can operate in the range of 23-85°C without mechanical clamps.

## INTRODUCTION

Over the last four decades, although integrated circuits double in computing power approximately every 18 months without increasing cost per IC, off-chip components are still needed to provide narrow-band filtering and stable reference frequencies. CMOS-MEMS technology is a platform to integrate narrow-band filters and mixer-filters (mixfilters) with active circuitry to realize single chip transceivers. However, several challenges, such as lowering termination resistance ( $R_T$ ), need to be addressed before their implementation in wireless systems.

In order to form a flat pass-band, microresonators need to be terminated to a  $R_T$  proportional to the 4<sup>th</sup> power of the electrode gap. Air-gap capacitive microresonators need relatively high termination resistance;  $R_T$  is 370 M $\Omega$  for devices with electrode gaps of 800 nm and  $Q$  of 10,000. Lowering  $R_T$  to a manageable level for on-chip circuits, for example 10 k $\Omega$ , is necessary for integration and requires a smaller electrode gap. In select processes, narrow gaps may be formed with sacrificial layers [1] and with solid-dielectric drives [2]. In CMOS-MEMS, narrow gaps may be achieved by self-assembly of electrodes [3].

Precise characterization of the sensing capacitance in the presence of large parasitic capacitance ( $C_p$ ) is important in understanding process and design limits. SEM image-based measurement and/or focused-ion-beam sectioning is the most common characterization technique where the capacitive gap and overlapped electrode area are measured and capacitance is extracted from a parallel-plate model. This technique is time-consuming for multiple-device measurement, impossible for automatic testing, and not accurate for sub-micron gaps due to significant geometry and material non-idealities. Within the integrated circuit community, a DC CBCM method has been widely used to measure inter-wire capacitance [4-7], and a bias-dependent technique was later developed to further reduce mismatch errors [8]. This technique is adopted here for the first-time to measure MEMS lateral gap capacitances and to study the temperature stability of SAE.

## SELF-ASSEMBLED ELECTRODE DESIGN

Narrow gap electrodes (NGEs) are crucial for increasing capacitive coupling especially for RF-CMOS-MEMS resonator/filter applications. Previously, approximately 500 nm gaps have been achieved with electrothermal gap-closing actuators

operating at 3.5mW power consumption [3]. Shown in Figure 1, a self-assembled actuator (SAAs) achieves electrode movement with no power consumption. The actuator comprises a beam flexure with individual beams made of the dielectric and metal layers in the CMOS. The beam cross section has laterally offset stacks of metal layers to create an embedded residual stress gradient transverse across the beam. After releasing the structures, the stress creates an internal bending moment that moves the device laterally. The final gap is defined by the difference between the initial electrode gap and the stopper gap. The inner-metal layers are offset to one side of the beam for half the beam length and offset to the other side of the remaining half of the beam length. This arrangement generates a guided-end condition that allows multiple beams to be placed in parallel to create a stiffer actuator. Theoretically, the displacement of SAAs is proportional to the square of actuator length and the inverse of the actuator beam width. The optimal beam design for maximizing displacement is discussed in [9].

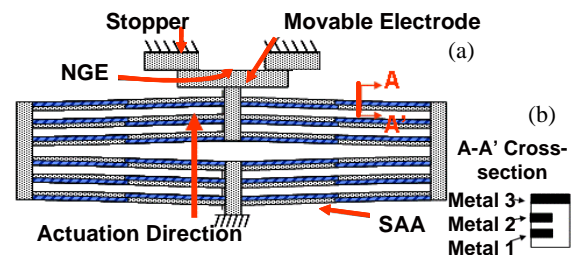


Figure 1: (a) The schematic of a self-assembled actuator, and (b) the cross-section of the self-assembled actuator at A-A'.

## THE DESIGN AND FABRICATION OF CMOS-MEMS FLEXURAL MODE RESONATORS

The FMR topology comprises two free-free beams coupled by supporting tethers, vibrates horizontally on the silicon substrate, It achieves high quality factor due to low anchor loss and low motional impedance with large electrode area, and was introduced for its high-order mode in oscillator applications [10].

The beams are actuated and the displacement sensed electrostatically through lateral air-gap electrodes. The actuating force at the center of each cantilever excites the FMR to move laterally in the x-direction, which generates output motional currents across a DC biased output capacitor. The output motional current is converted into a voltage by passing through the input capacitance of the pre-amplifier. With the assumption of identical input and output electrode geometry, the transfer function of the differential FMR is

$$H(\omega) \approx \frac{-4j\epsilon_0^2 A^2 V_p^2 G_v}{Kg^4 \left(1 - \frac{\omega^2}{\omega_R^2} + j\frac{\omega}{Q\omega_R}\right)} \quad (1)$$

where  $\epsilon_0$  is the permittivity of free space,  $A$  is the electrode overlap area,  $V_p$  is a DC polarization voltage,  $G_v$  is the ratio of the voltage amplification of the amplifier to the input capacitance of the amplifier,  $K$  is the equivalent stiffness of the coupled resonators,  $g$  is the electrode gap,  $\omega$  is the frequency of the input signal, and  $\omega_R$  is the resonant frequency.

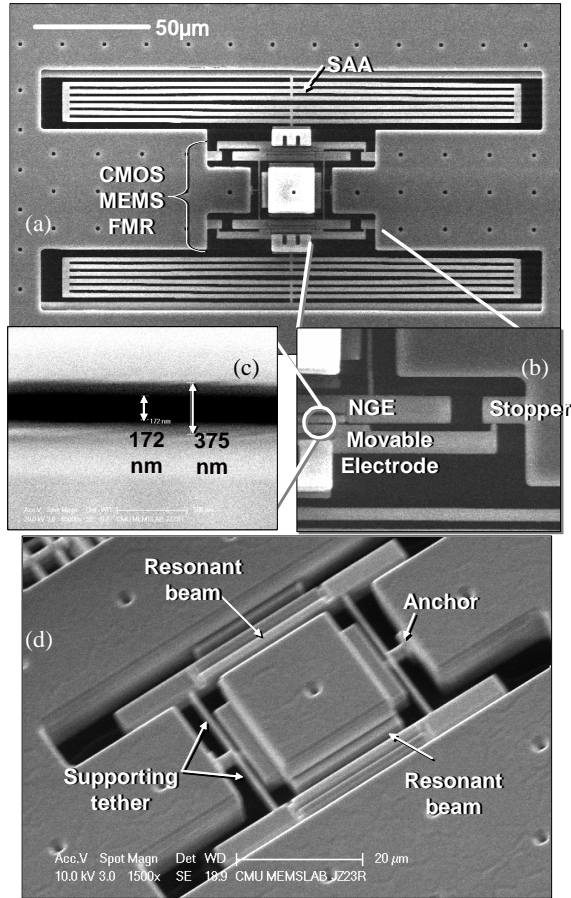


Figure 2: CMOS-MEMS flexural mode resonators. (a) Design with SAA electrodes. (b) A close-up view of a stopper and narrow-gap electrode (NGE). (c) Further close-up of NGE where mechanical gap is 172nm, and (d) A FMR fixed gap design.

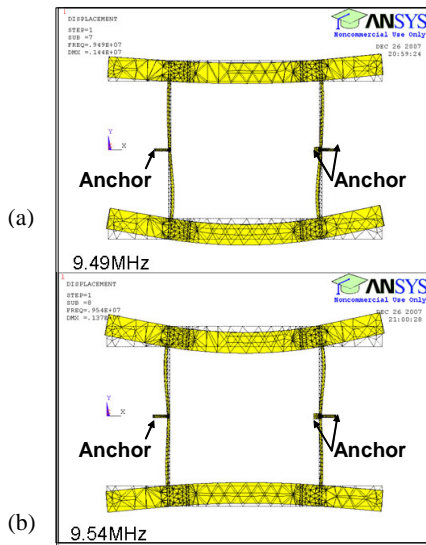


Figure 3: (a) The 1<sup>st</sup> and (b) 2<sup>nd</sup> mode of the CMOS-MEMS flexural mode resonator. A homogeneous Young's modulus of 70 GPa and density of 2200 kg/m<sup>3</sup> is assumed.

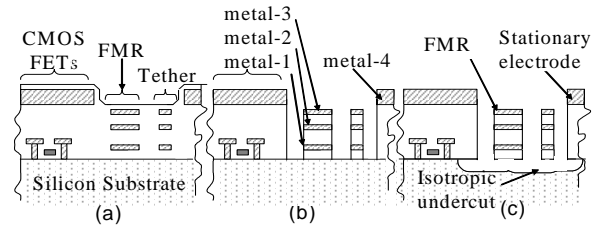


Figure 4: Cross-sections of CMOS-MEMS micro-machining process: (a) after foundry CMOS processing, (b) after SiO<sub>2</sub> etch, (c) after isotropic etch to release the resonator.

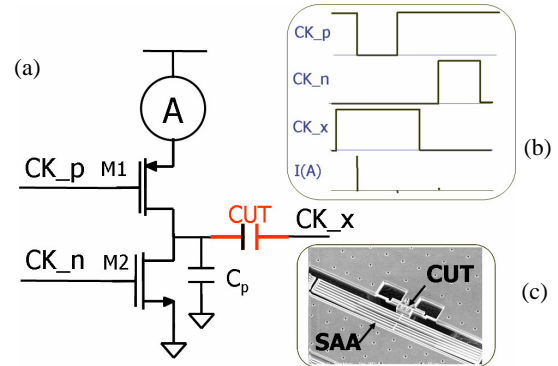


Figure 5: (a) The CBCM circuit diagram. (b) Timing diagrams of the three non-overlapping clocks (CK<sub>p</sub>, CK<sub>n</sub>, and CK<sub>x</sub>). (c) An implemented CUT with a SAA narrow gap.

Figure 2 (a) shows the SEM of a FMR with SAA electrodes, (b) and (c) illustrate close-up views of stoppers and NGEs, respectively and (d) is the SEM of a fixed-gap (FG) FMR for comparison. The finite-element analysis results of the first two resonant modes are illustrated in Figure 3, where the pole splitting due to the stiffness of supporting tethers is observed. This effect is employed to construct the bandpass response.

As illustrated in Figure 4(a), the post CMOS micromachining process [3] starts with a foundry-fabricated four-metal 0.35 μm CMOS chip. A CHF<sub>3</sub>:O<sub>2</sub> RIE removes all of the dielectric stacks which are not covered by top metal layers as shown in Figure 4(b). After the dielectric etch, a timed isotropic/anisotropic silicon etch releases the resonator and its SAA electrode simultaneously, resulting in Figure 4(c).

## DC CHARGE-BASED CAPACITANCE MEASUREMENT

The bias-dependent CBCM method, shown in Figure 5, requires two transistor switches, a DC precision current meter, and three clocks [8]. The capacitor under test (CUT) is charged and discharged through control of two transistor switches, M1 and M2. The CUT capacitance is extracted by subtracting two charging-current readings of the DC current meter with different amplitudes of the clock CK<sub>x</sub>. In the first measurement cycle, CK<sub>x</sub> is ground and the average current reading is  $I_1$ . In the second measurement cycle, CK<sub>x</sub> is  $\Delta V_{CK_x}$  and the average current reading is  $I_2$ . The extracted capacitance is

$$C_x = \Delta I_{avg} / (f \cdot \Delta V_{CK_x}) \quad (2)$$

where the  $\Delta I_{avg} = I_2 - I_1$  is the difference of measured DC currents, and  $f$  is the clock frequency. This differential technique eliminates errors from charge injection into  $C_p$ , even if  $C_p$  is orders of magnitude larger than CUT. The limitation on the  $C_p$  to CUT ratio is defined by the resolution of DC current meter, and is about 300X for the Agilent/HP 4140B used in the measurements.

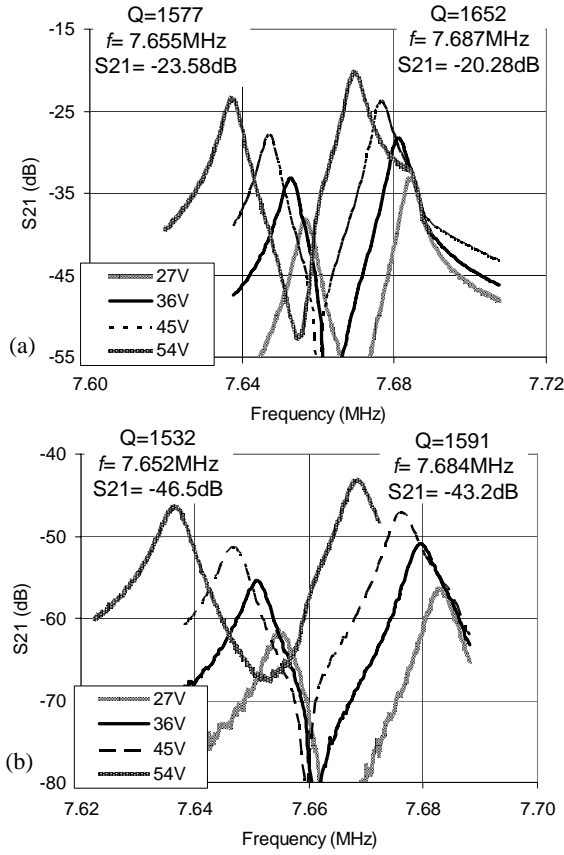


Figure 6: Measured frequency response of the (a) 1<sup>st</sup> and (b) 2<sup>nd</sup> mode of CMOS-MEMS FMRs with SAA and fixed electrodes at four different polarization voltages. The input power is 0dBm. Pressure is less than 50mTorr. Feedthrough is subtracted from the data.

## EXPERIMENTAL RESULTS

Figure 6 provides the measured results of FMRs with self-assembled and fixed gaps. The two devices have identical resonator designs with the parameters listed in Table 1. An on-board unity-gain circuit buffered the output signal, which is then measured by a network analyzer. Comparing the plots in Figure 6 (a) and (b), a 23 dB enhancement in  $S_{21}$  occurred between the average 274 nm SAA gap, in Figure 2(c), and the fixed gap of 1.1  $\mu\text{m}$ . This improvement is lower than the analytic prediction of 48 dB and the discrepancy is believed to be the result of low  $G_r$ , due to the larger parasitic capacitance loading for the SAA electrodes and the non-ideal sidewall (i.e. not vertical profile) of the NGEs. The self-assembled sidewall capacitance is also limited by a 50-100 nm thick sidewall polymer deposited during the CMOS-MEMS processing.

To characterize the narrow-gap electrode capacitance, SAA CUTs with CBCM switches were implemented as illustrated in Figure 7(a-d). The finite-element method (FEM) was employed to compare the simulated capacitance from the physical geometry with the extracted CBCM capacitance. Two sidewall geometries were compared: the simplified model geometry with parallel-sidewall electrodes in Figure 8(a) and a modified model with process related non-ideality, including top-metal slops, sidewall polymers, inner-metal pull-ins, and bottom-widening gaps, shown in Figure 8(b). The modified model geometry is extracted from a series of side-view SEMs of electrode sidewalls, with one example

Table 1: SAA FMR parameters and characteristics

Items	Parameters
Resonator (Beam) width	4 $\mu\text{m}$
Resonator (Beam) length	53 $\mu\text{m}$
Electrode length	20 $\mu\text{m}$
Electrode height	4.8 $\mu\text{m}$
Tether length	13 $\mu\text{m}$
Tether width	0.5 $\mu\text{m}$
SAA length, single side	100 $\mu\text{m}$
Polarization voltage, $V_p$	27-54 V
Pressure	< 50 mTorr
Resonant frequency, 1st & 2nd mode	7.65 & 7.68 MHz
$S_{12}$ (w/on-chip amp.), 1st & 2nd mode	-23.6 & -20.3 dB
Q, 1st & 2nd mode	1577 & 1652

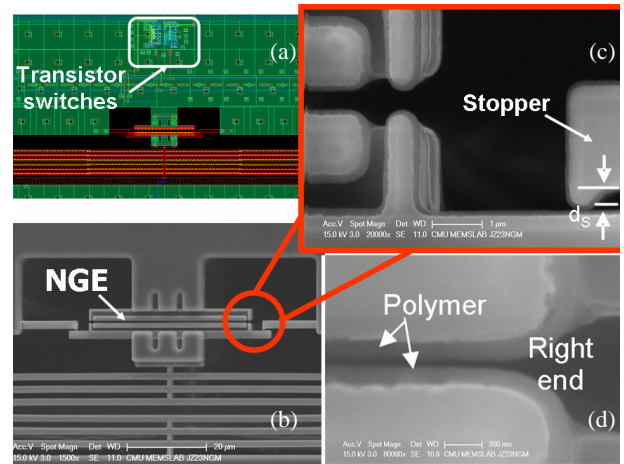


Figure 7: (a) The layout of the switches and SAA CUT. (b) The SEM of CUT. (c) The close-up view of a stopper for a 450 nm gap defined by the stub length of  $d_s$ . (d) The SEM of a narrow gap of about 230 nm.

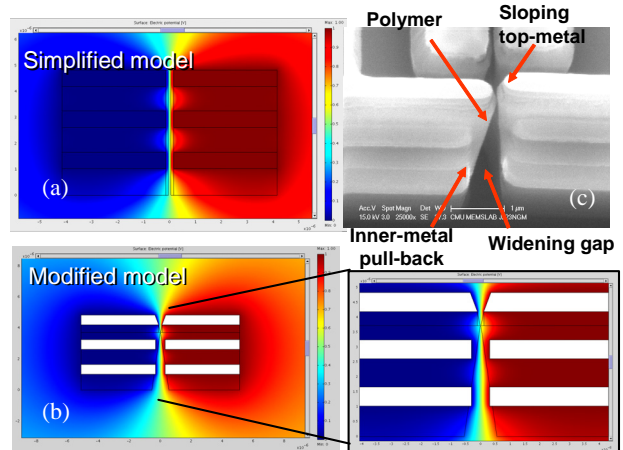


Figure 8: (a) The 2-D FEM (COMSOL) capacitance model of parallel narrow gap electrodes. (b) The modified capacitance model with geometry extracted from (c). (c) The SEM of close-up view of electrodes.

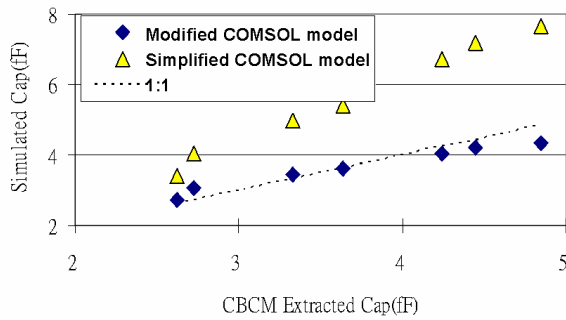


Figure 9: The comparison of CBCM extracted capacitance value and FEM simulated capacitance with simplified and modified models.

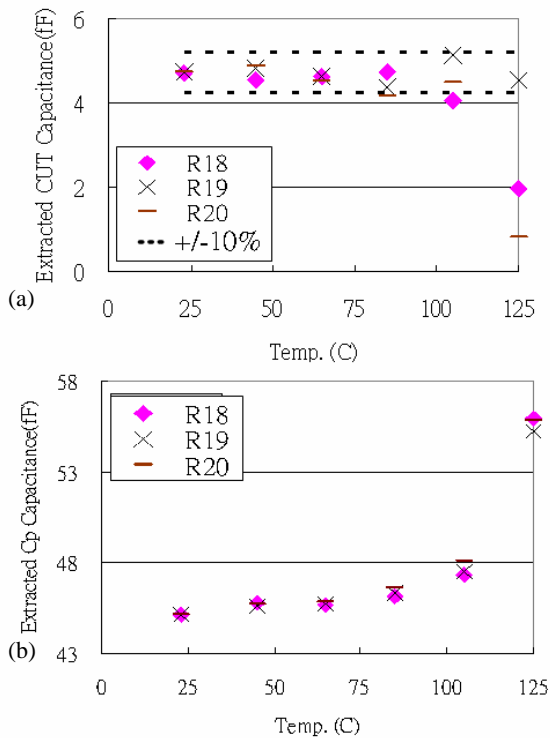


Figure 10: (a) CUT value and (b) parasitic capacitance  $C_p$  for three different test chips labeled as R18, R19 and R20, extracted directly from CBCM measurements. The calculated  $\pm 10\%$  region is based on the average capacitance at room temperature.

given in Figure 8(c).

Seven CUTs were tested with gaps ranging from 218nm to 564nm. The CBCM extracted capacitances and the corresponding FEM results with the two different models are compared in Figure 9. The CBCM extracted capacitance matches the simulations from measured sidewall geometry. The conventional parallel-plate model overestimates the capacitance by around 80% for the narrowest gaps.

A temperature stability test on SAA devices was conducted on three CUTs. The results in Figure 10 demonstrates that the SAA devices can operate up to 85 °C, which fulfills the temperature requirements of commercial and automotive standards. In addition, by adding mechanical clamps to constrain the pull-back electrode movement for high temperature operation, the upper operational limit could be extended further.

## CONCLUSIONS

This paper presents a self-assembled capacitive electrode to enlarge input/output capacitive coupling and its application in CMOS-MEMS flexural mode resonators (FMRs). The 275 nm self-assembled gap provides 23 dB gain without consuming actuation power. It should be possible to achieve even smaller gaps with future stopper designs and minimization of sidewall polymer formation. The DC charge-based capacitance measurement method was demonstrated through detailed FEM modeling to provide an accurate measure of the femto-Farad sidewall capacitance even with the existence of 9.6 times larger parasitic capacitance to ground. The temperature stability test demonstrates the SAA electrodes can operate within the range of 23-85°C. The high temperature limit could be extended with the help of mechanical clamps. The self-assembled electrodes and CBCM method are integrated on-chip directly, require little or no addition equipments, and therefore reduce process and testing complexity, respectively.

## REFERENCES

- [1] W. T. Hsu, J. R. Clark, and C. T. C. Nguyen, "A sub-micron capacitive gap process for multiple-metal-electrode lateral micromechanical resonators," presented at The 14th IEEE International Conference on Micro Electro Mechanical Systems, Interlaken, Switzerland, 2001.
- [2] S. A. Bhavne and R. T. Howe, "Silicon nitride-on-silicon bar resonator using internal electrostatic transduction," presented at The 13th International Conference on Solid-State Sensors, Actuators and Microsystems, Seoul, Korea, 2005.
- [3] C.-C. Lo, C. Fang, and G. K. Fedder, "Integrated HF CMOS-MEMS square-frame resonators with on-chip electronics and electrothermal narrow gap mechanism," presented at The 13th International Conference on Solid-State Sensors, Actuators and Microsystems, Seoul, Korea, 2005.
- [4] R. Bach, B. Davis, and R. Laubhan, "Improvements to CBCM (charge-based capacitance measurement) for deep submicron CMOS technology," presented at International Society for Quality Electronic Design, San Jose, CA, 2006.
- [5] J. C. Chen, B. W. McGaughy, D. Sylvester, and H. Chenming, "An on-chip, attofarad interconnect charge-based capacitance measurement (CBCM) technique," presented at International Electron Devices Meeting, San Francisco, CA, 1996.
- [6] D. Sylvester, J. C. Chen, and H. Chenming, "Investigation of interconnect capacitance characterization using charge-based capacitance measurement (CBCM) technique and three-dimensional simulation," IEEE Journal of Solid-State Circuits, vol. 33, pp. 449-453, 1998.
- [7] L. Vendrame, L. Bortesi, F. Cattane, and A. Bogliolo, "Crosstalk-based capacitance measurements: theory and applications," IEEE Transactions on Semiconductor Manufacturing, vol. 19, pp. 67-77, 2006.
- [8] Y.-W. Chang, C. Hsing-Wen, L. Tao-Cheng, K. Ya-Chin, T. Wenchi, K. Yen-Hui Joseph, and L. Chih-Yuan, "Charge-based capacitance measurement for bias-dependent capacitance," IEEE Electron Device Letters, vol. 27, pp. 390-392, 2006.
- [9] P. J. Gilgunn, J. Liu, N. Sarkar, and G. K. A. F. G. K. Fedder, "CMOS-MEMS Lateral Electrothermal Actuators," Journal of Microelectromechanical Systems, vol. 17, pp. 103-114, 2008.
- [10] G. K. Ho, K. Sundaresan, S. Pourkamali, and F. A. A. F. Ayazi, "Low-motional-impedance highly-tunable  $I_{\text{sup}}^2$  resonators for temperature-compensated reference oscillators," presented at The 18th IEEE International Conference on Micro Electro Mechanical Systems, Maimi, FL, 2005.

# SYNTHESIS AND CHARACTERIZATION OF HYBRID ORGANIC-INORGANIC THIN FILMS VIA ATOMIC LAYER DEPOSITION FOR MEMS/NEMS

D. Seghete<sup>1</sup>, Y. J. Chang<sup>2</sup>, B. Davidson<sup>2</sup>, V.M. Bright<sup>2</sup>, and S.M. George<sup>1</sup>

<sup>1</sup> Department of Chemistry and Biochemistry, University of Colorado at Boulder

<sup>2</sup> Department of Mechanical Engineering, University of Colorado at Boulder

## ABSTRACT

We report a hybrid atomic layer deposition (ALD) / molecular layer deposition (MLD) approach that produces a new class of hybrid organic-inorganic films. These novel films have very low densities, yet display typical ALD characteristics: controllable linear growth, conformality, low roughness, and uniform composition. The etch behavior of these materials indicates that they are completely removed in acidic solutions. Due to their low density and high carbon content, the new hybrid materials are promising as protective coatings and sacrificial layers in MEMS/NEMS devices.

## INTRODUCTION

Atomic layer deposition (ALD) is a thin film deposition technique that produces accurately controlled, dense inorganic films at low processing temperatures. Al<sub>2</sub>O<sub>3</sub> ALD has been used previously as micro-/ nano-scale structural material [1-3] (Fig. 1) and protective and wear resistant coating in MEMS devices [4, 5].

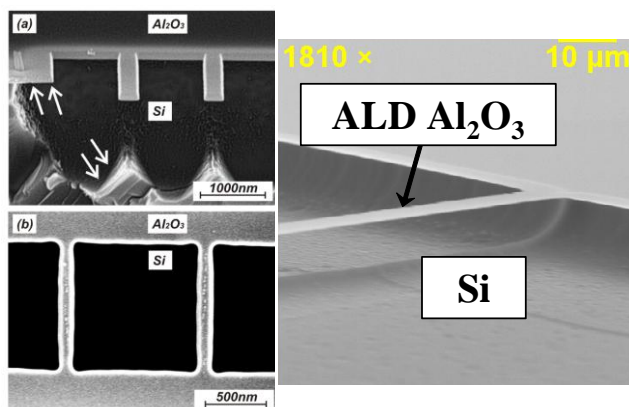


Figure 1. ALD Al<sub>2</sub>O<sub>3</sub> structures grown at either 177°C or 120°C.

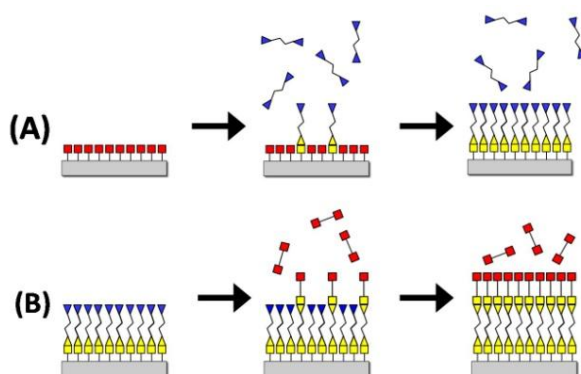


Figure 2. Schematic of the most general binary ALD or MLD system. For ALD the precursors are small inorganic molecules, while in MLD they are larger bifunctional organic species.

Molecular layer deposition (MLD) is a sequential self-limiting surface chemistry process similar to atomic layer deposition (ALD) [6]. As shown in Fig. 2, during MLD growth two bifunctional organic precursors are used to produce a purely organic film [7, 8]. The ability to perform ALD for inorganic materials and MLD for organic materials suggests an extension to a hybrid MLD/ALD approach using organic and inorganic precursors for hybrid organic-inorganic film growth.

Two general classes of hybrid ALD/MLD materials are reported. First is a binary system, where two precursors are used: an inorganic reactant, trimethylaluminum (TMA) and an organic reactant, ethylene glycol (EG). This hybrid system produces polymeric aluminum alkoxides, or alucones [9]. The second class of hybrid systems uses three reactants: an inorganic molecule, TMA, a heterobifunctional organic molecule, ethanolamine (EA), and a cyclic molecule, maleic anhydride (MA) [10]. This new approach requires three steps, and the obtained hybrid organic / inorganic films is referred to as “ABC”. The extension to three-step ABC MLD processes expands the variety of reactants and compositional diversity that can be achieved with MLD.

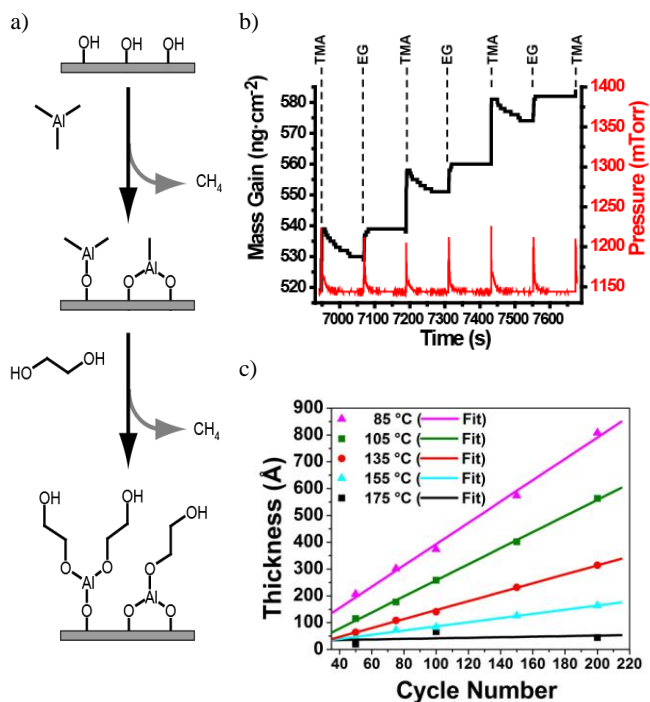


Figure 3. Surface chemistry and growth characteristics for the AB alucone: (a) schematic of the reaction mechanism, (b) quartz crystal microbalance mass gains during TMA and EG exposures, and (c) linear growth vs. number of cycles for various growth temperatures, as measured by x-ray reflectivity

## RESULTS AND DISCUSSION

### Alucone Growth

As illustrated in Figure 3a, the alucone growth is a binary self-limiting process [9]. The initial exposure of the surface to trimethylaluminum leads to a reaction with the -OH hydroxyl species on the surface. At the end of this reaction, when all the hydroxyls are consumed, the surface functionality is changed entirely from hydroxyl to -AlCH<sub>3</sub> methyl species. After a purge of the extra reactants and biproducts, the surface is exposed to ethylene glycol. One hydroxyl end of this molecule reacts with the -AlCH<sub>3</sub> methyl species, producing an aluminum alkoxide on the surface. The other end of the molecule regenerates the hydroxyl terminated surface. After all the -AlCH<sub>3</sub> methyl species have reacted, a purge step removes the extra reactants and products. Since the newly formed surface has the same hydroxyl functionality as the initial surface, the process can be repeated in a cyclic fashion.

Figure 3b displays the mass gains during TMA and EG exposures for steady state growth recorded by the *in situ* quartz crystal microbalance (QCM) at 135 °C [9]. Details about our experimental setup have been given elsewhere [11]. The decrease in mass gain during TMA exposure occurred over a period of 60-90s. This long progressive decrease is much longer than the time required for the TMA to return back to the baseline pressure in other ALD systems. Mass gains with decreases of this type have been observed previously during Al<sub>2</sub>O<sub>3</sub> ALD on polymers [12].

*Ex situ* x-ray reflectivity (XRR) scans confirmed the linear growth of alucone films versus number of cycles over a wide range of temperatures [9]. As shown in Figure 3c, the alucone growth rates were inversely proportional to the growth temperature. Growth rates varied between 4 Å per cycle at 85°C and 1.7 Å per cycle at 135°C. The growth rates measured with XRR agreed very well with *in situ* results from the QCM. Although the growth rates varied inversely proportional to temperature, the density of the films remained relatively constant at 1.5 g/cm<sup>3</sup> [9].

### ABC Growth

The surface chemistries involved in the growth of the new ABC films is schematically shown in Figure 4a [10]. Similar to alucone, TMA is the inorganic species used in the first step to react with the hydroxylated surface and produce -AlCH<sub>3</sub> methyl species. In the second step, ethanolamine, a hetero-bifunctional molecule is used to change the functionality from methyl to amine. In the third step, maleic anhydride is dosed to react with the amine groups in a ring-opening reaction to produce carboxyl groups on the surface. The resulting carboxyls are identical in functionality to the hydroxyls in the first step and allow the three step process to be repeated in a cyclic fashion. The resulting polymeric film is composed of monomer units that contain one Al atom, six C atoms, four O atoms and one N atom.

*In situ* QCM studies showed that the ABC hybrid material grows linearly versus number of cycles, as indicated in Figure 4b [10]. Similar to the alucone mass gain profile, the slow decrease in mass after the TMA dose suggests the low density, and hence polymeric character of the grown ABC film. As measured *ex situ* by XRR, the average growth rate for the ABC film was 23 Å/cycle at 90°C and 11 Å/cycle at 110°C (Figure 4c) [10].

### Physical Properties

XRR scans revealed that the ABC films had very low roughness and very uniform composition. As shown in Figure 5, Bragg peaks are sharp even past 8000 arcseconds. Such high reflectivity at large angles in an XRR experiment suggests minimum scattering at the interfaces. This behavior is obtained for

very smooth films that have a roughness correlated with the underlying layer. For the film in Figure 5, the 560 Å thick film had a roughness of 5 Å, which is similar to the typical roughness of the Si substrates used in the experiment. The good agreement between the experimental scan and the theoretical fit confirms the uniform composition of the obtained ABC film.

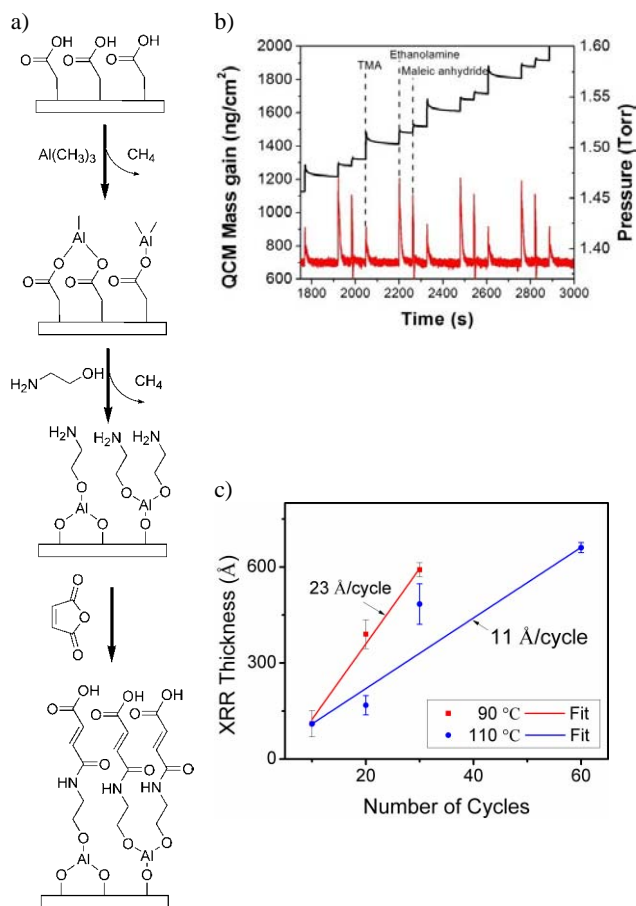


Figure 4. Surface chemistry and growth characteristics for the ABC films: (a) reaction mechanism, (b) QCM mass profile for four cycles, and (c) linear growth vs. number of cycles for different growth temperatures, as measured by XRR

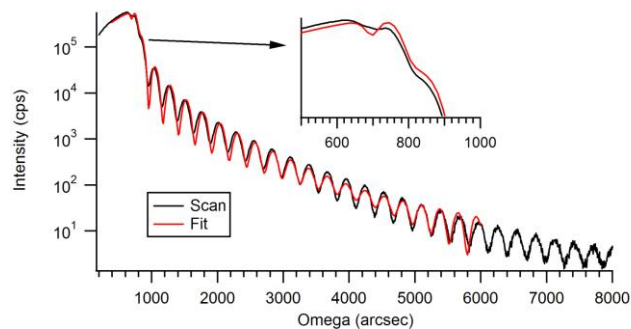


Figure 5. XRR scan of a typical ABC film grown at 90°C. The critical angle (inset) provides the density of the material, 1.6g/cm<sup>3</sup>, while the periodicity of the Bragg peaks confirms the low roughness and uniformity of the ABC films.

Nanoindentation of alucone films measured an average Young's modulus of 18.8 GPa and an average Berkovitch hardness of 1.46 GPa. These values are higher than those of typical polymers (~10 GPa and ~0.5 GPa) but lower than values typical for metals or ceramics (~100 GPa and ~10 GPa).

### Etch Behavior

Both dry-etching and wet-etching behaviors of the ABC film were investigated. Reactive ion etch (RIE) with oxygen was performed on the ABC films. The smooth initial ABC film was transformed into two layers. The bottom layer had the same density as the initial ABC film, while the top layer was denser. The plasma process leads to the formation of a passivation layer that prevent further etching as shown in Table 1.

Table 1. Film structure before and after reactive ion etching with oxygen, as measured by XRR

Material	Thickness (Å)	Density (g/cm <sup>3</sup> )	Roughness (Å)
<b>Initial</b>			
ABC	591.5	1.59	6.2
<b>After O<sub>2</sub> plasma</b>			
ABC	223.0	1.59	50.0
Unknown	289.7	2.08	6.6

As for wet-etching behavior, the ABC film was immersed into different solutions. As shown in Table 2, aprotic solvents did not interact with the ABC material. This result confirmed that the ABC film contains covalently bonded organic molecules. If the organic precursors were simply condensed on the surface, or if the amide linkage would not have been achieved, the aprotic solvents were expected to solvate the hydrophobic organic backbone of the molecule. Consequently, some of the ABC film would have been etched.

Table 2. Wet etch behavior of the ABC films in various solutions

Solvent	Solvent type	Observations after 90 min	Film structure by XRR after 90 min
Toluene	non-polar	no visible change	no change
Acetone	polar aprotic	no visible change	no change
Isopropanol	polar protic	color change formation of spots	thickness decrease film roughening two films formed
Water	polar protic	color change formation of spots	thickness decrease film roughening two films formed
1M NaOH	basic	formation of a spotted white film	too rough to measure
1M HCl	acidic	complete removal of polymer film	bare Si substrate

Both protic solvents had similar effects on the ABC film. The resulting two layer structure with the formation of a denser layer at the top is similar to the result obtained after the dry etch process. The interaction with the proton-containing solutions is in agreement with the observation that the alucone MLD films were susceptible to degradation upon exposure to water. The exact mechanism of this proton-mediated process is not yet understood.

While the 1M basic solution led to the formation of a white precipitate on the sample, the 1M acidic solution was successful in etching the ABC film. This contrasting behavior can be explained by the chemical composition of the ABC film. The existing amide linkage could react with the base solution to form carboxylic acid salts that are insoluble. In contrast, the ammonium chloride salt formed in the reaction with the acid solution is soluble, leading to a complete etch of the ABC film. The acid etching is promising for using the ABC layer as a sacrificial material in MEMS/NEMS structures.

### Potential Applications

Multilayers that combine alternate soft/flexible layers with hard/brittle layers have extraordinary mechanical properties. These multilayer structures are exploited in one of the strongest structures in nature, the nacreous layer of the mollusk shell [13, 14]. The unique organic-inorganic structure of nacre produces approximately two times the mechanical strength and approximately one thousand times the fracture toughness of its inorganic material [15]. Given the contrast between Young's modulus values of the alucone and ABC films and other typical ALD systems (e.g. alumina, tungsten), alternating multilayer structures could be fabricated to imitate the nacreous shell structure (Figure 6). Such high toughness structures could be used to coat conformally MEMS devices and improve their wear resistance.

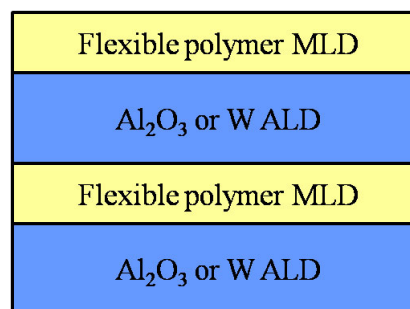


Figure 6. High toughness hard/soft multilayer to be used as wear resistant coating for MEMS/NEMS devices.

Ultra-thin film micro-/nano-scale resonators are another promising application of the novel hybrid materials. Nano-resonators have been used for precise mass detection [16] or high frequency applications [17]. The availability of ALD materials with contrasting mechanical properties allows for the design of composite materials with desired mechanical properties for MEMS/NEMS devices. The composite mechanical properties of a multilayer structure could be tuned by varying the ratio of organic to inorganic material. This control over the mechanical properties could be used to create a resonator with a tunable resonant frequency.

Alucone and ABC films can also be used as sacrificial spacer layers for MEMS/NEMS structures. Very thin hybrid organic/inorganic film can be grown at low temperatures with high conformity and low roughness. Embedding these films as sacrificial layers in the manufacturing process can produce MEMS devices with Ångstrom-level precision vertical gaps after release.

A layer of 80 nm thick MLD alucone was first deposited on silicon substrates at 80°C. 2 nm Al<sub>2</sub>O<sub>3</sub> and 20 nm W were deposited on top of the alucone layer at 120°C. After patterning AZP photoresist on the ALD W layer, tungsten etchant and 0.05% HF were used to etch the ALD W and ALD alumina, respectively. The patterned AZP photoresist was then removed by acetone.

Diluted NaOH was used to remove the MLD alucone under W ALD structure. The sample was then immersed in methanol and dried in a CO<sub>2</sub> critical point dryer. The released structure is shown in Figure 7. The upright W ALD structure is due to the mechanical stress within the W ALD thin film. This residual stress can be further tuned by varying the growth temperature and film thickness of the W ALD layer.

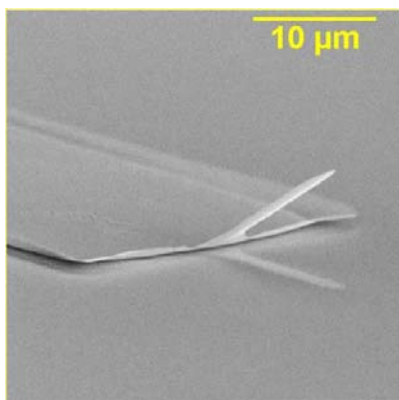


Figure 7. ALD W cantilever released via wet-etch from 80nm ALD/MLD alucone layer.

## CONCLUSIONS

We demonstrated the growth of novel hybrid organic-inorganic films using ALD/MLD techniques. In situ characterization showed the self-limiting and linear growth behaviors typical for ALD systems. The physical properties of these materials suggest a polymeric character. Due to their high carbon content and since they etch in acidic solutions, these new materials are suitable as sacrificial layers in MEMS devices. In addition, the reported films could be used as protective layers for MEMS applications when embedded in periodic organic/inorganic structures with exceptional mechanical properties.

## ACKNOWLEDGEMENTS

This research was supported by DARPA NEMS (SPAWAR Contract No.: N66001-07-1-2033), DARPA Award # HR0011-06-1-0048, the DARPA Focus Center for Integrated Micro/NanoMechanical Transducers (iMINT Center) at the University of Colorado, Boulder and the Air Force Office of Scientific Research.

## REFERENCES

- [1] Y. J. Chang, K. Cobry, and V. M. Bright, "Atomic Layer Deposited Alumina for Micromachined Resonators," *21st IEEE International Conference on Micro Electro Mechanical Systems (MEMS 2008), Tucson, USA, Jan. 13-17, 2008*, pp. 387-390.
- [2] M. K. Tripp, C. F. Herrmann, S. M. George, and V. M. Bright, "Ultra-thin multilayer nanomembranes for short wavelength deformable optics," *17th IEEE International Conference on Micro Electro Mechanical Systems. Maastricht MEMS 2004 Technical Digest*. pp. 77-80.
- [3] M. K. Tripp, C. Stampfer, D. C. Miller, T. Helbling, C. F. Hermann, C. Hierold, K. Gall, S. M. George, and V. M. Bright, "The mechanical properties of atomic layer deposited alumina for use in micro- and nano-electromechanical systems," *Sensors and Actuators A - Physical*, vol. 130, pp. 419-429, Aug, 2006.

- [4] N. D. Hoivik, J. W. Elam, R. J. Linderman, V. M. Bright, S. M. George, and Y. C. Lee, "Atomic layer deposited protective coatings for micro-electromechanical systems," *Sensors and Actuators A - Physical*, vol. A103, no. 1-2, pp. 100-8, 2003.
- [5] T. M. Mayer, J. W. Elam, S. M. George, P. G. Kotula, and R. S. Goeke, "Atomic-layer deposition of wear-resistant coatings for microelectromechanical devices," *Applied Physics Letters*, vol. 82, no. 17, pp. 2883-2885, 2003.
- [6] S. M. George, A. W. Ott, and J. W. Klaus, "Surface chemistry for atomic layer growth," *Journal of Physical Chemistry*, vol. 100, no. 31, pp. 13121-13131, Aug, 1996.
- [7] Y. Du, and S. M. George, "Molecular layer deposition of nylon 66 films examined using in situ FTIR spectroscopy," *Journal of Physical Chemistry C*, vol. 111, no. 24, pp. 8509-8517, Jun, 2007.
- [8] N. M. Adamczyk, A. A. Dameron, and S. M. George, "Molecular Layer Deposition of Poly(p-phenylene terephthalamide) Films Using Terephthaloyl Chloride and p-Phenylenediamine," in press, *Langmuir*, 2008.
- [9] A. A. Dameron, D. Seghete, B. B. Burton, S. D. Davidson, A. S. Cavanagh, J. A. Bertrand, and S. M. George, "Molecular Layer Deposition of Alucone Polymer Films Using Trimethylaluminum and Ethylene Glycol," *Chemistry of Materials*, in press, 2008.
- [10] B. Yoon, D. Seghete, and S. M. George, to be published, 2008.
- [11] J. W. Elam, M. D. Groner, and S. M. George, "Viscous flow reactor with quartz crystal microbalance for thin film growth by atomic layer deposition," *Review of Scientific Instruments*, vol. 73, no. 8, pp. 2981-2987, Aug, 2002.
- [12] C. A. Wilson, R. K. Grubbs, and S. M. George, "Nucleation and growth during Al<sub>2</sub>O<sub>3</sub> atomic layer deposition on polymers," *Chemistry of Materials*, vol. 17, no. 23, pp. 5625-5634, Nov, 2005.
- [13] F. Barthelat, H. Tang, P. D. Zavattieri, C. M. Li, and H. D. Espinosa, "On the mechanics of mother-of-pearl: A key feature in the material hierarchical structure," *Journal of the Mechanics and Physics of Solids*, vol. 55, no. 2, pp. 306-337, Feb, 2007.
- [14] G. Mayer, "Rigid biological systems as models for synthetic composites," *Science*, vol. 310, no. 5751, pp. 1144-1147, Nov, 2005.
- [15] B. Yeom, S. Kim, J. H. Cho, J. Hahn, and K. Char, "Effect of interfacial adhesion on the mechanical properties of organic/inorganic hybrid nanolaminates," *Journal of Adhesion*, vol. 82, no. 5, pp. 447-468, May, 2006.
- [16] Z. J. Davis, G. Abadal, O. Kuhn, O. Hansen, F. Grey, and A. Boisen, "Fabrication and characterization of nanoresonating devices for mass detection," *Journal of Vacuum Science & Technology B*, vol. 18, no. 2, pp. 612-616, Mar-Apr, 2000.
- [17] M. Li, H. X. Tang, and M. L. Roukes, "Ultra-sensitive NEMS-based cantilevers for sensing, scanned probe and very high-frequency applications," *Nature Nanotechnology*, vol. 2, no. 2, pp. 114-120, Feb, 2007.

# A MEMS PHOSPHONATE SENSOR

C.N. Monty<sup>1</sup>, I. Oh<sup>1</sup>, M.A. Shannon<sup>2</sup>, R.I. Masel<sup>1</sup>

<sup>1</sup> Department of Chemical & Biomolecular Engineering, University of Illinois, Urbana, IL 61801 USA

<sup>2</sup> Department of Mechanical Science & Engineering, University of Illinois, Urbana, IL 61801 USA

## ABSTRACT

The objective of this paper is to report the modeling and optimization of a new MEMS-based phosphonate sensor that utilizes a porous membrane between a gas and a liquid stream to allow operation at low liquid and high gas flow rates. Previous work from our laboratory has demonstrated that phosphonate molecules can be detected with such a device, but the sensitivity was insufficient for certain applications (e.g. detection of pesticides in foodstuffs). In this paper COMSOL simulations and design of experiments were used to optimize the device. We find that both the simulation and the experiment show that i) the size and hydrophilicity of the pores in the membranes and ii) the liquid channel height make the most difference to the sensor response. For example, we calculate that the response increases by 80 mV/mm as the channel depth decreases and the experiments show a 296 mV/mm change for decreased channel depths. Also, by optimizing the geometry the sensitivity of the device could be enhanced. The optimized device can detect  $10^9$  molecules with good signal to noise.

## INTRODUCTION

A multiphase microchemical system, by definition, contains processes occurring at an interface of two or more phases (gas, liquid, solid)[1]. The design and fabrication of a gas-liquid interface is especially difficult because, unlike solid-gas or solid-liquid interfaces, both media are fluidic and hard to control. There are two main strategies for the fabrication of micro-channel gas-liquid interfaces: 1) gas-liquid segmented flow [2-8] and 2) gas-liquid parallel flow [9-12]. Gas-liquid segmented flow was used by Jensen to take advantage of the shortened liquid diffusion distances in order to resolve fast transient responses in cell signaling networks [4]. Previously published research reported by Kobayashi et al used a gas-liquid parallel flow regime to perform hydrogenation of benzalacetone on a palladium catalyst [10]. In order to create gas-liquid parallel flow, Kobayashi *et al* functionalized the channel walls into hydrophilic and hydrophobic regions. The liquid then flows near the hydrophilic walls, while the gas stays in the hydrophobic regions.

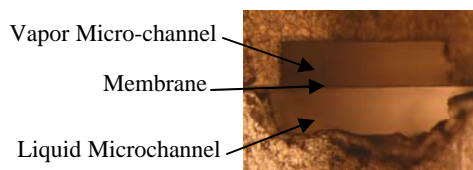
Recently we reported on a sensor that utilizes a micro-scale gas-liquid interface to create a multiphase micro-reactor for selective vapor detection [13, 14]. Our previous work studied the use of liquid acetylcholinesterase biochemistry and oxime chemistry to selectively detect trace amounts of phosphonate vapor. From these micro-reactors it was determined that the mass-transport of vapor molecules across the gas-liquid interface is rapid enough that the micro-reactor design can be used as a viable, rapid-response phosphonate detector. The results also show that specific liquid chemistry provides the sensitivity and selectivity needed to lower the detection limit and detection time when compared with previous methods. Before such a sensor can be developed into a reproducible device, however, there is a need to study the effect of various geometric reactor parameters on response and to more accurately understand the underlying transport phenomena in the system.

## EXPERIMENTAL METHODS

### Fabrication of Micro-channel Sensor

The assembly of the micro-channel sensor involves three steps: 1) fabrication of micro-channels, 2) deposition of the electrode onto a nanoporous membrane, and 3) assembly of the gas and liquid micro-channels and the nanoporous membrane. The micro-channels were machined into a small polycarbonate block. To coat the membrane with an electrode material, track-etch polycarbonate membranes of various pore size (thickness 10 $\mu$ m; SPI) are sputtered with a 40-nm thick layer of gold on the side of the liquid micro-channel. Some track-etch membranes are purchased with a hydrophilic poly(vinyl pyrrolidone) (PVP) coating. The gas micro-channel is made to overlap the liquid micro-channel. The membrane is sandwiched between the two polycarbonate micro-channels and the assembly is clamped using 5 screws. A picture of the final assembly is found in Figure 1A.

A)



B)

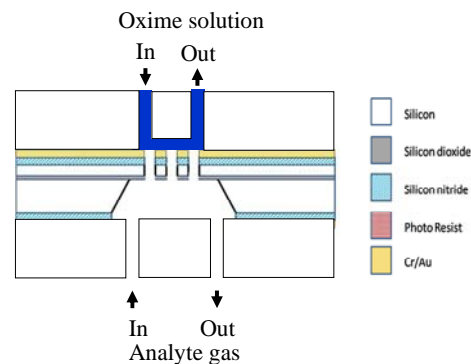


Figure 1: A) Cross-sectional view of the phosphonate sensor. The upper channel is the liquid micro-channel (0.25 mm wide by 0.1 mm deep). The lower channel is the vapor micro-channel (0.25 mm wide by 0.1 mm deep). The two micro-channels are separated by a nanoporous polycarbonate membrane (0.006 mm thick). The lower micro-channel was distorted during cutting. B) Schematic of silicon design. Oxime solution enters the liquid microchannel and is separated from the gas by a hydrophobic membrane.

Figure 1B shows a schematic of a Si based phosphonate sensor. The sensor is composed of three parts: Si/SiO<sub>2</sub> pore layer, liquid microchannel, and gas microchannel. The middle layer is the 6x6 circular straight Si pore with about 100 microns diameter. An SOI (silicon on insulator) wafer is etched using KOH wet etch and ICP-DRIE process leaving a membrane. After cleaning in a piranha solution, the Si pore surface is made hydrophobic with FDTs (perfluorodecyltrichlorosilane) in an MVD (molecular vapor

deposition) process. The Si pore is filled with photoresist and sputtered with 40-nm gold layer so that only the top surface of the Si pore is coated with gold. After removing the photoresist with organic solvent, liquid and gas microchannels are attached to the Si pore layer.

### Testing of Micro-channel Sensor

The testing set-up of the oxime sensor is taken from our previous work by Oh et al [14]. The oxime solution is passed along the liquid micro-channel using a manually-operated syringe. During electrochemical measurements, the liquid in the micro-channel remains stagnant. The vapor sample is introduced into the gas micro-channel using a syringe pump containing the diluted chemical sample at the flow rate of 1 mL/min. The open-circuit potential between the working electrode and the reference electrode is measured as the output signal from the micro-channel sensor.

## NUMERICAL SIMULATION

A numerical simulation of cyanide concentration in the liquid micro-channel and phosphonate concentration in the vapor micro-channel was performed over a range of channel geometry, membrane pore size, and pore hydrophilicity using COMSOL Multiphysics 3.3 with the Chemical Engineering Module. The vapor and liquid micro-channels can be considered two-dimensional and possessing fluidics which are incompressible and low-Reynolds number. There is no flow parallel to the membrane in the liquid micro-channel and only diffusive transport perpendicular to the membrane is considered in the liquid micro-channel and through the membrane itself.

The constants used in the simulation are as follows. Air and liquid diffusion coefficients of  $D_{\text{gas}} = 0.01 \text{ cm}^2/\text{sec}$  and  $D_{\text{liquid}} = 1 \times 10^{-5} \text{ cm}^2/\text{sec}$  were used [15]. The diffusivity of phosphonate vapor through a hydrophobic membrane,  $D_m$ , was estimated using a model for gas diffusion in porous media [16]:

$$D_m = D_{\text{gas}} \varepsilon^{\frac{4}{3}} \quad (1)$$

where  $\varepsilon$  is the porosity of the nanoporous membrane. Porosity varies with the size of the pore in the nanoporous membrane.

## RESULTS AND DISCUSSION

### Numerical Simulation

Figure 2 shows simulations of how the phosphate concentration should vary perpendicularly to the membrane at a point 0.125 cm from the leading edge of a 0.0075 cm deep 0.25 cm long microchannel covered by a 0.0006 cm thick membrane with 50 nm hydrophobic pores. In this simulation, the liquid micro-channel contains 10 mM oxime solution and 1 cm<sup>3</sup>/min of gas containing 100 ppb of analyte flows in the vapor micro-channel. Notice that the analyte concentration is almost constant in the gas phase then decays exponentially into the liquid. These results suggest that most of the mass transfer resistance is in the liquid side of the membrane, since diffusivities are so much higher in the gas phase than in the liquid.

Figure 3 shows simulation results for the effect of pore size in the nanoporous membrane on sensor response for a micro-channel 0.25 mm wide, 0.1 mm deep, and 5 mm long with hydrophobic pores. Notice as pore size increases from 10 nm to 50 nm the sensor response increases in the form of cyanide ion concentration. These results show that mass-transport across the membrane increases with larger pores due to an increase in open surface area and therefore porosity of the nanoporous membrane. The larger open surface area increases the gas-liquid interface and

allows more phosphate molecules to cross into the liquid microchannel.

Figure 4 shows the effect of channel depth on sensor response from the COMSOL simulation for a micro-channel 0.25 mm wide and 1 cm long with 50 nm hydrophobic pores. Notice as the channel depth decreases from 0.2 to 0.05 mm the sensor response increases in the form of increased cyanide concentration. The increase in response may be due to a build up of cyanide ions or phosphate molecules near the gas-liquid interface caused by a smaller amount of liquid in reduced channel depths.

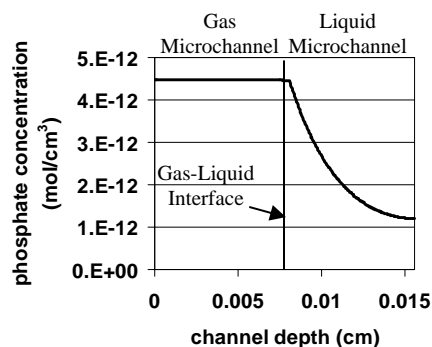


Figure 2: Simulation results for concentration profile of phosphonate concentration along channel depth

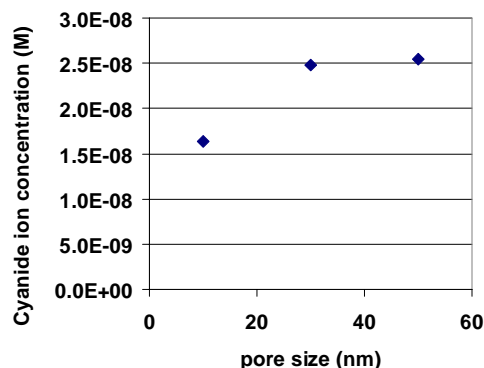


Figure 3: Simulation results for the effect of pore size of the nanoporous membrane on sensor response. The micro-channel dimensions and analyte concentration were the same as the experimental set-up. The simulation results also show that with an increase in pore size from 10 nm to 50 nm there is an increase in sensor response in the form of an increase in cyanide ion concentration. These results indicate that the mass transfer through the pore is faster with larger pores, leading to a faster response.

### Experimental Results

After study of the statistical analysis of the COMSOL simulation, a design of experiments was completed. From the simulation results it was noted that varying channel length and channel width did not have a large effect on sensor response while varying channel depth, pore size, and pore hydrophilicity greatly affected response (channel width was varied in our two-dimensional simulation by varying the superficial velocity). Testing of the oxime microreactor focused on changing channel geometry, pore size, and membrane coatings to determine the effect of each on sensor response.

Figure 5 shows experimental results for the effect of the pore size in the nanoporous membrane on sensor response for a liquid microchannel 0.25 mm wide, 0.10 mm deep. Notice that as the pore size increases from 10 nm to 50 nm the response of the sensor also increases from 11 mV to 60 mV (Pore sizes above 50 nm could not be tested due to flooding of the oxime solution into the vapor micro-channel). These results show that mass-transport across the membrane increases with larger pores due to an increase in open surface area and therefore porosity of the nanoporous membrane. The larger open surface area increases the gas-liquid interface and allows more phosphate molecules to cross into the liquid microchannel.

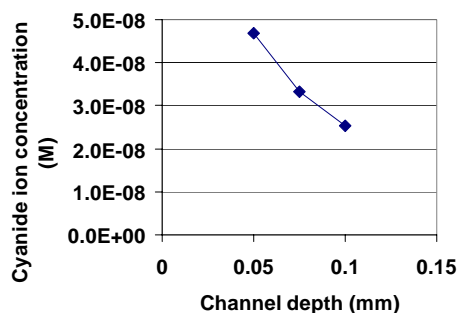


Figure 4: Simulation results for the effect of channel depth on cyanide ion concentration for a micro-channel that is 0.25 mm wide and 1 cm long. The liquid micro-channel contains 10 mM oxime solution in borate buffer (pH=10) with 100 ppb analyte gas at a flow rate of 1 cm<sup>3</sup>/min in the vapor micro-channel. As the channel depth decreases from 0.05 mm to 0.1 mm the cyanide ion concentration increases. This result may be due to an increased build-up of cyanide ions at the electrode surface for smaller channel depths.

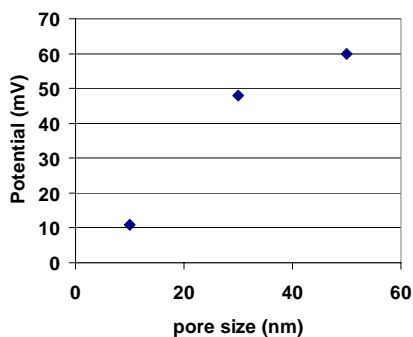


Figure 5: Experimental results for the effect of pore size of the nanoporous membrane on sensor response. The liquid micro-channel (250 μm wide x 100 μm deep x 0.5 cm long) contains 10 mM oxime solution in borate buffer (pH=10) with 100 ppb analyte gas at a flow rate of 1 cm<sup>3</sup>/min in the vapor micro-channel. As the pore size increases from 10 nm to 50 nm the response of the sensor also increases from 11 mV to 60 mV.

The effect of channel depth on sensor response is shown in Figure 6. Notice that as the channel depth decreases from 0.05 mm to 0.2 mm the sensor response increases, for all channel widths. These results may be due to an increased build-up of cyanide ions or phosphate molecules at the electrode surface for smaller channel depths.

The effect of vapor residence time on the microreactor was also studied. Figure 7 shows that a longer residence time does not affect sensor response experimentally.

### Comparison of Simulation and Experiment

A comparison of the statistical analysis of numerical simulation and experimental data is shown in Table 1. Notice in both experimental results and numerical simulations, varying the channel length and channel width had little to no effect on sensor response. Experiments show that the effect of channel width is only seen at widths less than 0.025 mm and at small channel depths. This result may be caused by entrance effects into the gas micro-channel that are not accounted for in our two-dimensional simulation. Conversely, channel depth has a large effect on sensor response. These results show that one rate-limiting step for phosphonate diffusion is perpendicular to the nanoporous membrane, and depth of the micro-channel is an important factor in sensor design.

Table 1 also shows that residence time also has little effect on the response of the sensor. This trend is due to the saturation of the gas-liquid interface with phosphonate molecules. Most importantly, this trend shows that a rate determining step in phosphonate molecule transport occurs at the gas-liquid interface and the pore size and pore hydrophilicity of the nanoporous membrane are therefore extremely important.

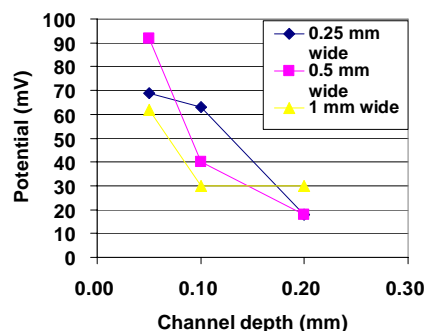


Figure 6: Experimental results for the effect of channel depth on sensor response. The liquid micro-channel is 0.5 cm long and the depth and width of the channel are varied (pore size = 50 nm). The liquid micro-channel contains 10 mM oxime solution in borate buffer (pH=10) with 100 ppb analyte gas at a flow rate of 1 cm<sup>3</sup>/min in the vapor micro-channel. As the channel depth decreases from 0.05 mm to 0.2 mm the sensor response increases, for all channel widths. This result may be due to an increased build-up of cyanide ions at the electrode surface for smaller channel depths.

Accordingly, Table 1 shows that increasing pore size has the largest affect on sensor response. This result shows that increasing the surface area of the gas-liquid interface has a large impact on sensor response. Also, in our simulation results, hydrophobic pores showed higher sensor response than hydrophilic pores due to wetting of the pores with oxime solution. In our experimental analysis, however, we were not able to test hydrophilic pores due to flooding of the gas micro-channel. This is most likely caused by the slight hydrophilic nature of the polycarbonate membrane and from contact angle measurements PVP-free polycarbonate membranes sputtered with gold still wick the pores with oxime solution and provide a lower sensor response. Using a more hydrophobic membrane should prevent wetting of the membrane with oxime solution and further improve sensor response.

## CONCLUSIONS

In this study a numerical simulation of a multi-phase microreactor for use as a phosphonate sensor was created. The simulation was used to design a set of experimental conditions, in order to further optimize the microreactor. The experimental results were then compared to the numerical simulation to further understand the underlying transport phenomenon. From the results, a microreactor with a 0.05 mm channel depth, 0.25 mm channel width, and 50 nm PVP-free nanoporous membranes provided the best sensor response. After the optimization of the sensor geometry the detection limit of our sensor has decreased from  $10^{11}$  to  $10^9$  phosphonate molecules.

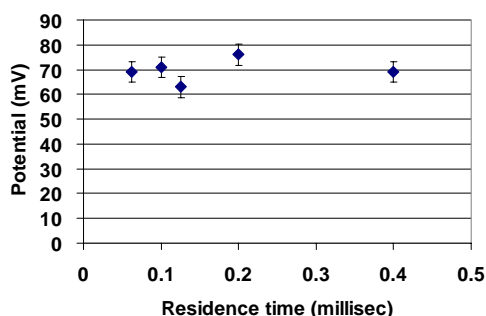


Figure 7: Experimental results for the effect of vapor residence time on sensor response. The liquid micro-channel contains 10  $\mu$ M oxime solution in borate buffer (pH=10) with 100 ppb phosphonate analyte gas at a flow rate of 1  $\text{cm}^3/\text{min}$  in the vapor micro-channel. Vapor residence time has very little effect on the sensor response with an average potential response of 73 mV and a standard deviation of 8.5 mV. This trend is also found from simulation results.

Both experimental results and numerical simulation show that a decrease in channel depth and an increase in pore size allow for faster mass-transport and faster sensor response. Comparison of experimental results and numerical simulations also shows that the PVP-free membranes treated with gold are wetted with oxime solution and preventing the fastest possible mass-transport of vapor molecules across the nanoporous membrane.

Table 1: Comparison of experimental data to simulation results for varying geometric reactor parameters.

Geometric Parameter	Range studied	Calculated slope	Measured Slope
Residence time	0.05 to 0.5 msec	0	$0.004 \pm 0.26$ mV/ms
Channel length	1 mm to 8 mm	0	$0.5 \pm 2.0$ mV/mm
Channel width	0.25 to 1 mm	0	$18 \pm 52$ mV/mm
Channel depth	0.05 to 0.25 mm	-80 mV/mm	$-296 \pm 90$ mV/mm
Pore size	10 to 100 nm	$125 \pm 38$ mV/ $\mu$ m	$1225 \pm 400$ mV/ $\mu$ m
Pore hydrophilicity	hydrophilic to hydrophobic	38 mV/change	Hydrophilic membrane leaked

The results from this study show that future work should be done to fabricate the microreactor in silicon wafers, such as in Figure 1B. For polycarbonate machining, 0.05 mm is the lower limit of channel depth. However, by moving the sensor into a silicon wafer we can create smaller channels and may be able to

further improve sensor response. Also, by creating a porous membrane with a silicon wafer we can create a more hydrophobic membrane with larger pores.

## ACKNOWLEDGEMENTS

This work was supported by the Defense Advanced Research Projects Agency (DARPA) under U.S. Air Force grant FA8650-04-1-7121. Any opinions, findings, and conclusions or recommendations expressed in this manuscript are those of the authors and do not necessarily reflect the views of the Defense Advanced Research Projects Agency, or the U.S. Air Force.

## REFERENCES

- [1] Gunther, A. and K.F. Jensen, *Multiphase microfluidics: from flow characteristics to chemical and materials synthesis*. Lab on a Chip, 2006. **6**(12): p. 1487-1503.
- [2] Chung, P.M.Y. and M. Kawaji, *The effect of channel diameter on adiabatic two-phase flow characteristics in microchannels*. International Journal of Multiphase Flow, 2004. **30**(7-8): p. 735-761.
- [3] Gunther, A., et al., *Micromixing of miscible liquids in segmented gas-liquid flow*. Langmuir, 2005. **21**(4): p. 1547-1555.
- [4] El-Ali, J., et al., *Cell stimulus and lysis in a microfluidic device with segmented gas-liquid flow*. Analytical Chemistry, 2005. **77**(11): p. 3629-3636.
- [5] Gunther, A., et al., *Transport and reaction in microscale segmented gas-liquid flow*. Lab on a Chip, 2004. **4**(4): p. 278-286.
- [6] de Mas, N., et al., *Scaled-out multilayer gas-liquid microreactor with integrated velocimetry sensors*. Industrial & Engineering Chemistry Research, 2005. **44**(24): p. 8997-9013.
- [7] Xu, J.H., et al., *Controllable gas-liquid phase flow patterns and monodisperse microbubbles in a microfluidic T-junction device*. Applied Physics Letters, 2006. **88**(13).
- [8] Yen, B.K.H., et al., *A microfabricated gas-liquid segmented flow reactor for high-temperature synthesis: The case of CdSe quantum dots*. Angewandte Chemie-International Edition, 2005. **44**(34): p. 5447-5451.
- [9] Zheng, B. and R.F. Ismagilov, *A microfluidic approach for screening submicroliter volumes against multiple reagents by using preformed arrays of nanoliter plugs in a three-phase liquid/liquid/gas flow*. Angewandte Chemie-International Edition, 2005. **44**(17): p. 2520-2523.
- [10] Kobayashi, J., et al., *A microfluidic device for conducting gas-liquid-solid hydrogenation reactions*. Science, 2004. **304**(5675): p. 1305-1308.
- [11] Zhao, B., J.S. Moore, and D.J. Beebe, *Surface-directed liquid flow inside microchannels*. Science, 2001. **291**(5506): p. 1023-1026.
- [12] Zhao, B., J.S. Moore, and D.J. Beebe, *Principles of surface-directed liquid flow in microfluidic channels*. Analytical Chemistry, 2002. **74**(16): p. 4259-4268.
- [13] Chelsea N. Monty, I.O. and R.I. Masel, *Enzyme-based Electrochemical Multiphase Microreactor for Detection of Trace Toxic Vapors*. IEEE Sensors, 2008.
- [14] Ilwhan Oh, C.N.M., Richard I Masel, *Electrochemical Multiphase Microreactor as Fast, Selective, and Portable Chemical Sensor of Trace Toxic Vapors*. IEEE SENSORS, 2008.
- [15] Welty, W., Wilson, Rorrer, *Fundamentals of Momentum, Heat, and Mass Transfer*. Fourth Edition ed. 2001, New York: John Wiley & Sons.
- [16] Millington, R.J., *"Gas Diffusion In Porous Media"*. Science, 1959. **130**(3367): p. 100-102.

# A MICRO-PRECONCENTRATOR/FOCUSER FOR A MICRO-GAS CHROMATOGRAPH: DEVICE AND MATERIALS CHARACTERIZATION

R. A. Veeneman<sup>1</sup> and E. T. Zellers<sup>1,2\*</sup>

Center for Wireless Integrated Microsystems, Departments of <sup>1</sup>Chemistry and <sup>2</sup>Environmental Health Sciences, University of Michigan, Ann Arbor, Michigan, USA

## ABSTRACT

The modeling and characterization of a microfabricated adsorbent preconcentrator/focuser ( $\mu$ PCF), designed for use in a micro-scale gas chromatograph ( $\mu$ GC) for the analysis of mixtures of vapors at parts-per-billion concentrations, are described. Classical models of vapor adsorption capacity and breakthrough volume are used to relate material properties and operating parameters to device performance. Adsorption studies on graphitized carbon adsorbents revealed two distinct adsorption-energy regimes that dictate the capacity for vapor adsorption over the relevant concentration range. Breakthrough volumes measured for two test vapors with the  $\mu$ PCF and a reference PCF of conventional design were in agreement and were used to define the upper limits on the allowable flow rate through the microfabricated device. The prediction of  $\mu$ PCF breakthrough volumes appears feasible.

## INTRODUCTION

It has been nearly 30 years since the first report of a microfabricated gas chromatograph ( $\mu$ GC) [1]. Since then numerous efforts have been mounted to develop low-power  $\mu$ GCs that are capable of capturing, separating, and detecting the components of mixtures of gases and vapors [2-6]. Most potential applications of such microsystems require detection of target compounds in the parts-per-billion or parts-per-trillion concentration range. Since most detector technologies are not sensitive enough to achieve limits of detection in this range, it is necessary to employ a preconcentration step prior to separation and detection.

The research described here is part of a larger effort within the Center for Wireless Integrated MicroSystems (WIMS) to develop a  $\mu$ GC for comprehensive analysis of complex mixtures of volatile organic compounds (VOC) of arbitrary composition [5-6]. Applications in indoor air quality monitoring, human exposure assessment, homeland security, and biomedical diagnostics are envisioned.

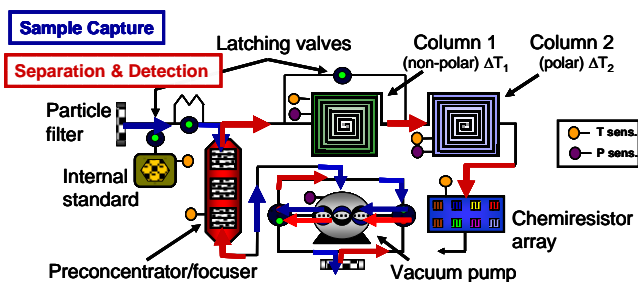


Figure 1. Block diagram of the WIMS  $\mu$ GC with arrows showing flow paths during sampling and analysis.

Figure 1 shows a block diagram of the WIMS  $\mu$ GC. The multi-stage  $\mu$ PCF is an integral component of the system, whose evolving design and associated fabrication techniques have been described elsewhere [7-9]. The  $\mu$ PCF is packed with different adsorbent materials to achieve quantitative trapping and efficient thermal desorption of VOCs spanning a wide range of structures

and volatilities (Figure 2). Operated at ambient temperature during sample collection, it is resistively heated to desorb trapped vapors for subsequent separation and detection by downstream components.

Although a number of other miniaturized or microfabricated preconcentrator devices have been reported [10-15], few consider explicitly the fundamental thermodynamic or kinetic factors affecting device design and operation [7, 14-15]. This study explores the application of some classical models of adsorption and breakthrough volume to the design and operation of the WIMS  $\mu$ PCF, and reveals some heretofore unrecognized factors affecting performance. Adsorption isotherms were collected for a series of vapors on two of the graphitized carbon adsorbents used in the  $\mu$ PCF, and breakthrough tests were conducted with a single adsorbent loaded into the  $\mu$ PCF as well as in a more conventional reference PCF. Results are considered in the context of the Dubinin-Radushkevich (D-R) and Wheeler Models for predicting the performance of the  $\mu$ PCF.

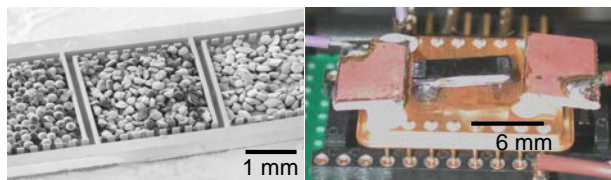


Figure 2. The WIMS  $\mu$ PCF filled with adsorbent (left) and a finished device in its testing package (right).

## THEORY

Among the thermodynamic models used to describe the equilibrium adsorption of vapors on porous and non-porous solids, the D-R model is perhaps the most widely applicable [16-18]. It is presented in its so-called linearized form in Eq. 1:

$$\ln W_e = \ln V_o \rho_L - \left[ \left( \frac{RT}{\beta E_o} \right) \ln \left( \frac{p_{sat}}{p} \right) \right]^2 \quad (1)$$

where  $W_e$  is the adsorption capacity (g/g),  $V_o$  is the micropore volume (cc/g),  $\rho_L$  is the analyte density (g/cc),  $R$  is the ideal gas constant,  $T$  is temperature (K),  $\beta$  is an affinity coefficient,  $E_o$  is the adsorption energy (kcal/mole) and  $p_{sat}/p$  is the inverse of the vapor concentration expressed as a fraction of its saturation vapor pressure,  $p_{sat}$ .

The D-R isotherm equation relates the adsorbed mass of vapor per unit mass of adsorbent to essential properties of the vapor and the adsorbent. A plot of uptake mass versus  $(\ln p_{sat}/p)^2$  yields  $E_o$  and  $V_o$  from the slope and y-intercept, respectively. Interestingly, most reports on the application of the D-R model to VOC adsorption have been restricted to vapor concentrations ranging from high-parts-per-million to saturation [16-18].

The Wheeler model has been used to describe the breakthrough of VOCs in packed adsorbent beds as a function of several key design and operating variables [19-20]. The most

common form of the equation is given in Eq. 2:

$$V_b = \frac{W_e W_B}{C_0} \left[ 1 - \frac{1}{k_v \tau} \ln \left( \frac{C_0}{C_x} \right) \right] \quad (2)$$

where  $V_b$  is the breakthrough volume (L) evaluated at some predetermined fraction of the challenge concentration,  $W_e$  the equilibrium adsorption capacity (g/g),  $W_B$  is bed mass (g),  $C_0$  is the challenge concentration (g/L),  $C_x$  is the concentration downstream from the bed (g/L),  $k_v$  is the kinetic rate coefficient ( $\text{min}^{-1}$ ), and  $\tau$  is the bed residence time (min), which is proportional to the volumetric flow rate,  $Q$  (L/min). The so-called 'critical bed residence time' is reached when the flow rate is such that  $V_b = 0$ .

Most applications of the Wheeler model have been related to predicting the performance of respirator cartridges [20], which contain very large beds and are challenged with high VOC concentrations. Its application to characterizing micro-scale preconcentrators is less common [7, 14-15].

## EXPERIMENTAL

### Devices and Materials

The  $\mu$ PCF consists of a series of three 450- $\mu\text{m}$ -deep Si cavities fabricated using DRIE and sealed using wafer-level Au-Au thermo-compression bonding. Backside Pt RTDs are integrated to monitor heating rates. Etched holes in the sealing plate accept deactivated fused-silica capillaries for connecting to upstream and downstream components. The volumes of the cavities are, in order, 4.41, 2.54, and 1.63  $\mu\text{L}$ , and were varied to accept different masses of three different adsorbent materials estimated to provide sufficient capacity for generalized use with the WIMS  $\mu\text{GC}$ . Overall device dimensions are 11mm  $\times$  4mm  $\times$  1mm.

A reference preconcentrator (PCF<sub>ref</sub>) of conventional design was constructed by packing a 2.5-mm section of stainless steel tubing (1.35 mm i.d.) with a quantity of adsorbent material similar to that contained in the  $\mu$ PCF and held in place by plugs of stainless steel mesh and silanized glass wool.

The two adsorbent materials studied here are the graphitized carbons Carbopack B (C-B, specific surface area = 100  $\text{m}^2/\text{g}$ ) and Carbopack X (C-X, specific surface area = 250  $\text{m}^2/\text{g}$ ) (Supleco, Eight-Four, PA) which were sieved to a size range of 112-140  $\mu\text{m}$ .

Adsorption isotherms were collected for 17 vapors. Eleven of these were tested on C-X and 12 were tested on C-B (five were tested on both adsorbents). The test compounds spanned a range of vapor pressures from 1.4 to 151 mm Hg and contained vapors with various functionalities (i.e., alkanes, aromatics, ketones, chlorinated hydrocarbons, alcohols, aldehydes, and esters).

### Adsorption Isotherms and Breakthrough Volumes

For the applications of interest, vapor concentrations are expected to be quite low, so tests focused on concentrations in the range of 10 to 2,000 parts-per-billion (ppb). Test atmospheres were generated by passing clean, dry air through a fritted bubbler containing the liquid analyte and diluting the saturated vapor stream with clean, dry air via calibrated mass flow controllers. Vapor concentrations were periodically verified by GC-FID (HP-6890, Agilent, Palo Alto, CA) via a gas sampling valve/loop. Vapor adsorption was measured with a thermogravimetric analyzer (TGA, Pyris 1, Perkin Elmer, Waltham, MA) loaded with 1-3 mg of adsorbent material and connected to the vapor stream with stainless steel tubing. Exposures were preceded and followed by purging with  $\text{N}_2$  for  $\sim 60$  min. Mass uptake by the empty sample pan was subtracted from all measurements. The minimum mass

change detectable by the instrument is  $\sim 1\mu\text{g}$ . The materials were preconditioned by heating under  $\text{N}_2$  to 270-300°C for 4.5 hr. The TGA was held isothermal at 26.6°C during vapor exposure. After each exposure series the adsorbent sample was heated to 300°C under  $\text{N}_2$  for 30 min to remove adsorbed vapors.

Breakthrough volumes were determined by drawing a known concentration of vapor through the preconcentrator. The outlet stream was periodically injected into a GC-FID via a six-port sampling valve. Breakthrough curves were constructed by plotting  $C_x/C_0$  versus the volume of air passed through the adsorbent at the specified flow rate. By convention,  $V_b$  was defined as the volume required for  $C_x/C_0$  to reach 0.1 (10% breakthrough). For the tests reported here, only the first cavity of the  $\mu$ PCF was used, and it was filled with 1.33 mg of C-X. The device was regenerated by heating under a flow of  $\text{N}_2$  at 200-300°C for 30 min.

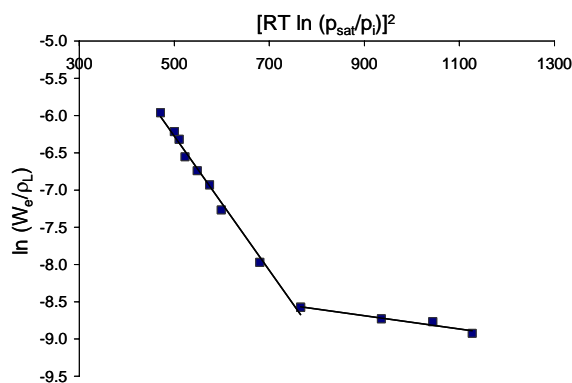


Figure 3. Representative linearized D-R plot for *m*-xylene on C-B showing two distinct regions, reflecting two different adsorption energies at different degrees of surface coverage.

## RESULTS AND DISCUSSION

### Adsorption Capacities

Of the 23 isotherms generated in this study, all but two gave D-R plots (cf. Eq. 1) similar to that shown in Figure 3 (for *m*-xylene on C-B) for both C-X and C-B. Two linear segments are apparent in all of these plots, the slopes of which are inversely proportional to the energy of the vapor-adsorbent interaction,  $E_o$  (note: values of  $\beta$  are calculated on the basis of the polarizability of each vapor [21], which can be found in standard references). The right-hand segment is the data at lower concentrations, which are

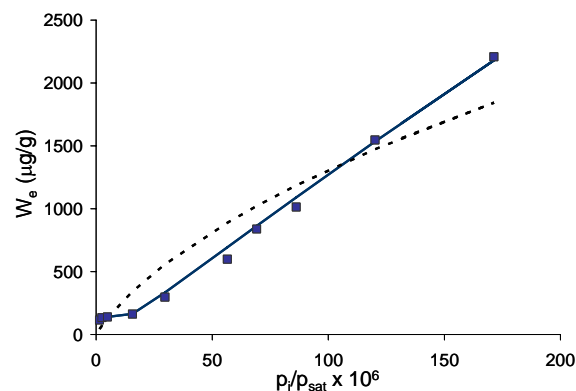


Figure 4. Isotherm for *m*-xylene (squares) and predictions using a single energy (dashed line) and dual energy (solid line) D-R equation.

characterized by a higher adsorption energy (shallower slope) for non-polar vapors. This is consistent with higher energy sites being filled in preference to lower energy sites. The left-hand segment is the data collected at higher concentrations and reflects adsorption at sites of lower energy.

For the polar vapors the slopes of each segment are reversed, in accordance with the lower affinity of polar vapors for the non-polar carbon surface at lower concentrations. At higher concentrations, vapor-vapor interactions become important for the polar vapors and lead to a higher apparent  $E_o$  value. Most studies report only a single linear relationship in such plots, consistent with experiments being conducted at higher concentrations [16-18].

The revelation of two regimes is quite significant, as it indicates, for example, that at low concentrations the capacity of the adsorbent for non-polar vapors is much higher than it is at even modestly higher concentrations. The values of  $V_b$  calculated were nearly zero in all cases (not shown), which is expected for C-B and C-X because they are nominally non-porous materials.

For both adsorbents, the points of discontinuity in the linearized D-R plots correspond to about the same (condensed) volume of sorbed vapor per gram of adsorbent material for all vapors tested:  $\sim 0.26 \mu\text{L/g}$  for C-B and  $\sim 1.2 \mu\text{L/g}$  for C-X. The lower value for C-B is attributed to its lower specific surface area.

This finding of two energy regimes has direct implications for modeling adsorption with the D-R equation. As shown in Figure 4, using a single (average) value of  $E_o$  leads to significant errors in the modeled adsorption isotherm (dashed line). When account is taken of the two energies (solid line) the average absolute error of the model is  $< 2\%$ .

#### Breakthrough Volumes as a Function of Bed Residence Time

Using the  $\mu\text{PCF}$  with the first cavity filled with 1.33 mg of C-X, breakthrough tests were performed with toluene and benzene over a range of flow rates ( $\tau$  values). A similar series of tests was performed with the reference PCF ( $\text{PCF}_{\text{ref}}$ ), which was packed with 1.35 mg of C-X. Figure 5 shows a representative  $\mu\text{PCF}$  breakthrough curve for toluene ( $C_o = 150$  ppb).

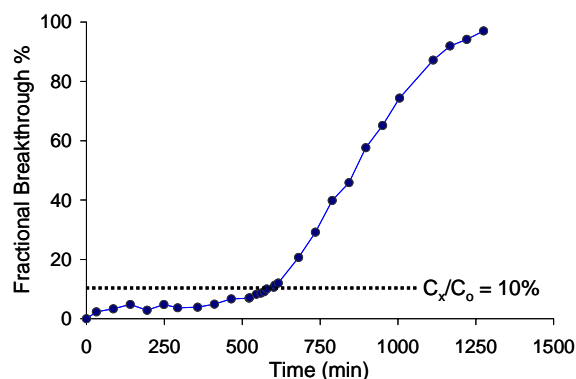


Figure 5. Example of a breakthrough curve of toluene on the C-X bed of the  $\mu\text{PCF}$  ( $Q = 4.1 \text{ mL/min}$ ;  $\tau = 11.8 \text{ msec}$ ).

Among other things, the Wheeler model (Eq. 2) predicts that  $V_b$  will decrease with decreasing  $\tau$  (increasing flow rate). Figure 6 shows the strong dependence of  $V_b$  on  $\tau$  for the  $\mu\text{PCF}$  (filled symbols), particularly at  $\tau$  values below 10 msec, which correspond to flow rates  $> 5 \text{ mL/min}$ . At lower flow rates, there is markedly less dependence. The critical bed residence time corresponds to a flow rate of  $16 \text{ mL/min}$  for toluene -- operation at

such high flow rates results in immediate breakthrough. Nearly identical results were obtained using the reference PCF (Figure 6, open symbols) indicating that bed geometry is not important and that data obtained with capillary-type devices are applicable to devices with rectangular cross sections, as long as the bed volumes are properly taken into account. Data collected for benzene thus far (not yet complete) are qualitatively consistent with that for toluene.

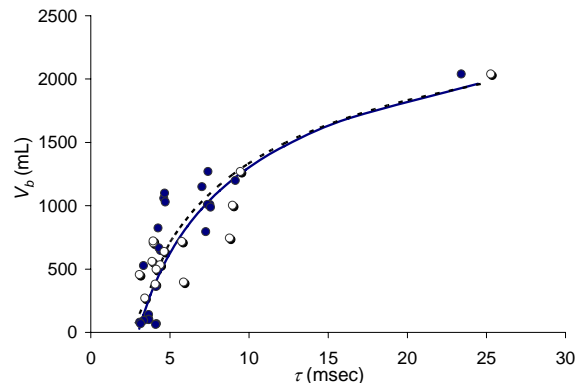


Figure 6. Dependence of  $V_b$  on bed residence time for toluene with the  $\mu\text{PCF}$  (filled symbols, solid curve) and the reference PCF (open symbols, dashed line).

#### Kinetic Rate Constants

Using values of  $W_e$  obtained from the TGA experiments and the values of  $V_b$  from the breakthrough experiments for the both the  $\mu\text{PCF}$  and reference PCF in the Wheeler model (Eq. 2), it was possible to calculate corresponding values of  $k_v$  for benzene and toluene over a range of linear velocities. Empirical models of  $k_v$  as a function of linear velocity,  $u$ , and particle diameter,  $d_p$  have been reported and are of the general form  $k_v = m(d_p^{-1.5})(u)^n$  where  $m$  and  $n$  are empirically determined coefficients [22].

Plots of  $k_v$  versus  $u$  are shown in Figure 7 for both vapors and both devices. Given the range of  $d_p$  ( $112\text{-}140 \mu\text{m}$ ) it was not possible to specify a value. Least-squares regression gave the following equations:  $k_v = 102 u^{0.6}$  for the  $\mu\text{PCF}$  and  $k_v = 73.8 u^{0.6}$  for the  $\text{PCF}_{\text{ref}}$  with  $r^2$  values  $> 0.95$  in both cases. Note that both vapors are described by the same relationship for a given device, consistent with the similarity in their diffusion coefficients. The difference in the coefficients is apparently due to small differences in average particle diameters loaded into the two devices. This suggests that  $k_v$  for a given bed may be effectively independent of vapor properties and dependent solely linear velocity.

#### Wheeler Model

Using the empirical equations derived for  $k_v$  and the D-R models for  $W_e$  it was possible to calculate modeled values of  $V_b$  for toluene from the Wheeler equation (Eq. 2) for the data shown in Figure 6. The curves shown in Figure 6 represent the modeled relationship for the  $\mu\text{PCF}$  (solid) and  $\text{PCF}_{\text{ref}}$  (dashed). As shown, the agreement between experimental and modeled  $V_b$  values is reasonably good.

#### CONCLUSIONS

This study has demonstrated the value of applying classical thermodynamic and kinetic models of adsorption to the design and operation of micro-scale preconcentrators for capturing vapors at trace-level concentrations. The finding of two adsorption energies among nearly all vapors on both adsorbents over the concentration

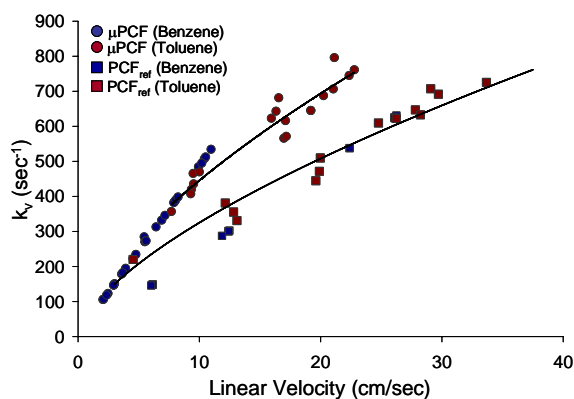


Figure 7. Kinetic rate coefficient ( $k_v$ ) vs. linear velocity for both benzene and toluene on Carboxpack X for the  $\mu$ PCF (circles) and the reference PCF (squares).

range of interest is noteworthy. The corresponding improvement in the accuracy of modeled adsorption capacities leads to more accurate estimates of required adsorbent masses in such devices.

The relationships shown here between breakthrough volumes and flow rates are also of value in defining limits on the sampling rates. Our data suggest that operation at bed residence times < 5 msec may lead to rapid breakthrough of target vapors which, in turn, reduces the preconcentration factor and the accuracy of quantitation when using such devices in microanalytical systems.

Empirical models of the kinetic rate coefficient and theoretical models of adsorption capacity were applied to the prediction of breakthrough volumes as a function of flow rate (bed residence time) with sufficient accuracy to guide design efforts and define operating limits on  $\mu$ PCF devices employing packed beds of adsorbents.

#### ACKNOWLEDGEMENTS

The authors wish to acknowledge Dr. Helena Chan and Ms. Katharine Beach for assistance in device fabrication.

#### REFERENCES

- [1] S. C. Terry, J. H. Jerman, and J. B. Angell, "A Gas Chromatograph Air Analyzer Fabricated on a Silicon Wafer," *IEEE Trans. Electron Dev.*, 26, 1880 (1979).
- [2] P. R. Lewis, R. P. Manginell, D. R. Adkins, R. J. Kottenstette, D. R. Wheeler, S. S. Sokolowski, D. E. Trudell, J. E. Byrnes, M. Okandan, J. M. Bauer, R. G. Manley, and G. C. Frye-Mason, "Recent Advances in the Micro Chem Lab," *IEEE Sensors J.*, 6, 784 (2006).
- [3] C. -J. Lu, W. H. Steinecker, W. -C. Tian, M. C. Oborny, J. M. Nichols, M. Agah, J. A. Potkay, H. K. L. Chan, J. Driscoll, R. D. Sacks, K. D. Wise, S. W. Pang, and E. T. Zellers, "First-Generation Hybrid MEMS Gas Chromatograph," *Lab on a Chip*, 5, 1123 (2005).
- [4] C2V Concept to Volume, 2/28/08 online, <http://www.c2v.nl>
- [5] E. T. Zellers, W. H. Steinecker, and K. D. Wise, "A Versatile MEMS Gas Chromatograph for Environmental Vapor Mixture Analysis", *Technical Digest 2004 Solid-State Sensor and Actuator Workshop*, Hilton Head, SC, 6/6-10/04 Transducer Res. Foundation, Cleveland (2004), pp. 61-66.
- [6] E. T. Zellers, S. Reidy, R. Veeneman, R. Gordenker, W. Steinecker, G. R. Lambertus, H. Kim, J. Potkay, M. P. Rowe, Q. Zhong, C. Avery, H. Chan, R. Sacks, K. Najafi, K. Wise, "An Integrated Micro-Analytical System for Complex Vapor Mixtures," *Proc. 2007 Solid-State Sensor and Actuator Conf.-Transducers 07*, Lyon, France, 6/10-14/07, pp. 2091 - 2094.
- [7] W. C. Tian, S. W. Pang, C. J. Lu, and E. T. Zellers, "Microfabricated Preconcentrator-Focuser for Microscale Gas Chromatograph," *J. Microelectromech. Sys.*, 12, 264 (2003)
- [8] W. C. Tian, H. K. L. Chan, C. J. Lu, S. W. Pang, and E. T. Zellers, "Multiple-Stage Microfabricated Preconcentrator-Focuser for Micro Gas Chromatography System," *J. Microelectromech. Sys.*, 14, 498 (2005)
- [9] H. K. L. Chan, S. W. Pang, R. A. Veeneman, E. T. Zellers, and M. Takei, "Microfabricated Preconcentrator for Quantitative Analysis of Low Concentration VOCs," *Proc. 2005 Solid-State Sensor and Actuator Conf.-Transducers-05*, Seoul, Korea, 6/5-6/9 (2005) pp. 2091 - 2094.
- [10] R. P. Manginell, G. C. Frye-Mason, R. J. Kottenstette, P. R. Lewis, and C. C. Wong, "Microfabricated Planer Preconcentrator," *Technical Digest Solid-State Sensor and Actuator Workshop*, Hilton Head, SC, 6/13-15/00 Transducer Research Foundation, Cleveland (2000), pp. 179-182.
- [11] C. E. Davis, C. K. Ho, R. C. Hughes, and M. L. Thomas, "Enhanced Detection of m-Xylene Using a Preconcentrator with a Chemiresistor Sensor," *Sens. Act. B.*, 104, 207 (2005).
- [12] I. Voiculescu, R. A. McGill, M. E. Zaghoul, D. Mott, J. Stepnowski, S. Stepnowski, H. Summers, V. Nguyen, S. Ross, K. Walsh, and M. Martin, "Micropreconcentrator for Enhanced Trace Detection of Explosives and Chemical Agents," *IEEE Sensors J.*, 6, 1094 (2006).
- [13] M. Kim, S. Mitra, "Microfabricated Microconcentrator for Sensors & Gas Chromatography," *J. Chrom.A.*, 996, 1 (2003).
- [14] C.-J. Lu and E. T. Zellers, "Dual-Adsorbent Preconcentrator for a Portable Indoor-VOC Microsensor System," *Anal. Chem.*, 73, 3449 (2001).
- [15] C.-J. Lu, E. T. Zellers, "Multi-Adsorbent Preconcentration/Focusing Module for Portable-GC/Microsensor-Array Analysis of Complex Vapor Mixtures," *The Analyst*, 127, 1061 (2002).
- [16] K. S. W. Sing and R. T. Williams, "Empirical Procedures for the Analysis of Physisorption Isotherms," *Ads. Sci. & Tech.*, 23, 839 (2005).
- [17] P. J. M. Carrott, and K. S. W. Sing, "Gas Chromatographic Study of Microporous Carbons," *J. Chrom.*, 406, 139 (1987).
- [18] A. Andreu, H. F. Stoeckli, and R. H. Bradley, "Specific and Nonspecific Interactions on Non-Porous Carbon Black Surfaces," *Carbon*, 45, 1854 (2007).
- [19] L.A. Jonas and J. A. Rehrmann, "The Kinetics of Adsorption of Organo-Phosphorous Vapors from Air Mixtures by Activated Carbon," *Carbon*, 10, 657 (1972).
- [20] G. O. Nelson and C. A. Harder, "Respirator Cartridge Efficiency Studies: VIII. Summary and Conclusions," *Am. Ind. Hyg. Assoc. J.*, 37, 514 (1976).
- [21] K. E. Noll, D. Wang, and T. Shen, "Comparison of Three Methods to Predict Adsorption Isotherms for Organic Vapors from Similar Polarity and Nonsimilar Polarity Reference Vapors," *Carbon*, 27, 239 (1989).
- [22] G. O. Wood and P. Lodewyckx, "An Extended Equation for Rate Coefficients for Adsorption of Organic Vapors and Gases on Activated Carbons in Air-Purifying Respirator Cartridges," *Am. Ind. Hyg. Assoc. J.*, 64, 646 (2003).

# DESIGN, MODELING AND FABRICATION OF MEMS-BASED MULTICAPILLARY GAS CHROMATOGRAPHY COLUMNS

M. A. Zareian-Jahromi<sup>1</sup>, M. Ashraf-Khorassani<sup>2</sup>, L. T. Taylor<sup>2</sup>, and Masoud Agah<sup>1</sup>

<sup>1</sup>VT MEMS Lab., Bradley Department of Electrical and Computer Engineering,

<sup>2</sup>Department of Chemistry, Virginia Tech., Virginia, USA

## ABSTRACT

This paper describes different approaches to achieve high-performance microfabricated silicon-glass separation columns for micro gas chromatographic ( $\mu$ GC) systems. The capillary width effect on the separation performance has been studied by characterization of 250  $\mu$ m-, 125  $\mu$ m-, and 50  $\mu$ m-wide single-capillary columns (SCCs) fabricated on a  $10 \times 8$  mm<sup>2</sup> die. To address the low sample capacity of these narrow columns, the paper presents the first generation of MEMS-based "multicapillary" columns (MCCs) consisting of a bundle of narrow-width rectangular capillaries working in parallel. The theoretical model for the high-equivalent-to-a-theoretical-plate (*HETP*) of rectangular MCCs has been developed, which relates the *HETP* to the discrepancies of the widths and depths of the capillaries in the bundle. Two-, four-, and eight-capillary MCCs have been designed and fabricated to justify the separation ability of these columns. These MCCs capable of multi-component gas separation provide a sample capacity as large as 200 ng compared to 10 ng for 50  $\mu$ m-wide single capillary columns.

## INTRODUCTION

Gas Chromatography is a unique and versatile technique for separation and identification of volatile and semivolatile organic mixtures. As an analytical tool, which was introduced in the 1950s, GC has a wide range of applications in the pharmaceutical industry, environmental monitoring, petroleum distillation, clinical chemistry, and food processing.

In a GC system, the mixture to be separated and analyzed is vaporized and injected into a column whose walls are coated by a polymer called stationary phase. The mixture components traverse the length of the column in a mobile phase (i.e., carrier gas) at rates determined by their retention in the stationary phase. If the column length and differences in the retention times are sufficient, a complete separation of components is possible. The separated components pass over a detector such as a flame ionization detector (FID), which generates a signal corresponding to the mass of the components in the mobile phase [1, 2].

Conventional GCs provide accurate analysis of complex mixtures but at the expense of using large, power-hungry, and relatively expensive table-top instruments. MEMS technology has already demonstrated the possibility of realizing micro gas chromatography systems ( $\mu$ GC) which exhibit faster analysis times, lower power consumption, and higher portability compared to bulky conventional GCs.

The development of high-speed and high-performance separation columns is of paramount importance in the world of  $\mu$ GC especially for public safety, homeland security, and environmental monitoring applications. The reported MEMS-based columns for high-speed GC (HSGC) have achieved separation of a few analytes in seconds but they have not been able to demonstrate highly efficient separations (complex mixture analysis) due to their significantly reduced column length (<50 cm) and their large channel width (>100  $\mu$ m). This paper addresses this situation by first demonstrating the successful design, fabrication, and stationary phase coating of very narrow-width columns. A new class of microfabricated columns called

multicapillary, consisting of a bundle of very narrow-width rectangular capillaries working in parallel, is also reported. The presented multicapillary columns enhance sample capacity and alleviate the stringent requirements on the amount of analyte that can be analyzed when using only a single narrow-width capillary column.

## THEORY

### I. Single-Capillary Column (SCC)

Analysis time, separation efficiency, and sample capacity are the main factors that need to be considered in the design and development of  $\mu$ GC columns for real-time trace analysis. Analysis time for a mixture is defined by the retention time,  $t_R$ , of the last target component peak to elute from the column [1, 3]:

$$t_R = \frac{L}{u}(k+1) \quad (1)$$

where  $u$  is the average linear carrier gas velocity,  $L$  is the column length, and  $k$  is the retention factor for the component, which depends on column temperature and stationary phase properties. For a given column cross section, the retention time can be decreased by operating at (1) a higher carrier gas velocity, (2) a higher temperature, or (3) using a shorter column. MEMS technology affords very high temperature programming rates (~600 °C/min) using on-chip heaters for ultra-low mass short separation columns [2, 4]. The major difficulty of using short columns for HSGC is the significant loss in column separation power. This amplifies the importance of using conditions that provide the maximum possible column efficiency.

The efficiency of GC columns is expressed by the height-equivalent-to-a-theoretical-plate (*HETP*). For rectangular channels, *HETP* is given by [5]:

$$HETP = \frac{2D_g}{u} f_1 f_2 + \left[ \frac{(1+9k+25.5k^2)}{105(k+1)^2} \frac{w^2}{D_g} \frac{f_1}{f_2} \dots + \frac{2}{3} \frac{k}{(k+1)^2} \frac{(w+h)^2 d_f^2}{D_s h^2} \right] u \quad (2)$$

where  $D_g$  and  $D_s$  are the binary diffusion coefficients in the mobile and stationary phases, respectively,  $d_f$  is the stationary phase thickness,  $w$  and  $h$  are the channel width and height, respectively, and  $f_1$  and  $f_2$  are the Gidding-Golay and Martin-James gas compression coefficients, respectively. Consequently, the number of theoretical plates ( $N$ ) can be calculated using *HETP* value:

$$N = L/HETP \quad (3)$$

Considering the second term in equation (2), it becomes clear that narrower columns (smaller  $w$ ) provide a smaller  $HETP$  or better separation efficiency. The downside of using HSGC columns with small widths is that for a given stationary phase thickness, the sample amount that can be injected without overloading the column is limited to several nano grams. The sample capacity drastically drops for narrow-width columns having a small cross-section area and small  $HETP$  (large  $N$ ) [6]. Another limitation of narrow-width columns is that the volumetric flow rate can be very low [1], which in turn puts limitations on the detector sensitivity. The following section addresses these problems by introducing the first generation of MEMS-Based multicapillary columns.

## II. Multicapillary Columns (MCC)

The idea of multicapillary columns was introduced by Golay in 1975 to increase the column separation efficiency without sacrificing sample capacity [3]. The main concept is that the reduced sample load, caused by using narrow-bore fused silica capillary columns, is compensated by increasing the number of capillaries,  $n$ , which work in parallel. Therefore, the sample capacity and flow rate can be theoretically increased by a factor of  $n$ . The  $HETP$  for a GC column is defined by the following equations [1]:

$$HETP = L \frac{\sigma^2}{t_R^2} \quad (4)$$

where  $\sigma^2$  is the peak variance. The  $HETP$  for MCCs can be defined in terms of the performance of its single capillaries, the stationary phase properties, and the structure features. By ignoring the details of derivation, an MCC with an average linear gas velocity of  $u_o$  has the following  $HETP$  :

$$HETP = \frac{u_o^2}{L[1+k_o]^2} \sigma_o^2 + L \left( \frac{\sigma_h}{h_o} \right)^2 + L \left( \frac{\sigma_w}{w_o} \right)^2 \quad (5)$$

where  $(\sigma_h/h_o)^2$  and  $(\sigma_w/w_o)^2$  are cross-section height and width variances normalized by the average height ( $h_o$ ) and width ( $w_o$ ), respectively.  $k_o$  is the retention factor in a capillary with cross-section area of  $a_o$  ( $h_o \times w_o$ ). In this equation, the first term,  $HETP_o$ , refers to the  $HETP$  of a capillary whose dimensions are the average of the dimensions of all capillaries in the bundle and can be calculated from equation (2). The other terms is related to the band broadening caused by inhomogeneity of the channels. If all the capillaries in the bundle have exactly the same dimensions ( $\sigma_h = \sigma_w = 0$ ), the second and third terms of the MCC performance equation would be zero, which means that MCC has an  $HETP$  equal to that of the single capillary while its sample capacity is multiplied by the number of capillaries in the bundle. Conventional MCCs comprising a bundle of round capillaries show a dispersion of 3-4% [7]. As shown later, highly homogenous rectangular capillaries can be fabricated by MEMS technology in order to minimize the second and third term in equation (5) and to increase the separation performance.

## FABRICATION

In order to study the width effect on  $HETP$ , SCC columns with three different capillary widths (50, 125, and 250  $\mu\text{m}$ ) were designed. Moreover, two-, four- and eight- capillary MCCs were fabricated to characterize the MCC performance.

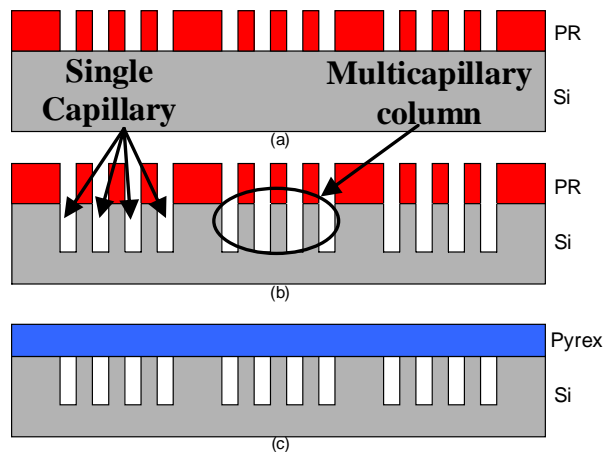


Fig. 1: Fabrication process flow for MEMS-based multicapillary columns. The column formed from silicon wafer etched using deep reactive ion etching (DRIE) technique (a-b) and bonded to a Pyrex wafer(c).

All the columns had a length of 25 cm and all the MCCs had a constant total width of 250  $\mu\text{m}$ . The fabrication of both silicon-glass SCCs and MCCs started with cleaning a silicon wafer in a Piranha solution. Then, a 10  $\mu\text{m}$ -thick layer of AZ9260 photoresist was spun on the wafer at 3 krpm for 60 seconds. After patterning the photoresist (Fig. 1a), the wafer was etched to a depth of 250  $\mu\text{m}$  using deep reactive ion etching (DRIE) technique to form channels with aspect ratios varying between 1 (for 250  $\mu\text{m}$ -wide columns) and 5 (for 50  $\mu\text{m}$ -wide columns) (Fig. 1b). After stripping the resist, the silicon wafer was anodically bonded to a Pyrex 7740 substrate (Fig. 1c). The final step is dicing the wafer to form  $10 \times 8 \text{ mm}^2$  chips, a picture of which is shown in Fig. 2. Fig. 3 shows SEM images of SCCs and MCCs before the channels were sealed. It should be mentioned that the serpentine design of the microfabricated columns compensates the peak broadening caused by turn-effect and equalize the length of all the capillaries in MCCs.

In order to connect the chips to the GC system, fused silica capillary tubing with 167  $\mu\text{m}$ -O.D. and 100  $\mu\text{m}$ -I.D. was used. The tubing was first deactivated at 400  $^\circ\text{C}$  with octamethylcyclotetrasiloxane (D4) as the deactivation agent using a previously published procedure [8]. After deactivation, the tubing was washed with 0.5 mL of methylene chloride and then

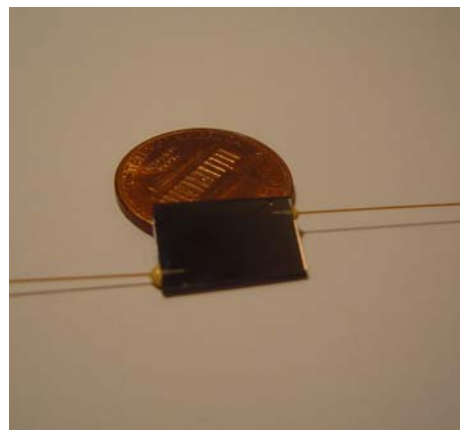


Fig. 2: GC column fabricated on an 8 mm square die after anodic bonding and attaching capillary tubes.

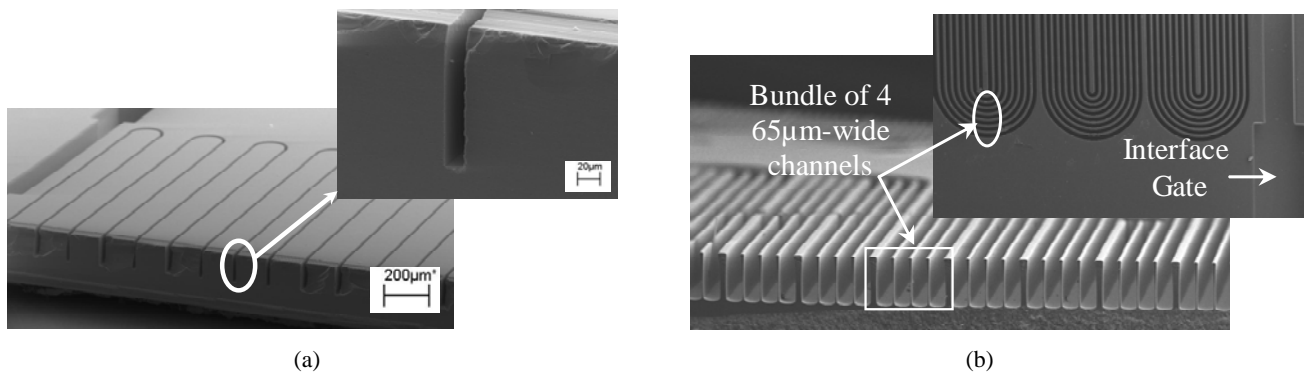


Fig. 3: SEM images of columns before anodic bonding. (a) Single Capillary Column (SSC), shows the vertical channels with aspect ratio of more than seven(onset) and (b) Cross-section view of 4-channel Multicapillary Column (MCC), top view (onset)..

purged with helium at 220 °C for 60 minutes. The tubing was then attached to the microfluidic ports of the chip using two-part adhesive (Epoxy 907, Miller-Stephenson). The deactivation procedure was repeated a second time to ensure deactivation of the chip. Due to temperature limitations of the epoxy, the deactivation procedure was performed at 250 °C, instead of 400 °C, for 90 minutes. The washing and purging procedures were also repeated. Then, a solution of polydimethylsiloxane (OV-1) dissolved in n-pentane was used to fill the column while one end of the column was blocked by pushing a small amount of wax into the capillary tubing. The concentration of the coating solution was calculated in the range of 4 mg/ml and 8 mg/ml for different columns in order to achieve an optimum coating thickness mentioned above. A vacuum was then applied to the other end while the column was kept in a water bath at 35 °C. This resulted in slow evaporation of the solvent leaving behind a thin layer of stationary phase on the column walls. In order to obtain a stable film, the OV-1 stationary phase was cross-linked by passing a vapor of azo-tetrabutane (AZT) through the column for 60 minutes. Finally, the column was sealed at both ends and heated at 220 °C for 60 minutes.

## RESULTS AND DISCUSSION

Table 1 summarizes the channel dimensions and statistical dispersion factors for different microfabricated MCCs. The cross-sectional dispersion of these MEMS MCCs is about 0.5% and is significantly lower than that of conventional columns (3-5%) [7]. Considering equation (5) and according to Table 1, the peak broadening resulting from inhomogeneities in the capillaries' dimensions (second term of equation 5) is one order of magnitude

less than that from the peak broadening resulting from a single capillary (first term).

In order to evaluate the capabilities of the microfabricated columns, several experiments were conducted using a conventional GC system (5890 Series II GC, Hewlett Packard) having a split inlet (200:1) and flame ionization detector (FID). The capillary column inside the GC was replaced by the MEMS column. The GC autosampler (7673B, Hewlett Packard) was used to inject the samples. Air was used as a carrier gas. All gases were purified with filters for water vapor and hydrocarbons. The injector and FID temperature were maintained at 280°C.

To determine the sample capacity, solutions of dodecane ( $C_{12}H_{26}$ ) in methylene chloride were prepared in increasing concentrations from 250 ng/ $\mu$ L to 10  $\mu$ g/ $\mu$ L and the *HETP* was calculated for each sample by an injection of 1  $\mu$ l of the solution at 60 °C with a split ratio of 200:1. The maximum sample amount without significant change in the *HETP* (less than 10%) was used to determine the column sample capacity. Table 2 lists the measured sample capacities of the columns. MCC columns are promising in that they can provide high efficiency of narrow columns while providing larger sample capacities. As listed in Table 2, the columns having more capillaries demonstrate higher sample capacity. The MCC with four 65  $\mu$ m-wide capillaries presented a much larger sample capacity (20 fold) compared to the 50  $\mu$ m-wide SCC.

The separation performance of the MCCs have been explored by separating a high-concentration gas mixture containing indoor air components (Sigma-Aldrich Inc., MO, US), in the conventional GC oven. Fig. 6 shows the chromatogram obtained using two-

Table 1: Statistical data obtained by SEM images to characterize the homogeneity of channels in different microfabricated MCCs at different cross sections.

MCC	Statistical Data to qualify fabrication process						$H_o$ cm	$L \left[ \frac{(\sigma_h)^2}{h_o^2} + \frac{(\sigma_w)^2}{w_o^2} \right]$ mm
	Average channel width(W) $\mu$ m	Average width dispersion $(\frac{\sigma_w}{W})\%$	Average channel depth(D) $\mu$ m	Average depth dispersion $(\frac{\sigma_D}{D})\%$	Average cross-section area(A) $(\mu$ m) <sup>2</sup>	Average area dispersion( $\frac{\sigma_A}{A}$ ) %		
2-capillary	126.5	0.27	256.7	0.43	32466	0.53	0.014	0.006
4-capillary	65.3	0.47	244.7	0.26	15983	0.51	0.009	0.007
8-capillary	36.2	0.52	231.4	0.19	8388	0.55	0.007	0.008

Table 2: Sample capacity measured using dodecane injection at 60°C, air as the carrier gas at 10psi column inlet pressure.

Column Design- Channel width(um)	Sample Capacity(ng)
SCC-50	10
SCC-125	12
SCC-250	19
MCC-125 (2-capillary)	50
MCC-65 (4-capillary)	200

channel MCC at a 30 °C/min temperature programming rate. The injection volume was 2 µl which can easily overload all the fabricated SCCs.

It should be emphasized that uniform stationary phase coating is a challenging step in the development of rectangular µGC columns. It becomes even more challenging for MCC columns with numerous parallel capillaries since all capillaries should have similar coating thickness to optimize the column performance. The primary experimental measurements of minimum *HETP*, under the same conditions mentioned above, showed a value of 0.05 cm and 0.12 cm for two- and four-capillary MCCs, respectively. This deviation from theory (see Table 1) is mainly attributed to the nonuniformity of the stationary phase coating. Work is currently under way to develop novel techniques based on self-assembly deposition of nano-structured materials to achieve a uniform thin layer of stationary phase in all the capillaries of the bundle in the presented microfabricated MCCs.

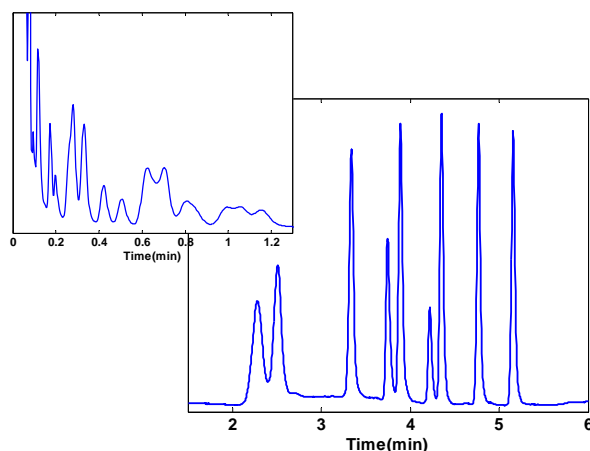


Fig.4: Chromatogram of high concentration standard mixture of indoor air components obtained by 2-channel MCC at a temperature rate of 30°C. Image onset is the first 1.2 min. of the analysis time.

## CONCLUSION

This paper has presented the development of silicon-glass high-efficient µGC columns. The tradeoff between separation efficiency and sample capacity has been addressed by presenting the MCCs. General correlations for the efficiency of rectangular

cross-section MCCs have been developed. The efficiency of such columns depends on the dispersion of the capillary dimensions in the bundle as well as the coating technique. The compatibility with unpredictable amount of environmental samples indicates the promise of MCCs for applications in environmental monitoring and homeland security.

## ACKNOWLEDGEMENTS

This work has been supported primarily by the National Science Foundation under Award Number ECCS-0601456.

## REFERENCES

- [1] R. L. Grob and E. F. Barry, *Modern Practice of Gas Chromatography* fourth ed. Hoboken, NJ: Wiley-Interscience, 2004.
- [2] M. Agah and K. D. Wise, "Low-mass PECVD oxynitride gas chromatographic columns," *Journal of Microelectromechanical Systems*, vol. 16, pp. 853-860, 2007.
- [3] M. J. E. Golay, "1ST INTERNATIONAL-SYMPOSIUM ON GLASS CAPILLARY CHROMATOGRAPHY, HINDELANG, GERMANY, MAY 4-7, 1975 - OPENING ADDRESS," *Chromatographia*, vol. 8, pp. 421-421, 1975.
- [4] M. Agah, G. R. Lambertus, R. Sacks, and K. Wise, "High-speed MEMS-based gas chromatography," *Journal of Microelectromechanical Systems*, vol. 15, pp. 1371-1378, Oct 2006.
- [5] E. S. Glenn, "Relationships for modeling the performance of rectangular gas chromatographic columns," *Journal of Microcolumn Separations*, vol. 13, pp. 285-292, 2001.
- [6] R. T. Ghijsen, H. Poppe, J. C. Kraak, and P. P. E. Duysters, "The Mass Loadability of Various Stationary Phases in Gas Chromatography," *chromatographia* vol. 27, p. 7, 1989.
- [7] V. P. Zhdanov, V. N. Sidelnikov, and A. A. Vlasov, "Dependence of the efficiency of a multicapillary column on the liquid phase loading method," *Journal of Chromatography A*, vol. 928, pp. 201-207, 2001.
- [8] C. W. R. Kong, S. Fields, and M. Lee., "Deactivation of small-diameter fused-silica capillary columns for gas and supercritical fluid chromatography," *Chromatographia*, vol. 18, pp. 362-266, 1984.

# DRIE-SI GAS CHROMATOGRAPHY COLUMNS: EFFICIENCY AND THERMAL STABILITY OF STATIONARY PHASES FOR COMPREHENSIVE TWO-DIMENSIONAL (GCxGC) SEPARATIONS

*G. Serrano,<sup>1</sup> S. M. Reidy,<sup>2</sup> K. D. Wise,<sup>3</sup> and E. T. Zellers<sup>1,2\*</sup>*

Center for Wireless Integrated Microsystems (WIMS), Departments of <sup>1</sup>Environmental Health Sciences, <sup>2</sup>Chemistry, and <sup>4</sup>Electrical Engineering and Computer Sciences, University of Michigan, Ann Arbor, MI, USA

## ABSTRACT

This study addresses some of the most critical factors affecting the performance of DRIE-Si/glass channels used as gas chromatographic (GC) separation microcolumns, namely, the consistency and uniformity of stationary phase deposition, deactivation of surface-adsorption sites on the microcolumn walls, and the stability of the stationary phase following repeated thermal cycling. Here, we demonstrate that films of PDMS can be reliably and reproducibly deposited in microcolumns 0.5 to 3-m long to provide unprecedented levels of separation efficiency and stable performance even up to 240°C in air. Use of HMDS as a surface deactivation agent is also demonstrated. The implementation of series-coupled microcolumns for comprehensive two-dimensional (GCxGC) separations employing pneumatic and thermal modulation at the junction point is also reported.

## INTRODUCTION

The measurement of gases and vapors in complex mixtures is critical to numerous efforts in public health and homeland security, including human exposure assessments, threat detection, air quality forecasting, and biomedical diagnoses. Current instrumentation is too large and expensive for routine implementation in many such applications. It is now well-known that stand-alone microsensor arrays can be used for the determination of only very simple mixtures [1,2] and, while progress continues toward micro-spectrometers capable of multi-component analysis [3-6], reliable quantitative analysis of complex gas/vapor mixtures demands temporal/spatial separation prior to measurement, regardless of the detector employed.

Several reports have appeared over the past decade on micromachined gas chromatographic ( $\mu$ GC) separation columns coupled with one or another sampling, pretreatment and/or detection devices [7-17]. A typical structure consists of a 0.25-3-m-long deep-reactive-ion-etched (DRIE) Si channel with an anodically-bonded Pyrex cover plate [11], although other designs have been reported [8,13]. A polymer layer is deposited on the channel walls and reversible partitioning of vapor-phase chemicals into the layer as they progress down the column in a carrier gas results in spatial separation.

Although single-column  $\mu$ GC separations are the most common, dual-column configurations have also been reported [14]. Comprehensive, two-dimensional (GCxGC) chromatography represents a special case, in which compounds are partially separated on a longer first-dimension column having a stationary phase of one polarity and then focused and re-injected into a shorter second column coated with a stationary phase of different polarity using a thermal or pneumatic modulator at the junction point of the two columns [18]. It is well-suited for separating complex vapor mixtures. GCxGC chromatography using microcolumns has not been reported.

Among the factors that affect the chromatographic resolution achievable with microcolumns is the uniformity of the stationary phase deposited on the walls of the channel. This will significantly affect the number of theoretical plates ( $N$ ) per unit length, which is

a standard measure of column efficiency that is related to chromatographic resolution. Deactivation of surface silanols on column walls is also important, as is the thermal stability of the stationary phase because temperature programming is typically used to accelerate separations.

This article examines the reproducibility achievable from multiple microfabricated GC columns statically coated with PDMS. The thermal stability of the PDMS stationary phase in air and He carrier gases is characterized, and the passivation of channel walls to reduce peak tailing for polar compounds is demonstrated. The use of microfabricated columns for pneumatically and thermally modulated GCxGC separations is also presented.

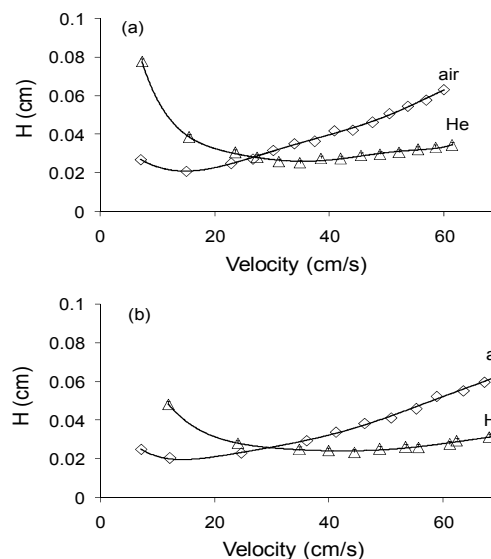


Figure 1. Golay plots (*n*-octane, 30 °C) for (a) 3-m and (b) 1-m PDMS-coated microcolumns using He and air as carrier gas. For He, the Golay plot is the average of five columns. For air, the plot is from a single column.

Table 1: Measures of efficiency for PDMS-coated microcolumns

	3-m column		1-m column	
	He <sup>a</sup>	Air	He <sup>a</sup>	Air
$N$	12500 (5)	14400	4270 (2)	4950
$H_{min}$ (cm)	0.024 (8)	0.021	0.023 (2)	0.021
$u_{opt}$ (cm/s)	33 (6)	15	44 (3)	12

<sup>a</sup> Average values,  $n = 5$ ; RSD (%) is given in parentheses.

## EXPERIMENTAL SECTION

### Microfabricated Columns

The microcolumn fabrication and stationary-phase deposition methods used in this study have been described previously [11,12,15]. Rectangular channels, 150  $\mu\text{m}$  wide by 240  $\mu\text{m}$  deep, were formed in Si by DRIE. A Pyrex cover was anodically bonded to the lower Si wafer to seal the channels. The 3-m microcolumns have a 3.2-cm  $\times$  3.2-cm footprint and the shorter microcolumns have correspondingly smaller footprints. Deactivated fused-silica capillaries (100- $\mu\text{m}$ -id) used for fluidic interconnections were secured by epoxy or silicone adhesive.

Five 1-m-long columns and five 3-m-long columns were coated with PDMS (OV-1, Ohio Valley, Marietta, OH), using a static coating method that entails filling the channel with a solution of PDMS and a cross-linking agent (dicumyl peroxide) in a volatile solvent, sealing one end, and then evaporating the solvent under vacuum at constant temperature [15]. Each column was then heated to 180°C to cross-link the polymer. A similar procedure was used for coating the moderately polar polymer, poly(trifluoropropylmethyl)siloxane (PTFPMS, OV-215, Ohio Valley) within microcolumns used for GCxGC separations. The calculated film thickness for both stationary phases was 0.15  $\mu\text{m}$ . To passivate the channel walls, a plug of liquid hexamethyl-disilazane (HMDS) was passed through the column under a flow of  $\text{N}_2$  gas. The column was then sealed, heated to 450 °C for 4 h, flushed with dichloromethane, and dried under  $\text{N}_2$  prior to stationary phase deposition as described above [19].

### Column Evaluations

Each column was evaluated using a bench-scale GC equipped with split-splitless injector, oven, and a flame-ionization detector (FID). For initial tests, n-octane was used as the probe vapor at a column temperature of 30°C with a carrier gas of He or air supplied from a compressed gas cylinder. Samples of n-octane vapor (2.5- $\mu\text{L}$ ) were drawn by syringe from the headspace of vial containing the pure solvent and injected with a split ratio of 1050:1. Golay plots (linear velocity vs. theoretical plate height) were used to determine the minimum plate height,  $H_{\text{min}}$ , and optimal linear velocity,  $u_{\text{opt}}$ . Chromatograms were processed with Grams/32 software (Galactic Industries, Salem, NH) and Excel.

To test thermal stability, two 3-m PDMS-coated columns were heated to several discrete temperatures between 30°C and 250°C and held at that temperature for 24 hr ( $\leq 100^\circ\text{C}$ ) or 48 hr ( $> 100^\circ\text{C}$ ) with He or air flowing through the column. Following each temperature excursion, the columns were cooled down to 30°C and chromatograms were run in a He or air carrier gas on separate mixtures of five alkanes, three aromatics, four ketones, and four alcohols by injecting a 0.1- $\mu\text{L}$  liquid sample of each mixture. The peak capacity, which is the number of peaks that can be separated in a specified amount of time at a specified resolution, was used as the metric of performance. It varies with  $N^{1/2}$  and, at a given column temperature, is a measure of column efficiency.

GCxGC separations were performed using split syringe injections, a 3-m PDMS microcolumn in series with a 0.5-m PTFPMS microcolumn, and an FID. For pneumatic modulation, a valve tee into the junction point of the two columns and connected to the carrier gas was used to equalize the pressure across the first column, thereby stopping flow in that column, while increasing the pressure at the junction point and the flow rate through the second column. Toggling this valve while a peak is eluting through the junction point allows for portions of the peak to be injected sequentially onto the second column and separated rapidly. A 2-D contour plot can be produced based on the retention time on each column. For thermal modulation, the junction-point

valve was replaced by a two-stage meso-scale device that uses forced-air cooling and resistive heating to sequentially focus peaks eluting from the first column and re-inject them piecemeal onto the second column [20]. The temperature range of the thermal modulator is -25 to  $\sim 200^\circ\text{C}$  and peak widths of 80-100 ms can be generated.

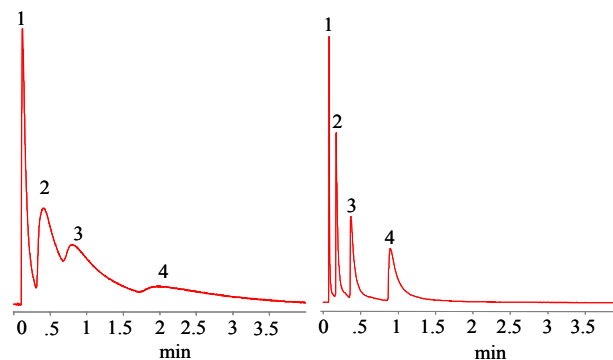


Figure 2. Chromatograms from untreated (left) and HMDS pretreated (right) 0.5-m PDMS-coated microcolumns for a mixture of alcohols: 1. 2-propanol, 2. 1-pentanol, 3. 1-hexanol, 4. 1-heptanol.

## RESULTS AND DISCUSSION

### Reproducibility of Coating Deposition

Figure 1 shows Golay plots for the 1-m and 3-m PDMS-coated columns using He and air carrier gases. Key metrics are presented in Table 1. Retention factors were 3.7 and 2.6 for the 3-m and 1-m columns, respectively, ensuring sufficient retention under the test conditions to obtain reliable measures of efficiency. The plate production is extremely reproducible, with RSD values of  $< 5\%$  for five replicates of each type of column. The  $N$  values of  $\sim 4,250$  and  $\sim 4,900$  plates/meter (for both the 1-m and 3-m columns) in He and air, respectively, are somewhat higher than those reported by Reidy et al. [17]. Part of this increase can be attributed to the higher split ratio used here. The calculated peak capacities (based on n-nonane in He) were 28 and 54 for the 1-m and 3-m columns, respectively. Although higher  $N$  values are produced in air, using He allows higher velocities (flow rates) to be used without loss of resolution, which reduces overall analysis times. These results demonstrate highly reproducible deposition of uniform films of stationary phase in microcolumns.

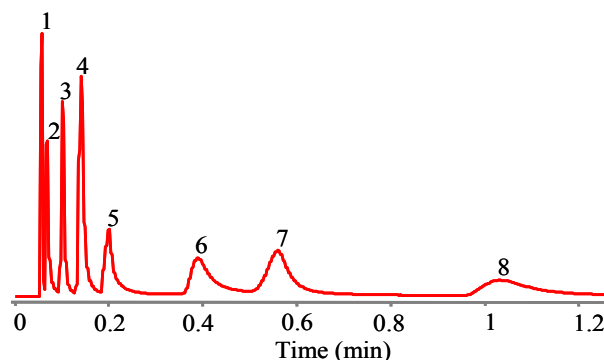


Figure 3. Test chromatogram of a multifunctional 8-component mixture separated isothermally at 30 °C using a 0.5-m HMDS-pretreated PDMS-coated microcolumn. Compounds: 1 pentane; 2 2-propanol; 3 n-heptane; 4 toluene; 5 1-pentanol; 6 3-heptanone; 7 2-chlorotoluene; 8 2-octanone.

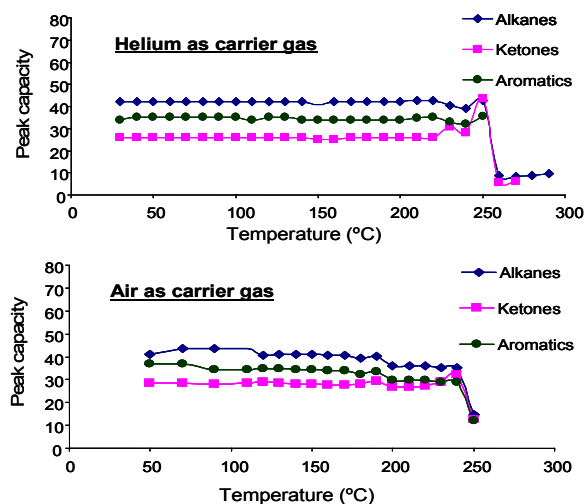


Figure 4. Peak capacity for different vapor subsets measured at 30 °C after pre-conditioning at the indicated temperature for 24-48 hrs, illustrating that the stationary phase is stable up to 240 °C in air or He.

### Column Deactivation

Although pretreatment is not necessary for achieving good separations of non-polar compounds [12,17], polar compounds interact with surface silanols on the channel walls, which degrades resolution. Pre-treatment with HMDS converts surface hydroxyl groups to trimethylsilyl ethers, rendering the sites non-polar. The improvement in peak shapes for the polar test vapors is apparent from the chromatograms shown in Figure 2 for a series of low-molecular-weight alcohols separated on 0.5-m PDMS-coated columns with and without pretreatment. The HMDS pre-treatment had no effect on the resolution of non-polar compounds or the total number of theoretical plates for the columns (not shown).

Figure 3 shows the separation of a mixture of alkanes, aromatics, ketones, and alcohols using the pre-treated 0.5-m PDMS column. The highly symmetric and baseline-resolved peaks achieved for this multi-vapor mixture in 70 sec illustrate the positive effect of the pre-treatment (note: post-treatment with HMDS vapor produces similar results without any apparent effect on the PDMS).

### Thermal Stability of PDMS-Coated Microcolumns

High-temperature operation can lead to oxidative decomposition of the stationary phase polymer and subsequent loss of resolution [21]. Figure 4 shows that the columns are stable in He and air up to 240-250°C. Above this temperature, peak capacity decreases significantly for all compounds. These results are very encouraging as they demonstrate the ability to ramp column temperatures to values high enough for rapid temperature-programmed separations of compounds that have very low vapor pressures at ambient temperature.

### GCxGC Separations

Figure 5 shows the configuration of the GCxGC system. The mid-point modulator comprises either a valve connected to the carrier gas supply (air) or a thermal cryo-trap/heater. We have succeeded in implementing GCxGC separation modules with our DRIE-Si/glass microcolumns employing pneumatic and thermal modulation. Figure 6a shows a “one-dimensional” chromatogram without any modulation of a 13-component mixture chosen to intentionally have several co-elutions. Figure 6b is a 2-D contour plot of the pneumatically modulated 13-component chromatogram.

Since the two separations are independent of each other there is a significant increase in peak capacity and all 13 components are completely separated. A mixture of aliphatic and aromatic hydrocarbons of similar complexity was analyzed using a thermal modulator in place of the pneumatic modulator (H<sub>2</sub> carrier gas, 0.25-m-long second column), with similar results (data not shown).

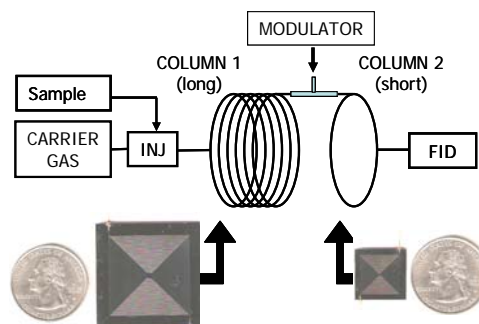


Figure 5. System configuration for comprehensive 2-D (GCxGC) separations using DRIE-Si microcolumns

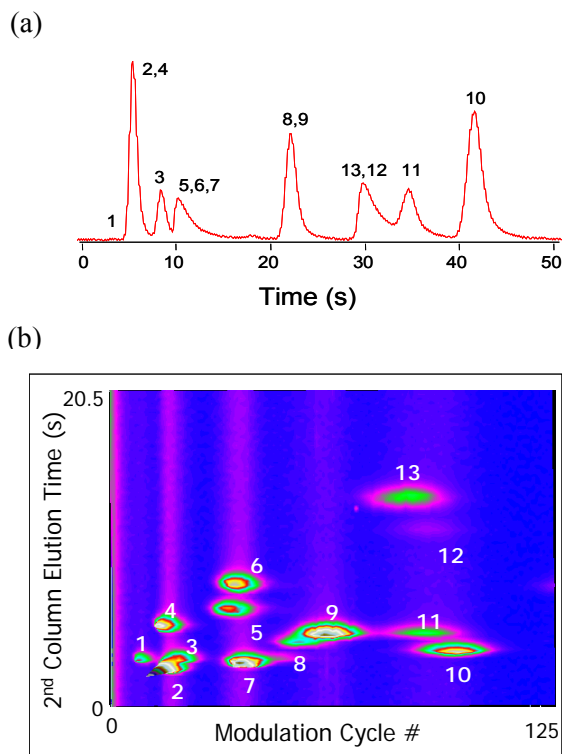


Figure 6. (a) One-dimensional chromatogram of a 13 component mixture. There are multiple sets of co-elutions. (b) A contour plot of the GCxGC separation of the 13 component mixture. The increase in peak capacity allows for the complete separation of all 13 components.

### CONCLUSIONS

This work has established that DRIE-Si/glass microcolumns with statically coated and cross-linked stationary phases of PDMS can be made reproducibly and can provide highly efficient separations -- the values of N achieved in this study, up to 4,900

plates/meter, are the highest values ever reported. Column pre-treatment with HMDS was successful in dramatically reducing peak broadening associated with wall adsorption by polar analytes. The PDMS stationary phase was found to be stable to very high temperatures in air, which bodes well for using such microcolumns to separate compounds with very low vapor pressures (e.g., explosives, pesticides, etc.) in field applications using air as the carrier gas. Results shown here also confirm that comprehensive GCxGC separations can be performed with either thermal or pneumatic modulation using DRIE-Si/glass microcolumns.

## ACKNOWLEDGMENTS

The authors wish to thank Ms. Katharine Beach for fabrication of the microcolumns employed here. This work was supported by the Engineering Research Center Program of the National Science Foundation under Award Number ERC-9986866 and by NASA Grant No. NNG06GA89G.

## REFERENCES

- [1] M.D. Hsieh, E.T. Zellers, "Limits of recognition for simple vapor mixtures determined with a microsensor array," *Anal. Chem.*, 76, 1885 (2004).
- [2] J.C. Jin, P. Kurzwaski, A. Hierlemann, E.T. Zellers, "Evaluation of multitransducer arrays for the determination of organic vapor mixtures," *Anal. Chem.*, 80, 227 (2008).
- [3] R.A. Miller, E.G. Nazarov, G.A. Eiceman, A.T. King, "A MEMS radio-frequency ion-mobility spectrometer for chemical vapor detection," *Sens. Actuat. A*, 91, 301 (2001).
- [4] C. Charlton, F. de Melas, A. Inberg, N. Croitoru, B. Mizaikoff, "Hollow-waveguide gas sensing with room-temperature quantum cascade lasers," *IEE Proc.Optolect.* 150, 306 (2003).
- [5] F.G. Bessoth, O.P. Naji, J.C.T. Eijkel, A. Manz, "Towards an on-chip gas chromatograph: the development of a gas injector and a dc plasma emission detector," *J. Anal. Atom. Spectrom.* 17, 794 (2002).
- [6] J. Moxom, P.T.A. Reilly, W.B. Whitten, J.M. Ramsey, "Analysis of VOCs in air with a micro ion trap mass analyzer," *Anal. Chem.*, 75, 3739 (2003).
- [7] A. deMello, "On-chip chromatography: the last twenty years," *Lab on a Chip*, 2, 48N (2002).
- [8] H. Noh, P.J. Hesketh, G.C. Frye-Mason, "Parylene gas chromatographic column for rapid thermal cycling," *IEEE J. Microelectromech. Syst.*, 11, 718 (2002).
- [9] A. Bhushan, D. Yemane, D. Trudell, E.B. Overton, J. Goettert, "Fabrication of micro-gas chromatograph columns for fast chromatography," *J. Microsyst. Tech.*, 13, 361 (2007).
- [10] P.R. Lewis, R.P. Manginell, D.R. Adkins, R.J. Kottenstette, D.R. Wheeler, S.S. Sokolowski, D.E. Trudell, J.E. Bymes, M. Okandan, J.M. Bauer, R.G. Manley, G.C. Frye-Mason, "Recent advancements in the gas-phase MicroChemLab," *IEEE Sensors J.*, 6, 784 (2006).
- [11] M. Agah, J.A. Potkay, G.R. Lambertus, R.D. Sacks, K.D. Wise, "High performance temperature-programmed microfabricated gas chromatography columns," *IEEE J. Microelectromech. Syst.*, 14 (5), 1039 (2005).
- [12] G.R. Lambertus, A. Elstro, K. Sensening, J. Potkay, M. Agah, S. Scheuering, K.D. Wise, F. Dorman, R. Sacks, "Design, fabrication, and microfabricated columns evaluation of for gas chromatography," *Anal. Chem.*, 76, 2629 (2004).
- [13] J.A. Potkay, G.R. Lambertus, R.D. Sacks, K.D. Wise, "A low-power pressure- and temperature-programmable micro gas chromatography column," *IEEE J. Microelectromech. Syst.*, 16, 1071 (2007).
- [14] C-J. Lu, W.H. Steinecker, W-C. Tian, M. Oborny, J. Nichols, M. Agah, J.A. Potkay, H.K. Chan, J. Driscoll, R.D. Sacks, K.D. Wise, S. Pang, E.T. Zellers, "First-generation hybrid MEMS gas chromatograph," *Lab on a Chip.*, 5, 1123 (2005).
- [15] S. Reidy, G. Lambertus, J. Reece, R. Sacks, "High-performance, static-coated silicon microfabricated columns for gas chromatography," *Anal. Chem.*, 78, 2623 (2006).
- [16] G.R. Lambertus, C. Fix, S.M. Reidy, R. Miller, D. Wheeler, E. Nazarov, R.D. Sacks, "Silicon microfabricated column with microfabricated differential mobility spectrometer for GC analysis of VOCs," *Anal. Chem.*, 77, 7563 (2005).
- [17] S. Reidy, D. George, M. Agah, R. Sacks, "Temperature-programmed GC using Si microfabricated columns with integrated heaters and temperature sensors," *Anal. Chem.*, 79, 2911 (2007).
- [18] M. Junge, S. Bieri, H. Huegel, and P. J. Marriott, "Fast comprehensive two-dimensional gas chromatography with cryogenic modulation," *Anal. Chem.*, 79, 4448 (2007).
- [19] R.C. Kong, G. Grob, "Deactivation of small diameter fused-silica capillary columns for gas and supercritical fluid chromatography," *Chromatographia*, 18, 362 (1984).
- [20] M. Libardoni, J. H. Waite, R. D. Sacks, "Electrically heated, air-cooled thermal modulator and at-column heating for comprehensive two-dimensional gas chromatography," *Anal. Chem.*, 77, 2786 (2005).
- [21] K. Grob, G. Grob, "Capillary columns with immobilized stationary phases. 5. Determination of column bleeding – re-silylation," *J. HRC & CC.*, 5, 349 (1982).

# A THERMALLY IMPROVED QUANTITATIVE PCR CHIP

Q.C. Quach and Y.C. Tai

Caltech Micromachining Laboratory, California Institute of Technology, Pasadena, CA, USA

## ABSTRACT

Here we present a thermally improved parylene-C based qPCR chip. The reaction chamber resides on a thermally isolated silicon island with an integrated heater connected to the main body via parylene-C bridges. This design allowed fast and efficient thermal cycling. By measuring the fluorescence of Sybr Green I during thermal cycling, detection of the M13 virus is demonstrated.

## INTRODUCTION

The polymerase chain reaction (PCR) is a well-established biochemical tool that can greatly benefit from miniaturization, leading to improved speed, portability, and ease of use. Although PCR has long been implemented on chips, quantitative PCR (qPCR) chips are less prominent. Polycarbonate [1], SU-8 [2], silicon-glass [3] and PDMS-based chips [4,5] have been realized; however, most utilize external, active heating and cooling elements. As these chips continue to mature, it becomes continually important to optimize thermal performance in terms of maximum heating and cooling rates with minimum power consumption.

## DESIGN

We choose parylene-C (poly(monochloro-p-xylylene)) as the channel material. It is biocompatible (USP Class VI) for minimal interference with the PCR reaction, optically transparent which allows DNA detection by optical fluorescence, and conformally deposited using a room temperature CVD process making it compatible with many standard MEMS procedures.

To optimize the thermal design, we use a unique technology developed by our group [6] to create a reaction chamber that sits on a 2mm x 2mm Si island surrounded by air and suspended by low-thermal-conductivity parylene bridges (Figs. 1 and 2). This design eliminates the need to heat the entire chip. Mechanical stability of the island was excellent as no relative movement with respect to the chip's main body was observed throughout the fabrication and testing phases of the device.

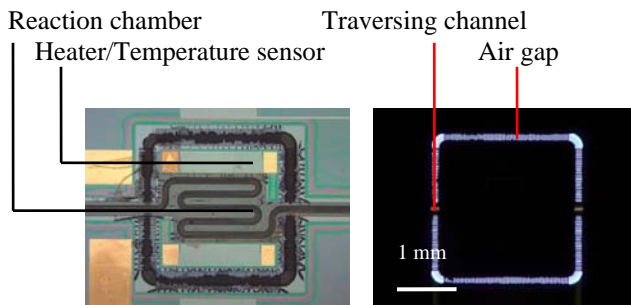


Figure 1: Thermally isolated reaction chamber with (left) front side lighting and (right) backlighting. The air gap is connected to the main body via parylene bridges. In this picture, wire bonds were removed for clarity

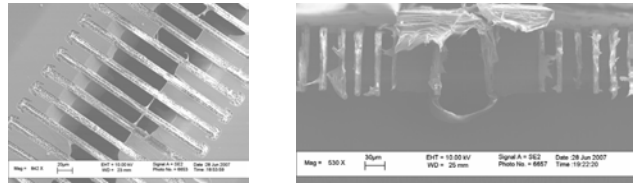


Figure 2: Air gap. (Left) top view of gap with parylene stitches. (Right) Cross sectional view showing bridges and air-gap-traversing channel

The 70nL qPCR reaction chamber is a serpentine channel embedded in the silicon. It is fabricated using a process that results in a clean parylene surface by avoiding the use of a photoresist sacrificial layer [7]. The channel is still fluidically connected to the main body via a parylene channel section that traverses the air gap (Fig. 1 and 2, right) to continue to the main body.

The integrated heater/temperature sensor is a 2.3 kOhm Ti/Pt metal trace. It is electrically connected to the main body by gold bridges formed by wire bonding. The main body (Fig. 3) contains the electrical contact pads and fluidic inlet and outlet holes. A customized Ultem and acrylic jig (Fig 4) is designed and fabricated in-house using a computer numerical control (CNC) milling machine.

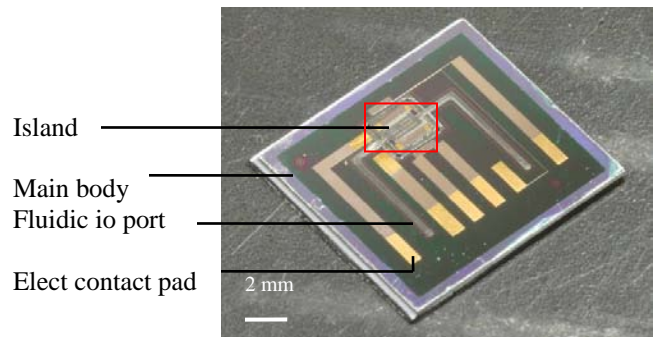


Figure 3: Entire chip view. Red square is the thermally isolated island enlarged for figure 1



Figure 4: Customized jig. Amber section is Ultem polymer while clear top plate is acrylic. Spring loaded conductive pins provide electrical contact with the chip

## FABRICATION

The fabrication is illustrated in figure 5. After growing 1 $\mu$ m of thermal oxide as an electrical insulation layer, the metal layer (300Å Ti, 2000Å Pt, 2000Å, Au) is deposited and patterned using a lift off technique. The gold is etched everywhere except at contact pads. Trenches for channel sidewalls and stitches are then etched using deep reactive ion etching (DRIE). The first parylene layer is then deposited to fill the trenches. The air gap and inlet/outlet holes are then simultaneously formed by etching the backside silicon using DRIE. Next, the parylene layer is etched to expose silicon and XeF<sub>2</sub> is used to etch the exposed silicon about

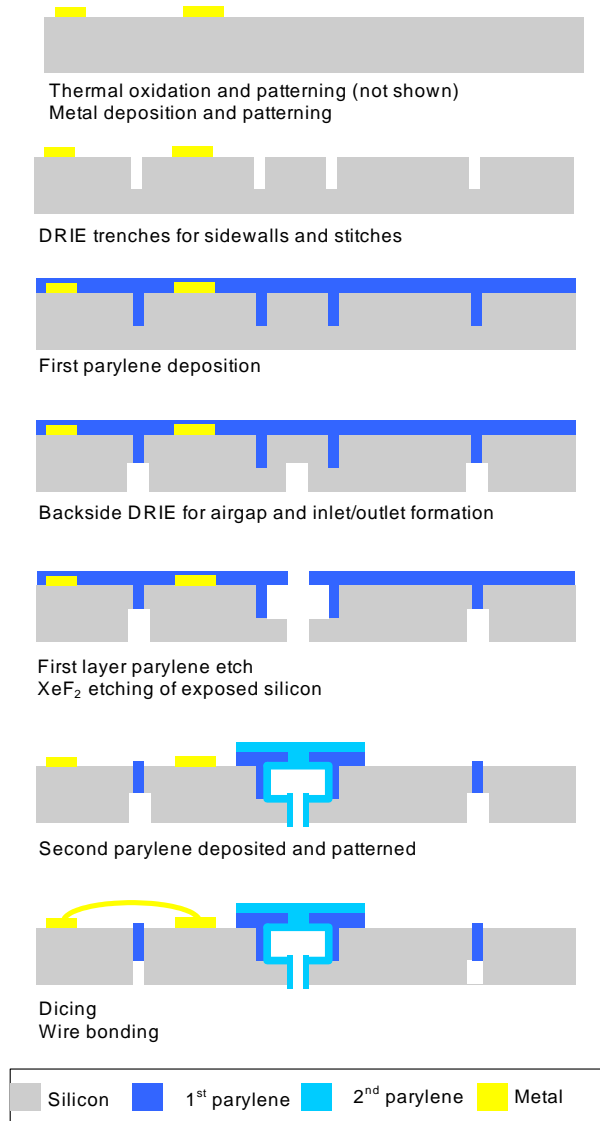


Figure 5: Fabrication process flow

100  $\mu$ m deep forming the fluidic channels. The sidewalls protect XeF<sub>2</sub> from excess lateral etching due to its isotropic silicon etching characteristic. Next, a second parylene layer is deposited and patterned to seal the channels. This embedded channel technology enables channels of arbitrary length by eliminating the diffusion-limited sacrificial material release step required for surface micromachining of parylene channels. After dicing, wire bonding is performed to electrically connect the heaters on the island to the main body.

## TESTING RESULTS AND DISCUSSION

### Thermal Characterization

The temperature coefficient of resistance was  $2.3 \times 10^{-3} / ^\circ\text{C}$  from the calibration curve (Fig 6). From this relationship between resistance and temperature, LabView was used to implement a PID scheme to feedback control a power source and a multimeter to supply programmed power and temperature profiles.

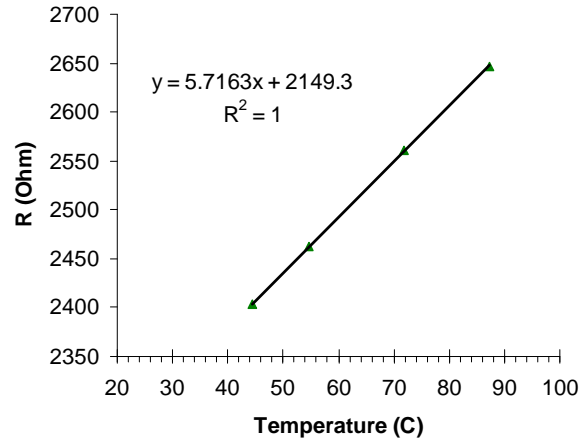


Figure 6: Temperature calibration. Resistance showed a highly linear relationship with temperature

The basic thermal characteristics of the dry chip (with empty channels) can be described using a simple analogy to a parallel RC circuit driven by a constant current source (figure 7).

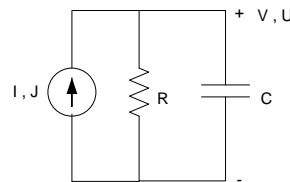


Figure 7: Variables for electrical, thermal circuit

In the electrical case, the voltage difference, V, observed in response to the applied current, I, is characterized by equation (1).

$$V(t) = V_0 e^{-t/RC} + IR(1 - e^{-t/RC}) \quad (1)$$

Transferring to the thermal case, the voltage difference is replaced by the temperature difference, U, between the chip and room temperature (taken as 23.5°C here). The applied current is replaced by the applied power, J.

$$U(t) = U_0 e^{-t/RC} + JR(1 - e^{-t/RC}) \quad (2)$$

$$U = T - T_{room}$$

$$\tau = RC$$

It should be noted that this simple model serves only to provide a framework to quantitate the thermal properties of the chip. A more thorough model would address assumptions relating to higher order effects such as differences in temperature, thermal conductivity, and heat capacities between the silicon island,

parylene channels, and PCR fluid.

The thermal resistance,  $R$ , is the resistance to the natural convection heat flow from the chip into the air. Hence,  $R = 1/hA$  where  $h$  is the heat transfer coefficient and  $A$  is the heat transfer area which is the top and bottom surface of the 2mm x 2mm island.  $R$  can be determined by measuring the steady state temperature for a given applied power. From figure 8, the thermal resistance is  $0.34 \text{ } ^\circ\text{C}/\text{mW}$  corresponding to a heat transfer coefficient of  $735 \text{ W}/\text{m}^2\text{ } ^\circ\text{C}$ .

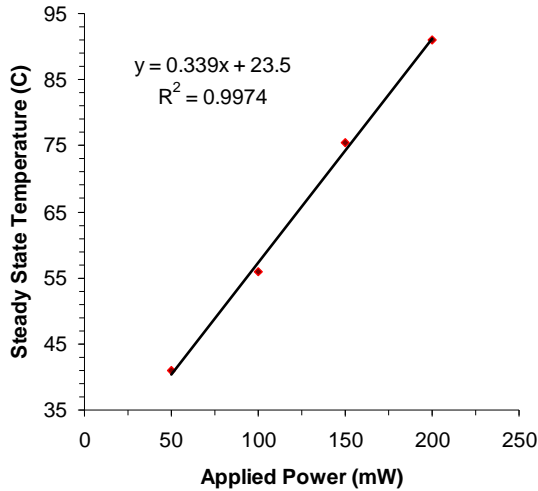


Figure 8: Steady State Power Response

The thermal time constant,  $\tau$ , was determined by fitting the model to the temperature response of the chip when the applied power is suddenly and instantaneously removed (figure 9). This yielded a time constant of approximately 2 seconds. From the values of  $\tau$  and  $R$ , the calculated thermal capacitance,  $C$  is  $5.9 \text{ mJ}/^\circ\text{C}$ . Given the rough nature of the model, the value for  $C$  was in fair agreement with the expected value of  $3.6 \text{ mJ}/^\circ\text{C}$  calculated from the heat capacity, density, and volume of the thermal island assuming it is comprised of only silicon.

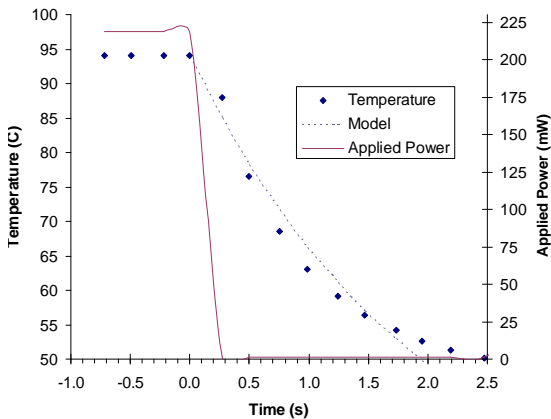


Figure 9: Step response to zero applied power

## PCR

Although the temperature could increase at about  $10^\circ\text{C}/\text{sec}$  and decrease at about  $14^\circ\text{C}/\text{sec}$  using only resistive heating and passive cooling, for simplicity all ramping times were set to 5 seconds for the PCR tests runs (Fig. 11). The rates were programmed as linear increases and decreases instead of aggressive step functions to minimize instability from the PID control algorithm, although better control and faster ramping times should be easily achieved with further experimentation with the control parameters.

We tested our qPCR chip using the M13 virus which has been shown to be an excellent model system for qPCR analysis [8]. The test solution was a freeze-dried seed sample of M13 from the American Type Culture Collection (ATCC #15669-B1) resuspended in 1mL of Tris-EDTA buffer pH 8.0. A standard Sybr Green I qPCR protocol was used with viral lysis occurring during the initial 2 min at  $95^\circ\text{C}$  “hot-start” procedure. Thermal cycling then proceeded with the following temperature schedule:  $95^\circ\text{C}$  for 15 sec,  $51^\circ\text{C}$  for 15sec, and  $72^\circ\text{C}$  for 15 sec for a total of 40 cycles. A fluorescence microscope and CCD camera were used to capture images of the chip and an image analysis program, ImageJ, [9] was used to extract the fluorescence data. Figure 10 shows that this device successfully discriminated between the no primers control and the test solution of  $10^7$  viral particles/ul. Based on the chamber volume, the total viral load was  $7 \times 10^5$  viral particles.

Improvements to the device can be made from both the engineering and biological standpoints. Although this work focuses on thermal optimization, optical performance is also an important factor for this device. Studies of the optical behavior of parylene and silicon will lead to future designs.

From the biological standpoint, total cycling time can be greatly reduced by optimizing the hold times for each temperature. Hold times down to 5 seconds at each temperature have been reported for on-chip PCR [10]. Although basic viral detection is demonstrated here further work needs to be done to determine the sensitivity of the device both in terms of minimum viral load and minimum DNA load that can be detected. It would also be natural to test the device with RNA samples.

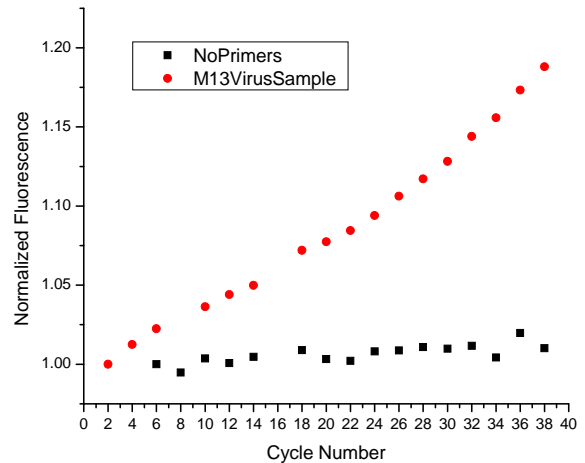


Figure 10: Example qPCR result. A fluorescence photograph of the chip was taken at the end of the  $72^\circ\text{C}$  extension step every 2 cycles. The image was then analyzed using the image analysis program ImageJ

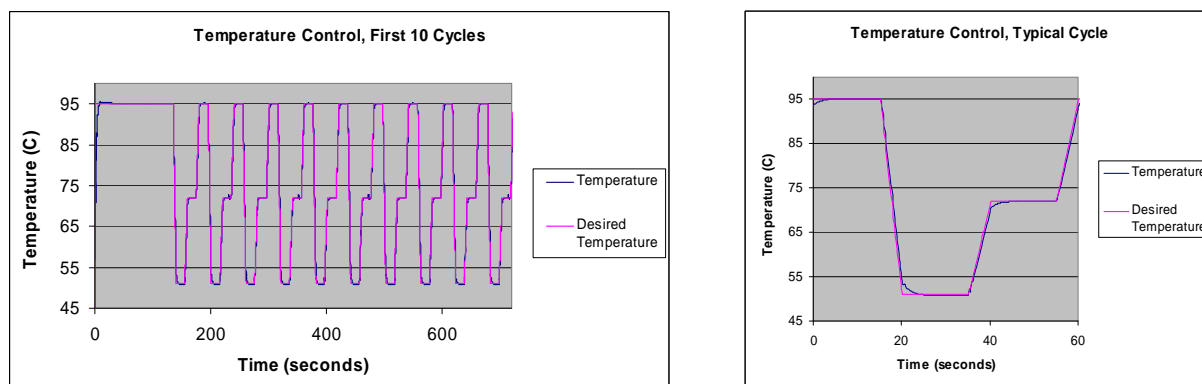


Figure 11: Temperature profiles for qPCR chip. Actual temperatures matched desired temperatures within 0.1°C. Left: First 10 cycles including initial 'hot-start' and viral lysing at 95 °C for 2 min. Right: Typical cycle

## CONCLUSIONS

These results demonstrate a thermally improved quantitative PCR chip based on parylene technology capable of detecting a model virus. The fast thermal response with low power consumption is crucial to the development of battery-powered portable instruments for quantitative PCR while the use of parylene allows future integration with the various other parylene based MEMS devices.

## ACKNOWLEDGEMENTS

This work was supported by The Boeing Company. We would like to thank the other members of the Caltech Micromachining Laboratory.

## REFERENCES

- [1] J. Yang, Y. Liu, C. Rauch, R. Stevens, R. Liu, R. Lenigk, P. Grodzinski, "High Sensitivity PCR Assay in Plastic Micro Reactors", *Lab on a Chip*, 2, pp.179-187 (2002)
- [2] M. Agirregabiria et al., "Concentration, Lysis and Real-Time PCR on a SU-8 Lab on a Chip for Rapid Detection of *Salmonella* spp. in Faeces", *Proceedings of the Eleventh International Conference on Miniaturized Systems for Chemistry and Life Sciences*, Paris, France, 10/7-11/2007, pp. 584-586
- [3] T.B. Taylor, E.S. Winn-Deen, E. Picozza, T.M. Woudenberg and M. Albin, "Optimization of the Performance of the Polymerase Chain Reaction in Silicon-Based Microstructures", *Nucleic Acids Research*, 25, 15, pp. 3164-3168 (1997)
- [4] Q.Xiang, B. Xu, R. Fu, and D. Li, "Real Time PCR on Disposable PDMS Chip with a Miniaturized Thermal Cycler", *Biomedical Microdevices*, 7:4, pp. 273-279 (2005)
- [5] N.C. Cady, Stelick, M.V. Kunnavakkam, C.A. Batt, "Real-Time PCR Detection of *Listeria Monocytogenes* Using an Integrated Microfluidics Platform", *Sensors and Actuators B* 107, pp.332-341 (2005)
- [6] C.Y. Shih, Y. Chen, J. Xie, Q. He and Y.C. Tai, "On-Chip Temperature Gradient Liquid Chromatography", *Technical Digest of the 18th IEEE International Conference on Micro Electro Mechanical Systems (MEMS 2005)*, Miami, Florida, 1/30/05 – 2/3/05, pp. 539-542
- [7] PJ Chen, C.Y. Shih, Y.C. Tai, "Design, Fabrication, and Characterization of Monolithic Embedded Parylene Microchannels in Silicon", *Lab on a Chip*, 6, pp. 803-810 (2006)
- [8] Sum et al., "Real-Time PCR Assay Using Molecular Beacon for Quantitation of Hepatitis B Virus DNA", *Journal of Clinical Microbiology*, 42(8), pp. 3438-3440 (2004)
- [9] Rasband, W.S., ImageJ, U. S. National Institutes of Health, Bethesda, Maryland, USA, <http://rsb.info.nih.gov/ij/>, 1997-2007
- [10] D.S. Lee, S.H. Park, H. Yang, K.H. Chung, T.H. Yoon, S.J. Kim, K. Kim, and Y.T. Kim, "Bulk Micromachined Submicroliter-volume PCR Chip with Very Rapid Thermal Response and Low Power Consumption", *Lab Chip*, 4, pp. 401-407 (2004)

# CONTINUOUS FLOW SEPARATION OF SUSPENDED CELLS IN HUMAN WHOLE BLOOD USING DIELECTROPHORESIS

Youngdo Jung<sup>1</sup>, Ki-Ho Han<sup>2</sup>, Yoonsu Choi<sup>1</sup>, and A. Bruno Frazier<sup>1</sup>

<sup>1</sup>Georgia Institute of Technology, Atlanta, Georgia, USA

<sup>2</sup>Inje University, Gimhae, Gyongnam, South Korea

## ABSTRACT

This paper is focused on the development of continuous flow dielectrophoretic (DEP) microsystems. The design and fabrication of the continuous flow DEP microsystems are presented along with the experimental characterization of the separation systems using human whole blood as sample material. The significance of this work is the development of the first continuous flow-based DEP microsystems for high-throughput separation of suspended cells in blood by cell type. Experimental results show that an angled-electrode type DEP microsystem can switch the flow stream of blood cells with  $96.16 \pm 2.48\%$  efficiency. Divergent type DEP microseparator can continuously separate out 87.0% of the red blood cells (RBCs) and 92.1% of the white blood cells (WBCs), while the convergent type DEP microseparator can separate 93.6% of the RBCs and 76.9% of the WBCs suspended in dilute human whole blood with a high conductivity of 17mS/cm.

## INTRODUCTION

Dielectrophoresis uses the electrical polarization of cells in a non-uniform electric field. Depending on the frequency of the applied AC electric field, a cell may feel an attractive force (positive DEP) in the electric field gradient or a repulsive force (negative DEP) in the opposite direction of the field gradient. Most cells experience a positive DEP force in the high frequency range and a negative DEP force in the low frequency region. At the crossover frequency, no DEP forces are exercised on the cells. The crossover frequency is dependent on various cell characteristics, such as the membrane characteristics, internal structures, or the size of cells, and the variability in the crossover frequency of cells is selective enough for DEP microsystems to differentiate between similar cell types. Microfluidic systems using DEP force have been shown to manipulate biological cells successfully using this intrinsic dielectric affinity differentiation and have demonstrated highly selective isolation of target rare cells from the mixture of various blood cells without any tagging [1-4].

However, most of conventional DEP microsystems require several discontinuous steps of retaining, washing and releasing samples. Recently, several continuous DEP microseparators were demonstrated for yeast cells, showing good positive and negative DEP action for viable and nonviable cells [5, 6].

The presented continuous flow-based DEP microsystems allow the high-throughput separation of suspended cells in human whole blood by cell type and would aid in the development of blood sample preparation and analysis systems for cell research and medical applications.

## METHOD

### Design Method

The conceptual view of an angled-electrode type DEP microsystem is shown in Fig. 1 (a) along with cell streams during operation. The input sample fluid is focused by two sided sheath flow (buffer #1, #2) and down stream comb-type angled electrodes. The electrodes are centered on the input sample channel and the outlet #1 channel with decreasing comb tooth length from the input to the output of the microseparator along the length of DEP chamber.

Without any force acting on cells, all cells travel with laminar flow and are collected into the outlet #2 (blue-line). Under a high gradient electric field created by the alternating electrodes, the cells experiencing positive DEP force are attracted toward the electrode edges, thus the cell stream is deflected toward outlet #1 (red-line), while the cells experiencing negative DEP force are levitated above the surface and swept with laminar flow to outlet #2 (blue-line). To manipulate biological cells more efficiently in a switching operation, the DEP system utilizes an induced hopping movement of the blood cells between neighboring electrodes by adjusting the release phase and attraction phase properly. Individual cell movement during one hopping period is described in Fig.1 (b).

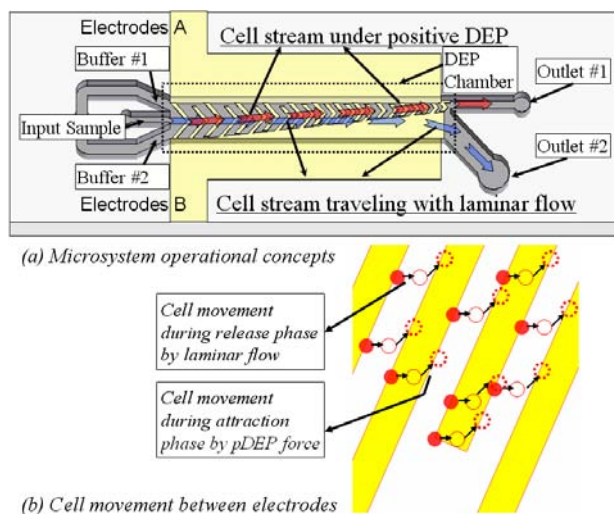


Figure 1: Operation principle of an angled-electrode type continuous DEP microsystem

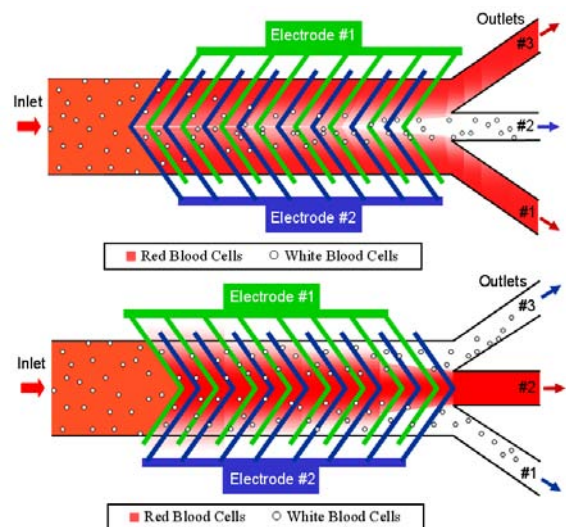


Figure 2: Operation principle of divergent and convergent type continuous DEP microsystems

The design of the divergent and convergent type DEP microseparators is shown in Fig. 2. At the crossover frequency of WBCs which is usually lower than that of RBCs, the DEP force on WBCs is much weaker than the DEP force on RBCs. Thus, weakly forced WBCs are diffused away from highly dense stream of RBCs. The RBCs and WBCs are continuously separated as the whole blood passes through the microchannel of the DEP microseparators.

**Fabrication Method**

The angled-electrode type DEP microsystem consisted of a glass microchannel, planar electrodes and microfluidic interfaces / system packaging. Cr/Au masking layers were sputtered on both sides of glass substrates (Schott Borofloat glass) with a DC sputterer. A 50 μm deep microchannel was etched through standard photolithography processes followed by HF wet etching of the glass for 30 minutes (Fig. 3 (a)). After removing all Cr/Au masking layers for the microchannel etching, additional Cr/Au layers for electrodes were sputtered on the surface of the etched glass substrate. The down stream comb-type angled electrodes were defined by another photolithography step using thick negative photoresist (Fig. 3 (b)).

A drilling guide, used to create the inlet and outlet ports in the top glass, the microfluidic interface, and microsystem packaging were designed and fabricated using stereolithography (Fig. 3 (e)).

The inlet and outlet holes along with electrode connection holes were drilled by diamond drill bits using a drilling guide for correct positioning on the top glass substrate. The drilled top glass was aligned and bonded with the patterned bottom glass by introducing UV cure adhesive resin between the two glass substrates by capillary force and curing them under a UV lamp for 30 minutes (Fig. 3 (c)). The microfluidic interface was bonded to the microseparator by repeating the UV adhesive bonding process (Fig. 3 (d)). Finally, two electric wires were connected to the electrode pads through the electrode connection holes using conductive silver paste.

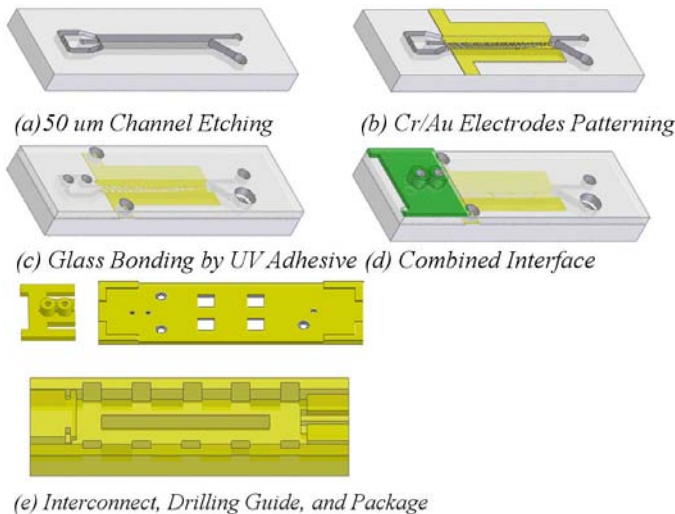


Figure 3: Fabrication process for an angled-electrode type microseparator

The divergent and convergent type DEP microseparators consisted of a PDMS microchannel from SU-8 mold structure, planar electrodes on the glass substrate, and the system packaging. Fig. 4 illustrates the fabrication process for the divergent and convergent type DEP microseparators.

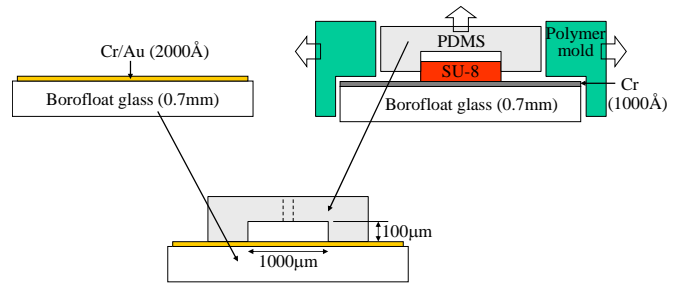


Figure 4: Fabrication process based on glass and PDMS for the divergent and convergent type DEP microseparators

**EXPERIMENTAL SETUP**

Human venous blood was collected at on-campus health center under the Institutional Review Board-approved protocol for blood collection for research purposes. The samples were drawn into evacuated glass tubes, containing EDTA as an anticoagulant. 8.5% (w/v) sucrose plus 0.3% (w/v) dextrose buffer solution was used to dilute human whole blood sample to the ratio of 10:1 and lower the conductance of the media. SYTO-13 fluorescent dye was used to identify the nucleated cells during experiments. The diluted blood sample with SYTO-13 fluorescent dye was incubated at 37°C for one hour.

The microseparator was treated with Pluronic® F108 block copolymer surfactant solution to reduce the adhesion of blood cells on the channel surface and washed several times with the buffer solution. The microsystem was assembled into the packaging and the attached electric wires were connected to the function generator output. A 500 uL gas tight glass syringe and a 3mL luer lock syringe were used to load the incubated blood sample and the buffer solution, and were connected to capillary tubing. The other ends of the tubing extending from the syringes were connected to the device inlet ports through the microfluidic interface. A syringe pump was used to provide the desired constant volumetric flow rates during the separation process.

The assembled microseparator was placed under a fluorescent microscope and the trajectory of blood cells was monitored and recorded using the microscope camera and video capture tools (Fig. 5). The separation efficiency of the magnetophoretic separation system was characterized by counting the number of the RBCs using a Coulter Cell Counter (Multisizer II, Beckman Coulter, Inc., Fullerton, CA)

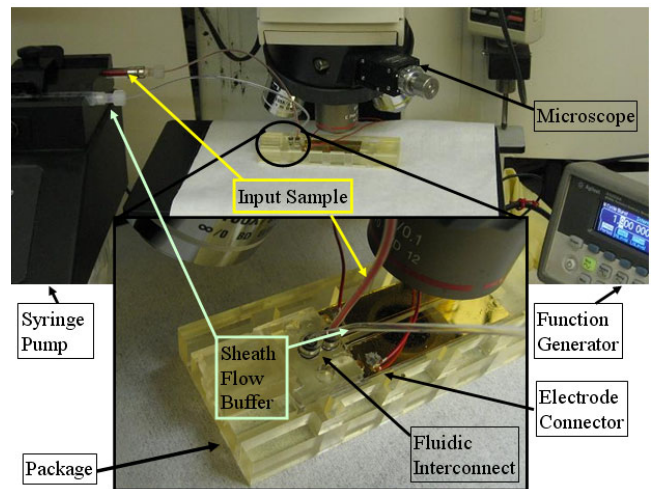


Figure 5: Instrument setup

## RESULTS

### Fabrication Results

The fabricated angled-electrode type microsystems are shown in Fig. 6. The microfluidic interface with two interconnection ports is shown bonded to the microseparator. Three input channels and comb-type angled electrodes which are centered on the input sample channel and the outlet #1 channel are shown. Two additional electrode connection holes were drilled to test the electrical connection after silver paste wire bonding. A narrow ditch was etched around the main separation chamber to prevent UV adhesive resin from flooding into the main channel during the bonding process.

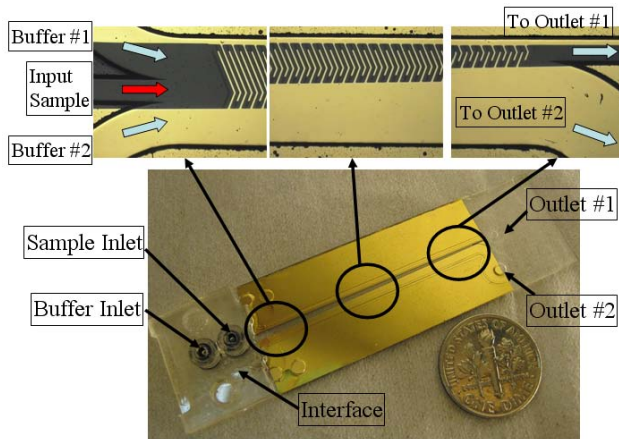


Figure 6: Fabricated hopping mode DEP microsystem

The fabricated divergent and convergent type DEP microseparators are shown in Fig. 7. The punched holes in the PDMS work as the microfluidic interfaces for blood sample introduction.

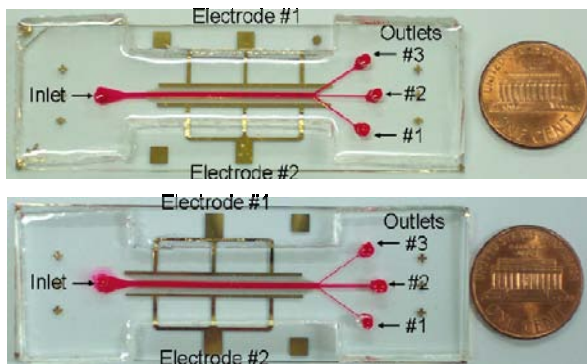


Figure 7: Fabricated convergent and divergent type microseparators

### Characterization Results

The images of a blood cell stream inside the angled-electrode type DEP microsystem with no electric field are shown in Fig. 8 (a). Without an applied DEP force,  $99.21 \pm 0.08\%$  of the cells from the input sample traveled in the laminar flow direction and were collected into outlet #2. A 2 MHz, 8 V<sub>p-p</sub> AC signal was supplied in burst mode (0.2 second ON and 1.3 second OFF) to create the hopping movement of the blood cells between adjacent electrodes in the angled-electrode type microsystem. Fig. 8 (b) shows switching of the input blood cell stream from outlet #2 to outlet #1. For switching operation,  $96.16 \pm 2.48\%$  cells were deflected from the

original flow direction and collected into outlet #1.

The volumetric flow rate for this demonstration was 20  $\mu\text{L/hr}$  ( $3.0 \times 10^3$  cells/sec). The configuration of the burst mode (periods for release and attraction phase) used for the switching operation was decided for the captured cells to cross one or two electrodes during one period based on the observed cell movement at the fixed volumetric flow rate

A 100 KHz, 8V p-p potential was applied to the electrodes for cell separation. The microscope images of the cell separation in the microsystem demonstrate the separation of WBCs (outlet #1) and RBCs (outlet #2). At this condition, most of RBCs did not experience the positive DEP force, and traveled in the laminar flow direction and were collected into outlet #2, while WBCs showed the positive DEP attraction to the electrode edges and moved toward outlet #1 (Fig. 9).

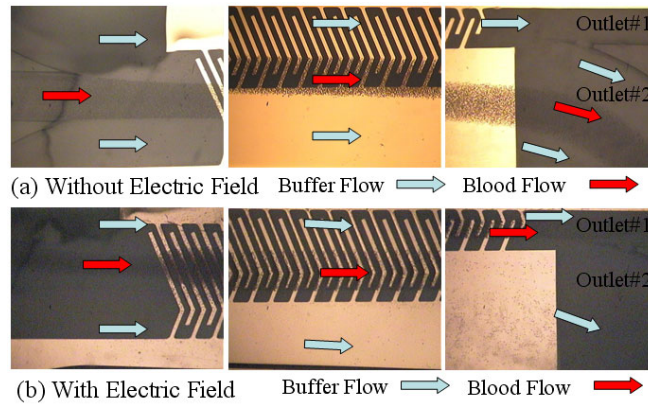


Figure 8: Micrograph of blood cells at the entrance, middle and exit of channel

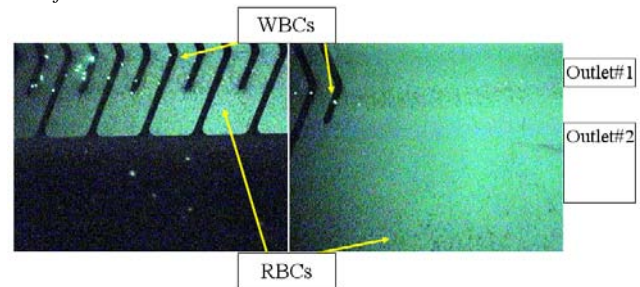


Figure 9: Blood cell separation in the microsystem

2 MHz, 3 V<sub>p-p</sub> sinusoidal voltage was applied to separate WBCs from RBCs by the DEP force inside the divergent and convergent type DEP microseparators. Suspending media with a high conductivity of 17 mS/cm comparable to the conductivity of human whole blood was used for the cell separation. Fig. 10 shows the images of RBCs and fluorescently dyed WBCs passing through the microchannel of the DEP microseparators. In the divergent type microseparator, the RBCs were drawn closer to the edges of the microchannel and flowed into the two outermost outlets (#1 and #3), while the WBCs were concentrated at the center of the microchannel and flowed into the central outlet (#2). In the convergent type microseparator, the RBCs were concentrated toward the center of the microchannel and flowed into the central outlet (#2), while the WBCs were drawn closer to the edges of the microchannel and flowed into the two outermost outlets (#1 and #3). The volumetric flow rate for this cell separation was 50  $\mu\text{L/hr}$  ( $4.0 \times 10^4$  cells/sec).

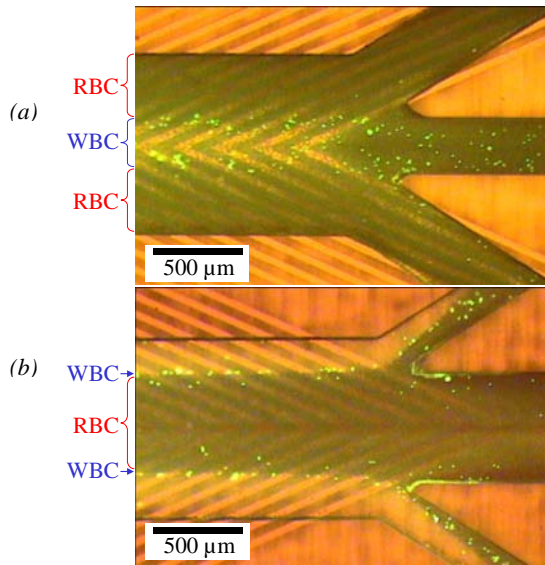


Figure 10: Micrograph of blood cell separation (a) in the divergent and (b) in the convergent type DEP microseparators

With the divergent type DEP microseparator, 87.0 % of RBCs passed through the outermost outlets (#1 and #3) while 92.1% of WBCs were diffused to the central outlet (#2) (Fig. 11 (a)). With the convergent type DEP microseparator, 93.6% of RBCs are separated into the central outlet (#2), while 76.9% of WBCs diffused to the two side outlets (#1 and #3) (Fig. 11 (b)).

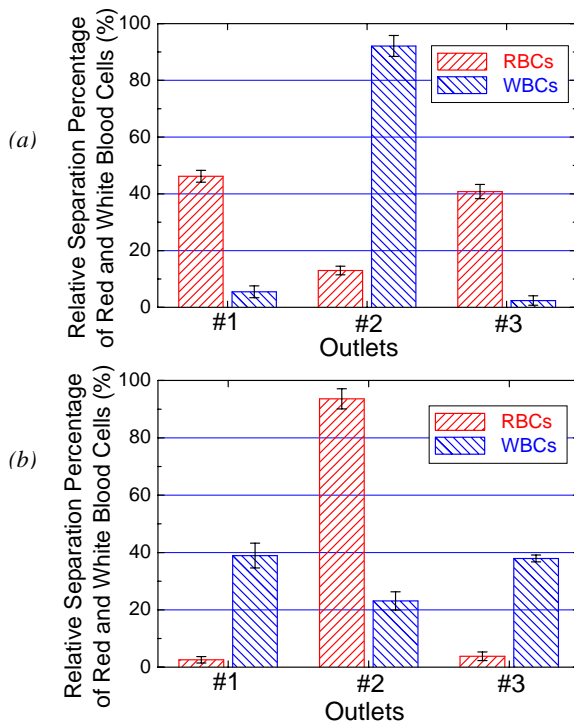


Figure 11: The measured relative separation percentage of RBCs and WBCs at each outlet of the continuous DEP microseparators for (a) divergent type and (b) convergent type design

For the angled-electrode type microsystem, it was observed that some captured cells moved only between the lower edges of the neighboring electrodes and did not change its direction enough toward the electrode center as desired. These cells were sometimes swept toward the undesired outlet. The electrode design that ensures the captured cells to move toward the desired outlet during the attraction phase will help increase the performance efficiency.

No clogging due to cell coagulation inside the chamber was observed during the experiments. However, when the frequency of the applied signal went below 100 Hz during frequency sweeping, the suspending media started to be electrolyzed and create bubbles inside the chamber, which obstructed the blood stream. At very low volumetric flow rate, unlike most of RBCs, some WBCs adhered to the electrode edge until strong negative force was exercised on the WBCs.

## CONCLUSION

The continuous flow DEP microsystems have successfully demonstrated the ability to switch the flow stream of blood cells between multiple outlet channels and to separate the WBCs from whole blood sample according to their native dielectric properties without the need for tagging or chemical modification of the blood sample. The presented microseparators combined further with miniaturized downstream cell detection and analysis system are expected to enable efficient and novel separation of suspended cells in blood with the potential for portability, reduced fabrication and operation cost, and future development of clinical point-of-care devices for abnormal cell isolation, analysis, and treatment.

## REFERENCES

- [1] P. R. C. Gascoyne, J. V. Vykoukal, J. A. Schwartz, T. J. Anderson, D. M. Vykoukal, K. W. Current, C. McConaghy, F. F. Becker, and C. Andrews, "Dielectrophoresis-based programmable fluidic processors," *Lab on a Chip*, vol. 4, pp. 299-309, 2004.
- [2] F. F. Becker, X. B. Wang, Y. Huang, R. Pethig, J. Vykoukal, and P. R. C. Gascoyne, "SEPARATION OF HUMAN BREAST-CANCER CELLS FROM BLOOD BY DIFFERENTIAL DIELECTRIC AFFINITY," *Proceedings of the National Academy of Sciences of the United States of America*, vol. 92, pp. 860-864, Jan 1995.
- [3] S. Fiedler, S. G. Shirley, T. Schnelle, and G. Fuhr, "Dielectrophoretic sorting of particles and cells in a microsystem," *Analytical Chemistry*, vol. 70, pp. 1909-1915, May 1998.
- [4] C. H. Tai, S. K. Hsiung, C. Y. Chen, M. L. Tsai, and G. B. Lee, "Automatic microfluidic platform for cell separation and nucleus collection," *Biomedical Microdevices*, vol. 9, pp. 533-543, Aug 2007.
- [5] I. Doh and Y. H. Cho, "A continuous cell separation chip using hydrodynamic dielectrophoresis (DEP) process," *Sensors and Actuators a-Physical*, vol. 121, pp. 59-65, May 2005.
- [6] Y. L. Li, C. Dalton, H. J. Crabtree, G. Nilsson, and K. Kaler, "Continuous dielectrophoretic cell separation microfluidic device," *Lab on a Chip*, vol. 7, pp. 239-248, 2007.

# CONTROLLED PICO-GRAM MATERIAL PLACEMENT ON SUSPENDED STRUCTURES USING SOLUTION WICKING

S. S. Bedair<sup>1</sup> and G. K. Fedder<sup>1</sup>

<sup>1</sup>Carnegie Mellon University, Pittsburgh, Pennsylvania, USA

## ABSTRACT

A fabrication method using inkjet printing of chemically sensitive materials into a suspended microgroove is explored. This involves wicking dissolved polymer into a suspended structure via a capillary groove running its length using surface tension forces. A “well” at the base of the suspended microgroove serves as the target for the inkjet drop. This work presents the theory behind the controlled material dosing, the fabrication method limits and the dried polymer profile measurements in the suspended capillary structures.

## INTRODUCTION

There has been a tremendous amount of work in miniaturized gas vapor detectors implementing several detection modes including: chemresistors, chemcapacitors and mass sensors. Arrayed and integrated sensors are needed for total gas analysis and discrimination [1] [2]. Arrayed sensors as well as arraying sensor modes necessitate a single-chip, multi-material fabrication method. Device scale deposition techniques that have been implemented include ink-jet printing [3] [4], micro-capillary deposition [5] and dip-pen nano-lithography [6 Piner]. For this work, drop-on-demand inkjet printing provides rapid ‘functionalization’ and multi-material placement. It is a mask-less process and pL quantities of solution can be deposited. Prior work includes successful deposition of multi-materials on mass-sensitive cantilever arrays using inkjet printing and micro-capillary deposition [5]. However, device scaling and narrow gaps are difficult with these methods.

In contrast, this work addresses a method to make inkjet printing compatible with scaled device size and  $\mu\text{m}$  and sub- $\mu\text{m}$  scaled air gaps. This is done by designing a well which serves as the target for the inkjet drop as shown in Fig. 1. A micro-capillary runs the length of the sensor device and upon solvent drying material originally suspended in solution is left in the capillary and on the scaled device.

We have previously shown a mass sensitive (75fg/Hz sensitivity) CMOS-MEMS cantilever oscillator with a  $2\ \mu\text{m}$  wide groove running its length as a successful vapor detector (Fig. 2 left) [3]. We explored a further scaled micro-slot cantilever design and showed a 25fg/Hz mass sensitivity (Fig. 2 right) [7]. Both demonstrate the proof of concept behind this method of polymer loading into micron-scaled cantilevers without destruction of the device or the narrow electrostatic gaps. This work addresses the theory, the microgroove aspect ratio limits, and the characterization of the dried polymer profile in the grooves. We demonstrate that this technique is not limited to mass sensitive materials, the solvent used or the concentration of the inkjet drop.

## THEORY

The theory of solute transfer in MEMS micro-capillaries is extended from the ‘coffee ring’ formation theory [8]. Consider a solution loaded well and capillary as illustrated in Fig. 1 where the capillary has length,  $L_c$ , height,  $h_c$ , and width,  $w_c$ . The solvent has density,  $\rho$ , and an evaporation rate per unit surface area  $J_s$  [ $\text{kg}/\text{m}^2/\text{sec}$ ]. The solvent mass rate of change,  $\rho \frac{\partial h_c}{\partial t} dx \cdot w_c$

[ $\text{kg}/\text{sec}$ ], in the differential element,  $dx$ , is described by

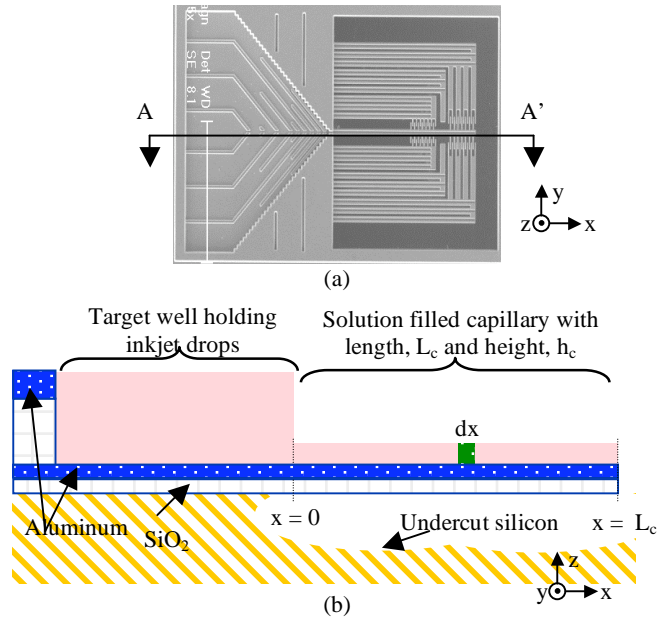


Figure 1: (a) Scanning electron micrograph (SEM) of the top view of the well and the capillary. (b) The cross section (A-A') illustrating the well with the inkjet drops and the filled capillary running the length of a MEMS device.

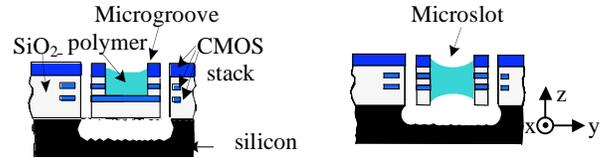


Figure 2: Cross sections of suspended micro-groove (left) and micro-slot (right) with dried polymer.

$$\rho \frac{\partial h_c}{\partial t} dx \cdot w_c = \rho w_c h_c v(x,t) - \rho w_c h_c v(x+dx,t) - J_s w_c dx \quad (1)$$

where the first term is the amount of solvent flowing into  $dx$ , the second term is the amount flowing out of  $dx$  and the final term describes the solvent mass loss due to evaporation from the top surface of the capillary. The velocity profile of the solvent as a function of time,  $t$ , and space,  $x$ , is described by  $v(x,t)$  where  $x=0$  is the entrance from the well into the capillary. The gradient of the velocity profile is described by

$$\frac{dv(x,t)}{dx} = -\frac{J_s}{h_c \rho} - \frac{1}{h_c} \frac{\partial h_c}{\partial t} \Rightarrow \frac{dv(x,t)}{dx} = -\frac{J_s}{h_c \rho} \quad (2)$$

The capillary height,  $h_c$ , does not change with time since the volume fill rate of solution from the well due to surface tension forces is much higher than the total volume of solvent evaporated from the capillary. This is a valid assumption for “short” capillary lengths,  $L_c < 500\ \mu\text{m}$ , based on calculations as well as experimental verification.

By similar analysis, the concentration profile,  $c(x,t)$  [ $\text{kg}$  of solute/ $\text{m}^3$  of solvent], is described by

$$\frac{\partial}{\partial t} (c(x,t)) = -\frac{\partial}{\partial x} (c(x,t)v(x,t)) + D \frac{\partial^2}{\partial x^2} c(x,t) \quad (3)$$

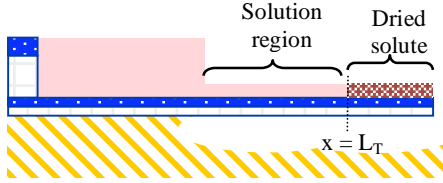


Figure 3: Cross section illustrating the drying process in the capillary. The dried solute extends from the end to  $L_T$ .

where  $D$  is the diffusion coefficient of the solute in the solution. Equations (2) and (3) are two coupled PDEs describing the solute transfer phenomenon with the following boundary conditions

$$\frac{v(0,t)}{dx} = -\frac{J_s}{h_c \rho}, \quad v(L_c, t) = 0 \quad (4a)$$

$$c(0,t) = c_o + \alpha \cdot t, \quad \frac{\partial c(L_c, t)}{\partial x} = 0 \quad (4b)$$

where  $c_o$  is the concentration of the inkjet drop and  $\alpha$  is a fitting coefficient. Equations (4a) and (4b) indicate that at the end of the capillary channel the solution velocity and the flux of solute are both zero. The solution concentration at the beginning of the channel varies linearly with time. The gradient of the velocity at the beginning of the channel is constant.

In Equation (2),  $J_s$  is assumed to be constant for a dilute solution concentration. However, once the concentration reaches a critical concentration,  $c_r$ , the solute originally suspended in solution becomes a semi-solid material with solvent diffusing out to the evaporation interface. A concentration dependent evaporation and, thus, velocity gradient describes this transition region

$$\frac{dv(x,t)}{dx} = -\frac{J_s}{h_c \rho} \cdot \frac{1}{1 + \exp\left[\frac{c(x,t) - c_r}{\mu}\right]} \quad (5)$$

where  $\mu$  is a transition coefficient.

During the drying process the concentration increases at a higher rate at the end of the capillary channel,  $L_c$ . Once the concentration at the end reaches a critical concentration,  $c_r$ , the solute once suspended in solution is considered a solid. Once a solid forms the velocity of the solution at this transition point becomes zero. The solute drying process, therefore, begins at the end of the capillary channel then recedes back. Figure 1 shows the profile of the solution in the well and capillary at an initial time,  $t_o$  where the drying process has begun. At later times Fig. 3 illustrates what the profile would be where  $x = L_T$  denotes the location of the transition between the solution and the solid solute.

## RESULTS

### Numerical Simulations

Equations (3) and (5) were solved by finite element analysis (FEA) using Comsol Multiphysics. The nondimensional quantities

$$x^* = \frac{x}{L_c}, \quad t^* = A \cdot t, \quad c^*(x^*, t^*) = \frac{c(x^*, t^*)}{c_r}, \quad v^*(x^*, t^*) = \frac{v(x^*, t^*)}{AL_c} \quad (6)$$

$$A = \frac{J_s}{h_c \rho} \quad (6a)$$

are substituted in Eqns. (3) and (5) to form the normalized coupled partial differential equations

$$\frac{dv^*(x^*, t^*)}{dx^*} = -\frac{1}{1 + \exp\left[\frac{c_r}{\mu} (c^*(x^*, t^*) - 1)\right]} \quad (7)$$

$$\frac{\partial}{\partial t^*} (c^*(x^*, t^*)) + \frac{\partial}{\partial x^*} (c^*(x^*, t^*) v^*(x^*, t^*)) - \frac{D}{AL_c^2} \frac{\partial^2}{\partial x^{*2}} c^*(x^*, t^*) = 0 \quad (8)$$

Channel length, $L_c$	120 $\mu\text{m}$
Channel height, $h_c$	3.2 $\mu\text{m}$
Solute density, $\rho$	1500 $\text{kg}/\text{m}^3$
Solute diffusion:evaporation ratio, $D/J_s$	$10^{-8} \text{m}^4/\text{kg}$
Initial solution concentration, $c_o$	5 $\text{kg}/\text{m}^3$
Solution to solid transition concentration, $c_r$	1000 $\text{kg}/\text{m}^3$
Well concentration fitting coefficient, $\alpha$	1.3 $\text{g}/\text{m}^3/\text{sec}$
Transition coefficient, $\mu$	50

Table 1: Channel dimensions and solution material properties.

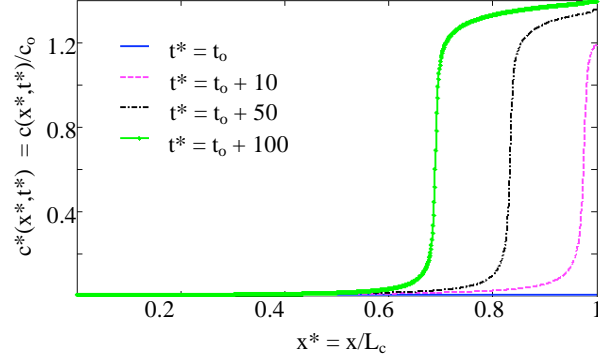


Figure 4: Concentration profile,  $c^*(x^*, t^*)$  at different times,  $t^*$ .

The parameters listed in Table 1 are used in the numerical analysis. Figure 4 shows the normalized concentration profiles along the capillary channel length at varying times during the drying process. The concentration increases at a higher rate at the end of the channel. At later times there is a large transition in the concentration. This is where  $L_T$  is located.

### Experiments

An array of suspended microgroove capillaries was fabricated using post-CMOS (Jazz 0.35  $\mu\text{m}$  BiCMOS) fabrication steps [3]. The final step involves polymer deposition using inkjet printing into the target well area. Three drops of 5  $\text{kg}/\text{m}^3$  of polythiophene suspended in trichlorobenzene (TCB) were deposited at the base of the suspended capillary with width, height, and length of 2  $\mu\text{m}$ , 3.2  $\mu\text{m}$  and 120  $\mu\text{m}$ , respectively. Trichlorobenzene is the solvent chosen for the experiments because of its ‘‘low’’ evaporation rate. Solvents with higher vapor pressures evaporate too fast to track the evaporation process with the current experimental setup. Figure 5 shows the snapshots in time of the solution drying. An arrow in each picture indicates the solution-solid transition region,  $L_T$ .

Video images of the drying process were taken at 10 frames per second. In each frame the transition between the ‘light’ and ‘dark’ portion in the channel is tracked. The initial concentration of the drop,  $c_o$ , was varied. The transition region was monitored for three drops with varying initial concentrations: 0.5  $\text{kg}/\text{m}^3$ , 1  $\text{kg}/\text{m}^3$ , 2.5  $\text{kg}/\text{m}^3$ , 5  $\text{kg}/\text{m}^3$  and 7.5  $\text{kg}/\text{m}^3$ . Figure 6 shows the normalized transition region location as a function of time for the various solution concentrations. Both the measured and the FEA model using  $A = 2.5$  are shown. There are two regions to note: an ‘accumulation region’ where there is some initial time for the solid solute to form at the end of the channel and the ‘solidification region’ where the transition location decreases with time. For the FEA data, the ‘accumulation region’ is located at  $t < 31$  sec,  $t < 28$  sec,  $t < 13.5$ ,  $t < 7.5$  sec and  $t < 5$  sec for the 0.5  $\text{kg}/\text{m}^3$ , 1  $\text{kg}/\text{m}^3$ , 2.5  $\text{kg}/\text{m}^3$ , 5  $\text{kg}/\text{m}^3$  and 7.5  $\text{kg}/\text{m}^3$  concentrations, respectively. For the measured data, this region is only seen with concentrations of 0.5  $\text{kg}/\text{m}^3$ , 1  $\text{kg}/\text{m}^3$ , 2.5  $\text{kg}/\text{m}^3$  at the respective times of  $t < 40$  sec,  $t < 26$  sec and  $t < 12$  sec. The ‘solidification region’ begins after these respective times.

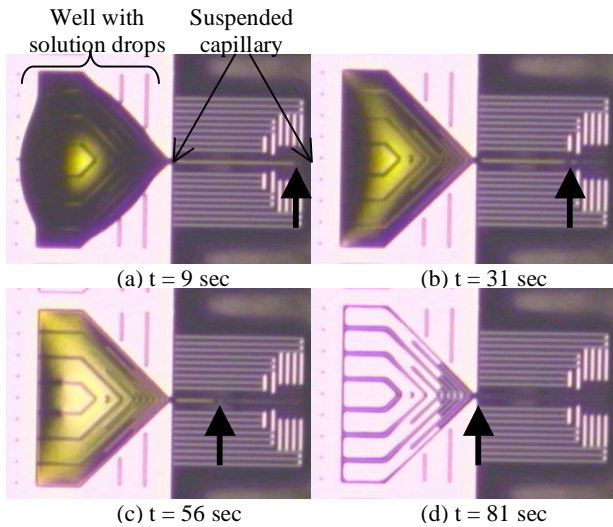


Figure 5: Images of the well and the suspended capillary ( $2 \mu\text{m}$  width,  $3.2 \mu\text{m}$  height and  $120 \mu\text{m}$  length) during the drying process after three  $5 \text{ kg/m}^3$  solution drops. An arrow in each image indicates the solution-solid transition location,  $L_T$ .

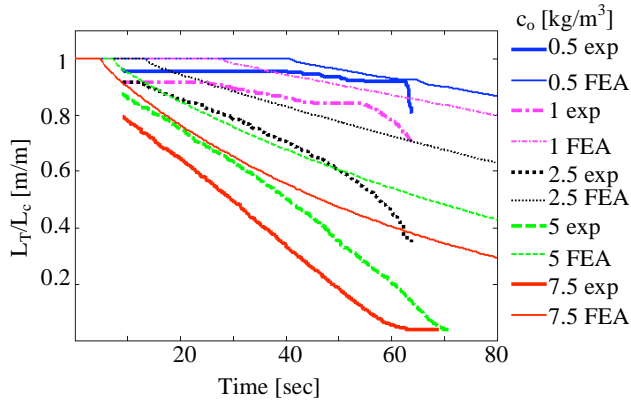


Figure 6: The measured transition location,  $L_T$ , after 3 solution drops of polythiophene in TCB with varying  $c_o$ . This is compared with the FEA model ( $A = 2.5$ ).

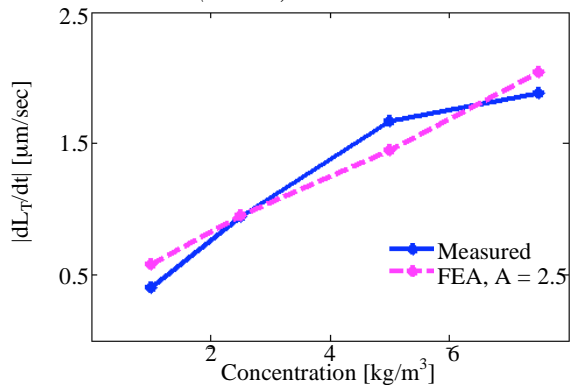


Figure 7: The measured and FEA solidification rate,  $|dL_T/dt|$ , versus the initial drop concentration.

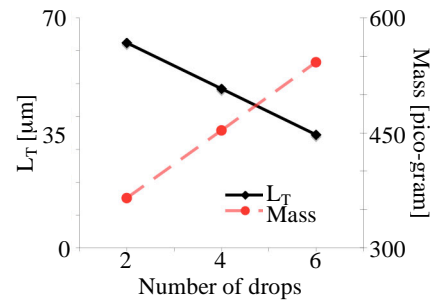


Figure 8: Polymer extent and corresponding mass after solvent drying with  $1 \text{ kg/m}^3$  of solution concentration.

At the initial measurement time, there is an apparent offset between the measured and FEA  $L_T$ . This is an artifact of the optics for the  $0.5 \text{ kg/m}^3$ ,  $1 \text{ kg/m}^3$  and  $2.5 \text{ kg/m}^3$  concentrations. However, for the larger concentrations the solidification begins at a time before the initial measurement time. During solidification, the measured fill rate digresses from the model at approximately  $t > 45$  sec for the  $1 \text{ kg/m}^3$  concentration,  $t > 55$  sec for the  $2.5 \text{ kg/m}^3$  concentration, and  $t > 35$  sec for the  $2.5 \text{ kg/m}^3$ ,  $5 \text{ kg/m}^3$  and  $7.5 \text{ kg/m}^3$  concentrations. This is probably due to a non-linear increase in concentration in the well area.

A small ‘dark’ region was observed at distances close to the solidification front,  $L_T$ . This region merges with the solidification front at later times during the drying process. This merger is seen as a ‘flat’ region in the curves in Fig. 6. This flat region is observed at times equal to 58 sec, 45 sec, 68 sec and 63 sec for the  $0.5 \text{ kg/m}^3$ ,  $1 \text{ kg/m}^3$ ,  $5 \text{ kg/m}^3$  and  $7.5 \text{ kg/m}^3$ .

The fill rate magnitude,  $|dL_T/dt|$ , is shown in Fig. 7 and compared to the model for varying initial concentrations. The measured fill rates are calculated between the time when the solidification begins and the merging time. For the FEA data, the rates indicated in Fig. 7 are calculated at the times shortly after solidification.

The number of drops was varied using an initial concentration of  $1 \text{ kg/m}^3$  and the final  $L_T$  was measured after complete solvent drying (see Fig. 8). The corresponding mass of the loaded material is indicated in the figure. With a proper number of drops the dried solute extent from the end of the channel can be set. This method provides controlled material placement from dilute solutions with a 100 pico-gram per drop resolution with a  $1 \text{ kg/m}^3$  initial concentration.

Capillary structures with varying groove aspect ratios and  $200 \mu\text{m}$  lengths were fabricated and the solidification front was monitored using 3 drops of  $5 \text{ kg/m}^3$  of polythiophene in TCB with each of the structures. The fill rate versus channel width with two channel heights,  $h_c$ , is shown in Fig. 9. There is a large aspect ratio dependence on the drying process. The meniscus of the liquid in the capillary has a large effect on the drying process and the solidification rate. The effective evaporation rate per unit surface area is observed to be larger with larger aspect ratio structures where the aspect ratio =  $h_c/w_c$ . In Fig. 9, the solidification rate dependence on the channel width varies with the channel height.

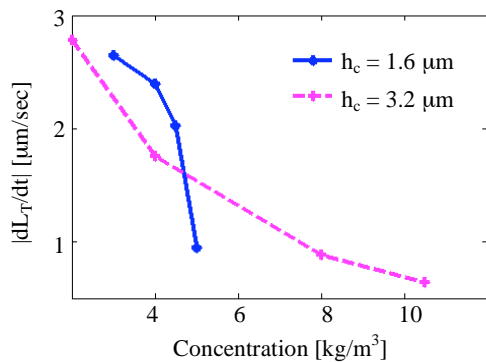


Figure 9: The measured solidification rate using 3 drops of 5 kg/m<sup>3</sup> in channels with varying aspect ratios.

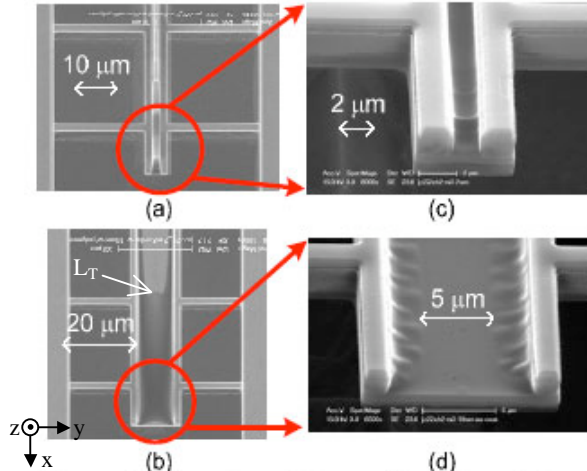


Figure 10: Top (a & b) and angled (c & d) SEM views of 1.8 μm and 10.5 μm wide grooves. The height for both structures is 3.2 μm.

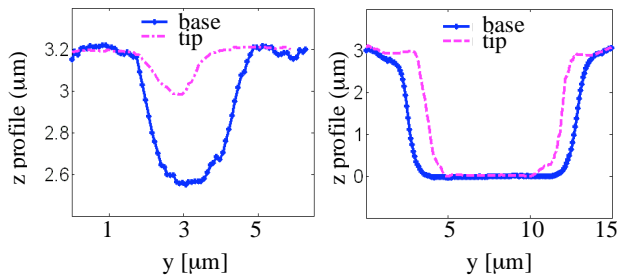


Figure 11: Measured polymer profile at the base and tip for the 1.8 μm wide (left) and 10.5 μm wide (right) grooves.

### Profile measurements

The scanning electron microscope images of two grooves with different aspect ratios are shown in Fig. 10 after solute solidification. The chip was sputter coated with gold for SEM contrast. The groove widths are 1.8 μm and 10.5 μm. Both grooves have 3.2 μm heights. The final polymer extent,  $L_T$ , is visible for the 10.5 μm groove (Fig. 11b). Profile measurements were taken using a white light interferometer. These are shown in Fig. 11. The profile of the dried material is dependent on the capillary groove aspect ratio. The meniscus effect is evident with the wider groove. There is more dried material along the channel sidewalls with the wider groove indicating that the 2-D evaporation profile must be considered with wider grooves. A maximum width for sustained capillary action was measured to be 7 μm and 14 μm for the 1.6 μm and 3.2 μm tall grooves,

respectively. At larger widths the solution fills and dries in the corners of the grooves.

### CONCLUSIONS

Inkjet printing into micro-capillaries is a viable mechanism for controlled, repeatable material placement. The theory of solute transfer in MEMS micro-capillaries is extended from the ‘coffee ring’ formation theory. The numerical analysis from the theory matches qualitatively with the experimental measurements of the ‘accumulation region’ and the solidification front. The experiments and FEM simulations verify that Eqn. 5 is a viable approach to handling the evaporation rate in the solution to solid transition regime. The accumulation time and the solidification rate are dependent on the initial concentration used.

Further experiments and analyses are needed to quantify two effects: the concentration change with time in the well and the evaporation rate dependence on the meniscus. The solution concentration in the well was assumed to be linear for the current model. However, it is evident that at later drying times this is not the case. This is probably due to the change in the exposed surface area at the times when the well begins to run out of solution. At these times the well is partial filled with solution.

### ACKNOWLEDGEMENTS

The authors thank Suresh Santhanam for post-CMOS MEMS fabrication and Lawrence Schultz for polymer preparation and jetting. This work is funded in part by NIOSH/CDC (contract 200-2002-00528) and a grant from AFOSR.

### REFERENCES

- [1] D. Lange, C. Hagleitner, A. Hierlemann, O. Brand, and H. Baltes, “Complementary Metal Oxide Semiconductor Cantilever Arrays on a Single Chip: Mass-Sensitive Detection of Volatile Organic Compounds”, *Analytical Chemistry*, 74, 13, (2002).
- [2] J. R. Stetter and W. R. Penrose, “Understanding Chemical Sensors and Chemical Sensor Arrays (Electronic Noses): Past, Present, and Future”, *Sensors Update*, 4, (2002).
- [3] S. S. Bedair and G. K. Fedder, “Polymer wicking to mass load cantilevers for chemical gravimetric sensors,” *IEEE Transducers '05*, Seoul, Korea, pp. 2035-9.
- [4] P. Cooley, D. Wallace and B. Antohe, “Applications of ink-jet printing technology to BioMEMS and microfluidic systems”, *SPIE Conf. on Micromachining and Microfabrication*, 2001.
- [5] A. Bietsch, J. Zhang, M. Hegner, H. P. Lang, and C. Gerber, “Rapid functionalization of cantilever array sensors by inkjet printing”, *Nanotechnology*, 15, (2004).
- [6] R. D. Piner, J. Zhu, F. Xu, S. Hong and C.A. Mirkin, “Dip Pen’ Nanolithography”, *Science*, 283, 661 (1999).
- [7] S. S. Bedair and G. K. Fedder, “Polymer mass loading of CMOS/MEMS microslot cantilever for gravimetric sensing”, *IEEE Sensors '07*, Atlanta, Georgia, pp 1164-7.
- [8] R. D. Deegan, O. Bakajin, T. F. Dupont, G. Huber, S. R. Nagel and T. A. Witten, “Contact line deposits in an evaporating drop”, *Physical Review E*, 62, 1, (2000).

# OPTICAL IMAGE-BASED DYNAMIC MANIPULATION OF AQUEOUS DROPLETS IMMERSED IN OIL MEDIUM

Sung-Yong Park<sup>1</sup>, Ting-Hsiang Wu<sup>2</sup>, Kenneth Wei<sup>1</sup>, Sheraz Kalim<sup>3</sup>, Caitlin Callahan<sup>3</sup>,  
Michael Teitell<sup>3</sup> and Eric P.Y. Chiou<sup>1</sup>

<sup>1</sup>The Department of Mechanical and Aerospace Engineering, University of California at Los Angeles,  
43-147 Eng. IV, 420 Westwood Plaza, Los Angeles, CA 90095-1597, USA

<sup>2</sup>The Department of Electrical Engineering, University of California at Los Angeles, USA

<sup>3</sup>The Department of Pathology and Pediatrics, University of California at Los Angeles, USA

## ABSTRACT

We report on an optically reconfigurable microfluidic platform enabling large scale, parallel processing of oil-immersed aqueous droplets on a featureless photoconductive glass substrate using direct optical images. Aqueous droplets containing chemical and biochemical contents are manipulated by optical image-patterned virtual electrodes through dielectrophoretic (DEP) forces to perform various droplet manipulation functions including (1) continuous 2D transport, (2) droplet merging, (3) and parallel processing of sixteen droplets. Our platform promises a low cost, silicon-coated microfluidic system for large scale, multiplexed droplet-based biochemical analysis.

## INTRODUCTION

Droplet-based microfluidic systems have the potential for high-throughput and speed chemical and biological analysis<sup>1-4</sup>. Thousands of highly uniform, isolated aqueous droplets containing chemical reagents can be generated in immiscible oil within seconds by flow-focusing devices. Applications such as fluorescent detection of millisecond chemical kinetics, laser Raman spectroscopic probing, and PCR reactions for high throughput DNA amplification have been demonstrated using droplet-based microfluidic devices<sup>5-7</sup>. A major difficulty associated with a droplet-based microfluidic system is in achieving active control of individual droplets confined in microchannels being driven by a continuous oil flow<sup>2-6</sup>. It has been shown that multiple droplets can be individually addressed in an open oil chamber using physically patterned electrodes, although complex wiring and interconnection issues arise for addressing numerically large droplet arrays<sup>8, 9</sup>. To solve this problem, a microfluidic device integrating a high voltage CMOS driving circuit recently achieved active and parallel droplet control. However, this approach increases the fabrication cost of microfluidic devices, which are often preferred to be disposable<sup>10</sup>.

Alternatively, a light-induced manipulation mechanism has been widely investigated to solve the wiring issues that arise for controlling a large array of electrodes<sup>11-14</sup>. For example, optoelectronic tweezers (OET) has recently been shown to manipulate single cells and microscopic particles sandwiched between an ITO electrode and a photoconductive electrode created by direct optical images<sup>14</sup>. However, due to impedance mismatch, it is difficult to modulate the electric field strength in electrically insulating mediums, such as oils used in two phase droplet based microfluidic systems, on an OET device since all of the applied voltage drops across the oil layer even without light illumination.

Our group has previously reported a novel floating electrode optoelectronic tweezers (FEOET) mechanism<sup>15</sup> enabling optical actuation of oil-immersed aqueous droplets using a circular laser beam with intensity as low as  $4 \mu\text{W}/\text{mm}^2$ . However, droplet movement is limited to a linear motion along the direction of electric field in the previous FEOET device, which strongly restricts its potentials in chemical and biological applications. Here, we demonstrate two-dimensional droplet manipulation functions on a

FEOET platform by utilizing diamond-shaped virtual electrodes patterned by a spatial light modulator. This opens up the possibility of massively parallel droplet manipulation on a featureless, silicon coated glass substrate using dynamic and reconfigurable optical images. Optically patternable virtual electrodes generate dielectrophoretic (DEP) forces to manipulate aqueous droplets containing chemical and biochemical contents and to perform various microfluidic functions such as two-dimensional transport, droplet merging and parallel processing of sixteen droplets.

## DEVICE STRUCTURE AND WORKING PRINCIPLE

Figure 1 shows the schematic structure of a FEOET device. It is fabricated by coating a glass wafer with two featureless a-Si:H layers ( $0.5\text{-}\mu\text{m}$  undoped and  $0.1\text{-}\mu\text{m}$   $n^+$ ). Two aluminum electrodes with a 6-cm lateral gap are deposited at the two edges of this device by e-beam evaporation and lift-off techniques. The Al electrodes also serve as an etching mask for removing the  $n^+$  a-Si:H layer using Reactive Ion Etcher (RIE). The  $n^+$  a-Si:H layer provides ohmic contacts with the Al electrodes. An open poly-dimethylsiloxane (PDMS) chamber housing aqueous droplets and immiscible oil (corn oil) is fixed on top of the undoped a-Si:H layer.

The previously reported FEOET device in our group was able to actuate an aqueous droplet by light-induced DEP forces with an intensity as low as  $4 \mu\text{W}/\text{mm}^2$ , an intensity promising a large area droplet manipulation platform with a regular and commercially available optical projector without extra optics components. However, DEP force induced on FEOET is dependent upon the direction of applied electric field and shape of optical virtual electrodes. In our previous experiment of droplet actuation using a circular light beam, DEP force induced in the direction parallel to

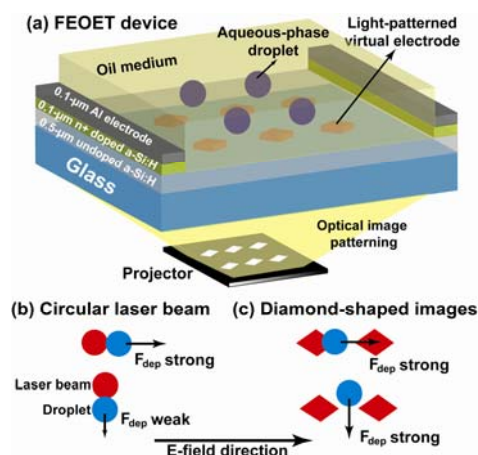


Figure 1: (a) Schematic structure of a FEOET device. (b) DEP forces induced by a circular light spot are weak in the direction perpendicular to applied field. (c) DEP forces induced by two diamond shaped virtual electrodes are strong in both parallel and perpendicular directions.

the applied electric field is strong, but the force in the perpendicular direction is weak (Fig. 1b). This limits the droplet motion to one direction, which restricts FEOET's future applications.

To provide FEOET two-dimensional manipulation functions, we propose to trap a droplet between the gap of two diamond-shaped virtual electrodes as shown in Fig. 1c. This unique shape of virtual electrode is able to provide a droplet with the same order of magnitude DEP forces in both directions parallel and perpendicular to the applied field.

## SIMULATION RESULTS

Numerical simulations of a three-dimensional electric field distribution in a FEOET chamber and on a droplet surface are performed using COMSOL Multiphysics 3.2. To reduce the simulation time, the device is simplified to two layers: a 5- $\mu\text{m}$  thick undoped a-Si:H and a 350- $\mu\text{m}$  thick oil medium. A 100 V DC bias is applied at the two end planes along the x direction, and a 300- $\mu\text{m}$  diameter aqueous droplet is loaded in a  $1.4 \times 0.8 \text{ mm}^2$  oil chamber. The dark conductivity of the homogeneous a-Si:H layer is assumed to be  $10^{-8} \text{ S/m}$ .

To compare the DEP forces induced by both a circular light beam and two diamond-shaped virtual electrodes, the circular light beam is assumed to have a 200- $\mu\text{m}$  full width half maximum (FWHM) spot size and it induces a peak photoconductive of  $10^{-4} \text{ S/m}$  in the center. The same peak photoconductivity is also assumed in the case of diamond-shaped virtual electrodes with a 200- $\mu\text{m}$  separation gap. The Maxwell stress tensor has been applied for calculating DEP forces on droplets<sup>16</sup>.

### Case of a Circular Laser Beam Illumination

Figure 2 shows the simulated electric field distribution around a droplet located at 150  $\mu\text{m}$  away from the center of a light beam along the direction parallel (Fig. 2a) and perpendicular (Fig. 2b) to the applied electric field.

Droplet actuation on FEOET results from the electrostatic dipole-dipole interactions between the droplet and virtual electrodes. Without light illumination, a droplet-induced dipole generates a symmetrical electric field distribution around a droplet surface, resulting in zero net DEP forces for transportation. To actuate a droplet, one can illuminate a light beam at one edge of a droplet to break this field symmetry around a droplet. As shown in Fig. 2(a), the electric field at the illumination side is greatly reduced, resulting in net DEP forces moving the droplet away from the light beam. The calculated DEP force is  $F_{dep} = [-9.46, 0.02, -2.87] \times 10^{-9} \text{ N}$ , corresponding the forces in x, y, z directions, respectively. The 0.02 nN force in the y direction comes from numerical errors.

Transporting droplet in the y direction, however, is not as effective as the one in the x direction using a circular light beam. Illuminating a droplet edge at the direction perpendicular (y direction) to the electric field fails to transport the droplet since the electric field strength difference between the illuminated and un-illuminated sides on the droplet surface is too small as shown in Fig. 2(b). The calculated DEP forces in this situation is  $F_{dep} = [-0.00, 0.12, 2.55] \times 10^{-9} \text{ N}$ . The y direction force is 78.8 times smaller than that of the x direction force in Fig. 2(a). For this reason, a circular light beam is not able to provide the required shape of virtual electrodes for 2D transportation in FEOET devices.

### Case of a Paired Diamond-Shaped Virtual Electrode

Figure 3 shows the simulation results of a droplet trapped by two diamond-shaped virtual electrodes. Without loading a droplet the electric field strength at the gap between these two electrodes is strongly enhanced (Fig. 3a at the top). When a droplet is loaded at 150  $\mu\text{m}$  away from the gap center along the x direction (Fig. 3b), the

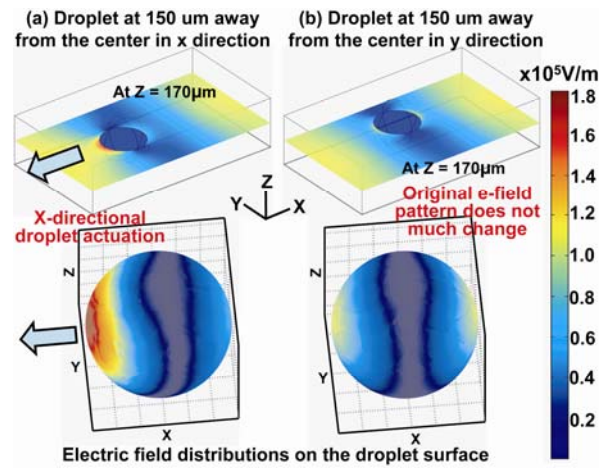


Figure 2: Numerical simulations of the electric field distributions by a circular laser beam illumination. (a) A droplet is located at 150  $\mu\text{m}$  away from the center along the x direction. (b) A droplet is located 150  $\mu\text{m}$  away from the center along the y direction.

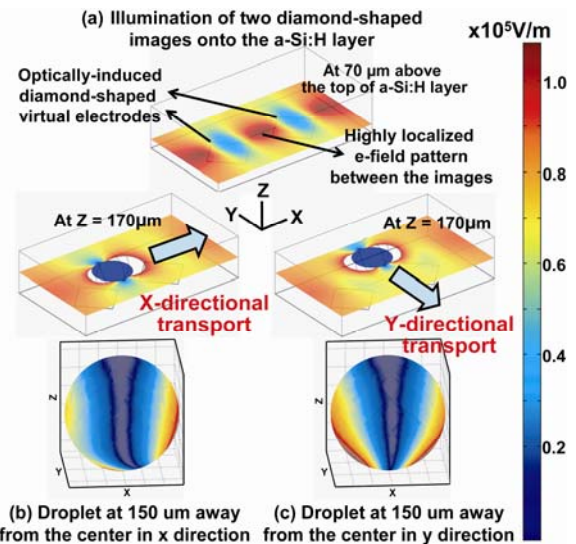


Figure 3: (a) Electric field distribution induced by two closely positioned diamond-shaped virtual electrodes separated by a 200  $\mu\text{m}$  gap. The strong electric field region is created at the gap. (b) A droplet is located 150  $\mu\text{m}$  away from the center along the x direction. The unbalanced e-field pattern in the x direction causes DEP force to drive and trap it to the right. (c) A droplet is located 150  $\mu\text{m}$  away from the center along the y direction. The e-field pattern is symmetric in x direction but asymmetric in the y direction, producing a net DEP force to attract the droplet back to the center

enhanced electric field can generate DEP forces pulling the droplet back to the center of the gap. The calculated DEP forces are  $F_{dep} = [1.45, 0.00, -2.48] \times 10^{-8} \text{ N}$ . The DEP force in the x direction is to the case of a circular laser beam.

For the situation of positioning a droplet 150  $\mu\text{m}$  away from the gap center along the y direction, the DEP force shows a dramatic increase compared to the y direction force in the case of a circular light beam. As shown in Fig. 3(c), the calculated DEP forces in this situation are  $F_{dep} = [0.00, -0.64, -2.51] \times 10^{-8} \text{ N}$ . The y direction force

is only 2.26 times smaller than the x direction force in the Fig. 3(b) situation. This value shows a dramatic improvement compared to the 78.8 times smaller in the circular light beam case. This y direction force is able to provide effective trapping and transporting of a droplet in the y direction. This also realizes the two-dimensional droplet manipulation functions on FEOET devices.

## EXPERIMENTAL DEMONSTRATIONS

With the capability of two-dimensional transport enabled by a paired diamond-shaped electrode, we have successfully demonstrated several important droplet manipulation functions on our FEOET platform, including continuous 2D transport, droplet merging, and parallel processing of 16 droplets.

Figure 4 shows the photo of a FEOET device with a  $6 \times 6 \text{ cm}^2$  active optical manipulation area. Two Al electrodes are applied by a 5 kV bias to power the entire device. Although the voltage is high, but the power consumption of the whole device is  $0.4 \mu\text{W}$  in the dark state and less than 4 mW in the bright state due to the large electrical impedance of the oil and a-Si:H thin film ( $\sim 10^{14} \Omega$  in the dark state) in the lateral direction.

Figure 5 shows the video snapshots of a 1.47 mm aqueous droplet containing the Trypan blue dye being trapped at the gap between two diamond-shaped virtual electrodes and transported in both x and y directions by reconfiguring projected optical images. The droplet transport speed is  $721 \mu\text{m}/\text{sec}$  in the x direction and  $363 \mu\text{m}/\text{sec}$  in the y direction. The two times difference between the speeds in the x and y direction matches well with the DEP force difference predicted in the simulation results in Fig. 3(b) and (c) using a  $300 \mu\text{m}$  droplet. Figure 6 shows that two 1-mm droplets containing yellow and green food coloring dyes are individually transported and merged together. When two aqueous droplets are driven close and aligned in the electric field direction, dipole-dipole interaction between two droplets induces electrocoalescence and combines two droplets together<sup>17</sup>.

Figure 7 demonstrates the flexibility and compatibility of FEOET devices with other microfluidic structures such as microwells. An example shown here is an array of PDMS microwells structure being positioned on top of a FEOET device. These wells are preloaded with aqueous solutions containing the Trypan blue dye and immersed in oil environment. A 1.28-mm de-ionized water droplet is transported by a paired diamond-shaped virtual electrode and delivered to the target well to dilute the dye concentration in that well.

The low light intensity requirement of FEOET and the two dimensional droplet transportation function realized by diamond-shaped virtual electrodes promise an FEOET platform

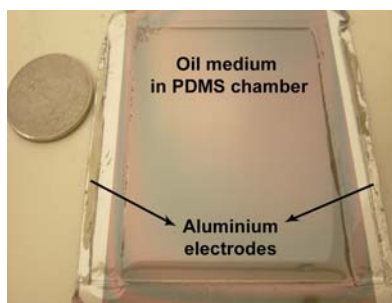


Figure 4: The photo of a FEOET device. The active area allowing optical manipulation of oil-immersed aqueous droplets is  $6 \times 6 \text{ cm}^2$ . A 5 kV electrical bias is applied through the two Aluminium electrodes to power this device.

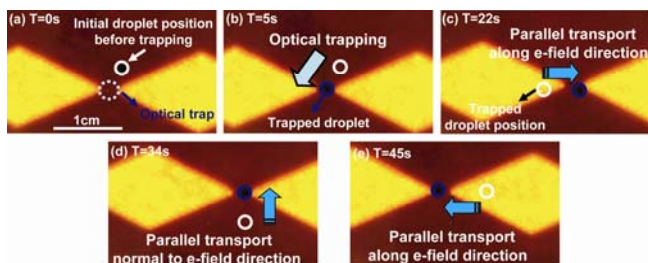


Figure 5: The video snapshots showing two-dimensional optical manipulation of a 1.47-mm droplet containing the Trypan blue dye on a FEOET device. The white and blue circles indicate droplet positions before and after movement (a) and (b) Two diamond-shaped virtual electrodes create strong electric field between the gap to trap the droplet. (c) The trapped droplet is transported to the right hand side along e-field direction. (d) The droplet is driven to the top side perpendicular to e-field direction. (e) It moves to the left hand side again.

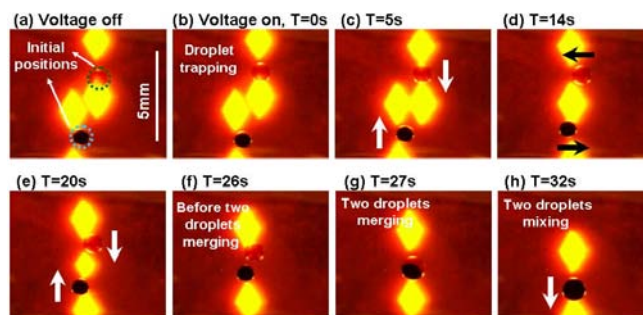


Figure 6: The video snapshots showing two 1-mm droplets containing different coloring dyes (yellow and green ones) are transported to merge.

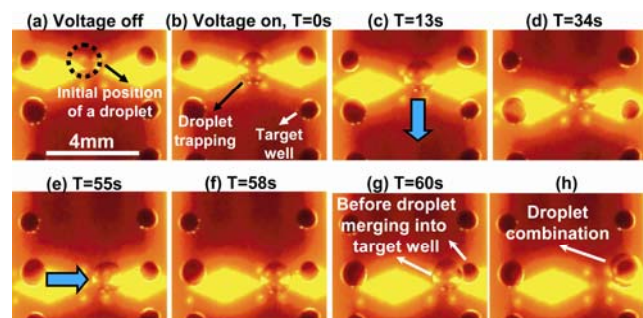
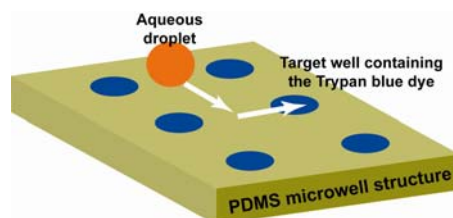


Figure 7: Snapshots of the video showing the function of delivery of aqueous droplets to target wells among an array of PDMS wells positioned on FEOET. (a) and (b) A 1.28-mm de-ionized water droplet is optically trapped between two diamond-shaped images. (c) through (g) Two-dimensional transport of the droplet is achieved by the corresponding optical image motions. (h) Finally, the droplet is merged into the target well containing Trypan blue.

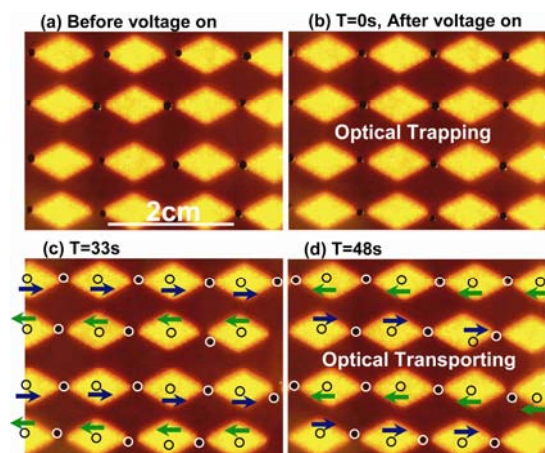


Figure 8: The video snapshots showing the large-scale, parallel manipulation of sixteen droplets of trypan blue dye with the range between 1.3-mm and 0.84-mm diameter. The black circles indicate the droplet position in previous step, while the white circles present the droplet position in the current step. a), (b) An array of diamond-shaped optical images generate sixteen traps and attract droplets between their gaps. (c),(d) Parallel transport of trapped droplets by dynamic optical images. (c) The droplets in the first and third rows are driven to the right side, while the droplets in the second and fourth rows are guided to the left.

capable of massively parallel processing a large number of droplets for high throughput chemical and biochemical screening applications. Figure 8 shows an example of parallel transporting 16 droplets. The droplet size in this experiment varies from 1.3-mm to 0.84-mm in diameter. Fig. 8(a) and (b) show the arrays of diamond-shaped virtual electrodes generate sixteen traps and position droplets between their gaps. In Fig. 8(c) and (d), the trapped droplets are transported to the left and right directions in parallel.

## CONCLUSIONS

We report on an optically reconfigurable microfluidic platform enabling parallel processing of oil-immersed aqueous droplets on a photoconductive glass substrate using direct optical images. This platform is realized by using paired diamond-shaped optically patterned virtual electrodes that allow transporting droplets on a two-dimensional FEOET surface. With this platform, we have demonstrated several important droplet manipulation functions including continuous 2D droplet transport, droplet merging and parallel processing of 16 droplets. This FEOET system is also compatible with other microfluidic structures such as an array of microwells. Our platform promises a low cost, droplet-based, microfluidic system for large scale, multiplexed chemical and biochemical screening applications.

## ACKNOWLEDGEMENTS

This project is supported by the NSF CAREER Award (ECCS-0747950), by the NIH Roadmap for Medical Research Nanomedicine Initiative PN2EY018228, and in part by NIH grants CA90571 and CA107300.

## REFERENCES

[1] D. Albrecht, G. Underhill, A. Mendelson S. Bhatia, "Multiphase electropatterning of cells and biomaterials", *Lab on a Chip*, **7**, 702-709 (2007).

[2] T. Tan, K. Hettiarachchi, M. Siu, Y. Pan, A. Lee, "Controlled microfluidic encapsulation of cells, proteins, and microbeads in lipid vesicles," *Journal of the American Chemical Society* **128**, 5656-5658 (2006).

[3] L. Li, J. Q. Boedicker, R. F. Ismagilov, "Using a multijunction microfluidic device to inject substrate into an array of preformed plugs without cross-contamination: Comparing theory and experiments", *Analytical Chemistry*, **79**, 2756-2761 (2007).

[4] D. Chen, L. Li, S. Reyes, D. Adamson, R. Ismagilov, "Using three-phase flow of immiscible liquids to prevent coalescence of droplets in microfluidic channels: Criteria to identify the third liquid and validation with protein crystallization", *Langmuir*, **23**, 2255-2260 (2007)

[5] H. Song, R. F. Ismagilov, "Millisecond kinetics on a microfluidic chip using nanoliters of reagents," *Journal of the American Chemical Society* **125**, 14613-14619 (2003).

[6] G. Cristobal, L. Arbouet, F. Sarrazin, D. Talaga, J. Bruneel, M. Joanicot, L. Servant, "On-line laser Raman spectroscopic probing of droplets engineered in microfluidic devices", *Lab Chip*, **6**, 1140-1146 (2006).

[7] M. Curcio, J. Roeraade, "Continuous segmented-flow polymerase chain reaction for high-throughput miniaturized DNA amplification", *Analytical Chemistry*, **75**, 1-7 (2003).

[8] J. Schwartz, J. Vykoukal, P. Gascoyne, "Droplet-based chemistry on a programmable micro-chip", *Lab on a Chip*, **4**, 11 (2004).

[9] Lee, C. C. et al., "Multistep synthesis of a radiolabeled imaging probe using integrated microfluidics", *Science*, **310**, 1793-1796 (2005).

[10] N. Manaresi, A. Romani, G. Medoro, L. Altomare, A. Leonardi, M. Tartagni, R. Guerrieri, "A CMOS chip for individual cell manipulation and detection," *IEEE Journal Of Solid-State Circuits* **38**, 2297-2305 (2003).

[11] A. Ohta, A. Jamshidi, J. Valley, H-Y Hsu, M. Wu, *Appl. Phys. Lett.* **91**, 074103 (2007).

[12] A. Ohta, P. Chiou, H. Phan, S. Sherwood, J. Yang, A. Lau, H. Hsu, A. Jamshidi, M. Wu, *J. Selec. Top. in Quantum electronics* **13**, 235-241 (2007).

[13] P. Y. Chiou, H. Moon, H. Toshiyoshi, C.J. Kim, M. C. Wu, "Light actuation of liquid by optoelectrowetting", *Sensors and Actuators a-Physical* **104**, 222-228 (2003).

[14] P. Y. Chiou, A. T. Ohta, and M. C. Wu, "Massively parallel manipulation of single cells and Microparticles using optical images", *Nature*, **436**, 370-372 (2005).

[15] S-Y. Park, C. Pan, T-H. Wu, S. Kalim, M. Teitell, and P.Y. Chiou, "Floating Electrode Optoelectronic Tweezers (FEOET): A Novel Mechanism Enabling Optical Manipulation of Oil Immersed Aqueous Droplets", in *Proceeding of the 11th International Conference on Miniaturized Systems for Chemistry and Life Sciences ( $\mu$ TAS) in Paris, France, Oct. (2007).*

[16] C. Rosale, K. Lim, "Numerical comparison between Maxwell stress method and equivalent multipole approach for calculation of the dielectrophoretic force in single-cell traps", *Electrophoresis* (2005), **26**, 2057-2065.

[17] J. Eow, M. Ghadiri, "Drop-drop coalescence in an electric field: the effects of applied electric field and electrode geometry", *Colloids and Surfaces A: Physicochem. Eng. Aspects* **219** (2003) 253-279.

# SMART MICROFABRICATED CHEMICAL PRECONCENTRATOR

R. P. Manginell<sup>1</sup>, D. R. Adkins<sup>2</sup>, M. W. Moorman<sup>1</sup>, R. Hadizadeh<sup>3</sup>, D. Copic<sup>3</sup>, D. Porter<sup>3</sup>, J. M. Anderson<sup>1</sup>,  
D. R. Wheeler<sup>1</sup>, K. B. Pfeifer<sup>1</sup> and A. Rumpf<sup>1</sup>

<sup>1</sup>Sandia National Laboratories, Albuquerque, NM

<sup>2</sup>Defiant Technologies, Inc., Albuquerque, NM

<sup>3</sup>University of Louisville, Louisville, KY

## ABSTRACT

The mass-sensitive smart preconcentrator (SPC) can determine when it has collected sufficient sample for analysis by a downstream chemical sensor system. The SPC consists of a Lorentz-Force-actuated MEMS resonator with an integral heater and surface coating for the collection of chemical analytes. The resonant frequency of the device varies with the mass of collected analyte. The limit of detection (LOD) of the SPC is less than 50 ppb for DMMP (dimethyl-methyl-phosphonate). At 1 ppm, 1 second collection of DMMP is sufficient to trigger analysis in a downstream microsystem. This paper gives a brief overview of the SPC and its integration into microanalytical systems. The theory of operation, which is applicable to other torsional oscillators, is used to predict a shear modulus of silicon(100) of  $G = 57.0 \text{ GPa} \pm 2.2 \text{ GPa}$ .

## INTRODUCTION

### Field Sensing and Preconcentration

A system approach, employing sample preconcentration, separation and detection functions, is necessary in reliable field detection units in order to separate target analytes from interferants [1-2]. Unlike previous microfabricated preconcentrators [3-7], this paper describes the first instance of a mass-sensitive microfabricated smart preconcentrator (SPC) for use in chemical detection microsystems [Fig. 1].

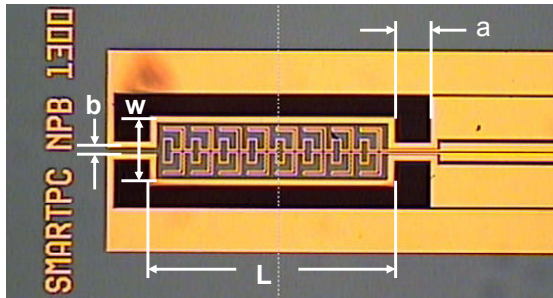


Figure 1: Top view photo and model dimensions.

### Operation

The smart preconcentrator (SPC) combines mass sensing and preconcentration functions, permitting it to determine when it has collected sufficient analyte for analysis by a downstream chemical microsystem. The SPC consists of a MEMS resonator with an integrated heater, and is constructed by silicon-on-insulator (SOI) micromachining [8]. It is similar in form to the oscillators described by Howe and Muller [9] and Evoy et al. [10], except that here Lorentz-force driving and electrical impedance measurements are used. Fig. 2 shows that a free-standing paddle of silicon is suspended from a silicon frame by two torsional beams. An AC current,  $i$ , passes through a metal transducer line on the right side of the paddle. This current interacts with a transverse, in plane magnetic field,  $B$ , generated by a pair of miniature permanent magnets situated along the die edges (not shown). The Lorentz Force ( $F \sim i \cdot B$ ) creates a torque on the paddle that changes sign

with the phase of the AC current oscillation. Sweeping the frequency of the drive current can be used to locate the resonant frequency of the SPC; the resonant frequency is measured via the induced current ( $i_p$ ) on the transducer line, shown on the left side of the paddle in Fig. 2. During use, the SPC has a thin-film adsorbent layer deposited on its surface to collect chemical analytes of interest. As analytes are adsorbed, the mass change of the system is measured by a change in  $i_p$ . When the mass change is sufficient for a downstream detection system, the serpentine heater is pulsed with a square wave voltage to rapidly heat and desorb the collected analyte. The SPC reaches a desorption temperature of  $200 \text{ }^\circ\text{C}$  in 20 msec, consuming 100 mW steady-state at that temperature.

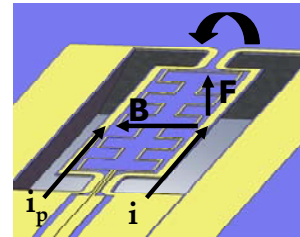


Figure 2: Solid model of the active area of the SPC. The drive current ( $i$ ) and magnetic field ( $B$ ) interact to create the Lorentz force ( $F$ ) that causes rotation of the paddle about the long symmetry axis of the torsional beams, as indicated by the block arrow. The induced pickup current ( $i_p$ ) is measured during operation.

## THEORY

The equation of motion [11] for the SPC is

$$I_m \ddot{\theta} + \gamma \dot{\theta} + k\theta = \frac{BwLi}{2}, \quad (1)$$

where  $\theta$  describes the angular motion around the central axis of symmetry generated by the Lorentz force. The right hand side of Eqn. 1 is the torque generated by the Lorentz force. The physical dimensions and parameters are shown in Figs. 1 and 2, with the exception of the oscillator thickness,  $c$ , which proceeds into the page in Fig. 1. Respectively, the moment of inertia, damping constant and torsion constant are

$$\begin{aligned} I_m &= \rho w c L \left( \frac{c^2 + w^2}{12} \right) \\ k &= 2 \frac{G}{a} b c^3 \beta \\ \gamma &= \frac{\sqrt{k I_m}}{Q} \end{aligned} \quad (2)$$

The  $Q$  of the oscillation appears in the denominator of the damping

constant. The density of the oscillator is  $\rho$  and the shear modulus of silicon is  $G$ .  $\beta$  is a dimensionless constant that depends on the ratio  $b/c$ , and has a limiting value of 1/3 for thin paddles. Eqn. (1) is solved in [11] in terms of the pickup impedance and current, and the sensitivity of the SPC to added mass is also derived. For the purposes of this discussion, we will restrict ourselves to the resonant frequency of the SPC:

$$\omega_o = \sqrt{\frac{k}{I_m}} = \sqrt{\frac{24\beta bc^2 G}{\rho w c L (c^2 + w^2)}} \quad (3)$$

To easily account for the mass of the metal lines and a thin adsorbent ( $t \ll c$ ), an effective density can be defined

$$\rho = \frac{M + \rho_{Si} w c L}{w c L} \quad (4)$$

$M$  takes into account the collective mass of the metal lines and the adsorbent, and  $\rho_{Si}$  is the silicon density. Defining a surface adsorption density  $\sigma$  [ $\text{g}/\text{cm}^2$ ] of adsorbed analyte, the resonant frequency with adsorbed analyte becomes

$$\omega_n = \sqrt{\frac{24\beta bc^2 G}{\rho w a L (\rho c + \sigma)(c^2 + w^2)}} \quad (5)$$

Equation (3) can be used to determine the shear modulus of silicon based on measured resonant frequency. The amount of adsorbed mass can be determined from Equation (5).

## FABRICATION

### Microfabrication

The microfabrication process is illustrated in Fig. 3. Silicon on insulator wafers (SOI) are used for starting material. The wafers nominally have a 5 micron device layer, a 1 micron BOX and 400 micron handle (Figure 3a). The first step is deposition and lift-off patterning of the metal heater and transducer lines (solid black boxes in Figure 3b) over a thin dielectric isolation layer (not shown). Metal patterning is followed by etching of two ‘u’-shaped patterns through the device layer, stopping on the BOX (buried oxide). Figure 3c provides side and top views of this step. This step defines the lateral dimensions of the paddle and suspension beams, while the thickness of the resonator ( $c$ ) is determined by the starting device layer thickness. In the final step, Figure 3d, the entire paddle is undercut by etching through the wafer, from the opposite side to the BOX. Alignment of the etch mask to the front side patterns is achieved using a Karl Suss MA/6 contact aligner. Both KOH and Bosch etching have been used for the latter etch step, though Figure 3d is indicative of Bosch etching given the sidewall angle illustrated. The choice of etching method does not influence device performance.

### Adsorbent coating

Subsequent to microfabrication, layers of adsorbent and reference materials are applied to the SPCs. Hydrogen-bond acid modified sol gels, which are selective towards organophosphonate compounds, were mainly used in this work. An automated spray system was developed for this purpose. An electrically-heated, computer-controlled stepper stage was used to raster several shadow-masked SPCs at a time under an ultrasonic nebulizer (Sono-Tek Corp, Milton, NY). The number of passes under the nebulizer controlled the thickness of the adsorbent.

Throughout the course of testing it was discovered that

uncoated SPCs, intended as reference devices, had non-negligible sensitivity to low levels of analyte through non-specific adsorption. Aminosilanes were synthesized and applied to both sol gel coated and uncoated SPCs. These contained a fluorinated alkyl chain to provide a reagent that would both lower the surface energy of a surface and passivate the surface. This functionalization chemistry can be performed in solution or in the gas phase. A 10 wt%/vol solution of  $\text{Me}_2\text{NMe}_2\text{SiCH}_2\text{CH}_2\text{C}_6\text{F}_{13}$  was generated in toluene. This solution was used to passivate reference SPCs, some of which were functionalized with a high surface area silica sol gel. The surfaces were allowed to react at room temperature for 30 minutes in solution followed by rinsing with toluene and air drying. The aminosilane functionalization of the silica gel did not appreciably affect its interaction with DMMP. Functionalization of bare resonators did, however, decrease the interaction of DMMP with the resonator, as seen below.

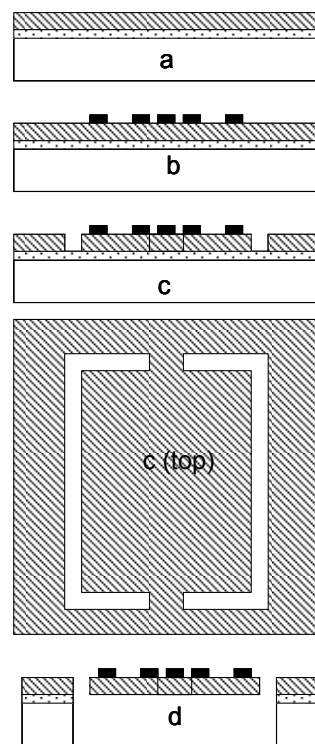


Figure 3: Microfabrication process steps illustrated in cross section and top views.

## CONTROL CIRCUIT

To drive the oscillator and measure its response to analyte capture, the circuit of Fig. 4 was developed. In brief, a ring oscillator is used to drive the circuit into resonance by driving one of the transducer wires on the paddle. This driving scheme is also illustrated in Fig. 2. The trans-impedance amplifier (Trans.) produces an output voltage proportional to the pickup current in the other transducer line. This voltage is input into a phase-locked loop (PLL) and compared with the PLL's onboard oscillator frequency. The oscillator frequency is controlled by a digital potentiometer (Dig. Pot), allowing computer control of the oscillator circuit. During initial set up, the circuit is auto tuned using the micro-controller and digital pot to the resonant frequency of the SPC. In subsequent operation, frequency changes brought

on by analyte challenges move the circuit away from the PLL oscillator frequency and an error voltage is produced. The error voltage is thus proportional to the frequency changes with exposed analyte. The error is sent through a 4-pole active low pass filter (Filter) and coupled to an A/D converter (ADC) via a calibration amplifier. The circuit is set such that 1 mV of error is equivalent to 1 Hz of frequency. The microcontroller (PIC16C62B) also has the ability to measure the frequency directly via a multiplexed counter circuit implemented on the board. Interface with a host PC is accomplished using RS-232 and a host shell program written in Visual-Basic. The heater portion of the circuit (Heat) is activated by the PIC to rapidly heat the SPC to its desorption temperature once sufficient analyte has been collected. The electrical low connection on the heater is connected to ground (not shown).

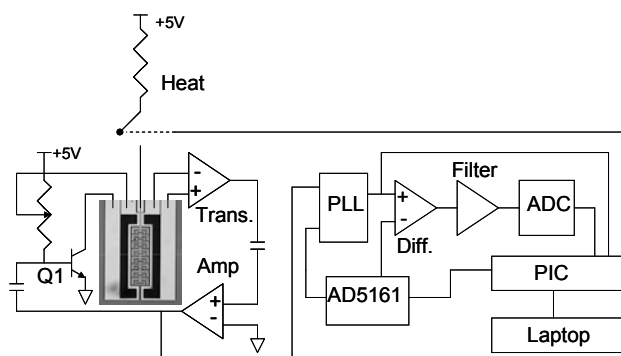


Figure 4: Oscillator circuit for autotuning and mass loading measurements. The desorption heater circuit (Heat) is switched by the PIC when the mass loading is adequate for the downstream system.

## TESTING

The SPC was inserted into drop-in test fixtures like those shown in Fig. 5. This packaging simultaneously creates a fluidic seal and electrical contact to the devices. When the plastic lids are fastened to the PEEK manifold, o-ring seals and miniature spring contacts are simultaneously compressed. A vapor generation system was developed to challenge the SPCs. A Lindberg-Blue oven (New Columbia, PA) was used to control the temperature of a diffusion vial containing DMMP. The flow rate of nitrogen through the system and the physical dimensions of the diffusion vial determined the concentration of DMMP delivered to the SPC. All flow lines exterior to the oven were heated in an insulated trunk line to prevent unwanted condensation. Test fixtures were connected to the output of the vapor system, while the control circuit of Fig. 4 was used for acquiring data. Raw data is shown in Fig. 6 for the response of an SPC to 400 ppbv of DMMP. The trace labeled 'sensor' is for an SPC coated with sol gel. The relatively flat response of the 'reference' device is due to the aminosilane treatment, mentioned above. After an initial precipitous drop, the sensor response tails off until the heater is pulsed at about 140 seconds and the response begins to return to baseline. The response of the SPC was tested down to 146 ppbv of DMMP, the minimum of the vapor system used.

In Figure 7, the time required for two devices to obtain a S/N ratio of 3:1 was determined as a function of concentration; the response times of the two devices were averaged to obtain the plot

of Fig. 7. This shows that as the concentration increases, the response time for the SPC to detect DMMP drops to less than 1 second. With typical preconcentrators an arbitrary collection time, normally set at one minute or greater, would be required. Therefore, the SPC diminishes collection times by a minute or more at high concentrations.

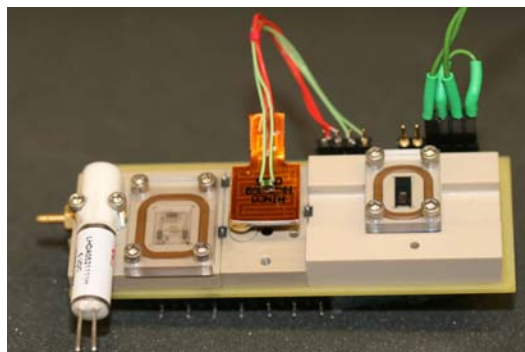


Figure 5: Packaging of a SPC (right), micro gas chromatograph with Minco heater (center), SAW array sensor (left) and Lee minivalve (far left). Electrical connections are made between the PCB and devices via miniature spring contacts. Miniature magnets (not shown) are placed in the recesses to either side of the SPC.

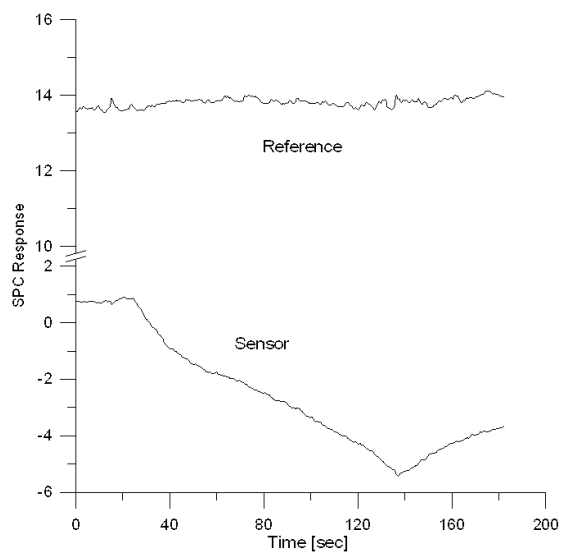


Figure 6: Response of an SPC to 400 ppbv of DMMP. The vertical axis is broken to allow simultaneous viewing of the sensor & reference response.

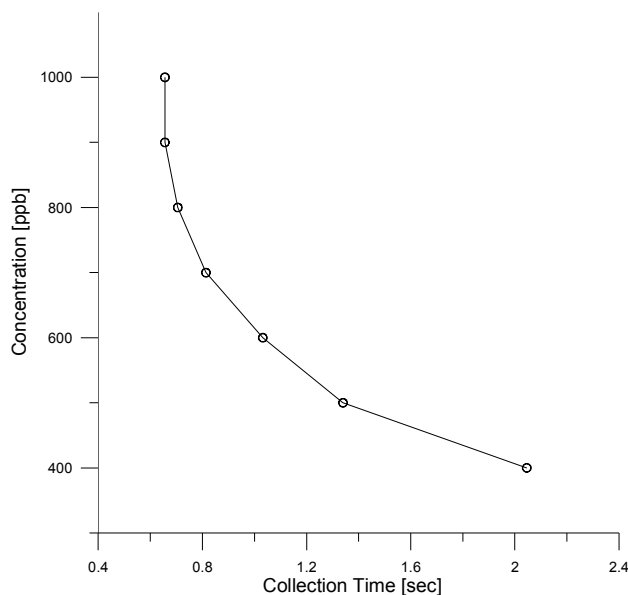


Figure 7: Response time required to reach 3:1 S/N as a function of concentration of DMMP.

## DISCUSSION

Several design variations were fabricated, and their resonant frequencies were measured (Table 1). In all cases,  $L = 1500$  micron,  $a = 200$  micron and  $c = 5$  micron were fixed. The values of  $\beta$  were taken from [12]. Based on Eqn. (3) the shear modulus of silicon (100) was predicted.

Table 1: Measured resonant frequency and predicted value of  $G$ .

Device	Resonant Frequency (kHz)	$\beta$	$G$ Predicted (GPa)	$w$ (micron)	$b$ (micron)
1	19.6	0.318	56.0	500	180
2	17.0	0.316	55.0	500	140
3	14.6	0.317	60	600	160
4	11.9	0.318	56.0	700	180
5	9.8	0.316	47.5	700	140

The average shear modulus of Si (100) from this analysis is  $54.9 \text{ GPa} \pm 5.5 \text{ GPa}$ . If  $47.5 \text{ GPa}$  is treated as an outlier, the average shear modulus becomes  $57.0 \text{ GPa} \pm 2.2 \text{ GPa}$ . In an analysis of nanopaddle oscillators Evoy [10], predicted that the modulus of SOI silicon (100) is 1.5 to 2 times lower than literature values. In a more detailed analysis Dowell [13] predicted a Young's modulus of  $122 \text{ GPa}$ ; this is more consistent with commonly stated range of  $E = 130 - 169 \text{ GPa}$ , but is still up to 28% softer. With the exception of the results for device 5, the present work predicts a shear modulus of Si (100) that falls in the range reported by Kim [14] of  $51 - 79 \text{ GPa}$ . Indeed, the average shear modulus, including the outlier, is in this range. Li [15] did report that SOI Si (100) is about 20% softer than nominal bulk silicon values. If this degree of softening is applied to the range given by Kim, the acceptable range of shear modulus for Si (100) drops to  $41 - 63 \text{ GPa}$ . The average shear modulus predicted here is also in this range.

## CONCLUSIONS

The SPC has the ability to detect when it has collected sufficient analyte for analysis by a downstream system. Ordinary preconcentrators, macro or micro-sized, would require an arbitrary collection time, wasting time at high concentrations. The SPC allows analysis times to be shortened drastically when ambient chemical concentrations are greatest, and most dangerous as in the case of toxic chemicals. Systems based on the SPC can have collection cycle times as short as 1 second with specificity at lethal concentrations. This is comparable, or shorter in duration than IMS-based systems. The existing SPC design has a LOD less than  $50 \text{ ppb}$  at 3:1 signal to noise. The theory of operation also allows for optimization of the SPC performance, and can be used in the measurement of the shear modulus of silicon.

## ACKNOWLEDGMENTS

The authors would like to thank many of the project staff of MESA, PETL and the IMRL at Sandia. The authors would like to acknowledge the financial support Sandia National Laboratories LDRD program. Sandia is a multiprogram laboratory operated by Sandia Corporation, a Lockheed Martin Company for the United States Department of Energy's National Nuclear Security Administration under contract DE-AC04-94AL85000.

## REFERENCES

- [1] E. B. Overton, et al., "Fast GC Instrumentation and Analysis for Field Applications," *Field Analytical Chemistry and Technology*, 5, 97 (2001).
- [2] P.R. Lewis, et al., "Recent Advancements in the Gas Phase Microchemlab," *IEEE Sensors Journal*, 6, 784 (2006).
- [3] R. P. Manginell and G. C. Frye-Mason, "Chemical Preconcentrator," U.S. Patent 6,171,378, January 9, 2001.
- [4] R. P. Manginell, et al., "Two dimensional modeling and simulation of mass transport in microfabricated preconcentrators," *IEEE Sensors Journal*, 7, 1032 (2007).
- [5] W. C. Tian, et al., "Microfab. Preconcentrator-Focuser for a Microscale Gas Chromatograph," *JMEMS*, 12, 264 (2003).
- [6] R. P. Manginell, et al., "Non-Planar Chemical Preconcentrator," U.S. Patent 7,118,712, October 10, 2006.
- [7] A. M. Ruiz, et al., "Membrane-Suspended Microgrid as a Gas Preconcentrator for Chromatographic Applications," *Sensors and Actuators A*, 135, 192 (2007).
- [8] R. P. Manginell, et al., "Mass-Sensitive Chemical Preconcentrator," U. S. Patent 7,168,298, January 30, 2007.
- [9] R. T. Howe and R. S. Muller, "Resonant-Microbridge Vapor Sensor," *IEEE Trans. Electron Devices*, ED-33, 499 (1986).
- [10] S. Evoy, et al, "Nanofabrication & electrostatic operation of paddle oscillators," *J. Appl. Physics*, 86, 6072 (1999).
- [11] R. P. Manginell, et al., "Mass Sensitive Microfabricated Chemical Preconcentrator," submitted to *JMEMS*.
- [12] H. Ford and J. Alexander, *Advanced Mechanics of Materials*, 2<sup>nd</sup> Ed. New York: John Wiley & Sons Inc., 1977.
- [13] E. H. Dowell et al., "Mathematical Model of a Nanopaddle Oscillator," *J. Appl. Phys.*, 90, pp. 5606-5611, December 2001.
- [14] J. Kim, D. Cho, and R. S. Muller, "Why is (111) Silicon a Better Mechanical Material for MEMS?," in *Transducers 2001 and EuroSensors XV*, 1 (2001) pp. 662-665.
- [15] X. Li, et al., "Mechanical Properties of Monocrystalline Silicon Thin Films Measured by Different Methods," in *2006 IEEE International Symposium on Micro-NanoMechatronics and Human Science* (2006) pp. 1-6.

# AN AGILE TIP-TILT-PISTON MICROMIRROR WITH LARGE APERTURE, LARGE SCANNING RANGE AND LOW DRIVING VOLTAGE

Kemiao Jia, Sagnik Pal, and Huikai Xie

Department of Electrical and Computer Engineering, University of Florida, Gainesville, FL 32611, USA

## ABSTRACT

This paper presents the design, fabrication and test results of an electrothermally-actuated tip-tilt-piston micromirror with a large optical aperture size of 1 mm. The mirror has a mechanical rotation angle of  $\pm 6^\circ$  about both x- and y- axis and displaces 141  $\mu\text{m}$  in z-axis all at dc voltages of less than 6 V. Dynamic test of the micromirror shows the electrothermal response time of each actuator is about 20 ms. The resonant frequencies of the piston and rotation motion are 664 Hz and 714 Hz, respectively. The large tip-tilt-piston scanning capability at low driving voltage makes this type of devices suitable for biomedical imaging and laser beam steering applications.

## INTRODUCTION

MEMS micromirrors have been widely used in various applications including optical communications, displays, medical imaging, and motion tracking [1]-[9]. For adaptive optics, optical phase arrays, and optical phase modulators, micromirrors with tip-tilt-piston (TTP) capability are required, which have been demonstrated using electrostatic, electrothermal and piezoelectric actuation [10]-[14][16][18]. Among various actuation mechanisms, electrothermal actuators usually are not very fast and consume relatively high power. On the other hand, electrothermal micromirrors produce large scan ranges at low driving voltages, making them very suitable for medical imaging applications, especially endoscopic imaging applications in which operating frequency is not high and power consumption is not critical.

Various bimorph-based electrothermal TTP micromirrors have been demonstrated [14]-[18]. For instance, Jain *et al.* demonstrated an electrothermal micromirror using a DRIE CMOS-MEMS process [15]. The device generated a maximum piston motion of 0.5 mm and tip/tilt optical scan angle of  $\pm 30^\circ$  at less than 15V DC. However, its mirror plate had a large lateral shift in the piston mode and its rotation axes of the tip/tilt modes shifted vertically during scanning. The large lateral shift of the mirror plate significantly reduces the effective optical aperture size, and the rotation-axis shift causes difficulty in optical alignment and image processing. In order to solve the lateral shift problem, Wu *et al.* developed a three-segment bimorph actuator design that achieved near lateral-shift-free large vertical actuation [16]. But its tip/tilt scan patterns are not horizontal, and the rotation-axis shift, though smaller, still exists. Todd *et al.* proposed an S-shaped, inverted-series-connected (ISC) bimorph actuator to overcome both mirror plate shift and rotation axis shift problems [17]. The ISC concept is illustrated in Fig. 1. With a single bimorph, as shown in Fig. 1(a), there exists a lateral shift and a tangential tilt angle at the tip of the bimorph. If two bimorphs with opposite layer compositions are connected in series to form an S-shaped beam, as shown in Fig. 1(b), the tilting angle at the tip of the second bimorph is compensated. However, the lateral shift still remains. If two S-shaped beams are connected with the second one inverted, as shown in Fig. 1(c), both the lateral shift and the tilt angle will be compensated. Jia *et al.* demonstrated the first working TTP micromirror based on this ISC bimorph actuation concept, but the scanning ranges were small and there were problems due to aluminum sidewall pileup and structural asymmetry [18]. Furthermore, the joints of the S-shaped beams in Fig. 1(b) and Fig. 1(c) are fragile.

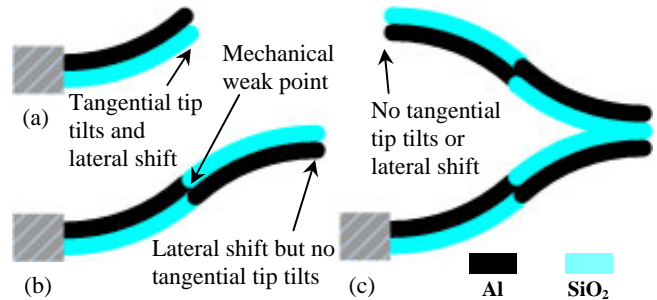


Fig. 1 ISC concept evolution. (a) Single bimorph with lateral shift and tangential tip tilt. (b) Series-connected bimorphs with zero tip tilt but nonzero lateral shift. (c) Inverted-series-connected bimorphs with zero tip tilt and zero lateral shift.

In this paper, we present a single-crystal-silicon based TTP micromirror employing a new ISC bimorph design that solves the above mentioned problems. The design, fabrication and test of the device will be presented and discussed in the following sections.

## DEVICE DESIGN AND FABRICATION

The new ISC bimorph actuator design is illustrated in Fig. 2(a), where the main improvement is adding an overlap at the middle of each S-shaped bimorph beam. The length of the overlap is optimized to approximately 1/3 of the total beam length to achieve maximum initial elevation of the mirror plate. The width of the overlap is widened to strengthen the connection as well as increase the stiffness of the actuator. Also, platinum instead of poly-silicon is used as the heater material. The temperature of the beams can be changed by applying a voltage to the Pt resistors embedded along the bimorph beams. By connecting four pairs of ISC actuators to the four sides of a square or circular mirror plate, tip-tilt-piston operation can be realized by controlling the voltages applied to the resistors. The 2D schematic of the device is shown in Fig. 2(b).

When a same voltage is applied to the four actuators simultaneously, the mirror plate moves vertically without any lateral shift. When different voltages are applied to the actuators, the mirror plate performs tip-tilt scanning. As shown in Fig. 2, point B, which connects a bimorph actuator to the mirror plate, moves pure vertically if the bimorph beam is heated evenly. This condition is achieved by embedding a heater along the entire bimorph path. When a same dc voltage is applied to all the four actuators and a pair of differential ac voltage signals is applied to one pair of opposing actuators, *i.e.*, Act 1 and Act 3, the mirror plate will rotate about the y-axis and the rotation axis is structurally fixed by the other two opposing actuators, *i.e.*, Act2 and Act4. Thereby, both piston motion decoupled from rotation and tip-tilt scanning with a fixed rotation axis can be obtained.

The fabrication process of the device is shown in Fig. 3. It starts from a bare silicon wafer. First, a 1 $\mu\text{m}$  thick PECVD SiO<sub>2</sub> is deposited and patterned to form the bimorphs that require SiO<sub>2</sub> to be the bottom layer (Fig. 3a). Then, the wafer is patterned, followed by a 0.25 $\mu\text{m}$  thick Cr-Pt-Cr sputtering and lift-off (Fig. 3b). After a thin SiO<sub>2</sub> layer is deposited, aluminum lift-off is performed to define the bimorphs and the mirror plate (Fig. 3c). This step has been modified from the previously reported process to solve the aluminum

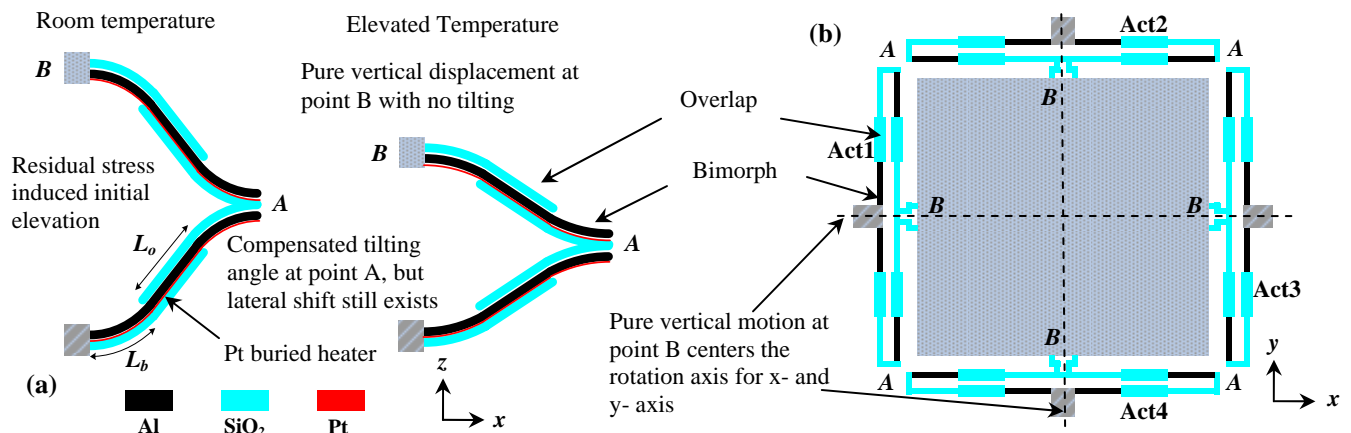


Fig. 2 (a) New ISC bimorph actuation concept. (b) Actuator configuration for the tip-tilt-piston mirror with centered rotation axes.

sidewall pileup problem [18]. Next, a second SiO<sub>2</sub> layer is deposited and patterned to form the bimorphs that require SiO<sub>2</sub> to be the top layer (Fig. 3d). A backside silicon etch is then proceeded to form the cavity under the mirror plate and the actuators, leaving a controllable thickness (~50  $\mu\text{m}$ ) of silicon to support the mirror plate (Fig. 3e). Finally, a front side silicon etch-through followed by an isotropic undercut is done to release the device (Fig. 3f).

An SEM of a fabricated device is shown in Fig. 4(a), where the mirror plate is 1 mm by 1 mm with an initial elevation of 141  $\mu\text{m}$ . Fig. 4(b) shows some details of a bimorph actuator and mechanical connections. Notice that in Fig. 4(c) a device with the mirror plate below the substrate surface is also obtained by simply swapping SiO<sub>2</sub> and Al in all bimorph segments. This design helps protect the fragile mirror surface for easy handling and packaging and has a similar piston stroke and optical scan range compared with the one in Fig. 4(a). The devices shown here have a fill factor of about 60%.

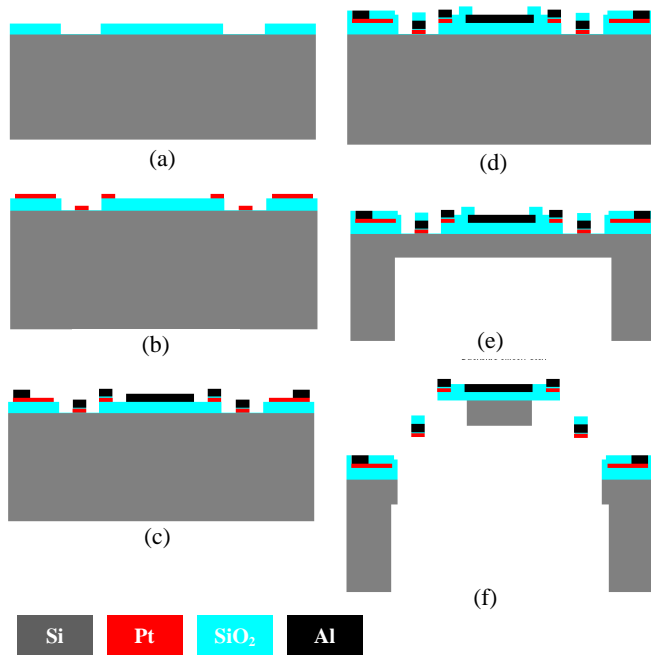


Fig. 3 Process flow: (a) Bottom oxide pattern. (b) Cr-Pt-Cr heater lift-off. (c) Insulation oxide deposition and Al lift-off. (d) Top oxide pattern. (e) Backside silicon etch. (f) Front side silicon etch-through and release.

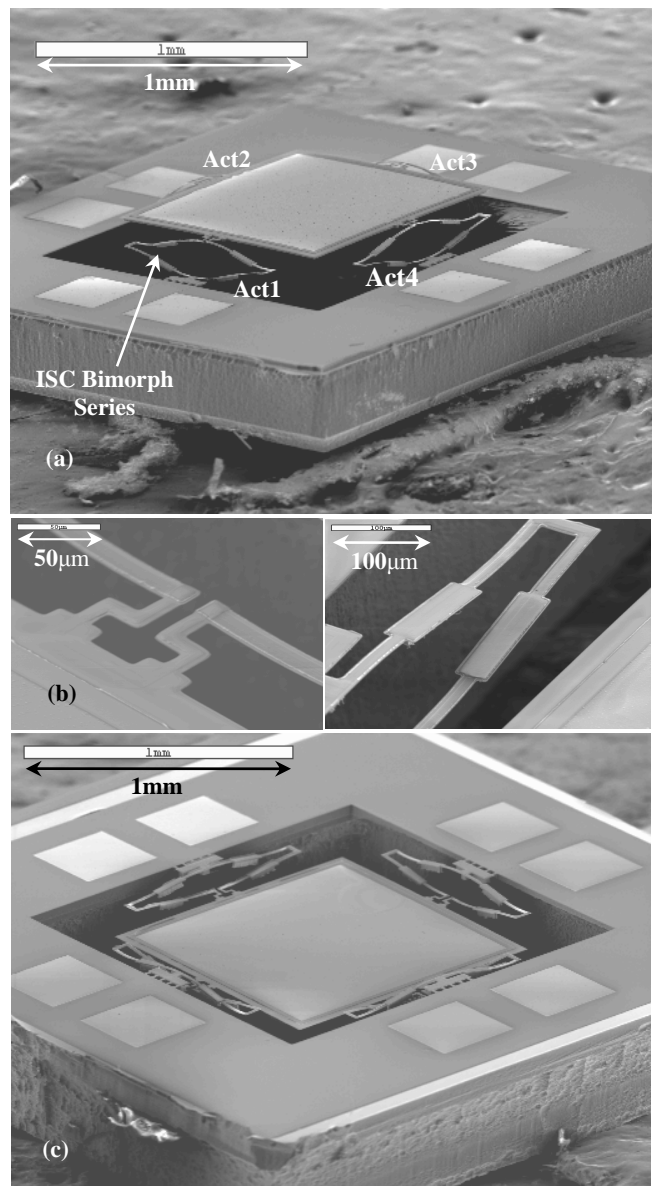


Fig. 4 (a) SEM image of a fabricated device. (b) Bimorph series and connections. (c) A device with mirror plate below substrate.

## EXPERIMENTAL RESULTS

### Static Measurement Results

Piston displacement of the mirror plate is achieved by driving the four actuators simultaneously with a same dc voltage. In this experiment, a wire-bonded device was placed under an Olympus BX51 optical microscope equipped with a Quadra-Chek 200 micro-position recorder to track the vertical displacement. After each increase of the supply voltage, the image was refocused and a reading of z position of the mirror plate was recorded. Data points for multiple locations on the mirror plate were taken to verify its piston motion. It was found that the tilting of the mirror plate was initially  $0.2^\circ$  and this tilting did not become larger during the actuation. It was also recorded from this test that the lateral shift of the mirror plate was only  $2\ \mu\text{m}$  over the entire actuation range of  $\sim 140\ \mu\text{m}$  at 5 V dc. The error in this measurement is  $\pm 1\ \mu\text{m}$  resulting from the refocusing step. Fig. 5 shows the static measurement result for the piston actuation.

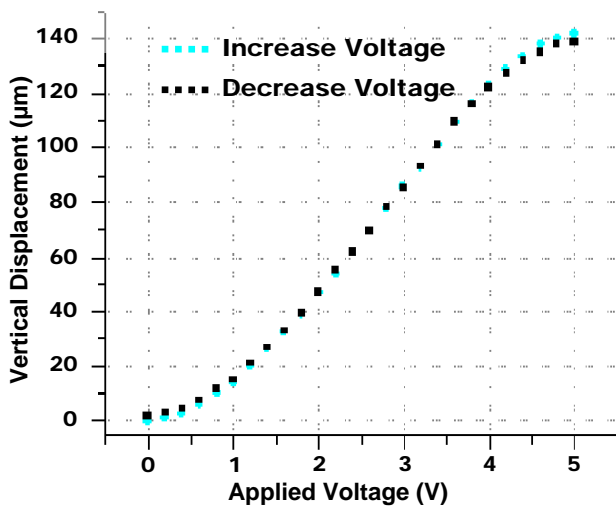


Fig. 5 Static measurement result for piston mode actuation. Same dc voltage was applied to all four actuators.

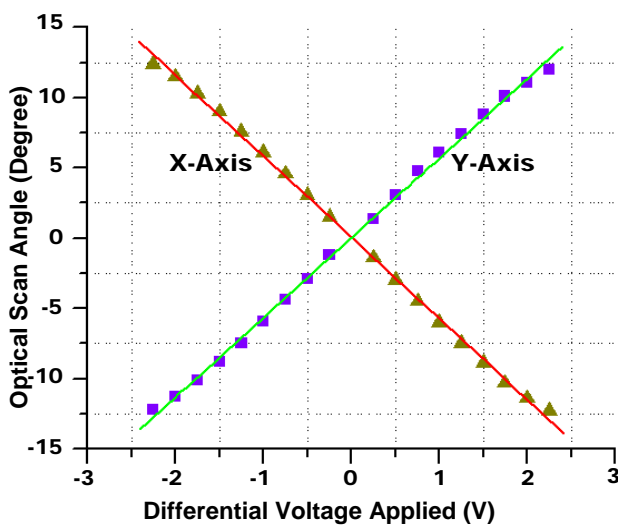


Fig. 6 Static measurement result for rotation mode actuation. All actuators had a dc voltage of 2.25V. Differential voltages were applied to opposing actuator pairs.

The static rotation measurement was taken by applying a same dc voltage of 2.25 V to all four actuators and at the same time superimposing two differentially varying voltages to one opposing actuator pair. A laser beam and a screen were used for this experiment. Fig. 6 shows the static measurement result for the rotation actuation. An optical scan angle of  $\pm 12^\circ$  was achieved for both x- and y-axis at a pair of 2.25 V differential voltages.

The measured resistances of the heaters are  $256 \pm 2\ \Omega$ . Notice that the highest voltage applied in the above measurements is 5 V dc. Thus, the maximum power consumption for each axis is less than 60 mW if we take into consideration the temperature coefficient of the platinum resistivity.

### Dynamic Measurement Results

The electromechanical response time of the actuator was measured by monitoring the light spot reflected by the mirror plate with a photosensitive device (PSD). A 2 Hz square-wave voltage (0-3.5 V) was applied to a single actuator. The voltage output from the PSD shows that the 10% to 90% response time is less than 20 ms, as shown in Fig. 7.

The frequency response of the mirror plate was also obtained with the PSD and an SRS 785 signal analyzer. For the piston mode measurement, a same 1 V dc superimposed by a 100 mV ac signal from the signal analyzer was applied to all four actuators. The light spot reflected by the mirror plate was monitored by the PSD whose output was fed back to the signal analyzer. For the rotation mode measurement, the same setup was used but the ac signal from the signal analyzer was inverted to make a differential pair and then applied to the two opposing actuators. The recorded resonance frequencies for piston and rotation modes are 664 Hz and 714 Hz, respectively.

One-dimensional (1D) line scans were generated by exciting one pair of the actuators, as shown in Fig. 8(a). Two-dimensional (2D) scans using this device were demonstrated by simultaneously exciting two pairs of the actuators. By varying the frequency and phase of the ac signals, different Lissajous patterns were generated and shown in Fig. 8(b)-(d). It was noticed that when the device was driven at its resonance frequency for the rotation mode, the optical scan angle can go up to  $\pm 30^\circ$  at 2.25 V differential voltages.

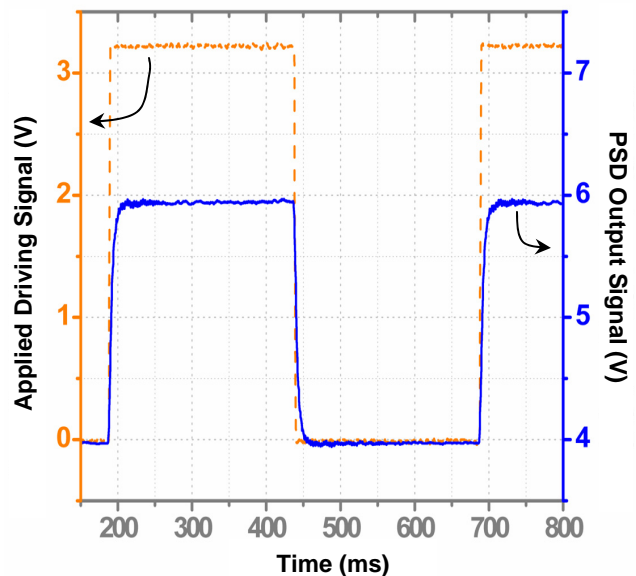


Fig. 7 Electromechanical transient response time measurement.

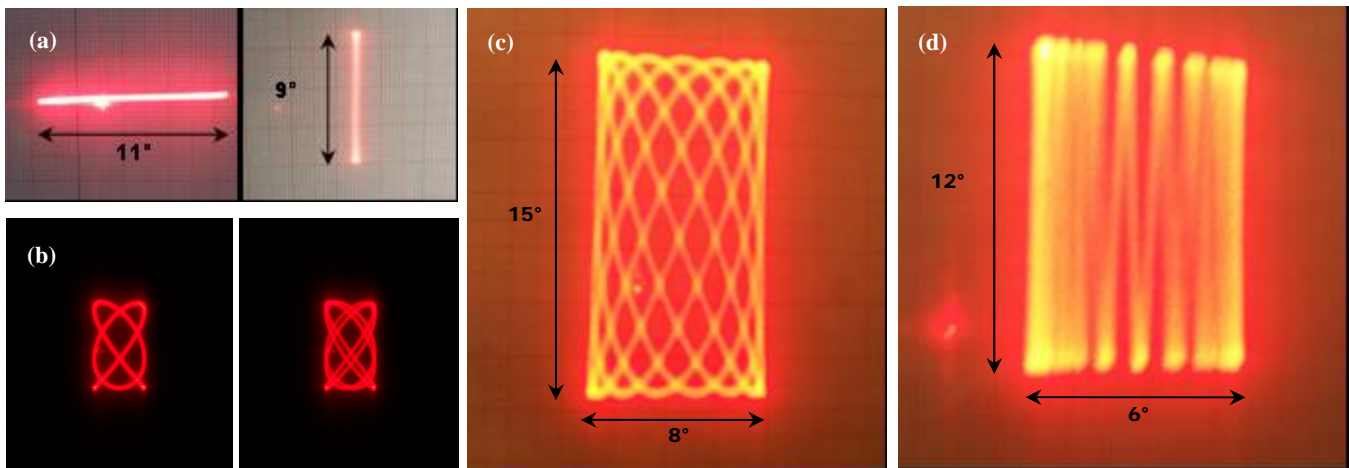


Fig. 8 Various Lissajous patterns generated by varying AC signal frequency ratio and phase difference between the two orthogonal actuator pairs. (a) 1-D scan for  $-x$  and  $-y$  axes; (b) Lissajous patterns with frequency ratio of 2:3 and a phase difference between two orthogonal actuator pairs; (c) Lissajous patterns with frequency ratio of 5:6; (d) Raster scanning pattern with frequency ratio of 1:9.

### Mirror surface quality measurement

The mirror surface quality was measured using a Wyko-Vision32 optical profilometer. The measured radius of curvature over the 1mm by 1mm mirror plate surface is 0.32 m with peak to valley deformation of 0.15  $\mu\text{m}$ . The surface roughness is about 20 nm.

### CONCLUSION

An agile tip-tilt-piston micromirror with 1mm by 1mm aperture size has been successfully demonstrated. The mirror can achieve a maximum 141  $\mu\text{m}$  piston stroke and  $\pm 12^\circ$  of 2D non-resonant optical scan range all at less than 6 V dc. This design solves the lateral-shift problem for the piston motion. The axis of rotation is also structurally fixed for the 2D scanning mode. The measured electromechanical response time is less than 20 ms. The device has performed various Lissajous patterns successfully. A study on the dynamic deformation of the mirror plate during linear and angular scanning is currently ongoing. Raster scanning for optical displays and optical imaging will be explored in the near future.

### ACKNOWLEDGEMENT

This project is supported by the National Science Foundation under award numbers CBET-0423557 and ECCS-0725598.

### REFERENCES:

- [1] K. E. Perterson, "Silicon torsional scanning mirror," *IBM Journal of Research and Developmen*, 24, pp. 631 (1980).
- [2] P. F. V. Kessel *et al.*, "A MEMS-based project display," *Proceedings of IEEE*, 86, pp. 1687 (1988).
- [3] U. Krishnamoorthy, et al., "Dual-mode micromirrors for optical phase array applications," *Sensors and Actuators A*, 97-98C, pp. 22-26 (2002).
- [4] J. B. Stewart *et al.*, "Open-loop control of a MEMS deformable mirror for large- amplitude wavefront control," *J. Opt. Soc. Am. A*, 24, pp. 3827-3833 (2007).
- [5] J. P. Yang, X. C. Deng, and T. C. Chong, "An electro-thermal bimorph-based micro actuator for precise track-positioning of optical disk drives," *J. Micromech. Microeng.*, 15, pp. 958-965 (2005).
- [6] A. D. Yalcinkaya *et al.*, "Two Axis Electromagnetic Microscanner for High Resolution Displays," *JMEMS*, 15, 4, pp. 786-794 (2006).
- [7] V. Milanovic, K. Castelino, and D. McCormick, "High adaptable MEMS-based display with wide projection angle," *MEMS'07*, pp. 143-146 (2007).
- [8] J. Tsai, and M. C. Wu, "Design, fabrication, and characterization of a high fill-factor, large scan-angle, two-axis scanner array driven by a leverage mechanism," *JMEMS*, 15, 5, pp. 1209- 1213 (2006).
- [9] W. Piyawattanametha *et al.*, "Three-dimensional in vivo real time imaging by a miniature dual-axes confocal microscope based on a two-dimensional MEMS scanner," *Transducers'07*, pp. 439-442 (2007).
- [10] V. Milanovic, G. A. Matus, and D. McCormick, "Gimbal-less Monolithic Silicon Actuators for Tip-Tilt-Piston Micromirror Applications," *Journal of Selected Topics in Quantum Electronics*, 10, 3, pp. 462-471 (2004).
- [11] I. W. Jung, U. U. Krishnamoorthy, and O. Solgaard, "High fill-factor two-axis gimballed tip-tilt-piston micromirror array actuated by self-aligned vertical electrostatic combdrive," *JMEMS*, 15, 3, pp. 563-571 (2006).
- [12] J. B. Stewart *et al.*, "Design and development of a 331-segment tip-tilt-piston mirror array for space-based adaptive optics," *Sensor and Actuators A*, 138, pp. 230-238 (2007).
- [13] F. Pardo *et al.*, "Flexible fabrication of large pixel count piston-tip-tilt mirror arrays for fast spatial light modulators," *Microelectronic Engineering*, 8, pp. 1157-1161 (2007).
- [14] J. Singh *et al.*, "A two axes scanning SOI MEMS micromirror for endoscopic bioimaging," *J. Micromech. Microeng.*, 18, *In Press* (2008).
- [15] A. Jain and H. Xie, "A single-crystal silicon micromirror for large bi-directional 2D scanning applications," *Sensors and Actuators A*, 130, pp. 454-460 (2006).
- [16] L. Wu and H. Xie, "A large-aperture piston-tip-tilt micromirror for optical phase array applications," *MEMS'08*, pp. 754-757 (2008).
- [17] S. Todd *et al.*, "A multi-degree-of-freedom micromirror utilizing inverted-series-connected bimorph actuators," *J. Opt. A: Pure Appl. Opt.* 8, pp. 352-359 (2006).
- [18] K. Jia and H. Xie, "Multi-axis electrothermal scanning micromirror with low driving voltage," *CLEO'07, Nanophotonic Structures and Devices*, CThJJ (2007).

# MICROMACHINED “SIDE-VIEWING” OPTICAL SENSOR PROBE FOR NON-INVASIVE DETECTION OF ESOPHAGEAL CANCERS

A. Garcia-Urbe<sup>1</sup>, K. C. Balareddy<sup>1</sup>, J. Zou<sup>1</sup>, A. Wojcik<sup>1</sup> and L. Wang<sup>2</sup>

<sup>1</sup>Department of Electrical and Computer Engineering, Texas A&M University, College Station, Texas, USA

<sup>2</sup>Department of Biomedical Engineering, Washington University, St. Louis, Missouri, USA

## ABSTRACT

In this paper, we report the design, fabrication and testing of a new miniaturized optical sensor probe with “side viewing” capability for oblique incidence diffuse reflectance spectrometry. The sensor probe consists of three micromachined positioning substrates and source/collection fibers to achieve 45° light incidence and collection of spatial resolved diffuse reflectance. Diffuse reflectance of human esophageal surface has been successfully measured for classification of cancerous tissues from normal ones for the first time.

## INTRODUCTION

In the United States, the American Cancer Society estimated that there were about 15,560 new cases of esophageal cancers with about 13,940 deaths in 2007 [1]. Esophageal cancer is 3 to 4 times more common among men than among women and 50% more common among African Americans than among whites.

Several different optical methodologies have been proposed to determinate the malignancy of tumors [2-4]. Among them, oblique incidence diffuse reflectance spectroscopy (OIDRS) is a novel non-invasive optical method for early diagnosis of epithelial types of cancer (e.g. skin and esophageal cancers), which utilizes a special optical fiber sensor probe to conduct comparative measurements of the diffuse reflectance spectra of interested tissues upon contact [5]. Unfortunately, OIDRS is currently limited to only skin applications by the available sensor probes, which are bulky and have only “front viewing” capability (Fig. 1a).

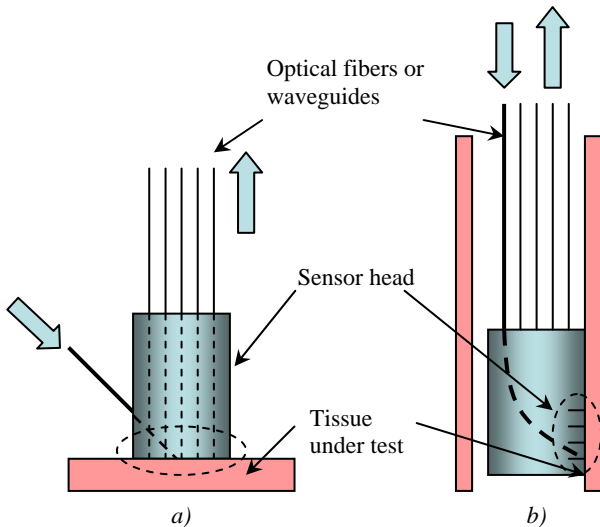


Figure 1: Schematic of OIDRS probe configuration: (a) front viewing and (b) side viewing.

To significantly extend OIDRS for the detection of a much wider variety of cancers inside human body, new sensor probes with much smaller size and more importantly “side viewing” capability are necessary for effective OIDRS measurement even in the narrow cavities (e.g. esophagus) (Fig. 1b). However, achieving

probe miniaturization and “side-viewing” capability requires dense placement and sharp bending of optical fibers, which would cause excessive light loss, cross-talk or even breaking of the fiber. To overcome these challenges, an entire new device design and structure need to be developed.

## THEORY

As shown in Fig. 2, when light is incident on the surface of an inhomogeneous media (e.g. biological tissue), part of the incident light will be directly reflected (specular reflectance) and the remaining will transmit into and interacts with the media. After undergoing multiples times of scattering and absorption, part of the transmitted light will be “turned” back and escape from the surface the media, which forms the diffuse reflectance. The spatially resolved steady-state diffuse reflectance for particular wavelength and oblique incidence can be calculated by [6].

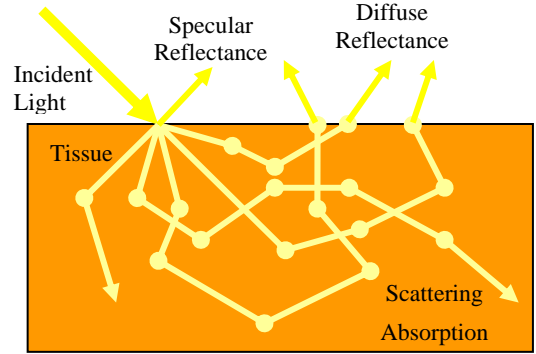


Figure 2: Illustration of OIDRS principle. After undergoing multiples times of scattering and absorption, part of the transmitted light is reflected back to form the diffuse reflectance.

$$R(x) = \frac{1}{4\pi} \left[ \frac{\Delta z(1 + \mu_{eff} \rho_1) \exp(-\mu_{eff} \rho_1)}{\rho_1^3} + \frac{(\Delta z + 2z_b)(1 + \mu_{eff} \rho_2) \exp(-\mu_{eff} \rho_2)}{\rho_2^3} \right] \quad (1)$$

where  $\rho_1$  and  $\rho_2$  are the distances between the source point and the observation point on the skin surface.  $\Delta z$  is the distance between the virtual boundary and the tissue depth, and  $z_b$  is the distance between the virtual boundary and the surface of the sample (Fig. 3). The distance from the point of incidence to the positive point source  $d_s = 3D$ . For oblique incidence the diffusion coefficient is  $D = (3(0.35\mu_a + \mu_s'))^{-1}$ , where  $\mu_a$  is the absorption coefficient and  $\mu_s'$  is the reduced scattering coefficient. The effective attenuation coefficient  $\mu_{eff} = (\mu_a/D)^{1/2}$ . The shift of the point sources in the  $x$  direction  $\Delta x = \sin(\alpha_i)/(3(0.35\mu_a + \mu_s'))$ , and  $\alpha_i$  is the angle of light transmission into the tissue. The absorption and reduced scattering coefficients can be calculated by [7]

$$\mu_a = \frac{\mu_{eff}^2 \Delta x}{3 \sin(\alpha_i)} \quad (2)$$

$$\mu_s' = \frac{\sin(\alpha_t)}{\Delta x} - 0.35\mu_a \quad (3)$$

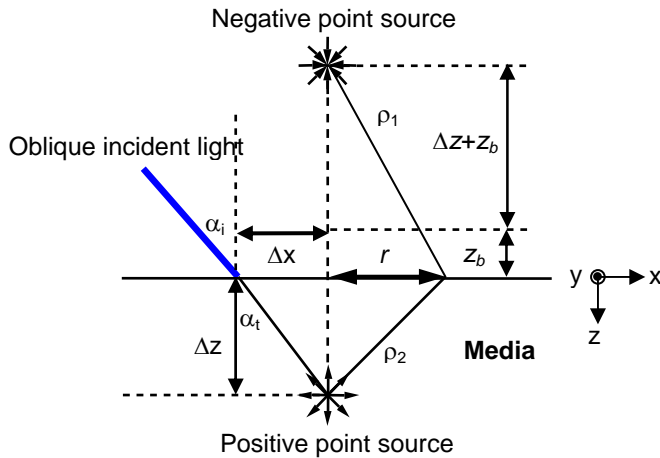


Figure 3: Schematic of the diffusion theory model for oblique incidence.

The diffusion equation assumes that the reduced scattering coefficient is much larger than the absorption. The source and detector must also be separated in space so that the light is diffuse when it reaches the detector. When the distance between the source and the detectors is comparable to the transport mean free path ( $\sim 1$  mm), diffusion theory does not apply. In this case, Monte Carlo simulation can be applied for the extraction of optical properties from the measured diffuse reflectance [8].

### PROBE DESIGN AND FABRICATION

To conduct OIDRS measurement, it is necessary to accurately deliver light of particular wavelength at a desirable oblique incidence angle on the tissue surface and also collect the one-dimensional linear distribution of the diffuse reflectance  $R(x)$ . While this can be achieved by placing the biological sample under an imaging setup, it will not be convenient and feasible to conduct in-vivo OIDRS measurements under ordinary clinical settings. To address this issue, we have investigated the idea of building a stand-alone fiber optic sensor probe for skin applications [9]. This skin probe takes a “front viewing” configuration, in which the sensor head is in line with the direction of the fiber bundle. Except the oblique incidence fibers, all other fibers remain straight without any need of bending, such that they can be arranged in a dense manner without possibility of fracture. However, the measurements from tissue inside human body, (such as esophagus) require a different configuration that allows the further miniaturization of the sensor and more importantly the side-view capability of the sensor, in which all the collection fibers have to undergo a sharp  $90^\circ$  turn within a tight space within 2~5 mm. This inevitably would cause significant light loss and leakage and also possible mechanical fracture of the collection fibers.

To address this problem, we have come up with a new probe design, which consists of three micromachined silicon substrates (Fig.4). The first substrate consists of a guiding structure made of  $100\ \mu\text{m}$  thick SU-8 (MicroChem, MA) layer, which serves as a position device for the source fiber to provide light incidence at an oblique angle ( $45^\circ$ ) (Fig. 5a). The source fiber with a diameter of  $200\ \mu\text{m}$  can be accommodated using a matching pair of two positioning substrates. The second substrate carries ten SU-8 waveguides ( $100\times 100\ \mu\text{m}^2$ ) with a  $90^\circ$  turn for collecting the spatially resolved diffuse reflectance from the tested tissue surface

(Fig. 5b). The third substrate consists of a 1D array of bulk-etched V-groves to ensure precise position of the 10 interconnection fibers to interface the  $90^\circ$  collection waveguides to OIDRS measurement setup (Fig. 5c). We choose SU-8 as structural materials for both the guiding structures of source fiber and also the curved waveguides for collecting the diffuse reflectance. SU-8 is preferable since it can be directly photolithographically patterned to form thick microstructures ( $100\ \mu\text{m}$ ) without further etching process, which results in a straightforward and low-cost fabrication process. Also, SU-8 has excellent optical transmittance over the visible light spectrum (where OIDRS works) (Fig. 6), which makes it a suitable optically conductive material for the curved waveguides. To prevent possible light leakage and cross-talk, the top/bottom surfaces and the two side walls of the SU-8 waveguides were coated with evaporated aluminum ( $180\ \text{nm}$  thick). To ensure a good coverage of the two side walls and the top surface, the aluminum depositions were conducted with the substrate placed at an oblique  $\pm 45^\circ$  with respect to the evaporation source.

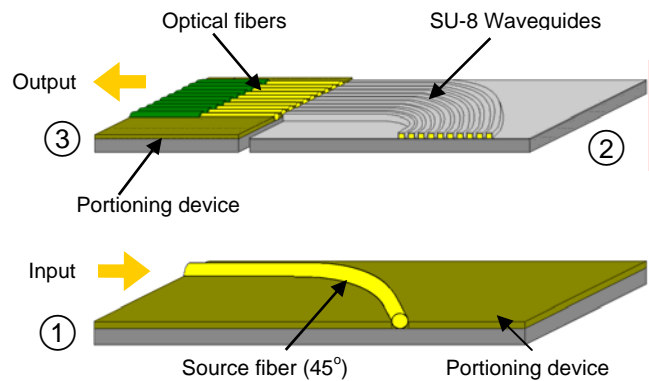


Figure 4: Schematic design of the new “side-viewing” OIDRS probe.

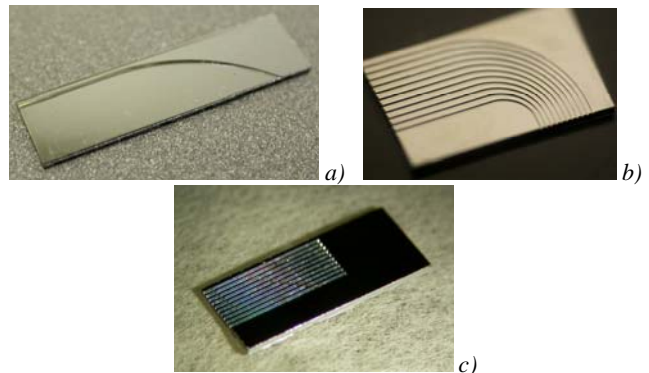


Figure 5: Micromachined silicon positioning substrates for the OIDRS probe (a) Source fiber guide; b) Collection waveguide substrates; and c) Interconnection fiber guide.

After the fabrication of three substrates, both the source fiber and the interconnection fibers were carefully placed into their positioning substrates and fixed in place with black epoxy. Next, all the substrates were aligned and glue together to complete the assembly of the entire probe in an aluminum holder for protection (Fig. 7a). The outer dimension of the sensor head is  $5\times 5\times 12\text{mm}^3$ , which is small enough for esophagus inspection. The source and collection fibers of the sensor probe were then connected to the system via SMA connectors (Fig. 7b).

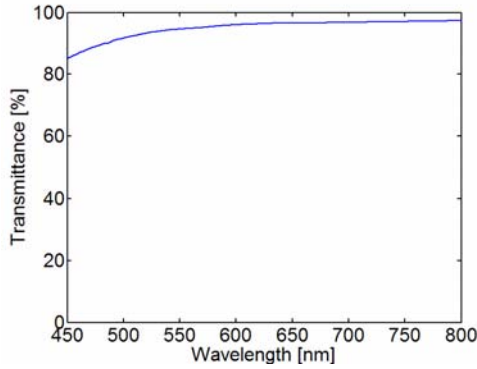


Figure 6: Optical transmittance of SU-8 in the visible spectrum (100 $\mu$ m thick film).

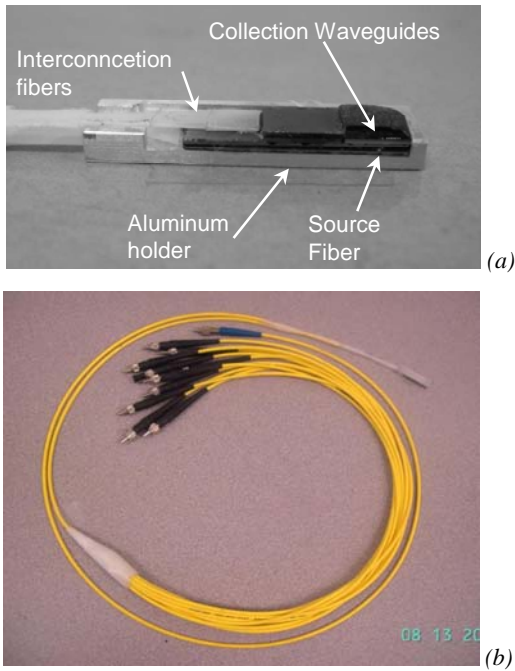


Figure 7: (a) OIRDS probe assembly. (b) Complete OIRDS probe.

### TESTING AND RESULTS

The testing set-up of the OIR is shown in Fig 8. It consists of halogen lamp, imaging spectrograph, CCD camera, and personal computer. Before an OIRDS measurement is conducted, the source fiber of the sensor probe is connected to the output of the light source via SMA connectors. The proximal end of each collection fiber is fitted with SMA 905 connectors and then connected to the input of the spectrograph through a custom-made interface. After the sensor probe gets into contact with the sample, white light is delivered through the source fiber and the diffuse reflectance is then captured by the collection fibers. The collection fibers are coupled with the imaging spectrograph that generates an optical spectrum for each fiber. The CCD camera collects the spectral-images from the wavelength range of 455 to 765 nm. The spectral images represent the steady-state diffuse reflectance spectra from each collection fiber, which are stored in the computer for further analysis. This system is capable of capturing one frame of spectral image in a fraction of a second.

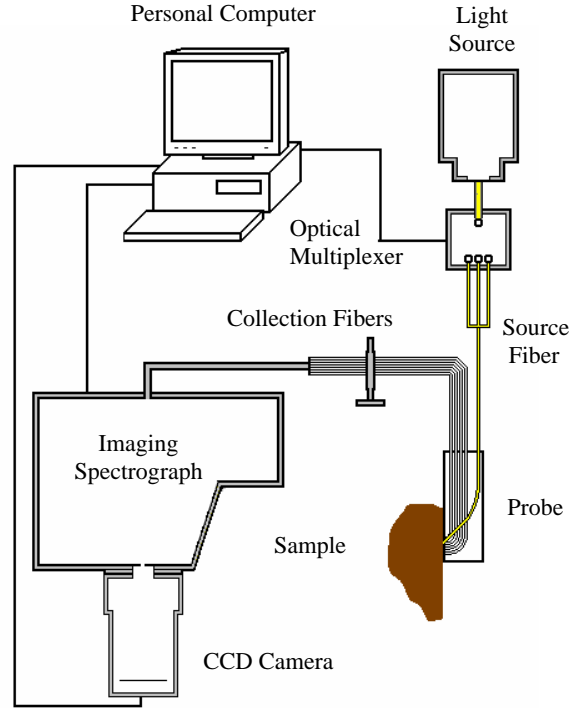


Figure 8: Experimental setup for OIRDS probe testing.

Before the real measurement, the fabricated OIRDS probe and image capture system were calibrated using a standard liquid phantom, which consists of trypan blue dyes as the absorbers and polystyrene microspheres as the scattering elements [10]. After the calibration, the entire OIRDS system was used to conduct ex-vivo measurement of human esophagus specimens with cancerous tissues (adenocarcinoma) for the first time (one specimen shown as an example) (Fig. 9). The measurement results by the ten collection channels clearly show different diffuse reflectance spectra for the normal and cancerous tissues (Fig. 10). The general lower diffuse reflectance of the cancerous tissue is caused by its darker color (causing more light absorption). The stronger scattering of the cancerous tissue is believed to be caused by the relatively larger cell nuclei as stronger optical scatter in malignant tumor cells, which is expected to serve as a good indicator to effectively differentiate cancerous tissue from benign ones [11].

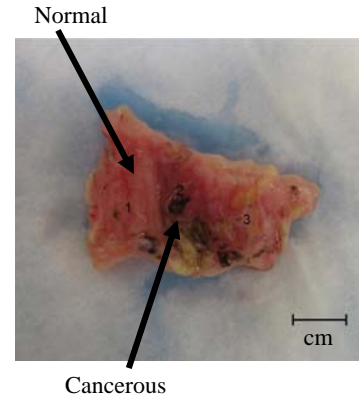


Figure 9: Esophagus cancer testing sample (adenocarcinoma).

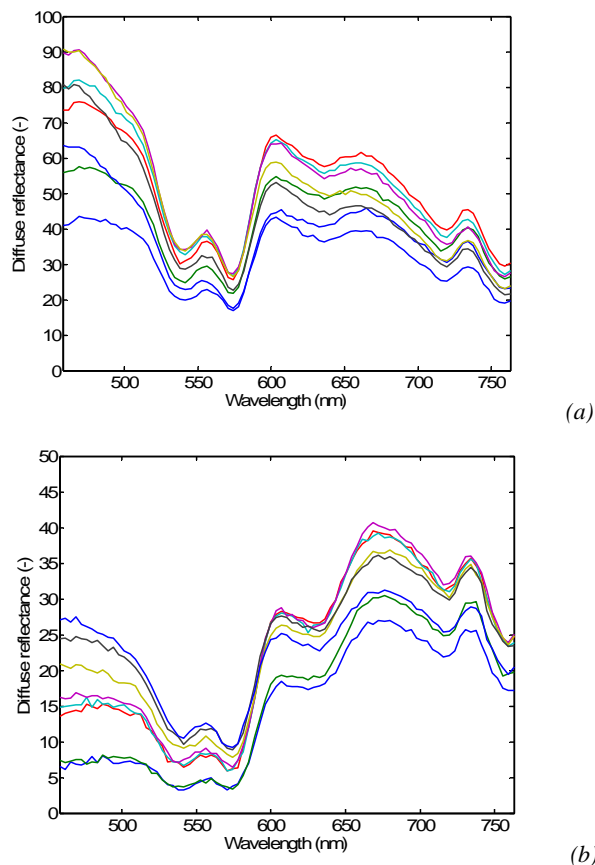


Figure 10: Diffuse reflectance spectra of human esophagus from ex-vivo OIRS measurement: (a) Normal tissue; and (b) Cancer tissue.

## CONCLUSIONS

A new miniaturized OIRS sensor probe has been successfully developed and used for ex-vivo testing of esophageal cancer for the first time. When used with medical endoscopes, the new sensor probe is expected to enable in-vivo non-invasive detection of esophageal cancer and many other epithelial types of cancers inside human body.

## ACKNOWLEDGMENTS

The authors thank Dr. Kenneth Wang of Mayo Clinic (Rochester, Minnesota) for his help during the data collection. This project is supported by National Institutes of Health under contract R01 CA106728.

## REFERENCES

[1] American Cancer Society website. <http://www.cancer.org>.  
 [2] P. R. Bargo, S. A. Prahl, T. T. Goodell, R. A. Sleven, G. Koval, G. Blair, S. L. Jacques, "In vivo determination of optical properties of normal and tumor tissue with white light reflectance and an empirical light transport model during endoscopy," *Journal of Biomedical Optics* 10, 034018, (2005).

[3] S. Brand, J. M. Ponomarev, B. E. Bouma, G. J. Tearney, C. C. Compton, N. S. Nishioka, "Optical Coherence Tomography in the Gastrointestinal Tract," *Endoscopy* 32, pp. 796-803 (2000)  
 [4] Messmann H, Knüchel R, Bäuml W, Holstege A, Schölmerich J. "Endoscopic fluorescence detection of dysplasia in patients with Barrett's esophagus, ulcerative colitis, or adenomatous polyps after 5-aminolevulinic acid-induced protoporphyrin IX sensitization," *Gastrointestinal Endoscopy*, 49(1), pp. 97-101, (1999).  
 [5] A. Garcia-Urbe, N. Kehtarnavaz, G. Marquez, V. Prieto, M. Duvic, and L. V. Wang, "Skin cancer detection by spectroscopic oblique-incidence reflectometry: classification and physiological origins," *Applied Optics* 43, pp. 2643-2650, (2004).  
 [6] L.-H. Wang and S. L. Jacques, "Use of a laser beam with an oblique angle of incidence to measure the reduced scattering coefficient of a turbid medium," *Applied Optics* 34, pp. 2362-2366, (1995)  
 [7] S.-P. Lin, L.-H. Wang, S. L. Jacques, and F. K. Tittel, "Measurement of tissue optical properties using oblique incidence optical fiber reflectometry," *Applied Optics* 36, 136-143 (1997).  
 [8] T. J. Farrell and M. S. Patterson, "A diffusion theory model of spatially resolved, steady-state diffuse reflectance for the noninvasive determination of tissue optical properties in vivo" *Medical Physics* 19, pp. 879-888, (1992)  
 [9] A. Garcia-Urbe, K. C. Balareddy, J. Zou and L. V. Wang, "Micromachined Fiber Optical Sensor for In-Vivo Measurement of Optical Properties of Human Skin," Submitted to *IEEE Sensor Journal*.  
 [10] G. Marquez and L.-H. Wang, "White light oblique incidence reflectometer for measuring absorption and reduced scattering spectra of tissue-like turbid media," *Optics Express* 1, 454-460 (1997).  
 [11] L. T. Perelman, V. Backman, M. Wallace et al. "Observation of periodic fine structure in reflectance from biological tissue—a new technique for measuring nuclear size distribution," *Physical Review Letters* 80, pp. 627-630, (1998).

# MONOLITHIC INTEGRATION OF BINARY-PHASE FRESNEL ZONE PLATE OBJECTIVES ON 2-AXIS SCANNING MICROMIRRORS FOR COMPACT MICROENDOSCOPES

Karthik Kumar<sup>1</sup>, Hung Cao<sup>2</sup>, and Xiaojing Zhang<sup>2</sup>

<sup>1</sup>Department of Electrical and Computer Engineering, University of Texas, Austin, Texas, USA

<sup>2</sup>Department of Biomedical Engineering, University of Texas, Austin, Texas, USA

## ABSTRACT

We demonstrated unique monolithic integration of Fresnel zone plate objective on 2-axis staggered vertical combdrive micromirror surface via direct patterning of reflective binary-phase-modulation elements on silicon. Need for focusing optics is thus obviated, simplifying microendoscope assembly and improving form factor. Micromirrors scanning  $\pm 9^\circ$  (optical) about both axes are patterned with elliptical zones designed for 7mm (8mm) focal length and  $20^\circ$  ( $45^\circ$ ) off-axis 635-nm illumination using 635nm (1310nm) laser. Videos of samples acquired with  $\sim 15\mu\text{m}$  lateral resolution over  $1\text{mm} \times 0.35\text{mm}$  field of view at 5.0 frames/second using the device in a bench-top single-fiber laser-scanning confocal microscope confirm applicability of the device to microendoscopy.

## INTRODUCTION

*In vivo* optical imaging is an important tool for medical diagnosis in situations where biopsy is difficult, and for image-guided microsurgery and photodynamic therapy [1]. Cellular-level imaging enables early detection of many diseases such as cancers, which can be crucial to effective treatment and patient survival chances [2]. Visualization in sensitive internal non-tubular human organs requires compact forward-imaging endoscopes, which have thus far proven to be difficult to assemble in small form factor, as opposed to sideways-imaging probes [3]. Microelectromechanical system (MEMS) technologies are uniquely positioned to provide distal beam deflection for image formation in microendoscopes. Vertical combdrive micromirrors have been shown to provide the large rotational torque, deflection angles and mirror surface quality for laser-scanned imaging systems [4]. However, catheter rigid length and outer diameter are mainly limited by focusing optics. Micromachined 3-D optics has been assembled into integrated free-space systems [5]. For multi-element systems, such as catheters, additional assembly becomes increasingly challenging and expensive. The present research addresses the above limitations by monolithically integrating a micromachined Fresnel zone plate objective directly on the surface of the micromirror via patterning of reflective binary-phase-modulation elements.

## THEORY

Coherent illumination incident on the micromirror surface at an angle to the mirror normal can be concentrated at a wavelength-dependent focal distance by an Elliptical Zone Plate (EZP, Figure 1) designed according to equation (1):

$$\left(\frac{x}{a_n \cos \theta}\right)^2 + \left(\frac{y - b_n}{a_n}\right)^2 = 1, \text{ where}$$

$$a_n = \frac{\sqrt{n\lambda \left(f \cos^2 \theta + \frac{n\lambda}{4}\right)}}{\cos^2 \theta} \text{ and } b_n = \frac{n\lambda \sin \theta}{2 \cos^2 \theta} \quad (1)$$

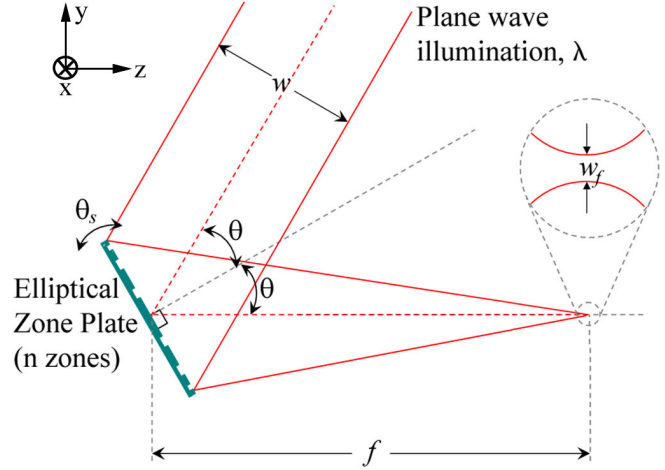


Figure 1: Illustration of design parameters for scanning binary-phase reflective Elliptical Fresnel Zone Plate (EZP).  $\theta$  is the off-axis illumination angle of wavelength  $\lambda$ ,  $\theta_s$  the micromirror scan angle,  $w$  and  $w_f$  are the incident and focused beam waists, and  $f$  is the focal length of the EZP with  $n$  zones.

$\theta$  is the off-axis illumination angle about the  $x$ -axis with respect to the micromirror normal,  $\lambda$  is the illumination wavelength,  $f$  is the focal distance, and  $a_n$  and  $a_n \cos(\theta)$  are the semi-major and semi-minor axes of the elliptical boundary of the  $n^{\text{th}}$  zone of the EZP. Degradation in focal spot size (indicated as  $w_f$  in Figure 1) due to changing illumination angle  $\theta$  (by micromirror rotation) and wavelength are negligible for optical path difference deviation at the zone boundaries of less than  $\lambda/4$  from nominal value [6, 7]. Therefore, the EZP can be fabricated for required focal spot size under maximum rotation angle to prevent aberrations using the following design constraints –

$$\text{Spherical Aberration: } n \approx \sqrt{2f / \lambda} \quad (2)$$

$$\text{Chromatic Aberration: } n \approx \lambda / \Delta\lambda \quad (3)$$

$$\text{Off-Axis Aberration: } \alpha \approx (3n)^{-1/2} \text{ (for small } n) \quad (4)$$

These conditions restrict the maximum number of EZP zones and micromirror scan angle (indicated as  $\theta_s$  in Figure 1), therefore determining the number of resolvable points in the image or the “numerical aperture” of the EZP. Variation of focal distance with wavelength may provide a new mechanism for 3-D imaging through axial scan [8].

## FABRICATION

The micromirror is actuated by staggered vertical comb drives fabricated by a comb self-alignment process in bonded double-SOI wafers [9, 10]. Coarse features of the stator are etched by Deep Reactive Ion Etching (DRIE) into  $25\mu\text{m}$  thick SOI <100> device

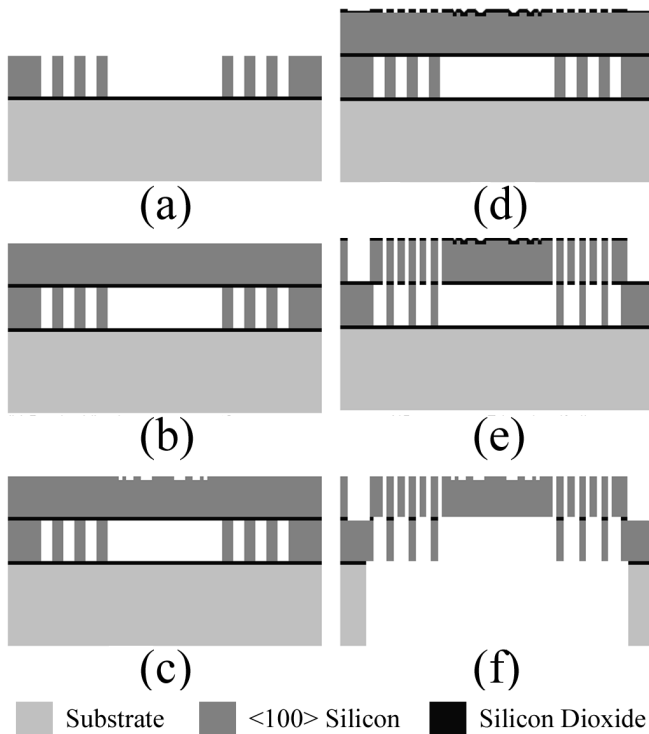


Figure 2: Device fabrication process sequence. (a) DRIE of coarse features in to SOI device layer. (b) Bond oxidized wafer, grind/polish. (c) Pattern binary-phase modulation elements of zone plate into micromirror surface. (d) Chemical vapor deposit silicon dioxide and pattern with exact micromirror features. (e) DRIE-Oxide RIE-DRIE sequence to create self-aligned actuators. (f) Backside DRIE to release micromirror, and oxide RIE on both sides to remove protective oxide.

layer (Figure 2). An oxidized <100> wafer is fusion bonded on top of the patterned wafer, and ground down to  $25\mu\text{m}$  thickness with  $<50\text{nm}$  surface roughness to form the micromirror surface. Features of the elliptical zone plate objectives are patterned on the surface to quarter-wavelength depth. Exact features of the actuators, aligned to the lower layer features, are etched into deposited silicon dioxide. DRIE-oxide RIE-DRIE etching sequence forms the self-aligned. Backside substrate DRIE and oxide RIE on both sides releases the mirror and removes remaining protective oxide. Scanning electron micrographs of the fabricated device are presented in Figure 3.

### DEVICE CHARACTERIZATION

Scanning EZPs designed for  $635\text{nm}$  ( $1310\text{nm}$ ) wavelength with focal lengths of  $7\text{mm}$  ( $8\text{mm}$ ) and off-axis illumination angles of  $20^\circ$  ( $45^\circ$ ) were fabricated on micromirrors of size  $500\mu\text{m}\times 700\mu\text{m}$ . Two-axis beam scanning is obtained by mounting the micromirror by torsion rods within a gimbal, which is suspended by torsion rods aligned in the orthogonal direction. Rotation about each axis is driven by two sets of staggered vertical comb drives. This configuration leads to two-axis angular scanning about a single pivot point at the center of the micromirror, which reduces optical field distortions.

Frequency response characteristics (Figure 4a) of the micromirror were tested by applying voltage of  $20.0+20.0\sin(\omega t)$  volts and varying the sinusoidal frequency. The micromirror

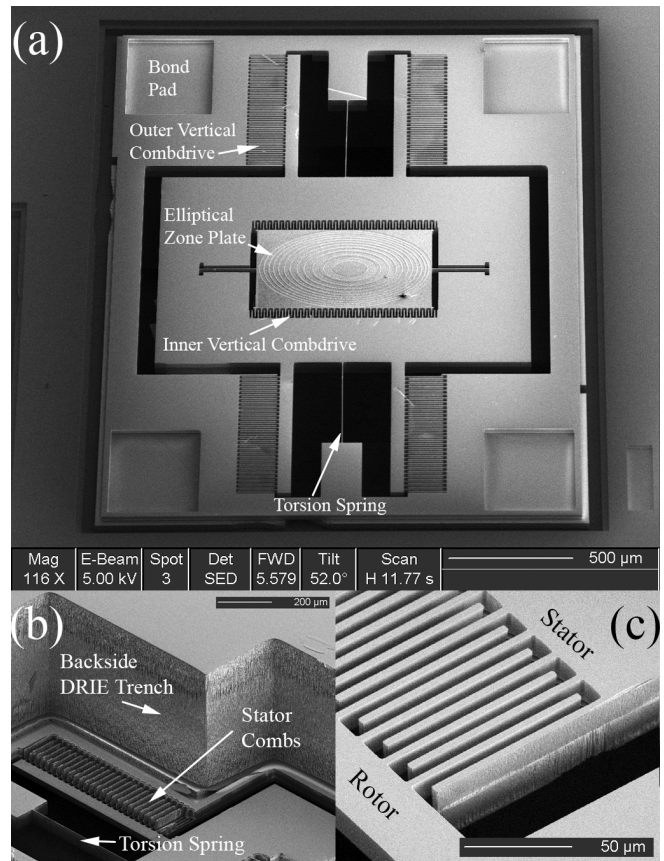


Figure 3: SEM images of the fabricated device. (a) Top view showing the EZP, vertical comb drives, torsion springs, and bond pads for electrical connection. (b) Backside view showing DRIE trench with vertical sidewalls to release the scanning micromirror. (c) Close-in view of vertical combdrive.

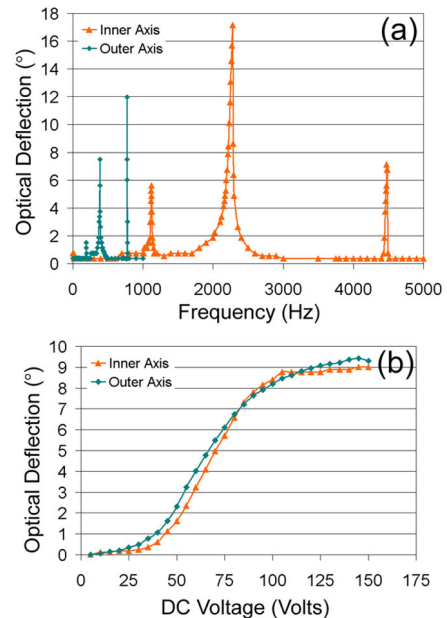


Figure 4: Micromirror operating characteristics. (a) Frequency response characteristics (Applied voltage =  $20.0 + 20.0\sin(\omega t)$  V). (b) Static deflection characteristics on driving one comb bank on each axis.

exhibits resonant out-of-plane rotation at 2280Hz and 383Hz for the inner and outer axes respectively. The static voltage deflection characteristics (Figure 4b) were determined by applying a DC voltage to one comb drive on each axis. Static voltage deflection of  $\sim 9^\circ$  (optical) was measured on application of 110 volts on both axes. Raster scan pattern was used for point-by-point image formation, employing resonant frequency operation of the inner axis for fast line scan, and non-resonant operation of outer-axis for frame scan.

Size of the focused spot of an EZP designed with 8mm focal length for 635nm illumination at  $45^\circ$  was profiled against micromirror rotation angle by measuring the far-field angular beam divergence ( $\theta$ ) of the Gaussian beam, and calculating the focused beam waist ( $w_f$ ) using the formula –

$$\theta \approx \frac{2\lambda}{\pi w_f} \quad (5)$$

The measured focused spot size shows little degradation (Figure 5) for micromirror scanning angles up to  $10^\circ$  (optical) about both axes.

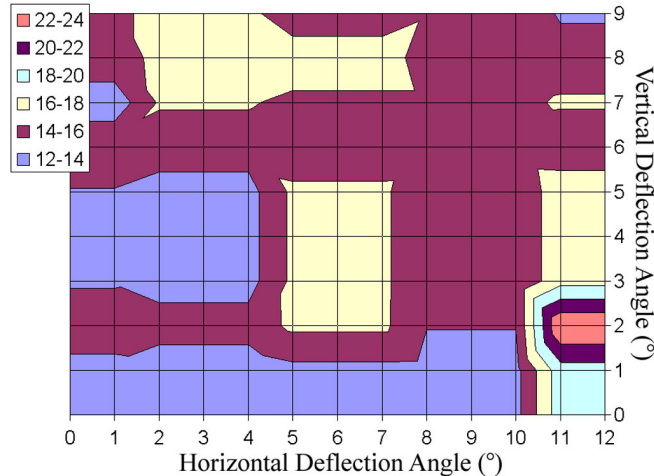


Figure 5: Map of diameter of the focused spot (in microns) created by an EZP with 8mm focal length for 635nm illumination at  $45^\circ$  nominal incidence as function of optical angular deflection of the micromirror.

## IMAGING RESULTS

### Transmission Barcode Imaging using EZP Micromirror

Preliminary testing of image-formation capabilities of the device was performed in a simple transmission-mode experiment, depicted in figure 6. A sample with spatially-varying transmission was placed in the focal plane of a scanning EZP, and transmitted light was concentrated into a photodetector using two collection lenses. Mylar transparencies printed with longhorn logos and numbers were imaged (Figure 7) using the system at 5 frames/second. Comparison with images obtained from an Olympus BX51 microscope using 10X objective indicated an estimated field of view of  $1\text{mm} \times 0.35\text{mm}$  at approximately  $15\mu\text{m}$  resolution.

### EZP Micromirror-Based Reflectance Confocal Imaging

The devices were then incorporated into a portable bench-top single-fiber laser-scanning reflectance confocal microscope

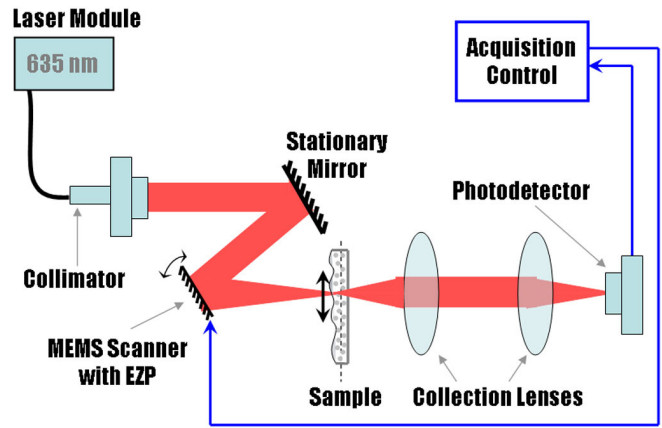


Figure 6: Schematic of transmission-mode imaging experiment used for preliminary device testing.

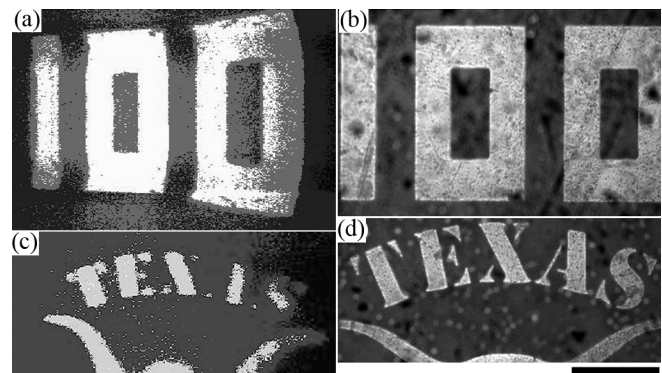


Figure 7: Results of imaging Mylar transparencies using preliminary transmission-mode imaging experiment. (a-b) Image calibration: (a) Image of number 100 (transparent) in opaque background, and (b) Image of sample using Olympus BX51 confocal microscope. (c-d) Image of longhorn symbol and text “TEXAS”: (c) using the device, and (d) using Olympus BX51 confocal microscope. Scale Bar:  $250\mu\text{m}$ .

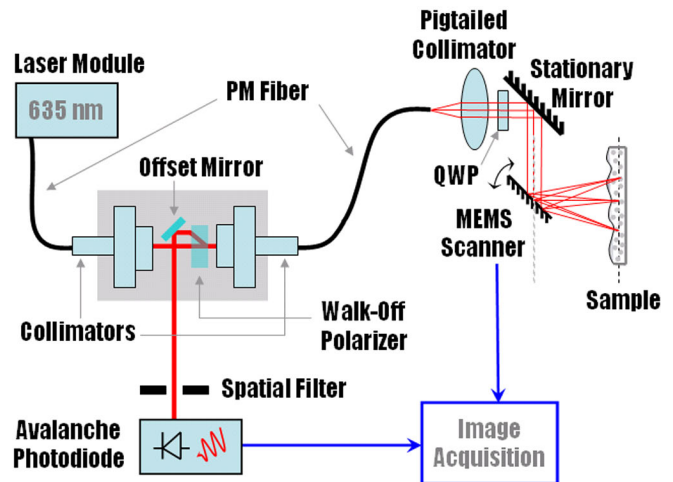


Figure 8: Schematic of single-fiber laser-scanning reflectance confocal microscope incorporating the micromirror with monolithically integrated EZP.

(Figure 8) that is better suited to eventual use in *in vivo* imaging applications. Polarized light from a 635nm semiconductor laser

diode is launched into a single-mode polarization-maintaining fiber, aligned to the fiber slow axis. After collimation into a beam matched to the size of the EZP, the linearly polarized light is converted into circularly polarized light by a quarter-wave plate (QWP) before being simultaneously focused and scanned across the sample by our device. Reflected light from the sample maintains some component of circularly polarized light, which is converted into light linearly polarized along the fiber fast axis, orthogonal to the incident illumination. This allows the walk-off polarizer to separate the sample reflection from laser illumination and direct it to an avalanche photodetector. Images using this system of a USAF1951 resolution target obtained are depicted in figure 9.

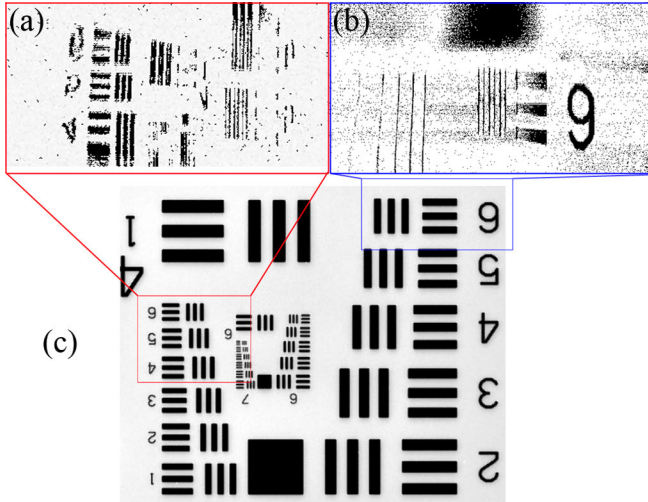


Figure 9: Results of imaging USAF1951 resolution target using laser-scanning reflectance confocal experiment using the device. Images of groups of elements from different parts of the target are depicted in (a)-(b). Field of view is  $1\text{mm} \times 0.35\text{mm}$ , and resolution is  $\sim 15\mu\text{m}$ . (c) Image of the target using Olympus BX51 confocal microscope with corresponding locations marked by colored rectangles.

Field of view of  $1\text{mm} \times 0.35\text{mm}$  and lateral resolution of  $15\mu\text{m}$  are estimated based on calculating the line width of the resolvable features in the resolution target images.

## CONCLUSIONS

Novel monolithic integration of reflective binary-phase-modulation elements on two-axis MEMS scanning micromirrors is

demonstrated for simultaneous beam scanning and focusing in a compact single-chip solution. This approach can potentially eliminate the need for focusing optics in a microendoscopes catheter, thus simplifying assembly and improving form factor. Elliptical zone plates integrated on two-axis self-aligned staggered vertical comb driven micromirrors, incorporated into a laser-scanning reflectance confocal microscope experiment, were shown to provide the cellular-level resolution required in microendoscopes without complex multi-element assembly.

## REFERENCES

- [1] R. S. Montgomery, and S. E. Wilson, "Intraabdominal abscesses: image-guided diagnosis and therapy", *Clinical Infectious Diseases*, 23, 28 (1996).
- [2] Y. T. Pan, T. Q. Xie, C. W. Du, S. Bastacky, S. Meyers, and M. L. Zeidel, "Enhancing early bladder cancer detection with fluorescence-guided endoscopic optical coherence tomography", *Optics Letters*, 28, 2485 (2003).
- [3] Z. Yaqoob, J. Wu, E. J. McDowell, X. Heng, and C. Yang, "Methods and application areas of endoscopic optical coherence tomography", *Journal of Biomedical Optics*, 11, 063001 (2006).
- [4] D. Hah, P. R. Patterson, H. D. Nguyen, H. Toshiyoshi, and M. C. Wu, "Theory and experiments of angular vertical comb-drive actuators for scanning micromirrors", *IEEE Journal of Selected Topics in Quantum Electronics*, 10, 505 (2004).
- [5] L. Y. Lin, S. S. Lee, K. S. J. Pister, and M. C. Wu, "Micro-machined three-dimensional micro-optics for integrated free-space optical system", *IEEE Photonics Technology Letters*, 6, 1445 (1994).
- [6] M. Young, "Zone plates and their aberrations", *Journal of the Optical Society of America*, 62, 972 (1972).
- [7] Q. Cao, and Jürgen Jahns, "Comprehensive focusing analysis of various Fresnel zone plates", *Journal of the Optical Society of America A*, 21, 561 (2004).
- [8] S. Cha, P. C. Lin, L. Zhu, P-C. Sun, and Y. Fainman, "Nontranslational three-dimensional profilometry by chromatic confocal microscopy with dynamically configurable micromirror scanning", *Applied Optics*, 39, 2605 (2000).
- [9] U. Krishnamoorthy, D. Lee, and O. Solgaard, "Self-aligned vertical electrostatic combdrives for micromirror actuation", *Journal of Microelectromechanical Systems*, 12, 458 (2003).
- [10] K. Kumar, K. Hoshino, H-J. Shin, R. Richards-Kortum and X. J. Zhang, "High-reflectivity two-axis vertical comb drive microscanners for confocal imaging applications", 2006 IEEE/LEOS International Conference on Optical MEMS and Their Applications, Big Sky, MT, 8/21-24/06, pp. 120 - 121.

# ROBUST OPTICAL DESIGN OF ANGLED MULTILAYER DIELECTRIC MIRRORS OPTIMIZED FOR RUBIDIUM VAPOR CELL RETURN REFLECTION

M.A. Perez<sup>1</sup>, J. Kitching<sup>2</sup> and A.M. Shkel<sup>1</sup>

<sup>1</sup>MicroSystems Laboratory, University of California, Irvine, CA, USA

<sup>2</sup>Time and Frequency Division, National Institute of Standards and Technology, Boulder, CO, USA

## ABSTRACT

This paper reports on the design and implementation of thin film multilayer dielectric to form Bragg reflectors on the sidewalls of micromachined atomic cells. Due to deposition shadowing, significant variations in the thicknesses of the thin films are encountered when the layers are deposited using PECVD. These gradients in thickness may limit optical performance of the reflector in atomic cells. An optimized design procedure is described to maximize the performance of the reflector at a wavelength of 795 nm under the variations in material thickness. In addition, an optical design based on two shifted quarter wave Bragg reflectors in series is used to form a reflector with extended optical bandwidth for added robustness. The extended reflectance range maintains high reflection at the  $D_1$  absorption wavelength of  $^{87}\text{Rb}$  despite variations in uniformity greater than 70%. The developed reflector technology is ideally suited for use in miniature rubidium vapor cells. We demonstrate less than 1.5 dB of return loss with circular polarization ellipticity maintained to  $\pm 2^\circ$  is demonstrated, as required for many atomic MEMS applications.

## INTRODUCTION

Miniature vapor cells for emerging atomic MEMS applications, such as chip scale atomic clocks [1], magnetometers [2], [3] and gyroscopes, depend on the efficient routing of laser light using micromachined reflectors. Cells containing rubidium alkali vapor need low reflection losses at the  $^{87}\text{Rb}$   $D_1$  transition wavelength of 795 nm after multiple reflections inside the vapor cell cavity formed in bulk micromachined wet-etched silicon (Figure 1).

However, uncoated silicon is not sufficiently reflective for use as a high performance mirror, losing 67% of optical energy in bulk transmission. Previously, rubidium vapor cells with optical return performance superior to uncoated silicon have been demonstrated by use of multilayer dielectric reflectors integrated on the sidewalls of wet-etched silicon cavities fabricated using Plasma Enhanced Chemical Vapor Deposition (PECVD) [4]. Although these reflectors have the potential to reflect light with negligible loss, large variations in the thin film thicknesses were observed due to the deposition technology, which limited the reflector performance.

PECVD has many practical advantages over other thin film fabrication methods, such as Physical Vapor Deposition (PVD), including higher deposition rates and the formation of films with better mechanically and environmental robustness [5]. However,

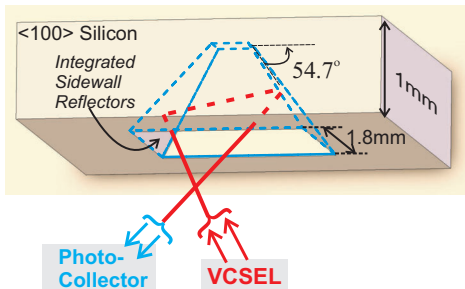


Fig. 1. Bulk micromachined reflector cell for atomic MEMS

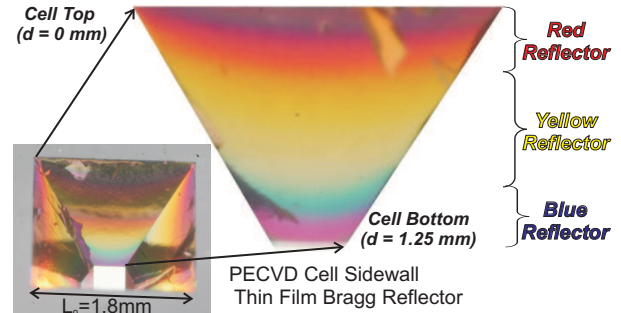


Fig. 2. PECVD Bragg reflector on the sidewall of a reflector cell with shifting wavelength reflectance from deposition nonuniformity

the thicknesses of PECVD fabricated thin films deposited onto the sidewalls of micromachined cavities rapidly decreases with cavity depth. This film thinning is due to the decrease in the arrival angle available to reactant species (shadowing) from the PECVD reactor chamber [6]. For the proposed vapor cell geometry, the resulting nonuniformity results in a reduction in layer thickness by over 70% down the cavity's sidewall.

When a multilayer reflector is deposited on the angled sidewalls (in this case at  $54.7^\circ$ ), this nonuniformity results in a shift in the reflection to lower wavelengths, as observed in the shift in the reflector color from red to yellow to blue down the sidewall face (Figure 2). Since the optimum reflectance wavelength varies over the area of the reflector, the efficiency at the design wavelength is compromised. By increasing the range of the high reflectance band (the range of wavelengths for which the reflectivity is optimized) and optimizing the deposition process for a particular wavelength, maximum reflectance is achieved down the entire sidewall at the design wavelength.

## REFLECTOR DESIGN

### Bragg Reflectors

The design of micromachined cells with integrated Bragg reflectors for rubidium vapor cells has been previously described in [4]. Briefly, the light reflected at the interface between each layer may be made to constructively interfere to maximize the total reflected optical power at a specific wavelength. The reflectivity is maximized if the structure is composed of alternating thin film layers each of optical thickness of one-quarter wavelength of the light to be reflected as given by [7]

$$t = \frac{\lambda_0}{4n}, \quad (1)$$

where  $t$  is the thickness of each layer,  $\lambda_0$  is the wavelength of light to be reflected and  $n$  is the index of refraction of each layer.

The high reflectance wavelength bandwidth is given by [7]

$$2\Delta g = \frac{4}{\pi} \sin^{-1} \left( \frac{n_H/n_L - 1}{n_H/n_L + 1} \right), \quad (2)$$

where  $g$  is the normalized wavenumber ( $g = \lambda_0/\lambda$ ) and  $n_H$  is the higher and  $n_L$  the lower index of refractions of each of the thin

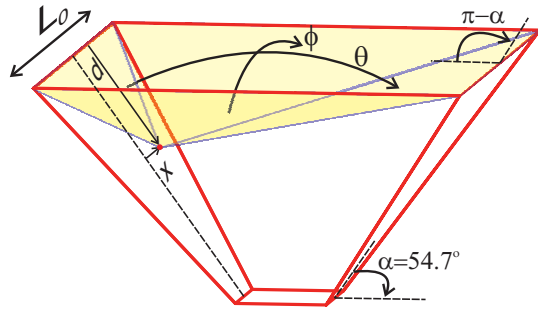


Fig. 3. Arrival angles on the sidewall of a reflector cell cavity

film materials. The wavelengths at the upper ( $\lambda_+$ ) and lower ( $\lambda_-$ ) limits of this reflectance band are given by

$$\lambda_+ = \frac{\lambda_0}{1 - \Delta g} \quad (3)$$

$$\lambda_- = \frac{\lambda_0}{1 + \Delta g}, \quad (4)$$

which yields the reflector bandwidth  $\Delta\lambda$  in wavelength units by

$$\Delta\lambda = \lambda_+ - \lambda_- = \frac{2\Delta g}{1 - (\Delta g)^2} \lambda_0. \quad (5)$$

The width of the reflectance band is maximized using high contrast ratio ( $n_H/n_L$ ) materials. Amorphous silicon ( $\alpha Si$ ,  $n_H = 3.9$ ) and silicon dioxide ( $SiO_2$ ,  $n_L = 1.45$ ) are readily deposited using PECVD and yield a high optical index contrast ( $\frac{n_H}{n_L} = 2.7$ ) and  $\Delta g = 0.3$ , such that for  $\lambda_0 = 795$  nm,  $\Delta\lambda = 520$  nm [8].

### Cavity Shadowing in PECVD

Commonly, PECVD process tools are designed and developed for use with planar substrates. Although PECVD is frequently used for conformal coverage over abrupt features such as the sidewalls of micromachined cavities, it has been shown that PECVD films deposited onto the sidewalls of etched cavities are not uniform and decrease with the depth into the trench [6]. These variations are attributed to the high mean free path of gas species during PECVD and limited film precursor migration along the sidewall surface.

The thin film deposition rate into a cavity is characterized by the arrival angles opposite ( $\theta$ ) and parallel ( $\phi$ ) to the deposition face open to the PECVD reactor vessel (Figure 3). The arrival angle  $\theta$  is calculated by

$$\theta = \sin^{-1} \left\{ \sqrt{\frac{L_0^2 \sin^2(\alpha)}{L_0^2 + d^2 - 2L_0 d \cos(\alpha)}} \right\}, \quad (6)$$

where  $d$  is the depth along the sidewall face,  $L_0$  is the cavity opening width,  $\alpha$  is the etch angle, and the oblique or acute angle solution for  $\sin^{-1}$  must be chosen to provide the physically suitable and continuous solution as a function of sidewall depth. Arrival angle  $\phi$  is calculated by

$$\phi = \tan^{-1} \left\{ \frac{L_0/2 + x}{d} \right\} + \tan^{-1} \left\{ \frac{L_0/2 - x}{d} \right\}, \quad (7)$$

where  $x$  is the horizontal displacement from the sidewall centerline.

The product of the two arrival angles may be used to estimate the total effect of arrival angle shadowing. When normalized by the arrival angles available to a planar substrate ( $\theta_{\perp} = \pi$ ,  $\phi_{\perp} = \pi$ ), the fractional change in the arrival angle may be used to estimate the change in the deposition rate onto a micromachined cavity sidewall from that onto a planar surface. This yields the ratio of thickness

of a thin film on a cavity sidewall  $t$  to the thickness on a planar surface  $t^{\perp}$  according to

$$\frac{t}{t^{\perp}} = \frac{\phi\theta}{\phi_{\perp}\theta_{\perp}} = \frac{\phi\theta}{\pi^2}. \quad (8)$$

From (1), the thickness variation in (8) results in two optical characteristics for a cavity sidewall integrated reflector: The first is the discrete shift in the reflectance band between a reflector deposited on a planar surface and onto cavity sidewall. The second characteristic is the continuous shift of the reflectance band to lower wavelengths down the reflector face into the cavity.

### Optimized Bragg Reflector for Cavity Sidewall Integration

PECVD process parameters are generally defined in terms of the planar deposition rate. Since the physical thickness of each layer will shift across the interface from planar to sidewall deposition, it is of interest to define the design wavelength for planar deposition  $\lambda_0^{\perp}$  that will achieve a sidewall reflector design at wavelength  $\lambda$ . In addition, it is desirable to optimize the planar design to maximize the reflectance at  $\lambda$  over as much of the sidewall as possible under the shift to lower wavelengths down the sidewall into the cavity.

The reflector may be optimized at  $\lambda$  if it is equal to the wavelength at the lower limit of the reflectance band  $\lambda_-$  at the top of the cavity sidewall. This provides that the entire reflectance band is available for decreasing film thickness and shifts to lower reflectance band wavelengths. Using (1), (4), and (8) yields

$$\frac{\phi\theta}{\phi_{\perp}\theta_{\perp}} = \frac{\lambda_-(1 + \Delta g)}{\lambda_0^{\perp}}. \quad (9)$$

Optimizing (9) by setting  $\lambda = \lambda_-$  and evaluating the left hand side for the shadowing at the top of the sidewall for  $d = 0$  yields

$$\lambda_0^{\perp} = \frac{\lambda(1 + \Delta g)}{1 - \alpha/\pi}, \quad (10)$$

where  $\alpha$  is evaluated in radian units. Equation (10) is used to determine the planar deposition design wavelength  $\lambda_0^{\perp}$  which yields a reflector designed to maximize the reflectance at a wavelength  $\lambda$  deposited on a sidewall at etch angle  $\alpha$ . For a  $\alpha Si / SiO_2$  system with  $\alpha = 54.7^\circ$  and  $\lambda = 795$  nm, we find  $\lambda_0^{\perp} = 1480$  nm.  $\lambda_0^{\perp}$  is used to establish the deposition time using the thin film thickness from (1) for the deposition rates in any particular PECVD system.

### Robustness to Film Thinning

The reflection bandwidth may be used as a measure of the robustness to film thinning due to cavity shadowing when used in narrowband (laser) applications at a wavelength  $\lambda$ . Thinning thin film layer thicknesses will shift the reflection wavelength according to (1). If the variation in thickness causes a shift in the target wavelength  $\lambda_0$  greater than the bandwidth of the reflector  $\Delta\lambda$ , the reflectance will be reduced at the target wavelength. Using (3) and (4) with (1) reflector wavelength limits over the fractional change in thin film thickness are evaluated according to

$$\frac{t}{t_0} = \frac{(1 - \Delta g)}{(1 + \Delta g)}, \quad (11)$$

where  $t_0$  is the thickness at  $d = 0$  and  $\lambda \equiv \lambda_- \equiv \lambda_+$  for a reflector ideally optimized to maximize reflectance at  $\lambda$ . For an  $\alpha Si / SiO_2$  Bragg reflector  $t/t_0 = 0.54$ , which indicates that the reflector may be optimized using (10) to be robust for up to a reduction in the thin film thicknesses of 46%.

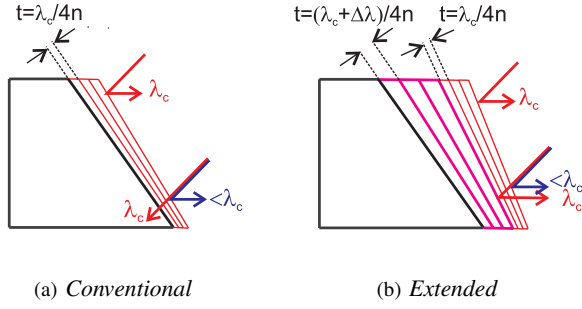


Fig. 4. Bragg reflector design for deposition shadowing robustness

### Extended Bragg Reflector

The variation in film thickness due to cavity shadowing in a particular cavity geometry may be too large to maintain high reflectance at the target wavelength using a conventional Bragg reflector despite optimization. The effect of cavity shadowing on deposition rate variation is shown in Figure 5(a) for the geometry explored in this work, which produces a pattern nearly identical to the color variation observed by the naked eye on the sidewall of the reflector cell (Figure 2). At the bottom of the sidewall, the film thickness will decrease to less than  $t/t_0 = 0.3$ , resulting in a reduction in the thickness of the reflector films of more than 70 %.

The effect of this shift in deposition rate on an optimized conventional Bragg reflector is shown in Figure 5(b). As the reduction in deposition rate exceeds 46 %, the reflectance band is shifted below  $\lambda = 795$  nm and the reflectance is reduced to below 50 % to as low as 10% on the lower face of sidewall reflector, becoming effectively transparent to the design wavelength over the lower region of the reflector (Figure 4(a)).

However, the bandwidth of the reflector may be extended by using two Bragg reflectors in series. A second, thicker Bragg reflector provides high reflectance at higher wavelengths and adds to the total reflectance bandwidth. The second reflectors then provides high reflectance in the region where the upper Bragg reflector is transparent (Figure 4(b)).

The design wavelength of the second reflector is optimally designed by shifting the design wavelength by the reflectance bandwidth to  $\lambda_0^S$ . Using (3) and (4) yields

$$\frac{\lambda_0^S}{\lambda_0} = \frac{(1 + \Delta g)}{(1 - \Delta g)}, \quad (12)$$

where the upper reflectance band limit of the original reflector is matched to the lower limit of the second reflector ( $\lambda_+ \equiv \lambda_-^S$ ) to

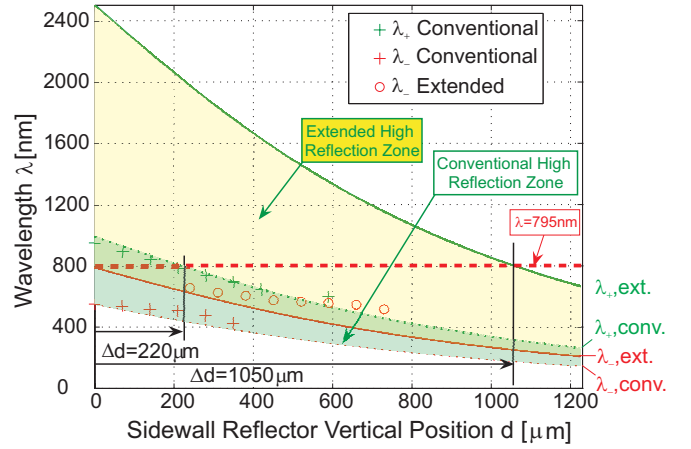


Fig. 6. Conventional vs. optimally designed Extended Bragg reflectors for use at 795 nm in micromachined reflector cell

create a composite reflector with an ideally extended reflectance to  $2\Delta g$ . For the  $\alpha Si / SiO_2$  Bragg reflector, the shifted reflector is optimally designed with  $\lambda_0^S = 1.8\lambda_0$ , increasing the thickness of the layers by 80 %. From (11) and  $2\Delta g = 0.6$ , the extended reflector is able to maintain high reflectance over thickness reductions due to cavity shadowing down to  $t/t_0 = 0.3$ . As shown in Figure 5(c), the use of an extended band reflector allows 90 % reflectance to be maintained down the sidewall for up to 70 % thinning due to cavity shadowing.

### EXPERIMENTAL RESULTS

Reflector cells were fabricated according to the process described previously in [4]. Briefly, a 1 mm thick  $\langle 100 \rangle$  silicon wafer is wet through-etched in potassium hydroxide (KOH) with a silicon nitride hardmask with 1.8 mm square lithographically patterned openings. This produces cavities with  $54.7^\circ$  sidewalls formed by the  $\langle 111 \rangle$  crystallographic planes. Optical thin films are sequentially deposited onto the sidewalls via PECVD in a PlasmaTherm 790 under continuous vacuum forming reflectors.

The reflector is composed of two six layer Bragg reflectors in series with a total of 12 alternating  $\alpha Si$  and  $SiO_2$  thin films. The top (thinner) six layers are of  $\alpha Si$  and  $SiO_2$  with 90 nm and 240 nm planar deposition thicknesses, respectively. Upon deposition onto the sidewall of the cavity, the thicknesses of the films are expected to reduce by 30 % according to (9), yielding estimated sidewall thicknesses of 60 nm and 170 nm, respectively. These layers provide high reflectance over the upper section of the cell. The bottom (thicker) six layers are of  $\alpha Si$  and  $SiO_2$  with planar

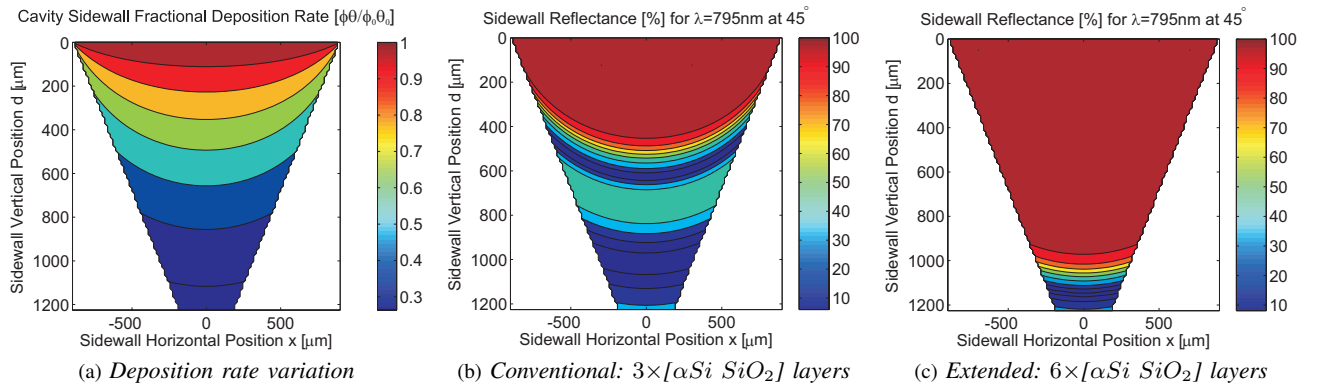


Fig. 5. Effect of cavity deposition shadowing on sidewall PECVD Bragg reflectors ( $L_0 = 1.8$  mm,  $\alpha = 54.7^\circ$ )

deposition thicknesses 170 nm and 430 nm, sidewall thicknesses of 120 nm and 300 nm, and provide high reflectance over the lower section of the cell.

The reflectance bandwidth of the cell reflector faces were characterized by using an Ocean Optics [9] USB2000 spectrometer with a reflection probe coupled to an LS-1 tungsten halogen light source. The lower wavelength limits of the reflection bandwidth was extracted from this broadband characterization. This is compared to the wavelength limits for the previously fabricated six layer conventional reflector not optimized for sidewall deposition, as well as the analytically projected reflectance bandwidths, in Figure 6. The optimized reflector is demonstrated to maintain high reflectance at 795 nm over more than 85 % of the cavity sidewall, compared to less than 20 % for the previously fabricated conventional Bragg reflector.

The performance of a complete cell is demonstrated at 795 nm by mounting a sample on a rotation stage from which the circularly polarized collimated beam from a ULM [9] VCSEL is directed via the sidewall reflectors into a Thorlabs [9] PAX polarimeter, as shown in Figure 7. Return reflection demonstrates optical losses of less than -1.5 dB and the polarization state is maintained to  $\pm 2^\circ$  of ellipticity over incident angles from  $10^\circ$  to  $30^\circ$ , as shown in Figure 8. This experimental results demonstrate applicability of the design to many atomic MEMS applications of interest, as both high reflectance and ellipticity maintenance is required for the propagation of circularly polarized light in those applications.

## CONCLUSIONS

An optimized design procedure for the integration of multilayer PECVD reflectors onto the sidewalls of bulk micromachined cavities has been described for the fabrication of reflector cells with improved optical return performance. This procedure optimizes the reflectance bandwidth for the cavity geometry to maintain high reflectance under deposition non-uniformities caused by deposition shadowing. A design for an extended reflectance band was introduced by using two shifted Bragg reflectors in series. The design was shown to be effective in maintaining high reflection at the  $D_1$  absorption wavelength of  $^{87}\text{Rb}$  despite non-uniformities in excess of 70 % for optical return applications. The fabricated cell was characterized to be able to return light at 795 nm with losses less than 1.5 dB while maintaining the polarization ellipticity of circular polarized light to  $\pm 2^\circ$ . In this paper we demonstrate an effective technique for the integration of multilayer reflectors with nonplanar microdevices, such as on the sidewalls of micromachined cavities. This work paves the way for the introduction of high performance optics into atomic MEMS sensors and other optical MEMS with nontrivial geometries.

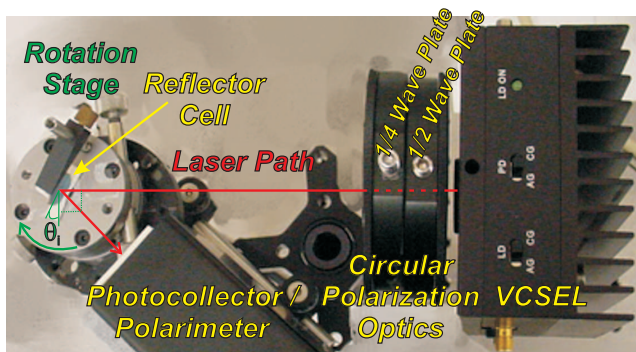


Fig. 7. Experimental stage for return reflection characterization of the Bragg reflector cell

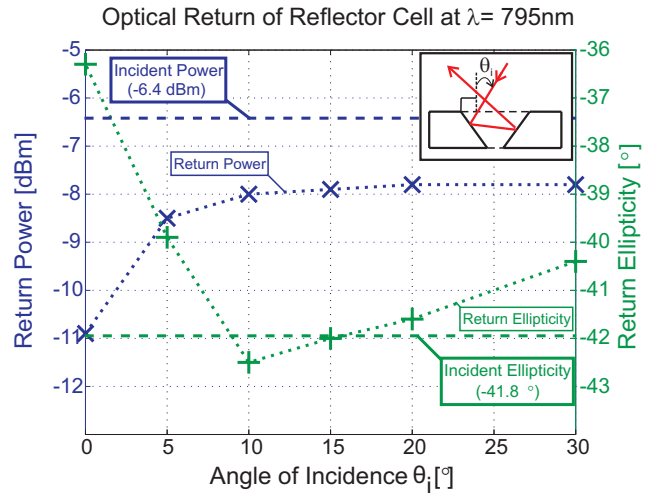


Fig. 8. Experimental return reflection characterization of the extended Bragg reflector cell

## ACKNOWLEDGMENT

The authors thank the staff of the Integrated Nanosystems Research Facility (INRF) for fabrication assistance. This work was supported in part by the Defense Advanced Research Projects Agency (DARPA) Navigation-Grade Integrated Micro Gyroscopes (NGIMG) program and is a partial contribution of the National Institute of Standards and Technology (NIST), an agency of the US government, and is not subject to copyright.

## REFERENCES

- [1] D. Younger, L. Lust, D. Carlson, S. Lu, L. Forner, H. Chanhvongsak, and T. Stark, "A manufacturable chip-scale atomic clock," in *Transducers '07 & Eurosensors XXI: The 14th International Conference on Solid-State Sensors and Actuators and Microsystems*, June 2007.
- [2] L.-A. Liew, S. Knappe, J. Moreland, H. Robinson, L. Hollberg, and J. Kitching, "Microfabricated alkali atom vapor cells," *Appl. Phys. Lett.*, vol. 84, p. 2694, 2004.
- [3] S. Knappe, V. Gerginov, P. D. D. Schwindt, V. Shah, H. G. Robinson, L. Hollberg, and J. Kitching, "Atomic vapor cells for chip-scale atomic clocks with improved long-term frequency stability," *Opt. Lett.*, vol. 30, pp. 351–2353, 2005.
- [4] M. Perez, U. Nguyen, S. Knappe, E. Donley, J. Kitching, and A. Shkel, "Rubidium vapor cell with integrated nonmetallic multilayer reflectors," in *IEEE 21st International Conference on Micro Electro Mechanical Systems, 2008. MEMS 2008*, 13–17 January 2008, pp. 790–793.
- [5] L. Martinu and D. Poitras, "Plasma deposition of optical films and coatings: A review," *Journal of Vacuum Science & Technology A: Vacuum, Surfaces, and Films*, vol. 18, no. 6, pp. 2619–2645, 2000.
- [6] A. Adams, "Plasma deposition of inorganic films," *Solid State Technology*, vol. 26, no. 4, pp. 135–139, April 1983.
- [7] H. A. Macleod, *Thin-Film Optical Filters*, 3rd ed. Institute of Physics Publishing, Bristol–Philadelphia, 2001.
- [8] E. D. Palik, *Handbook of Optical Constants of Solids*, E. D. Palik, Ed. Elsevier, 1998, vol. 1.
- [9] "Products or companies named here are cited only in the interested of complete scientific description, and neither constitute nor imply endorsement by NIST or by the US government."

# A CAVITY-LESS MICROMACHINED CAPACITIVE PRESSURE SENSOR FOR WIRELESS OPERATION IN LIQUID AMBIENT

K. Takahata<sup>1</sup> and Y.B. Gianchandani<sup>2</sup>

<sup>1</sup>Department of Electrical and Computer Engineering, University of British Columbia, Vancouver, Canada

<sup>2</sup>Department of Electrical Engineering and Computer Science, University of Michigan, Ann Arbor, USA

## ABSTRACT

This paper reports a micromachined capacitive pressure sensor that does not use the traditional cavity and diaphragm, and its use in aqueous environment. The device is fabricated with two micromachined plates of stainless steel and an intermediate polymer layer that is soft enough to deform in the target pressure range. A polyurethane room-temperature-vulcanizing liquid rubber of 38- $\mu\text{m}$  thickness is used as the deformable material. For frequency-based interrogation of the capacitance, a passive inductor-capacitor tank is fabricated by combining the capacitive sensor with an inductive coil, which is formed using an 80- $\mu\text{m}$ -diameter copper wire. Wireless sensing in liquid is demonstrated by monitoring the variation in the resonant frequency of the tank via an external coil that is magnetically coupled with the tank. The sensitivity at room temperature is measured to be 23-33 ppm/KPa over a dynamic range of 340 KPa, which is shown to match a theoretical estimate obtained by a bonded elastomer model. The geometrical impact on the frequency response is also evaluated.

## INTRODUCTION

Capacitive pressure sensors are favored for low-power and telemetric applications since they draw no DC power, and conveniently form passive inductor-capacitor (L-C) tank circuits for frequency-based measurement of pressure [1-3]. Micromachined capacitive pressure sensors typically use an elastic diaphragm with fixed edges and a sealed cavity in between the diaphragm and the substrate below [4, 5]. Since this configuration relies on the deflection of a relatively thin diaphragm against a sealed cavity, in some applications there is a concern of robustness of the diaphragm and leaks in the cavity seal. For example, in implantable applications, diaphragm or cavity failure is unacceptable. Survivability with high over-pressures and mechanical robustness are critical for certain military uses. Lead transfer for the sealed electrode has also been a persistent challenge.

This research explores a capacitive pressure sensor that consists of two micromachined metal plates with an intermediate polymer layer, eliminating the need of diaphragms and cavities. Use of polymeric material that is soft enough to deform over a target pressure range allows thickness of the polymer, or capacitance of the parallel plate capacitor, to be dependent on hydraulic pressure that surrounds the device (Fig. 1). This capacitive change can be interrogated by monitoring the resonant frequency of an L-C tank in which the sensor serves as a capacitor of the tank. The tank can be formed by coupling an inductor coil with the sensor separately, or it can be done by winding an insulated wire directly on the sensor [6]. The wireless interrogation can be implemented using an external antenna/inductor that is magnetically coupled with the L-C tank device (Fig. 2). The simple sandwich configuration of the pressure sensor provides not only mechanical robustness by eliminating the risk of cavity/diaphragm failures but also more freedom in the selection of structural materials. The latter feature will allow us to use appropriate materials to achieve an inherent compatibility of the device with target environments, e.g., those in corrosive liquid and the human body, circumventing packaging-related limitations that can negatively impact the cost and applicability of the device.

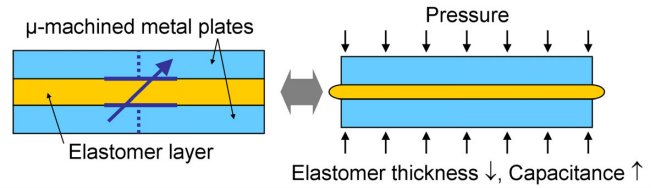


Figure 1: Cross sectional view of the cavity-less bulk-metal/elastomer capacitive pressure sensor.

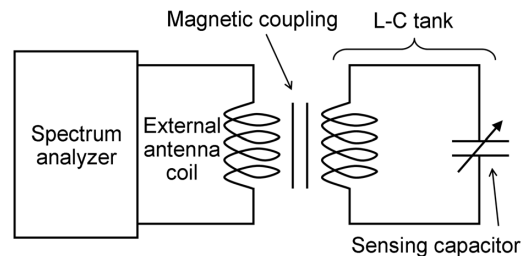


Figure 2: Electrical representation of the wireless measurement set-up for the L-C tank device.

## THEORY

The capacitance of the device is determined by the thickness of the intermediate elastomer that is varied with the ambient pressure. For a rectangular layer of an incompressible, homogeneous elastomer that is bonded with rigid plates on both sides, the relationship between an applied pressure,  $P$ , on each of the plates and the resultant strain,  $e$ , can be expressed as [7]:

$$P = \frac{EA}{2} (S^2 - S_0^2) - E \left[ 1 + \frac{1}{3} \left( \frac{Y^2 - W^2}{Y^2 + W^2} \right)^2 \right] \log(1 - e) \quad (1)$$

where  $E$  is the Young's modulus of the elastomer,  $2Y$  and  $2W$  are the length and width of the rectangle layer, respectively.  $A$  is a constant given by

$$A = \frac{4}{3} + \frac{W}{Y} \left( 2 - \frac{11W}{10Y} \right). \quad (2)$$

$S$  is a geometric parameter called shape factor, which is approximately represented for the structure by

$$S = \frac{YW}{2T(Y+W)} = \frac{S_0}{(1-e)}, \quad (3)$$

where  $2T$  is the resultant thickness of the layer upon the compression and  $S_0$  is the original shape factor with the initial thickness ( $2T_0$ ) before the compression. The strain can be expressed as  $e = 1 - T/T_0$ . The final thickness determines the capacitance of the structure  $C = \epsilon(4YW)/(2T)$ , where  $\epsilon$  is the permittivity of the elastomer, and then the resonant frequency of the L-C tank,  $f = 1/(2\pi\sqrt{LC})$ , where  $L$  is the inductance of the tank. The permittivity of polyurethane is reported to be stable over the pressure range that is involved in this effort [8]. With these, the ratio of the resonant frequency after the compression to the original

one and that for capacitance can be coupled with the strain as

$$\left(\frac{f}{f_0}\right)^2 = \frac{C_0}{C} = \frac{T}{T_0} = 1 - e \quad (4)$$

where  $C_0$  and  $f_0$  are the original capacitance and resonant frequency prior to the compression, respectively. Therefore, the relationship between the applied pressure and the ratio in the resonant frequency,  $f/f_0 = F$ , can be expressed using Eqs. (1) and (4) as

$$P = \frac{EAS_0^2}{2} \left( \frac{1}{F^4} - 1 \right) - E \left[ 1 + \frac{1}{3} \left( \frac{Y^2 - W^2}{Y^2 + W^2} \right)^2 \right] \log(F^2). \quad (5)$$

## FABRICATION

Figure 3 illustrates the fabrication process for the sensors. The base and top plates with the indicated dimensions were cut from type-304 stainless steel sheets with thickness of 100  $\mu\text{m}$  and 50  $\mu\text{m}$ , respectively, using micro-electro-discharge machining ( $\mu\text{EDM}$ ) [9] (Fig. 4). The top plate was designed to be slightly smaller than the base plate (50- $\mu\text{m}$  offset from all sides of the base plate) to assist with the self-alignment of the two plates in the assembly step performed later. The base plate was still connected to the original foil with two tethers after the machining as shown in Fig. 4. A two-part polyurethane RTV liquid rubber (Poly 74-20, part-A: polyurethane pre-polymer, part-B: polyol, Polytek Development Co., PA, USA) with the softener (part-C: plasticizer) was used to form very soft (<20 Shore A) and robust rubber. This effort used the formulation of parts A:B:C=1:1:1, which provides rubber with the Young's modulus of 67 KPa [6]. After applying the mixed solution to the upper surface of the base plate, the top plate was placed on it. The top plate was self-aligned to the base due to surface tension of the solution. After curing, the device was released from the original foil (Fig. 5a). The cured polyurethane had  $\sim 38\text{-}\mu\text{m}$  thickness (Fig. 5b), providing the nominal capacitance of 6.0 pF. An inductive coil

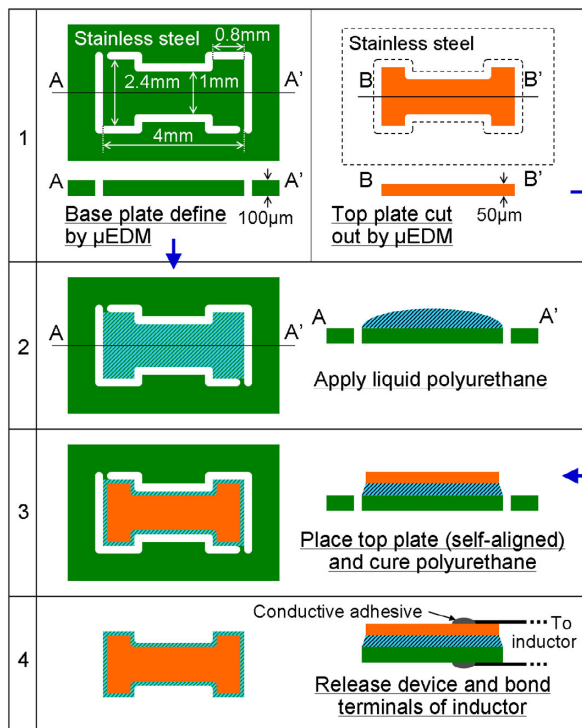


Figure 3: Fabrication process flow.

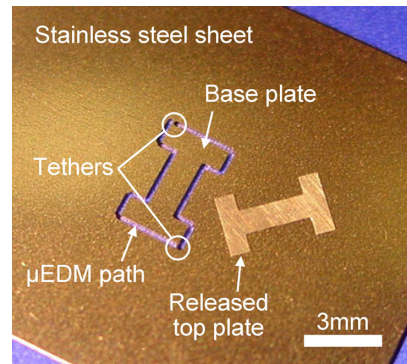


Figure 4: Individual capacitive plates fabricated by  $\mu\text{EDM}$  of type-304 stainless steel foil.

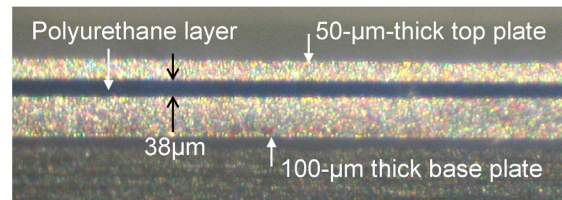
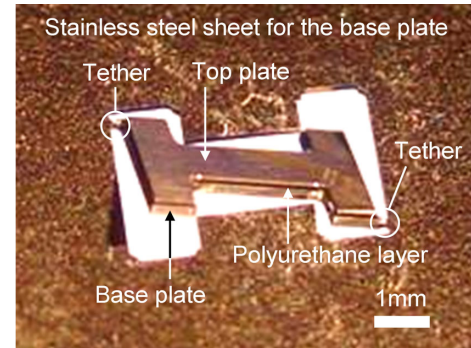


Figure 5: (a: upper) Fabricated device with the cured polyurethane being released from the original stainless-steel foil by breaking the tethers; (b: lower) sidewalls of the capacitive device showing stainless-steel/polyurethane layers.

(5-mm diameter, 5 turns) of 80- $\mu\text{m}$ -thick enamelled copper lead was coupled with the device to form an L-C tank by bonding the terminals of the coil to the capacitive plates with conductive adhesive. The oxide layers of the stainless steel were mechanically removed prior to the bonding to lower the contact resistance, i.e., increase the quality factor of the tank. The resonant frequency of the fabricated L-C tank was measured to be 95 MHz in air, which is close to the theoretical value ( $\sim 80$  MHz) obtained with the measured capacitance and inductance of the tank.

## EXPERIMENTAL RESULTS

Figure 6 illustrates the set-up used for the wireless sensing tests. The fabricated L-C tank devices were placed within a sealed plastic chamber, and magnetically coupled with an external coil through the chamber walls. The resonant frequency of the tank was monitored by tracking the frequency of the characteristic peak, which was reflected by the resonance of the tank, in an s-parameter ( $s_{11}$ ) of the external coil that was connected to a network-spectrum analyzer while changing pressure inside the chamber. The chamber was filled with deionized water to demonstrate operation in liquid. The devices provided a distinct resonant peak, even without packaging/coating for electrical protection. With the same set-up, the frequency dependence on temperature was also evaluated at atmosphere pressure. Temperature of the chamber was controlled

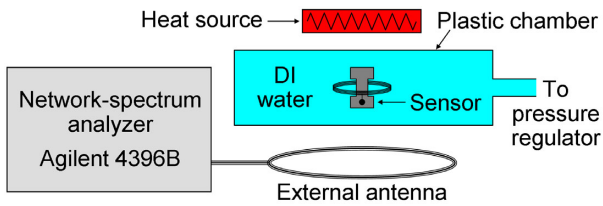


Figure 6: Set-up for wireless testing.

by changing the distance between the device and a source of heat located outside of the chamber as shown in Fig. 6.

Figure 7 shows a typical measured response with the wireless set-up at room temperature in DI water. Compared to the 95 MHz resonant frequency in air, the reduced resonant frequency was expected with the increased parasitic capacitance due to the operation in water. The sensitivity is calculated to be 23-33 ppm/KPa for the pressure range up to 340 KPa. The same measurement at 40 °C also plotted in Fig. 7 exhibits a similar curve with an offset of about +0.4 MHz from that at room temperature. The resonant frequency measured with varying temperature at atmosphere pressure is plotted in Fig. 8, indicating a linear dependence with its coefficient of +783 ppm/°C. The increase of the resonant frequency suggests the decrease of the capacitance, which can be due to the thermal expansion of the polyurethane. (The dielectric constant of polyurethane elastomer was reported to be stable at the temperature range used in this experiment [10].)

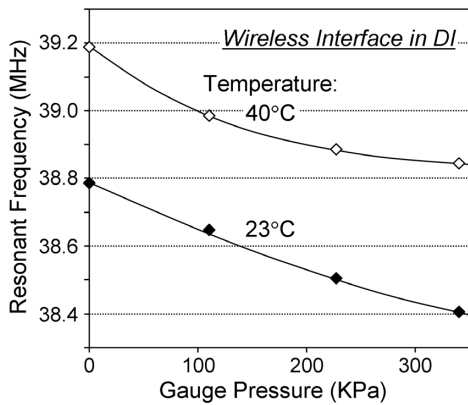


Figure 7: Typical frequency response of the fabricated device vs. pressure measured with the wireless set-up in Fig. 6 at room and elevated temperatures.

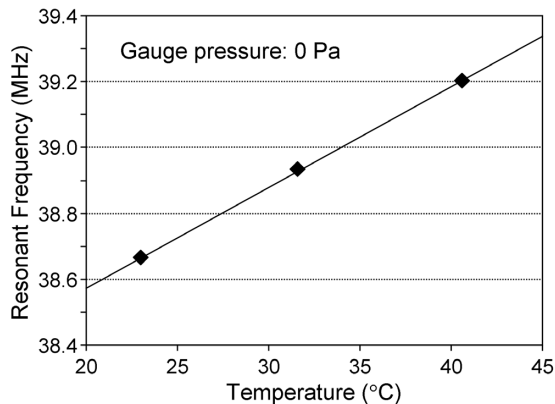


Figure 8: Typical frequency dependence on temperature measured at atmosphere pressure.

## THEORETICAL EVALUATION

It is worth evaluating the measurement results obtained and their consistency with the theoretical estimation. To simplify the task for this initial analysis using Eq. (5), the following calculation assumes that the capacitive structure has a simple rectangular shape with  $4 \times 1\text{-mm}^2$  area, which corresponds to the largest rectangular portion of the actual design (Fig. 3). It further assumes that the dimensions of the top and base plates as well as the intermediate elastomer layer are all identical.

With the measured polyurethane thickness  $2T_0=38\ \mu\text{m}$  and the lateral dimensions of the selected rectangle, i.e.,  $2Y=4\ \text{mm}$  and  $2W=1\ \text{mm}$ , the constant  $A$  and the shape factor  $S_0$  are calculated to be 1.76 and 10.5, respectively. Using Eq. (5) with these values and  $E=67\ \text{KPa}$ , the normalized resonant frequency,  $F$ , as a function of hydrostatic pressure,  $P$ , is numerically solved and plotted in Fig. 9. The “band” shown in the graph represents the possible range of the theoretical response with an assumption of  $\pm 5\%$  variations in the thickness and Young’s modulus of the polyurethane layer. The measurement result in Fig. 7 at room temperature is also plotted in the graph for comparison. It is clearly seen that the theoretical estimation matches well with the measured response at lower pressure. It can also be seen that the measured response deviates from the theoretical response as the pressure is increased.

Figure 10 shows calculated frequency change ( $F$ ) with pressure as a function of the width-to-thickness ratio ( $W/T$ ) of the rectangular

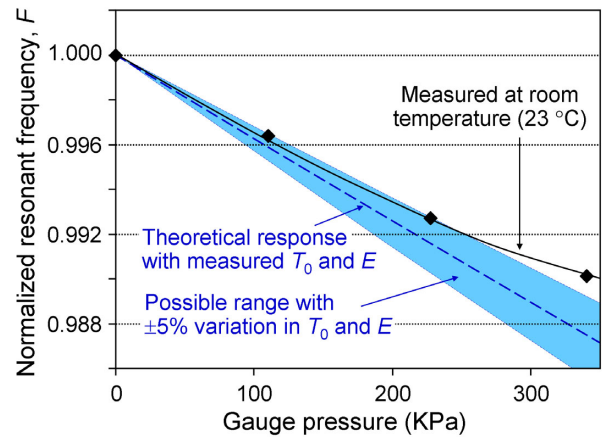


Figure 9: Comparison of relative frequency changes ( $F$ ) between the measured result from Fig. 7 and the theoretical response of the device with the simplified  $4 \times 1\text{-mm}^2$  rectangular shape.

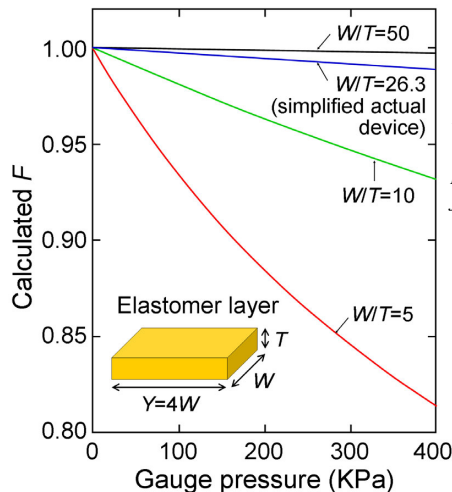


Figure 10: Calculated  $F$  vs. pressure as a function of the  $W/T$  ratio of the rectangular elastomer layer. The result indicates higher sensitivity with lower  $W/T$ .

elastomer layer. The calculation assumes the length-to-width ratio ( $Y/W$ ) of 4 as in the simplified shape of the fabricated device used for the analysis in Fig. 9. The plot for  $W/T=26.3$  corresponds to the actual device and identical to the theoretical plot in Fig 9. The result indicates the strong dependence of the sensor response on the  $W/T$  ratio.

## DISCUSSION

The slightly lower response and deviation from the theoretical estimation seen in Fig. 9 could be partially because of the presence of the extra portions (four  $0.8 \times 0.7\text{-mm}^2$  rectangles) in the actual device that were excluded in the analysis – these portions partially increase the width ( $W$ ), i.e., the  $W/T$  ratio of the device, leading to a reduced response as predicted in Fig. 10. Another hypothesis may be related to the deformation of the capacitive plates especially in the thinner top plate. The compressive strain of the polymer layer depends on the lateral location on the structure under a uniform applied pressure [11]. Hence the upper plate can bend if it is not completely rigid, which is the real case. This deformation, i.e., non-uniform displacement of the plate, may also be a partial source of the deviation. Non-ideal factors attributed to thin layer of the polyurethane material including inhomogeneity of the material and inclusion of particles while mixing the liquid components of the material can be a potential contributor as well. Nevertheless, it is noteworthy that the theoretical model for the bonded elastomer, which was originally developed for macro-scale blocks, is useful to find an approximate response, within a limited pressure range (up to 300 KPa), of a micromachined device with an elastomer layer whose thickness is only a few tens of microns.

The device construction will need some optimization for improved performance and practicality of the device. The analytical result in Fig. 10 suggests a path to achieving higher sensitivity with modified designs of the device. The high temperature coefficient of this device may limit its applications. One of potential options to address the issue would be the use of composite rubbers that incorporate inorganic negative thermal expansion (NTE) nanoparticles [12]. The device will need to be coated with a dielectric layer for electrical insulation when the device is surrounded by a conductive medium. This will be important especially for biomedical and implant applications where the device makes direct contact with polarizable liquids such as body fluid and blood. These electrical and biological insulations can be easily achieved by the use of Parylene materials – the flexible, stretchable feature of the material is expected to minimize the impact of coating on the mechanical behavior of the device.

## CONCLUSIONS

This research has explored a micromachined capacitive pressure sensor that eliminated both a diaphragm and a sealed cavity from its construction. The sensor consists of two metal plates and an intermediate polymer, which is expected to offer high mechanical robustness and reliability. The device was constructed with stainless-steel plates fabricated by a  $\mu$ EDM technique and polyurethane liquid rubber as the polymer layer that permitted self-aligning of the micromachined plates in the assembly process. This material combination can offer good corrosion resistance and fracture toughness, potentially reducing the difficulties associated with packaging for selected applications. The sensor and a 5-mm-diameter copper coil were combined to form an L-C tank, which was successfully used to implement wireless frequency readout for pressure monitoring up to 340 KPa gauge pressure in liquid. The maximum sensitivity was observed to be 33 ppm/KPa. The comparison between the measured result and theoretical

response obtained with a bonded elastomer model revealed the effectiveness of the model in predicting the sensor response.

## ACKNOWLEDGMENTS

The authors would like to thank TRIUMF, Vancouver, B.C., Canada, for providing access to their measurement equipment and Mr. Mark Richardson at the University of Michigan, Ann Arbor, for his assistance in the micromachining work. Y. Gianchandani acknowledges partial support from the IR/D program of the National Science Foundation (NSF), USA. The findings do not necessarily reflect the views of the NSF.

## REFERENCES

- [1] A.D. DeHennis and K.D. Wise, "A Wireless Microsystem for the Remote Sensing of Pressure, Temperature, and Relative Humidity," *IEEE/ASME J. Microelectromech. Syst.*, 14(1), 2005, pp. 12-22.
- [2] K.H. Shina, C.R. Moona, T.H. Leeb, C.H. Limb, and Y.J. Kimb, "Flexible Wireless Pressure Sensor Module," *Sensor. Actuator.*, A 123-124, 2005, pp. 30-35.
- [3] M.A. Fonseca, J.M. English, M. von Arx, and M.G. Allen, "Wireless Micromachined Ceramic Pressure Sensor for High-Temperature Applications," *IEEE/ASME J. Microelectromech. Syst.*, 11(4), 2002, pp. 337-343.
- [4] H. Chau and K.D. Wise, "An Ultraminiature Solid-State Pressure Sensor for a Cardiovascular Catheter," *IEEE Trans. Electron Dev.*, 35(12), 1988, pp. 2355-2362.
- [5] W.H. Ko and Q. Wang, "Touch Mode Capacitive Pressure Sensors for Industrial Applications," *Proc. IEEE Int. Conf. Micro Elec. Mech. Syst. (MEMS)*, 1997, pp. 284-289.
- [6] K. Takahata and Y.B. Gianchandani, "A Micromachined Polyurethane/Stainless-Steel Capacitive Pressure Sensor Without Cavity and Diaphragm," *Proc. IEEE Int. Conf. Solid-State Sensor. Actuator. Microsyst. (Transducers)*, 2005, pp. 483-486.
- [7] J.M. Hill and A.I. Lee, "Large Elastic Compression of Finite Rectangular Blocks of Rubber," *Q. J. Mech. Appl. Math.*, 42(2), 1989, pp. 267-287.
- [8] Z.Y. Cheng, S. Gross, J. Su, and Q.M. Zhang, "Pressure-Temperature Study of Dielectric Relaxation of a Polyurethane Elastomer," *J. Polymer Sci. B Polymer Phys.*, 37(10), 1999, pp. 983-990.
- [9] K. Takahata and Y.B. Gianchandani, "Batch Mode Micro-Electro-Discharge Machining," *IEEE/ASME J. Microelectromech. Syst.*, 11(2), 2002, pp. 102-110.
- [10] J. Su, Q.M. Zhang, C.H. Kim, R.Y. Ting, and R. Capps, "Effects of Transitional Phenomena on the Electric Field Induced Strain-Electrostrictive Response of a Segmented Polyurethane Elastomer," *J. Appl. Poly. Sci.*, 65(7), 1997, pp. 1363-1370.
- [11] B.P. Holownia, "Compression of Bonded Rubber Blocks," *J. Strain Anal.*, 6(2), 1971, pp. 121-123.
- [12] G. Agostini and F.G. Corvasce, "Tire with Low Thermal Expansion Component," United States Patent Application No. 20070074801, 2007.

# A LATERALLY-IMPLANTED PIEZORESISTIVE SKIN-FRICTION SENSOR

Y. Li, V. Chandrasekharan,, B. Bertolucci, T. Nishida, L. Cattafesta, D.P. Arnold and M. Sheplak

Interdisciplinary Microsystems Group, University of Florida, Gainesville, Florida, USA

## ABSTRACT

This paper presents the packaging, fabrication, and calibration of a piezoresistive skin-friction sensor for the direct measurement of wall shear stress. The floating-element structure integrates laterally-implanted piezoresistors into the tether sidewalls to form a fully active Wheatstone bridge for electromechanical transduction. Experimental characterization at a bias voltage of 1.5 V indicates a sensitivity of  $4.24 \mu V/Pa$ , a noise floor of  $11.4 mPa/\sqrt{Hz}$  at  $1 kHz$ , a linear response up to the maximum testing range of  $2 Pa$ , and a flat dynamic response up to the testing limit of  $6.7 kHz$ .

## INTRODUCTION

The measurement of wall shear stress is of vital importance in a variety of applications. For example, in the design of aerospace and naval vehicles, this measurement provides physical insight into the skin-friction drag distributions, flow separation fronts and transition to turbulent flow. From a scientific perspective, the measurement of the mean wall shear stress,  $\bar{\tau}_w$ , is essential for the nondimensionalization of a turbulent boundary layer profile via the friction velocity,  $u^* = \sqrt{\bar{\tau}_w/\rho}$ , where  $\rho$  is the fluid density. Moreover, as computing power continues to increase, measurement of fluctuating wall shear stress will be essential for validating direct numerical simulations, a process of considerable value to the turbulence modeling community. Furthermore, since shear stress is a vector field, it may provide advantages over pressure sensing in feedback flow control applications involving separated flows [1]. Unfortunately, the time-accurate, direct measurement of fluctuating shear stress has not yet been fully realized [2]. MEMS-based devices with high-bandwidth and fine spatial resolution capabilities offer the potential to capture physics of the relevant length scales in at least moderate  $Re$  flows.

Both thermal and floating element micromachined shear stress sensors have been developed for various flow applications.[2] Thermal devices infer the shear-stress via the measurement of Joulean heating rate, hence calibration for quantitative measurements is difficult. Direct sensors measure the integrated shear force on a floating-element using capacitive, [3-5] piezoresistive,[6, 7] or optical [8-10] transduction schemes. None of these devices have successfully transitioned to wind tunnel measurement tools because of performance limitations and/or packaging impracticalities [2]. For use in a wind tunnel, the sensor package must be flush mounted in an aerodynamic model, robust enough to tolerate humidity variations and immune to electromagnetic interference (EMI). We have attempted to address these limitations via the development of a side-implanted piezoresistive sensor. Figure 1 illustrates the floating element device and the junction-isolated sidewall implanted p-type silicon piezoresistors.

The physical structure consists of a  $50 \mu m$  thick,  $1 mm \times 1 mm$  element suspended by four  $1 mm$  long,  $30 \mu m$  wide and  $50 \mu m$  thick tethers. The shear force on the element induces a mechanical stress field in the tethers and thus a resistance change. The piezoresistors are arranged in a fully-active Wheatstone bridge to ideally provide rejection to common mode disturbances, such as pressure fluctuations. A dummy bridge

located next to the sensor is used for temperature corrections. The device modeling and design have been previously reported [11].

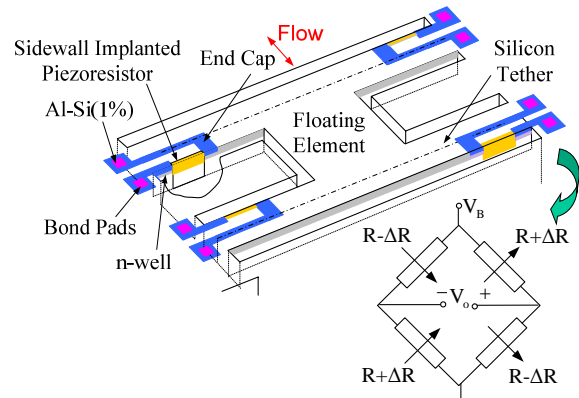


Figure 1: A 3D schematic of the side-implanted piezoresistive shear-stress sensor and equivalent Wheatstone bridge.

## FABRICATION AND PACKAGING

In this section, a brief overview of the main sensor fabrication process is given. A discussion of the sensor package and associated interface circuit follows.

The device is fabricated from a SOI wafer using an 8-mask process. A detailed description of the fabrication process development has previously been reported [12]. The process begins with a phosphorus blanket implantation that forms an n-well. Boron implantation forms a heavily doped Ohmic contact. The tethers and floating element are defined by patterning PECVD oxide via RIE (Figure 2 (A)). The patterned Si is etched vertically  $8 \mu m$  via DRIE to form the trench for the sidewall implant. The scallops formed on the sidewalls during DRIE are smoothed by hydrogen annealing. A  $100 nm$  thick oxide layer is thermally grown as a thin implant oxide on the sidewall. After a preamorphization implant, boron is implanted at an oblique angle of  $54^\circ$  to achieve a  $5 \mu m$  shadow side-wall implantation (Figure 2 (B)). The oxide on the sidewall is etched via BOE, followed by a boron drive-in process to form the piezoresistors. A thin oxide layer is thermally grown as a passivation layer. The tether is defined via DRIE using the BOX layer as an etch stop (Figure 2 (C)). After trench filling with photoresist, the oxide is patterned and etched via BOE to open contact vias, followed by  $1 \mu m$  thick Al-Si(1%) metallization layer. The metal layer is patterned and RIE etched to form the metal contacts. A PECVD silicon nitride layer is then deposited and RIE etched to expose the bond. The structure is released from the backside using DRIE and RIE (Figure 2 (D)). Finally, the sensors are annealed in forming gas for noise floor improvement. An optical photograph of the fabricated device is shown in Figure 3.

After fabrication, the individual die ( $6.2 mm \times 6.2 mm$ ) were separated and then packaged in a printed circuit board (PCB) ( $20 mm \times 20 mm$ ). Figure 4 illustrates the sensor die embedded in the printed circuit board and sealed with glue at the perimeter, which in turn is flush-mounted in a Lucite package for easy wind-tunnel mounting. An interface circuit board was designed for offset compensation. This board includes two sets of

compensation circuitry: one for the active bridge and another for the dummy bridge. This board is attached on the backside of the device package and supported by two screws connected to the Lucite package. The copper wires for the signal output or voltage supply in the device package are soldered to the PCB feedthrough vias.

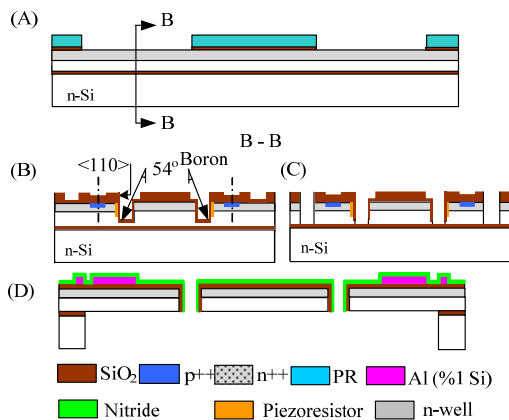


Figure 2: Process flow to fabricate the shear stress sensor.

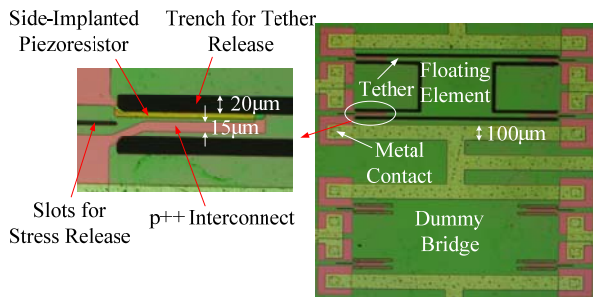


Figure 3: An optical photograph of the fabricated device with a close up view of the tether and side-implanted piezoresistor.

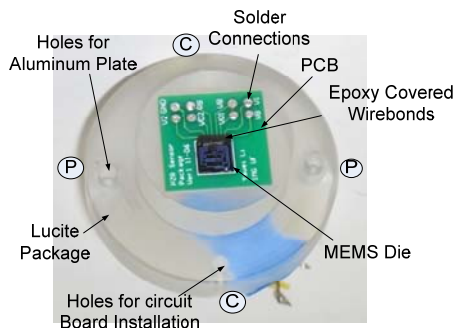


Figure 4: An optical photograph of the sensor package.

## EXPERIMENTAL RESULTS

The experiments were performed in the Interdisciplinary Microsystems Laboratory at the University of Florida. Several tests were performed to determine the electrical and shear stress transduction properties.

### Electrical Characterization

After fabrication, wafer-level electronic testing of the bridge resistance and junction isolation was conducted using an Agilent 4155C semiconductor parameter analyzer and a wafer level probe station. The leakage current is less than  $0.1 \mu A$  up to a reverse bias voltage of  $-10 V$  (Figure 5), after that point a soft break down initiates at  $-20V$  (Figure 6). The input and output resistances of the

bridge are  $414 \Omega$  and  $397 \Omega$  (Figure 7), respectively.

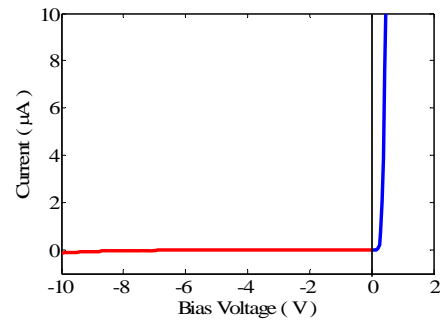


Figure 5: The forward and reverse bias characteristics of p/n diode illustrating the junction isolation of the Wheatstone bridge.

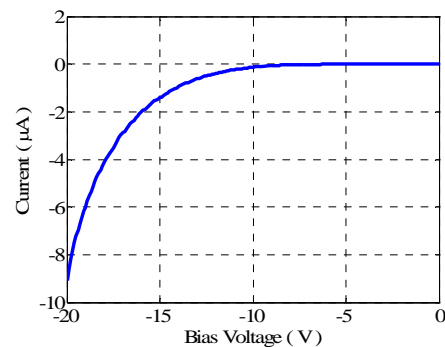


Figure 6: I-V characteristics of the Wheatstone bridge illustrating the breakdown voltage of the p/n diode.

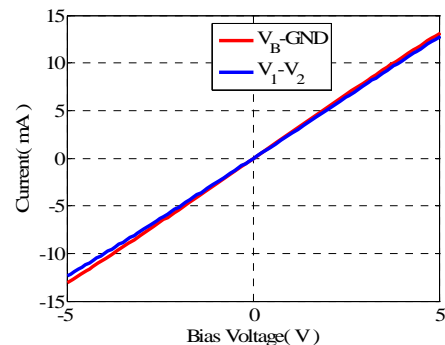


Figure 7: The I-V characteristics of the Wheatstone bridge to extract the input and output resistance.

### Dynamic Characterization

The frequency response and linearity were studied using Stokes' layer excitation of shear-stress in a plane-wave tube (PWT). This technique utilizes acoustic plane waves in a duct to generate known oscillating wall shear stresses [13]. A conceptual schematic of the dynamical calibration setup is shown in Figure 8. The plane wave is generated by a BMS 4590P compression driver that is mounted at one end of the PWT. The PWT consists of a rigid-wall 1"x1" duct with an anechoic termination (a 30.7" long fiberglass wedge), which supports acoustic plane progressive waves propagating along the duct. The sensor and a reference microphone (B&K 4138) are flush-mounted at the same axial position from the driver. The usable bandwidth for plane waves in the PWT is determined by the cut-on frequency of the first higher order mode and is  $6.7 kHz$  in air and  $20 kHz$  in helium. The compensated output voltage from the interface circuit is ac-coupled

and amplified 46 dB by SR560 low noise preamplifier. A B&K PULSE Multi-Analyzer System (Type 3109) is used as the microphone power supply, data acquisition unit, and signal generator for the source signal in the plane wave tube.

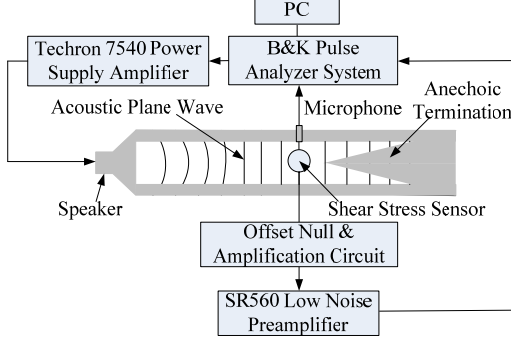


Figure 8: Schematic of experimental setup for the sensor characterization via Stokes' layer excitation.

The dynamic sensitivity and linearity of the sensor was tested with a single tone of 2088 Hz as a function of increasing sound pressure levels (SPL) in air. The sensor was operated at bias voltages of 1.0V, 1.25V, and 1.5V. This is substantially lower than the optimized bias voltage of 10 V to avoid resistor self-heating [11]. Any resistor self-heating will lead to temperature-resistive voltage fluctuations due to unsteady convective cooling [14]. The acoustically-generated wall shear stress for the frequency range of excitation in this paper is approximated by [13]

$$\tau'_{wall} = \frac{p' \sqrt{j\omega\nu}}{c} e^{j(\omega t - kx - \frac{\pi}{2})} \tanh\left(\sqrt{\frac{j\omega b^2}{\nu}}\right), \quad (1)$$

where  $p'$  is the amplitude of the acoustic perturbation,  $j = \sqrt{-1}$ ,  $\nu$  is the kinematic viscosity,  $\omega$  is the angular frequency,  $k = \omega/c$  is the acoustic wave number, and  $b$  is the duct width.

By adjusting the SPL from 123dB to 157dB, the induced shear stress varies from 0.04 Pa to 2.0 Pa. Figure 9 shows normalized output voltages at bias voltages of 1.0 V, 1.25 V and 1.5 V in response to the shear stress variation. The normalized sensitivity is defined as the ratio of the normalized differential sensor output voltage (output voltage/bias voltage) to the input wall shear stress. For all bias conditions, the sensor responds linearly up to 2.0 Pa and the normalized sensitivities (slopes of the plots) are 2.905  $\mu\text{V}/\text{V}/\text{Pa}$ , 2.882  $\mu\text{V}/\text{V}/\text{Pa}$  and 2.828  $\mu\text{V}/\text{V}/\text{Pa}$ , respectively. The predicted normalized sensitivity is 3.65  $\mu\text{V}/\text{V}/\text{Pa}$ . For a balanced Wheatstone bridge without resistor self-heating, the normalized sensitivity should be constant. If resistor self-heating occurs, a power-law dependence on the power dissipation is expected. The close match in normalized sensitivities (<3% variation) indicates that the sensor is responding solely to the integrated shear force fluctuations and not unsteady convective cooling.

The frequency response at bias voltage of 1.5 V is also investigated in this experiment. The normalized frequency response function of the shear stress sensor is given as [13]

$$H(f) = \frac{V(f)}{\tau_{wall}(f)} \frac{\partial \bar{\tau}}{\partial \bar{V}}, \quad (2)$$

where  $V(f)$  is the sensor output with a known input,  $\tau_{wall}(f)$  is obtained via Equation (1), and  $\partial \bar{\tau}/\partial \bar{V}$  is the static sensitivity. For this experiment, we normalized with the 2.088 kHz sensitivity.

Figure 10 demonstrates the magnitude and phase of the actual frequency response function of the shear stress sensor for a nominal input shear-stress magnitude of 0.3 Pa. The gain factor is flat and is between  $-3.01$  dB to  $0.09$  dB for this test. The phase is flat up to 4.552 kHz. These results are not corrected for non-idealities in the anechoic termination which result in finite reflected waves [13]. In addition, there is some suspicion that the results above 4.552 kHz may be corrupted by the scattered evanescent field near the termination. Regardless, there is no apparent resonance in this sensor up to 6.7 kHz. Future experiments will be conducted in helium to obtain the resonant frequency.

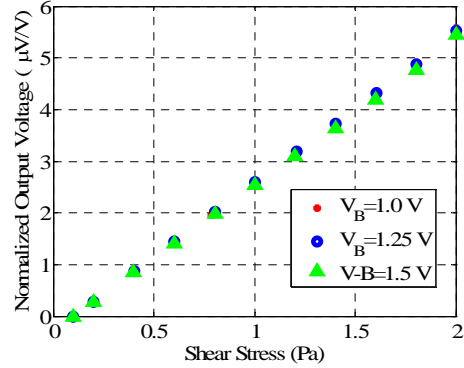


Figure 9: The normalized sensitivity at forcing frequency of 2088Hz with different bias voltages.

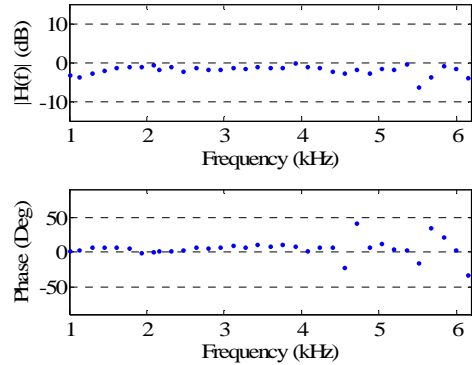


Figure 10: Magnitude and phase of the frequency response function at bias voltage of 1.5V.

### Noise Measurement

The lower end of the dynamic range of the sensor is ultimately limited by the device noise floor. This measurement is made by mounting the sensor in the sidewall of the plane wave tube with the speaker amplifier turned off. This provides a reasonable estimate of the entire sensor system noise floor as installed in a calibration chamber. The compensated voltage output is amplified by the SR560 low noise preamplifier (ac coupled), and then fed into the SRS785 spectrum analyzer [14]. The spectrum analyzer measures the noise power spectral density (PSD), using a Hanning window to avoid the PSD leakage. The measured noise PSD includes the sensor noise and the setup noise, such as EMI, noise of amplifier, the spectrum analyzer and power supply. LabView is used for data acquisition and manipulation. The measured output-referred electrical voltage noise floor is shown in Figure 11 for a bias voltage of 1.5 V. As expected, the electronic noise spectrum is dominated by  $1/f$  noise indicating

that the signal-to-noise ratio for this sensor is a strong function of frequency. At  $1\text{ kHz}$  (with  $1\text{ Hz}$  bin) the noise floor is  $48.2\text{ nV}/\sqrt{\text{Hz}}$  which corresponds to minimum detectable shear stress of  $11.4\text{ mPa}$ .

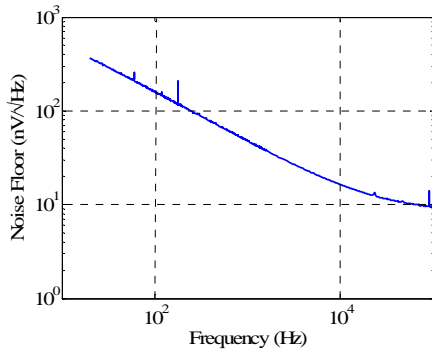


Figure 11: Noise floor of the measurement system.

## CONCLUSION

A proof-of-concept micromachined, floating element shear-stress sensor was developed that employs laterally-implanted piezoresistors. A dynamic characterization of the device revealed a linear response up to  $2.0\text{ Pa}$  and a flat response up to the frequency testing limit of  $6.7\text{ kHz}$ . The theoretically predicted resonant frequency is  $9.8\text{ kHz}$ . Noise floor measurements indicate that  $1/f$  noise dominates and a minimum detectable shear stress of  $11.4\text{ mPa}$  at  $1\text{ kHz}$ . Therefore, the experimentally determined dynamic range is  $11\text{ mPa} - 2\text{ Pa}$ . The theoretically predicted upper end of the dynamic range at 3% static non-linearity is  $5\text{ Pa}$ . The upper ends of the dynamic range and bandwidth, however, could not be verified due to constraints in our calibration apparatus. A summary of the experimental results compared to the theoretical results for a bias voltage of  $1.5\text{ V}$  are listed in Table 1. The normalized sensitivity is close to the predicted design value, but resistor heating precluded using higher bias voltages thus lowering the maximum allowable sensitivity by  $16.5\text{ dB}$ . Furthermore, the noise floor is roughly a factor of 7 higher than predicted. This may be because the measured noise floor is the total system noise, which includes setup noise and sensor noise, whereas the predicted value is just due to the sensor and the SR560 preamplifier. There are also substantial differences in the predicted versus realized bridge impedance which means that the voltage noise of the resistors may also be higher than predicted. Isolated measurements of the resistors must be made to quantify this noise source [15].

Table 1: Performance comparison

Parameters	Predicted Value	Experimental Results
Normalized Sensitivity ( $\mu\text{V}/\text{V}/\text{Pa}$ )	3.65	2.83
Noise Floor ( $\text{nV}$ )	6.5	48.2
MDS ( $\text{mPa}$ )	1.2	11.4
Bandwidth ( $\text{kHz}$ )	9.8	$> 6.7$
Resistance ( $\Omega$ )	1000	397
$\tau_{\text{max}}$ ( $\text{Pa}$ )	5	$> 2$

## REFERENCES

- [1] M. Sheplak, L. Cattafesta, and Y. Tian, "Micromachined Shear Stress Sensors for Flow Control Applications," in Proceedings of the IUTAM Symposium Held at the Royal Geographical Society, London, England 2007.
- [2] J. W. Naughton and M. Sheplak, "Modern Development in Shear Stress Measurement," Prog. Aerosp. Sci., Vol. 38, pp. 515-570, 2002.
- [3] M. A. Schmidt, R. T. Howe, S. D. Senturia, and J. H. Haritonidis, "Design and Calibration of a Micromachined Floating-Element Shear-Stress Sensor," IEEE Trans. Electron Devices, Vol. 35, pp. 750-757, 1988.
- [4] T. Pan, D. Hyman, and M. Mehregany, "Microfabricated Shear Stress Sensors, Part 1: Design and Fabrication," AIAA J., Vol. 37, pp. 66-72, 1999.
- [5] J. Zhe, V. Modi, and J. Kenneth. R. Farmer, "A Microfabricated Wall Shear-Stress Capacitive Sensing," J. Microelectromech. Syst., Vol. 14 (1), pp. 167-175, Feb. 2005.
- [6] J. Shajii, K.-Y. Ng, and M. A. Schmidt, "A Microfabricated Floating Element Shear Stress Sensor Using Wafer-bonding Technology," J. Microelectromech. Syst., Vol. 1 (2), pp. 89-94, June 1992.
- [7] A. A. Barlian, S.-J. Park, V. Mukundan, and B. L. Pruitt, "Design and characterization of microfabricated piezoresistive floating element-based shear stress sensors," Sensors and Actuators A, Vol. 134 (1), pp. 77-87, Feb 2007.
- [8] A. Padmanabhan, H. Goldberg, K. D. Breuer, and M. A. Schmidt, "A Wafer-Bonded Floating-Element Shear Stress Microsensor with Optical Position Sensing by Photodiodes," J. Microelectromech. Syst., Vol. 5 (4), pp. 307-315, 1996.
- [9] F.-G. Tseng and C.-J. Lin, "Polymer MEMS-Based Fabry-Perot Shear Stress Sensor," IEEE Sensors J, Vol. 3, pp. 812-817, Dec. 2003.
- [10] S. Horowitz, T.-A. Chen, V. Chandrasekaran, K. Tedjojuwono, L. Cattafesta, T. Nishida, and M. Sheplak, "A Micromachined Geometric Moiré Interferometry Floating-Element Shear Stress Sensor," in IEEE Solid-State Sensor and Actuator Workshop, 2004, pp. 13-18.
- [11] Y. Li, M. Papila, T. Nishida, L. Cattafesta, and M. Sheplak, "Modeling and optimization of a side-implanted piezoresistive shear stress sensor," in Proceeding of SPIE 13th Annual International Symposium on Smart Structures and Materials, San Diego, CA, 2006. Paper No. 6174-7,
- [12] Y. Li, T. Nishida, D. P. Arnold, and M. Sheplak, "Microfabrication of a wall shear stress sensor using side-implanted piezoresistive tethers," in Proceeding of SPIE 14th Annual International Symposium on Smart Structures and Materials, San Diego, CA, 2007, pp. Paper No. 6529-13.
- [13] V. Chandrasekaran, A. Cain, T. Nishida, L. N. Cattafesta, and M. Sheplak, "Dynamic calibration for thermal shear-stress sensors with mean flow," Exp Fluids, Vol. 39, pp. 56-65, 2005.
- [14] T. V. Papen, H. Steffes, H. D. Ngo, and E. Obermeier, "A micro surface fence probe for the application in flow reverse area," Sensors and Actuators A, Vol. 97-98, pp. 264-270, 2002.
- [15] R. Dieme, G. Bosman, M. Sheplak, and T. Nishida, "Source of excess noise in silicon piezoresistive microphones," J. Acoustical Society of America, Vol. 119, pp. 2710-2720, May 2006.

# A MICROMACHINED WIRELESS GAMMA RADIATION DETECTOR USING BULK METAL CONVERSION LAYERS

Christine K. Eun and Yogesh B. Gianchandani

Department of Electrical Engineering and Computer Science, University of Michigan, Ann Arbor

## ABSTRACT

This paper reports a micromachined wireless gamma radiation sensor. The gas-based detector is comprised of a patterned bulk metal conversion layer assembled on top of a pair of thin-film copper electrodes electroplated on a glass substrate. The metal layer converts gamma radiation into photoelectrons, which ionize the sensing gas. A bias between the electrodes creates an electric field that accelerates the charged particles, resulting in a current pulse. These current pulses generate a wideband signal extending into the GHz frequency range. Experiments were conducted in two gas environments: in an  $N_2/Ne$  mixture at 640 Torr and in air at 760 Torr. Two types of metals (platinum-rhodium and tungsten) for the conversion layer were evaluated using  $1.0 \mu Ci$  gamma sources of  $^{65}Zn$  and  $^{22}Na$ . By using a trench pattern ( $1.5 \text{ mm} \times 1.8 \text{ mm}$ ), machined in a  $200 \mu m$ -thick Pt-Rh metal layer, the count rate from the detector exceeded 28 kcpm and showed  $>10X$  improvement in sensing when compared to an un-patterned metal layer. The detector operated under partial pressure in the nitrogen/neon mixture. Other metal conversion patterns and stack configurations were also investigated.

## INTRODUCTION

Sensing gamma radiation is important for many homeland security applications. Other forms of radiation (alphas and betas) have limited ranges and can be shielded more easily. For example, sheets of paper easily block alpha particles, while beta particles have ranges on the order of meters in air. Gamma-rays are high-energy photons that are emitted from many dangerous radioisotopes. Depending on their initial energy, they can travel up to tens of meters in air and require thick layers of lead for shielding. However, they are difficult to detect because of their low probability of interaction with matter. Miniaturized wireless gamma sensors could someday be used in a network configuration to monitor areas with high pedestrian traffic (e.g. shopping malls, football stadiums, subway stations). They would offer ultra-compactness and low power consumption, enabling rapid deployment and reconfiguration.

A miniaturized gas-based beta sensor with wireless capability has been reported in [1]. It is comprised of thin-film metal electrodes deposited on a glass substrate surrounded by a sensing gas mixture. Beta particles (or high-energy electrons) ionize the gas atoms and initiate electron avalanche breakdown, which results in a current pulse. These current pulses have been shown to generate a wireless signal for use in networking applications.

Gamma radiation is not detected directly by gas-based devices because the low density of gas provides low probability of interaction with the incident radiation. Conventional Geiger counters detect gamma radiation by the photoelectric effect. Gamma photons bombard the metal encapsulation of the sensing gas, producing photoelectrons within the Geiger tube, that avalanche and create current pulses. The use of metals to convert gamma-rays into photoelectrons is well established [2-6].

This paper presents a micromachined gas-based wireless gamma radiation detector that uses a bulk metal layer for gamma-to-photoelectron conversion. In particular, it explores the impact of thickness and structural shape of the metal conversion layer on two device configurations.

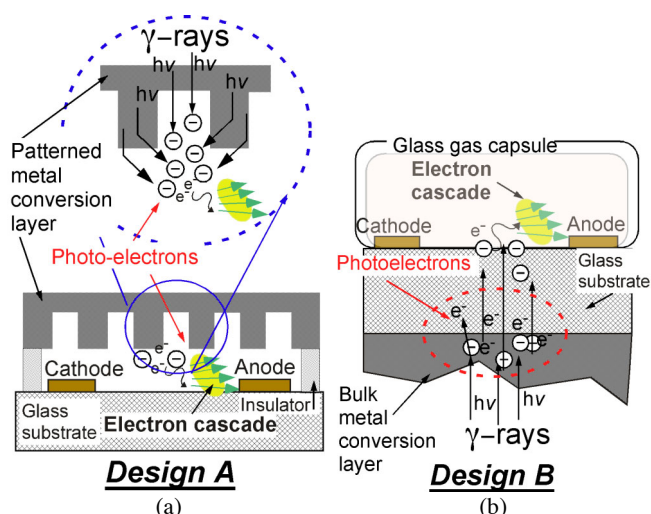


**Fig. 1:** (a) **Design A** - Cross-section of gamma detector with patterned bulk metal conversion layer. As gamma radiation interacts with the metal conversion layer, the generated photoelectrons ionize the surrounding gas between the electrodes, initiating a gas discharge and current pulse. Design A can facilitate a higher collection efficiency of these scattered events. (b) Cross-section of preliminary device structure (**Design B**) with an un-patterned metal layer. The photoelectrons penetrate through the glass substrate to ionize the gas atoms.

## DEVICE CONCEPTS AND OPERATION

One device structure (**Design A**) consists of a glass substrate with electroplated copper electrodes and assembled on top of it, a micromachined conversion layer patterned from bulk metal (Fig. 1a). When gamma radiation interacts with the metal conversion layer (MCL), photoelectrons are emitted and ionize the surrounding gas. An electric field between the electrodes accelerates the electrons, leading to an avalanche breakdown measured as a current pulse. Two machining patterns that increase the exposed surface area for the **Design A** MCL are proposed: (1) A groove or trench-style pattern (TRENCH MCL) and (2) a square well or column-style pattern (COLUMN MCL). These structures can enhance the generation and collection efficiency of photoelectrons. Increasing the metal surface area exposed to the sensing gas can decrease photoelectron re-absorption probability in the MCL [2, 3].

**Design B** (Fig. 1b) is a simpler configuration that uses an un-patterned MCL (SOLID MCL) to achieve the basic conversion efficiency without structural enhancement. (In this, the MCL is located on the backside of the glass substrate.) The photoelectrons travel through the back of the glass substrate and ionize the gas atoms located near the electrodes.

Another choice for the substrate material is mica. In conventional Geiger counters, alpha particles and lower energy beta particles must travel through a thin mica window ( $70\text{-}100 \mu m$ ) in order to reach the sensing gas. Factors that need to be considered in choosing an appropriate substrate material include stiffness, yield strength, temperature coefficient, and charging issues.

The emission and scattering processes are statistically determined by gamma energy (Fig. 2). Gamma radiation ionizes via three main processes: (1) the photoelectric effect, in which the gamma-ray imparts all its energy to a photoelectron, which scatters at an angle determined by the gamma energy (low-energy photons); (2) Compton scattering, in which the gamma-ray imparts only a portion of its energy to the photoelectron resulting in multiple photoelectrons per gamma-ray (medium-energy photons); and (3) pair production, in which the energy of the gamma radiation is converted to an electron/positron pair (high-energy photons).

Higher-density metals (e.g. tungsten and platinum-rhodium) are desirable for the MCL because of their higher interaction probabilities. Figure 3 shows the attenuation coefficient as a function of photon energy for W and Pt-Rh [7]. Having similar densities and excitation energies, they share similar collision processes. At higher photon energies (>1 MeV), Compton scattering dominates and results in multiple photoelectrons generated in the metal layer per gamma-ray. Figure 4 compares the theoretical range of photoelectrons through various media such as air, Pyrex glass, and metals [8]. Photoelectrons have similar theoretical ranges in W and Pt-Rh. Even though photon interactions increase with metal thickness, the resulting photoelectrons have a higher probability of re-absorption back into the metal layer, instead of being ejected out. The optimal relationship is to have photoelectron mean-free-range comparable to the MCL thickness.

Table I lists gamma-emitting radioisotopes used in the testing phase of this effort: 1.0  $\mu\text{Ci}$   $^{65}\text{Zn}$  and 1.0  $\mu\text{Ci}$   $^{22}\text{Na}$ . Both are relatively high-energy gamma radiation sources that emit beta particles in conjunction with gamma radiation. Unlike beta radiation that is emitted over a spectrum of radiation energy levels, gamma radiation is emitted at specific energies. The interactions of W and Pt-Rh with these sources are primarily the photoelectric effect, and Compton scattering.

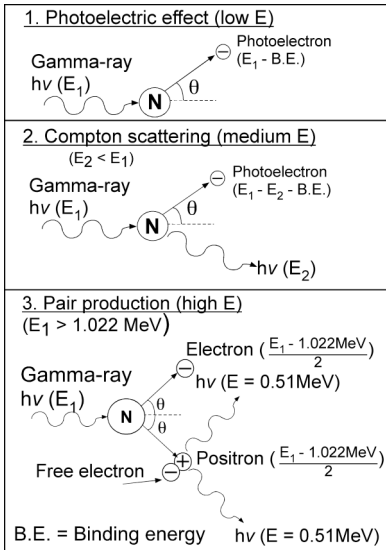


**Fig. 2:** Collision processes for gamma radiation interacting in a medium. The photon energy determines the type of collision as well as the scattering angle of the resulting photoelectron.

**Table I:** List of gamma-emitting radioisotopes by type and energy of emissions.  $\beta$ -particles are commonly released in conjunction with gamma radiation.

*Most frequent emission	Gamma Energies (MeV)		Beta Energies (MeV)	
	$E_{\text{MIN}}$	$E_{\text{MAX}}$	$E_{\text{MIN}}$	$E_{\text{MAX}}$
Isotope				
Na-22		*1.274		*0.546
Zn-65	0.345	*1.115		*0.330

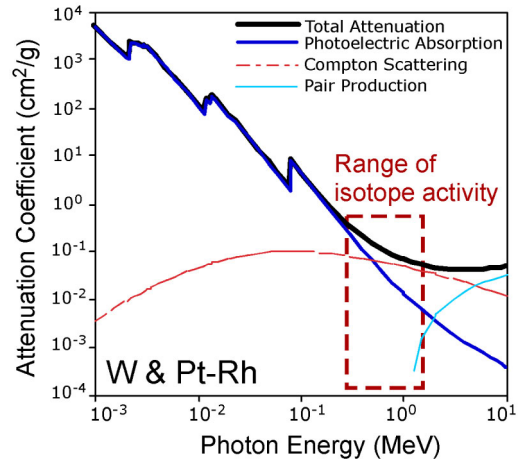


**Fig. 3:** Theoretical plot of different collision processes as a function of gamma energy for tungsten and platinum-rhodium [7]. Atten. coefficient has been normalized by material density ( $\text{g}/\text{cm}^3$ ).

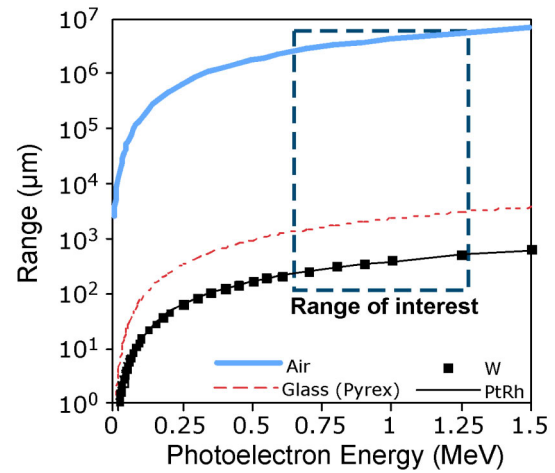


**Fig. 4:** Theoretical range of electrons through tungsten (W), platinum-rhodium (Pt-Rh), glass and air [8]. The thickness of the metal layer should be less than the range of the photoelectrons in order to maximize interaction with the gas.

## FABRICATION

The Pt-Rh metal conversion layer is patterned by batch mode micro-electro-discharge machining ( $\mu\text{EDM}$ ). Figure 5 shows the machining process. In  $\mu\text{EDM}$ , controlled spark discharges (80 V, 100 pF, 5 kW) between a tool cathode and workpiece anode thermally erode conductive material. In batch mode, the entire pattern is machined in parallel, increasing throughput. The 175  $\mu\text{m}$ -tall copper tool is fabricated with a PMMA LIGA process but an SU-8 process can also be used. A 200 nm silicon coating is deposited on the tool and selectively removed at the top to limit the effects from debris buildup [9].

The finished COLUMN MCL pattern is an 8 X 8 array of 110  $\mu\text{m}$  square holes with 90  $\mu\text{m}$  spacing, giving a total active area of 1.5 mm X 1.5 mm. To form the TRENCH MCL, the same tool was dithered laterally by 150  $\mu\text{m}$  during machining, giving an active area of 1.5 mm X 1.8 mm. Each pattern was machined to a depth of 110  $\mu\text{m}$  in a 200  $\mu\text{m}$ -thick Pt-Rh foil. Assembly of the final device includes attaching an insulator layer (63  $\mu\text{m}$ -thick Kapton foil) followed by alignment of the patterned conversion metal to the electrode structure. Figure 6 shows photographs of the assembled detectors with the (a) TRENCH MCL and (b) COLUMN MCL.

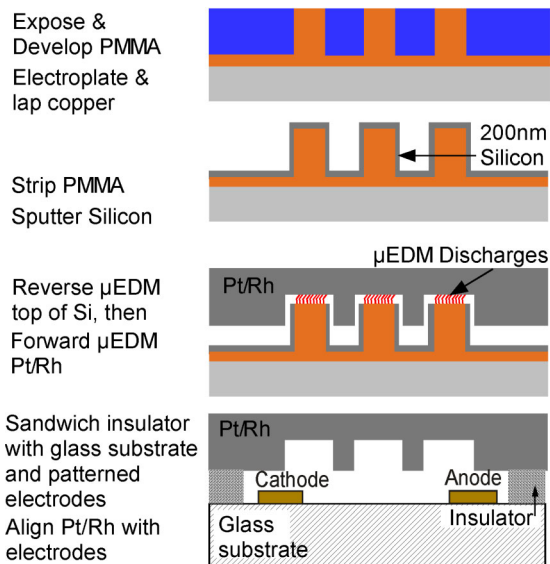


**Fig. 5:** Process flow for batch-mode micro-electro-discharge machining to pattern the **TRENCH MCL** and **COLUMN MCL** for *Design A*.

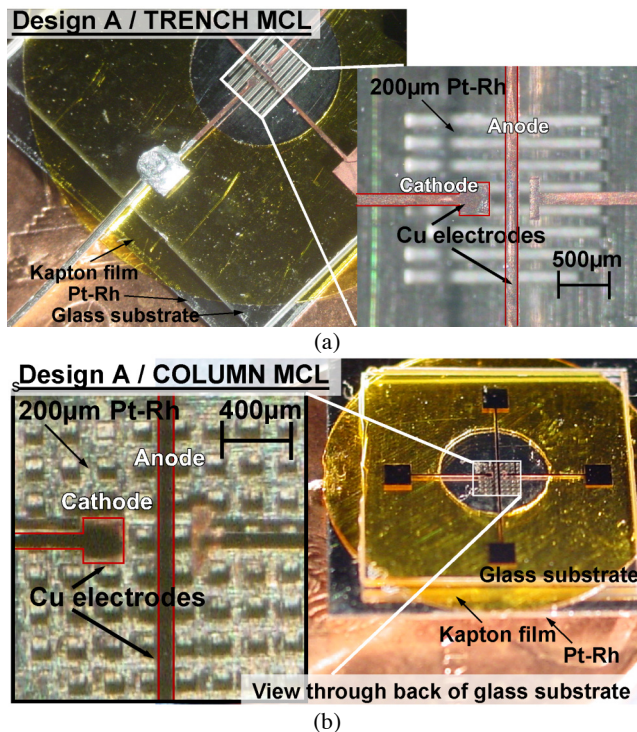


**Fig. 6:** Photograph of assembled *Design A* with 200  $\mu\text{m}$ -thick Pt-Rh layer using the (a) **TRENCH MCL** and (b) **COLUMN MCL**. Shown through the back of the glass substrate.

## RESULTS AND DISCUSSION

To determine the effectiveness of the MCL, the gamma sensors were tested with and without the metal layer present. Since each source emits both beta particles and gamma radiation, without the MCL for gamma conversion, the count rate should be primarily due to beta particles alone. With the MCL present, the count rate should be higher because the photoelectrons (from the gamma converter) can be sensed in addition to the beta particles.

Experiments were conducted for *Design A* and *Design B* in two sensing gases and pressures: air at 760 Torr and a nitrogen-to-neon gas ratio of 5:2 at 640 Torr. Also, two bulk metals (50  $\mu\text{m}$ -thick W and 200  $\mu\text{m}$ -thick Pt-Rh) and two radioisotopes (1.0  $\mu\text{Ci}$   $^{22}\text{Na}$  and 1.0  $\mu\text{Ci}$   $^{65}\text{Zn}$ ) were evaluated. W and Pt-Rh have similar bulk properties and consequently have comparable conversion efficiencies. Finally, the performance of two machined patterns (**TRENCH MCL**, **COLUMN MCL**) in Pt-Rh were evaluated and compared to the performance of a **SOLID MCL** of Pt-Rh.

*Design A* with the Pt-Rh **TRENCH MCL** was evaluated in the presence of  $^{22}\text{Na}$ , in air at 760 Torr and in the  $\text{N}_2/\text{Ne}$  sensing gas mixture under partial pressure. The count rate with the  $\text{N}_2/\text{Ne}$  gas mixture ( $>28$  kcounts-per-minute) appeared to be almost twice the count rate in air. The operating voltage was fixed at 900 V. Figure 7 compares the relative count ratios for *Design A*, while detecting  $^{22}\text{Na}$ . Relative count ratio is defined as the count rate with a patterned MCL over the count rate with the **SOLID MCL**. The **TRENCH MCL** and **COLUMN MCL** in 200  $\mu\text{m}$ -thick Pt-Rh were evaluated at two different pressures (640 Torr, 760 Torr) and sensing gases ( $\text{N}_2/\text{Ne}$  mixture, air). The **TRENCH MCL** demonstrated a  $>10\text{X}$  improvement in count rate over the **SOLID MCL**, while the **COLUMN MCL** showed  $\approx 6\text{X}$  increase. The **TRENCH MCL** showed comparable performance in count ratios ( $>10\text{X}$ ) in the  $\text{N}_2/\text{Ne}$  mixture at 640 Torr and in air at 760 Torr.

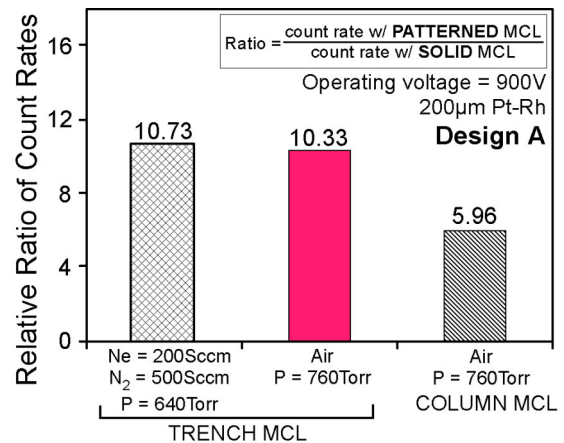


**Fig. 7:** Comparison of count ratios for *Design A* with two different machined patterns (**TRENCH MCL**, **COLUMN MCL**) in Pt-Rh and evaluated at two different pressures (640 Torr, 760 Torr) and sensing gases ( $\text{N}_2/\text{Ne}$  mixture, air). Operated at 900 V.

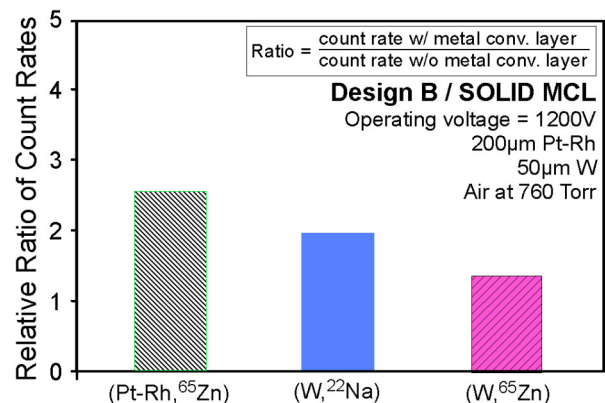


**Fig. 8:** Comparison of the conversion efficiency for different thicknesses in MCLs (200  $\mu\text{m}$ -thick Pt-Rh, 50  $\mu\text{m}$ -thick W) with *Design B*. Applied voltage is 1200 V in ambient air.

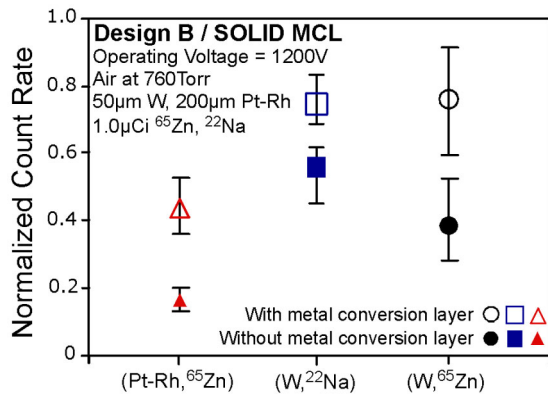


**Fig. 9:** Comparing normalized count rates from Design B with un-patterned MCLs of Pt-Rh and W, in the presence of different isotopes. Error bars indicate the range of measured count rates.

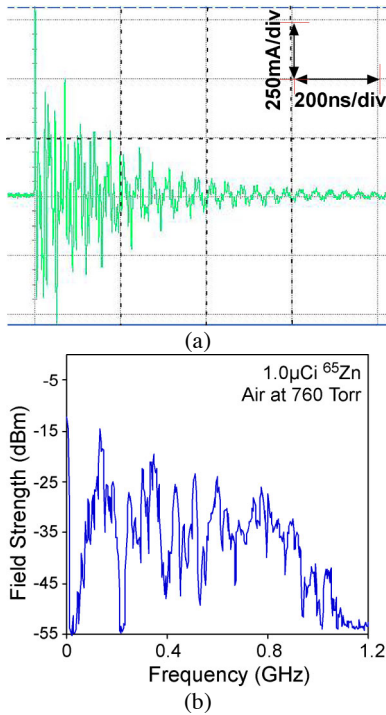


**Fig. 10:** (a) Current pulses during gamma radiation detection using Design A with a Pt-Rh SOLID MCL, measured with a high frequency current probe. These pulses show very fast current peaks ( $\approx 600$  ns), which result in (b) a wireless signal with a bandwidth  $>1.2$  GHz, measured with an antenna placed 30 cm from the device.

Design B was tested in an air environment at 760 Torr. Higher conversion efficiencies (higher relative count ratios) were measured for 200  $\mu\text{m}$ -thick Pt-Rh over 50  $\mu\text{m}$ -thick W, because interaction probability increases with layer thickness (Fig. 8). Higher count ratios for Design B were measured while detecting  $^{22}\text{Na}$  compared to  $^{65}\text{Zn}$ , because  $^{22}\text{Na}$  emits (on average) 5X more gamma-rays per decay than  $^{65}\text{Zn}$ . Figure 9 compares the normalized count rates for Design B and shows the range of statistical variation in count rates. A consistently higher count rate with an MCL shows the efficacy of the gamma-to-electron conversion method. For Design B, the overall count rates were lower with the Pt-Rh SOLID MCL compared to the W SOLID MCL. However, there was an overall improvement in operational stability with the Pt-Rh when compared to Design B with W. In the absence of an MCL (using Design B), a higher relative count rate was observed in the proximity of  $^{22}\text{Na}$  ( $\approx 0.55$ ) compared to  $^{65}\text{Zn}$  ( $\approx 0.38$ ), because  $^{22}\text{Na}$  has a higher rate of beta emission (90%) compared to  $^{65}\text{Zn}$  (1.4%). A glass substrate was used for preliminary tests, but future efforts can use thin mica for increased photoelectron detection efficiency.

Current pulses (of duration  $\approx 600$  ns) were measured with a wideband oscilloscope and the wireless signal emitted during sensor operation in the proximity of  $^{65}\text{Zn}$  was received remotely using a spectrum analyzer and antenna positioned  $\approx 30$  cm from the detector (Fig. 10). The measured bandwidth extended beyond 1.2 GHz. The MCL showed minimal impact on the resulting RF field strength.

## CONCLUSIONS

The proposed concept for a wireless micromachined gamma radiation sensor has been experimentally validated. The gas-based detector includes a layer of bulk metal on top of a glass substrate containing metal electrodes. The bulk metal converts gamma radiation to photoelectrons that ionize the gas medium, resulting in a current pulse. These fast current pulses generate a wideband wireless signal ( $>1.2$  GHz). The impact of two different structures patterned in the MCL was tested: TRENCH MCL and COLUMN MCL. The TRENCH MCL showed a count rate exceeding 28 kcpm and a  $>10\text{X}$  improvement in sensing when compared to an un-patterned MCL. The detector operated under partial pressure in an  $\text{N}_2/\text{Ne}$  mixture in the proximity of 1.0  $\mu\text{Ci}$  of  $^{22}\text{Na}$ . Operation in air with Pt-Rh and W MCLs located on the backside of the glass substrate showed a higher count rate with the MCL than without.

Overall, this work has shown that integrating micromachined metal layers for enhanced gamma detection efficiency provides important new functionality to miniaturized wireless gas-based sensors for beta particles. In doing so, it enables longer detection distances and detection of concealed nuclear materials. In the future, the metal conversion layer can be integrated into the gas packaging for the sensor.

## ACKNOWLEDGEMENTS

This work was supported primarily by the Engineering Research Centers Program of the National Science Foundation under Award Number EEC-9986866. The facilities used for this research include the Michigan Nanofabrication Facility (MNF) at the University of Michigan. Y.G. acknowledges support through the IR/D program while working at the National Science Foundation. The findings do not necessarily reflect the views of the NSF. The authors would like to thank Mark T. Richardson for his help in machining the metal conversion layers.

## REFERENCES

- [1] C.K. Eun et al, "A magnetically enhanced 3-electrode wireless micro-Geiger counter," *IEEE MEMS*, Jan. 2007.
- [2] B. Shafir and A. Seidman, "High efficiency gamma-ray metal converters," *Nucl. Instr. & Meth.*, vol. 129, 1975 pp. 177-186.
- [3] U. Shimoni et al., "Investigations on metal converters for gamma-ray detection and mapping," *Nucl. Instr. & Meth.*, vol. 117, 1974, pp. 599-603.
- [4] M. Nakamura, "The energy spectra and the quantum efficiencies of electrons emitted from the metallic elements irradiated by 60Co gamma-rays," *J. Appl. Phys.*, 54(6) Jun. 1983, pp. 3141-3149.
- [5] J.O. Hirschfelder et al., "The penetration of gamma-radiation through thick layers," *Phys. Rev.*, 73(8), Apr. 1948, pp. 852-862.
- [6] J. Martin, *Physics of Radiation Protection*, 2nd Ed., Ch.3, Wiley-VCH, 2006, Appendix B&D.
- [7] M.J. Berger et al., "XCOM: Photon Cross Sections Database," *NIST Standard Reference Database*, Mar. 1998. <http://physics.nist.gov/PhysRefData/Xcom/Text/XCOM.html>
- [8] H.H. Anderso, et al., "ESTAR: Stopping power and range tables for electrons," *NIST Standard Reference Database*, <http://physics.nist.gov/PhysRefData/Star/Text/ESTAR.html>
- [9] M.T. Richardson and Y.B. Gianchandani, "Achieving precision in high density batch mode micro-electro-discharge machining," *J. Micromech. Microeng.*, vol. 18, pp. 1-12, 2008.

# AN IMPLANTABLE CAPACITIVE MICROMACHINED ULTRASONIC IMAGER PROBE FOR PHOTOACOUSTIC IMAGING

Xiaoyang Cheng<sup>1</sup>, Jinguang Chen<sup>1</sup>, Sheng-Wen Huang<sup>2</sup>, Russell S. Witte<sup>3</sup>, and Pinyen Lin<sup>4</sup>

<sup>1</sup>Dept. of Electrical and Computer Engineering,

The University of New Mexico, Albuquerque, NM 87131

<sup>2</sup>Dept. of Biomedical Engineering, The University of Michigan, Ann Arbor MI 48109

<sup>3</sup>Dept. of Radiology, The Univ. of Arizona, Tucson, AZ 85721

<sup>4</sup>Infotonics Technology Center, Canandaigua, NY

## ABSTRACT

This paper reports the development of a miniature slab-shaped capacitive micromachined ultrasonic transducer (CMUT) array for photoacoustic imaging (PAI). As a minimally invasive imager, this device is capable of receiving relatively weak ultrasound signals that are difficult to access with non-invasive transducers and is useful for acquiring photoacoustic images of biological structures. This CMUT imager probe was fabricated using a two-layer polysilicon surface micromachining process, followed by a double-sided deep silicon etching process for shaping the silicon substrate into a thin probe. New CMUT structures were developed for this implantable imager probe, aiming at reducing the effective gap height and the driving voltage, as well as alleviating the charging trap effect. Photoacoustic imaging of the nerve cord of a lobster using this miniature CMUT array has been demonstrated.

## INTRODUCTION

Capacitive Micro-machined Ultrasonic Transducers (CMUT) is considered as an alternative to the piezoelectric transducers for ultrasonic imaging. Extensive research on the fabrication and modeling of CMUT devices began in the early 1990s [1-2]. Compared to piezoelectric ultrasonic transducers, CMUT has the advantages of a broader acoustic bandwidth, feasibility of direct transducer-transistor integration, and a lower fabrication cost. Densely populated CMUT arrays can be manufactured using standard micro-fabrication techniques for high-frequency applications.

Photoacoustic imaging (PAI) [3-5] constructs images using ultrasounds generated by a target object which is under pulsed infrared illumination. The target object is flashed with a laser pulse, leading to optical absorption and thermoelastic expansion. This expansion generates ultrasound, which can be detected by an ultrasound transducer or an array of receivers to form images. Whereas traditional pulse-echo ultrasound imaging has low contrast in soft tissue due to similar acoustic impedances, PAI benefits from high optical contrast combined with excellent spatial resolution determined primarily by the ultrasound wavelength, approaching cellular resolution [6]. Contrast in PAI depends primarily on the optical wavelength and absorption spectrum of the tissue. Thus, PAI provides an appreciably higher contrast than pulse-echo ultrasonic imaging. Moreover, when the light source is tuned to the near infrared, PAI can be used to form an image well over a centimeter into tissue. For photoacoustic imaging of live human or animal tissue with red blood cells, hemoglobin provides significant help in boosting the contrast ratio. Hemoglobin has a very high optical contrast in the visible and infrared spectra. As a result, high-contrast imaging of blood containing structures in tissue such as tumors or blood vessel is one of the unique

advantages of PAI. Compared to other techniques, PAI is a safe process that uses nonionizing radiation and fluences within standards set by ANSI and could provide 3D images with high resolution and contrast. In addition to viewing anatomical structure, photoacoustic imaging is capable of detecting composition of tissue and functional activities [5] of an organ based on blood-related infrared absorption rate difference and sensitivity of the optical spectrum of hemoglobin to oxygenation saturation [6].

Currently the vast majority of photoacoustic imaging experiments reported relied on use of single or an array of piezoelectric transducer for the ultrasound detection. CMUT [6-8] device is a promising alternative for PAI because of the broad acoustic bandwidth it provides. Fabricated using silicon-based integrated circuits technology, CMUT devices can be implemented into various 1-D [7], 2-D [7], or 3-D [8] arrays for PAI. In contrast to a regular laboratory-scale CMUT array [9], a miniature CMUT array [10] can be used in an invasive PAI system and would provide information not available from a non-invasive system. In this paper, the design of a miniature slab-shape CMUT array is reported, along with its application in photoacoustic imaging. Figure 1 illustrates the schematic of a PAI process using a miniature CMUT array.

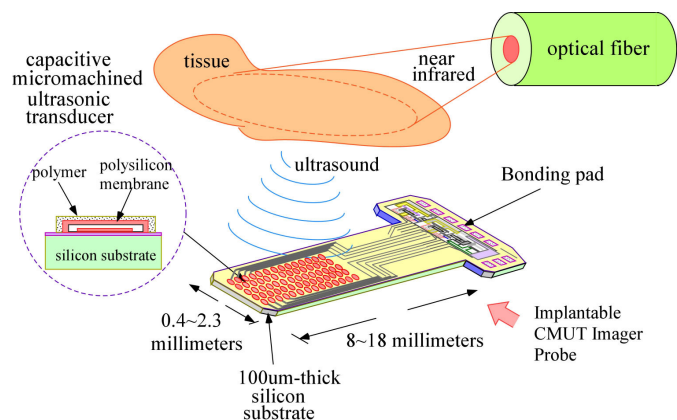


Figure 1: Schematic of the CMUT imager probe and its application in a photoacoustic imaging process.

## MINIATURE CMUT ARRAYS

In many CMUT devices reported in the literature, a dielectric layer is embedded between the membrane and its counter electrodes to prevent electrode-membrane shorting. One of the problems associated with this embedded dielectric film is the charging problem. The charge stored in the dielectric-conductor

interface will alter actuation voltages of the CMUT device. One of the solutions to alleviate the dielectric charging problem is to use a bipolar AC signal for driving the transducer [11] in a transmission process. However, even with application of these bipolar signals the charging effect cannot be completely eliminated. An embedded dielectric layer also increases the effective gap height of a CMUT, resulting in a higher driving voltage. For a CMUT with a dielectrics layer of thickness  $x_0$ , the effective gap is defined as [12]

$$t_{eff} = S_0 + \frac{x_0}{\epsilon_r} \quad (1)$$

Where  $S_0$  is the gap distance,  $\epsilon_r$  is the relative dielectric coefficient of the material. The “pull-in” voltage for an ideal CMUT device with piston-like membrane is expressed as:

$$V_{collapse} = \sqrt{\frac{2kx}{\epsilon_0 A}} \times (S_0 + \frac{x_0}{\epsilon_r} - x) = \sqrt{\frac{8k(S_0 + x_0/\epsilon_r)^3}{27\epsilon_0 \pi a^2}} \quad (2)$$

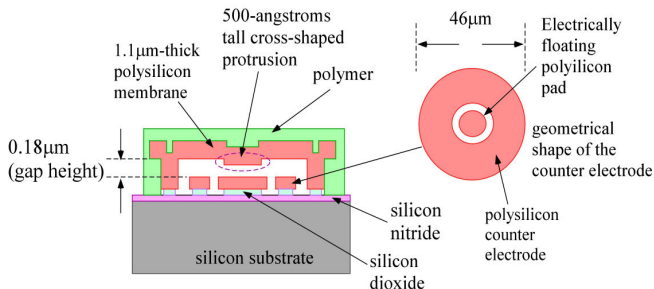


Figure 2: Poly-silicon capacitive micro-machined ultrasonic transducer with a circular-shaped buffering pad in the middle of the counter electrode.

A new CMUT structure was developed and used on this miniature PAI CMUT array as shown in Figure 2 to alleviate the aforementioned problems associated with an embedded dielectric layer. Instead of embedding a dielectric layer (either patterned or un-patterned) between the membrane and its counter electrode as commonly used for many CMUT devices, this new design used a pad-buffering structure for preventing shorting of the membrane to its counter electrode during ultrasound transduction. Because the dielectric layer is removed, the charging effect will be reduced. A circular-shaped 500Å-high poly-silicon protrusion reaching out from the lower surface of the poly-silicon membrane works as the counter pad for the poly island. The polysilicon protrusion would land on the poly island when excessive electrical voltage or acoustic impingement is applied, preventing shorting of this device. Without an embedded dielectric layer, the effective gap distance [12] was reduced, at the cost of a smaller counter electrode area. For comparison, theoretical calculation was conducted based on the assumption that the electrodes act like parallel plates. The device parameters used in this calculation are listed in table 1. It was found that the island-insulated CMUT may be operated at a lower bias than its dielectric insulation counterpart under a comparable operation condition. Table 2 listed the calculated capacitance, collapse voltage, and effective gap height of 46µm-diameter CMUT devices with an embedded dielectric layer or with a polysilicon island.

Table 1: CMUT Devices Parameters

Cell diameter ( $\mu\text{m}$ )	46
Gap distance ( $\mu\text{m}$ )	0.3
Membrane thickness ( $\mu\text{m}$ )	1.0
Insulating layer thickness ( $\mu\text{m}$ )	0.12
Poly Island diameter ( $\mu\text{m}$ )	5.0
Gap between the island and the ring-shaped counter electrode ( $\mu\text{m}$ )	1.5

Table 2: The calculated results

Parameters	CMUT with dielectric layer	CMUT with poly circular protrusion
Effective gap distance ( $\mu\text{m}$ )	0.22	0.2
Capacitance ( $fF$ )	70	65
Collapse voltages ( $V$ )	125	113

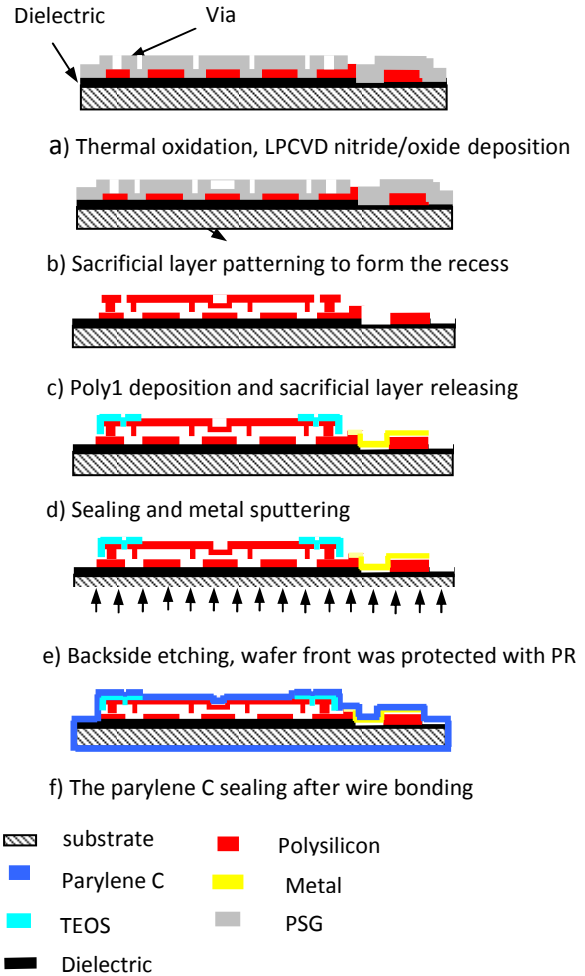
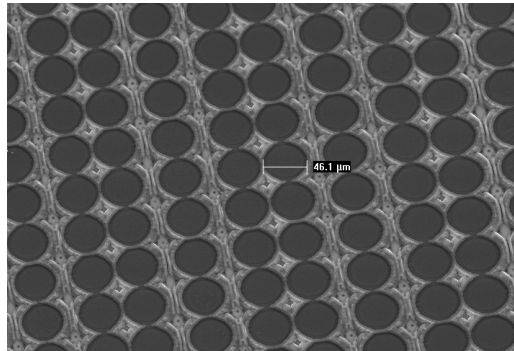


Figure 3: the fabrication process flow

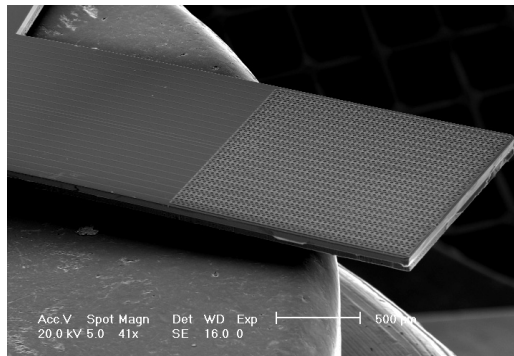
Two-layer-polysilicon micromachining process was employed to fabricate this device. The similar fabrication steps including surface micromachining and bulk micromachining can be found in

[10] in detail. The big difference is that after the sacrificial layer (PSG) was deposited and the anchor was etched, the center of sacrificial layer was patterned and timely-control etched so that the circular protrusion could be formed during the Poly1 deposition. The process flow was illustrated in Figure 3.

The SEM pictures of fabricated CMUT probes were shown in Figure 4. The array width of this 1D CMUT array varies from 1mm to 4mm, depending on the frequency of the transducer. The length and thickness of the silicon substrate of the CMUT array are typically 1.2-2 cm and 100  $\mu\text{m}$ , respectively. Such miniature CMUT arrays are suitable for implanting application or minimally invasive applications in surgery.



a)



(b)

Figure 4: (a) SEM photograph of a two-dimensional CMUT array comprising 1058 transducers for photoacoustic imaging. (b) top view of the CMUT devices on this probe.

### DEVICE CHARACTERIZATION

The CMUT array was tested both as a transmitter and a receiver in water. Figure 5 (a) & (b) show the time- and frequency-domain ultrasound signal transmitted by a 46 $\mu\text{m}$ -diameter CMUT and received by a commercial piezoelectric transducer; Figure 5 (c) & (d) show the time- and frequency-domain ultrasound signal transmitted by a commercial piezoelectric ultrasound transducer and received by a 46 $\mu\text{m}$ -diameter CMUT. The center frequency of the transmitting signal is about 5.2MHz, which is close to the theoretical natural frequency 6 MHz. For CMUT working in the receiving mode, the center frequency is almost the same. The fractional bandwidth is around 98%.

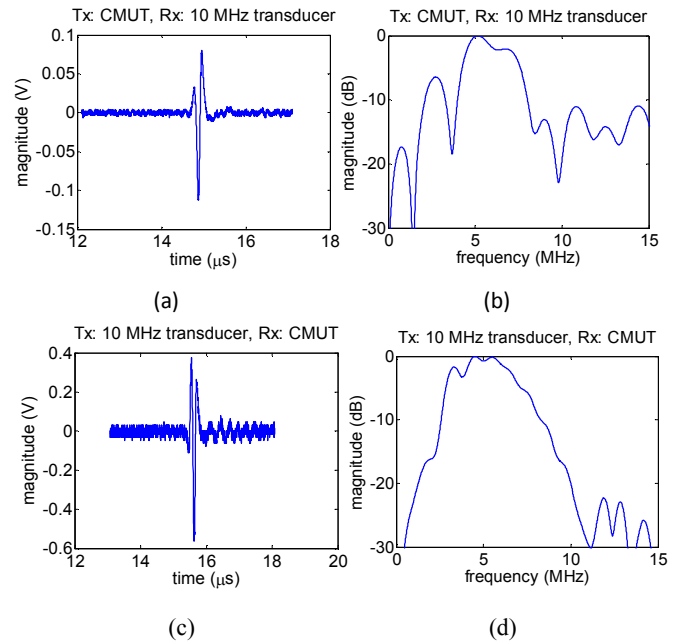


Figure 5: (a) & (b) Time- and frequency-domain ultrasound signal in transmitting mode; (c) & (d) time- and frequency-domain ultrasound signal in receiving mode.

Electrical testing was also performed to identify the charge trapping effect for this new design CMUT probe. For comparison, the previously designed CMUT with dielectric film covering the bottom electrode was biased at 50Vdc under receiving mode. It is observed that the received signal amplitude started to attenuate after 1hr due to charge trapping. In the test with this miniature slab-shaped CMUT, the received signal amplitude was not attenuated until the device continuously worked for 4 hours.

### PHOTOACOUSTIC IMAGING EXPERIMENT

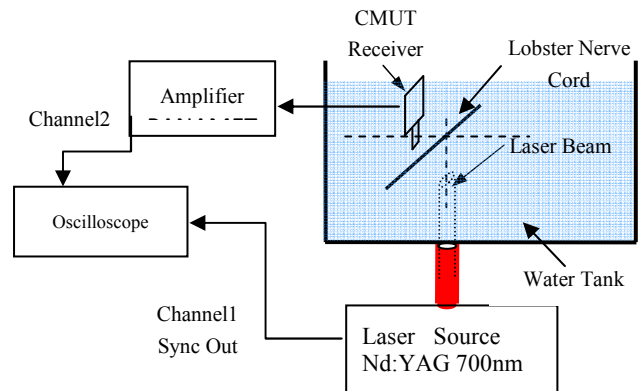


Figure 6: Schematic setup for the photoacoustic imaging system

In the photoacoustic imaging experiment, the miniature CMUT array was used as the receiving transducer for photoacoustic imaging of the lobster tissue. The schematic setup for the photoacoustic imaging is shown in Figure 6. The abdominal segment of the nerve cord of a lobster was excised, stained (with

dye NK2761) and positioned in the testing water tank. A tunable laser source was used to generate laser pulses and create the approximate illumination pattern (0.2x2cm) on the nerve cord. The CMUT probe was placed perpendicularly to the laser beam axis and faced the nerve cord. The laser fired at PRR of 20Hz with the wavelength at 700nm. The power intensity was approximately 20mJ/cm<sup>2</sup>. The signals were amplified with a 40dB gain and digitized and then transferred to a computer. All post-processing was done using MATLAB. A synthetic aperture focusing technique (SAFT) was employed for imaging reconstruction. The reconstructed photoacoustic image of the stained nerve cord of a lobster is shown in Figure 7.

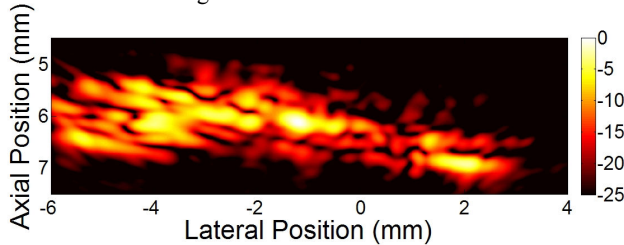


Figure 7: Photoacoustic image (dynamic range: 25dB) of the nerve cord of a lobster shot by the implantable CMUT probe. .

## CONCLUSION

A miniature slab-shaped capacitive micromachined ultrasonic transducer (CMUT) imager and its application for photoacoustic imaging (PAI) were proposed in this research. The CMUT imager probe was fabricated using a two-layer polysilicon surface micromachining process. This image array reduced the effective gap. The experiment has shown that the charge trapping problem was alleviated. Photoacoustic imaging of the nerve cord of a lobster using this miniature CMUT array has also been successfully demonstrated.

## REFERENCES

- [1] M. I. Haller and B. T. Khuri-Yakub, "A surface micromachined electrostatic ultrasonic air transducer," in *Proc. IEEE Ultrason. Symp.*, 1994, pp. 1241-1244.
- [2] F. V. Hunt, "Electroacoustic: The analysis of transduction, and its historical background". New York, NY: Acoustical Society of America, 1982.
- [3] J. E. Schneider, S. D. Bamforth, S. M. Grieve, K. Clarke, S. Bhattacharya, and S. Neubauer, "High resolution, high-throughput magnetic paragraph sign resonance imaging of mouse embryonic paragraph sign anatomy using a fast gradient-echo sequence." *Magma* 16, 443-51 (2003).
- [4] P. Mansfield, and P. G. Morris, *NMR Imaging in Biomedicine*, New York: Academic Press (1982).
- [5] X. Wang, Y. Pang, G. Ku, X. Xie, G. Stoica, and L.-H. Wang, "Non-invasive laser-induced photoacoustic tomography for structural and functional imaging of the brain in vivo," *Nature Biotechnology* 21 (7), 803-806 (2003).
- [6] M. Xu and L. V. Wang, "Photoacoustic imaging in biomedicine," *Review of Scientific Instruments* 77, 041101, pp. 1-22, 2006.
- [7] Y. Huang, A. S. Ergun, M. H. Badi, and B. T. Khuri-Yakub, "Fabricating Capacitive Micromachined Ultrasonic Transducers with Wafer-Bonding Technology," *IEEE Journal of Micromechanical Systems*, vol. 12, no. 2, pp. 128-137, 2003.
- [8] J. Chen, X. Cheng, I.-M. Shen, J. Liu, P.-C. Li, and M. Wang, "A Monolithic Three-Dimensional Ultrasonic Transducer Array for Medical Imaging," *IEEE Journal of Microelectromechanical Systems*, vol. 16, no. 5, pp. 1015-1024, October 2007.
- [9] I. O. Wygant, X. Zhuang, P. S. Kuo, D. T. Yeh, O. Oralkan, B. T. Khuri-Yakub, "Photoacoustic Imaging Using a Two-Dimensional CMUT Array". 2005 IEEE Ultrasonics Symposium.
- [10] J. Chen, X. Cheng, C. Chen, P. Li, J. Liu, and Y. Cheng, "A Capacitive Micromachined Ultrasonic Transducer Array for Minimally Invasive Medical Diagnosis " to be published in June/2008 issue of *IEEE Journal of Microelectromechanical Systems*.
- [11] H. R. Shea, A. Gasparyan, H. B. Chan, S. Arney, R. E. Frahm, D. Lopez, S. Jin, R. P. McConnel, "Effects of electrical leakage currents on MEMS reliability and Performance". *IEEE Trans. on Device and Materials Reliability*, 2004, 4(2)198-207.
- [12] M. I. Haller and B. T. Khuri-Yakub, "A surface micromachined electrostatic ultrasonic air transducer," in *Proc. IEEE Ultrason. Symp.*, 1994, pp. 1241-1244.

# FULLY BATCH-FABRICATED LINEAR QUADRUPOLE MASS FILTERS

*K. Cheung, L. F. Velásquez-García, and A. I. Akinwande*  
Massachusetts Institute of Technology, Cambridge, MA 02139 USA

## ABSTRACT

We report the design, fabrication, and characterization of a fully batch-fabricated linear quadrupole mass filter. The device demonstrates for the first time, a microfabricated quadrupole mass filter that doesn't require any post-fabrication electrode assembly. Utilizing a design with non-conventional square electrodes, a 30 mm quadrupole with an effective electrode diameter of  $\sim 1.7$  mm, and integrated ion optics was fabricated. At a driving frequency of 2 MHz and a maximum applied voltage of 100 V, a mass range of 250 a.m.u. was achieved in the first stability region, and a half-height peak-width of 0.7 a.m.u. was obtained in the second stability region at mass 28.

## INTRODUCTION

Mass spectrometers are powerful analytical tools that can identify the composition of unknown compounds, and quantify compounds that are known. Scaling-down this device will permit faster analysis times, power savings through operation at higher pressures, portability, and reduced costs [1, 2]. A popular method of miniaturization is through the use of microelectromechanical systems (MEMS) fabrication technologies because it permits batch-processing. The development of micro-scaled gas analyzers will have applications in national security, environmental safety and monitoring, satellites and space exploration, industrial processing, as well as biological research and healthcare.

Mass spectrometers comprise primarily of an ionizer to create charged species, a mass filter to sort the ions according to their mass-to-charge ratios, and a detector to measure the quantity of the filtered ions. Batch-fabricated ionizers and detectors have already been developed for a micro-gas analyzer system [3, 4]. In order to produce these systems inexpensively and efficiently, the mass filter component should also be completely batch-fabricated.

Linear quadrupoles are popular mass filters due to their simplicity in design and usage. Researchers have demonstrated mass filtering with MEMS-based quadrupole mass filters (QMFs) [5-7]. Reported designs utilize metallic rods or metalized glass rods as electrodes, which required manual assembly of these electrodes after the MEMS components were fabricated. This methodology places a bottleneck on the manufacturing and sets a limit on the precision that can be achieved.

We propose using a non-conventional square electrode geometry that can be fully batch-fabricated, thus taking advantage of the dimensional precision associated with MEMS technology. This paper reports the design, fabrication, and characterization of the micro-square electrode quadrupole mass filter (MuSE-QMF). The operating principles of a QMF will be described, followed by an overview of the optimization process. The fabrication process flow will be presented, and the experimental results discussed.

## THEORY

An ideal QMF utilizes four hyperbolic electrodes aligned in a symmetric manner to generate an ideal quadrupole field. If the applied potential is a combination of r.f. and d.c. voltages, the equations of motion for a charged ion in this field would be given by the Mathieu equation [8]. This equation has stable and unstable solutions that can be mapped as a function of two parameters. Overlapping the Mathieu stability diagrams for the directions orthogonal to the quadrupole axis define stability regions, shaded areas in Fig. 1, where ion motion is stable in both directions.

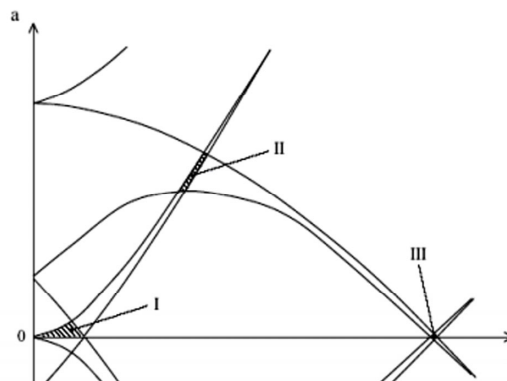


Figure 1: The Mathieu stability diagram showing quadrupole stability regions I, II, and III. The Mathieu parameters,  $a$  and  $q$ , are functions of the device geometry and the operating conditions.

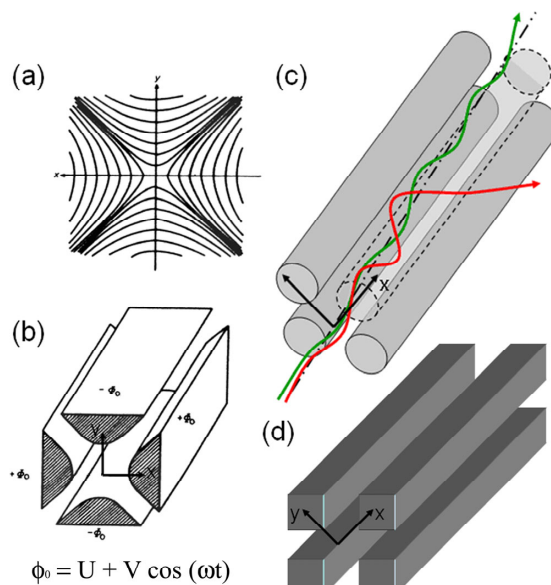


Figure 2: (a) Ideal quadrupole potential field [8], (b) Hyperbolic electrodes with standard applied voltages for an ideal QMF [8], (c) Conventional cylindrical electrode QMF (transmitted ion trajectories are in green), (d) Proposed square electrode geometry.

Most commercial QMFs and reported MEMS-based versions utilize cylindrical electrodes instead of hyperbolic ones due to the reduced complexity in manufacturing. To compensate for the distortion that comes from using non-hyperbolic electrodes, optimization was conducted to minimize the higher-order field components that are a result of this non-ideality. Continuing the technological progression shown in Fig. 2, optimization can be conducted on the MuSE-QMF to minimize unwanted field components as well.

QMFs are typically operated in stability region I but there are reports of higher resolution and improved peak-shapes that come with operation in stability region II [8, 9]. Driving the MuSE-QMF in a higher stability region can serve to further improve the performance of the device aside from the geometric optimization.

## DESIGN AND OPTIMIZATION

Analysis of the field components of the MuSE-QMF was conducted in a manner similar to that reported in [10]. A general schematic of the device was conceived and critical dimensions were parameterized as illustrated in Fig. 3. Maxwell 2D was used to calculate the potentials for the various geometries. The field data was then exported into a MATLAB script which decomposed the potentials into corresponding multipole terms.

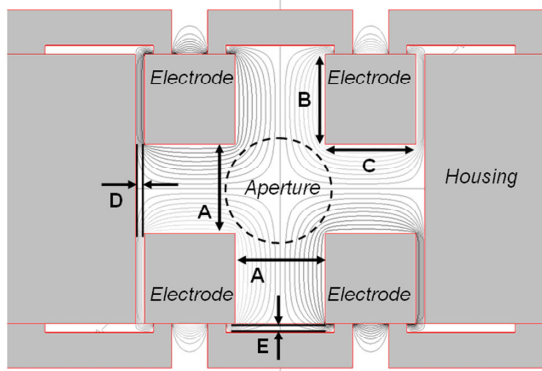


Figure 3: Cross section of the device geometry used during optimization, with field lines generated by Maxwell 2D. The critical dimensions are A (the characteristic dimension of the quadrupole aperture), B (the thickness of the electrodes), C (the width of the electrode), D (the horizontal electrode-to-housing spacing), and E (the vertical electrode-to-housing spacing).

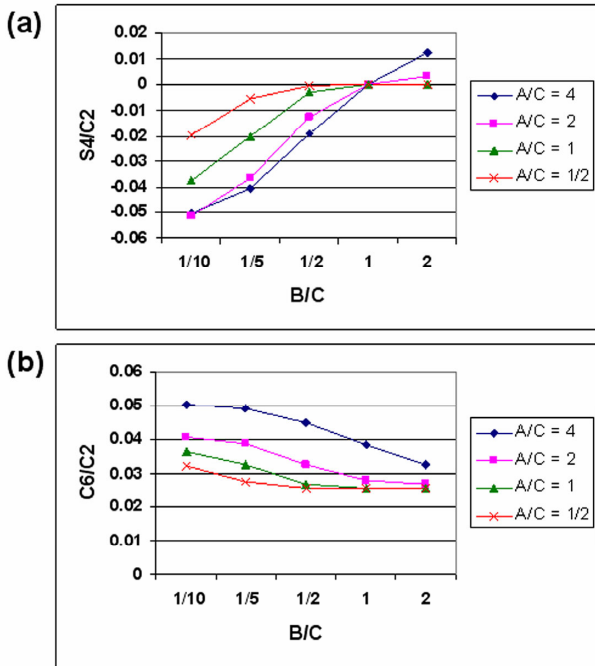


Figure 4: Optimization results using dimensions A, B, and C. Electrode dimensions and aperture size were parameterized without including the housing in the simulations.

From the boundary conditions established by symmetry of the electrodes, the first three significant terms in the expansion are  $C_2$ ,  $S_4$ , and  $C_6$ .  $C_2$  corresponds to the ideal quadrupole term, while  $S_4$  and  $C_6$  are the first odd and even higher-order terms respectively. The ratios  $S_4/C_2$  and  $C_6/C_2$  give an indication of the significance of

the unwanted field components that should be minimized. The results shown in Fig. 4 led to the conclusion that setting the dimensions  $A = B = C$  will minimize the undesirable terms. Data in Fig. 5 show that  $S_4/C_2$  is optimal when  $D = E$ , and  $C_6/C_2$  is a minimum when  $D$  is large. For fabrication and testing considerations, dimension A was set to 1 mm and E to 100  $\mu\text{m}$ . A large device aperture will increase the signal strength of the transmitted ions, while a small electrode-to-housing distance will improve processing uniformity.

Maximum transmission through a QMF occurs when the incoming ions enter near the central axis of the device [8]. The inclusion of integrated ion optics, as shown in Fig. 6, can help focus the ion stream towards the axis, as well as control the inlet and outlet conditions, thus improving overall performance.

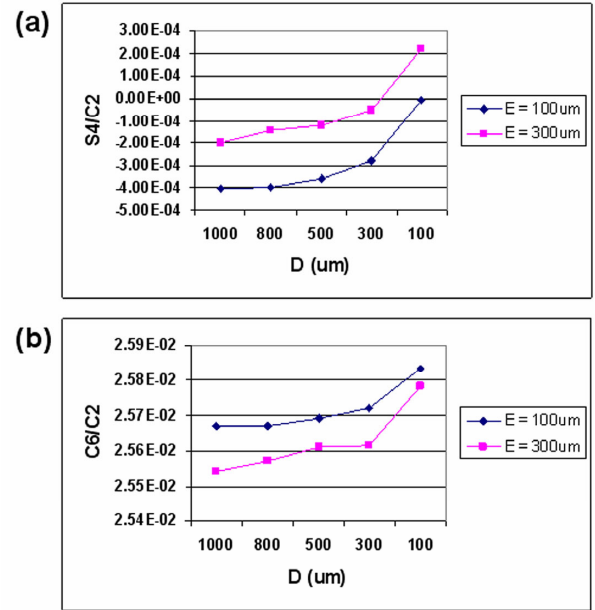


Figure 5: Optimization results using  $A = B = C = 1\text{mm}$ , while varying the dimensions D and E. The full geometry shown in Fig. 4 is used in these simulations.

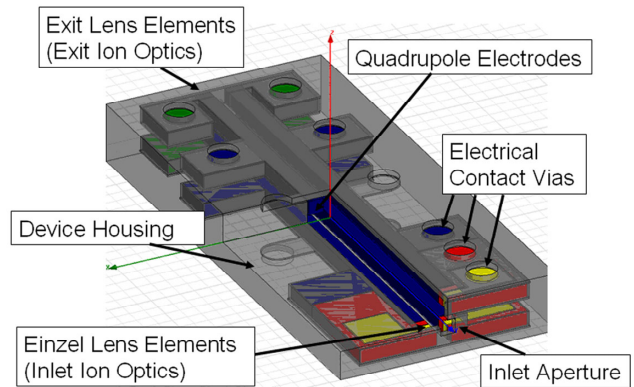


Figure 6: Schematic of the MuSE-QMF. The device has integrated ion optics denoted in red (Einzel lens 1 & 3), yellow (Einzel lens 2), and green (exit lens). The electrodes are shown in blue.

## DEVICE FABRICATION

Five highly-doped silicon double-side polished (DSP) wafers are needed to complete the device. Two  $500 \pm 5 \mu\text{m}$  wafers are

used as the capping layers, two  $1000 \pm 10 \mu\text{m}$  wafers serve as the electrode layers, and another  $1000 \pm 10 \mu\text{m}$  is utilized as a spacer layer. All the wafers initially have  $0.3 \mu\text{m}$  of oxide to serve as a protective layer during processing.

A series of deep reactive ion etches (DRIE), wet thermal oxidation, and silicon fusion bonding is used to realize the device. The cap wafers are defined with release trenches  $100 \mu\text{m}$  deep that are required for the electrode etch (Fig. 7a), and through-wafer vias for electrical contact. The cap wafers then have  $1 \mu\text{m}$  of thermal oxide grown to serve as an electrical isolation barrier (Fig. 7b). The electrode wafers have  $250 \text{ nm}$  of silicon rich nitride deposited on one side to serve as an oxide wet-etch barrier (Fig. 7c). The exposed oxide is removed with a buffered oxide etch (BOE) before bonding to the cap wafers and annealing. The electrodes are defined in the bonded stack with a DRIE halo-etch (Fig. 7d), followed by nitride removal with hot phosphoric acid. The spacer wafers are coated on both sides with  $4 \mu\text{m}$  of plasma enhanced chemical vapor deposited (PECVD) silicon oxide to serve as hard masks for a nested etch. On both sides, the PECVD oxide is patterned with reactive ion etching (RIE), followed by DRIE of  $450 \mu\text{m}$  to begin defining the aperture (Fig. 7e). The entire wafer is then etched  $100 \mu\text{m}$  on each side, followed by an oxide strip (Fig. 7f). The nested etch completes the aperture and defines recesses in the spacer wafer which prevents electrical shorting in the final device. The thin protective oxide on the cap-electrode stacks are removed with BOE. The two stacks and the spacer wafer are then cleaned and fusion bonded, followed by die-sawing to complete the device (Fig. 7g).

Measuring  $15 \text{ mm} \times 4 \text{ mm} \times 33 \text{ mm}$ , the MuSE-QMF contains a  $30 \text{ mm}$  quadrupole with an effective electrode diameter of  $\sim 1.7 \text{ mm}$ , and integrated ion optics (Fig. 8 – 10).

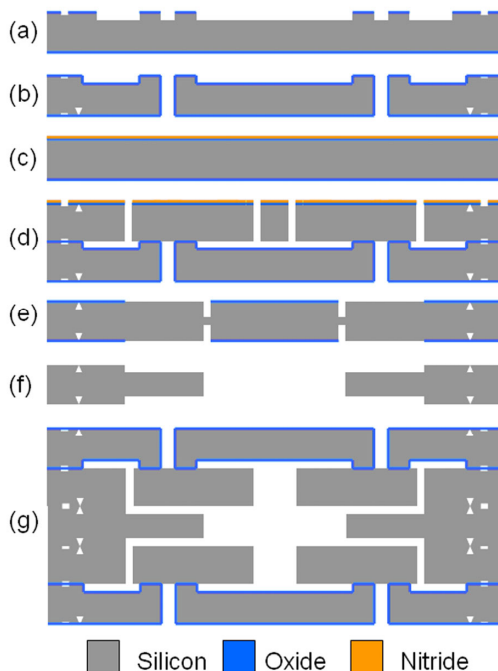


Figure 7: Device process flow - (a) Cap wafer after release trench etch, (b) Completed cap wafer, (c) Electrode wafer with nitride deposition, (d) Bonded cap-electrode stack with patterned electrodes, (e) Spacer wafer with patterned oxide for nested etch, and partial aperture etch, (f) Completed spacer wafer, (g) Final device with two complete cap-electrode stacks bonded to one spacer wafer.

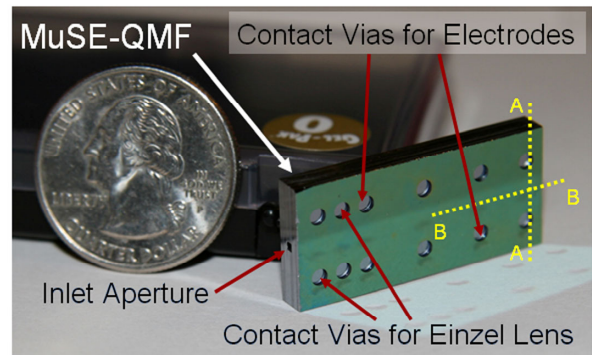


Figure 8: Completed device. The cross section along A is shown in Fig. 9, while the cross section along B is shown in Fig. 10.

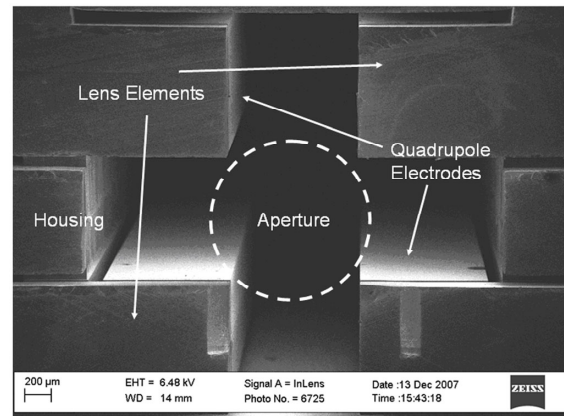


Figure 9: SEM of device interior - cross section across electrodes looking from the exit of the device.

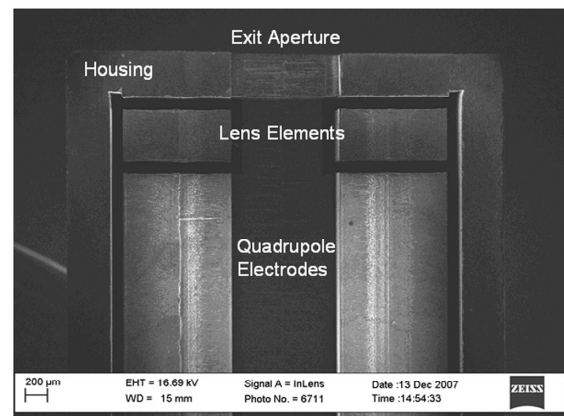


Figure 10: SEM of device interior - cross section along the length of the device at the exit aperture.

## EXPERIMENTAL RESULTS

Testing was conducted at Ardara Technologies (Ardara, PA). The experimental setup comprised of a vacuum chamber that allowed the introduction of air or FC-43 (perfluorotributylamine) into the system at a pressure of  $5 \times 10^{-5}$  Torr. A hot filament ionizer was used to generate the ions, and a conversion dynode multiplier was used to detect the signal. A self resonating r.f. supply was set to drive the device at  $2 \text{ MHz}$  with a maximum voltage of  $100 \text{ V}$ . A d.c. supply was combined with the r.f. signal through a bias-tee network consisting of  $30 \text{ M}\Omega$  resistors, and  $47 \text{ pF}$  blocking capacitors. Control of the voltage supplies, the ionizer

current, the detector gain, and the ion optics are managed through a Merlin® data acquisition system. The multiplier signal is measured through a preamplifier at a rate of 12.5 kS/s.

A spectrum for FC-43 was obtained in region I to demonstrate the maximum mass range achievable for the MuSE-QMF. Fig. 11 shows a mass range of 250 a.m.u. with prominent peaks at mass 69, 131, and 219. To explore the minimum peak-width obtainable, air was used due to its closely spaced peaks. A spectrum for air was obtained in region II to validate the notion that operation in a higher stability region will enhance resolution, and improve peak shape. Fig. 12 shows a minimum half-height peak-width of 0.7 a.m.u. at mass 28 with clear indication of peaks at mass 32, 40, and 44. The relative peak-intensities of the measured spectra are in good agreement with the NIST library spectra.

This data was obtained without functional integrated ion optics due to structural integrity issues of the lens components. Attempts to drive the device with a voltage greater than 100 V resulted in electrical breakdown of the insulating oxide. These two limitations diminished the performance of the MuSE-QMF by reducing the maximum mass range achievable, and by exaggerating the peak-shape non-idealities that arise from poor control of the quadrupole inlet and exit conditions.

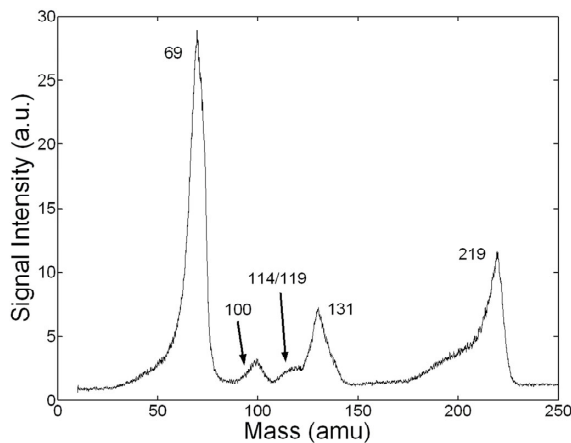


Figure 11: Mass spectrum of FC-43 at 2 MHz, Region I. Precursor peaks located on the low mass side of the peaks are apparent.

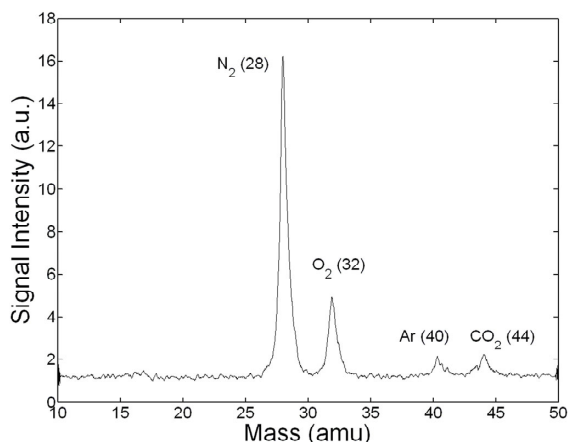


Figure 12: Mass spectrum of air at 2 MHz, Region II. Higher resolution and reduced precursor peaks are observed.

## CONCLUSIONS

The ability of a fully batch-fabricated linear quadrupole mass filter with non-conventional square electrodes to perform mass filtering was demonstrated. Potential field calculations with a multipole expansion provided a means of minimizing undesirable higher-order components, thus optimizing the design. Testing of the MuSE-QMF showed increased resolution and improved peak-shape when operated in a higher stability region, and the recorded performance is on par with other MEMS-based QMFs. This device design is scalable to smaller dimensions and can readily include integrated pre-filters for enhanced performance.

## ACKNOWLEDGEMENTS

The authors would like to thank Dr. Randy Pedder and the staff at Ardara Technologies (Ardara, PA) for their assistance in the testing of our device. This work was sponsored by DARPA/MTO and the US Army Soldier Systems Center (Natick, MA) through contract # W911QY-05-1-0002 (DARPA program manager Dennis Polla, and Army program manager Henry Girolamo).

## REFERENCES

- [1] S. Taylor, J. R. Gibson, and B. Srigengan, "Miniature mass spectrometry: implications for monitoring of gas discharges", *Sensor Review*, vol. 23, no. 2, pp. 150 – 154, 2003.
- [2] E. R. Badman, and R. G. Cooks, "Miniature mass analyzers", *Journal of Mass Spectrometry*, vol. 35, pp. 659 – 671, 2000.
- [3] L-Y. Chen, L. F. Velásquez-García, X. Wang, K. Teo, and A. I. Akinwande, "A Micro Ionizer for Portable Mass Spectrometers using Double-gated Isolated Vertically Aligned Carbon Nanofiber Arrays", *Technical Digest IEEE International Electron Device Meeting*, Washington DC, USA, pp. 843 – 846, December 2007.
- [4] Y. Zhu, J. Lee, and A. Seshia, "System-level simulation of a micromachined electrometer using a time-domain variable capacitor circuit model", *Journal of Micromechanics and Microengineering*, vol. 1, no. 5, pp. 1059 – 1065, 2007.
- [5] S. Taylor, R. Tindall, R. R. A. Syms, "Silicon based quadrupole mass spectrometry using microelectromechanical systems", *Journal of Vacuum Science and Technology B*, vol. 19, no. 2, pp. 557 – 562, 2001.
- [6] M. Gear, R. R. A. Syms, S. Wright, and A. S. Holmes, "Monolithic MEMS Quadrupole Mass Spectrometers by Deep Silicon Etching", *Journal of Microelectromechanical Systems*, vol. 14, no. 5, pp. 1156 – 1166, October 2005.
- [7] L. F. Velásquez-García, A. I. Akinwande, "An Out-of-Plane MEMS Quadrupole for a Portable Mass Spectrometer", *Technical Digest of the 14th International Conference on Solid-State Sensors, Actuators, and Microsystems*, Lyon, France, vol. 2, pp. 2315 – 2320, 2007.
- [8] P. Dawson, *Quadrupole Mass Spectrometry and Its Applications*, AIP, 1997.
- [9] L. F. Velásquez-García, K. Cheung, A. I. Akinwande, "An Application of 3D MEMS Packaging: Out-Of-Plane Quadrupole Mass Filters," *Journal of Microelectromechanical Systems*, submitted for publication.
- [10] R. R. A. Syms, T. J. Tate, M. A. Ahmad, S. Taylor, "Design of a microengineered electrostatic quadrupole lens", *IEEE Transactions on Electron Devices*, vol. 45, no. 11, pp. 2304 – 2311, November 1998.

# HOT SELF BOLOMETER PHOTONIC CRYSTAL BASED HYDROCARBON SENSOR

A.D. Oliver, M.U. Pralle, P. Loges, I. Puscasu, and E.A. Johnson

ICx Photonics, Billerica, MA, USA

## ABSTRACT

We report a novel combination infrared source and bolometer that uses a photonic crystal to emit narrow band infrared energy that is used to measure hydrocarbon gasses. The device emits infrared radiation aided by a photonic crystal at the hydrocarbon wavelength of  $3.3\ \mu\text{m}$  and suppresses emission at other wavelengths. The amount of radiation that returns to the device after emission, reflection off a mirror, and passing through a gas sample is related to the partial pressure of methane or other hydrocarbons in the sample being measured. The device can detect gas concentrations down to 500 ppm of methane and has a sensitivity of up to  $4\ \mu\text{V/ppm}$ .

## INTRODUCTION

We present a novel photonic crystal based combination infrared source and bolometer that is used to detect hydrocarbon gasses. The highly integrated single component infrared device contains all the elements of a non dispersive infrared optical bench in a single MEMS chip, unlike most infrared based gas sensors which separate the infrared source and detector. The device emits infrared radiation via a photonic crystal with a tuned output of 90% of the theoretical maximum at the hydrocarbon wavelength of  $3.3\ \mu\text{m}$  and suppresses emission at other bands. The amount of infrared radiation that returns to the device after bouncing off a retro-reflecting mirror depends on the concentration of methane present between the device and the mirror. This paper will present the operation, fabrication, wafer level packaging, testing, and performance of the device. This is the first time that this device has been reported in the trade or technical literature and the first time that this type of device has been reported to the MEMS community [1].

## OPERATION

The device uses two thermally isolated filaments,  $1.5\ \text{mm} \times 3\ \text{mm}$  in size that are resistively heated to  $300^\circ\ \text{C}$ . A photonic crystal, incorporated into the thermally isolated bulk-micromachined filaments, facilitates emission of infrared radiation, at the methane absorption wavelength of  $3.3\ \mu\text{m}$  and suppresses blackbody emission at wavelengths outside this band yielding high power efficiency and gas specificity. Without the photonic crystal, the peak of the emitted blackbody radiation would be near  $5.2\ \mu\text{m}$  in accordance with Wein's law. Because of the photonic crystal's geometry, the infrared emission is non-Lambertian and is emitted preferentially in a direction normal to the surface of the filament. The infrared radiation passes through a silicon cap wafer and out of the vacuum sealed package and then through the gas being analyzed. The infrared radiation reflects off a mirror and back through the gas being analyzed, through the silicon cap and onto the filament. In our test setup, the optical path length is about 5 cm. The photonic crystal has a high emissivity at  $3.3\ \mu\text{m}$  (approximately 90%), and does not transmit infrared radiation so almost all of the infrared radiation that is incident on the photonic crystal is absorbed. Because of the high thermal resistance of the filament ( $150\ \text{K/W}$ ), the incident infrared energy causes the temperature of the filament to increase. The filament has a temperature coefficient of resistance of 0.4%, and thus operates as a bolometer, making the resistance change of the sensor dependent on the partial pressure of the gas species being analyzed. To compensate for changes in the ambient temperature and the supply

voltage and to allow incorporation of the device into a Wheatstone bridge circuit, one of the two filaments is blinded with a gold film on the cap wafer. The device also has an on-chip thermistor to facilitate second order temperature corrections. The vacuum encapsulation and very high power conversion efficiency combine to keep the case temperature just above the ambient temperature, thus enabling intrinsically safe operation in potentially explosive environments. Any breach in the wafer level package that would expose the hot filaments to flammable gasses would immediately cause the device to lose thermal isolation and cool the filament. Figure 1 pictorially demonstrates how the device operates as a gas sensor.

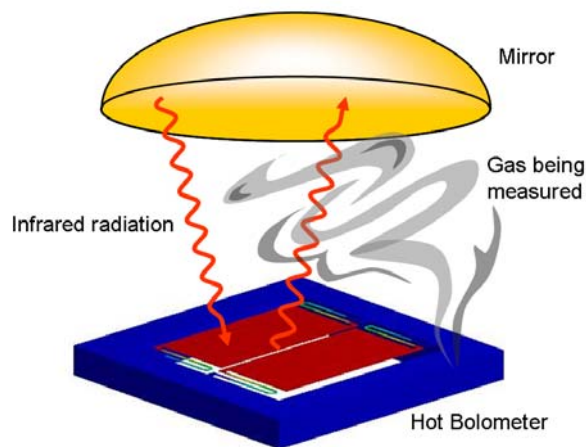


Figure 1 Pictorial depiction of device operation that shows infrared energy generation, absorption of the infrared by gasses, reflection off the mirror and return to the device. A change in the amount of infrared energy absorbed by the device is proportional to a temperature change and a resistance change in the filament, which is proportional to a change in the concentration of the gas being measured.

## PHOTONIC CRYSTAL THEORY

The photonic crystal is used in this device to increase the efficiency and decrease the cross sensitivity of the device by reducing the out of band emission of infrared light. Narrow emission is important to reducing cross sensitivity because some common atmospheric gasses absorb infrared radiation near the methane  $3.3\ \mu\text{m}$  line including water vapor at  $2.7\ \mu\text{m}$  and  $\text{CO}_2$  at  $4.2\ \mu\text{m}$ . Therefore, tailoring the emission of infrared energy so there is no radiation at these bands is critical to eliminating cross sensitivity. If the radiation emitted by the device was absorbed by a gas species other than the species of interest, the sensor would indicate a higher gas concentration than what was actually present. A device that emits a narrow band of infrared eliminates this cross sensitivity. Also, by reducing the bandwidth of the emitted infrared light, the energy loss due to radiation is reduced and less energy is needed to heat the device.

We fabricate the photonic crystals from a silicon substrate, a thin insulating oxide layer, and a conductive metal filament layer on top. The entire structure is pierced with an array of micrometer sized holes that have a periodic spacing. In the same way that the

periodic arrangements of atoms in a solid state device changes the allowed and forbidden energy bands and energy bandgaps for electrons from the energy levels available in individual atoms, the periodic arrangement of recesses form alternating regions of low pressure gas and silicon or a two dimensional photonic crystal, which causes the establishment of photonic bandgaps. Photonic bandgaps are analogous to electron bandgaps, they are regions where certain wavelengths are not allowed. Our periodic structure creates a sharp photon absorption profiles aided by surface plasmons, which are longitudinal modes of electromagnetic radiation propagating along the surface that exponentially decay away from the interface. Photonic crystals are usually designed using finite element codes. Faraday's law and Ampere's law are expressed in terms of the magnetic field,  $\mathbf{H}$ , and the Maxwell eigen-value problem is solved. Equation 1 shows the solution of Faraday's and Ampere's law in terms of the magnetic field where  $\epsilon$  is the dielectric constant and  $\omega$  equals  $2\pi$  times the frequency.

$$\nabla \times \frac{1}{\epsilon} \nabla \times \mathbf{H} = \left(\frac{\omega}{c}\right)^2 \mathbf{H} \quad (1)$$

A good summary of our photonic crystal structure can be found in references [2-4]. A SEM image of the photonic crystal is shown in figure 2.

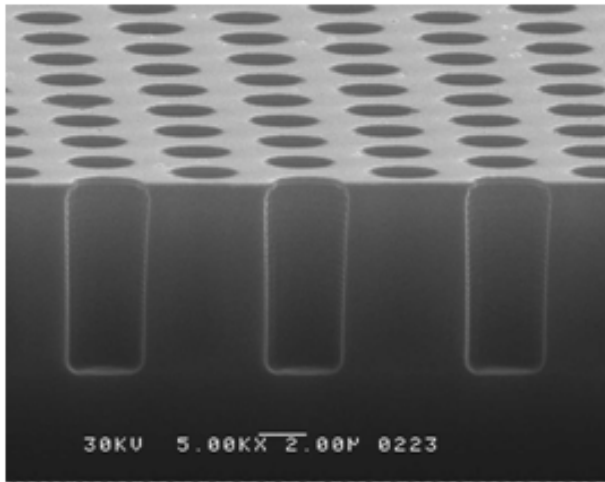


Figure 2 Photograph of the dry etched photonic crystal.

**FABRICATION**

To improve efficiency, the filaments are thermally isolated from the substrate with a bulk micromachining etch and vacuum encapsulation. All the fabrication is done by Innovative Micro Technology of Santa Barbara, California [5]. The three wafer stack is bonded together using a glass frit bonding process. The top wafer in the stack is high resistivity silicon that is transparent in the infrared and allows optical energy to enter and leave the device. The proprietary vacuum bonding process has a stabilized base pressure of less than 20 mT. Figure 3 is a photograph of the devices after dicing.

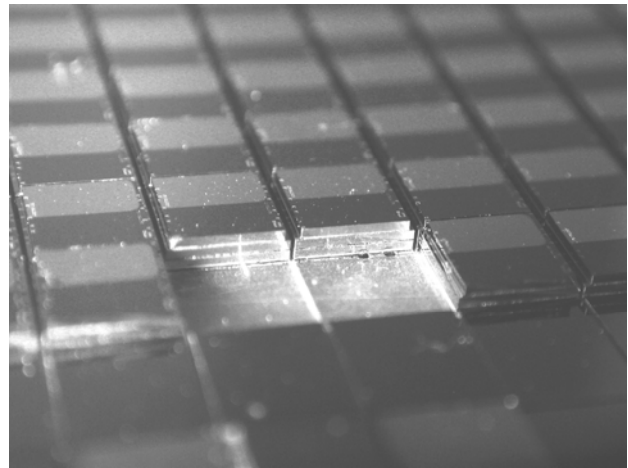


Figure 3 Devices after dicing. The photograph illustrates the 3 wafer stack and the blinding of one filament to form a reference. The device is constructed from a three wafer stack. The wire bond connections are made to the exposed ledge on the middle wafer.

Figure 4 shows the relationship between the pressure inside the devices and the high current resistance (10 mA) divided by the low current resistance (100  $\mu$ A). The ratio is close to 1.0 at atmospheric pressure. Figure 4 implies the increased sensitivity that is created by vacuum sealing the device. At low pressures, the thermal resistance of the filament is dominated by the structural silicon support arms. At high pressures, the thermal resistance is dominated by the thermal conductivity of the gasses surrounding the sensor and is not dependent on the pressure because the mean free path of the gas molecules is much smaller than the distance from the filament to the cap wafer. Thermal isolation is one characteristic measured during testing that separates acceptable device from rejected devices.

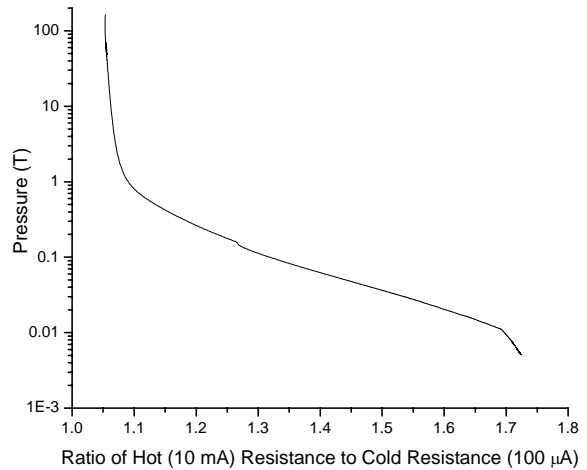


Figure 4 The  $R_{hot}/R_{cold}$  resistance ratio as a function of pressure.  $R_{hot}$  is measured at 10 mA and  $R_{cold}$  is measured at 100  $\mu$ A. At very high and very low pressures, this ratio and the thermal isolation is independent of pressure. If the experiment had been continued to 0.001 or 0.0001 T the hot resistance to cold resistance would not have exceeded 1.75.

One interesting discovery was that the amount of surface area of the photonic crystal and the diameter of the holes influenced the final base pressure that was reached during packaging. During the prototyping of the device, we varied the size of the photonic crystal holes and changed the spacing. The pressure inside the wafer level package increased as the diameter of the photonic crystal holes decreased because of the decreased pumping conductance. Conductance is dependent on the cube of the diameter when molecular flow is the dominate flow mechanism. We also changed the density of the holes in the photonic crystal and discovered that devices with a higher density of holes, and more surface area, had a higher base pressure than units with a lower hole density. This correlates with theory because the main cause of residual gasses inside the devices after sealing is outgassing from surfaces. In this device, about 50% of the total surface area inside the devices is from the sides of the holes. The results of this experiment are shown in figures 5 and 6.

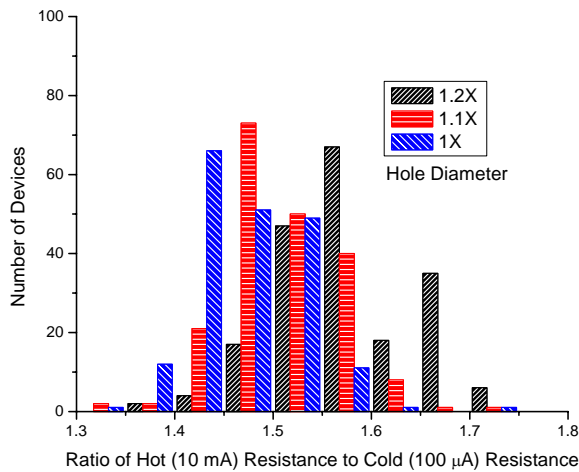


Figure 5 Pressure histogram showing the relationship between photonic crystal hole diameter and the thermal isolation (ratio of 10 mA resistance to 100  $\mu$ A resistance). The diameters are expressed as in terms of the smallest hole diameter or 1.1 or 1.2 times the smallest hole diameter. A value of 1.7 corresponds to a pressure of 9mT and a value of 1.4 corresponds to a pressure of 60 mT. Hole density was held constant in this experiment.

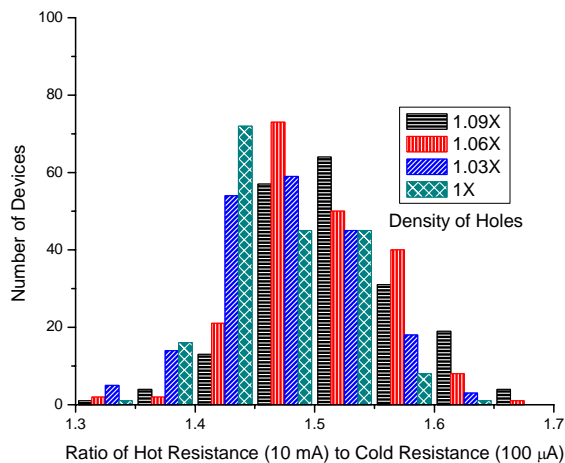


Figure 6 Pressure histogram showing the relationship between the number of holes in the filament and the thermal isolation (ratio of 10 mA resistance to 100  $\mu$ A resistance). The holes account for about 50% of the surface area that is sealed inside the device.

## FINAL ASSEMBLY AND TESTING

To reduce costs and monitor yield, the devices are tested on a wafer level before dicing. The defects that are found during this step are thermal isolation problems and electrical resistance problems. Thermal isolation is determined by using the device as a pirani gauge and measuring the ratio of the resistance at a high current level (10 mA) and a low current level (100  $\mu$ A). If the device is thermally isolated, the resistance changes by more than 50% from the low to the high current level. Devices that are not vacuum sealed, in contrast, exhibit a less than 10% change in resistance between the high and low current levels. Figure 2 shows a graph of the ratio of hot resistance to the cold resistance as function of pressure.

After testing on a probe station at Innovative Micro Technologies, the devices are shipped to Solid State Testing of Billerica, MA where they are die attached into 28 pin leadless chip carriers LCCs and wire bonded using thermosonic gold ball bonding [6]. Then they are shipped to ICx Photonics where they undergo gas testing. The electrical circuit is a Wheatstone bridge followed by amplification. The ICx Photonics automatic gas testing station, shown in figure 7, can expose several sensors in parallel to a predetermined series of gas concentrations. The gas sensitivity is influenced by defects in the transparent cap wafer. Issues in packaging and those due to electrical noise are also discovered and eliminated during gas testing.

Using results similar to figures 8 and 9 the performance of the device was analyzed. For an optical path length of 5.2 cm and a bridge voltage of 5 V, the device has a noise equivalent methane level in the 500 ppm range, a sensitivity of 3 to 4  $\mu$ V/ ppm, and a response time of 1 s.



Figure 7 Automatic testing setup. The test gas flows through the tubes to the twelve gas testing locations. The domes are the mirrors and the sensors sit beneath them along with the amplification circuitry.

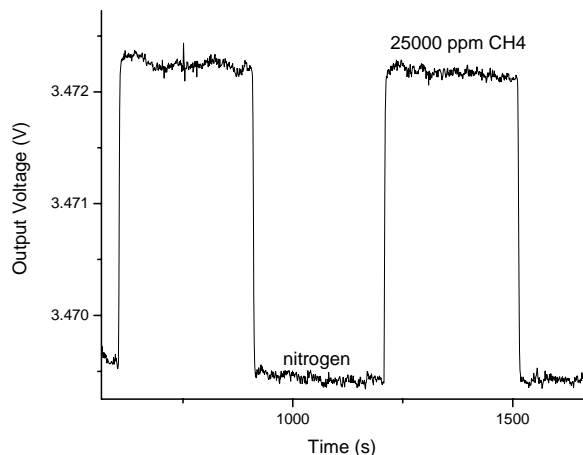


Figure 8 Time response of the gas sensor to 25000 ppm of methane alternating with nitrogen.

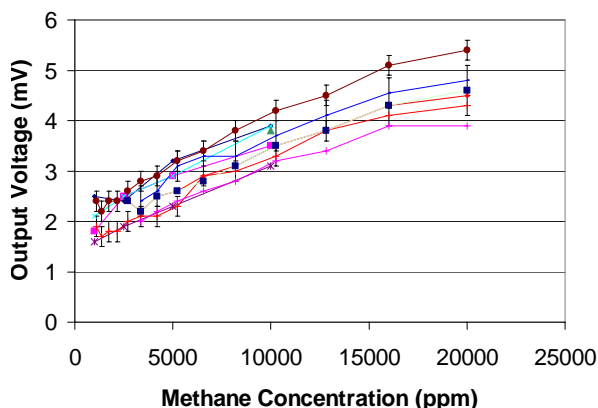


Figure 9 Output voltage as a function of gas concentration for a series of devices. . These devices were tested at half the gain setting of the device in figure 8. The minimum concentration in this graph is 1000 ppm.

## APPLICATIONS

The 70 mW that this device consumes makes it ideal for low power portable safety applications such as detecting explosive gasses in coal mines. The sensor and supporting circuitry are intrinsically safe because the voltages, capacitance and surface temperatures provide certifiable protection ignition in a potentially explosive atmosphere. The low power levels also make it

compatible with battery powered portable operation and remote monitoring applications. Because of the tailored infrared emission, the device has a low response to humidity, CO<sub>2</sub>, and other gasses that are found in coal mines. Because the gas does not contact the sensing element, it is not susceptible to poisoning and hysteresis that plague electrochemical sensors. The device is compatible with the ICx Photonics 4P sensor readout module [7].

## CONCLUSION

This paper reports a novel combination infrared source and bolometer that uses a photonic crystal to emit and detect precisely tailored infrared energy that is used to detect hydrocarbon gasses. The highly integrated single component infrared device contains all the elements of a non dispersive infrared optical bench in a single MEMS chip, unlike most infrared based gas sensors which separate the infrared source and detector. The device emits infrared radiation with a photonic crystal with a tuned output of 90% of the theoretical maximum at the hydrocarbon wavelength of 3.3  $\mu\text{m}$  and suppresses emission at other bands. The amount of radiation that returns to the device after emission, reflection off a mirror, and passing through a gas sample is related to the partial pressure of methane or other hydrocarbons in the sample being measured. The device can detect gas concentrations down to 500 ppm of methane and has a sensitivity of up to 4  $\mu\text{V/ppm}$ .

## ACKNOWLEDGEMENTS

The authors wish to thank Pat Feierabend, Jeff Summers, Doug Thompson, and the staff at Innovative Micro Technologies in Santa Barbara, California as well as Tracey Hines and the staff of Solid State Testing for building these devices. Brent Schell, Adam Yannopoulos, David Chin, and Nitin Thaker developed much of the test infrastructure at ICx Photonics.

## REFERENCES

- [1] A. C. Greenwald, M. U. Pralle, M. P. McNeal, N. Moelders, I. Puscasu, J. T. Daly, E. A. Johnson, "Modeling Combined Thermal, Electrical, Optical And Mechanical Response For MEMS Spectroscopic Gas Sensor Based On Photonic Crystals", Proc. MRS, paper, v741, paper J12.3.1 (2003).
- [2] M. U. Pralle, N. Moelders, M. P. McNeal, I. Puscasu, A. C. Greenwald, J. T. Daly, E. A. Johnson, T. George, D. S. Choi, I. El-Kady, and R. Biswas, "Photonic Crystal Enhanced Narrow-Band Emitters", Applied Physics Letters, vol 81, no. 25, pp. 4685-4687, (2002).
- [3] I. Puscasu, M. U. Pralle, M. P. McNeal, J. T. Daly, A. C. Greenwald, E. A. Johnson, R. Biswas and C. G. Ding. "Extraordinary Emission from Two-Dimensional Plasmonic-Photonic Crystals," J. Appl. Phys., 98, 13531 (2005).
- [4] R. Biswas, C. G. Ding, I. Puscasu, M. U. Pralle, M. P. McNeal, J. T. Daly, A. C. Greenwald and E. A. Johnson, "Theory of subwavelength hole arrays coupled with photonic crystals for extraordinary thermal emission", Phys. Rev. B 74, 045107 (2006).
- [5] <http://www.imtmems.com>
- [6] <http://www.solidstatetesting.com>
- [7] <http://www.icx-precision-photonics.com/iirss.shtml>

# HYBRID ULTRA-COMPACT 4<sup>TH</sup> ORDER BAND-PASS FILTERS BASED ON PIEZOELECTRIC ALN CONTOUR-MODE MEMS RESONATORS

C. Zuo, N. Sinha, C.R. Perez, R. Mahameed, M.B. Pisani, and G. Piazza

Penn Micro and Nano Systems Laboratory (PMaNS), Department of Electrical and Systems Engineering  
University of Pennsylvania, Philadelphia, PA 19104, USA

## ABSTRACT

This work reports on the design, fabrication and testing of a new class of hybrid (filter design using combined electrical and mechanical coupling techniques) ultra-compact ( $800 \times 120 \mu\text{m}$ ) 4<sup>th</sup> order band-pass filters based on piezoelectric Aluminum Nitride (AlN) contour-mode microelectromechanical (MEM) resonators. The demonstrated 110 MHz filter shows a low insertion loss of 5.2 dB in air, a high out-of-band rejection of 65 dB, a fractional bandwidth as high as 1.14% (hard to obtain when only conventional electrical coupling is used in the AlN contour-mode technology), and unprecedented 30 dB and 50 dB shape factors of 1.93 and 2.36, respectively. All these are achieved in an extremely small footprint and by using just half the space that any other 4<sup>th</sup> order filter would have taken. In terms of nonlinearities, the 110 MHz filter shows a 1 dB compression point higher than +63 dBmV and input third order intercept point (IIP<sub>3</sub>) values well beyond +153 dBmV. This new hybrid design represents a net improvement over the state of the art and constitutes a very promising solution for intermediate frequency (IF) filtering in many wireless communication systems.

## INTRODUCTION

To further reduce the fabrication cost and form factor of personal telecommunication systems, there have been tremendous efforts in both academia and industry to realize fully integrated CMOS radio frequency (RF) solutions using low-IF and zero-IF radio architectures [1]. However, due to the lack of high quality factor ( $Q$ ) filtering components, which used to be implemented by off-chip quartz crystal and Surface Acoustic Wave (SAW) devices,

homodyne architectures generally have poorer sensitivity, image rejection and dynamic range than superheterodyne transceivers. These issues lead to look at alternative ways of developing post-CMOS compatible high- $Q$  MEMS resonators that enable low cost and small footprint IF and RF filtering and, most importantly, improve flexibility in defining multi-frequency and multi-band RF architectures.

Several research groups have been developing MEMS resonator technologies based on electrostatic [2] and piezoelectric [3] transduction mechanisms that are capable of providing multiple frequencies of operation on the same silicon substrate (in contrast with conventional FBAR or quartz crystal technologies for which only one frequency per substrate is possible). Among these, the aluminum nitride (AlN) contour-mode RF MEMS technology [4] stands out as one of the most promising and capable of immediately satisfying the critical requirements of the rapidly developing wireless industry. It is currently the only technology that can reliably span a wide frequency range from 10 MHz up to several GHz (operating in the fundamental mode of vibration) on the same silicon chip, and simultaneously offer high  $Q$  in air (1,000 – 4,000) and low motional resistance (25 – 700  $\Omega$ ), which makes the devices readily matched to conventional 50  $\Omega$  RF systems.

Based on this new AlN contour-mode MEMS technology, VHF band-pass filters have been demonstrated using electrical [5, 6] and mechanical coupling [7, 8] techniques. For electrical coupling, several AlN contour-mode resonators are cascaded in a ladder or self-coupling topology to realize higher order filtering. The fractional bandwidth of these filters is generally set by the

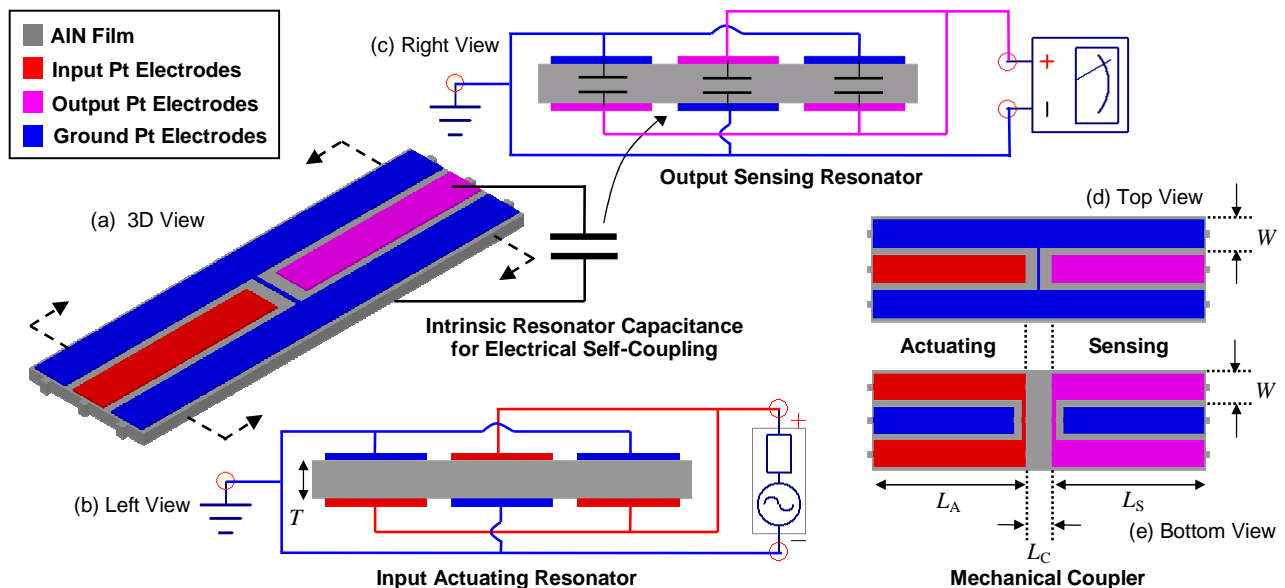


**Fig. 1:** (a) 3D, (b) left, (c) right, (d) top and (e) bottom schematic views of the 2<sup>nd</sup> order sub-filter stage. It consists of an input actuating AlN contour-mode piezoelectric resonator, an output sensing resonator and a rectangular mechanical coupler in between with lengths of  $L_A$ ,  $L_S$  and  $L_C$ , respectively.  $W$  is the finger width which determines the resonant frequency of the resonators and therefore the center frequency of the filter, while  $T$  is the AlN film thickness. All  $L_A$ ,  $L_S$ ,  $L_C$  and  $W$  values can be defined by photolithography, which enhances designer's freedom in setting filter center frequency ( $W$ ), bandwidth ( $L_C/W$ ) and termination ( $L_A$  and  $L_S$ ) independently.

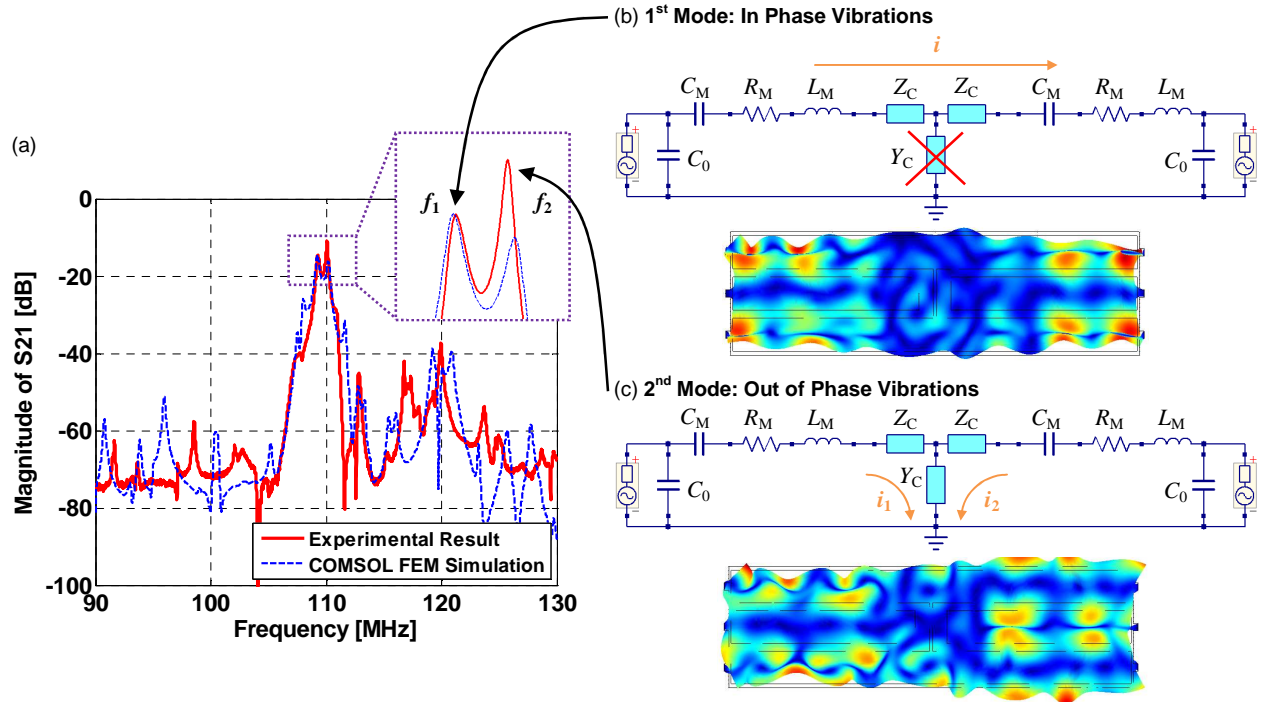


**Fig. 2:** (a) Unmatched transmission ( $S_{21}$  at  $50 \Omega$  termination) curves are given for the mechanically coupled 2<sup>nd</sup> order sub-filter stage. The curves show a good agreement between the experimental data and the COMSOL<sup>®</sup> FEM simulation (discrepancies likely due to theoretically unpredictable  $Q$  values for different vibration modes). Two transmission peaks can be seen: (b) for the first peak, the output resonator is vibrating in phase with the input one; (c) for the second peak, the two resonators are moving out of phase. The equivalent circuits are also given to illustrate the function of the mechanical coupler.

effective electromechanical coupling coefficient  $k_t^2$ , which is a material property and limits the bandwidth to be 0.2% to 1% in the AlN contour-mode technology. Both mechanical coupling and dual mode techniques can be adopted to increase the bandwidth to a certain extent, as shown in [7–9]. However, the pass band shape and spurious modes are very difficult to control when the filter order is higher than 2. Therefore, with this work we propose a new hybrid solution that takes advantage of both electrical and mechanical coupling techniques to implement small form factor, high order and spurious free filtering functions. The demonstrated 110 MHz filter shows a low insertion loss of 5.2 dB in air, a high out-of-band rejection greater than 65 dB, a fractional bandwidth as high as 1.14% (hard to achieve when only conventional electrical coupling is used), and unprecedented 30 dB and 50 dB shape factors of 1.93 and 2.36, respectively. All these are achieved in an extremely small footprint and by using just half the space that any other 4<sup>th</sup> order filter would have taken.

### FILTER DESIGN

The 4<sup>th</sup> order hybrid filter consists of two mechanically coupled sub-filter stages electrically cascaded and coupled by the intrinsic capacitance existing in the piezoelectric AlN contour-mode resonators, as illustrated in Fig. 1.

### Mechanical Coupling

Each sub-filter stage can be treated as a 2<sup>nd</sup> order filter which has a one-port input actuating resonator [10], an output sensing resonator and a passive mechanical coupler in between (Fig. 1). The mechanical coupler is equivalent to an electrical T-network which includes two series components with impedance  $Z_C$  and a parallel component with admittance  $Y_C$  (Fig. 2) [7]. Both the values of  $Z_C$

and  $Y_C$  can be capacitive or inductive depending on the geometrical dimensions of the mechanical coupler. The 2<sup>nd</sup> order system has two modes of mechanical vibration, as explained by the equivalent circuits of Fig. 2. In the first mode, the input and output resonators vibrate in phase with each other and the coupling element  $Y_C$  has no effect on the first system resonance at  $f_1$ . In the second mode, the two resonators vibrate out of phase and the coupling admittance  $Y_C$  can be equally split into input and output branches causing a higher system resonance at  $f_2$ . The frequency separation between  $f_1$  and  $f_2$  is primarily set by the value of  $Y_C$ , and the filter bandwidth can then be engineered at the CAD layout level by defining the coupler dimension,  $L_C$ , through photolithography. All this analysis has been verified by COMSOL<sup>®</sup> FEM simulations, which indicate that the fractional bandwidth can be varied from 1% to 2% by designing the length to half wavelength ( $W=\lambda/2$ ) ratio ( $L_C/W$  in Fig. 1) of the mechanical coupler, as shown in Fig. 3.

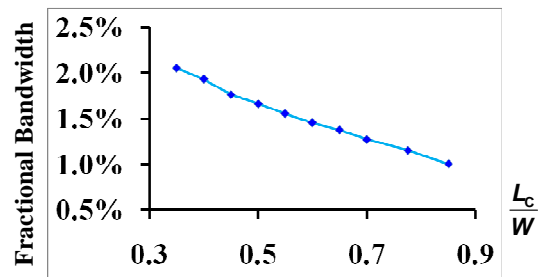


**Fig. 3:** Filter fractional bandwidth plotted as a function of the length to half wavelength ratio  $L_C/W$ , obtained from COMSOL<sup>®</sup> FEM simulations.

The unmatched transmission curves ( $S_{21}$  at  $50 \Omega$  termination) of such a mechanically coupled sub-filter are also given in Fig. 2. They show a good agreement between the experimental result and the COMSOL<sup>®</sup> FEM simulation that was employed for the design of this filter. Compared with the dual-mode AIN mechanical filters using an annular geometry [8, 9], this new rectangular topology drastically reduces the die space of the single-stage 2<sup>nd</sup> order filter by eliminating the inevitable empty space present in the annulus. Further, differently from any other mechanically coupled MEMS filter demonstrated to date, this device requires a mechanical coupler whose dimensions are comparable to the acoustic wavelength instead of being a significant fraction of it. Therefore its frequency of operation can be extended to the GHz range.

### Electrical Self-Coupling

This work increases the filter order of any previously demonstrated low-loss and spurious free mechanically coupled filter from a mere 2<sup>nd</sup> order to a 4<sup>th</sup> order by electrically coupling two of the mechanically coupled sub-filter stages using the intrinsic capacitance,  $C_0$ , of the resonators. In this way the first ever hybrid MEMS filter (Fig. 4) has been realized. The principle of electrical coupling is explained in further details in [11]. In the case of AIN contour-mode resonators, the electromechanical transducer itself is an electrical capacitor  $C_0$ , so that no external coupling element is needed for the electrical coupling of two sub-filter stages. This

electrical self-coupling technique can improve manufacturing yield by employing single-frequency resonators for filter synthesis [6] and reduce the overall device size by eliminating external coupling elements. As we can see from Fig. 4, a much cleaner filter response is obtained after electrical coupling. Shape factors are almost halved and out-of-band rejection is improved from 50 to 65 dB. All these are achieved in a small silicon area of just  $800 \times 120 \mu\text{m}$ .

### EXPERIMENTAL RESULTS

The filters were fabricated using a simple five-mask, low-temperature, potentially post-CMOS compatible process [3]. The two Pt electrode layers were sputter-deposited and patterned by lift-off. The AIN layer in between was sputter-deposited using a Tegal/AMS<sup>®</sup> PVD tool and exhibits rocking curves as low as  $1.4^\circ$ . An additional electroplated Au layer was finally added on top of the routing electrodes to reduce the electrical resistance of the pads. The electrical test setup included a Desert Cryogenics<sup>®</sup> TTP6 probe station, an Agilent<sup>®</sup> N5230A network analyzer (for 2 port S-Parameter measurements), an Agilent<sup>®</sup> 8562EC Spectrum Analyzer and an Agilent<sup>®</sup> E8257D PSG Analog Signal Generator (for power handling and intermodulation distortion measurements). The devices under test were directly probed and connected to the measurement instrumentation without the use of any external electronic interface.

The measured transmission response for a 110 MHz hybrid 4<sup>th</sup>

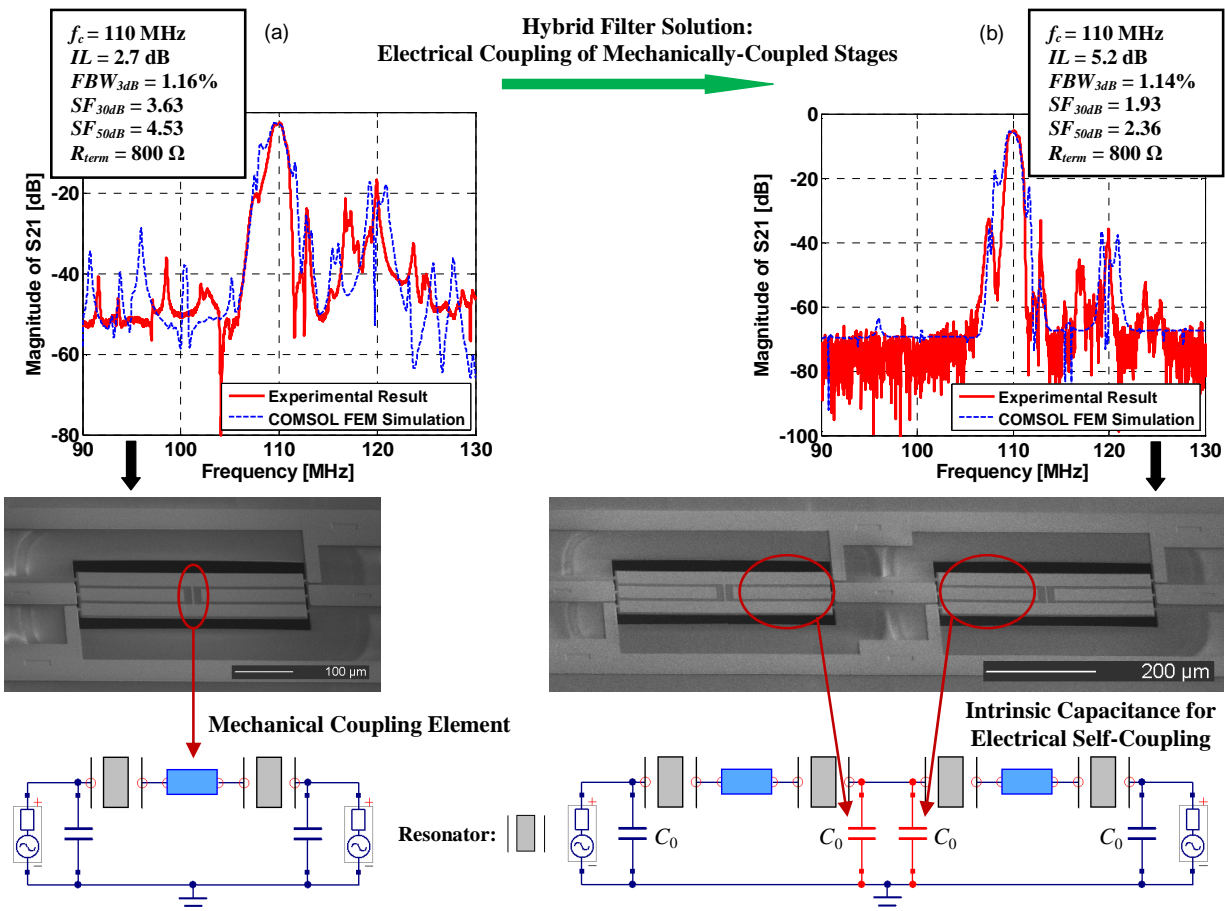


**Fig. 4:** (a) Transmission response ( $S_{21}$  at  $800 \Omega$  termination) and SEM picture (below) of the single-stage mechanically coupled 2<sup>nd</sup> order sub-filter. (b) Transmission response ( $S_{21}$  at  $800 \Omega$  termination) and SEM picture (below) of the two-stage 4<sup>th</sup> order filter, which is formed by electrically cascading two single stages and coupling them using the intrinsic capacitance of the AIN contour-mode piezoelectric resonators.

order filter using 800  $\Omega$  termination is shown in Fig. 4 (b). The electrical self-coupling technique suppresses most of the spurious modes that appear in the mechanically-coupled single stage (Fig. 4 (a)) by pushing them below the feed-through level. In this way a much cleaner filter response is obtained. The few discrepancies between COMSOL<sup>®</sup> simulations and experimental results (evident in the presence of two additional out-of-band peaks) are probably caused by the fact that a  $Q$  of 500 was assumed for all the modes of vibration and which is likely not to be the case in reality. A lower  $Q$  for spurious modes masks their presence in the final transmission plot of the experimental data. The 4<sup>th</sup> order filter has a low insertion loss of 5.2 dB in air, a high out-of-band rejection of 65 dB, a fractional bandwidth as high as 1.14%, and especially unprecedented 30 dB and 50 dB shape factors of 1.93 and 2.36, respectively. Simulations also show that the insertion loss can be further improved to 2.6 dB if a  $Q$  of 1000 is achieved.

Power handling and nonlinearity characterization were also performed for the same 110 MHz 4<sup>th</sup> order filter. The results show that a 1 dB compression point higher than +63 dBmV (max allowed by the test set up) can be obtained. Furthermore, a two-tone test technique [12] was used to measure the input third order intercept point ( $IIP_3$ ) values.  $IIP_3$  values well beyond +153 dBmV were recorded for all three analyzed cases: (a) both of the two interfering tones are in the pass band; (b) one tone in band and the other out of band; (c) both are out of the pass band. These data show superior performance of this filter design in terms of immunity to intermodulation distortions over other electrically coupled AlN contour-mode devices [6], electrostatically-transduced resonators [12] or SAW counterparts [13].

The temperature coefficient of frequency (TCF) of the filter was measured to be linear in the 300 to 400 K range and equal to -25.7 ppm/K, as shown in Fig. 5.

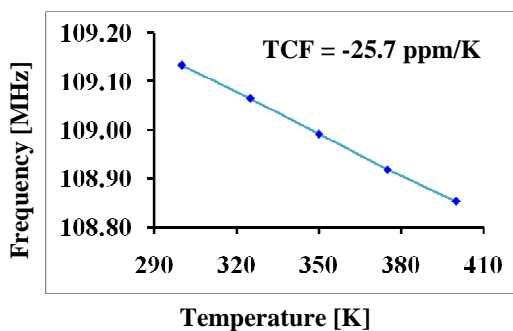


Fig. 5: Temperature coefficient of frequency (TCF) of the hybrid 4<sup>th</sup> order filter.

## CONCLUSION

The first ever hybrid MEMS filter has been designed, fabricated and tested. The device consists of two mechanically coupled sub-filter stages electrically cascaded and coupled by the intrinsic capacitance existing in the piezoelectric AlN contour-mode resonators. The demonstrated 110 MHz filter shows unprecedented rejection, shape factor and bandwidth performances, which would have otherwise not been possible if simply mechanical (pass band shape and spurious modes are hard to control in 3<sup>rd</sup> or 4<sup>th</sup> order filters [7]) or electrical (wide bandwidth, sharp roll off and small area are hard to achieve [5, 6]) coupling techniques were to be used. Therefore, this new hybrid design represents a net improvement over the state of the art and constitutes one of the most promising solutions for IF filtering in many wireless communication systems. On-going research is aimed at lowering the filter termination

impedance, as well as expanding this coupling technique to GHz frequencies for RF filtering.

## ACKNOWLEDGEMENTS

This work was supported by the DARPA ASP/Honeywell grant. The authors offer special thanks to Philip J. Stephanou, Justin P. Black at Harmonic Devices and the Wolf Nanofabrication Lab staff at Penn for their help with part of the fabrication steps.

## REFERENCES

- [1] H.-K. Yoon and M. Ismail, "A Fully-Integrated CMOS RF Front-End for Wi-Fi and Bluetooth," *The 2nd Annual IEEE Northeast Workshop on Circuits and Systems*, pp. 357-360, NEWCAS 2004.
- [2] C. T.-C. Nguyen, "MEMS technology for timing and frequency control," *IEEE Trans. On Ultrasonics, Ferroelectrics, and Frequency Control*, vol. 54, no. 2, pp. 251-270, Feb. 2007.
- [3] G. Piazza, P. J. Stephanou, and A. P. Pisano, "Piezoelectric Aluminum Nitride Vibrating Contour-Mode MEMS Resonators", *Journal of MicroElectroMechanical Systems*, vol. 15, no.6, pp. 1406-1418, December 2006.
- [4] G. Piazza, P. J. Stephanou, and A. P. Pisano, "AlN Contour-Mode Vibrating RF MEMS for Next Generation Wireless Communications," *ESSDERC 2006*, Montreux, Switzerland, Sep 2006.
- [5] G. Piazza, P. J. Stephanou, and A. P. Pisano, "Single-Chip Multiple-Frequency AlN MEMS Filters Based on Contour-Mode Piezoelectric Resonators", *Journal of MicroElectroMechanical Systems*, vol. 16, no.2, pp. 319-328, April 2007.
- [6] C. Zuo, N. Sinha, M. B. Pisani, C. R. Perez, R. Mahameed, and G. Piazza, "Channel-Select RF MEMS Filters Based On Self-Coupled AlN Contour-Mode Piezoelectric Resonators", *2007 IEEE International Ultrasonics Symposium*, New York, October 2007.
- [7] P. J. Stephanou, G. Piazza, C. D. White, M. B. J. Wijesundara, and A. P. Pisano, "Mechanically Coupled Contour Mode Piezoelectric Aluminum Nitride MEMS Filters," *IEEE MEMS 2006*, pp. 906-909, 2006.
- [8] P. J. Stephanou, G. Piazza, C. D. White, M. B.J. Wijesundara, A. P. Pisano, "Piezoelectric Aluminum Nitride MEMS Annular Dual Contour Mode Filter", *Sensors and Actuators A-Physical*, vol. A134, 2007.
- [9] R. H. Olsson III, J. G. Fleming, K. E. Wojciechowski, M. S. Baker, and M. R. Tuck, "Post-CMOS Compatible Aluminum Nitride MEMS Filters and Resonant Sensors", *2007 IEEE International Frequency Control Symposium*, Jun 2007.
- [10] G. Piazza a, P. J. Stephanou, and A. P. Pisano, "One and Two Port Piezoelectric Higher Order Contour-Mode MEMS Resonators for Mechanical Signal Processing", *Solid-State Electronics*, vol. 51, pp. 1596-1608, 2007.
- [11] S. Pourkamali and F. Ayazi, "Electrically coupled MEMS bandpass filters Part I: With coupling element", *Sensors and Actuators A*, vol. 122, pp. 307-316, 2005.
- [12] R. Navid, J. R. Clark, M. Demirci, and C. T.X. Nguyen, "Third-Order Intermodulation Distortion in Capacitively-Driven CC-Beam Micromechanical Resonators", *MEMS 2001*, pp. 228 - 231, Jan 2001.
- [13] Yoshio Satoh, Osamu Ikata, Tsutomu Miyashita, and Hideki Ohmori, "RF SAW Filters", *International Symposium on Acoustic Wave Devices for Future Mobile Communication Systems*, March 2001.

# LOW VOLTAGE COMPLEMENTARY MEMS LOGIC USING PIEZOELECTRIC ACTUATORS

Daniel C. Judy, Ronald G. Polcawich, and Jeffery S. Pulskamp  
U.S. Army Research Laboratory, Adelphi, MD 20783

## ABSTRACT

Microelectromechanical systems (MEMS) based on piezoelectric thin films continue to be examined for a variety of versatile sensors and actuators [1,2]. The most promising piezoelectric material for actuators is lead zirconate titanate (PZT) because of its large piezoelectric coefficient relative to other piezoelectric thin films such as aluminum nitride and zinc oxide [1]. One drawback of using PZT based MEMS is the difficulty associated with integrating PZT with CMOS to enable embedded control with MEMS components. This paper presents results on using piezoelectrically-actuated MEMS switches for simple logic circuits.

## INTRODUCTION

Rather than combining PZT based MEMS with CMOS to enable an on-chip control logic integrated with the MEMS components, one approach is to integrate MEMS logic components within the same process as PZT based MEMS actuators and sensors. Instead of using electronic logic, this approach relies on using mechanical switching elements configured to create the necessary logic components. Lee et. al. successfully demonstrated the concept of MEMS logic components fabricated using the polymumps fabrication process.[3,4] Leveraging this past work, we have developed complementary MEMS logic (CML) components based on the Army Research Laboratory's PZT MEMS fabrication process. The ARL process has previously been used to develop RF MEMS switches capable of operating as low as 2 volts.[5,6] Using the same process flow, PZT mechanical switches configured for optimal operation at DC have been designed and integrated to demonstrate several logic elements.

## CONCEPT

The previously reported PZT switch fabrication process created normally open switches by stress engineering the PZT actuator to possess a negative curvature after fabrication. In its simplest form, an inverter requires both normally open (NO) and normally closed (NC) mechanical switching components (see Figure 1). A normally closed PZT switch was designed such that the DC contact cantilever comprised of gold was anchored to the end of the actuator. As the actuator deforms into the wafer plane, the gold cantilever contacts the DC control lines completing the electrical circuit (see Figure 2). The inverter operates as follows. When the input is low (typically 0V) the NC actuator is in contact and the actuation voltage ( $V_{act}$ ) is presented to the output, which can then be used to actuate the next logic gate. When the input is high ( $V_{act}$ ) the NC switch opens up and the normally open (NO) switch is closed presenting ground to the output.

## RESULTS

The inverter shown in Figure 2 has demonstrated operation as low as  $1 V_{DC}$  (see Figure 3). Successful inversion is illustrated by the output waveform (blue trace) of the inverter always being in the opposite state of the input waveform (red trace) (see Figure 3). The current version of the CML inverter has a length of  $125 \mu m$  with a fundamental resonance frequency of approximately 38 kHz.

Shorter, faster devices designed within the design tolerances of the current fabrication process are being investigated for improved performance and a reduction in scale. Alternative fabrication processes including the use of sub-micron lithography and electron beam lithography are being investigated as a means to enable nanoelectromechanical (NEMS) logic.

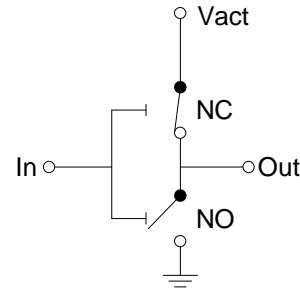


Figure 1: Schematic description of a CML inverter based on using normally closed (NC) and normally open (NO) mechanical switches.

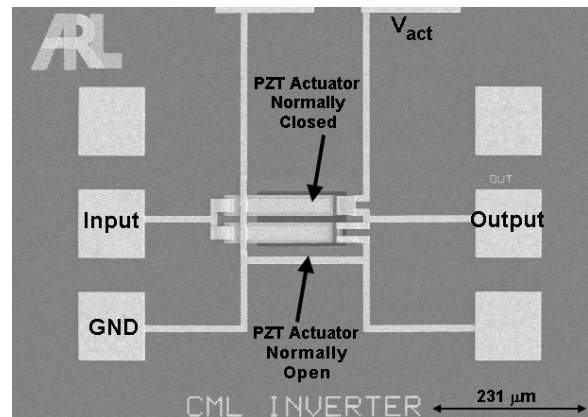


Figure 2: SEM image of a PZT inverter with a normally closed and a normally open switch.

These inverters have exhibited lifetimes in excess of  $10^6$  cycles (see Figure 4). Referring to Figure 4, a digital voltmeter was used to measure the RMS voltage on the output of the inverter, and a computer logged the time and cycle count. When the device fails open the RMS voltage jumps to  $V_{act}$ , and if the device fails closed the RMS voltage goes to zero. The plot shows that some intermittent high resistance failures occurred before the stuck closed failure at around 20 million cycles. The typical failure for these types of devices is due to high contact resistance. This failure mechanism is likely related to contact contamination either from residual organics from the processing or frictional polymers generated during contact, although this is still an area of investigation.

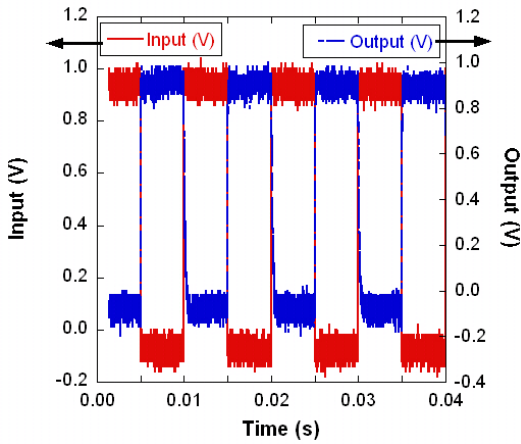


Figure 3: Experimental operation of a one volt PZT based CML inverter.

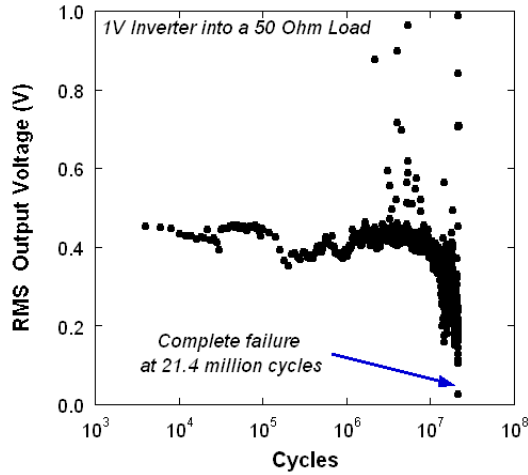


Figure 4: Inverter reliability with  $5V_{DC}$  operation into a 50 Ohm load. Failure mode are currently under investigation with high contact resistance generated by contact contamination is a leading possibility.

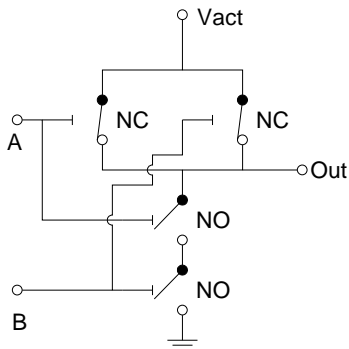


Figure 5: Schematic representation of a CML NAND gate based on using two normally closed (NC) switches in parallel, and two normally open (NO) switches in series.

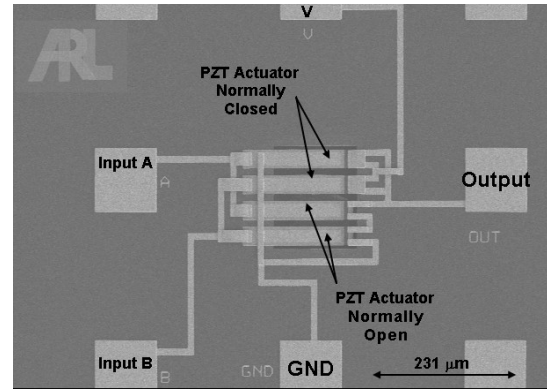


Figure 6: SEM image of a CML NAND gate with two normally closed and two normally open switches.

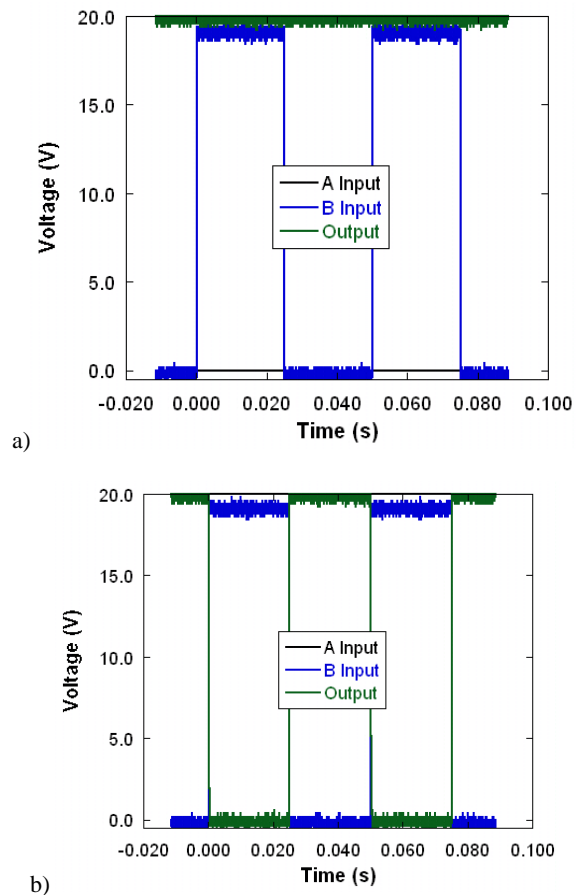


Figure 7: CML NAND gate experimental operation altering the A input between 0V (a) and 20 V (b).

In addition to the CML inverter, NAND gates and ring oscillators have been demonstrated. The NAND gate is shown schematically in Figure 6 and the actual device is shown in Figure 6. The typical CMOS inverter consists of two normally closed transistors wired in parallel to  $V_{act}$ , and two normally open transistors wired in series to ground (Figure 5). The CML NAND consists of two normally closed switches wired in parallel, and two

normally open switches wired in series, analogous to the CMOS implementation (see Figure 6).

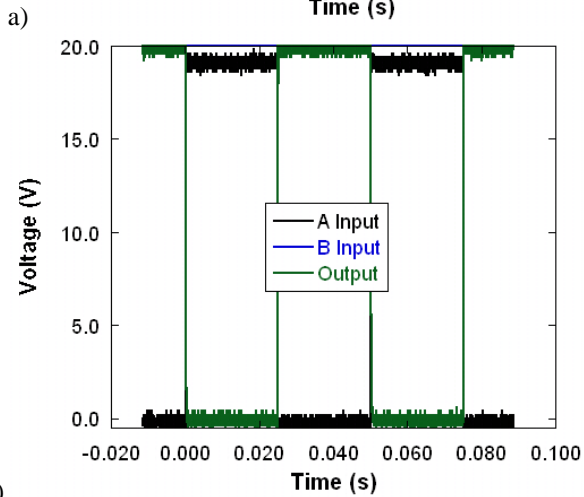
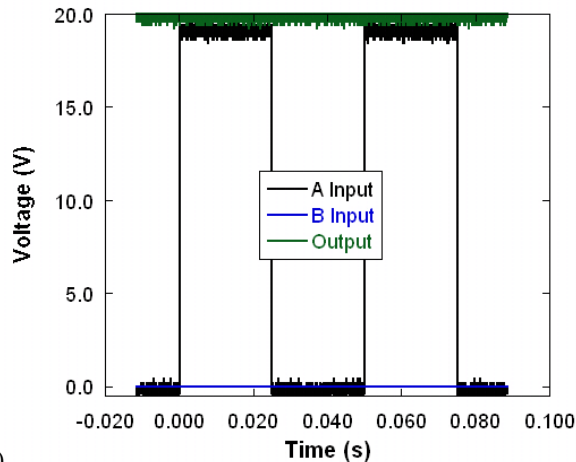


Figure 8: CML NAND gate experimental operation altering the B input between 0V (a) and 20 V (b)

The operation of the CML NAND gate is shown in Figure 7 and 8. A NAND gate has the interesting property that it behaves as a switchable inverter. For instance, when input A (black trace in Figure 7a) is high, then the signal on input B (blue trace in Figure 7a) is blocked, and the output is held high (green trace in Figure 7a). Conversely, if input A is held low then the input B signal is inverted on the output of the device (see Figure 7b). The opposite case, where input B is used to control the input A signal is illustrated in Figure 8. The successful NAND gates have only been operated at elevated voltages (at or near 20 V), although it is expected contact conditioning and actuator poling should allow for a decrease in operating voltage similar to the CML inverter.

Finally, a ring oscillator was successfully demonstrated using CML technology. A ring oscillator typically involves cascading an odd number of logic inverters and feeding the output of the last stage back to the first. This creates and instability which causes the output to toggle back and forth from high to low. Figure 9 shows the realization of the ring oscillator using MEMS logic. The SEM of the actual device is shown as the inset. A close inspection of the SEM shows the requisite odd number of inverters with the output

section on the right feed back to the input section on the left. The output waveform is shown in the graph. The asymmetric waveform is believed to be due to different contact resistances for the normally open and normally closed switches. In addition we were only able to demonstrate the ring oscillator for a few seconds at a time. In most instances, the oscillations would stop after a few seconds of operation, but could be started again by turning the power on and off. We also believe the presumed contact asymmetry is responsible for the intermittent operation of this device. The long term stability and reliability of this device is currently being investigated.

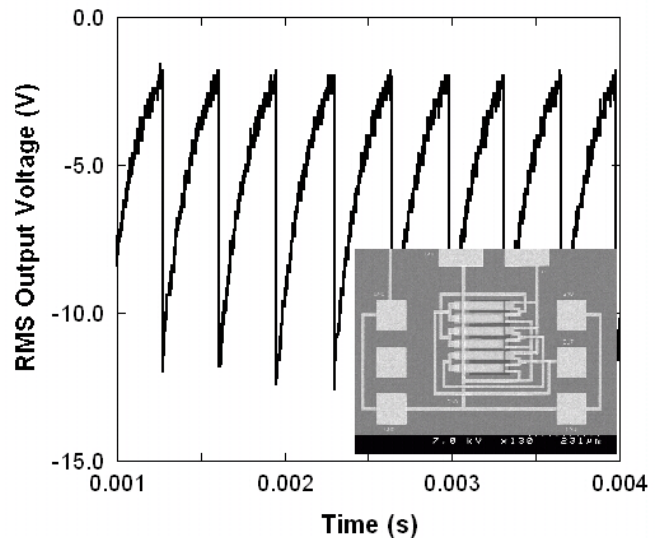


Figure 9: CML ring oscillator experimental performance with a frequency of operation of 2.9 kHz with an applied voltage of 11.2 V. The asymmetry in the output waveform is believed to be due to a difference in the NO and NC contact resistance. The actual device is shown in the inset SEM.

## CONCLUSION

This effort has demonstrated low voltage CML components compatible with an existing PZT MEMS fabrication process. This could overcome the problems of integration of CMOS with our PZT process, and all of the potential process compatibility issues involved. One application that is currently being pursued is the integration of phase state control logic within the PZT phase shifter outlined in Reference 6. If successful, we could reduce the required 16 control inputs of a 4 bit phase shifter to 4 logic lines. The same technology can be applied to a wide variety of PZT MEMS components including PZT resonators [7] and microrobotics relying on PZT thin film actuators [8].

## REFERENCES:

- [1] P. Muralt, IEEE Trans. UFFC, vol. 47, pp 903 - 915, 2000.
- [2] K. Prume, et. al., IEEE Trans. UFFC, vol. 54, pp. 8 – 14, 2007.
- [3] S.-W. Lee, R. W. Johnstone, and A. M. Parameswaran, IEEE CCECE/CCGEI, Saskatoon, May 2005, pp. 1513 – 1516.
- [4] S.-W. Lee, R. W. Johnstone, and A. M. Parameswaran, Proc. SPIE, 6037, pp. 1A1-1A10, 2005.
- [5] R. Polcawich, et. al., IEEE Trans. Microw. Theory Techn., vol 55, pp. 2642 – 2654, 2007.

- [6] R. Polcawich, et. al., IEEE Proc. Internat. Microw. Symp., pp. 2083 – 2086, 2007.
- [7] H. Chandralim, et. al., submitted to Proc. Solid-State Sensor Actuator Workshop, 2008.
- [8] K. Oldham, et. al., Integ. Ferro., vol. 95, pp. 54 - 65, 2007.

# MICRODISCHARGE-BASED PRESSURE SENSORS FOR OPERATION AT 1000°C

Scott A. Wright\* and Yogesh B. Gianchandani

Engineering Research Center for Wireless Integrated MicroSystems (WIMS)  
University of Michigan, Ann Arbor, MI, USA

## ABSTRACT

This paper reports microdischarge-based pressure sensors which operate by measuring the change in spatial current distribution of pulsed DC microdischarges. The sensors are composed of 3D arrays of horizontal bulk metal electrodes embedded in quartz substrates. Microdischarge-based pressure sensors are well-suited for high temperature operation because of the inherently high temperatures of the charged species that are generated. In this effort, temperatures of up to 1000°C are tested. The pressure sensors have a measurable pressure range of 10-760 Torr and require an active area of only 0.8 mm<sup>2</sup>. The sensor structures are designed to allow for unequal expansion of electrodes and substrate, during high temperature operation. The sensors demonstrate a maximum sensitivity of 5,000 ppm/Torr and temperature coefficients of sensitivity as low as 44 ppm/K.

## INTRODUCTION

Pressure sensors amenable to high temperatures have uses in numerous industrial segments including the combustion section of gas turbine engines, coal boilers, furnaces, and oil/gas exploration. A variety of microscale solutions have been explored. Fabry-Perot, and other interferometers, have been used on the ends of fiber optic cables and have been operated at temperatures of 800°C using sapphire membranes [1]. Bragg gratings have been photo inscribed into fibers and used to trace wavelength shifts caused by pressure changes at temperatures exceeding 350°C, with the potential of operating at temperatures over 1,500°C [2]. High temperature piezoresistive pressure sensors in silicon carbide [3], and more recently even in Si [4], are capable of operating at 600°C; sensors operating at 800°C using sapphire membranes have also been developed [5].

Microdischarges are miniature plasmas created in gases between electrodes and are used for on-chip chemical sensing and other applications. Devices utilizing microdischarges are well suited for high temperature operation as the electrons have thermal energies exceeding 6.1 eV (70,787 K), and are not adversely affected by a high or low temperature ambient [6].

Microdischarge-based pressure sensors can be conceivably operated by measuring the change in spatial current distribution of microdischarges with pressure. As gas pressure increases, the mean free path of ionized molecules reduces and consequently, their spatial confinement changes. To measure the current distribution and microdischarge confinement, the microdischarges are created between a single anode and multiple cathode electrodes as shown in Fig. 1. The fractional current flowing through each cathode can be measured. At low pressures current favors the farthest cathodes while at high pressures, the opposite occurs. A repeatable relationship between current distribution and pressure allows such devices to be used as pressure sensors. A planar thin-film version of the microdischarge-based pressure sensor was first reported in [7], and operated at temperatures up to 200°C.

Microdischarge-based sensors are fundamentally different than ion gauges, which are not effective at atmospheric pressure because the small mean free path of the ions makes thermionic emissions difficult to detect [8].

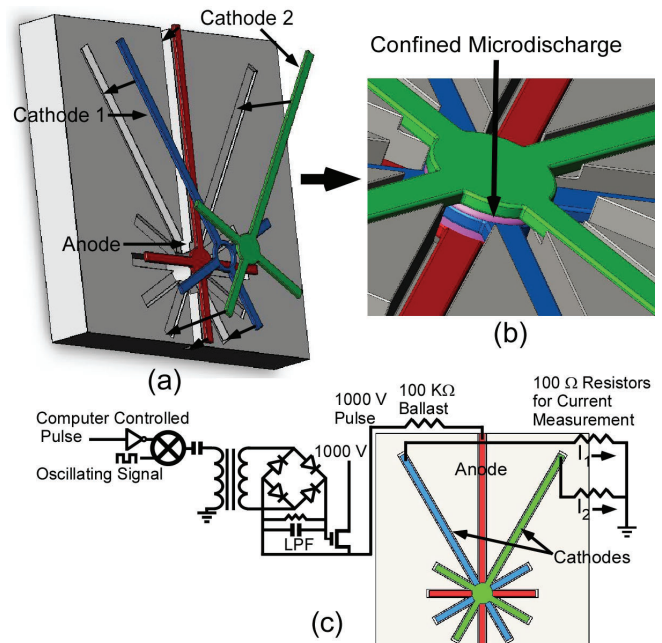


**Fig. 1:** Schematic of (a) electrodes above quartz chip illustrating placement, (b) microdischarge chamber during operation, and (c) isolation and readout circuitry.

This paper describes a new microdischarge-based microscale pressure sensor geometry that uses bulk foils in a multi-cathode stack in a quartz substrate. In this effort, we explore the use of multiple cathodes. In fact, multiple anodes may also be used. However, anode current shows excessive pressure dependence because of the high mobility of electrons that dominate it [9]. For this reason, measuring anode current results in pressure sensors with relatively small dynamic ranges.

## DEVICE DESIGN AND OPERATION

The pressure sensor structure consists of several electrodes suspended over a cavity in a quartz chip. Each electrode has a single lead for electrical contact and between one and three additional supports, which maintain the suspended position of the electrode. A microdischarge chamber exists in the center of the chip, in a chip through-hole as shown in Fig. 1b. This chamber is formed by the sandwich of circular electrodes, in which microdischarges are created. A single disk-shaped anode electrode serves as the bottom of the chamber while the center electrodes are torus-shaped, allowing the discharges to exist between the bottom anode and all other electrodes. The top cathode is disk-shaped as well, confining the discharges.

To reduce power consumption and parasitic heating in the pressure sensors, pulsed DC microdischarges are used. At lower pressures ( $\approx <100$  Torr), a steady state DC current can be measured in the discharges, but as the pressure increases, thermal instabilities can occur which make DC measurements difficult. These plasma variations can be further influenced by electrode wear, re-

\* 1301 Beal Ave., Ann Arbor, MI 48109, USA; Tel: (734) 763-6132, E-mail: scottwri@umich.edu

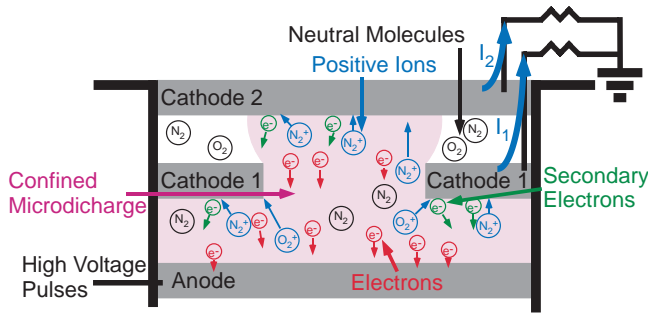


**Fig. 2:** Theoretical diagram of a microdischarge between a single anode and multiple cathodes in a microdischarge chamber. Changes in the ion distribution vary the currents in the cathodes.

deposition, and other factors. In our work, these issues are circumvented by using relatively short, pulsed DC microdischarges. A computer controlled, single ended, transformer coupled, gate drive circuit creates the pulses and is shown in Fig. 1c. A current limiting 100-k $\Omega$  ballast resistor is used, and 100- $\Omega$  resistors are used in series with each cathode to measure current.

Figure 2 shows electron movement, ion movement, and current distribution in the microdischarges. The electrons are drawn towards the positive anode, creating positive ions from neutral molecules in the process which are drawn to the two separate cathodes. Based on the pressure, the fraction of the total ions reaching each cathode varies, which varies  $I_1$  and  $I_2$ . Upon cathode impact, the energetic ions eject high energy secondary electrons from the cathodes, which sustain the DC microdischarges by ionizing additional neutral molecules and continuing the breakdown process. The current in each cathode is composed of the ions impacting the cathode and the secondary electrons leaving the cathode. While electrons carry most of the current in the plasma itself, they cannot reach the cathodes because of surrounding sheaths that are positively charged.

When designing the sensors, the spacing between the anode and the multiple cathodes is determined through theoretical calculations to allow for high sensitivity or a large dynamic range. The breakdown voltage between the anode and each cathode is a function of pressure ( $p$ ), spacing ( $d$ ), and density ( $\rho$ ) which is dependent on temperature and pressure. This breakdown voltage is used to estimate the threshold pressure, above which current deviates from a cathode further from the anode to one closer. The threshold pressure determines the dynamic range, as the sensors will not function effectively once current does not reach a cathode. The equation considering the dependence between breakdown voltage, pressure, spacing, and temperature is:

$$V_b = Bp \left( \frac{\rho}{\rho_0} \right) d \left[ \ln \left[ \frac{Ap \left( \frac{\rho}{\rho_0} \right) d}{\ln(1/\gamma)} \right] \right]^{-1} \quad (1)$$

where in air the constant  $A = 15\text{cm}^{-1}\text{Torr}^{-1}$ ,  $B = 365\text{Vcm}^{-1}\text{Torr}^{-1}$ , and the secondary emission coefficient  $\gamma = 0.025$  for  $\text{N}_2^+$  [10].

When designing the sensors to operate with a set operating voltage over pressure and temperature ranges of interest, the necessary electrode spacing can be calculated. Conversely for a set operating voltage and electrode spacing, the threshold pressure for cathode dominance, and dynamic range, can be found at different temperatures as illustrated in Table 1. As shown in the table, the dynamic range of the sensors increases with increasing

**Table 1:** Threshold pressure above which current deviates to closer cathodes for different anode/cathode spacing at various temperatures with 1000 V applied.

Cathode (Minimum spacing from anode)	Estimated Pressure for Cathode Dominance (Torr)			
	23°C	500°C	800°C	1000°C
1 (225 $\mu\text{m}$ )	454	1185	1645	1951
2 (300 $\mu\text{m}$ )	340	889	1233	1463
3 (400 $\mu\text{m}$ )	255	666	925	1098

temperature. This is because for a single cathode location, the threshold pressure increases with increasing temperature. However, the actual threshold pressures may differ from the predicted threshold pressures due to secondary electron emissions from the other cathodes, which continue to ionize surrounding gases. When operating within a sensor's dynamic range, changes in pressure will cause gradual fractional changes in current distribution between cathodes due to gradual changes in the mean free path, which affect the percentage of ions reaching each cathode.

The sensitivity and dynamic ranges are tuned by adjusting the number of electrodes, electrode thicknesses, inter-electrode spacing, and electrode diameter based on equation 1. A typical Three Cathode design with electrodes 50  $\mu\text{m}$  thick, 3 mm in diameter, and spaced 100  $\mu\text{m}$  apart is shown in Fig. 3a. These sensors have active areas of 7  $\text{mm}^2$  and are fabricated on 4  $\text{cm}^2$  chips. A typical Two Cathode design with electrodes 125  $\mu\text{m}$  thick, 1-2 mm in diameter, and spaced 50-100  $\mu\text{m}$  apart is shown in Fig. 3b. These sensors have active areas of 0.8-3  $\text{mm}^2$  and are fabricated on 1  $\text{cm}^2$  chips. The Two Cathode design has electrode supports as well as electrical leads, to ensure horizontal orientation. The sensors are designed to function with an applied voltage of 1000 V, but altering the voltage results in different sensitivities.

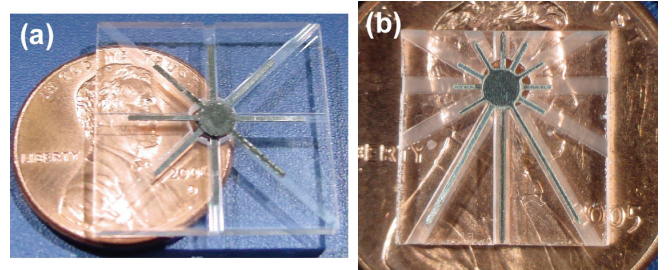


**Fig. 3:** Pressure sensors with (a) three cathodes and (b) two cathodes on pennies.

## FABRICATION

A fabrication method that accommodates the expansion mismatch between electrodes and substrate is used (Fig. 4). The electrodes are lithographically patterned and etched from stainless steel, using chemical spray etching. Stainless steel is used for its robustness and oxidation resistance at high temperatures. Trenches of specified depths and a through-hole in the center are cut into a quartz chip. Both mechanical and wet-etch processes can be used for this purpose. The electrodes are assembled into the trenches, and the circular electrodes are placed in the through-hole. The different depths between the various trenches specify the discharge gap spacing, as the electrodes lie flush with the bottom of the trenches. Ceramic epoxy holds the electrode lead and support arms in place, without adhering to the stainless steel. This allows the leads and supports to expand separately from the quartz chip

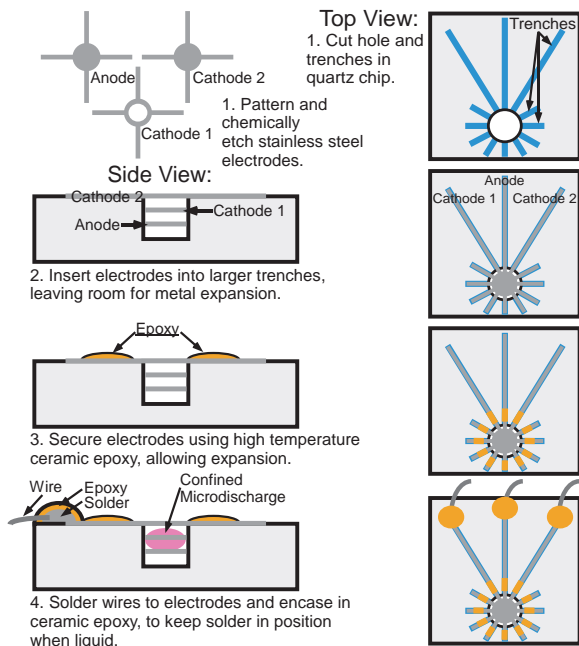


**Fig. 4:** Top and side view of a Two Cathode fabrication process.

and the ceramic epoxy without buckling. High temperature wires are soldered to the electrodes and the solder is encased in ceramic. This ceramic keeps the solder in position so it maintains electrical contact, even when the solder is liquefied at high temperatures.

## RESULTS AND DISCUSSION

Individual pressure sensors were fabricated, operated, and characterized at temperatures between 23°C and 1000°C, measuring pressures between 10 Torr and 760 Torr. Sensors were operated for over 10 hours at various temperatures to demonstrate durability. Pulses 1 ms in duration were applied at a rate of 40 Hz to the sensors with voltages between 700 V and 1000 V. The pulses consumed between 168 μJ and 400 μJ each. The sensors were tested in a temperature controlled vacuum chamber.

Pressure was determined by measuring the percentage of total current in each cathode and calculating the differential current output between two cathodes. Figures 5 and 6 illustrate this, as

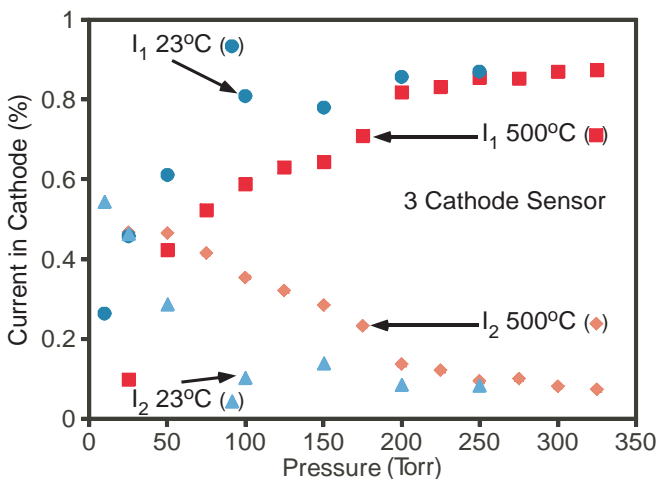


**Fig. 5:** Current distribution in a Three Cathode sensor. The sensor has electrodes 50 μm thick, 3 mm in diameter, and spaced 100 μm apart. Each data point is the average of 100 measurements.

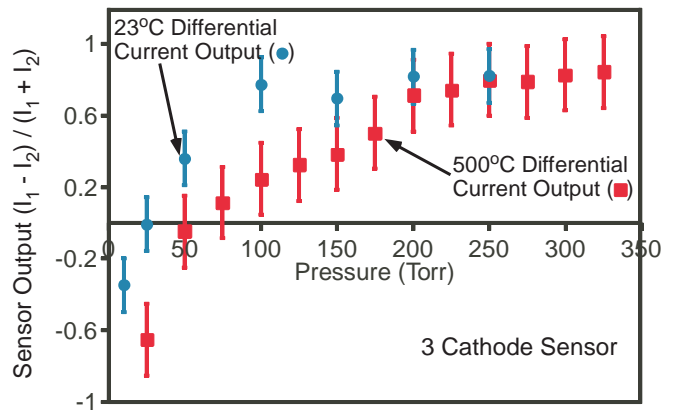


**Fig. 6:** Differential current output used to determine pressure from the current distribution in Fig. 5 at 23°C and 500°C.

Fig. 5 presents the percentage of total current in two cathodes in a typical Three Cathode sensor at 23°C and 500°C. (The third cathode only functioned to stabilize the microdischarges.) Figure 6 presents the differential current output calculated from the data in Fig. 5, used to determine the pressure. This sensor demonstrated relatively high sensitivities of 4,875 ppm/Torr and 4,979 ppm/Torr at 23°C and 500°C respectively, between 10 Torr and 300 Torr. It

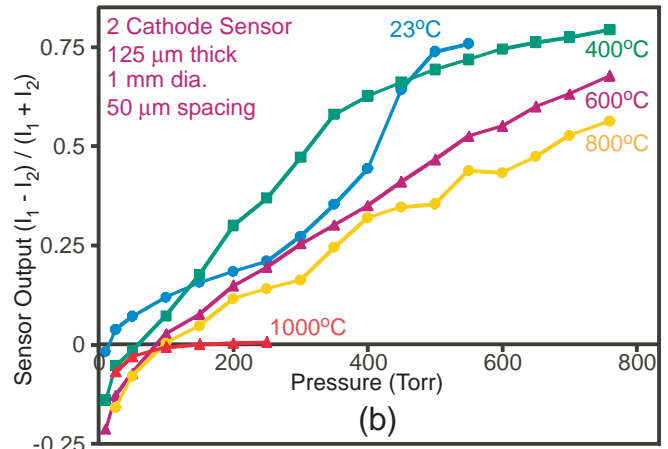
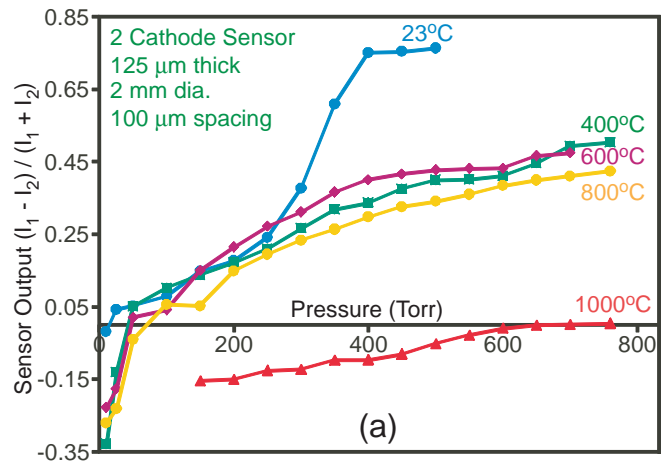


**Fig. 7:** Sensor output as a function of pressure in sensors with two cathodes and 125 μm thick electrodes. (a) Output from a sensor with (a) 2 mm diameter electrodes spaced 100 μm apart and (b) 1 mm diameter electrodes spaced 50 μm apart. Each data point is the average of 100 measurements.

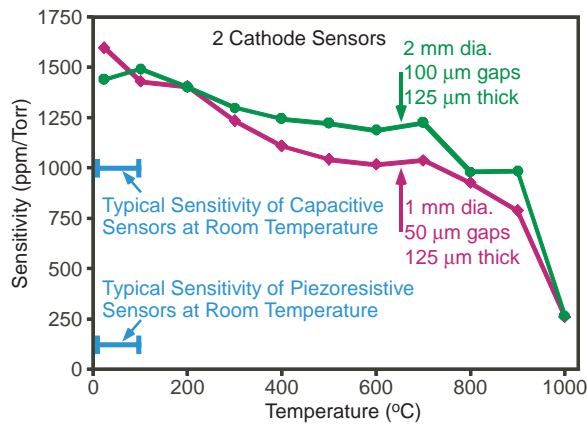


**Fig. 8:** The average sensitivities of the sensors in Fig. 7 as a function of temperature.

also had very little temperature dependence as shown by the 104 ppm/Torr sensitivity difference between 23°C and 500°C.

The Two Cathode sensors were operated between 23°C and 1000°C over the pressure range of 10-760 Torr. Figure 7 illustrates the differential current output used to determine pressure from two different, typical Two Cathode sensor designs. The first (Fig. 7a) is from a sensor with electrodes 125 μm thick, 2 mm in diameter, and spaced 100 μm apart while the second (Fig. 7b) is from a sensor with electrodes 125 μm thick, 1 mm in diameter, and spaced 50 μm apart. The average sensitivities of these two sensors are shown in Fig. 8 as a function of temperature. The sensitivities decreased with pressure, potentially as a result of the gas rarefaction, which occurred with increasing temperature. These sensors had smaller sensitivities but larger dynamic ranges than the previously described sensors (Figs. 5, 6) as shown by comparing the sensitivities in Figs. 6 and 8.

Sensitivity, dynamic range, and the temperature coefficient of sensitivity are metrics which are used to compare microdischarge-based pressure sensor designs to one another and to other pressure sensors. The performance of four different sensor designs (data from one is not presented in this paper) are shown in Table 2 with the highest performance in each category. The data in the table represents typical operation of each sensor design. For comparison, typical piezoresistive and capacitive pressure sensors have sensitivities of 100 ppm/Torr and 1,000 ppm/Torr respectively, and temperature coefficients of sensitivity of  $\pm 1,000$  ppm/K to  $\pm 5,000$  ppm/K [11, 12].

## CONCLUSIONS

Microdischarge-based pressure sensors have been developed and demonstrate an ability to operate from room temperature to 1000°C over the pressure range of 10-760 Torr. These sensors can also potentially operate at temperatures below room temperature and over larger pressure ranges. The sensors currently occupy active areas as small as 0.8 mm<sup>2</sup> on chips 1 cm<sup>2</sup>. They demonstrate sensitivities as high as 5,000 ppm/Torr and temperature coefficients of sensitivity as low as 44 ppm/K. A new fabrication method is used which allows for expansion and contraction of electrodes with temperature variations, and may be of use in future high temperature microscale devices.

## ACKNOWLEDGMENTS

The authors are grateful for the fabrication assistance received from Mr. M. Richardson. This work was supported primarily by

**Table 2:** Performance summary of four different sensor designs.

Sensor Parameters	Max Sensitivity (ppm/Torr)	Dynamic Range (Torr)	Temperature Coefficient of Sensitivity (ppm/K)
2 cathodes 2mm dia. 100μm gaps	1,500	<b>750</b>	-857
2 cathodes 1mm dia. 50μm gaps	1,500	<b>750</b>	-912
2 cathodes 1mm dia. 100μm gaps	2,000	<b>750</b>	-1043
3 cathodes 3mm dia. 100μm gaps	<b>5,000</b>	300	<b>44</b>

the Engineering Research Center Program of the National Science Foundation under Award No. EEC-9986866. Y. Gianchandani acknowledges support through the IR/D program while working at the National Science Foundation. The findings do not necessarily reflect the views of the NSF.

## REFERENCES

- [1] R. Fielder, K. Stingson-Bagby, M. Palmer, "State of the art in high-temperature fiber optic sensors," *SPIE*, 5589(1), pp. 60-69, 2004.
- [2] T. Li, Z. Wang, Q. Wang, X. Wei, B. Xu, W. Hao, F. Meng, S. Dong, "High pressure and temperature sensing for the downhole applications," *SPIE*, 6757(1), pp. 1-7, 2007.
- [3] A. Ned, R. Okojie, A. Kurtz, "6H-SiC pressure sensor operation at 600°C," *HITEC*, Albuquerque, NM, pp. 257-260, 1998.
- [4] S. Guo, H. Eriksen, K. Childress, A. Fink, M. Hoffman, "High temperature high accuracy piezoresistive pressure sensor based on smart-cut SOI," *MEMS*, Tucson, AR, pp. 892-895, 2008.
- [5] S. Fricke, A. Friedberg, T. Ziemann, E. Rose, G. Muller, D. Telitschkin, S. Ziegenhagen, H. Seidel, U. Schmidt, "High temperature (800°C) MEMS pressure sensor development including reusable packaging for rocket engine applications," *MNT for Aerospace Applications, CANEUS*, pp. 5p, 2006.
- [6] M. Kushner, "Modeling of microdischarge devices: Plasma and gas dynamics," *J. Phys. D: App. Phys.*, 38(11), pp. 1633-1643, 2005.
- [7] S. Wright, Y. Gianchandani, "A harsh environment, multi-plasma microsystem with pressure sensor, gas purifier, and chemical detector," *MEMS*, Kobe, Japan, pp. 754-757, 2007.
- [8] C. Edelmann, "Measurement of high pressures in the vacuum range with the help of hot filament ionization gauges," *Vacuum*, 41(7-9), pp. 2006-2008, 1990.
- [9] C. Wilson, Y. Gianchandani, R. Arslanbekov, V. Kolobov, A. Wendt, "Profiling and modeling of dc nitrogen microplasmas," *J. Appl. Phys.*, 94(5), pp. 2845-2851, 2003.
- [10] J. Cobine, *Gaseous Conductors Theory and Engineering Applications*, New York, Dover Publications, 1958.
- [11] Y. Zhang, K. Wise, "Performance of nonplanar silicon diaphragms under large deflections," *J. Microelectromech. Sys.*, 3(2) pp. 59-68, 1994.
- [12] M. Gad-el-Hak, *The MEMS Handbook, Second Edition*, Boca Raton, FL, CRC Press, 2006.

# RADIOISOTOPE-POWERED IMPULSE RADIO FREQUENCY SENSOR NODE

S. Tin, R. Duggirala, A. Lal, and C. Pollock

SonicMEMS Laboratory, School of Electrical and Computer Engineering, Cornell University  
Ithaca, NY, USA

## ABSTRACT

We demonstrate a radioactive thin-film powered wireless sensor node which can transmit an RF signal coded with the environmental information gathered by a passive capacitive sensor. Sensor nodes operate for several decades and transmit data over RF links at powers of 100-1000 milliWatts. In our active sensor node, radioisotope energy emitted in electrons from  $^{63}\text{Ni}$  thin films is used to electrostatically charge a cantilever over several minutes, and the stored electrical energy is released over a nano-second time scale, achieving a collected-to-released power amplification of  $10^9$  (10 mins/10ns). Even when the radioisotope emitted power is nanowatts from a benign amount of  $^{63}\text{Ni}$ , over 500mW of transmitted RF power has been remotely detected. Since the half life of  $^{63}\text{Ni}$  is 100 years, this RF transmitter can work autonomously for several decades. In our prototype wireless sensor node, a humidity sensitive polymer capacitance is used to demonstrate sensor node functionality. A transmitted frequency shift of 4.27 MHz over 150 MHz is achieved when the humidity changes from 22% to 97%.

## INTRODUCTION

A critical requirement for the success of autonomous remote systems is the realization of miniature power sources with long lifetimes, especially for sensor networks working in harsh, inaccessible environments. While traditional power sources can only work up to several years without replacement or refueling, radioactive isotope power sources can work for 100 years with their performance mostly unaffected by environment. This is possible due to the high energy density ( $\sim 10^5 \text{kJ/m}^3$ ) and long half-life (100.2 years) of the  $^{63}\text{Ni}$  radioisotope fuel used in the device. Nickel-63 emits  $\beta$ -particles with an average energy  $E_{avg}=17.3\text{keV}$  and a maximum penetration depth  $<10\mu\text{m}$  in solids. As a result, devices powered by  $^{63}\text{Ni}$  thin-films can be deployed safely with microscale shielding.

The power requirements for a typical low-power wireless sensor node are shown in Figure 1. Power requirements are 1-10 nW for retaining memory state, 0.1-1 mW for periodic sensing and processing, and 1-100 mW for periodic wireless communication

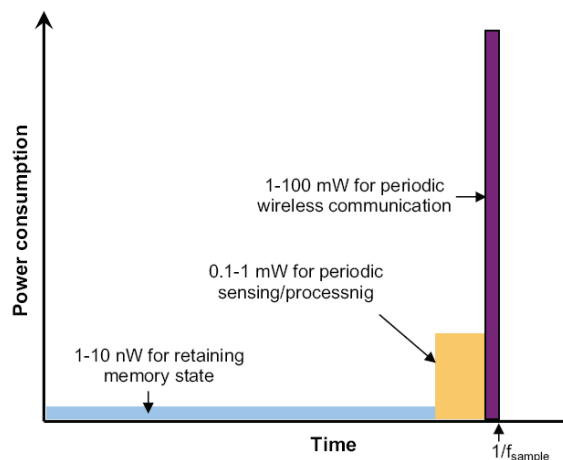


Figure 1: Schematic illustrating the power requirements of typical periodically sampling low power wireless sensor microsystems [1].

communication. The power to retain memory state can be provided by betavoltaics as reported in [2] even with the low activity radioactive thin films presented here. Furthermore, MEMS radioisotope-powered piezoelectric power generator [3] can generate output power needed for periodic sensing and processing. In this paper, we focus on the radioactive RF power generation that can be used as a CMOS compatible wireless beacon and communications. A sensing network can thus be powered entirely with thin films of low activity radioisotope.

Nickel-63 radioisotope actuated reciprocating piezoelectric [3] and piezoelectric unimorph cantilevers [4] have been previously reported to generate RF pulses upon radioisotope discharge. These were limited to pulses generated from dielectric waveguides integral to the self-reciprocating cantilever. In this paper, the cantilever is a simple micromachined gold cantilever limiting its function only for charge collection and release (Figure 2).  $^{63}\text{Ni}$  isotope source have been used to bias sensors [5] and generate RF signal [6]. In this paper we demonstrate a fully self-powered sensor node with hundreds of milliwatts of RF transmitter power output. An RF equivalent circuit model of the self-reciprocating cantilever system has been developed that agrees with the experimentally observed frequency output versus sensor capacitance.

## PRINCIPLE OF OPERATION

As illustrated in Figure 2, a gold cantilever is placed about  $500\mu\text{m}$  above a  $^{63}\text{Ni}$  radioactive thin film with 1.5 mCi activity. Positive charges are accumulated on an electrically isolated  $^{63}\text{Ni}$  thin film due to the continuous emission of  $\beta$ -particles (electrons), which are collected on the gold cantilever. The accumulated charge increases with time, increasing the electrostatic force which eventually pulls the cantilever into the radioisotope thin-film. When the gap between the cantilever and radioactive source is small enough, arc discharge through the gap occurs. As the electrostatic force is eliminated, the beam oscillates, and the process repeats itself.

When the gap between the cantilever and radioactive source is  $500\mu\text{m}$ , the pull-down cycle requires 3 minutes. As the cantilever approaches the source, tunneling and direct conduction-based current results in a pulse that is very short in time ( $<1\text{ns}$ ). The energy integrated over the reciprocation period is released in a very

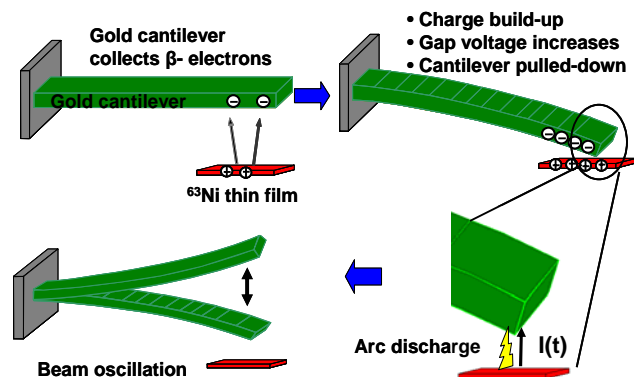


Figure 2: The beta-radioisotope actuated reciprocation of gold cantilever

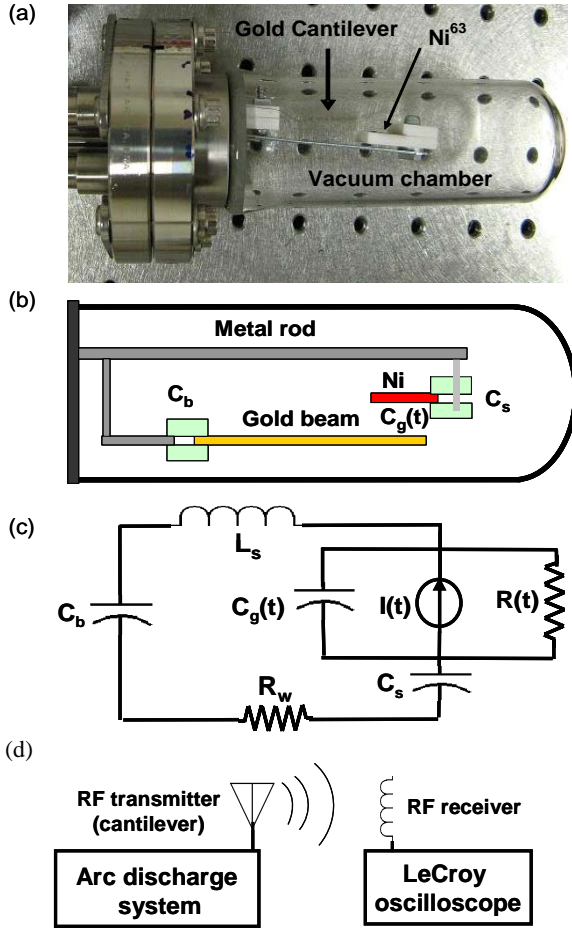


Figure 3. (a) Photograph, (b) schematic, and (c) equivalent LC circuit of the self-powered wireless discharge system; (d) schematic of wireless detection system

short time allowing us to greatly amplify the power from the radioactive source. The discharge current pulse passes through the RF circuit formed by the device exciting its impulse response.

As shown in Figure 3(a), a gold cantilever ( $5\text{cm} \times 0.8\text{cm} \times 300\mu\text{m}$ ) and  $^{63}\text{Ni}$  source discharging system is

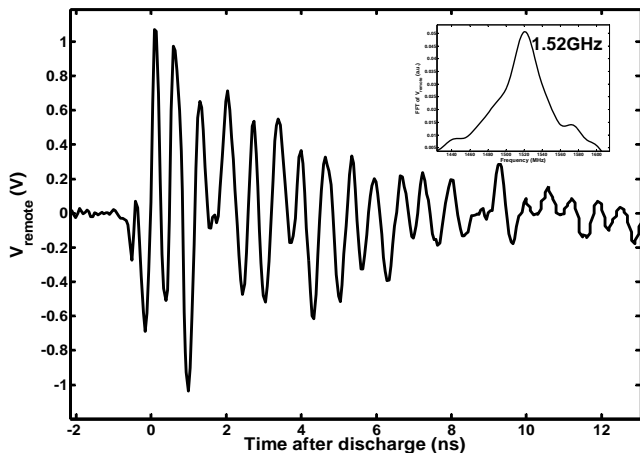


Figure 4. Magnitude and frequency of the remotely detected RF signal of the arc discharge system

Table 1: Representation and measured values of  $R$ ,  $L$ ,  $C$  components in circuit model in Figure 3(c)

Component	Representation	Value
$C_s$	Source holder capacitance	8.3pF
$C_b$	Beam holder capacitance	8.3pF
$R_w$	Resistance of metal beams and rod	0.1 ohm
$L_s$	Equivalent inductance of the arc discharge system	2.4nH
$C_g(t)$	Air gap capacitance	Time dependent
$I(t)$	Air gap current	Discharge pulse
$R(t)$	Equivalent resistance across the air gap	Arc resistance

housed inside a small glass vacuum chamber that is evacuated and sealed. Connected to a vacuum pump, the chamber is pumped down to  $10^{-3}$  mTorr. Both the gold cantilever and the  $^{63}\text{Ni}$  source are held in place with quarter-inch thick Teflon plates, which forms a capacitor  $C_b$  at the beam holder, and a capacitor  $C_s$  at the radioactive source holder (Figure 3(b)).  $C_g(t)$  is the air-gap capacitance at any given time  $t$ . An RF receiver (air-core coils with 21 turns and 1.5cm inner diameter) is connected to a high bandwidth oscilloscope (LeCroy WaveMast 8500) placed outside the chamber to detect and record the RF signal (Figure 3(d)). RF signal with frequency of 1.52GHz, which lasts for around 10ns, is remotely detected upon cantilever discharge (Figure 4.)

An LC circuit model is developed for the wireless RF discharge system (Figure 3(c)) with the measured values of the components list in Table 1. When an arc discharge occurs across the air gap, a sub-nanosecond high power current pulse is released which generates oscillations in the RLC circuit at hundreds of megahertz for hundreds of nanoseconds. After the discharge, the cantilever is effectively at rest because of mechanical inertia. Then the gap between the cantilever and the source is very small, which means the value of  $C_g$  is very large at that moment compared to other capacitors in the circuit.

To verify the circuit model, the circuit in Figure 3(c) is simulated in SPICE with the capacitance across the discharge air

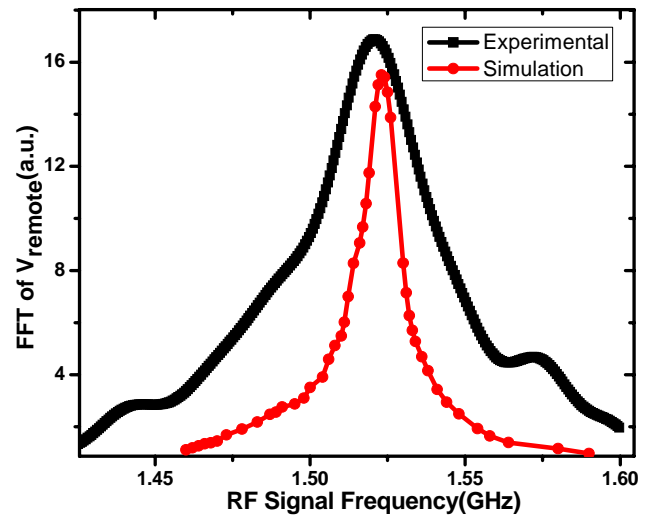


Figure 5. Resonance response of the arc discharge system from SPICE simulation and experimental measurement.

gap,  $C_g$  is estimated to be 100pF with contact area of  $100 \mu\text{m}^2$ . Capacitance  $C_g \gg C_s$  and acts as a short compared to other impedances in the circuit.  $R(t)$  is relatively large and is ignored in this simulation, as it is shorted out by  $C_g$  at the time scales involved. The values of other capacitors and inductors used in the simulation are listed in Table 1. The cantilever reciprocation period is 3 minutes with 0.64cm of the cantilever area exposed to the radiation. Therefore, with 9pA (1.5mCi) electron current, the totally charge across the air gap at the time of arc discharge is 1nC. Assuming the discharge lasts 1ns, the average discharge current will be 1A. A pulse current of 1A with rising and falling time of 0.1 ns (time estimated from experimental values) and duration time of 1ns are chosen to excite the LC circuit in the simulation (resonance frequency of the circuit is independence of pulse magnitude and duration). The simulated resonance frequency of the LC circuit is plotted in Figure 5, together with the frequency of remotely measured RF signal from device shown in 3(a). The simulation result agrees with the experimental result, both of which are around 1.52 GHz.

### EXPERIMENTAL SETUPS AND RESULTS

The high power pulses from the arc discharge system can be utilized to generate wireless RF signals detectable over long distances. As shown in Figure 1, wireless communication is the most power consuming process in the sensor network. Equipped with a self-powered RF signal source, one needs to modulate the RF output with the sensing signal. In the system shown in Figure 3(a), all the parameters inside the glass chamber have fixed values. The RF frequency can only be modulated with components outside the chamber. As shown in Figure 6(a), external capacitor is connected to the arc discharge system. In the equivalent circuit (Figure 6(b)), the circuit inside the dotted box is the arc discharge system, while  $C_{sc}$  is the external

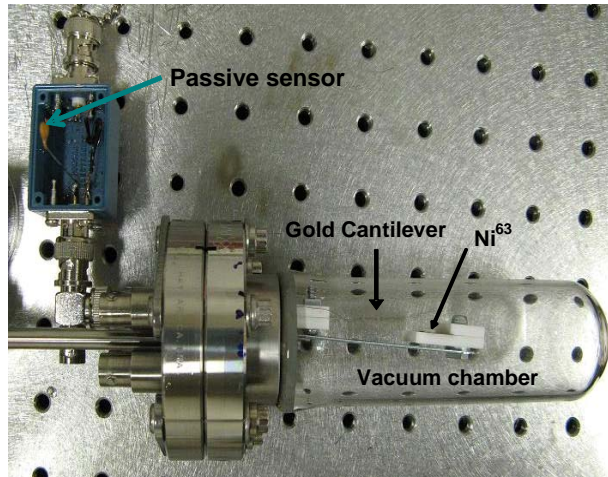


Figure 6. (a) Photograph, (b) equivalent LC circuit of the self-powered wireless discharge system with external capacitance

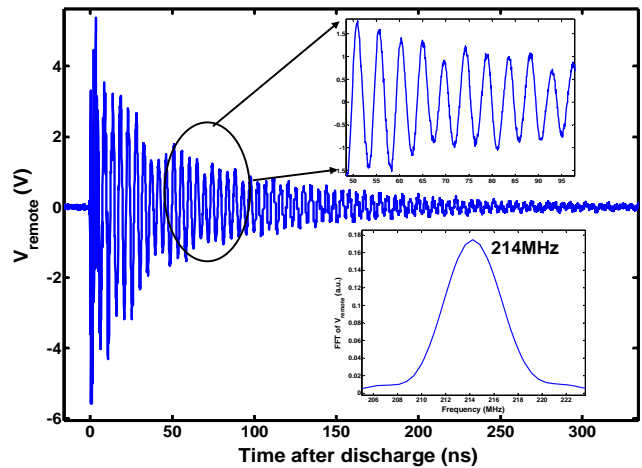


Figure 7. Magnitude and frequency of the remotely detected RF signal with 20pF external capacitance wireless RF sensor node

capacitance.  $L_w$ , and  $R_e$ , the inductance and resistance introduced by wire connections to the external capacitor, are measured to be 61nH and 0.8 Ohm respectively using LCR meter (HP 4275A). To check the impact of the external capacitor, a 20pF capacitor is connected to 1.52GHz signal still exist for the first 10ns, an additional 214MHz the system, while the RF signal is measured remotely. While the RF signal is remotely detected upon cantilever discharge (Figure 7.) The RF signal lasts for more than 300 ns with a maximum of 500mW detected 20 cm away from the chamber via the RF receiver. The SPICE simulation result of the new LC circuit (Figure 6(b)) with 20pF external capacitor agrees with the experimental measurement (Figure 8.)

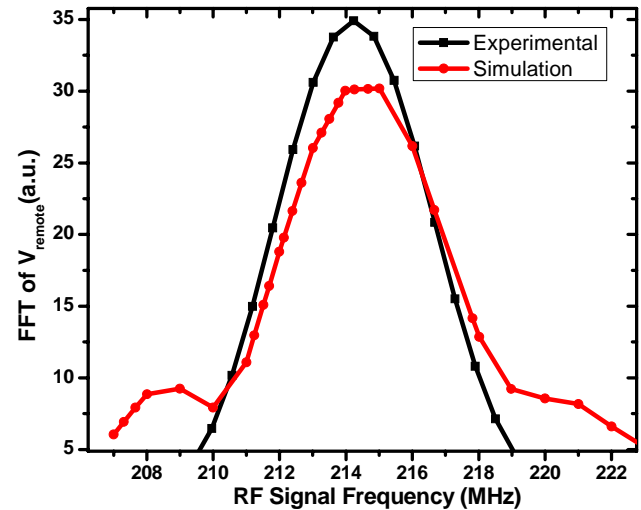


Figure 8. Resonance response of system with 20pF external capacitor from SPICE simulation and experimental measurement.

External capacitors with different values are then used to examine their impact on the frequency of the RF signal. The output RF signals are remotely detected with receiver and analyzed. The frequency of the RF signal is plotted versus the external capacitance in Figure 9. The frequency decreases with increasing external capacitance. When the capacitance increases from 12pF to 75pF, a frequency shift of 63 MHz is achieved (239MHz to 176MHz). The result of the SPICE simulation of LC circuit model matches the measurement results. Therefore, with the circuit model, the value of the external capacitor can be extracted from the

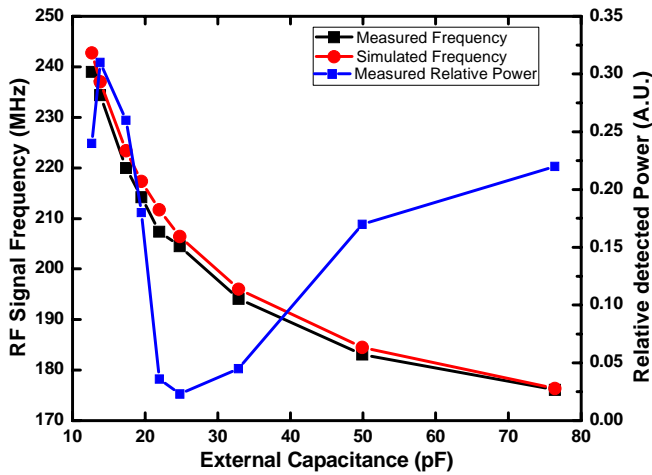


Figure 9. Experimental and simulated RF signal frequency with different external capacitance.

frequency of the remotely detected RF signal. The relative power of detected RF signals with different external capacitor values is also plotted in Figure 9. With cantilever reciprocation period almost stays the same, the transmitted RF signal power is consistent for all external capacitance values. However, the RF receiver has different gains at different frequencies, which causes the variation in detected RF signal power.

To implement a completely self-powered wireless sensor node, a capacitive polymer humidity sensor (Figure 10) is connected to the discharge system. The capacitance of the sensor at different humidity levels are first characterized (Figure 10). The different levels of relative humidity are generated by exposing the humidity sensor to different saturated salt solutions (with known relative humidity values) in a closed chamber. The capacitance of the sensor increases with the relative humidity. The RF signal is remotely measured at different humidity levels. The frequency of the signal is analyzed and plotted in Figure 11. A frequency shift of 4.27 MHz is achieved when the humidity changes from 22% to 97% (Figure 11). The experiment results match SPICE simulation outputs when the capacitance values of the humidity sensor are used in the LC circuit model in Figure 6(b).

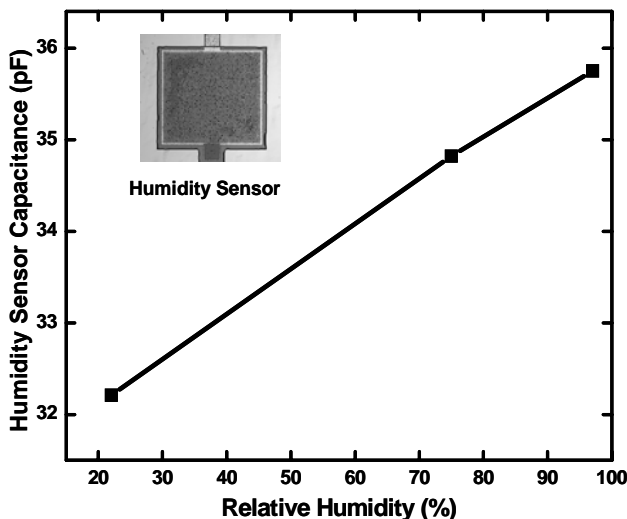


Figure 10. Measured humidity sensor capacitance at different relative humidity levels.

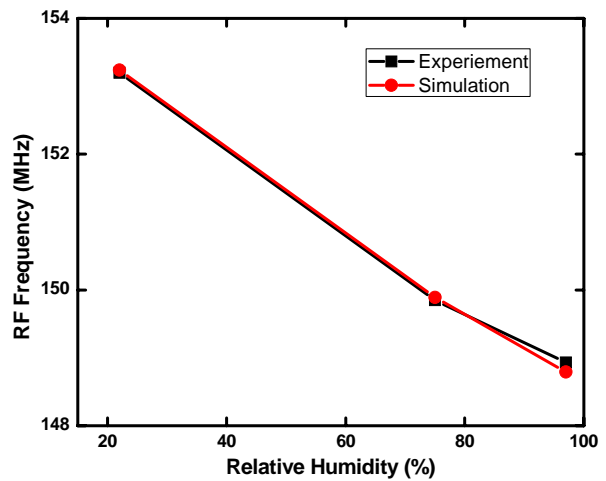


Figure 11. Measured remotely detected RF signal frequency at different relative humidity levels.

## CONCLUSIONS

In this paper, we demonstrated a completely self-powered wireless sensor node which can transmit an RF signal coded with the environmental information gathered by a passive capacitive sensor. Sensor nodes that can operate for several decades and transmit data over RF-links at power of 100-1000 milliWatts without environmental energy harvesting can potentially revolutionize reliable long-term monitoring, such as water content in building foundations or detection of leached chemicals in chemical processing plants. These sensors need to be buried deep into structural constructs such as steel and concrete, where changing batteries or harvesting vibration or EM energy is not a reliable option. In the near future, efforts in developing microscale vacuum packages will be undertaken to reduce volume. Furthermore, transmission line equivalent models are also being developed to engineer desired frequency output from the all-self-powered RF sensor node.

## ACKNOWLEDGEMENT

This work was supported by DARPA-MTO, and contracted under the U. S. SPAWAR R7D center.

## REFERENCES

- [1] S. Roundy, D. Steingart, L. Frechette, P. Wright, and J. Rabaey, "Power Sources for Wireless Sensor Networks," Berlin, Germany, 2004, pp. 1-17
- [2] R. Duggirala, S. Tin, and A. Lal, "3D Silicon Betavoltaics Microfabricated using a Self-Aligned Process for 5 Milliwatt/CC Average, 5 Year Lifetime Microbatteries," Transducers 2007, Lyon, France, Jun. 2007, pp 279-282
- [3] H. Li, A. Lal, J. Blanchard, and D. Henderson, "Self reciprocating Radioisotope powered Cantilever," Transducers, 2001, Munich, pp. 744-747
- [4] R. Duggirala., A. Polcawich, E. Zakar, M. Dubey, and A. Lal, "MEMS Radioisotope-powered Piezoelectric Power Generator," MEMS 2006, Istanbul, Jan. 2006, pp.94-97.
- [5] R. Duggirala, M. Kranz, C. Pollock, and A. Lal, "Self-powered Humidity Sensor powered by Nickel-63 Radioisotope," 2006 Solid State Sensor and Actuator Workshop, Hilton Head Island, June 2007.
- [6] S. Tin, R. Duggirala, R. Polcawich, M. Dubey, and A. Lal, "Self-powered Discharge-based Wireless Transmitter", MEMS 2008, Tucson, Jan. 2006, pp. 988 - 991

# VERTICALLY ALIGNED SILICON NANOWIRE ACTUATORS AND SWITCHES

L. Tsakalagos, K. Subramanian, X. Wang, M.F Aimi, C.F. Keimel, J.E. Balch, A.T. Byun, J.A. Fronheiser, J. Iannotti, L. Yan, T.P. Feist, J.B. Fortin

General Electric – Global Research Center, Niskayuna, New York, USA

## ABSTRACT

We report the development of novel, vertically aligned silicon nanowire electrostatic switches targeting 1V operation and 1 nanosecond switching times for future computing applications. Analytical and finite element models show that it is possible to obtain 1V operation and nanosecond switching. The source, gate, and drain electrodes of the nanoswitch are fabricated using standard MEMS processes. Silicon nanowires are subsequently grown by chemical vapor deposition. Electrostatic actuation of a Si nanowire in a two-terminal configuration was demonstrated *in situ* in a scanning electron microscope, and preliminary electrical tests showed repeated actuation of nanowires with an on-state resistance of ~342 M $\Omega$ .

## INTRODUCTION

As the push towards faster, more powerful electronics continues, scaling of metal oxide semiconductor field-effect transistors (MOSFETs) along Moore's Law leads to significant design challenges, including on state losses and leakage currents associated with an ever-thinning gate dielectric [1]. These lead to severe thermal management problems that must be overcome by novel approaches at the device and system level. Here we propose a small footprint, low power consumption, and mass producible nanoelectromechanical switch design that offers an innovative solution to the above-mentioned problems. Switches based on nanoelectromechanical systems (NEMS) in particular have unique properties such as a physical air gap between source and drain that have the potential to alleviate many of the power losses in solid-state switches. Furthermore, they may enable all mechanical computing or the ability to create computers without the need for any cooling by allowing the active devices to operate at high temperature.

Inorganic nanowires are of particular interest in high frequency mechanical switching applications owing to the fact that their relatively high elastic modulus and small dimensions provides a high resonant frequency (Table1). Indeed, the potential for nanowire/tube NEMS devices for GHz operation has been studied theoretically. Kinaret *et al.* [2] showed that horizontally-aligned carbon nanotube triode devices have the potential to switch in the nanosecond time regime. Jonsson *et al.* [3] also showed that such device could operate as GHz switches, though they also calculated that there is a non-linear resonant behavior at such frequencies.

Table 1. Calculated resonant frequency for a silicon and silicon carbide cantilever rod with various dimensions.

Resonator material	Dimensions (L (nm), r (nm))			
	1000,60	300,30	100,10	30,3
Silicon (E=108 GPa, $\rho$ =2.3 g/cm <sup>3</sup> )	110 MHz	636 MHz	1.9 GHz	6.36 GHz
Silicon Carbide (E=400 GPa, $\rho$ =3.2 g/cm <sup>3</sup> )	190 MHz	1 GHz	3.1 GHz	10 GHz

There have been few published experimental works on nanowire/tube switches. Ke and Espinosa [4,5] demonstrated a bistable NEMS device based on multi-walled carbon nanotubes by *in situ* SEM analysis, whereas Cruden and Cassell [6] demonstrated a vertically oriented carbon nanofiber-based device. We note that in

those works the nanostructures were actuated using external probes or structures, not by integrated microelectrodes. Blick and co-workers [7] fabricated silicon nano-pillar structures using top-down nanofabrication and demonstrated that field emission can be useful mechanism in identifying their resonant behavior. On the other hand, horizontally aligned carbon nanotube NEMS switches were demonstrated by Cha *et al.* [8], and in-plane silicon nanowire switches were shown by Li *et al.* [9].

Here we propose the use of integrated, vertically aligned silicon nanowire devices for switching applications. **Figure 1** shows a schematic of our device structure. The electrodes are fabricated using standard MEMS/microfabrication methods, whereas the nanowires are synthesized using bottoms-up catalytic growth processes. In this work we show that such devices structures have potential to act as high-speed switches, and demonstrate DC actuation of integrated two-terminal Si NW devices.

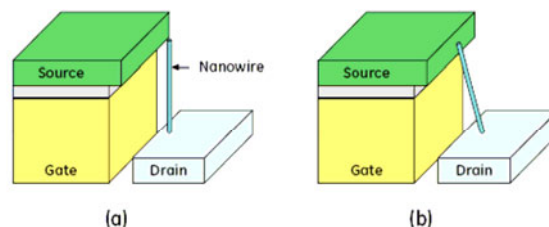


Figure 1: Schematic of the proposed electrostatically-actuated nanoelectromechanical switch consisting of gate, drain, and source electrodes and a nanowire actuator in (a) the open state and (b) closed state.

## EXPERIMENTAL PROCEDURE

### Device Fabrication

The nanoswitch fabrication process is shown in **Figure 2**. We are interested in both two and three-terminal devices. Two-terminal devices have only gate and drain terminals and were used to study the electrostatic actuator performance. The 2-terminal device fabrication process begins with a degenerately-doped Si <111> substrate. A 0.5-1  $\mu$ m silicon dioxide film is first grown on the substrate. Then a thin (100-300 nm) metal layer, typically titanium or chromium, is deposited on top of the oxide. This metal film both acts as a mask for reactive ion etching (RIE) of the oxide film, and as the top contact/gate electrode for the device. The metal film is wet etched to form the electrode structure. RIE is then used to etch the SiO<sub>2</sub> film down to the Si substrate. A 5-10nm thin Au catalyst film is shadow evaporated on the substrate for growth of the Si NWs.. Then the substrate is placed in a 5'' horizontal chemical vapor deposition (CVD) reactor (Tylan) capable of growth on 4'' wafers. Silicon nanowires are grown using the vapor-liquid-solid growth mechanism [10]. Typical growth times are 1-5 minutes. P-type doping in the nanowires has been confirmed in separate experiments [11,12].

### Testing & Characterization

Electrical testing was performed using a semiconductor parameter analyzer (HP 4154B) in both DC and pulsed modes. The

devices were characterized in a field emission scanning electron microscope (LEO 1530VP) equipped with an electrical feedthrough. *In situ* actuation of Si NWs in the SEM was performed by connecting probes through the electrical feedthroughs and connecting the devices to a DC power supply.

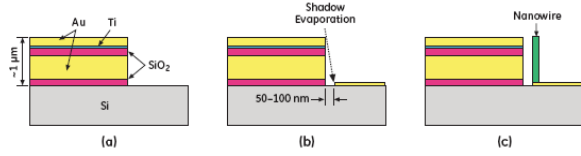


Figure 2: Schematic of nanoswitch fabrication process. (a) Conventional photolithography and liftoff methods are used to build a film stack comprising (top down) Au/Ti/SiO<sub>2</sub>/Au/SiO<sub>2</sub> layers (for 3 terminal switch) or Ti/SiO<sub>2</sub> layers (for 2 terminal switch); (b) Shadow evaporation produces a thin (5~10 nm) Au film as a catalyst for nanowire growth. (c) Vertically oriented nanowires are grown by CVD method.

## RESULTS AND DISCUSSION

### Device Performance Modeling

An analytical model was first used to establish the basic geometrical parameters required to fabricate NEMS switches that can operate in the GHz regime with low operating voltages. A silicon nanowire with circular cross section was assumed to have bulk elastic constants ( $E = 108$  GPa) and density ( $2330$  kg/m<sup>3</sup>). The first resonant mode ( $f_r$ ) was evaluated using the following equation:

$$f_r = \frac{3.52}{2\pi} \sqrt{\frac{EI}{\rho_{\text{length}} l^4}} \quad (1)$$

where  $I$  is the area moment of inertia ( $0.25 \cdot r^4$ ) and  $\rho_{\text{length}}$  is the density per unit length ( $\rho \cdot \pi \cdot r^2$ ). **Figure 3** shows a contour plot of the expected first resonant mode, from which it is evident that nanowires with diameters on the order of 20-80 nm in diameter and 200-1000 nm in length are required for such high-speed switching applications. The gap required to actuate a silicon nanowire was first evaluated analytically by assuming a uniform load applied to 4/5 of the nanowires (representing the gate, with the upper 1/5 representing the top contact). **Figure 3b** shows the pull in voltages for various wire and gap dimensions. It is found that for a nanowire with a resonance frequency of 250 MHz, a gap between the nanowire and the gate electrode on the order of 5-20 nm is required to achieve 1 V actuation.

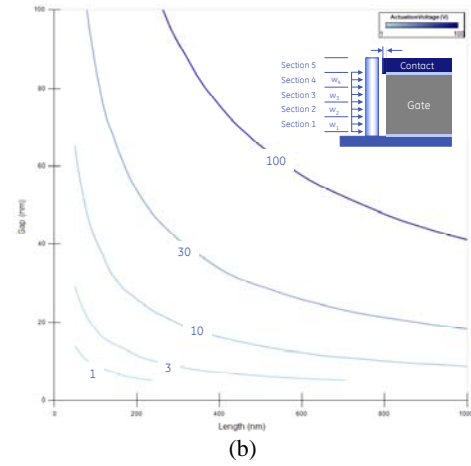
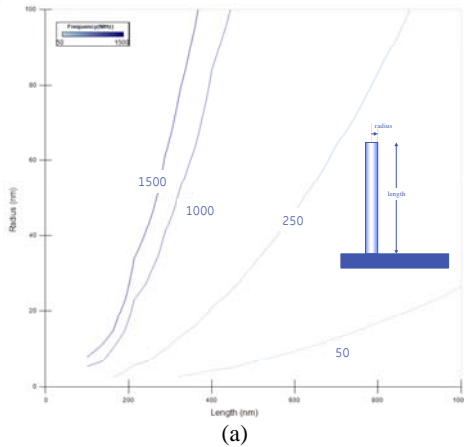


Figure 3: (a) Contour plot showing the impact of nanowire radius and length on the first order resonance frequency and (b) contour plot showing the nanowire-gate gap and length for a Si NW with a  $f_r = 250$  MHz.

A more detailed analysis of the expected device performance was undertaken using finite element analysis. Five critical factors were investigated: 1) impact of quality factor ( $Q$ ) on the device performance; 2) Casimir force [13] at the length scales of interest; 3) effect of high surface-to-volume ratio in nanowires on their elastic properties and device performance; 4) effect of additional device parameters such as gate length and the presence of the catalyst particle on the mechanical response; and 5) optimal device geometry required to achieve nanosecond switching times.

**Figure 4** shows the effect of  $Q$  on open time for the case of no damping, as well as overdamping ( $Q = 0.4$ ) and under-damping ( $Q = 8.3$ ), assuming a nanowire length of 500 nm, a diameter of 50 nm, and a gap of 20 nm. It is noted that no distinction is made here between damping due to the external environment and materials damping due to planar or line defects, grain boundaries, etc. In the case of overdamping, oscillation of the nanowire about the rest position is suppressed, though at the cost of increased open time. When the wire is underdamped the oscillations about the rest position are significant, though this is mitigated by the fact that the actual electrical open time is significantly shorter than the time it takes for the nanowire to initially reach the rest position, and hence the nanowire can be re-actuated to the closed position before settling at the rest position. A  $Q$  of 1-3 will thus be preferable for these Si NW devices.

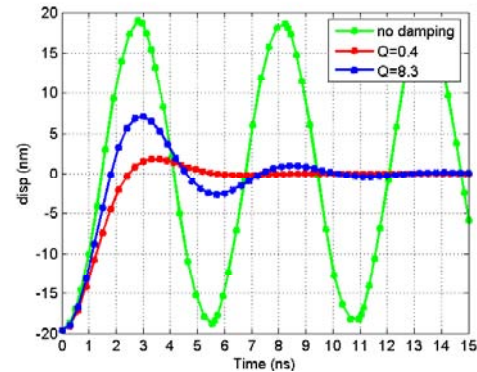


Figure 4: Effect of quality factor on open time for a 500 nm long, 50 nm diameter Si nanowire placed 20 nm from the gate electrode

We also studied the impact of the Casimir force on Si NW NEMS switch devices, which may lead to an additional attractive force between the nanowires and the gate electrode. In the case of two parallel plates, this force ( $F_c$ ) scales as  $A/d^4$ , and for a sphere in the vicinity of a parallel plate  $F_c \propto R/d^3$ , where  $A$  is the area,  $R$  is the radius, and  $d$  is the distance between conductors [14]. We calculate a Casimir force of  $\sim 0.2$  nN for our typical device dimensions, which if assumed to act as a point load will lead to a displacement of  $\sim 2$  nm. This displacement will be less for a distributed load, and hence the Casimir force can be neglected for gaps greater than 5 nm.

Surface elasticity has recently been studied theoretically as a possible mechanism by which the elastic constants of a nanostructure can be modified compared to their bulk counterparts [15]. However, a recent study has shown that for silicon the nanostructure must have a critical dimension below 5 nm in order for the surface to significantly impact the mechanical properties of the nanostructure [16]. Since our nanowires have diameters in the range of 40-80 nm, surface elasticity will not be a factor in the devices studied here. Indeed, recent studies of semiconducting and metallic nanowires show that their elastic constants and strength are similar to bulk materials [17,18].

Having ruled out significant contributions of the above non-classical effects to the device performance, the impact of gate length on pull-in voltage ( $V_{pull-in}$ ) and close time was evaluated. Assuming the device parameters discussed above, it was found that decreasing the gate length from 1000 nm to 700 nm led to an  $\sim 24\%$  increase in pull-in voltage and a 20% increase in close time. Therefore, these device parameters will not drastically affect the device dynamics. The impact of the catalyst particle present at the tip of the nanowire, which also acts as the contact material, was also found to have a limited effect on the resonant frequency of a typical Si NW. Indeed by a detailed design of experiments, it was found that close times as low as 1.7 nsec with  $V_{pull-in} = 0.5$  V can be obtained for 1000 nm long, 40 nm diameter nanowires placed 5 nm away from the gate electrode (Figure 5). The open time is on the order of 7-10 nsec (depending on  $Q$ ), but as noted above the nanowire can be actuated prior to reaching the rest position.

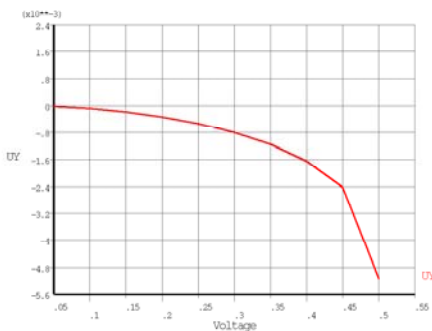


Figure 5: Simulated displacement-voltage curve showing  $V_{pull-in} = 0.5$  for a design capable of 1.7 nsec closing time.

### Si NW NEMS Device Fabrication

As noted above, we have fabricated two-terminal Si nanowire devices on 4" wafers. In the vicinity of the electrode there are typically many nanowires, though few are close enough to be actuated at low voltages. At present the placement of the nanowires is not deterministic, and various methods are being explored so that nanowires can be placed at well-defined locations 5-20 nm away from the microfabricated electrodes. This fact does not, however, hinder our ability to test the nanowire actuators (see

below). Nevertheless, fabrication of the two-terminal Si NW NEMS actuators on large-area wafers clearly shows the potential of this technology to be mass-manufacturable. A three-terminal process has also been developed and is currently under fabrication. Testing data reported below is focused on two-terminal devices.

### Testing

A typical wafer contains  $\sim 1000$  devices; hence autoprobing was used to determine which devices are functional at reasonable voltages. In devices tested to date the pull-in voltage was in the range of 25-35 V, hence we typically observed stiction of the device as evidenced by repeated DC current-voltage (I-V) measurements on a given device. Calculations show that the local temperature at the contact at such relatively high voltage will be several hundred degrees, hence it is not surprising that stiction occurs. Of course, in three-terminal devices the actuation voltage is independent of the source-drain voltage, which will be on the order of  $10^2$ 's of mV. Hence, stiction due to local heating should not be a problem for three-terminal devices.

After autoprobing, functional devices were subject to low frequency pulsed testing and indeed showed actuation above the measured DC  $V_{pull-in}$  and no actuation below  $V_{pull-in}$ , though a leakage current was observed (Figure 6). The typical on resistance was several 100 M $\Omega$ . High speed switching experiments will be performed on future three-terminal devices to assess the switching time and reliability issues that may arise in such nanoscale switches.

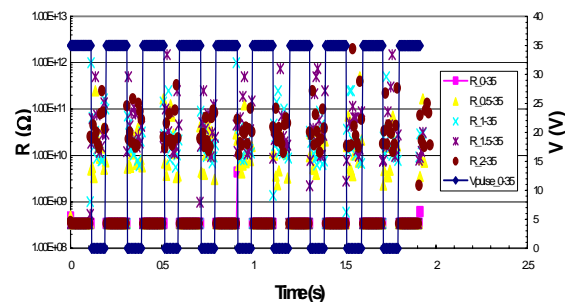
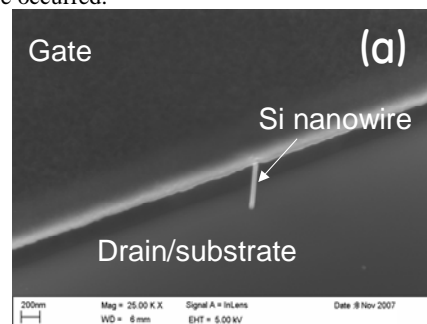


Figure 6: Pulsed gate voltage test data showing repeated actuations of a 2-terminal device with pull-in voltage of  $\sim 27$  V. The on-state resistance of the device is  $\sim 342$  M $\Omega$ . The off-state resistance is  $\sim 2080$  M $\Omega$ , indicating the presence of a residual leakage path, which is currently under investigation. No switching was observed when the device was actuated at 25 V.

We also studied actuation of Si NWs using *in situ* scanning electron microscopy (SEM). Figure 7 shows that upon application of 10 V, actuation/bending of the NW was clearly observed. Release of the applied voltage did not restore the nanowire to its rest position, indicating stiction between the top electrode and the nanowire occurred.



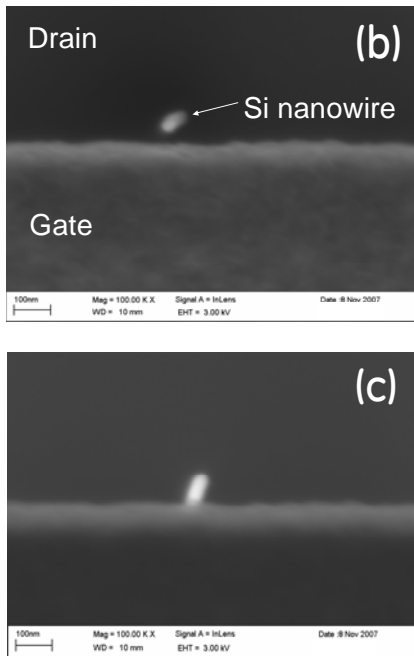


Figure 7. SEM images of a  $\sim 38$  nm diameter Si nanowire  $\sim 33$  nm away from a gate electrode (a) a 30 degree angle view; (b) top view at 0 V actuation voltage, (c) (top view) after application of a 10V actuation voltage, the nanowire was actuated to contact the gate electrode. After removal of the applied voltage the nanowire remained bonded to the top electrode. The expected pull-in voltage for this device was calculated to be 4.7 V.

## CONCLUSIONS

We proposed and demonstrated vertically-aligned silicon nanowire switches. Detailed modeling studies showed that non-classical effects such as the Casimir force and surface elasticity will not impact the performance of these devices, and that it is possible to obtain device designs that can yield low-voltage, high-speed switches. Two-terminal Si NW actuators were fabricated with integrated electrodes on 4" wafers, thus showing the potential of this technology for mass manufacturing. Electrical testing showed repeated actuation of these devices, and actuation of an individual Si NW was observed via *in situ* scanning electron microscopy. Future work is focused on fabricating three-terminal switches and testing their high-speed response and lifetime.

*The authors gratefully acknowledge the DARPA NEMS program (Dr. Amit Lal) for funding this work, which was prepared with the support of the U.S. Navy under Award No. N66001-07-C-2038. However, any opinions, findings, conclusions or other recommendations expressed herein are those of the author(s) and do not necessarily reflect the views of the U.S. Navy. We thank M. Knussman for technical assistance with the SEM.*

## REFERENCES

- [1] D. A. Muller, T. Sorsch, S. Moccio, F. H. Baumann, K. Evans-Lutterodt, and, G. Timp, "The electronic structure at the atomic scale of ultrathin gate oxides", *Nature*, 399, 758 (1999).
- [2] J. M. Kinaret, T. Nord, and S. Viefers, "A carbon nanotube-based nanorelay", *Appl. Phys. Lett.* 82, 1287 (2003).
- [3] L. M. Jonsson, S. Axelsson, T. Nord, S. Viefers, and J.M. Kinaret, "High frequency properties of a CNT-based

- nanorelay", *Nanotechnology*, 15, 1497 (2004).
- [4] C. Ke and H. D. Espinosa, "Feedback controlled nanocantilever device", *Appl. Phys. Lett.*, 85, 681 (2004).
- [5] C. Ke and H. D. Espinosa, "In situ Electron Microscopy Electromechanical Characterization of a Bistable NEMS Device", *Small*, 2, 1484 (2006).
- [6] B. A. Cruden and A. M. Cassell, "Vertically oriented carbon nanofiber based nanoelectromechanical switch", *IEEE Trans. Nanotech.*, 5, 350 (2006).
- [7] H. S. Kim, H. Qin, M. S. Westphal, Lloyd M Smith, and R.H. Blick, "Field emission from a single nanomechanical pillar", *Nanotechnology*, 18, 065201 (2007).
- [8] S. N. Cha, J. E. Jang, Y. Choi, G. A. J. Amaratunga, D.-J. Kang, D. G. Hasko, J. E. Jung and J. M. Kim, "Fabrication of a nanoelectromechanical switch using a suspended carbon nanotube", *Appl. Phys. Lett.*, 86, 083105 (2006).
- [9] Q. Li, S-M. Koo, C. A. Richter, M. D. Edelstein, J. E. Bonevich, J. J. Kopanski, J. S. Suehle, and E. M. Vogel, "Precise Alignment of Single Nanowires and Fabrication of Nanoelectromechanical Switch and Other Test Structures", *IEEE Trans. Nanotech.*, 6, 256 (2007).
- [10] R. S. Wagner and W. C. Ellis, "Vapor-liquid-solid growth mechanism of single crystal growth", *Appl. Phys. Lett.*, 4, 89 (1964).
- [11] L. Tsakalakos, S. T. Taylor, R. R. Corderman, J. Balch, J. Fronheiser, "Heterogeneous integration of semiconducting and carbide nanowires with Si substrates", *Proc. SPIE*, 6370, 637019 (2006).
- [12] L. Tsakalakos, J. D. Michael, R. Wortman, J. Balch, J. Fronheiser, S. F. LeBoeuf, R. Boone, D. White, "Time Resolved Photoconduction Studies of Uniformly Doped and pn Junction Si Nanowires", *Mater. Res. Soc. Symp. Proc.*, 958, 0958-L10-36 (2007).
- [13] H. B. G. Casimir, "On the attraction between two perfectly conducting plates", *Proc. Koninklijke Nederlandse Akad. Wetenschappen*, B51, 793 (1948).
- [14] F. Capasso, J. N. Munday, D. Iannuzzi, and H. B. Chan, "Casimir forces and quantum electrodynamic torques: physics and nanomechanics", *IEEE J. Select. Top. Quantum Electron.* 13, 400 (2000).
- [15] P. Sharma, S. Ganti, and N. Bhate, "The Effect of Surfaces on the Size-Dependent Elastic State of (Nano) Inhomogeneities", *Appl. Phys. Lett.*, 82, 535 (2003).
- [16] R. Maranganti and P. Sharma, "Length Scales at Which Classical Elasticity Breaks Down for Various Materials", *Phys. Rev. Lett.*, 98, 195504 (2007).
- [17] A. San Paulo, J. Bokor, R. T. Howe, R. He, P. Yang, D. Gao, C. Carraro, and R. Maboudian, "Mechanical elasticity of single and double clamped silicon nanobeams fabricated by the vapor-liquid-solid method", *Appl. Phys. Lett.*, 87, 053111 (2005).
- [18] S. Hoffmann, I. Utke, B. Moser, J. Michler, S. H. Christiansen, V. Schmidt, S. Senz, P. Werner, Ulrich Go1sele, and C. Ballif, "Measurement of the Bending Strength of Vapor-Liquid-Solid Grown Silicon Nanowires", *Nano Lett.*, 6, 622 (2006).

# A MEMS BASED MINIATURE HYDROGEN FUEL CELL FOR PORTABLE POWER GENERATION

K.Y. Lin<sup>1</sup>, R.D. Morgan<sup>1</sup>, H.S. Kim<sup>1</sup>, L. Zhu<sup>2</sup>, B. Gurau<sup>1</sup>, M.A. Shannon<sup>2</sup>, R.I. Masel<sup>1</sup>

<sup>1</sup> Department of Chemical & Biomolecular Engineering, University of Illinois, Urbana, IL 61801 USA

<sup>2</sup> Department of Mechanical Science & Engineering, University of Illinois, Urbana, IL 61801 USA

## ABSTRACT

MEMS based fuel cells have been proposed as replacements for batteries in distributed sensor networks, on chip power, and implantable devices. In this paper we will present the design and fabrication of new MEMS based fuel cells that show a factor of 4 higher power output than any MEMS based hydrogen/air fuel cell reported previously. Our approach is to base the fabrication on a single wafer compared to conventional two bonded wafers. Our hybrid microfabricated hydrogen fuel cell has an open cell voltage of 1.02V, a peak power density of 284 mW/cm<sup>2</sup> and fuel utilization rate close to 90%.

## INTRODUCTION

Portable devices have become much more feature packed and require much more power than before. However, they have been facing a persistent problem as rechargeable battery technology hasn't kept pace with the rapid advancements in chip designs. Bridging that gap may now be possible through fuel cells, a clean-energy technology that produces electricity from the electrochemical reactions between hydrogen and oxygen. Potential military applications are: a lightweight alternative to the heavy batteries soldiers have to carry into battle to power various high-tech gears.

Fuel cells convert chemical energy directly to electric power. There are different types of fuel cells characterized by the electrolyte material. Among them, proton exchange membrane (PEM) fuel cells are regarded as most suitable for portable applications. Figure 1 shows a schematic of a typical PEM fuel cell and how it works. Using hydrogen as the fuel, reactions at the anode and cathode of the PEM fuel cell are:



The protons produced at the anode are transported through the proton exchange membrane to the cathode, and the electrons travel through the external circuit thereby producing electricity. Protons and electrons are reacted with oxygen at the cathode with water being the only product. Catalyst layers on the electrodes are necessary for both anode and cathode reactions to occur efficiently.

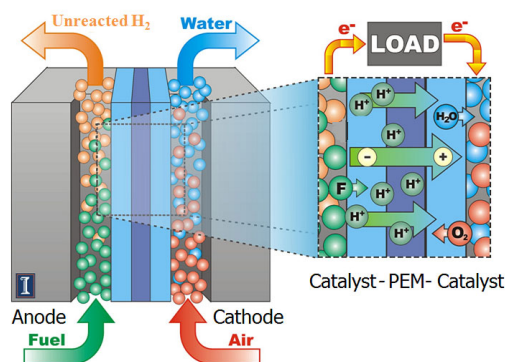


Figure 1: Schematic of a typical PEM fuel cell.

Recent interests have been on MEMS microfabrication rather than traditional manufacturing processes due to ease of miniaturization and reduction of cost. The high cost to build fuel cells is one of the biggest impediments to their commercialization. Traditionally, fuel cells are built similarly to a car, with pieces manufactured separately and then assembled. There is high variability, and the process is costly and time consuming. With microfabrication, instead of assembling the separate parts, the fuels cells are made by addition and subtraction on a base structure; the same way current microelectronic devices are made.

Previous works on MEMS based fuel cells can be categorized into four different areas [1]: Silicon base structures, porous silicon as the membrane, metal based materials, and polymer based materials such as PDMS and PMMA. Silicon based fuel cells will be the focus on this paper since silicon is the most common material used in MEMS, and many fabrication techniques have already been developed. Several groups have worked in this area using a conventional "sandwich" method: fabrication was done on two separate silicon wafers along with MEA and sandwich it with a proton conducting layer. Table 1 shows the fuel cell peak power performance reported for H<sub>2</sub>/O<sub>2</sub> system and open cell voltage (OCV) vary among different system designs.

In this paper we will present the design and fabrication of new MEMS based fuel cells that show a factor of 4 higher power output than any MEMS based hydrogen/air fuel cell reported previously [4-9]. Our approach is to work on single wafer MEMS fabrication. The advantage of fabricating using only a single wafer compared to two wafers is ease of miniaturization by eliminating the need for bonding two separate wafers onto a Nafion® sheet. Our design uses a hybrid proton conducting membrane: silicon base structure filled with Nafion® ionomer solution.

## EXPERIMENTAL

### Microfabrication of Silicon Dies

The Si based micro fuel cells were fabricated from 100 mm P type boron-doped double sided polished prime <1-0-0> SOI wafers (Ultrasil Corp., Hayward, CA) with 300 μm thick handle wafer (0.1-1.0 ohm-cm resistivity), 40 μm thick device layer (1-10 ohm-cm resistivity), and 0.5 μm thick buried oxide using conventional MEMS fabrication processes. Square windows of 2.4 mm x 2.4 mm were patterned on the handle wafer (anode side) while a 6 x 6 array of circular windows of 100 μm diameter and 100 μm apart were patterned on the device layer (cathode side) as shown on Fig. 2.

Table 1: A comparison of the performance of our device operated on  $H_2$  at 25 °C to those reported previously. We only included references where hydrogen was the fuel and the peak power was more than 10 mW/cm<sup>2</sup>.

	Open Cell Voltage (V)	Cell Area (mm <sup>2</sup> )	Design	Peak Power Density (mW/cm <sup>2</sup> )
Yu <i>et al.</i> [8]	0.95	506	Silicon wafers bolted to conventional MEA	195 (with pure O <sub>2</sub> running on the cathode side)
Modroukas <i>et al.</i> [5]	0.85	100	Silicon wafers bonded to conventional MEA	70 (with flowing air on the cathode side)
Meyers <i>et al.</i> [4]	0.9	n/a	Silicon wafers bonded to conventional MEA	63 (with pure O <sub>2</sub> running on the cathode side)
Yeom <i>et al.</i> [7]	0.95	44	Silicon wafers bonded to Nafion®	35 (with stagnant air on the cathode side)
Zhiyong <i>et al.</i> [9]	0.96	143	Silicon wafers bonded to Nafion®	13.7 (with pure O <sub>2</sub> running on the cathode side)
Pichonat <i>et al.</i> [6]	0.8	7	Nafion® filled silicon MEA	18 (with pure O <sub>2</sub> running on the cathode side)
<b>Our Device</b>	1.02	5.76	Nafion® filled silicon MEA	284 (with stagnant air on the cathode side)

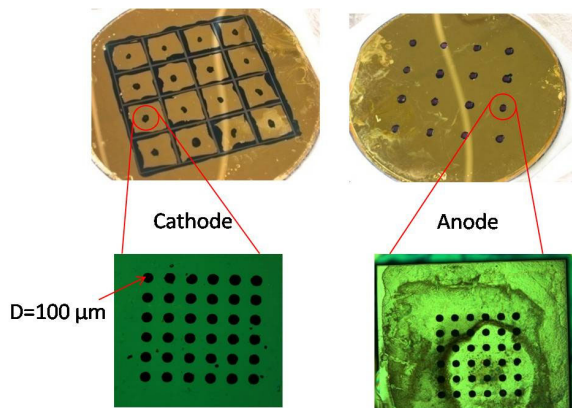


Figure 2: (Top) Picture showing finished wafer from cathode side and anode side views. (Bottom) Picture taken from microscope focusing on one device: showing the circular channels from cathode side and square window from anode side.

Figure 3 shows the microfabrication steps for the making of the Si dies: (A) the native oxide layer was removed by immersion in the buffered oxide etch (BOE) solution and the wafer was cleaned by 3:1 by volume of sulfuric acid and 30 wt% hydrogen peroxide; (B) roughly 100 nm thick silicon nitride layer was grown on both sides of the wafer by low pressure chemical vapor deposition (LPCVD); (C) photolithography using AZ 4620 photoresist was applied to pattern on the silicon nitride of the handle wafer (anode side) to make the square windows (2.4 mm sides); (D) dry etching using an inductively coupled plasma deep reactive ion etcher (ICP-DRIE, Plasma-Therm SLR770) was done to create square windows in the nitride layer on the anode side; (E) photoresist was removed by photoresist stripper AZ-400T, then 300 μm exposed silicon substrate was wet etched to the oxide

layer using a 35% potassium hydroxide solution at 85°C with silicon nitride as the mask; (F) again, using standard photolithography, a 6x6 array of circular windows (100 μm diameter) was patterned on the silicon nitride of the device layer (cathode side); (G) dry etching using ICP-DRIE was done to create the circular windows in the silicon nitride on the cathode side; (H) dry etching using the BOSCH process was done to etch 40 μm exposed silicon substrate down to the oxide layer; (I) dry etching using a Freon reactive ion etcher system (Freon RIE, PlasmaLab) was done to etch through the oxide layer; (J) using a DC-Magnetron sputtering system, roughly 150 nm of gold (50 nm of chrome as an adhesion layer) was sputtered (everywhere on both sides of the wafer except the openings on both sides) to serve as the current collector.

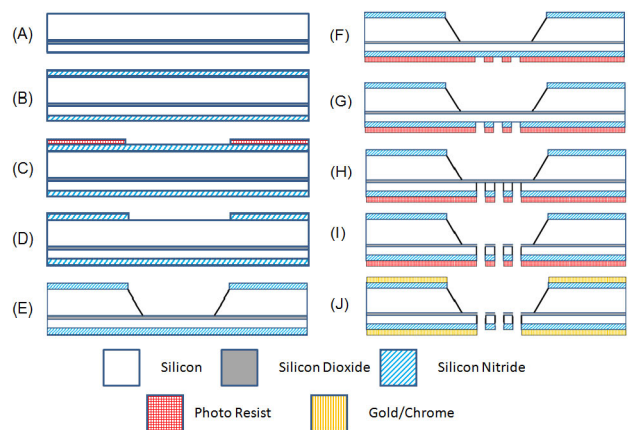


Figure 3: Microfabrication steps for silicon fuel cell dies.

### Preparation of Membrane Electrode Assembly

The membrane electrode assembly (MEA) was directly applied on the fabricated silicon structure as shown on Fig. 4. To prepare the MEA, ~28  $\mu\text{L}$  of 5 wt% Nafion<sup>®</sup> ionomer 1100 EW (Solution Technology Inc., Mendenhall, PA) was applied to the membrane area to fill the channels for proton conduction as well as to serve as an adhesion layer for the anode and cathode catalyst layers. The Nafion<sup>®</sup> layer was then allowed to dry. A leak test was performed using an in-house device. Catalyst inks were then prepared by dispersing platinum black (HiSPEC 1000, Alfa Aesar, Wardhill, MA) with Nafion<sup>®</sup> solution, Millipore water, and isopropanol via sonication. Using the direct paint method, the catalyst inks were painted onto the Nafion<sup>®</sup> layer of the anode and cathode to form the membrane electrode assembly. The resulting catalyst loading was approximately 20 mg/cm<sup>2</sup>. In addition to the membrane area, a small amount of catalyst ink was painted onto the gold current collectors to provide electrical connection.

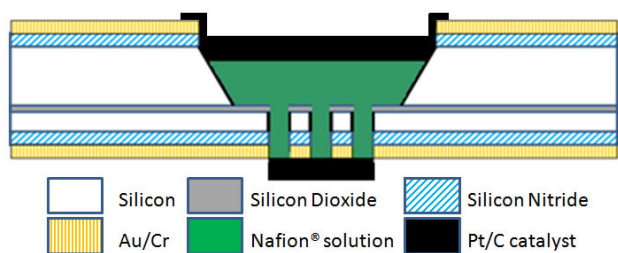


Figure 4: Membrane Electrode Assembly for the Si fuel cell.

### Hydrogen Fuel Utilization Rate Measurement

High fuel utilization rate of the fuel cell is essential for high energy density of the power generator device. The fuel utilization rate of the hydrogen fuel cell was obtained using a glass tube filled with hydrogen gas as shown on Fig. 5. The cell was run for 30 min from the hydrogen gas supplied from the glass tube. The water level at the glass tube was measured before and after the life test to estimate the amount of hydrogen supplied to the fuel cell.

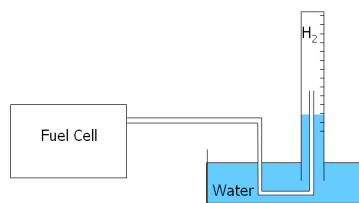


Figure 5: Schematic of the apparatus for measuring hydrogen utilization rate.

### Fuel Cell Testing

In order to test the fuel cell, a Teflon holder had to be fabricated in house as shown in Fig. 6. It consisted of two pieces. The bottom piece allowed hydrogen to flow over the anode, while the top piece allowed stagnant air to diffuse to the cathode. The test was to determine the performance of the fuel cell by determining the voltage-current (VI) relationship. The fuel cell was placed in the Teflon housing and connected to the potentiostat (Solartron SI-1287, Hampshire, UK). Dry hydrogen was passed over to the anode, and stagnant air was allowed on the cathode. Once the fuel cell reached a steady OCV, the potential was then stepped from OCV to 0.1V.

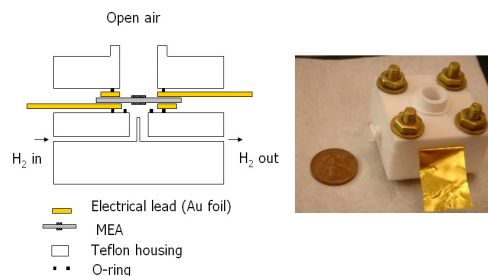


Figure 6: In house made Teflon housing for silicon fuel cell.

## RESULTS AND DISCUSSION

### Hydrogen Fuel Utilization Rate

Figure 7 shows the life test curves obtained at various operating voltages. Table 2 summarizes the calculation results under various conditions. The utilization rate turned out to be quite high (83~90%) and the rate was higher at lower voltage (higher current) indicating that there is some fuel leakage during operation. Therefore, the fuel utilization rate may be enhanced if the fuel leakage is reduced.

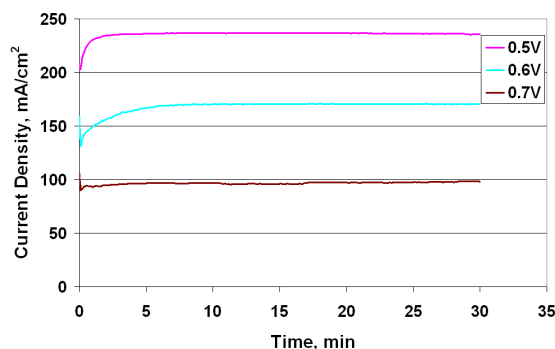


Figure 7: Constant voltage life test for fuel utilization calculation with the setup shown in Figure 5.

Table 2: Some of the characteristics of our devices operating on pure hydrogen and stagnant air at 25 °C.

Voltage	Current (mA/cm <sup>2</sup> )	Power (mW/cm <sup>2</sup> )	Hydrogen utilization
0.4 V	710	284	
0.5 V	480	240	90.2%
0.6 V	310	186	88.9%
0.7 V	260	182	83.6%

### Fuel Cell Performance

Table 1 and Figure 8 highlight the performance of our device. The fuel cell has an open cell voltage of 1.02V, a peak power density of 284 mW/cm<sup>2</sup> and fuel utilization rate close to 90%. Table 1 compares these results to several devices from previous literature. Prior to our work the best MEMS based hydrogen/air fuel cell only produced 70 mW/cm<sup>2</sup> compared to 284 mW/cm<sup>2</sup> in our device. Yu *et al.* [8] showed 195 mW/cm<sup>2</sup> by running pure oxygen on the cathode, but note that power is 4-5 times higher with oxygen than with air. Our device shows the highest power output of those shown previously, and it is a true MEMS device. There are no bolts or clamps holding on the MEA, and the device can be fully integrated with a miniature hydrogen generator as shown in Fig. 9.

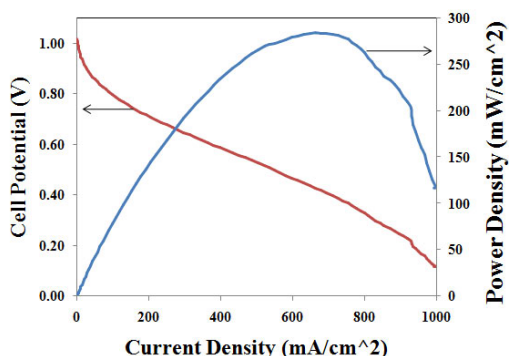


Figure 8: A polarization curve at 25 °C with flowing hydrogen on the anode and stagnant air (air-breathing) on the cathode.

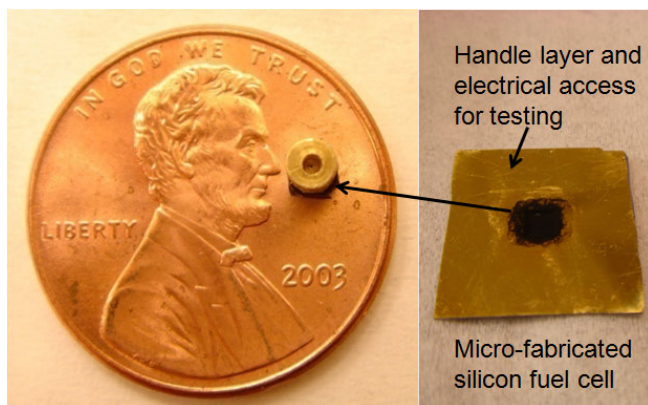


Figure 9: A picture of a hydrogen generator integrated with a silicon fuel cell both sitting on a penny.

Although the cell performance was greatly improved by the new MEA design, the performance still deviates from the ideal behavior as illustrated in Fig. 10. Low open cell potential is a sign of hydrogen crossover from the anode to the cathode side. The large slope of VI curve indicates that the current performance is mainly limited by parasitic resistance of the cell. Rapid drop of the cell voltage at high current density region designates mass transfer resistance mainly caused by the large amount of water produced at the cathode.

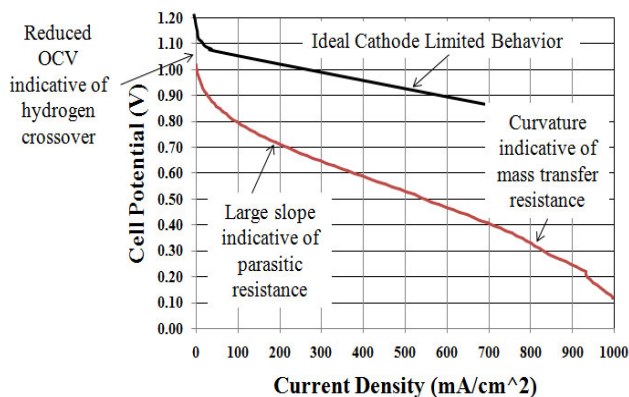


Figure 10: Comparison with ideal cathode limited behavior curve.

## CONCLUSIONS

In this paper, single wafer fabrication process was successfully demonstrated. Our hybrid microfabricated hydrogen fuel cell has shown an open cell voltage of 1.02V, a peak power density of 284 mW/cm<sup>2</sup> and fuel utilization rate close to 90%. The new MEMS based fuel cells show a factor of 4 higher power output than any MEMS based hydrogen/air fuel cell reported previously.

## ACKNOWLEDGEMENTS

This research is funded by the Defense Advanced Research Projects Agency (DARPA) under grant 2007-0299513-000. Any opinions, findings, and conclusions or recommendations expressed in this manuscript are those of the authors and do not necessarily reflect the views of the US Government. Micro-Nano-Mechanical Systems Cleanroom along with Micro and Nanotechnology Laboratory in University of Illinois at Urbana-Champaign provided the use of microfabrication facilities.

## REFERENCES

- [1] Pichonat, T. and B. Gauthier-Manuel, *Recent developments in MEMS-based miniature fuel cells*. *Microsystem Technologies*, 2007. **13**(11): p. 1671-1678.
- [2] Kuan-Lun, C., A.S. Mark, and I.M. Richard, *Porous silicon fuel cells for micro power generation*. *Journal of Micromechanics and Microengineering*, 2007(9): p. S243.
- [3] Kuan-Lun, C., M.A. Shannon, and R.I. Masel, *An improved miniature direct formic acid fuel cell based on nanoporous silicon for portable power generation*. *Journal of the Electrochemical Society*, 2006. **153**(8): p. 1562-7.
- [4] Meyers, J.P. and H.L. Maynard, *Design considerations for miniaturized PEM fuel cells*. *Journal of Power Sources*, 2002. **109**(1): p. 76-88.
- [5] Modroukas, D., V. Modi, and L.G. Frechette, *Micromachined silicon structures for free-convection PEM fuel cells*. *Journal of Micromechanics and Microengineering*, 2005. **15**(9): p. 193-201.
- [6] Pichonat, T. and B. Gauthier-Manuel, *Mesoporous silicon-based miniature fuel cells for nomadic and chip-scale systems*. *Microsystem Technologies*, 2006. **12**(4): p. 330-4.
- [7] Yeom, J., et al., *Microfabrication and characterization of a silicon-based millimeter scale, PEM fuel cell operating with hydrogen, methanol, or formic acid*. *Sensors and Actuators B: Chemical*, 2005. **107**(2): p. 882-891.
- [8] Yu, J., et al., *Fabrication of miniature silicon wafer fuel cells with improved performance*. *Journal of Power Sources*, 2003. **124**(1): p. 40-46.
- [9] Zhiyong, X., et al., *A silicon-based fuel cell micro power system using a microfabrication technique*. *Journal of Micromechanics and Microengineering*, 2006(10): p. 2014.

# A SELF-RESONANT, MEMS-FABRICATED, AIR-BREATHING ENGINE

Florian Herrault<sup>1</sup>, Thomas Crittenden<sup>2</sup>, Svyatoslav Yorish<sup>2</sup>, Edward Birdsell<sup>1</sup>, Ari Glezer<sup>1</sup>, and Mark G. Allen<sup>1</sup>

<sup>1</sup>Georgia Institute of Technology, Atlanta, Georgia, USA

<sup>2</sup>Virtual AeroSurface Technologies, Atlanta, Georgia, USA

## ABSTRACT

This paper reports the design, fabrication, and characterization of a self-resonant, MEMS-fabricated, air-breathing engine. Commonly known as a valveless pulsejet, this device converts chemical energy from fuel into pulsatile thrust which may be used for propulsion or converted into vibrational mechanical energy suitable for electrical power generation. The engine is fabricated by laser machining of ceramic sheets, followed by lamination and sintering. Using hydrogen fuel, the engine resonates in a frequency range of 0.9-1.6kHz with pressure differentials in the combustion chamber up to 10kPa. When coupled with a Lorentz-force type generator, the system delivers 2.5 $\mu$ W to an external electrical load at a frequency of 1.5kHz.

## INTRODUCTION

Due to the increasing demand for small-scale, portable, self-powered systems, chemical-to-electrical converters have been an active research area as potential replacements for existing batteries. Hence, efforts have been partly dedicated to heat-engine-based electrical power generation systems [1]. However, while MEMS-based, high power density, mechanical-to-electrical energy converters have been successfully demonstrated [2, 3], MEMS-based, heat engines for chemical-to-mechanical conversion systems remain elusive. As their dimensions shrink, they become difficult to fabricate and operate. First, it is challenging to reproduce the complexity and three-dimensionality of heat engines at a small scale using microfabrication approaches. Secondly, as the size of these converters decreases, the operating frequency required to maintain appreciable output power increases, which in turn results in very high required rotational speeds. Air-driven, silicon-based, multi-wafer, micro-turbines have demonstrated rotational speeds beyond one million of revolutions per minute [1]. In addition, and as a part of the same research effort, micro-combustors have been successfully fabricated [4]. However, severe constraints on materials and fabrication tolerances have been observed. As a result, the fabrication and operation of devices combining the combustor and the turbine for chemical-to-mechanical conversion is still very challenging. Thus, at smaller scales, a tradeoff between simplicity of operation (e.g., no valves, rotating parts, or seals) and ultimate efficiency may be desirable. As a consequence, we investigate the application of MEMS fabrication techniques to the development of a valveless pulsejet, a small-scale, reduced-complexity, air-breathing engine.

Valveless pulsejet combustor designs with no moving parts at larger scales have been known since the early 1900s. Recently, a 15-cm long, conventionally fabricated system has been reported [5, 6], where various system measurements such as temperature, pressure, operation frequency and thrust measurements have been described. To our knowledge, there is no literature reporting on the design, and fabrication of such engines at smaller scales (i.e. combustion chamber volume below 1cm<sup>3</sup>). The relatively low efficiency of this type of engine has always been seen as a major drawback as compared to that of other heat engines. However, at a small-scale, this issue is counterbalanced by the extreme simplicity of design and operation, as mentioned previously. In this paper, we present the development of a MEMS-fabricated, ceramic-based, valveless pulsejet supplied by hydrogen. The device converts

chemical energy from a source of hydrogen fuel into an oscillating thrust, which can be either used for micro-propulsion, or converted into vibrational mechanical energy. Such energy could be used as a platform for mechanical-to-electrical converters using vibration-based, electromagnetic power generation systems. The air-breathing engine self-resonates in the kHz range; this high mechanical frequency is potentially suitable for high energy density generators.

## SYSTEM DESIGN

The self-resonant, air-breathing engine includes a combustion chamber with air and fuel inlets, and a resonant tailpipe. Openings are also designed in the combustion chamber to integrate two spark plugs for initial ignition. Fig. 1 shows a three-dimensional (3-D) rendering of the MEMS-fabricated engine with integrated fuel inlets. As opposed to other heat engines, this combustor does not have any moving parts.

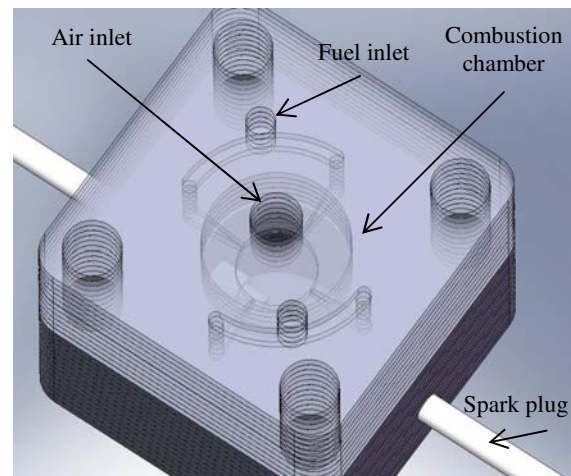


Figure 1: 3-D renderings of the MEMS-fabricated, self-resonant, air-breathing engine with integrated fuel inlets.

## Operation Cycle

The typical operation cycle of the air-breathing, self-resonant engine is shown in Fig. 2. As illustrated in Fig. 2a, the cycle begins with a single spark ignition accompanying a small amount of force-fed air into the inlet, and the fuel supply. The spark ignites the fuel/air mixture in the combustion chamber with a corresponding pressure rise, pushing exhaust products out of the inlet pipe and out toward the end of the exhaust pipe, as presented in Fig. 2(b-c). After a short period of time, the pressure in the chamber decays to below atmospheric level, creating a phenomenon of suction. This induces fresh air to flow into the chamber from the air inlet, and hot gases and radicals to return to the chamber from the exhaust pipe, as described in Fig. 2d. Consequently, the combustion is automatically re-ignited without any additional spark, and the sequence (2.b-2.e) resumes as long as fuel is supplied. The net result is an air-breathing engine capable of producing oscillating thrust with no moving parts. Furthermore, the single spark ignition is a major advantage over other combustion engines.

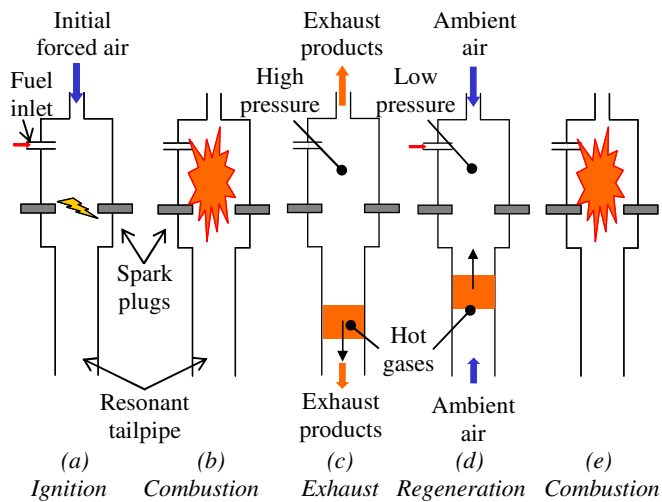


Figure 2: Conceptual schematic of typical valveless pulsejet operation.

### SYSTEM FABRICATION

Laser micromachining of ceramic sheets (Alumina A-16), followed by mass-manufacturable lamination and sintering is used to fabricate the primary elements of this device [7, 8]. The three-dimensional design of the device is divided into CAD layers of a thickness of approximately 1mm. Those individual layers are patterned onto ceramic sheets by infrared laser micromachining. The multiple layers are then accurately positioned on top of each other using alignment pins, and laminated for 5min at a temperature of 85°C, and a pressure of 50kg/cm<sup>2</sup>. The device is finally sintered at a temperature of 1500°C for several hours. Fig. 3 illustrates the described fabrication concept. Shrinkage of approximately 15% occurs during the sintering process, and must be considered in the design. Such a process enables the integration of complex, three-dimensional microfluidic ports for the fuel and air inlets, the exhaust as well as the spark initiation.

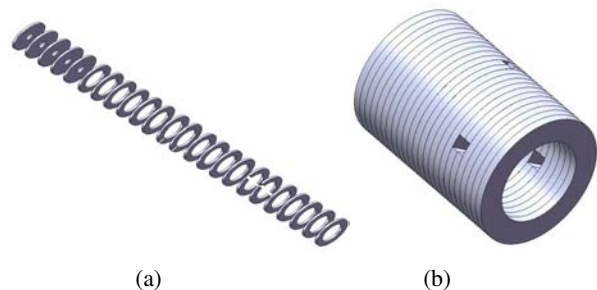


Figure 3: Conceptual renderings of laser micromachined, laminated sheets: (a) Ceramic layers are individually laser machined, (b) and then aligned, laminated, and finally sintered.

### First generation air-breathing engine

The first generation device has been fabricated by stacking laser machined rings with integrated ports, as illustrated in Fig. 4. The fabricated elements of the first generation device are shown in Fig. 5. The combustion chamber has an inner diameter of 7.5mm, and an internal volume of approximately 0.8cm<sup>3</sup>. As shown in Fig. 5c, the experimental setup consists of the hydrogen feed line, and the conventional, 3.2mm diameter, resonant tailpipe. The area ratios between the air inlet, combustion chamber, and resonant tailpipe are critical for the operation of the engine. If the amount of

air that is sucked back in the chamber is too low, the device will not resonate. In addition, if the exhaust pipe is too short, the hot gases will not remain within it, which will prevent the regeneration phase from taking place. Operating conditions have been determined by experimental investigations.

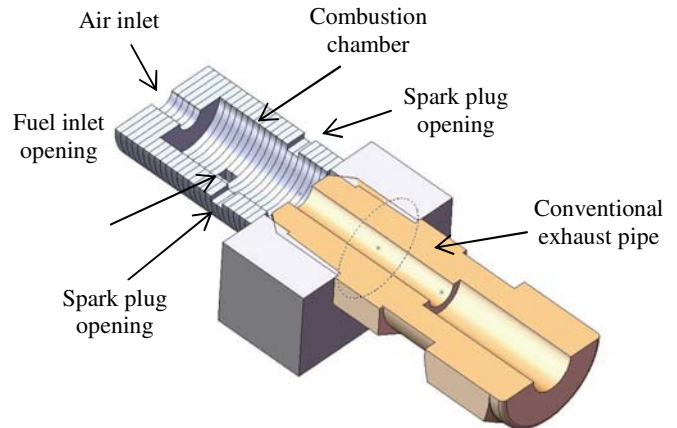


Figure 4: 3-D cross-sectional renderings of the self-resonant combustion device with conventional exhaust pipe.

Note that the inlet system and the combustion chamber have been fabricated separately to allow testing of several inlet and exhaust configurations with the same chamber.

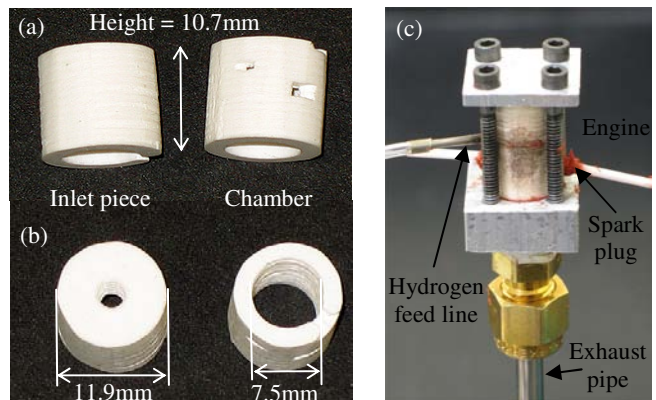


Figure 5: Self-resonant, combustion engine: The air inlet piece has been fabricated separately to test different configurations with the same combustion chamber: (a) Side-view, (b) Top-view, and (c) Test setup.

### Second generation air-breathing engine with integrated inlets

Proper designs of the fuel and air inlets are required to obtain the correct gas mixture, and an operating device. Large-scale devices integrate conventional pipes to supply the fuel inside the chamber [5, 6]. MEMS fabrication approaches offer the opportunity of fully integrated, microfluidic inlet channels. In addition, complicated, and non-conventional designs can be achieved. Fig. 6 depicts the second generation device with integrated, multi-directional fuel inlets. The four inlets are located at the periphery of the chamber, and direct the flow of fuel toward the center of the chamber. The combustion chamber, which is shown in Fig. 6c, is similar to the first generation engine, and the same resonant tailpipe has been used for system characterization.

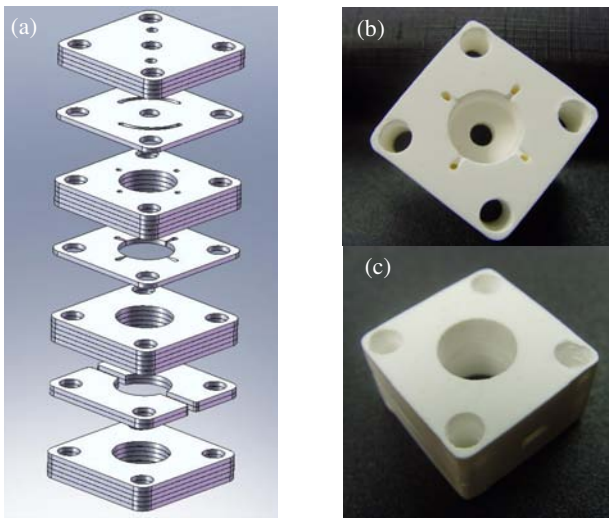


Figure 6: Self-resonant, air-breathing engine with integrated fuel inlets: (a) Exploded rendering of the design, (b) Integrated, multi-directional fuel/air inlet, and (c) Combustion chamber.

## SYSTEM CHARACTERIZATION

### First generation device

A pressure transducer is implemented to measure the variation of pressure inside the combustion chamber as a function of time and fuel flow-rates. The acquisition of the data is performed with the assistance of LabView software. A 1mm diameter opening that is located in the center of the combustion chamber is integrated in the fabrication process to allow the pressure measurements. Fig. 7 depicts the time-dependent pressure variation. At a hydrogen flow rate of 2.5L/min, a pressure differential of 9kPa, and a resonant frequency of 1.38kHz have been measured. The pressure differential is calculated by measuring the peak-to-peak values between the high pressure and the low pressure phases. As can be seen, the pressure goes below the atmosphere level as previously detailed in the operation cycle in Fig. 2.

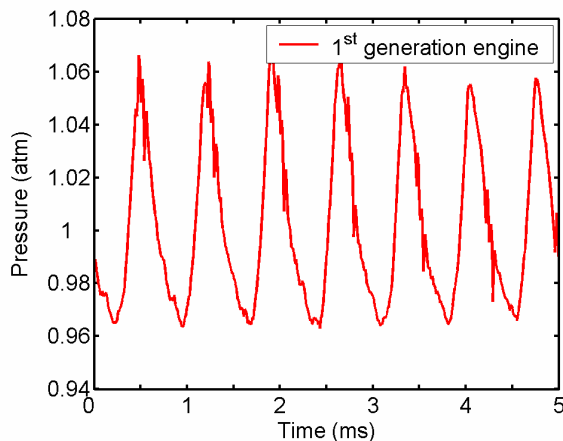


Figure 7: First generation device: Pressure variation as a function of time using a hydrogen flow-rate of 2.5L/min.

As shown in Fig. 8, both the resonant frequency and the pressure differential vary with hydrogen flow rates. Furthermore, the fabricated combustion engine resonates for flow rates in the 1-4L/min range where the air/fuel mixing occurs properly. A maximum of 10kPa of pressure differential has been measured inside the chamber.

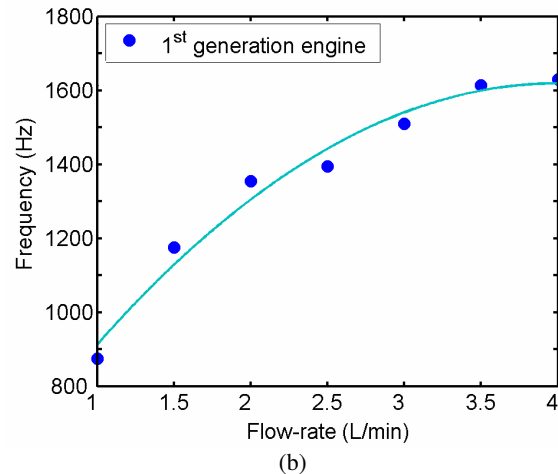
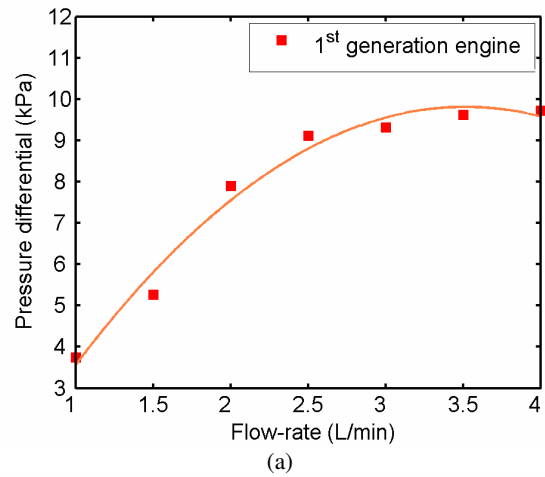


Figure 8: First generation device: (a) Pressure differential and (b) resonant frequency as a function of hydrogen flow-rate.

The flow structure of the air inlet has been recorded using a Schlieren system. Schlieren flow visualization is an optical system based on the deflection of light. Because the jet is three-dimensional, and there is significant wasted heat, it is difficult to have a clear picture of the phenomenon. The suction phase, or regeneration phase, is shown in Fig. 9.

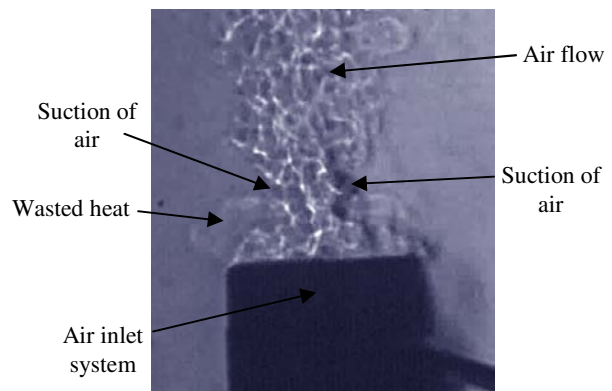


Figure 9: Visualization of the air flow on the inlet side using a Schlieren optical system.

## Second generation device

Similar experiments have been performed using the engine with integrated, multi-directional fuel inlets. The pressure variation as a function of time is shown in Fig. 10 for a hydrogen flow-rate of 2L/min. The functional range of operation has been measured from approximately 1L/min to 3L/min. However, both the resonant frequency and the pressure differential vary with time, as depicted in Fig. 10. This is presumably due to unequal mixing and also ineffective mixture ratio from pulse to pulse in this unoptimized structure. In this regard, having the fuel inlet at the center of the chamber yields better results than having the fuel inlets on the periphery. Since the primary air flow is along the centerline of the chamber, the hydrogen needs to penetrate to the center of the chamber and have enough time to remain for complete mixing on the time scale of the resonator.

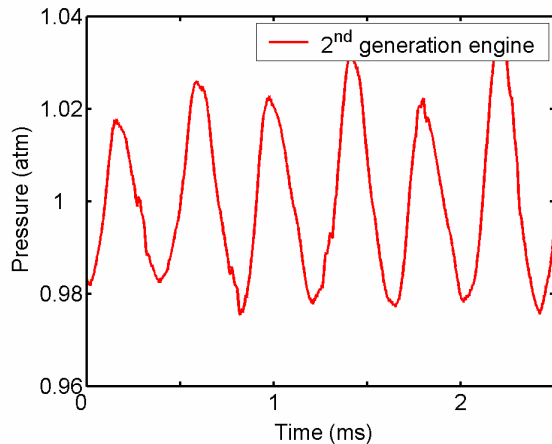


Figure 10: Second generation device: Pressure variation as a function of time using a hydrogen flow-rate of 2L/min.

## Electrical Power Measurements

To demonstrate the feasibility of electrical power generation using the air-breathing engine as a source of mechanical energy, an electromagnetic, Lorentz-force type generator has been placed in fluidic contact with the engine exhaust. The generator membrane is mechanically driven by the oscillating thrust of the device. As a result, electrical power is delivered to an external load resistance. The first version of the air-breathing engine has been used for this experiment. The results are presented in Fig. 11. An output voltage of approximately 40mV<sub>rms</sub> peak to peak has been measured across an 8Ω load at a frequency of 1.5kHz, which corresponds to an output power of 2.5μW<sub>rms</sub>. Although this experiment is not optimized for maximum efficiency and high power output, it demonstrates the potential for MEMS-scale, combustion-based fuel-to-electrical power generation. More robust mechanical power transmission is expected to produce significantly higher electrical output.

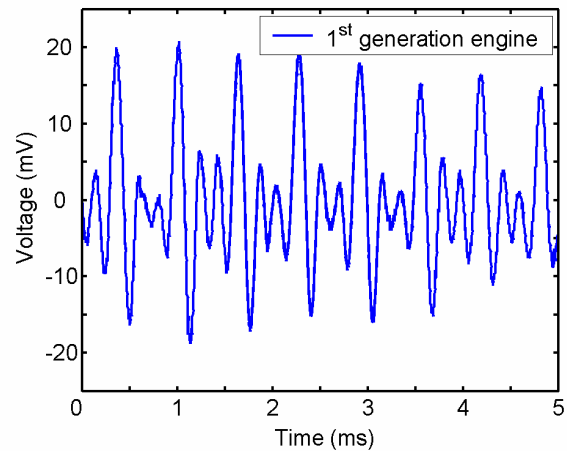


Figure 11: First generation device: Electrical output as a function of time measured by placing a Lorentz-force generator in fluidic contact with the oscillating exhaust. (Hydrogen flow-rate = 3.5L/min).

## CONCLUSIONS

We have introduced the fabrication and measurement results of a small-scale, self-resonant, ceramic-based, air breathing engine. When supplied by hydrogen fuel, the system generates a pressure differential up to 10kPa inside the combustion chamber, at a resonant frequency of 1.5kHz. Improvements may include the use of hydrocarbon fuels, or higher level of compactness of the engine. Furthermore, the implementation of a vibration-based magnetic power generator onto the self-resonant engine is envisioned as the next step toward a fully-integrated, MEMS-based, chemical-to-electrical converter, as suggested by the last detailed experiment.

## REFERENCES

- [1] Epstein, *et al.*, "Power MEMS and Microengines", *Proc. Transducers '97*, pp. 753-756, vol. 2, (1997).
- [2] D. P. Arnold, F. Herrault, I. Zana, J.-W. Park, S. Das, J. H. Lang, and M. G. Allen, "Design optimization of an 8 W, microscale axial-flux, permanent-magnet generator," *J. Micromech. Microeng.*, v. 16, n. 9, pp. 290-296, (2006).
- [3] H. Raisigel, O. Cugat, and J. Delamare, "Permanent magnet planar micro-generators," *Sensors and Actuators A*, vol. 130-131, pp. 438-444, (2006).
- [4] C. M. Spadaccini, A. Mehra, J. Lee, X. Zhang, S. Lukachko, and I. A. Waitz, "High power density Silicon combustion systems for micro gas turbine engines," *J. Eng. Gas Turbines Power*, vol. 125, issue 3, pp. 709-719, (2003).
- [5] T. Geng, M. A. Schoen, A. V. Kuznesov, and W. L. Roberts, "Combined numerical and experimental investigation of a 15-cm valveless pulsejet," *Flow turbul. Combust.*, vol. 78, n. 1, pp. 17-33, (2007).
- [6] Schoen, M.: "Experimental investigations in 15 centimeter class pulsejet engines," Master dissertation, Mechanical and Aerospace Engineering Department, North Carolina State University, Raleigh, North Carolina, (2005).
- [7] M. G. Allen, and A. Glezer, "Alternative Micromachining Technologies for the Realization of Robust MEMS," *American Institute of Aeronautics and Astronautics Conference*, AIAA 2000-248, (2000).
- [8] E. Birdsell, J. Park, and M. G. Allen, "Wireless ceramic sensors operating in high temperature environments," *40th AIAA Joint Propulsion Conference*, AIAA 2004-3990, (2004).

# AUTOMATIC MODE MATCHING FOR HIGH-Q VIBRATORY RATE GYROSCOPES

C.D. Ezekwe<sup>1,2</sup> and B.E. Boser<sup>1</sup>

<sup>1</sup>University of California, Berkeley, California, USA

<sup>2</sup>Robert Bosch Research and Technology Center, Palo Alto, California, USA

## ABSTRACT

We demonstrate automatic mode-matching for high-Q micromachined vibratory rate gyroscopes. Unlike previously proposed techniques, our approach continuously tunes the sense resonance frequency to match the drive frequency and achieves a stable scale factor and more than 50Hz of bandwidth regardless of fabrication and drift.

## INTRODUCTION

In a vibratory rate gyroscope, the readout interface senses the Coriolis acceleration, from which the angular rate is inferred. The Coriolis acceleration is sensed by detecting the capacitance between the moving proof mass and fixed electrodes. In converting the capacitance to either voltage or current, the front-end amplifier, invariably, introduces circuit noise, which limits the minimum detectable signal. Matching the drive and sense modes increases the acceleration-to-capacitance sensitivity by the Q-factor of the sense mode, which can be in excess of 1000 in vacuum packaged devices. With *mode matching*, the same Coriolis acceleration produces a much larger capacitance change, significantly reducing the impact of the circuit noise. This paper describes the techniques used to exploit mode matching effectively to achieve a Brownian motion limited noise floor of  $0.004^\circ/\text{s}/\sqrt{\text{Hz}}$  over a 50Hz band while dissipating 1mW.

## MODE MATCHING CHALLENGES

While mode matching amplifies the Coriolis acceleration induced motion by the Q-factor of the sense mode, it gives rise to several challenges that must be addressed in a practical system. With mode matching, the Coriolis signal is centered at the sense mode frequency, and, thus, the sensor bandwidth is fixed by the sense mode frequency and Q-factor. The resulting difficulty is illustrated by the system in [1], where the use of mode matching,

together with a traditional open-loop readout interface, limits the sensor bandwidth to below 1Hz, much less than the 50Hz required in automotive and consumer applications [2]. Furthermore, the bandwidth and scale factor in that system are poorly controlled due to the normally substantial variation of the Q-factor with the manufacturing process and the ambient. Figure 1 illustrates this problem. Besides, due to the limited accuracy of any practical mode-matching scheme, a residual frequency mismatch will invariably exist. The uncertainty in the residue due to process and ambient variations gives rise to further uncertainty in the scale factor. With the very abrupt change in the phase response near the sense mode frequency, the uncertainty exacerbates the task of synchronously demodulating the Coriolis signal with the correct phase, which is necessary for rejecting quadrature error. Figure 2 illustrates this problem.

Due to these difficulties, many gyroscope implementations avoid mode-matching altogether and, instead, operate away from the sense mode frequency, obtaining a larger bandwidth and better defined scale factor and phase response at the expense of sensitivity [3]. A practical readout interface exploiting the sense resonance must overcome the problems arising from mode matching in a way that neither interferes with gyroscope performance nor negates the advantage derived from mode matching.

## FORCE FEEDBACK

Feedback is widely used in electronics to obtain precise characteristics, for example precise gains, from imprecise elements. It has been used in sensors to improve bandwidth, dynamic range, linearity, and drift [4]. Especially in high-Q vibratory gyroscopes with matched drive and sense modes, feedback is imperative to ensure proper operation.

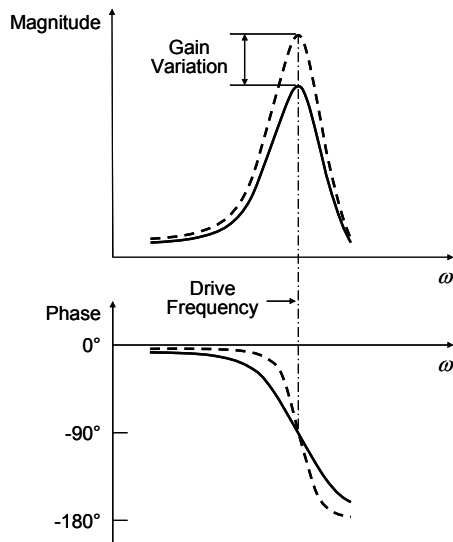


Figure 1: Scale factor (gain) variation with Q-factor.

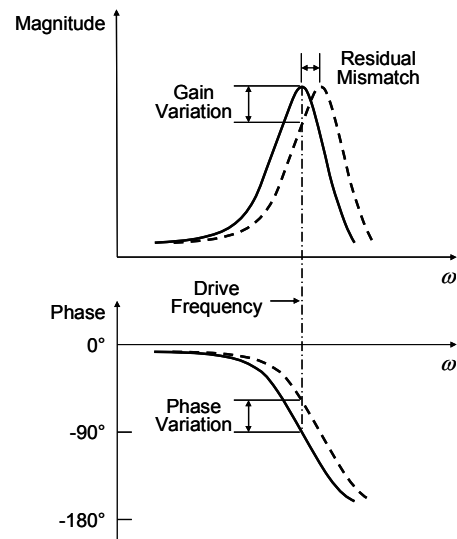


Figure 2: Scale factor and phase response variations with residual mismatch.

Figure 3 shows the sense dynamics enclosed in a force feedback loop. A compensator and a force transducer are added to the basic *open-loop* readout interface to form a *closed-loop* readout interface. Based on the motion sensed by the front-end, the compensator produces an estimate of the Coriolis force which the force transducer applies with opposite polarity on the proof mass to null its motion. Perfect nulling of the proof mass motion implies that the feedback force is exactly equal and opposite to the Coriolis force. While this is impossible to achieve over all frequencies in practice, adequate nulling is possible within a limited frequency band where the force feedback open-loop gain is sufficiently high. Within that frequency band, the output of the closed-loop interface is an accurate representation of the Coriolis acceleration.

Figure 4 compares the frequency responses of the open-loop sensor and that of a closed-loop interface that has a high open-loop gain over a frequency range that extends beyond the sense mode frequency. Electronic circuits implementing the compensator provide the open-loop gain necessary for a closed-loop response that is flat and stable over a much wider frequency range, regardless of the variations of the sensor parameters. This obviates the traditional tradeoff of mechanical sensitivity for larger bandwidth and better defined scale factor and phase response.

In this work, the feedback force is applied by reusing the sense combs as differential electrostatic actuators. Electrostatic actuators also produce spring softening, which, if not handled with care, results in the parasitic tuning of the sense mode frequency by the feedback voltage, with the unintended consequence of increasing the uncertainty in the residual mismatch.

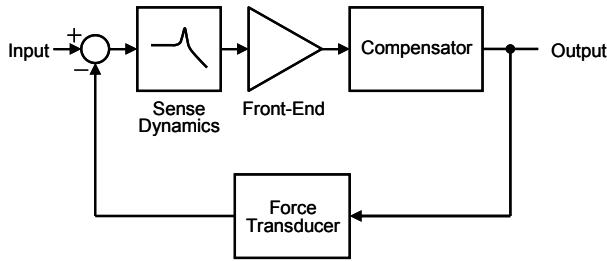


Figure 3: Basic force feedback loop.

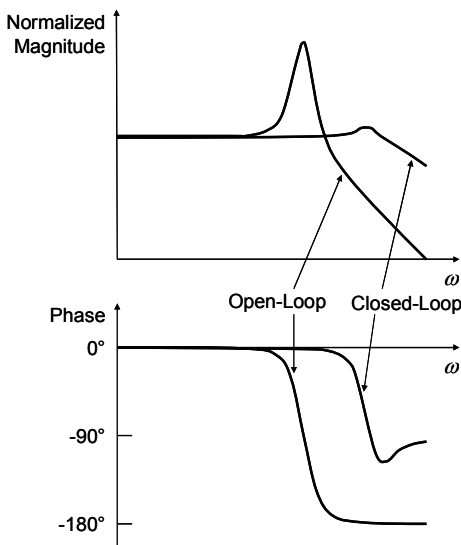


Figure 4: Illustration of the closed-loop response versus open-loop response of the sensor.

As an illustration of this problem, consider the schematic shown in Figure 5, where the proof mass is grounded, and the top and bottom electrodes are biased at  $V_{bias}$  and driven differentially by the feedback voltage  $v_{fb}$ . The feedback force applied on the proof mass for displacements that are small relative to the gap is

$$F_{fb} = 2 \underbrace{\frac{C_{s0}}{x_g}}_{\text{actuator gain}} V_{bias} v_{fb} + 2 \underbrace{\frac{C_{s0}}{x_g^2} (V_{bias}^2 + v_{fb}^2)}_{\text{signal dependent stiffness}} x \quad (1)$$

where  $x_g$  is the nominal gap and  $C_{s0}$  is the nominal sense capacitance between the proof mass and each pair of connected electrodes. In addition to the desired voltage controlled force with the indicated actuator gain, the actuator produces an unwanted stiffness term that also depends on the feedback voltage. With proportional control, this problem results in about 1% dynamic variation of the sense mode frequency in the experimental prototype, whereas an error of much less than 0.3% is required.

Bang-bang control, a feedback control strategy in which the feedback voltage is restricted to just two levels, overcomes this problem. With bang-bang control, the feedback voltage toggles between  $V_{bias}$  and  $-V_{bias}$  in such a way that its time-average approximates the feedback voltage under proportional control. The technique converts the dynamic frequency variation into a static error since, regardless of the spectral content of the feedback voltage, the square is constant,  $V_{bias}^2$ . The resulting static error is removed by calibration. Though bang-bang control results in a highly nonlinear force feedback loop, we use linear system techniques in the subsequent sections since they lead to useful results when used to analyze certain aspects of the loop behavior.

#### AUTOMATIC FREQUENCY CALIBRATION

Calibration is also necessary to guarantee resonance frequency matching in the presence of fabrication tolerances and ambient variations. Previously proposed calibration schemes determine the frequency mismatch by monitoring properties of the open-loop sensor [1], and therefore are incompatible with force feedback, which is imperative in a mode-matched gyroscope to stabilize the scale factor and widen the bandwidth. In this work, we inject a calibration signal into the force feedback loop to monitor the mismatch between the drive and sense resonance frequencies. Figure 6 shows the force feedback loop with the calibration input. The transfer function from the calibration input to the output assuming a high open-loop gain is

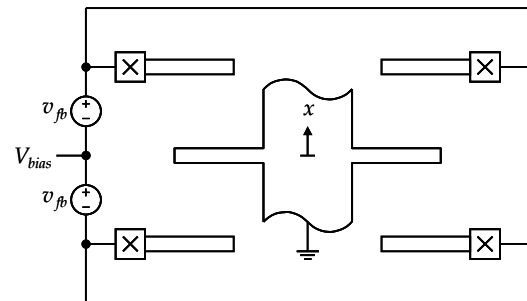


Figure 5: Schematic diagram of a differential electrostatic actuator.

$$G_{cal}(s) = \frac{1}{K_{v-f}K_{x-v}H_s(s)} \propto \frac{1}{H_s(s)} \quad (2)$$

$G_{cal}(s)$ , which is simply the inverse transfer function of the sense element, has a frequency response that, as shown in Figure 7, vertically mirrors the second-order response of the sensor and, thus, serves as a good proxy for  $H_s(s)$ . In fact,  $G_{cal}(s)$  is preferable over  $H_s(s)$  because it has zeros in place of the high-Q poles in  $H_s(s)$  that severely limit the tracking bandwidth of conventional open-loop sensing based frequency calibration techniques such as the one in [1].

Two pilot tones serve as the calibration signal. The tones are at approximately  $\pm 250\text{Hz}$  offset from the drive frequency to avoid interference with the Coriolis signal, enabling continuous background calibration. Their output amplitudes are nearly equal when the drive and sense resonance frequencies match. When the sense resonance frequency is *higher* (or *lower*) than the drive frequency, the amplitude of the higher frequency tone is *smaller* (or *larger*) than that of the lower frequency tone. Thus, the amplitude difference indicates the magnitude and direction of frequency mismatch. Figure 8 illustrates the estimation principle.

Figure 9 shows a simplified diagram of the complete calibration loop. The same tones that are applied at the calibration

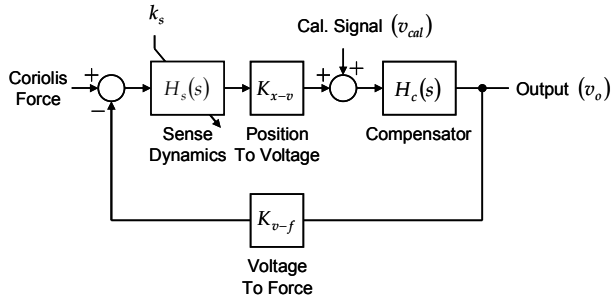


Figure 6: Force feedback loop with added calibration input.

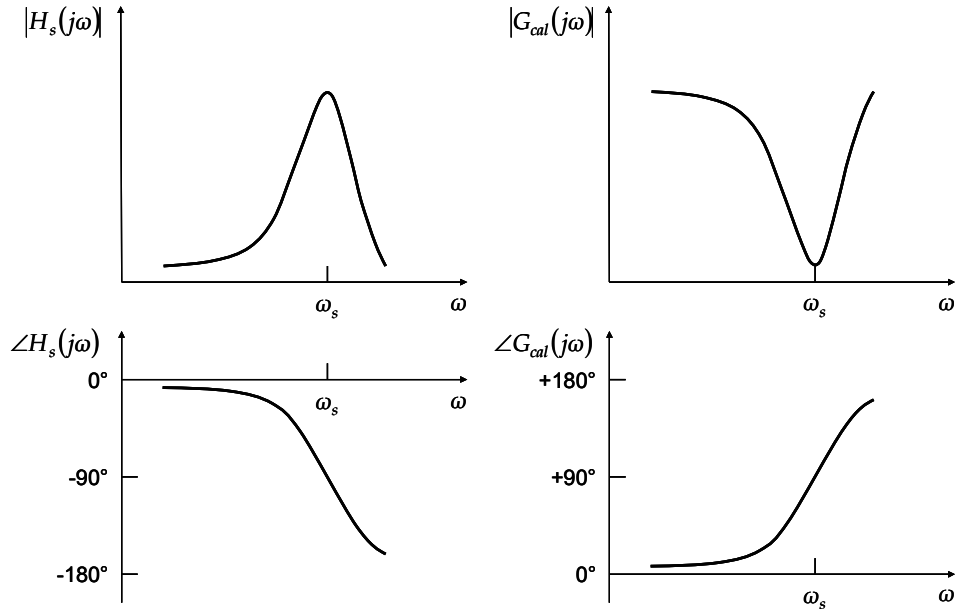


Figure 7: Comparison of  $H_s(j\omega)$  and  $G_{cal}(j\omega)$ .

input are used to demodulate the amplitude information. The mean of the demodulated signal is, to first order, linearly proportional to the difference between the drive and sense resonance frequencies. Adjustment of the sense resonance frequency is accomplished using electrostatic spring softening obtained through a set of tuning combs dedicated to frequency tuning. A digital loop filter with infinite DC gain drives the mismatch to zero.

## EXPERIMENTAL RESULTS

The frequency calibration technique was implemented as part of the readout interface described in [5]. Figure 10 shows the

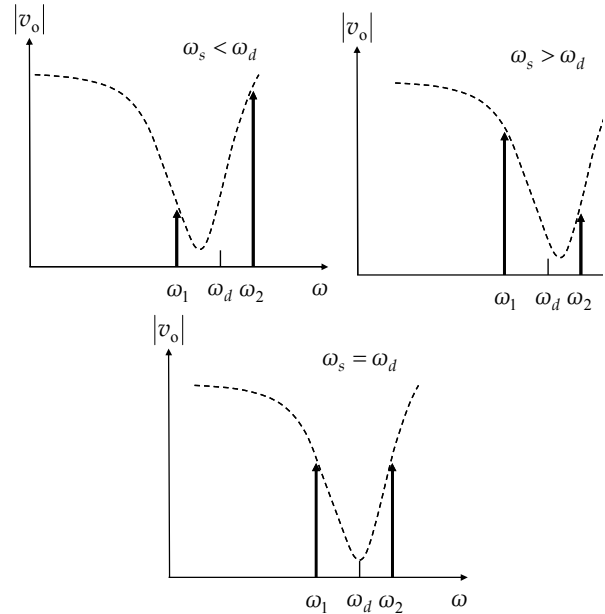


Figure 8: Frequency mismatch estimation using two out-of-band pilot tones. The dashed curves represent  $G_{cal}(j\omega)$ , whose minimum occurs at the sense mode frequency.



# FUNDAMENTAL AND OVERTONE ALUMINUM NITRIDE DUAL MODE RESONATOR FILTERS

*R.H. Olsson III and M.R. Tuck*

Sandia National Laboratories, Albuquerque, New Mexico, USA

## ABSTRACT

This paper reports post-CMOS compatible aluminum nitride dual mode resonator filters that realize 4<sup>th</sup> order band-pass filters in a single resonator device. Dual mode filters at 106 MHz operating in their fundamental mode are reported with insertion losses as low as 5.5 dB when terminated with 150  $\Omega$ . A notching technique is demonstrated for varying the 3 dB bandwidth of these filters from 0.15 to 0.7%, overcoming a significant limitation of previous work. Dual mode filters operating at their 5<sup>th</sup> and 10<sup>th</sup> overtones are reported scaling the operating frequencies of this class of device to 0.55 and 1.1 GHz.

## INTRODUCTION

Aluminum nitride (AlN) MEMS filters are a promising technology for the miniaturization of RF communication systems [1-3]. The small size and single chip integration of filters operating from 1 MHz to several GHz enable real time spectrum analyzers and multi-channel software defined radios with greatly reduced size and power consumption. These applications require banks of greater than 100 filters, placing added emphasis on small size and a minimum number of devices. Dual mode filters, which realize a 4<sup>th</sup> order band-pass filter in a single device, are ideal for such applications. AlN dual mode filters were first reported at 23 MHz in [4] and later scaled to 108 MHz utilizing the ring device in Fig. 1 [3]. It was demonstrated in [3] that varying the ratio,  $R/W$ , changes the separation between the two resonant modes shown in Fig. 2 that comprise the dual mode filter and thus the filter bandwidth. This technique, however, was limited and the minimum separation between the two resonant peaks could only be reduced to 0.3%. Due to the high-Q of these devices, large peak separations result in excessive pass-band ripple (PBR) even with large resistive filter terminations. Furthermore, it is often desirable in spectrum analyzer and RF communications applications to reduce filter bandwidth to improve sensitivity. Utilizing a notching technique [5] the resonant peak separation for the dual mode filters has been reduced to less than 0.1%, resulting in low insertion loss (< 7dB), low termination impedance (150  $\Omega$ ) filters with bandwidths as small as 0.15% and no PBR.

In order to address the applications outlined above it is necessary that the dual mode MEMS filter technology be able to cover the VHF (30-300 MHz) and UHF (0.3-3 GHz) frequency range. Scaling the dual mode filter in Fig. 1 to higher frequencies while operating in the fundamental mode requires a subsequent reduction in resonator width,  $W$ , which increases the filter impedance due to the smaller transduction area. While this increased impedance can be compensated by a subsequent increase in ring radius,  $R$ , this results in an excessively large filter area. It was demonstrated in [3] that operating an AlN ring resonator in overtone modes scales the operating frequency while maintaining a constant device size and impedance. This technique has been applied to dual mode filters where operation at the 5<sup>th</sup> and 10<sup>th</sup> overtones has scaled these filters to 550 and 1080 MHz, the highest frequency dual mode filters reported to date. These overtone filters can function as a 2, 3, or 4-port networks corresponding to single-ended, single-ended-to-differential (balun), or fully differential operation, which can be used to improve the rejection of out-of-band signals and spurious modes.

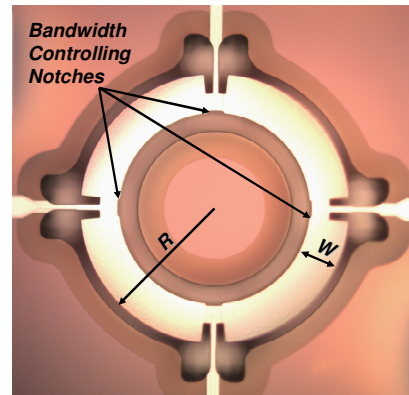


Figure 1: Fundamental dual mode AlN MEMS filter with bandwidth controlling notches and 4-anchors.

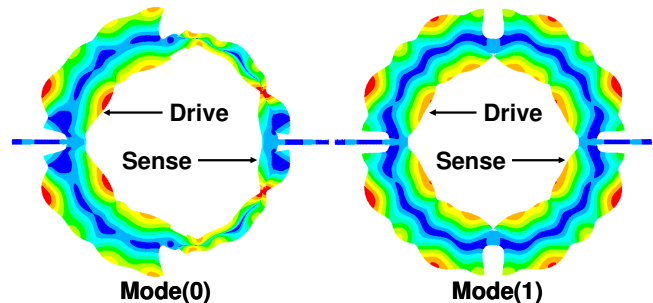


Figure 2: Anti-symmetric,  $Mode(0)$ , and symmetric,  $Mode(1)$ , resonant modes that comprise the dual mode filter shown for a 2-anchor filter.

## FUNDAMENTAL DUAL MODE FILTERS

A photo of the fundamental dual mode filter is shown in Fig. 1. The filter was fabricated using the process detailed in [3] which achieves highly oriented AlN films (rocking curve full-width-half-maximum of 1°) necessary for constructing low impedance filters. For the fundamental mode filters reported here, the bottom oxide thickness in [3] has been increased to 0.6  $\mu\text{m}$  in an ongoing effort to achieve passive temperature compensation. The dual mode filter in Fig. 1 has small internal notches that change the coupling stiffness between the drive and sense halves of the ring resulting in a decrease in the separation between  $Mode(0)$  and  $Mode(1)$  in Fig. 2 and filter bandwidth. The measured results from four dual mode filters with radius,  $R = 140\mu\text{m}$ , width,  $W = 40\mu\text{m}$ , 2-anchors and notching,  $N$ , of 0, 2, 3 and 4  $\mu\text{m}$  are shown in Fig. 3. Utilizing notching the resonant peak separation can be changed by nearly an order of magnitude providing the ability to design dual mode filters in the 0.1% to 1% bandwidth range. The measured and modeled (ANSYS finite element model) peak separations are shown in Fig. 4, demonstrating good agreement between the theoretical and experimental results. Since the impedance of each dual mode filter is approximately 150  $\Omega$ , that termination impedance was chosen for all the filters for comparison. The measured results of the dual mode filters with different amounts of notching are shown in Fig. 5 and a close-up

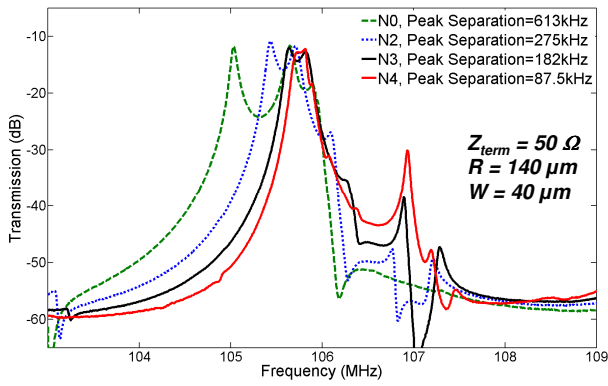


Figure 3: Measured transmission of dual mode AlN filters with an outer radius,  $R$ , of  $140 \mu\text{m}$ , width,  $W$ , of  $40 \mu\text{m}$ , 2-anchors and internal notching of 0, 2, 3, and 4  $\mu\text{m}$ . Notching decreases the peak separation from 613 kHz to 87.5 kHz.

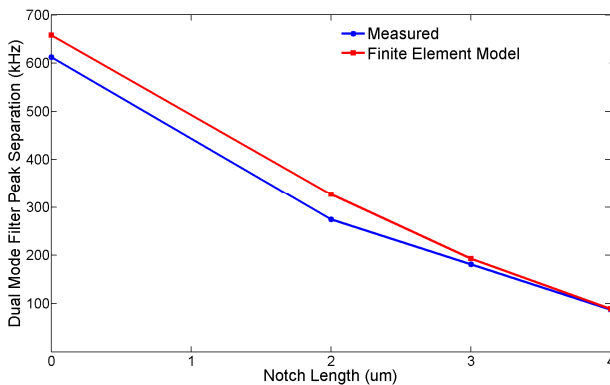


Figure 4: Measured and predicted peak separation vs. notching.

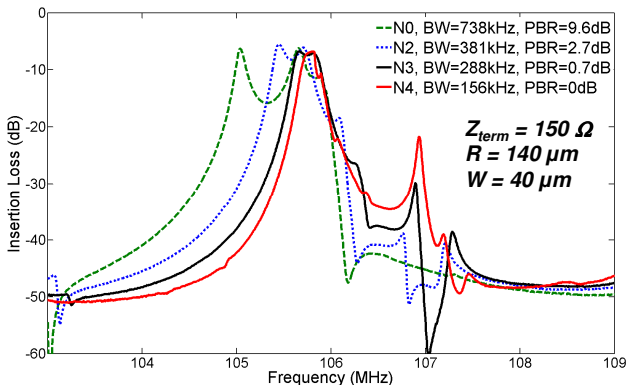


Figure 5: Measured transmission of dual mode AlN filters with,  $R = 140 \mu\text{m}$ ,  $W = 40 \mu\text{m}$ , 2-anchors and internal notching of 0, 2, 3, and 4  $\mu\text{m}$  when terminated with  $150 \Omega$ . The PBR is reduced to below 3 dB for all notched filters.

of the filter pass-bands are shown in Fig. 6. The ripple of each filter with notching is reduced to below 3 dB while the unnotched filter ripple is nearly 10 dB. While further increases in the termination impedance will continue to reduce the ripple, impedance increases are limited to a maximum of  $800 \Omega$  by the 1.8 pF shunt transducer and pad capacitance of the device. The wide bandwidth response of a dual mode filter is shown in Fig. 7 demonstrating greater than 50 dB of stop-band rejection. Since the motivation of this work is to construct single-chip filter banks it is important that the frequency spacing between filters be well

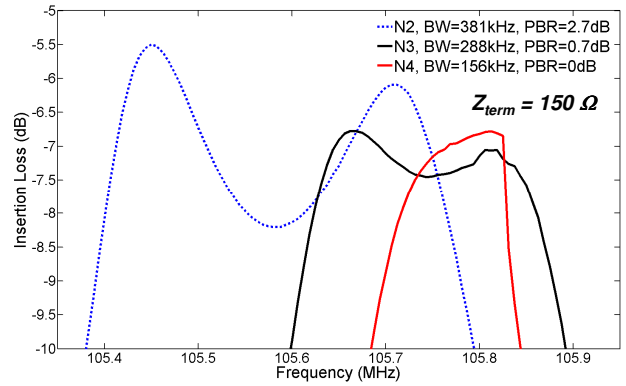


Figure 6: Close-up of the filter pass-bands from Fig. 5.

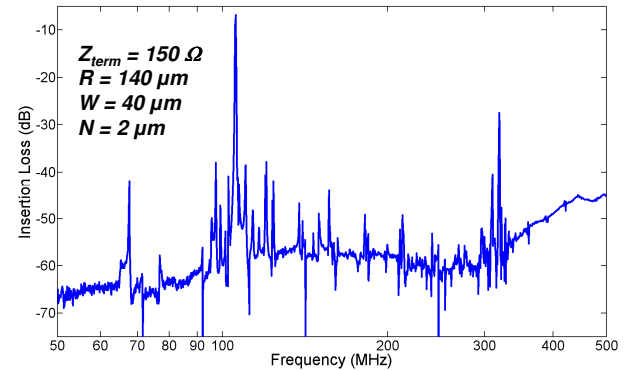


Figure 7: Wideband frequency response of the dual mode filter.

controlled and that the crosstalk between filters be low. Shown in Fig. 8 is the response of a bank of four dual mode filters located on the same  $1.7 \times 0.7 \text{ mm}$  die, all with radius,  $R = 140 \mu\text{m}$ , notching,  $N = 3 \mu\text{m}$ , 4-anchors, and widths,  $W$ , varying from  $40.25$  to  $41 \mu\text{m}$  in  $0.25 \mu\text{m}$  increments for a filter bandwidth of 250 kHz and a center-to-center frequency spacing of 600 kHz. The increase in termination impedance to  $200 \Omega$  (compared to the  $150 \Omega$  in Fig. 5) is needed to offset the slight decrease in Q for the 4-anchored filters compared to those with 2-anchors. Also shown in Fig. 8 is the crosstalk between physically adjacent filters spaced  $300 \mu\text{m}$  apart and frequency adjacent filters physically located  $500 \mu\text{m}$  apart. It can be seen in Fig. 8 that the filter bandwidths and frequency spacings are well controlled and that the crosstalk between filters is well below the filter stop-band rejection. Table 1 summarizes the performance of the notched fundamental dual mode filters and filter bank.

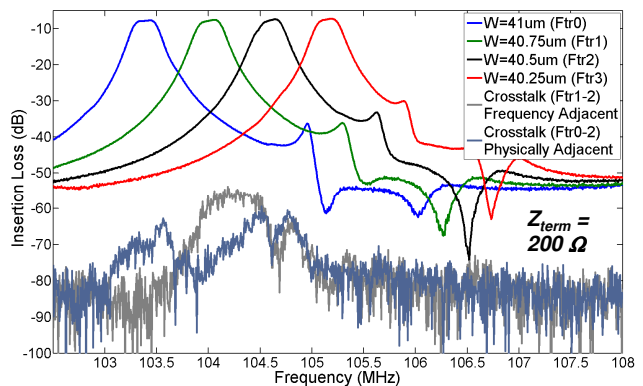


Figure 8: Frequency response and crosstalk performance of a 4-element, single-chip dual mode filter bank.

Table 1: Fundamental dual mode filter performance.

R ( $\mu\text{m}$ )	W ( $\mu\text{m}$ )	N ( $\mu\text{m}$ )	Termination Impedance ( $\Omega$ )	Insertion Loss (dB)	Center Frequency (MHz)	3 dB Bandwidth (kHz)	Pass-band Ripple (dB)	20 dB Shape Factor
140	40	0	150	6.2	105.4	744	9.6	1.8
140	40	2	150	5.5	105.6	381	2.7	2.6
140	40	2	200	5.2	105.6	394	1.7	2.6
140	40	3	150	6.8	105.7	288	0.7	3.2
140	40	4	150	6.8	105.8	156	0	4.5
140	40.25	3	200	7.7	103.4	260	0	3.1
140	40.5	3	200	7.6	104.0	252	0	3.2
140	40.75	3	200	7.4	104.6	240	0	3.5
140	41	3	200	7.3	105.2	244	0	3.5

## OVERTONE DUAL MODE FILTERS

In order to scale the dual mode filter architecture and its advantages of ultra-small size, a minimum number of devices for manufacturability, variable bandwidth and excellent stop-band rejection to higher frequencies without increasing size or insertion loss overtone operation is employed. It was demonstrated in [3] that through appropriate top Al electrode patterning on a single ring resonator that overtones can be selectively transduced and higher frequencies can be achieved without increasing motional impedance or device footprint. The 5<sup>th</sup> overtone dual mode filter (4-anchors) shown in Fig. 9 utilizes this technique to scale the 4<sup>th</sup> order fundamental dual mode filter in Fig. 1 to 550 MHz. The mode shapes in Fig. 2 now appear as overtones as shown in Fig. 10 (2-anchors), with the symmetric mode occurring at lower frequency. Overtone operation also allows for 3-port (balun) or 4-port (fully differential) dual mode filters. The measured 2 and 3-port frequency response of a 5<sup>th</sup> overtone dual mode filter with radius,  $R = 140 \mu\text{m}$ , width,  $W = 40 \mu\text{m}$ , notching,  $N = 4 \mu\text{m}$ , and 2-anchors is shown in Fig. 11. Inside the filter bandwidth S31 and S41 are 180° out-of-phase while transmission outside the filter bandwidth is dominated by capacitive feed-through placing S31 and S41 in phase. Thus, subtracting S41 from S31, which forms a single-ended-to-differential converter or balun, improves the stop-band rejection by 16 dB while reducing the insertion loss by 3 dB due to the increased transduction area. Further increases in stop-band rejection can be achieved utilizing fully differential operation as shown in Fig. 12, where the frequency response of two 5<sup>th</sup> overtone dual mode filters with 3 and 4  $\mu\text{m}$  of notching are presented. The notching technique demonstrated above for the fundamental dual mode filters can be used to control the bandwidth of overtone dual mode filters. As was the case for the fundamental

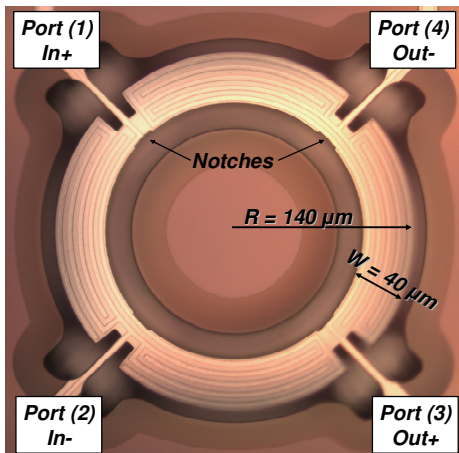


Figure 9. Fully differential 5<sup>th</sup> overtone dual mode AlN filter.

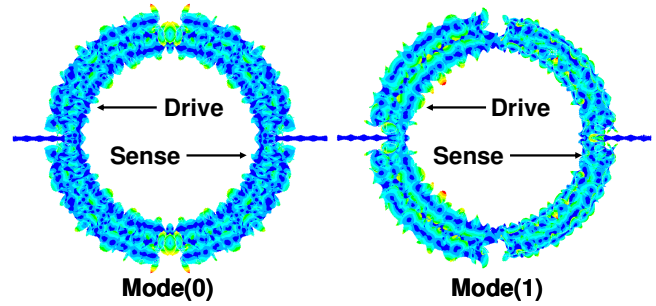


Figure 10: Symmetric, Mode(0), and anti-symmetric, Mode(1), resonant modes that comprise the 5<sup>th</sup> overtone dual mode filter.

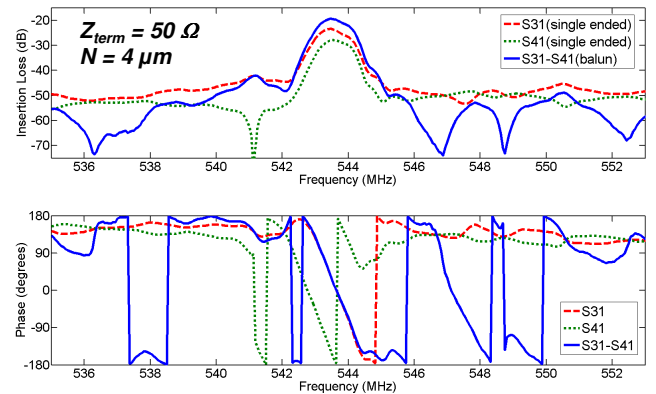


Figure 11: Frequency response of a 5<sup>th</sup> overtone dual mode filter when operated as a 2 and 3 port network. Ports 3 and 4 are 180° out of phase in the filter pass-band and in phase outside the pass-band. Subtracting the outputs to form a balun reduces insertion loss by 3 dB and increases stop-band rejection by 16 dB.

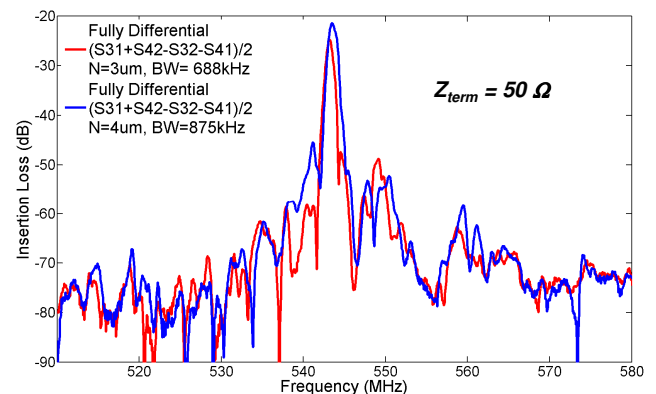


Figure 12: Fully differential frequency response of the 5<sup>th</sup> overtone dual mode filter with 3 and 4  $\mu\text{m}$  bandwidth controlling notches.

Table 2: Performance of 5<sup>th</sup> and 10<sup>th</sup> overtone dual mode filters with radius,  $R = 140 \mu\text{m}$ , and width,  $W = 40 \mu\text{m}$ .

Over-tone	# of ports	N ( $\mu\text{m}$ )	# of anchors	Insertion Loss (dB) @ 50 $\Omega$	Center Frequency (MHz)	3 dB Bandwidth (kHz)	PBR (dB)	20 dB Shape Factor	Stop-band Rejection (dB)	Min. Off-Overtone Rejection (dB)
5th	2	4	2	23.5	544	875	0	2.9	32	22
5th	3	4	2	19.4	544	875	0	2.6	48	35
5th	4	4	2	21.4	544	875	0	2.5	58	49
5th	4	3	2	22.7	543	688	0	3	56	47
5th	4	2	4	22.7	559	813	0	2.7	57	62
5th	4	0	4	24.7	559	625	0	3.5	55	60
10th	2	0.5	4	41.1	1084	750	0	-	9	0
10th	3	0.5	4	39.1	1084	750	0	9.2	20	24
10th	4	0.5	4	39.2	1084	750	0	11.8	24	46
10th	4	0.5	4	39.8	1084	1500	0	4.4	24	46

mode devices, notching has a much larger effect on the frequency of the anti-symmetric mode, controlling the bandwidth by moving it closer or further in frequency from the symmetric mode which is comparatively constant with notching. The wideband response of the 5<sup>th</sup> overtone dual mode filter is shown in Fig. 13 for 2, 3, and 4-port operation, where balun and fully differential configurations not only improve the stop-band rejection by 16 and 26 dB, but also the rejection of lower overtones by 13 and 27 dB. Table 2 summarizes the results for the 5<sup>th</sup> overtone dual mode filters and presents additional data on 10<sup>th</sup> overtone dual mode filters operating at 1.1 GHz.

## DISCUSSION AND CONCLUSIONS

Fundamental and overtone dual mode filters that realize a 4<sup>th</sup> order band-pass filter in a single device have been demonstrated at 100, 550, and 1085 MHz. A notching technique has been developed capable of controlling the bandwidth of these filters between 0.1 and 1%. Banks of dual mode filters around 100 MHz have shown excellent bandwidth and frequency spacing control and the crosstalk between filters is below the filter stop-band rejection. When scaled to overtone operation, these filters demonstrate higher than expected insertion loss. The 106 MHz fundamental dual mode filter with 4  $\mu\text{m}$  of notching in Fig. 3 and the 544 MHz, 5<sup>th</sup> overtone fully differential dual mode filter with 4  $\mu\text{m}$  of notching in Fig. 12 both have 0.16% bandwidth. The insertion loss of the 106 MHz filter at 50  $\Omega$  is 12.7 dB and is expected to be 3 dB higher in the 544 MHz filter due to the 25% reduction in transduction area (the input signal is divided between  $\text{in}^+$  and  $\text{in}^-$  from Fig. 9) if the quality factor,  $Q$ , of the resonant

modes are the same for the two filters. The measured insertion loss of the 5<sup>th</sup> overtone filter, however, is 21.4 dB, 5.7 dB higher than expected and increases slightly for the filter with 3  $\mu\text{m}$  of notching and decreased bandwidth of 688 kHz. It is suspected that resonator  $Q$  is being reduced at higher frequencies by the tapered sidewall of the AlN etch. AlN resonators measured at frequencies in excess of 1 GHz often exhibit two closely spaced resonant peaks due to the AlN taper. This particularly degrades the insertion loss of the 1.1 GHz 10<sup>th</sup> overtone filters due to their narrow bandwidth and high operating frequency. On going work in realizing a vertical AlN sidewall should significantly reduce dual mode filter insertion loss at higher frequencies. A path has been demonstrated for the realization of miniature, single device, 4<sup>th</sup> order filters covering the VHF and UHF frequency range for real time spectrum analysis and cognitive radio applications.

## ACKNOWLEDGEMENTS

The authors would like to thank the Microelectronics Development Laboratory staff at Sandia National Laboratories including Jim Stevens and Craig Nakakura for AlN process development. This work was supported by the Laboratory Directed Research and Development program at Sandia National Laboratories. Sandia National Laboratories is a multiprogram laboratory operated by the Sandia Corporation, Lockheed Martin Company, for the United States Department of Energy's National Nuclear Security Administration under contract DE-AC04-94AL85000.

## REFERENCES

- [1] G. Piazza, P. J. Stephanou and A. P. Pisano, "Single-Chip Multiple Frequency ALN MEMS Filters Based On Contour-Mode Piezoelectric Resonators," *Journal of Microelectromechanical Systems*, 16, 2, pp. 319-328, (2007).
- [2] D. J. D. Carter, J. Kang, D. White and A. E. Duwel, "Fabrication and Measurement of an IC-Compatible GHz-Range Piezoelectric Longitudinal Bar Resonator," *Proc. of the Solid-State Sensor, Actuator, and Microsystems Workshop*, (2004), pp. 254-257.
- [3] R. H. Olsson III, J. G. Fleming, K. E. Wojciechowski, M. S. Baker and M. R. Tuck, "Post-CMOS Compatible Aluminum Nitride MEMS Filters and Resonant Sensors," *Proc. IEEE Frequency Control Symposium*, (2007), pp. 412-419.
- [4] P. J. Stephanou, G. Piazza, C. D. White, M. B.J. Wijesundara and A. P. Pisano, "Piezoelectric Aluminum Nitride MEMS Annular Dual Contour Mode Filter," *Sensors and Actuators A*, 134, pp. 152-160, (2007).
- [5] G. K. Ho, Personal Communication, June 2007.

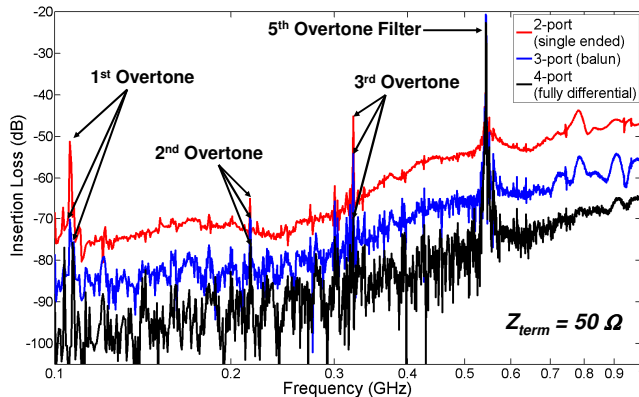


Figure 13: Wideband response of a 5<sup>th</sup> overtone dual mode filter. Utilizing balun and fully differential operation reduces feed-through of lower overtones by 13 and 27 dB.

# INFLUENCE OF SILICON ON QUALITY FACTOR, MOTIONAL IMPEDANCE AND TUNING RANGE OF PZT-TRANSDUCED RESONATORS

Hengky Chandralim<sup>1</sup>, Sunil A. Bhawe<sup>1</sup>, Ronald Polcawich<sup>2</sup>, Jeff Pulskamp<sup>2</sup>,  
Daniel Judy<sup>2</sup>, Roger Kaul<sup>2</sup> and Madan Dubey<sup>2</sup>

<sup>1</sup>OxideMEMS Laboratory, Cornell University, Ithaca, NY 14853, USA

<sup>2</sup>US Army Research Laboratory, Adelphi, MD 20783, USA

## ABSTRACT

This paper provides a quantitative comparison and explores the design space of PZT-only (Lead Zirconium Titanate) and PZT-on-Silicon length-extensional mode resonators for incorporation into RF MEMS filters and oscillators. We experimentally measured the correlation of motional impedance ( $R_X$ ) and quality factor ( $Q$ ) with the resonators' silicon layer thickness ( $t_{Si}$ ). For identical lateral dimensions and PZT-layer thickness ( $t_{PZT}$ ), the PZT-on-Silicon resonator has higher resonant frequency (dominated by silicon), higher  $Q$  (5,100 vs. 140) and lower motional impedance (51  $\Omega$  vs. 205  $\Omega$ ). However, PZT-only resonator demonstrated much wider frequency tuning range (5.1% vs. 0.2%).

## INTRODUCTION

Numerous applications in wireless communications and sensor networks have motivated the development of on-chip, high- $Q$  MEMS resonators and filters to realize portable radios that consume low power and operate at the global range of frequency standards. Dielectrically transduced thickness shear mode and contour-mode resonators have the capability to reach high frequency of operation while maintaining high  $Q$  and low motional impedance [1,2]. A band-pass filter can be constructed by electrically or mechanically coupling an array of these resonators. However, the inadequate effective coupling efficiency of the dielectrically transduced resonators limits the bandwidth of the filter, creating a demand for transducers with high electromechanical coupling coefficient.

Aluminum Nitride (AlN) is a popular material for fabrication of thin film bulk acoustic wave (BAW) and contour-mode resonators and filters because it possesses a high acoustic velocity, high quality factor and post-CMOS integration capability [3,4]. However, intermediate frequency applications have driven the investigations for new piezoelectric/ferroelectric materials for resonators. At low frequencies, ferroelectrics like PZT are better suited as they avoid thick film requirements and reduce the area required for the filters. Furthermore, PZT exhibits larger electromechanical coupling coefficient than AlN, enabling the design of larger % bandwidth filters [5].

A resonator with dynamically tunable center frequency will not only overcome fabrication tolerances and thermal drift, but will also facilitate filter design that has the ability to discern bandwidths between 0.1 MHz to 5 MHz, enabling a handheld analog spectral processor with voltage dependent dynamic frequency trimming and tuning. PZT has been previously shown to have frequency tuning capabilities in [6,7]. However, PZT-only resonators are well known to have low quality factor ( $Q < 300$ ) [5,8]. In order to overcome the low quality factor of PZT-only resonators, we developed a new fabrication technology to integrate PZT transduction with single-crystal silicon resonators.

## LENGTH-EXTENSIONAL MODE RESONATORS

Previous results have shown that length-extensional mode vibrations can be excited by sandwiching a piezoelectric transducer (AlN, Zinc Oxide, PZT, etc.) between metal electrodes [4,9].

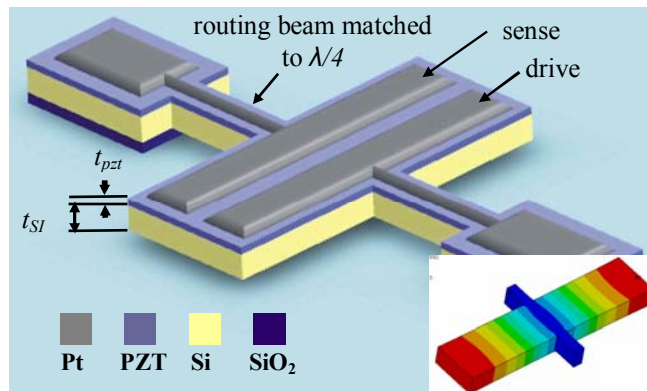


Figure 1: 3D schematic of PZT-on-silicon length-extensional mode resonator, and (inset) ANSYS mode shape.

However due to poor crystallinity and repeatability of the piezoelectric thin-films, several research groups have chosen to use the piezoelectric material for actuation and sensing, while utilizing single-crystal silicon (SCS) as the resonating structure [10,11] (Figure 1). In this effort, PZT transduced resonators were fabricated with and without a 10  $\mu\text{m}$  thick silicon device layer to explore the insertion loss and  $Q$  trade-offs between the two types of resonators. The frequency independent motional impedances of the fundamental mode of PZT transduced length-extensional mode two-port resonators are

$$R_{X\_PZT\text{-on-SOI}} = \frac{\pi}{2} \cdot \frac{\sqrt{E_{\text{Eff}} \cdot \rho_{\text{Eff}}}}{Q} \cdot \left( \frac{t_{Si} + t_{PZT}}{E_{PZT}^2 \cdot W \cdot d_{31}^2} \right) \dots (1)$$

$$R_{X\_PZT\text{-only}} = \frac{\pi}{2} \cdot \frac{\sqrt{E_{PZT} \cdot \rho_{PZT}}}{Q} \cdot \left( \frac{t_{PZT}}{E_{PZT}^2 \cdot W \cdot d_{31}^2} \right) \dots (2)$$

where  $\rho_{\text{Eff}}$  and  $E_{\text{Eff}}$  are the effective (PZT + silicon) density and Young's modulus,  $W$  is the resonator width,  $d_{31}$  is the transverse piezoelectric coefficient, and  $\rho_{PZT}$  and  $E_{PZT}$  are the density and Young's modulus of the PZT thin-film. PZT is acoustically lossy material resulting in PZT-only resonators having low  $Q$ . Integrated PZT transduction with single-crystal silicon resonators retains the mechanical energy within the high quality silicon device layer. Equation 1 indicates that there will be a net decrease in  $R_X$  if the improvement in  $Q$  outweighs the increase in  $t_{Si}$  for PZT-on-silicon resonators. However, due to the silicon carrier layer, the PZT-on-silicon resonators have to perform extra work in order to overcome the inertia of the proof-mass. Hence the PZT-only resonators will exhibit higher pole-zero separation than PZT-on-silicon resonators in a one-port configuration. Therefore by changing  $t_{Si}$  we can tradeoff between narrow bandwidth and wide bandwidth filters.

## FABRICATION PROCESS

The fabrication process flow for the PZT-on-silicon resonators is shown in Figure 2. We started with an SOI wafer with 10  $\mu\text{m}$

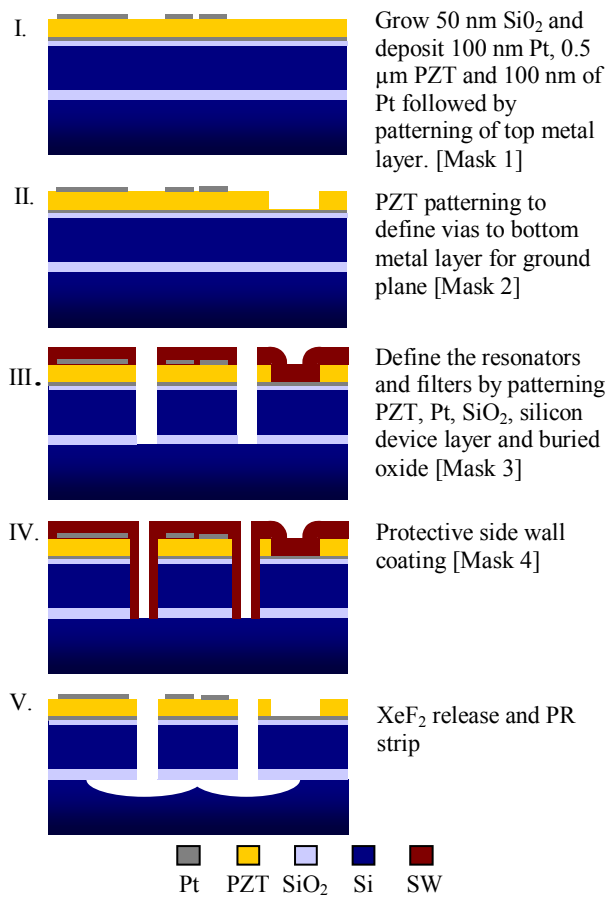


Figure 2: Fabrication process-flow for PZT-on-Silicon resonators. By replacing the SOI wafer with a Silicon wafer, we used the same fabrication process to manufacture PZT-only resonators.

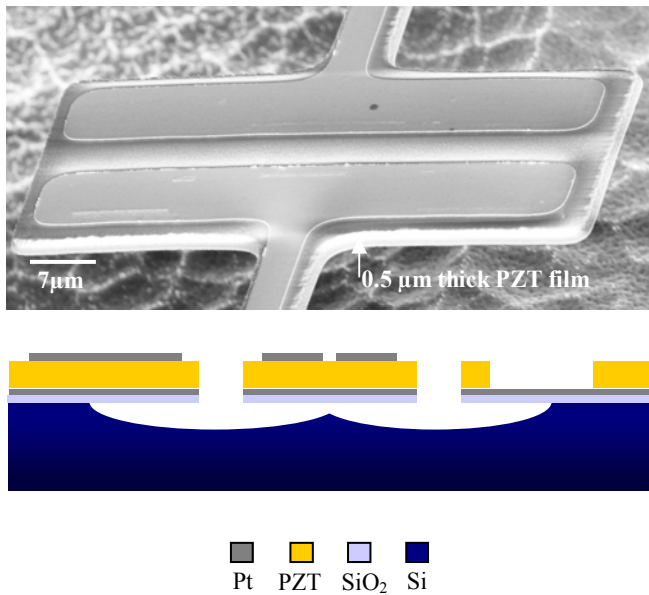


Figure 3: SEM and process cross-section of a released PZT-only resonator. The cross-section is drawn in such a way as to identify the signal and ground pads, the drive and sense electrodes and the released resonator.

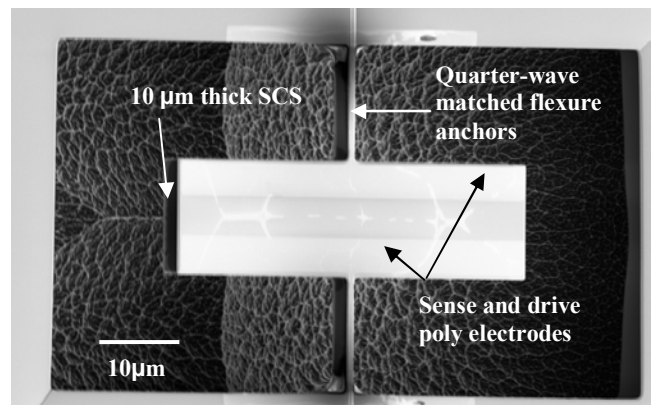


Figure 4: SEM of released PZT-on-silicon resonator. The isotropic pit due to the  $\text{XeF}_2$  etch can be seen in the background.

thick silicon device layer. We deposited 50 nm  $\text{SiO}_2$  to mitigate lattice mismatch issues between the PZT-metal stack and the silicon. Then we successively deposited 100 nm platinum bottom metal, 0.5  $\mu\text{m}$  PZT [12] and another 100 nm platinum top metal. We patterned the top metal electrodes and signal pads using lift-off followed by pattern and wet-etch of PZT to open ground pads. The resonator was then defined by anisotropic etching of the PZT, platinum, silicon dioxide, silicon device layer and the buried oxide. A novel technique of dry releasing the devices using a gentle front-side  $\text{XeF}_2$  alleviated the need for backside DRIE used in [13]. Figures 3 and 4 show PZT-only and PZT-on-silicon bar resonators fabricated in this process.

## MEASUREMENT RESULTS

The resonators were characterized after performing SOLT calibration followed by SOT de-embedding. Measured transmission response of the PZT-only and PZT-on-silicon resonators with the exact same lateral dimensions in air at room temperature and pressure are shown in Figure 5. The PZT-on-silicon resonators exhibit higher  $Q$ , higher resonant frequency and lower motional impedance compared to their PZT-only counterparts. These measurement results confirm that integrating

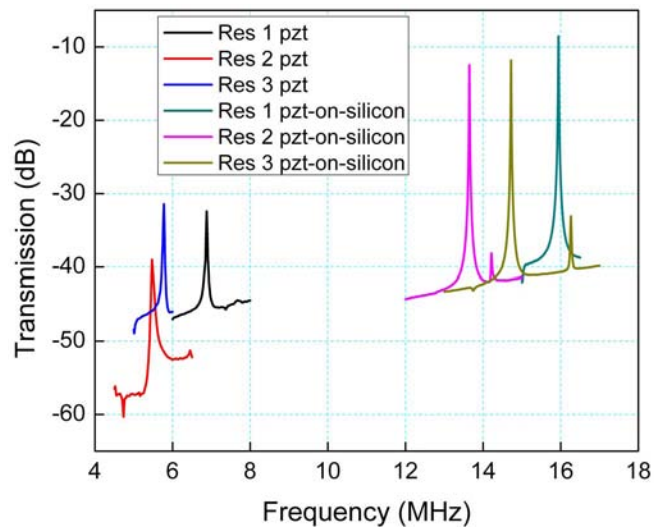


Figure 5: Measured transmission response of PZT-only and PZT-on-Silicon resonators with the exact same lateral dimensions in air at room temperature and pressure.

PZT transduction with single-crystal silicon retains the mechanical energy within the high quality silicon device layer. The improvement in  $Q$  ( $35\times$ ) outweighs the increase in  $t_{Si}$  ( $10\ \mu\text{m}$ ), resulting in a net decrease in  $R_X$  (Tables 1 and 2).

Table 1: The measured characteristics of PZT-only resonators.

	Res 1 PZT	Res 2 PZT	Res 3 PZT
Dimensions ( $\mu\text{m}^2$ )	240 x 40	280 x 60	260 x 60
$Q$	202	91	241
$f_{CENTER}$ (MHz)	6.88	5.47	5.78
$R_X$ ( $\Omega$ )	4,078	8,812	3,628

Table 2: The measured characteristics of PZT-on-SOI resonators.

	Res 1 PZT-on-silicon	Res 2 PZT-on-silicon	Res 3 PZT-on-silicon
Dimensions ( $\mu\text{m}^2$ )	240 x 40	280 x 60	260 x 60
$Q$	5,040	3,820	4,224
$f_{CENTER}$ (MHz)	15.94	13.65	14.72
$R_X$ ( $\Omega$ )	167	319	290

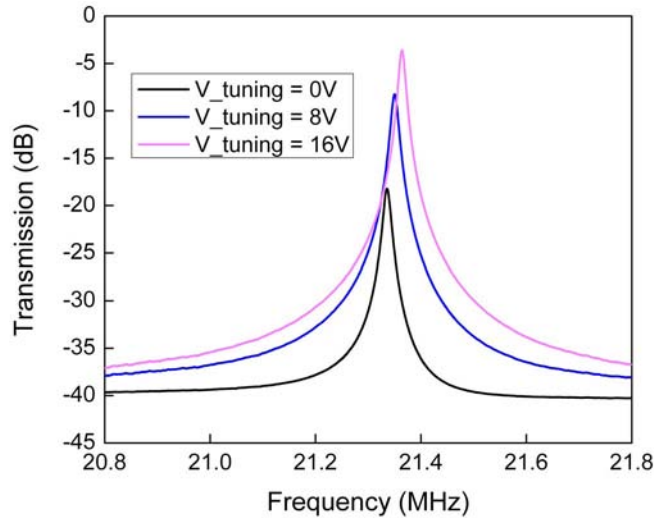


Figure 6: Measured transmission of a  $190\ \mu\text{m} \times 40\ \mu\text{m}$  PZT transduced resonator on  $10\ \mu\text{m}$  silicon with different bias voltages in air at room temperature and pressure. 0.2% frequency tuning capability is observed due to DC bias dependent Young's modulus and density of PZT thin film. (only 3 transmission plots are shown to avoid crowding).

Table 3: The measured characteristics of PZT-on-SOI resonator with five different bias voltages.

Tuning Voltage	0 V	4 V	8 V	12 V	16 V
$Q$	2,020	2,021	2,021	2,022	2,023
$f_C$ (MHz)	21.332	21.340	21.345	21.355	21.365
$R_X$ ( $\Omega$ )	582	223	142	83	50

## DC VOLTAGE TUNING

Wang *et al* and Cho *et al* have demonstrated that PZT has a DC-bias dependent Young's modulus, density and permittivity [6,7]. As DC bias increases, the increase in the piezoelectric coefficient,  $d_{31}$ , and decrease in permittivity leads to an overall increase in the electromechanical coupling coefficient and decrease in  $R_X$ . By taking an advantage of the DC bias dependent piezoelectric coefficient  $d_{31}$ , we can compensate insertion loss of the resonators due to air damping, anchor losses and fabrication errors. The measured transmission of a  $190\ \mu\text{m} \times 40\ \mu\text{m}$  PZT transduced resonator on  $10\ \mu\text{m}$  silicon with different bias voltages is shown in Figure 6. A 0.2% frequency tuning capability is observed due to the DC bias dependent Young's Modulus of PZT thin film. Since the resonant frequency is dominated by the silicon device layer, there is very little resonant frequency tuning, whereas the improvement in electromechanical coupling leads to  $11\times$  improvement in motional impedance at 16V DC bias. The measured characteristics of the resonator are summarized in Table3.

In contrast, the measured transmission of a  $90\ \mu\text{m} \times 20\ \mu\text{m}$  PZT-only resonator with different bias voltages in air at room temperature and pressure is shown in Figure 7. The PZT-only resonators demonstrate 5.1% DC bias dependent frequency tuning capability, the highest tuning range reported by any piezoelectrically transduced contour mode resonators to date. The measured characteristics of the resonator are summarized in Table4.

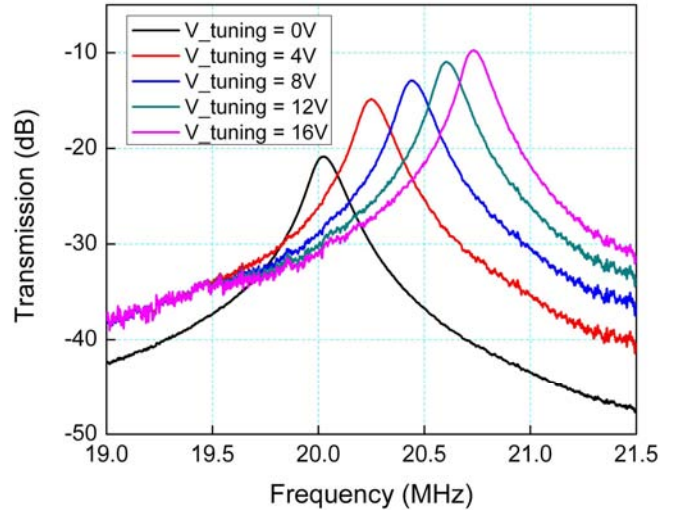


Figure 7: Measured transmission of a  $90\ \mu\text{m} \times 20\ \mu\text{m}$  PZT-only resonator with five different bias voltages in air at room temperature and pressure. 5.1% frequency tuning capability is observed due to DC bias dependent Young's modulus and density of PZT thin film.

Table 4: The measured characteristics of PZT-only resonator with different bias voltages.

Tuning Voltage	0 V	4 V	8 V	12 V	16 V
$Q$	125	126	136	147	148
$f_C$ (MHz)	20.025	20.250	20.440	20.610	20.730
$R_X$ ( $\Omega$ )	1,004	453	343	253	207

## CONCLUSION

We have fabricated and characterized DC field dependent PZT transduced length-extensional mode resonators with and without silicon device layer. By varying the silicon thickness (thereby the % mass of crystalline silicon in the resonator) and DC bias voltage we can define the desired  $Q$  and frequency tuning range of the resonators, and tradeoff between steep-walled narrow-bandwidth filters, low- $Q$  wide-bandwidth filters and center frequency agility.

## ACKNOWLEDGEMENTS

The authors wish to acknowledge the assistance and support of Joel Martin and Brian Power of General Technical Services and Richard Piekarski from the ARL for their hard work with device fabrication.

## REFERENCES

- [1] H. Chandralim, D. Weinstein, L. F. Cheow and S. A. Bhave, "Channel-select micromechanical filters using high- $\kappa$  dielectrically transduced MEMS resonators," *MEMS 2006*, Istanbul, Turkey, January 22-26, 2006, pp. 894-897.
- [2] H. Chandralim and S. A. Bhave, "Digitally-tunable MEMS filter using mechanically-coupled resonator array," *MEMS 2008*, Tucson, Arizona, January 13-17, 2008, pp. 1020-1023.
- [3] R. C. Ruby, A. Barfknecht, C. Han, Y. Desai, F. Geefay, G. Gan, M. Gat, and T. Verhoeven, "High-Q FBAR filters in a wafer-level chip-scale package," *ISSCC 2002*, San Francisco, California, February 3-7, 2002, pp. 184-185.
- [4] G. Piazza, P. J. Stephanou and A.P. Pisano, "Single-chip multiple-frequency AlN MEMS filters based on contour-mode piezoelectric resonators," *JMEMS* 16 (2) 2007, pp. 319-328.
- [5] J. D. Larson, S. R. Gilbert and B. Xu, "PZT material properties at UHF and microwave frequencies derived from FBAR measurements," *Ultrasonics Symposium 2004*, Montreal, Canada, August 24-27, 2004, pp. 173-177.
- [6] Q. Wang, *et al*, "Effect of DC bias field on the complex materials coefficients of piezoelectric resonators," *Sensors and Actuators A: Physical* 109 (1-2) 2003, pp. 149-155.
- [7] J. Cho, *et al*, "Optimization of electromechanical coupling for a thin-film PZT membrane: II. Experiment," *Journal of Micromechanics and Microengineering* 15 (10) 2005, pp 1804-1809.
- [8] B. Piekarski, D. DeVoe, M. Dubey, R. Kaul and J. Conrad, "Surface micromachined piezoelectric resonant beam filters," *Sensors and Actuators A: Physical* 91 (3) 2001, pp. 313-320.
- [9] B. Antkowiak, *et al*, "Design of a high-Q, low-impedance, GHz-range piezoelectric MEMS resonator," *Transducers'03*, Boston, Massachusetts, June 8-12, 2003, pp. 841-846.
- [10] S. Humad, R. Abdolvand, G. K. Ho, G. Piazza and F. Ayazi, "High frequency micromechanical piezo-on-silicon block resonators," *IEDM 2003*, Washington DC, December 8-10, 2003, pp. 957-960.
- [11] A. Jaakkola, *et al*, "Piezotransduced single-crystal silicon BAW resonators," *Ultrasonics Symposium 2007*, New York City, New York, October 28-31, 2007, pp. 1653-1656.
- [12] S. Dey, K. Budd, and D. Payne, "Thin-film ferroelectrics of PZT of sol-gel processing," *TUFFC* 35 (1) 1988, pp. 80-81.
- [13] G. Ho, R. Abdolvand and F. Ayazi, "High order composite bulk acoustic resonators," *MEMS 2007*, Kobe, Japan, January 21-25, 2007, pp. 791-794.

# NOISE ANALYSIS OF A TUNNELING ACCELEROMETER BASED ON STATE SPACE STOCHASTIC THEORY

L.A. Oropeza-Ramos<sup>1</sup>, N. Kataria<sup>2</sup>, C.B. Burgner<sup>1</sup>, K.J. Åström<sup>1</sup>, F. Brewer<sup>2</sup> and K.L. Turner<sup>1</sup>

<sup>1</sup>Mechanical Engineering Department <sup>2</sup>Computer Science Department  
University of California, Santa Barbara, CA, 93106 USA

## ABSTRACT

This paper presents noise analysis of a lateral tunneling accelerometer, considering Brownian motion, Nyquist-Johnson and shot noise. The tunneling accelerometer has been fabricated; a low noise differential transresistance amplifier and a digital integral controller have been designed and implemented. Noise analysis has been made based on state space models and compared with experimental results.

## INTRODUCTION

The measurement of acceleration, in addition to being a central element of inertial guidance systems, has application to a wide variety of commercial problems (including automotive, medical, industrial, aeronautics and defense sectors). Different transducer mechanisms have been used in micro fabricated accelerometers [1].

Tunneling is a highly sensitive method for measuring position, which was inspired by the early work on scanning tunneling microscope. An electrostatic actuator is used, which has the advantage over capacitive, piezo-resistive and piezoelectric displacement transducers that the critical sensing area is reduced, and sensitivity and bandwidth are higher. The tunneling current is also largely independent of temperature.

## Motivation

An understanding of the effects of noise is important to determine the factors that limit sensor resolution. There has been considerable work on tunneling accelerometers [2-8]. The analysis presented by Gabrielson [10] concludes that thermal noise is the main factor for most of the tunneling accelerometers. Work from JPL and Stanford reported large amounts of noise at low frequencies (below 100 Hz), and their origin is still under investigation. A mathematical model to simulate the 1/f noise related to surface adsorption-desorption process is presented in [9]. In this paper, we use a different theoretical approach that makes it very easy to investigate the effects of different noise sources on a tunneling accelerometer. The analysis is compared to the experimental data using a simple integrating controller.

## Principle

In tunneling displacement transducers, the theoretical relationship between the tunneling electrode gap and the tunneling current is given by

$$I_t \propto V_b e^{-\alpha\sqrt{\Phi}x_o} \quad (1)$$

where  $I_t$  is the tunneling current,  $V_b$  is tunneling bias across the tunneling electrode gap;  $\alpha$  is the tunneling constant;  $\Phi$  is the effective height of the tunneling barrier or the effective work function and  $x_o$  is the shortest tunneling gap between tunneling tip and the proof-mass electrode. Electron tunneling can only be observed when the gap between a pair of clean metal electrodes is nearly on the order of 1 nm.

When the micro machined tunneling accelerometer is accelerated, the proof-mass experiences an inertial force that causes its motion (see Figure 1). Because of the strong exponential dependence of current distance, it is necessary to use force feedback with the tip to keep a constant tunneling current. In this

case, an electrostatic force is used to control the position of the proof mass. Comparing the tunneling current to a reference signal, the feedback control adjusts the electrostatic rebalance force that maintains a constant tunneling electrode separation, as is represented by the block diagram in Figure 2. The feedback force is the measurement of the external acceleration.

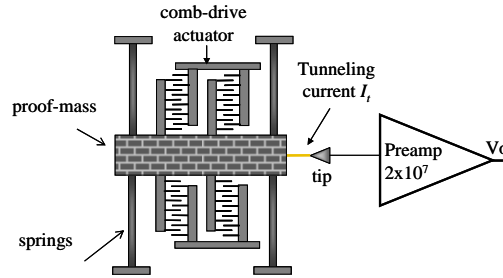


Figure 1. Schematic of a tunneling accelerometer structure.

## THE SYSTEM

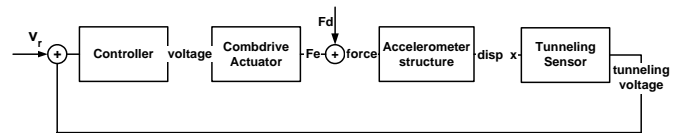


Figure 2. Schematic block diagram of the closed loop tunneling accelerometer system.

As shown in Figure 1, the basic design of a lateral tunneling accelerometer consists of four elements: the proof-mass that moves relative to the substrate in response to an external stimulus, a sensor based on the tunneling tip, an electrostatic actuator with interleaved comb fingers, and folded flexural springs. The oscillatory can be simplified as a lumped model of a spring-mass-damper system. The equation of motion is:

$$m \frac{d^2x}{dt^2} + c \frac{dx}{dt} + kx = F_e + F_d \quad (2)$$

where  $x$  is displacement,  $m$  is the mass,  $k$  and  $c$  are the stiffness and damping coefficients respectively,  $F_e$  is the electrostatic force and  $F_d$  is the external disturbance.

Our device is based on the device designed in [11]. It consists of a large proof-mass actuated laterally by an electrostatic actuation force governed by:

$$F_e = N \frac{\epsilon \cdot h}{d} V^2 \quad (3)$$

where  $N$  is the number of movable fingers,  $\epsilon$  is the air dielectric constant,  $d$  is the space between fingers,  $h$  is the depth of the fingers and  $V$  is the voltage applied.

## NOISE ANALYSIS

In this section the stochastic dynamical model of the closed loop system is constructed using stochastic control theory [12]. Thermo-mechanical noise from the proof-mass motion, shot noise in the tunneling junction, and Johnson-Nyquist resistor noise are considered. The analysis is based on linearized models which block diagram is shown in Figure 4.

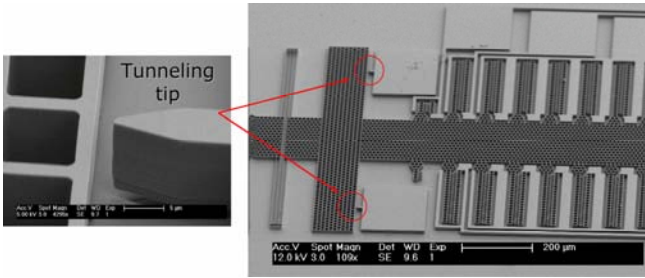


Figure 3. Electron micrograph of the large lateral tunneling accelerometer fabricated in a SOI wafer (20 $\mu$ m Si/5 $\mu$ m SiO<sub>2</sub>).

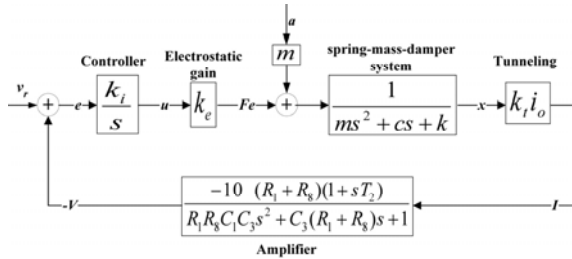


Figure 4. Block Diagram of the linearized model.

### Suspended Mass

The accelerometer structure is modeled by equation (2). The force-voltage relation of the comb actuator is  $F_e = IV^2$  where  $I = N\epsilon h/d$ . Let  $V^2 = (V_o + u)^2$ , where  $V_o$  is the bias voltage necessary to reach the tunneling operating point and  $u$  is the feedback control signal. Thus  $V^2 = (V_o^2 + 2V_o u + u^2)$ . The middle term dominates since  $V_o \gg u$ . Introducing gain  $k_e = 2IV_o$ , the force  $F_e$  in (2) is simply  $F_e = k_e u$ . The disturbances represented by  $F_d$  in (2) correspond to the external acceleration and the thermal forces  $r$  and  $n_{th}$ , hence  $F_d = r + n_{th}$ .

Introducing  $a = (k/m)^{1/2}$  and  $c/m = 2\zeta a$  and the state variables  $x_1 = x$  and  $x_2 = \dot{x}$ , the spring-mass-damper system (2) is given by:

$$\dot{x}_a = A_a x_a + B_a (k_e u + r + n_{th}); \quad y_a = C_a x_a$$

where

$$x_a = \begin{pmatrix} x_1 \\ x_2 \end{pmatrix}; \quad A_a = \begin{pmatrix} 0 & 1 \\ -a^2 & -2\zeta a \end{pmatrix}; \quad B_a = \begin{pmatrix} 0 \\ \frac{1}{m} \end{pmatrix}; \quad C_a = (1 \quad 0)$$

Modeling the noise as ideal white noise, the system can be described by the linear stochastic differential equation:

$$dx_a = A_a x_a dt + B_a w_{th} \quad (5)$$

where  $w_{th}$  is a Wiener process with incremental covariance  $Edw_{th}^2 = r_{th} dt$ . The parameter  $r_{th}$  can be determined from the Boltzmann's equipartition law which gives  $r_{th} = 2ck_B T$ , where  $T$  is the absolute temperature. The corresponding spectral density is  $\Phi(\omega) = ck_B T / \pi [N^2 / \text{rad/s}] = 2ck_B T [N^2 / \text{Hz}]$ . Notice that spectral density is proportional to the damping coefficient  $c$  (dissipation-fluctuation property).

### Tunneling Detector

The relation between tunneling current and tip-electrode distance is given by equation (1). Linearizing it around the operating point  $x_o = 10\text{\AA}$  gives

$$k_t = \left. \frac{dI_t}{dx} \right|_{x=x_o} = \alpha \sqrt{\Phi} i_o \quad [A/m]$$

The total current is then

$$I = k_t (i_o) x + n_t (i_o) \quad (6)$$

where the gain and the noise intensity depends on the nominal tunneling current  $i_o$ . The tunneling noise  $n_t$  is attributed to the

discreteness of the electrical charges, known as shot noise, which has an incremental covariance of  $E(dw_t)^2 = r_t dt$  with  $r_t = qi_o [A^2/\text{Hz}]$ .

### Preamplifier

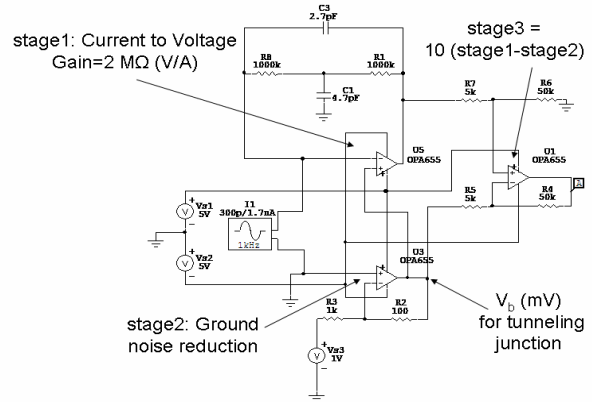


Figure 5. Circuit diagram of the differential preamplifier with a gain of  $2 \times 10^7$  V/A.

A low noise transimpedance amplifier based on differential voltage sensing scheme is implemented for tunneling detection. It is designed to alleviate ground noise and ground loop problems. The circuit diagram is shown in Figure 5.

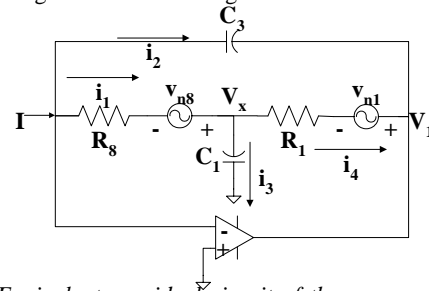


Figure 6. Equivalent non-ideal circuit of the preamp stage 1. The voltage sources represent the resistors fluctuations.

Resistors are modeled as ideal resistors with a series voltage source representing Johnson-Nyquist noise, as shown in Figure 6. The noise in the first stage dominates and we will therefore only consider noise in resistors  $R1$  and  $R8$ . Introduce  $x_3 = V_x$  and  $x_4 = 10V_1$  (note that the last stage of the circuit adds a gain of 10 to the output  $V_1$ ), the state space representation of the preamplifier is given by

$$\dot{x}_d = A_d x_d + B_d I + B_R n_R \quad y_d = C_d x_d \quad \text{where}$$

$$x_d = \begin{pmatrix} x_3 \\ x_4 \end{pmatrix}; \quad A_d = \begin{pmatrix} -\left(\frac{1}{C1R8} + \frac{1}{10R1C1}\right) & \frac{1}{R1C1} \\ \frac{-10}{C3R8} & 0 \end{pmatrix}; \quad B_d = \begin{pmatrix} 0 \\ \frac{10}{C3} \end{pmatrix}$$

$$B_R = \begin{pmatrix} \frac{-1}{R1C1} & \frac{1}{C1R8} \\ 0 & \frac{10}{C3R8} \end{pmatrix}; \quad C_d = (0 \quad 1)$$

The vector  $n_R$  represents the noise in the preamplifier which primarily is due to the resistors in the first stage. Substituting  $I$  with equation (6), the tunneling detector with noise sources can be represented as a stochastic differential equation:

$$dx_d = A_d x_d dt + B_d k_t (i_o) x_t dt + B_d dw_t + B_R dw_R \quad (7)$$

$y_d = C_d x_d$ ;  $w_t$  and  $w_R$  are Wiener processes with incremental

covariance:  $R_d = B_d r_t B_d^T + B_R R_R B_R^T$ ;  $r_t = qi_o$ ;  $R_R = \begin{pmatrix} r_{R1} & 0 \\ 0 & r_{R8} \end{pmatrix}$

and  $r_{R1} = 2k_B TR_1$   $r_{R8} = 2k_B TR_8$ .

## Controller

The integral controller can be modeled as

$$u = k_i \int_0^t (v_r(\tau) - x_4(\tau)) d\tau$$

where  $k_i$  is determined by the design procedure in [13] and  $v_r$  is the reference voltage corresponding to the tunneling set point. Defining a new state  $x_5$  such that  $\dot{x}_5 = v_r - x_4$ , the differential equation that describes the control action is defined as

$$dx_c = -x_4 dt + v_r dt \quad y_c = u = k_i x_5 \quad (8)$$

## The Complete System

The realization of accelerometer, tunneling detector and controller systems, equations (5), (7) and (8), is incorporated into a state space model and its stochastic differential equation is described as:

$$dx = Axdt + dw \quad (9)$$

where  $w$  is a Wiener process with incremental covariance  $Edwdw^T = Rdt$ , and

$$R = \begin{pmatrix} R_a & 0 & 0 \\ 0 & R_d & 0 \\ 0 & 0 & 0 \end{pmatrix} \quad R_a = B_a r_{th} B_a^T = \begin{pmatrix} 0 & 0 \\ 0 & \frac{r_{th}}{m^2} \end{pmatrix}$$

$$A = \begin{pmatrix} 0 & 1 & 0 & 0 & 0 \\ -a^2 & -2ga & 0 & 0 & \frac{k_b k_i}{m} \\ 0 & 0 & -(\frac{1}{C_{1RS}} + \frac{1}{C_{1RI}}) & \frac{1}{C_{1RI}} & 0 \\ 0 & 0 & \frac{1}{C_{3RS}} & 0 & 0 \\ 0 & 0 & 0 & -1 & 0 \end{pmatrix} \quad B = \begin{pmatrix} 0 & 0 & 0 & 0 & 0 \\ \frac{1}{m} & 0 & 0 & 0 & 0 \\ 0 & 0 & \frac{1}{C_{1RI}} & \frac{1}{C_{1RS}} & 0 \\ 0 & \frac{1}{C_3} & 0 & \frac{1}{C_{3RS}} & 0 \\ 0 & 0 & 0 & 0 & 0 \end{pmatrix}$$

The steady state covariance of the fluctuations are given by the Lyapunov equation [12]

$$AP + PA^T + R = 0 \quad (10)$$

which can be solved numerically with a standard Matlab program.

Table 1. System parameters.

$h=18 \mu m$	$T=293 K$	$f_o=4.2 kHz$	$i_o=1.75 nA$
$m=4.917 \mu g$	$N=540 fingers$	$R1=1 M\Omega$	$k_i=4.01 A/m$
$Q=10$	$\epsilon_o=8.854 \times 10^{-12} F/m$	$R8=1 M\Omega$	$k_e=9.2 \times 10^{-7} N/V$
$d=2.65 \mu m$	$\alpha=1.025 [A^{-1} eV^{0.5}]$	$C1=4.7 pF$	$k_i=45$
$\Phi=0.05 eV$	$k_B=1.3807 \times 10^{23} J/K$	$C3=10 pF$	$V_o \sim 14.2 V$

The contributions of the different noise sources can be computed by setting corresponding parameters to zero. Thus, the standard deviation of the output of the preamplifier ( $\sigma_{*} = p_{44}^{1/2}$ ) due to each noise source is calculated and presented in Table2.

Table 2. Contribution to different noise sources (units: mV)

$\sigma_{th}=3.052$	$r_{th} \neq 0$	$r_i=0$	$r_{R1}=0$	$r_{RS}=0$
$\sigma_i=0.056$	$r_i \neq 0$	$r_{th}=0$	$r_{R1}=0$	$r_{RS}=0$
$\sigma_{R1}=0.14$	$r_{R1} \neq 0$	$r_{th}=0$	$r_i=0$	$r_{RS}=0$
$\sigma_{R1}=0.17$	$r_{RS} \neq 0$	$r_{th}=0$	$r_i=0$	$r_{R1}=0$
$\sigma_{tot}=3.1$	$r_{th} \neq 0$	$r_i \neq 0$	$r_{R1} \neq 0$	$r_{RS} \neq 0$

It is clear that the noise is dominated by the thermal noise. Considering contributions from all the noise sources, the fluctuations in the preamplifier output have a standard deviation of  $\sigma_{tot}=3.1 mV$ .

To analyze the noise behavior in the frequency domain, lets consider the theorem of the spectral factorization of continuous time process [12], which establishes that a stochastic input signal with spectral density  $\Phi_u(\omega)$  propagates into a stable dynamical system  $G(s)$  in such a way that the output signal has a spectral density  $\Phi_y=G(i\omega)G(-i\omega)\Phi_u(\omega)$ . Figure7 is the plot of the spectral

densities of the preamp output due to each noise source and the total sum. Notice that at low frequencies, the thermo-mechanical noise  $n_{th}$  has the larger contribution but at high frequencies it is the resistor noise  $n_{RS}$  of the amplifier who dominates, as expected.

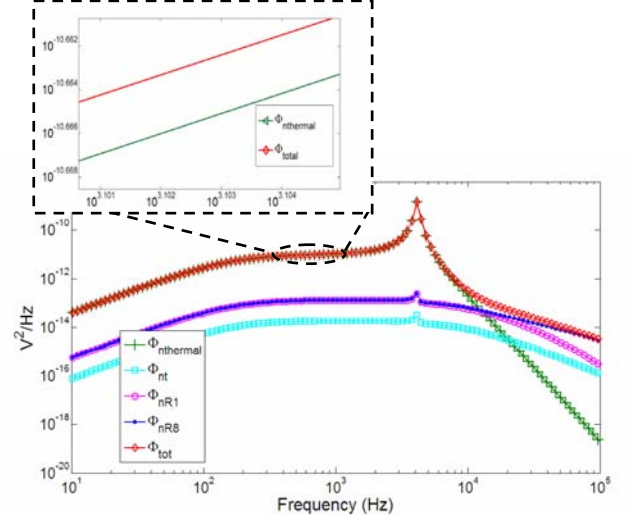


Figure 7. Power spectral densities of the tunneling voltage due to each noise source.

## EXPERIMENTAL RESULTS

The controller is implemented in a digital platform based on Mathworks© xPC Target prototyping.

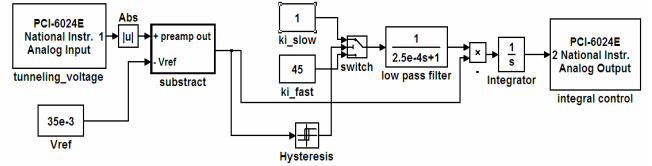


Figure 8. Simulink model of the controller implementation, including the I/O blocks that represent the analog input/output of the NI 6024E DAQ board.

Figure 8 shows the Simulink model of the system. The analog input from the DAQ board corresponds to the tunneling voltage of the preamplifier. This signal is compared to a reference of  $35 mV$  which corresponds to a tunneling current of  $1.75 nA$ . The difference between the tunneling voltage and the reference is the error signal to the controller, which is simply and integrator with gain  $k_{i\_fast}$ . This gain is used during tunneling.

To start tunneling it is necessary to move the mass gradually towards the tunneling tip. This is also accomplished using the integrating controller but with a lower gain. When the mass is far away from the tip it thus moves with constant speed given by the set point. When tunneling starts, the error signal becomes small and the gain is switched to the larger value automatically. A hysteresis has been introduced to avoid spurious switches. This simple device has proven very robust and its use is straightforward.

The smallest possible sampling time, due to hardware limitations, is  $T_s=2 \times 10^{-4} sec$ . Figure9 shows the responses of the tunneling transient and the control action  $u$  during  $100 sec$  monitoring. There is no tunneling initially and observe that the variations in the measured signal are due to resistor noise. The control signal increases linearly and the mass approaches the tunneling tip. Tunneling begins after  $50 sec$  at which point the tunneling current grows exponentially towards  $35 mV$ . The controller gain is then switched keeping the tunneling current close

to the set point. The experiment is robust and reproducible but the noise level varies somewhat depending on the general noise level in the lab. From the curves shown in Figure 9 the standard deviation of the noise is  $\sigma_{exp}=0.26\text{ mV}$  before tunneling starts, and  $\sigma_{exp}=2.3\text{ mV}$  during tunneling. Considering the gain of the preamplifier and  $k_t$ , these fluctuations correspond to variations of  $0.016\text{ \AA}$  and  $0.14\text{ \AA}$  before and after tunneling. The increment of the noise level is primarily due to thermal noise. The values are close to the values obtained by analysis of the model, and the difference may be due to inaccuracies of the tunneling model. It has been observed that environmental conditions change the value of the work function  $\Phi$  [8], which is considered constant in the theoretical tunneling-electrode distance relation.

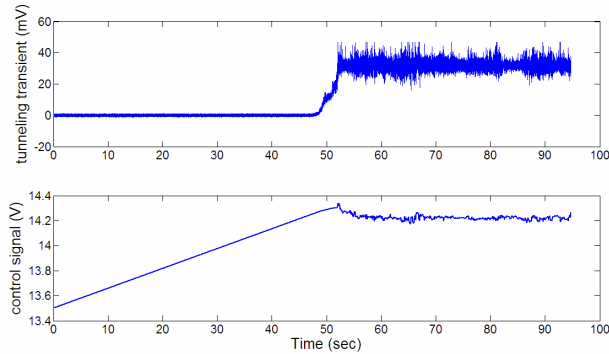


Figure 9. Exponential transient response of the tunneling signal (top) compared to the actuation voltage corresponding to the control action  $u$  (bottom).

The distribution of the experimental tunneling signal is plotted in Figure 10. The signal has a Gaussian distribution as is expected for a linear system with white noise excitation.

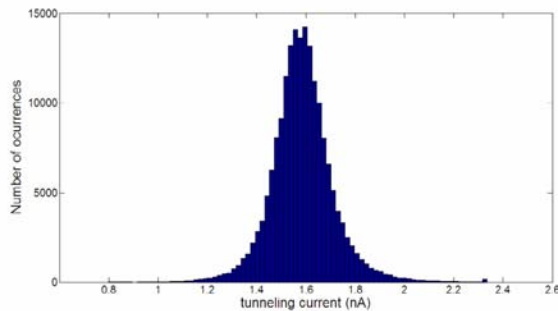


Figure 10. Histogram of the tunneling current. It is clear the signal has a Gaussian distribution as expected for white noise.

### Shaker Testing

The tunneling accelerometer was placed in a Brüel&Kjaer 4808 vibration exciter [14] to test the sensor operation. The top plot in Figure 11 corresponds to the tunneling current and the bottom trace is the control signal. Notice that the integral controller is not able to overcome the complete external shaking as expected. However, this result shows the operation of our inertial sensor with a simple tracking closed loop.

### CONCLUSIONS

A noise analysis of a tunneling accelerometer based on stochastic state space theory is developed. Considering Brownian, Johnson, and shot noise as sources, the theoretical standard deviation of the tunneling signal is calculated to be  $\sigma_{tot}=3.1\text{ mV}$  and it is compared with experimental observations  $\sigma_{exp}=2.3\text{ mV}$ . This

difference may be contributed by inaccuracies of the work function  $\Phi$  in our tunneling model.

The state space analysis presented here gives a good insight of the stochastic behavior of the tunneling current and how noise propagates in the system. The controller used was a simple integrating controller which gave a fairly low bandwidth. With the current experimental set up, our results confirm Gabrielson's conclusion that thermal noise gives the major contribution. The bandwidth can be increased by using a more sophisticated controller. Such a controller will have a higher bandwidth and more resistor noise will be fed into the systems. We are currently exploring the effect of more complicated controllers that will give an instrument with higher bandwidth.

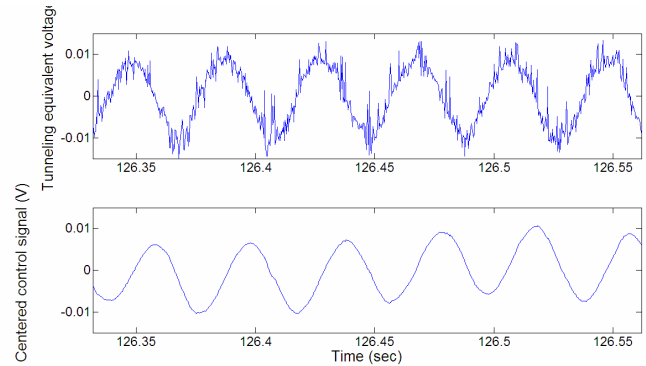


Figure 11. Shaker testing results. The input signal is a sine of 25 Hz frequency and 400 mV amplitude.

### REFERENCES

- [1] N. Yazdi, F. Ayazi, and K. Najafi, "Micromachined inertial sensors," *Proceedings of the IEEE*, vol. 86, pp. 1640–1659, August 1998.
- [2] T. Kenny, S. Waltman, J. Reynolds, and W. Kaiser, "A micromachined silicon electron tunneling sensor," *Proceedings, An Investigation of Micro Structures, Sensors, Actuators, Machines and Robots*, pp. 192–196, February 1990.
- [3] —, "Micromachined silicon tunnel sensor for motion detection," *Appl. Phys. Lett.*, vol. 58, pp. 100–102, January 1991.
- [4] H. Rockstad, T. Kenny, J. Reynolds, W. Kaiser, and T. Gabrielson, "A miniature high-sensitivity broad-band accelerometer based on electron tunneling transducer," *Sensors and Actuators A*, vol. 43, January 1994.
- [5] H. Rockstad, J. Reynolds, T. Tang, T. Kenny, W. Kaiser, and T. Gabrielson, "A miniature, high-sensitivity, electron tunneling accelerometer," *Transducers'95*, vol. 2, June 1995.
- [6] P. Scheeper, J. Reynolds, and T. Kenny, "Development of a modal analysis accelerometer based on a tunneling displacement transducer," *Transducers'97*, vol. 2, pp. 867–870, June 1997.
- [7] C. Yeh and K. Najafi, "A low-voltage tunneling-based silicon microaccelerometer," *Transactions on Electronic Devices, IEEE*, vol. 44, pp. 1875–1882, Nov 1997.
- [8] P. Hartwell, F. Bertsch, S. Miller, K. Turner, and N. MacDonald, "Single mask lateral tunneling accelerometer," *Proceedings of MEMS'98*, pp. 340–344, Jan 1998.
- [9] J. Wang, P. Zavracky, N. McGruer, and R. Morrison, "Study of tunneling noise using surface micromachined tunneling tipdevices," *Transducers'97*, vol. 1, pp. 467–470, June 1997.
- [10] T. Gabrielson, "Mechanical-thermal noise in micromachined acoustic and vibration sensors," *IEEE transactions on Electron Devices*, vol. 40, pp. 903–909, May 1993.
- [11] P. Hartwell, "Velocity and displacement measurements of microelectromechanical systems using laser vibrometry," PhD Thesis, Cornell University, August 1999.
- [12] K. J. Åström, *Introduction to Stochastic Control Theory*. Dover, 1970.
- [13] K. J. Åström and R. M. Murray, *Feedback Systems. An Introduction for Scientists and Engineers*. Princeton University Press, 2008.
- [14] [www.bksv.com](http://www.bksv.com)

# PIEZORESISTIVE SENSING OF A DIELECTRICALLY ACTUATED SILICON BAR RESONATOR

Dana Weinstein and Sunil A. Bhave

OxideMEMS Lab, Cornell University, Ithaca, New York 14853, USA

## ABSTRACT

This paper reports on a dielectrically actuated and piezoresistively sensed 4.41 GHz silicon bar resonator with an electromechanical  $Q$  ( $Q_{em}$ ) of 8180. The 2-port piezoresistive transconductance measurement performed provides a promising alternative to capacitive measurement at high frequencies, where nominal and feed-through capacitance often dominates the output signal. The electromechanical  $fQ$  product of the silicon-based resonator is  $3.6 \times 10^{13} \text{ s}^{-1}$ , the highest reported to date for a silicon resonator using a direct 2-port measurement.

## INTRODUCTION

Silicon-based high frequency electromechanical resonators offer low power, small footprint, high-Q solutions for a variety of applications including microprocessing, RF communications, and sensor networks. In recent years, much of MEMS resonator research has focused on different mechanisms for driving and sensing acoustic resonance at frequencies exceeding 1 GHz. Promising transduction methods include solid dielectric capacitive transduction [1,2], piezoelectric transduction [3,4], and air-gap capacitive actuation with piezoresistive sensing [5].

The authors previously demonstrated the internal dielectric transduction of a 4.51 GHz silicon bar resonator [2]. The 3<sup>rd</sup> and 9<sup>th</sup> longitudinal-mode harmonics of the device were excited and detected capacitively with dielectric films sandwiched inside the resonator body at displacement nodes (Figure 1). The 9<sup>th</sup> harmonic resonance at 4.51 GHz with a mechanical quality factor of 11,200, demonstrated a 9.8 dB improvement in signal strength over the 3<sup>rd</sup> harmonic at 1.5 GHz. The resulting mechanical  $fQ$  product of  $5.1 \times 10^{13} \text{ s}^{-1}$  is the highest measured to date in silicon. The analytical and experimental study of internal dielectric transduction performed in [2,6] indicates improved transduction efficiency with increasing frequency, enabling mechanical resonance at previously unattainable frequencies.

A three-port scalar mixer measurement [7] was used to characterize the internal dielectrically transduced resonator. However, the large nominal and feed-through capacitance inherent in high-frequency capacitive sensing makes such resonators impractical in most integrated CMOS applications.

In this work, the 9<sup>th</sup> harmonic of a longitudinal mode silicon bar resonator is detected in a two port measurement, coupling the benefits of internal dielectric capacitive actuation with the piezoresistive sensing demonstrated by van Beek et al [5].

## THEORY

### Capacitive Actuation and Sensing

Internal dielectric transduction employs capacitive drive and sense to excite and detect acoustic resonance. In [2], a longitudinal-mode bar resonator is driven and sensed electrostatically with thin vertical dielectric layers, as shown in Figure 1. The resonator body is biased to  $V_{DC}$ , and a harmonic excitation of amplitude  $v_{in}$  is applied to the drive electrode at the resonant frequency. The amplitude of vibrations of the  $n^{\text{th}}$  harmonic resonance is given by

$$U_0 = \frac{2Q\epsilon_f V_{DC} v_{in}}{n^2 \pi^2 Y} \frac{L}{g^2} \left[ \sin\left(k_n d - \frac{k_n g}{2}\right) - \sin\left(k_n d + \frac{k_n g}{2}\right) \right] \quad (1)$$

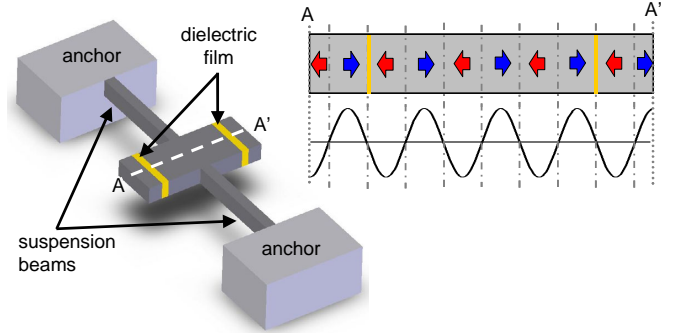


Figure 1: Schematic of internal dielectric transduced longitudinal-mode bar resonator. The dielectric films (yellow) are incorporated into the resonant mode shape. A cross section of the bar along A-A' is illustrated on the right. The 9<sup>th</sup> harmonic longitudinal mode is shown, with dielectric films for driving resonance positioned at displacement nodes.

where  $Q$  is the quality factor, and  $Y$  and  $\rho$  are the Young's modulus and mass density of the resonator, respectively. Here,  $\epsilon_f$  is the dielectric permittivity,  $g$  is the dielectric thickness,  $d$  is the position of the dielectric along the bar,  $A$  is the transduction area, and  $k_n = n\pi/L$  is the resonance wave number. The 2-port motional impedance  $R_X \equiv v_{in}/i_{out}$  for the  $n^{\text{th}}$  harmonic of the resonator is given by

$$R_X = \frac{n\pi\sqrt{Y\rho}}{2QA\epsilon_f^2 V_{DC}^2} \frac{g^4}{\cos^2(k_n d) \sin^2(k_n g/2)} \quad (2)$$

The quartic dependence of the motional impedance on dielectric thickness requires the thinnest dielectric possible, limited by fabrication and material properties. As the resonator scales to higher frequencies and the acoustic half-wavelength  $\lambda/2 \rightarrow g$ , the  $\sin^2$  term in the denominator approaches unity, reducing motional impedance. Internal transduction incorporates the dielectric film into the resonant mode shape, resulting in increased transduction efficiency without degradation of the  $fQ$  product as frequency extends into the GHz range.

### Capacitive Actuation and Piezoresistive Sensing

Capacitive sensing at GHz frequencies is challenging due to large nominal and feed-through capacitance intrinsic to the device; three-port scalar-mixer measurements are often required. To overcome this obstacle, piezoresistive sensing of a capacitively actuated resonator is implemented. There are several benefits to piezoresistive detection. Geometric and frequency scaling are considerably more favorable than in the case of capacitive sensing. Additionally, independent control of the drain current enables us to set the piezoresistive transconductance  $g_m$  to be as large as possible. When a drain current  $I_d$  flows through a mechanically resonating structure, the piezoresistive change in the resistance  $dR/R$  generates a transconductance

$$g_m = \frac{dR}{R} \frac{I_d}{v_{in}} \quad (3)$$

where  $v_{in}$  is the AC voltage across the dielectric films capacitively exciting resonance. The change in the resistance due to piezoresistivity follows

$$\frac{dR}{R} = \pi_t \sigma_t + \pi_l \sigma_l \quad (4)$$

where  $\pi_t$  and  $\pi_l$  are the transverse and longitudinal piezoresistive coefficients, and  $\sigma_t$  and  $\sigma_l$  are the transverse and longitudinal stresses, respectively. The stress is defined by the resonant mode shape with amplitude of vibrations given by equation 1. Summing equation 4 over all points in the resonator, weighting each point by the ratio of total current density at that point to the total current density, the total fractional piezoresistive change is given by

$$\frac{dR}{R} = \frac{\sum_i j_i (\pi_{ti} \sigma_{ti} + \pi_{li} \sigma_{li})}{\sum_i j_i} \quad (5)$$

In the case of the dielectrically actuated longitudinal-mode resonator, acoustic waves travel perpendicular to the drain current, as shown in Figure 2. Figure 3 presents the analytical results of the contribution to the piezoresistive signal distributed over the resonator body, as defined by equation 5. The symmetry of the resonant mode and uniformity of the current flow result in a cancellation of most of the signal. With this geometry, the primary contribution to the output signal comes from vibrations in and near the suspension beams.

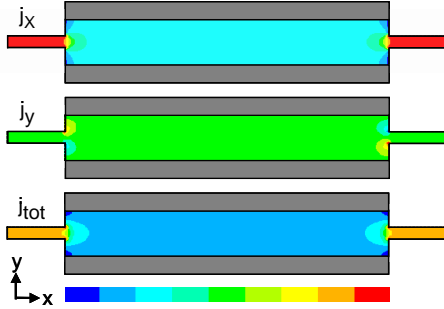


Figure 2: Contour plot of current density in the resonator. Current flow is uniform through most of the resonator body. Current non-uniformity at the input and output of the resonator is the primary source of piezoresistive signal.

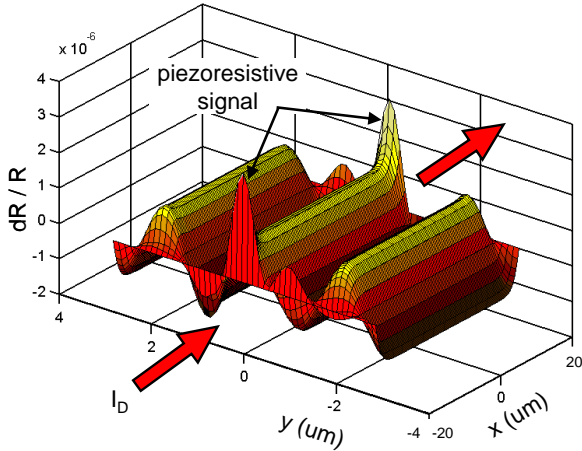


Figure 3: Spatial distribution of piezoresistive signal. The symmetry of the strain in the resonator results in cancellation of the signal in the majority of the body. The piezoresistance peaks near the routing beams generate the detected resonant signal.

## CALIBRATION AND MEASUREMENT

The resonator was fabricated as described in [2], in a combined SOI-polysilicon process using a 15 nm silicon nitride film for dielectric actuation. Figure 4 shows a scanning electron micrograph of the 8.5  $\mu\text{m}$  long  $\times$  2.5  $\mu\text{m}$  thick  $\times$  40  $\mu\text{m}$  wide silicon bar resonator, with a 9<sup>th</sup> harmonic longitudinal resonance at 4.5 GHz.

The resonator was tested at room temperature in a vacuum probe station. A schematic of the experimental setup is shown in Figure 5. A short-open-load-through calibration on a ceramic substrate was first performed to remove parasitics up to the probe tips, followed by de-embedding using short, open, and through structures on-chip. Both ends of the resonator were biased to a  $V_G$  of 10V, and a 0 dBm (0.2 V) AC excitation from an Agilent parametric network analyzer (PNA) was superimposed to capacitively generate resonance. A drain current across the resonator, defined by a bias voltage  $V_d$ , was modulated piezoresistively and detected by the PNA. The transconductance is given by

$$g_m = Y_{21} - Y_{12} \quad (6)$$

This technique is identical to microwave frequency measurement of the transconductance in transistors.

## EXPERIMENTAL RESULTS

The measured frequency response of the 9<sup>th</sup> harmonic longitudinal mode with drain currents of 1.22, 11.82, and 23  $\mu\text{A}$  is presented in Figure 6. At 23  $\mu\text{A}$ , a resonant frequency of 4.41 GHz with an electromechanical  $Q$  of 8180 is observed with a piezoresistive transconductance of 1.1  $\mu\text{A}/\text{V}$ . The power dissipated in the resonator is 0.46 mW.

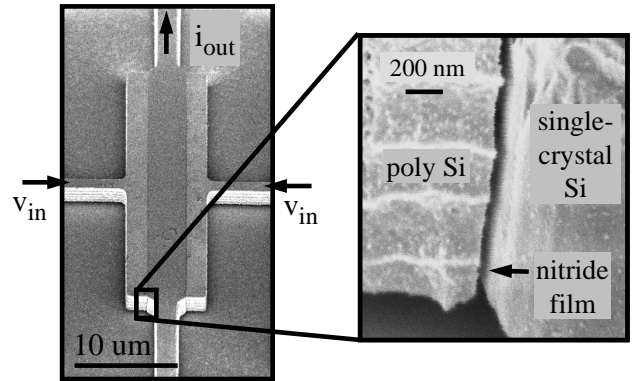


Figure 4: SEM of silicon bar resonator: 8.5  $\mu\text{m}$  long  $\times$  2.5  $\mu\text{m}$  thick  $\times$  40  $\mu\text{m}$  wide. An input AC voltage  $v_{in}$  superimposed on a bias voltage  $V_G$  applied to both ends of the bar drives resonance, while the output current  $i_{out}$  is detected across the center of the bar. The inset image shows the thin nitride gap between the polysilicon and single crystal regions of the resonator.

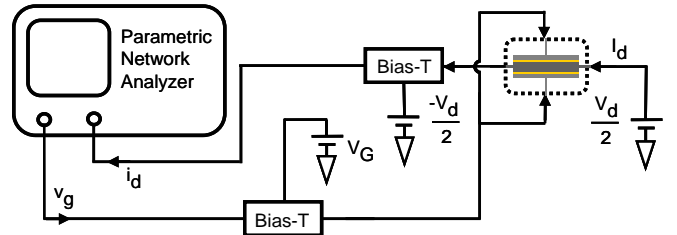


Figure 5: Schematic of measurement setup for internal dielectric actuation and piezoresistive detection.

Several trends occur as the drain current through the resonator increases. As expected, the resonant frequency decreases with increasing bias current, as shown in Figures 6 and 7. This is due to thermal expansion of the silicon bar as a result of Joule heating. A 1.6% tuning is observed varying the current flow through the resonator from 1.22  $\mu\text{A}$  to 23  $\mu\text{A}$ .

Figure 8 presents the experimental shift in electromechanical  $Q$  as the current increases. The increasing  $Q$  is a result of desorption of molecules from the surface of the resonator as the device is heated. At a maximum current of 23  $\mu\text{A}$ , the resonant signal exhibits an electromechanical  $f \cdot Q$  product of  $3.6 \times 10^{13} \text{ s}^{-1}$ . While the three-port scalar mixer measurement of [2] provides an accurate measure of the resonator's mechanical  $Q$ , the quality factor obtained in the two-port piezoresistive measurement combines both mechanical and electrical contributions to  $Q$ , resulting in the electromechanical  $Q$  commonly quoted in literature. The observed electromechanical  $f \cdot Q$  product is the highest measured to date in silicon. Moreover, this  $f \cdot Q$  product is in very good agreement with the theoretical upper bound on  $Q$  presented in [8]. This indicates that the quality factor of the RF longitudinal bulk-mode resonator is limited by normal and Umklapp phonon scattering described by the Akheiser Effect.

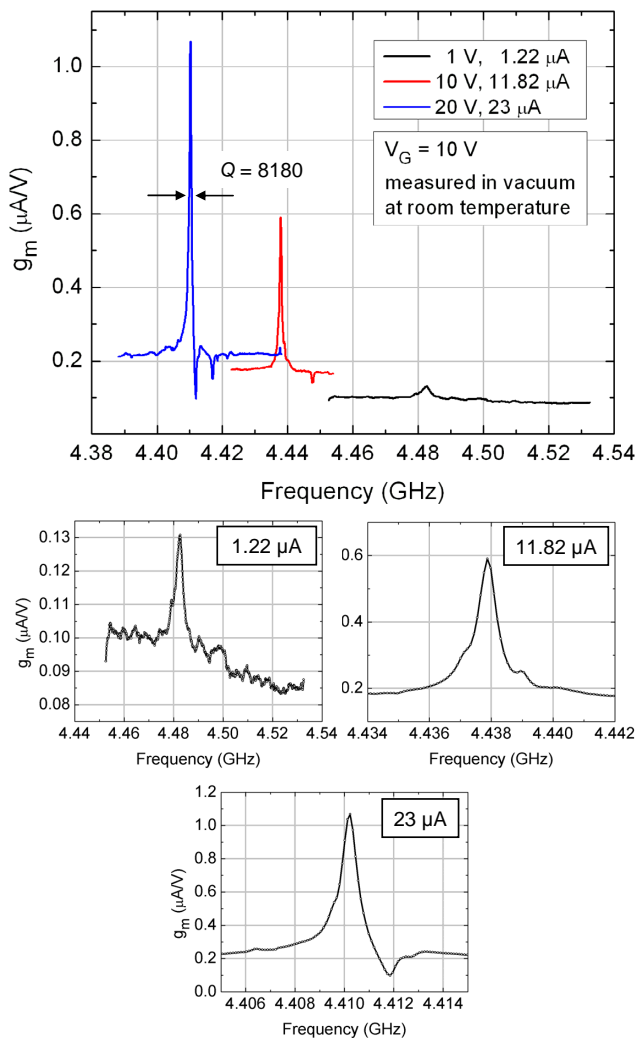


Figure 6: Measured frequency response of piezoresistive transconductance  $g_m$  of the resonator for varying drain currents.

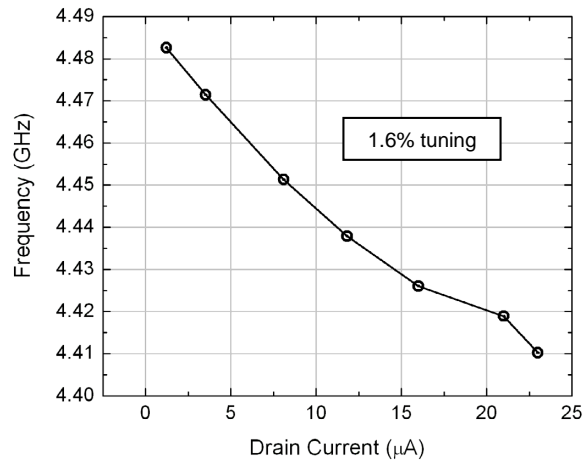


Figure 7: Measured resonant frequency scaling with increasing drain current. Resistive heating thermally expands the resonator, decreasing resonant frequency with increasing internal temperature.

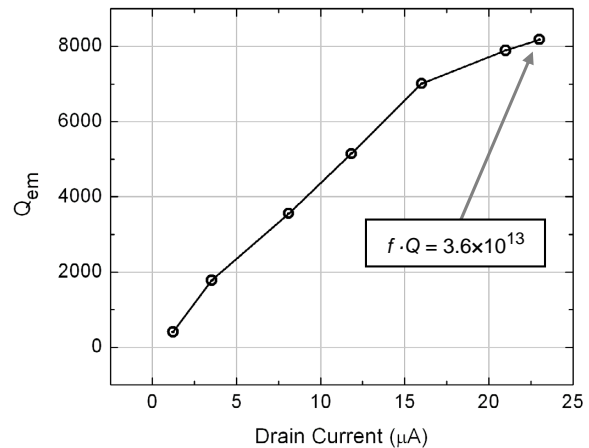


Figure 8: Measured electromechanical  $Q$  scaling with increasing drain current. The increasing trend results from desorption of molecules from the resonator surface as the device is resistively heated.

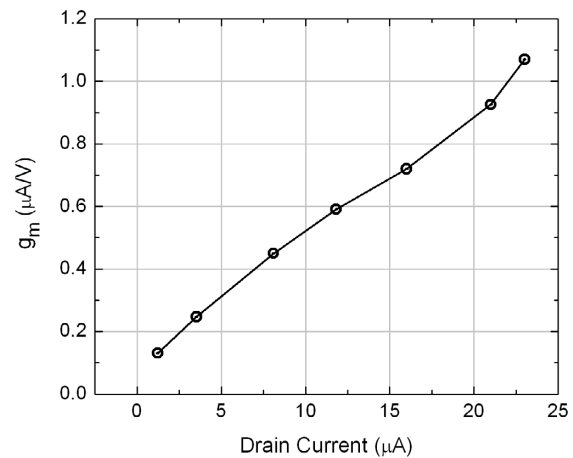


Figure 9: Experimental  $g_m$  scaling with increasing drain current. This trend is directly dependent on  $Q$ , and therefore reflects the effects of surface desorption as the drain current increases and the resonator heats.

As seen in Figure 9, piezoresistive transconductance scales linearly with drain current, dictated by equation 3, with a 1.1  $\mu\text{S}$  signal at 23  $\mu\text{A}$  of drain current. The extracted piezoresistive  $dR/R$  for this device is 1%. However, the transconductance is directly proportional to the resonant  $Q$ , whose rising trend with increasing current flow was affected by desorption on the resonator surface. It should be noted that the measured fractional piezoresistance is therefore not indicative of equilibrium conditions.

## CONCLUSION

Piezoresistive sensing was presented as a viable improvement over internal dielectric capacitive sensing in high frequency resonators, offering a two-port configuration to facilitate direct incorporation of RF MEMS resonators into integrated circuit applications. The measured resonance at 4.41 GHz demonstrates an electromechanical  $Q$  of 8180. The resulting  $f \cdot Q$  product of the resonator is higher than previously measured in silicon, indicating the promise of internal dielectric actuation in  $>1\text{GHz}$  resonators. Piezoresistive sensing, which does not require a scalar mixer measurement, yields a measurement of the electromechanical  $Q$  as opposed to a purely mechanical  $Q$ . This is the value of  $Q$  used in the design of integrated devices. A low power consumption of  $<1\text{ mW}$  and control of  $g_m$  make these NEMS-Transconductor hybrid resonators ideal candidates for integration into high-frequency CMOS technology.

## REFERENCES

- [1] Y.-W. Lin, S.-S. Li, Z. Ren, and C. T.-C. Nguyen, "Vibrating micromechanical resonators with solid dielectric capacitive-transducer 'gaps'," Joint IEEE Int. Frequency Control/Precision Time & Time Interval Symposium, Vancouver, Canada, 08/29-31/05, (2005), pp. 128 – 134.
- [2] D. Weinstein, S.A. Bhave, "Internal dielectric transduction of a 4.5 GHz silicon bar resonator," IEEE International Electron Devices Meeting, Washington, DC, 12/10-12/07, (2007), pp. 415 - 418.
- [3] G. Ho, R. Abdolvand and F. Ayazi, "High order composite bulk acoustic resonators," 20<sup>th</sup> IEEE International Conference on Micro Electro Mechanical Systems, Kobe, Japan, 01/21-25/07, (2007), pp. 791 - 794.
- [4] G. Piazza, P. J. Stephanou and A.P. Pisano, "Single-chip multiple-frequency AlN MEMS filters based on contour-mode piezoelectric resonators," Journal of Micro Electro Mechanical Systems, 16 (2), 319 - 328 (2007).
- [5] J.T.M. van Beek, G.J.A.M Verheijden, G.E.J. Koops, K.L. Phan, C. van der Avoort, J. van Wingerden, D. Ernur Badaroglu, J.J.M. Bontemps, "Scalable 1.1 GHz fundamental mode piezoresistive silicon MEMS resonator," IEEE International Electron Devices Meeting, Washington, DC, 12/10-12/07, (2007), pp. 411 - 414.
- [6] D. Weinstein, S.A. Bhave, "Internal dielectric transduction: optimal position and frequency scaling," IEEE Transactions on Ultrasonics, Ferroelectrics, and Frequency Control, 54(12), 2696 - 98 (2007).
- [7] A.-C. Wong, T.-C. Nguyen, "Micromechanical Mixer-Filters ('Mixlers')," Journal of Micro Electro Mechanical Systems, 13(1), 100-112 (2004).
- [8] S.A. Chandorkar, M. Agarwal, R. Melamud, R.N. Candler, K.E. Goodson, T.W. Kenny, "Limits of quality factor in bulk-mode micromechanical resonators," 21<sup>st</sup> IEEE International Conference on Micro Electro Mechanical Systems, Tuscon, Arizona, 01/13-17/08, (2008), pp.74 - 77.

# POST-CMOS COMPATIBLE ALUMINUM NITRIDE RING WAVE GUIDE (RWG) RESONATORS

K. E. Wojciechowski, R. H. Olsson III and M. R. Tuck  
Sandia National Laboratories, Albuquerque, NM, USA

## ABSTRACT

This work presents a new type of MEMS resonator based on launching an acoustic wave around a ring. Its maximum frequency is set by electrode spacing and can therefore provide a means for developing resonators with center frequencies in the GHz. In addition since the center frequency is dependent on the average radius it is not subject to lithographic process variations in ring width. We have demonstrated several Ring Waveguide (RWG) Resonators with center frequencies at 484 MHz and 1 GHz. In addition we have demonstrated a 4<sup>th</sup> order filter based on a RWG design.

## INTRODUCTION

For MEMS devices to be incorporated into RF systems it is desirable to provide CMOS compatible MEMS filters with multiple high frequencies (GHz) and low insertion loss (50Ω impedance). This has yet to be accomplished however great strides are being made in this area [1-6]. One of the limiting factors to developing devices at GHz frequencies is the need to create half-wavelength device features (usually several microns). Recent piezoelectric MEMS devices are employing a method to selectively transduce device harmonics/overtones through use of electrode spacing to determine device harmonic selected. This method has been used by the harmonic contour mode devices proposed and demonstrated in [1,2]. In these devices the mechanical structure can be many times larger than the desired wavelength. Therefore resonator size and hence power handling can be controlled independently of resonant frequency.

Ring waveguide resonators are similar to Surface Acoustic Wave (SAW) devices where lithographically defined electrode spacing,  $w_E$ , and average ring radius,  $R_{avg}$ , determine the resonator center frequency (Fig. 1). In fact RWG device resonances are created by acoustic wave propagation around the ring. The dependence on average ring radius and electrode spacing enables accurate control of the RWG center frequencies when compared to contour-mode devices [1,3,4,6] where the size mechanical structure determines the center frequency. Additionally, since smaller feature size can be achieved lithographically on metal, higher frequency devices are easier to realize with these resonators. Unlike SAW resonators, which require exotic substrates, and cannot be easily integrated with CMOS processes the RWG devices presented in this work have been fabricated in a post-CMOS compatible aluminum nitride process [1]. Devices implemented in this process are isolated from the substrate by trench isolation (Figure 2). Hence, they are expected to have less loss than typical SAW devices. Finally, the RWG resonator adds an additional degree of freedom in the resonator design as resonances set by electrode spacing, and average radius, can be combined with contour modes set by ring width,  $w_R$ . Most importantly, these resonances can be independently tuned. This creates a direct path to the implementation of multi-pole filters.

Two different size RWG resonators have been demonstrated. The first device has an average radius, of 260 μm and a center frequency of 484 MHz (Figure 3). It has a loaded Q of 746 and its motional impedance is 474 Ω. The second device ( $R_{avg} = 120 \mu\text{m}$ ) center frequency is 998 MHz with a Q = 363 and motional impedance of 2.69 kΩ (Table 1).

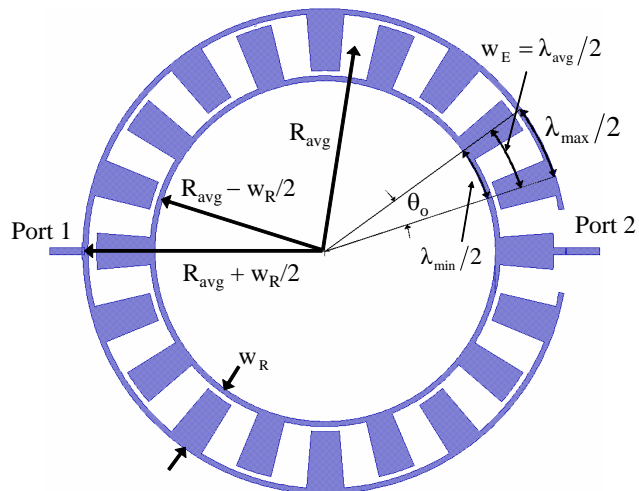


Figure 1: Schematic of ring wave guide resonator electrode configuration. Acoustic wave propagation is around the ring.

## DEVICE THEORY

In this section we develop a simple analytical model for the device based on Figure 1. The acoustic wave propagating around the center of the ring has a wavelength,  $\lambda_{avg}$ .

$$\lambda_{avg} = 2R_{avg}\theta_o \quad (1)$$

The nominal center-to-center electrode spacing is  $\lambda_{avg}/2$  and the angle at which the electrode configuration repeats is  $\theta_o$ . This leads to a device resonant frequency of:

$$f_o = \frac{c_R}{2R_{avg}\theta_o} \quad (2)$$

Where  $c_R$  is the speed of the material, and is determined by the effective density and stiffness of resonator. This can be estimated from the film thickness of the aluminum nitride (AlN), oxide and metal electrodes. Since the resonant frequency is dependent on the average radius, process variation of the outer and inner radius does not affect it. Note that the number of electrodes,  $N_e$ , must be even (3). If this constraint is not followed there will be a discontinuity in the electrodes which may cause unwanted spurious modes.

$$N_e = \frac{\pi}{\theta_o} = \text{even integer} \quad (3)$$

## Multiple Modes

Multiple modes can be transduced in the RWG since the average distance between the center of its electrodes varies (Figure

1). In fact the range of wavelengths that can exist in the wave guide is bounded by  $[\lambda_{\min}, \lambda_{\max}]$ .

$$\lambda_{\min} = 2R \left( R_{\text{avg}} - \frac{W_R}{2} \right) \theta_o, \quad (4)$$

$$\lambda_{\max} = 2 \left( R_{\text{avg}} + \frac{W_R}{2} \right) \theta_o$$

Since the mechanical resonances in AlN are fairly high Q we can expect to see separate peaks in the frequency spectrum corresponding to wavelengths in the range of  $[\lambda_{\min}, \lambda_{\max}]$ . In addition, due to the electrode configuration, device harmonics at odd multiples of the fundamental wavelengths (electrode spacing) can be supported while even harmonics are suppressed. This is also true for the harmonic contour mode devices [1, 2]. Finally, an analytical model for a similar SAW resonator has been developed in [7].

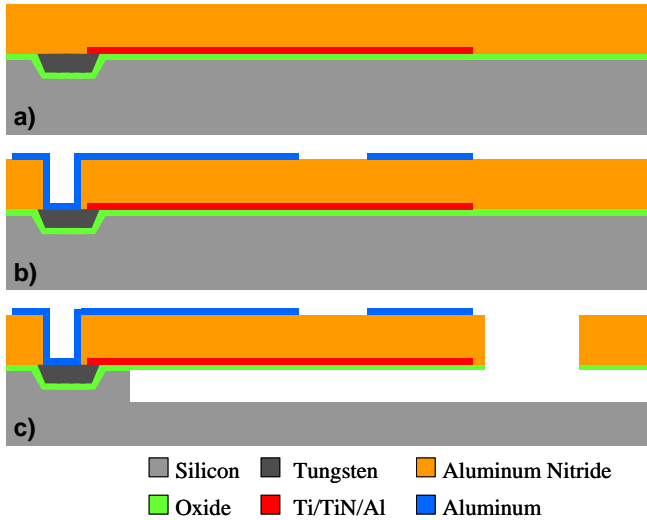


Figure 2: Aluminum nitride microfilter fabrication process.

## FABRICATION PROCESS

The process flow used to fabricate the AlN resonators, is shown in Figure 2. The process replaces the platinum bottom electrode in [3] with standard CMOS metals, aluminum (Al), titanium (Ti), titanium nitride (TiN) and tungsten (W). (a) The process begins with an anisotropic silicon (Si) etch and the deposition of a silicon dioxide ( $\text{SiO}_2$ ) layer to isolate the bottom electrode from the substrate. Tungsten is then deposited by chemical vapor deposition (CVD) and chemically mechanically polished (CMP) until it remains only where Si was etched. An oxide touch polish is then performed to further smooth the wafer surface prior to the sputter deposition and patterning of the bottom electrode. The bottom electrode processes utilizes a Ti(20 nm)/TiN(50 nm)/Al(50 nm) bottom electrode. Next, 750 nm of AlN is sputter deposited at 350 °C. Using this process highly oriented c-axis AlN films necessary for realizing low impedance resonators can be reliably formed. Typical rocking curve full width half maximum values for the AlN film measured using X-ray diffraction are 1-1.2° on Ti/TiN/Al. (b) Contacts to the W areas are etched in the AlN and a 100 nm thick Al top electrode is deposited and patterned. (c) Finally, the resonator frequency is lithographically defined by etching trenches in the AlN and  $\text{SiO}_2$  to bulk Si and the devices are released using an isotropic etch in dry  $\text{SF}_6$ . The maximum temper-

ature in this process is 350 °C and all of the materials are post-CMOS compatible and can be deposited and etched using standard CMOS tools.

## EXPERIMENTAL RESULTS

Several RWG devices were fabricated. Two of the devices fabricated are shown in Fig. 3. The first device (Figure 3a) has an average radius of 120  $\mu\text{m}$  and angular electrode pitch of 2 degrees. The second device average radius is 260  $\mu\text{m}$  with identical pitch. The resonant frequencies of these devices can be calculated from (2) and are 1022 MHz and 472 MHz respectively (Table 1).

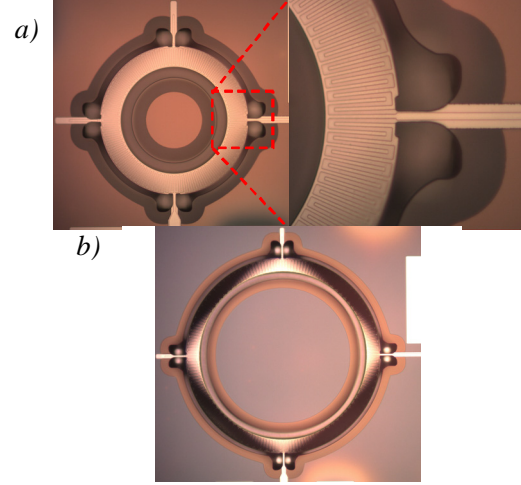


Figure 3: Photomicrographs of RWG resonators, a) Small ring device ( $R_{\text{avg}} = 120\mu\text{m}$ ). b) Large ring device ( $R_{\text{avg}} = 260\mu\text{m}$ ).

Table 1: Parameters of RWG resonators

Parameter	Large Ring	Small Ring
$R_{\text{avg}}$	260 $\mu\text{m}$	120 $\mu\text{m}$
Ring width, $w_R$	40 $\mu\text{m}$	
$\theta_o$	2 deg	2 deg
$\lambda_{\text{avg}}/2$ (electrode spacing)	9.08 $\mu\text{m}$	4.19 $\mu\text{m}$
$c_R$ , Material speed (calculated)	8569 m/s	
$f_o$ (calculated)	472 MHz	1022 MHz
$f_o$ (measured)	484 MHz	998 MHz
Insertion Loss (measured)	20.4 dB	34.8 dB
Q	746	363
$R_x$	474 $\Omega$	2690 $\Omega$
$L_x$	116.287 $\mu\text{H}$	155.639 $\mu\text{H}$
$C_x$	0.932 fF	0.163 fF
Ring resonator bulk extensional mode	107 MHz	

As can be seen from Table 1 there is close agreement with the calculated and the measured resonant frequencies. The differences are due to AlN thickness variation which results in material speed variation. We are presently working on methods for more accurately controlling AlN film thickness. Figure 4 shows the S21 transmission spectrum for these devices. The small ring device has similar performance to the lateral field excitation device presented in [4].

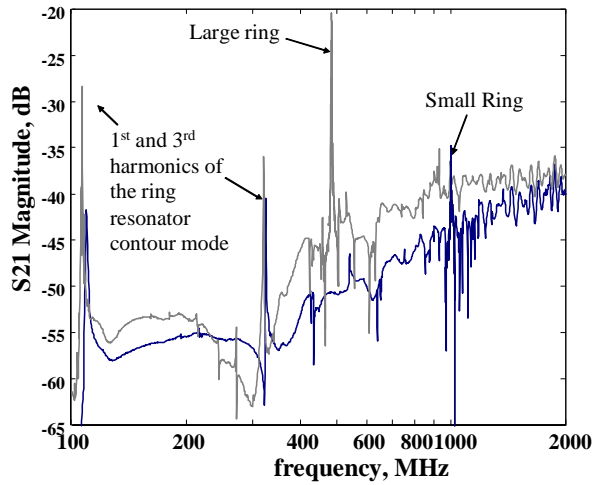


Figure 4:  $S_{21}$  transmission in dB of the large (grey) and small ring (blue) RWG resonators. Note that the contour modes ( $1^{st}$  harmonic at 107 MHz and  $3^{rd}$  harmonic at 321 MHz) are present for both rings. Measured in air with an AGILENT E5071C,  $P_{in} = 0$  dBm, Termination =  $50\Omega$ .

We also designed a  $4^{th}$  order filter response (Fig. 5) with a RWG filter. It was implemented by placing the ring contour-mode (214MHz) close to the RWG resonance (209MHz) set by the electrode spacing. Since the contour mode is dependent on ring width,  $w_R$ , and the average RWG mode is independent of  $w_R$  these resonances can be placed close to one another by choosing,  $w_R$  and  $\theta_o$ . This particular RWG filter has an average radius of  $120\mu\text{m}$  and ring width of  $20\mu\text{m}$ . The electrode pitch,  $w_E$ , is  $20.4\mu\text{m}$  which corresponds to an electrode angular pitch ( $\theta_E$ ) of 9 degrees.

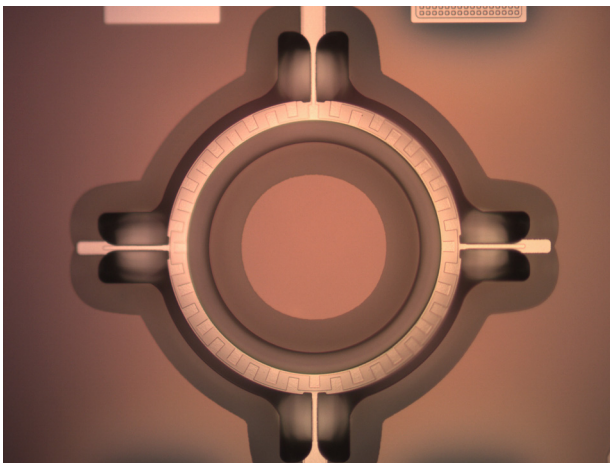


Figure 5: Photomicrograph of a  $4^{th}$  order filter implemented with a combination of contour and RWG modes.

We observed spurious parasitic modes outside the filter band ( $\sim 200\text{MHz}$ ). The cause of these spurious modes and designs to suppress them are being investigated. A differential electrode design could potentially cancel these spurious modes in the filter response.

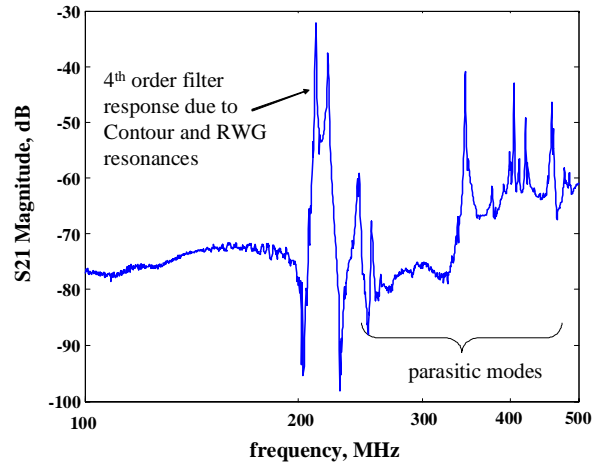


Figure 6:  $S_{21}$  transmission of the  $4^{th}$  order filter realized by combining the  $1^{st}$  harmonic contour-mode of the ring with the SAW like resonance created with the electrode spacing. Measured in air with an AGILENT E5071C,  $P_{in} = 0$  dBm, Termination =  $50\Omega$ .

Another interesting result was obtained from a RWG with an electrode angular pitch of 6 degrees, average radius of  $120\mu\text{m}$ , and width of  $40\mu\text{m}$ . This shows an example of an RWG exhibiting three modes (Fig. 7) due to the difference in electrode spacing from the inner to outer radius.

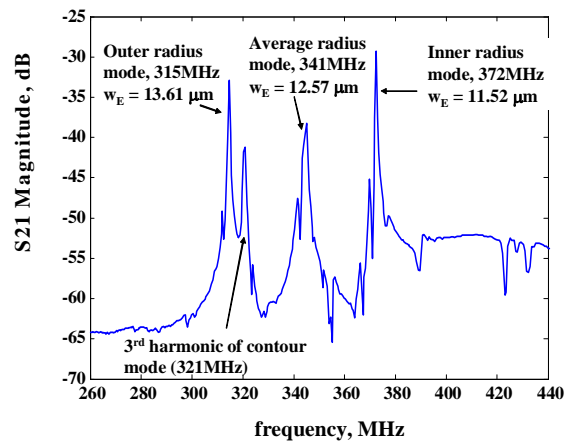


Figure 7:  $S_{21}$  transmission of a RWG resonator where the change in electrode pitch allows for multiple modes to exist. Measured in air with an AGILENT E5071C,  $P_{in} = 0$  dBm, Termination =  $50\Omega$ .

Finally, a fully differential large ring device was implemented on a subsequent fabrication run. In this device four electrodes were used to implement a completely differential device. Otherwise it is identical to the device shown in Fig 3a. It was expected to have significantly lower device feed through and lower insertion loss. This was verified by the measured results (Fig. 8). However, unlike the single ended device which exhibited only one mode due to the average radius, the differential device has modes corresponding to the average and inner ring radii. It is not clear why the inner radius mode is present for the differential device while it does not exist in the single ended one. It may be due to the differential drive and sense. Interestingly the outer radius mode is not present and may be suppressed by the anchoring or notching on the outside of the ring. Notching at the anchor, as can be seen in

Figure 3a, was done for stress relief. Finally, with the reduction in the device feed through other modes in the wave guide bandwidth (below -40dB) can be observed in the frequency response of the waveguide (Figure 8).

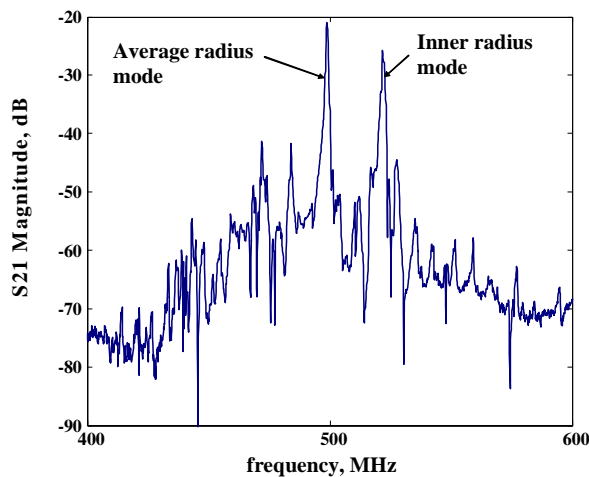


Figure 8:  $S_{21}$  transmission of a fully differential large ring. RWG (260 $\mu$ m average radius,  $\theta_o = 2$  degrees). Measured in air with an AGILENT E5071C,  $P_{in} = 0$  dBm, Termination = 50 $\Omega$ .

## CONCLUSIONS

In this work we have presented a RWG device which represents a new type of MEMS resonator. Our first results demonstrate their potential for high-frequency, multi-pole filtering and wide-bandwidth filter implementations in a post-CMOS compatible process. Two RWG resonators have been demonstrated with center frequencies of 484MHz and 1GHz, motional impedances of 474 $\Omega$  and 2.69 k $\Omega$ , and Q's of 746 and 363 respectively. We also demonstrate a 4<sup>th</sup> order filter response (Figure 6) with a RWG filter implemented by placing the ring contour-mode close to the RWG resonance.

Finally it was experimentally shown that RWG resonators support multiple modes inside the waveguide. This may have possible application in making wide band filters which are difficult to implement with current devices. Additionally, it may be possible to develop multi-pole filters with RWG filters based on electrode configuration alone. This can be achieved by varying electrode pitch around the ring similar to established methods used to achieve multi-pole devices in SAW filters. Alternatively, we could take advantage of the fact that the electrode pitch can be varied from the inner section to the outer section of the ring. With a large enough difference, multiple modes can be excited leading to wider bandwidth filters.

## ACKNOWLEDGEMENTS

The authors would like to thank the Microelectronics Development Laboratory staff at Sandia National Laboratories including Jim Stevens and Craig Nakakura for AlN process development. This work was supported by the Laboratory Directed Research and Development program at Sandia National Laboratories. Sandia National Laboratories is a multiprogram laboratory operated by the Sandia Corporation, Lockheed Martin Company, for the United States Department of Energy's National Nuclear Security Administration under contract DE-AC04-94AL85000.

## REFERENCES

- [1] R. H. Olsson III, J. G. Fleming, K. E. Wojciechowski, M. S. Baker, M. R. Tuck, "Post-CMOS Compatible Aluminum Nitride MEMS Filters and Resonant Sensors," IEEE International Frequency Control Symposium, 2007 Joint with the 21st European Frequency and Time Forum., vol., no., pp.412-419, May 29 2007-June 1 20.
- [2] P. J. Stephanou, A. P. Pisano, "PS-4 GHz Contour Extensional Mode Aluminum Nitride MEMS Resonators," Ultrasonics Symposium, 2006. IEEE , vol., no., pp.2401-2404, 2-6 Oct. 2006.
- [3] G. Piazza, P. J. Stephanou, A. P. Pisano, "Single-Chip Multiple-Frequency AlN MEMS Filters Based on Contour-Mode Piezoelectric Resonators," Journal of Microelectromechanical Systems, vol.16, no.2, pp.319-328, April 2007.
- [4] J. Wang, J. E. Butler, T. Feygelson, C. T-C. Nguyen, "1.51-GHz nanocrystalline diamond micromechanical disk resonator with material-mismatched isolating support," *Micro Electro Mechanical Systems, 2004. 17th IEEE International Conference on. (MEMS)*, vol., no., pp. 641-644, 2004.
- [5] D. Weinstein, S. A. Bhawe, "Internal dielectric transduction: optimal position and frequency scaling," *IEEE Transactions on Ultrasonics, Ferroelectrics and Frequency Control*, vol.54, no.12, pp.2696-2698, December 2007
- [6] B. Bircumshaw, G. Liu, H. Takeuchi, T.-J. King, R. Howe, O. O'Reilly, A. P. Pisano, "The radial bulk annular resonator: towards a 50 $\Omega$  RF MEMS filter," TRANSDUCERS, 12th International Conference on Solid-State Sensors, Actuators and Microsystems, , 2003 , vol.1, no., pp. 875-878 vol.1, 8-12 June 2003.
- [7] S. V. Biryukov, G. Martin, M. Wehnacht, "Closed Regular Electrode Structure for SAW Resonators," IEEE International Frequency Control Symposium, 2007 Joint with the 21st European Frequency and Time Forum., vol., no., pp.168-171, May 29 2007-June 1 2007.

# CARBON NANOTUBE MEMBRANE IN MICROCHANNEL FOR ELECTROPHORETIC SEPARATION OF PROTEINS

Rathish Dorairaj<sup>1</sup>, Thomas J. Roussel<sup>2</sup>, Gamini Sumanasekera<sup>3</sup>, Palaniappan Sethu<sup>2</sup>,  
Carolyn M. Klinge<sup>4</sup> and Robert S. Keynton<sup>2</sup>

<sup>1</sup>Departments of Electrical and Computer Engineering, <sup>2</sup>Bioengineering, <sup>3</sup>Physics,

<sup>4</sup>Biochemistry and Molecular Biology, University of Louisville, Louisville, KY

## ABSTRACT

We report the development of a simple microfluidic device, which uses a carbon nanotube (CNT) membrane (CNTM) to separate two proteins based on their molecular weights (MW). The device was fabricated by traditional microfabrication techniques and chemical vapor deposition (CVD). Protein A (MW= 42 kDa) and Aprotinin (MW= 6.5 kDa) were flowed through the CNTM in separate identical electrophoresis runs. The larger protein was observed to accumulate ahead of the CNTMs, whereas in the case of the smaller protein, no accumulation was observed, indicating that the buildup was due to the larger size of the higher MW protein.

## INTRODUCTION

Traditional polymeric gels used in gel electrophoresis (GE) suffer from several limitations. Namely, the polymerization process involved in making the gels is sensitive to ambient conditions like, humidity, temperature and other local disturbances, causing gel structural heterogeneity [1], resulting in migration velocities that are non-uniform for identical gels necessitating the use of a molecular weight ladder in conjunction with the analytes during electrophoresis. Subsequently, experimental reproducibility and repeatability between GE runs are very difficult to attain. Additionally, the gels can only be used once and the polyacrylamide gel monomer is highly neurotoxic. Therefore, researchers have investigated the feasibility of microfabrication methodologies [2,3] that incorporated “gels” or “sieving matrices” made out of silicon substrates. This methodology has an inherent limitation in that photolithographic processing techniques determine pore size (~1 $\mu$ m), making them unsuitable for protein separations. Duke and Austin [3] were successful in demonstrating diffusion-based macromolecular sorting using a microfabricated platform because of a minimal dependence on pore size. Thus far, the only CNTM-related work, reported by Bakajin et al [4], focused on developing a CNTM to filter large polystyrene beads under pressure-driven flow. However, no study has been performed, to date, to investigate separation and/or filtration of proteins using electrophoretic flow through a CNTM. CNTMs offer several advantages including mechanical rigidity, chemical inertness, sub-micron sized pores and good thermal conductivity, which could facilitate dissipation of heat generated during electrophoresis. Therefore, this paper focuses on the development of a simple microfluidic device, consisting of two reservoirs connected by a microchannel containing CNTMs, to separate two proteins based on their molecular size.

## MATERIALS AND METHODS

### Fabrication

Our group has previously reported the fabrication methodology [5] of the device (figure 1A) consisting of a quartz bottom substrate and a PDMS top substrate. The quartz substrate obtained from Chemglass Inc. (Vineland, NJ) is RF sputter coated with Cr (40 nm), followed by a DC sputter deposition of Au (200 nm), which acted as the etching mask. Positive photoresist AZ 1813 is spun on (4000 rpm, 20 s). After photolithographic

patterning by exposure to UV light and development in Microposit<sup>TM</sup> MF<sup>TM</sup>-319 (Rohm and Haas, Phoenix, AZ), the metal layers were etched: Cr in Microchrome etchant (Microchrome Tech., Inc., San Jose, CA) for 30 s and Au in Potassium Iodide (Alfa-Aesar, Ward Hill, MA) for 30 s. The underlying exposed quartz is etched in buffered-oxide etch 6:1 (J. T. Baker, Phillipsburg, NJ) for 19 minutes to form the microchannel. Positive photoresist AZ 1805 is spun on (spread: 500 rpm, 0.2 s; spin: 4000 rpm, 20 s) and patterned to define the area where the CNTMs are to be deposited and developed. The thinner photoresist allows patterning within the microchannel. A thin-film Iron catalyst (5 nm) is deposited using an e-beam evaporation system (Kurt J. Lesker Co., Philadelphia, PA), followed by an ultrasonic lift-off process in an acetone bath and metal etching. Thermal CVD is performed using ethylene as the carbon source and 10% H<sub>2</sub>/ 90% Ar as the carrier gas at 700 °C for 15 minutes to grow the CNTM inside the microchannel defined by the Iron catalyst. The PDMS substrate is cut out to the desired size from a sheet of PDMS made from Sylgard® 184 silicone elastomer kit (Dow Corning Corp., Midland, MI) and access holes are punched. Finally, the quartz and PDMS substrates are bonded by exposure to Oxygen plasma followed by a rapid aging process (60 °C for 12 hours) to increase the bond strength. Two different chip designs were fabricated. Device 1 contained a single, 1 mm long CNTM (2  $\mu$ m thick; figure 1B) and device 2 contained a series of 6 CNTM strips (length= 30  $\mu$ m; spacing= 100, 200, 400, 800, 1200  $\mu$ m; figure 2A), all located in the microchannel (width= 500  $\mu$ m; length= 3175  $\mu$ m; depth= 1.7  $\mu$ m).

CNTM strip thickness measurements were performed using a surface profilometer (Dektak, Veeco, Woodbury, NY) and were validated with an SEM. The channel depth was specifically chosen to enable the PDMS top substrate to slightly compress the CNTs preventing the passage of analyte above the membranes. Testing was performed using a fluorescent microscope (Nikon TE2000-E, Melville, NY) and phosphate buffer (pH= 7.4, 20 mM). The proteins investigated were Protein A (42 kDa; 0.24 mM) and Aprotinin (6.5 kDa; 1.54 mM), which were fluorescently labeled using a fluorescein labeling kit (Pierce Biotechnology, Inc., Rockford, IL). A Keithley 2400 sourcemeter (Cleveland, OH) was employed to apply the desired electric field (95 V/cm).

## RESULTS

Figure 1A-C shows fabricated device 1 and a cross-sectional SEM image of the “as-grown” CNTM, with an average CNT diameter of ~50 nm. Thickness measurements from surface profilometry indicated that the CNTM strips were 1.8-1.9  $\mu$ m thick (figures 2A). SEM images taken at 5° and 30° angles to the surface of the substrate (figures 2B,C) validated these values, yielding thicknesses of 1.91  $\mu$ m and 1.84  $\mu$ m, respectively. In the preliminary studies on device 1, when the 95 V/cm electric field was applied, the dye migrated to the edge of the CNTM (figure 1D) and abruptly stopped. No further migration was observed, irrespective of the duration or magnitude of electric field applied.

Studies on device 2 under the same testing conditions showed the complete migration of the dye to the exit reservoir. The

incomplete electrophoretic migration through the CNTM in device 1 was due to the conductive nature of the CNTs, which produced a break in the electric field and a significant interruption in the voltage gradient (figure 3B). To confirm this phenomenon, the CNTM was replaced by a Pt metal strip (80 nm thick) of identical footprint as the CNTM in device 1 and the same result (no migration through the Pt strip, in spite of the empty gap now present between the quartz substrate and the PDMS) was observed. Also, the voltage gradient in device 2 (figure 3C) more closely approximates an empty channel (figure 3A) with a resulting electroosmotic flow capable of transporting the dye through the narrow CNTM strips.

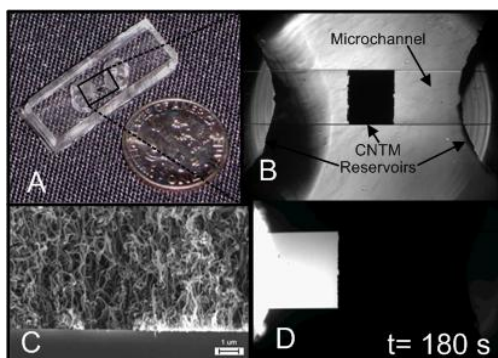


Figure 1: Electrophoresis device 1 (A) with a microscopic image of the inset (B) showing CNTM in the microchannel. (C) Cross-sectional SEM image of a CNTM (D) Absence of fluorescein migration through the CNTM, 180 s after the application of electric field. Electroosmotic flow was from left to right.

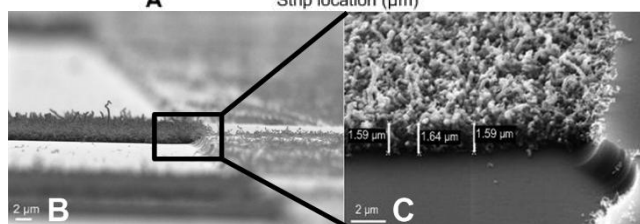
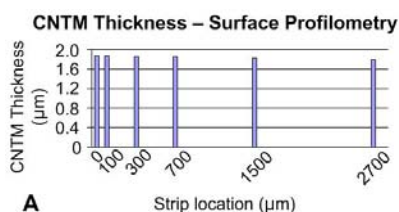


Figure 2: Thickness of individual CNTM strips (device 2) obtained from Dektak surface profilometer (A). SEM micrographs at 5° (B) and 30° (C) angles. CNTM thickness =  $1.6 / \cos 30 = 1.84 \mu\text{m}$ .

Subsequently, to test the separation capabilities of the membranes, electrophoresis of Protein A and Aprotinin were performed separately but under identical test conditions. In the case of Protein A (figure 4A), accumulation of the protein was observed in front of all six CNTM strips. About 90 s after the application of the electric field, Protein A accumulation ahead of the first strip reached a critical limit that prevented incoming molecules from migrating further. This caused the “band” ahead of first strip to significantly increase in length than those ahead of the other strips as time progressed (compare  $t=120\text{s}$  and  $t=150\text{s}$ ). In the case of Aprotinin (figure 4B) however, no accumulation was observed indicating that the smaller molecule was able to migrate freely through the pores in the CNTM.

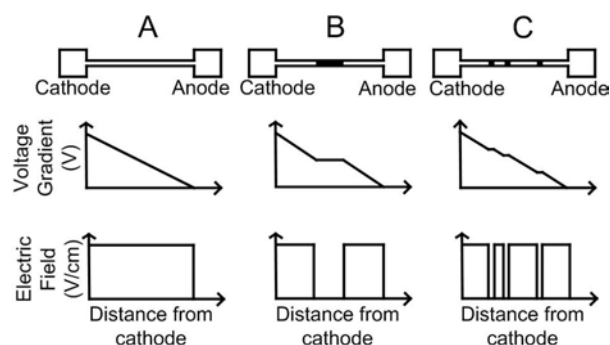


Figure 3: Comparison of voltage gradients between a design (device 1) with a single long CNTM (B) and a design (device 2) with multiple narrow CNTMs (C). The voltage gradient in C more closely approximates a channel without CNTM (A), whereas the voltage gradient in B severely interrupts the voltage gradient.

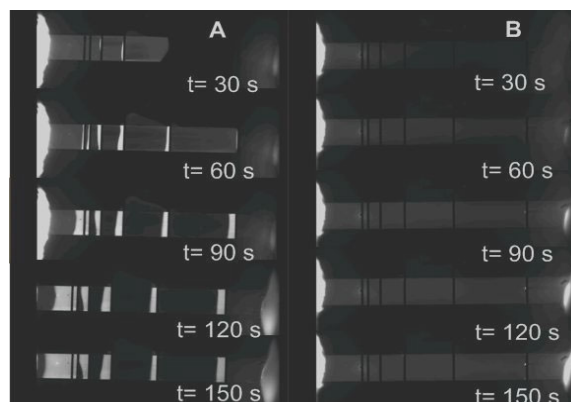


Figure 4: Protein electrophoresis using Protein A (A; 42 kDa) and Aprotinin (B; 6.5 kDa). Protein A formed bands, while Aprotinin did not. Applied electric field = 95 V/cm. Electroosmotic flow was from left to right.

Further studies will investigate varying the density of the CNTM strips along the length of the microchannel. This will establish a gradient separation of molecules based on MW. It is believed that this device will eventually duplicate the performance of gel-based electrophoretic separation techniques for not only protein identification, but also isolating specific types of proteins.

## REFERENCES

- [1] R. Ruchel, R.L. Steere and E.F. Erbe, “Transmission-Electron Microscopic Observations of Freeze-etched Polyacrylamide Gels”, *J. Chromat.*, 166, (1978), 563-575.
- [2] C.D. Furlong and D.J. Beebe, “A Microfabricated Device for the Study of the Sieving Effect in Protein Electrophoresis”, 18<sup>th</sup> Annual Intl. Conf. of the IEEE EMBS, Amsterdam 1996.
- [3] T.A.J. Duke and R.H. Austin, “Microfabricated Sieve for the Continuous Sorting of Macromolecules”, *Phys. Rev. Lett.*, 80, (1998), 1552-1555.
- [4] O. Bakajin, N. Ben-barak, J. Peng, A. Noy, “Carbon Nanotube based Microfluidic elements for Filtration and Concentration”, 7th Intl. Conf. on Miniaturized Chem. and Bio. Anal. Sys., October 5-9, 2003, Square Valley, CA, USA.
- [5] R. Dorairaj, S.D. Cambron, G. Sumanasekera et al., “Fabrication of Carbon Nanotube-filled microchannels for Biological Separations”, 2007 SEM Annual Conf. and Exposition on Experimental and Applied Mechanics, June 4-6, 2007, Springfield, MA, USA.

# CHARACTERIZATION OF DUAL-AXIS PIEZORESISTIVE MEMS FORCE SENSORS

G.C. Hill, D.R. Soto, J.E. Oliver, and T.W. Kenny  
Stanford University, Stanford, California, USA

## ABSTRACT

Dual-axis piezoresistive MEMS force sensors were rigorously characterized to improve their calibration. Displacement sensitivity was measured directly as in [1], while spring constants were calculated using resonant frequency measurements and finite element modeling (FEM) [1, 2]. Similar devices have been described in the literature [3, 4], but this is the first report of a robust calibration process that corrects for the expected variability of critical parameters.

## INTRODUCTION

The stiffness of MEMS cantilevers is difficult to measure directly. Some have fabricated and calibrated reference springs for this purpose[5], a method limited by the reference calibration and the ability to control the orientation and position of interaction. The use of analytical formulas for stiffness predictions is limited by the applicability of the formula and the accuracy of material and geometry parameters.

These dual-axis sensors have distinct regions of lateral and normal compliance (Figure 1). The tip half is 1  $\mu\text{m}$ -tall and bends

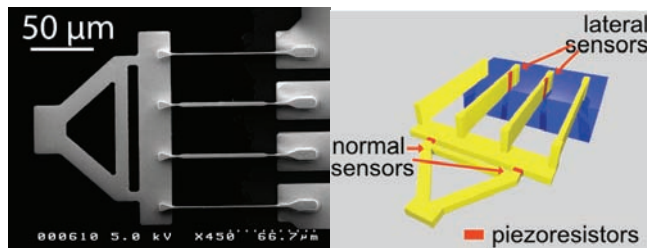


Figure 1: SEM of cantilever (left) and schematic (right) showing piezoresistive implants that transduce forces applied at the tip. Sensors are located in regions of high stress under deflection (see Figure 2). In the SEM, “normal” forces are out of the page, while “lateral” forces are vertical on the page.

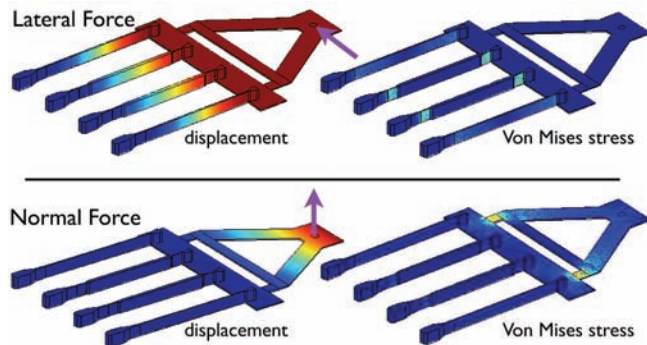


Figure 2: Finite element model (FEM) of a cantilever with force applied laterally (top) and normally (bottom), where color shows displacement (left) and von Mises stress (right). Lateral compliance is achieved primarily in the long, thin “ribs”, with stress concentrated at the location of the lateral sensors, and normal compliance is primarily in the triangular tip, with stress concentrated at the normal sensors.

in response to normally applied forces, while resisting lateral forces (Figure 2). Four tall (10  $\mu\text{m}$ ), skinny (0.75-1.5  $\mu\text{m}$ ), long (80-200  $\mu\text{m}$ ) ribs connect the triangle tip to the base. These ribs comply with lateral forces but are stiff to normal forces. Piezoresistors are strategically implanted in high-stress regions, and are read by a Wheatstone-bridge signal conditioning circuit.

## RESULTS

### Displacement sensitivity

The voltage output from the signal conditioning circuit is linearly related to tip deflection by the displacement sensitivity parameter. Displacement sensitivities of  $\sim 0.1$ -1 V/ $\mu\text{m}$  were measured using a computer-controlled piezoelectric stage to move the cantilever into a fixed bristle (Figure 3). These sensitivities were highly reproducible, with less than 1% variation in successive measurements at the same point (Figure 4). Sensitivities varied by 5% (normal direction) and 10% (lateral direction) with repositioning. In particular, applying normal forces offset from the tip center did not affect displacement sensitivity (Figure 5). Sensitivity measurements made over several months do not show drift greater than the repositioning variability. Thus, once measured, the displacement sensitivity may be used with confidence in later experiments.

### Force constants

A 3-D FEM (COMSOL 3.3a) was constructed for each cantilever and used to predict its lateral and normal stiffnesses and resonant frequencies. Input parameters included mask dimensions and bulk silicon material properties. The critical dimension in each analysis (rib thickness  $t_{rib}$  for lateral, cantilever thickness  $t_{cant}$  for normal) was not well described by mask dimensions. Both these dimensions are set in a timed 9  $\mu\text{m}$ -etch of the ribs pattern into the 10  $\mu\text{m}$ -device layer of a silicon-on-insulator wafer. The remaining “1  $\mu\text{m}$ ” device layer is the nominal cantilever thickness; however, 5% etch rate variability across a wafer results in cantilever thicknesses from 0.55 to 1.45  $\mu\text{m}$ . Similar variability was noted during fabrication, but cantilever thicknesses were difficult to measure precisely after processing. SEM measurements of rib thicknesses were taken and showed significant thinning from the mask dimensions ( $\sim 50\%$ ), as well as significant variability in thickness along each rib.

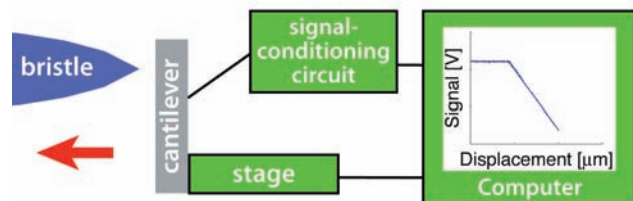


Figure 3: Experimental set-up for displacement sensitivity measurement. Cantilever is mounted on a computer-controlled piezoelectric stage and moved into a bristle. As the cantilever deflects, a Wheatstone bridge signal-conditioning circuit measures the change in piezoresistance. The displacement sensitivity is the slope of a linear fit to voltage output vs. displacement.

Table 1: Fitting geometry parameters in a finite element model (FEM) to measured resonant frequencies. Lateral- and normal-mode resonant frequencies were measured for each cantilever using a laser-Doppler vibrometer. Model 1 uses average SEM measurements for rib thickness  $t_{rib}$  and the nominal cantilever thickness  $t_{cant} = 1\mu\text{m}$ . Predicted frequencies are off by an average of 20% (normal-mode) and 90% (lateral). Model 2 uses the optimized thicknesses for each cantilever (see Figure 6) such that modeled resonant frequencies match observation within 1-2%. Frequencies are in kHz and dimensions in  $\mu\text{m}$ . Stiffness parameters from Model 2 are to be used in future work.

Cantilever	Measured		Model 1				Model 2			
	$f_{lat}$	$f_{norm}$	$t_{rib}$	$t_{cant}$	$f_{lat}$	$f_{norm}$	$t_{rib}$	$t_{cant}$	$f_{lat}$	$f_{norm}$
1	122	204	1.44	1.00	198	185	1.01	1.11	122	204
2	52	92	1.06	1.00	107	93	0.62	0.98	52	92
3	20	59	0.97	1.00	55	68	0.46	0.87	20	59
4	14	41	0.95	1.00	29	45	0.55	0.89	14	41
5	63	72	0.87	1.00	83	92	0.67	0.76	63	72
6	25	68	0.79	1.00	42	89	0.51	0.73	25	68
7	24	50	0.79	1.00	41	67	0.49	0.72	24	50
8	36	64	0.75	1.00	68	92	0.44	0.67	36	64

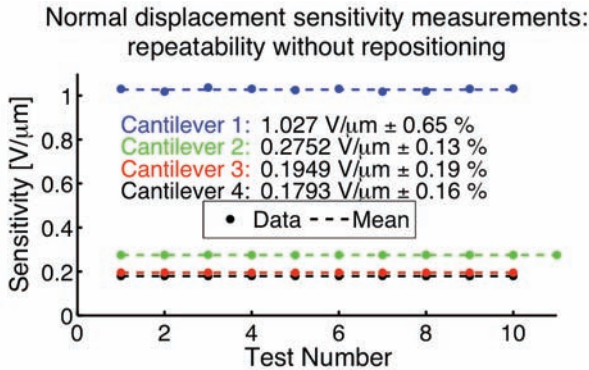


Figure 4: Displacement sensitivity measurements are highly reproducible (standard deviation < 1%) if the cantilever is not repositioned between measurements. Ten measurements each of four cantilevers shown. Errors are standard deviations of values.

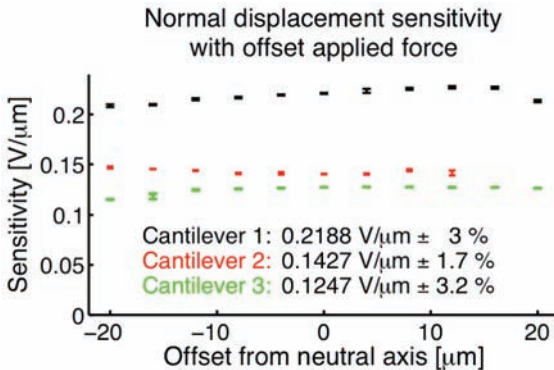


Figure 5: Normal displacement sensitivity measurements versus offset from neutral axis along cantilever tip. Averages shown with error bars. Sensitivity is only weakly related to offset.

Initial models used the measured rib thicknesses and nominal cantilever thickness (Table 1). The predicted lateral and normal resonant frequencies of each device were then compared to actual resonant frequencies measured with a laser-Doppler vibrometer. The predictions were off by 20% (normal-mode) and 90% (lateral-mode), revealing modest inaccuracies in  $t_{cant}$  and significant inaccuracies in  $t_{rib}$ . This result, consistent with the observed variable rib thinning, suggests that the visually observed rib thicknesses were greater than the mechanically effective rib thicknesses. For each mode of each device, the critical parameter was adjusted until the resonant frequency predicted by the model matched observation (Figure 6).

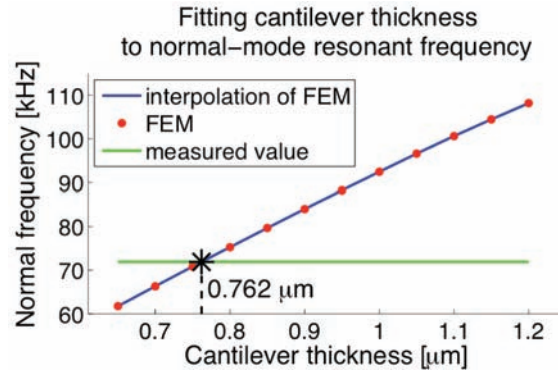


Figure 6: The cantilever thickness in an FEM is adjusted to match the observed normal-mode resonant frequency for a specific cantilever. This model fits at a cantilever thickness of  $0.762\mu\text{m}$ .

## CONCLUSIONS

In conjunction with the measured displacement sensitivities, using stiffnesses predicted by resonant frequency-corrected models will improve the accuracy of two-component force measurements made with these sensors in future experiments.

## ACKNOWLEDGEMENTS

The National Science Foundation partially supported this work under grants ECS-9731293 and EEC-0425914. A Kirby Stanford Graduate Fellowship and Stanford's Summer Undergraduate Research Institute partially supported G.H. and J.O.

## REFERENCES

- [1] T. Gotszalk, P. Grabiec, and I. W. Rangelow, "Calibration and examination of piezoresistive Wheatstone bridge cantilevers for scanning probe microscopy", *Ultramicroscopy*, 97, 385-9, (2003).
- [2] J. L. Hazel and V. V. Tsukruk, "Friction force microscopy measurements: normal and torsional spring constants for V-shaped cantilevers", *J. Tribology*, 120, 814-19, (1998).
- [3] K. Autumn, Y. A. Liang, S. T. Hsieh, W. Zesch, W. P. Chan, T. W. Kenny, R. Fearing, and R. J. Full, "Adhesive force of a single gecko foot-hair." *Nature*, 405, 681-5, (2000).
- [4] B. W. Chui, T. W. Kenny, H. J. Mamin, B. D. Terris, and D. Rugar, "Independent detection of vertical and lateral forces with a sidewall-implanted dual-axis piezoresistive cantilever", *Applied Physics Letters*, 72, 1388-1390, (1998).
- [5] P. J. Cumpson, P. Zhdan, and J. Hedley, "Calibration of AFM cantilever stiffness: a microfabricated array of reflective springs", *Ultramicroscopy*, 100, 241-51, (2004).

# ENDOTOXIN REMOVAL USING MICROMACHINED SILICON NANOPOROUS MEMBRANES

R.A. Smith<sup>1,2</sup>, K. Goldman<sup>3</sup>, A.J. Fleischman<sup>1</sup>, W.H. Fissell<sup>1</sup>, C.A. Zorman<sup>2</sup>, and S. Roy<sup>1</sup>

<sup>1</sup>Department of Biomedical Engineering, Cleveland Clinic, Cleveland, Ohio, USA

<sup>2</sup>Dept. of Electrical Engineering and Computer Science, Case Western Reserve University, Cleveland, Ohio USA

<sup>3</sup>H-Cubed, Inc., Cleveland, Ohio USA

## ABSTRACT

In this work, micromachined silicon nanoporous membranes (MSNM) are introduced as a means for removing endotoxin from water for medical uses. MSNM with critical pore dimensions of 35 nm and 42 nm and a 0.2  $\mu\text{m}$  syringe filter were challenged with feed solutions containing endotoxin activities of around 20,000 EU/mL. MSNM filters showed a reduction in endotoxin activities by 2 to 3 orders of magnitude.

## INTRODUCTION

Endotoxins are lipopolysaccharide fragments from the outer cell membrane in Gram-negative bacteria that are known to cause septic shock, tissue injury, and death in organisms [1]. As such, it is critical for the endotoxin levels in medical solutions to be minimized. For intravenous (IV) use, the limit of acceptable endotoxin presence has been set by the United States at 0.25 endotoxin units (EU) per mL. Previous work in endotoxin removal has focused on methods based on size exclusion [2], charge exclusion [3], and adsorption [3-4]. Ceramic filters are attractive for endotoxin removal because of their ability to withstand the harsh environments employed during cleaning [5]. Ceramic filters generally have a wide pore size distribution based on their method of manufacture. With endotoxin levels of 1000 EU/mL in the feed solution, these filters are capable of reducing endotoxin activity in the filtrate to IV use specifications in dead-end filtration, but not when used in cross-flow filtration applications [5]. Cross-flow filtration is desirable for many applications because it generally extends filter lifetime by reducing filter fouling.

## DEVICE DESCRIPTION

Micromachined silicon nanoporous membranes (MSNM) with monodispersed pore size distributions of the type shown in the schematic of Fig. 1 are an attractive alternative to ceramic filters for size-exclusion based endotoxin removal. Like ceramic membranes, MSNM are chemically, mechanically, and biologically stable [6]. The membranes are made of polysilicon films that are deposited on nitride-coated (100) Si wafers. Standard Si micromachining techniques combined with Si thermal oxidation can be used to produce nanopore membranes with very tight tolerances on pore dimensions and distribution; the critical dimensions of all pores varying by only 5% [7]. MSNM are currently of interest as size-exclusion based filters for use in renal replacement applications [8]. Based on previous work in molecular sieving, we hypothesize that MSNM can deliver superior functionality and performance over conventional size-exclusion based filtration technologies since the pore geometries are more tightly controlled [9].



Figure 1: Cross-sectional schematic of a MSNM used in this study. Pores are formed by selective removal of a sacrificial oxide that is thermally grown on the sidewalls of a patterned polysilicon film.

## EXPERIMENTAL

In this study, MSNMs of the type shown in Fig. 2 with pore sizes of 35 nm and 42 nm and a commercially-available 0.22  $\mu\text{L}$  syringe filter were evaluated for their effectiveness in endotoxin removal. Using the apparatus shown in Fig. 3, a mixture composed of 1 mL concentrated endotoxin solution and 100 mL of filtered DI water was circulated by a peristaltic pump in a closed circuit from the liquid reservoir past the MSNM chip in a cross-flow orientation. The filtrate was collected in a sterile microcentrifuge tube. For each filter, three 1 mL samples of filtrate and three 1 mL samples of the feed solution were collected, though only one feed sample for the syringe filter was tested for endotoxin activity. In addition, 1 mL samples of filtered DI water and endotoxin-free water were collected for comparison purposes. After collection, the samples were sent to Nelson Labs (Salt Lake City, UT) to determine endotoxin levels. The test employed for EU quantification was the LAL kinetic turbidimetric test which had a range of 0.005 EU/mL to 5 EU/mL. If the filtrate had an endotoxin content greater than the available range, serial dilutions were performed until a reading could be made.

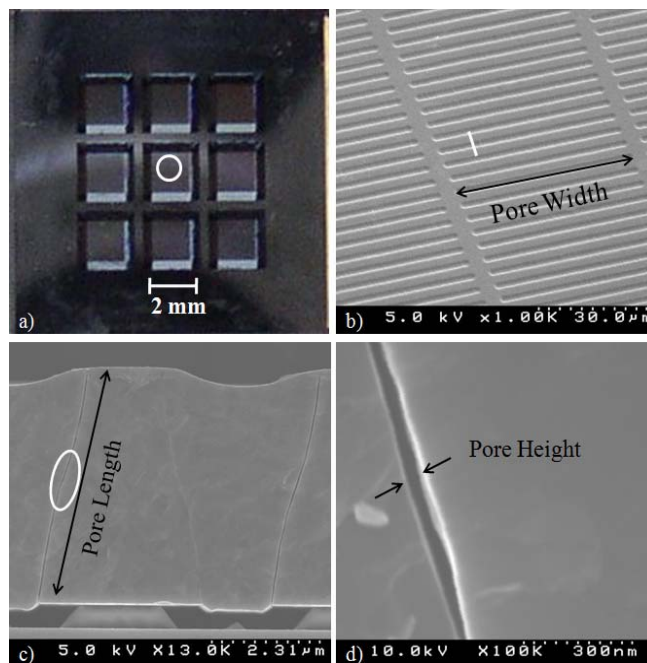


Figure 2: Images of a micromachined silicon nanoporous membrane chip: a) An optical image of an entire chip. b) An SEM of the top surface of the membrane which illustrates the width of the nanopores. c) A cross-sectional SEM of a nanoporous membrane which illustrates the length of the nanopores. d) A close-up cross sectional view showing an individual nanopore. At this magnification, the pore height (the critical dimension) can be measured (42 nm in this case).

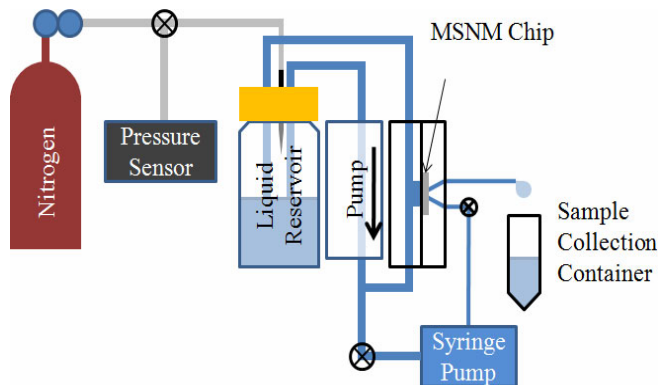


Figure 3: Schematic diagram of the experimental setup used to evaluate the MSNM filter chips. Pressure is applied to a liquid reservoir that contains the feed solution. The pressurized feed solution is circulated past the MSNM chip by a peristaltic pump. Filtrate is collected in a sterile microcentrifuge tube. The MSNM is mounted in a cross-flow filtration.

## RESULTS

Table 1 summarizes the measured endotoxin levels for all samples. Both MSNM chips were capable of dramatically reducing the endotoxin levels, whereas the syringe filter did not appreciably reduce endotoxin levels. Although the endotoxin levels in the MSNM filtrate were not at levels suitable for IV use, the endotoxin levels in the feed solutions were more than 100x higher than those found in typical tap water (125 EU/mL) [10]. The extremely high endotoxin level in the feed solution was chosen to provide high contrast between the feed solution and filtrate. A comparison of endotoxin in the filtrate with that in the feed as a function of pore size is shown in Fig. 4. These data suggest that pore sizes below 30 nm are required to achieve filtrate that meets IV standards when feed stock with high endotoxin concentrations is used. MSNM with pore sizes below 10 nm are readily achievable and evaluation of these membranes is currently underway.

Table 1: Endotoxin levels in the feed solution and filtrate. Uncertainties for endotoxin level measurements are +100%/-50%.

MSNM-35	
Feed (EU/mL)	Filtrate (EU/mL)
22000	390
21000	15
19000	9.7
MSNM-42	
Feed (EU/mL)	Filtrate (EU/mL)
23000	61
25000	80
23000	16
SYRINGE	
Feed (EU/mL)	Filtrate (EU/mL)
24000	22000
	17000
	26000
Other Data	
DI Water (EU/mL)	Endotoxin-Free Water (EU/mL)
0.12	<0.005

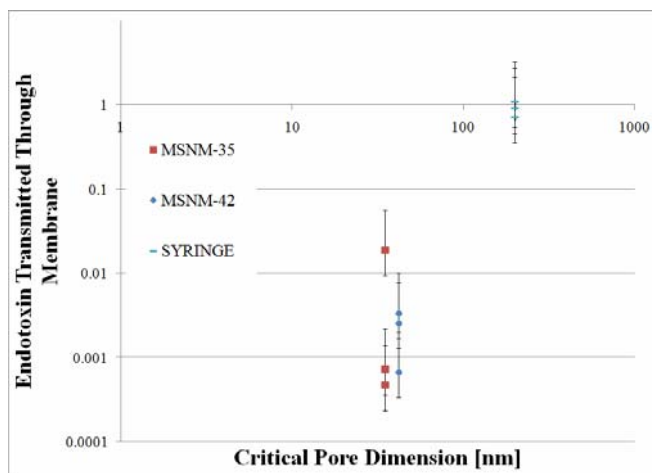


Figure 4: Measurement of endotoxin activity in the filtrate relative to endotoxin activity in the feed solution as a function of MSNM pore size. By comparison, a 0.22  $\mu\text{m}$  syringe filter did not exhibit any endotoxin rejection.

## ACKNOWLEDGEMENTS

This work was made possible by NASA STTR Grant # 06 T3.02-9924.

## REFERENCES

- [1] P. Magalhães, et al., "Methods of endotoxin removal from biological preparations: a review", *Journal of Pharmaceutical Science*, 10, 271-287 (2007).
- [2] K.J. Sweander, M.Forte, and L. Nelson, "Filtration removal of endotoxin(pyrogens) in solution in different states of aggregation", *Applied and Environmental Microbiology*, 34, 382-385, (1977).
- [3] C.P. Gerba and K. Hou, Kenneth. "Endotoxin removal by charge-modified filters" *Applied and Environmental Microbiology*, 50, 1375-1377, (1985).
- [4] R.L. Machado, et al., "Evaluation of a chitosan membrane for removal of endotoxin from human IgG solutions" *Process Biochemistry*, 41, 2252-2257, (2006).
- [5] P. Czermak, M. Ebrahimi, and G. Catapano. "New generation ceramic membranes have the potential of removing endotoxins from dialysis water and dialysate", *International Journal of Artificial Organs*, 28, 694-700 (2005).
- [6] F.J. Martin, and C. Grove, "Microfabricated Drug Delivery Systems: Concepts to Improve Clinical Benefit" *Biomedical Microdevices*, 3, 97-108, (2001).
- [7] T.A. Desai, D.J. Hansford, and M. Ferrari, "Micromachined Interface: New Approaches in Cell Immunoisolation", *Biomolecular Engineering*, 17, 23-26 (2000).
- [8] W.H. Fissell, et al., "Dialysis and Nanotechnology: Now, 10 Years, or Never?" *Blood Purification*, 25, 12-17, (2007)
- [9] J. Han, J. Fu, and R.B. Schoch, "Molecular sieving using nanofilters: Past, present and future", *Lab on a Chip*, 8, 23-33 (2008)
- [10] W.B. Anderson, R.M. Slawson, and C.I. Mayfield, "A review of drinking-water-associated endotoxin, including potential routes to human exposure", *Canadian Journal of Microbiology*, 48, 567-587 (2002).

# MECHANICAL ENERGY SCAVENGING FROM FLYING INSECTS

Ethem Erkan Aktakka<sup>1</sup>, Hanseup Kim<sup>1</sup>, Massood Atashbar<sup>1,2</sup>, and Khalil Najafi<sup>1</sup>

<sup>1</sup> Department of Electrical Engineering and Computer Science

Center for Wireless Integrated Microsystems (WIMS ERC), University of Michigan, Ann Arbor, MI, USA

<sup>2</sup> Department of Electrical and Computer Engineering

Center for Advanced Smart Sensors and Structures, Western Michigan University, Kalamazoo, MI, USA

## ABSTRACT

This paper reports the first effort to generate power from a live insect (*Cotinis nitida* - Green June Beetle) during its tethered flight, by utilizing piezoelectric devices in the d31 bending mode to convert mechanical vibrations of a beetle into electrical output. We measured available deflection, force and power output from oscillatory movements at different locations on a beetle with an unmounted piezoelectric beam and showed that up to ~115  $\mu\text{W}$  power generation is possible. Two initial generator prototypes were fabricated, mounted on a beetle, and harvested 11.5  $\mu\text{W}$  and 7.5  $\mu\text{W}$  in device volumes of 11.0  $\text{mm}^3$  and 5.6  $\text{mm}^3$  respectively, from 85 Hz-100 Hz wing strokes. A final prototype was designed to enable minimum disturbance of free-flight while maximizing power output. ANSYS simulations predict an output of 101.6  $\mu\text{W}$ .

## INTRODUCTION

One of the main constraints in the development of Micro-Air-Vehicles (MAVs) is the limited weight and volume reserved on the device for a long-life power source. Studies towards creating cyborg insects have demonstrated reliable tissue-electronics neuromuscular interfaces [1], and flight modulation through an implantable microsystem [2]. These initial implanted systems used batteries to power the microcontroller and muscle stimulator. However energy scavenging from an insect's high frequency body movements would achieve an unlimited source of power over the insect's life-time.

## MEASUREMENTS ON BEETLE

Several measurements were performed during tethered flight of a subject beetle, including acoustic measurements to define the average fundamental wing-stroke frequency, 92.1 Hz. Fig.1 summarizes the high speed (6000 fps) camera measurements of deflection and frequency at various body sections. Available force and power output measurements at various locations of the body were performed with an unmounted macro-scale piezoelectric beam (Fig.2-3). Force and power output (directly proportional to Frequency $\times$ Force $\times$ Deflection) increased towards the flight muscle base. These experimental measurements demonstrated ~115  $\mu\text{W}$  power generation due to elytra vibration close to the wing base, where both peak force input (35 mN-40 mN) and oscillatory displacement (0.8  $\text{mm}_{\text{pp}}$ ) are considerably large.

## INITIAL PROTOTYPE EXPERIMENTS

Two initial back-pack type energy scavenger prototypes were fabricated from 380  $\mu\text{m}$  thick PZT-Brass-PZT bimorphs, then mounted and tested on beetles. Prototype-I (Fig.4), stretching from thorax to far abdominal end of elytra, generated 11.5  $\mu\text{W}$  in 11.0  $\text{mm}^3$  device volume by delivering 874 mV<sub>RMS</sub> to a 66.6 k $\Omega$  load. Prototype-II (Fig.5), again mounted on the thorax, generated 7.5  $\mu\text{W}$  in a device volume of 5.6  $\text{mm}^3$  from two short piezoelectric beams each actuated by left/right elytra upstrokes.

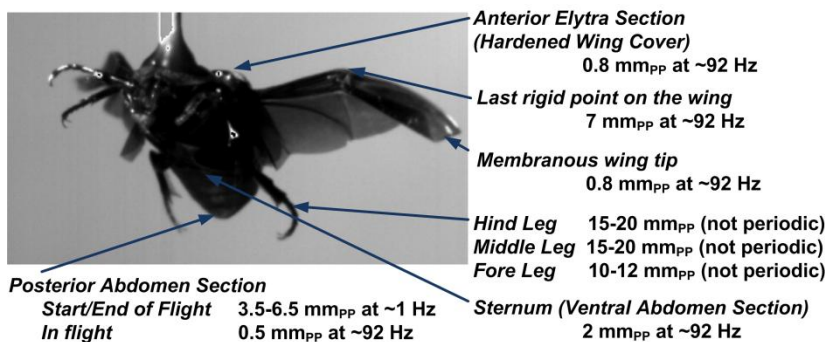


Figure 1: Deflection and frequency measurements on a beetle in flight.

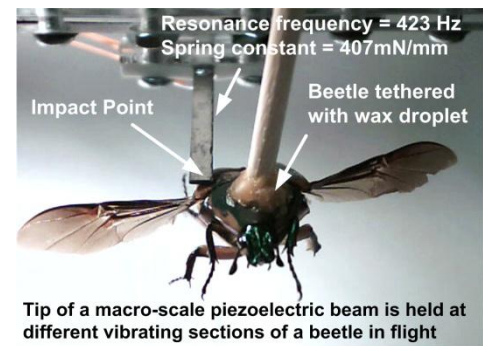


Figure 2: Measuring available power from a beetle.

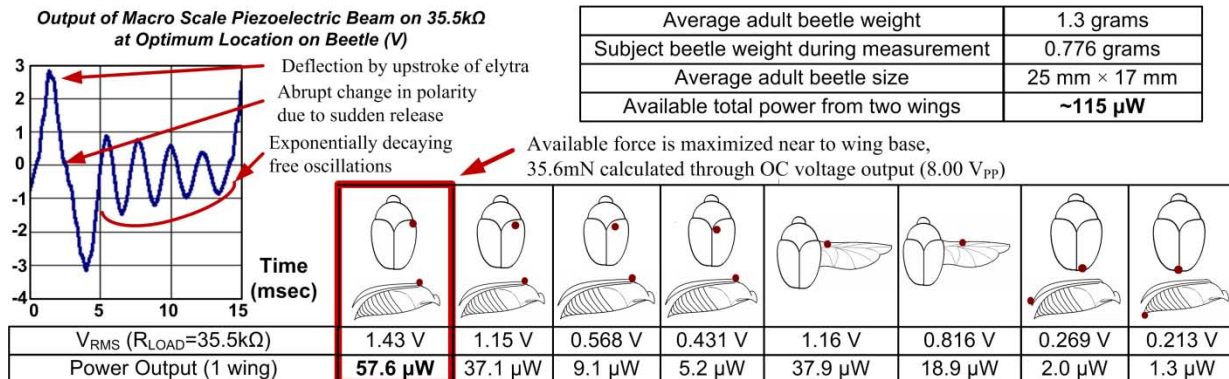


Figure 3: Available power measurements on *Cotinis nitida* during its tethered flight using the setup shown in Figure 2.

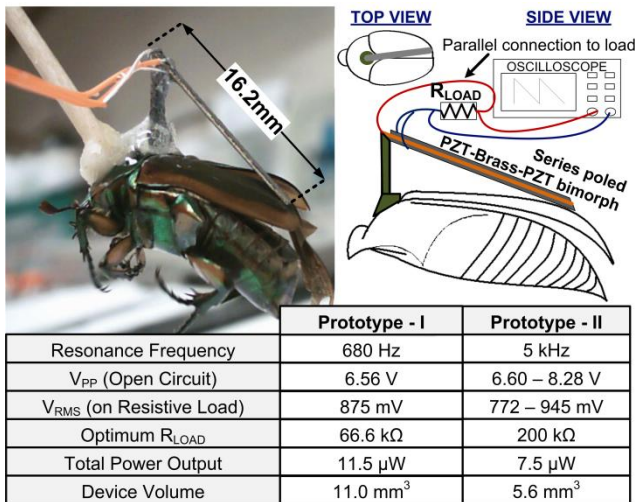


Figure 4: Prototype-I and output values of both prototypes.

The second prototype provided higher normalized output, (Power/Force/Deflection), 17.5  $\mu$ W/mN/mm, as it was hit by a higher force source. Since these initial prototypes had high beam stiffness, their vibrating tips could not be attached directly to the actuation site, therefore a gap between the device tip and the elytra was provided. From these experiments, it was concluded that the final prototype should take advantage of the full deflection of the elytra with a lower spring constant, while keeping maximum beam stress lower than the material yield stress (~20 MPa).

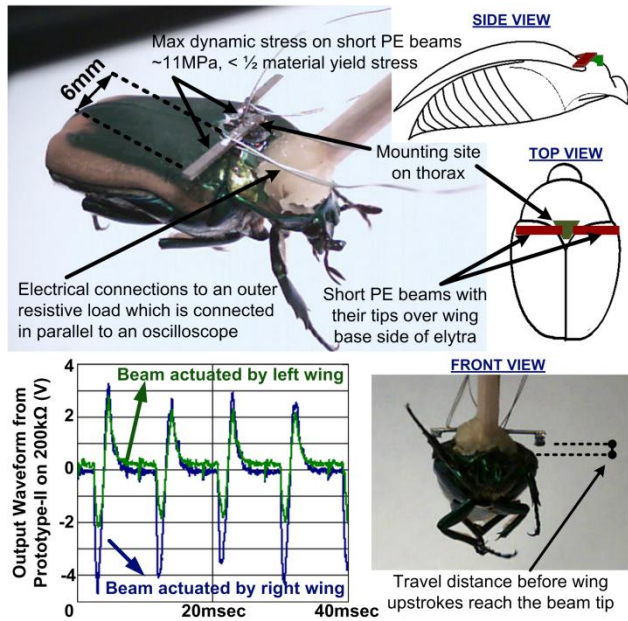


Figure 5: Prototype-II and its voltage output on a 200 k $\Omega$  load.

## FINAL PROTOTYPE DESIGN

A final energy scavenger prototype (Fig.6) was designed to provide a lower spring constant, while still occupying a limited area (5 mm  $\times$  5 mm) and maximizing strain on the piezoelectric layer, by employing a spiral beam geometry. For realization of the device, reliable low temperature solder bonding of piezoceramics was developed, and re-polarization and laser ablation of bulk piezoelectric layers were characterized. ANSYS simulations

indicate that a force of <2 mN is required for this design, and that 50.8  $\mu$ W can be generated per device at the insect's flapping frequency and elytra deflection. Placement of one coil design per wing can provide a total output >100  $\mu$ W, which is greater than the worst case average power consumption (80  $\mu$ W) of the wing muscle neural stimulator used in [2]. A direct connection from the device's impact point to the wing base (Fig.7), where the asynchronous flight muscle can supply up to ~0.9 N [3], would further improve power output.

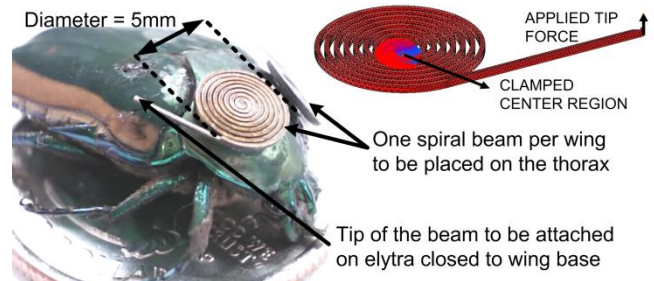


Figure 6: Final prototype; conceptual device geometry constrained in a 5 mm  $\times$  5 mm area, and device placement on a beetle's dorsal thorax.

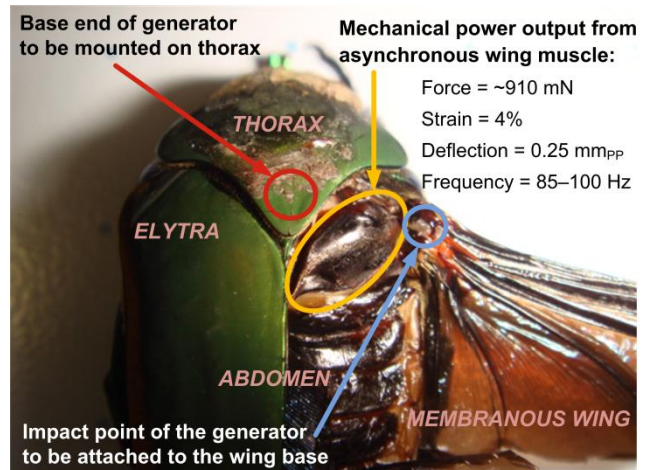


Figure 7: Conceptual device connection to the beetle's wing base, where flight muscles can provide up to 910 mN [3].

## REFERENCES

- [1] A. Bozkurt, R. Gilmour, D. Stern, A. Lal, "MEMS Based Bioelectronic Neuromuscular Interfaces for Insect Cyborg Flight Control", IEEE Conference on Micro Electro Mechanical Systems (MEMS 2008), Tucson, USA, pp. 160-163, 2008.
- [2] H. Sato, C.W. Berry, B.E. Casey, G. Lavella, Y. Yao, J.M. Vanderbrooks, and M.M. Maharbiz, "A Cyborg Beetle: Insect Flight Control Through an Implantable, Tetherless Microsystem", IEEE Conference on Micro Electro Mechanical Systems (MEMS 2008), Tucson, USA, pp. 164-167, 2008.
- [3] G.N. Askew, R.L. Marsh, "Review Muscle Designed for maximum short-term power output: quail flight muscle" The Journal of Experimental Biology 205, pp. 2153-2160, 2002.

# HIGH FREQUENCY ZNO-ON-DIAMOND MONOLITHIC FILTERS

R. Abdolvand<sup>1</sup> and F. Ayazi<sup>2</sup>

<sup>1</sup>School of Electrical and Computer Engineering, Oklahoma State University, Stillwater, Oklahoma, USA

<sup>2</sup>School of Electrical and Computer Engineering, Georgia Institute of Technology, Atlanta, Georgia, USA

## ABSTRACT

This paper reports on the design and implementation of acoustically-coupled thin-film ZnO-on-diamond resonators fabricated on a single resonant structure (monolithic filter). These small devices benefit from the large elastic modulus of diamond (largest in nature) to reach higher center frequencies while the frequency-determining dimension of the device stays in a range comfortably feasible to fabricate using conventional photolithography and etching tools. Lateral mode filters with center frequencies up to 900MHz are demonstrated with 1.4x frequency increase compared to the devices made on silicon.

## INTRODUCTION

In a monolithic acoustic filter multiple modes of a single resonant structure are coupled in order to achieve a higher order system. The same technique has been implemented in monolithic crystal filter (MCF) technology for decades [1]. The majority of the MCF's have been designed based on coupled thickness modes of a quartz plate [1,2]. With the emergence of thin-film technologies very high frequency (few GHz) piezoelectric filters are demonstrated and commercialized (e.g. film bulk acoustic resonator filters). However, the technique most attractive for low-frequency crystal filters (monolithic mode coupling) have not been yet adopted for these new-generation of acoustic devices. Lateral and thickness mode monolithic thin-film piezoelectric-on-silicon (TPoS) filters were demonstrated for the first time in [3]. In this work, we use a nanocrystalline diamond (NCD) film as the resonant structure in place of the silicon to achieve higher center frequencies.

## FILTER DESIGN

A monolithic thin-film piezoelectric-on-diamond (TPoD) filter is structurally the same as a two-port TPoD resonator (Fig. 1) [4]. The difference between a TPoD resonator and a filter is mainly in the top electrode pattern. In a filter configuration the top electrode is properly patterned to enable excitation of the dual resonance modes of a released structure. These two modes include a symmetric mode in which the displacement under both electrodes is in-phase, and an asymmetric mode in which the developed strain field under the two electrodes is 180° out of phase.

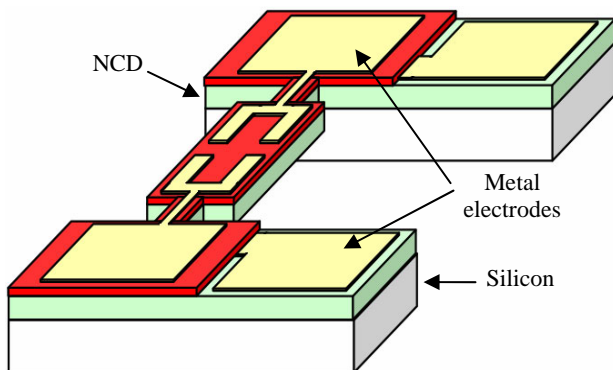


Figure 1: The schematic diagram of a piezoelectric-on-diamond monolithic filter.

In Fig. 2 the dual third harmonic lateral extensional mode-shapes that can be excited by the electrode pattern shown in Fig. 1 are simulated using the COMSOL package.

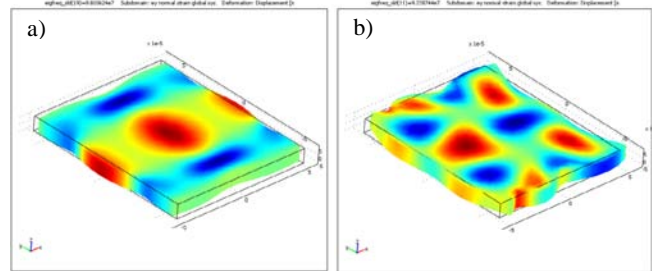


Figure 2: The simulated dual third harmonic lateral extensional mode-shapes which are coupled in the filter shown in Fig. 1; a) in-phase and b) out-of-phase.

Theoretically, all classes of resonance modes including flexural and extensional can be employed in a monolithic filter. In this work, a flexural-mode as well as a high-frequency (RF) lateral-extensional mode ZnO-on-diamond filter is presented. For the flexural-mode filter, the resonant structure is a long beam. The top electrode in this device is a metal strip which is split in half on top of the ZnO layer. The simulated dual flexural mode-shapes excited in this filter are presented in Fig. 3.

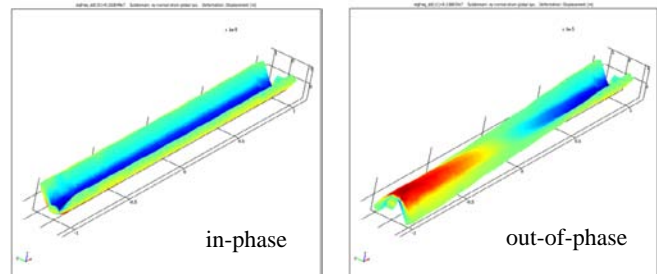


Figure 3: The simulated dual width flexural mode-shapes of a long beam.

On the other hand, the extensional mode filter consists of a wide rectangular membrane with a plurality of metal fingers on top of the ZnO layer. These fingers are designed to match the strain field pattern in a high-order lateral-extensional mode-shape of the structure (extension of the device shown in Fig. 1 in width direction).

## EXPERIMENTAL RESULTS

The process flow for fabrication of ZnO-on-diamond filters is schematically presented in Fig. 4. The resonant structure consists of a stack of ZnO on NCD. However, an optional thin layer of polished silicon dioxide can be included in the structure. The starting substrate is a silicon wafer with ~2μm of NCD deposited on top. The surface roughness of the diamond crucially affects the quality of the sputter-deposited piezoelectric layer. Therefore, the optional intermediate oxide layer is used to act as a buffer layer to compensate for the roughness of the diamond after polishing [4]. It also performs as a passive temperature compensation mechanism.

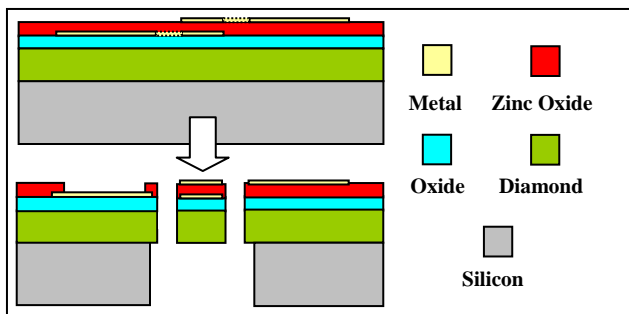


Figure 4: The schematic of the process flow

After depositing all the layers on the substrate, the access hole to the bottom electrode is etched in ZnO. Then, the resonant structure is defined by etching the stack from the top and is released by etching the silicon from the backside.

Fabricated devices are characterized on a high frequency probe station using GSG probes. The proper calibration procedure is performed before each measurement. The frequency response of Fig.5 is measured from the flexural-mode filter shown in the inset SEM picture. The device is a 20 $\mu\text{m}$  wide, 400 $\mu\text{m}$  long beam. The measured high out-of-band rejection (-50dB@78MHz) is due to the electrical isolation between the input and output ports which is a signature characteristic of acoustically-coupled filters. The insertion loss and the pass-band ripple of the filter are improved by terminating the filter with 500 $\Omega$  loads.

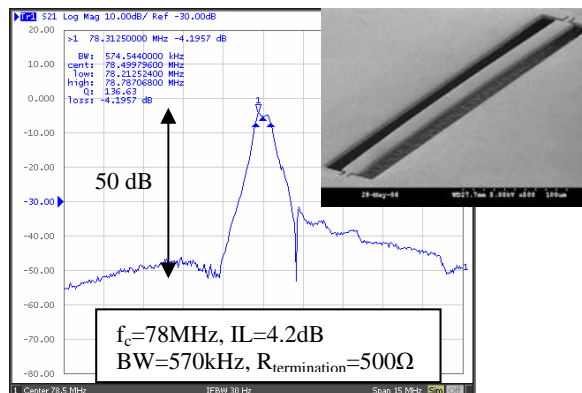


Figure 5: The frequency response of the flexural ZnO-on-nanocrystalline diamond monolithic filter

In this flexural mode device a thin layer of silicon dioxide (0.5 $\mu\text{m}$ ) was deposited and polished to promote the growth of c-plane ZnO grains on the rather rough surface of the NCD film. The temperature coefficient of frequency in this device was measured to be less than 8ppm/ $^{\circ}\text{C}$  as a result of including the oxide film in the structure. By modifying the deposition parameters, the grain size in the NCD film can be controlled. Smaller grain size NCD layer translates into a smoother surface which may eliminate the need for a polished intermediate layer.

Frequency responses of two lateral-extensional filters with identical layout (Fig. 6) fabricated on different substrates are compared in Fig. 7. The device fabricated on a 4 $\mu\text{m}$  SOI substrate has a center frequency of 640MHz (BW~1.5MHz) where as the same device made on the 2 $\mu\text{m}$  thick NCD film shows a 1.4x increase in the center frequency (~900MHz) with a 3MHz bandwidth. The ZnO is directly deposited on the NCD film with less than 10nm surface roughness. Relatively high insertion loss of the filter can be partially attributed to the lower coupling coefficient of the piezoelectric film.

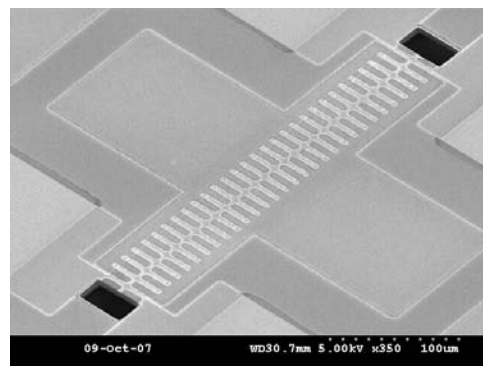


Figure 6: The SEM picture of the lateral-mode monolithic filter. The center-to-center finger pitch is 10 $\mu\text{m}$  in this device.

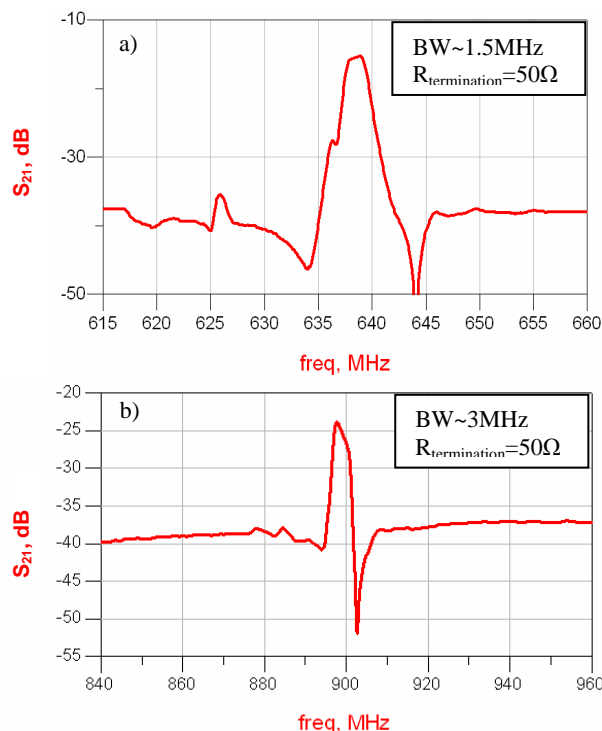


Figure 7: Measured frequency response plots of the device shown in Fig.6 fabricated on; a)SOI and b)Nanocrystalline diamond.

#### ACKNOWLEDGEMENT

Authors wish to thank Advanced Diamond Technology for providing the nanocrystalline diamond films.

#### REFERENCES

- [1] W. D. Beaver, "Theory and design of the monolithic crystal filter," *21st Annual Symposium on Frequency Control*, pp. 179-199, 1967.
- [2] R. G. Kinsman, "A history of crystal filters," *Proceedings of the 1998 IEEE International Frequency Control Symposium*, May 1998, pp.563-570.
- [3] R. Abdolvand, F. Ayazi, "Monolithic thin-film piezoelectric-on-substrate filters" *Proc. IEEE MTT-S International Microwave Symposium (IMS 2007)*, June 2007, pp. 509-512.
- [4] R. Abdolvand, G. K. Ho, J. Butler, F. Ayazi, "ZnO-on-nanocrystalline-diamond lateral bulk acoustic resonators," *Proc. of IEEE Micro Electro Mechanical Systems Conference*, Jan. 2007, pp. 795-798.

# POLYMER-BASED MICROSYSTEM FOR MECHANICAL CHARACTERIZATION OF CELLS

M. Gnerlich<sup>1</sup>, W.-Y. Zhang<sup>1</sup>, H. Donahue<sup>2</sup>, A. Voloshin<sup>1</sup>, and S. Tatic-Lucic<sup>1</sup>  
<sup>1</sup>Lehigh University, USA and <sup>2</sup>Pennsylvania State University, USA

## ABSTRACT

A BioMEMS platform has been developed to measure the mechanical compliance of live biological cells. It integrates a V-shaped electrothermal actuator (ETA) array, a force sensor, a displacement sensor, a thermal sensor, and a cell-positioning system in a single chip. By compressing a cell and measuring the reaction force with a biocompatible polymer-based system, the mechanical compliance can be measured without damaging the cell. Here, we present the initial characterizations of the integrated sensors and actuators, as well as temperature measurements during actuation in liquid environments including cell medium.

## INTRODUCTION

Determining the mechanical compliance of bone cells is considered to be of paramount importance to research for a more effective cure for osteoporosis, an illness that is impacting a significant portion of the world's senior population [1]. However, there is a lack of accurate and rapid systems that could reliably measure the mechanical properties of multiple biological cells at the same time [2,3], and a BioMEM system has been designed for this purpose. In our previous publications [4,5], we have presented the initial actuator characterization and detailed fabrication process. Here, for the first time, we describe the characterization of all of the constitutive modules, including the temperature measurements in the surrounding cell medium and the preliminary characterization of the force sensor which measures the force exerted onto the cell.

## METHOD

The BioMEM system is illustrated in Fig. 1 and the system functions as follows. First, a cell is trapped in the desired position (between an actuator and a cantilever based force sensor) using a set of four dielectrophoresis (DEP) electrodes stimulated with a 10 V<sub>p-p</sub> sinusoidal signal at 1 MHz, as shown in Fig. 5. Then, a force is applied to the cell using a polymer based electrothermal actuator. The resulting deformation of the cell is measured, and from these two measurements (force and deformation) the Young's modulus can be extracted using the Hertz contact model [6]. The temperature in the area immediately next to the actuator is measured using an integrated platinum resistance temperature detector (RTD) sensor and Wheatstone bridge. The temperature of the surrounding medium was measured using an external type K bead thermocouple placed 1 mm from the device and compatible digital multimeter (DMM) with temperature readout.

Power was applied to the actuator as an 800 KHz controlled voltage sinusoidal signal using a high-power operational amplifier. The tests were controlled and measured with a custom LabView program, which allowed integration of the data acquisition from the temperature bridge with GPIB communication to the DMM and function generator instruments. The instantaneous power delivered to the actuator was measured with a 4-point RMS voltage and current setup at 0.5 second intervals and recorded with the temperature data. Optical images were captured at 4 second intervals for displacement measurements using calibrated image capture software.

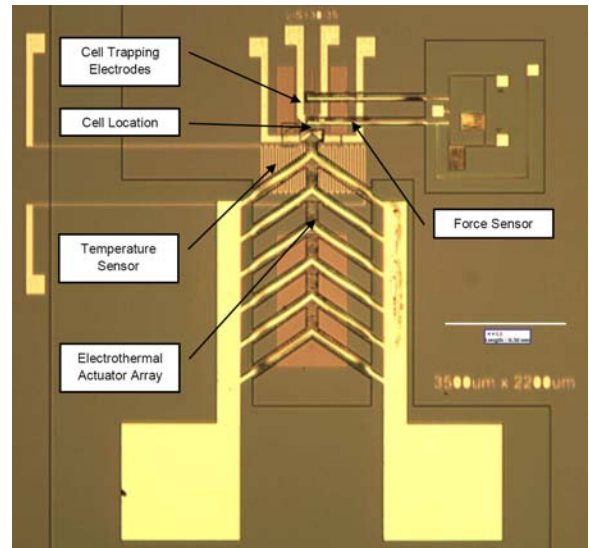


Figure 1. Optical image of a fabricated device with all the constitutive modules (the scale bar is 500  $\mu\text{m}$ ) [4]

## RESULTS

The initial characterization of all modules has been completed. The targeted range of up to 4  $\mu\text{m}$  motion of the actuator has been reached, as documented on Fig. 2. In addition to the actuator displacement in cell medium, characterization has been performed in three media so far: air, DI water, and cell medium. Temperature during the operation of the actuator has also been measured because we were concerned that the elevated temperature during electrothermal actuation could compromise the health of the living cell.

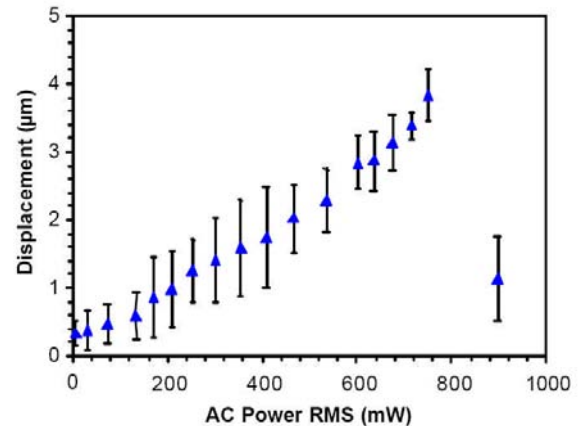


Figure 2. Electrothermal actuator array displacement as a function of applied AC RMS power (800kHz) in cell medium [5]

The temperature data from the on-chip sensor during 40 second long electrothermal actuator tests in deionized (DI) water shows that the maximum temperature is 45  $^{\circ}\text{C}$  (+/- 2 $^{\circ}\text{C}$ ) at the location of the cell at an applied RMS power level of 316 mW, and maximum 51  $^{\circ}\text{C}$  (+/- 2 $^{\circ}\text{C}$ ) at an RMS power of 444 mW, as documented on Fig. 3. Using the nearby thermocouple, the

temperature was measured to be 32 °C (+/- 1°C) at 316 mW and 35 (+/- 1°C) at 444 mW. The nominal cell medium temperature at zero power was 1 °C (+/- 1°C) higher at the end of the test. It was determined that cells would not sustain heat damage during a typical 2.5 second long compression test, since they can withstand temporary 40 °C temperature elevations above the normal cell culture temperature of 37 °C [7].

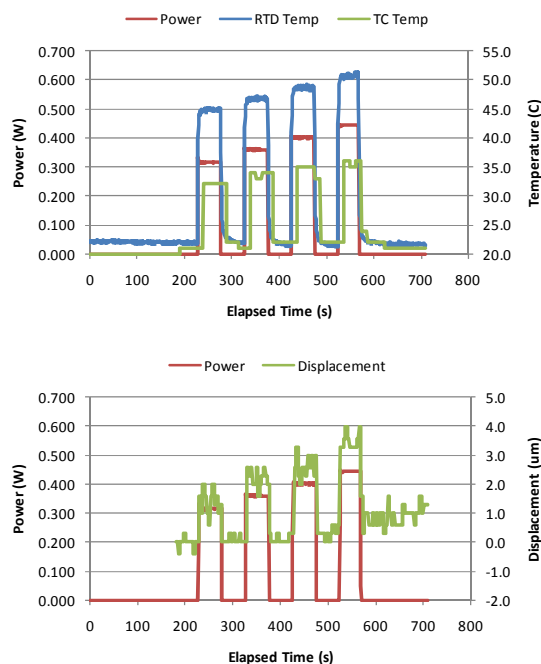


Figure 3. Temperature measured by the on-chip RTD sensor and nearby type K bead thermocouple (top) and corresponding displacement measured optically (bottom) when the actuator is powered in 40 second bursts in deionized water.

Initial characterization results for the force sensor are presented in Fig. 4. We estimate that we can currently resolve a force of 36 µN at 1 µm displacement for the tested device.

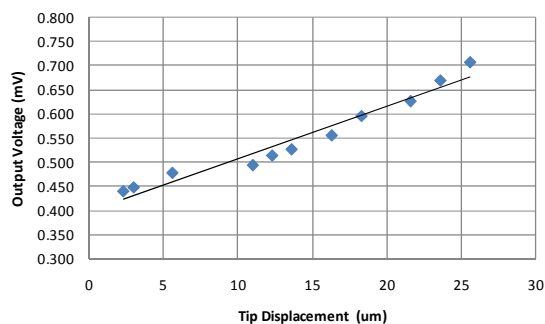


Figure 4. Output voltage as a function of lateral displacement of the cantilever force sensor with integrated Wheatstone's bridge.

In addition to force, measurements of corresponding cell deformation are required to complete mechanical characterization. The original design included a displacement sensor based on a cantilever strain gage attached to the electrothermal actuator array, but its performance was unsatisfactory due to stiction problems and deformation during electrothermal actuation. Therefore, the displacement measurement was performed with an optical

microscope requiring only calibration of the image capture software and the achieved optical resolution limit was +/- 0.5 µm. We have also tested the performance of the cell positioning module, and NIH3T3 fibroblast cells were successfully trapped using the dielectrophoretic electrodes, as documented on Fig. 5 which shows four different snapshots in the cell capturing process.

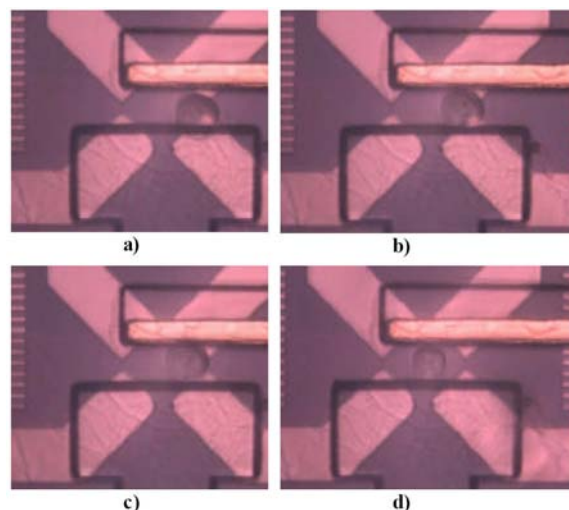


Figure 5. Cell capture with dielectrophoresis electrodes in cell medium. The fibroblast cell is attracted towards the center of the electrodes (a - c) and is kept in place as the cell settles to the bottom of the substrate directly in front of the actuator (d)

## CONCLUSION

Characterization of the components for mechanically testing living cells show that cell trapping, force measurements and electrothermally actuated compression may be accomplished at temperatures suitable for live biological cells while in cell medium. Successful cell compression with physiologically meaningful strain of 25% has been accomplished, as documented on the cell compression movie [8]. The measurement of mechanical properties of cells is underway.

## REFERENCES

- [1] U.S. Department of Health and Human Services. "Bone Health and Osteoporosis: A Report of the Surgeon General" (<http://www.surgeongeneral.gov/library/bonehealth/>)
- [2] Miyazaki, H., Hasegawa, Y. and Hayashi, K. "A newly designed tensile tester for cells and its application to fibroblasts". J. of Biomechanics, 33 (2000), pp. 97 - 104.
- [3] Scuor, N., et al. "Design of a novel MEMS platform for the biaxial stimulation of living cells". Biomedical Microdevices, 8 (2006), pp. 239 - 246.
- [4] Zhang, Wenyue, et al. "Polymer MEMS system for measuring the mechanical modulus of a biological cell". BioDevices 2008, 2 (2008), pp. 146 - 150.
- [5] Zhang, W.-Y. et al. "Polymer V-Shaped Electrothermal Actuator Array for Biological Applications". Journal of Micromechanics and Microengineering (2008) (submitted).
- [6] Zhang, W.-Y. Ph.D. Dissertation. ECE Department, Lehigh University. Bethlehem, PA: Lehigh University, 2007.
- [7] Chronis N. and Lee L.P., "Polymer MEMS-Based Microgripper for Single Cell Manipulation". 17th IEEE International Conference on Micro Electro Mechanical Systems, Maastricht, 1/25 - 1/29 (2004), pp. 17 - 20.
- [8] See <http://www.lehigh.edu/~mag305/cellcompression/>

# RAPID SACRIFICIAL GERMANIUM ETCHING USING XENON DIFLUORIDE

Garrett D. Cole and Elaine Behymer

Center for Micro- and Nanotechnologies, Lawrence Livermore National Laboratory,  
7000 East Avenue, Livermore, California 94550, USA

## ABSTRACT

We present a novel micromachining procedure employing the noble gas halide, xenon difluoride ( $\text{XeF}_2$ ), to rapidly undercut a sacrificial layer comprised of low-temperature deposited amorphous germanium ( $\alpha\text{-Ge}$ ). As a proof of concept, this process is utilized to fabricate electrostatically-actuated suspended Bragg mirrors applicable to wavelength-tunable surface-normal photonic devices. Exploiting  $\text{XeF}_2$  as the release etchant, we observe a truly remarkable lateral etch rate in excess of  $150 \mu\text{m}/\text{min}$  for a  $1\text{-}\mu\text{m}$ -thick sacrificial  $\alpha\text{-Ge}$  film. Given the rapid nature of this etch, we envision this procedure to be a promising approach for the lateral undercutting of large-area microdevices.

## INTRODUCTION

The sacrificial etch method is a fundamental technique for the construction of microelectromechanical systems (MEMS). Within this framework, processes employing gas-phase etchants such as  $\text{XeF}_2$ , bromine trifluoride [1], and HF vapor [2] have proven quite successful; particularly in the case of  $\text{XeF}_2$  for sacrificial silicon etching. As opposed to wet chemistry mediated undercutting, these processes enable rapid lateral etching without inducing capillary forces, thus eliminating the need for post-release critical point drying (CPD) and enabling efficient penetration into narrow micro/nanoscale vias. In this manuscript we present a novel micromachining procedure utilizing  $\text{XeF}_2$  to selectively etch a sacrificial  $\alpha\text{-Ge}$  film. When compared with sacrificial silicon etching, this process exhibits a significant enhancement in the achievable lateral etch rate. Additionally, the fabrication sequence may be tailored to incorporate low temperature deposition steps, ranging from thermal or electron-beam evaporation of  $\alpha\text{-Ge}$  at room temperature (enabling deposition rates of  $100 \text{ \AA}/\text{s}$  [3]), to CVD processes producing high quality polycrystalline germanium films at temperatures below  $450^\circ \text{C}$  [4].

## GAS-PHASE GERMANIUM ETCHING

The results from a preliminary investigation of the lateral etch rate of  $\alpha\text{-Ge}$  in  $\text{XeF}_2$  are presented in Fig. 1. For this experiment the  $\alpha\text{-Ge}$  is deposited by room temperature electron-beam evaporation onto single-crystal GaAs substrates. This procedure results in extremely smooth films with surface roughness values ranging from  $8\text{--}11 \text{ \AA}$ . Following evaporation, a  $\text{SiN}_x$  structural film is deposited via PECVD at  $200^\circ \text{C}$ . A pattern consisting of circular etch vias and orthogonal stripes is then transferred into the  $\text{SiN}_x$  with dilute HF. Finally, the  $\alpha\text{-Ge}$  layer is selectively undercut in a pulsed  $\text{XeF}_2$  etching system [5]. From the circular vias we measure a lateral etch rate of approximately  $55 \mu\text{m}/\text{min}$  for the  $1\text{-}\mu\text{m}$ -thick  $\alpha\text{-Ge}$  sample. This value is comparable to that recently presented for crystalline germanium samples [6] and largely exceeds the maximum typical silicon etch rate of approximately  $10 \mu\text{m}/\text{min}$  [7]. However, for the  $30\text{-}\mu\text{m}$ -wide orthogonal stripes surrounding the circular apertures (see inset image in Fig. 1), we measure a remarkable lateral etch rate of nearly  $160 \mu\text{m}/\text{min}$ . Given the rapid nature of this process, we propose that  $\text{XeF}_2$  etching of germanium is a promising approach for undercutting large-area devices or for the lift-off of continuous films from a potentially re-usable handle substrate, as in the epitaxial liftoff process pioneered by Yablonovitch [8].

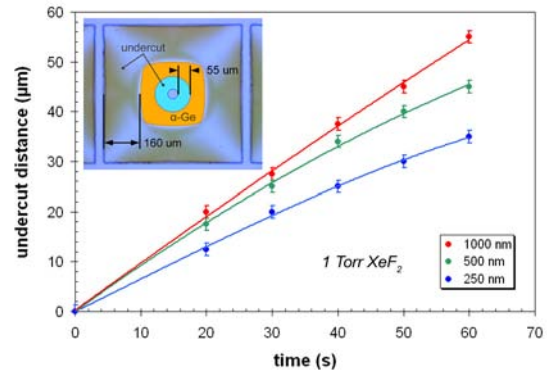


Figure 1: Undercut distance as a function of time for various thickness  $\alpha\text{-Ge}$  films. The data corresponds to the position of the lateral etch front with respect to the  $40\text{-}\mu\text{m}$ -diameter etch vias. Inset: micrograph of  $1\text{-}\mu\text{m}$   $\alpha\text{-Ge}$  sample after 60 s of etching.

## SUSPENDED DIELECTRIC BRAGG MIRRORS

The viability of our novel micromachining process is demonstrated through the development of electrostatically-actuated suspended dielectric Bragg reflectors (see Fig. 2), applicable to wavelength-tunable vertical-cavity lasers (VCSELs) [9,10] and amplifiers [11]. The detailed fabrication sequence for these devices may be found in [12]. Although  $\text{XeF}_2$  has been applied extensively in silicon-based microfabrication, to the best of our knowledge, this is the first use of this etchant for the development of MEMS with a germanium sacrificial layer, as well as the first use of  $\text{XeF}_2$  for MEMS on a compound semiconductor substrate.

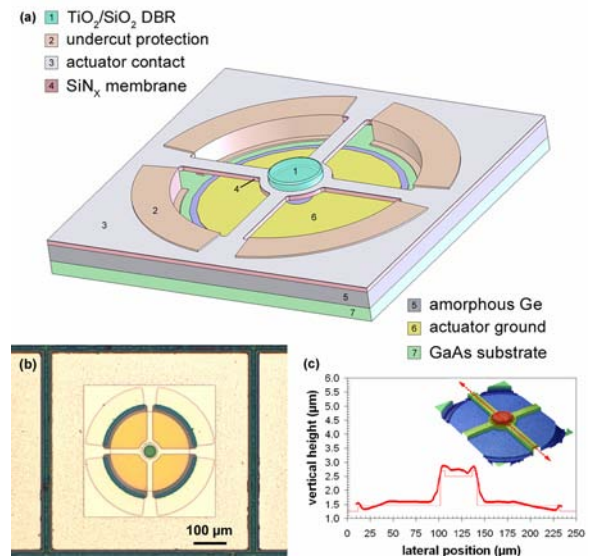


Figure 2: (a) Solid model of the suspended Bragg mirror. (b) Optical micrograph of a completed micromirror. (c) Line scan recorded with an optical profilometer; the inset includes the original 3-D mapping and indicates the path of the 2-D plot. The ideal profile is depicted along with the measurement. A minor upward bowing extends the nominal  $1000\text{-nm}$  air gap to  $1150 \text{ nm}$ .

As with sacrificial silicon etching, this process results in excellent selectivity over most metals, dielectrics, polymers, etc. Additionally, the use of the non-plasma etch eliminates surface damage induced by ion bombardment, while the simplicity of the etching system allows for *in situ* viewing of the lateral etch front. Compared with previous implementations [11], the fabrication of the suspended mirror structures is greatly simplified through: 1) the elimination of the CPD process, 2) the ability to monitor the lateral etch front beneath the transparent mirror structure, and 3) the largely reduced release etch time. In fact, for the devices presented in this manuscript, the total time required to successfully undercut an 80- $\mu\text{m}$  diameter membrane is less than 20 seconds (achieved through two 10-s pulses or one single 20-s etch pulse).

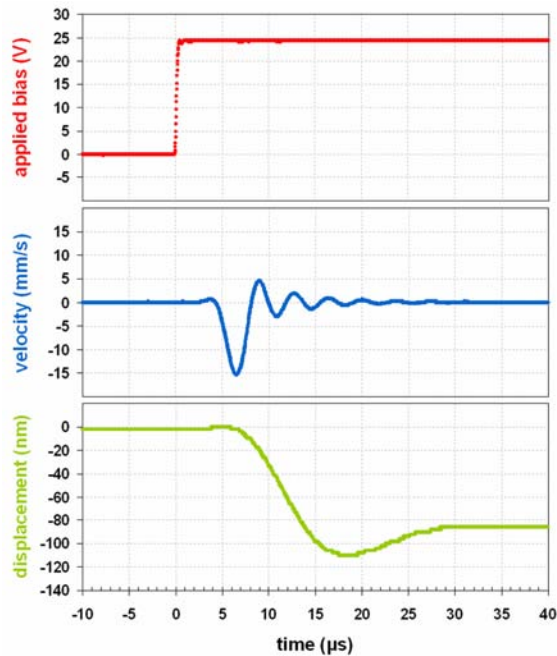


Figure 3: Step response (atmospheric pressure) for a 60  $\mu\text{m}$  diameter membrane with 70  $\mu\text{m}$  long by 20  $\mu\text{m}$  wide tethers at a bias of 24 V; negative values indicate vertical motion towards the substrate. Ringing leads to a settling time of just under 30  $\mu\text{s}$ .

Following fabrication we investigate the static and dynamic characteristics of the suspended reflector using a laser-Doppler-vibrometer-based MEMS motion characterization system [13]. Fig. 3 presents the step response of the suspended mirror structure, while the compiled displacement versus bias data are included in Fig. 4. It is important to note that the step response exhibits temporal smoothing due to the limited 3-dB bandwidth of the vibrometer (250 kHz for velocity and 50 kHz for displacement). The settling time of this structure may be reduced by optimizing the geometry of the actuator to achieve sufficient squeeze-film damping for a near critically-damped response [14].

From the theoretical fit of the static deflection data, the estimated snap-down voltage (displacement) is 30.9 V (447 nm) with the best fit achieved for an air-gap thickness of 1120 nm. This value compares well with the profilometer measurements of the air-gap thickness (1150 nm). Assuming this mirror is incorporated on a GaAs-based  $1-\lambda$  semiconductor cavity with a hypothetical center wavelength of 1000 nm, the measured deflection would result in a wavelength tuning range of 37 nm at 30 V bias (this calculation includes the penetration depth for a 25.5 period GaAs/AlAs bottom mirror).

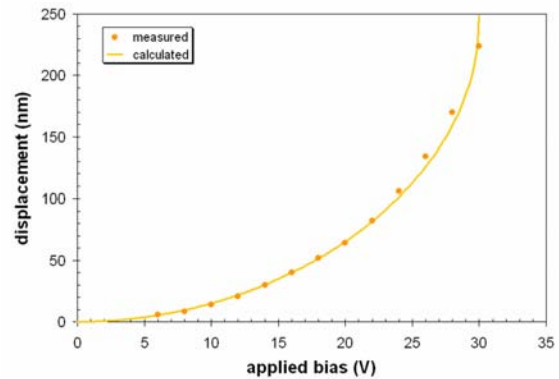


Figure 4: Static deflection characteristics of the suspended mirror. The theoretical curve is generated from the iterative solution of a one-dimensional electromechanical model [12]. Current-voltage measurements demonstrate leakage currents below 20 pA at 30 V.

## SUMMARY AND FUTURE WORK

We have demonstrated a novel micromachining process exploiting  $\text{XeF}_2$  to rapidly remove an evaporated  $\alpha\text{-Ge}$  sacrificial layer. For large etch apertures we record undercut rates exceeding 150  $\mu\text{m}/\text{min}$ . Further investigation will be necessary to quantify the lateral etch rate for narrow (sub-micron) vias. Finally, this procedure has been utilized to demonstrate high-performance arrays of electrostatically actuated suspended Bragg reflectors.

## ACKNOWLEDGMENTS

This work performed under the auspices of the U.S. DOE by Lawrence Livermore National Laboratory under Contract DE-AC52-07NA27344. GDC thanks Professor Roger T. Howe of Stanford University for a number of insightful discussions.

## REFERENCES

- [1] T. Yao, X. Yang, Y.C. Tai, Sens. Actuators A **97**, 652 (2002).
- [2] Y.I. Lee, K.H. Park, J. Lee, C.S. Lee, H.J. Yoo, C.J. Kim, Y.S. Yoon, J. MEMS **6**, 226 (1997).
- [3] M.L. Rappaport, B. Berkovitz, J. Vac. Sci. Technol. **21**, 102 (1982).
- [4] A.E. Franke, J.M. Heck, T.J. King, R.T. Howe, J. MEMS **12**, 160 (2003).
- [5] P.B. Chu, J.T. Chen, R. Yeh, G. Lin, J.C.P. Huang, B.A. Warneke, S.J. Pister, Proc. Transducers '97, Chicago, IL, USA, paper 2D3.01, p. 665.
- [6] G. Xuan, T.N. Adam, J. Suehle, E. Fitzgerald, P. Lv, N. Sustersic, M.J. Copping, J. Kolodzey, Proc. ISTDM 2006, Princeton, NJ, paper 5P.44.
- [7] K.R. Williams, R.S. Muller, J. MEMS **5**, 256 (1996).
- [8] E. Yablonovitch, D.M. Hwang, T.J. Gmitter, L.T. Florez, J.P. Harbison, Appl. Phys. Lett. **56**, 2419 (1990).
- [9] M. Maute, B. Kögel, G. Bohm, P. Meissner, M.-C. Amann, IEEE Photon. Technol. Lett. **18**, 688 (2006).
- [10] M.C. Huang, K.B. Cheng, Y. Zhou, A.P. Pisano, C.J. Chang-Hasnain, IEEE J. Sel. Top. Quantum Electron. **13**, 374 (2007).
- [11] G.D. Cole, E.S. Björlin, C.S. Wang, N.C. MacDonald, J.E. Bowers, IEEE Photon. Technol. Lett. **17**, 2526 (2005).
- [12] G.D. Cole, E. Behymer, L.L. Goddard, T.C. Bond, J. Vac. Sci. Technol. B **26**, 593 (2008).
- [13] K.L. Turner, P.G. Hartwell, N.C. Macdonald, Proc. Transducers '99, Sendai, Japan, p. 1144.
- [14] G.D. Cole, J.E. Bowers, K.L. Turner, N. C. MacDonald, IEEE/LEOS Optical MEMS 2005, Oulu, Finland, paper F4.

# REAL-TIME SYNTHESIS AND MANIPULATION OF PHOTOPOLYMERIZED MICROSTRUCTURES USING OPTOFLUIDIC MASKLESS LITHOGRAPHY AND OPTICAL TWEEZERS

K. Yu<sup>1</sup>, H. Park<sup>2</sup>, N. Park<sup>2</sup>, and S. Kwon<sup>2</sup>

<sup>1</sup>University of California, Berkeley, CA, USA

<sup>2</sup>Seoul National University, Seoul, Korea

## ABSTRACT

We report on a microfluidic platform for real-time synthesis, manipulation, and assembly of free-floating heterogeneous polymeric microstructures. We generate polymeric microparticles with various sizes, shapes, and composition using in-situ photopolymerization process with a dynamic spatial light modulator, and manipulate their relative positions and orientations using an optical tweezer for particle transportation, sorting, assembly, and reordering. Rapid prototyping of composite polymeric structures by assembling smaller microstructures with different shapes and materials is experimentally demonstrated. The integration of optical tweezers and maskless lithography with the microfluidic channels enables dynamic particle generation and manipulation in a single compact platform.

## INTRODUCTION

Microscopic structures made of multiple polymeric materials with different physical and/or chemical properties have important applications in the various disciplines of microsystems engineering, including photonic devices [1], self-assembly process [2], and biocompatible materials [3, 4]. Rapid lab-on-a-chip prototyping of such composite microstructures can provide a number of advantages in terms of time, cost, and portability over conventional fabrication technologies with mask-based lithography [3-6]. However, in previous in-situ photopolymerization techniques for multi-faced microparticle generation, the number of materials and their boundary shapes within one microparticle are generally limited by microfluidic streams inside the channel [4-6]. In this paper, we demonstrate that an optical tweezer can manipulate polymerized microstructures inside the microfluidic channel [7], and can be used for in-situ fabrication of complicated composite microstructures.

## EXPERIMENTAL SETUP

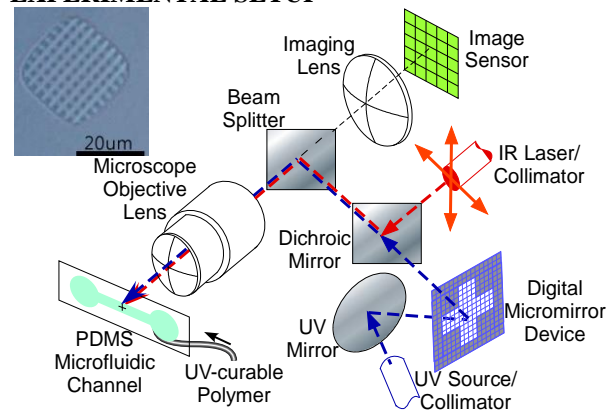


Figure 1: Schematic diagram of the experimental setup. The inset shows a microscope photograph of a polymeric two-dimensional lattice structure synthesized by the setup.

Figure 1a schematically shows our experimental setup based on an inverted microscope. Extruded polymeric microparticles with various shapes and sizes can be synthesized inside the microfluidic channel by selectively solidifying the liquid-phase photocurable

oligomer stream with the ultraviolet (UV) light exposure [3-6]. A high magnification microscope objective lens demagnifies computer-controlled image patterns from a two-dimensional spatial light modulator (SLM) [8] onto the microfluidic channel placed on the object plane of the microscope [6]. The illumination source for the SLM is a UV light source with the center wavelength of 365 nm.

The objective lens also focuses the high-intensity infrared (IR) optical beam from a continuous-wave 1060 nm Ytterbium fiber laser source for optical manipulation. The optical tweezing IR beam is spatially combined with the UV exposure pattern using a dichroic mirror as shown in Fig. 1. The beam spot size at the object plane is approximately 2µm with a 60× objective lens (numerical aperture: 0.65). The fiber laser output is mounted on a translational stage as shown in Fig. 1a, and, therefore, the beam spot position can be controlled independently from the UV exposure pattern. Since the optical tweezer wavelength is far from the UV photopolymerization wavelength, the IR beam does not solidify the photocurable oligomer, but only exerts force on the polymerized microparticles. The particle synthesis and manipulation processes are monitored and analyzed in real-time by a charge coupled device camera and a computer machine vision system.

The microfluidic channel is fabricated using a standard soft lithography technique with polydimethylsiloxane (PDMS) material as described in Fig. 2 [9]. Since the inhibition layer near the PDMS channel surface prevents the photopolymerization process [5], the cured microstructures can be made either free-flowing or adhered on the surface of the microfluidic channel depending on the UV exposure time. The photocurable oligomer used in our experiments is polyethylene glycol diacrylate (PEG-DA) with 10% UV photoinitiator (2, 2-dimethoxy-2-phenylacetophenone).

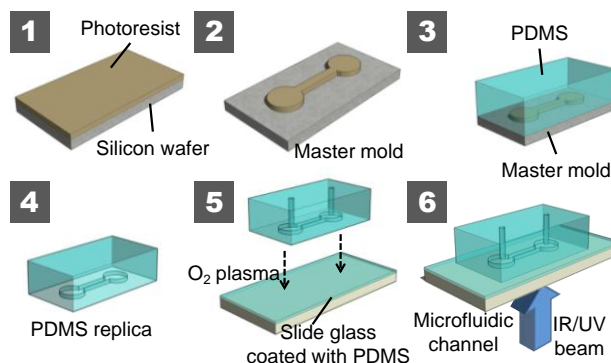


Figure 2: Fabrication process for the PDMS microfluidic channel. The channel height and the inhibition layer thickness are 12 µm and 1.5 µm, respectively.

An optical microscope photograph of a two-dimensional polymeric lattice structure synthesized by our experimental setup is shown in the inset of Fig. 1. All UV curing processes in this paper are performed with a 60× objective lens. Since the SLM pixel size is 13.68 µm, one pixel corresponds to 0.228 µm at the object plane. However, the spatial resolution of our maskless lithography is currently ~1 µm, and limited by the diffraction, non-ideal transfer modulation function, and the depth of focus.

## EXPERIMENTS AND RESULTS

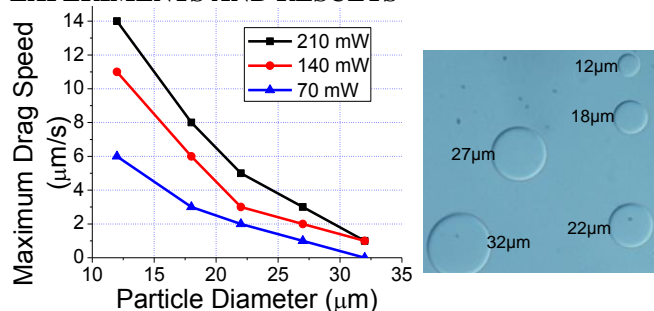


Figure 3: Maximum drag speed as a function of the synthesized particle size for the optical tweezer beam power of 70, 140, and 210 mW. The experiments are performed with the cylindrical microparticles shown in the inset.

The trapping force of an optical tweezer depends on the IR beam intensity and the refractive indices of prepolymer solution and polymerized structures. Figure 3 shows the relationship between the maximum dragging speed, polymer particle size, and optical power. Higher optical power increases the tweezer force, and can compensate for larger friction force.

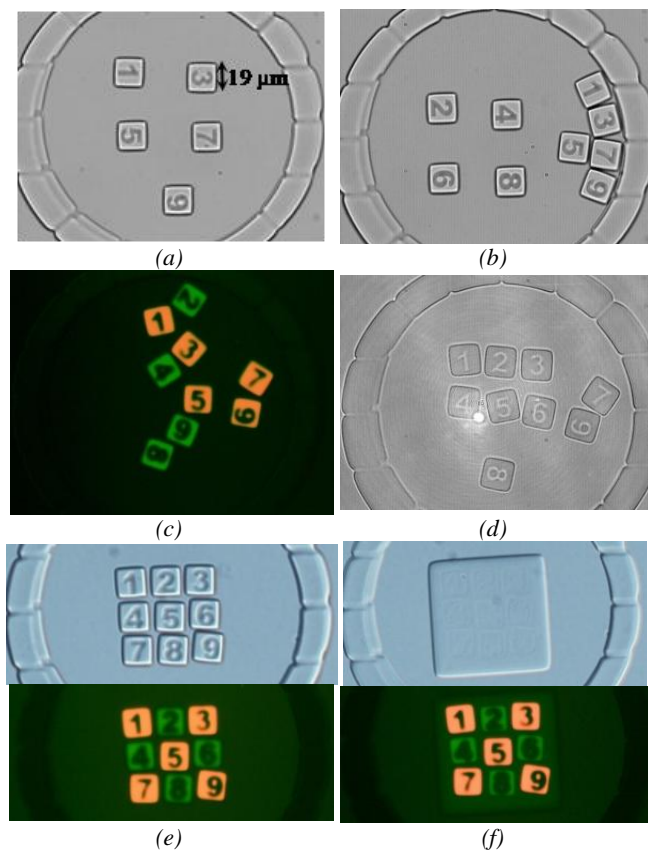


Figure 4: Synthesis of heterogeneous polymeric microstructures using in-situ photopolymerization and photocurable resin solution exchange. Microparticle synthesis with (a) Rhodamine B and (b) fluorescein. (c) Fluorescent image of nine polymeric microparticles. (d) Assembly of microparticles using the IR optical tweezer. Brightfield and fluorescent image of the assembled microparticle array (e) before and (f) after photocuring.

Figure 4 shows our proof-of-concept experiment, which generates a composite polymeric structure by assembling nine smaller microstructures with different shapes and materials. A

ring-shaped cage structure is first generated with long UV exposure time of 5 seconds (Fig. 4a). The fixed ring-shaped border passes the liquid-phase prepolymer material through its small openings when the microfluidic channel is pressurized by a syringe pump, but keeps the solidified polymeric particles inside the cage.

Using several solution exchanges, we then create nine different particles with two different material properties as shown in Fig. 4abc (red and green fluorescent for odd- and even-numbered particles, respectively). Five free-flowing microparticles (Particle: 1, 3, 5, 7, 9) are first synthesized inside the cage area after Rhodamine B (red) is added to the photocurable oligomer stream (Fig. 4a). The particle size is approximately  $19 \mu\text{m} \times 19 \mu\text{m}$  (86 pixels by 86 pixels on the SLM), and the UV exposure time is 0.2 second. Due to short exposure time, the inhibition layer is not completely depleted, and therefore, the particles are free-floating inside the PDMS microfluidic channel [5-6]. The unpolymerized material is then washed away, and the oligomer stream with fluorescein (green) is injected into the channel for subsequent photocuring of four additional microparticles (Particle: 2, 4, 6, 8, Fig. 4b). Next, we wash away the unpolymerized material and fill the channel with the original oligomer stream again (Fig. 4c).

The optical tweezer moves and rotates these microparticles to form a  $3 \times 3$  array pattern as shown in Fig. 4de. The last UV exposure combines the assembled heterogeneous particles, and creates a bigger structure composed of nine different regions (Fig. 4f). Figure 4f shows that the fluorescent property of each microparticle is preserved. Synthesizing such a structure using conventional fabrication techniques would require at least several deposition and etching steps with multiple masking patterns.

In summary, we have demonstrated a compact optofluidic platform for real-time synthesis, manipulation, and assembly of free-floating heterogeneous polymeric microstructures using in-situ photopolymerization and optical tweezer. Our technique provides flexible and interactive environments in the fabrication and manipulation of microstructures inside the microfluidic channels.

## REFERENCES

- [1] Y. Lu, Y. Yin, and Y. Xia, "Three-Dimensional Photonic Crystals with Nonspherical Colloids as the Building Blocks," *Adv. Materials*, 13, 415 (2001).
- [2] N. Bowden, A. Terfort, J. Carbeck, and G. M. Whitesides, "Self-Assembly of Mesoscale Objects into Ordered Two-Dimensional Arrays," *Science*, 276, 233 (1997).
- [3] Y.K. Cheung, B.M. Gillette, M. Zhong, S. Ramcharan, and S.K. Sia, "Direct patterning of composite biocompatible microstructures using microfluidics," *Lab. Chip*, 7, 574 (2007).
- [4] W.G. Koh and M.V. Pishko, *Anal. Bioanal. Chem.* "Fabrication of cell-containing hydrogel microstructures inside microfluidic devices used as cell-based biosensors," 385, 1389 (2006).
- [5] D. Dendukuri, D. C. Pregibon, J. Collins, T. A. Hatton, and P. S. Doyle, "Continuous-flow lithography for high-throughput microparticle synthesis," *Nat. Mater.*, 5, 365 (2006).
- [6] S. E. Chung, W. Park, H. Park, K. Yu, N. Park, and S. Kwon, "Optofluidic maskless lithography system for real-time synthesis of photopolymerized microstructures in microfluidic channels," *Appl. Phys. Lett.*, 91, 041106 (2007).
- [7] M. Ozkan, M. Wang, C.S. Ozkan, R. Flynn, and S. Esener, "Optical manipulation of objects in microfluidic devices," *Biomed. Microdevices*, 5, 61 (2003).
- [8] D. Dudley, W. M. Duncan, and J. Slaughter, "Emerging digital micromirror device applications," *Proc. SPIE*, 4985, 14 (2003).
- [9] J. C. McDonald, and G. M. Whitesides, "Poly(dimethylsiloxane) as a material for fabricating microfluidic devices," *Acc. Chem. Res.*, 35, 491 (2002).

# Author Index

Scroll to the author and select a [Blue](#) link to open a paper. After viewing the paper, use the bookmark “Go to Previous Document” to return to the same page in the Table of Contents.

**Acrobat Reader 8 Users:** Need to select View\Go To\Previous Document from the menu bar instead of using the bookmark.

---

## A

Abbaspour-Tamijani, A. ....	36
Abdolvand, R. ....	384
Adachi, T. ....	72
Adams, G.G. ....	186
Adkins, D.R. ....	280
Agah, M. ....	118, 256
Agarwal, N. ....	166
Aguilar, H.P. ....	154
Ai, L. ....	142
Aimi, M.F. ....	340
Akinwande, A.I. ....	316
Aktakka, E.E. ....	382
Alfeeli, B. ....	118
Allen, M.G. ....	348
Aluru, N.R. ....	166
Anderson, D.Z. ....	212
Anderson, J.M. ....	280
Arnold, D.P. ....	304
Arzt, E. ....	26
Ashraf-Khorassani, M. ....	118, 256
Åström, K.J. ....	364
Atashbar, M. ....	382
Autumn, K. ....	130
Averitt, R.D. ....	54
Ayazi, F. ....	384

## B

Babu, S.R. ....	72
Bae, B. ....	68, 88
Bahl, G. ....	102
Bajikar, S. ....	72
Balareddy, K.C. ....	288
Balch, J.E. ....	340
Bancu, M.G. ....	150
Barlian, A.A. ....	98
Bathurst, S. ....	224

Beamesderfer , M.A. ....	72
Beardslee, L.A. ....	190
Bedair, S.S. ....	272
Behymer, E. ....	388
Beloin St-Pierre, D. ....	86
Bernstein, J.J. ....	150
Berry, C.W. ....	90
Bertolucci, B. ....	304
Bhave, S.A. ....	360, 368
Bingham, C. ....	54
Birdsell, E. ....	348
Boser, B.E. ....	352
Bradley, R. ....	72
Brand, O. ....	190
Brewer, F. ....	364
Bright, V.M. ....	182, 212, 244
Brown, J.J. ....	182
Burgner, C.B. ....	364
Byun, A.T. ....	340

## C

Cai, Y. ....	84
Callahan, C. ....	276
del Campo, A. ....	26
Candler, R.N. ....	102, 162
Cao, H. ....	292
Cattafesta, L. ....	304
Chae, J. ....	36, 138, 232
Chandorkar, S. ....	48, 102
Chandrahalim, H. ....	360
Chandrasekharan, V. ....	304
Chang, C.C. ....	110
Chang, M.-P. ....	122
Chang, Y.J. ....	244
Chen, C.F. ....	110
Chen, J. ....	312
Chen, L. ....	186
Chen, P.-C. ....	114
Chen, P.-J. ....	146
Cheng, M.M.-C. ....	1
Cheng, X. ....	312
Cheung, K. ....	316
Chiou, E.P.Y. ....	276
Choi, S.H. ....	138
Choi, Y. ....	268
Chou, J.B. ....	80

Chuang, H.C. ....	212
Chwalek, J. ....	92
Ciocan, R. ....	150
Cole, G.D. ....	388
Cong, H. ....	228, 236
Copic, D. ....	280
Costa, J. ....	18
Costen, N.P. ....	72
Cote, R.J. ....	134
Crist, S. ....	18
Crittenden, T. ....	348
Culpepper, M.L. ....	60
Cutkosky, M. ....	130

## **D**

Daly, P. ....	198
Datta, P. ....	114
Davidson, B. ....	244
Delametter, C. ....	92
Demirci, K.S. ....	190
Deng, S. ....	6
Deng, W. ....	220
Dening, D. ....	18
Denis, K. ....	72
Dest, Y. ....	114
DeVoe, D.L. ....	110
Dikin, D.A. ....	182
Donahue, H. ....	386
Donald, B.R. ....	202
Dorairaj, R. ....	376
Dribinsky, A. ....	84
Du, Y. ....	186
Dubey, M. ....	360
Duggirala, R. ....	336
Dusatko, T.A. ....	216

## **E**

Eaton, J.W. ....	106
Elata, D. ....	102, 178
El-Gamal, M.N. ....	216
Esparza, N. ....	130
Eun, C.K. ....	308
Ewin, A.J. ....	72
Ezekwe, C.D. ....	352

## F

Fan, K. ....	54
Fedder, G.K. ....	10, 240, 272
Feist, T.P. ....	340
Ferrari, M. ....	1
Fettig, R. ....	72
Fissell, W.H. ....	380
Fitzgerald, A.M. ....	106
Fleischman, A.J. ....	380
Fortin, J.B. ....	340
Frangioni, J.V. ....	150
Franz, D. ....	72
Frazier, A.B. ....	268
Fréchette, L.G. ....	86
Fronheiser, J.A. ....	340
Fung, T.H. ....	98
Furlani, E. ....	92

## G

Garcia-Uribe, A. ....	288
Geil, B. ....	220
George, S.M. ....	244
Gering, J. ....	18
Ghodssi, R. ....	170
Gianchandani, Y.B. ....	126, 158, 300, 308, 332
Gilgunn, P.J. ....	10
Givrad, T.K. ....	32
Glass, E. ....	18
Glezer, A. ....	348
Gnerlich, M. ....	386
Golda, D.S. ....	60
Goldman, K. ....	380
Gomez, A. ....	220
Gorisse, P. ....	18
Green, S.R. ....	158
Gritsch, H.A. ....	28
Gu, H. ....	84
Gupta, N.K. ....	126
Gupta, P. ....	6
Gurau, B. ....	68, 344

## H

Hadizadeh, R. ....	280
Hammond, J. ....	18
Han, J. ....	88
Han, K.-H. ....	268

Harrison, J.C. ....	232
Hartwell, P. ....	194
Hawkins, G. ....	92
Hennessey, R.G. ....	102, 178
Herrault, F. ....	348
Hess, L. ....	72
Hill, G.C. ....	378
Hintsala, J. ....	198
Hirshberg, A. ....	178
Holschneider, D.P. ....	32
Hopcroft, M.A. ....	48, 102
Horsley, D.A. ....	80
Howe, R.T. ....	102, 162, 178
Hsiai, T.K. ....	142
Hu, R. ....	72
Hu, W. ....	162
Hua, Y. ....	84
Huang, S.W. ....	312
Huigens, B.M. ....	106
Humayun, M. ....	146
Hung, L.-W. ....	208

## I

Iannotti, J. ....	340
Ivanishev, A. ....	150
Ivanov, T. ....	18

## J

Jackson, K. ....	72
Jacobson, Z.A. ....	208
Jankowski, N.R. ....	220
Javey, A. ....	208
Je, S.-S. ....	232
Jeanmaire, D. ....	92
Jeon, J. ....	224
Jha, C.M. ....	102
Jhabvala, C.A. ....	72
Jhabvala, M.D. ....	72
Jia, K. ....	284
Jiang, H. ....	76
Jiang, L. ....	84
Johnson, E.A. ....	320
Jorgenson, J. ....	18
Judy, D.C. ....	328, 360
Jung, Y. ....	268

## K

Kadirvel, K. ....	64
Kalim, S. ....	276
Kataria, N. ....	364
Kaul, R. ....	360
Keimel, C.F. ....	340
Kelly, D. ....	72
Kenny, T.W. ....	48, 102, 130, 378
Kerr, D. ....	18
Keynton, R.S. ....	376
Khang, D. ....	154
Kim, B. ....	48, 102
Kim, C.-J. ....	28
Kim, D. ....	68
Kim, E.S. ....	142
Kim, H. ....	382
Kim, H.S. ....	68, 344
Kim, N. ....	114
Kim, S. ....	18
Kim, S.G. ....	224
King, T.T. ....	72
Kitching, J. ....	296
Klejwa, N. ....	162, 178
Kletetschka, G. ....	72
Klinge, C.M. ....	376
Kloner, R.A. ....	142
Korin, Y. ....	28
Kozicki, M.N. ....	232
Kumar, K. ....	292
Kutyrev, A.S. ....	72
Kwon, S. ....	390

## L

Lal, A. ....	336
Lang, J.H. ....	52
Lebens, J. ....	92
Lee, H.K. ....	48
Lee, H.W. ....	224
Lee, T.Y. ....	114
Lenkinski, R.E. ....	150
Leung, A. ....	84
Leus, V. ....	178
Levey, C.G. ....	202
Li, M.J. ....	72
Li, P.-Y. ....	32
Li, W.-C. ....	40

Li, Y. ....	304
Lin, H.K. ....	134
Lin, J.C.-H. ....	146
Lin, K.Y. ....	68, 344
Lin, P. ....	312
Lin, Y. ....	40
Liu, H. ....	84
Liu, J. ....	110
Lo, C.-C. ....	240
Loges, P. ....	320
Lu, F. ....	84
Lu, J. ....	154
Lutz, M. ....	6
Lynch, B.A. ....	72

## M

Maarek, J.-M.I. ....	32
MacDonald, N.C. ....	154
Mahameed, R. ....	22, 324
Maharbiz, M.M. ....	90, 122, 126
Mäkinen, J. ....	198
Mallon Jr., J.R. ....	98
Manginell, R.P. ....	280
Mardilovich, P. ....	224
Marquis, R. ....	150
Martin, D.T. ....	64
Masel, R.I. ....	68, 88, 248, 344
Mathai, S. ....	80
McCarthy, M. ....	170
McGruer, N.E. ....	186
Melamud, R. ....	48, 102
Meng, E. ....	32
Meng, M. ....	84
Mercier, T. ....	18
Mikula, V. ....	72
Miller, T. ....	72
Monty, C.N. ....	248
Moorman, M.W. ....	280
Morgan, B. ....	220
Morgan, R.D. ....	68, 344
Moseley, S.H. ....	72
Mott, B. ....	72
Murphy, M.C. ....	114

## **N**

Nabki, F. ....	216
Najafi, K. ....	382
Nguyen, C.T.-C. ....	40, 208
Nikitopoulos, D.E. ....	114
Nishida, T. ....	64, 304
Nunan, K. ....	198

## **O**

O'Brien, G. ....	84
Oh, I. ....	248
Oh, L. ....	72
Oliver, A.D. ....	320
Oliver, J.E. ....	378
Olsson III, R.H. ....	356, 372
Oropeza-Ramos, L.A. ....	364

## **P**

Padilla, W.J. ....	54
Pal, S. ....	284
Pan, T. ....	228, 236
Paprotny, I. ....	202
Paquin, M. ....	86
Parameswaran, M. ....	174
Park, D.S. ....	114
Park, H. ....	390
Park, N. ....	390
Park, S.-J. ....	98
Park, S.-Y. ....	276
Park, T. ....	114
Parness, A. ....	130
Partridge, A. ....	6
Peramaih, G. ....	6
Perez, C.R. ....	22, 324
Perez, M.A. ....	296
Pfeifer, K.B. ....	280
Piazza, G. ....	22, 324
Pierce, D.M. ....	106
Pisani, M.B. ....	22, 324
Pittenger, B. ....	44
Plesa, C. ....	174
Polcawich, R.G. ....	328, 360
Pollock, C. ....	336
Pontius, J. ....	72
Porter, D. ....	280
Pralle, M.U. ....	320

Provine, J. ....	178
Pruitt, B.L. ....	98
Pucci, G. ....	84
Pulskamp, J.S. ....	328, 360
Puscasu, I. ....	320

## Q

Qiu, Z. ....	236
Quach, Q.C. ....	264

## R

Radadia, A.D. ....	88
Radza, E. ....	6
Rao, M.P. ....	154
Rapchun, D. ....	72
Rastegar, A.J. ....	98
Ray, C. ....	72
Ray, K. ....	72
Reed, E.F. ....	28
Reed, J. ....	18
Reidy, S.M. ....	260
Ren, Z. ....	40, 208
Revzin, A. ....	236
Rouhanizadeh, M. ....	142
Roussel, T.J. ....	376
Roy, S. ....	380
Rumpf, A. ....	280
Ruoff, R.S. ....	182

## S

Saati, S. ....	146
Salvia, J. ....	48, 102
Sameoto, D. ....	174
Sandow, P. ....	198
Sato, H. ....	90
Sawyer, W. ....	198
Schofield, A.R. ....	14
Schulman, J.H. ....	56
Schulte, E. ....	72
Schwinger, D.S. ....	72
Seghete, D. ....	244
Seo, J.H. ....	190
Serrano, G. ....	260
Sethu, P. ....	376
Shah, G.J. ....	28
Shannon, M.A. ....	68, 88, 248, 344

Sharma, J. ....	6
Sheplak, M. ....	64, 304
Sheridan, R. ....	6
Shkel, A.M. ....	14, 296
Shu, P.K. ....	72
Silverberg, R.F. ....	72
Singh, G. ....	182
Sinha, N. ....	22, 324
Slocum, A.H. ....	52
Smith, R.A. ....	380
Smith, W.W. ....	72
Snodgrass, S. ....	72
Sohl, D. ....	72
Song, T. ....	110
Soper, S.A. ....	114
Soto, D.R. ....	130, 378
Sparr, L.M. ....	72
Stark, B.H. ....	6
Steptoe-Jackson, R. ....	72
Strikwerda, A. ....	54
Subramanian, K. ....	340
Suen, S. ....	6
Suk, J.W. ....	182
Sumanasekera, G. ....	376

## **T**

Tai, Y.-C. ....	134, 146, 264
Takahata, K. ....	300
Tan, M. ....	80
Tao, H. ....	54
Tasciotti, E. ....	1
Tatic-Lucic, S. ....	386
Taylor, L.T. ....	118, 256
Teitell, M. ....	276
Tin, S. ....	336
Trauernicht, D. ....	92
Truax, S. ....	190
Trusov, A.A. ....	14
Tsai, K.L. ....	162
Tsakalagos, L. ....	340
Tsao, C.W. ....	110
Tuck, M.R. ....	356, 372
Turner, K.L. ....	44, 364

## V

Varghese, M. ....	84
Varma, R. ....	146
Veale, J.L. ....	28
Veeneman, R.A. ....	252
Velásquez-García, L.F. ....	316
Vengallatore, S. ....	216
Veronica, V. ....	72
Virwani, K. ....	44
Visvanathan, K. ....	126
Voloshin, A. ....	386

## W

Waits, C.M. ....	170, 220
Walmsley, R. ....	194
Wang, L. ....	288
Wang, L.L. ....	72
Wang, S.X. ....	162
Wang, S.Y. ....	80
Wang, W. ....	236
Wang, X. ....	340
Weber, A.C. ....	52
Webster, T.J. ....	154
Wei, K. ....	276
Weinstein, D. ....	368
Wheeler, D.R. ....	280
Whiston, S. ....	198
White, C.D. ....	106
Wise, K.D. ....	260
Witte, R.S. ....	312
Wojciechowski, K.E. ....	372
Wojcik, A. ....	288
Wright, S.A. ....	332
Wu, M.C. ....	80
Wu, T.-H. ....	276

## X

Xie, H. ....	284
Xu, W. ....	36

## Y

Yama, G. ....	102
Yan, L. ....	340
Yang, Q. ....	92
Yang, Y. ....	138
Yeom, J. ....	88
Yoneoka, S. ....	102
Yorish, S. ....	348
You, B.H. ....	114
Yoxall, B. ....	80
Yu, H. ....	36, 142
Yu, K. ....	80, 390

## Z

Zareian-Jahromi, M.A. ....	256
Zellers, E.T. ....	252, 260
Zeng, X. ....	76
Zeyen, B. ....	44
Zhang, W. ....	84
Zhang, W. ....	194
Zhang, W.-Y. ....	386
Zhang, X. ....	36
Zhang, X. ....	54
Zhang, X. ....	292
Zhao, S. ....	236
Zhao, Y. ....	84
Zheng, S. ....	134
Zheng, Y. ....	72
Zhu, H. ....	236
Zhu, L. ....	68, 344
Ziaei-Moayyed, M. ....	162
Zincke, C. ....	72
Zorman, C.A. ....	380
Zou, J. ....	288
Zuo, C. ....	22, 324

# Keyword Index

Scroll to the keyword and select a **Blue** link to open a paper. After viewing the paper, use the bookmark “Go to Previous Document” to return to the same page in the Table of Contents.

*Acrobat Reader 8 Users: Need to select View\Go To\Previous Document from the menu bar instead of using the bookmark.*

---

## A

Accelerometer .....	84, 364
Acoustic .....	64
Actuator .....	162
Adhesion .....	26, 186
Adsorption .....	252
Aluminum Nitride .....	22, 356, 372, 324
Atom Chips .....	212
Atomic Force Microscopes .....	44
Atomic Layer Deposition .....	208, 244
Atomic MEMS .....	296
Atomization .....	220

## B

Ball Bearings .....	170
Band-Pass Filters .....	324
Batch-Fabricated .....	316
Biliary Stent .....	158
Bimorph Actuator .....	284
Biological Cell .....	386
Biomaterial .....	1
Bion™ .....	56
Biosensor .....	138
Blood .....	134
Blood Cell Separator .....	268
Bose-Einstein Condensations .....	212
Bragg Reflector .....	296
Brittle and Ductile Separation .....	186

## C

Calibration .....	352, 378
Cancer Detection .....	288
Cantilever .....	98, 378
Capacitive .....	64, 312
Capillary Loading .....	272
Carbon Nanotube Membrane .....	376
Cardiovascular .....	142
Cell Separation .....	28

Ceramic Device .....	348
Characterization .....	174
Charge Models .....	102
Charge-Based Capacitance Measurement .....	240
Circulating Tumor Cells .....	134
Closed-Loop Feedback Control .....	80, 190
CMOS .....	84
Column .....	260
Complementary Metal-Oxide-Semiconductor Microelectromechanical Systems .....	10
Composite Resonator .....	48
COMSOL Simulation .....	248
Conductive Photoresist .....	228
Contact .....	18
Contact Mechanics .....	26
Continuous Flow Polymerase Chain Reaction .....	114
Continuous Separation .....	268
Contour-Mode Resonators .....	22, 324
Cyborg Insect .....	382

## **D**

Damping .....	194
Dielectric Charge .....	102
Dielectric Transduction .....	368
Dielectrophoresis .....	268
Dielectrophoretic Manipulation .....	276
Diffuse Reflectance .....	288
Directional Microphone .....	232
DRIE .....	86
Droplet Manipulation .....	276
Drug Delivery .....	1
Dual Beam Actuation .....	22

## **E**

Elastomer .....	122
Electrode .....	86
Electromechanical Testing .....	182
Electrostatic Actuation .....	122, 178
Electrostatic Actuator .....	388
Electrostatic Comb Drive .....	80
Electrostatic Tuning .....	48
Electrothermal Actuator .....	386
Electrothermal Stimulation .....	126
Electrothermal Valve .....	32
Electrowetting-on-Dielectric (EWOD) .....	28
Encapsulated Resonator .....	48
Enclosed Package .....	194

Endoscopic Medical Imaging .....	284, 292
Endotoxin .....	380
Energy Scavenging .....	382

## **F**

Fabrication .....	10
Ferroelectric Imaging .....	44
Fibrillar Adhesive .....	130
Field Sensing .....	280
Film Bulk Acoustic Resonator .....	36
Filtration .....	134, 376, 380
Finite Element Analysis .....	106
Flip-Chip Bonding .....	10, 72
Fluidics .....	92
Force Feedback .....	352
Force Sensor .....	378
Forward Imaging .....	292
Fracture Prediction .....	106
Frequency Tuning .....	360
Fresnel Zone Plate .....	292
Friction .....	170
Frictional Adhesion .....	130

## **G**

Gamma Radiation .....	308
Gas Chromatography .....	256
Gas-Liquid Interface .....	248
Gate Oxide Quality .....	198
Gecko .....	130
Gecko Tape .....	26
Germanium .....	388
Gettering .....	198
Glaucoma Drainage Device .....	146
Gold Nanoparticles .....	76
Green June Beetle .....	126
Gyroscope (s) .....	14, 352

## **H**

Harmonic Amplification .....	44
Hearing Aid Applications .....	232
High Temperature .....	332
Hydrocarbon Sensor .....	320
Hydrogen Generator .....	68

## **I**

Impedance .....	182
Implantable System .....	90

In Vivo .....	142
Inertial Sensors .....	14
Infusion Pump .....	32
Ink-Jet .....	92, 224, 272
In-Liquid Sensing .....	36
Insect Flight Control .....	90
In-Situ Microdevices .....	232
Intraocular Pressure .....	146

## **L**

Lab-on-a-Chip .....	28
Laterally Implanted .....	304
Lead Zirconate Titanate .....	224
Light-Responsive Hydrogel .....	76
Liquid Microlenses .....	76
Low Temperature .....	216

## **M**

Magnetic .....	162
Magnetic Beads .....	28
Magnetic Microactuator .....	60
Magnetic Resonance Imaging .....	150
Magnetoelastic Sensors .....	158
Make-Break Power Switching .....	52
Maskless Lithography .....	390
Material Properties .....	174
Mechanical Modulus .....	386
Membrane Electrode Assembly .....	344
MEMS (Micro-Electro-Mechanical-System) .....	18, 72, 92, 118, 150, 194, 224, 236, 256, 324, 386
MEMS Logic .....	328
MEMS Resonator .....	40, 372
Meso-Scale Nanopositioner .....	60
Metal Converter for Radiation .....	308
Metamaterial .....	54
Micro Air Vehicle .....	90, 126
Micro Engine .....	348
Micro Fuel Cell .....	86
Micro Power Generator .....	382
Microactuators .....	202
Microanalytical Systems .....	118
Microassembly .....	202
Microcolumn .....	88
Microcombustion .....	220
Microdischarge .....	332
Microfabrication .....	54, 344
Microfilter .....	356

Microfluidic (s) .....	86, 138, 236, 264, 390
Microfluidic Channel .....	36
Microfluidic Functions .....	276
Microfluidic System .....	268
Micro-Flying Air Vehicle .....	382
Micro-Fuel Cell .....	68
Micro-Gas Chromatography System .....	88, 118, 252, 260, 280
Microlens Scanner .....	80
Micromachined Optical Probe .....	288
Micromechanical Filter .....	208
Micromechanical Resonator .....	208
Micromirror .....	284
Microphone .....	64
Microplasma .....	332
Micro-Power Source .....	68
Micro-Preconcentrator .....	252
Microresonator .....	240, 356
Microrobots .....	202
Microsecond .....	88
Microshutter .....	72
Microtribology .....	26
Microturbines .....	170
Microvalve .....	88, 146
Mode Matching .....	352
Modeling .....	252
Molecular Layer Deposition .....	244
Monolithic Filter .....	384
MS Interfacing .....	110
Multicapillary .....	256
Multilayer Protective Coating .....	244
Multiplexed Electrospray .....	220
Multi-Reactor Platform .....	114

## N

Nanocrystalline Diamond .....	384
Nano-Electrodeposits .....	232
Nanoelectromechanical Systems .....	340
Nanofibers .....	182
Nanoparticle .....	162
Nanopatterning .....	154
Nanoporous Membrane .....	248
Nanoporous Silicon Membranes .....	380
Neural Stimulation .....	90
Neuroimaging .....	32
Noise .....	364

## O

Optical Interconnect .....	80
Optical Tweezer .....	390
Oscillator .....	6

## P

Packaging .....	6
Parylene .....	32, 146, 264
Phosphonate Detection .....	248
Photoacoustics .....	312
Photoelectron Detection .....	308
Photolithography .....	228
Photonic Crystal .....	320
Piezoelectric .....	328, 384
Piezoelectric Resonators .....	324
Piezoresistive .....	98, 304, 368
Piezoresistor .....	378
Piezothermal .....	126
Polydimethylsiloxane .....	228, 390
Polyimide .....	236
Polymer MEMS .....	174
Polymer Sacrificial Layer .....	244
Polymerase Chain Reaction .....	264
Polyurethane .....	300
Pop Up .....	54
Porous Silicon .....	1
Potassium hydroxide (KOH) .....	52
Power Amplifier .....	40
Power Generation .....	348
Preconcentrator .....	280
Pressure Sensor .....	300, 332
Printing .....	92, 224, 236
Protein Electrophoresis .....	376
Protein Sensor .....	138
Proteomics .....	1
Proton Exchange Membrane Fuel Cell .....	344
PZT .....	328, 360

## Q

Q-Factor .....	190
Quadrupole Mass Filter .....	316
Quality Factor .....	36

## R

Radio Frequency Microelectromechanical Systems .....	22, 356
Radio Frequency Sensor Node .....	336
Radioisotope Power .....	336

Reconfigurable Microfluidics .....	122
Reliability .....	106
Relay .....	52
Resonance .....	40
Resonant Sensors .....	158
Resonator (s) .....	150, 190, 194, 216, 368
RF CMOS-MEMS .....	240
RF MEMS .....	186, 360, 368
RF MEMS Switch .....	40
RF Tags .....	150
Ring Resonator .....	372
Robotic Spotting .....	110
Robust Designs .....	14

## S

Sacrificial Etching .....	388
Scanning Micromirror .....	292
Scratch-Drive Actuators .....	202
Second Stability Region .....	316
Self-Assembled Narrow Gap .....	240
Self-Regulating .....	68
Sensor .....	56
Sensor-IC Integration .....	198
Separation .....	260, 376
Separation Columns .....	256
Shear Stress .....	304
Shear Stress Sensor .....	142
Silicon .....	344
Silicon Carbide .....	216
Silicon Dioxide .....	102
Silicon Nanowire .....	340
Silicon Nozzles .....	220
Silicon Resonators .....	102
Silicon-on-Insulator (SOI) .....	10, 18
Silver Powder .....	228
Six-Axis Compliant Mechanism .....	60
Skin Friction .....	304
Small Footprint .....	114
SOI Wafers .....	198
Solution Wicking .....	272
Space Telescope .....	72
Sputtering .....	216
Square Electrodes .....	316
Stainless Steel .....	300
Stents .....	154
Stimulator .....	56

Stochastic .....	364
Stochastic Collocation .....	166
Stochastic Modeling .....	166
SU-8 .....	130, 162, 174
Switch .....	18, 52, 166, 340
Switch Contact.....	186

## **T**

Temperature Stability .....	48
Terahertz .....	54
Thermal Convection .....	84
Thermal Desorption .....	118
Thin Films .....	296
Three-Axis .....	84
Through-Wafer Interconnects .....	212
Tip-Tilt-Piston .....	284
Torsion .....	280
Tunable Focus .....	76
Tunneling .....	364

## **U**

Ultra-High-Vacuum .....	212
Ultrasound .....	312
Ultrathin .....	6
Uncertainties .....	166

## **V**

Valveless Pulsejet .....	348
Vapor Analysis .....	260
Virtual Electrodes .....	276
Virus Detection .....	264
Viscosity Sensors .....	158

## **W**

Wafer Thinning .....	6
Weibull .....	106
Wireless .....	300
Wireless Nuclear Sensor .....	308

## **X**

XeF2 .....	360
Xenon Difluoride .....	388

# 2008

## Solid-State Sensors, Actuators, and Microsystems Workshop

Hilton Head Island, South Carolina • June 1 - 5, 2008

All opinions expressed in this digest are those of the authors and are not binding on Transducer Research Foundation, Inc.

Copies of available volumes of this digest may be obtained from the Transducer Research Foundation, Inc., c/o 307 Laurel Street, San Diego, California 92101-1630 USA (+1-619-232-9499)

Copyright and Reprint Permission: Abstracting is permitted with credit to the source. Libraries are permitted to photocopy beyond the limit of U.S. copyright law for private use of patrons those articles in this volume that carry a code at the bottom of the first page, provided the per-copy fee indicated in the code is paid through Copyright Clearance Center, 222 Rosewood Drive, Danvers, MA 01923. For other copying, reprint or republication permission, contact Transducer Research Foundation, Inc., c/o 307 Laurel Street, San Diego, California 92101-1630 USA, [info@transducer-research-foundation.org](mailto:info@transducer-research-foundation.org). All rights reserved. Copyright ©2010 by the Transducer Research Foundation, Inc. Personal use of this material is permitted. However, permission to reprint/republish this material for advertising or promotional purposes or for creating new collective works for resale or redistribution to servers or lists, or to reuse any copyrighted component of this work in other works must be obtained from the Transducer Research Foundation, Inc.

TRF Catalog Number: 08TRF-0001

Library of Congress Control Number: 2008924361

ISBN Number: 0-9640024-7-7

ISSN: 1539-2058 (Print) ISSN: 1539-204X (Electronic)

DOI 10.31438/trf.hh2008.0

This product contains Adobe Acrobat software. Copying this product's instructions and/or designs for use on future CD-ROMs or digital products is prohibited without written permission from The Printing House and Adobe Systems Incorporated. The Printing House or its suppliers are not liable for any direct, indirect, special, incidental, or consequential damages to your hardware or other software arising out of the use—or the inability to use—the material on this CD-ROM. This includes, but is not limited to, the loss of data or loss of profit. Adobe, Acrobat and the Acrobat logo are trademarks of Adobe Systems Incorporated or its subsidiaries and may be registered in certain jurisdictions.

If you have questions regarding the installation, please contact:



The Printing House, Inc.

Phone: +1-608-873-4500 Fax: +1-608-873-4558

Hours: Monday through Friday, 8 am - 5 pm CST

E-mail: [graphics@printinghouseinc.com](mailto:graphics@printinghouseinc.com)